PROCEEDINGS BOOK OF THE 6TH INTERCONTINENTAL GEOINFORMATION DAYS 13-14 JUNE 2023 Baku, AZERBAIJAN

MERSIN UNIVERSITY-ENGINEERING FACULTY
DEPARTMENT OF GEOMATICS ENGINEERING

ISBN: 978-605-72800-4-6 https://igd.mersin.edu.tr/

The proceedings of the

6th Intercontinental Geoinformation Days

ISBN: 978-605-72800-4-6

Baku, 2023

6th Intercontinental Geoinformation Days

I would like to thank all of the contributing authors and reviewers to the 6th Intercontinental Geoinformation (IGD) Symposium, 13-14 June 2023. In this international symposium there are 105 presentations. 52 of them are from Türkiye and the other 53 papers are from 11 different countries.

Best regards

Prof. Dr. Murat YAKAR

Honor Board

Ali Hamza PEHLİVAN – Governor of Mersin Province
Prof. Dr. Erol YAŞAR – Rector of Mersin University
Prof. Dr. Orhan AYDIN – Rector of Tarsus University
Prof. Dr. Ömer ARIÖZ – Rector of Toros University
Mehmet Zeki ADLI – Director of Turkish Land Registry and Cadastre
Prof. Dr. Diane DUMASHIE– FIG President
Prof. Dr. Lena Halounová – ISPRS President
Prof. Dr. Chryssy POTSIOU – FIG Honorary President
Prof. Dr. Haluk ÖZENER – Boğaziçi University Director of Kandilli Observatory
Dr. Orhan ERCAN – FIG Vice President

Organizing Committee

Mersin University – Faculty of Engineering – Department of Geomatics Engineering
Prof. Dr. Murat Yakar – Conference Chairman
Prof. Dr. Zakir Eminov – Director of Institute of Geography, Co-Chairman
Prof. Dr. Said Safarov – head of Caspian Sea hydrometeorology department
Assoc. Prof. Dr. Erdinç Avaroğlu
Assoc. Prof. Dr. Jalal Shiri
Prof. Dr. Behrouz Sari Sarraf
Prof. Dr. Khalil Valizadeh Kamran
Assoc. Prof. Dr. Bakhtiar Feizizadeh
Prof. Dr. Maryam Bayati Khatibi
Assoc. Prof. Dr. Aboulfazl Ghanbari
Asst. Dr. Sadra Karimzadeh
Asst. Dr. Iraj Teymouri
Asst. Dr. Husain Karimzadeh
Prof. Dr.Saeid Jahabakhsh
Prof. Dr. Shahram Rostaei
Assoc. Prof. Dr. Shahrivar Rostaei
Assoc. Prof. Dr.- Zaur Imrani
Asst. Dr. Mohsen Aghayari
Asst. Prof. Dr. Ali Ulvi
Asst. Prof. Dr. Fatma Bünyan Ünel
Asst. Prof. Dr. Lütfiye Kuşak
Dr. Behnam Khorrami
Dr. - Elnur Safarov
Dr. - Rovshan Kerimo
Dr. - Sabuhi Talibov
Dr. Hakan Doğan
Lect. Atilla Karabacak
Lect. Şafak Fidan
Res. Asst. Abdurahman Yasin Yiğit
Res. Asst. Aydın Alptekin
Eng. Engin Kanun
Eng. Mücahit Emre Oruç
Eng. Seda Nur Gamze Hamal
Eng. Huseynova Bayimkhanim
Eng. Emil Jabrayilov
Eng. Rasulzade Vusale

Executive Committee

Prof. Dr. Abdurrahman EYMEN – Erciyes University, TURKEY
Prof. Dr. Alexander SAGAYDAK – State University of Land Use Planning, RUSSIA
Prof. Dr. Alias Abdul RAHMAN – Universiti Teknologi Malaysia (UTM), MALAYSIA
Prof. Dr. Andreas GEORGOPOULOS – National Technical University of Athens, GREECE
Prof. Dr. Ariel BLANCO – University of Philippines at Daliman, PHILIPPINES
Prof. em. Dr.-Ing. Dr.h.c. Armin GRÜN – ETH Zürich, SWITZERLAND
Prof. Dr. Ashutosh MOHANTY – Shoolini University, INDIA
Prof. Dr. Edmönd Höxha (Albania University, Titana Albania)
Prof. Dr. Aydın ÜSTÜN – Kocaeli University, TURKEY
Prof. Dr. Bashkim IDRIZI – University of Prishtina, KOSOVO
Prof. Dr. Bülent BAYRAM – Yıldız Technical University, TURKEY
Prof. Dr. Charles TOTH – Ohio State University, USA
Prof. Dr. Chryssy POTSIOU – National Technical University of Athens, GREECE
Prof. Dr. Çetin CÖMERT – Karadeniz Technical University, TURKEY
Prof. Dr. Dursun Zafer ŞEKER – Istanbul Technical University, TURKEY
Prof. Dr. Erkan BEŞDOK – Erciyes University, TURKEY
Prof. Dr. Ferruh YILDIZ – Konya Technical University, TURKEY
Prof. Dr. Fevzi KARSLI – Karadeniz Technical University, TURKEY
Prof. Dr. Füsun BALIK ŞANLI – Yıldız Technical University, TURKEY
Prof. Dr. Hacı Murat YILMAZ – Aksaray University, TURKEY
Prof. Dr. Hediye ERDOĞAN – Aksaray University, TURKEY
Prof. Dr. Haluk ÖZENER – Boğaziçi University, TURKEY
Prof. Dr. Hande DEMİREL – Istanbul Technical University, TURKEY
Prof. Dr. Jiyoon KIM – University of Seoul, REPUBLIC OF KOREA
Prof. Dr. Maria Antonia BROVELLI – Politecnico di Milano, ITALY
Prof. Dr. Mevlüt YETKİN – İzmir Katip Çelebi University, TURKEY
Prof. Dr. Muhammad Bilal – Nanjing University of Information Science and Technology, CHINA
Prof. Dr. Mustafa YANALAK – Istanbul Technical University, TURKEY
Prof. Dr. Naser EL-SHEIMY – University of Calgary, CANADA
Prof. Dr. Nebiye MUSAOĞLU – Istanbul Technical University, TURKEY
Prof. Dr. Nilanchal PATEL – Birla Institute of Technology Mesra, INDIA
Prof. Dr. Niyazi ARSLAN – Çukurova University, TURKEY
Prof. Dr. Pal NIKOLLI – University of Tirana, ALBANIA
Prof. Dr. Reha Metin ALKAN – Istanbul Technical University, TURKEY
Prof. Dr. Sebahattin BEKTAŞ – Ondokuz Mayıs University, TURKEY
Prof. Dr. Sujit MANDAL – Diamond Harbour Womens' University, INDIA
Prof. Dr. Tahsin YOMRALIOĞLU – Beykent University, TURKEY
Prof. Dr. Tayfun ÇAY – Konya Technical University, TURKEY
Prof. Dr. Tamer BAYBURA – Afyon Kocatepe University, TURKEY
Prof. Dr. Tarık TÜRK – Cumhuriyet University, TURKEY
Prof. Dr. Taşkın KAVZOĞLU – Gebze Technical University, TURKEY
Prof. Dr. Uğur DOĞAN – Yıldız Technical University, TURKEY
Prof. Dr. Yasemin ŞİŞMAN – Ondokuz Mayıs University, TURKEY
Prof. Dr. Youkyung HAN – Kyungpook National University, REPUBLIC OF KOREA
Prof. Dr. Fetullah ARIK – Konya Technical University, TURKEY
Prof. Dr. S. Kazem Alavipanah – University of Tehran, Turkey
Prof. Dr. Manouchehr Farajzadeh – Tarbiat Modares University, Iran
Prof. Dr. Orhan Gündüz – İzmir Institute of Technology, Turkey
Prof. Dr. Seyed Ali Almodaresi – Islamic Azad University,Yazd
Prof. Dr. Timo Balz, Wuhan University, China
Assoc. Prof. Dr. Bakhtyar Feizizadeh – University of Tabriz, IRAN
Assoc. Prof. Dr. Anargha DHORDE – Nowrosjee Wadia College, INDIA
Assoc. Prof. Dr. Aziz ŞİŞMAN – Ondokuz Mayıs University, TURKEY
Assoc. Prof. Dr. Bihter EROL – Istanbul Technical University, TURKEY
Assoc. Prof. Dr. Cevdet Coşkun AYDIN – Hacettepe University, TURKEY
Assoc. Prof. Dr. Erol YAVUZ – Uşak University, TURKEY
Assoc. Prof. Dr. Fatih DÖNER – Gümüşhane University, TURKEY

Assoc. Prof. Dr. Fatih POYRAZ – Cumhuriyet University, TURKEY
Assoc. Prof. Dr. Halil AKINCI – Artvin Çoruh University, TURKEY
Assoc. Prof. Dr. Khalil Valizadeh KAMRAN – University of Tabriz, IRAN
Assoc. Prof. Dr. Lyubka PASHOVA – Bulgarian Academy of Sciences, BULGARIA
Assoc. Prof. Dr. Murat UYSAL – Afyon Kocatepe University, TURKEY
Assoc. Prof. Dr. Özgün AKÇAY – Çanakkale Onsekiz Mart University, TURKEY
Assoc. Prof. Dr. Serdar EROL – Istanbul Technical University, TURKEY
Assoc. Prof. Dr. Şükran YALPIR – Konya Technical University, TURKEY
Assoc. Prof. Dr. Uğur AVDAN – Eskişehir Technical University, TURKEY
Assoc. Prof. Dr. Zaide DURAN – Istanbul Technical University, TURKEY
Assoc. Prof. Dr. Alireza Gharagozlou – Shahid Beheshti University
Assoc. Prof. Dr. Ali Shamsoddini – Tarbiat Modarres University
Assoc. Prof. Dr. Gordana Kaplan – Eskisehir Technical University
Assoc. Prof. Dr. Babak Vaheddoust– Bursa Technical University
Assoc. Prof. Dr. Najmeh Neysani Samany– University of Tehran
Assoc. Prof. Dr. Ara Toomanian – University of Tehran
Asst. Prof. Dr. Sadra Karimzadeh – University of Tabriz, Iran
Asst. Prof. Dr. Mehrdad Jeihouni – University of Tabriz, Iran
Asst. Prof. Dr. Berk ANBAROĞLU – Hacettepe University, TURKEY
Asst. Prof. Dr. Esra TEKDAL YILMAZ – Nicholls State University, USA
Asst. Prof. Dr. Jorge ROCHA – University of Lisbon, TURKEY
Asst. Prof. Dr. Kemal ÇELİK – Gümüşhane University, TURKEY
Asst. Prof. Dr. Khalid MAHMOOD – University of Punjab, PAKISTAN
Asst. Prof. Dr. Mahmut Oğuz SELBESOĞLU – Istanbul Technical University, TURKEY
Asst. Prof. Dr. Mustafa Utkan DURDAĞ – Artvin Çoruh University, TURKEY
Asst. Prof. Dr. Mustafa ÜSTÜNER – Artvin Çoruh University, TURKEY
Asst. Prof. Dr. Nizar POLAT – Harran University, TURKEY
Asst. Prof. Dr. Osman Sami KIRTILOĞLU – İzmir Katip Çelebi University, TURKEY
Asst. Prof. Dr. Sadra KARIMZADEH – University of Tabriz, IRAN
Asst. Prof. Dr. Serdar BİLGİ – Istanbul Technical University, TURKEY
Asst. Prof. Dr. Subija IZEIROSKI – Geo-SEE Institute, NORTH MACEDONIA
Asst. Prof. Dr. Surendra Pal SINGH – Wollega University, ETHIOPIA
Asst. Prof. Dr. Süleyman Sefa BİLGİLİOĞLU – Aksaray University, TURKEY
Asst. Prof. Dr. Serdar BİLGİ – Istanbul Technical University, TURKEY
Asst. Prof. Dr. Tae-Suk BAE– Sejong University, REPUBLIC OF KOREA
Asst. Prof. Dr. Tirthankar BANERJEE – Banaras Hindu University, INDIA
Asst. Prof. Dr. Volkan YILMAZ – Artvin Çoruh University, TURKEY
Asst. Prof. Dr. Shirin Mohammadkhan – University of Tehran
Asst. Prof. Dr. Hossein Aghighi– Shahid Beheshti University
Asst. Prof. Dr. Samira Abushova – Azerbaijan National Academy of Science
Asst. Prof. Dr. Hamid Reza Ghafarian Malamiri– Yazd University
Dr. Behnam Khorrami – 9 Eylul University, Turkey
Dr. Abdel Aziz ELFADALY – Nat. Auth. for Remote Sensing and Space Science, EGYPT
Dr. Abdul-Lateef BALOGUN – Universiti Teknologi PETRONAS (UTP), MALAYSIA
Dr. Artur GIL – University of the Azores, PORTUGAL
Dr. Ajoy DAS – Gujarat University, INDIA
Dr. Bayartungalag BATSAIKHAN – Chairwoman of Mongolian Geo-spatial Association, MONGOLIA
Dr. Cesar CAPINHA – University of Lisbon, PORTUGAL
Dr. Erman ŞENTÜRK – Kocaeli University, TURKEY
Dr. Gojko NIKOLIC – University of Montenegro, MONTENEGRO
Dr. Ismail KABASHI – Angst, AUSTRIA
Dr. Narendra KUMAR – HNB Garhwal University, INDIA
Dr. Krishna Prasad BHANDARI– Tribhuvan University, NEPAL
Dr. Adamu BALA – China University of Geosciences, CHINA
Dr. MD Firoz KHAN – University of Malaya, MALAYSIA
Dr. Muhammad IMZAN BIN HASSAN – Universiti Teknologi Malaysia, MALAYSIA
Dr. Eng. Colonel Altan YILMAZ – Turkish Gen. Directorate of Mapping, TURKEY
Dr. Ali Keshavarzi-University of Tehran, Iran

13 JUNE 2023

Azerbaijan Time	Opening Ceremony
09.30-10.00	Chairman-Conveners-Session chairs

Azerbaijan Time	Sesssion 1: UAV Photogrammetry Session Chair: Prof. Ben Jarihani, James Cook University, Australia
10.00-10.10	Investigation of linear and logarithmic regression between measured and calculated parameters of Eldarica pine tree Ali Hosingholizade
10.10-10.20	The 3D virtual restitution of historical buildings using photogrammetry: A case study of the Dungeon-Cistern structure in the Ancient City of Dara (Anastasiopolis), Mardin Lale Karataş, Murat Dal, Aydın Alptekin, Murat Yakar
10.20-10.30	Stone material damage detection in restoration using Virtual Reality: The case of Virgin Mary Church and Patriarchate in Midyat, Türkiye Lale Karataş, Murat Dal, Aydın Alptekin, Murat Yakar
10.30-10.40	Game development in Unity game engine using optical UAV data Mertcan Nazar, Umut Gunes Sefercik
10.40-10.50	Assessment of structural degradation at Germus Church: A UAV-based Study Emine Beyza Dörtbudak, Şeyma Akça, Nizar Polat

Azerbaijan Time	Session 2: Geographic Information Systems Session Chair: Prof. Manuchehr Farajzadeh, Tarbiat Modares University, Iran
11.00-11.10	Ecological risk analysis with the help of geographic information systems in fruit growing; Manisa in Türkiye example Emre Yeniay, Aydın Şik
11.10-11.20	Using GIS to identify and assess renewable energy sources Nijat Imamverdiyev
11.20-11.30	Locating the best place to build a desalination plant with artificial intelligence (Chabahar study area, Iran) Saeed Rasti, Fatemeh Tamnia, Mostafa Mahdavifard, Majid Kiavarz Moghaddam
11.30-11.40	Investigation of drought status of Konya Closed Basin with Percent of Normal Index Beyza Değişli, Durdane Akçay, Hanife Nur Şimşekli, İsa Alperen Pınar, Gaye Aktürk, Bilal Candan, Mehmet Ali Tamer, Vahdettin Demir, Mehmet Faik Sevimli
11.40-11.50	Study of industrial production in Azerbaijan based on anamorphosis maps Zaur Imrani

Azerbaijan Time	Session 3: Remote Sensing Session Chair: Prof. Mohammad Hossein Rezaei Moghaddam, University of Tabriz, Iran
12.00-12.10	Air pollution monitoring in Tehran using Sentinel_5 satellite (2022) Nilufar Makky, Khalil Valizade Kamran, Sadra Karimzade
12.10-12.20	Comparative study of hyperspectral imagery classification with SVM and ensemble machine learning methods Saziye Ozge Atik
12.20-12.30	Upwelling events in the Caspian Sea Said Safarov, Vusal Ismayilov, Elnur Safarov
12.30-12.40	Flood risk susceptibility and evaluation by AHP technique in Denizli, Türkiye Hamed Reza Vafa, Dursun Zafer Seker
12.40-12.50	Improving the accuracy of classification of multispectral Images using an anisotropic diffusion neural network algorithm (ADNNA) and machine learning SVM algorithm. Behnaz Torkamani Asl, Parviz Zeaieanfirouzabadi, Seyed Mohammad Tavakkoli Sabour

Azerbaijan Time	Session 4: Geographic Information Systems Session Chair: Prof. Bakhtiar Feizizadeh, Humboldt-Universität zu Berlin, Germany
13.00-13.10	Flood risk assessment and mapping: a case study of the Aksu River Basin (Giresun), Türkiye Halil Burak Akdeniz, Emre Can Tuzcu
13.10-13.20	Implementation of GIS in Mingachevir city Aliyeva Seyidnisa Xoshbext
13.20-13.30	Modelling future land use/land cover and seasonal land surface temperature changes based on CA-ANN algorithm to assess its impacts on Chennai Metropolitan Area (CMA), India Mohammed Faizan, Manas Hudait
13.30-13.40	Improving of groundwater level estimation using SMOTE technique Emine Dilek Taylan, Tahsin Baykal, Özlem Terzi
13.40-13.50	Using frequency ratio model for flood susceptibility mapping of Mandaue City, Cebu Jao Hallen Bañados, Isabella Pauline Quijano, Chito Patiño

Azerbaijan Time	Session 5: Remote Sensing Session Chair: Prof. Sadra Karimzadeh, University of Tabriz, Iran
14.00-14.10	Investigating the flooded area of Bangladesh by Sentinel_1 and CHIRPS images in the GEE system Khalil Valizadeh Kamran, Nilufar Makky, Neda Kaffash Charandabi
14.10-14.20	Monitoring long term shoreline changes along Caspian Sea, Azerbaijan using geospatial techniques Turkan Mamishova
14.20-14.30	Analysis of the relationship between meteorological and agricultural drought of 2007 in Bartın province, Türkiye Ali Levent Yagci
14.30-14.40	Change detection of buildings using high spatial resolution images and deep learning Saeid Abdolian, Ali Esmaeily, Mohammad Reza Saradjian Maralan
14.40-14.50	Monitoring of ground displacement of Warri metropolis using persistent scatterer interferometry (PSI) and small baseline subset (SBAS) time series Oluibukun Gbenga Ajayi, Bilyaminu Yusuf, Yusuf Drisu Opaluwa

Azerbaijan Time	Session 6: Geographic Information Systems Session Chair: Prof. Bakhtiar Feizizadeh, Humboldt-Universität zu Berlin, Germany
15.00-15.10	Modeling spatial distribution of bark beetle susceptibility using the maximum entropy approach Fatih Sivrikaya, Gonca Ece Özcan
15.10-15.20	Importance of using space information and GIS technologies in the process of selecting analogue terrains in hydrological research Rza Mahmudov, Movlud Teymurov
15.20-15.30	Comparative analysis of image classification capabilities of support vector machine (SVM) and random forest (RF) with google earth engine (GEE) platform: A case study of Sangamner, Maharashtra Prasad Balasaheb Wale, Vinit Dhaigude, Satyam Mishra
15.30-15.40	Analyzing optimal routes to safe areas using OpenStreetMap and very high-resolution remote sensing imagery Obaidurrahman Safi, Muhammed Enes Atik
15.40-15.50	Development of aggregated risk matrix for assessing the pipeline multiple natural disasters and their visualization using GIS Aslan Babakhanov

Azerbaijan Time	Session 7: UAV Photogrammetry Session Chair: Nizar Polat, Harran University, Türkiye
16.00-16.10	Production of digital maps by unmanned aerial vehicle (UAV) Murat Yakar, Abdurahman Yasin Yiğit, Ali Ulvi
16.10-16.20	Utilizing UAVs for rapid spatial data acquisition in disaster management: A case study of Islahiye Casım Öncel, Bünyamin Ataş, Nurullah Börü, Nizar Polat
16.20-16.30	Generating a thermal index map with Unmanned aerial vehicles (UAVs) with thermal sensors Yunus Kaya, Abdulkadir Memduhoğlu, Nizar Polat
16.30-16.40	Documenting historical buildings using high-resolution photographs obtained with smartphones: The Case of Latifiye (Abdullatif) Mosque, Mardin/Türkiye Lale Karataş, Murat Dal, Aydın Alptekin, Murat Yakar
16.40-16.50	Architectural documentation with terrestrial laser scanning (TLS) data: Case study of Lutfu Pasa caravanserai (Mathius Caravanserai), Izmir Lale Karataş, Murat Dal, Aydın Alptekin, Murat Yakar

Azerbaijan Time	Session 8: Remote Sensing Session Chair: Prof. Said Safarov, Academician Hasan Aliyev University, Azerbaijan
17.00-17.10	Comparison of active and passive remote sensing data in extracting coastlines Sheida Fathi, Seyed Mohamad Tavakkoli Sabour, Parviz Zeaiean Firouzabadi, Ali Hosingholizade
17.10-17.20	Land Cover Classification Utilizing PlanetScope SuperDove Data in GEE Gulden Reshidoglu Sahin, Gordana Kaplan
17.20-17.30	Classification of hybrid maize seeds (Zea mays) with object-based machine learning algorithms using multispectral UAV imagery Ismail Colkesen, Umut Gunes Sefercik, Taskin Kavzoglu, Hasan Tonbul, Muhammed Yusuf Ozturk, Osman Yavuz Altuntas, Mertcan Nazar, Ilyas Aydin
17.30-17.40	Study of land subsidence induced by oil extraction in the Tengiz oilfield of Kazakhstan using radar interferometry (InSAR) Emil Bayramov, Manfred Buchroithner, Martin Kada
17.40-17.50	Consequent increase of the Caspian level in the coastal zone of the Republic of Azerbaijan (according to aerospace data) Amir Aliyev, Dilshad Suleymanli, Ramin Atakishiyev, Dilara Hasanova

Azerbaijan Time	Session 9: Geographic Information Systems Session Chair: Prof. Iraj Teimouri, University of Tabriz. Iran
18.00-18.10	Investigation of the causes of the flood disaster GIS-based in the city center of Şanlıurfa (Türkiye) in 2023 Faruk Bingöl, ibrahim Halil Yildirim, Ahmet Serdar Aytaç, Ömer Kayli, Sezgin Abukan, Nizar Polat
18.10-18.20	The effect of climatic factors on the cotton productivity using machine learning approaches Bakhtiyar Babashli
18.20-18.30	Analysis of Investment Planning in Electricity Distribution Systems with GIS Kadri Kaya, Abdulkadir Menduhoğlu
18.30-18.40	The recreational potential of waterfalls (in the example of Gabala district) Shahla Ismayilova
18.40-18.50	Preparing soil protection map using GIS: A case study from Türkiye Nuri Bozali, Fatih Sivrikaya

Azerbaijan Time	Session 10: Remote Sensing Session Chair: Prof. Omid Ghorbanzadeh, Institute of Geomatics, University of Natural resources and life sciences, Austria
19.00-19.10	Using EO1 Hyperspectral Images for Rock Units Mapping Parisa Safarbeyranvand, Parviz Zeaiean Firouzabadi, Ali Hosingholizade, Reza Bastami
19.10-19.20	Bathymetric model generation in shallow waters with optical satellite images and machine learning algorithms Fatma Karlığa, Ugur Alganci, Dursun Zafer Şeker
19.20-19.30	Creation of Land Use and Land Cover maps of the Khachmaz-Shabran region of Azerbaijan using machine learning methods Nariman Imranli, Raziye Hale Topaloglu , Elif Sertel
19.30-19.40	Displacement Analysis of Aftershocks Occured After 6 February 2023 Kahramanmaraş Earthquakes Dilara Solmaz, Nusret Demir

14 JUNE 2023

Azerbaijan Time	Session 11: Surveying and Geodesy Session Chair: Prof. Aziz Şişman, 19 May University, Türkiye
10.00-10.10	NMF-based ensemble clustering for GNSS velocity field: tectonic insights Seda Özarpacı Batuhan Kılıç
10.10-10.20	Lake Level Forecasting with Radial Based Neural Networks Mehmet Fehmi Yıldız, Vahdettin Demir
10.20-10.30	Comparison of Web Based Online GNSS Data Evaluation Services Mehmet Emin Tabar, Yasemin Sisman
10.30-10.40	A Detection Method of Mismatched Measures in GNSS Coordinate Time Series: Fuzzy Logic and IQR (Interquartile Range) Based Approach Hüseyin Pehlivan
10.40-10.50	Evaluation of satellite altimetry-derived gravity field models with shipborne gravity data in the Mediterranean Sea Aslınur Bahçekapılı, Bihter Erol
10.50-11.00	Compliance analysis in polynomial surface determination with ANOVA Ulku Kirici Yildirim, Yasemin Sisman
11.00-11.10	Continuous decimeters level real-time Precise Point Positioning in Polar high latitude region Reha Metin Alkan, Mahmut Oğuz Selbesoğlu, Hasan Hakan Yavasoğlu, Bilal Mutlu

Azerbaijan Time	Session 12: Geographic Information Systems Session Chair: Dr. Mehrdad Jeihuni, University of Tabriz. Iran
11.20-11.30	The importance of using GIS technology in conducting geographic research in the Republic of Azerbaijan Zakir Eminov
11.30-11.40	Determination of suitable areas for Wind Power Plant installation in Şanlıurfa with GIS and AHP Tacettin Ataş, Abdulkadir Memduhoğlu
11.40-11.50	Relief morphometry as a factor of formation and spatial differentiation of highland landscapes of the major Caucasus Ulviye Qasimova
11.50-12.00	Identifying Urban Landscape Patterns and Influences on Dengue Incidence in Mandaue City, Philippines Isabella Pauline Quijano, Jao Hallen Banados
12.00-12.10	Investigation of land use and land cover in urban landscape based on GIS Shahnaz Amanova

Azerbaijan Time	Session 13: Land Administration, Cadastre and Land Use Session Chair: Prof. Atta –ur Rahman, University of Peshawar, Pakistan
12.20-12.30	Spatio-temporal Appraisal of Glacial Lakes, Susceptibility Analysis and Po-tentials of Glacial Lake Outburst Floods in the Peri-Glacial Environment of Western Himalayas Atta-ur Rahman
12.30-12.40	Analysis of rural ethnosettlement in Balakan administrative region based on GIS method Bayimkhanim Huseynova
12.40-12.50	Relief influence on plant cover of Zangilan District Gulnar Hajiyeva, Aytan Mammadova
12.50-13.00	Critical issues in emergency planning for radiological accidents Maryna Batur, Reha Metin Alkan
13.00-13.10	Vegetation indices in the assessment and management of soil fertility Matanat Asgarova

Azerbaijan Time	Session 14: Geographic Information Systems Session Chair: Dr. Aydın Alptekin, Mersin University, Türkiye
13.20-13.30	Wildfire hazard and risk assessment at the instance of qabala district Firuza Aghayeva
13.30-13.40	What is the best spatial interpolation technique for evaluating droughts? Ahmad Abu Arra, Eyüp Şişman, Mehmet Emin Birpinar
13.40-13.50	Investigating urban livability using global TOPSIS in Bojnord city Foroogh Khazaei Nezhad, Ali Hosingholizade, Kimiya Momen
13.50-14.00	Studying the distribution of population of Mountain Shirvan in the GIS environment Rovshan Karimov, Natavan Jafarova
14.00-14.10	Modern methods of studying inaccessible mountain relief with GIS technology Kazimova Latifa

Azerbaijan Time	Session 15: Remote Sensing Session Chair: Prof. Hasan Tombul, Gebze Technical University, Türkiye
14.20-14.30	Efficient use of wind energy in Lankaran zone Vusala Rasulzada
14.30-14.40	Innovative Trend Analysis of Downward Surface Shortware Radiation in Türkiye during 1984-2021 Seyma Akca, Eyüp Sisman
14.40-14.50	Rapture and Surface Deformation mapping of Turkey 2023 Earthquake using DInSAR with Sentinel-1 Satellite Data Pouya Mahmoudnia, Mohammad Sharifikia
14.50-15.00	Comparison of different land surface temperature (LST) estimation algorithms using remotely sensed images Ali Hosingholizade, Parviz Zeaiean Firouzabadi, Foroogh Khazaei Nezhad, Mozhgan Dehghani Aghchekohal
15.00-15.10	Index-based mapping of floating algae blooms observed on Lake Iznik using Landsat-8 imagery Ismail Colkesen, Muhammed Yusuf Ozturk, Osman Yavuz Altuntas

Azerbaijan Time	Session 16: Close-Range and Aerial Photogrammetry Session Chair: Prof. Bakhtiar Feizizadeh, Humboldt-Universität zu Berlin, Germany
15.20-15.30	3D modeling of historically important columns Abdurahman Yasin Yiğit, Murat Yakar, Ali Ulvi
15.30-15.40	Modeling of ancient period Sarcophagus with close range photogrammetry Ali Ulvi, Abdurahman Yasin Yiğit, Murat Yakar,
15.40-15.50	Comparing conventional and photogrammetric methods for volume calculation of stone piles: A case study in the Karacadağ Region Cömert Oso, Hasan Lafci, Nizar Polat
15.50-16.00	Comparative Analysis of Semantic Segmentation of Terrestrial Images Using DeepLabv3+ Ahmet Verani, Muhammed Enes Atik, Zaide Duran

Azerbaijan Time	Session 17: Geographic Information Systems Session Chair: Dr. Leila Naghipour, University of Tabriz. Iran
16.10-16.20	Possibilities of applying smart technologies in agriculture (after the Pandemic) Nazim Garayli
16.20-16.30	Studying the influence of mudflows on the geomorphological structure of rivers using by GIS technologies Samira Abushova, Aytan Maharramova
16.30-16.40	Getting disaster information through the web Lutfiye Kuşak
16.40-16.50	Defining the specific weights of morphometric indicators of relief for the evaluation of the ecological-geomorphological condition (A case study of the Eastern part of the Kura depression) Jeyhun Gasimov
16.50-17.00	Determination of Fire Susceptible Areas and Location Selection of Fire Stations by Geographical Analytical Method Sayed Payamuddin Danish, Mevlut Uyan, Mehmet Ertaş

Azerbaijan Time	Session 18: Remote Sensing Session Chair: Prof. Dursun Zafer Şeker, İstanbul Technical University, Türkiye
17.20-17.30	Comparison of soil moisture estimation based on LST-NDVI of Landsat 8 images with field soil sampling Mozhgan Dehghani aghchekohal, Parviz Zeaiean Firouzabadi, Ali Hosingholizade
17.30-17.40	High resolution remote sensing data and environmental data for the classification of a square in Rome, Italy Lorenza Fiumi Fiumi, Francesco Atanasio Carolei, Fabrizio Filiberti, Marco Torre
17.40-17.50	Comprehensive soil erosion risk assessment using remote sensing (on the example of Zangilan region) Guliyev İsmayil, Rauf Huseynov
17.50-18.00	An evaluation of the effectiveness of spectral bands and indices on semantic segmentation with Attention U-Net using Sentinel-2A imagery and ESA WorldCover products Elif Ozlem Yilmaz, Taskin Kavzoglu
18.00-18.10	Analysis of the sea surface temperature (SST) of the Caspian Sea from NOAA satellites Ismayil Zeynalov, Aybeniz Akhmedova, Rena Akhmedova, Almaz Rustamova

Azerbaijan Time	Session 19: Cartography Session Chair: Dr. Lütfiye Kuşak, Mersiun University, Türkiye
18.20-18.30	Contemporary characteristics of air temperature distribution in the territory of Azerbaijan Camal Hüseynov
18.30-18.40	How is Mathematics Popularized as the Basis of Engineering Education? Nuri Erdem, Battal Yıldırım
18.40-18.50	Compilation of environmental protection maps by region, economic area and scale Magsad Gojamanov, Ilhama Garibova

Azerbaijan Time	Session 20: LiDAR - 3D Laser Scanning Session Chair: Prof. Ali Shamsoddini, Tarbiat Modares University, Iran
19.00-19.10	Enhancing Ground Point Extraction in Airborne LiDAR Point Cloud Data Using the CSF Filter Algorithm Berkan Saritas, Gordana Kaplan
19.10-19.20	3D visualization of pavement distress using terrestrial LIDAR data N H Riyaz Khan, S Vasanatha Kumar
19.20-19.30	Extraction of tree parameters using terrestrial 3D LIDAR data Sangeetha Gaikadi, Vasantha Kumar S

Azerbaijan Time	Session 21: Land Administration, Cadastre and Land Use Session Chair: Prof. Tayfun Çay, Konya Technical University, Türkiye
19.40-19.50	Analysis of the vulnerability of rural settlements to earthquakes in TMA using fuzzy inference system and spatial statistics techniques Bahman Tahmasi, Hassan Ali Faraji Sabokbar, Seyed Ali Badri
19.50-20.00	Assessing Land Use and Land Cover Changes in Kigali City, Rwanda Katabarwa Murenzi Gilbert, Yishao Shi
20.00-20.10	Comparison of different valuation methods in land consolidation studies Tayfun Çay, Musa Nehir SÖZEN
20.10-20.20	Four-Dimensional Cadastre Modeling with UML Diagram Tayfun Çay, Hasan Çevik
20.20-20.30	Analysis of real estate values and economic indicators in extraordinary situations Fatma Bunyan Unel
20.30-20.40	Value Based Land Regulation Model and Its Applicability in Türkiye Mehmet Koçoğlu, Mehmet Ertaş, Mevlüt Uyan
20.40-20.50	Geoinformation Systems for Early Warning and Assessment of Climate Change Impacts on Wheat Yields in Azerbaijan Sona Guliyeva
20.50-21.00	Investigation of Drought-Threatened Areas through Different Drought Indexes: A Case Study in Mersin, Türkiye Mehmet Özgür Çelik, Murat Yakar
21.00-21.10	Analysis of Land Surface Temperature Distribution in Response to Land Use Land Cover Change in Agroforestry Dominated Area, Gedeo Zone, Southern Ethiopia Wendwesen Taddesse Sahile, Gashaw Kibret Goshem[1], Seid Ali Shifaw, Muh Rais Abidin

6th Intercontinental Geoinformation Days

igd.mersin.edu.tr

Investigation of linear and logarithmic regression between measured and calculated parameters of Eldarica pine tree

Ali Hosingholizade *[1]

[1]*University of Tehran, Department of Remote Sensing and GIS, Tehran, Iran*

Keywords
UAV
Segmentation
Classification
Crown Area
Bojnord

Abstract

Man-made forests are created with various goals, including reducing the pressure on natural forests. Therefore, the knowledge of the status of their quantitative characteristics for planning and achieving primary goals has always been of interest to the managers of these types of forests. In this research, field data collection of parameters such as height, DBH and crown area was done with Phantom 4 UAV RGB images (2 Cm), Total Station TS02 (7″) and standard metal meter(1mm). Then it was obtained by calculating the parameters with the help of paired images (crown area) and point cloud (Height and Diameter at breast height). In the next step, two-by-two linear and logarithmic regression relationships were created between H, DBH and crown area parameters, and the value of R^2 was also obtained. The results showed that linear regression is better than logarithmic regression. Also, the amount of R^2 between DBH and H parameters in two cases of data from field measurements (R^2=0.75) and data from calculations (R2=0.83) gave better results than the comparison of other parameters. Therefore, it is possible to use linear regression equations between DBH and H in very few statistics, similar environmental conditions and no need for very high accuracy.

1. Introduction

Studying the physical quantities of trees provides the possibility of optimal forest management to achieve the desired structure. Among these physical quantities are the diameter at breast height (DBH), height, crown area (the largest diameter and the perpendicular to it for calculation area), which in addition to the importance of each one, examining the relationship between them is importance (Liao et al. 2022; Tienaho et al. 2022). For example, DBH, the crown area and the height of the tree are among the variables that are measured in order to estimate forest inventory, biomass, forest simulation, tree growth theory, carbon estimation and volume measurement. All of which require accurate models between the physical parameters of the tree. (Lou et al. 2022). In forest statistics, tree height is often estimated from the measured diameter of the tree at breast height. The diameter of the tree can be measured easily and at low cost. Measuring tree height is relatively more difficult and costly (Moreira et al. 2021; Iizuka et al. 2017). Therefore, models that are measured exclusively based on diameter have a great impact on cost. With the importance of breast diameter as the main biometric variable of forest trees, its study has particular importance (Nazariani et al. 2021). This variable has a high correlation with the variables of height, volume and other tree sizes and is considered an important factor in the study of these characteristics (Arabatzis and Burkhart. 1992). Another important physical parameter that is used in modeling the growth and performance of forest is the crown area, which is highly correlated with tree growth and its accurate measurement in the forest, especially for adult trees are challenge (Hosingholizade et al. 2022). In order to solve these challenges such as time-consuming and expensive in large areas, the use of Unmanned aerial vehicle (UAV) paired images and the resulting point cloud can solve the problems (Hosingholizade et al. 2022). Therefore, the evaluation of single trees in forest is highly considered for the use of UAV technology in large-scale forests. These separations are based on single trees in coniferous forests with good accuracy (Iqbal et al. 2021). Based on, different equations have been developed between the physical parameters of

* **Corresponding Author**

*(a.hosingholizade@ut.ac.ir) ORCID ID 0000–0001–5286–1361

Cite this study

Hosingholizade, A. (2023). Investigation of linear and logarithmic regression between measured and calculated parameters of Eldarica pine tree. Intercontinental Geoinformation Days (IGD), 6, 1-4, Baku, Azerbaijan

the tree, but since the growth of different parts of a tree depends on different parameters, such as soil type, moisture, type and species of tree, amount of sunlight, rainfall, temperature and human factors (pollutants). (Jones et al. 2020; D'Odorico et al. 2021). Therefore, a general equation cannot be used for all conditions and species across the globe. Nowadays, the use of local equations and its development according to the existing conditions in order to study more and more accurately It is widely used. (Goodbody et al. 2017).

Also, continuous imaging and parameter calculations are not economical for small levels and it also results in limitations of local flights and permits. On the other hand, the lack of flight teams and specialist forces for image processing, sampling, quick and low count investigations (very few number), makes the use of regression equations still justified despite the capabilities of UAVs. Therefore, in this research, while using paired images of UAVs and the resulting point cloud and considering the ground measurements, we tried to establish equations using the appropriate in SPSS V.26 between physical parameters such as crown area and diameter. so that these equations can be used according to similar environmental conditions in other places or small number of investigations. "Figure 1" shows the process.

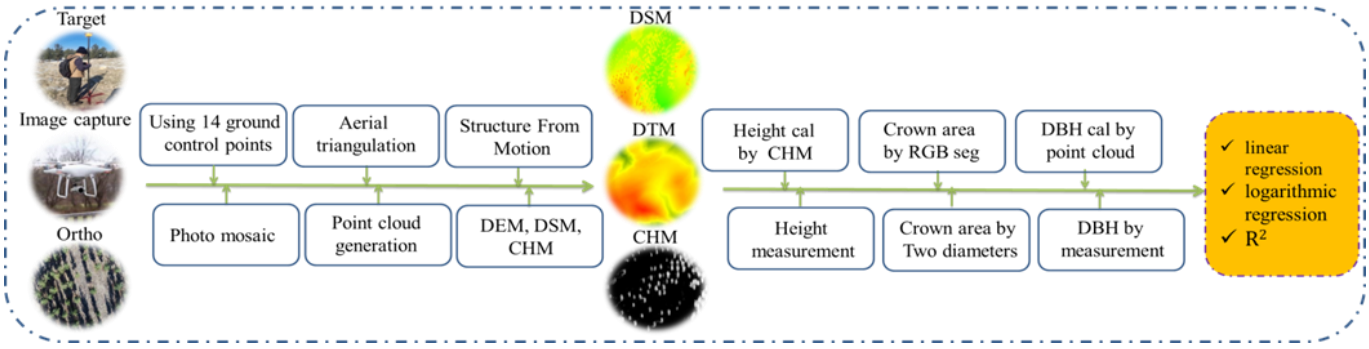

Figure 1. Workflow of the study

2. Method

2.1. Study area

Pardisan Park of North Khorasan is located at the eighth kilometer of Bojnord-Mashhad Road (37° 28 ' 57 N "-57° 25 ' 49 " E, Zone 40 N), at an average altitude of 1080 meters above sea level. This complex is purely covered with Tehran pine (Pinus eldarica). The region is cold semi-arid according to the coupon criteria and has a relatively high slope in topography (1112 to 1037 meters). The average rainfall and its temperature according to the statistics of Bojnord Airport Meteorological Synoptic Station (the closest station to the study area) for a period of 10 years (2011-2021) are 260 mm and 15 ° C, respectively.

2.2. Field data collection and processing

In this research, 324 Eldarica pine trees were registered using dual-frequency GPS Raymand 3GB with the definition of horizontal (0.5 cm) and vertical (1 cm) accuracy thresholds. Then, the direction of the reference ground and the better construction of the model were marked on the ground from 14 control points with proper dispersion and visibility from all directions and recorded accurately with a dual-frequency GPS. In the next step, 952 images were recorded with Phantom 4 UAV with 90-degree angles as Crossing with 80 and 40 percent longitudinal and sidelab coverage and at a height of 40 meters from the ground. Due to restrictions on presence in the area and permits, the flight took place at 14:30 local time (11:30 UTC) on March 4, 2021. For field data collection, the height of all the trees was measured using a TS02 TotalStation (accuracy of 7 seconds of degrees). Finally, by using a standard metal meter, the diameter at breast height and the two perpendicular diameters of the crown (to calculate the area with the ellipse formula) were accurately measured. After field imaging and data collection, a three-dimensional model of the area and a mosaic image was obtained using the PIX4D software using the SFM algorithm. To calculate the area of the crown, segmentation of the RGB image of the region using parameters Compactness, Scale and Shape in Ecognition V9.1 was used. By generating point cloud from RGB images, products such as Digital Terrain Models (DTM), Digital Surface Models (DSM) and from the difference between these two Canopy Height Models (CHM) (height of each tree) were obtained by using Cloudcompare v11. Then, the diameter at breast height (height of 1.30 cm) was calculated on the Trimble Business Center (TBC) software. Finally, the calculated and measured data were statistically analyzed in SPSS V.26 software.

3. Results

In this research, the number of 324 pine trees in Tehran with different diameters and heights according to the difference in the year of their planting were directly measured in the field. "Table 1" shows a summary of field measurements. Torres-Sanchez et al. (2018) also studied 325 tree bases in estimating the characteristics of single almond trees on UAV data, which is similar to the number of samples in the present study. As can be seen, the studied pine trees had a relatively diverse range of diameter and height, and this issue plays an important role in establishing equations and evaluations. "Table 2" also shows the linear and logarithmic regression equations between the parameters of tree height (H), DBH and crown area.

Table 1. Summary of statistical characteristics of the crown area of 324 pine trees Estimated UAV events

Method	Characteristic	Min	Max	Mean	STD	CV (%)
Field	Height (meter)	0.54	13.07	6.62	2.60	38.91
	DBH (meter)	0.10	0.62	0.37	0.11	30.29
	Crown area (square meter)	0.81	49.94	15.95	7.92	49.74
Calculation	Height (meter)	0.68	13.14	6.78	2.56	37.86
	DBH (meter)	0.11	0.72	0.44	0.13	30.96
	Crown area (square meter)	5.85	44.35	17.22	6.43	37.01

Table 2. Linear and logarithmic equations by using Field (F) and calculated (Cal) data

Parameter	Linear Equation	R^2	Logarithmic Equation	R^2
H(F) < > DBH(F)	y = 0.0379x + 0.118	0.75	y = 0.1724ln(x) + 0.062	0.67
H(F) < > Crown area(F)	y = 1.3904x + 6.552	0.21	y = 5.9275ln(x) + 5.198	0.16
DBH(F) > Crown area(F)	y = 0.0105x + 0.204	0.52	y = 0.1469ln(x) - 0.016	0.51
H(Cal) < > DBH(Cal)	y = 0.0479x + 0.110	0.83	y = 0.2302ln(x) + 0.018	0.74
H(Cal) < > Crown area (Cal)	y = 1.3583x + 8.008	0.29	y = 6.055ln(x) + 6.241	0.22
DBH(Cal) < > Crown area(Cal)	y = 0.0159x + 0.161	0.63	y = 0.2887ln(x) - 0.367	0.60

4. Discussion

As shown in "Table 1". The physical parameters (DBH, H, crown area) resulting from calculations generally have lower standard deviation (STD) and Coefficient of variation (CV) compared to field measurements, which indicates less dispersion of this type of data. Among the parameters, the DBH standard deviation is lower than the height and crown area parameters, which means that the field measurement as well as calculations in DBH have been done more accurately than the height and crown area, which can cause different reasons. One of these reasons is direct access to the tree trunk. In other words, calculation of height and crown area is indirect, which can be the correct sign error for measurement, not taking the staff to calculate the length of the diameters (for use in area estimation) and the total station level error to measure the height. Regarding the height, as is clear in "Table 1", it has less standard deviation than the crown area, which measurement with total station and marking is more accurate than visually finding the dimensions and border of the crown and measuring it can be one of the reasons. Also, the values of statistical parameters such as: Max, Min and Mean indicate the diversity in the physical parameters of pine trees in the study area.

By examining the data in "Table 2", in general, it can be seen that in the Eldarica pine trees in the study area, in the linear regression mode, the R2 value was higher than the logarithmic mode. In simpler words, in the linear mode, the relationship between the variables has been associated with a higher correlation. Of course, this correlation and changes in it were not the same for all parameters. For example, by examining the relationship between DBH and H parameters, it has the highest R2 in linear (R2=0.75) and logarithmic (R2=0.67) data for direct field measurements. The same advantage exists when using data from calculations, that is, in the case of using calculation data, the R2 value for DBH and H parameters has a higher value. On the other hand, the amount of R2 in parameters H and crown area in two modes of direct field data collection and computational data has the lowest correlation for pine trees in the region in linear mode (R2=0.16 and R2=0.21). logarithmic result is (R2=0.22 and R2=0.29).

5. Conclusion

Estimation of physical parameters in man-made forests is an important goal for applications using UAVs. However, the use of UAVs and their accuracy in estimating physical parameters have been proven many times in forest studies. In some cases, due to the small number of trees, the use of UAV is not economical and even in some areas, it is not possible to issue a flight permit. Therefore, quick and low-cost evaluation so that even non-experts can collect data is becoming more necessary and the use of regressions has a special value. Based on the obtained results, the use of linear regression in estimating the physical parameters of Eldarica pine trees has brought better results. Also, the use of DBH and H parameters in two modes of direct field data collection and the data obtained from calculations has a much higher correlation rate than other physical parameters. Therefore, it is suggested to use these equations between DBH and H to estimate parameters (linear regression) for areas with soil, weather and other parameters similar to the studied area.

Acknowledgement

The authors of the study are grateful to the General Directorate of Environmental Protection of North Khorasan province. Also, part of the costs of this research has been provided through the plan number 4003393 approved by the Fund for Support of Researchers and Technologists of the country.

References

Arabatzis, A. A., & Burkhart, H. E. (1992). An evaluation of sampling methods and model forms for estimating height-diameter relationships in loblolly pine plantations. Forest science, 38(1), 192-198. https://doi.org/10.1093/forestscience/38.1.192

D'Odorico, P., Schönbeck, L., Vitali, V., Meusburger, K., Schaub, M., Ginzler, C., & Ensminger, I. (2021). Drone-based physiological index reveals long-term acclimation and drought stress responses in trees. Plant, Cell & Environment, 44(11), 3552-3570. https://doi.org/10.1111/pce.14177

Fradette, O., Marty, C., Tremblay, P., Lord, D., & Boucher, J. F. (2021). Allometric equations for estimating biomass and carbon stocks in afforested open woodlands with black spruce and jack pine, in the eastern canadian boreal forest. Forests, 12(1), 59. https://doi.org/10.3390/f12010059

Goodbody, T. R., Coops, N. C., Marshall, P. L., Tompalski, P., & Crawford, P. (2017). Unmanned aerial systems for precision forest inventory purposes: A review and case study. The Forestry Chronicle, 93(1), 71-81.

Hosingholizade, A., Erfanifard, Y., Alavipanah, S. K., Latifi, H., & Jouybari-Moghaddam, Y. (2022). An assessment of support vector machines for crown delineation of pine single trees on unmanned aerial vehicle imagery. Intercontinental Geoinformation Days, 4, 17-20.

Hosingholizade, A., Erfanifard, Y., Alavipanah, S. K., Latifi, H., & Jouybari Moghaddam, Y. (2022). Comparison of unmanned aerial vehicle (UAV) RGB imagery and point clouds in crown area estimation of individual trees within pine (Pinus eldarica) man-made forests. Journal of RS and GIS for Natural Resources.

Iizuka, K., Yonehara, T., Itoh, M., & Kosugi, Y. (2017). Estimating tree height and diameter at breast height (DBH) from digital surface models and orthophotos obtained with an unmanned aerial system for a Japanese cypress (Chamaecyparis obtusa) forest. Remote Sensing, 10(1), 13. https://doi.org/10.3390/rs10010013

Iqbal, I. A., Osborn, J., Stone, C., & Lucieer, A. (2021). A comparison of als and dense photogrammetric point clouds for individual tree detection in radiata pine plantations. Remote Sensing, 13(17), 3536. https://doi.org/10.3390/rs13173536

Jones, A. R., Raja Segaran, R., Clarke, K. D., Waycott, M., Goh, W. S., & Gillanders, B. M. (2020). Estimating mangrove tree biomass and carbon content: a comparison of forest inventory techniques and drone imagery. Frontiers in Marine Science, 6, 784. https://doi.org/10.3389/fmars.2019.00784

Liao, K., Li, Y., Zou, B., Li, D., & Lu, D. (2022). Examining the Role of UAV Lidar Data in Improving Tree Volume Calculation Accuracy. Remote Sensing, 14(17), 4410. https://doi.org/10.3390/rs14174410

Lou, X., Huang, Y., Fang, L., Huang, S., Gao, H., Yang, L., ... & Hung, I. K. (2022). Measuring loblolly pine crowns with drone imagery through deep learning. Journal of Forestry Research, 33(1), 227-238. https://doi.org/10.1007/s11676-021-01328-6

Moreira, B. M., Goyanes, G., Pina, P., Vassilev, O., & Heleno, S. (2021). Assessment of the influence of survey design and processing choices on the accuracy of tree diameter at breast height (DBH) measurements using UAV-based photogrammetry. Drones, 5(2), 43. https://doi.org/10.3390/drones5020043

Nazariani, N., Hamidi, S. K., & Mansour Samaei, R. (2021). Investigating Diameter-Height Models of Fagus and Carpinus betulus Forest in Area 40 A of Noshahr (Mazandaran). Natural Ecosystems of Iran, 12(1), 70-83.

Tienaho, N., Yrttimaa, T., Kankare, V., Vastaranta, M., Luoma, V., Honkavaara, E., ... & Saarinen, N. (2022). Assessing Structural Complexity of Individual Scots Pine Trees by Comparing Terrestrial Laser Scanning and Photogrammetric Point Clouds. Forests, 13(8), 1305. https://doi.org/10.3390/f13081305

Torres-Sanchez, J., de Castro, A. I., Pena, J. M., Jimenez-Brenes, F. M., Arquero, O., Lovera, M., & Lopez-Granados, F. (2018). Mapping the 3D structure of almond trees using UAV acquired photogrammetric point clouds and object-based image analysis. Biosystems engineering, 176, 172-184. https://doi.org/10.1016/j.biosystemseng.2018.10.018

6th Intercontinental Geoinformation Days

igd.mersin.edu.tr

The 3D virtual restitution of historical buildings using photogrammetry: A case study of the Dungeon-Cistern structure in the Ancient City of Dara (Anastasiopolis), Mardin

Lale Karataş*[1], Murat Dal [2], Aydın Alptekin [3], Murat Yakar [4]

[1]*Mardin Artuklu University, Department of Architecture and Urban Planning, Türkiye*
[2]*Munzur University, Department of Architecture, Türkiye*
[3]*Mersin University, Department of Geological Engineering, Türkiye*
[4]*Mersin University, Department of Geomatics Engineering, Türkiye*

Keywords
3D Documentation
Photogrammetry
Restitution
Virtual Restitution
Mardin

Abstract

To accurately document cultural heritage buildings, a preliminary study phase that assesses the building's characteristics is crucial. Historical data is necessary to have a basic understanding of the building's past, so both geometric surface surveys and in-depth historical and archival research should be conducted. In recent years, 3D digitization and geomatics technologies have been applied in the field of cultural heritage, particularly for documentation and preservation purposes. The goal is to document and preserve the significant historical features (form, appearance) of a cultural heritage structure along with relevant data, in case of natural or other damages. In this context, the purpose of the presented paper is to propose the restitution of the Zindan-Sarnıç structure in Dara (Anastasiopolis) ancient city, which is a unique cultural heritage site, through a three-dimensional model created using photogrammetry. The documentation/survey, dating/reconstruction, conservation/restoration, and consolidation interventions, including the three-dimensional model, encompass the identification of problems related to the structure and its immediate surroundings, determining the life process/history and values/potentials from its construction periods to the present, and establishing the fundamental principles and approaches for the conservation and consolidation interventions of the structure.

1. Introduction

Cultural heritage, especially immovable assets such as monuments, archaeological sites, etc., is the primary application area for new approaches. A digital 3D model, produced as part of the documentation process for architectural structures, is now an urgent necessity. The digital 3D model should be transformed into a vital reference framework for conservation experts. This will enable the creation of a suitable data source (graphic and semantic) to assist restoration and reconstruction systems (Penttilä et al., 2007).

In recent years, 3D digitization and geomatic technologies have been applied in the field of cultural heritage, particularly for documentation and preservation purposes. The aim is to document and preserve the significant historical features (such as form and appearance) of a cultural heritage structure using relevant data, in case of natural or other damages (Gomes et al., 2014).

To document cultural heritage buildings accurately, it is crucial to conduct a preliminary study phase where building features are evaluated (Karataş & Dal, 2023). Since having basic information about the building's history is necessary, both geometric surface investigation and in-depth historical and archival research should be conducted (Karataş, 2022a, b, c, d).

The aim of this study is to present a restitution proposal for the Zindan-Cistern structure in the unique cultural heritage site of Dara (Anastasiopolis) ancient city, using a 3D model created through photogrammetry.

1.1. Study area and significance of the structure

Dara (Anastasiopolis), located approximately 30 km southeast of Mardin, is an important ancient border city

* **Corresponding Author**

*(lalekaratas@artuklu.edu.tr) ORCID ID 0000-0001-8582-4612
(muratdal@munzur.edu.tr) ORCID ID 0000-0001-5330-1868
(aydinalptekin@mersin.edu.tr) ORCID ID 0000-0002-5605-0758
(myakar@mersin.edu.tr) ORCID ID 0000-0002-2664-6251

Cite this study

Karataş, L., Dal, M., Alptekin, A., & Yakar, M. (2023). The 3D virtual restitution of historical buildings using photogrammetry: A case study of the Dungeon-Cistern structure in the Ancient City of Dara (Anastasiopolis), Mardin. Intercontinental Geoinformation Days (IGD), 6, 5-8, Baku, Azerbaijan

dating back to the late antique period. It is known as Dara in the local language and has historical significance as a city established during the 6th century, similar to other newly founded cities of that era such as Rusafa and Zenobia in Syria, and Justiniana Prima in Serbia. This city, established in the 6th century, provides valuable tangible evidence of urban planning, different types of structures, and their functions, serving as important documents that convey knowledge about the urban development of that period (Al-Mashhadani, 2017; Celik, 2018; Mardin Governorship, 2013).

Figure 1. The location of Dara Ancient City

Figure 2. 3D model of the Dara Necropolis Area.

The archaeological remains of Dara, including the city walls, public structures, private residential areas, necropolis, and stone quarries, are among the important features that make Dara city significant (Karataş, 2016). The Zindan-Cistern structure, belonging to the ancient city of Dara/Anastasiopolis, is one of the notable structures in the area (Figure 3).

2. Method

The initial stage of the restitution study involved archival research on the structure. The 3D model generated using various software and programs forms the basis for analysis and examination. The archival research started with the evaluation and interpretation (periodization-contextualization) of the structure's historical, architectural, and lived aspects from its construction period to the present day. It concluded with the interpretation of the area's historical, cultural, and natural values in order to ensure their preservation and continuity, following the principles of scientific conservation. The study provided details on physical/spatial interventions for conservation/restoration and consolidation, in line with the scientific conservation principles.

(a)

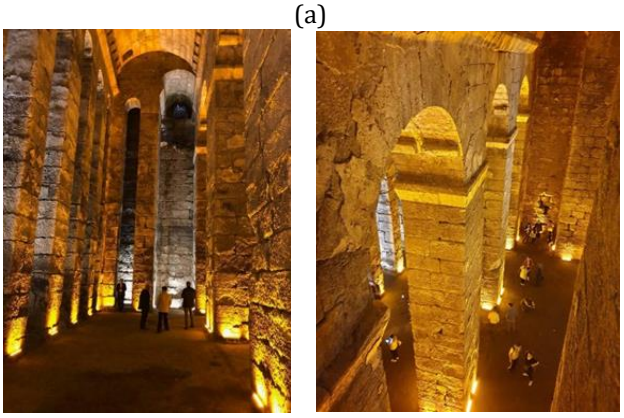

(b)

Figure 3. Dara (Anastasiopolis) ancient city Zindan-Cistern structure: (a) Exterior appearance (b) Interior space

In the second stage of the study, the documentation of the original state of the structure revealed through archival research was carried out using a 3D model. For this purpose, the Zindan-Sarnıç structure of Dara/Anastasiopolis ancient city was examined on-site and photographed. During these fieldwork activities, two cameras were used: a Fuji FinePix HS10 model with 30X optical zoom, panoramic shooting feature, and 10.3-megapixel resolution, and an Olympus SP-550UZ model with 18X optical zoom and 7.1-megapixel resolution, both operated with tripod stands. Numerous photographs were taken from different perspectives to thoroughly and comprehensively document all parts of the structure, capturing both general views and detailed components (Figure 4).

Photoscan software was used to merge the photos. A total of 120 photos taken from different angles of the structure were utilized. Initially, the photo data of the structure was introduced to the software. The processing of the images captured with a smartphone was carried

out using PhotoScan Professional software developed by Agisoft LLC, which utilizes the Shape from Motion (SFM) algorithm (Agisoft, 2018). PhotoScan applies the SFM algorithm to generate a 3D model from the images. During the image processing phase with PhotoScan, the uploaded photos were adjusted using the software. A total of 120 high-resolution photo frames were obtained and the previously determined 9 coordinate points, latitude, longitude, and elevation information were entered to align the photos in a coordinated manner. In this phase of photo correction, PhotoScan calculated the camera positions and orientations for each image, resulting in the production of orthophotos. As a result of all these processes, a 3D model and orthophoto of the Dara church-underground structure were generated. The restitution descriptions were defined based on these 3D documents.

The Table 1 summarizes the methodology followed step by step.

3. Results

Within the scope of the study and the proposed restitution for the structure, a detailed archival research and photogrammetric-based 3D modeling approach were followed. The findings regarding the restitution of the obtained structure in the study are explained below:

The Dungeon-Cistern structure of the ancient city of Dara (Anastasiopolis) is located approximately 100 meters northwest of Agora Street. It is a large cistern with well-cut stone walls, and its original entrance is on the eastern facade. Despite the fact that the connected structures and adjacent spaces are still underground and a house has been built on top of the structure at a later date, the structure still retains its grandeur. Above the two-story structure, the city's cathedral (great church) is located, of which only one wall remains standing today in the western part. According to the historian Procopius, there are two significant churches in Dara. One of them is the 'Great Church,' and the other is the Bartholomew Church. According to the historian Theodorus Lector, Saint Bartholomew appeared in the dream of Anastasius and asked for the protection of the city. In response to this, Anastasius had Bartholomew's bones brought from Cyprus to Dara. Until the 14th century, there was a Syriac metropolitanate in Dara (Gabriel, 1940; Abdulgani Efendi, 1999).

According to Honatio Southgate, there are ten cisterns located next to the hill where the Muslim settlement is situated. Each cistern is approximately 150 steps long, 75 steps deep, and 15 or 20 steps wide. Currently, three out of these ten cisterns have disappeared, while the remaining seven, although not actively used by the villagers, still defy time. These cisterns were constructed by excavating the bedrock and then completing the upper parts with small stones. The bedrock was hollowed out from top to bottom, allowing water collected from the mountains to reach and be stored in these cisterns without waste. According to some historians, Dara was the city where the first dam and irrigation channels were established in Mesopotamia. The water cisterns comprised a system that could control the flow, proportion, and retention of water. In the ancient city of Dara, outside the city walls, another cistern, dating back to the 6th century and known as the "zindan" among the locals, was identified. The interior of the cistern, which had its upper covering collapsed, was filled with 18 meters of soil. Through excavation, the soil filling inside the cistern, which was used as a stable, was emptied, and its vaulted upper covering was restored using its original stones without the use of any new stones (Gabriel, 1940; Abdulgani Efendi, 1999; Akyüz, 1988). The interior of the structure is a symmetrical rectangle approximately 23x16 meters in size, extending in the east-west direction. Its height is approximately 15 meters (Figure 4).

Table 1. Workflow

	Step	Description
1	**Archival Research**	Historical documents, old photographs, drawings, and written sources related to the structure were examined. These archival materials provided information about the original design and details of the structure, forming the basis for the restitution study.
2	**Photo Analysis**	The 120 photographs used in the restitution process were thoroughly analyzed using a detailed photo analysis method. The details, angles, perspectives, and different sections of the structure depicted in the photographs were carefully evaluated.
3	**Photo Processing and 3D Modeling**	The processing of the photographs and the generation of a 3D model were carried out using the Photoscan software. The photographs were analyzed using the SFM algorithm to create a 3D model. In this stage, the coordination of the photographs, calculation of camera positions and orientations, and production of orthophotos were ensured.
4	**Restitution Study**	A restitution study was conducted using the obtained 3D model and other archival information. Missing or damaged parts of the structure were reconstructed or restored according to the original design and details. The restitution process was based on the information obtained from archival research and examinations conducted on the structure.
5	**Restitution Proposal**	As a result of the restitution study, a detailed 3D model of the structure has been obtained. The work carried out during the restitution process has been documented, and the methodology of restitution has been explained. These findings can be utilized in restoration projects with the aim of preserving the original details, design, and historical features of the structure.

(a) (b)

Figure 4. a) A professional digital camera, Fuji FinePix HS10 model, with 30X optical zoom, panoramic shooting feature, and a resolution of 10.3 megapixels.
b) A semi-professional digital camera, Olympus SP-550UZ model, with 18X optical zoom and a resolution of 7.1 megapixels.

4. Discussion and Conclusion

The restitution study conducted within the scope of this project aims to recreate the original appearance of the structure and provide a foundation for restoration efforts, using a detailed approach that includes archival research and photogrammetric-based 3D modeling processes. In this article, the Dungeon-Cistern structure in the ancient city of Dara (Anastasiopolis) is examined as a case study. Due to the continuous need for restoration and maintenance works, as well as its complexity, size, and unique features, the Dara Dungeon-Cistern structure presents a significant example of challenges and issues, making it a suitable case study to apply the proposed methodology. However, the methodology applied can also be applied to other similar historical buildings.

According to the findings of the study, the Dara Dungeon-Cistern structure is dated back to the 6th century and has survived to the present day. Currently, the main issues are related to structural integrity and material deterioration. Regarding the former, these mainly arise from the high loads on the columns within the immense volume of the structure and the weight of the stones, which result in significant protrusions on the side walls and compression of the elements below. As for material deterioration on the exterior facades, it is caused by the presence of limestone, which is highly sensitive to atmospheric agents and tends to undergo layer separation and fragmentation. In future studies, integrated visualized damage assessment techniques are seen as key elements to identify material damages, aiming to preserve the structure and transmit it to future generations.

Acknowledgement

We extend our gratitude to the local community for their assistance during the data collection phase of this study at Dara Ancient City.

References

Abdulgani Efendi. (1999). Mardin Tarihi. (Çev. Burhan ZENGİ). Ankara: Afşaroğlu Matbaa.

Agisoft. (2018). [Agisoft website]. Retrieved from https://www.agisoft.com/

Altun, A. (2011). Mardin'de Türk Devri Mimarisi. İstanbul, 43.

Al-Mashhadani, F. B. (2017). The Urban Design and Planning of Dara Ancient City in Mardin, Turkey. Alexandria Engineering Journal, 56(2), 221-231.

Celik, Z. H. (2018). The Urban History and Development of Dara Ancient City. International Journal of Environmental Science and Development, 9(5), 142-146.

Gabriel A. (1940). Voyages Archeologiques Dans La Turquie Orientale. Paris.

Gomes, L., Pereira Bellon, O. R., & Silva, L. (2014). 3D reconstruction methods for digital preservation of cultural heritage: A survey. Pattern Recognition Letters, 50, 3-14. https://doi.org/0.1016/j.patrec.2014.03.023

Mardin Valiliği İl Kültür ve Turizm Müdürlüğü. (2013). Mardin Kültür Envanteri. İstanbul.

Karataş, L. (2016). Mardin Kentsel Sit Alanındaki İbadet Yapılarında Malzeme Kullanımı ve Sorunları Üzerine Bir Araştırma (Master's Thesis, Uludağ University, Fen Bilimleri Enstitüsü, Bursa, 340p).

Karataş, L., Alptekin, A., Kanun, E., & Yakar, M. (2022a). Tarihi kârgir yapılarda taş malzeme bozulmalarının İHA fotogrametrisi kullanarak tespiti ve belgelenmesi: Mersin Kanlıdivane ören yeri vaka çalışması. İçel Dergisi, 2(2), 41-49.

Karataş, L., Alptekin, A., & Yakar, M. (2022b). Detection and documentation of stone material deterioration in historical masonry structures using UAV photogrammetry: A case study of Mersin Aba Mausoleum. Advanced UAV, 2(2), 51-64.

Karataş, L., Alptekin, A., Karabacak, A., & Yakar, M. (2022c). Detection and documentation of stone material deterioration in historical masonry buildings using UAV photogrammetry: A case study of Mersin Sarisih Inn. Mersin Photogrammetry Journal, 4(2), 53-61.

Karataş, L., & Menteşe, D. H. (2022). Dara Antik Kenti (Anastasiopolis) Nekropol Alanının Malzeme Sorunlarının Yersel Lazer Tarama Yönteminden Elde Edilen Ortofotolar Yardımıyla Belgelenmesi. Türkiye Fotogrametri Dergisi, 4(2), 41-51.

Karataş, L., Alptekin, A., & Yakar, M. (2022). Documentation of stone material deterioration on the facades of historical masonry buildings by terrestrial laser scanning: A case study of a Mansion in Mardin. Intercontinental Geoinformation Days, 5, 172-175.

Karataş, L., & Dal, M. (2023). Deterioration analysis of historical village house structure in Mersin Kanlıdivane archaeological area by UAV method. Mersin Photogrammetry Journal, 5(1), 32-41.

Penttilä, H., Rajala, M., & Freese, S. (2007). Building information modelling of modern historic buildings. In Proceedings of the 25th eCAADe Conference on Predicting the Future (pp. 607-613).

Yakar, M., Orhan, O., Ulvi, A., Yiğit, A. Y., & Yüzer, M. M. (2015). Sahip Ata Külliyesi Rölöve Örneği. *TMMOB Harita ve Kadastro Mühendisleri Odası*, *10*

6th Intercontinental Geoinformation Days

igd.mersin.edu.tr

Stone material damage detection in restoration using Virtual Reality: The case of Virgin Mary Church and Patriarchate in Midyat, Türkiye

Lale Karataş*[1], Murat Dal [2], Aydın Alptekin [3], Murat Yakar [4]

[1]*Mardin Artuklu University, Department of Architecture and Urban Planning, Türkiye*
[2]*Munzur University, Department of Architecture, Türkiye*
[3]*Mersin University, Department of Geological Engineering, Türkiye*
[4]*Mersin University, Department of Geomatics Engineering, Türkiye*

Keywords
Photogrammetry
Virtual Reality
Stone Material Deteriorations
Historic Buildings
Cultural Heritage

Abstract

With the advancements in technology, various methods are being used for documenting cultural heritage. However, three-dimensional (3D) documentation techniques have some drawbacks. For instance, terrestrial laser scanning techniques are not widely used due to their high costs and the expertise required. Photogrammetry can generate point clouds at a lower cost but involves managing large data files, which require additional time. In this context, the aim of this study is to present a method that integrates photogrammetry and virtual reality technologies to examine a stone building in three dimensions in a cost-effective and timely manner, and to investigate stone material deterioration on the obtained 3D model. The virtual 3D environment of the structure can be created using the proposed method from global panoramic photographs on various open-source platforms at a reasonable cost and within a short period. The results of the study demonstrate that stone material deterioration can be easily identified in these environments consisting of a three-dimensional virtual tour of the structure.

1. Introduction

Using 360-degree panoramic images to conduct virtual reconstruction and damage assessment in historical buildings is an important method for digitally recreating buildings and identifying potential damages. Scientific studies highlighting the significance of virtual reality-based damage assessment in historical buildings and the benefits of the techniques used in this field indicate significant progress in the processes of identifying structural damage, planning restoration, and making conservation decisions. These techniques have provided important advancements in the assessment of structural damage, restoration planning, and decision-making for the preservation of historical buildings. Zhang et al. (2020) conducted research on how 3D laser scanning and virtual reconstruction can be used in the damage assessment of historical buildings, and it was determined that significant benefits were achieved in damage assessment. Gül & Özşahin (2019) emphasized the importance of virtual reality applications in the damage assessment of historical structures and highlighted the usability of virtual reality technology in areas such as structural analysis, restoration processes, and conservation decision-making. Ioannidis & Soile (2019) emphasized the benefits of virtual reality technologies, particularly in the preservation of cultural heritage, in areas such as damage assessment of historical buildings, restoration processes, and visitor experiences. Costa et al. (2017) examined how virtual reality technology can be used in the preservation of historical buildings through a case study, highlighting that augmented reality technology is an effective tool in areas such as damage detection, restoration processes, and visitor interaction.

The stage of restoration and restitution proposal is the most important step carried out before applying interventions to a structure. Building upon the positive findings obtained in previous literature studies, this paper presents a case study of the Virgin Mary Church and Patriarchate. Within this scope, the identification of stone material issues will be discussed through virtual reconstruction of the building. Located in the urban conservation area of Mardin, the Virgin Mary Church and Patriarchate are historical monuments with distinct

* **Corresponding Author**

*(lalekaratas@artuklu.edu.tr) ORCID ID 0000-0001-8582-4612
(muratdal@munzur.edu.tr) ORCID ID 0000-0001-5330-1868
(aydinalptekin@mersin.edu.tr)ORCID ID 0000-0002-5605-0758
(myakar@mersin.edu.tr) ORCID ID 0000-0002-2664-6251

Cite this study

Karataş, L., Dal, M., Alptekin, A., & Yakar, M. (2023). Stone material damage detection in restoration using Virtual Reality: The case of Virgin Mary Church and Patriarchate in Midyat, Türkiye. Intercontinental Geoinformation Days (IGD), 6, 9-12, Baku, Azerbaijan

characteristics influenced by factors such as topography, materials, climate, and surrounding cultural elements. In this study, a virtual simulation was created from 360-degree panoramic photographs of the historical monument, which is of great necessity for the sustainable preservation of cultural heritage, and stone material deteriorations were attempted to be identified through this virtual reconstruction.

1.1. The history and significance of the structure

The Virgin Mary Church and Patriarchate are located in the district of Midyat, which is part of the Mardin province in Türkiye. Midyat is situated in a region surrounded by the fertile lands of Mesopotamia and has a significant historical background. The district is renowned for its rich cultural heritage and historical structures (Abdulgani Efendi, 1999).

The Virgin Mary Church is one of the most important religious structures in Midyat. It has a history that dates back to the 4th century and belongs to the Syriac Orthodox Church. The church is believed to have been built on a site where the tomb of Mor Şleymun (Saint Simon), one of the apostles of Antioch, is located. The architecture of the Virgin Mary Church bears resemblance to traditional Syriac churches in the Middle East, and it serves as a significant religious and touristic attraction in the region (Alioğlu, 2000).

The Midyat Patriarchate is the central location of the Syriac Orthodox Church. This building was relocated from the Deyrulzafaran Monastery in Mardin to Midyat in 1994. The Midyat Patriarchate serves as the residence of the Syriac Orthodox Patriarch, who is the religious leader of the Syriac Orthodox Church. The Patriarchate building is a beautiful example of Syriac church architecture and holds significant importance as a tourist attraction for visitors to the region (Altun, 2011; Ahunbay, 2005) (Figure 1).

Figure 1. Images of the Virgin Mary Church and Patriarchate

2. Method

Steps for Virtual Reconstruction and Damage Assessment in Historical Buildings Using 360-Degree Panoramic Imaging:

2.1. Capturing panoramic images

To capture 360-degree panoramic images that encompass the entire surroundings of the historical building, special equipment such as dedicated 360-degree cameras, cameras with a 360-degree shooting mode, or smartphones with 360-degree capabilities can be used. It is important to carefully capture the shots to obtain high-resolution and sharp images. Sufficient photographs should be taken to capture all the details, both indoors and outdoors of the building (Karataş, 2022a; b; c). In this study, the selected structures were visited, and panoramic images of the buildings were captured using a panoramic imaging device (NCTech iris360º Model) (Figure 2) for the creation of three-dimensional virtual environments (Figure 3).

Figure 2. The NCTech iris360º Model is a panoramic imaging device used for capturing 360-degree panoramic images. (TMMOB Jeoloji Mühendisleri Odası ,2023).

Figure 3. 360-degree panoramic images of the Virgin Mary Church and Patriarchate taken by the NCTech iris360º

2.2. Image stitching and virtual reconstruction

360-degree panoramic images are stitched together using specialized software or online platforms. In this step, the captured photographs are merged to create a complete 360-degree image. The image stitching process involves analyzing the overlapping points of the photos to ensure perspective alignment and create a seamless panoramic view (Karataş, 2022).

In recent years, with the advancement of technology and the widespread availability of open-source software, it has become possible to generate virtual models from 360-degree panoramic photographs for the 3D examination of historical structures. Even on open-source platforms, various studies have been conducted in this regard. Examples of open-source software and platforms include Matterport (https://matterport.com/), Kuula (https://kuula.co/), Roundme (https://www.roundme.com/), 3DVista (https://www.3dvista.com/), and Mozilla Hubs (https://hubs.mozilla.com). These platforms can be used to upload, edit, and create virtual tours using 360-degree photographs.

Within the scope of the study, the obtained panoramic images were transformed into navigable 3D environments within structures by leveraging the capabilities provided by various open-source virtual reality platforms. These platforms offer the ability to convert panoramic images into 3D environments, allowing users to navigate within the structures.

Within the scope of the study, a 3D virtual environment was created based on the 360-degree panoramic photographs of the building, and the damages occurring in the structure were identified. The virtual environment of Virgin Mary Church and Patriarchate was generated using the Mozilla Hubs program from the 360-degree panoramic photos. The details of the building can be perceived clearly in the virtual environment, allowing users to navigate and zoom in or out using avatars to view detailed information about materials and material deterioration. The virtual tour images conducted through avatars for damage assessment in the virtual environment are presented as shown in the figures (Figure 4).

2.3. Damage assessment

The created virtual model and tour were utilized to detect material damages in Virgin Mary Church and Patriarchate structure. Through analyses conducted on the virtual model, cracks, wear and tear, structural issues, or other signs of damage could be identified. Additionally, comparing the virtual model with historical records or photographs will aid in determining changes that have occurred over time in its current condition.

3. Results

According to the findings, the facade walls of Virgin Mary Church and Patriarchate structure have experienced surface loss, voids, and color changes due to the damaging effects of moisture and sunlight on the stone material. Surface loss and color changes are the most common problems observed in monuments located in Mardin (Karataş, 2016; Karataş et al., 2022d, e, f, g, h; Karataş et al., 2023a, b, c, d, e).

Based on these results, it can be concluded that the material issues identified in Virgin Mary Church and Patriarchate located in Midyat, a district of Mardin, are similar to historical structures in Mardin. Improper material repairs are partially present due to the failure to use original materials resulting from the deterioration of the original material. Plant growth and moss formation have been detected in the flat courtyard. Wear and tear are observed on the stairs. Cracks, deformations, wear, and color changes are found in the frames and wings of the wooden windows. Wear is observed on the thresholds. No material deterioration has been detected in the arches. Decorative elements on the building facade show loss of form and surface contamination.

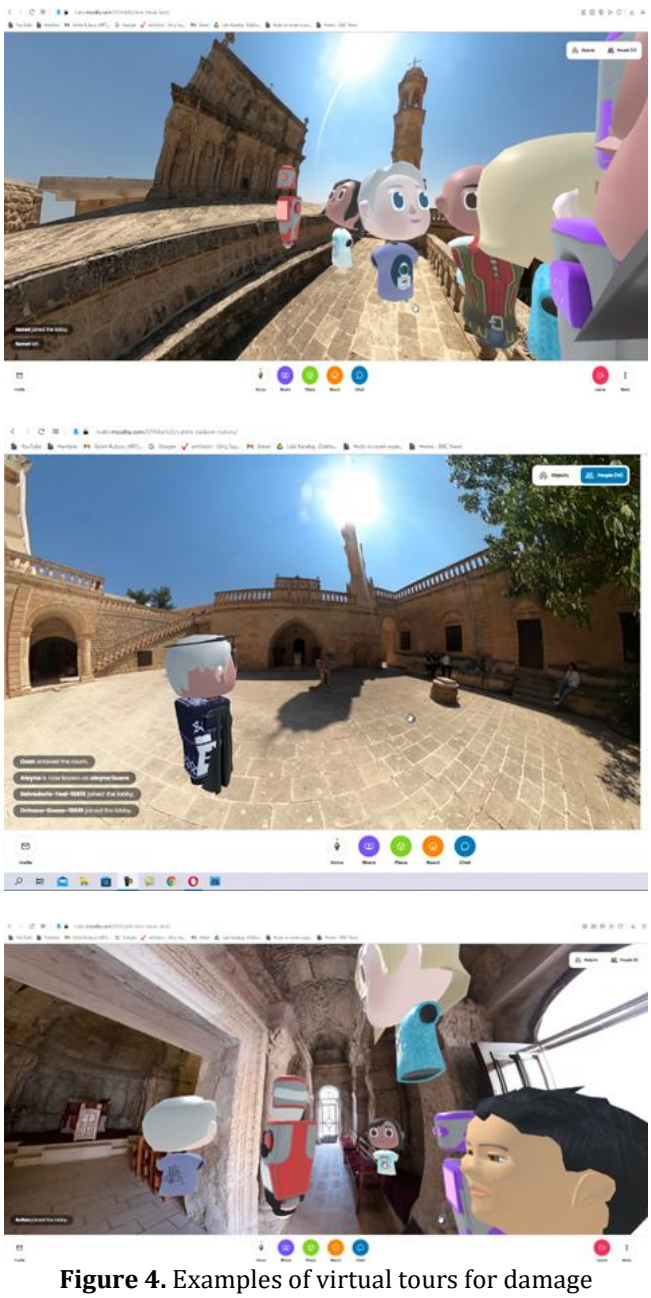

Figure 4. Examples of virtual tours for damage assessment

4. Conclusion

The study presents a method that integrates photogrammetry and virtual reality technologies to obtain a virtual tour containing a 3D model of a stone building in a cost-effective manner and within a short timeframe. The detectability of stone material deterioration was investigated within the obtained 3D virtual environment. As a result of this study, it was concluded that the proposed method enables the creation of a virtual 3D environment of the structure from global panoramic photographs in a cost-effective and efficient manner. It was also found that stone material deterioration within the structure can be easily identified using avatars in this virtual environment.

In future studies, it is recommended to use the systematic approach followed in our research to create virtual environments of historical structures from different countries and share them on open platforms such as Sketchfab (https://sketchfab.com) on the web. This would allow for the creation of an open-source library on stone material deterioration and provide individuals from anywhere in the world with the opportunity to freely view, explore, and examine all documented historical buildings in this environment.

References

Abdulgani Efendi. (1999). Mardin Tarihi. (Çev. Burhan ZENGİ). Ankara: Afşaroğlu Matbaa.

Ahunbay, Z. (2005). Antik Mardin: Taşın Belleği. Mardin, Türkiye: Yapı Kredi Yayınları.

Alioğlu, E. F. (2000). Mardin Şehir Dokusu Ve Evler. Tarih Vakfı, İstanbul.

Altun, A. (2011). Mardin'de Türk Devri Mimarisi. İstanbul, 43.

Costa, E., et al. (2017). Augmented reality for historical building preservation: A case study in the portuguese route of the romanesque. International Archives of the Photogrammetry, Remote Sensing and Spatial Information Sciences, 42(2), 241-248.

Gül, M., & Özşahin, T. Ş. (2019). The importance of virtual reality applications in damage assessment of historical structures. Journal of Cultural Heritage Management and Sustainable Development, 9(2), 178-192.

Ioannidis, C., & Soile, S. (2019). Augmented and virtual reality in heritage preservation. Journal of Cultural Heritage, 37, 137-143.

Karataş, L. (2016). Mardin Kentsel Sit Alanındaki İbadet Yapılarında Malzeme Kullanımı ve Sorunları Üzerine Bir Araştırma (Master's Thesis, Uludağ University, Fen Bilimleri Enstitüsü, Bursa, 340p).

Karataş, L. (2022). Integration of 2D mapping, photogrammetry and virtual reality in documentation of material deterioration of stone buildings: Case of Mardin Şeyh Çabuk Mosque. Advanced Engineering Science, 2, 135–146.

Karataş, L., Alptekin, A., & Yakar, M. (2022a). Restitution suggestion for Mardin TatlıDede Mansion. Advanced Engineering Days (AED), 4, 61-63.

Karataş, L., Alptekin, A., & Yakar, M. (2022b). Investigation of Molla Hari (Halil) Süleyman Paşa Mosque's material deteriorations. Advanced Engineering Days (AED), 4, 55-57.

Karataş, L., Alptekin, A., & Yakar, M. (2022c). Contribution of architectural design of ancient city Dara's water cisterns to the water efficiency of the city. Advanced Engineering Days (AED), 4, 52-54.

Karataş, L., Alptekin, A., & Yakar, M. (2022d). Material deteriorations occurring on the facades of the Mor Sergios Bakhos Church. Advanced Engineering Days (AED), 4, 48-51.

Karataş, L., Alptekin, A., & Yakar, M. (2022e). Documentation of Mardin Kadife Ertem Mansion's architectural characteristics. Advanced Engineering Days (AED), 4, 58-60.

Karataş, L., Alptekin, A., & Yakar, M. (2022f). Mardin historical Kasaplar (Butchers) Bazaar restoration evaluation. Advanced Engineering Days (AED), 5, 5-7.

Karataş, L., Alptekin, A., & Yakar, M. (2022g). Mardin historical Marangozlar (Neccarlar) Bazaar architectural features. Advanced Engineering Days (AED), 5, 12-14.

Karataş, L., Alptekin, A., & Yakar, M. (2022h). Mardin historical Kuyumcular (Jewelers) Bazaar restoration evaluation. Advanced Engineering Days (AED), 5, 15-17.

Karataş, L., Alptekin, A., Yakar, M., & Dal, M. (2023a). Investigation of the historical process of the Mardin Castle. Advanced Engineering Days (AED), 6, 1-4.

Karataş, L., Alptekin, A., Yakar, M., & Dal, M. (2023b). Mardin Castle building material and construction technique analysis. Advanced Engineering Days (AED), 6, 5-8.

Karataş, L., Alptekin, A., Yakar, M., & Dal, M. (2023c). Assessment of structural problems in Mardin Castle. Advanced Engineering Days (AED), 6, 9-13.

Karataş, L., Alptekin, A., Yakar, M., & Dal, M. (2023d). Evaluation of conservation and restoration works in protected areas: A case study of Mardin Castle. Advanced Engineering Days (AED), 6, 14-17.

Karataş, L., Alptekin, A., Yakar, M., & Dal, M. (2023e). Mardin Castle landscaping and landscape interventions proposal. Advanced Engineering Days (AED), 6, 18-21.

Unal, M., Yakar, M., & Yildiz, F. (2004, July). Discontinuity surface roughness measurement techniques and the evaluation of digital photogrammetric method. In *Proceedings of the 20th international congress for photogrammetry and remote sensing, ISPRS* (Vol. 1103, p. 1108).

Yakar, M., & Doğan, Y. (2017). Uzuncaburç Antik Kentinin İHA Kullanılarak Eğik Fotogrametri Yöntemiyle Üç Boyutlu Modellenmesi. 16. *Türkiye Harita Bilimsel ve Teknik Kurultayı. TMMOB Harita ve Kadastro Mühendisleri Odası, Ankara*.

Yakar, M., Orhan, O., Ulvi, A., Yiğit, A. Y., & Yüzer, M. M. (2015). Sahip Ata Külliyesi Rölöve Örneği. *TMMOB Harita ve Kadastro Mühendisleri Odası*, *10*.

Zhang, X., Wang, C., Liu, Y., Huang, J., & Zou, W. (2020). Damage assessment of historic buildings based on three-dimensional laser scanning and virtual reconstruction. Sustainability, 12(6), 2243.

6th Intercontinental Geoinformation Days

igd.mersin.edu.tr

Game development in Unity game engine using optical UAV data

Mertcan Nazar*[1], Umut Gunes Sefercik [1]

[1]*Gebze Technical University, Department of Geomatics Engineering, Kocaeli, Türkiye*

Keywords
UAV
Structure from Motion
3D Model
Virtual Reality
Unity

Abstract

Computer graphics have become highly advanced with the ability to offer users to experience a synthetic world and interact with the digital environment in a realistic manner. Within this concept, game engines are prominent tools for the visualization of three-dimensional (3D) geospatial data and for creating virtual reality (VR) based applications. Moreover, advancements in game engine technology, and easier and free access to powerful game engines have increased the number of VR-based games. Optical UAVs are the most demanded UAV systems due to their ability to produce precise and true color three-dimensional (3D) object models with a broad array of objects in different sizes and forms. However, the optical UAV technique has some disadvantages in 3D modeling including dependence on sunlight due to the passive remote sensing principle and lack of vegetation penetration capability compared to active remote sensing systems. Also, the geometry of image acquisition and low correlation land cover cause distortions and inaccurate depictions on the generated 3D models. In this study, the factors that will affect the performance of the game in the 3D model production stages and within the Unity environment are investigated and relevant solutions have been proposed.

1. Introduction

In recent years, there has been an increasing interest in unmanned aerial vehicle (UAV) technologies, which have emerged as an alternative to traditional aerial photogrammetric systems. One of the reasons why optical UAV systems are preferred is the low cost and periodically achievable very high-resolution data. In addition, the ability to fly at desired altitudes, the placement of different detection sensors, and the possibility of working in various capturing geometries are among the advantages offered by optical UAV systems. Within the scope of basic photogrammetric work steps, three-dimensional (3D) data such as digital surface models (DSM), digital terrain models (DTM), contour lines, textured 3D mesh models and vector data can be produced using UAV data (Remondino et al. 2011). Usage areas of optical UAV systems include cultural heritage documentation (Bakirman et al. 2020), archeological studies (Ulvi 2022), natural disaster monitoring (Lindner et al. 2016), smart agriculture (Almalki et al. 2021), and 3D virtual reality (VR) integration (Sefercik et al. 2022). Moreover, the creation of digital twins of non-terrain objects is among the areas where optical UAV systems are used.

Computer systems offer users the opportunity to experience an interactive digital environment through VR technology. Developments in game engines have led to an increased interest in VR technology. In addition, VR systems have become an important tool for the visualization of geospatial data and the creation of high-quality 3D models. Lately, free access to powerful game engines and the easier learning phase of game development have increased the number of VR-based games and applications. Unity game engine is a cross-platform game development platform used by a large group of users because it is free to use and it has a user-friendly interface. In this study, the factors including depth filtering level selection, gaps in 3D models due to object form, visualization of texture data in Unity, application of rendering optimization algorithms and lastly inaccurate depiction of object geometry due to the lack of penetration capability of optical UAV systems, that will affect the performance of the game in the 3D model production stages and within the Unity environment are investigated and relevant solutions are proposed.

* **Corresponding Author**

*(mnazar@gtu.edu.tr) ORCID ID 0000 – 0002 – 3280 – 5685
(sefercik@gtu.edu.tr) ORCID ID 0000 – 0003 – 2403 – 5956

Cite this study

Nazar, M., & Sefercik, U. G. (2023). Game development in Unity game engine using optical UAV data. Intercontinental Geoinformation Days (IGD), 6, 13-16, Baku, Azerbaijan

2. Dataset and materials

A dataset consisting of aerial photos which were captured over the Gebze Technical University (GTU) campus, located in the Gebze district of Kocaeli province, Türkiye, using DJI Phantom 4 Pro V2.0 UAV with a 20-megapixel (MP) Sony Exmor RGB camera was utilized for producing high-quality 3D textured mesh models. UAV flights were carried out in bundle grid, polygonal and circular modes, and flight elevations were chosen as 30 m and 80 m. A total of 8333 aerial RGB photos were captured while front and side overlap ratios were determined as 80% and 60%, respectively, and the achieved ground sampling distance (GSD) was ≤ 2.2 cm. Specifications of the utilized UAV are shown in Table 1.

Table 1. Specifications of the DJI Phantom 4 Pro V2.0 UAV

DJI Phantom 4 Pro V2.0 UAV

Specification	Value
Camera	4K, HD, 1080p, 1", effective pixel resolution 20 MP
Gimbal	3-axis (pitch, roll, yaw)
Image size	3:2 Aspect Ratio: 5472×3648 4:3 Aspect Ratio: 4864×3648 16:9 Aspect Ratio: 5472×3078
Flight duration	Max. 30 minutes
Weight	1375 g
Speed	Max 20 m/s in S-mode
Wind speed resistance	Max. 10 m/s
Outdoor positioning module	GPS/GLONASS dual
Hover accuracy range	± 0.1 m V, ± 0.5 m H (Vision); ± 0.3 m V, ± 1.5 m H (GPS)

3. Methodology

The methodology of this study consists of two main parts including the production of 3D textured mesh model generation and the creation of a game in the Unity environment (Figure 1).

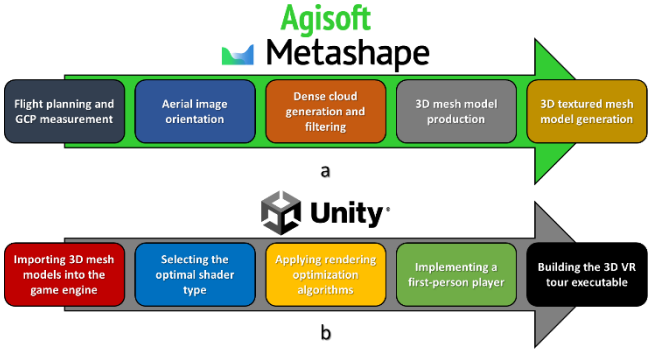

Figure 1. The methodology of the study area 3D textured mesh model generation (a) and 3D VR tour creation (b)

3D textured mesh model generation steps were carried out in structure from motion (SfM) based Agisoft Metashape Professional photogrammetric evaluation software. Before the aerial image orientation, flight planning was done in DJI Ground Station (GS) Pro software and homogenously distributed ground control points over the study area were measured using the real-time kinematic (RTK) GNSS technique. After the relative orientation of aerial photos, absolute orientation was done using GCPs with the root mean square error (RMSE) of ± 2 cm (~0.9 pixels). After the sparse point cloud production is completed as a result of aerial photo orientation, it is important to perform dense point cloud production in order to obtain a high-quality and detailed 3D mesh model. In Agisoft Metashape, depth maps containing depth information are created for dense point cloud production by processing photos. However, when creating depth maps, outliers or extreme values can be observed as a result of situations that cause noise-containing data such as differences in illumination in the photographs or unclear focus. In order to eliminate these extreme values, a depth filtering option with four filtering levels is used in the software. When these four levels are examined, the aggressive filter is recommended in areas where there are no important small details, while the mild level filter preserves the important small details that can be distinguished. Apart from that, while the moderate option gives results between mild and aggressive, depth filtering can be turned off and operations can be performed. Another important issue during the production of a 3D mesh model with high-quality and realistic depiction capability is that the objects merge with the bare topography by elongating with the effect of interpolation during the transformation from a dense point cloud to a mesh model. Lastly, 3D textured mesh models were produced using high-resolution aerial photos.

3D VR tour creation was done in the Unity game engine by the integration of produced 3D textured mesh models into the virtual environment. Firstly, 3D mesh models were imported as the wavefront .OBJ format into Unity. This format is conventionally utilized in exporting 3D mesh models and it stores 3D coordinates and triangle data and is employed by a wide number of 3D CAD software (Kato and Ohno 2009). For accurate and realistic visualization of texture data over the 3D mesh models a material object was created and texture data was implemented on this material. Then the shader type was changed from standard to unlit/texture. For improving the game performance occlusion culling rendering optimization algorithm was applied. The occlusion culling algorithm is utilized for the recognition and rendering of visible surfaces of 3D objects so that the objects positioned at the rear side of a particular viewpoint are not rendered for increasing performance and minimizing hardware bottlenecks (Coorg and Teller 1997). Users should be able to move around the 3D mesh models and interact with the environment freely. So a player with a first-person camera was added to the game environment and this player can be controlled with mouse and movement keys to provide users a realistic VR experience. In the last step, a game executable was built in Unity for providing users access to the game.

4. Results

After the methodology steps were completed, results were investigated and solution proposals were presented. Different depth filtering options were examined in dense point cloud generation (Figure 2).

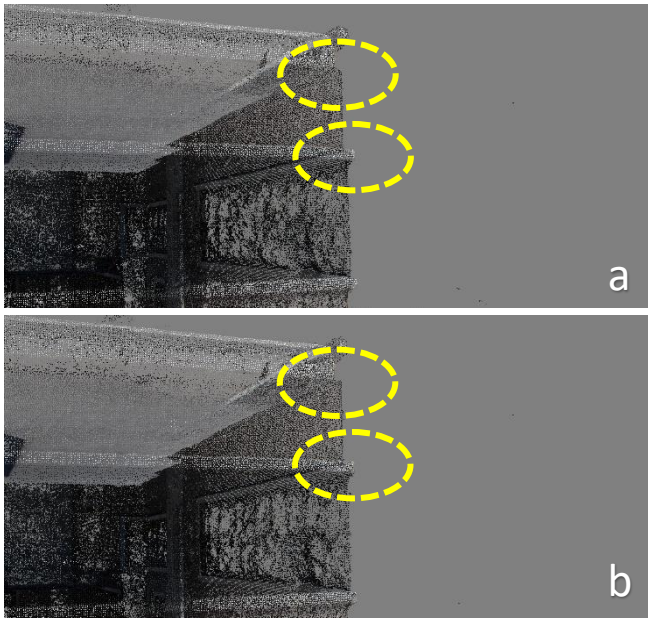

Figure 2. Produced dense point clouds when depth filtering was aggressive (a) and disabled (b)

When the depth filtering was chosen as aggressive building corners were smoother in 3D models and when it was disabled corners were sharper and seem to be more similar to the real structure. Moreover, object form seems to be another factor affecting the 3D modeling performance (Figure 3).

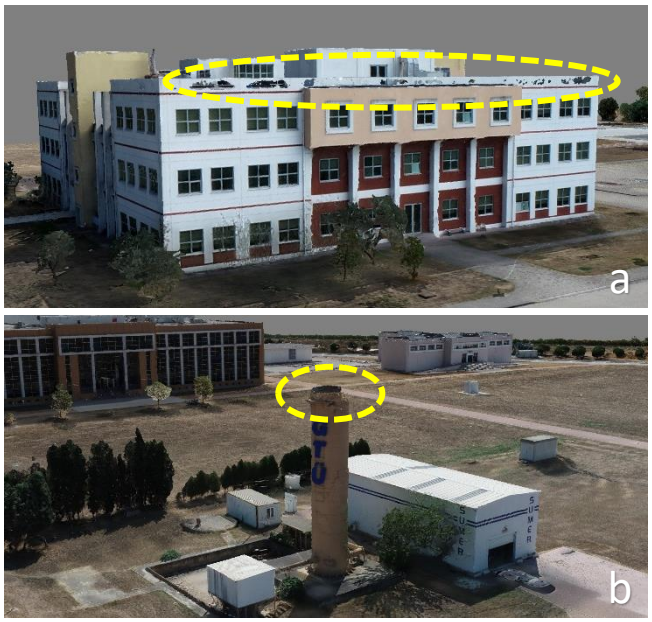

Figure 3. Gaps in the 3D model of a building (a) and a chimney (b)

In order to eliminate gaps resulting from object forms additional circular flights can be made with the UAV at oblique (inclined) camera angles (≤70°) on building facades. Another solution is to use checkerboards on objects that are thought to have issues before the UAV flight and take terrestrial photos of these objects to be used in absolute orientation, and use both aerial and terrestrial photos together in relative orientation. Moreover, the hole filling tool in Agisoft Metashape can be utilized to eliminate some of the gaps. In Unity imported texture data is applied to 3D mesh models by creating a material object and implementing the texture data on the material. However, a suitable shader type should be selected for the created material so that the texture is displayed correctly and in high detail (Figure 4).

Figure 4. Shader type of the material as standard (a) and unlit/texture (b)

The optimal shader type should be selected for accurate visualization of the texture data. The unlit/texture shader type displays the texture data more accurately and realistically compared to the standard shader type. Apart from the visual performance, the functional performance of a game is evenly important. Moreover, high polygonal data size and bottlenecks due to the limitation of utilized hardware appear to be negative factors in game performance. To improve the game performance and eliminate the hardware bottlenecks rendering optimization algorithms such as occlusion culling are applied. After the occlusion culling algorithm was applied to the created 3D VR tour frame per second (FPS) or in other words the number of frames that appears within a second, was increased to 51-122 FPS from 51-55 FPS. Boost in FPS values resulted in increased game performance and a smoother game experience for users. Optical UAV systems lack object penetration ability due to their operation based on the remote sensing principle. Especially in dense vegetation cover, forests, and underground passes a low number of points are generated due to overlaying objects obstructing the viewpoint of the optical UAV systems. The resulting 3D mesh models are inaccurate and incomplete depictions of real objects because of this problem (Figure 5). In such areas, multi-return laser scanning capable UAVs may be used, but since the original color information of the point cloud is also provided by digital cameras integrated into the laser scanner, it is not possible to obtain the original color.

Figure 5. 3D model of the underground pass produced using RGB UAV dense cloud (a) and using the fusion of RGB UAV dense cloud and colored terrestrial laser scanner dense cloud (b)

Terrestrial photogrammetry is also not recommended due to correlation problems in orientation. In light of all these issues, the most accurate production of 3D models in their original color is possible with the fusion of optical UAV and colored terrestrial laser scanner data in the correct geometry.

5. Conclusion

Within the scope of this study, the factors in the 3D textured mesh model production and in the integration of generated models into the Unity engine are investigated for improving game performance, and encountered problems are explored with relevant solution proposals. It has been observed that the parameters affecting the 3D modeling performance in SfM-based image matching software including the production of dense point clouds, generation of 3D mesh models, and appropriate texture graphics, significantly affect the performance of the created game. Apart from factors affecting 3D modeling performance, elements such as the selection of proper shader type for texture applied material object, and application of occlusion culling rendering optimization algorithm appear to greatly affect the both visual and functional performance of the game. Object geometry is another aspect affecting visual performance, gaps formed due to object forms lead to 3D mesh models with inaccurate geometry and decreased game performance. Lastly, the lack of penetration capability of optical UAV systems emerges as another issue affecting 3D modeling performance, especially in areas obscured by overlaying objects. A solution proposal for this issue is merging the optical UAV dense cloud with the color terrestrial laser scanner dense cloud. In conclusion, the game performance of the created 3D VR tour is affected greatly by parameters in 3D model generation and factors in setting up the game environment.

References

Almalki, F. A., Soufiene, B. O., Alsamhi, S. H., & Sakli, H. (2021). A low-cost platform for environmental smart farming monitoring system based on IoT and UAVs. Sustainability, 13(11), 5908. https://doi.org/10.3390/su13115908

Bakirman, T., Bayram, B., Akpinar, B., Karabulut, M. F., Bayrak, O. C., Yigitoglu, A., & Seker, D. Z. (2020). Implementation of ultra-light UAV systems for cultural heritage documentation. Journal of Cultural Heritage, 44, 174-184. https://doi.org/10.1016/j.culher.2020.01.006

Coorg, S., & Teller, S. (1997). Real-time occlusion culling for models with large occluders. In Proceedings of the Symposium on Interactive 3D Graphics, 83-90, Providence RI, USA.

Kato, A., & Ohno, N. (2009). Construction of three-dimensional tooth model by micro-computed tomography and application for data sharing. Clinical oral investigations, 13, 43-46. https://doi.org/10.1007/s00784-008-0198-4

Lindner, G., Schraml, K., Mansberger, R., & Hübl, J. (2016). UAV monitoring and documentation of a large landslide. Applied Geomatics, 8, 1-11. https://doi.org/10.1007/s12518-015-0165-0

Remondino, F., Barazzetti, L., Nex, F., Scaioni, M., & Sarazzi, D. (2011). UAV photogrammetry for mapping and 3D modeling–current status and future perspectives. International Archives of the Photogrammetry, Remote Sensing and Spatial Information Sciences, 38(1), 25-31. https://doi.org/10.5194/isprsarchives-XXXVIII-1-C22-25-2011

Sefercik, U. G., Kavzoglu, T., Nazar, M., Atalay, C., & Madak, M. (2022). Creation of a virtual tour .exe utilizing very high-resolution RGB UAV data. International Journal of Environment and Geoinformatics, 9(4), 151-160. https://doi.org/10.30897/ijegeo.1102575

Ulvi, A. (2022). Using UAV photogrammetric technique for monitoring, change detection, and analysis of archeological excavation sites. Journal on Computing and Cultural Heritage, 15(3), 1-19. https://doi.org/10.1145/3522742

6th Intercontinental Geoinformation Days

igd.mersin.edu.tr

Assessment of structural degradation at Germus Church: A UAV-based study

Emine Beyza Dörtbudak*[1], Seyma Akca [1], Nizar Polat [1]

[1]*Harran University, Geomatic Engineering Department, Sanliurfa, Türkiye*

Keywords
Germus Church
UAV
Photogrammetry
Digital Documentation

Abstract

Turkiye, with its rich history, has witnessed the rise and fall of many civilizations over the centuries. The preservation and documentation of historical artifacts and archaeological sites left behind by these civilizations are vital for the transmission of cultural heritage to future generations. In this regard, the application of photogrammetry has emerged as a promising method for modeling cultural heritage, and it has gained significant popularity in recent years, especially with the advancements in unmanned aerial vehicles (UAVs). In a recent study, researchers conducted the UAV-based photogrammetric reconstruction of the Germus Church, a historical structure believed to have been constructed in the 19th century. This innovative approach combines the use of UAVs and photogrammetry techniques to create accurate and detailed 3D models of the church. By capturing high-resolution aerial photographs from different angles, the researchers were able to reconstruct the entire structure digitally, capturing its intricate architectural details. The utilization of UAVs in photogrammetry not only allows for efficient data collection but also offers a non-intrusive method for surveying cultural heritage sites. This technology enables researchers and conservationists to document and study historical structures with precision, aiding in their preservation and restoration efforts. The study on the Germus Church serves as an example of how modern techniques can contribute to the safeguarding and understanding of Turkey's diverse cultural heritage. By employing UAV-based photogrammetry, researchers are able to create virtual representations of historical sites, ensuring that the knowledge and beauty of these structures are preserved for generations to come.

1. Introduction

It is possible, and indeed necessary, to transmit historical artifacts that encompass all stages of history and provide us with every clue related to history to future generations through a robust documentation process. Documentation of historical or cultural structures encompasses determining the current state of the structure (shape and position) in three-dimensional space, creating its map, conducting studies, processes, storage, and presentation steps necessary for all possible analyses (Kaya et al., 2019).

Until recent times, terrestrial observation systems have been widely used in the documentation of cultural heritage. However, in last decades, satellite technologies with higher spatial resolution have provided new opportunities for modeling efforts worldwide. With advancements in aviation and remote sensing technologies, photogrammetry and Unmanned Aerial Vehicle (UAV) systems have also started to be utilized more effectively in the field of modeling. (Toprak et al., 2019)

The photogrammetric applications conducted using photographs captured by a camera integrated into an unmanned aerial vehicle (UAV) are referred to as UAV photogrammetry (Ulvi, 2018). UAV photogrammetry, which we frequently encounter in the literature, has emerged in the field of 3D modeling of cultural heritage, thanks to its advantages in terms of time, cost, and data collection (Ulvi, 2021; Polat et al., 2020)

With the production of unmanned aerial vehicles in various shapes, sizes, and features, it is observed that 3D modeling has also advanced, making it easier to detect the current state and deformations of structures. (Uysal et al., 2015). In this study, the advantages of UAV photogrammetry were utilized to create a 3D model of the Germus Church, which is a cultural heritage site.

* **Corresponding Author**

*(beyzadbk@gmail.com) ORCID ID 0009 – 0001 – 6523 – 6060
(seymaakca@harran.edu.tr) ORCID ID 0000-0002-7888-5078
(nizapolat@harran.edu.tr) ORCID ID 0000-0002-6061-7796

Cite this study

Dörtbudak, E. B., Akca, Ş., & Polat, N. (2023). Assessment of structural degradation at Germus Church: A UAV-based study. Intercontinental Geoinformation Days (IGD), 6, 17-19, Baku, Azerbaijan

2. Method

The production of the model consists of two stages: fieldwork and office work.

During the fieldwork stage, data acquisition takes place. This involves capturing aerial photographs or images of the Germus Church using the unmanned aerial vehicle (UAV) equipped with a camera. The UAV is flown over the site, and high-resolution images are taken from different angles and positions. The purpose of this stage is to collect visual data that will be used for the subsequent modeling process (Uslu et al. 2016).

In this study, the DJI Mavic 2 Pro, a UAV system from the DJI brand, was used to generate a 3D model of the historical church. The DJI Mavic 2 Pro is a successful system with features such as an effective range of 8 km, a maximum flight time of 31 minutes, 4K recording with a Hasselblad camera, a 1" CMOS sensor, GPS sensor, 4-way obstacle sensing, automatic return to home, and a weight of approximately 1 kg (Akca and Polat, 2022). The UAV used in the study is depicted in Figure 1.

Figure 1. DJI Mavic 2 Pro UAV system used in the study

For the photo capture in the flight plan, a 80% overlap in the flight direction and a 60% overlap in the cross direction were set. The flight progressed for 20 minutes, and a total of 239 photos were taken. After the flight, aerial photographs of the area were obtained. Blurry photos taken during takeoff and landing were excluded from the dataset due to weather conditions. Once the fieldwork is completed, the collected images are transferred to the office for processing. This is where the office work stage begins. In this stage, specialized software is used to process the images and create a 3D model. The software analyzes the images, identifies common points and features, and reconstructs the three-dimensional structure of the Germuş Church based on these data points. The acquired images from the unmanned aerial vehicle were processed using Agisoft Photoscan, an independent software that offers significant capabilities for performing photogrammetric operations on digital images. A point cloud and a 3D model were created based on the evaluation of the images.

3. Study area

The selected study area, Germuş Church, is located in the Dagetegi near at the foothills of Germus Mountain, which is situated 10 kilometers northeast of the city center of Sanliurfa. The historical church is positioned at coordinates 37°12'06.0" latitude and 38°51'04.2" longitude and is located 5 kilometers away from Göbekli Tepe, which is known as the "zero point" of history. The location information for the study area is depicted in Figure 2.

Figure 2. The study area

4. Discussion

In this study, UAV-based 3D modeling of the historical heritage site known as Germuş Church, located in the Haliliye district of Sanliurfa province, has been successfully accomplished. The use of UAVs was employed to contribute to the surface investigation prior to the planned restoration of the historical church and to produce topographic products that could serve as a basis for the restoration works. The findings and processes involved in the production of the 3D model reveal that the UAV-based capture, which is overlapping, precise, and highly accurate, plays a significant role in generating the point cloud. The generated dense point cloud contains 7,800,413 points. The obtained point cloud is presented in Figure 3.

Figure 3. The generated point cloud

When evaluating the Agisoft software used for image processing, it can be observed that photos with regular overlap rates are processed accurately, resulting in a 3D model that closely resembles reality (Yakar et al. 2016). However, it is noted that as the number of added photos increases for the purpose of achieving greater accuracy, the processing time of the model also increases. Therefore, it is important to aim for an optimal balance between image input parameters and processing time (Atik and Duran, 2022).

When evaluating the generated 3D model and the fieldwork, it is clearly visible that the domes of the historical church have collapsed and the side facades have suffered damage. The deformed parts of the historical church are indicated on the 3D model in Figure 4 and Figure 5.

During the fieldwork, it was observed that both the interior and exterior of the church had been explored and excavated by individuals searching for artifacts. This

situation demonstrates the suitability of using unmanned aerial vehicles in the documentation of historical sites that are dangerous to enter and explore. Furthermore, the obtained 3D model can serve as a reference for comparing the current state of the church with any future deformations it may undergo. The damaged interior of the Germus Church is depicted in Figure 6. The final version of the 3D model of Germus Church is depicted in Figure 7.

Figure 4. The deformed parts of the historical church

Figure 5. The deformed parts of the historical church

Figure 6. Interior view of Germus Church

Figure 7. The 3D model of Germus Church

5. Conclusion

The modeling of Germus Church holds great importance in terms of preserving cultural heritage and passing it on to future generations. As seen in the obtained 3D model, both the interior and exterior of Germus Church have suffered various deformations due to damage and the passage of time. There are cracks on the walls, and collapses can be observed in the ceiling and dome areas. Additionally, the religious figures, mosaics, and other decorations inside the church have been damaged or lost over time. To ensure the preservation of this endangered structure and to recognize its value, efforts should be made to restore it and promote it for tourism.The three-dimensional modeling of Germus Church using UAV technology has documented the deformations of this cultural heritage and contributed to its restoration efforts, thus facilitating its introduction to tourism.

References

Atik, M. E., & Duran, Z. (2022). An Efficient Ensemble Deep Learning Approach for Semantic Point Cloud Segmentation Based on 3D Geometric Features and Range Images. Sensors, 22(16), 6210.

Akca, S., & Polat, N. (2022). Semantic segmentation and quantification of trees in an orchard using UAV orthophoto. Earth Science Informatics, 15(4), 2265-2274.

Kaya, Y., Şenol, H. İ., Memduhoğlu, A., Akça, Ş., Ulukavak M., & Polat, N. (2019). Hacim Hesaplarında İHA Kullanımı: Osmanbey Kampüsü Örneği. Photogrammetry Journal of Turkey, 1(1), 07-10.

Polat, N., Mehmet, Ö. N. A. L., Ernst, F. B., Şenol, H. İ., Memduhoglu, A., Mutlu, S., ... & Hüseyin, K. A. R. A. (2020). Harran Ören Yeri Arkeolojik Kazı Alanınındın Çıkarılan Bazı Küçük Arkeolojik Buluntuların Fotogrametrik Olarak 3B Modellenmesi. Türkiye Fotogrametri Dergisi, 2(2), 55-59.

Toprak, A. S., Polat, N., & Uysal, M. (2019). 3D modeling of lion tombstones with UAV photogrammetry: a case study in ancient Phrygia (Turkey). Archaeological and Anthropological Sciences, 11(5), 1973-1976.

Ulvi, A. (2018). Analysis of the Utility of the Unmanned Aerial Vehicle (UAV) in Volume Calculation by Using Photogrammetric Techniques. International Journal of Engineering and Geosciences, 3(2), 43-49.

Ulvi, A. (2021). Documentation, Three-Dimensional (3D) Modelling and visualization of cultural heritage by using Unmanned Aerial Vehicle (UAV) photogrammetry and terrestrial laser scanners. International Journal of Remote Sensing, 42(6), 1994-2021.

Uslu, A., Polat, N., Toprak, A. S., & Uysal, M. (2016). Kültürel Mirasın Fotogrametrik Yöntemle 3B Modellenmesi Örneği. Electronic Journal of Map Technologies, 8(2), 165-176.

Uysal, M., Toprak, A. S., & Polat, N. (2015). DEM generation with UAV Photogrammetry and accuracy analysis in Sahitler hill. Measurement, 73, 539-543.

Yakar, M., Kabadayı, A., Yiğit, A. Y., Çıkıkçı, K., & Catin, S. (2016). Emir Saltuk Kümbeti Fotogrametrik Rölöve Çalışması ve 3 Boyutlu Modellenmesi. Geomatik1(1),14-18.

6th Intercontinental Geoinformation Days

igd.mersin.edu.tr

Ecological risk analysis with the help of geographic information systems in fruit growing; Manisa in Türkiye example

Emre Yeniay[*1], **Aydın Şık** [2]

[1]*Republic of Türkiye Ministry of Agriculture and Forestry, General Directorate of Plant Production, Ankara, Türkiye*
[2]*Gazi University Faculty of Architecture, Department of Industrial Design, Ankara, Türkiye*

Keywords
GIS
Risk Analysis
MCDM
AHP
Fault Tree Model
Agricultural Crop Risk Maps

Abstract

With the help of information technologies, which are developing day by day, it has become easier to perform agricultural analyzes. Positional analyses can be performed with the help of Geographical Information Systems by gathering Climate, Soil, Topography and İrrigation data related to Agriculture. These analyses enables to generate analyses for agricultural investment maps, areas of agricultural conformity, plant pattern determination, etc. The purpose of this study is to prepare "Product Based Fruit Growing Risk Analysis Maps". Climate, Soil, Topography and Irrigation data, which are important in the growing of agricultural products are collected, severity and prospects for risk analysis are determined separately and risk values are established for each risk factor. The total risk value was calculated by prioritizing risk factors using the Analytical Hierarchy Process (AHP), one of the multi-criteria decision-making methods. Thanks to AHP, a methodology for calculating scenario-based risk values has been developed taking into account different probabilities. With the developed model, risk maps were created for climate, soil, topography and water constraints. The total risk map was obtained by combining the risk maps created with AHP. In this study, a model was created by selecting the Manisa Province Peach product in Türkiye. As a result of the model, the total risk values were divided into classes as "High Risk Areas", "Medium Risk Areas", "Low Risk Areas" and "Strongly Not Recommended Areas" according to the points they received spatially.

1. Introduction

The existing agricultural areas in the world are decreasing by 0.1-0.2% every 5 years, and the world population has increased by 30% in the last 20 years and reached 8 billion. (UN, 2022). In Türkiye, the amount of cultivated area decreased by 12 percent in the last 20 years and decreased to 23.5 million hectares. In the same period, the population of the country increased by 28 percent and reached 84 million.

The increasing world population increases the demand for food, but the disasters caused by climate change and deteriorating agricultural lands cause serious decreases in food supply at the opposite rate. At this point, the way out seems to be to switch from traditional farming methods to smart, planned and precision agriculture, also called Agriculture 4.0, where information systems are used. In smart and planned agriculture, determining what to grow where and how, thanks to the products grown in ideal conditions, it ensures that the products that are least affected by diseases and pests are obtained. However, it is not always possible to choose land with ideal conditions. Thanks to the studies carried out at this point, knowing in advance what kind of risks the existing land has, allows the creation of artificial conditions to correct the factors that cause damage.

Risk is the value determined according to the probability of damage that may be caused by dangerous situations. The purpose of risk management is to control the consequences of this uncertainty. For this, it is necessary to identify and analyze the risk factors. Risk management will be easier when risk factors are analyzed beforehand. As seen in the "risk = severity × probability" formula, the degree of risk revealed by severity and probability values can have the same value for very different conditions. In the first case, systems that will cause less damage should be considered, taking into account the situations that will occur when the event occurs. For the second case, the reasons leading to the occurrence of the event should be determined and an attempt should be made to eliminate them effectively. (Senel et al., 2013).

In this study, land suitability, site selection and ecological risk analysis for the fruit growing sector are discussed with the help of GIS applications. With GIS applications that make a significant contribution to the processing of big data, researchers, practitioners and policy makers are provided with the opportunity to successfully present advanced agricultural analyzes.

* **Corresponding Author**

*(eyeniay@yahoo.com) ORCID ID 0000-0002-4063-3502
(aydins024@gmail.com) ORCID ID 0000-0002-8977-9094

Cite this study

Yeniay, E, & Şık, A. (2023). Ecological risk analysis with the help of geographic information systems in fruit growing; Manisa in Türkiye example. Intercontinental Geoinformation Days (IGD), 6, 20-23, Baku, Azerbaijan

2. Method

The study was developed on the basis of site selection analysis on ArcGIS model builder application. For risk analysis, severity and probabilities were determined and geographical layers that could cause yield loss in crop production were listed on the fault tree with the help of Analytical Hierarchy Process (AHP).

2.1. Dataset

Statistical and digital data obtained from various institutions were transferred to the geographic database created in ArcGIS 10.5 application. By converting statistical data into geographic data format, climate, soil, topography and water presence maps shown in Figure 1 were created.

30 years of statistical climatic data were transformed into geographic data by using "co-kriging" and inverse distance weighting (IDW) methods.

Climate Data	*Soil Data*
Temperature	Soil Depth
Average Temperature on a Monthly	Lithosolic
Maximum Temperature on a Monthly	Very Shallow (0-30cm)
Minimum Temperature on a Monthly	Shallow (30-50cm)
Extreme Maximum Temperature on a Monthly	Medium Deep (50-90cm)
Extreme Minimum Temperature on a Monthly	Deep (90-150cm)
Precipitation	Very Deep (>150cm)
Total Precipitation on a Monthly	Soil Erosion
Summer Months Total Precipitation	Wind Erosion
Total Annual Precipitation	Rain Erosion
Sunbathing	Land Use Capability
Total Sunbathing Times on a Monthly	1-8th Class Land
Annual Total Sunbathing Time	Available Land Use
Evaporation	Absolute Irrigated Farmland
Evaporation Values on a Monthly	Marginal Irrigated FarmLand
Average Annual Evaporation Amount	Absolute Dry Farmland
Humidity	Marginal Dry Farmland
Average Humidity value on a Monthly	Planted Agricultural Land
Spring Months Average Humidity value	Meadow and Pasture Areas
Summer Months Average Humidity Value	Wetlands
Wind	Forest Areas
Average Wind Speed on a Monthly	More Fields
Soil Temperature	Drainage
Water Data	*Topography*
Irrigation	Height
Streams	Slope
Dams and Lakes	Aspect

Figure 1. GIS Datasets

2.2. Agricultural Risk Analysis

Fault tree analysis (FTA) is a tool that can be used to help the analyst identify, evaluate, and analyze all root causes and pathways leading up to the occurrence of a particular event. (Jafarian et al. 2012)

To construct a tree, a top event is placed at the top and then connected to logic symbols representing the conditions for the event to occur, and then connected to the intermediate events that caused the top event.

The risks faced by farmers are grouped under two headings: ecological risks arising from natural events and economic risks arising from financial conditions. Today, risks such as increasing disasters (drought, hurricane, flood, frost, and hail), change of seasons, erosion, diseases and pests due to climate change are grouped under the title of ecological risks. In a recent study, researchers estimated that 23% of field crops were lost due to adverse weather conditions. In horticultural crops, this rate increases remarkably. (Islam at al., 2018).

In this study, spatial risk analysis was performed with a model developed in GIS on the determination of ecological risks in fruit growing. The process proceeds in three steps. The first step is to establish the model with the FTA method, the second step is to enter the intensities and probabilities of the causes, and the third and last step is to run the model developed on the ArcGIS software and create the maps.

In the climate, soil, topography and water presence layers, the values that may pose a risk during the growth of the plant and value of the severity and probability this risk are entered. Suitable areas where a selected plant grows with high yield, that is, with the least risk, will receive the lowest score, while areas where the growing conditions for the plant are unfavorable and contain high risk will receive the highest score in the risk matrix.

In addition, by assigning values between these layers according to their importance, the risk scores from the layers can be re-scored hierarchically thanks to the Weighted Overlay Analysis tool. (Ahmed et al., 2013).

First of all, the process begins with the collection of data and recording it on the database after standardization. Then, the risks that may cause yield loss for each product and the probability and severity values of these risks should be determined. AHP priority values created for each sub-risk value of the risk analysis will be determined. Finally, the final total risk map will be created by combining all sub-risk layers according to hierarchical ranking and scoring according to the fault tree logic in Figure 2.

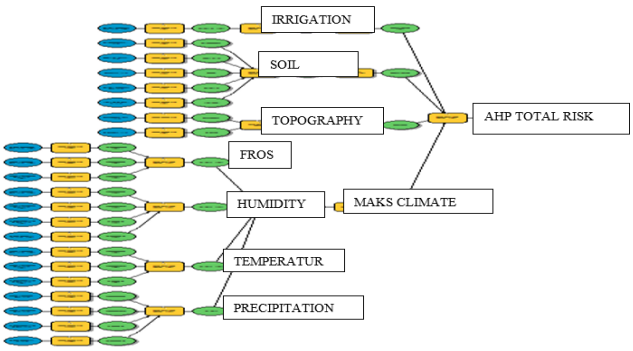

Figure 2. GIS Model Fault Tree

The Risk Matrix was created in table 1 using the formula "Risk= Severity x Probability (Probability)". According to the scores they got after the entered values;

- Green areas: 1-6 low risk (1 pointless risk)
- Yellow areas: 6 -12 medium risk
- Red areas: 12-25 are determined as high risk (25 irreparable risk).

Table 1. Risk Matrix

MATRIX	**Severity**				
Probability	**Very Light 1**	**Light 2**	**Moderate 3**	**Serious 4**	**Very Serious 5**
Very Small 1	Meanless 1	Low 2	Low 3	Low 4	Low 5
Small 2	Low 2	Low 4	Low 6	Medium 8	Medium 10
Medium 3	Low 3	Low 6	Medium 9	Medium 12	High 15
High 4	Low 4	Medium 8	Medium 12	High 16	High 20
Too High 5	Low 5	Medium 10	High 15	High 20	Irreparable 25

The GIS model assigns the probability values entered for the layers as values into each cell spatially. The average temperature value of a point selected as an example in Manisa in April is -1 °C and the severity of frost damage to the peach trees at this point is moderate 3. The average temperature value of the same point is -5 °C in March and +3 °C in May. Therefore, the average temperature value in March and May will be 4 and 1 frost severity. However, considering the blooming periods of the peach trees at the chosen point, the probability of frost in April, when the flowering is the highest, is 5, and the probability of frost is 3 and 1 due to the low flowering in March and May (Gerçekçioğlu, 2008; Gür et al., 2011).

Table 2. Risk Factors

Selected Point Layers	Temperature	Severity	Probabilities	Risk Severity	Frost Risk Factor
March	-5 °C	Serious 4	Medium 3	4x3 12	**Maximum Risk Severity 15**
April	-1 °C	Moderate 3	Too High 5	3x5 15	
May	+3 °C	Very Light 1	Small 1	1x2 1	

For this reason, for each risk factor, a sample table is filled as in Table 2 and a "Significance Evaluation" is made by using the AHP over the risk factors. AHP is used to prioritize risk factors among risk factors. This is done with the "Weighted Overlay" analysis tool in GIS.

After the criteria and sub-criteria are determined by using the Super Decision program, the criteria that affect each other can be determined by analyzing the interactions between the criteria, and the network structure in Figure 3 is created by making connections between the criteria, internal and external dependencies, and feedbacks with the help of the program.

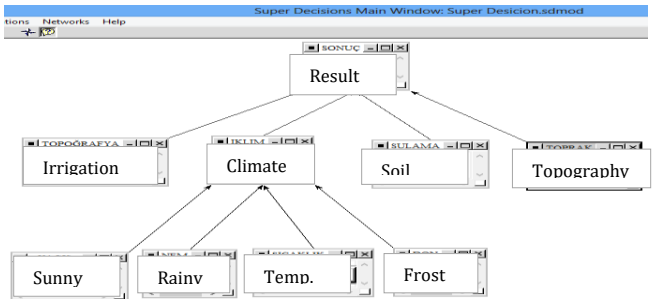

Figure 3. Super Decision Program Interface

After entering the risk probability and severity values of all layers under the climate, soil, topography and irrigation layer groups for the peach crop, the "superiority" importance scores among the risk factors are entered in Table 3.

After this stage, risk factors ranging from 0 to 25 values were obtained in each group. “AHP priority values” between climate, soil, topography and irrigation layers are entered in the “weighted overlay” tool in GIS. Since the sum of the values entered in the AHP is equal to the full value of "1", the final values will be "total risk" values between 0 and 25. In the peach sample, the “frost risk factor” took a value of 15 at a selected point. Again, the same point took the values of "humidity", "temperature", "precipitation" 10, 12, 8 by manual calculation. While calculating the climate risk factor, the value of 15, which is the maximum risk among the subgroups, was taken as shown in Table 3.

Table 3. Total Risk Superiority Table

Risk Factors			Severity Weight	Total Risk
Irrigation			0,10303	
Soil			0,11887	**Climate + Topography + Soil + Irrigation = 1**
Topography			0,29271	
	Layers	**Climate Max Risk**		
Climate	Frost Humidity Temperature Precipitation	Max (Frost, Humidity, Temperature, Precipitation)	0,4809	

Climate Risk Factor=Maksimum[Frost Risk, Humidity Risk, Precipitation Risk, Temperature Risk]

Climate Risk Factor=Maksimum[15, 10, 12, 8]=15

Again, in the manual calculations made for the same point, the soil took the risk value of 8, the topography 12, and the irrigation 18 risk value. The final ecological risk value was calculated by entering the prioritization scores for climate, soil, topography and irrigation with AHP.

Final Risk =Climate x 0,48 + Soil x 0,12 + Topography x 0,30 + Irrigation x 0,10

Final Risk =15 x 0,48 + 13 x 0,12 + 8 x 0,30 + 16 x 0,10 =12,40

3. Results

As a result of the process, it is seen that the point selected for the cultivation of peach crops is "moderate" in the risk matrix according to the calculations. This manual calculation for a single point was automatically performed on the GIS for millions of points and risk maps were generated for all sublayers and group layers separately, as shown in Figure 4.

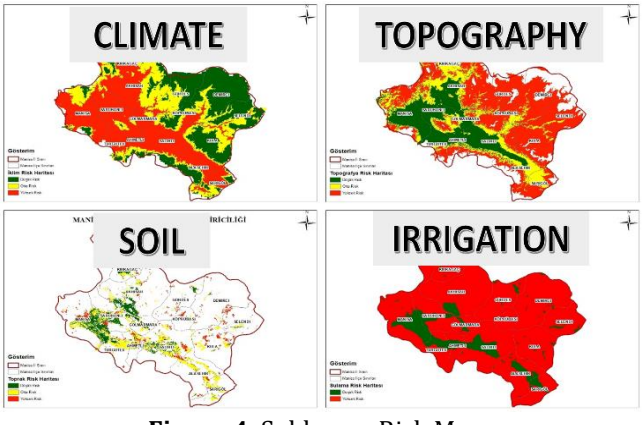

Figure 4. Sublayers Risk Maps

The negative impact of each sub-risk factor on crop yield is different. Therefore, the effect of the sub-risk factor on the total risk will be different according to the AHP priority value. The final risk map of the peach crop in Figure 5 was obtained by combining the climate, soil, topography and irrigation sub-risks as a result of hierarchical scoring.

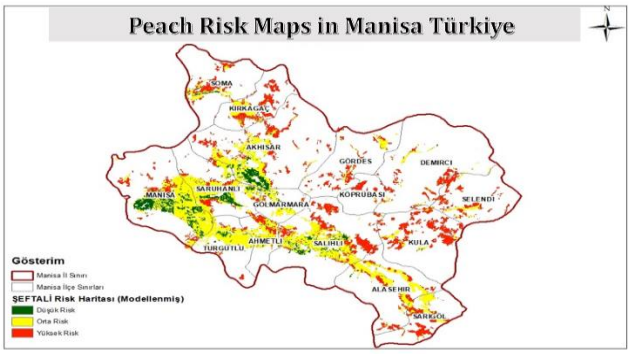

Figure 5. Peach Risk Maps in Manisa Türkiye

4. Discussion

According to the 2020 data of the Turkish Statistical Institute, the maximum peach yield per tree in Türkiye is 85 kg, and the average yield is 49 kg. According to the same data, peach yield is high in Manisa Province Center, Saruhanlı, Akhisar, Turgutlu, Salihli and Sarıgöl districts. In the high-risk red areas in the risk map created as a result of the model, the yield is low in direct proportion to the statistics, while the yield is high in the low-risk green areas. Most of the Manisa Plain appears to be medium risk. When the sub-risk factors are examined, the plain region seems to be low risk in soil, topography and irrigation layers, but climatic factors, which are the main limiting factors in fruit growing, resulted in high risk in the plain.

5. Conclusion

It has been determined that the peach is highly affected by the risk factors coming from the climate and topography layers. Although the soil and topography risk is low in the lands in the plain region, it has been adversely affected by climatic factors. Because in the months of high temperatures, the risks against diseases and pests increase due to climatic conditions. It is evaluated that the risk factors of peach can be reduced by cultural and mechanical climate improvements. As a result of the digitization of the maps, a total of 215.000 hectares of land can be grown in peach, and 27.500 hectares of these areas are low risk, 112.000 hectares are medium risk, and 67,000 hectares are high risk.

Thanks to the risk analysis model developed on GIS; Site selection and risk analysis can be made for all plant products whose climate, soil, topography and irrigation data and ecological demands are known. By examining the risk maps created, the risks that may cause yield loss during the production phase of agricultural activities can be determined in advance, and high yields can be obtained with the measures taken.

This study is a methodology study to encourage the use of developing technologies such as Geographic Information Systems (GIS) in land-based agriculture. It will become a necessity for us to use smart agricultural systems in order to meet the food needs of humanity against all the negativities experienced on our planet. Intelligent farming systems called Agriculture 4.0 will also be possible as a result of the integration of GIS and agricultural activities.

References

El-Sheikh, R. F. A., Ahmad, N., Shariff, A. R. M., Balasundram, S. K., & Yahaya, S. (2010). An agricultural investment map based on geographic information system and multi-criteria method. *Journal of Applied Sciences*, *10*(15), 1596-1602.

Gitz, V., Meybeck, A., Lipper, L., Young, C. D., & Braatz, S. (2016). Climate change and food security: risks and responses. *Food and Agriculture Organization of the United Nations (FAO) Report*, *110*(2).

Gerçekçioğlu, T., (2008). Tokat Kazova arazilerinin şeftali yetiştiriciliğine uygunluklarının coğrafi bilgi sistemi yardımıyla belirlenmesi. Tekirdağ Ziraat Fakültesi Dergisi, 5(2), 215-225.

Gür, İ., & Pırlak, L. (2011). Eğirdir ekolojik şartlarında yetiştirilen bazı şeftali çeşitlerinin fenolojik ve pomolojik özelliklerinin tespiti. Batı Akdeniz Tarımsal Araştırma Enstitüsü Derim Dergisi, 28(2), 27-41

Islam, M. M., Ahamed, T., & Noguchi, R. (2018). Land suitability and insurance premiums: A GIS-based multicriteria analysis approach for sustainable rice production. *Sustainability*, *10*(6), 1759.

Mokarram, M., Marnani, S. A., Moezi, A. A., & Hamzeh, S. (2011). Land suitability evaluation using ordered weight averaging with fuzzy quantifier in Shavoor plain, Iran. *Research on Crops*, *12*(2), 593-599.

Nyeko, M. (2012). GIS and multi-criteria decision analysis for land use resource planning. Journal of Geographic Information System, 4(04), 341-348.

Pablo J., Hubbard, N., & Loudjani, P. (2014). Precision Agriculture: An Opportunity for Eu Farmers - Potential Support with The Cap 2014-2020, Directorate-General for Internal Policies, Agriculture and Rural Development, European Parlement.

Sharma, R., Kamble, S. S., & Gunasekaran, A. (2018). Big GIS analytics framework for agriculture supply chains: A literature review identifying the current trends and future perspectives. *Computers and Electronics in Agriculture*, *155*, 103-120.

Tuncay, D., & Demirel, N. (2017). Reliability analysis of a dragline using fault tree analysis. Bilimsel Madencilik Dergisi, 56(2), 55-64.

Yasin, A., & Keskin, İ. (2018). Determination of factors affecting wheat production in altınekin district by risk analysis, Selcuk Journal of Agriculture and Food Sciences, 32 (3), 496-501

Yeniay, E., & Şık, A. (2022). Risk Analysis Using Geographic Information Systems by Determining the Factors Affecting Yield in Plant Production: A case study from Ankara, Turkey. Journal of Agricultural Sciences, 28 (4), 677-69

6th Intercontinental Geoinformation Days

igd.mersin.edu.tr

Using GIS to identify and assess renewable energy sources

Imamverdiyev Nijat Sohrab

Institute of Geography, Ministry of Science and Education of Azerbaijan

Keywords
Renewable energy
Energy assessment
GIS
Energy mapping
Energy resources

Abstract

This article describes the use of Geographic Information Systems (GIS) in identifying and assessing alternative energy sources. GIS is a powerful tool that can be used to analyze various factors, such as geography, climate, and land use, to identify the most suitable locations for renewable energy projects. This paper provides an overview of the different types of alternative energy sources and their potential for energy production. The use of GIS in mapping and analyzing solar, wind, hydroelectric, geothermal, biomass, and tidal energy resources are discussed, along with case studies and examples of successful projects. The paper first presents an overview of GIS technology and its application in energy assessment. The material also highlights the importance of stakeholder engagement and community involvement in the planning and development of alternative energy projects. Also, it demonstrates the potential of GIS in promoting the transition to a more sustainable and renewable energy future. Finally, the paper highlights the benefits of using GIS for energy analysis, including its ability to provide accurate and detailed information about the potential of different energy sources in a specific location. Overall, in this article aims to demonstrate the importance of GIS technology in promoting the adoption of alternative energy sources and contributing to a more sustainable energy future.

1. Introduction

GIS (Geographic Information System) is a powerful tool that can be used to identify and assess alternative energy sources. GIS is enabling new energy production by identifying sites of maximum energy potential and optimized economic development while minimizing environmental impact. GIS can be used to explore renewable energy resources using remote sensing and GIS (Avtar et al. 2019). The renewable energy technical potential of a technology is its achievable energy generation given system performance, and topographic, environmental, and land-use constraints. The benefit of assessing technical potential is that it establishes an upper-boundary estimate of development potential (Lopez et al. 2012). It can help identify areas with high potential for developing renewable energy sources (RES), and regions with restrictions on their exploitation, such as environmentally or culturally sensitive areas (Jordao, 2010).

GIS can save time and money when determining where and how renewable energy sources should be exploited and used (Jordao, 2010). It can also help monitor fluctuations over time, evaluate the feasibility of proposed projects and predict their effects on the environment (Resch et al. 2014).

Furthermore, one example of a successful renewable energy project that used GIS is the Cape Wind Project in Massachusetts, USA. The Cape Wind Project is a proposed offshore wind farm that aims to generate up to 468 MW of electricity, enough to power more than 200,000 homes. To determine the best location for the wind farm, the developers used GIS to analyze various factors such as wind speed, ocean depth, and proximity to shore. They collected data from various sources such as weather stations, buoys, and remote sensing, to create a wind resource map of the area (Kimmell and Stalenhoef, 2011). They also used GIS to analyze the seabed to identify areas with suitable soil conditions for anchoring the turbines. Besides, GIS is enabling new energy production by identifying sites of maximum energy potential and optimized economic development while minimizing environmental impact (Lopez et al. 2012).

2. Material and method

Geographic Information Systems (GIS) were used to identify and assess renewable energy sources by

* **Corresponding Author**

*(imamverdiyev.nicat@gmail.com) ORCID ID 0000-0002-5573-0209

Cite this study

Sohrab, I. N. (2023). Using GIS to identify and assess renewable energy sources. Intercontinental Geoinformation Days (IGD), 6, 24-27, Baku, Azerbaijan

combining spatial data on various factors, such as land use, topography, climate, and existing infrastructure. It was taken the following steps for this:

Data collection: Gather data on topography, climate, land use, etc. Data integration: Integrate the different types of data into a GIS software such as ArcGIS or QGIS. Analysis: Performed spatial analysis to identify areas that are suitable for renewable energy sources, such as wind, solar, hydro, and geothermal. Mapping: Created maps showing the potential locations for renewable energy sources based on the analysis. Evaluation: The potential of each renewable energy source and comparing them to one another. Implementation: Determination of the most viable renewable energy source based on the evaluation.

There are several software options that can be used for renewable energy analysis. Here are a few of the most used: ArcGIS, QGIS, GRASS GIS, Wind Navigator and PVsyst. These GIS software options are used by renewable energy developers to identify and assess renewable energy sources, analyze the potential for energy production, and make decisions about renewable energy projects.

3. Results

GIS maps allow users to assess the potential for renewable energy sources in particular areas based on criteria such as wind speed, solar irradiance, and topography. For instance, to identify suitable sites for wind turbines, GIS tools can generate maps of wind speed and direction along with data from remote sensors based on topography. The same methods are used to identify suitable areas for solar panel installation.

One example of the use of GIS in renewable energy planning is the Renewable Energy Zones (REZ) Toolkit, which provides a step-by-step process for identifying and designating renewable energy zones (Lee and Roberts, 2018). This toolkit includes steps for process design, candidate zone selection, transmission options development, final transmission plan designation, and transmission system upgrade. GIS is used extensively in this process for renewable energy resource assessment, candidate zone identification, and transmission system design.

Another study applies the Analytic Hierarchy Process (AHP) and develops a systematic approach and decision support system to assess energy alternatives and help municipalities select the most suitable alternatives (Budak et al. 2019). This methodology involves integrating experts' input and data analytics and helps decision-makers form long-term strategies for renewable energy development.

This study was investigated by applying spatial analysis in GIS. GIS spatial analyses offer an effective method for identifying and assessing renewable energy sources, providing a comprehensive understanding of the potential for renewable energy in a given area. GIS (Geographic Information System) technology can be utilized to identify and assess renewable energy sources (Maclaurin et al. 2019). Spatial analysis is a crucial tool within GIS that allows users to combine and analyze data from various sources, helping to answer complex spatial questions (Ramachandra and Shruthi, 2007). This analysis calculates renewable energy capacity, generation, and cost based on geospatial intersection with grid infrastructure and land-use characteristics.

It is determined that the spatial analysis mapping method in Azerbaijan has a significant untapped potential for renewable energy sources (IEA, 2020). The potential of renewable energy sources, which are economically viable and technically feasible, is estimated at 27 000 MW, including 3 000 MW of wind energy, 23 000 MW of solar energy, 380 MW of bio-energy potential, and 520 MW of mountain rivers (The Ministry… 2022). Azerbaijan's renewable energy potential is estimated to be at around 27,000 megawatts, the largest share of which belongs to solar energy (23,000 megawatts) (Jafarova 2019). According to a report by the International Renewable Energy Agency (IRENA), Azerbaijan has the potential to generate over 27,000 megawatts of wind and solar power combined. This is a significant figure, considering that Azerbaijan's current electricity demand is around 7,000 megawatts. In recent years, Azerbaijan has made significant strides in renewable energy development, including the construction of some wind and solar power plants across the country. One such example is the Gobustan Wind Farm, which has a capacity of 50 megawatts and produces enough electricity to power around 35,000 homes. Generally, Azerbaijan has excellent solar power potential. The country has an estimated technical potential of around 23,000 MW for solar energy generation and receives 2,400 to 3,200 sunshine hours annually with an estimated solar intensity of 1,500 kWh/m^2 to 2,000 kWh/m^2 (The Ministry… 2022). Additionally, Azerbaijan has significant prospects for renewable energy development, including solar energy. The country has excellent solar resources and is considered to be a suitable area for solar energy potential. Therefore, it can be inferred that Azerbaijan is a suitable location for the deployment of solar energy infrastructure.

Azerbaijan has immense potential for offshore wind power, with a technical offshore wind resource of around 157GW - over 20 times the country's current installed energy capacity. Current wind farms are mainly located in the regions of Absheron, Khizi, and Gobustan, but other regions of Azerbaijan also have the potential based on wind power density (Jafarova, 2019).

In addition, in 2019, Azerbaijan adopted a law on renewable energy which aims to increase the share of renewable energy in the country's energy mix to 30% by 2030. The government has also implemented several incentives to attract investment in the sector, including tax breaks for renewable energy projects and a feed-in tariff system for electricity generated from renewable sources. Currently, the largest renewable energy project in Azerbaijan is the 200 MW wind farm in the Caspian Sea, which is expected to be completed in 2022. The country also has several solar power projects in the pipeline, including a 240 MW solar power plant in the Gobustan region. In addition to wind and solar power, Azerbaijan has the potential for geothermal and biomass energy. The government has installed some energy stations in the country. Here are a few examples (The Ministry, 2022):

1. Gobustan Wind Farm: This 52 MW wind farm, located in the Gobustan region, was commissioned in 2019 and is currently the largest wind farm in Azerbaijan. The project was developed by the state-owned company Azerenerji and is expected to generate around 200 GWh of electricity per year.

2. Solar power plant in Pirallahi: This 10 MW solar power plant, located on the Pirallahi Island in the Caspian Sea, was commissioned in 2019. The project was developed by the Norwegian company Scatec Solar and is expected to generate around 16 GWh of electricity per year.

3. Geothermal power plant in Nakhchivan: This 8 MW geothermal power plant, located in the Nakhchivan Autonomous Republic, was commissioned in 2018. The project was developed by the Turkish company MB Holding and is expected to generate around 60 GWh of electricity per year.

4. Baku White City Solar Power Plant: This 1 MW solar power plant, located in the Baku White City development, was commissioned in 2018. The project was developed by the German company Solarwatt and is expected to generate around 1.2 GWh of electricity per year.

The government of Azerbaijan has set ambitious targets for the development of renewable energy in the country. The primary target is to increase the share of renewable energy in the country's energy mix to 30% by 2030. This target is part of the country's broader efforts to reduce its dependence on fossil fuels and diversify its energy sources. In addition to the 30% target, the government has set a number of specific targets for different types of renewable energy. For example, the goal is to install 420 MW of wind power capacity and 650 MW of solar power capacity by 2025. The government has also set a target of 440 MW of geothermal power capacity by 2030. To achieve these targets, the government has implemented a range of incentives and support measures for renewable energy projects, including feed-in tariffs, tax breaks, and simplified permitting processes (Jafarova, 2019).

4. Discussion

While Azerbaijan has the potential to become a leader in renewable energy, there are several challenges that must be addressed to achieve this goal. Some of the main challenges facing the renewable energy sector in Azerbaijan include:

1. Lack of investment: Despite the incentives offered by the government, investment in renewable energy projects in Azerbaijan remains relatively low. This is partly due to the country's dependence on natural gas exports, which has traditionally been the main source of revenue for the government and the economy.

2. Limited infrastructure: Azerbaijan's renewable energy sector is still in its early stages, and there is limited infrastructure in place to support it. This includes a lack of transmission lines and interconnectors to connect renewable energy sources to the national grid.

3. Regulatory barriers: The regulatory framework for renewable energy in Azerbaijan is still developing, and there are several barriers to entry for investors. These include bureaucratic procedures, complex permitting processes, and a lack of transparency in decision-making.

4. Technical issues: Azerbaijan's climate and terrain can make it difficult to develop certain types of renewable energy, particularly wind power. There are also technical challenges associated with integrating intermittent energy sources like wind and solar into the grid.

5. Public awareness: There is still a lack of public awareness and understanding of renewable energy in Azerbaijan, which can make it difficult to build support for the sector and attract investment.

Overall, addressing these challenges will be critical to the development of Azerbaijan's renewable energy sector and the achievement of its ambitious targets for renewable energy deployment. Thus, Azerbaijan's renewable energy potential is largely untapped, with practical deployment limited compared to the scale of available resources and long-term ambitions (IEA, 2020).

To promote the development of renewable energy in the country, Azerbaijan passed the "Law on Renewable Energy" in May 2021, which established a regulatory framework for renewables and support mechanisms for renewable energy projects. This law aims to promote the use of renewable energy sources in the production of electricity, reduce greenhouse gas emissions, and increase energy efficiency.

The government of Azerbaijan has also taken other measures to promote renewable energy, such as setting a target to increase the share of renewable energy in the country's electricity mix to 30% by 2030 [3]. The country has also participated in international renewable energy initiatives, such as the International Renewable Energy Agency (IRENA) and the European Union's Eastern Partnership initiative, to share knowledge and best practices and to attract investment in the renewable energy sector (IEA, 2020).

5. Conclusion

GIS-based spatial analyses are an important aspect of renewable energy research, enabling researchers to make informed decisions about energy planning and production. GIS is an important tool for conducting spatial analyses related to renewable energy research. This technology enables researchers to produce maps, analyses, models, applications, and visualizations that inform energy planning and production. It was determined that Azerbaijan has significant potential for renewable energy development, with excellent solar and wind resources and significant prospects for biomass, geothermal, and hydropower. As of 2020, the country had installed 12 large and 7 small hydroelectric plants, 6 wind, 10 solar, and 6 biomass power plants, with an installed capacity of 420 megawatts (MW.

Moreover, it is noted that Azerbaijan has a high potential for renewable energy sources, with an estimated 27,000 MW of economically viable and technically feasible potential, including 3,000 MW of wind energy, 23,000 MW of solar energy, 380 MW of bioenergy potential, and 520 MW of mountain rivers. In

2019, the total renewable energy supply in Azerbaijan was around 66%, out of which hydropower, wind, solar, and biomass power plants were the main sources of renewable energy. Azerbaijan has 12 big and 7 small hydroelectric plants, and 6 wind, 10 solar, and 6 biomass power plants that were constructed from 2018 to 2020, which are expected to have an installed capacity of 420 MW.

Acknowledgement

Acknowledgements of support for the Ministry of Energy of the Republic of Azerbaijan are welcome.

References

Avtar, Sahu, Aggarwal, Chakraborty, Kharrazi, Yunus, Dou, et al. (2019). Exploring Renewable Energy Resources Using Remote Sensing and GIS—A Review. Resources, 8(3), 149. MDPI AG. Retrieved from http://dx.doi.org/10.3390/resources8030149

Budak, G., Chen, X., Celik, S., & Ozturk, B. (2019). A systematic approach for assessment of renewable energy using analytic hierarchy process. Energy, Sustainability and Society, 9, 1-14.

IEA (2020), Azerbaijan energy profile, IEA, Paris https://www.iea.org/reports/azerbaijan-energy-profile, License: CC BY 4.0

Jafarova, E. (2019). Renewable Energy Renews Azerbaijan's Energy Strategy. The Georgetown Journal of International Affairs, NW Washington, D.C. 20057.

Jordao, Ticiano Costa. (2010). GIS and renewable energy sources. GIM International, 24.

Kimmell, K., & Stalenhoef, D. S. (2011). The cape wind offshore wind energy project: a case study of the difficult transition to renewable energy. Golden Gate U. Envtl. LJ, 5, 197.

Lee, N., & Roberts, B. J. (2018). Technical Potential Assessment for the Renewable Energy Zone (REZ) Process: A GIS-Based Approach (No. NREL/TP-7A40-71004). National Renewable Energy Lab. (NREL), Golden, CO (United States).

Lopez, A., Roberts, B., Heimiller, D., Blair, N., & Porro, G. (2012). Us renewable energy technical potentials. a gis-based analysis (No. NREL/TP-6A20-51946). National Renewable Energy Lab. (NREL), Golden, CO (United States).

Maclaurin, G., Grue, N., Lopez, A., Heimiller, D., Rossol, M., Buster, G., & Williams, T. (2019). The renewable energy potential (rev) model: a geospatial platform for technical potential and supply curve modeling (No. NREL/TP-6A20-73067). National Renewable Energy Lab. (NREL), Golden, CO (United States).

Ramachandra, T. V., & Shruthi, B. V. (2007). Spatial mapping of renewable energy potential. Renewable and sustainable energy reviews, 11(7), 1460-1480.

Resch, B., Sagl, G., Törnros, T., Bachmaier, A., Eggers, J. B., Herkel, S., ... & Gündra, H. (2014). GIS-based planning and modeling for renewable energy: Challenges and future research avenues. ISPRS International Journal of Geo-Information, 3(2), 662-692.

The Ministry of Energy of the Republic of Azerbaijan: The Use of Renewable Energy Resources in Azerbaijan [Electronic resource] / Aprel 24, 2022. URL: The Use of Renewable Energy Resources in Azerbaijan |Ministry of Energy of Azerbaijan (minenergy.gov.az).

6th Intercontinental Geoinformation Days

igd.mersin.edu.tr

Locating the best place to build a desalination plant with artificial intelligence (Chabahar study area, Iran)

Saeed Rasti*[1], Fatemeh Tamnia[2], Mostafa Mahdavifard[3], Majid Kiavarz Moghaddam[1]

[1] *University of Tehran, Department of Remote Sensing and GIS Tehran, Iran*
[2] *University of Kharazmi, Department of Remote Sensing and GIS Tehran, Iran*
[3] *University of Tabriz, Department of Remote Sensing and GIS Tabriz, Iran*

Keywords
Locating
Desalination
Artificial intelligence
GIS
Chabahar

Abstract

Due to the increase in world population, water consumption will increase significantly It has become one of the main problems of drinking water supply. On the one hand, compensable water resources are declining, and on the other hand, in some areas due to drought due to lack of rainfall and lack of access to surface and groundwater resources, drilling wells does not help to solve this problem. Therefore other methods such as water desalination or desalination should be considered. In Iran, due to the climatic conditions of the country, the need to produce drinking water in low capacities, for sparsely populated and remote areas, is an issue that has received less attention so far. While in arid and desert areas, which are large in the central regions of Iran, on the one hand, the need for fresh water is one of the main problems of the people of these areas and on the other hand, solar energy with appropriate radiation intensity in this area available. Artificial intelligence is expanding in all sciences and all walks of life, and this technology is advancing day by day. Scientists hope that thanks to recent advances in artificial intelligence, control and monitoring methods for water treatment plants will be simpler and cheaper than before. This research, uses artificial intelligence and criteria such as the topography of the region, the distance between Chabahar and Konarak, and type of land use. Distance from communication roads, distance from the river, proximity to water areas (beach) to the location of desalination has been done.

1. Introduction

Recycling effluents, rainwater collection, bottled water, and cross-country pipelines are some of the alternatives. There are advantages and disadvantages to each of these strategies. Desalination is a low-cost approach of supplying drinking water to places where there is water scarcity. Desalination is the most well-known method arising from changes in both the availability and demand for freshwater supplies, both of which are anticipated to increase exponentially in future years (Bremere, 2001).

One of the most promising techniques to deal with water shortages is desalination which converts mildly saline or seawater to drinkable freshwater (Grubert, et al., 2014; Ziolkowska., 2015).

In terms of sea areas, the largest number of desalination plants exist in the Gulf with a total seawater desalination capacity of approximately 12.1 Mm3/d—or about 44% of the worldwide daily production. The largest producers of desalinated water in the Gulf (and worldwide) are Saudi Arabia (25% of the worldwide seawater desalination capacity, of which 11% are in the Gulf region, 12% in the Red Sea region, and 2% in unknown locations), the United Arab Emirates (23% of the worldwide seawater desalination capacity), and Kuwait (6%)) El-Ghonemy, 2012).

Access to appropriate and sustainable water resources is one of the most important factors for a country's long-term development. This is especially critical in the Middle East and countries surrounding the Persian Gulf because of its placement in the world's dry belt. Desalination is one of the human techniques to deal with a water shortage, and it is a technology that the Arab countries of the Persian Gulf have employed to supply water. Despite its unlimited access to seawater in the Persian Gulf and the Sea of Oman and the great potential for water desalination, Iran has not been effective at using it, and continues to have water shortages and secondary issues, making a barrier to increasing economic progress. Despite the high efficiency of water

* **Corresponding Author**

*(saeedrasti13744@gmail.com) ORCID ID 0000 – 0002 – 8159 – 9144
(tamniafateme417@gmail.com) ORCID ID 0009-0003-1747-2258
(mostafamahdavi842@gmail.com) ORCID ID 0000 – 0001– 9811 – 5428
(kiavarzmajid@ut.ac.ir l) ORCID ID 0000 – 0003 – 0335 – 3795

Cite this study

Rasti, S., Tamnia, F., Mahdavifard, M., & Moghaddam, M. K. (2023). Locating the best place to build a desalination plant with artificial intelligence (Chabahar study area, Iran). Intercontinental Geoinformation Days (IGD), 6, 28-31, Baku, Azerbaijan

desalination, finding a suitable location for desalination plants is one of the most difficult challenges facing water basin planners and managers. They must, in accordance with the principle of low-consequence development, inflict the least environmental damage on the environment, and at the same time, take into account future needs in accordance with the framework of sustainable development without destroying resources. Many studies have been conducted around the world and in Iran to develop optimal methodology and to identify the most suitable sites for desalination. There have been studies on the selection of suitable sites for desalination plants, which include solar desalination plants in Türkiye (Aydin et al., 2020).

2. Methodology

2.1. Study area

Chabahar is one of the southeastern cities of Baluchistan, Iran and the only ocean port in the country, which is located on the shores of the Makran Sea and the Indian Ocean. Chabahar port is of great importance due to its strategic location, which is the closest way for landlocked countries in Central Asia to access open waters. It is located at 60 degrees and 37 minutes east longitude and 25 degrees and 17 minutes north latitude. It is bounded on the north by Iranshahr and Nikshahr counties, on the south by the Oman Sea, on the east by Pakistan and on the west by the provinces of Kerman and Hormozgan. The area of Chabahar city is about 9739 square kilometers, the height of this city is 7 meters above sea level and it has 130 kilometers of land border and about 115 kilometers of water border in the Oman Sea. The population of Chabahar city is 291910 people.

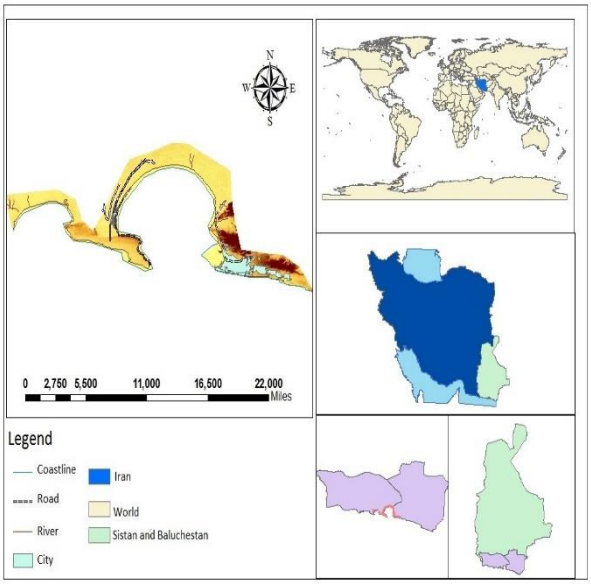

Figure 1. Geographical location of Chabahar in southeastern Iran

2.1.1. Artificial neural network

An artificial neural network is an idea for processing information that is inspired by the biological nervous system. Like the human brain, it processes information. In a nervous system, neurons (nerve cells) are known to be the main processing element for Problem solving works in unison: ANNs, like humans, learn by example and transfer knowledge, or the law behind experimental data, to the network structure by processing it into experimental data. It is called intelligent because it learns general rules based on calculations on numerical data or examples. Each network consists of at least two layers, an input layer and an output layer. At the same time it can have several hidden layers between the input and output layers, usually a single neuron with multiple inputs alone is not enough to solve the problem.

2.2.1. How to prepare data in GIS software

Before building a neural network, data needs to be prepared. First, we select the desired parameters based on the project theme. After selecting the effective parameters, data collection is needed. The effective parameters for identifying the area need desalination water, inter-city distance, geological structure, land use, proximity to communication roads, distance from the river, and proximity to water areas (Beach).

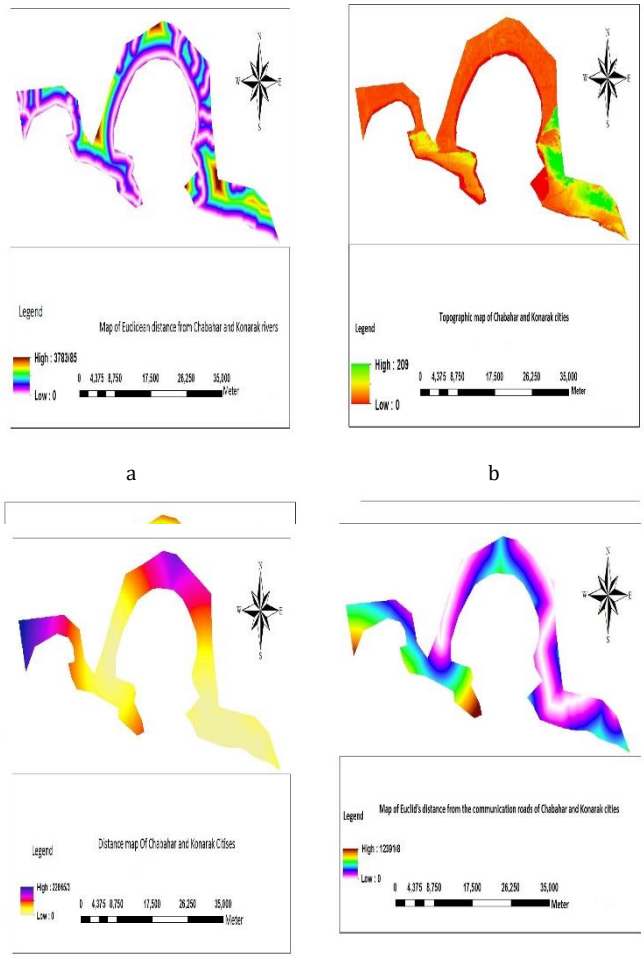

Figure 2. Map prepared from data in GIS software(a), inter-city distance (b), geological structure (c), proximity to communication roads (d), land use (e), proximity to water areas (Beach). Are. (f) proximity to communication roads

2.2.3. Compiling an artificial neural network

The compilation is essentially the application of a descending random gradient to the entire neural network. optimizer is a method for optimizing weights, such as adam, rmsprop .... The first parameter is an algorithm that is to be used to obtain the optimal set of weights in the neural network. . There are several types of these parameters. One of the most effective algorithms for this is Adam. The second parameter is the loss function in the stochastic reduction gradient algorithm. Because classes are binary, the binary-crossover loss is used. Otherwise, categorical_crossentopy is used. The final argument is the criterion used to evaluate the "model". In this example, "(accuracy) is used to evaluate the model. As a result, we fit the data to our model.

2.2.4. Regularization term

Small changes in input size to changes in output can solve these problems Used with a common term in harms. This is the middle that measures the banks in the neural network. Adding it causes damage can reduce our weight and bias. L1, L2 are used. In weight L1 is absolute, L2 in weight is multiplied by two

Overfitting in machine learning occurs when the model learns the details of the noise in the dataset and thus performs poorly on the test dataset. This happens when there is a big difference between the accuracy of the test set and There is a training set or when there is a high variance when applying cross-validation K fold is available. In artificial neural networks, this problem is addressed using a method called "Dropout Regularization". Dropout Regularization works by accidentally deactivating some neurons in each repetition of training to prevent them from becoming too independent of each other.

```
model_3 = Sequential ([Dense (10, activation='sigmoid',
t_shape= (9,)), kernel_regularizer=regularizers.l2 (0.01),
inpuDropout (0.3),
=regularizers.l2 (0.01)), Dense (5, activation='relu',
kernel_regularizer Dropout (0.3), (1,
activation='sigmoid', Dense
kernel_regularizer=regularizers.l2 (0.01)),])
model_3.compile
(optimizer='sgd',loss='binary_crossentropy',
metrics= ['accuracy'])
hisr_3=model.fit(x_train,y_train,batch_size=10,epochs=1
00, ,validation_data=(x_val,y_val))
```

2.2.5. Adjust parameters

Once the desired accuracy is achieved, the parameters can be adjusted for higher accuracy. Grid search enables the user to calculate various parameters to get the best parameters.

```
from sklearn.model_selection import GridSearchCV
```

Also, the make_classifier function must be edited according to the following tutorial. A new variable called optimizer is also created to add more than one optimizer to the params variable.

```
def make_classifier(optimizer):
() classifier=Sequential
classifier.add(Dense(10,kernel_initializer =
"uniform",activation='relu'))
classifier.add(Dense(1,activation = 'relu'))
classifier.compile(optimizer=optimizer,loss =
"binary_crossentropy",metrics = ["accuracy"])
return classifier classifier = KerasClassifier(build_fn =
make_classifier)
params={'batch_size':[5,10],'nb_epoch':[1,10],
'Optimizer':['adam','rmsprop'] }
```

batch size: The number of courses and the optimizer function is among these parameters.

rmsprop and adam: Here they are as optimizers**.**

Grid Search is then used to test these parameters. Grid Search function from the parameter estimator that was defined. Demands scoring and number of k-folds

```
grid search= GridSearchCV (estimator=classifier,
param_grid= prams, scoring='accuracy', cv= 10)
```

```
grid search= grid search.fit (x_trian, y_trian)
```

You can get the best selection of parameters using the best_params from the grid search object. Similarly, best_score is used to get the best score.

```
best_param= grid_search.best_params_best_param
    {'batch_size': 5, 'epochs': 10, 'optimizer': 'rmsprop}'

best_accuracy=grid_search.best_score_best_accuracy
0.812
```

To predict new data:

```
Kol=pd.read_csv("/home/khu/Downloads/dade20.csv"
)
```

Calling data that has no output and the output of this data is predicted using training data

```
test_x=data1.drop (['X','Y', 'class', 'SUTIABILIT'],
axis=1).values test_x
x_kol=kol.iloc [: 2:10]
x_kol=x_scale.fit_transform(x_kol)
kol_prdict=model. Predict (x_kol)
kol_prdict
```

3. Results

Neural network training based on trial and error so that the optimal network arrangement is achieved by changing the number of hidden layers and neurons of that type of moving function of training algorithms and

the number of repetitions of the training stage to calculate the output coefficient. The optimal model is when the neural network performs the best fit with the least error (Saadi et al., 1399). 2% loss performance. The line diagram (1,2) shows the correlation between the loss function and the accuracy of the training and validation data.

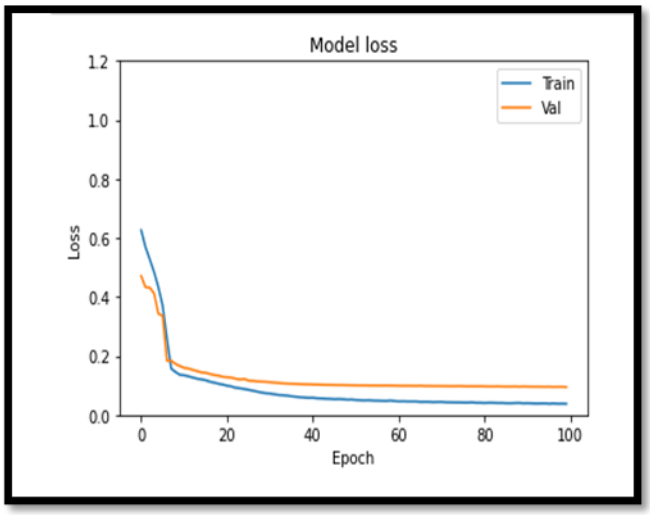

Figure 3. Correlation diagram of the function of educational data loss and validation

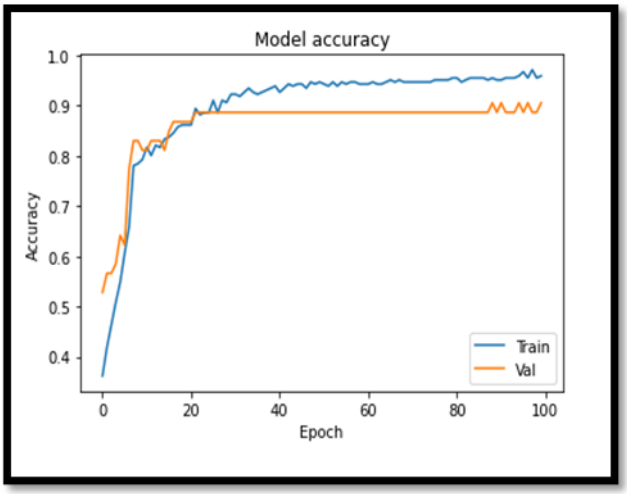

Figure 4. Correlation between the accuracy and validity of educational data

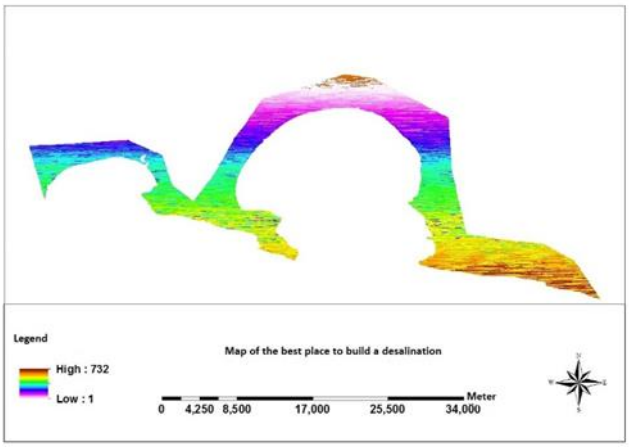

Figure 5. Map of the best place to build a desalination plant

4. Conclusion

Today, with the shortage of fresh water, humans have turned to use other available non-fresh water sources such as seawater and oceans, and in this regard, new technologies in the field of seawater treatment and desalination have been formed. Due to its proximity to the waters of the Oman Sea and the Persian Gulf, Iran has a good potential for the development of desalination units and the production of fresh water for industrial, agricultural, and even drinking purposes. It is necessary to increase and develop desalination units. It requires compliance with environmental laws and standards to prevent the increase of pollutants in the marine environment due to the effluent of these units. According to the results and output of Figure 3, the best places to build on the map according to the criteria are dark yellow to dark red.

References

Aydin, F., & Sarptas, H. (2020). Spatial assessment of site suitability for solar desalination plants: a case study of the coastal regions of Turkey. Clean Technologies and Environmental Policy, 22, 309-323.

Bremere, I., Kennedy, M., Stikker, A., & Schippers, J. (2001). How water scarcity will effect the growth in the desalination market in the coming 25 years. Desalination, 138(1-3), 7-15.

El-Ghonemy, A. M. K. (2012). Future sustainable water desalination technologies for the Saudi Arabia: a review. Renewable and Sustainable Energy Reviews, 16(9), 6566.

Grubert, E. A., Stillwell, A. S., & Webber, M. E. (2014). Where does solar-aided seawater desalination make sense? A method for identifying sustainable sites. Desalination, 339, 10-17.

Ziolkowska, J. R. (2015). Is desalination affordable?—regional cost and price analysis. Water Resources Management, 29, 1385-1397.

6th Intercontinental Geoinformation Days

igd.mersin.edu.tr

Investigation of drought status of Konya Closed Basin with Percent of normal index

Beyza Değişli [1], Durdane Akçay [1], Hanife Nur Şimşekli[1], İsa Alperen Pınar [1], Gaye Aktürk [2], Bilal Candan [1], Mehmet Ali Tamer *[1], Vahdettin Demir [1], Mehmet Faik Sevimli [1]

[1]*KTO Karatay University, Engineering and Natural Sciences Faculty, Civil Engineering Department, Konya, Türkiye*
[2]*Kırıkkale University, Engineering and Natural Sciences Faculty, Civil Engineering Department, Kırıkkale, Türkiye*

Keywords
Drought
Konya Closed Basin
PNI
IDW
Interpolation

Abstract

In this study, meteorological drought situation of Konya Closed Basin was analyzed by PNI method. In the analysis, annual total precipitation data covering the records of 11 meteorological stations in the basin between 1972 and 2020 were used. Drought classes obtained from the analyzes made according to the PNI index were interpreted in the entire data period and the results of the last years (2015-2020) were mapped using the Inverse Distance Weighting (IDW) method. When the results were examined, it was determined that 2 of the 11 stations (Konya and Niğde stations) in the region had 4 extreme dry years at most. According to the PNI method analyzes of the last 5 years of the basin, it was observed that the driest year was 2020. The IDW map provides information about the spatial distribution of results. When the IDW interpolation map of the results was examined, it was observed that the drought values changed in our basin over time (2015-2020).

1. Introduction

Drought is an event that can significantly affect the level of welfare of the people with the country's economy and development capacity. For this reason, the evaluation of drought scenarios that may occur in the future has great importance for many components of the country's economy such as agriculture, energy, ecology, biodiversity, forestry, health and water sectors (Osuch et al. 2016).

Drought is a meteorological natural catastrophe that seriously affects daily life, restricts people's activities, and creates ecological issues. The time of occurrence, duration, severity and area of impact of drought change every year.That is why drought leads to environmental, social and economic impacts.

Over time, changes in temperature and precipitation in a region cause important events that affect human life and should be taken seriously. As a result of the constantly increasing trend of temperature values and the continuous decreasing trend of precipitation values, drought-desertification phenomenon, which is a phenomenon that takes place in long periods, occurs.

On the contrary, the continuous increase in precipitation or the tendency of instantaneous precipitation to increase continuously cause dangers such as floods and landslides.

In this study, meteorological drought situation in Konya Closed Basin was analyzed by PNI method. The annual total precipitation data recorded over the years from 11 meteorological stations in the basin were used. The drought classes obtained according to the PNI index were interpreted in the entire data period and the situation in recent years (2015-2020) was examined with the IDW interpolation maps obtained using the value of the last years.

2. Method

2.1. Percentage Index of Normal (PNI)

The Percentage Index of Normal (PNI) is a method widely used among drought indices and is based on precipitation data. PNI is a method that is widely used among drought indices and is based on precipitation data. It is a method that finds the PNI value by dividing

* **Corresponding Author**

*(mehmet.ali.tamer@ogrenci.karatay.edu.tr) ORCID ID 0000-0001-7656-6543

Cite this study

Değişili, B., Akçay, D., Şimşekli, H. N., Pınar, İ. A., Aktürk, G., Candan, B., Tamer, M. A., Demir, V., & Sevimli, M. F. (2023). Investigation of drought status of Konya Closed Basin with Percent of normal index. Intercontinental Geoinformation Days (IGD), 6, 32-35, Baku, Azerbaijan

the amount of precipitation in a certain time period by the average amount of precipitation in the same time period and multiplies it by a multiplier of 100 and finds the PNI value converted to a percentage. The general equation of the method is given below.

$$\text{PNI} = \frac{P_i}{P_{i(avr)}} \times 100 \qquad (1)$$

Here, PNI, Percentage of Normal Index value. Pi(mm), the current amount of precipitation. Pi (avg, mm) refers to the average amount of precipitation (McKee et al. 1993). The classification for the 12-month period given in Table 1 is included. According to PNI values, there are 4 different drought classes for 5 different periods.

Table 1. Percentage Index Classes of Normal

Period	Normal	Slightly Arid	Medium Arid	Severe Arid
1	> % 75	% 65 - % 75	% 55 - % 65	< %55
3	> % 75	% 65 - % 75	% 55 - % 65	< %55
6	> % 80	% 70 - % 80	% 60 - % 70	< %60
9	> % 83.5	% 73.5 - % 83.5	% 63.5 - % 73.5	< %63.5
12	> % 85	% 75 - % 85	% 65 - % 75	< %65

2.2. IDW (Inverse Distance Weighting) Method

This method will be used to obtain interpolation maps of PNI index results. IDW is an interpolation method used to generate data from non-sampleable data with sample points. The general equations of the method are given below.

$$f(x.y) = \sum_{i=1}^{n} w_i f_i \qquad (2)$$

$$w_i = \frac{h_i^{-p}}{\sum_{j=1}^{n} h_i^{-p}} \qquad (3)$$

Here; p, Is taken as the power parameter and is denoted by the exponent. Hi, represents the spatial distance between Decimation points and interpolation points. wi, Refers to the sum of weights and values. fi: Represents the known height value (Krige, 1951).

2.3. Study Area

Konya Closed Basin, located in Central Anatolia in Türkiye and encompassing most of Konya's lands, is one of the most important basins of the country in terms of agriculture. Semi-arid continental climate conditions prevail in the basin. It is located between latitudes 36° 51' N and 39° 29'N and longitudes 31° 36'E and 34° 52'E. The province of Konya, located in this basin, is the largest city in Türkiye in terms of surface area and is approximately 38,257 km long, excluding the area where it was established and the lakes. The average elevation of the city above sea level is 1016 m. The study area is shown in Figure 1.

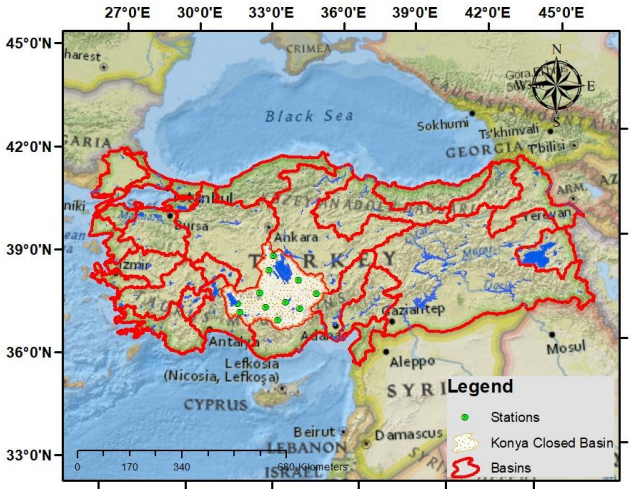

Figure 1. Konya Closed Basin and Other Basins in Türkiye

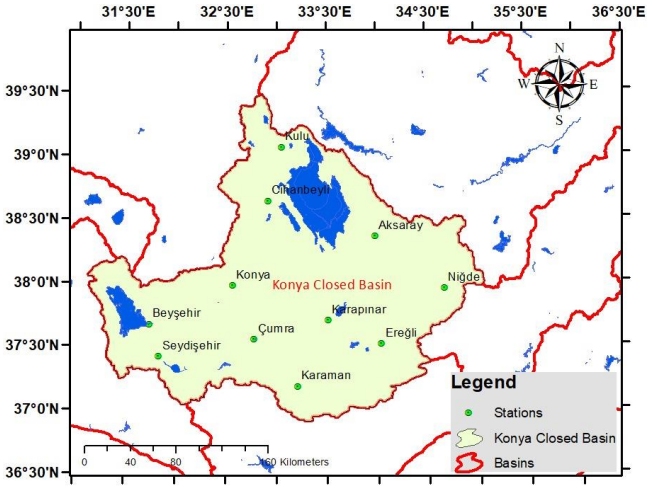

Figure 2. Stations used in the study

3. Application

According to the PNI method, the number of occurrences of drought classes between 1972 and 2020, which is the data period, is given in Table 2.

PNI values for the last years are given in Table 3.

The maps obtained by using the IDW method of the PNI values in Table 3 are given in Figure 3-9.

Table 2. The number of drought indices

Stations	Normal	Slightly Arid	Medium Arid	Severe Arid
AKSARAY	36	5	7	1
BEYŞEHİR	37	6	6	0
CİHANBEYLİ	38	3	6	2
ÇUMRA	34	8	4	3
EREĞLİ	37	7	3	2
KARAMAN	35	7	6	1
KARAPINAR	36	9	2	2
KONYA	36	6	3	4
KULU	38	6	3	2
NİĞDE	37	5	3	4
SEYDİŞEHİR	36	6	6	1

Table 3. PNI values of recent years

İSTASYON ADI	2020	2019	2018	2017	2016	2015	2010
AKSARAY	112.33	87.07	126.60	89.34	103.94	114.28	135.08
BEYŞEHİR	85.27	114.00	100.54	118.35	96.00	79.60	120.10
CİHANBEYLİ	80.01	85.71	118.61	84.03	86.20	138.85	106.04
ÇUMRA	66.61	114.83	138.72	117.46	90.25	76.68	122.56
EREĞLİ	73.92	96.42	104.46	91.30	114.12	114.42	112.56
KARAMAN	82.70	144.16	113.58	106.40	123.21	86.66	99.76
KARAPINAR	83.70	144.55	133.96	124.66	105.99	88.96	116.38
KONYA	89.54	111.80	115.27	95.85	87.02	114.84	108.20
KULU	75.48	88.83	122.57	87.76	96.36	111.62	112.13
NİĞDE	91.60	97.57	143.25	69.12	93.66	120.23	142.11
SEYDİŞEHİR	78.52	98.95	94.39	110.77	95.46	92.72	121.66

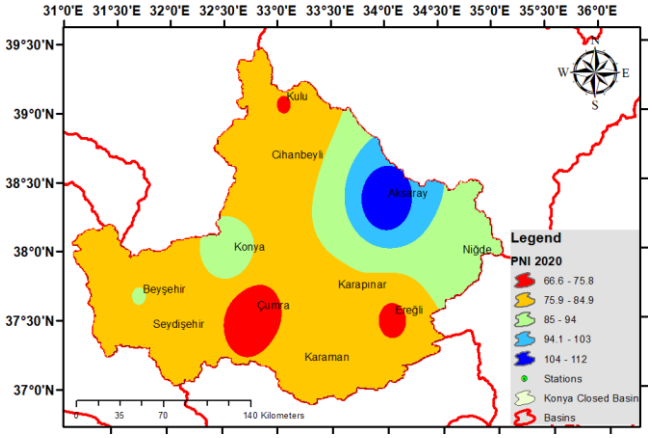

Figure 3. PNI-IDW map of 2020 year

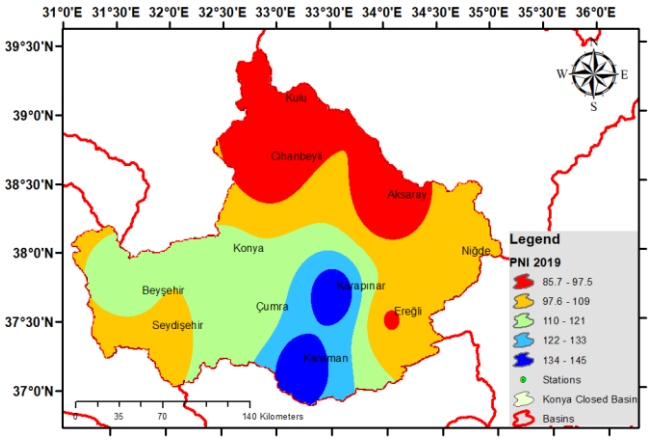

Figure 4. PNI-IDW map of 2019 year

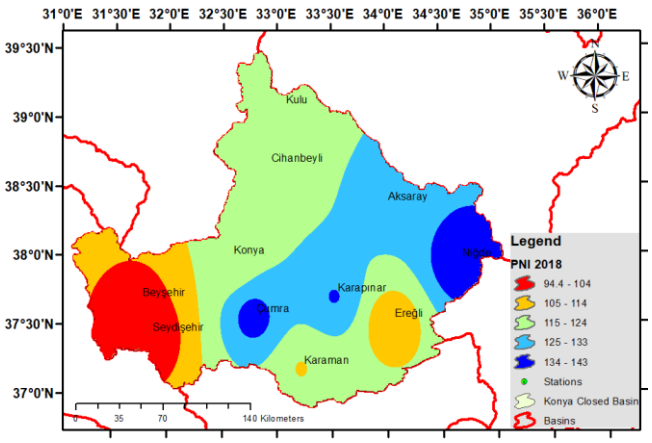

Figure 5. PNI-IDW map of 2018 year

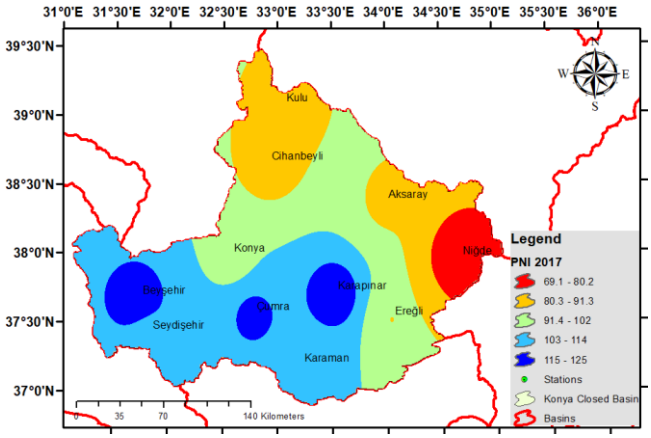

Figure 6. PNI-IDW map of 2017 year

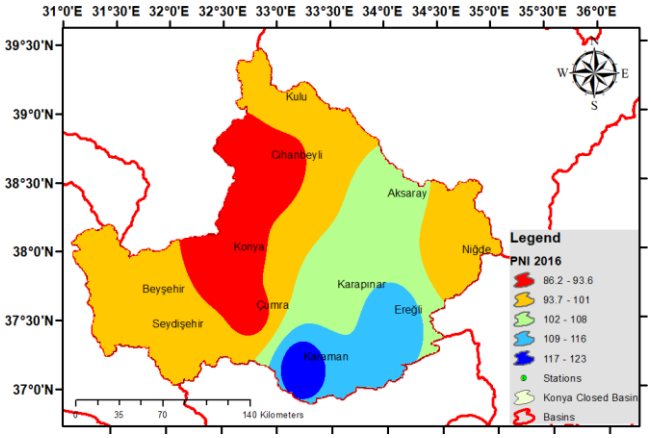

Figure 7. PNI-IDW map of 2016 year

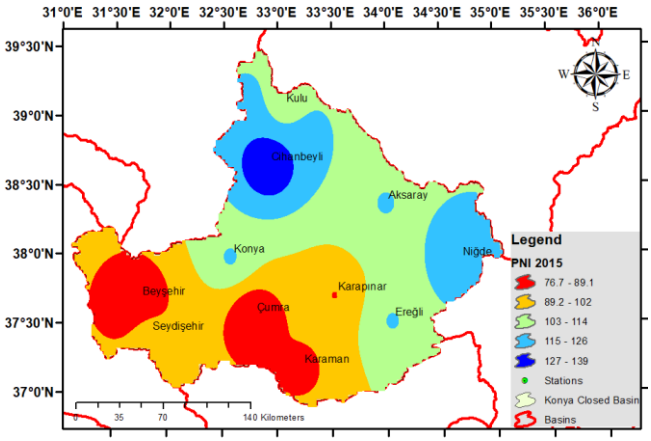

Figure 8. PNI-IDW map of 2015 year

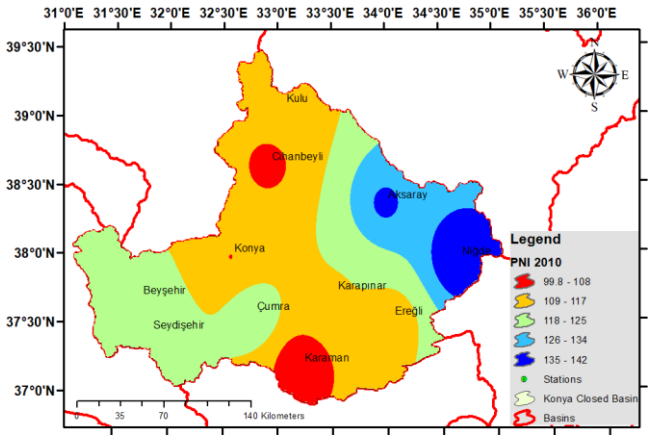

Figure 9. PNI-IDW map of 2010 year

4. Discussion

Duygu, Kirmencioğlu and Aras created a comprehensive drought management plan of the Konya closed basin with Standard Precipitation Index (SPNI), Percent of Normal Method (PNI) and other methods. To determine Water Management, precipitation data between 1972 and 2013 were analyzed (Duygu et al. 2017). Dalkılıç, et al. 2021 evaluated the combined use of the precipitation data of the Konya closed basin between 1981-2010 with SPNI, PNI and other known drought indices. As a result of their studies, the reliability of the drought index methods was determined. Efe and Özgür examined the drought data between 1972 and 2013 with SPNI and PNI methods in the study covering Konya and its surroundings. As a result of the annual evaluation of their work, severe drought was observed in 6 of 20 stations Efe and Özgür, 2014. As a result of the PNI tests conducted in Kulu and Çumra, which are included in our study, drought was observed and adaptation to this study was achieved. As a result, our study is different from other studies in terms of timeliness and stations.

5. Conclusion

In this study, annual total precipitation data recorded between 1972 and 2020 at 11 meteorology observation stations located in the Konya Closed Basin were used. According to the PNI method, the annual drought status of the total precipitation was examined for the basin. As a result of the analysis, when we examined the last 5 years, it was seen that the driest years were 2019 (especially around Karaman and Karapınar) and 2018 (around Çumra and Niğde).

Acknowledgement

The authors thank KTO Karatay University, Kırıkkale University, and TÜBİTAK.

Funding

This study is supported by the application numbered 1919B012201319 within the scope of the 2209-A University Students Research Projects Support Program 2022-1, carried out by the TÜBİTAK Scientist Support Programs Presidency (BİDEB).

References

Osuch, M., Romanowicz, R. J., Lawrence, D., & Wong, W. K. (2016). Trends in projections of standardized precipitation indices in a future climate in Poland. *Hydrology and Earth System Sciences*, *20*(5), 1947-1969.

McKee, T. B., Doesken, N. J., & Kleist, J. (1993, January). The relationship of drought frequency and duration to time scales. In *Proceedings of the 8th Conference on Applied Climatology* (Vol. 17, No. 22, pp. 179-183).

Krige, D. G. (1951). A statistical approach to some basic mine valuation problems on the Witwatersrand. *Journal of the Southern African Institute of Mining and Metallurgy*, *52*(6), 119-139.

Duygu, M. B., Kirmencioğlu, B., & Aras, M. (2017). Essential Tools to Establish a Comprehensive Drought Management Plan-Konya Basin Case Study. *Turkish Journal of Water Science and Management*, *1*(1), 54-70.

Dalkilic, H. Y., Bayçinar, M., & Samui, P. (2021). Evaluation of combined use of drought indices in the case of Konya Closed Basin. *International Journal of Global Warming*, *23*(2), 169-190.

Efe, B., & Özgür, E. (2014). Standart Yağış İndeksi (SPI) ve Normalin Yüzdesi Metodu (PNI) İle Konya ve Çevresinin Kuraklık Analizi. 1(1), 343–354.

6th Intercontinental Geoinformation Days

igd.mersin.edu.tr

Study of industrial production in Azerbaijan based on anamorphosis maps

Zaur Imrani

Ministry of Science and Education of the Republic of Azerbaijan, Institute of Geography named after acad. H. A. Aliyev, Azerbaijan

Keywords
Industry
Production
Productivity
Sustainable development
Anamorphosis map

Abstract

The industry is the leading area of material production and was formed during the division of social production. The availability of natural resources and market demand for the manufactured product is the main condition for its formation. Industrial development promotes the rational territorial organization of productive forces, regions' comprehensive development, and the appropriate use of natural resources. In recent years, a significant increase in the specific weight of science-intensive industries has become a defining feature of the development trend of world industry. The application of the achievements of scientific and technical progress in production areas leads to the specialization of not only finished products but also their constituent parts. For this reason, the approach to industrial production from an economic-geographic point of view is of particular importance. Spatial analysis of industry constitutes a logical paradox (contradiction) about regional sustainable development. In this regard, many specialists use the method of multidimensional approach (logical description) in industrial geography. The multidimensional approach is based on the analysis of the operational processing of the information entered into the database management system with the help of a computer. One of the methods of such an approach is related to the preparation of anamorphosis maps, in which we tried to reveal regional differences with the help of these maps in our research.

1. Introduction

The volume and development of industrial production depend on its specific characteristics, the geopolitical position of the country, the degree of provision of natural resources, the industrialization of production, the level of application of the achievements of scientific and technical progress to production, investment and so on (Shafizade, 2016). The guarantor of the sustainable development of industrial production is determined by the scientific necessity of all components. This is also measured by the geographical location of industrial production, its competitiveness, constant updating of the management mechanism, tolerance to external environmental influences, and so on.

The traditional fields of industry are determined by the rational material needs of economic subjects based on the pyramid of individual needs in sustainable industrial production (Maevsky et al. 2016). However, the research conducted in this direction shows that the sustainability of industrial production is studied mainly in the financial and economic aspects. This ensures the stable use of income, free manoeuvring of the resources of the production enterprise, and uninterrupted production and sale of products (Rodionova and Fedotova, 1995).

The development of industry causes an increase in labour productivity, an expansion of the possibilities for using manufactured products in all areas of the economy, an intensification of the efficiency of social production, etc. This suggests that industry is the leading sector of production and the national economy. The role of the industry in the sustainable development of the country consists of the following:

- the volume of production in the industry is greater than in other areas of production;
- the largest share of the value of production fixed funds (active and passive) is concentrated in the industry;
- the industry contributes to the development of other sectors of the economy;
- serves to expand industrial economic cooperation;
- enables more rational use of industrial labour resources, etc.

* **Corresponding Author**

*(zaur_imrani@mail.ru) ORCID ID 0000-0002-0606-3753

Cite this study

Imrani, Z. (2023). Study of industrial production in Azerbaijan based on anamorphosis maps. Intercontinental Geoinformation Days (IGD), 6, 36-40, Baku, Azerbaijan

2. Method

The assessment of the sustainable development of industrial production is carried out based on the economic-statistical analysis method. However, the use of this analysis method is not enough to conduct a comprehensive approach. At this time, there is a need for new non-standard methods, and the development of industrial production requires new scientific-methodological approaches based on logic. One such approach is related to anamorphic maps.

An anamorphosis map means a distorted map. An anamorphosis map is a description of the territory of the state according to the variable of the given cartographic map scheme in scientific language (Strelova and Panevina, 2010). That is, anamorphosis is a map-like representation in which the size of an object (country, region, etc.) is proportional to the value of its numerical indicators (GDP, population, etc.) (Sokolov and Titkova, 2018). The creation of anamorphosis maps is very useful in many cases in terms of the modified structure of the interaction of several factors for visual analysis (Serdyutskaya el at. 2008). Anamorphosis maps are compiled based on statistical indicators. The advantage of these maps over cartograms is that the mapped indicators are relatively easy to evaluate because they cause continuous change.

3. Results

The industrial geography of Azerbaijan is mainly characterized by oil and gas extraction, mining, light and food industries based on local raw materials, and construction industries (Imrani and Zeynalova, 2014). If we analyze the location of industrial areas using the historical approach, we will see that the achievements in this area have led to the development of some regions at a high pace, while others have been left behind. From a comprehensive point of view, this division has become an integral part of sustainable economic-geographical development or regional policy. The level of economic development of the country is closely related to the principles of proper positioning and coordination of its regional policy and industries.

The economic development of Azerbaijan affects the increase in the number of industrial enterprises operating in the territory and their production capacity. If we analyze the years 1995-2021, we will see that the number of industrial enterprises increased by 1595 enterprises to 3689 enterprises (Figure 1). Among these enterprises, the mining and processing industries are mostly selected with their own development pace. Although this growth rate was recorded in all sectors, a higher growth number was recorded in the processing industry, with 933 enterprises. The increase in the mining industry was 263 enterprises, in water supply 258 enterprises, and electricity and gas production 171 enterprises. Although the overall growth rate of the processing industry is sharply different from other industries, it has been observed in the sub-sectors of this industry in a decreasing trend. Production of food products 90 enterprises, installation and repair of machinery and equipment 20 enterprises, and to a lesser extent 8 enterprises of wood processing, 8 enterprises of machinery and equipment production suffered a decrease more. Although there was a sharp decrease in the production of food products in 1998 (329 enterprises), in the following years there was a trend observed with an increase and sometimes a decrease. The sharp decrease in the number of other enterprises coincides with 1998. For example, 218 enterprises in the installation and repair of machinery and equipment, 68 enterprises in the production of beverages (alcoholic and non-alcoholic), and 60 enterprises in the production of construction materials were terminated in just one year (Industry of Azerbaijan, 2003; Industry of Azerbaijan, 2022). The reason for this was the observation of deflation (a drop in production and income) in the country. Deflation hurt the development of all areas, slowed regional development, and reduced the volume of industrial output and the number of jobs, as well as the income of the population.

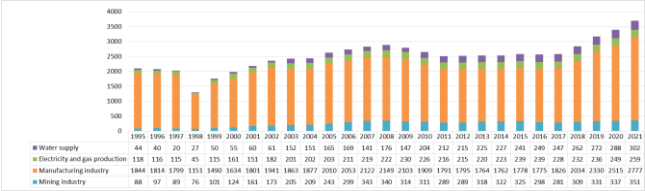

Figure 1. Number of industrial enterprises, unit

If we look at the percentage of industries, we will see that most of the total industrial enterprises, i.e. 75.3%, belong to the processing industry. Mining has a very low figure of 9.5%, water supply 8.2%, electricity and gas production 7.0% (Industry of Azerbaijan, 2022). The distribution of industrial enterprises operating in Azerbaijan by types of ownership has undergone significant changes in recent decades. In connection with the privatization policy in the country, in 1993 the Law "On Privatization of State Property" (Law of the Republic of Azerbaijan, 1993), in 1995, the State Program "Privatization of State Property in 1995-1998" (The Law of the Republic of Azerbaijan, 1995) was adopted and already in 1998, a new form of ownership was created in connection with the privatization of state property. In that year, the share of state ownership in the industry was 44.7%, and the share of non-state ownership was 55.3%. 28 enterprises privatized by foreign companies made up only 3.9% of the non-state sector. However, in 2021, the share of state ownership decreased to 15.3%, and the share of non-state ownership increased to 84.7%, of which 9.8% (307 enterprises) belonged to foreign companies.

While there has been a significant change in the composition of industrial enterprises in Azerbaijan in recent years, quality changes have also occurred. In the most general form, these changes were more evident in the ratio difference between the mining and processing industries. If we look at the production volume of industrial enterprises in 1995-2021, we will see that growth has been noticeable in all areas. The increase in the volume of total industrial products was 31.2 times. This growth trend is reflected by various indicators in the fields. An increase of 104.5 times in the mining industry, 15.1 times in the processing industry, 13.8 times in water

supply, and 7.8 times in the production of electricity and gas was recorded (Figure 2). Such growth occurred in all areas of production. However, during the studied years, the highest growth indicators were in the production of metal ores 10.7-387.5 million manats, installation and repair of machines and equipment 4.1-516.0 million manats, furniture production 344.3-33710.1 million manats, production of finished metal products 4.4-381.6 million manats, etc. fields (Industry of Azerbaijan, 2003; Industry of Azerbaijan, 2022). It can be concluded that not only the production of mining industrial products, which occupies a leading position in the country's economy but also other sectors and all their sub-sectors have seen a growing trend. In certain years, this increase has gone along with the decline, even if slight, due to the economic crisis observed in the world (a sharp increase in inflation in the countries of the world) and devolution in the country (depreciation of the national currency unit compared to the dollar).

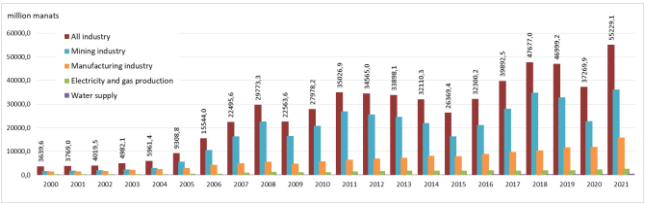

Figure 2. The volume of products produced by industrial enterprises, million manats

Industrial production acts not only as a leading force but also as a provider of the country's economy and economic sectors, regional development. Since the industry is valued as an economic power, social security, employment and infrastructure provision, regional advantages should be studied accordingly, because the development of industrial production in any region leads to the comprehensive rise and stability of that region. For example, Baku city accounts for 98.7% of oil production and 99.9% of gas production, which is considered the leading force of industrial production in the country, and the rest for Shirvan, Salyan, Neftchala and Siyazan regions. This factor has led to the development of Baku city at a higher pace than other regions and the emergence of regional inequality. In addition to oil and gas production, in the exploitation of other valuable mineral deposits in the country: gold Dashkasan 57.1%, Gadabey 42.9%, silver Dashkasan 86.1%, Gadabey 13.9%, copper Gadabey takes a leading place at 100%. Apart from these, the extraction of gravel, crushed stone and small river stone building materials have been expanded in the regions in connection with the development of the construction industry in recent years. While in 2011, the production of basic construction materials was in 7 regions, in 2021 this indicator was increased to 13 regions. The cities and regions where gravel, crushed stone and small river stone materials intended for construction are extracted include Imishli 49.1%, Gabala 15.5%, Guba 10.4%, Baku 8.6%, Absheron 7.0% and so on. In the production of sand for construction, Nakhchivan 32.9%, Imishli 22.6%, Gabala 21.5%, Baku 19.8%, etc.; limestone Baku 66.2%, Absheron 22.9%, Gazakh 9.9%, gypsum Goranboy 93.5%, Baku 6.5% (Industry of Azerbaijan, 2022).

Gadabey, Dashkasan, Imishli, Gabala and other regions take the leading place in the above-mentioned minerals, except for oil and gas production. However, these regions lag in general development. This can be seen more clearly in the analysis of regional industrial production.

The disparity of resources (natural resources, skilled workforce, science-intensive production, social infrastructure, etc.) between regions and the unique developmental characteristics of society lead to the creation of potential but unidirectional areas. The economic, social and ecological aspects of these areas act as an integrated tool in regional planning. That is, the main goal of regional planning is to achieve at least a small amount of disparity between regions. National priorities are defined and the policy interface (interaction) is created within the regulatory regional strategy (Williamson, 1965). Industrial production is an important component of the development of resources in terms of socio-economic efficiency in this process. Because well-organized industrial areas are an integral part of the regional strategy, in addition to increasing the quality of production.

If we analyze the number of industrial enterprises in Azerbaijan, their production capacity and their share in the non-state sector, we will see that there is a constant growth trend. This growth is observed in all economic regions. In a small period, i.e., between 2005 and 2021, the highest growth is Nakhchivan 26.0 times, Karabakh 23.8 times, Mil-Mugan 22.3 times, Shaki-Zagatala 23.0 times, and the least Baku 5.9 times, Shirvan-Salyan 5.6 times, Central Aran 3.9 times (able 1.). However, in terms of regional development, these indicators are not fully justified. As in previous years, some economic regions lag behind the general development trend and continue to do so.

If we prepare the anamorphosis map of the industrial map of Azerbaijan on the main indicators of industrial production, we can see the extent of the changing trend. It turns out that a changing trend was observed as a result of the analysis of anamorphosis maps prepared by us, reflecting the years 2000 and 2021. Although this change is based on the principles of regional development, the Baku economic region is always at the forefront. In 2000, the Central Aran economic region, which developed relatively regionally, lagged behind its development pace in 2021 and was replaced by Absheron-Khizi and Nakhchivan, as well as Ganja-Dashkasan and Shirvan-Salyan economic regions (Figure 3). The advantage of anamorphic maps is that regional differences are more clearly revealed, which can be seen more clearly in Figure 3.

Anamorphosis maps are very suitable for visual analysis of regional phenomena, and modelling of the structure of their interaction. These maps help to see the real dangers. In the future, anamorphosis maps can be used to improve the development of regional strategic plans.

Table 1. The main indicators of industrial production

Economic regions	Years					
	2005			2021		
	Number of enterprises, units	Product production, million manats	The share of the non-state sector, in %	Number of enterprises, units	Product production, million manats	The share of the non-state sector, in %
Baku	1302	7725,1	72,9	1999	45309,7	85,9
Nakhchivan	96	41,2	66,6	111	1069,6	92,3
Absheron-Khizi	217	224,7	15,2	381	4125,8	69,9
Mountainous Shirvan	39	6,0	42,7	57	88,9	81,0
Ganja-Dashkasan	190	137,7	24,9	197	860,8	60,8
Karabakh	60	8,2	46,9	85	194,8	66,3
Kazakh-Tovuz	96	31,8	17,4	98	416,3	76,5
Guba-Khachmaz	76	37,7	50,1	124	306,0	64,2
Lankaran-Astara	78	18,2	70,2	118	340,8	80,3
Central Aran	141	190,5	13,6	158	646,1	45,4
Mil-Mugan	66	24,9	64,4	85	554,5	92,6
Sheki-Zagatala	106	21,0	34,0	164	440,6	83,6
Eastern Zangezur	1	0,8	0,0	12	7,9	61,5
Shirvan-Salyan	85	153,6	47,2	100	867,3	65,5

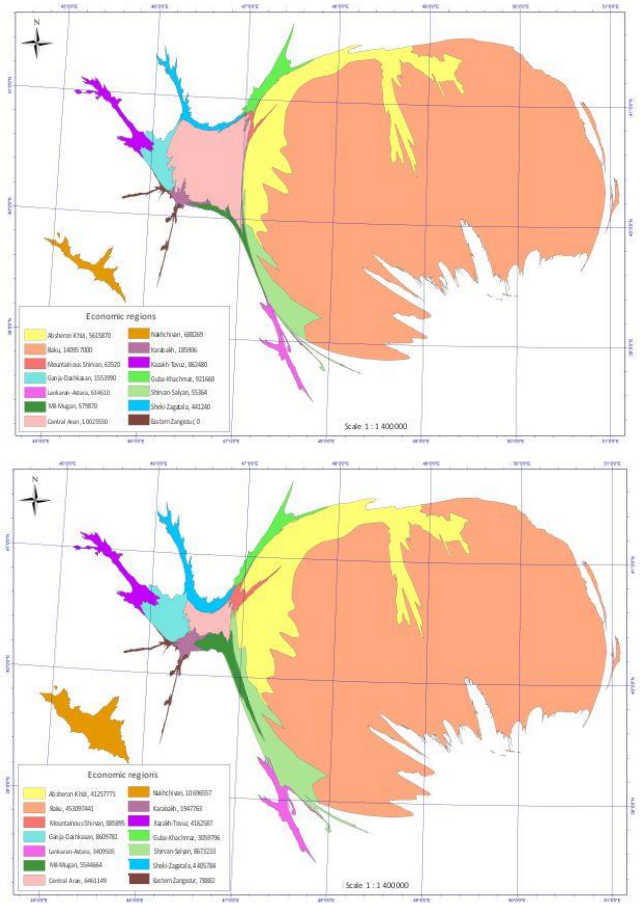

Figure 3. Map of industrial production anamorphoses

4. Discussion

One of the problems arising in the territorial organization of the industry is the coordination of production. The correct organization of production coordination has a significant impact on the formation and development of industries. Because production relations play an important role in the formation of the economy. And the specialization of production is significantly important in the establishment of production relations between small industries whose complex development is related to each other. Analysis of these relationships is possible with the help of anamorphosis maps.

5. Conclusion

Based on the anamorphosis map of industrial production, it was partially possible to reveal several socio-economic problems in the economic regions of Azerbaijan. Despite the measures taken to improve the field and territorial structure of the industry in recent years, large enterprises based on the more efficient use of local resources should be created and their full capacity should be ensured. Only in this case, it is possible to significantly increase production in industrial enterprises and achieve innovations in the direction of efficient operation in the future. The analysis of all these on the map is possible based on the anamorphosis approach method.

References

Imrani, Z. T. & Zeynalova, K. Z. (2014). Economic-geographic features of the territorial organization of the economy in Azerbaijan. Baku: 2014. 232.

Industry of Azerbaijan, statistical collection (2003). Head A. Valiyev. Baku: 202;

Industry of Azerbaijan, statistical collection (2022). Head T. Budagov. Baku: 212.

Law of the Republic of Azerbaijan on the privatization of state property in the Republic of Azerbaijan (1993). Adopted on January 7, 1993. Baku: 6.

Maevsky, V. I., Malkov, S. Yu. & Rubinshtein, A. A. (2016). New theory of capital reproduction: development and practical application. Moscow-St. Petersburg: 260.

Rodionova, V. M. & Fedotova, M. D. (1995). Financial stability of the enterprise in terms of inflation Moscow: 320.

Serdyutskaya, L. F., Bakhmatsky, E. A. & Yatsyshin, A. V. (2008). Anamorphoses as an instrument of spatial analysis of ecological and geographical phenomena. Geoinformatics. 1. 60-66.

Shafizade, E. R. (2016). Analysis of industrial production in Azerbaijan and its econometric model. Proceedings of the Institute of Applied Mathematics. 5(2).224-234.

Sokolov, A. S. & Titkova, Yu. N. (2018). The use of non-traditional electronic maps in ecological education. Sakharov readings of 2018: ecological problems of the XXI century, materials of the 18th international scientific conference. 172-173.

Strelova, O. Yu. & Panevina, G. N. (2010). Didactic resources of the anamorphosis map. Municipal formation: innovations and experiment. 2. 64-70,

The Law of the Republic of Azerbaijan on the approval of the State Program of Privatization of State Property in the Republic of Azerbaijan in 1995-1998 (1995). Adopted on September 29, 1995. Baku: 22.

Williamson, J. G. (1965). Regional Inequality and the Process of National Development. Economic Development and Cultural Change. 13(4). 1-84

6th Intercontinental Geoinformation Days

igd.mersin.edu.tr

Air pollution monitoring in Tehran using Sentinel_5 satellite (2022)

Nilufar Makky *[1], **Khalil Valizade Kamran** [1] **Sadra Karimzadeh** [1]

[1]*University of Tabriz, Enviromental Science, RSGIS, Tabriz, Iran*

Keywords
Remote sensing
Air pollution
TROPOMI
Sentinel_5
Population

Abstract

Tehran, one of the largest cities globally, has been severely impacted by excessive pollution, posing a significant threat to vulnerable people with heart disease and asthma. However, utilizing Sentinel_5 (TROPOMI) sensor images, we can monitor and map the concentration levels of CO, NO2, O3, and aerosols, including fine airborne particles. With this data, it is possible to identify areas that are excessively polluted and apply necessary measures for effective crisis management. Considering the influence of city temperature changes, construction, and the NDBI index, the amount of air pollution deserves thorough investigation. These findings not only provide essential scientific insights but also have practical implications for sustainable urban development policies and public health strategies.

1. Introduction

The extent of climate change (Eghrari et al, 2023, Musavi et al,2023) has already had significant impacts that can be seen in several dimensions. Managing climate challenges is very important for researchers. In addition, it has many bad effects on human life (Karimzade & Matsuoka, 2018. Musavi et al,2023). Also, urban management can improve our life (Makky & Kaffash, 2017). The average surface temperature of the Earth has been increased by about (1.62) degrees Fahrenheit since the late 19th century in all over the world (Boer et al., 2000; Kaufmann et al., 2011; Damtoft et al., 2008). Also, air pollution is a very destroyer global crisis and it has a death toll of 7 million people per year, of which (600,000) of them are children (UN). In addition, air pollution is a dangerous global threat that has many bad effects on human health and ecosystems. One of the most dangerous and toxic air pollutants is (NO_2). It is responsible for respiratory diseases, cardiovascular diseases, reduced capacity of self-cleaning air the weakened immune function of the lungs, asthma, and many more (Srokzynski, 1988; WHO). According to the European Environment Agency (EEA), in 2018 year, 55,000 premature deaths from NO2 gas occurred across Europe (EEA). In addition, high nitrogen concentrations damage ecosystems due to eutrophication and acidification (along with sulfur dioxide, and SO2). This, in turn, leads to changes in the diversity of species (reduction in the level of existing species and invasion of new species) as well as an increase in the concentration of toxic metals in water and soil (Dopre et al,2010). A major advance in satellite NO_2 observations was the TROPOSpheric Monitoring Instrument (TROPOMI), which was mounted on the Sentinel-5 Precursor (Sentinel-5P, S-5P) satellite launched by the European Space Aency. Atmospheric NO2 pollution has become even more threatening since the start of the COVID-19 pandemic, and many scientific studies have explained this. In this regard, a decrease in NO2 levels was reported in 2020. On a global and regional scale, they analyzed NO_2 TVCD data in 33 cities worldwide, and only in more than 1 city (Isfahan) did atmospheric NO_2 concentrations increase during the pandemic. The reason for this increase was ignoring the restrictions of COVID-19 in Iran (Bauwns et al, 2020). Fossil fuel CO_2 emissions are mainly through the combustion of oil and coal, leading to climate change and disease in organisms globally (Li et al., 2021). O_3 is a gas often formed from NOx (nitrogen oxides) and hydrocarbons, released in the form of nanoparticles and ultra-fine particles with atmospheric contaminants (whether organic or inorganic). O3 is released in large quantities by thermoelectric power plants and the internal combustion engines of motor vehicles, thus raising levels of atmospheric contamination on a global scale (Dong et al., 2021; Forest, 2021).

Aerosols are compounds capable of containing high loads of atmospheric contaminants that spread over large regions, absorbing solar radiation, and leading to a greater imbalance in temperature in cities around the world (Mei et al., 2020; Fernandez-Moran et al., 2021; Bodah et al., 2022). Today, energy consumption and air

* **Corresponding Author**

*(nilufar_makky73@yahoo.com)
(valizadeh@tabrizu.ac.ir) ORCID ID 0000-0003-4648-842X
(sadra.karimzadeh@gmail.com) ORCID ID 0000-0002-5645-0188

Cite this study

Makky, N., Kamran, K. V., & Krimazadeh, S. (2023). Air pollution monitoring in Tehran using Sentinel_5 satellite (2022). Intercontinental Geoinformation Days (IGD), 6, 41-45, Baku, Azerbaijan

pollution are metropolitans' important transportation issues. In these cities, most people consider their mode of transportation based on the appropriate means, including passenger, travel characteristics, population growth, urban space, and transportation (Bagheri et al,2020). Tehran is the most populated city in Iran its capital of it, has a population of 8.5 million, and this number reaches about 12.5 million people due to the daily commute of people who come from nearby cities such as Qom, Qazvin, and Karaj for work and education every day (Hosseini et al, 2016; Bayat et al, 2019) The other types of transportation in Tehran (smart modes, cycling, public transport) are marginal compared with the private mode in daily trips in Tehran city. In 2017, Tehran Traffic Organization information showed that the Tehran bus system was giving service to passengers by 10 BRT lines and 240 regular buses every day. Also, the important change in Tehran's urban transportation has been related to the metro, which started its operation in 1990. The information showed that in 2017, about 732 million trips were made by the metro in Tehran (Mojtehedzadeh et al, 2019).

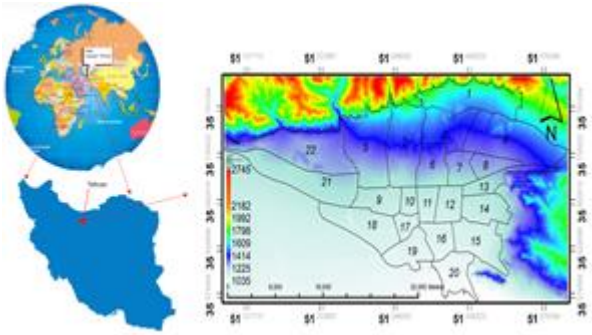

Figure 1. Tehran location

In this map, the elevation position of Tehran is displayed by The Shuttle Radar Topography Mission with a resolution of about 30 meters.

2. Method

Using remote sensing data to monitor air quality is important for environmental research. The Sentinel-5 satellite with the Tropomi sensor enables the tracking of gaseous pollutants. In this research, the TROPOMI sensor of the Sentinel 5 satellite was used to determine the number of suspended particles including NO2, O3, CO, and AEROSOL. All extracted gases have units based on mol/m^2. The GEE environment was used for coding. The extracted maps were designed and displayed in ARC MAP 10.8 software.

3. Results

Nitrogen dioxide (NO_2) and nitrogen oxide (NO) are trace gases found in both the troposphere and stratosphere layers of the Earth's atmosphere. They are released into the atmosphere through anthropogenic activities like fossil fuel combustion and natural processes such as wildfires and microbiological processes in soils. NO2 is a reliable measure for concentrations of nitrogen oxides due to its conversion from NO through a photochemical cycle involving ozone (O_3) in the presence of sunlight. The distribution map of NO_2 in Tehran city for 2021 and 2022 was presented (tropomi.eu).

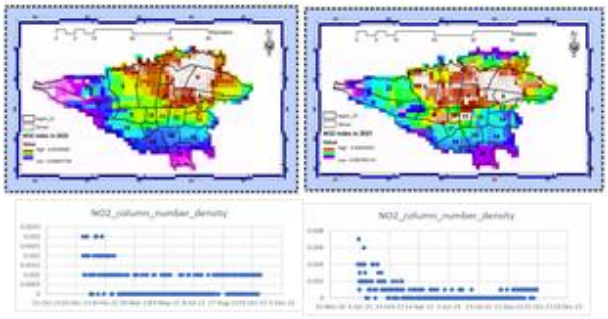

Sentinel-5 offers high-resolution imagery of the UV Aerosol Index (UVAI), also known as the Absorbing Aerosol Index (AAI), which provides near real-time data. AAI relies on wavelength-dependent variations in Rayleigh scattering in the UV spectral range for a pair of wavelengths. The difference between observed and modeled reflectance yields the AAI. Positive AAI values indicate the presence of UV-absorbing aerosols like dust and smoke, making it useful for tracking episodic aerosol plumes originating from events such as dust outbreaks, volcanic ash, and biomass burning. (tropomi.eu). Here the map of Aerosol was shown.

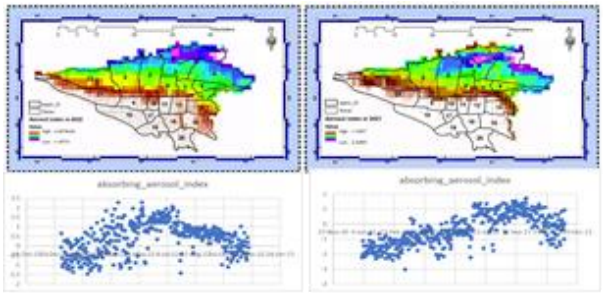

Figure 3. Aerosol distribution in Tehran

Carbon monoxide (CO) is a significant atmospheric trace gas that plays a vital role in the understanding of tropospheric chemistry. In several urban regions, it is a significant atmospheric pollutant. The primary sources of CO are fossil fuel combustion, biomass burning, and the atmospheric oxidation of methane and other hydrocarbons.

Fossil fuel combustion is the primary source of CO at northern mid-latitudes, whereas the oxidation of isoprene and biomass burning have a crucial impact in the tropics (tropomi. eu).

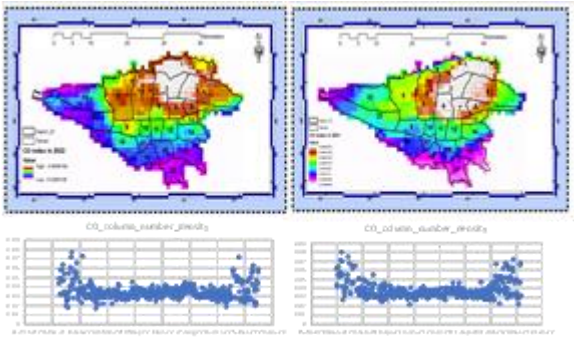

Figure 4. CO distribution in Tehran

The ozone layer in the stratosphere serves as a protective shield for the biosphere against hazardous solar ultraviolet radiation, while in the troposphere, it functions as an effective purifying agent. However, high concentrations of ozone can have adverse effects on human health, animals, and vegetation. Additionally, ozone is a significant greenhouse gas that contributes to ongoing climate change. Following the detection of the Antarctic ozone hole in the 1980s and the establishment of the Montreal Protocol regulating the production of chlorine-containing ozone-depleting substances, ozone has been routinely monitored from both ground-based and spaceborne platforms. (tropomi.eu).

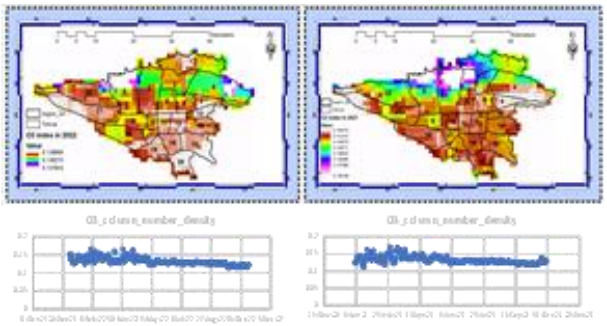

Figure 5. O_3 distribution in Tehran

Land surface temperature (LST) is a critical climatic parameter that has a substantial impact on the energy balance of the Earth's surface. Several factors affect LST, including the thermal properties of the surface, subsurface media, and the energy balance between the surface and atmosphere. (Anggoro et al., 2017; Almy and Astrolabe, 2021). LST is defined as the average surface temperature of a given area, represented by a range of pixels with different surface types. The formula used to calculate LST in this study is as follows (Rongali et al, 2011).

$$LST = \frac{BT}{1+(\lambda . BT/\rho)\ln \varepsilon} - 273,15 \qquad (1)$$

LST: Land surface temperature (in $°C$)

BT: At-satellite brightness temperature (in $°C$)

λ: Band 10 radiation wavelength (10,6 μm)

ρ: $(h.\ c)/\ \sigma$ (1,438 × 10−2 mK), where σ is Boltzmann constant, which value was 1,38 × 10−23 J/K;
h is Planck's constant whose value was 6,626 .10^{-34} Js; and c is the speed of light which value was 2,998 × 108 m/s.

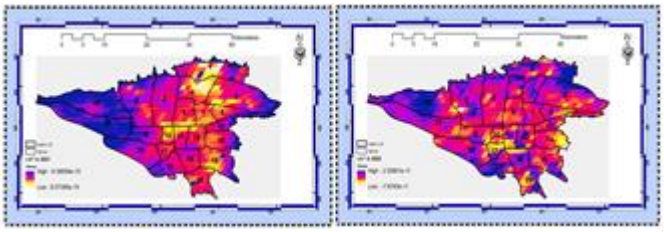

Figure 6. LST in Tehran

NDBI is used to extract built-up features of the city and the NDBI raster map is derived from the short-wave infrared (SWIR) and (NIR) channels of multiband remotely sensed imagery from Landsat8 in Gee (Garg et al.,2016). The formula for calculating NDBI is shown:

$$\mathbf{NDBI} = \frac{(SWIR - NIR)}{(SWIR + NIR)} \qquad (2)$$

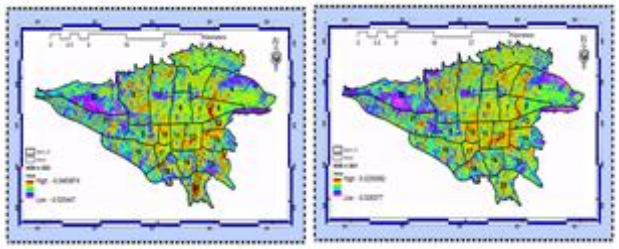

Figure 7. NDBI Index in Tehran

Vegetation indices based on visible and near-infrared bands have been widely used in vegetation detection and health assessments (Ke et al, 2015), among which the NDVI is most commonly used in vegetation-related monitoring. The definition of the NDVI is shown by Formula (Rouse et al, 2022):

$$\mathbf{NDVI}\ (LANDSAT\_8) = \frac{B5\_B4}{B5 + B4} \qquad (3)$$

Researches utilized the Normalized Difference Vegetation Index (NDVI) to quantify vegetation coverage in remote-sensing images. The NDVI formula for Landsat 8 L2 was used, where RED (B4) is the reflectance in the red band and NIR (B5) is the reflectance in the near-infrared band. The NDVI has a range of [-1, 1], where values less than 0 indicate non-vegetated areas such as clouds, snow, and water. An NDVI value of 0 indicates bare soil or rocks, while values greater than 0 indicate vegetation coverage, with the value increasing as the coverage increases. Only valid NDVI values were used, with pixel values filtered to exclude those with NDVI less than 0, and only values with NDVI greater than or equal to 0 were retained for further analysis. (Zhao et al ,2023).

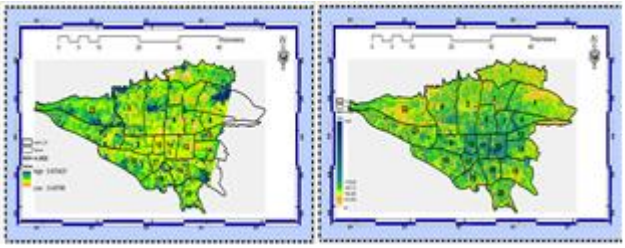

Figure 8. NDVI Index in Tehran

4. Discussion

In this study, using remote sensing and the GEE system, our goal is to determine the areas prone to pollution in order to introduce people with respiratory diseases to maintain their health by not visiting these places.

5. Conclusion

This study aimed to identify high-risk polluted areas in Tehran based on the presence of nitrogen dioxide, ozone, aerosols, and carbon monoxide using Sentinel 5 images. Results showed that in 2022, there was a significant increase in construction and urban density in regions 12, 16, 19, 20, and 4 compared to 2021. The highest concentration of aerosols was observed in the southern areas of Tehran, which remained at its maximum level in 2022. Nitrogen dioxide and ozone gases increased in certain regions. However, carbon monoxide gas reached its minimum in 2022 in high-risk areas. Additionally, vegetation coverage and health declined slightly in Tehran in densely populated areas in 2022 compared to 2021. These findings can contribute to the identification of polluted areas and help prevent respiratory diseases for individuals living in these areas.

References

Almy, F. N. I., & F. V. Astrolabe, S. P. (2019) Sebaran Land Surface Temperature Dan Indeks Vegetasi.Di Wilayah Kota Semarang Pada Bulan Oktober. Bulletin Poltanesa 22(1) 45-52.

Anggoro, W. U., Andri. S., & Bandi, S. (2017). Analisis Hubungan Variasi Land Surface Temperature Applications.

Bagheri, M, Ghafourian H., Kashefioasl M., Taghi Sadatipour M., Rabbani M. (2020) Transport network traffic management and urban travel demand to reduce air pollution (Case study: Shiraz), Department of Environmental Engineering, North Tehran Branch, Islamic Azad University, Tehran, Iran.10.22075/ijnaa.2023.29603.4213.

Bauwens, M., Compernolle, S., Stavrakou, T., Müller, J., Van Gent, J., Eskes, H., Levelt, P.F., van der A, R., Veefkind, J.P., Vlietinck, J., et al. (2020). Impact of Coronavirus Outbreak on NO2 Pollution Assessed Using TROPOMI and OMI Observations. Geophys. Res. Lett. 47, e2020GL087978.

Bayat, R., Ashrafi, K., Motlagh, M.S., Hassanvand, M.S., Daroudi, R., Fink, G., Künzli, N. (2019). Health impact and related cost of ambient air pollution in Tehran. Environ. Res. 176, 108547.

Boer, E. P. J., & Hendrix, E. M. (2000). Global optimization problems in optimal design of experiments in regression models. Journal of Global Optimization, 18(4), 385–398.

Boer, E. P. J., & Hendrix, E. M. (2000). Global optimization problems in optimal design of

Damtoft, J. S., Lukasik, J., Herfort, D., Sorrentino, D., & Gartner, E. M. (2008). Sustainable development and climate change initiatives. Cement and Concrete Research, 38(2), 115–127.

Dengan Kelas Tutupan Lahan Menggunakan Data Citra Satelit Landsat (Studi Kasus: Kabupaten Pati) J. Geodesi Undip 6(2) 71-80.

Duprè, C., Stevens, C. J., Ranke, T., Bleeker, A., Peppler-Lisbach, C. O. R. D., Gowing, D.J., Dise, N. D., Dorland, E., Bobbkink, R., Diekmann. M. (2010). Changes in species richness and composition in European acidic grasslands over the past 70 years: The contribution of cumulative atmospheric nitrogen deposition. Glob. Chang. Biol. 2010, 16, 344–357.

Eghrari,Z. Delavar ,M. R., M, Zare., Beitollahi, A., Nazari,B, (2023), LAND SUBSIDENCE SUSCEPTIBILITY MAPPING USING MACHINE LEARNING ALGORITHMS. ISPRS Ann. Photogramm. Remote Sens. Spatial Inf. Sci., X-4/W1-2022, 129–136, 2023.https://doi.org/10.5194/isprs-annals-X-4-W1-2022-129-2023.

European Environment Agency. Air Quality in Europe—2020. Report. EEA Report No 9/2020. Available online: https://www.eea.europa.eu/publications/air-quality-in-europe-2020-report (accessed on 10 October 2021).

Garg, A., Pal, D., Singh H., Pandey, D.C. (2016). A comparative study of NDBI, NDISI and NDII for extraction of urban impervious surface of Dehradun (Uttarakhand, India) using Landsat 8 imagery. International Conference on Emerging Trends in Communication Technologies (ETCT), pp. 1-5, doi: 10.1109/ETCT.2016.7882963.

Hosseini, V., Shahbazi, H. (2016). Urban Air Pollution in Iran. Iran. Stud. 49, 1029–1046.

http://www.tropomi.eu/data.products

https://doi.org/10.3390/geosciences8120487

https://ntrs.nasa.gov

Izanlou, S., Amerian, Y. & Seyed Mousavi, S. M. (2023). GNSS-DERIVED PRECIPITABLE WATER VAPOR MODELING USING MACHINE LEARNING METHODS, ISPRS Ann.2022. Photogramm. Remote Sens. Spatial Inf. Sci., X-4/W1-2022, 307–313, https://doi.org/10.5194/isprs-annals-X-4-W1-2022-307-2023, 2023.

Karimzadeh, S., & Matsuoka, M. (2018). A Weighted Overlay Method for Liquefaction-Related Urban Damage Detection: A Case Study of the 6 September 2018 Hokkaido Eastern Iburi Earthquake, Japan. Geosciences, 8(12), 487.

Kaufmann, R. K., Kauppi, H., Mann, M. L., & Stock, J. H. (2011). Reconciling anthropogenic climate change with observed temperature 1998–2008. Proceedings of the National Academy of Sciences, 108(29), 11790–11793.

Ke, Y.H., Im, J., Lee, J., Gong, H. L., Ryu, Y. (2015). Characteristics of Landsat 8 OLI-derived NDVI by comparison with multiple satellite sensors and in-situ observations. Remote Sens. Environ, 164, 298–313.

Li, M., W, Liu., W, Liu., M, Bi., Z, Cui (2021). Dynamic substance flow analysis of lead in the fossil fuel system of China from 1980 to 2018 J. Clean. Prod. 313, Article 127918, 10.1016/j.jclepro.2021.127918

Makky, N., Kaffash Charandabi, N., (2017). Surveying the landscape of Tabriz city from the point of view of tourists. National Conference of new geomatics technologies and applcation.

Mojtehedzadeh, M. (2019) Assessment of Urban Transport System in Tehran. Suti Report; United Nation Economic and Social Commission for Asia and Pacific (ESCAP): Bangkok, Thailand. Available online: https://www.unescap.org/sites/default/files/Tehran.pdf (accessed on 17 July 2019).

Rongali, G., Keshari, A. K., & Gosain, A. K. (2018). A Mono-Window Algorithm for Land Surface Temperature Estimation from Landsat 8 Thermal Infrared Sensor Data: A Case Study of the Beas River Basin, India. Pertanika Journals, 26(2), 829–840.

Rouse, J. W., Haas, R. W., Schell, J. A. (2022). Monitoring the Vernal Advancement and Retrogradation (Greenwave Effect) of Natural Vegetation. NASA/GSFCT Type III Final Report. Available.

Seyed Mousavi, S.; M. & Akhoondzadeh. M. A. (2023). QUICK SEASONAL DETECTION AND ASSESSMENT OF INTERNATIONAL SHADEGAN WETLAND WATER BODY EXTENT USING GOOGLE EARTH ENGINE CLOUD PLATFORM, ISPRS Ann. Photogramm. Remote Sens. Spatial Inf. Sci., X-4/W1-2022, 699–706, https://doi.org/10.5194/isprs-annals-X-4-W1-2022-699-2023, 2023.

Sroczyński, J. (1988). The Impact of Atmos. In Air Pollution on Human Health; PAN: Wrocław, Poland. (In Polish)

UN. With a Premature Death Every Five Seconds, Air Pollution Is Violation of Human Rights. Available online: https://www.un.org/sustainabledevelopment/with-a-premature-death-every-five-seconds-air-pollution-is-violation-of-human-rights-says-un-expert-2/

Veefkind, J., Aben, I., McMullan, K., Förster, H., de Vries, J., Otter, G., Claas, J., Eskes, H., de Haan, J., Kleipool, Q. (2012). TROPOMI on the ESA Sentinel-5 Precursor: A GMES mission for global observations of the Atmos. composition for climate, air quality and ozone layer applications", Remote Sens. Environ. 120, 70–83.

World Health Origination (WHO) Air Quality Guidelines for Particulate Matter, Ozone, Nitrogen Dioxide and Sulfur Dioxide. Available online: https://apps.who.int/iris/handle/10665/345329 (accessed on 10 October 2021).

Zhao, Y., Hou., Peng, Jiang., J, Zhao., J, Chen., Y, Zhai., J. (2023), High-Spatial-Resolution NDVI Reconstruction with GA-ANN, Sensors, 23(4), 2040; https://doi.org/10.3390/s23042040

6th Intercontinental Geoinformation Days

igd.mersin.edu.tr

Comparative study of hyperspectral imagery classification with SVM and ensemble machine learning methods

Saziye Ozge Atik[*1]

[1]*Gebze Technical University, Faculty of Engineering, Department of Geomatics Engineering, Kocaeli, Türkiye*

Keywords
Hyperspectral Imagery
Classification
Machine Learning
Ensemble Methods
Artificial Intelligence

Abstract

Hyperspectral images are usually high-dimensional data consisting of hundreds of spectral bands. Thanks to the spectral details they provide, they are preferred in many ground observation tasks such as forest areas, vegetation, and harvest forecasting. With the widespread use of artificial intelligence in many areas, the use of machine learning algorithms in highly complex data such as hyperspectral data continues to increase. In this study, the Indian Pines dataset was classified using three different machine learning algorithms. In the experiments, the performance of the Support Vector Machines algorithm was compared with the performance of the Random Forest and XG Boost ensemble methods. According to the results obtained, the highest performance was obtained with the XG Boost algorithm as 90.88%. The worst result was obtained with Random Forest as 79.61%. The SVM algorithm, on the other hand, took second place in the performance obtained with an accuracy of 85.12%. The results obtained are presented together with the visuals and the performance metrics are also evaluated as precision, recall, and F1 score.

1. Introduction

Early on in the 1970s, remote sensing was the primary use of hyperspectral imaging then it spread out to other many fields (Amigo et al. 2015). Many methods have been developed to extract information in many fields from data consisting of hundreds of spectral bands. Machine learning is one of the popular methods used in this field. In this study, the performance of the Support Vector Machine algorithm was compared with the other ensemble machine learning algorithms, Random forest and eXtreme Gradient Boosting (XG Boost). While the XG Boost method gave the best results, the lowest accuracies were obtained with the experiments using the RF algorithm. The performances of the items were tested with precision, recall, f1-score and gestational accuracy criteria. The classification maps obtained as a result of the experiments are presented as images.

Experiments in the study were carried out on the Indian Pines data set (URL-1). The dataset image and ground truth are shown in Figure 1. The Indian Pines test site is in Northwest Indiana and the images of the dataset consist of 224 spectral bands and 145 x 145 pixel images in the wavelength range of 0.4–2.5 ± 10^{-6} meters. The image of the data set includes 16 classes, mostly agriculture, forest and vegetation classes. The class names and sample numbers for each class is shown in Table 1. In the study, 200 bands of the dataset was used in the experiments. The class distribution is showed in Table 1.

Figure 1. Indian pines dataset image and ground truth with legend

* **Corresponding Author**

*(soatik@gtu.edu.tr) ORCID ID 0000-0003-2876-040X

Cite this study

Atik S. O. (2023). Comparative study of hyperspectral imagery classification with SVM and ensemble machine learning methods. Intercontinental Geoinformation Days (IGD), 6, 46-48, Baku, Azerbeijan

Table 1. Indian pines class names and sample numbers

Class	Samples
Alfalfa	46
Corn-notill	1428
Corn-mintill	830
Corn	237
Grass-pasture	483
Grass-trees	730
Grass-pasture-mowed	28
Hay-windrowed	478
Oats	20
Soybean-notill	972
Soybean-mintill	2455
Soybean-clean	593
Wheat	205
Woods	1265
Buildings-Grass-Trees-Drives	386
Stone-Steel-Towers	93

The general flowchart of the study is illustrated in Figure 2. The selected samples of the Indian Pines were shown in Figure 3.

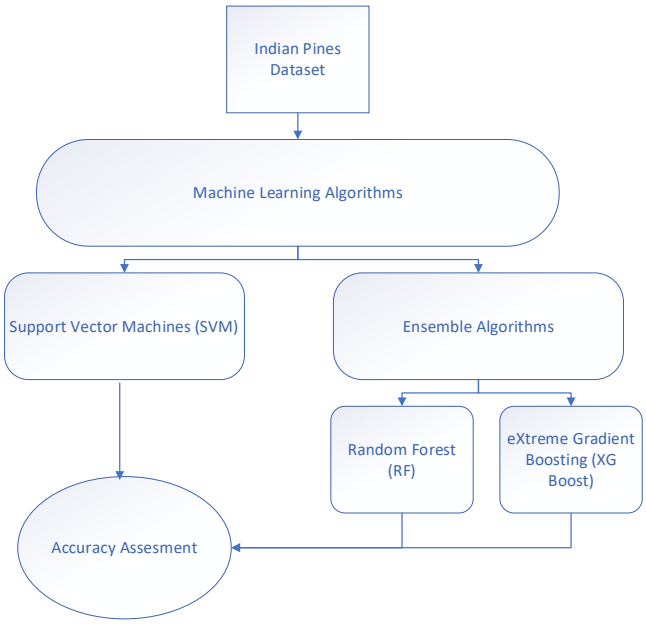

Figure 2. General flowchart of the study

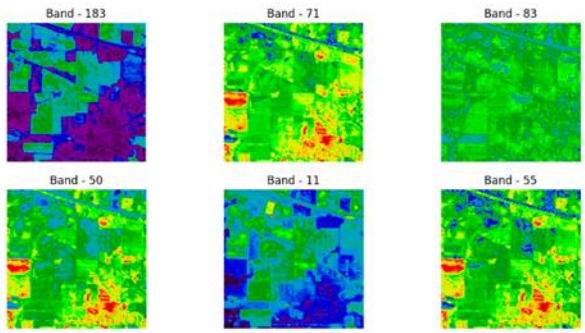

Figure 3. Band Samples of Indian Pines Dataset

2. Method

Machine learning algırithms that are used in the experiments are explained shortly below.

2.1. Support Vector Machines

The supervised machine learning technique Support Vector Machines (SVM) (Cortes and Vapnik, 1995) is utilized for both classification and regression tasks. When the data has distinct boundaries that can be easily separated or when moving the data into a higher-dimensional feature space helps improve separation, it performs particularly well.

In a number of fields, including text classification, image recognition, and bioinformatics, SVM has been shown to be successful. They have effective high-dimensional data-handling skills and good generalization capabilities. SVMs, however, may be sensitive to parameter adjustment and kernel selection.

2.2. Random Forests

A capable and common non-parametric machine learning algorithm, Random Forest (Breiman, 2001) is used for both classification and regression tasks. It functions by building a group of decision trees, then making predictions based on the combined output of these trees. The final prediction is obtained using a voting or averaging method, and each decision tree is trained independently on a part of the data that has been randomly selected.

2.3. Extreme Gradient Boosting (XGBoost)

Extreme Gradient Boosting, or XGBoost(Chen et al., 2015) is a robust and widespread machine learning algorithm that is mainly applied to regression and classification issues. It is an improved version of the machine learning technique known as gradient boosting, which combines the predictions of several weak models (often decision trees) to produce a powerful predictive model (Budholiya et al., 2022). The function is shown in Equation 1.

Objective Function = Loss Function + Regularization Term (1)

2.4. Evaluation Metrics

The evaluation metrics are selected as precision, recall, F1-score and general accuracy. The general formulas are shown in Equations 3-6.

$$Precision = \frac{TP}{TP + FP} \quad (3)$$

$$Recall = \frac{TP}{TP + FN} \quad (4)$$

$$F1\ score = 2\ \mathrm{x} \frac{Precision\ \mathrm{x}\ Recall}{Precision + Recall} \quad (5)$$

$$Overall\ accuracy = \sum_{i=1}^{k} \frac{N_{ii}}{N} \quad (6)$$

TP İS true positive, FP is false positive, FN is false negative and N is the number of samples in the equations.

3. Results

According to the results obtained in the study, the best result was 90,88 % overall accuracy with XG Boost. With the SVM machine learning method, 85, 12 % accuracy was achieved. 79,61 % accuracy has been achieved with the RF algorithm. The performances are listed in Table 2.

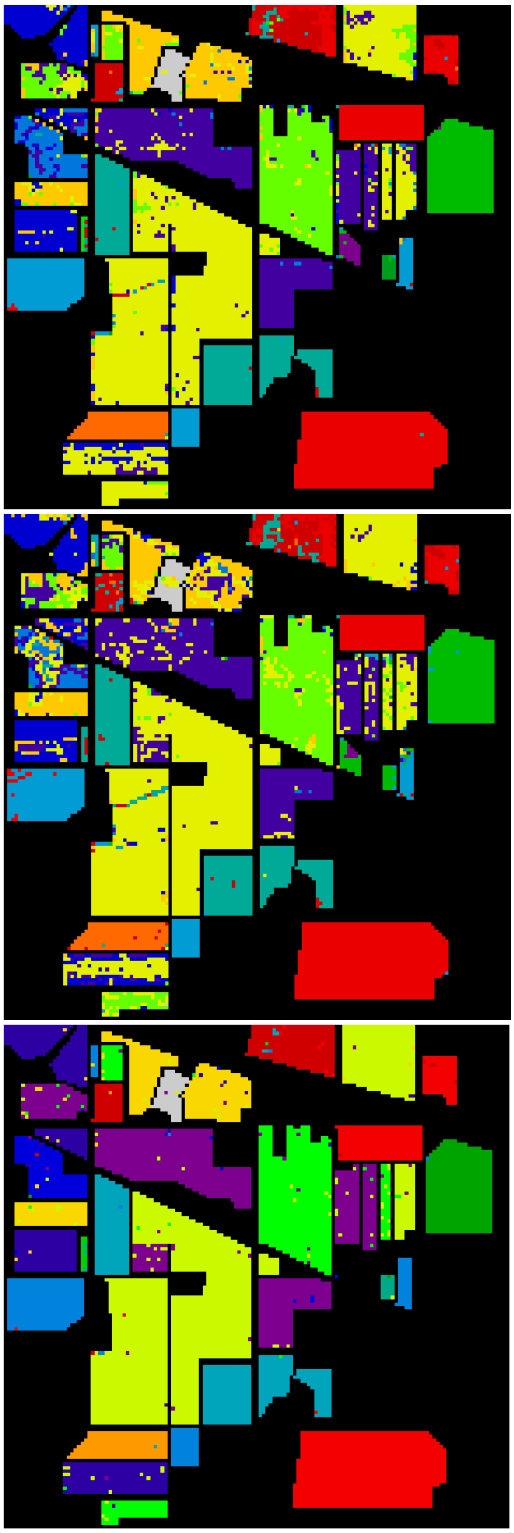

Figure 4. SVM(top), RF (middle) and XGBoost (bottom) classification results by order

Table 2. Performance metrics of the experiments

Methods	Precision	Recall	F1score	Accuracy
SVM	85,94	81,25	83,01	85,12
RF	72,39	64,65	67,20	79,61
XGBoost	90,32	84,49	86,74	90,88

The classification maps are shown in Figure 4. According to classification results generally XG Boost algorithm gave the best performances for most classes. However, in the classification performed using this algorithm, the confusion in the corn no-till and alfalfa classes is remarkable. On the other hand, in SVM and RF results the salt and pepper effect seems to be more common.

4. Discussion

According to the results of the study, one of the ensemble methods was found to be superior to SVM in all conditions, while the other lagged behind the performance of SVM. In this case, it was concluded that it would not be appropriate to generalize the performance of ensemble methods when compared to SVM. The numerical results obtained differ depending on the algorithm used for classification. At the same time, the results obtained may vary depending on the hyperparameter optimization of the algorithms used. In this study, experimentally suitable parameters were sought and used for all three algorithms. The fact that XG boost gives better results than other algorithms may be since it is a new generation technique that includes an iterative optimization.

5. Conclusion

The study can be enriched with more machine learning algorithms and the application of the ensemble method. At the same time, the use of a large number of spectral bands in experiments can be reduced by feature extraction or dimension reduction techniques, and its effect on performance in experiments can be investigated.

References

Amigo, J. M., Babamoradi, H., & Elcoroaristizabal, S. (2015). Hyperspectral image analysis. A tutorial. Analytica chimica acta, 896, 34-51.

Breiman, L. (2001). Random forests, Machine learning, 45(1), 5-32

Budholiya, K., Shrivastava, S. K., & Sharma, V. (2022). An optimized XGBoost based diagnostic system for effective prediction of heart disease. Journal of King Saud University-Computer and Information Sciences, 34(7), 4514-4523.

Chen, T., He, T., Benesty, M., Khotilovich, V., Tang, Y., Cho, H., ... & Zhou, T. (2015). Xgboost: extreme gradient boosting. R package version 0.4-2, 1(4), 1-4.

Cortes, C., & Vapnik, V. (1995). Support-vector networks, Machine learning, 20(3), 273-297.

URL-1. The Indian Pines hyperspectral dataset, Purdue University, Retrieved April 20, 2023, fromhttps://engineering.purdue.edu/~biehl/MultiSpec/hyperspectral.html

6th Intercontinental Geoinformation Days

igd.mersin.edu.tr

Upwelling events in the Caspian Sea

Said Safarov [1], Vusal Ismayilov [2], Elnur Safarov[1]

[1]*Institute of Geography of Ministry of Science & Education, Caspian Sea Hydrometeorology Department, Baku, Azerbaijan*
[2] *Baku State University, Geography Faculty, Baku, Azerbaijan*
[3] *Institute of Geography of Ministry of Science & Education, Caspian Sea Level Department, Baku, Azerbaijan*

Keywords
Caspian Sea
MODIS Aqua
Upwelling phenomenon
Sea surface temperature
Advection

Abstract

In this article, upwelling phenomena that are observed in the surface waters of the Caspian Sea were studied. For this purpose, we used data from MODIS-Aqua satellite observations in the infrared range of 11 microns, with a spatial resolution of 4 km, for the period 2003-2021, which are available through the NASA Giovanny on-line data system databases. It has been established that in the eastern part of the Middle and South Caspian, upwelling phenomena are mainly observed from May to September. The most intense upwelling is observed on the eastern coast of the Middle Caspian in July-August. According to averaged long-term data, the upwelling phenomenon during this period is mainly observed between 40-44º latitude, and its width increases from north to south, reaches 60-70 km in the direction of the Kazakh Gulf and decreases to the south. In the upwelling zone, the temperature gradient sometimes reaches 4.0ºC/100 km. In some years, the upwelling zone that has arisen on the eastern coasts can spread over long distances and even reach the western coasts. In most cases, the upwelling phenomenon occurs against the background of advection of warm waters from the South Caspian to the Middle Caspian.

1. Introduction

In the eastern and western coasts of the Middle and partly Southern Caspian, a thin strip of deep cold waters rises, which is called the upwelling phenomenon

The phenomenon of upwelling in the Caspian Sea and its causes are the subject of many scientific works. A number of researchers (Kosarev 1980) showed in their studies that the rise of deep waters to the surface is due to the water cycle under the influence of wind.

Thus, long-term studies show that easterly winds prevail over the eastern part of the Caspian Sea from mid-July to October (Dyakonov & Ibraev 2019). These winds drive relatively warm water from the sea surface into the open sea, and it is replaced by cold water rising to the surface from the deep layers.

On the other hand, currents directed from the shore to the open sea create reverse currents of water in the lower layers, i.e., currents of cold water directed towards the shore.

There are different explanations for the occurrence of upwelling. So, in the 1960s. it was suggested that groundwater is the cause of temperature anomalies in the eastern part of the Middle Caspian (Mayantsev & Osyanin 1965). One of the arguments against this idea is the observed homogeneity of salinity and other hydrochemical properties of the waters of the eastern part of the Middle Caspian.

In 1977 A.A. Karimov and N.T. Klevtsova put forward a hypothesis about the relationship between temperature anomalies and internal waves (Kerimov & Klevtsova, 1977). The study of temperature anomalies occurring in the western part of the Middle Caspian showed that they are of a "synoptic" nature (Monakhova & Akhmedova, 2010).

The upwelling phenomenon is observed both on the eastern and western coasts of the Middle and South Caspian. However, it should be noted that if on the east coast in May-September upwelling is systematic, then on the west coast it is relatively episodic. From this point of view, and since the study considered only long-term average monthly, average seasonal and average annual distributions, it is difficult to identify and study the manifestations of upwelling on the west coast based on the corresponding satellite images.

* **Corresponding Author**

*(safarov53@mail.rul) ORCID ID 0000-0002-8447-2843
(vusalhakimoglu@gmail.com) ORCID ID xxxx – xxxx – xxxx – xxxx
(elnur.safarov854@gmail.com) ORCID ID xxxx – xxxx – xxxx – xxxx

Cite this study

Safarov, S., Ismayilov, V., & Safarov, E. (2023). Upwelling events in the Caspian Sea. Intercontinental Geoinformation Days (IGD), 6, 49-52, Baku, Azerbaijan

2. Method

The present study used water surface temperature (SST) data (2003-2021) from the NASA Giovanni online information system database based on nighttime measurements of the MODIS radio spectrometer installed on the Aqua satellite. The MODIS spectroradiometer with a wavelength of 11 μm has a horizontal spatial resolution of 4 km, which makes it possible to detect mesoscale anomalies in the distribution of the surface temperature of the Caspian Sea, especially upwelling zones, and their characteristic features.

3. Results and discussion

As can be seen from Figure 1, the upwelling in May is not very intense, but the size and intensity of the upwelling zone in May in different years can be different (Ginzburg et al., 2020; Lavrova et al., 2011). Upwelling, which began mainly in the eastern part of the Middle Caspian in May, relatively weakens the advection of warm water mass from the South Caspian to the Middle Caspian.

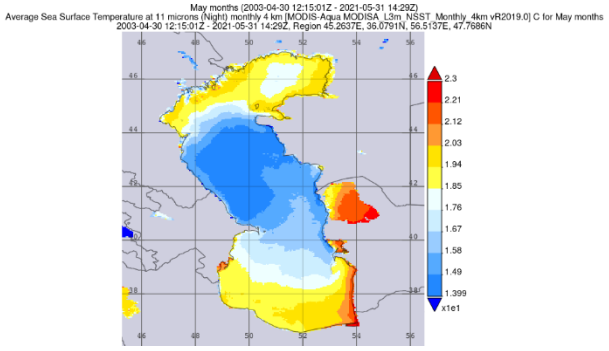

Figure 1. Distribution of sea surface temperature in the Caspian Sea in May

In June, the upwelling phenomenon, which began from the eastern coast of the sea, begins to manifest itself more clearly (Figure 2). Thus, the upwelling zone extends along the eastern part of the sea along the 20.2 ^{0}C isotherm from latitude 44,2^0 to 39,5^0 and covers large areas to the west. It can spread to the western coast of Ogurchink Island (Ginzburg et al., 2020). As can be seen from Figure 2, the minimum surface temperature in the up-welllling zone is 18 ^{0}C, but in some years it can drop to 14^{0}C.

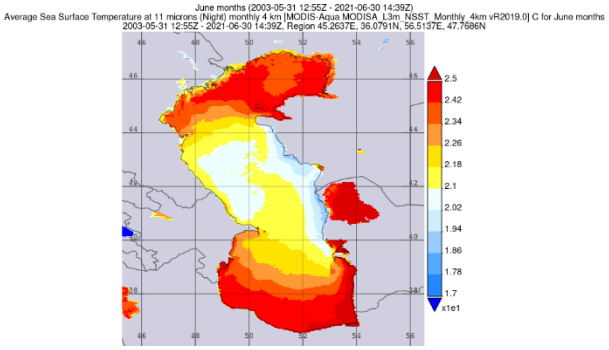

Figure 2. Distribution of sea surface temperature in the Caspian Sea in June

In June, the intensification of the upwelling phenomenon in the eastern part of the Middle and partly the South Caspian is accompanied by a noticeable weakening of the advection of warm water masses from the east of the South Caspian and its deviation to the west.

In July, a pronounced upwelling was recorded on the eastern coast of the Middle and partly Southern Caspian (Figure 3). As can be seen from the figure, the width of the upwelling zone increases from north to south, and in some places even reaches 60 km. In the east of the Middle Caspian, the water surface temperature drops from 25 ºC to 21 ºC from west to east. The temperature gradient is 4.2 ºC/100 km.

Figure 3 shows that the upwelling zone extends from the 40th parallel to the 44.5th parallel, expands to the south from Cape Peschany and even penetrates the South Caspian. Intense upwelling partially extinguishes the advection of warm water mass from the South Caspian to the Middle Caspian, and even the reverse process occurs, i.e., advection of the upwelling mass of cold water from the Middle Caspian to the South Caspian.

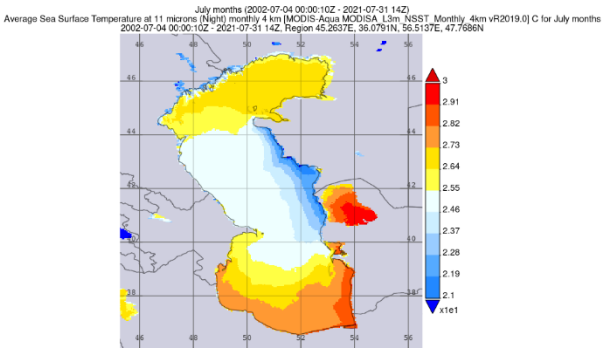

Figure 3. Distribution of sea surface temperature in the Caspian Sea in July

As can be seen from Figure 4, the upwelling process in August remains intense, but compared to July, its southern border shifts by about 0.5÷0.7º to the north, and the process cannot penetrate the South Caspian. As can be seen from the figure, the reason for this is the advection of warm waters from the South Caspian to the Middle Caspian more often than in July. In the western part of the South Caspian, on the contrary, advection of relatively cold waters from the Middle Caspian prevails. Lower upwelling temperatures (22 ºC) are observed in the area from the southern coast of Cape Peschanyi to the northern part of the Kazakh Bay.

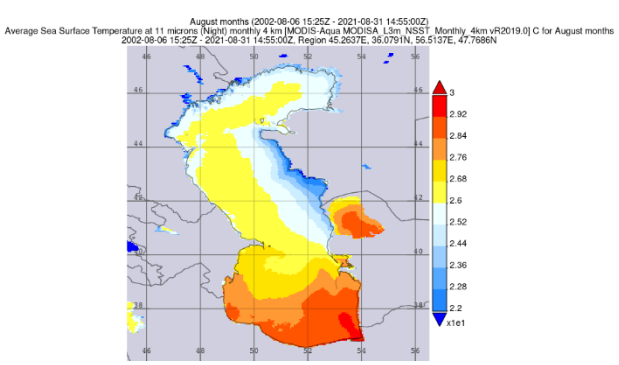

Figure 4. Distribution of sea surface temperature in the Caspian Sea in August

It should be noted that in some years the nature of the distribution of the average surface temperature in August may undergo certain changes. Figure 5 shows the distribution of the average sea surface temperature for August 2009 over the sea area. As can be seen, there is a strong advection of warm water masses from the eastern part of the South Caspian to the Middle Caspian, as evidenced by the convexity of the corresponding isotherms to the north. This process prevents the upwelling zone from spreading to the south. Instead, the rising cold-water mass extends to the west in a strip about 200 km long and about 100 km wide from the direction of Cape Peschany, and even individual jets of cold water reach the western coast.

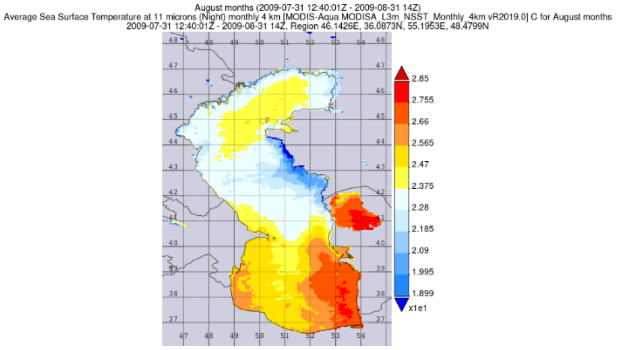

Figure 5. Distribution of the average water surface temperature in the Caspian Sea area in August 2009

The upwelling event, which took place in August 2014, is of greater interest due to its uniqueness. The distribution of the average surface temperature for August 2014 is shown in Figure 6. As can be seen from the Figure 6, the upwelling phenomenon here occurs under conditions of strong temperature advection, which originates in the eastern part of the South Caspian and is directed to the north, which prevents upwelling from spreading to the south. Temperature advection from the eastern part of the South Caspian to the north extends along the eastern coast of the Middle Caspian to the Kazakh Gulf, and therefore the southern border of the upwelling zone begins only from the northern coastal waters of this bay. From the north, the upwelling zone is limited by the southern coastal waters of the Tyube-Karagan peninsula.

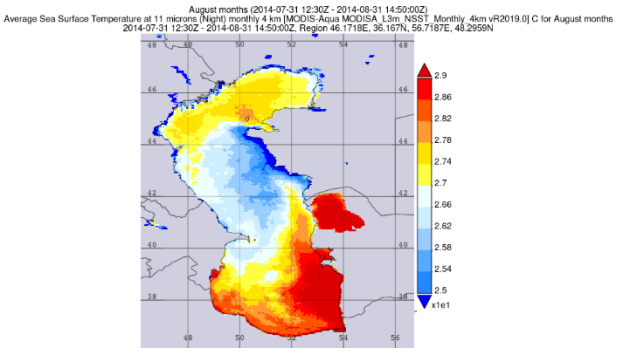

Figure 6. Distribution of the average water surface temperature in the Caspian Sea area in August 2014

As can be seen from Figure 6, the upwelling waters, which could not penetrate south from the Kazakh Gulf due to strong temperature advection from the southeast, spread to the west and south, reaching a very significant part of the Middle Caspian and even the northeastern coastal waters of the South Caspian, or rather the Azerbaijani sector of the sea. From this point of view, this effect can explain the sometimes-sharp cooling of the waters of the western coast of the sea during hot periods of the year. On the other hand, the penetration of upwelling waters into the South Caspian leads to anomalous changes in the distribution of surface waters here (Figure 6).

In September, the southern border of the upwell-ling zone in the east of the Caspian Sea (isotherm 22.6 ºC) passes through the latitude 40.5 º, as in August. Since the water temperature in the North Caspian begins to decrease in September, it becomes difficult to determine the northern boundary of the upwelling zone. The main difference between the upwelling observed in this month and August is that the upwelling zone is narrower, against the background of a relatively lower temperature.

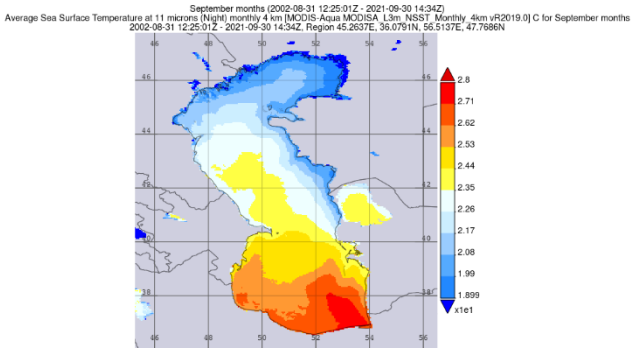

Figure 7. Distribution of sea surface temperature in the Caspian Sea in September

It should be noted that the upwelling processes observed in September of different years can manifest themselves in different ways. During the years of intense advection of warm water mass from the South Caspian to the Middle Caspian, the southern border of upwelling is significantly shifted to the north. For example, in September 2014, warm advective currents moving north along the east coast from the South Caspian extended to about the 42th parallel, preventing the upwelling process from spreading south, and instead, the transformed upwelling waters moved westward from the coastal zone to the direction to the south and reached a latitude of 38.5º in the South Caspian (Ginzburg et al., 2020). On the contrary, in years when there is no advection of the waters of the South Caspian into the Middle Caspian, the southern boundary of the upwelling belt can move up to the 40th parallel (Lavrova et al., 2011).

4. Conclusion

Analysis of MODIS Aqua data showed that in the period May-September, upwelling occurs in the eastern and western coastal waters of the Middle Caspian and partly in the South Caspian. It occurs regularly on the east coast, and fragmentarily on the west coast. The most intense upwelling is observed on the eastern coast of the Middle Caspian in July-August. According to averaged

long-term data, the upwelling phenomenon during this period is mainly observed between 40-44º latitude, and its width increases from north to south, reaches 60-70 km in the direction of the Kazakh Gulf and decreases to the south. In the upwelling zone, the temperature gradient sometimes reaches 4.0 ºC/100 km. In some years, the upwelling zone that has arisen on the eastern coasts can spread over long distances and even reach the western coasts. In most cases, the upwelling phenomenon occurs against the background of advection of warm waters from the South Caspian to the Middle Caspian.

References

Dyakonov, G. S., & Ibraev, R. A. (2019). Dynamics of the waters of the Caspian Sea over the Apsheron threshold in 2003. Marine Hydrophysical Journal, 35(6), 633-645

Ginzburg, A. I., Kostyanoy, A. G., & Sheremet, N. A. (2020). Dynamics of the upwelling zone near the eastern coast of the Caspian Sea in the seasonal cycle (May-September) according to satellite long-term average temperature data (2003–2019). Modern problems of remote sensing of the Earth from space, 17(7), 215–226

Kerimov, A. A., & Klevtsova, N. T. (1977) Anomaly of water temperature and internal waves in the Middle Caspian. Proceedings of the TCRIH, 70, 53-63

Kosarev, A. N. (1980). Water structure and conditions for the formation of biological productivity in the Middle and South Caspian. Water resources, 3, 26-36

Lavrova, O. Yu., Kostyanoy, A. G., Lebedev, S. A., Mityagina, M. I., Ginzburg, A. I., & Sheremet, N. A. (2011). Integrated satellite monitoring of the seas of Russia. M. IKI RAN, 470

Mayantsev, G. P., & Osyanin, Yu. A. (1965). On underground runoff from Mangyshlak to the Caspian Sea. Oceanology, T. 5., 5, 854-855.

Monakhova, G. A., & Akhmedova, G. A. (2010). Rise of deep waters near the western coast of the Middle Caspian. Scientific journal of KubGAU, 63 (09), 1-12

6th Intercontinental Geoinformation Days

igd.mersin.edu.tr

Flood risk susceptibility and evaluation by AHP technique in Denizli, Turkiye

Hamedreza Vafa[*1], **Dursun Zafer Seker** [2]

[1]*Istanbul Technical University, Graduate School, Geographical Information Technologies Program, Istanbul, Turkiye*
[2] *Istanbul Technical University, Civil Engineering Faculty, Department of Geomatics Engineering, Istanbul, Turkiye*

Keywords
Remote sensing
Google Earth Engine
Flood Hazard Map
Geographic Information system
Analytical Hierarchy Process

Abstract

Flood remains one of the most devastating natural calamities worldwide, inflicting irreparable damage upon society, the environment, and critical infrastructure. The compounding effects of climate change have only deepened the complexity of this challenge. Hence, a comprehensive exploration of the flood phenomenon from diverse perspectives becomes imperative, necessitating interdisciplinary collaboration with specialists from various fields of study. In this vein, the present study endeavors to evaluate eleven influential factors utilizing advanced technologies such as Google Earth Engine (GEE), Geographic Information System (GIS), and the Analytical Hierarchy Process (AHP). The outcome of this concerted effort is the development of a Flood Hazard Map (FHM), which accuracy was verified through a rigorous comparison with historical events. This model proves highly effective in discerning flood-prone regions, garnering substantial acceptance from rational perspectives. The ensuing results reveal that nearly half of the region under scrutiny is characterized by high and very high hazard levels, underscoring the urgent need for further in-depth investigations in this domain. Moreover, it is of paramount importance to acknowledge the profound impact of the June 2023 flood, a pivotal and well-documented factor influencing the outcomes of this study. Overlooking this critical aspect could portend irreversible consequences for the future. Therefore, it is imperative to recognize the significance of interdisciplinary cooperation, the potential ramifications of climate change, and the crucial historical events that shape our understanding of floods. Effective strategies to mitigate flood risks, safeguard lives, and protect irreplaceable resources can be developed by adopting a holistic strategy.

1. Introduction

Globally, floods continue to be a great natural hazard (Kreibich et al., 2022), causing over 4,000 fatalities in 2021 (Global Natural Disaster Assessment Report, 2021). Meanwhile, according to (Statista, 2023), 146 people died in the 2021 flash and river floods in the USA. This is the greatest amount between 1995 and 2021, after its peak in 2015 with 176 deaths. Floods can potentially destroy infrastructure, interrupt vital services, relocate populations, and threaten lives and livelihoods. Considering population expansion and climate change, this issue gets progressively more complicated. Flash floods and river floods are classified as two main types of floods. The first group generally leads to greater loss of life, and the latter issues damage to properties (USGS, 2023).

Flash floods (or Pluvial floods) are destructive floods that occur in a short period, generally caused by heavy rainfall or the unexpected release of water from either natural or artificial sources. Heavy rains in June 2019 caused flash floods in Denizli, a southwestern province of Turkiye. The flood destroyed infrastructure, residences, and agricultural fields in various regions, including Pamukkale. Flash floods immediately overwhelmed the region, causing fatalities and disrupting routines. Meanwhile, flooding in June 2022 affected the agricultural areas of the province.

River floods (or Fluvial floods) occur when rivers overflow their banks and inundate adjacent areas with

* **Corresponding Author**

*(vafa21@itu.edu.tr) ORCID ID 0000-0002-8171-9206
(seker@itu.edu.tr) ORCID ID 0000-0001-7498-1540

Cite this study

Vafa H., & Seker D. Z (2023). Flood risk susceptibility and evaluation by AHP technique in Denizli, Turkiye. Intercontinental Geoinformation Days (IGD), 6, 53-56, Baku, Azerbaijan.

water. The Büyük Menderes River in Denizli experienced a flood with spring run-off between March 10 and March 15, 2006.

Besides, addressing the impacts of floods in the era of climate change requires a comprehensive approach based on scientific understanding. Mitigation efforts to reduce greenhouse gas emissions are crucial in slowing down the pace of climate change and limiting its long-term impacts on flood patterns (IPCC, 2018). Despite the global concerns resulting from Covid-19, (Vafa et al. 2021, 2022) showed that mandatory quarantines reduced air pollution in Khuzestan province and Istanbul city, which are among the most polluted regions in Iran and Turkiye. Tackle the multidisciplinary issue, which is directly and indirectly affected or related to the trend of expanding urbanization, loss of agricultural land, changes in rain patterns, droughts, and depletion of water supplies needs the attention of numerous world specialists and international collaboration. This subject may be investigated from several perspectives. One of the most critical challenges is the availability of a Flood Map (FM) or flood-prone areas to make wise decisions to protect human, natural, and financial resources.

Despite the numerous floods that occurred in Turkiye and their financial and human losses, Haltas et al., (2021) discovered a significant disparity in the number of flood records and their accuracy between agencies. This study fills that gap by providing valuable flood event inventories. It should be mentioned that both the population and the number of floods depicted an increasing pattern. According to this research, floods killed over a thousand people (human resources), damaged nearly two thousand square kilometers of agricultural land (food scarcity and economic loss) and resulted in the loss of approximately two thousand million TL (financial resources) between 1930 to 2020 years. Meanwhile, Denizli province has taken fourth place in terms of floods, trailing only Istanbul, Antalya, and Rize. Due to the limited number of studies conducted in Denizli province, this area has been selected as a case study.

This study aims to investigate the flood hazard by producing a flood hazard map (FHM) for the region using the AHP method and validating it by overlaying the results with a layer of historical events (archive data).

2. Method

2.1. Study Area

Denizli province is in the southwest of Turkiye, between longitudes 28.55° E and 30.04° E and latitudes 36.87° N to 38.45° N, and covers an area of around 11,000 km^2 with a population of around 1,061,000 people. There are currently 36 meteorological stations in the region. Based on the stations' coordinates, monthly rainfall information was extracted from the (NASA power data access viewer) for eight of these stations. The maximum slope of the region is approximately 70 degrees with an average of 11. Meanwhile, the average elevation is approximately 962 meters above sea level, ranging from 105 to 2531 meters "Figure 1".

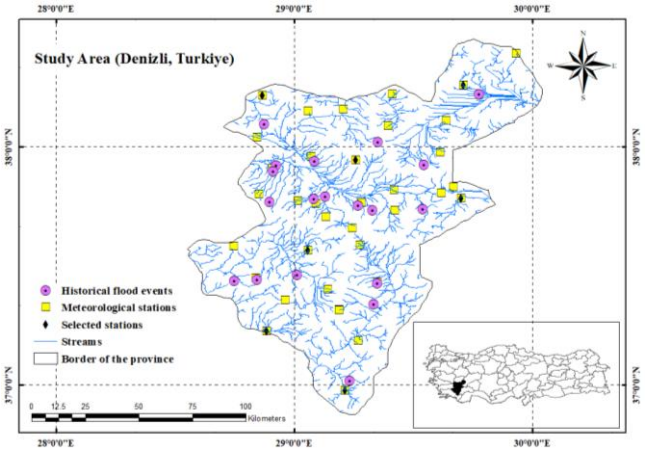

Figure 1. Study Area

2.2. Data

Shuttle Radar Topography Mission (SRTM) data was utilized to ascertain the Digital Elevation Model (DEM), as well as elevation (ELV), slope (SLP), curvature (CRV), distance to stream (DtS), drainage density (DD), flow accumulation (FA), and topographic wetness index (TWI) from the DEM.

The monthly precipitation data from the chosen stations between 1981 and 2021 are used in the equation (1), Modified Fournier Index (MFI) to generate the rainfall intensity map (Chen, 2022):

$$MFI = \sum_{1}^{12} \frac{{p_n}^2}{P} \quad (1)$$

Where P and p_n are the average annual and monthly rainfall, respectively.

Corine 2018 was used to generate the LULC map. Remote Sensing (RS) indices such as NDVI, MNDWI, and NDBI were derived from Landsat images with the aid of Google Earth Engine (GEE). Also, the soil type (ST) layer of the region has been obtained according to the layer provided by the Food and Agriculture Organization of the United Nations (FAO).

Then, using the Jenk algorithm, the 8 parameters ELV, SLP, DtS, DD, TWI, NDVI, FA, and MFI were divided into 5 categories. CRV, ST, and LULC are also classified as 1 to 5 based on expert's opinions and previous researches (Ozay and Orhan, 2023; Talukdar et al., 2020; Khosravi et al., 2019; Tehrany et al., 2014). Curvature was classified as concave, flat, and convex which were 5, 3, and 1, respectively. LULC has been classified as 5 for built-up and water bodies. Barren, agriculture, sparse vegetation, and forest were assigned 4 to 1, respectively. Also, ST had been classified as Calcic and Eutric Cambisols, Calcaric Fluvisol, Lithosols, Calcic Xerosols, and water as one, three, four, and five.

2.3. Analytic Hierarchy Process

The analytic hierarchy process (AHP) is a mathematical technique for evaluating complex decision problems with multiple criteria (Saaty, 1988). So, the weight values of each GIS layer were determined utilizing

the AHP. The initial step is identifying the decision dilemma. Then using a pairwise comparison matrix in which all detected important properties of the GIS layer are compared with preference factors, AHP calculates the necessary significant weighting factors for each GIS layer (Yuan et al., 2022). In the pairwise comparison matrix of the AHP, ratings range continuously from 1 (least significant) to 9 (most significant). The importance rating of each criterion was introduced by Saaty (1977).

This study's proposed methodology suggests an 11 by 11 pairwise comparison matrix. The criteria are arranged hierarchically. Each row's values characterize the relative importance between the two factors. So, a pairwise comparison matrix was developed based on Saaty's rating, literature review, and expert opinions. Table 1 represents the normalized comparison matrix.

The obtained weight for each layer is given in Table 2.

Table 1. Normalized pairwise comparison matrix

Factor	DtS	SLP	DD	ELV	FA	NDVI	MFI	LULC	TWI	ST	CRV
DtS	0.29	0.35	0.28	0.34	0.32	0.23	0.21	0.20	0.17	0.17	0.16
SLP	0.15	0.17	0.28	0.11	0.19	0.23	0.21	0.20	0.17	0.17	0.16
DD	0.15	0.09	0.14	0.23	0.19	0.14	0.13	0.14	0.12	0.13	0.12
ELV	0.10	0.17	0.07	0.11	0.13	0.14	0.13	0.14	0.12	0.13	0.12
FA	0.06	0.06	0.05	0.06	0.06	0.14	0.13	0.09	0.12	0.09	0.09
NDVI	0.06	0.03	0.05	0.04	0.02	0.05	0.13	0.09	0.07	0.09	0.09
MFI	0.06	0.03	0.05	0.04	0.02	0.02	0.04	0.09	0.12	0.09	0.09
LULC	0.04	0.02	0.03	0.02	0.02	0.02	0.01	0.03	0.07	0.06	0.09
TWI	0.04	0.02	0.03	0.02	0.01	0.02	0.01	0.01	0.02	0.06	0.05
ST	0.03	0.02	0.02	0.02	0.01	0.01	0.01	0.01	0.01	0.02	0.03
CRV	0.03	0.02	0.02	0.02	0.01	0.01	0.01	0.01	0.01	0.01	0.02

Table 2. Factors' weight by AHP method

Factor	DtS	SLP	DD	ELV	FA	NDVI	MFI	LULC	TWI	ST	CRV
Weight	0.25	0.19	0.14	0.12	0.08	0.06	0.06	0.04	0.03	0.02	0.01

And finally, the hazard map of the area was generated by Equation (2) in the raster calculator.

$$FHI = \sum_{i=1}^{n} W_i F_i = W_{Dts} Dts + W_{SLP} SLP + W_{DD} DD + W_{ELV} ELV + W_{FA} FA + W_{NDVI} NDVI + W_{MFI} MFI + W_{LULC} LULC + W_{TWI} TWI + W_{ST} ST + W_{CRV} CRV \quad (2)$$

Where;
FHI: Flood Hazard Index
W_i: Weights derived via the AHP
F_i: Flood factor's raster layers

3. Results

To demonstrate the reliability of the flood hazard map, the results were validated using historical flood events "Figure 2".

4. Discussions

AHP was able to classify the previously selected events as having a hazard level between 2 and 5, except for a single point that is classified as having a very low hazard level. On this basis, the implementation of the AHP method to generate the area's flood hazard map was deemed effective.

Accordingly, approximately 26% and 22% of the region are at high and very high inundation hazard levels, respectively.

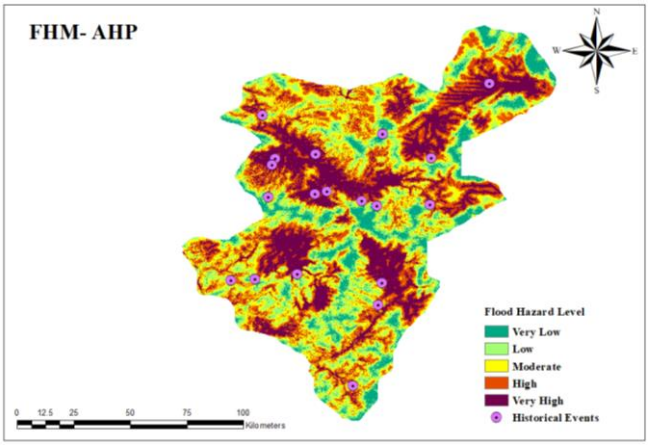

Figure 2. Flood Hazard Map

5. Conclusions

In this study, the AHP method was used to develop a map of the region's flood hazard, and nearly fifty percent of the region was classified as having a high or very high flood hazard level. Due to the presence of agricultural lands and gardens, urban areas, mines, construction and industrial spots in the region, it is essential to develop a comprehensive crisis management plan.

Acknowledgment

This research represents the preliminary phase of a master's thesis currently being finalized at Istanbul Technical University. It is anticipated that this endeavor will serve as a foundation for defining additional multidisciplinary initiatives to reduce the province's vulnerability and devising effective action plan scenarios.

References

Chen, Y. (2022). Flood hazard zone mapping incorporating geographic information system (GIS) and multi-criteria analysis (MCA) techniques. Journal of Hydrology, 612(C). https://doi.org/10.1016/j.jhydrol.2022.128268

Corine from Copernicus. Date retrieved: February 2023. https://land.copernicus.eu/pan-european/corine-land-cover/clc2018?tab=download

FAO. (2023). Food and Agriculture Organization of United Nations. Date retrieved: February 2023.

Global Natural Disaster Assessment Report. (2021). Date retrieved: May 2023. https://www.preventionweb.net/quick/74710

Haltas, I., Yildirim, E., Oztas, F. & Demir, I. (2021). A comprehensive flood event specification and inventory: 1930–2020 Turkey case study. International Journal of Disaster Risk Reduction, 56. https://doi.org/10.1016/j.ijdrr.2021.102086

IPCC. (2018). Global warming of 1.5°C. An IPCC Special Report on the impacts of global warming of 1.5°C above pre-industrial levels and related global greenhouse gas emission pathways, in the context of strengthening the global response to the threat of climate change, sustainable development, and efforts to eradicate poverty [V. Masson-Delmotte, P. Zhai, H. O. Pörtner, D. Roberts, J. Skea, P.R. Shukla, A. Pirani, W. Moufouma-Okia, C. Péan, R. Pidcock, S. Connors, J. B. R. Matthews, Y. Chen, X. Zhou, M. I. Gomis, E. Lonnoy, T. Maycock, M. Tignor, T. Waterfield (eds.)]. In Press. https://www.ipcc.ch/sr15/

Kreibich, H., Van. Loon, A.F., Schröter, K., ..., Mård, J., Mathew, H, et al. (2022). The challenge of unprecedented floods and droughts in risk management, Nature 608, 80–86. https://doi.org/10.1038/s41586-022-04917-5

Khosravi, K., Shahabi, H., Pham, B.T., Adamowski, J., Shirzadi, A., Pradhan, B., Dou, J., Ly, H.B., Grof, G., Ho, H.L., Hong, H., Chapi, K. & Prakash, I. (2019). A comparative assessment of flood susceptibility modeling using Multi-Criteria Decision-Making Analysis and Machine Learning Methods, Journal of Hydrology. 573, 311-323. https://doi.org/10.1016/j.jhydrol.2019.03.073

NASA power data access viewer. Date retrieved: May 2023. https://power.larc.nasa.gov/

Ozay, B., Orhan, O. (2023). Flood susceptibility mapping by best–worst and logistic regression methods in Mersin, Turkey. Environmental Science and Pollution Research, 30, 45151–45170. https://doi.org/10.1007/s11356-023-25423-9

Saaty, T. L. (1977). A scaling method for priorities in hierarchical structures, Journal of Mathematical Psychology, 15, 3, 234-281. https://doi.org/10.1016/0022-2496(77)90033-5

Saaty, T. L. (1988). What is the Analytic Hierarchy Process? In: Mitra, G., Greenberg, H.J., Lootsma, F.A., Rijkaert, M.J., Zimmermann, H.J. (eds) Mathematical Models for Decision Support. NATO ASI Series, 48. Springer, Berlin, Heidelberg. https://doi.org/10.1007/978-3-642-83555-1_5

Statista. Date retrieved: May 2023. https://www.statista.com/statistics/203709/number-of-fatalities-caused-by-floods-and-flash-floods-in-the-us/

Talukdar, S., Ghose, B., Shahfahad, Salam, R., Mahato, S., Pham, Q.B., Linh, N.T.T., Costache, R., & Avand, M. (2020). Flood susceptibility modeling in Teesta River basin, Bangladesh using novel ensembles of bagging algorithms. Stochastic Environmental Research and Risk Assessment. 34, 2277–2300. https://doi.org/10.1007/s00477-020-01862-5

Tehrany, M.S., Lee, M.J., Pradhan, B., Jebur, M.N., & Lee, S. (2014). Flood susceptibility mapping using integrated bivariate and multivariate statistical models. Environmental Earth Sciences, 72(10):4001–4015. https://doi.org/10.1007/s12665-014-3289-3

USGS. United States Geological Survey. Date retrieved: May 2023. https://www.usgs.gov/

Vafa, H., Dogru, A.O., & Seker, D.Z. (2021). Monitoring air pollution in Khuzestan before and during the COVID-19 Pandemic through remote sensing technology. International Symposium on Applied Geoinformatics. https://doi.org/10.15659/isag2021.12585

Vafa, H., Dogru, A.O., & Seker, D.Z. (2022). Istanbul air pollution analysis from January 2019 till April 2022 through remote sensing technology. 4th Intercontinental Geoinformation Days (IGD), Mersin, Turkiye.

Yuan, Z., Wen, B., He, C., Zhou, J., Zhou, Z., & Xu, F. (2022). Application of multi-criteria decision-making analysis to rural spatial sustainability evaluation: a systematic review. International Journal of Environmental Research and Public Health. 19(11):6572. https://doi.org/10.3390/ijerph19116572

6th Intercontinental Geoinformation Days

igd.mersin.edu.tr

Improving the accuracy of classification of multispectral Images using an anisotropic diffusion neural network algorithm (ADNNA) and machine learning SVM algorithm

Behnaz Torkamani Asl*[1], Parviz Zeaieanfirouzabadi [1], Seyed Mohammad Tavakkoli Sabour [1]

[1]*Kharazmi University, Senior Graduate, the Department of Remote Sensing and Geographical Information System, Tehran, Iran*

Keywords
Unsupervised classification
ADNN
Multi-Level classification
Multispectral Images
Remote Sensing

Abstract

To improve image classification accuracy, one common practice is to add specific information like image texture, DEM and different indices to satellite image datasets. Here, an attempt has been made to include outputs of Anisotropic Diffusion Neural Network algorithm (ADNNA) to satellite image datasets during classification stages. The unsupervised multi-level neural network (or anisotropic diffusion neural network) modifies the pixel values of the input image by consecutive weighted averaging with neighboring pixels. It performs simultaneous modification of all input multi-spectral image at five level of scale/resolution. The algorithm can process both spectral information of the image and textural details resulting from wavelet transformation simultaneously in a multi-scale representation. To perform this task Landsat 8 Surface reflectance images pertaining to Miandoab region have classified with and without adding outputs of ADNNA (five levels) by support vector machine (SVM) algorithm. Different dataset was created. First dataset was a composite of bands of original images only, second dataset was a composite of different outputs of anisotropic diffusion neural network algorithm only and third dataset contains band of original image and each output of anisotropic diffusion neural network algorithm and the last had bands of original image together with all outputs of anisotropic diffusion neural network algorithm**.** SVM classification algorithm was used to classify all datasets separately with the same training site input. Classification accuracy was performing through Kappa coefficient of agreement. Results show that the highest kappa coefficient of agreement in classifying the Landsat 8 image is with level 2 of the ADNNA pluse original image bands with approximately 86% compare to other datasets (original images, all 5 level ADNNA outputs, other levels pluse original images). It is concluded that ADNNA outputs can improve classification results effectively.

1. Introduction

Image classification is one of the most important methods to Interpretation of satellite images and change detection of land use (Ehsani and Shakeryari, 2018). researchers have tried to develop methods and advanced classification techniques to improve the accuracy of classification, these including artificial neural networks, fuzzy logic and intelligent systems (Lu and Weng, 2007). The main advantage of artificial neural networks compared to other methods is that it requires less training data for accurate analysis (Bui, et al. 2012). A better classification result is obtained using the edge preservation filter based on the anisotropic diffusion equation before classification, compared to other methods such as the Gaussian filter or the original images without smoothing with low-pass linear filters (Yuan and He, 2008). This algorithm performs multilevel segmentation of an image at many scales using a multiresolution texture representation. Each level uses anisotropic diffusion to segment a multispectral image at successively lower resolutions. Texture and statistical similarities between and within levels guides the diffusion process. The restriction of coarse-to-fine segmentation is removed, and one operates at all levels simultaneously. In this manner the labeling process can choose the scale or scales at which useful segments exist (Fernandesl and Jernigan, 1992). Since the anisotropic neural network algorithm does not perform classification, no training data is required for this algorithm and it also does not produce any thematic map (Perona and Malik, 1990). This algorithm has a more

* **Corresponding Author**

*(behnaz.torkaman@gmail.com) ORCID ID xxxx – xxxx – xxxx – xxxx
(pzeaiean@gmail.com) ORCID ID xxxx – xxxx – xxxx – xxxx
(tavakkoli.khu_ac@yahoo.com) ORCID ID xxxx – xxxx – xxxx – xxxx

Cite this study

Asl, B. T. Zeaieanfirouzabadi, P., & Sabour, S. M. T. (2023). Improving the accuracy of classification of multispectral Images using an anisotropic diffusion neural network algorithm (ADNNA) and machine learning SVM algorithm. Intercontinental Geoinformation Days (IGD), 6, 57-60, Baku, Azerbaijan

acceptable result in classifying satellite images with high resolution than fuzzy clustering algorithms (Fernandesl and Jernigan, 1992).

The main goal of this work is to investigate the effect of anisotropic diffusion neural network algorithm on classification accuracy. To do this, different dataset was created. First dataset was a composite of bands of original images only, second dataset was a composite of different outputs of anisotropic diffusion neural network algorithm only and third dataset contains band of original image and each output of anisotropic diffusion neural network algorithm and the last has bands of original image together with all outputs of anisotropic diffusion neural network algorithm**.** SVM classification algorithm was used to classify all datasets separately with the same training site input. Classification accuracy was performing through Kappa coefficient of agreement.

2. Research background

The anisotropic diffusion algorithm was first introduced by Prona and Malik (1990), which is an adaptive smoothing method. This method is attractive due to its preservation of edge localization and the ability to control feature scale. The principal of a diffusion-based smoothing method is to allow diffusion where the local gradient magnitude is low, and prevent diffusion at the intensity edges, where the gradient magnitude is relatively high. Therefore, anisotropic diffusion allows intra-region smoothing without inter-region smoothing (Perona and Malik, 1990).

In 2003 Daryaei (2003) used the anisotropic diffusion algorithm and multi-scale wavelet transform for change detection. this study was to reveal urban/agriculture changes using multi-scale analysis by using multi-resolution/multi-temporal image data in Esfahan city in Iran.

In 2007, Noberga et al. (2007) compared the classification accuracy of 3 different image types, an original LiDAR image, an image filtered with a low-pass kernel filter, and an image filtered with an anisotropic diffusion filter, both Anisotropic diffusion filter and filter with low-pass kernel are used to remove noise from images. They found that anisotropic diffusion method with the best result among others.

3. Anisotropic diffusion neural network framework

Anisotropic Diffusion Neural Network is a five-level network where the lowest l having one node per pixel in the full resolution image, and successive levels are connected to each other in the manner of a quad tree. Each node at the lowest level is connected to the output, the highest frequency of the texture map, at the same location, and the nodes of successive levels are connected to the lower frequencies of the texture maps (Fernandesl and Jernigan, 1992).

Perona and Malik pursued 3 basic goals to present the 5-level neural network of the space scale of the anisotropic diffusion equation:

1. No artificial details should be created from smaller scales to larger scales.
2. At each level, the boundaries of each region should be preserved and correspond to meaningful boundaries in the same image resolution.
3. Anisotropic diffusion allows intra-regional smoothing to occur without inter-regional smoothing [6].

The general formula of anisotropic diffusion neural network is given in equation (Perona and Malik, 1990 (1):

$$I_t = div(c(x.y.t)\nabla I) = c(x.y.t)\Delta I + \nabla c \cdot \nabla I \qquad (1)$$

In the above equation, the diffusion coefficient is assumed to be constant and independent of the location. Perona and Malik believed that by modifying the anisotropic diffusion formula they could achieve the goals stated in the previous section, they explained how a suitable choice of c(x,y,t) can satisfy the criteria 2 and 3 listed in the section He estimated the previous one**.**

Div is the divergence operator, Δ and ∇ represent the gradient and Laplacian operators, respectively, according to the distance variables. In the relation of I_t = cΔI, if c (x,y,t) is constant, the isotropic heat diffusion equation is obtained. Suppose we know the locations of the boundaries of the region in the time scale and we want to perform smoothing throughout the ranges instead of smoothing at the edge and borders; This result can be reached by placing the diffusion coefficient c=1 inside each region and c=0 at the borders (Perona and Malik, 1990).

According to Equation (2) each network level is an implementation of anisotropic diffusion equation discretized using 4-neighbour connections on a square lattice as suggested by Perona and Malik (1990).

$$I_{i.j}^{t+1} = I_{i.j}^{t} + \lambda[c_N \cdot \nabla_N I + c_S \cdot \nabla_S I + c_E \cdot \nabla_E I + C_W \cdot \nabla_w I]_{i.j}^{l} \qquad (2)$$

where (4) CN, CS, CE and CW are the direction coefficients in the north, south, east and west direction respectively at time t, and λ is an update rate between [0,1.4]. Prona and Malik use conductivity coefficients that are proportional to the local illumination gradient in the direction shown (Fernandesl and Jernigan, 1992).

Other conductivity coefficients have been proposed, but none of them deal with multispectral images and all of them only depend on gradient information from the same scale (Fernandesl and Jernigan, 1992).

The followings are the advantages of this method:

1- Unlike other low-pass linear filters, the image smoothed using the anisotropic diffusion neural network will be displayed on several scale levels, in contrast to the common simultaneous filtering methods, which are only performed on one scale level (Yuan and He, 2008)**.**
2- This algorithm processes all input spectral channels at the same time, but other filters process each spectral channel independently Richmond, (2008).
3- Anisotropic Diffusion Neural Network Algorithm simultaneously uses both local spectral and texture information to determine the amount of accumulation in a certain level. Spectral information is extracted from the input multispectral image and texture information is extracted from texture-context maps. Most filters are

invariant to spectral or texture information Richmond, (2008).

4. Materials and Methods

In this research, level 2 Landsat 8 satellite images acquired on March 11, 2022 have been used. This image is corrected for atmospheric and radiometric distortions (U.S. Geological Survey).

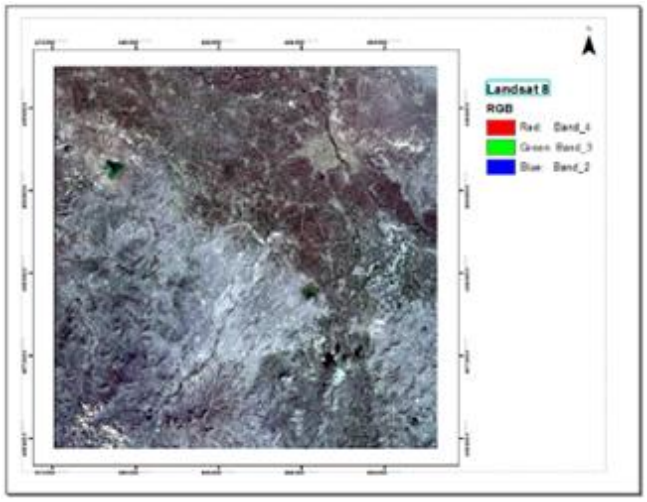

Figure 1. Landsat 8 false color composite (U.S. Geological Survey)

4.1. Study area

Satellite image is pcovering Miandoab region of West Azerbaijan province, Iran which is located at a distance of 164 km far from Urmia and in the south of the province (Figure 2). The approximate area of this region is 2,694 Km2 and it is located at the longitude of 46 degrees and 6 minutes east of the Greenwich Meridian and within 36 degrees and 58 minutes north of the equator in the middle of the plains leading to Lake Urmia with a height of 1,314 meters above sea level. This area has been chosen due to the presence of different land use land cover including vegetation, barren lands and pastures (soil), as well as numerous waterbodies.

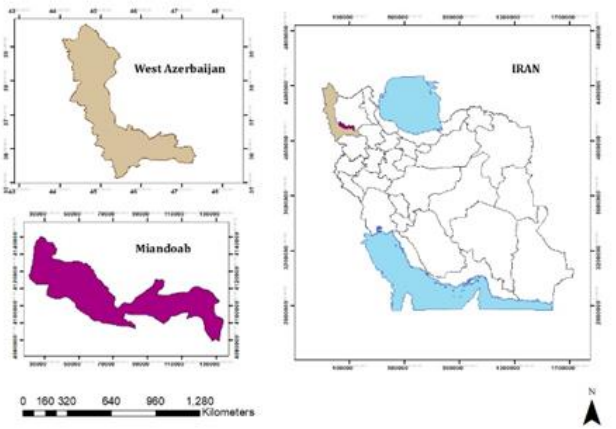

Figure 2. The geographical location of Miandoab region in West Azarbaijan province of Iran

4.2. Methodology

In this study, OLI data was used for classification. A multi-level segmentation algorithm, which is an anisotropic diffusion neural network implementation, was evaluated to generate multi-spectral/multi-scale images using spectral and texture information (wavelet transform method). Since the neural network algorithm does not perform classification and is like a filter, the SVM algorithm was used on all output levels of the neural network for classification. In this study, to evaluate and compare the multi-level network design, the original image was also classified with SVM. Finally, the accuracy of the classification, which is measured by the Kappa coefficient of agreement, was extracted from the independent data set and evaluated for validation. As it can be seen, the output of the classification network algorithm does not separate complications. In this study, multi-resolution data was used for unsupervised classification of Miandoab city, West Azarbaijan province. Anisotropic diffusion neural network, which is a multilevel segmentation algorithm, was used to generate multispectral images using spectral and texture information. From bands 2, 3, 4, 5 and 6, the Landsat 8 image was extracted as the main multi-spectral image, and from band 7, the texture map was extracted by using wavelet transformation.

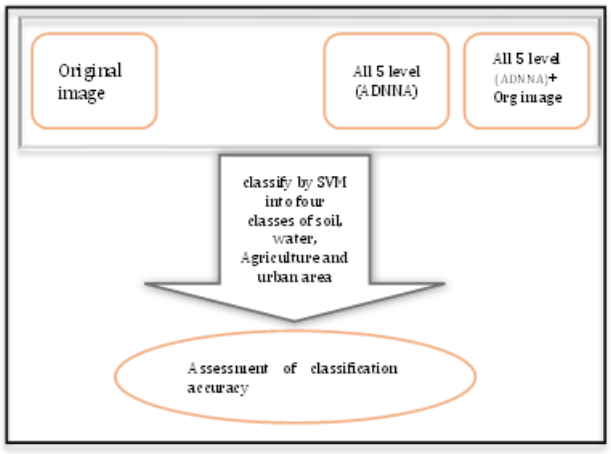

Figure 3. The flowchart of methodology

Finally, the output of the anisotropic propagation neural network was obtained in 5 levels.

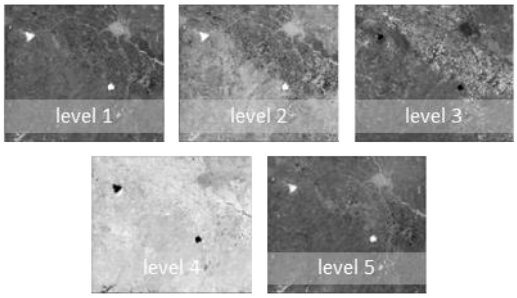

Figure 4. 5-level classification output of anisotropic diffusion neural network algorithm on Landsat 8 image using spectral and texture information

Since the neural network algorithm does not perform classification and has an approach similar to image filters, to compare the output of the algorithm, each level was combined with 2 bands from the original image (band 4 and 7) And all 5 levels combined with the original image and also combined all 5 level together and SVM (Support Vector Machine) algorithm was used to classify the image into four classes of soil, water, Agriculture and urban area**.**

As a result, the multi-level network algorithm using texture analysis on the Landsat 8 image, the output of level 2 of the network with a classification kappa of 0.86 is more accurate than the rest of the levels (Table 1). If the primary image has 512x512 pixels, the output of the first level of the network is the size of the primary image, the second level is 256x256, and the subsequent levels are smaller in the same way and are multiplied by the power of 2 (here the first level is 2048x2048). According to the Figure 3, the first level of the images has a lot of noise (spots) and the details were lost in the third scale and later, as a result, the most suitable level for classifying the output image is the second level.

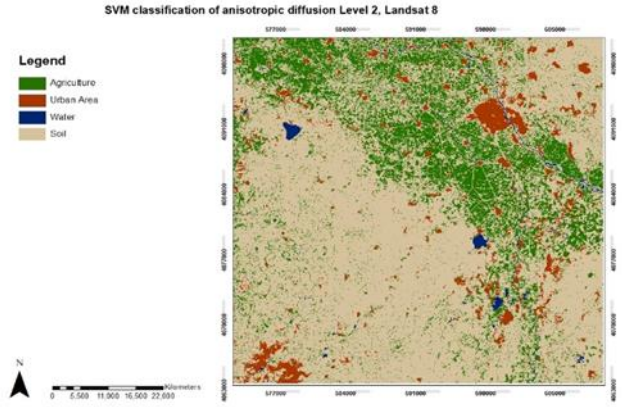

Figure 5. SVM Classification of anisotropic diffusion Level 2 on Landsat 8 image (the best accuracy)

Table 1. Classification kappa

	Level 1+ ORG Image	Level 2+ ORG Image	Level 3+ ORG Image	Level 4+ ORG Image
Kappa	0.84	0.86	0.8	0.76
	Level 5+ ORG Image	All 5 Level+ ORG Image	All 5 Level	Org Image
Kappa	0.63	0.69	0.73	0.67

5. Conclusion

Classification of remote sensing images for interpretation and preparation of thematic maps is one of the most important issues of remote sensing science. Due to the importance of classification in extracting information from multispectral satellite images in remote sensing, this research tried to use the anisotropic diffusion neural network algorithm to classify the basic pixels of multispectral images such as Landsat 8. Increase accuracy Anisotropic Diffusion Neural Network algorithm is described as a multi-level scheme where each level uses the anisotropic diffusion equation to classify a multi-spectral image in successively lower spatial resolution. Texture and statistical similarities between and within each level guide the diffusion process. Since the anisotropic neural network algorithm does not perform classification, no training set is required for this algorithm and it also does not produce any topic map. In this study, we classified the result of the network algorithm with the use of texture information by support vector machine classification and compared each level, all level together, stacked all levels and original image and also original image singly. The level of two network algorithms in classification of support vector machine in Landsat 8 image with Kappa of 0.86 is more accurate than the SVM classification of original image with kappa of 0.67and also original image + All levels with kappa of 0.69. The poor result of clarification of all 5 level and all 5 level + original image was not unexpected due to a lot of noise (spots) in level 1 and the details were lost in the third scale and later.

References

Daryaei, J. (2003). Digital Change Detection Using Multi-Scale Wavelet Transformation & Neural Network. In International Institute for Aerospace survey and Earth Sciences.

Ehsani, A., & Shakeryari, M. (2018). Determining the optimal method of land use classification and mapping by comparing artificial neural network algorithms and support vector machines using satellite data (Case study: Hamoon International Wetland). Environmental Science and Technology,20.

Fernandes, R. A., & Jernigan, M. E. (1992, August). Unsupervised multi-level segmentation of multispectral images. In Neural Networks for Signal Processing II Proceedings of the 1992 IEEE Workshop (pp. 363-372). IEEE.

Lu, D., & Weng, Q. (2007). A survey of image classification methods and techniques for improving classification performance. International journal of Remote sensing, 28(5), 823-870.

Nobrega, R., Quintanilha, J., & Hara, C. O. (2007). A Noise-Removal Approach for Lidar Intensity Images Using Anisotropic Diffusion Filtering to Preserve Object Shape Characteristics. American Society for Photogrammetry and Remote Sensing - ASPRS Annual Conference: Identifying Geospatial Solutions 2 (February), 471–481.

Perona, P., & Malik, J. (1990). Scale-space and edge detection using anisotropic diffusion. IEEE Transactions on pattern analysis and machine intelligence, 12(7), 629-639.

Richmond, H. (2008). PCI Geomatics User's Guide, Ontario, Canada; 2008.

Tien Bui, D., Pradhan, B., Lofman, O., & Revhaug, I. (2012). Landslide susceptibility assessment in vietnam using support vector machines, decision tree, and Naive Bayes Models. Mathematical problems in Engineering,

Yuan, J., & He, G. (2008). Application of an Anisotropic Diffusion Based Preprocessing Filtering Algorithm for High Resolution Remote Sensing Image Segmentation. Congress on Image and Signal Processing, 629–633.

6th Intercontinental Geoinformation Days

igd.mersin.edu.tr

Flood risk assessment and mapping: a case study of the Aksu River Basin (Giresun), Türkiye

Halil Burak Akdeniz*[1], Emre Can Tuzcu[1]

[1]*Konya Technical University, Engineering and Natural Sciences Faculty, Geomatics Department, Konya, Türkiye*

Keywords
Flood risk
Flood vulnerability
Flood hazard
GIS
AHP

Abstract

Flood is considered to be the most common natural disaster worldwide during the last decades. Flood risk potential mapping is required for mitigation of flood, preventing, management, and minimizing losses. The purpose of this study is to present flood risk potentiality areas in the Aksu River Basin using Multi-Criteria Decision Making method and Geographic Information Systems and risky structures were identified in basin. Within the scope of this purpose, six criteria (slope, aspect, rainfall, land use, distance to river, and geology) that will affect the flood risk were determined. As a result of the study, it was determined that 0.64% of the basin is very high risk, 9.59% high risk, 50.54% moderate risk, 33.54% low risk, and 5.69% very low risk. Also, it was determined that there are 110 real estate within the very high flood risk area and 1362 real estate within the high flood risk area. Declaring areas with very high and high risk as "disaster-prone zones" in accordance with Article 2 of Law No. 7269 dated 1959 and not allowing construction and should be relocated to more suitable areas is crucial. The zoning plans should be updated accordingly.

1. Introduction

Flood is a recurrent hazardous phenomenon that has become the most common natural disaster worldwide during the past decades, causing many environmental and socio-economic consequences within the affected area (Rahmati et al. 2016). The intensity of flood risk is directly related to several associated factors such as urbanization, inefficient drainage system, improper river improvement works, inadequate infrastructure, inappropriate land use change, climate change, etc. and results in loss of life and property. Therefore, assessing, managing, and mapping flood risk is crucial to combating and preventing the adverse effects of severe floods. Flood risk maps are useful tools for planning the future direction of city growth and are usually used to identify flood-susceptible areas (Tehrany et al. 2014).

Flood risk analysis and assessment often involve multiple criteria that have to be geographically related to one another. Therefore, Geographic Information Systems (GIS) possessing the capabilities of collecting, storing, analyzing, managing, and visualizing large amounts of spatial data are an important tool. Multi-Criteria Decision Making (MCDM) methods provide convenience to decision makers in designing and solving complex problems with many criteria or evaluating possible alternative ways (Feizizadeh et al. 2014). Spatial MCDM methods, on the other hand, were developed on the basis of combining spatial analyzes in GIS with MCDM methods. Today, many MCDM methods such as Analytical Hierarchy Process (AHP), Analytic Network Process (ANP), Technique for Order of Preference by Similarity to Ideal Solution (TOPSIS) in GIS has proven successful in natural disaster analysis and other geo-environmental studies (Radwan et al. 2019; Pathan et al. 2022).

The purpose of this study is to present flood risk potentiality areas using MCDM methods with GIS support and risky structures were identified in these areas.

2. Study Area

The Aksu River Basin is located within the borders of the Giresun province in the northeast of Türkiye (Figure 1). The basin is located between 40°54'50''-40°27'16'' north latitudes and 38°34'11''-38°10'00'' east longitudes. The area of the Aksu River Basin is 899.4349 km^2. According to the census data of 2022, the total population of the settlements within the basin is 183,653.

Aksu River, which gave its name to the basin, is the most important water source of the basin. Aksu River originates from the Karagöl region at an altitude of 3039 meters and flows into the Black Sea. The elevation difference in the basin is quite high with 3107 meters and the slope values vary between 0° and 70°. Settlements in the basin have developed along the riverbeds and steep slopes due to the rugged topography. Floods of disaster

* **Corresponding Author**

*(hbakdeniz@ktun.edu.tr) ORCID ID 0000 – 0002 – 9504 – 051X
(cantuzcuemre@gmail.com) ORCID ID 0009-0006-4286-6883

Cite this study

Akdeniz, H. B., & Tuzcu, E. C. (2023). Flood risk assessment and mapping: a case of the Aksu River Basin (Giresun), Türkiye. Intercontinental Geoinformation Days (IGD), 6, 61-64, Baku, Azerbaijan

magnitude occur during periods of heavy rainfall because flood risk was not taken into account in the urban development (Avcı and Sunkar 2015).

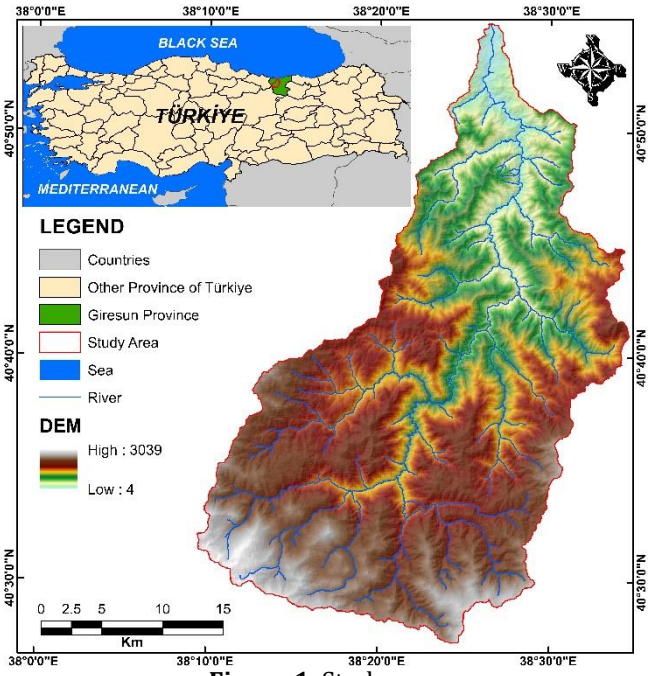

Figure 1. Study area

3. Materials and Methods

Six criteria were used to identify flood risk areas. These criteria are "slope, aspect, land use, distance to river, geology, and rainfall." The criteria were determined based on literature research, consultation with five expert academics, and the characteristic features of the study area (Özcan 2017; Pathan et al. 2022). The criteria were obtained from various data sources. Slope and aspect data were generated from Digital Elevation Model (DEM) data. The DEM data were obtained from the United States Geological Survey data portal. The land use and land cover map of the study area was obtained from the CORINE 2018 data produced by the European Environment Agency. The riverbeds were digitized using 1:25000 topographic maps and OpenStreetMap data. The geological structure of the study area was digitized from 1:100000 geological maps obtained from the Mineral Research and Exploration Regional Directorate II (Konya). Rainfall was obtained by interpolating data from the Meteorology General Directorate stations within the basin using the Schreiber method. ArcGIS software was used for data collection, storage, processing, spatial analysis, and mapping.

The risk classes and scores of the criteria were determined through literature research and adjusted to fit the environmental conditions of the Aksu River Basin based on expert opinions (Figure 2). The risk classification of the criteria (very low, low, moderate, high, very high) was determined through literature research (Radwan et al. 2019). Very high was scored as 5, while very low was scored as 1. The risk classes and scores of the criteria are shown in Table 1.

The AHP, one of the MCDM methods, was used to determine the relative importance of criteria in identifying flood risk areas. To evaluate the consistency of expert judgments in pairwise comparisons, the consistency ratio (CR) should be calculated. If CR ≤ 0.10, the pairwise comparison matrix is considered consistent, and the generated weights can be used. If CR ≥ 0.10, the pairwise comparison matrix is considered inconsistent, and it needs to be revised (Saaty 1990). The criterion maps and weights determined by the AHP method were combined using the weighted overlay method to determine flood risk areas in the Aksu River Basin. In the final stage of the study, risky structures (residential, commercial, industrial, social facilities, etc.) located in flood risk areas were identified.

3.1. Identification of criteria

As the degree of slope increases, the water holding capacity of the soil decreases, and the flow rate and amount of erosion and surface water increases (Özdemir 2020). Therefore, low slope areas cause water accumulation and flood risk. In the study, the degree of slope >30% were classified as very low risk, while the degree of slope <%3 were classified as very high risk.

Aspect affects the amount of heat energy received from the sun, and therefore affects water loss through sweating and evaporation. Due to the orographic structure and aspect, north-facing slopes in the Eastern Black Sea region receive excessive rainfall (Avcı and Sunkar 2015). Therefore, north-northeast directions were classified as "very high risk" and south-southeast-southwest directions were classified as "very low risk".

The most important factor in frequent floods and inundations in Giresun is the high amount of rainfall (Avcı and Sunkar 2015). As the amount of rainfall increases, the probability of flood risk also increases (Souissi et al. 2020). Therefore, in the study, areas with an annual average rainfall of more than 2820 mm were classified as very high risk (Table 1).

Land use is a factor that directly affects the flood risk. There is an inverse relationship between flooding and vegetation density, meaning that an area with high vegetation density has a lower risk of flooding (Rahmati et al. 2016). Forest, due to its characteristic structure, retain flowing water, slow down its speed, and enable it to penetrate the soil. Therefore, in this study, forest areas were classified as very low risk, while settlement and wetland areas were classified as very high risk and high risk, respectively (Figure 2).

One of the most significant criteria affecting flood risk is the distance from the river. Areas closer to the riverbed are at a higher risk of flooding than those farther away (Fernandez and Lutz 2010). Thus, in this study, areas within 250m of the river were classified as very high risk.

Another important criterion in flood risk assessment is the geological structure of the area. This is because the type, porosity, and permeability of geological structures in the study area are important factors in surface water flow and therefore in flood risk. Therefore, areas with meta-siltstone geological structure were classified as very low risk, while alluvium and carbonate geological structure were classified as high risk (Figure 2, Table 1).

Table 1. The risk classes, scores, weights and consistency ratio of flood risk criteria

Criteria	Unit	Very High (5)	High (4)	Moderate (3)	Low (2)	Very Low (1)	Weight	Consistency Ratio
Slope	%	0-3	>3-10	>10-20	>20-30	30<	0.180	0.07
Aspect	-	North, Northeast	Northwest	West, East	-	South, Southwest, Southeast	0.033	
Rainfall	mm	>2530	<2530-2230	<2230-1930	<1930-1630	<1630-1320	0.273	
Land use	-	Wetlands and Water bodies	Artificial surfaces	Agricultural	-	Forest	0.144	
Distance to river	m	<250	>250-500	>500-1000	>1000-1500	>1500	0.261	
Geology	-	-	Alluvium, Carbonate	Volcanic rocks	Limestone	Metasiltstone	0.109	

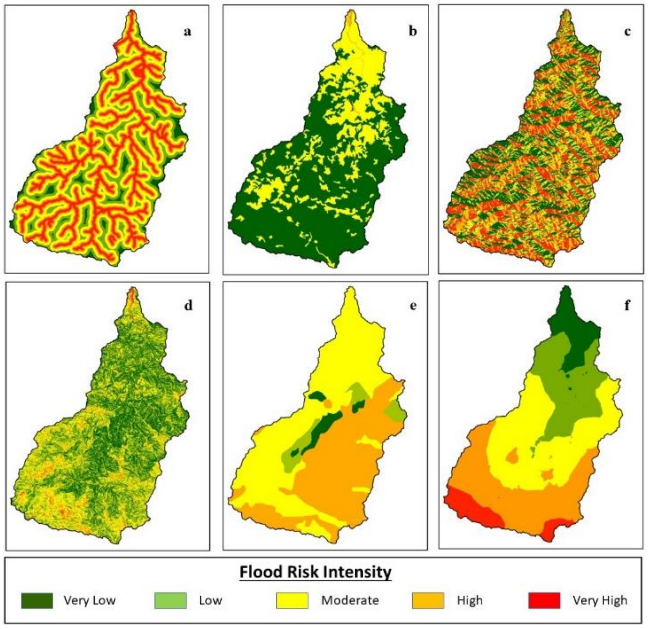

Figure 2. Flood risk maps of criteria (a) distance to river, (b) land use, (c) aspect, (d) slope, (e) geology, (f) rainfall

4. Results

When the criteria weights determined by the AHP method were compared, the criteria with the highest importance were calculated as "rainfall (0.273)" (Table 1). This criterion is followed by "distance to river (0.261), slope (0.180), land use (0.144), geology (0.109), aspect (0.033)" criteria, respectively. The consistency ratio of the pairwise comparison matrix created for the criteria was calculated as 0.07. This result indicates that the pairwise comparison matrices made by the experts are consistent (CR ≤ 0.10).

The flood risk areas map of the Aksu River Basin is shown in Figure 3. When the areas under flood risk in the study area were examined, it was determined that 0.64% very high risk, 9.59% high risk, 50.54% moderate risk, 33.54% low risk, and 5.69% very low risk (Table 2).

In the study, the number of real estates located within the very high and high flood risk areas were calculated. Accordingly, it was determined that there are 110 real estate within the very high flood risk area and 1362 real estate within the high flood risk area. Some of the real estates located in the high-risk area is shown in Figure 4.

Table 2. Areal extent of flood risk within in Aksu (Giresun) River Basin

Flood Risk Classes	Area (km²)	Rate (%)
Very Low	51.1793	5.69
Low	301.6518	33.54
Moderate	454.5338	50.54
High	86.3006	9.59
Very High	5.7694	0.64

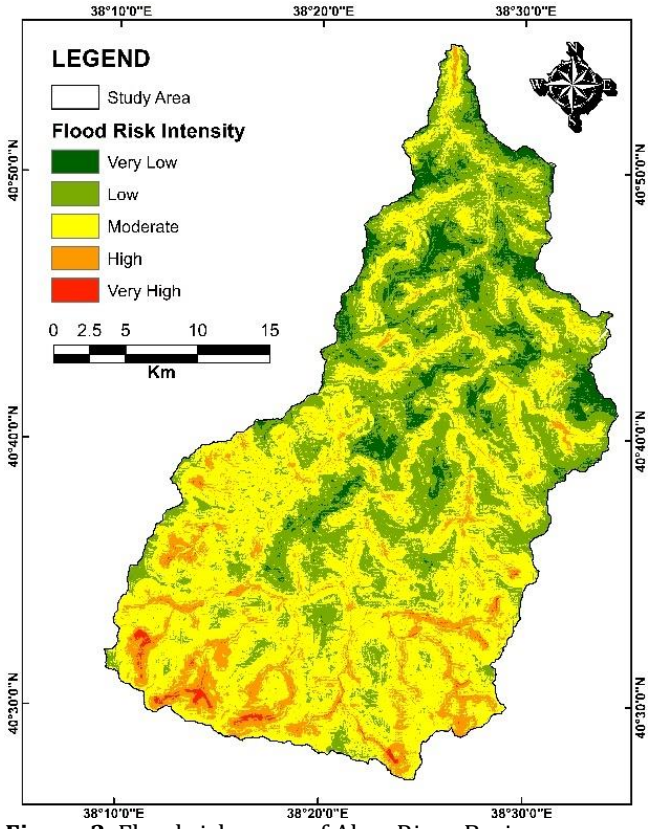

Figure 3. Flood risk maps of Aksu River Basin

5. Discussion

The flood risk mostly occurs in valley bottoms and at the mouth of rivers in the study area. When the causes of flood risks are examined, it is seen that the area receives rainfall throughout the year, which leads to quick saturation of the soil. In addition, the high slope of the area, high velocity of the streamflow, accumulation of material due to erosion in the valley bottoms where the slope decreases, and narrowing of the riverbed due to the accumulated material are other factors. Unplanned

urbanization, settlements in riverbeds, narrowing of the river width, and inadequate rainwater drainage and discharge lines also contribute to the problem.

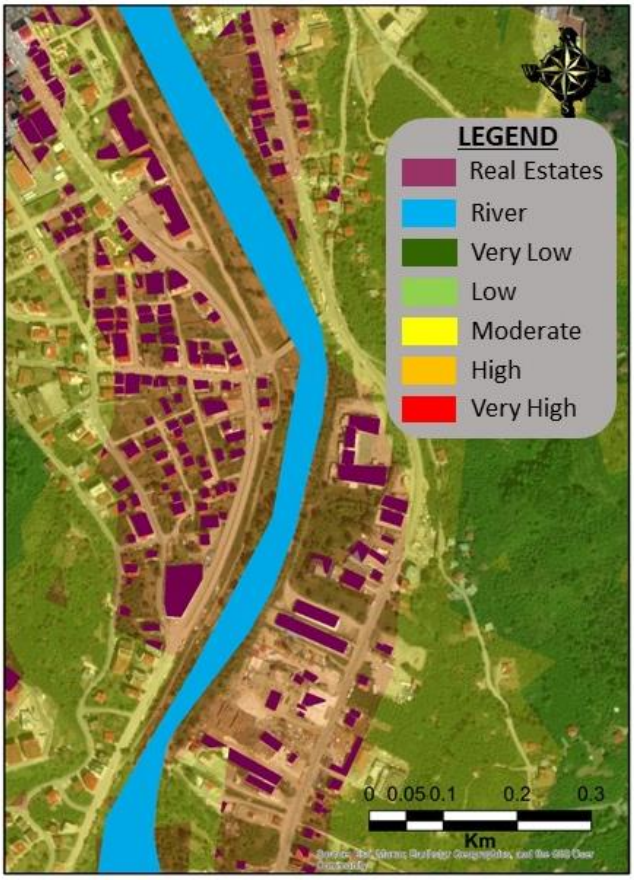

Figure 4. The map of real estates within the high flood risk

In order to reduce and prevent the risk and impact of floods in the study area, necessary measures must be taken. To achieve this, blockages caused by sediment and waste in the engineering structures within the riverbed should be prevented. The cross sections of existing engineering structures should be improved. Taking material from or discharging material into the riverbed, which could affect the flow regime and bed morphology, should be prohibited. Settlements identified as having a very high or high risk of flooding should be relocated to more suitable areas, and zoning plans should be updated accordingly.

6. Conclusion

The ratio of flood damages to total natural disaster damages in the study area is approximately 40%, which is the highest percentage. In addition to residential and commercial buildings, flood damages also affect roads and all infrastructure facilities. Therefore, flood damages, which cause significant economic losses in addition to threats to human life, disrupt the normal flow of life and affect large areas. Taking into account this situation and the other reasons mentioned in the study, conducting flood risk analysis throughout the basin, updating the risk maps at regular intervals, prioritization studies, and incorporating risk maps into zoning plans are of great importance. In addition, declaring areas with very high and high risk as "disaster-prone zones" in accordance with Article 2 of Law No. 7269 dated 1959 and not allowing construction in these areas is crucial.

Acknowledgement

This study was extracted from the second author's "Bachelor's degree graduation project".

References

Avcı, V., & Sunkar, M. (2015). Giresun'da sel ve taşkın oluşumuna neden olan Aksu Çayı ve Batlama Deresi Havzalarının morfometrik analizleri. Coğrafya Dergisi, 30, 91-119.

Feizizadeh, B., Roodposhti, M.S., Jankowski, P., & Blaschke, T. (2014). A GIS-based extended fuzzy multi-criteria evaluation for landslide susceptibility mapping. Computers & geosciences, 73, 208-221.

Fernández, D. S., & Lutz, M. A. (2010). Urban flood hazard zoning in Tucumán Province, Argentina, using GIS and multicriteria decision analysis. Engineering Geology, 111(1-4), 90-98.

Radwan, F., Alazba, A. A., & Mossad, A. (2019). Flood risk assessment and mapping using AHP in arid and semiarid regions. Acta Geophysica, 67, 215-229.

Rahmati, O., Zeinivand, H., & Besharat, M. (2016). Flood hazard zoning in Yasooj region, Iran, using GIS and multi-criteria decision analysis. Geomatics, Natural Hazards and Risk, 7(3), 1000-1017.

Özcan, O. (2017). Taşkın tespitinin farklı yöntemlerle değerlendirilmesi: Ayamama Deresi örneği. Doğal Afetler ve Çevre Dergisi, 3(1), 9-27.

Özdemir, A. (2020). Determination of protection zones in drinking water basins: a case study from Turkey, Sapanca Lake Basin. Environmental Earth Sciences, 79(8), 1-15.

Pathan, A. I., Girish Agnihotri, P., Said, S., & Patel, D. (2022). AHP and TOPSIS based flood risk assessment-a case study of the Navsari City, Gujarat, India. Environmental Monitoring and Assessment, 194(7), 509.

Tehrany, M. S., Lee, M. J., Pradhan, B., Jebur, M. N., & Lee, S. (2014). Flood susceptibility mapping using integrated bivariate and multivariate statistical models. Environmental Earth Sciences, 72, 4001-4015.

Saaty, T. L (1990). How to make a decision: the analytic hierarchy process. European Journal of Operational Research, 48(1), 9-26.

Souissi, D., Zouhri, L., Hammami, S., Msaddek, M. H., Zghibi, A., & Dlala, M. (2020). GIS-based MCDM–AHP modeling for flood susceptibility mapping of arid areas, southeastern Tunisia. Geocarto International, 35(9), 991-1017.

6th Intercontinental Geoinformation Days

igd.mersin.edu.tr

Implementation of GIS in Mingachevir city

Aliyeva Seyidnisa Xoshbext

Azerbaijan State Pedagogical University, Department of General Geography, Azerbaijan

Keywords
Central Aran
Systems
Structure
Planning

Abstract

Geographic information systems (GIS) are a special type of information systems that serve to collect, store and process data consisting of certain information about certain areas of the earth's surface. In modern times, maps are more necessary for studying, systematizing, analyzing the current situation in the environment and protecting the fragile balance between people and the environment than for the purpose of describing geographical objects. Forecasts provide us with ample opportunities to plan the future and model human and environmental relations. . CIS has an important role in the development of all administrative regions included in the Central Aran economic region. Mingachevir is the fourth largest city of Azerbaijan. From GIS in almost all fields is used. We can say that GIS was used for the first time in the preparation of a city map. Research is conducted there, aerial photographs are taken, etc., maps are prepared. The city was built in connection with the construction of a hydroelectric power station on the Kura River November 11. It received city status in 1948. The city of Mingachevir is 17 km away from the Baku-Tbilisi sea road is located at a distance. 30 km from the national airport located in Yevlakh district, 8 km from the international airport located in the city of Ganja it is far away.

1. Introduction

Looking at all this, we see that the development of the CIS in our country is important. Many GIS companies operate in the Republic of Azerbaijan. They use modern methods and technologies for the future development of the Republic of Azerbaijan. It is no coincidence that a number of state structures and departments in the Republic of Azerbaijan already use GIS.

Figure 1. Location map of the study area

These include the State Land and Mapping Committee, the State Registry Service of Real Estate, the State Committee for Real Estate Issues, the Ministry of Emergency Situations, etc. an example can be given. About 10 GIS companies are already operating in the Republic of Azerbaijan.

2. Method

Many studies on Geographical Information Systems have been conducted in Mingachevir, located in the Central Aran, and these systems have been used for planning, territorial management, productivity growth, etc. It has been found to be useful in some areas.

Many changes have been observed in the infrastructure of the city in the field of Geographic information systems applied in the city of Mingachevir. Many projects related to the application of geographic information systems have been developed, and thanks to these projects, many benefits have been achieved in urban planning and development.

One of the biggest benefits of applying Geographic Information Systems in Central Aran, especially in Mingachevir, is the management and development of the infrastructure of the area. In the field of these systems, it is possible to evaluate, strengthen and plan the environment, architecture and infrastructure in Mingachevir.

* **Corresponding Author**

*(e-mail) ORCID ID xxxx – xxxx – xxxx – xxxx

Cite this study

Xoshbext, A. S. (2023). Implementation of GIS in Mingachevir city. Intercontinental Geoinformation Days (IGD), 6, 65-67, Baku, Azerbaijan

2.1. The importance of implementing GIS in Mingachevir

In this area, development plans are implemented more appropriately and the City's layout and infrastructure are made more efficient. Another benefit of applying Geographical Information systems in Mingachevir is its use for territorial planning.

One of the most important components of GIS is "data". GIS can combine spatial data with other data sources. In this way, information related to many organizations and structures is organized, local information is clarified. Although experts recognize data as a key element for GIS, it appears to be the most difficult component to obtain. Data sources are aggregated, multifaceted and have different structures, and data collection takes a lot of time and money. Necessary funds have been allocated to this field in recent years in the city of Mingachevir. The fact that the city is developing day by day is a clear proof of this.

2.2 .Fields of application of GIS in Mingachevir

Geographic Information Systems (GIS) are widely used in a variety of sectors. The following are the fields where GIS is used in Central Aran:

~ **Urban planning and construction:** Aranda Geographic Information Systems are used in urban planning and construction, such as building location, road and bridge planning and construction.

~ **Urban and rural planning:** Agriculture, external road planning, construction of internal ring roads and power lines, etc. from Central Aran Geographical Information Systems. It is used for carrying out work in the fields of village and settlement planning.

~ **Urban and rural planning:** planning of agriculture, external roads, construction of internal ring roads and power lines, etc. from Geographical Information Systems in the Central Aran economic region. It is used for carrying out work in the fields of village and settlement planning.

~ **Water management:** Geographic Information Systems are used in water management, water resource protection, water level measurement and water quality management.

~ **Culture and tourism:** In the Central Aran economic region, Geographic Information Systems are used in the fields of culture and tourism, such as planning and management of museum and tourism sites, tourism statistics and data analysis.

~ **Security and defense:** Security planning, threat assessment, military power, etc. from GIS in the Central Aran economic region. It is used for work in security and defense fields.

~ **Urban economics and marketing:** Urban planning, investment and development evaluation, finding the most popular commercial locations in the Central Region from Geographical Information Systems, etc. It is used for business in urban economy and marketing.

3. Results

The Center for Geographic Information Systems facilitates the provision of geographic information to both internal and external customers in Aran. This allows us to serve customers faster and more efficiently. Geographic Information Systems, when implemented, can lead to changes in the business processes of a company, institution or organization.

Through GIS, opportunities such as more efficient production, efficient use of supplies, or better customer service can be achieved. If a company, institution or organization does all the steps correctly when implementing GIS, it can be more successful in achieving its goal.

However, the results of the application will not always be positive, as there may be problems such as incorrect data entry, incorrect data analysis, application usage or outdated requirements.

4. Discussion

In addition to these fields, Geographical Information Systems are used for public relations of citizens of Zardab district and presentation of information of organizations in relevant fields. Zardab district creates a solid economic base for its population with the land it owns. Due to its proximity to the capital Baku, this region has areas suitable for use in military, construction, petrochemical, and agricultural fields. For this reason, the territory of the district is suitable for the use of Geographical Information Systems (GIS). These systems help monitor and manage planting, irrigation, crop storage and transportation. However, GIS systems are also used in central administration bodies, project preparation and development areas.

5. Conclusion

Looking at all this, we see that the development of the CIS in our country is important. Many GIS companies operate in the Republic of Azerbaijan. They use modern methods and technologies for the future development of the Republic of Azerbaijan. It is no coincidence that a number of state structures and departments in the Republic of Azerbaijan already use GIS. These include the State Land and Mapping Committee, the State Registry Service of Real Estate, the State Committee for Real Estate Issues, the Ministry of Emergency Situations, etc. an example can be given. About 10 GIS companies are already operating in the Republic of Azerbaijan.

References

Aronoff, S. (1991) Geographic Information Systems: A management Perspective, WDL Publications, canada.

Bayramova L.Ə. (2011). Coğrafi Ekologiya kafedrasinda həyata keçirilən beynəlxalq layihələrdə CIS texnologilayalarinin tətbiqi- Bakı Dövlət Universitetinin "Tətbiqi ekologiyanın problemləri" Elmi Konfransı. Bakı.

Ershad Ali, (2018). Geographic Information System (GIS): Definition, Development, Applications &

Components. International Journal of Scientific Research and Reviews

ESRI (1990). Understanding GIS

Heywood, I., Cornelius, S., & Carver, S. (1998) An Introduction to Geographical Information Systems.

Longley, P. A., Goodchild, M. F., Maguire, D. J. & Rhind, D. W. (eds) (1999) Geographic Information Systems.

Mehdiyev A. & İsmayilov A. (2011). Coğrafi İnformasiya Sistemləri. Bakı, "Müəllim" nəşriyyatı, 232

Rasouli, A. A., MammadovG. Sh., Asgarova, M. M. (2021). Mastering Spatial Data Analysis Inside the GIS Setting. Azerbaijan, Baku: "Science"publishing house of Azerbaijan National Academy of Sciences, 398

6th Intercontinental Geoinformation Days

igd.mersin.edu.tr

Modelling future land use/land cover and seasonal land surface temperature changes based on CA-ANN algorithm to assess its impacts on Chennai Metropolitan Area (CMA), India

Mohammed Faizan [*1], **Manas Hudait** [2]

[1] *Institute of Remote Sensing, College of Engineering Guindy, Anna University, Chennai 600021, India*
[2] *International Institute of Geospatial science and Technology (IIGST), Kolkata, India*

Keywords
Remote sensing
Land use/Land cover
Land surface temperature
Artificial neural network
Cellular automata

Abstract

Urbanization may cause huge amount of Land use and land cover (LULC) changes, which creates a significant influence on land surface temperature (LST) in fast developing megacities. This study first analyzed the pattern of LULC changes and then evaluated their implications on LST in the Chennai Metropolitan Area (CMA) for the years 2000, 2010, and 2020 using Landsat TM/EMT+/OLI satellite images. The study ultimately predicted the future LULC and LST scenarios for the years 2030 and 2040 using Artificial neural network and cellular automata algorithms based on previous predicted change maps of LULC and LST. The study then used correlation analysis to examine the relationship between LULC, LST, and other vital spectral indices such as NDVI, NDWI, and NDBI for both the summer and winter seasons. Overall accuracy assessment of 91% in 2000, 89% in 2010 and 92% in 2020, with Kappa coefficients more than 85% for LULC. The results indicated a considerable decrease in agricultural land (40.91 %), Forest land (51.60 %) and an increase in built-up area (64.39 %) from 2000 to 2020, respectively. Maximum LST increases from 34.29°C in 2000 to 41.51°C in 2020 and 35.06°C in 2000 to 41.26 in 2020 during summer and winter seasons respectively and with substantial LST differences seen among different LULC classes. The predicted outcomes for 2030 and 2040 show considerable losses of agricultural land, forest land by 4.69 % and 38.95 %, respectively, as well as increases in built-up areas by 16.96 %. The predicted seasonal LST revealed that in 2030 and 2040, more than 70% and 80% of the summer and 22% and 13% of the winter seasons will likely have LSTs in the 32-34 °C range. The study shows that LST with NDVI and NDWI are negative correlation and on the other hand, LST with NDBI are positive correlation. This study can help urban planners, environmental engineers and agricultural officers design successful policy efforts to protect agricultural and forest areas for sustainable development.

1. Introduction

Urbanization has a challenge for many countries. Developed nations have less daunting issues than underdeveloped countries, because of fast and unplanned urbanization . Population expansion and industrialization have also worked as a stimulant in the process of urban in-migration. In 1950, 30 percent of the world's population lived in cities , a rate that increased to 54 percent in 2014 and is predicted to rise to 66 percent by 2050. India's urban population was 217 million in 1991, but it increased to 377 million in 2011. According to Census of India 2011 statistics, India's urban population has grown considerably during the previous two decades. According to a United Nations assessment, India's urban population would grow by approximately 500 million during 2010 and 2050 (United Nations 2012). Tamil Nadu has experienced significant urbanization, for the last two decades. Chennai, India's fourth biggest metropolis, is the greatest accomplishment of Tamil Nadu's urbanization. According to 2011 Census statistics, more individuals in Tamil Nadu have relocated from rural to urban regions in the past ten years than in other states.

The use of Remote Sensing (RS) and Geographic Information Systems (GIS) has made it possible to estimate LULC variations and LST distribution in a given region. Several studies have used multi-temporal Landsat imagery to characterize the LULC change and its effects on LST. Several studies used Logistic Regression

* **Corresponding Author**

*(faizan15273@gmail.com) ORCID ID 0000 – 0001 – 8110 – 4087
(mh.iigst@gmail.com) ORCID ID 0000 – 0002 –0313– 1183

Cite this study

Faizan, M., Hudait, M. (2023), Modelling future land use/land cover and seasonal land surface temperature changes based on CA-ANN algorithm to assess its impacts on Chennai Metropolitan Area (CMA), India, Intercontinental Geoinformation Days (IGD), 6, 68-73, Baku, Azerbaijan

(LR), Cellular Automata (CA), Markov Chain (MC), and Artificial Neural Network (ANN) to predict LULC and LST changes. Each approach has its own set of advantages and disadvantages. The CA-ANN model, which predicts the future LULC and LST change matrix by integrating the previous pattern of change, is extensively used for prospective LULC and LST simulation. CA-ANN, in connection with related LULC indices like as NDVI, NDWI, and NDBI, can accurately predict LST . As a result, CA-ANN is often considered as the most accurate approach for forecasting the LULC and LST consequences.

The study makes use the advantage of the geospatial technologies and the historical record of Landsat Satellite imagery data to analyse land use change in CMA. The objectives of this study to (i) Map and examine the different changes in CMA LULC pattern during the past 20 years (i.e., 2000–2020); (ii) analyse the distribution of LST, NDVI, NDWI, and NDBI in the city; (iii) To determine the relationship between LST and other spatial indices (i.e., NDVI, NDWI, and NDBI); (iv) In addition, CA-ANN algorithms were employed in this work to predict future LULC and LST scenarios for CMA in 2030 and 2040.

2. Study area and datasets

2.1 Study area

The Chennai Metropolitan Area (CMA), seen in Figure 1, is India's fourth largest metropolitan region. It is Asia's 22nd most populous city and the world's 40th most densely populated city. CMA covers an area of 1189 km^2 and includes Chennai district, parts of Kancheepuram and Tiruvallur districts, with Chennai district covering an area of 176 km2. Chennai is situated on the southeastern coast of India, at 13.04° N 80.17° E, in the northeastern side of Tamil Nadu. According to the Chennai Metropolitan Development Authority (CMDA), the CMA encompasses 176 km2 of Chennai district, 637 km2 of Thiruvallur district (including Ambattur, Tiruvallur, Ponneri, and Ponnamallee taluks), and 376 km2 of Kancheepuram district (including Tambaram, Sriperumbudur, and Chengalpattu taluks). It is located on the eastern sea side fields, a coastal plain. The city has a typical elevation of 6 m (20 ft), with the highest point being 60 m (200 ft).

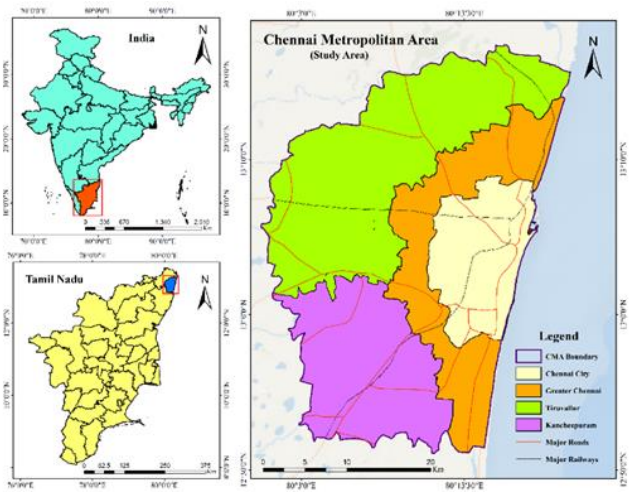

Figure.1 Location map of the study area

2.2 Datasets

The study focuses on multi-temporal satellite images Landsat 4-5 Thematic Mapper (TM), Landsat 7 Enhanced Thematic Mapper Plus (ETM+), and Landsat 8 Operational Land Imager (OLI) acquired from the US Geological Survey (USGS) website (https://earthexplorer.usgs.gov) where path is 141 and row is 51 for the years 2000, 2010, and 2020. The images all have a spatial resolution of 30m. Using the WGS-84 datum, the Landsat images (Level 1 Terrain Correction product) was projected to UTM zone 44 North projection. Satellite images of the summer and winter seasons from the time series 2000, 2010, and 2020 were downloaded at ten-year intervals to assess the variance in LULC and LST in the study area. Landsat images from March to May were collected in order to predict the summer season LST of the study area for the mentioned years. Landsat images from January to February were used for winter season LST.

3.Methodology

3.1 Method for calculating NDVI, NDWI, NDBI and LST

The NDVI value ranges from -1 (negative) to +1 (positive). Values ranging from 0 to +1 (positive) indicate vegetation cover, whereas values near to 1 indicate dense vegetation.

$$NDVI = \frac{NIR_{Band} - RED_{Band}}{NIR_{Band} + RED_{Band}} \quad (1)$$

The NDWI value ranges from -1 (negative) to +1 (positive). Water bodies are represented by values ranging from 0 to +1 (positive), with values near to 1 indicating a high density of water bodies

$$NDWI = \frac{Green_{Band} - NIR_{Band}}{Green_{Band} + NIR_{Band}} \quad (2)$$

The NDBI ranges from -1 to +1, with negative values indicating water bodies and vegetation, positive values indicating built-up areas, and low positive values indicating barren soil types.

$$NDBI = \frac{MIR_{Band} - NIR_{Band}}{MIR_{Band} + NIR_{Band}} \quad (3)$$

LST was estimated using the Digital Number (DN) of a thermal band. Thermal band 6 was taken into account for Landsat 5 TM and Landsat 7 EMT+. LST was calculated for Landsat 8 OLI utilizing bands 10 during the summer and winter seasons. The DNs in the downloaded data were transformed to LST. However, the extraction of LST from Landsat TM, EMT+, and OLI is slightly different in terms of calculating spectral radiance.

3.2 LULC Classification

In this study, LULC types were classified into five categories in the years of 2000, 2010 and 2020 respectively (Water bodies, Urban/Built-up land, Open land, Forest land and Agricultural land. To categorize

LULC for the various study periods, we used Maximum Likelihood (ML) and the supervised classification technique. The categorized maps were validated using random sample ground truth data from 100 Google Earth images. For accuracy assessment, user accuracy, producer accuracy, the overall accuracy, and kappa statistics were computed, and one of the best quantitative techniques for image classification accuracy was used.

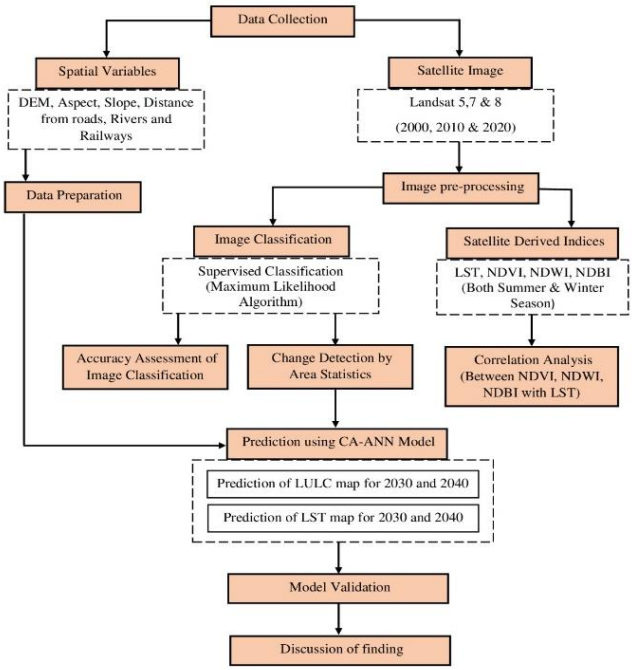

Figure 2. Methodological flow chart of the study

3.4 LULC and LST predictions for 2030 and 2040

For this study, the MOLUSCE plugin tool in QGIS software was used to predict the 2030 and 2040 LULC and LST distributions, which is considered as one of the best prediction models. This study's input module includes dependent variables such as LULC maps and LST distribution and independent variables such as Distance from Road, Railways, Rivers, Slope, Aspect and elevation (for LULC prediction) and NDBI, NDVI, and NDWI (for LST prediction). The validation step provided several kappa statistics such as percent of correctness, kappa histogram, standard kappa, and kappa location for the accuracy validation of the predicted LULC map.

4. Results and discussions

4.1 Variation in past LULC patterns and Accuracy Assessments

The LULC classification maps for the years 2000, 2010, and 2020 are shown in Figure 4. The ML classifier showed good overall accuracies for Chennai, with evaluations of 91 percent (2000), 89 percent (2010) and 92 percent (2020), respectively, and Kappa accuracies of 88% (2000), 86% (2010), and 90% (2020). The accuracy study showed that the verification rates for all years were more than 85%, suggesting an excellent accuracy match.

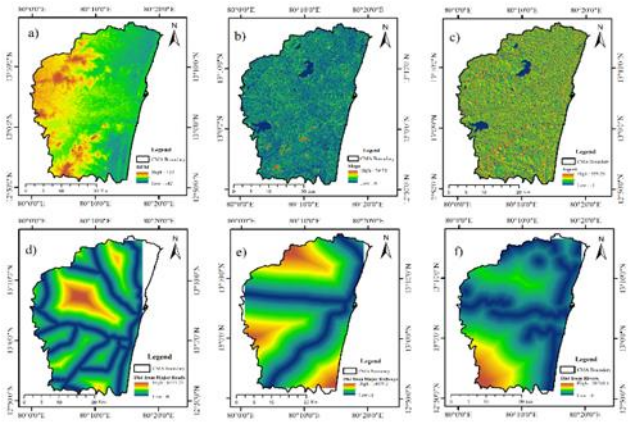

Figure 3. Factors contributing to LULC change and urban growth a) DEM, b) Slope, c) Aspect, d) Dist from major roads e) Dist from major railways f) Dist from rivers

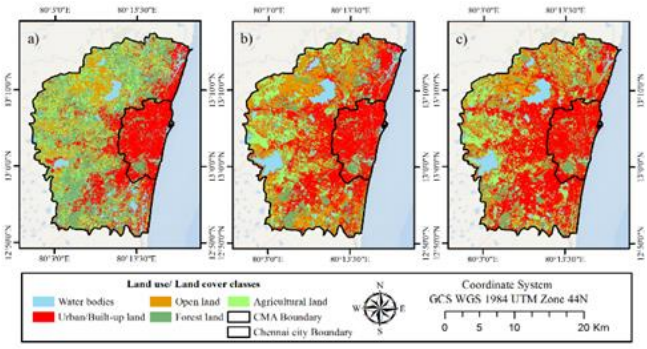

Figure. 4 Land use land cover map of a)2000, b)2010, c)2020

4.2 Changing pattern of seasonal LST

The summer season LST distribution for the years of 2000,2010, and 2020 are shown in Figure 5. In 2000, 0.5% (6.28 km) of the study area was experienced temperatures between 30-<32°C. Also, 1% (1 km^2) of the study area came under the range of 32- <34 °C in 2010 and was increased to 41.61 % (511.23 km^2) in 2020.

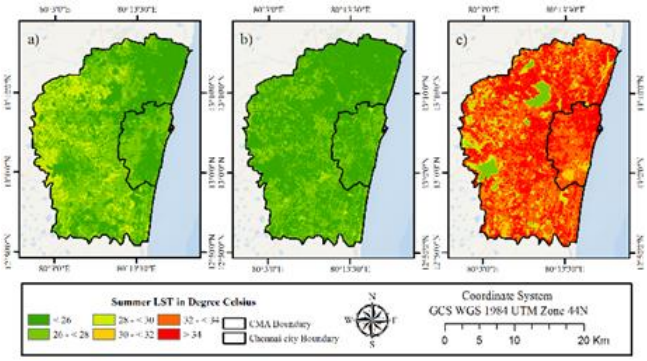

Figure 5. Spatial distribution of summer LST a)2000, b)2010, c)2020

For the study area, zone-wise winter LST variation is shown in Figure 6. In 2000, 2010, and 2020, around 7.47% (91.77km^2), 17.63% (216.58 km^2) and 17.43% (214.09 km^2) of the area in study region were recorded temperatures from 28-<30°C.

4.3 Impact of NDVI, NDWI and NDBI on LST

According to the literature, a greater degree of LST is related with a lower NDVI in this study. The lowest NDVI is observed in built-up areas that dominate the residential areas in chennai. NDVI is found to be a negative regulator of LST.

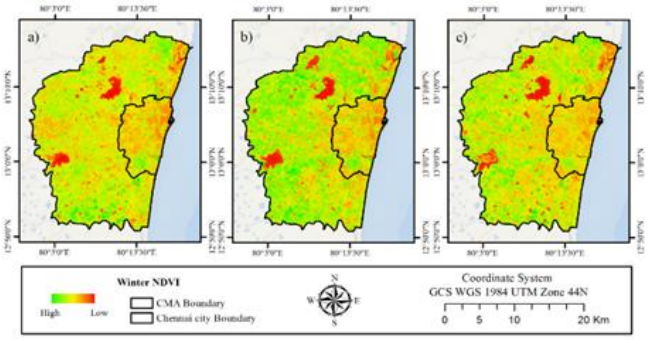

Figure 6. Spatial distribution of winter LST a)2000, b)2010, c)2020

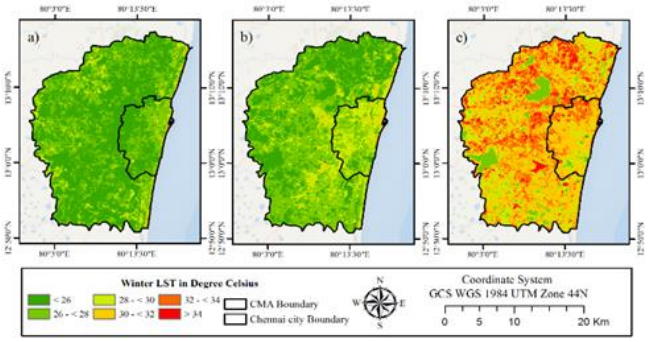

Figure 7. Spatial distribution of Summer NDVI a)2000, b)2010, c)2020

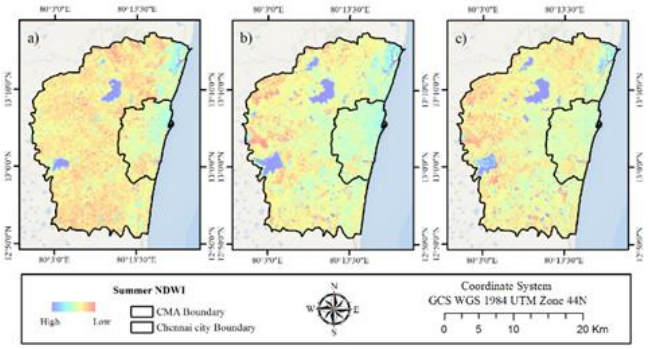

Figure 8. Spatial distribution of winter NDVI a)2000, b)2010, c)2020

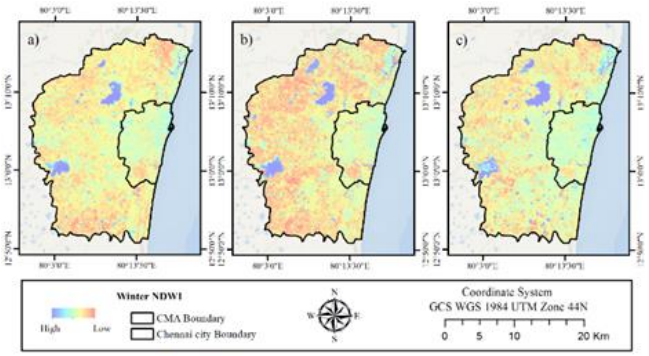

Figure 9. Spatial distribution of summer NDWI a)2000, b)2010, c)2020

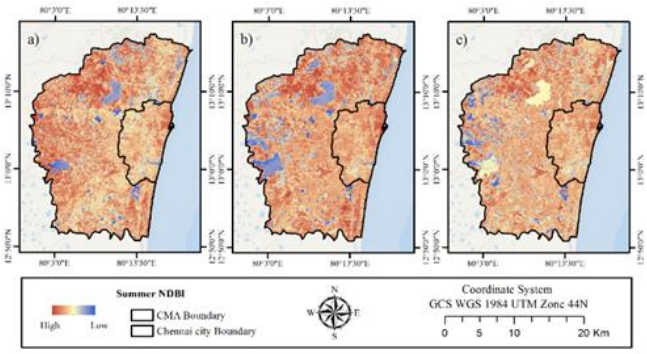

Figure 10. Spatial distribution of Winter NDWI a)2000, b)2010, c)2020

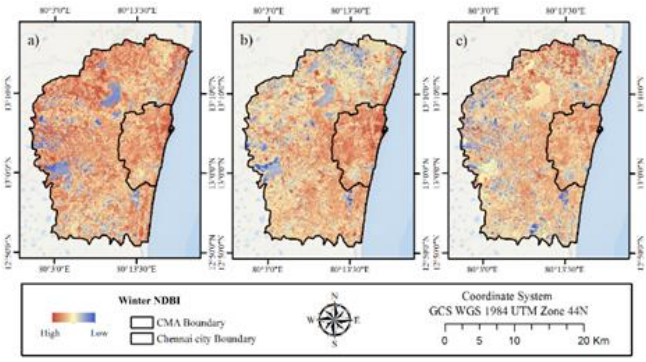

Figure 11. Spatial distribution of summer NDBI a)2000, b)2010, c)2020

Water has a lower temperature than other patterns of land usage. In lower NDWI, the LST was increasing.NDWI is found to be a negative regulator of LST.

The NDBI value steadily increased, resulting in a larger LST value. It demonstrates a positive relationship between LST and built-up regions. According to the results, lower LST values associated with lower NDBI, whereas higher LST values correlated to densely built-up regions.

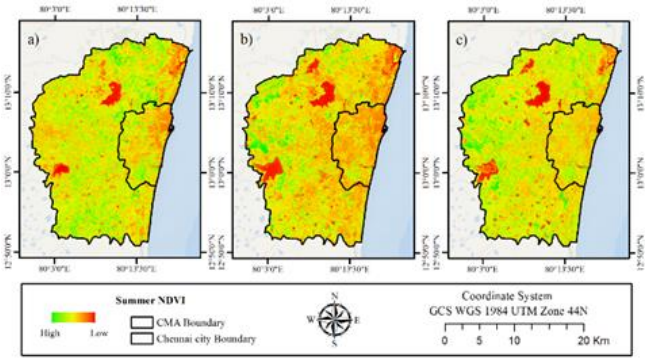

Figure 12. Spatial distribution of Winter NDBI a)2000, b)2010, c)2020

4.4 Predicted LULC for 2030 and 2040

According to the predicted LULC map, if the current trend of expanding built-up area continuing without any planned steps, the increasing urban areas will be 53.73 percent in 2030 and 62.84 percent in 2040, with bare land and forest land being displaced by built-up areas. Forest land and agricultural land were also reduced by 12.71 percent in 2030 and 7.76 percent in 2040,

compared to 13.19 percent in 2020. The predicted LULC scenario of 2040 would confront a 121.58 percent rise in built-up areas, followed by a significant decline in open land, forest land, and agricultural land by 35.19 percent, 71.52 percent, and 44.19 percent, respectively, compared to the initial year 2000.

Reduced forest cover and increasing urbanization may have an impact on the ecosystem services, urban health, and thermal features of a city. If the unplanned urban growth trend continues, the effects of UHI will be exacerbated, leading to an increase in environmental, economic, and medical issues in the study region. Appropriate land-use planning, water-body preservation, and an increase in urban greeneries will all help to make the CMA more ecologically sustainable by minimizing the consequences of UHI.

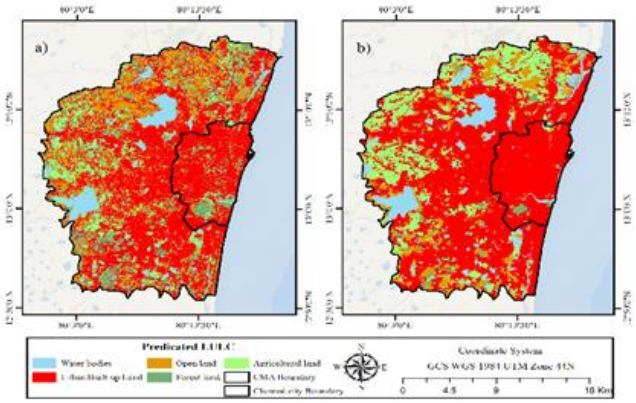

Figure 13. LULC prediction for the year a) 2030 b) 2040

4.7 Predicted Seasonal LST for 2030 and 2040

As a result, increased LST will have a direct influence on air temperature. In the summer of 2030, around 69.74 percent of the study area would be in the high temperature zone (32 - 34 °C), while just 0.01 percent will be in the low temperature zone (26 - 28 °C). For winter LST, the years 2029 and 2039, respectively, only 21.79 percent and 13.47 percent of the study area would likely be in the high-temperature zone (32-34°C), whereas 0.03 percent and 2.92 percent will be in the 36-28 °C. Because the forecast LST was calculated using the trends of past years' LST patterns (2000-2020), the forecast findings also indicated a substantial probable increase in the LST value for the years 2030 and 2040.

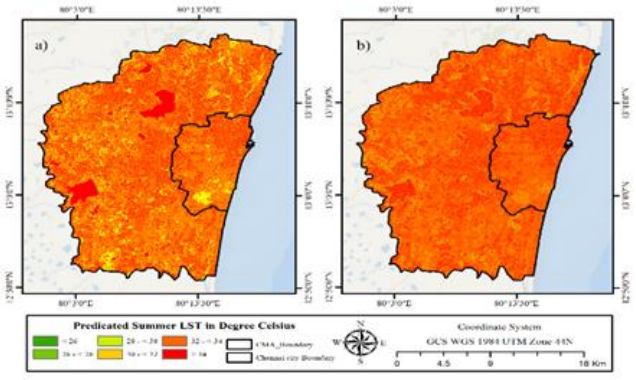

Figure 14. Summer LST prediction for the year a) 2030 and b) 2040

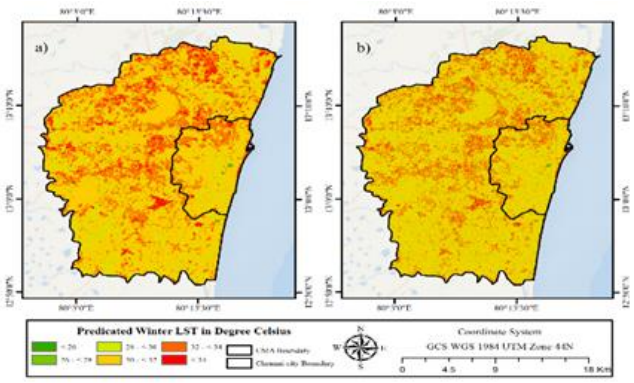

Figure 15. Winter LST prediction for the year a) 2030 and b)2040

5.Conclusion

The study's aim is to assess changes in LULC and LST in the CMA from 2000 to 2020. Finally, this analysis predicted the LULC and LST for the years 2030 and 2040 using CA-ANN model. The investigation indicated that the study region has seen enormous agricultural land loss, with more to emerge in the future years. This study also looked at the effects of land cover change, temperature rise, and climate change in the study area. Finally, this study suggested a sustainable land use management plan for the Chennai Metropolitan Area based on expert viewpoints and taking into account the implications of unplanned infrastructure expansion, loss of green cover, and climate change

The study's findings will be useful to Chennai City authorities, government officials, policymakers, and urban planners, who will be able to use the study's findings for future planning and decision making. City officials can also develop rules, restrictions, and initiatives to help minimize LST in the city. Furthermore, incorporating the study's findings will make Chennai more ecologically and environmentally sound, inclusive, and sustainable. Future study may concentrate on the effects of LST change as seen by city inhabitants. Furthermore, human-environment interactions must be explored in order to have a better understanding of the causes and effects of LST change. Other Tamil Nadu cities' urban expansion, changes in LULC, and spread of LST should be evaluated and simulated to determine that they develop in a sustainable manner. The research concluded by suggesting a variety of solutions for mitigating the negative impact of LULC changes through sustainable land-use practices.

References

Aboelnour, M., & Engel, B. A. (2018). Application of remote sensing techniques and geographic information systems to analyze land surface temperature in response to land use/land cover change in Greater Cairo Region, Egypt. Journal of Geographic Information System, 10(1), 57-88.

Balew, A., & Korme, T. (2020). Monitoring land surface temperature in Bahir Dar city and its surrounding using Landsat images. The Egyptian Journal of Remote Sensing and Space Science, 23(3), 371-386.

Faizan, M. O. (2020). Assessment of Urban Heat Island using GIS and Remote Sensing -A Case Study of Chennai City, India. Conference: Global to Local Sustainability & Future Earth at Udaipur, India

Faizan, M. O. (2022). Monitoring Land Use/Land Cover Change and Its Impact on Variations of Land Surface Temperature Rapidy Urbanizing Island Using Google Earth Engine (GEE) -A Case Study of Delhi, India.

Kafy, A. A., Rahman, M. S., Hasan, M. M., & Islam, M. (2020). Modelling future land use land cover changes and their impacts on land surface temperatures in Rajshahi, Bangladesh. Remote Sensing Applications: Society and Environment, 18, 100314.

Pal, S., & Ziaul, S. K. (2017). Detection of land use and land cover change and land surface temperature in English Bazar urban centre. The Egyptian Journal of Remote Sensing and Space Science, 20(1), 125-145.

6th Intercontinental Geoinformation Days

igd.mersin.edu.tr

Improving of groundwater level estimation using SMOTE technique

Emine Dilek Taylan*[1], Tahsin Baykal [1], Özlem Terzi [2]

[1]*Suleyman Demirel University, Civil Engineering Department, Isparta, Türkiye*
[2]*Isparta Applied Sciences University, Civil Engineering Department, Isparta, Türkiye*

Keywords
Groundwater
SMOTE
ET algorithm
Denizli

Abstract

Accurate estimation of the groundwater level is very important for sustainable water management and planning of water resources. Since the groundwater field studies are time consuming and costly, the use of machine learning techniques for the groundwater level estimation is proposed in this study. Also, synthetic minority oversampling technique (SMOTE) algorithm was used to increase the success of the extra tree (ET) algorithm, which is one of the machine learning techniques, in estimating the groundwater level. For this, precipitation, elevation, slope, and curvature data, which are effective on groundwater, were used. First, the groundwater level was classified as very low, low, medium high and very high. When the result of the model developed with ET algorithm was evaluated, the accuracy value was calculated as 0.53 and the Cohen's Kappa value as 0.36. Then, to increase the success of the extra tree model, data irregularities were removed with the SMOTE algorithm. It was observed that the accuracy of the SMOTE-ET model increased to 0.69 and the Cohen's Kappa value to 0.62. When the results are evaluated, it is thought that the SMOTE algorithm increases the success of the ET algorithm in estimating the groundwater level.

1. Introduction

Accurate estimation of groundwater level is one of the requirements for sustainable use and management of water resources. Modeling of groundwater level provides benefits to managers and engineers in decision making, especially due to increasing groundwater demands for agricultural use. In recent years, groundwater level modeling studies done by many researchers (Daliakopoulos 2005; Poursaeid et al. 2022; Sahoo and Jha 2013; Yadav et al. 2020) Afzaal et al. (2020) estimated groundwater levels for the Baltic River and Long Creek watersheds in Canada using deep learning and artificial neural networks with stream level, stream flow, precipitation, relative humidity, mean temperature, evapotranspiration, heat degree days, dew point temperature, and evapotranspiration variables. They said that these techniques are convenient and accurate. Dash et al. (2010) tried the ANN-GA hybrid model for groundwater level estimation and found that it was successful. Synthetic minority oversampling technology (SMOTE) is used to eliminate class imbalance and improve model performance with new samplings between minority classes and their neighbors in the input dataset. It has been widely preferred in the field of class imbalance in recent years. Wang et al. (2019) produced landslide susceptibility maps with higher accuracy using SMOTE with machine learning techniques such as support vector machine (SVM), logistic regression (LR), artificial neural network (ANN) and random forest (RF). Tang et al. (2022) stated that more appropriate estimations will be made with the XGBoosting method using SMOTE for the precipitation forecast in the Danjiangkou River basin. Razali et al. (2020) stated that the decision tree machine learning technique applied using SMOTE achieved 99.92% success in flood risk estimation for the Kuala Krai region in Kelantan, Malaysia.

In this study, the model was developed to estimate groundwater level with extra tree (ET) algorithm using precipitation, elevation, slope, and curvature data for Denizli province in Türkiye. In addition, improvement of ET model was made by SMOTE.

2. Method

2.1. Study region and data

Denizli province, located in the Aegean Region, is located between 28° 30' – 29° 30' east meridians and 37°

* **Corresponding Author**

*(dilektaylan@sdu.edu.tr) ORCID ID 0000 – 0003 – 0734 – 1900
(tahsinbaykal@gmail.com) ORCID ID 0000 – 0001 – 6218 – 0826
(ozlemterzi@isparta.edu.tr) ORCID ID 0000 – 0001 – 6429 – 5176

Cite this study

Taylan, E. D., Baykal, T., & Terzi, Ö. (2023). Improving of Groundwater Level Estimation Using SMOTE Technique. Intercontinental Geoinformation Days (IGD), 6, 74-77, Baku, Azerbaijan

12' – 38° 12' north parallels. It has a mild and rainy climate in winters. It is bordered by Burdur and Afyon in the east, Aydın and Manisa in the west, Uşak in the north and Muğla in the south. The study region map was given in Figure 1.

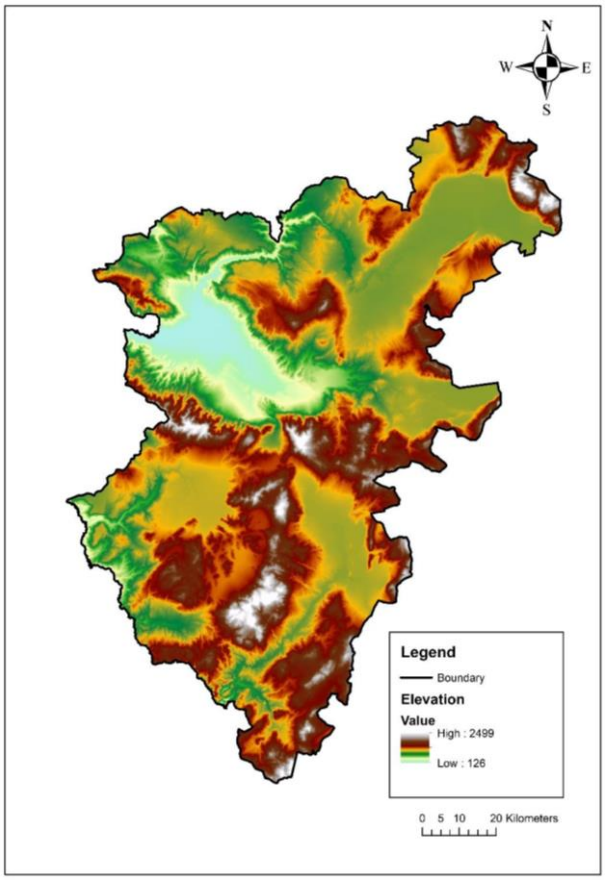

Figure 1. The study region map

Groundwater levels taken from Çıldır (2017) consist of 258 well measurements in Denizli, Türkiye. Monthly precipitation data were obtained from Nasa Power for the years 1981-2021 of Çardak, Buldan, Çivril, Acıpayam, Beyağaç and Çameli districts. Groundwater level and precipitation maps were created with Inverse Distance Weighting (IDW) in ArcGIS environment. Elevation, slope, and curvature data were obtained from SRTM dem data in ArcGIS environment. All maps have pixel dimensions set to 1x1 km.

2.2. Synthetic minority oversampling technique (SMOTE)

SMOTE algorithm, which is an oversampling method, creates new samples from minority classes without repetition. So, it can simply and effectively reduce the phenomenon of imbalance. The SMOTE algorithm creates new instances of the minority class using the Euclidean distance between instances of the minority class (x_i) and obtains k-nearest neighbors. A sampling rate M is calculated to determine the new proportion of various samples in accordance with the imbalance rate of the applied dataset. For x_i, several samples are randomly selected from the k-nearest neighbors, assuming that the chosen nearest neighbor is x_m. For each randomly selected neighbor x_m, a new sample is created from the original sample based on Equation 1.

$$x_{new} = x + rand(0,1) \times |x_i - x|, new \in 1,2,\dots,M \quad (1)$$

Here, rand (0,1) denotes a random number in the range 0 to 1. The above steps are repeated M times to create M new samples. That is, if the total number of the minority category is T, new samples are generated MT. After combining the new samples with several original samples, a new balanced dataset is obtained. (Chen et al. 2022; Geetha et al. 2019; Ishaq et al. 2021). The main processes of the SMOTE algorithm are given in Figure 2.

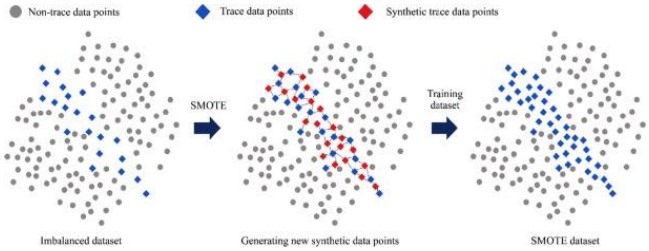

Figure 2. SMOTE algorithm main processes (Chen et al. 2022)

2.3. Extra tree algorithm

Extra trees are one of the decision tree-based ensemble learning methods. Unlike other tree-based ensemble methods, extra tree separates nodes with randomly chosen cut-points and develops trees using the entire learning sample to minimize bias (Geurts et al. 2006). Each decision tree is created from the dependency relationship of the extracted data samples (Kumar et al. 2020; Sharaff and Gupta 2019). At the same time, each decision tree selects the best features based on the mathematical basis of the Gini Index given in Equation 2.

$$gini\ (D) = 1 - \sum_{i=1}^{m} P_i^2 \quad (2)$$

where m represents the number of output labels and pi indicates the probability that a sample belongs to the i^{th} output label in dataset D (Du et al. 2023).

2.4. Evaluate metrics

Cohen's Kappa coefficient (k) represents a measure of how many samples are classified in the machine learning model (Equation 3).

$$K = \frac{(p0-pe)}{(1-pe)} \quad (3)$$

Here, p0 and pe show the total accuracy and random accuracy of the model, respectively (Vujović 2021). Precision is obtained by dividing the true positive (TP) predictions by the total number of true positive and false positive (FP) predictions (Equation 4). The recall given in Equation 5 is obtained by dividing the correct positive predictions by the total number of positives.

$$Precision = \frac{TP}{TP+FP} \quad (4)$$

$$Recall = \frac{TP}{TP+FN} \quad (5)$$

Here FN is false negative. Accuracy is one of the most popular criteria in multiclass classification and is calculated directly from the confusion matrix (Equation 6)

$$Accuracy = \frac{TP+TN}{TP+TN+FP+FN} \quad (6)$$

F1-Score, which collects precision and recall measures under the concept of harmonic mean, is given in Equation 7:

$$F1 - Score = 2 \times \left(\frac{precision \times recall}{precision+recall}\right) \quad (7)$$

The best value for the F1 score is obtained at 1 and the worst value at 0 (Grandini et al. 2020).

3. Results and Discussion

In this section, the modeling results for the estimation of the groundwater level are presented. By using precipitation, elevation, slope and curvature data, groundwater level was estimated with the extra tree (ET) algorithm. Then, SMOTE algorithm on data were used to improve the performance of the ET algorithm. While developing the model, the data were randomly divided into 80% training and 20% testing. Cohen's Kappa, Accuracy, Recall, Precision and F1-Score metrics were used to evaluate the model result.

Groundwater level is divided into five classes as very low, low, medium, high, and very high. Before the ET model was developed, the ratio of each class to the total data was examined. It is seen that the very high class constitutes only 4% of the total data and the data is unbalanced distributed.

In the study, firstly, the ET model was developed by ignoring the data unbalance. The accuracy value of the developed model was calculated as 0.53 and the Cohen's Kappa value as 0.36. Precision, recall and F1-score values calculated for each class in the test set are given in Table 1, and confusion matrix is given in Figure 3.

Table 1. Evaluation metric results of ET model test set

Class	Precision	Recall	F1 score
Very low	0.63	0.65	0.64
Low	0.51	0.61	0.56
Moderate	0.46	0.42	0.44
High	0.51	0.42	0.46
Very high	0.35	0.13	0.19

When the accuracy and Cohen's Kappa values calculated for the ET model and Table 1 are examined, it is seen that this model is not sufficient for estimating the groundwater level. Then, the SMOTE algorithm was used to increase the success of the ET model. The ratio of each class belonging to the groundwater level to the total number of data was balanced with the SMOTE algorithm.

After each class was equalized with the SMOTE algorithm, the ET model was reapplied to the new data set. The accuracy value of the reconstructed SMOTE-ET model was 0.69 and the Cohen's Kappa value was 0.62. Precision, recall and F1-score values calculated for each class in the test set are given in Table 2, and confusion matrix is given in Figure 4.

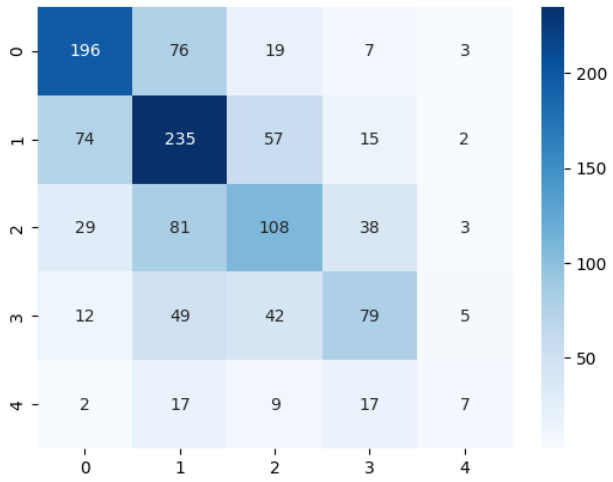

Figure 3. Confusion matrix of ET model test set (0-Very low, 1-Low, 2-Moderate, 3-High and 4-Very high)

Table 2. Evaluation metric results of SMOTE-ET model test set

Class	Precision	Recall	F1 score
Very low	0.68	0.76	0.72
Low	0.59	0.49	0.54
Moderate	0.63	0.61	0.62
High	0.70	0.72	0.71
Very high	0.83	0.88	0.86

Figure 4. Confusion matrix of SMOTE-ET model test set (0-Very low, 1-Low, 2-Moderate, 3-High and 4-Very high)

When the SMOTE-ET model accuracy and Cohen's Kappa value are examined, it is seen that it gives better results than the ET model. In addition, when Tables 1 and 2 are compared, it is seen that although the recall and F1-Score values of the Low class in the SMOTE-ET model are lower than the recall and F1-Score values of the Low class in the ET model, it gives better results in other classes.

4. Conclusion

In this study, ET algorithm was used to estimate the groundwater level of Denizli, Türkiye. In order to

increase the success of the estimation results obtained with ET algorithm, the imbalanced data in the groundwater level are eliminated with the SMOTE algorithm. Thus, more accurate groundwater level estimates were obtained.

References

Afzaal, H., Farooque, A. A., Abbas, F., Acharya, B., & Esau, T. (2020). Groundwater estimation from major physical hydrology components using artificial neural networks and deep learning. Water, 12(1), 5. https://doi.org/10.3390/w12010005

Chen, J., Huang, H., Cohn, A. G., Zhang, D., & Zhou, M. (2022). Machine learning-based classification of rock discontinuity trace: SMOTE oversampling integrated with GBT ensemble learning. International Journal of Mining Science and Technology, 32(2), 309-322. https://doi.org/10.1016/j.ijmst.2021.08.004

Çıldır, M. A. (2017). measurement of groundwater levels in Denizli and mapping with geographic information systems (Master's thesis, Pamukkale University Institute ff Science).

Daliakopoulos, I. N., Coulibaly, P., & Tsanis, I. K. (2005). Groundwater level forecasting using artificial neural networks. Journal of hydrology, 309(1-4), 229-240. https://doi.org/10.1016/j.jhydrol.2004.12.001

Dash, N. B., Panda, S. N., Remesan, R., & Sahoo, N. (2010). Hybrid neural modeling for groundwater level prediction. Neural Computing and Applications, 19, 1251–1263. https://doi.org/10.1007/s00521-010-0360-1

Du, Y., Liu, Y., Yan, Y., Fang, J., & Jiang, X. (2023). Risk management of weather-related failures in distribution systems based on interpretable extra-trees. Journal of Modern Power Systems and Clean Energy. https://doi: 10.35833/MPCE.2022.000430.

Geetha, R., Sivasubramanian, S., Kaliappan, M., Vimal, S., & Annamalai, S. (2019). Cervical cancer identification with synthetic minority oversampling technique and PCA analysis using random forest classifier. Journal of medical systems, 43, 1-19. https://doi.org/10.1016/j.ijmst.2021.08.004

Geurts, P., Ernst, D., & Wehenkel, L. (2006). Extremely randomized trees. Machine learning, 63, 3-42. https://doi.org/10.1007/s10994-006-6226-1

Grandini, M., Bagli, E., & Visani, G. (2020). Metrics for multi-class classification: an overview. arXiv preprint arXiv:2008.05756. https://doi.org/10.48550/arXiv.2008.05756

Ishaq, A., Sadiq, S., Umer, M., Ullah, S., Mirjalili, S., Rupapara, V., & Nappi, M. (2021). Improving the prediction of heart failure patients' survival using SMOTE and effective data mining techniques. IEEE access, 9, 39707-39716. https://doi: 10.1109/ACCESS.2021. 3064084.

Kumar, P., Singh, S. N., & Dawra, S. (2022). Software component reusability prediction using extra tree classifier and enhanced Harris hawks optimization algorithm. International Journal of System Assurance Engineering and Management, 13(2), 892-903. https://doi.org/10.1007/s13198-021-01359-6

Poursaeid, M., Poursaeid, A. H., & Shabanlou, S. (2022). A comparative study of artificial intelligence models and a statistical method for groundwater level prediction. Water Resources Management, 36(5), 1499-1519. https://doi.org/10.1007/s11269-022-03070-y

Razali, N., Ismail, S., & Mustapha, A. (2020). Machine learning approach for flood risks prediction. IAES International Journal of Artificial Intelligence, 9(1), 73. https://doi:10.11591/ijai.v9.i1.pp73-80

Sahoo, S., & Jha, M. K. (2013). Groundwater-level prediction using multiple linear regression and artificial neural network techniques: a comparative assessment. Hydrogeology Journal, 21(8), 1865. https://doi: 10.1007/s10040-013-1029-5

Sharaff, A., & Gupta, H. (2019). Extra-tree classifier with metaheuristics approach for email classification. In Advances in Computer Communication and Computational Sciences: Proceedings of IC4S 2018, 189-197, Springer Singapore.

Tang, T., Jiao, D., Chen, T., & Gui, G. (2022). Medium-and long-term precipitation forecasting method based on data augmentation and machine learning algorithms. IEEE Journal of Selected Topics in Applied Earth Observations and Remote Sensing, 15, 1000-1011. https://doi: 10.1109/JSTARS.2022.3140442.

Vujović, Ž. (2021). Classification model evaluation metrics. International Journal of Advanced Computer Science and Applications, 12(6), 599-606. https://doi:10.14569/IJACSA.2021.0120670

Wang, Y., Wu, X., Chen, Z., Ren, F., Feng, L., & Du, Q. (2019). Optimizing the Predictive Ability of Machine Learning Methods for Landslide Susceptibility Mapping Using SMOTE for Lishui City in Zhejiang Province, China. International Journal of Environmental Research and Public Health, 16(3), 368. MDPI AG. Retrieved from http://dx.doi.org/10.3390/ijerph16030368

Yadav, B., Gupta, P. K., Patidar, N., & Himanshu, S. K. (2020). Ensemble modelling framework for groundwater level prediction in urban areas of India. Science of the Total Environment, 712, 135539. https://doi.org/10.1016/j.scitotenv.2019.135539

6th Intercontinental Geoinformation Days

igd.mersin.edu.tr

Using frequency ratio model for flood susceptibility mapping of Mandaue City, Cebu

Jao Hallen Bañados *[1], **Isabella Pauline Quijano**[1], **Chito Patiño**[1]

[1]*University of the Philippines Cebu, SMART-TUrF, College of Science, Cebu City, Philippines*

Keywords
Flood susceptibility
Frequency ratio
GIS
ROC

Abstract

Floods cause damage to the global economy and environment, leading to the loss of lives; therefore, identifying flood-vulnerable locations is essential for complete flood risk management. As a highly dense and low-lying city, Mandaue City in Cebu, Philippines, easily gets flooded during heavy downpours leading to heavy traffic and damages in the area. This study utilized a geospatial approach to generate a flood susceptibility map of the city using the frequency ratio (FR) model. The flood susceptibility analysis considered eight flood conditioning factors: elevation, slope, Topographic Wetness Index (TWI), curvature, river density, land use, Normalized Difference Vegetation Index (NDVI), and rainfall. The FR model results exhibited high accuracy, with an AUC value of 0.902. Five percent of the city falls under high hazard classification, encompassing industrial, commercial, and critical facilities.

1. Introduction

Rapid urbanization and climate change have resulted in numerous environmental issues and tragedies (Rahmati et aal. 2019). The Philippines experiences around 20 tropical cyclones annually, with the peak season occurring from July to October, accounting for about 70% of all typhoons (Santos 2020).

Mandaue City is prone to flooding during heavy downpours, causing traffic congestion and damage. Hence, flood prevention is crucial to protect livelihoods and the environment (Huang et al. 2008). Geographic information systems (GIS) and remote sensing have been used in various studies to analyze flood hazards and map flood susceptibility (Bates 2004; Paul et al. 2019; Rahmati et al. 2016; Yariyan et al. 2020). Accurate identification of flood-prone areas is essential for effective flood management and prevention (Termeh et al. 2018). Flood susceptibility modeling, incorporating GIS and remote sensing, helps identify vulnerable areas (Wang 2019). Flood inventory maps serve as primary data sources for flood susceptibility mapping, and techniques like logistic regression and frequency ratio (FR) models are used to assess flood risk (Ullah et al. 2020). The FR model, known for its simplicity and satisfactory risk analysis, was chosen for this study (Ullah et al. 2020). Although not commonly used for flood hazards, the FR model has shown promising results for other natural hazards like landslides (Nicu 2017; Aditian et al. 2018; Regmi et al. 2014)

The study's main objective is to generate a flood susceptibility map of Mandaue City, focusing on the Butuanon river basin, using the FR model and identify potential flood risk areas within the city.

2. Method

2.1. Description of study area

Mandaue City, located in the province of Cebu in the Philippines, is a commercial and industrialized urban area situated at coordinates 10.3321° N and 123.9357° E. It is a high-income city and is surrounded by other highly-urbanized cities, as shown in Figure 1. The climate in the region follows a wet and dry season pattern, with the rainy season lasting from June to November, classified as Coronas climate type 3. The city receives an average annual precipitation of 1,570 millimeters (JICA 2010).

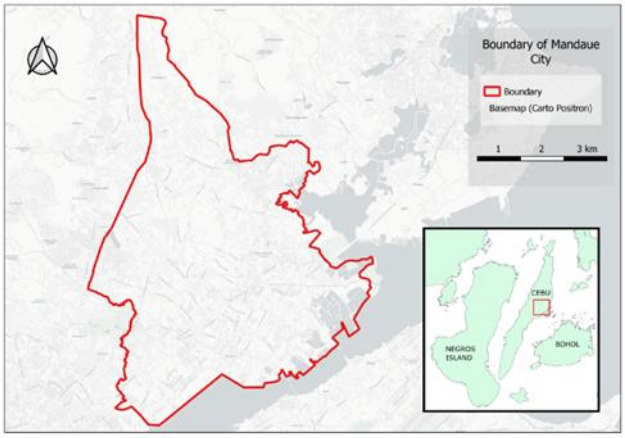

Figure 1. Mandaue City, Cebu, Philippines

* **Corresponding Author**

*(jlbanados@up.edu.ph) ORCID ID 0000-0002-7675-1762
(ilquijano@up.edu.ph) ORCID ID 0000-0002-7579-7267
(clpatino@up.edu.ph) ORCID ID 0000-0001-6879-2268

Cite this study

Bañados, J. H., Quijano, I. P., Patiño, C. (2023). Using frequency ratio model for flood susceptibility mapping of Mandaue City, Cebu. Intercontinental Geoinformation Days (IGD), 6, 78-82, Baku, Azerbijan

2.2. Flood inventory mapping

The accuracy of flood susceptibility mapping relies on accurate historical flood data (Ullah et al. 2020). In this study, flood-prone areas were identified based on the city's 2020 Comprehensive Drainage Master Plan and Drainage Impact Assessment. 163 flood points were recognized and categorized in the flood inventory database with input from residents.

2.3. Flood conditioning factors

Flood susceptibility assessment requires considering multiple flood-triggering and causing factors and their relationship to flooding. The selection of flood-controlling factors is not standardized and varies across studies (Samanta et al. 2018; Das 2019; Dou et al. 2018). In this study, flood conditioning factors were chosen based on the physical and natural characteristics of the study area and data availability. The flood conditioning parameters included elevation, slope, Topographic Wetness Index (TWI), river density, land use, rainfall, Normalized Difference Vegetation Index (NDVI), and curvature.

The Interferometric Synthetic Aperture Radar (IFSAR) Digital Elevation Model (DEM) was utilized to generate the elevation, slope, TWI, and curvature rasters. Land use and river density datasets were extracted by the City Planning Division of the city. The NDVI and rainfall datasets were obtained using the Google Earth Engine platform. The NDVI raster was specifically acquired using the Landsat-8 images collection, which covers the 2013-2022 dataset. Meanwhile, the rainfall raster was extracted from Climate Hazards Group InfraRed Precipitation with Station Data (CHIRPS). All factors were then reclassified into six classes using the natural break classification, except for the curvature raster (Pawar et al. 2022).

2.4. Frequency ratio (FR) model

Frequency ratio is an extensively used model in the analysis and mapping of different types of natural hazards, including floods, landslides, and forest fires (Rehman et al. 2022). Each independent flood triggering factor's relationship to the likelihood of flooding determined its measure of probability. The link between flood incidence and flood-triggering factors is strongest when the probability is larger (greater than 1) and weakest when the probability is lower (less than 1) (Samanta et al. 2018). The FR formula is expressed in Equation 1:

$$FR = \frac{Flood\ Points\ per\ Factor\ Class\ /\ Total\ Flood\ Points\ per\ Factor\ Class}{Area\ per\ Factor\ Class/\ Total\ Area} \quad (1)$$

The results were then normalized as relative frequency (RF) into a range of probability values [0, 1]. Even after normalization, the RF still has the flaw of assigning equal weight to each contributing factor. A prediction rate (PR) was produced by grading each flood conditioning factor with the training data set to solve this issue. Finally, the flood susceptibility map can be generated using the summation of the PR of each factor and the RF of each class using the Equation 2.

$$FS = \sum_{i=1}^{n} PR_i \times RF_i \quad (2)$$

3. Results

The FR model was used to assess Mandaue City's flood susceptibility by analyzing the relationship between flood-prone areas and flood conditioning factors. Table 1 presents the reclassification results and occurrences of each factor related to flood hazards.

Low-lying areas, accounting for 38.15% of the city, had a high RF value (0.304) and were prone to flooding. Nearly 92% of past floods occurred in the first three elevation classes are consistent with previous research (Khosravi et al. 2019). Low-gradient slopes in lower regions were found to be more susceptible to flooding compared to high-gradient slopes (Ramesh et al. 2020). The lowest slope gradient class (<1.838°) covered 70.36% of the study area and had a high occurrence of past floods (74.58%). The TWI factor in this study was categorized into five classes. Flood occurrences were lower in the last TWI class, while classes ranging from 5.903 to 9.2 had a higher susceptibility to flooding. Reclassification results revealed that higher TWI values were predominantly found in streams and low-lying areas, while the uplands had lower TWI values. Flooding in the watershed was more likely in areas with higher TWI values (Tehrany et al. 2015).

Drainage density plays a critical role in flooding, as higher density indicates increased surface runoff and a greater likelihood of flooding (Ullah et al. 2020) The study found that the highest drainage density was near the Butuanon River, which is located in the middle of the city and is a major contributor to flooding (Maglana et al. 2020). The occurrence of flooding was most likely in areas classified in the third to fifth classes, with a probability of 70.08%. Regions with high drainage density have a higher risk of flooding due to increased surface runoff (Das 2019). Land use patterns reflect how the city utilizes its land. In terms of flooding, built-up areas contribute to increased runoff due to extensive impermeable surfaces and a lack of vegetation to slow down or absorb water. Barren ground also enhances runoff. In this study, higher weights were assigned to waterbodies (RF of 0.285) and mangrove forest areas (RF of 0.329). Built-up areas near rivers, with their economic resources, infrastructure, and large population, are particularly susceptible to flooding (Khosravi et al. 2016). Positive NDVI values indicate vegetation, while negative values represent water. Therefore, higher NDVI levels suggest a lower risk of flooding, while lower NDVI values indicate a higher potential for flooding (Khosravi et al. 2016). For the NDVI of the area, values range from -0.224 to 0.745. The curvature analysis, derived from the same DEM as elevation and slope, represented the topography's morphology. It was divided into three classes: convex, flat, and concave. Positive curvature values indicated convex surfaces, zero represented flat surfaces, and negative values indicated concave surfaces. The study found that the majority of the study area

belonged to the middle class, which had relatively flat topography and accounted for 93.47% of flood occurrences.

Table 1. Flood conditioning factors and classes

Factor	Class	Occurrence	%
Elevation (m)	0-7.61	23278	54.65
	7.61-17.26	5424	12.73
	17.26-29.95	10516	24.69
	29.95-49.25	2022	4.75
	49.25-77.17	956	2.24
	77.17-129.97	398	0.93
Slope (degree)	0-1.84	31881	74.85
	1.84-5.18	6363	14.94
	5.18-10.03	2348	5.51
	10.03-16.38	1143	2.68
	16.38-23.9	509	1.2
	23.9-42.78	350	0.82
TWI	2.52-5.9	4783	11.23
	5.9-7.64	11922	27.99
	7.64-9.2	11724	27.53
	9.2-10.85	8376	19.66
	10.85-13.36	4402	10.33
	13.36-24.72	1387	3.26
Drainage	0-0.76	490	10.47
Density	0.76-2.01	425	9.08
	2.01-3.16	1042	22.26
	3.16-4.31	1116	23.84
	4.31-5.71	1123	23.99
	5.71-9.2	486	10.38
Land Use	Brush/Shrubs	138	2.32
	Built-up	4432	74.59
	Inland Water	970	16.32
	Mangrove Forest	97	1.63
	Open/Barren	293	4.93
	Perennial Crop	12	0.2
Rainfall (mm)	53.54-56.38	655	14.15
	56.38-61.15	26	0.56
	61.15-66.94	3471	75
	66.94-72.42	6	0.13
	72.42-76.48	127	2.74
	76.48-79.52	343	7.41
NDVI	-0.22-0.06	559	12.1
	0.06-0.14	1013	21.94
	0.14-0.23	1068	23.13
	0.23-0.32	910	19.71
	0.32-0.44	686	14.85
	0.44-0.75	382	8.27
Curvature	-12.47--1.31	809	1.9
	-1.31-0.56	39813	93.47
	0.56-12.81	1972	4.63

4. Discussion

To create the final flood susceptibility map, the weights of each factor and the RF of each class were summed using the flood susceptibility index equation in the ArcGIS 10.8 environment (Samanta et al. 2018). The resulting raster was divided into four classes, with only three classes representing hazard levels: low, moderate, and high, as shown in Figure 2. The analysis reveals that approximately 5% of the total area is in a high-hazard zone, 27% in a moderate zone, and 36% in a low-hazard zone. The remaining 32% of the city is considered safe, as summarized in Table 2.

Table 2. Hazard classes

Hazard Class	Class Area (sq. m)	% of Area
Very Low	10719	32
Low	12076	36
Moderate	9242	27
High	1634	5

Figure 2 illustrates that the high-risk areas for flooding are primarily located near the banks and mouth of rivers and streams, particularly along the Butuanon River. Upon examining the intersection of flood susceptibility and the buildings dataset, it becomes evident that numerous residential areas, commercial buildings, industrial zones, and critical facilities are highly vulnerable to future flooding.

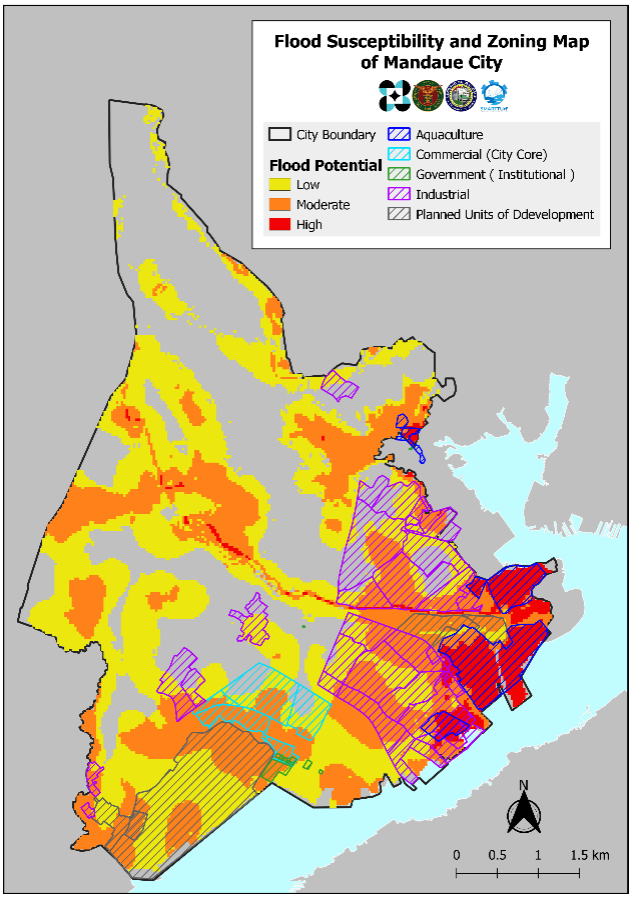

Figure 2. Flood susceptibility map and zoning map of Mandaue City

5. Conclusion

Floods are a significant global environmental hazard, causing widespread devastation. To mitigate the impact of floods, it is essential to assess flood vulnerability and generate flood susceptibility maps. This study utilized a

GIS-based approach with the frequency ratio method to create a flood susceptibility map of Mandaue City. Eight flood conditioning factors, including elevation, slope, TWI, river density, land use, rainfall, NDVI, and curvature, were analyzed. The effectiveness of the frequency ratio model was evaluated using the ROC curve, resulting in a success rate of 90.2% as depicted in Figure 3. The flood conditioning factors played a crucial role in mapping flood vulnerability.

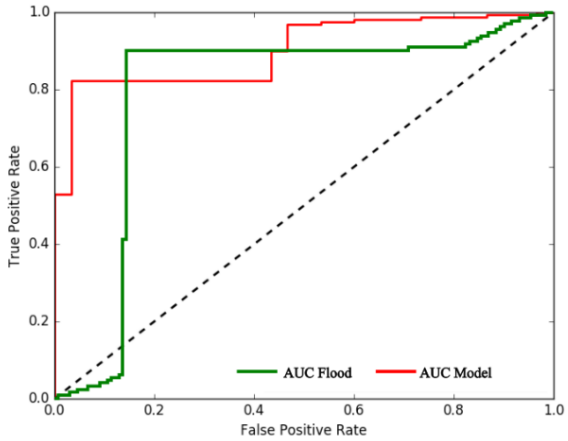

Figure 3. AUC graph of the FR model and flood hazard

Acknowledgement

This research was conducted by the Smart City Solutions to Urban Flooding Program. We are grateful to the Department of Science and Technology (DOST) for the financial support, with the DOST Philippine Council for Industry, Energy, and Emerging Technology Research and Development as the monitoring agency and the University of the Philippines Cebu as the implementing agency.

References

Aditian, A., Kubota, T., & Shinohara, Y. (2018). Comparison of GIS-based landslide susceptibility models using frequency ratio, logistic regression, and artificial neural network in a tertiary region of Ambon, Indonesia. Geomorphology, 318, 101-111.

Bates, P. D. (2004). Remote sensing and flood inundation modelling. Hydrological processes, 18(13), 2593-2597.

Das, S. (2019). Geospatial mapping of flood susceptibility and hydro-geomorphic response to the floods in Ulhas basin, India. Remote Sensing Applications: Society and Environment, 14, 60-74.

Debabrata, S., & Mondal, P. (2020). Flood vulnerability mapping using frequency ratio (FR) model: a case study on Kulik river basin, Indo-Bangladesh Barind region. Applied Water Science, 10(17).

Dou, X., Song, J., Wang, L., Tang, B., Xu, S., Kong, F., & Jiang, X. (2018). Flood risk assessment and mapping based on a modified multi-parameter flood hazard index model in the Guanzhong Urban Area, China. Stochastic environmental research and risk assessment, 32, 1131-1146.

Huang, X., Tan, H., Zhou, J., Yang, T., Benjamin, A., Wen, S. W., ... & Li, X. (2008). Flood hazard in Hunan province of China: an economic loss analysis. Natural Hazards, 47, 65-73.

Japan International Cooperation Agency (JICA). (2010).

Khosravi, K., Pourghasemi, H. R., Chapi, K., & Bahri, M. (2016). Flash flood susceptibility analysis and its mapping using different bivariate models in Iran: a comparison between Shannon's entropy, statistical index, and weighting factor models. Environmental monitoring and assessment, 188, 1-21.

Khosravi, K., Melesse, A. M., Shahabi, H., Shirzadi, A., Chapi, K., & Hong, H. (2019). Flood susceptibility mapping at Ningdu catchment, China using bivariate and data mining techniques. In Extreme hydrology and climate variability (pp. 419-434). Elsevier.

Maglana, J. M. R., Parmes, H. O. O., Yu, A. C. C., Fornis, R. L., & Oraya, A. F. A. (2020, October). An attempt to classify landcover of the Butuanon river catchment using Landsat images covering the years 1993 to 2019 for rainfall-runoff modelling. In AIP Conference Proceedings (Vol. 2278, No. 1). AIP Publishing.

Nicu, I. C. (2017). Frequency ratio and GIS-based evaluation of landslide susceptibility applied to cultural heritage assessment. Journal of Cultural Heritage, 28, 172-176.

Paul, G. C., Saha, S., & Hembram, T. K. (2019). Application of the GIS-based probabilistic models for mapping the flood susceptibility in Bansloi sub-basin of Ganga-Bhagirathi river and their comparison. Remote Sensing in Earth Systems Sciences, 2, 120-146.

Pawar, U., Suppawimut, W., Mutiil, N., & Rathnayake, U. (2022). A GIS-Based Comparative Analysis of Frequency Ratio and Statistical Index Models for Flood Susceptibility Mapping in the Upper Krishna Basin, India. Water, 14, 3771.

Rahmati, O., Zeinivand, H., & Besharat, M. (2016). Flood hazard zoning in Yasooj region, Iran, using GIS and multi-criteria decision analysis. Geomatics, Natural Hazards and Risk, 7(3), 1000-1017.

Rahmati, O., Darabi, H., Haghighi, A. T., Stefanidis, S., Kornejady, A., Nalivan, O. A., & Tien Bui, D. (2019). Urban flood hazard modeling using self-organizing map neural network. Water, 11(11), 2370.

Ramesh, V., & Iqbal, S. S. (2020). Urban flood susceptibility zonation mapping using evidential belief function, frequency ratio and fuzzy gamma operator models in GIS: a case study of Greater Mumbai, Maharashtra, India. Geocarto International.

Regmi, A. D., Yoshida, K., Pourghasemi, H. R., Dhital, M. R., & Pradhan, B. (2014). Landslide susceptibility mapping along Bhalubang—Shiwapur area of mid-Western Nepal using frequency ratio and conditional probability models. Journal of Mountain Science, 11, 1266-1285.

Rehman, A., Song, J., Haq, F., Mahmood, S., Ahamad, M. I., Basharat, M., ... & Mehmood, M. S. (2022). Multi-hazard susceptibility assessment using the analytical hierarchy process and frequency ratio techniques in the Northwest Himalayas, Pakistan. Remote Sensing, 14(3), 554.

Samanta, R. K., Bhunia, G. S., Shit, P. K., & Pourghasemi, H. R. (2018). Flood susceptibility mapping using geospatial frequency ratio technique: a case study of

Subarnarekha River Basin, India. Modeling Earth Systems and Environment, 4, 395-408.

Santos, G. D. (2021). 2020 Tropical Cyclones in the Philippines: A Review. Tropical Cyclone Research and Review, 10(3), 191-199.

Tehrany, M. S., Pradhan, B., Mansor, S., & Ahmad, N. (2015). Flood susceptibility assessment using GIS-based support vector machine model with different kernel types. Catena, 125, 91-101.

Termeh, S. V. R., Kornejady, A., Pourghasemi, H. R., & Keesstra, S. (2018). Flood susceptibility mapping using novel ensembles of adaptive neuro-fuzzy inference system and metaheuristic algorithm. Sci. Total Environ., 615, 438-451.

Ullah, K., & Zhang, J. (2020). GIS-based flood hazard mapping using relative frequency ratio method: A case study of Panjkora River Basin, Eastern Hindu Kush, Pakistan. PLoS ONE, 15(3), e0229153.

Wang, Y. (2019). Flood susceptibility mapping in Dingnan County (China) using adaptive neuro-fuzzy inference system with biogeography-based optimization and imperialistic competitive algorithm. Journal of Environmental Management, 247, 712-729.

Yariyan, P., Avand, M., Abbaspour, R. A., Torabi Haghighi, A., Costache, R., Ghorbanzadeh, O., ... & Blaschke, T. (2020). Flood susceptibility mapping using an improved analytic network process with statistical models. Geomatics, Natural Hazards and Risk, 11(1), 2282-2314.

6th Intercontinental Geoinformation Days

igd.mersin.edu.tr

Investigating the flooded area of Bangladesh by Sentinel_1 and CHIRPS images in the GEE cloud-based platform

Nilufar Makky*[1], Khalil Valizadeh Kamran [2], Neda Kaffash Charandabi [3]

[1,2] *University of Tabriz, Environmental science, RSGIS department, Tabriz city, Iran*
[3] *University of Tabriz, Marand Technical department, Marand City, Tabriz, Iran*

Keywords
Sentinel_1
Flood
NDBI
Climate change
CHIRPS

Abstract

Climate change has been linked to the occurrence of severe weather events such as storms, droughts, and floods. The utilization of remote sensing technology has shown promise in predicting these events and supporting crisis management planning efforts. A noteworthy example is the catastrophic flooding that occurred in Bangladesh in May 2022, resulting in a significant loss of life and displacement of hundreds of thousands of individuals. In response, remote sensing techniques, including CHIRPS satellite imagery and Synthetic Aperture Radar (SAR) data, were employed to monitor and assess the extent and impact of the flooding. The Normalized Difference Built-Up Index (NDBI) was utilized to demonstrate a decrease in urban development by 10% in areas affected by floods. Moreover, the public's preference for urban development was found to be clustered around the northwestern border with India, indicating potential areas of focus for future urban development planning. These findings highlight the utility of remote sensing technology in the realm of crisis management and urban development

1. Introduction

The 2020 average global surface temperature statistically matched 2016 as the warmest year on record, continuing a long-term warming trend due to human activities (climate.nasa.gov). Managing climate challenges is very important for researchers. In addition, it has many bad effects on human life (Karimzade & Matsuoka, 2018). Also, urban management can improve our life (Makky & Kaffash, 2017). Disaster risk from rainfall is now universally discussed due to its possible connection with global warming. Catastrophic rainfall has been decreasing until the mid-2010s, after which it is likely to increase due to increased rainfall intensity (Towhata ,2022). Of course, natural disasters such as floods happen all over the world. Due to their negative impact on various social, economic and environmental aspects, the need to monitor and map these phenomena has increased. In fact, we use open-source remote sensing (RS) images obtained by optical and radar sensors to access flood-affected areas. In addition, by using Sentinel-1 images, we suggest using ground range detected images (GRD) (Benzougagh et al,2021). Geospatial resources, including satellite-based Synthetic Aperture Radar (SAR) and optical data, have been very useful in providing time-sensitive information on the extent and impact of natural hazard events such as floods to support emergency response and crisis management efforts (Hertel et al, 2023). For example, 41.98 percent of the disaster events that occurred in 2021 in Indonesia were flood disasters. A rainfall of 2.08 billion cubic meters occurred in the second week of January 2021 in South Kalimantan, Indonesia, where the volume of rainwater was not proportional to the capacity of the Barito watershed, causing flooding in 11 cities/districts (Adiba and Bioresita, 2022). Konawa Utara District is one of the southeast Sulawesi districts that experienced flash floods in 2019. As a result, this flood caused significant environmental and economic damage and damaged several public infrastructures. Mangidi et al used Sentinel 1 SAR images and the Sigma-Naught Index (NDSI) to investigate this incident. This method can identify the backscatter value comparison from the image before and during the flood. Then the extraction of flood information, the results of this study show that floods occurred in some important areas of North Kunawe region and six (6) regions namely Wiwirano region, Oheo region, Molawe region, Langgikima region, Asera region, Andowia region are under the water is a slave.

* **Corresponding Author**

*(nilufar_makky73@yahoo.com)
(n_kaffash@tabrizu.ac.ir) ORCID ID 0000-0002-6281-9009
(valizadeh@tabrizu.ac.ir) ORCID ID 0000-0003-4648-842X

Cite this study

Makky, N., Kamran, K. V., & Charandabi, N. K. (2023). Investigating the flooded area of Bangladesh by Sentinel_1 and CHIRPS images in the GEE cloud-based platform. Intercontinental Geoinformation Days (IGD), 6, 83-88, Baku, Azerbaijan

This area included 186.24 hectares of residential and commercial area, 664.39 hectares of agricultural land. The rest of the flood zone consisted of forests, shrubs and wastelands. More importantly, the flood also inundated the center of North Kunawe district located in Asra district with an area of 25.76 hectares (Mangidi and Mandaya, 2019). He et al analyzed flood survey data sets in 18 different study areas including 18 countries from Sentinel-2 and Sentinel-1 post-disaster data, named CAU-Flood, with detailed image preprocessing and human annotation. A new Deep Convolutional Neural Network (CN), called Mutual Change Detection Network (CMCDNet) was used and also proposed to use multispectral and SAR images for flood detection. The proposed network uses encode decode structure and combines features in It gives several steps using Gating and Self-attention modules. The proposed (CMCDNet; cross-modal change detection) performed better than state-of-the-art (SOTA) methods in terms of flood detection accuracy and achieved 89.84% accuracy [He et al, 2023]. In Vietnam, the recent historical flood events caused a lot of damage to property, there was an urgent need for detailed remote sensing to help the government respond quickly to reduce loss of life. However, flooding usually occurs when most of the sky is covered with clouds. In such weather conditions, satellite radar images such as Copernicus Sentinel-1 Synthetic Aperture Radar (SAR) images are a valuable data source in flood monitoring tasks. The aim of this study was to design a method based on Convolutional Neural Network (CNN). The CNN model was empirically obtained by modifying the model based on visual inspection on the generated flood masks. Experimental results showed that the pre-trained CNN model provides similar results compared to the conventional Google Earth Engine (GEE) method, but significantly reduces the time required for flood mapping, which allows it to be used for immediate flood investigation. be (Phu and Van, 2023). In recent decades, the use of machine learning algorithms for predicting natural hazards has been of great importance for high efficiency, (Hayder et al) a prediction model based on the structure of short-term memory (ES-LSTM) and recurrent neural networks (RNNs) for They proposed hourly precipitation season forecast and precipitation was classified using artificial neural network (ANN) model and decision tree (DT) algorithm. The Australian Bureau of Meteorology dataset named the historical daily weather dataset was used to test the effectiveness of the proposed model. The findings showed that ES-LSTM and RNN achieved 17.3 and 42.6 in terms of mean absolute percentage error (MAPE), respectively. Meanwhile, the ANN and DT models achieved the prediction.

Among these regions, the Ohio region suffered the most flooding with 1,836.88 hectares (4.1% of the total area of the Ohio region). showed that ES-LSTM and ANN obtained the best results compared to other models (Hayder et al, 2023). Previous work was done on building flood forecasting models with the aim of reducing risks, proposing policies, reducing mortality and limiting property damage caused by floods. The massive amount of data generated by social media platforms such as Twitter opens the door to flood analysis. Due to the insitu nature of Twitter data, some government agencies and authorities have used it to track natural disaster events in order to develop a faster rescue strategy. However, due to the shorter duration of tweets, it is difficult to build a complete forecasting model for flood determination. Machine learning (ML) and deep learning (DL) methods can be used to statistically develop flood forecasting models. At the same time, the large volume of tweets makes it necessary to use big data analysis (BDA) tools for flood forecasting. In this regard, this work presents an optimal flood forecasting model based on deep learning with big data analysis (ODLFF-BDA) based on Twitter data. The proposed ODLFF-BDA technique aims to predict the presence of floods using tweets in a big data environment. The ODLFF-BDA technique involves data preprocessing to convert incoming tweets into a usable format. In addition, a bidirectional coder representation of transformers (BERT) model is used to generate emotional textual embeddings of tweets. In addition, a gated regression unit (GRU) with a multi-layer convolutional neural network (MLCNN) is used for local data mining and flood forecasting. Finally, an equilibrium optimizer (EO) is used to fine-tune the meta-parameters of the GRU and MLCNN models in order to enhance the prediction performance. If compared with other algorithm techniques, the memory usage is less than 3.5 MB. The performance of the ODLFF-BDA technique was verified using the Kaggle benchmark dataset, and the findings showed that it significantly outperformed other recent approaches (Indra and Duraipandian et al ,2023). The operating conditions of large cascade hydropower plants are complex. Improving the accuracy of water level prediction of large cascade hydropower plants is significant for flood control, transportation, irrigation, etc. To create input data in the form of a feature map so that the model can weight features of each of the influencing factors when the water level changes, speed, flow and output data of the hydropower plant were also created. In this process, the LSTM parameters are optimized using the Archimedes optimization algorithm, and the output results of the LSTM and GRU net accuracy of 96.65% and 84.0%, respectively were good.

The water level downstream of Xiangjiaba Hydropower Station, outperforms existing artificial intelligence and hydrodynamic methods, and has strong scalability in flood forecasting and urban rainwater forecasting (Ma et al, 2023). Understanding the different characteristics of rainfall is essential for water resources management. However, the highly variable nature of rainfall is important in accurately estimating rainfall in a particular region. Such variability in rainfall leads to floods or droughts, both of which are potentially catastrophic (Anandh et al, 2022). Knowing the precipitation trends using time series observations is the key to reliably determining the behavior of future observations. In fact, precipitation is an important part of the hydrological cycle, and its gradual change over time, due to ongoing climate change, is of interest to water resource managers and hydrologists. Indeed, global climate change affects the distribution of rainfall, altering water availability by increasing the length of dry periods and increasing the frequency of floods (Kessabi et a, 2023). CHIRPS combines satellite images with a resolution of 0.05° with insitu station data to create

gridded rainfall time series for trend analysis and seasonal drought monitoring (chc.ucsb.edu). Many studies have been conducted to investigate the error characteristics of precipitation products in different temporal and spatial scales. In the Adige basin, CHIRPS was shown to be the best product, and all products show larger errors in terms of overall statistical measures in the winter months (Duan et al, 2016). Based on this research, we used Chirps satellite to check it. Mardab al-Hawiza is one of the important marshes in the south of Iraq and near the Iranian border. They are rich in distinctive nature and in the past centuries, large rural communities have been formed around them and their water is taken from the Euphrates and Tigris. In 2018, a destructive flood in the Tigris river basin affected many areas. Ahmed et al. by comparing the land use before and after the flood season for Al-Hawiza swamps and also determined water reflection values using remote sensing and geographic information systems for the years 2018 and 2019, water reflection values using Landsat-8 images between the years It was calculated on 3/4/2018 and 3/7/2019 and before and after the flood wave that covered the southern swamps. The results showed that remote sensing can accurately determine the water and the extent of the flooded area caused by flooding in swamps and extracted from Landsat 8 using the NDBI, NDWI index (AHMED et al., 2022, Mousavi et al.,2023).

Works are weighted to obtain a more accurate water level forecast. The proposed model achieves good accuracy and efficiency in forecasting.

2. Method

By using VH polarizations for vertical transmission and horizontal reception, VV for vertical transmission and vertical reception, and (IW) in the Google earth engine system, a radar image of flooded areas was created. The interferometric wide band (IW) mode is the primary ground acquisition mode and meets most service requirements, acquiring data over a 250 km band with a spatial resolution of 5 meter and 20 meters. Sentinel_1 image on the surface of our study identified with the ground range (GRD) were uploaded in the engine environment, the data of the said polarizations were processed for flood mapping for its accuracy in flood detection, also from decibel images due to the high quality in determining the flood was used. CHIRPS is a 35-year quasi-global rainfall dataset covering 50°S to 50°N from 1981 that integrates indoor climatology, CHPclim, satellite imagery, and rain gauge data (Funk et al ,2016). The best spatial resolution of CHIRPS is 0.05 degrees.

Our study area is located in Bangladesh, which is one of the most flood-prone areas in the world. Bangladesh is a country located in South Asia. The total area of this country is 143,998 square kilometers with a population of 149.7 million people. The population density is 1039 per square kilometer, which is one of the highest in the world. Geographically, it extends from 20°34' to 26°38'N latitude and from 88°01' to 92°41'E longitude. Except for the hilly areas of the southeast, most of the country is a low-lying plain land. In terms of climate, this country belongs to subtropical regions where Dushanbe weather prevails throughout the year. The average temperature of the country in winter is between 7.20 and 12.80 degrees Celsius and 23.90 and 31.10 degrees Celsius (SHAHID et al, 2006). The choice of this country as a study area was due to the fact that in 2022, a flood occurred on the 11th of MAY, which caused the death of hundreds of people and the displacement of several thousand people. Examining and presenting flood prevention methods can be effective.

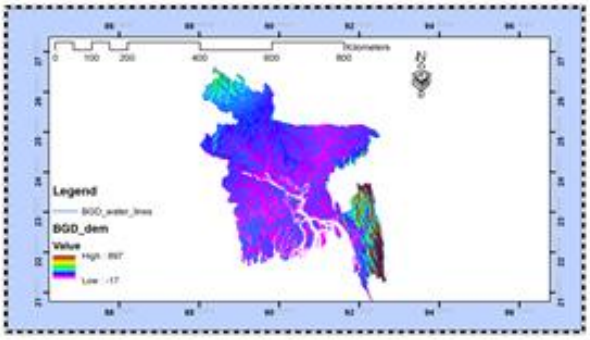

Figure 1. Case study

3. Results

The radar image after the flood was created by two polarizations VV and VH in the GEE system. MAX and MIN numbers indicate greater accuracy in detailing flood effects in VV polarization.

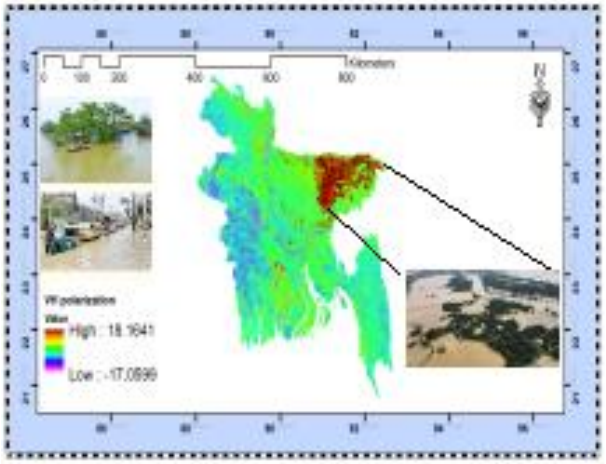

Figure 2. Radar image of the flooded area with VH polarization

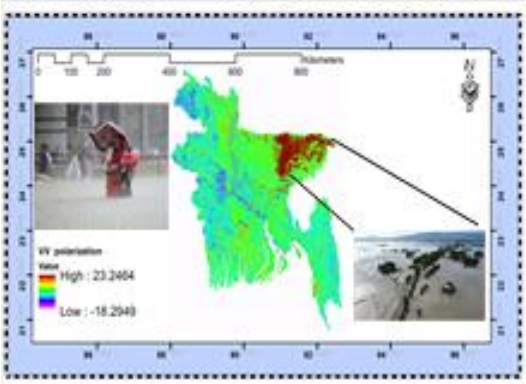

Figure 3. Radar image of the flooded area with VH polarization

Table 1. Table of coverage details by two polarizations

	VV	VH
MAX effect	23.2464	18.2949
MIN effect	18.1641	17.0599

Due to the fact that a severe flood occurred on 11/05/2022 in Bangladesh and had a destructive effect on large parts of this country, we used the GEE system to analyze the rainfall images obtained from the CHIRPS satellite for 14 months. The start date was selected from 05/2021 to 07/2022. The amount of precipitation two months after the flood was extracted for further investigation. The results showed that in the months close to the date of the flood, this country has seen a lot of rain. In the months of MAY, JUNE, 2021, and 2022, the amount of precipitation has increased sharply. The area marked with a dark color is the area of SYLHET state, which has heavy rainfall and there was a destructive flood in that area. The graph of the one year rainfall time series indicates the severity of flooding caused by heavy rainfall. The graph of the one-year's rainfall time series indicates the severity of flooding caused by heavy rainfall.

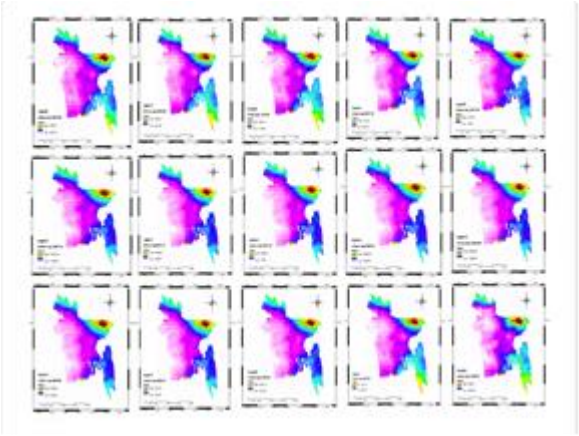

Figure 4. Rainfall images from CHIRPS satellite

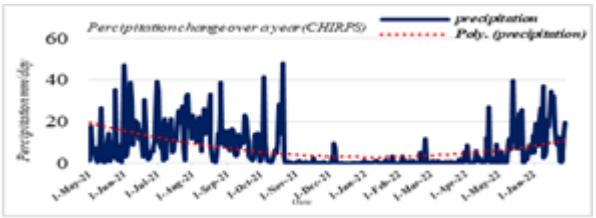

Figure 5. Time series diagram of rainfall in Bangladesh during one year

In addition, the resulting time series graph shows abundant rainfall in the months of MAY and June. One of the important reasons for this flood is heavy and continuous rain. These rainfalls are increasing due to global warming and the necessary forecasts must be made in all countries due to the increase of these rainfalls. Global warming increases the probability of heavy precipitation (from 40 to 60 mm/h) by about 1.3 to 1.8 times, but at the same time reduces the probability of light precipitation (from 1 to 10 mm/h) by about 20%. Gives. Urban development increases the probability of urban rainfall in all intensity ranges. It is worth noting that the effects of rapid urban development could be as important as global warming in the near future in intensifying heavy hourly rainfall in coastal megacities [Chenix et al,2023]. In addition to high rainfall, land subsidence may be another effective factor in flooding (Jiang et al, 2023). Land subsidence (LS) is one of the most challenging natural disasters that has potential consequences such as damage to infrastructure and buildings, creating sinkholes and leading to soil degradation (Eghrari et al., 2023, Mousavi et al,2023).

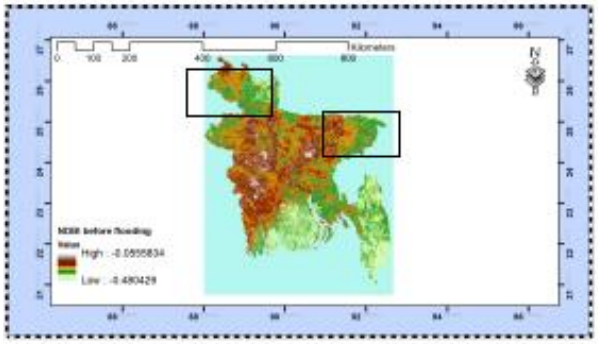

Figure 6. NDBI_Before flooding

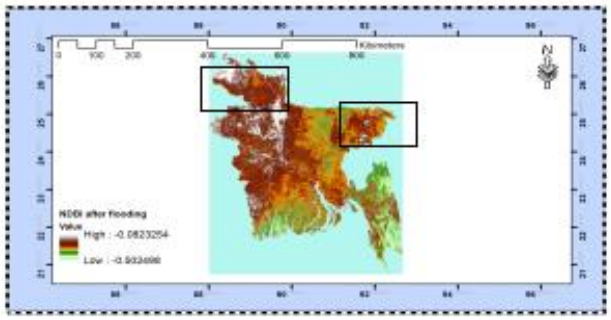

Figure 7. NDBI_After flooding

The NDBI index, which was extracted with the Landsat_8 sensor, shows the developed areas and is calculated from the following formula.

$$NDBI = (SWIR - NIR) / (SWIR + NIR) \quad (1)$$

4. Discussion

Flood mapping using Synthetic Aperture Radar (SAR) and precipitation data from satellites such as Climate Hazards Group InfraRed Precipitation with Station (CHIRPS) is crucial in managing flood risks globally. SAR uses microwaves to detect changes in water coverage and is useful in monitoring flood extent and level conditions day or night. CHIRPS produces high-quality precipitation estimates and combines satellite measurements and ground-based rainfall data to calculate rainfall patterns, aiding in flood risk management and climate change adaptation. The integration of SAR and CHIRPS data provides a comprehensive image of water inundation helping determine volume, speed, direction, and flooded regions, supporting flood risk assessment, prevention, and monitoring. Given the significant impact of flooding worldwide, the use of SAR and CHIRPS technologies is essential to aid decision-making for flood management programs.

5. Conclusion

Floods are known to have severe negative impacts on human life, finances, and urban development. In 2022, Sentinel-1 radar data was utilized to identify areas affected by floods in Bangladesh. The observed CHIRPS satellite images validated heavy precipitation surrounding the estimated flood-affected locations. During May, the northeastern region of Bangladesh experienced torrential rains that culminated in severe flooding. Due to its low-lying environment and numerous rivers, Bangladesh is particularly vulnerable to flooding, mandating a minimum distance between the waterways during periods of heavy rainfall. Analysis utilizing the NDBI index revealed a 10% decrease in urban growth and development rates in the flooded area, indicating that the costly damage caused by the floods had discouraged construction activities in the region.

Currently, there is ongoing developmental work in the northwest region of Bangladesh, which shares its borders with India. With global warming, major cities may experience increased rainfall, underscoring the requirement for proactive measures such as precise predictions and necessary preparations to alleviate the risks associated with flooding.

Acknowledgement

References

Adiba, A., Bioresita, F., (2022). Sentinel-1 SAR Polarization Combinations for Flood Inundation Spatial Distribution Mapping (Case Study: South Kalimantan)", IOP Conference Series: Earth and Environmental Science, Volume 1127, Geomatics International Conference (GEOICON) 2022 25/07/2022- 26/07/2022 Online. DOI 10.1088/1755-1315/1127/1/012009.

AHMED, A., HASHESH, T., (2022). USING SATELLITE IMAGES CLASSIFICATION TO ESTIMATE WATER LEVEL IN THE SOUTHERN MARSHLANDS AFTER THE FLOODS WAVE", nternational Journal of Applied Sciences and Technology.

Anandh, P. C., Krishna Vissa, N., Tyagi, B. (2022). Statistical Characteristics of Extreme Rainfall Events Over the Indian Subcontinent", Extreme Natural Events pp 109–127Cite as. DOI: 10.1007/978-981-19-2511-5_4.

Benzougagh, B., Louis Frison, P., Gajbhiye Meshram, S., Boudad, L., Dridri, Driss Sadkaoui, A., Mimich, Kh., Khedher, Kh.,2021," Flood Mapping Using Multi-temporal Sentinel-1 SAR Images: A Case Study—Inaouene Watershed from Northeast of Morocco", https://link.springer.com/journal/40996.

Chenix, Hu., Chi, young tom., Xinwei ,li ,.2023" Mega-city development impact on hourly extreme rainfall over the South China Greater Bay Area under near-future climate warming", Urban Climate. Volume 48, March 2023, 101389, https://doi.org/10.1016/j.uclim.2022.101389

https://www.chc.ucsb.edu/data/chirps

https://climate.nasa.gov/vital-signs/global-temperature.

Duan, Z., Liu, J., Tuo, Y., Chiogna, G., Disse, M, 2016, ."Evaluation of eight high spatial resolution gridded precipitation products in Adige Basin (Italy) at multiple temporal and spatial scales", Sci, Total Environ. 2016, 573, 1536–1553.

Eghrari,Z., Delavar ,M. R ., M, Zare., Beitollahi, A., Nazari,B, 2023, "LAND SUBSIDENCE SUSCEPTIBILITY MAPPING USING MACHINE LEARNING ALGORITHMS", ISPRS Ann. Photogramm. Remote Sens. Spatial Inf. Sci., X-4/W1-2022, 129–136, 2023.https://doi.org/10.5194/isprs-annals-X-4-W1-2022-129-2023.

Funk, C., Peterson, P., Landsfeld, M.,Pedreros, Verdin .,D , Shukla., J , Husak., S , Rowland., G, Harrison .,J , Hoell., L , A.; et al,2015," The climate hazards infrared precipitation with stations-a new environmental record for monitoring extremes", Sci, Data 2015, 2, 150066. Volume 285, 1 February 2023, 113388. https://doi.org/10.1016/j.rse.2022.113388.

He., X., Zhang, Sh., Xue, B., Zhao,T., Wu, T,(2023). Cross-modal change detection flood extraction based on convolutional neural network", International Journal of Applied Earth Observation and Geoinformation. https://doi.org/10.1016/j.jag.2023.103197

Hertel, V., Chow, C., Wani, O., Wieland, M., & Martinis, S. (2023). Probabilistic SAR-based water segmentation with adapted Bayesian convolutional neural network. *Remote Sensing of Environment*, *285*, 113388.

Hayder, I., Al-Amiedy, T., Ghaban, W., Saeed, F., Nasser, M., Abdulnabi Al-Ali, Gh., A Younis, H. (2023). An Intelligent Early Flood Forecasting and Prediction Leveraging Machine and Deep Learning Algorithms with Advanced Alert System" , MDPI, Processes 2023, 11(2), 481; https://doi.org/10.3390/pr11020481.

Indra, G., Duraipandian, N, (2023). Modeling of Optimal Deep Learning Based Flood Forecasting Model Using Twitter Data", Intelligent Automation & Soft Computing. 2023, Vol. 35 Issue 2, p1455-1470. 16p.

Jiang, H., Zhang, J., Liu, Y., Li, J., Fang, J. (2023). Does flooding get worse with subsiding land? Investigating the impacts of land subsidence on flood inundation from Hurricane Harvey", Science of The Total Environment.Volume 865, 20 March 2023, 161072.

Kessabi, R., Hanchane, M., Caloiero,T .,Pellicone, G .,Addou ,R .,Krakauer ,NY,2023," Analyzing Spatial Trends of Precipitation Using Gridded Data in the Fez-Meknes Region, Morocco", Hydrology 2023, 10(2), 37; https://doi.org/10.3390/hydrology10020037.

Mangidi, U., Mandaya, I., Ngii, E.,2019," Utilization of Sentinel 1 SAR for Flood Mapping in North Konawe Regency, Southeast Sulawesi Province, Indonesia", Published under license by IOP Publishing Ltd. DOI 10.1088/1755-1315/1134/1/012019.

Ma., X, Hu, H, Ren, Y, (2023). A hybrid deep learning model based on feature capture of water level influencing factors and prediction error correction for water level prediction of cascade hydropower stations under multiple time scales", Journal of Hydrology, https://doi.org/10.1016/j.jhydrol.2022.129044.

SHAHID, SH, CHEN, X, KUMAR HAZARIKA, M, (2006). EVALUATION OF GROUNDWATER QUALITY FOR IRRIGATION IN BANGLADESH USING GEOGRAPHIC INFORMATION SYSTEM", J. Hydrol. Hydromech., 54, 2006, 1, 3–14.

Towhata,I. ,2022" Views on Recent Rainfall-Induced Slope Disasters and Floods", Springer Transactions in Civil and Environmental Engineering.

Phu La, H. Van Ngo, Q,2023," Application of Convolution Neural Network for Rapid Flood Mapping Using Sentinel-1 Imagery—A Case Study in Central Region of Vietnam", Environmental Science and Engineering book series (ESE). DOI: 10.1007/978-3-031-17808-5_26.

Karimzadeh, S., & Matsuoka, M. (2018). A Weighted Overlay Method for Liquefaction-Related Urban Damage Detection: A Case Study of the 6 September 2018 Hokkaido Eastern Iburi Earthquake, Japan. Geosciences, 8(12), 487. https://doi.org/10.3390/geosciences8120487.

Makky, N., Kaffash Charandabi, N., (2017). Surveying the landscape of Tabriz city from the point of view of tourists. National Conference of new geomatics technologies and applcation.

Seyed Mousavi, S.; M. and Akhoondzadeh. M. A QUICK SEASONAL DETECTION AND ASSESSMENT OF INTERNATIONAL SHADEGAN WETLAND WATER BODY EXTENT USING GOOGLE EARTH ENGINE CLOUD PLATFORM, ISPRS Ann. Photogramm. Remote Sens. Spatial Inf. Sci., X-4/W1-2022, 699–706, https://doi.org/10.5194/isprs-annals-X-4-W1-2022-699-2023, 2023.

Izanlou, S.; Amerian, Y.; and Seyed Mousavi, S. M. GNSS-DERIVED PRECIPITABLE WATER VAPOR MODELING USING MACHINE LEARNING METHODS, ISPRS Ann.2022. Photogramm. Remote Sens. Spatial Inf. Sci., X-4/W1-2022, 307–313, https://doi.org/10.5194/isprs-annals-X-4-W1-2022-307-2023, 2023.

6th Intercontinental Geoinformation Days

igd.mersin.edu.tr

Monitoring long term shoreline changes along Caspian Sea, Azerbaijan using geospatial techniques

Turkan Mamishova[*1]

[1]*Baku State University, Ecology and soil sciences, Ecological geography, Baku, Azerbaijan*

Keywords
Digital shoreline analysis
Remote sensing
Coastal management

Abstract

Since the Caspian Sea has no access to the ocean, its level changes cover a wide range. Thus, the change of the level affects the coastal zone and leads to a change in its geomorphological structure. In the study, the displacement dynamics of the coastline of Azerbaijan for the years 2005 and 2021 were determined using the Sentinel 2A and Landsat 7 satellite images and remote sensing data. Tasseled Cap Transformation (TCT) and different Normalized Difference Water Index, Normalized Difference Vegetation Index have been used to demarcate the shorelines. According to the established coastline, the increasing and decreasing land areas were calculated.The main objectives of the study are to demarcate the shorelines of 2005 and 2021 from the different sensor satellite images, to identify the quantitative and qualitative shoreline changes for above mentioned periods.

1. Introduction

The coastal zone is one of the most dynamic areas on Earth, with changes occurring at a wide range of time and spatial scales. Shoreline is defined as the line of contact between land and water body (Kajichang, et al. 2013). They are continuously modified by natural and human made process. This fact, makes systematic mapping of this type of regions a challenge. Coastal zones is of particular importance for the presence of availability of settlements and economic activities, most of which are related to tourism. Accurate demarcation and monitoring of shorelines necessary for understanding various coastal process. Shoreline delineation is difficult, time consuming and sometimes impossible for entire coastal system when using traditional grand survey in techniques. The coastline is not a straight line to all locations; it has many modulations and undulations because some geomorphological features are easily washed out by wave energy, like limestone. Shoreline changes resulting from natural and anthropogenic activities are interrelated. International Geographic Data Committee (IGDC) is recognized the shoreline as the one of the 27 most important features-to be mapped and monitored (Kajichang et al. 2010). The shoreline change studies help in the different application fields such as shoreline erosion monitoring, coastal zone management, flood prediction, and evaluation of water resources (Yashon et al. 2006). In this study, coastline demarcation is an important and challenging task as it forms the basis for further research such as coastline changes, forecasting and detection of vulnerabilities, etc. Understanding coastal dynamics requires a broader temporal and spatial scale approach that time-limited and localized research cannot provide. Over the past several decades, remote sensing and geographic information systems techniques have led to improvements in coastal geomorphological research. Currently, the development of remote sensing and GIS technologies has established itself as the most powerful and reliable tools for mapping coastline changes.

Tasseled Cap Transformation (TCT) and different Normalized Difference Water Index, Normalized Difference Vegetation Index have been used to demarcate the shorelines and vector change detection method has been employed to access the changes of coastal zone Caspian Sea territory of Azerbaijan by using Sentinel 2A and Landsat 7 (ETM+) sensor data (Thieler et al. 2009).

The main objectives of the study are to demarcate the shorelines of 2005 and 2021 from the different sensor satellite images, to identify the quantitative and qualitative shoreline changes for above mentioned periods.

By using these methods, the study aims to provide valuable insights into the dynamics of the coastal zone in the study area. The results of the analysis can be used to develop effective coastal management strategies and to promote the sustainable development of the coastal ecosystem.

* **Corresponding Author**

*(tukan.mamishova@gmail.com) ORCID ID 0000-0003-2729-5067

Cite this study

Mamishova T. (2023). Monitoring long term shoreline changes along Caspian Sea, Azerbaijan using geospatial techniques. Intercontinental Geoinformation Days (IGD), 6, 89-92, Baku, Azerbaijan

2. Method

In this study for to identify occur changes in the coastal zone for sixteen years was used ortho rectified and geodetic dataset of Landsat Enhanced Thematic Mapper plus (+ETM 2005) and Sentinel 2A (2021) data. Based on accessible databases, some pre-preprocessing methods were first involved for correction of atmospheric inaccuracy using dark object subtraction. Dark object subtraction (DOS) is perhaps the simplest and most widely used image based relative atmospheric correction approach for classification and change detection applications (Markhamet al. 2000). In the second stage, the process of geometric correction which is known as orthorectification was applied to the Landsat images. During this process, data is corrected according to the user's ground reference system. The Sentinel-2A product has radiometric and geometric corrections. An atmospheric correction operation was performed by applying a Sen2Cor processor to the satellite image in the SNAP software package provided by ESA (European Space Agency) (Mamishova, 2022).

2.1. Determination coastline

For extract of the shoreline, we used the Tasseled Cap Transformation method and NDVI (Normalized Difference Vegetation Index). Determining the Normalized Difference Vegetation Index (NDVI) in this technique uses a composite red band and Near Infrared (NIR) to determine the level of greenness and classification of vegetation areas. The next step uses Tasseled Cap to convert band channel into a new band set with clear interpretation for vegetation mapping, this transformation already proven fit for shoreline extraction. Tasseled cap transformation (TCT) is a usually used remote-sensing technique and has been successfully used in various remote sensing-related applications. However, the TCT coefficient set is sensor-specific, and therefore, in this article, we developed the TCT coefficients specifically for Sentinel-2 multispectral instrument at-sensor reflectance data [4]. Tasseled Cap process are using composite bands of red, green, blue, NIR, short wave infrared-1 (SWIR-1) and short wave infrared-2 (SWIR-2) to find out the level of brightness, greenness and wetness of an object.

Brightness, a measurement value for the ground; greeness, a measured value for the vegetation; wetness, a measured value for interactions of soil and canopy moisture (Figure 1) (Yamamoto and Finn, 2012).

After this analysis shoreline of the river from Samurchay to the Astarachay coastal of the Caspian Sea was extracted (Figure 1).

The extracted shoreline can provide valuable information for further analysis and management of the coastal zone. It can help to identify areas that are prone to erosion or accretion, track changes in the shoreline over time, and support the development of coastal management strategies.

Overall, the extraction of the shoreline from Samurchay to the Astarachay coastal of the Caspian Sea represents an important step in understanding the dynamics of the coastal zone in the study area. The extracted data can provide a valuable resource for researchers, policymakers, and other stakeholders interested in the sustainable management of coastal ecosystems.

Figure 1. Shoreline extraction results for 2005 to 2021

2.2. Caspian Sea level

In Caspian Sea, the minimum sea level for the past years was registered in 1977 by a ground station at -29 m. Since 1978, the sea level has risen, and in 1995 it was registered at -26.66 m and whereupon the sea level was almost stable with slight decrease. In 2016-2020, a 0.2-meter descent was observed in the Caspian Sea (Figure 3).

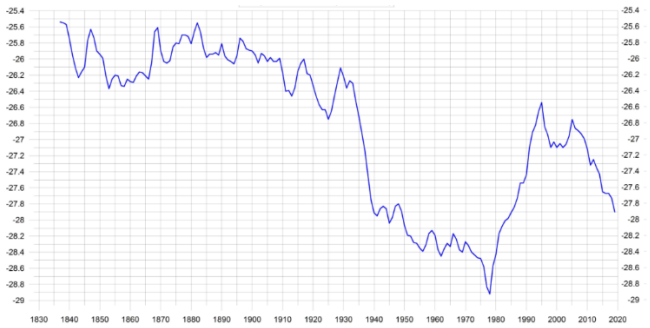

Figure 3. Sea level changes in the Caspian Sea (1837-2019)

3. Results

The Digital Shoreline Analysis System (DSAS) is a GIS-based system established by the USGS. DSAS 5.0 has six

statistical methods to measure variations. In this study, Net shore Movement (NSM) was used. NSM measuring net shoreline change according to distance rather than mean value. NSM relates to date and only two shorelines require, i.e. total distance among the earliest and the latest of coastline in each transect (Thieler et al. 2009). Where, the NSM positive and negative value shows seaward and landward movement of the coastline respectively. Baseline, historical seashores and coastlines uncertainty are input data delivered in the model for during simulation phase. The spaces among transects alongside the baseline and transects length were demarcated based on the Coastline pattern. DSAS creates transects that are cast perpendicular to the baseline at a user definite spacing along the coast. The transect coastline intersections along this baseline are then used to compute the rate of change statistics. Based on the logical conditions in DSAS, 6758 transects has been created that are oriented perpendicular to the baseline at each 100 m spacing along from river of Samurchay to the Astarachay coastline.

The results of coastline analysis show that the NSM distance positive values follow the 0,02 m between 10804 m, negative values follow (-907.54 m) between (-0.02 m). The maximum accretion distance 10804 m, maximum erosion distance -907.54 m (Figure 4).

a

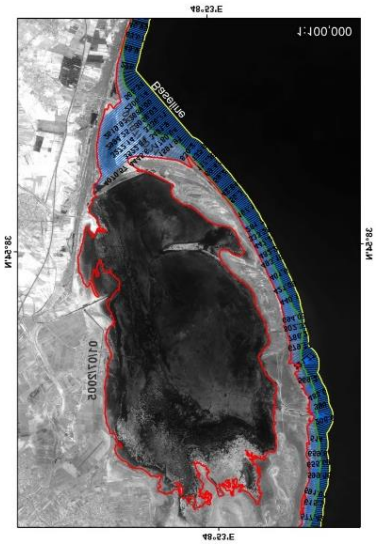

b

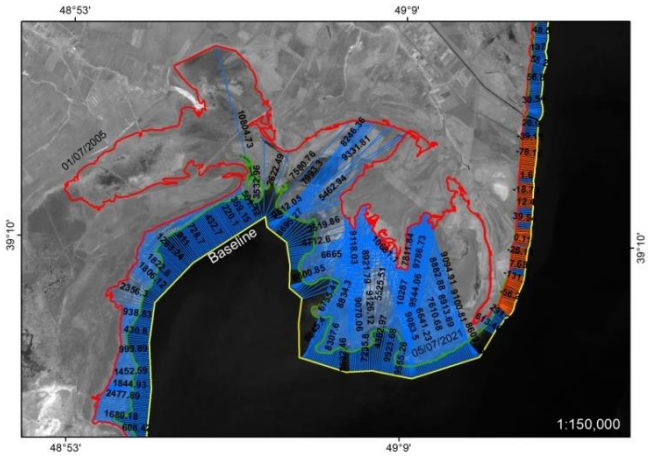

c

Figure 4. Net Shoreline Movement (NSM) Change Rate 2016 to 2021 (same areas)

The rates of shoreline position variations measured by the NSM method during this period show that the coastline is principally subjected to accretion (Figure 5).

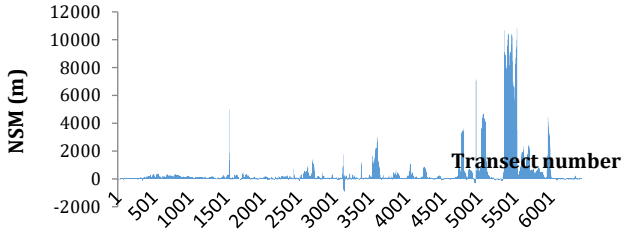

Figure 5. Net Shoreline Movement (NSM) Change Rate 2016 to 2021

4. Discussion

It is worth noting that while the overall trend indicates a net gain in the area due to accretion, there have been some losses of land due to erosion. These losses of land could have significant implications for the ecosystem of the study area, including changes in the habitat and biodiversity of the shoreline.

Therefore, it is essential to monitor and manage the coastline to. The findings of this study can provide valuable information for coastal management planning, including the implementation of measures such as beach nourishment, sediment management, and shoreline stabilization.

Overall, the results of this study provide important insights into the dynamics of the study area's shoreline and highlight the need for continued monitoring and management of the coastline to ensure its sustainability and resilience.

5. Conclusion

According to the results, in period form, 2016 to 2021 the rates of shoreline position changes indicate that all transects are accretional and less erosion was observed.

Study area shoreline is changing over time because of accretion and erosion process. However, the whole area of the coastline is almost gone through the accretion

process whereas the erosion also occurred but not like the accretion through the entire period. From 2005-2021 most of the accretion took place having 16.85473.41 sq. km of the net gain of the area although in this period coastline has lost about 0.12 31.15 sq. km of the land.

Acknowledgement

I would like to express my sincere appreciation to my supervisor, Rauf Gardashov, for their guidance, encouragement, and valuable insights throughout the research process. His expertise and constructive feedback have been instrumental in shaping the direction and scope of this study. I am grateful for the time and effort my supervisor has dedicated to this project. Their support has been essential in helping me to complete this research successfully. Thank you, Rauf Gardashov, for your invaluable contributions to this study.

References

Frazier, P. S., & Page, K. J. (2000). Water body detection and delineation with Landsat TM data. Photogrammetric engineering and remote sensing, 66(12), 1461-1468.

Kuleli, T., Guneroglu, A., Karsli, F., & Dihkan, M. (2011). Automatic detection of shoreline change on coastal Ramsar wetlands of Turkey. Ocean Engineering, 38(10), 1141-1149.

Kumaravel, S., Ramkumar, T., Gurunanam, B., Suresh, M., & Dharanirajan, K. (2013). An application of remote sensing and GIS based shoreline change studies–a case study in the Cuddalore District, East Coast of Tamilnadu, South India. International Journal of İnnovative Technology and Exploring Engineering, 2(4), 211-215.

Li, R., Di, K., & Ma, R. (2003). 3-D shoreline extraction from IKONOS satellite imagery. Marine Geodesy, 26(1-2), 107-115.

Mamishova, T. (2022). Due to the drop in the level of the Caspian Sea evaluation of the geomorphologic properties of the coastal region based on the processing of satellite images. Intercontinental Geoinformation Days, 4, 266-269.

Markham, B. L. (1986). Landsat MSS and TM post-calibration dynamic ranges, exoatmospheric reflectances and at-satellite temperatures. Landsat Technical Notes, 1, 3-8.

Ouma, Y. O., & Tateishi, R. (2006). A water index for rapid mapping of shoreline changes of five East African Rift Valley lakes: an empirical analysis using Landsat TM and ETM+ data. International Journal of Remote Sensing, 27(15), 3153-3181.

Thieler, E. R., Himmelstoss, E. A., Zichichi, J. L., & Ergul, A. (2009). The Digital Shoreline Analysis System (DSAS) version 4.0-an ArcGIS extension for calculating shoreline change (No. 2008-1278). US Geological Survey.

Yamamato, K. H., & Finn, M. P. (2012). Approximating Tasseled Cap Values to Evaluate Brightness, Greenness, and Wetness for the Advanced Land Imager (ALI). US Department of the Interior, US Geological Survey.

6th Intercontinental Geoinformation Days

igd.mersin.edu.tr

Analysis of the relationship between meteorological and agricultural drought of 2007 in Bartın province, Türkiye

Ali Levent Yagci[*1]

[1]*Gebze Technical University, Faculty of Engineering, Department of Geomatics Engineering, Kocaeli, Türkiye*

Keywords
Meteorological Drought
Agricultural Drought
SPI
VCI
NDVI

Abstract

Drought is a recurring climatic event that devastates agriculture and depletes surface and subsurface water resources. While it cannot be avoided, it can be monitored to mitigate its negative effects on economy. In recent decades, remote sensing has played a major role to track droughts from space. In this study, the 16-day composite Normalized Difference Vegetation Index (NDVI) images collected by the Moderate Resolution Imaging Spectroradiometer onboard the Terra satellite between 2000 and 2016 along with the Vegetation Condition Index (VCI) was used to monitor the drought event of 2007 in Bartın province, Türkiye. Later, the Standard Precipitation Index (SPI) was calculated using precipitation observations recorded at the meteorological station managed by the Turkish State Meteorological Service (MGM) to validate the drought findings of the VCI method. The results indicated that there was a 4-month lag of vegetation to precipitation and meteorological drought signaled by SPI led to agricultural drought indicated by VCI in 2007 in the study area.

1. Introduction

Drought is a direct result of a prolonged precipitation deficit which recurs frequently as a part of climate variability. Because the occurrence of drought can be seen with the human eye, drought indices have been developed to detect drought events.

So far, precipitation observations recorded at the meteorological stations have been heavily used to detect meteorological drought, a prolonged precipitation deficit in comparison to the historical precipitation average. The Standard Precipitation Index (SPI) is selected as a standard index to monitor meteorological drought worldwide by the World Meteorological Organization (WMO 2012). However, this method calculates a point-based estimate of meteorological drought that can not be used to estimate regional drought conditions since meteorological towers are very far away from each other.

Satellite remote sensing is a proven tool to monitor droughts from space (Deng et al. 2013). Because satellites collect spatially continuous observations over the Earth surface every day, they can be used to estimate regional drought conditions with spatially interpolating point-based drought estimates. Agricultural drought is a result of depleted soil moisture that cannot sustain healthy vegetation growth. Vegetation condition can be observed from satellites using proxy indicators such as Normalized Difference Vegetation Index (NDVI). When agricultural drought strikes, it affects vegetation health and growth relative to historical vegetation growth conditions over a region of interest. There have been many studies to track agricultural drought using remotely-sensed images (Yağcı 2018; Deng et al. 2013; Yagci 2021; Tucker and Choudhury 1987; Yagci et al. 2018; Kogan 1997). The vegetation condition index (VCI) calculated from the multi-year NDVI data has been found simple, effective and accurate to identify agricultural drought conditions over the globe (Yagci, Di, and Deng 2013; Kogan 2001; Deng et al. 2013).

In this study, the relationship between meteorological and agricultural drought is investigated by taking the drought event that took place in 2007 in Bartın Province, Türkiye as an example. The time series of SPI and VCI are compared in 2007 at the location of the meteorological tower to reveal the lagged relationship between vegetation condition and precipitation deficit.

* **Corresponding Author**

*(e-mail) ORCID ID 0000-0003-1094-9204

Cite this study

Yağcı, A. L. (2023). Analysis of the relationship between meteorological and agricultural drought of 2007 in Bartın province, Türkiye. Intercontinental Geoinformation Days (IGD), 6, 93-96, Baku, Azerbaijan

2. Data and Methods

2.1. The study area

The study area is selected as Bartın Province, Türkiye. There is a meteorological station (Station code = 17020) managed by MGM with a long record of precipitation observations spanning from 1961 to 2017. The location of the tower with respect to Bartın province are shown in Figure 1.

The study area features a temperate climate with no dry seasons and hot summer (e.g., Cfa) according to Köppen-Geiger (Beck et al., 2018). The landscape is dominated by the mixed forestland.

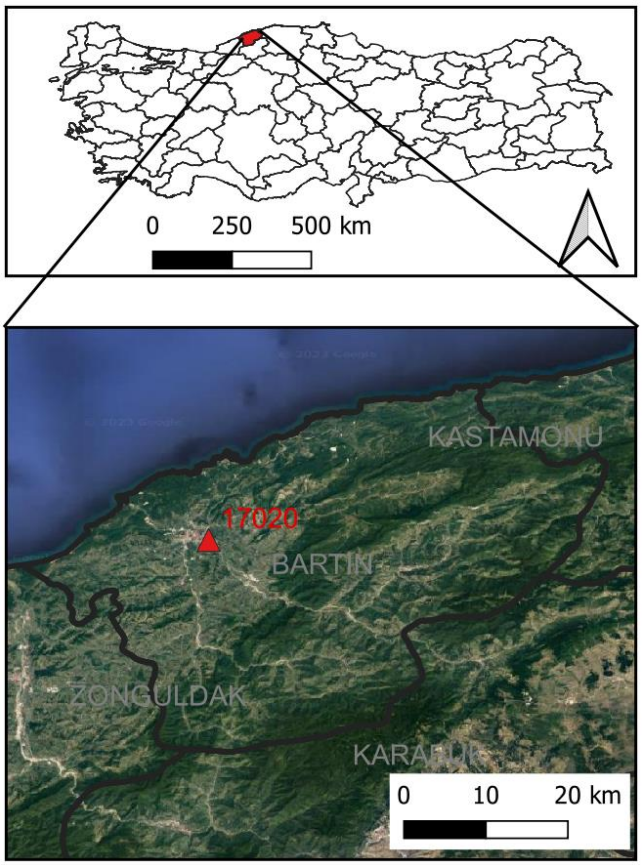

Figure 1. The location of the tower in the study area

2.2. Data

The version 6.1 Vegetation Index Products collected by the Moderate Resolution Imaging Spectroradiometer onboard the Terra satellite between 2000 and 2016 was retrieved from LP DAAC data pool website. The product name of the dataset is MOD13A2. Each granule has a NDVI and pixel reliability layer with 16-day temporal and 1-km spatial resolutions.

The pixel reliability layer holds critical quality information about each pixel in the NDVI layer (Table 1). NDVI pixels as indicated by fill/no data, snow/ice and cloudy in the pixel reliability layer were removed from the analysis. The resulting gaps were temporally interpolated from good quality observations. Later, the VCI was calculated by Equation (1) using only good quality NDVIs.

Table 1. Pixel values and their description in the pixel reliability layer of MODIS vegetation index products

Key	Summary	Description
-1	Fill/No data	Not processed
0	Good Data	Use with confidence
1	Marginal Data	Useful, check QA information
2	Snow/Ice	Target is snow or ice
3	Cloudy	Target is cloudy

Table 2. Drought classification scheme of the VCI

Range	Category
41 - 100	No drought
21 - 40	Abnormally dry
16 - 20	Moderate drought
11 - 15	Severe drought
6 - 10	Extreme drought
0 - 5	Exceptional drought

In addition to NDVI data, the monthly precipitation observations recorded at the station, 17020, were downloaded from the MGM website through the data distribution tool, MEVBIS, between 1961 and 2016.

Table 3. Drought classification scheme of the SPI (WMO 2012)

Range	Category
> 2.0	Extremely wet
1.5 to 1.99	Very wet
1.0 to 1.49	Moderately wet
0.99 to -0.99	Near normal
-1.0 to -1.49	Moderately dry
-1.5 to -1.99	Severe dry
< -2.0	Extremely dry

2.3. Methods

In this study, two drought indices were used to examine the relationship between meteorological and agricultural drought. The first index is the VCI, an agricultural drought index, whereas the other one is SPI, a meteorological drought index. The VCI highlights vegetation variation induced by annual prevailing conditions and can be calculated by the Equation 1.

$$VCI_i = 100\ x\ \frac{NDVI_i - NDVI_{min}}{NDVI_{max} - NDVI_{min}} \qquad (1)$$

where $NDVI_{ij}$ is the NDVI value at i^{th} day of year, j, while $NDVI_{max}$ and $NDVI_{min}$ are the maximum and minimum NDVI values for a given pixel between 2000 and 2016, respectively. In the final step, the drought maps were constructed from the VCI using the classification scheme given in Table 2.

The SPI is a statistical indicator of precipitation deficit normalized by the sample standard deviation on multiple timescales (e.g., 1, 2, 3 …, 12 months). Before transformation to a normal distribution, long-term precipitation records collected at the tower between 1961 and 2016 are fitted to a 3 parameter pearson probability distribution. Then, the SPI can be calculated by the Equation 2.

$$SPI_{ij} = 100\ x\ \frac{P_{ij} - \bar{P}_i}{s_i} \qquad (2)$$

where P_{ij} precipitation value at i^{th} month j year, while $\bar{P}_{ij}$ and s_{ij} mean and standard deviation of long-time precipitation records at i^{th} month, respectively. Later, SPI values were categorized by the classification scheme given in Table 3.

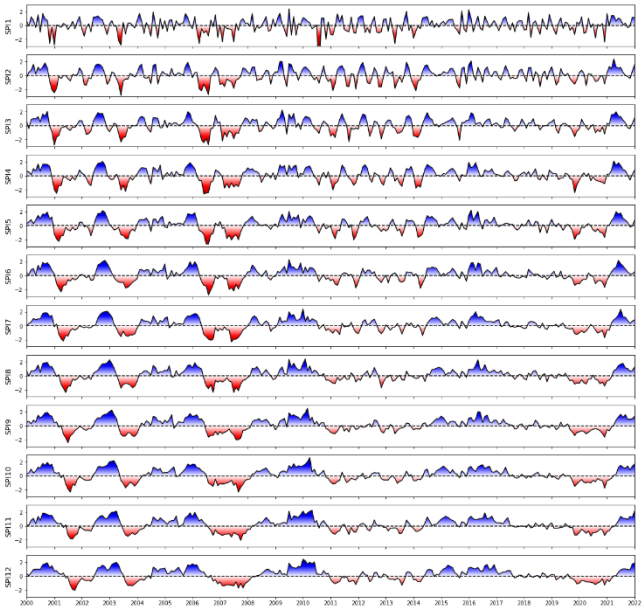

Figure 2. The time series of SPI on multiple timescales from 1-month to 12-month between 2000 and 2016.

3. Results

In the first step, the drought years at the station was found based on the SPI time series analysis given in Figure 2. The 12-month SPI (SPI-12) indicated that the most severe drought occurred from winter 2006 until the end of winter of 2008. In other words, the year 2007, was the month when the drought hit the study area hard. The second severe drought started in the winter of 2019 and continued until the spring season in 2021. Furthermore, the other notable drought events took place in the summer-fall season of 2001 and the fall-winter season 2013.

The frequency of changes in the 1-month SPI (SPI-1) was high and impacted by monthly rainfall. The time series of SPI-12 varied slowly in comparison to other SPI on time scales less than 12-month. It is more suitable to determine drought events using SPI with long-timescales (>4 months) .

The correlation analysis was conducted between VCI and all SPIs in the 2007 drought year (Figure 3). The VCI was highly correlated with 4-month SPI (SPI-4). This implies that there was a 4-month lag between vegetation and meteorological drought. The second highest correlation was observed between VCI and 6-month SPI (SPI-6). The lowest correlation coefficient values were seen between VCI and SPI-11, and VCI-SPI-1. This demonstrated that the short-term rainfall deficit does not impact the vegetation growth.

The time series of SPI-4, SPI-6 and VCI was plotted together for visual analysis of the 2007 drought event (Figure 4). SPI-4 showed that the drought started in April 2007 and ended in October 2007, while SPI-6 indicated the onset of drought was May 2007 and the drought event continued until October 2007. On the other hand, VCI was more in line with SPI-4, indicating that drought event occurred between April and October of 2007.

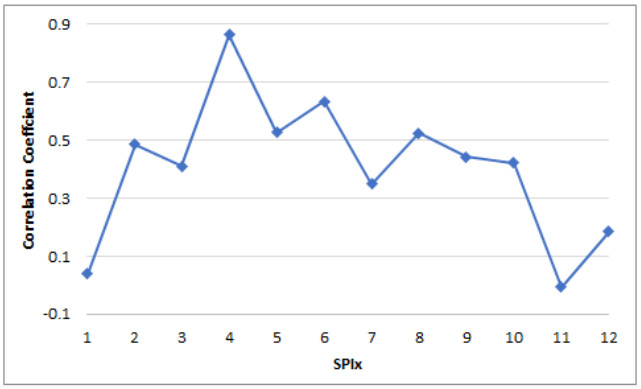

Figure 3. Correlation coefficient (r) values between VCI and SPI1-SPI12 in 2007

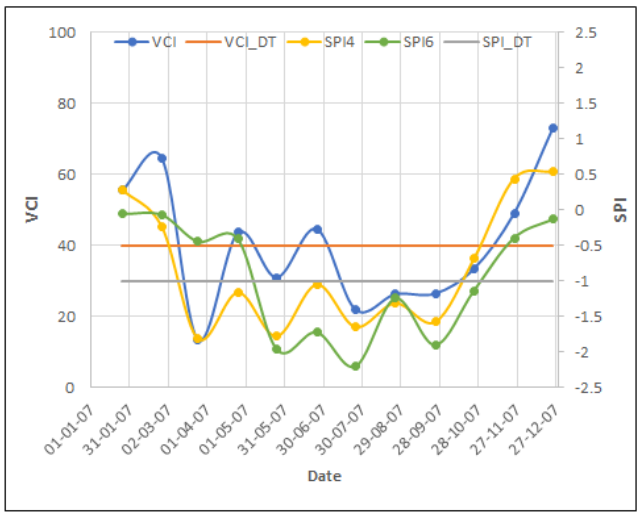

Figure 4. Comparison of VCI and SPI4-SPI-12 in 2007. VCI-DT and SPI-DT are the drought thresholds, respectively

4. Conclusion

In this study, a relationship between meteorological and agricultural drought was examined in the 2007 drought event. VCI is employed to track agricultural drought as whereas the SPI was the indicator of meteorological drought. During the study period (2000-2017), Bartın province experienced the most severe drought in 2007.

In the study area, 4 months lag was found between precipitation deficit and vegetation stress. In other words, vegetation in this area can sustain 4 months long rainfall deficit. Overall, agricultural drought can develop in this region after more than 4 months long meteorological droughts.

Acknowledgement

Author would like to thank MGM for distributing the meteorological observations collected at the station, 17020 at no cost to researchers.

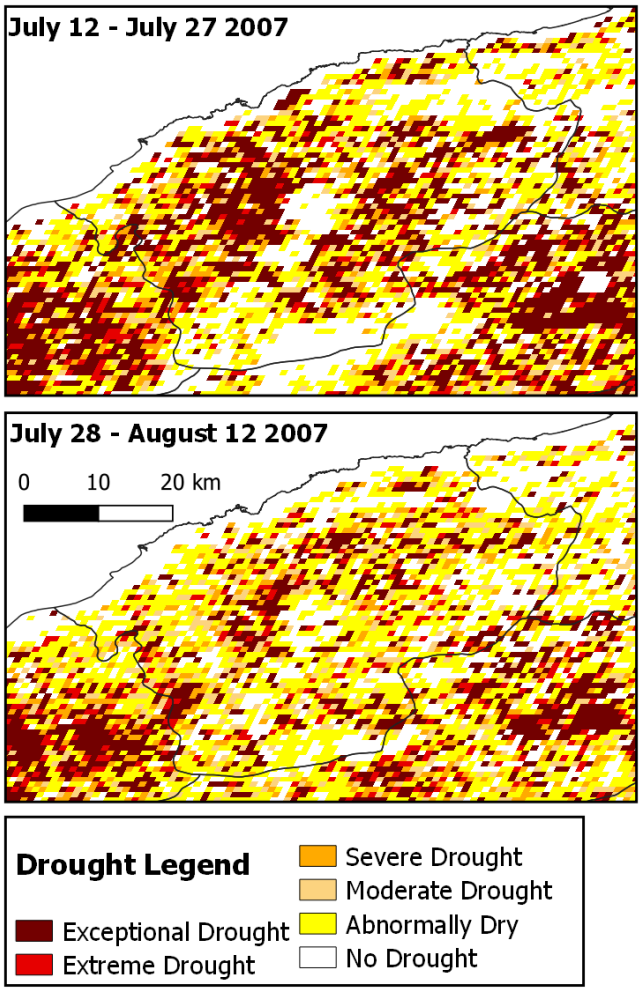

Figure 5. VCI-based drought maps between July 12 and July 27, 2007 (above) and July 28 and August 12, 2007 (below) for Bartın Province

References

Beck, H. E., Zimmermann, N. E., McVicar, T. R., Vergopolan, N., Berg, A., & Wood, E. F. (2018). Present and future Köppen-Geiger climate classification maps at 1-km resolution. Scientific data, 5(1), 1-12.

Deng, M., Di, L., Han, W., Yagci, A. L., Peng, C., & Heo, G. (2013). Web-service-based monitoring and analysis of global agricultural drought. Photogrammetric Engineering & Remote Sensing, 79(10), 929-943.

Kogan, F. N. (1997). Global drought watch from space. Bulletin of the American Meteorological Society, 78(4), 621-636.

Kogan, F. N. (2001). Operational space technology for global vegetation assessment. Bulletin of the American meteorological society, 82(9), 1949-1964.

Tucker, C. J., & Choudhury, B. J. (1987). Satellite remote sensing of drought conditions. Remote sensing of Environment, 23(2), 243-251.

WMO. (2012). Standardized Precipitation Index User Guide. WMO, No. 1090. Geneva: World Meteorological Organization. http://www.wamis.org/agm/pubs/SPI/WMO_1090_EN.pdf.

Yagci, A. L. (2021). Fully automated drought analysis from the products of the moderate resolution imaging spectroradiometer (MODIS). Intercontinental Geoinformation Days, 3, 105-108.

Yagci, A. L., Di, L., & Deng, M. (2013). The effect of land-cover change on vegetation greenness-based satellite agricultural drought indicators: a case study in the southwest climate division of Indiana, USA. International journal of remote sensing, 34(20), 6947-6968.

Yagci, A. L., Santanello, J. A., Rodell, M., Deng, M., & Di, L. (2017). Detecting the 2012 Drought in the Southeastern United States with Moderate Resolution Imaging Spectroradiometer-and Gravity Recovery and Climate Experiment-Based Drought Indicators. In Remote Sensing of Hydrometeorological Hazards (pp. 85-101). CRC Press.

Yağcı, A. L. (2018). Uzaktan Algılama Görüntülerinden Tarimsal Kuraklığın Belirlenmesi. Uzaktan Algılama ve Coğrafi Bilgi Sistemleri Sempozyumu (UZAL-CBS). Eskişehir, Turkey: Eskişehir Teknik Üniversitesi.

6th Intercontinental Geoinformation Days

igd.mersin.edu.tr

Change detection of buildings using high spatial resolution images and deep learning

Saeid Abdolian[1], Ali Esmaeily[1], Mohammad Reza Saradjian*[2]

[1] *Graduate University of Advanced Technology, Faculty of New Sciences and Technologies, Kerman, Iran*
[2] *University of Tehran, College of Engineering, School of Surveying and Geospatial Engineering, Tehran, Iran*

Keywords
Change detection
Deep learning
Relevant training dataset
Buildings
Newly constructed areas

Abstract

The main aim of this study is to detect changes in buildings. The data required to achieve this goal are high spatial resolution images and the method used to achieve the goal is the use of a deep neural network and a new relevant dataset. In this research, the training and testing of a deep neural network is investigated to detect changes in buildings such that the accuracy is improved. The deep learning networks have not been previously used in industrial areas that have different characteristics such as building structures, building construction methods, materials and color variety of the roofs of the buildings. In this research, it is assumed that the development of networks alone does not improve the accuracy of the results considerably, but the training of previously developed networks with the relevant training dataset greatly increases the accuracy. Accordingly, a training dataset to detect the changes in the buildings of industrial areas have been produced to train an already developed deep learning network with the relevant data to detect the change in buildings. As a result, the trained network with relevant data was tested, and reasonable average accuracy and recall achieved.

1. Introduction

Deep neural networks, which use multiple layers between the input and output layers, have been widely used by providing solutions in solving problems that were very complex previously. Hinton and Salakhutdinov in 2006 applied deep learning to data processing and showed that the depth of the artificial neural network can be very effective in the learning ability of the network (Hinton and Salakhutdinov, 2006). Optimal features can be directly extracted from raw data by deep learning methods and the network can reach maximum accuracy in many applications such as building change detection.

2. Study area

The study area is two industrial parks named Mobarakeh Industrial Park in Mobarakeh City and Shamsabad Industrial Park in Rey City in Iran. Mobarakeh Industrial Park is located on the Isfahan-Shiraz Road and 28 km away from Mobarakeh city. It is located between 51.71° to 51.75° East longitude and 32.40° to 32.44° North latitude. Shamsabad Industrial Park is located in the south of Tehran province in Rey city. Shamsabad Industrial Park is the largest industrial park in Iran with an area of over 3 thousand hectares. The location of Shamsabad Industrial Park is at 45 km of Tehran-Qom highway, in the district of Hassanabad city. Shamsabad Industrial Park is located between 51.18° to 51.29° East longitude and 35.30 to 35.38° North latitude.

3. The Data

In order to collect training dataset, satellite images from the two industrial parks were downloaded through Google Earth Pro software (Figure 1). When downloading Google Earth images, the specification of the images is selected by image dimensions and scale. The images in this study were divided into three groups, each group containing two time series images. Two groups were used as network training and one group as network testing. Also, the test dataset is selected from another part of Shamsabad Industrial Park. Details of images including date, dimensions, and loading scale are provided in Table 1.

Due to the lack of internal training datasets, an external dataset selection has been used in the training process. The LEVIR-CD dataset is a new large-scale remote sensing binary structural change detection dataset that helps develop new deep learning-based algorithms for change detection in remote sensing images. The introduced dataset is a new benchmark for evaluating change detection algorithms, especially deep learning-based algorithms.

* **Corresponding Author**

*(sarajian@ut.ac.ir) ORCID ID 0000 – 0002 – 1734 – 5860
(aliesmaeily@hotmail.com) ORCID ID 0000 – 0002 – 5463 – 5613
(saeid.abdolian.rs@gmail.com) ORCID ID xxxx – xxxx – xxxx – xxxx

Cite this study

Abdolian, S., Esmaeily, A., & Saradjian, M. R. (2023). Change detection of buildings using high spatial resolution images and deep learning. Intercontinental Geoinformation Days (IGD), 6, 97-100, Baku, Azerbaijan

Figure 1. The study area: top) Shamsabad Industrial Park (green box, training area and yellow box, test area), bottom) Mobarakeh Industrial Park (green box, training area).

Table 1. Images used as a training set

Location	Image date	Image dimensions
Shamsabad Industrial Park	2005/03/09 2017/03/13	2086 × 4195
Shamsabad Industrial Park	2002/05/05 2017/03/31	2071 × 4739

The LEVIR-CD set consists of 637 pairs of very high resolution (0.5 m/pixel) image segments with a size of 1024 × 1024 pixels. These two-time images with a period of 5 to 14 years have significant land use changes, especially the growth of constructions. LEVIR-CD covers different types of buildings such as villas, high-rise buildings, garages and warehouses. In this collection, an attempt has been made to focus on building-related changes, including change from soil/vegetation/built-up land or building under construction to new construction areas, and also building decline. These two-time images are labeled by remote sensing image interpretation experts using binary labels (i.e., 1 for change and 0 for no-change). LEVIR-CD contains 31,333 examples of change building. Using this dataset, it was tried to create a separate dataset for large warehouses and create a new dataset. This new dataset, which contains 522 images in dimensions of 256 × 256, was added to internal dataset to increase the volume of training data.

4. Method

Change detection in Shamsabad Industrial Park was done by STANet (Spatial-Temporal Attention-based neural network). This network consists of convolutional deep learning algorithm (CNN) (Shen et al. 2019), advanced ResNet *(He et al. 2016)* model and combination of several modules in order to improve the training process. In other networks, two-time images are normally coded separately, while in this network, a self-attention change detection mechanism is designed. This module makes full use of the spatio-temporal relationship to obtain features. By doing this, the examination of pixels that have become challenging in terms of brightness and misregistration have also been improved to some extent.

The STANet (Zhou et al. 2022) network consists of three general parts: 1) Basic feature extractor by ResNet architecture with FCN (Sun et al. 2020) algorithm based on transfer learning approach, 2) Extraction of more distinct and accurate features by PAM (Pyramid spatial-temporal Attention Module) (Chen and Shi 2020), and 3) Check changes by metric module.

5. Implementation

In order to implement and analyze the results, the training dataset for the detection of construction changes produced from Shamsabad and Mobarakeh industrial parks were used to train the STANet network. After the training of STANet network, a part of Shamsabad Industrial Park was tested by this network. First, data preparation, then network training and hyperparameter estimation were done. Then the network was tested and the test results were presented along with their performance analysis. At the end, the test output was validated and a more detailed change representation was provided. Data preparation consists of three parts, geometric corrections, change label generation, and image patches generation.

First, geometrical corrections were made. Then, the change label was generated to train the network and validate the experiment. The actual land change image, which is a binary image, is a change map or label, where the white color represents the areas of change and the black color represents the areas of no change. By visually comparing the time series images, the pixels of newly built buildings were changed to white and other areas of the image were changed to black. In this research, in order to train the STANet network, a change map was produced from the two industrial parks. After training the STANet network, it is necessary to test the network. For this purpose, a part of Shamsabad Industrial Park was tested by this network. Then, in order to validate the test from this region, the change label of this region was used and the validation criteria were applied.

In order to train and test the STANet network, input images with specific dimensions should be input to the network. These dimensions may be set to 32, 64, 128, 256, 512 and 1024 pixels. In dimensions smaller than 32 pixels, the amount of information for analysis is too little. Dimensions larger than 1024 pixels slow down the processing speed. The smaller the size, the less RAM is used for processing which increases the processing speed and vice versa. The dimensions of the images downloaded from Google Earth are larger than the dimensions defined in the grid input because they were taken from the entire area. Therefore, the original images

were divided into smaller patches. The dimensions of 256 × 256 were appropriate in terms of the amount of RAM used for processing speed and the amount of information for network analysis.

The STANet network was trained in two stages, and tested in three stages according to Figure (2). First, the STANet network which was trained by the LEVIR-CD dataset, was tested for the internal region to determine the capability of the network as well as the capability of the LEVIR-CD training dataset. In the following, first dataset of Mobarakeh Industrial Park, which contains 117 images of 256 × 256 pixels was combined with a selection of warehouse changes of the LEVIR-CD dataset. Then, the STANet network was trained using the combination of this dataset, and a part of Shamsabad Industrial Park was tested. Then, the second training dataset of Shamsabad Industrial Park which contains 128 images with dimensions of 256 × 256 pixels, were added to this dataset. By combining these three datasets, a more appropriate dataset was obtained. In the last step, the STANet network was trained again using the combination of this newly formed dataset. The same part of Shamsabad Industrial Park was tested again. As a result, the importance of adding internal training data was revealed.

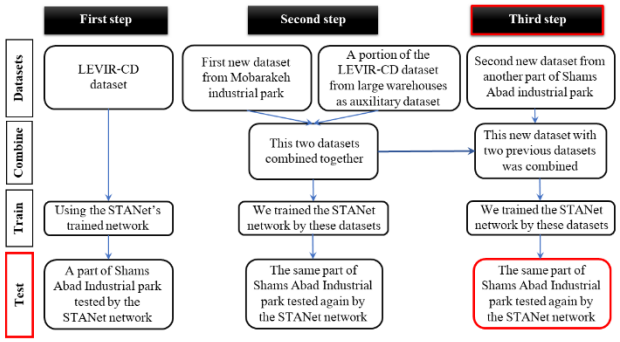

Figure 2. Research stages in which, in the first stage, only the network trained using the external region was tested for the internal region and in the second and third stages, the network was trained and tested with the addition of new datasets of the internal regions.

5.1. Tools and processing environment

The programming code in this research was written in Python language. Python as an object-oriented and high-level programming language has many applications in various fields of data science, machine learning, deep learning, data mining, etc. The code was implemented in the Google Colab environment with free GPU (graphic processing units) which makes it possible to run heavy computer programs at a very high speed. The STANet network was implemented by two main libraries in deep learning. Pytorch library was used for vector calculations through GPU and deep neural network construction based on autodiff system. The second library was Torchvision library which was used to detect the edges of buildings in the image.

5.1.1. Network training

Network training was done in two stages. First, the setting of the algorithm and hyperparameters for the purpose of training and then the training steps were performed.

Choosing the right optimization algorithm for the deep learning model is very important and has a great impact on the time to reach the desired result. In this network, the Adam's optimization algorithm was used. This algorithm is a method that adjusts the learning rate during the training process. Adam's optimization algorithm is a generalized version of the stochastic gradient descent (SGD) algorithm, which has recently been widely used for deep learning applications in the field of computer vision. In the following, the hyperparameters set in the training process are explained.

In order to increase the amount of data and enrich (i.e. augmentation) the training dataset, the network creates a set of data different from the existing data by rotating and cropping the images. In this way, the amount of data increases and leads to an increase in accuracy. In the learning phase, the rotation rate was applied as a random rotation (-15° to 15°).

The whole training process was set to 200 epochs. The entire dataset was trained in each epoch and the training accuracy was validated by a series of training data. In each epoch compared to the previous epoch, the training process got better by resetting the new learning parameters.

The learning rate controls how much the model changes in response to the estimation error each time the model weights are updated. Determining learning rate is considered as a hyperparameter. If the learning rate is chosen low, the algorithm may get stuck in local minima. If a large training rate is selected, the network may reach an unstable state. The learning rate in this network was set to 0.001 for the first 100 epochs and then it was set to zero in the next 100 epochs with a linear decrease.

In stage 1 training, the first dataset was selected for training from an industrial park that has examples of change and no-change in proportion. The network was trained for both the changed buildings and the buildings that had a color difference in the two images as the no-change. Due to the lack of training data produced inside the country, the LEVIR-CD dataset was also used in the training process and a selection of large warehouses in this dataset was extracted and integrated with the internal training dataset. The learning process of the network in the first stage in 200 epochs is presented in four diagrams in Figure 3.

Stages 2 and 3 of training are combined here. In order to increase the internal training dataset, a second internal training dataset was also produced. This dataset was a part of Shamsabad Industrial Park. In the second and third stages of training, network training was performed by combining two internal training datasets (i.e. first and second datasets) and a selection of large buildings and warehouses (i.e. LEVIR-CD dataset). The training process of the network in these stages in 200 epochs is presented in four diagrams in Figure 4.

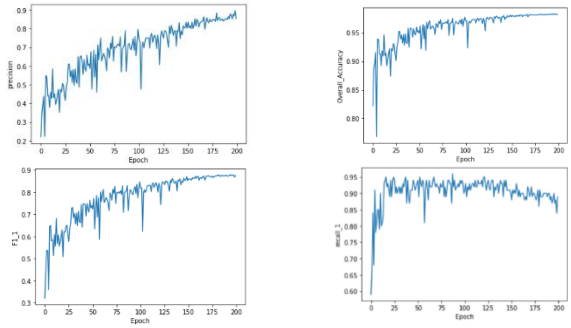

Figure 3. Four evaluation criteria of the training process of stage 1 in 200 epochs: the top-left graph shows the accuracy criterion, the top-right graph is the precision criterion, the bottom-left graph is the F1 criterion, and the bottom-right graph is the recall criterion.

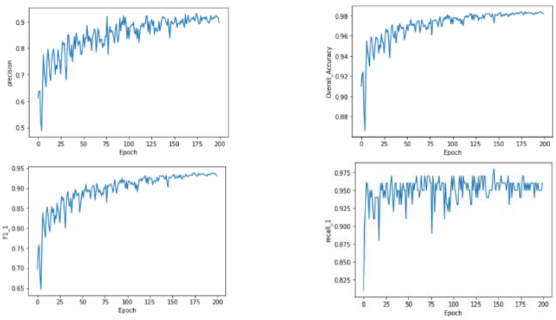

Figure 4. Four evaluation criteria of the training process of stages 2 and 3 in 200 epochs: the top-left graph shows the accuracy criterion, the top-right graph is the precision criterion, the bottom-left graph is the F1 criterion, and the bottom-right graph is the recall criterion.

5.1.2. Network testing

To carry out the test phase, after training the network, ready weights were generated so that during the test, only by introducing these weights, the test processed at a very high speed. The algorithm processed the data after installing the necessary libraries with the prepared weights obtained in the training stage. As a result, the binary image of the changes was produced as a prediction. The test phase was performed in three stages. In the third stage test, the network was trained by combining the two previous training datasets and the second internal training dataset (Shamsabad Industrial Park). The test was again performed on Shamsabad Industrial Park and reached a much better result than the previous two tests. The results showed that with the increase of the internal training dataset, the results continued to increase with great accuracy. Figure 5 shows the total result of change detection obtained from Shamsabad Industrial Park by STANet network. The first, second and third rows show the first, second and third stages of predicted changes, respectively. The left column shows the predicted change and no-change and the right column shows the correctness of the predicted change and no-change. In the left column, the white color is the change and the black color is no-change. In the right column, the white color is the obtained change, the blue color is the unpredicted change, and the red color is no-change that were classified as change mistakenly.

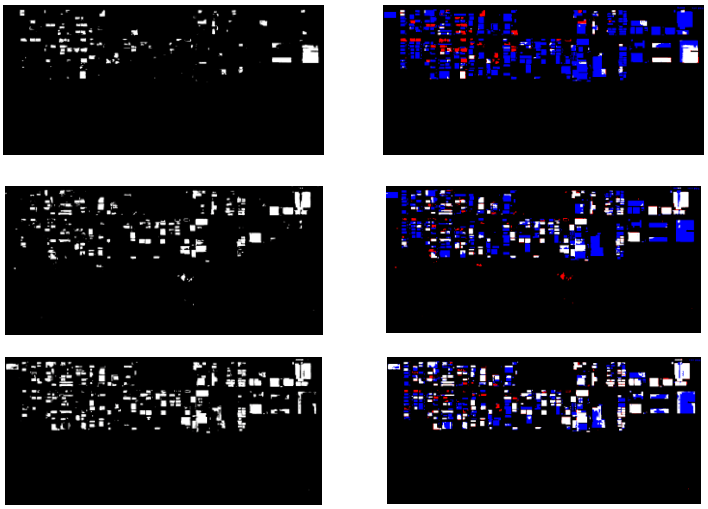

Figure 5. The total result of change detection obtained from Shamsabad Industrial Park by STANet network.

6. Conclusion

As mentioned, the result of prediction in the first stage was not accurate. In the second stage of the test, the average accuracy was 52% and the recall was 37% due to the training of the network by combining two datasets of internal and external training. The first training dataset were selected in such a way that the ratio of change and no-change was the same so that the network pays enough attention to both modes during learning. In this phase of testing, the network error was reduced. Next, the network was trained with more internal data. As a result, in the last stage of the test, the average accuracy was 69% and the recall was 57%. In addition, it was shown in this study that development of networks alone does not improve the accuracy of the results considerably, but the training of previously developed networks with the relevant training dataset greatly increases the accuracy.

References

Chen, H., & Shi, Z. (2020). A spatial-temporal attention-based method and a new dataset for remote sensing image change detection. Remote Sensing, 12(10), 1662.

He, K., Zhang, X., Ren, S., & Sun, J. (2016). Deep residual learning for image recognition. In Proceedings of the IEEE conference on computer vision and pattern recognition (pp. 770-778).

Hinton, G. E., & Salakhutdinov, R. R. (2006). Reducing the dimensionality of data with neural networks. science, 313(5786), 504-507.

Zhou, S., Dong, Z., & Wang, G. (2022). Machine-learning-based change detection of newly constructed areas from GF-2 imagery in Nanjing, China. Remote Sensing, 14(12), 2874.

Sun, Y., Zhang, X., Huang, J., Wang, H., & Xin, Q. (2020). Fine-grained building change detection from very high-spatial-resolution remote sensing images based on deep multitask learning. IEEE Geoscience and Remote Sensing Letters, 19, 1-5.

6th Intercontinental Geoinformation Days

igd.mersin.edu.tr

Monitoring ground displacement of Warri metropolis using persistent scatterer interferometry (PSI) and small baseline subset (SBAS) time series

Oluibukun Gbenga Ajayi*[1,2], Bilyaminu Yusuf [2], Yusuf Drisu Opaluwa[2]

[1]*Namibia University of Science and Technology, Faculty of Engineering and the Built Environment, Department of Land and Spatial Sciences, Windhoek, Namibia*
[2]*Federal University of Technology, Minna, School of Environmental Technology, Department of Surveying and Geoinformatics, Minna, Nigeria*

Keywords
PSI
Small Baseline subset
Ground displacement
Ground subsidence
InSAR

Abstract

Ground subsidence is a major challenge faced by many cities worldwide, with infrastructure damage costing billions annually. This study aims to retrieve the subsidence of Warri, a coastal city in Southern Nigeria, using interferometry synthetic aperture radar (InSAR). Persistent Scatterer Interferometry (PSI) and Small Baseline Subset (SBAS) methods were used for the retrieval of the subsidence in the city. Results obtained show that Warri experiences subsidence, with PSI revealing a displacement of -0.5 to 1.5 mm/year, and SBAS showing 0.33 to 0.65 cm/year. The standard deviation for PSI ranges between 0.7 and 7.8 mm/year, and 0.2 to 1 cm/year for SBAS. Our study highlights the exceptional capabilities of InSAR in effectively and precisely monitoring subsidence across extensive urban regions, achieving remarkable accuracy down to millimetre scale.

1. Introduction

Urban growth often leads to increased infrastructure development, such as roads, highways, bridges, railways, buildings, and groundwater extraction. However, these developments can also lead to ground subsidence, which is a phenomenon that affects many cities around the world. Ground subsidence can be caused by a variety of factors, including earthquakes, landslides (Abraham, 2021), excessive groundwater extraction (Muhammad et al., 2016b), mining and construction, volcanic activity, and oil and gas exploration (Muhammad et al., 2016b).

Subsidence has the potential to cause damages to infrastructure, such as roads, highways, buildings, railways, and communication masts. It can also be a threat to human existence and lead to economic loss with high maintenance costs (Chen et al., 2012). Therefore, it is important for city planners to measure and monitor ground displacement.

Conventionally, geodetic surveying, levelling measurement, and Global Navigation Satellite System (GNSS) were used to measure displacement at very precise accuracy up to millimetre level but only small area can be covered in a short time. For large areas, the method is costly and time consuming (Chen et al., 2020; Nam et al., 2020), hence the need to explore other alternative approaches. Interferometry Synthetic Aperture Radar (InSAR) is a remote sensing method that is used in the monitoring of ground displacement. It involves the use of Synthetic Aperture Radar (SAR) images obtained through satellite at different time over the same area to study the ground deformation and displacement taking place (Abraham, 2021) over regions of interest. InSAR have demonstrated over time to be an efficient and valuable geohazard risk analysis method that is based on multiple radar images and has played an important role in recent years as a cost-effective and alternative method to geological and geotechnical investigations (Alesssandro et al., 2017).

Persistent Scatterer Interferometry (PSI) and Small Baseline Subset (SBAS) are powerful remote sensing techniques based on multi-temporal images and time series used to study the displacement of the ground surface. PSI as the name implies, is based on Permanent Scatterer (PS) while Small BAseline Subset is based on Distributed Scatterer (DS). They were developed to solve the problem of geometric decorrelation, temporal deorrelation and atmospheric delay encountered by Differential Interferometry Synthetic Aperture Radar (DInSAR).

In this study, we aimed at depicting the ground displacement of Warri, Delta State, Nigeria using PSI and SBAS.

* **Corresponding Author**

*(ogbajayi@gmail.com) ORCID ID 0000-0002-9467-3569
(yusufbilyaminu72@gmail.com) ORCID ID 0009-0003-9345-7658
(opaluwayd@futminna.edu.ng) ORCID ID 0000-0002-6897-1714

Cite this study

Ajayi, O. G, Yusuf, B., & Opaluwa, Y. D. (2023). Monitoring of ground displacement of Warri metropolis using persistent scatterer interferometry (PSI) and small baseline subset (SBAS) time series. Intercontinental Geoinformation Days (IGD), 6, 101-104, Baku, Azerbaijan

2. Method

This study used 17 Sentinel-1A images acquired in IW mode over a period of 13 months from 15 May 2019 to 31 July 2020. A time series analysis was performed using interferograms generated from co-registered stack images. The phase difference of each interferogram reflected the influence of various factors such as topography, atmospheric phase, displacement phase, orbital and noise phase. To eliminate the topography artefact, a digital elevation model (DEM) was used.

Two methods were used to build the stack of interferograms: single master used by PSI and multiple master was used for SBAS. Various techniques have been used to perform the analysis of small base line (SBAS) and PSI. PSI determines phase changes by examining permanent and dominant scatterer (persistent scatterer) while the SBAS approach measures surface displacement associated with homogenously distributed scatterers which results in improved spatial coverage (Fabio et al., 2020; Osmanoglu et al., 2016).

2.1. Persistent scatterer interferometry (PSI)

The Stanford Method for Persistent Scatterer (StaMPS) was used in this study. The preprocessing was done using snap to stamps developed by Jose et al. (2019) which can be retrieved on the GitHub repository (https://github.com/mdelgadoblasco/snap2stamps).

The processing framework is subdivided into two main steps: preprocessing and postprocessing, and the summary of the processing steps are as follows;

Preprocessing

i. Master selection and splitting: The InSAR overview stack feature within SNAP was used to choose the primary (master) image. After the selection, TopSAR split was used for the subsetting.
ii. Slave splitting: Here, the specific subswath and burst that covered the desired region of interest were selected while also applying the precise orbit file. The precise orbit is automatically downloaded approximately 20 days after acquisition.
iii. Coregistration and interferogram generation: The auxiliary file (Digital Elevation Model) was subset using a bounding box to extract the desired area of interest while also saving the amplitude coregistered master, the slaves stack, and the interferograms with autorectified coordinate (latitude and longitude) and elevation as output.
iv. Export: This include the export of master-slave pair that is coregistered, along with its corresponding interferograms incorporating elevation and autorectified coordinate band.

Postprocessing

i. Data loading: The data was converted to a format compatible with PSI and saved in MATLAB workplace.
ii. Estimate phase noise: Here, the phase noise in each pixel candidate in every interferograms was estimated.
iii. PS selection: The PS were selected considering their noise properties while also estimating the proportion of random element (non-PS).
iv. PS weeding: Noisy PS selected in step 3 were eliminated and discarded and those that resulted from signals contributed by nearby ground resolution elements were removed.
v. Phase correction: In this step, the correction for wrapped phase due to DEM error was performed.
vi. Phase unwrapping: Phase unwrapping has the ability to resolve the ambiguity of modulus of 2π and obtain the absolute change of phase. It is always recommended to re-run steps 6 and 7 in order to determine the spatially correlated look angle and master atmosphere while compensating for the orbit error prior to the unwrapping process.
vii. Spatially correlated look angle error estimation: This error arises from spatially correlated DEM (this includes error within the DEM and incorrect mapping of the DEM into radar coordinate). Also, the estimation of both master atmosphere and orbit error phase occurs simultaneously.
viii. Atmospheric filtering: After the StaMPS processing in MATLAB, the linear-based correction in TRAIN is applied. At this stage, a specific reference area is chosen and an average velocity usually derive from GNSS data is introduced. By default, StaMPS utilizes the entire extent as the referenced area. In this study, we opted for the default mode due to lack of GNSS data at the time of processing.

2.2. Small baseline subset (SBAS)

This study used Mintpy incorporated in OpenSARLap, a cloud-based system for processing of synthetic aperture radar (SAR) workflows. First, interferograms of the imagery were generated using the OnDemand platform on the Alaska Satellite Facility (ASF) website.

To prepare the data, the HyP3 InSAR Stack for Mintpy was used. In this phase, the data were added and checked for the presence of DEM, incident angle map, and azimuth angle map. The area of interest was also subset and areas of no interest were removed. Finally, post-processing using Mintpy Time-series for processing of small baseline subset was carried out.

Interferometry Synthetic Aperture Radar (InSAR) time series analysis using Mintpy and HpP3 products based on the Losangeles_timeseies notebook by Yunjun et al. (2019) was used for the processing of small baseline subset.

3. Results

The PSI displacement map is presented in Figure 1 while the PSI time series of Warri metropolis is presented in Figure 3. An average subsidence of -13.9 to 13.4 mm/year and standard deviation of 0.7 to 7.8 mm/year was observed for the period of observation for

PSI, with the riverine and rural areas having the highest standard deviation which can be attributed to insignificant or complete absence of PS.

For SBAS (see Figure 2), an average of -6 to 2 cm/year was observed having a standard deviation of 0.2 to 1 cm/year.

In the metropolis, a subsidence of -0.5 to 1.5 mm/year for PSI and 0.65 to 0.33 cm/year for SBAS was obtained. In both PSI and SBAS, we observed a negative deformation in the metropolis which suggests the presence of subsidence.

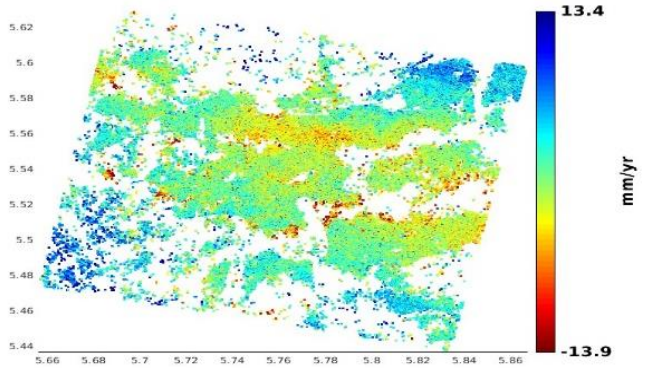

Figure 1. PSI Displacement map. Northing represent y-axis and Easting x-axis

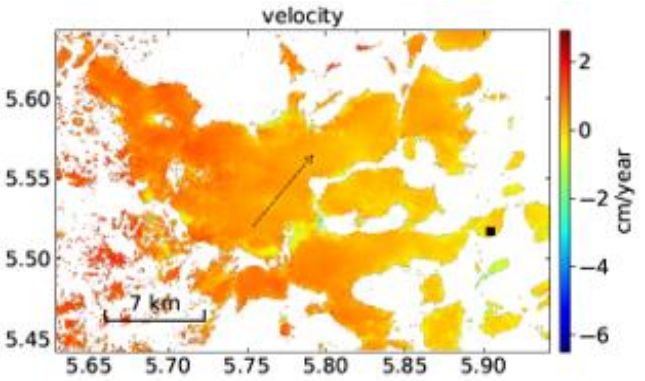

Figure 2. SBAS Displacement map overlayed on google earth image. Northing represent y-axis and Easting x-axis

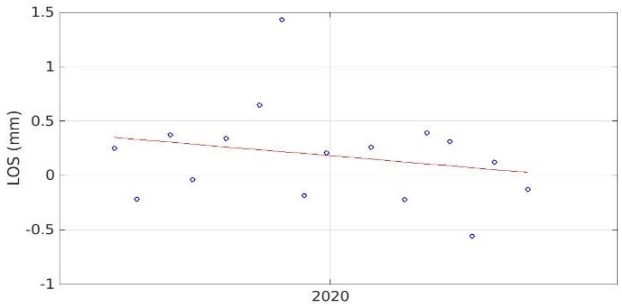

Figure 3. PSI Time series of the metropolis

4. Discussion

The ground displacement of Warri has been analysed using two different methods; Persistent Scatterer Interferometry (PSI) and Small Baseline Subset (SBAS). Results obtained from both methods showed negative deformation in the metropolis. Figure 1 shows PSI average annual displacement. From the Figure 4, it was observed that the average annual velocity obtained for the PSI method was between -13.9 mm/year to 13.4 mm/year. Also, some positive deformation (uplift) upward toward North east of Warri and downside of the area was observed. Figure 3 shows the deformation pattern in the urban centre which suggests that a deformation of -1 to 1.5 is inherent in the metropolis.

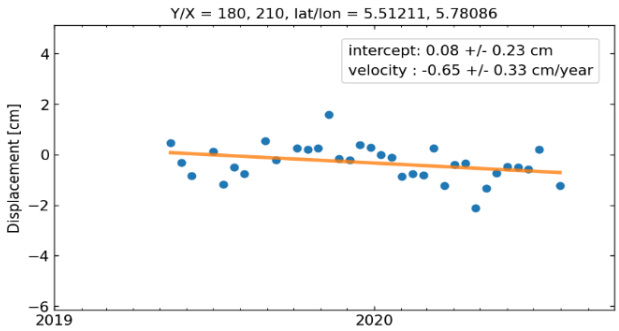

Figure 4. SBAS Time series of the metropolis

Figure 2 presents the displacement map of SBAS. On the map, an annual displacement of -6 cm/year to 2 cm/year can be observed. In the metropolis, SBAS subsidence of between 0.33 to 0.65 cm/year was obtained. Unlike the PSI where the upward and the downward show uplift, here, uplift is observed only in the western part of the study area. The time series of the SBAS in the metropolis (Figure 4) also shows a negative deformation at the rate of -0.65 cm/year to 0.33 cm/ year.

This implies that despite the differences in the rate of deformation, both methods confirmed that the urban centre is subsiding, and both methods detect an uplift on the Warri seaport which consequentially can result in increase in flooding and sea level rise due to climate change. The difference in the number of images used for both methods may be the main reason for the large differences in the average velocity between the two methods. The observed deformations may be caused by a combination of ground water withdrawal and excessive flooding.

The findings of this study are consistent with findings of Muhammad et al. (2016a) which also reported active subsidence in Warri. Their study specifically showed a deformation of -5 mm/year to 5 mm/year in the metropolis of Warri.

However, it is important to validate the results using other methods such as Global Navigation Satellite System (GNSS) in the future work to further confirm the findings of this study which are very important for city planning and policy developments by city planners and government authorities as it will aid in mitigating the urban risk of subsidence, and developing effective early-warning systems.

5. Conclusion

This study utilized remote sensing techniques, particularly the Interferometry Synthetic Aperture Radar (InSAR) with emphasis on persistent scatterer interferometry (PSI) and Small Baseline Subset (SBAS),

to detect ground deformation in Warri, a coastal city in southern Nigeria. The results revealed several degrees of deformation in Warri metropolis, with subsidence ranging from -0.5 to 1.5 mm/year using PSI, and -0.65 to 0.33 cm/year using SBAS in different areas of the study area. The findings of this study can offer significant insight to city planners and government authorities to develop effective mitigation strategies and to design better drainage systems and overall city development plans. Further work will consider the validation of the results using global navigation satellite system (GNSS).

References

Abraham, T. (2021). Mapping of surface deformation associated with the 5.2 magnitude Stilfontein earthquake of 3 April 2017 using radar interferometry. The Egyptian Journal of Remote Sensing and Space Sciences 24, 85–108

Osmanoglu, B., Sunar, F., Wdowinski, S., & Cabral-Cano, E. (2016). Time series analysis of InSAR data: Methods and trends. ISPRS Journal of Photogrammetry and Remote Sensing 115, 90–102

Nam, B. X., Tran Van Anh, Luyen K. Bui, Nguyen Quoc Long, Thi Le Thu Ha, & Ropesh Goyal (2020). Mining-Induced Land Subsidence Detection by Persistent Scatterer InSAR and Sentinel-1: Application to Phugiao Quarries, Vietnam. Proceedings of the International Conference on Innovations for Sustainable and Responsible Mining, LNCE 108, 18–38, 2021.https://doi.org/10.1007/978-3-030-60269-7_2

Chen, F., Lin, H., Zhang, Y., & Lu, Z. (2012). Ground subsidence geo-hazards induced by rapid urbanization: Implications from InSAR observation and geological analysis. Natural Hazards and Earth System Sciences, 12(4), 935-942.

Chen, Y., Tong, Y., & Tan, K. (2020). Coal mining deformation monitoring using SBAS-InSAR and offset tracking: A case study of Yu County, China. IEEE Journal of Selected Topics in Applied Earth Observations and Remote Sensing, 13, 6077-6087.

Gama, F. F., Mura, J. C., R. Paradella, W., & G. de Oliveira, C. (2020). Deformations prior to the Brumadinho dam collapse revealed by Sentinel-1 InSAR data using SBAS and PSI techniques. Remote sensing, 12(21), 3664.

Mancini, F., Grassi, F., & Cenni, N. (2021). A workflow based on SNAP–StaMPS open-source tools and GNSS data for PSI-Based ground deformation using dual-orbit sentinel-1 data: Accuracy assessment with error propagation analysis. Remote Sensing, 13(4), 753. https://doi.org/10.3390/rs13040753

Mahmud, M. U., Yakubu, T. A., Oluwafemi, O., Sousa, J. J., Ruiz-Armenteros, A. M., Arroyo-Parras, J. G., ... & Perissin, D. (2016a). Application of multi-temporal interferometric synthetic aperture radar (MT-InSAR) technique to land deformation monitoring in Warri Metropolis, Delta State, Nigeria. Procedia Computer Science, 100, 1220-1227.

Muhammad U. M., Tahir A. Y., Taiyte O. A., Joaquim J. S., Antonio M. R., Matus B., Milan L., & Daniele P. (2016b). Subsidence monitoring in the coastal region of Nigeria using multi-temporal interferometric synthetic aperture radar (MT -InSAR). Proc. 'Living Planet Symposium 2016', Prague, Czech Republic_9–13 May.

Yunjun, Z., Fattahi, H., & Amelung, F. (2019). Small baseline InSAR time series analysis: Unwrapping error correction and noise reduction. Computers & Geosciences, 133, 104331.

6th Intercontinental Geoinformation Days

igd.mersin.edu.tr

Modeling spatial distribution of bark beetle susceptibility using the maximum entropy approach

Fatih Sivrikaya [*1], **Gonca Ece Özcan** [1]

[1]*Kastamonu University, Faculty of Forestry, Department of Forest Engineering, Kastamonu, Türkiye*

Keywords
Bark beetle
Ips sexdentatus
MaxEnt
Bioclimatic variables

Abstract

Bark beetles cause significant damage to forests, which are valuable natural resources. The creation of susceptibility maps for bark beetles is a significant stage in the management and reduction of bark beetle-related harm. The present investigation involved the development of a susceptibility map for bark beetles, utilizing the Maximum Entropy (MaxEnt) model, a machine learning technique, and incorporating 19 different bioclimatic climate variables. The model's accuracy was evaluated through receiver operating characteristic (ROC) analysis, and the area under the curve (AUC) was computed to be 0.705. The MaxEnt model indicated that the annual mean temperature (BIO 1) had the greatest impact on the susceptibility of bark beetles. Categorization of bark beetles' susceptibility was delineated into four different categories, namely low, moderate, high, and extreme. Based on the results, approximately 58% of the study area included areas that exhibit vulnerability to bark beetle infestation. The accuracy of the bark beetle susceptibility map, which was developed based on these results, was found to be high and consistent with the observed bark beetle damage.

1. Introduction

Epidemics of bark beetles (Coleoptera: Curculionidae, Scolytinae), which have affected the global region and caused tree deaths, have increased considerably in recent years all over the world (Hlásny et al. 2019; Hlásny 2021; Sommerfeld et al. 2021). Current projections indicate that these outbreaks will increasingly continue (Evagelista et al. 2011; Seidl et al. 2014). 16 species of the genus Ips, one of the taxonomically defined bark beetles in the world, are distributed in Eurasian forests (Cognato and Felizet 2000). One of these species, Ips sexdentatus Boerner (Coleoptera: Curculionidae: Scolytinae), is a natural species of Turkey's forests and causes damage in pine, fir, and spruce forests (Bernard 1935; Oymen 1992; Ozcan et al. 2011). In such endemic populations, this species prefers to colonize weakened, stressed, and recently dead trees (Gil and Pajares 1986). However, when the presence of suitable hosts increases, it can also attack healthy trees and cause an epidemic level infestation (Raffa and Berryman 1983).

The prevalence of aggressive bark beetle species is influenced by certain stand and climatic factors (Fttig et al. 2007; Mezei et al. 2012; Salinas Moreno et al. 2004; Sivrikaya et al. 2023; Sproull et al. 2017; Stadelmann et al. 2013; Özcan et al. 2022). Extreme temperatures and droughts due to climate change will increase insect outbreaks and thus increase tree deaths (García de la Serrana et al. 2015; Raffa et al. 2008). The life cycles of bark beetles are also regulated by climate (Evangelista et al. 2011). Of course, the climate tends to favor bark beetle populations, which will cause infestations to occur in previously unrecorded forests (Buotte et al. 2017). Therefore, accurately modeling the spatial distributions of species is of greatest significance (González-Hernández et al. 2020; Phillips and Dudik 2008). These models are important for forestry activities (Graham et al. 2004).

Various modeling methods are used to predict suitable habitat based on future conditions (Smith et al., 2013). The MaxEnt performs better than other methods, and the software is relatively easy to use (Elith et al. 2006; Merow et al. 2013). It stands out with its high estimation accuracy and good results with smaller sample sizes compared to other methods (Phillips and Dudik 2008). There are studies that determine the potential distribution of different bark beetle species with the MaxEnt approach (Dowling 2015; Evangelista et al. 2011; González-Hernández et al. 2020; Li et al. 2021; Sarıkaya et al. 2018; Sivrikaya et al. 2023; Şen et al. 2020). Presently, there is currently a scarcity of

* **Corresponding Author**

*(fsivrikaya@kastamonu.edu.tr) ORCID ID 0000-0003-0860-6747
(goncaece@kastamonu.edu.tr) ORCID ID 0000-0003-0141-1031

Cite this study

Sivrikaya, F., & Özcan, G. E. (2023). Modeling Spatial Distribution of Bark Beetle Susceptibility Using the Maximum Entropy Approach. Intercontinental Geoinformation Days (IGD), 6, 105-109, Baku, Azerbaijan

research that demonstrates the sensitivity of forests to Ips sexdentatus utilizing this specific modeling approach. The aim of this study is to reveal the susceptibility map of Ips sexdentatus according to bioclimatic variables with MaxEnt, which is a machine learning approach.

2. Materials and Method

2.1. Study area

This study was conducted in the Sarıçam planning unit in Kastamonu, which is located in the north of Türkiye. The study area is 10272 ha, of which 7672 ha are forested. 87% of the forest area is productive, and 13% is degraded forest. The most common tree species in the study area are Crimean pine, Calabrian pine, oak, and fir. The climate of the area is continental. The winter months are usually snowy, and the spring and autumn are cold. Summers are hot and mostly dry.

2.2. Dataset

Between 2008 and 2018, the Kastamonu Regional Directorate of Forestry (RDF) conducted a field study to assess the extent of damage caused by *I. sexdentatus*. 120 beetle damaged points in Sarıçam planning unit were obtained from the Kastamonu RDF as point layers. Bioclimatic variables were obtained from the WorldClim website in raster format (WorldClim, 2023) (Table 1). The presence of a strong correlation between variables may result in overfitting of the model, thereby impacting the accuracy of the predictions (Méndez-Encina et al. 2021). The Pearson correlation coefficient (r) was employed as a means of assessing the correlation between variables. The Band Collection Statistics tool in ArcGIS 10.6 was utilized to exclude one of the two associated variables that exhibited a correlation exceeding 0.90 from the model (Yusup et al. 2018). The preparation of bark beetles' susceptibility map was carried out through the utilization of MaxEnt 3.4.4. The training dataset consisted of 70% of beetle damage points, and the rest was used for model validation. The susceptibility map of the bark beetle was classified into four distinct categories, namely low, moderate, high, and extreme, using the natural break method within the ArcGIS 10.6 software.

3. Results and Discussion

In order to minimize the risk of overfitting, a correlation analysis was conducted. The analysis revealed that 11 variables exhibited a strong correlation (>0.90) with other variables. The MaxEnt model utilized eight distinct and uncorrelated variables to predict the vulnerability of bark beetles. The modeling procedure comprised of the variables BIO 1, BIO 4, BIO 7, BIO 12, BIO 14, BIO 17, BIO 18, and BIO 19.

The accuracy of the bark beetle susceptibility map generated using the MaxEnt model was evaluated through ROC analysis. Based on the analysis results, the training data showed an AUC value of 0.742, while the test data revealed an AUC value of 0.705. The results indicate that the model that was created shows a high level of accuracy and suitability for practical use (Fig. 1). According to González-Hernández et al. (2020), temperature, which is considered, one of the bioclimatic variables, played a crucial role in determining the potential areas of the bark beetle Dendroctonus mexicanus as determined by MaxEnt. The potential distribution models generated AUC values that were in close proximity to 1. A recent investigation employed MaxEnt to generate susceptibility maps of Pityokteines curvidens in fir forests, revealing that NDVI, elevation, and stand structure were the most critical parameters. The AUC metric was calculated for the susceptibility maps pertaining to this particular species, yielding a value of 0.739 (Sivrikaya et al. 2023).

Table 1. The bioclimatic variables

Variables	Code	Unit
Annual mean temperature	BIO 1	°C
Mean diurnal range	BIO 2	°C
Isothermality	BIO 3	%
Temperature seasonality	BIO 4	°C
Max temperature of warmest month	BIO 5	°C
Min temperature of coldest month	BIO 6	°C
Temperature annual range	BIO 7	°C
Mean temperature of wettest quarter	BIO 8	°C
Mean temperature of driest quarter	BIO 9	°C
Mean temperature of warmest quarter	BIO 10	°C
Mean temperature of coldest quarter	BIO 11	°C
Annual precipitation	BIO 12	mm
Precipitation of wettest month	BIO 13	mm
Precipitation of driest month	BIO 14	mm
Precipitation seasonality	BIO 15	%
Precipitation of wettest quarter	BIO 16	mm
Precipitation of driest quarter	BIO17	mm
Precipitation of warmest quarter	BIO18	mm
Precipitation of coldest quarter	BIO19	mm

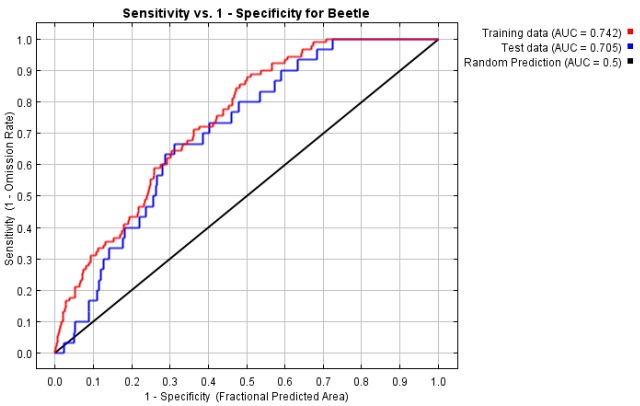

Figure 1. AUC values in ROC curve for bark beetle susceptibility map based on the MaxEnt

The bark beetle susceptibility map was found to be primarily influenced by the BIO 1 and BIO 19 variables, as indicated by the MaxEnt model output. These variables accounted for 35.8% and 35.3% of the overall contribution, respectively. Furthermore, it can be observed from Table 2 that the variables BIO 1, BIO 19, and BIO 14 collectively account for approximately 82% of the model. The variables BIO 17, BIO 19, BIO 18, and BIO1 were identified as the top four variables with the highest permutation importance for bark beetle susceptibility when analyzed independently. These

variables accounted for 27.2%, 24.6%, 11.2%, and 10.9% of the permutation importance, respectively. The results indicate that the model developed exhibits a high degree of accuracy and applicability. The potential distribution of *Ips amitinus* was predicted using MaxEnt models under both current and future climate conditions. The species is likely to expand its range in Central, Southeastern, and Southern Europe. The MaxEnt estimate was primarily influenced by temperature, which accounted for 70.8% of the variation in the climate parameter (Økland et al. 2019). According to a study conducted by Méndez-Encina et al. (2021), the process of developing ecological niche models for the three primary Pinus species of *Dendroctonus mexicanus* revealed that a solitary variable (BIO 1) accounted for 93.9% of the model.

Table 2. Contribution and importance percentage of variables for MaxEnt

Variable	Contribution (%)	Permutation Importance (%)
BIO 1	35.8	10.9
BIO 19	35.3	24.6
BIO 14	11.0	10.0
BIO 17	4.2	27.2
BIO 4	4.0	4.2
BIO 12	3.3	4.4
BIO 18	3.3	11.2
BIO 7	1.1	7.5

Comparable outcomes were likewise noted in the jackknife analysis utilizing the training dataset. As per the Jackknife method, it was observed that BIO 1, BIO 19 and BIO 12 variables demonstrated the maximum level of influence among the variables present in the model (Fig. 2). At the same time, the jackknife test results indicate that the environmental variable exhibiting the highest gain in isolation is BIO 1, implying that it possesses the most valuable information independently. The variable that exhibits the most substantial reduction in gain upon its exclusion from the model is BIO 19.

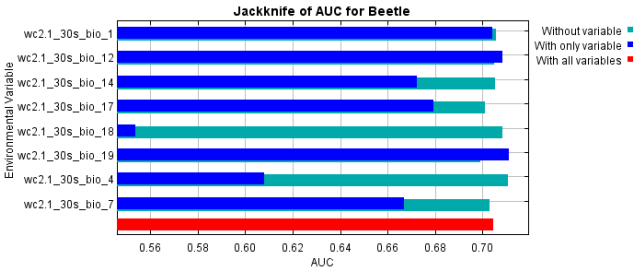

Figure 2. The utilization of jackknife estimations to determine variable importance in MaxEnt

The susceptibility of bark beetles can be classified into four distinct categories, namely low, moderate, high, and extreme, as illustrated in Figure 3. According to Table 3, the study area can be categorized into four sensitivity levels, with 30.5% classified as being in the extreme sensitivity category, 27.7% in the high sensitivity category, 21.3% in the medium sensitivity category, and 20.5% in the low sensitivity category. To clarify, it can be stated that around 58% of the study area comprises regions that are susceptible to bark beetle infestation.

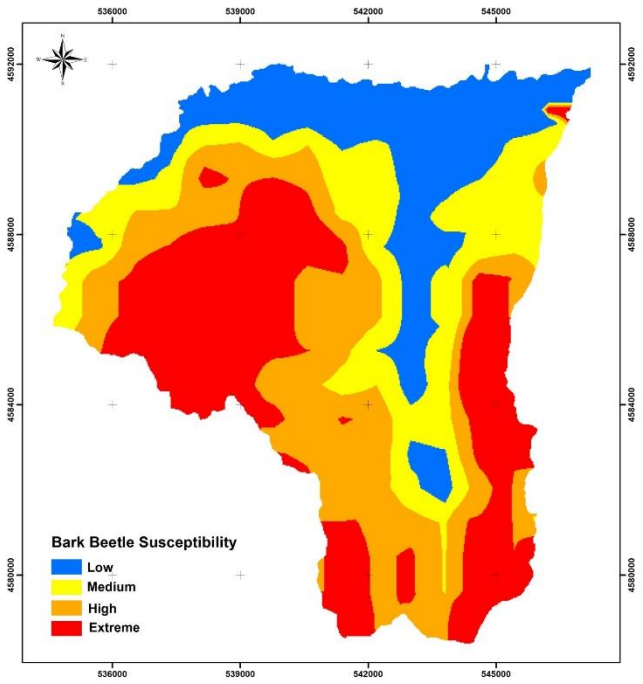

Figure 3. Bark beetle susceptibility map

Table 3. The area of bark beetle susceptibility classes

Bark Beetle Susceptibility Class	Area	
	ha	%
Low	2115.1	20.5
Moderate	2190.6	21.3
High	2837.2	27.7
Extreme	3129.2	30.5
Total	10272.1	100.0

4. Conclusion

Accurately and reliably predicting the potential distributions of harmful species holds significant importance in the sustainable planning of forests. MaxEnt, which utilizes data from prediction models, has gained significant popularity in recent times. The MaxEnt model utilized nineteen bioclimatic variables to forecast the sensitivity of *Ips sexdentatus*. The two most significant contributors were the BIO 1 and BIO 19 variables, which had values of 35.8% and 35.3%, respectively. Thus, it was determined that around 58% of the study area was susceptible to the detrimental effects caused by *I. sexdentatus*. The results of this investigation possess the potential to facilitate the monitoring of *I. sexdentatus* and similar species of bark beetles.

Acknowledgement

We would like to thank the Kastamonu Regional Directorate of Forestry for providing us with the bark beetle information.

References

Bernhard, R. (1935). Türkiye ormancılığının mevzuatı, tarihi ve vazifeleri. Yüksek Zirraat Enstitüsü Neşriyatı, Ankara, 15.

Buotte, P. C., Hicke, J. A., Preisler, H. K., Abatzoglou, J. T., Raffa, K. F., & Logan, J. A. (2017). Recent and future climate suitability for whitebark pine mortality from mountain pine beetles varies across the western US. Forest Ecology and Management, 399, 132-142. https://doi.org/10.1016/j.foreco.2017.05.032

Cognato, A.I., & Felix, A. (2000). Phylogeny of Ips DeGeer species (Coleoptera: Scolytidae) inferred from Mitochondrial Cytochrome Oxidase I DNA sequence. Molecular Phylogenetics and Evolution, 14, 445–460. https://doi.org/10.1006/mpev.1999.0705

Dowling, C. R. (2015). Using MaxEnt modeling to predict habitat of mountain pine beetle in response to climate change. PHD Thesis, University of Southern California.

Elith, J., Graham, C.H., Anderson, R.P., Dudik, M., Ferrier, S., Guisan, A., Hijmans, R. J., Huettmann, F., Leathwick, J. R., Lehman, A., Li, J., Lohmann, L. G., Loiselle, B. A., Manion, G., Moritz, C., Nakamura, M., Nakazawa, Y., Overton, J. M. M. O., Peterson, A. T., Phillips, S. J., Richardson, K., Scachetti-Pereira, R., Schapire, R. E., Soberon, J., Williams, S., Wisz, M. S., & Zimmermann, N. E. (2006). Novel methods improve prediction of species' distributions from occurrence data. Ecography, 29, 129–151. https://doi.org/10.1111/j.2006.0906-7590.04596.x

Evangelista, P. H., Kumar, S., Stohlgren, T. J., & Young, N. E. (2011). Assessing forest vulnerability and the potential distribution of pine beetles under current and future climate scenarios in the Interior West of the US. Forest Ecology and Management, 262(3), 307-316. https://doi.org/10.1016/j.foreco.2011.03.036

Fettig, C. J., Klepzig, K. D., Billings, R. F., Munson, A. S., Nebeker, T. E., Negrón, J. F., & Nowak,J.T. (2007). The effectiveness of vegetation management practices for prevention and control of bark beetle infestations in coniferous forests of the western and southern United States. Forest Ecology and Management, 238, 24–53. https://doi.org/10.1016/j.foreco.2006.10.011

García de la Serrana, R., Vilagrosa, A., & Alloza, J. A. (2015). Pine mortality in southeast Spain after an extreme dry and warm year: interactions among drought stress, carbohydrates and bark beetle attack. Trees, 29, 1791-1804. https://doi.org/ 10.1007/s00468-015-1261-9

Gil, L., & Pajares, J. A. (1986). Los escolıtidos de las conıferas en la Penınsula Ibérica. Monografıas INIA, (53), 194.

González-Hernández, A., Morales-Villafaña, R., Romero-Sánchez, M. E., Islas-Trejo, B., & Pérez-Miranda, R. (2020). Modelling potential distribution of a pine bark beetle in Mexican temperate forests using forecast data and spatial analysis tools. Journal of Forestry Research, 31(2), 649-659. https://doi.org/10.1007/s11676-018-0858-4

Graham, C. H., Ferrier, S., Huettman, F., Moritz, C., & Peterson, A. T. (2004). New developments in museum-based informatics and applications in biodiversity analysis. Trends in Ecology & Evolution, 19(9), 497-503. https://doi.org/10.1016/j.tree.2004.07.006

Hlásny, T., König, L., Krokene, P., Lindner, M., Montagné-Huck, C., Müller, J.,Qin, H., Raffa, K.R., Schelhaas, M-J, Svoboda,M., Viiri, H., & Seidl, R. (2021). Bark beetle outbreaks in Europe: state of knowledge and ways forward for management. Current Forestry Reports, 7, 138-165. https://doi.org/10.1007/s40725-021-00142-x

Hlásny, T., Krokene, P., Liebhold, A., Montagné-Huck, C., Müller, J., Qin, H., Raffa, K., Schelhaas, M-J, Sield, R., Svoboda, M., & Viiri, H., (2019). Living with bark beetles: impacts, outlook and management options European Forest Institute. ISBN 978-952-5980-76-9

Li, Y., Johnson, A. J., Gao, L., Wu, C., & Hulcr, J. (2021). Two new invasive Ips bark beetles (Coleoptera: Curculionidae) in mainland China and their potential distribution in Asia. Pest Management Science, 77(9), 4000-4008. https://doi.org/10.1002/ps.6423

Méndez-Encina, F. M., Méndez-González, J., Mendieta-Oviedo, R., López-Díaz, J. Ó., & Nájera-Luna, J. A. (2021). Ecological niches and suitability areas of three host pine species of bark beetle Dendroctonus mexicanus Hopkins. Forests, 12(4), 385. https://doi.org/10.3390/f12040385

Merow, C., Smith, M. J., & Silander Jr, J. A. (2013). A practical guide to MaxEnt for modeling species' distributions: what it does, and why inputs and settings matter. Ecography, 36(10), 1058-1069. https://doi.org/10.1111/j.1600-0587.2013.07872.x

Mezei, P., Jakuš, R., Blaženec, M., Belánová, S., & Šmídt, J. (2012). The relationship between potential solar radiation and spruce bark beetle catches in pheromone traps. Annals of Forest Research, 55, (2), 243-252.

Økland, B., Flø, D., Schroeder, M., Zach, P., Cocos, D., Martikainen, P., Siitonen,J., Mandelshtam,M.Y., Musolin,D.L., Neuvonen, S., Vakula,J., Nikolov,C., Lindelow,A., & Voolma,K. (2019). Range expansion of the small spruce bark beetle Ips amitinus: a newcomer in northern Europe. Agricultural and Forest Entomology, 21(3), 286-298. https://doi.org/10.1111/afe.12331

Oymen, T. (1992). The forest scolytidae of Turkey. Journal of the Faculty of Forestry Istanbul University, 42, I, 77–91.

Özcan, G. E., Sivrikaya, F., Sakici, O. E., & Enez, K. (2022). Determination of some factors leading to the infestation of Ips sexdentatus in crimean pine stands. Forest Ecology and Management, 519, 120316. https://doi.org/10.1016/j.foreco.2022.120316

Özcan, G. E., Eroğlu, M., & Alkan-Akıncı, H. (2011). Use of pheromone-baited traps for monitoring Ips sexdentatus (Boerner) (Coleoptera: Curculionidae) in oriental spruce stands. African Journal of Biotechnology, 10(72), 16351-16360. https://doi.org/10.5897/AJB11.1709

Phillips, S. J., & Dudík, M. (2008). Modeling of species distributions with MaxEnt: new extensions and a comprehensive evaluation. Ecography, 31(2), 161-175. https://doi.org/10.1111/j.0906-7590.2008.5203.x

Raffa, K. F., & Berryman, A. A. (1983) The role of host plant-resistance in the colonization behavior and

ecology of bark beetles (Coleoptera, Scolytidae). Ecological Monographs 53, 27– 49.

Raffa, K. F., Andersson, M. N., & Schlyter, F. (2016). Host selection by bark beetles: playing the odds in a high-stakes game. In Advances in Insect Physiology. 50, 1-74. https://doi.org/10.1016/bs.aiip.2016.02.001

Salinas-Moreno, Y., Mendoza, M.G., Barrios, M.A., Cisneros, R.., Macias-Samano, J., & Zuniga, G. (2004). Aerography of the genus Dendroctonus (Coleoptera: Curculionidae: Scolytinae) in Mexico. Journal of Biogeography, 31(7), 1163-1177. https://doi.org/10.1111/j.1365-2699.2004.01110.x

Sarikaya, O, Karaceylan, I. B., & Sen, I. (2018). Maximum entropy modeling (MaxEnt) of current and future distributions of Ips mannsfeldi (Wachtl, 1879) (Curculionidae: Scolytinae) in Turkey. Applied Ecology and Environmental Research, 16(3), 2527-2535.http://dx.doi.org/10.15666/aeer/1603_25272535

Seidl, R., Schelhaas, M. J., Rammer, W., & Verkerk, P. J. (2014). Increasing forest disturbances in Europe and their impact on carbon storage. Nature Climate Change, 4(9), 806-810.

Sivrikaya, F., Özcan, G. E., Enez, K., & Sakici, O. E. (2022). Comparative study of the analytical hierarchy process, frequency ratio, and logistic regression models for predicting the susceptibility to Ips sexdentatus in crimean pine forests. Ecological Informatics, 71, 101811. https://doi.org/10.1016/j.ecoinf.2022.101811

Sivrikaya, F., Özcan, G.E., & Enez, K. (2023). Predicting the Susceptibility to Pityokteines curvidens Using GIS with AHP and MaxEnt Models in Fir Forests, Chapter: Analytic Hierarchy Process - Models, Methods, Concepts, and Applications. IntechOpen

Smith, S. E., Mendoza, M. G., Zúñiga, G., Halbrook, K., Hayes, J. L., & Byrne, D. N. (2013). Predicting the distribution of a novel bark beetle and its pine hosts under future climate conditions. Agricultural and Forest Entomology, 15(2), 212-226. https://doi.org/10.1111/afe.12007

Sommerfeld, A., Rammer, W., Heurich, M., Hilmers, T., Müller, J., & Seidl, R. (2021). Do bark beetle outbreaks amplify or dampen future bark beetle disturbances in Central Europe? Journal of Ecology, 109(2), 737-749. https://doi.org/10.1111/1365-2745.13502

Sproull, G.J., Bukowski, M., McNutt, N., Zwijacz-Kozica, T., & Szwagrzyk, J. (2017). Landscape-level spruce mortality patterns and topographic forecasters of bark beetle outbreaks in managed and unmanaged forests of the Tatra Mountains. Polish Journal of Ecology, 65, 24–37. https://doi.org/10.3161/15052249PJE2017.65.1.003

Stadelmann, G., Bugmann, H., Wermelinger, B., & Bigler, C. (2014). Spatial interactions between storm damage and subsequent infestations by the European spruce bark beetle. Forest Ecology and Management, 318, 167–174.

Şen, I., Sarikaya, O., & Örücü, Ö. K. (2020). Current and future potential distribution areas of Carphoborus minimus (Fabricius, 1798) in Turkey. Folia Biologica, 68 (4), 141-148. http://doi.org/10.3409/fb_68-4.16

Yusup, S., Sulayman, M., Ilghar, W., & Zhang, Z. X. (2018). Prediction of potential distribution of Didymodon (Bryophyta, Pottiaceae) in Xinjiang based on the MaxEnt model. Plant Science Journal, 36(4), 541-553.

6th Intercontinental Geoinformation Days

igd.mersin.edu.tr

Importance of using space information and GIS technologies in the process of selecting analogue terrains in hydrological research

Rza Makhmudov [1], **Movlud Teymurov** [1]

[1]*Institute of Geography, Land Hydrology and Water Resources Department, Baku, Azerbaijan*

Keywords
Water resources
Space information
GIS technologies
Analogue terrains
Flow-forming factors

Abstract

The research is devoted to the wider application of GIS technologies in hydrological studies, especially in the assessment of water resources of rivers. Runoff formation is a very complex process that occurs under the influence of multiple factors. Studies show that the more flow-forming factors that are considered in the assessment process, the more accurate and reliable the results are. The practice of studying water resources based on the analogy of observed and unobserved river basins is a widespread approach in hydrology. Previously, analogies created on the basis of one or several predictors did not allow to obtain reliable results in the selection of analogue terrains. Modern scientific innovations have enabled more detailed analysis and modeling of runoff-forming processes. With our proposed method, analog geospaces are selected based on the similarity of most components through space information, and assessment is performed using GIS and other multifunctional technologies. Another advantage of the assessment with the new method is the ability to easily restore climate and runoff data for unobserved and extreme regions. Thus, on the basis of basins with hydrometeorological data, it is possible to estimate the water resources of any other unstudied rivers with high accuracy without time-space restrictions. Comparison of the actual and calculated by the proposed method of runoff for most of the river basins of Azerbaijan shows that the error between them was up to 10% in 92 cases out of 100.

1. Introduction

It is impossible to imagine modern scientific research without the use of space imagery and geospatial data. Previously, scientific-experimental researches were mainly carried out by terrestrial visual methods by organizing field expeditions, but now 80-90% of them are performed on the basis of space information. The Earth sciences section is the most widespread field of multi-functional operations performed through geospatial data and GIS technologies. Geoinformation data are also widely used in the field of hydrology, especially in the recovery of hydrometeorological data and the estimation of water resources (Abanish, et al. 2021; Gokhan Cuceloglu, et al. 2017).

2. Method

Our main goal in the submission is to investigate the role of space images and geoinformation during the restoration of hydrometeorological quantities and the assessment of water resources in unobserved areas. For this purpose, a number of traditional and modern methods have been used. Even during the application of traditional methods, the study processing was carried out completely with modern GIS-technologies (Mahmudov and Teymurov 2022). The scientific research process is based on 3 important sources: primary reliable data, modern scientific approach methods and high-precision computing technologies. To obtain accurate results, first of all, it is important to have

* **Corresponding Author**

*(rza_hidromet@mail.ru) ORCID ID xxxx – xxxx – xxxx – xxxx
(movludteymurov@yahoo.com) ORCID ID xxxx – xxxx – xxxx – xxxx

Makhmudov, R., Teymurov, M. (2023). Importance of using space information and GIS technologies in the process of selecting analogue terrains in hydrological research. Intercontinental Geoinformation Days (IGD), 6, 110-112, Baku, Azerbaijan

reliable research materials. During the study, information about most of the factors influencing water resources is collected without physical contact of the territory. LULC data (Land use & Land cover) are obtained on the basis of fragments of multispectral (hyperspectral) satellite images. Various difference indices (NDIs) are used to determine the landscape and soil cover, vegetation density, humidity and aridity of the area. The most important of these are indices for vegetation (NDVI), water (NDWI), build-up (NDBI), urban (UI), erosion and bare soil (NDBaI), salinization (NDSI), drought (NDDI) and humidity (NDMI) (Teymurov, 2023).

The heigh, slope, aspect indicators of the relief are determined by the digital elevation model (DEM); and using the Hydrology, Surface and Density program in ArcGIS, the morphometric features of rivers and the range of horizontal and vertical fragmentation of the surface are found. İn procces restoring climate data from traditional methods, the methods of Graphical Relationships, Interpolation and Analogy were used; and modern methods, preference was given to Counter-approach and NDI methods.

3. Results

It is known that all the components that make up natural complexes are closely related and interact with each other. These effects occur in a regular manner, and changes observed in any component are reflected in other components as well. Among the natural components, relief, heat and humidity level have a leading effect. During the study, most of the factors that play a role in the flow-formation and the change in the volume of water resources are taken into account. These factors are divided into 3 groups:

1) **Inputs that make up the surface cover of the territory**. These include LULC (land use & land cover) and HSG (Hydrological soil groups). LULC–is the sum of natural and anthropogenic landscapes characterizing the general appearance of the surface cover of the territory. HSG–is an indicator reflecting the surface runoff and infiltration capacity of soils. According to the granulometric composition, 4 HSG are separated (A, B, C, D). From group A to group D, there is a tendency to weaken infiltration and increase flow. 2) **Morphometric quantities**. These include the relief of the area (height, slope degree, exposure of slopes), river basins area, horizontal and vertical fragmentation of the surface, river network density, etc. includes. 3) **Climate and humidity factors**. These include factors such as air temperature, atmospheric precipitation, actual and potential evaporation, humidity coefficient, maximum water retention of soils, actual soil moisture, hydrological losses, initial abstraction. Flow factors can be combined in 2 groups in terms of obtaining information about them: 1. Geospatial data components that can be obtained through space information. This includes most flow factors. 2. Components restored on the basis of a database of similar locations. It includes climate indicators.

The most widely used methods when studying the water resources of the ungauged areas were the Counter-approach and Analogue terrains selection.

Analogue terrains–are areas with similar physical and geographical conditions between river basins with measurement data and no observations. The functional mechanism of terrains analogy is designed to search unknown elements in areas without data by using the relationship between components (especially in quantitative terms) based on the database of long-term observation areas. The results of long-term observations and artificially created experimental river basins showed that the greater the number of runoff-forming components included in the calculations, the closer the relationship between the components. This thesis showed itself in the higher correlation in the estimation of flow quantities. So, the more similar the physical-geographic conditions in which the flow is formed, if the analogy is made with the maximum number of factors affecting, the flow quantities are closer to each other.

The Counter-approach technology is based on the fact that if most of the flow factors are known, the unknown parameters are recovered from the database of available factors. In other words, when using Counter-approach technology, the research process is performed from the end to the beginning. A suitable place and time to be compared is selected, and the influence of factors is checked individually or by joining them in a complex manner.

At present, it is possible to achieve maximum (sometimes 100%) similarities between river basins through satellite images and modern GIS technologies. Similar terrains are distinguished not only by the complex factors themselves, but also by their different quantitative and gradational limits. As a result, inter terrain analogy sometimes appears in millions of variants during the processing carried out in ArcGIS various calculation, comparison and probabilistic software. Figure 1 shows analogue terrains in the forested areas of the Karabakh region, distinguished by the combination of the forest with other flow-forming factors.

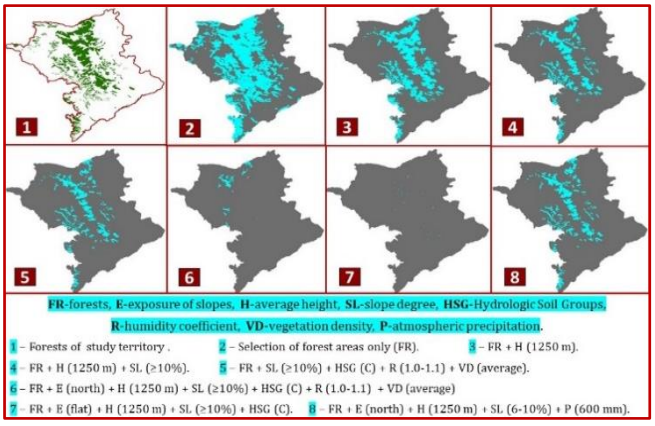

Figure 1. Selection of analogue terrains with the joint participation of various factors

As the intraspecies diversity of components and their quantities change, the number of similar spaces (polygons) decreases. Using ArcGIS program, the number

of similar polygons in the Karabakh region, separated only with the participation of forests, was 388506. Each time a new predictor was added to the processing, the number of analogue terrains changed as follows: average elevation – 142141, slope – 71536, humidity coefficient and vegetation density – 12268, exposure (north) – 1728, flat surfaces – 26. As it can be seen, the geospaces that are similar for most predictors in terms of physical-geographical conditions only within the study area are a minority. Therefore, when selecting similar terrains, no distinction is made for the location of the river basin with measurement data. Thus, the principle of similarity of the same river basin located in the same physical-geographic provinces, different rivers in the same province, rivers located in different provinces and even in other countries can be referred to.

4. Discussion

Currently, the world's fresh water resources are rapidly decreasing. Assessment of water resources is very important in terms of water supply of the economy and population, protection of the existing ecosystem, territorial planning and solving other problems. Through our proposed new method (CWBM), the entire research process is performed without space-time limitations based on satellite images of the area and GIS technologies. CWBM is an innovative and operative-interactive method. The results obtained with it are distinguished by their sensitivity and adequacy to any changes, being of high accuracy. The advantages of the new method make it urgent to promote it and expand the use of its application possibilities.

5. Conclusion

The following scientific innovations were applied for the first time during the assessment of flow-forming factors and water resources: 1. Simultaneous application of new different scientific approaches in the processing process, such as Counter-approach technology and Analogue terrains selection. 2. Participation of complex flow-forming factors in the selection of analogue areas. 3. Adding new predictors such as vegetation density, aspect (exposure of slopes), horizontal fragmentation of the surface, humidity level of territory to the process of selecting similar places. 4. Assessment the impact of each of the flow-forming factors on water resources both separately and together. 5. Separate calculation of the natural and anthropogenic impact on the change in the volume of water resources, etc.

Acknowledgement

Currently, the integration of scientists and fields of science representing different countries, especially the goals of expanding the application of GIS technologies in this process, is one of the most urgent problems of world science. Such international projects serve the exchange of scientific ideas between different countries and the development of science as a whole. We express our gratitude to the initiators of the project and all their hardworking staff for ensuring our participation in this important event.

References

Cuceloglu, G., Abbaspour, K. C., & Ozturk, I. (2017). Assessing the water-resources potential of Istanbul by using a soil and water assessment tool (SWAT) hydrological model. Water, 9(10), 814.

Kumar, A., Kanga, S., Taloor, A. K., Singh, S. K., & Đurin, B. (2021). Surface runoff estimation of Sind River basin using integrated SCS-CN and GIS techniques. HydroResearch, 4, 61-74.

Mahmudov, R. N. & Teymurov, M. A. (2022). The importance of space images and information in the assessment of water resources of the terrıtory (by the example of Shusha dıstrıct). AR Ministry of Science and Education, BSU, AR Space Agency (Azerkosmos). Materials of the scientific-practical conference. Baku. I., 340-351.

Teymurov, M. A. (2023). Assessment of soil-vegetation cover and water resources on the basis of modern scientific innovation. Scientific advances and innovative approaches Proceedings of the III International Scientific and Practical Conference. Tokyo. Japan, 28-32.

6th Intercontinental Geoinformation Days

igd.mersin.edu.tr

Comparative analysis of Image classification capabilities of Support Vector Machine (SVM) and Random Forest (RF) with Google Earth Engine (GEE) platform: A case study of Sangamner, Maharashtra

Prasad Balasaheb Wale*[1], Vinit Dhaigude [1], Satyam Mishra[1]

[1]*NIIT University, PhD Scholar, Geographic Information System (GIS) Area, Neemrana, Rajasthan, India*

Keywords
Google Earth Engine
Support Vector Machine
Random Forest
Sentinel MSI

Abstract

Support Vector Machine (SVM) and Random Forest are supervised machine learning algorithms known for their ability to precisely classify complex landscapes on earth surface. These advancements have been very productive for Geographical Information System domain to monitor natural and anthropogenic transformation using remotely sensed datasets. In the present study, Google Earth Engine (GEE) platform has been utilized to identify different land use land cover zones of Sangamner tehsil of Maharashtra. Sentinel MSI satellite images of January 2019 have been accessed and classified over GEE with both SVM and RF classifier. The classification results demonstrate that the SVM classifier performs better than RF over study area with 94.50% and 78.38% overall accuracy. The results obtained from the study illustrate that the major area is utilized for agricultural and urban practices.

1. Introduction

Machine Learning (ML) algorithms play an important role in multiple fields to solve the various complex regression and classification problems (Mariana and Dragut, 2016). In the field of Remote Sensing (RS) and Geographical Information System (GIS), ML algorithms significantly play an crucial role in different studies including Land Use Land Cover (LULC) analysis, Agricultural studies, Precise monitoring and mapping of Natural Resources (Phan Thanh Noi, 2018). Near real time face recognition, tree species identification and urban infrastructure mapping using high resolution drone images are recent applications of machine learning algorithm. Intensive transformation in anthropogenic activities to sustain increasing population with limited geographical area initiated some environmental issues including climate change. Therefore, sustainable planning and management of environment studies have got higher importance (Duraisamy, 2018).

Advancement in computer science, space technology allows us to carry out precise mapping and monitoring of natural and manmade resources at different spatial and temporal scale with greater accuracy (Claudia Maria de Almeida and Liesenberg, Veraldo, 2017). Information from RS satellites are preferable in such studies due to their global coverage and continuous illumination efficiency. The increasing number of Earth Observation (EO) satellites with higher spatial, temporal and spectral resolution revolutionizing scientific studies. (Mathias et al. , 2018).

Image classification is commonly preferred approach in GIS to study dynamics of LULC using RS datasets (Shelestov *et al.*, (n.d.)). There are two primary methods of image classification in GIS including Supervised and Unsupervised (Phan Thanh Noi, 2018). Both methods have their potentials and limitation (Donald and Weih, 2005). Supervised classification approach is further classified in pixel and object based classification approach (Blaschke *et al.*, 2000).

Recent studies of LULC analysis demonstrated that ML based classification approaches including Support Vector Machine (SVM), Random Forest (RF) and Artificial Neural Network (ANN) can detect and classify the earth surface features precisely than traditional classification techniques (Claudia Maria de Almeida and Liesenberg, Veraldo, 2017). Potential of RF in classification involves its ability to overcome the problem of overfitting very accurately whereas SVM has ability to precisely detect and separate the classes and avoid the outliers (Xiong *et al.*, (n.d.)). Recently, there have been few studies carried out to compare various supervised classification techniques. However, the accuracy may vary for each case study depending upon quality and quantity of

* **Corresponding Author**

*(prasad.wale20@st.niituniversity.in) ORCID ID 0009-0000-2701-9340
(vinit.dhaigude20@st.niituniversity.in) ORCID ID 0009-0005-4344-0561
(satyam.mishra22@st.niituniversity.in) ORCID ID 0009-0007-8349-0410

Cite this study

Wale, P. B., Dhaigude, V., & Mishra, S. (2023). Comparative analysis of Image classification capabilities of Support Vector Machine (SVM) and Random Forest (RF) with Google Earth Engine (GEE) platform: A case study of Sangamner, Maharashtra. 6th Intercontinental Geoinformation Days (IGD), 6, 113-116, Baku, Azerbaijan

training samples, dataset preferences, classifier selection and landscape complexity (Phan Thanh Noi, 2018) & (Claudia Maria de Almeida and Liesenberg, Veraldo, 2017). The major challenge of machine algorithm involves its higher computational time, high training sample requirements, more complex structure and consume more resources compare to traditional analysis techniques (Nitze, U SCHULTHESS, 2012). The satellite images, comprises of multiple spectral bands with high resolution create another challenge known is "Big Data" problem in the classification (Shelestov *et al.*, (n.d.)).

GEE is a cloud based, planetary scale platform design to access, and analyze the open source geo spatial data of different satellites including Landsat and Sentinel imagery (Xiong *et al.*, (n.d.)) & (Dimosthenis Traganos, Bharat Aggarwal, Dimitris Paursanidis, 2018). The primary objective of the present study is to prepare LULC map of Sangamner tehsil of Ahmednagar district of Maharashtra. Whereas, the Second objective is to compare the SVM and RF technique with GEE platform to evaluate its efficiency in terms of computation and classification task.

2. Study Area

Sangamner is one of the fastest growing tehsils located in Ahmednagar district of Maharashtra. The spatial extend of Sangamner lies between 19.5678 N latitude to 74.2115 E longitude. Pravara river flows from the middle of the city. Pravara river originates in Western Ghats region near Ratanwadi and it merges in to the Godavari river(Veena U Joshi, 2009).

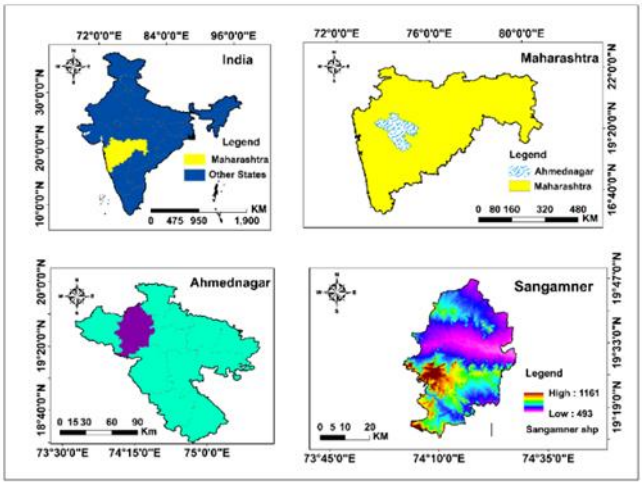

Figure 1. Study Area location with respect to country, state, and district level.

The primary activity of the study area is agriculture because of availability of fertile alluvial soil and constant water supply. Sangamner falls under rainfall shadow zone created by Western ghats, where rainfall ranges around 416mm per annual. Whereas, minimum and maximum temperature lies between 18°c to 32°c. Due to extensive agricultural practices located at the central portion of the study area, has been declared as "Overexploited" groundwater zone by Central groundwater board (Duraisamy, 2018). The construction of Nilwande damn at upper region of the study area, has brought a significant change in the socio-economic activities of the Sangamner.

3. Method

3.1. Dataset

In the present study, one Sentinel-2 MSI image captured in January 2019 has been accessed through GEE. to perform Both RF and SVM classification. Sentinel images have spatial resolution of 10 m in visible and NIR region and other 6 bands are having 20m and 3 bands are having 60 m resolution (Xiong *et al.*, (n.d.)). It Is successfully launched in 2015 and is has been providing precise information of earth surface without any cost for researchers (Son *et al.*, 2017).

3.2. Methodology

The methodology section primarily divided into three section such as accessing the sentinel MSI images of Sangamner and loading the layers on console of GEE. Supervised classification using SVM and RF classifier and analysis of their ability to separate the defined classes. Accuracy assessment and further processing of export layers and classified maps layout preparation has been prepared using ArcPro software.

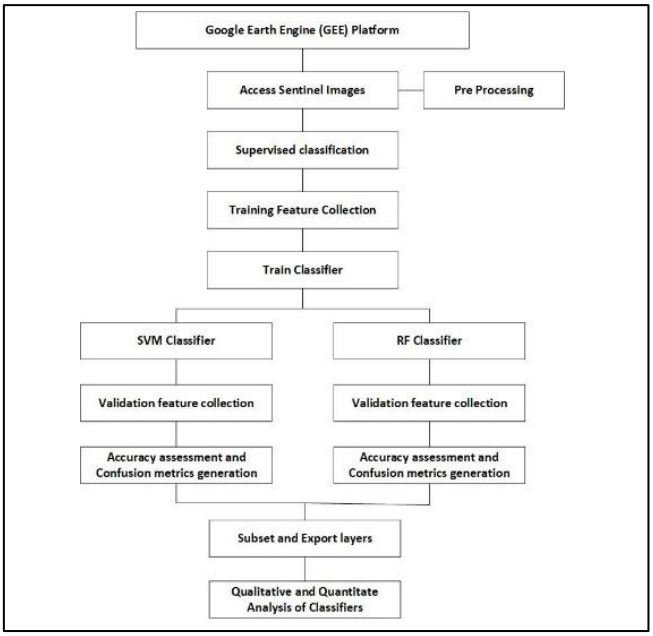

Figure 2. Methodological flow chart showing the major steps which have been followed in present study.

Fundamentally, satellite images are very complex in nature, and it is very difficult to classify with parametric classifiers. Therefore, Non- parametric classifiers e.g., RF, SVM, ANN have been booming and getting more attention from RS discipline.

In the present study, we have utilized SVM and RF classifiers to analyze LULC analysis of the study area. In order to compare both classification techniques, the same training samples and validation sample feature collection dataset have been used in this study.

3.2.1 Random Forest (RF) and Support Vector Machine (SVM) classifiers:

RF classification technique has efficiency to handle the large and complex dataset and overcome the very common issue of overfitting accurately (Raczko and Zagajewski, 2017). RF classification has performed using RandomForest classifier command in GEE. The decision trees are created by making divisions of training samples and decision trees train randomly to avoid overfitting (Kremic and Subasi, 2016). Each decision tree independently classifies the probability of feature to classify in one class among the classes defined by user. The final classification result takes all decision trees probability into account to split features into various classes(Mariana and Dragut, 2016).

$$\{h(x, \theta_k), k = 1,2,3.. \ i \ ..\} \quad (1)$$

Where, h is RF classifier, x is input variable or vector, θ_k is independent and randomly distributed sample vectors use to create decision tree(Son *et al.*, 2017). More detailed illustration of random forest classifier mentioned in (Mariana and Dragut, 2016).

SVM is another commonly use classifier introduced by vapnik (Chang-an *et al.*, 2019). SVM classifier can precisely classify the linearly and non- linearly distributed data by hyperplane. Hyperplane is line that can separate the two classes in n-dimensional space distinctly (Kremic and Subasi, 2015). The data points or Vectors which are located near to hyperplane are called as support vectors (Kremic and Subasi, 2016). Support vectors plays an extraordinary role to separate two classes with high margin. Margin is distance between two hyperplane that split the classes from each other. We must choose the hyperplane, which has the highest and equal distance from support vectors. Following figure no 3 gives basic idea of SVM and referred from (Shujun Huang, Nianguang Cai, Pedro Penzuti Pacheco, 2018).

In the linear classification, SVM can accurately classified two classes but in the real world we deal with more complex classes where linear classification may give poor results. To avoid this problem, we use non-linear SVM classification techniques. Nonlinear function uses kernel trick to avoid problem of mix classification and dimensionality (Kremic and Subasi, 2016). Kernels generally transform the low dimensional input space into higher and accurately separable dimensional space. There are four important kernels in non-linear SVM classification these are: Linear, Polynomial, Radial Basis Function (RBF) and sigmoid (Claudia Maria de Almeida and Liesenberg, Veraldo, 2017).

In this study we have used Radial Bias Function (RBF) kernel for SVM classification, because it is the most popular kernel and shows better performance than other kernels (Phan Thanh Noi, 2018). More detailed illustration about SVM classifier and RBF kernel mentioned in (Phan Thanh Noi, 2018) and (Raczko and Zagajewski, 2017).

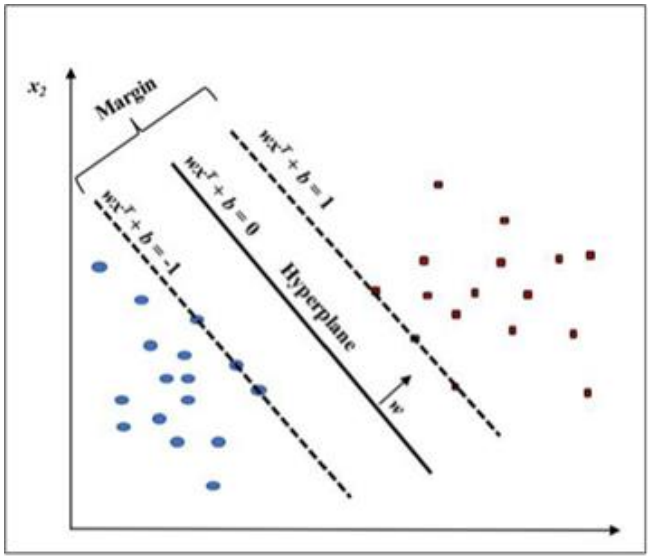

Figure 3. Detailed illustration of SVM algorithm its important components including Hyperplane, Margin and support vectors

4. Results and Discussion

In the present study LULC map of study area is prepared based on sentinel MSI data of January 2019. SVM and RF classification techniques have been utilized with GEE platform to use to classify image of Sangamner tehsil into different classes. The image has been classified into 4 different LULC classes including Forest, Water, Agriculture and Barren Land.

Table 1. Indicates the area (sq km) of Water, Urban, Agriculture and Barren land as per the result of SVM and RF classification analysis

Class	Area sq km (SVM)	Area Sq Km (RF)
Water	14.35	45.22
Urban	55.64	558.85
Agriculture	196.20	147.00
Barren Land	1394.03	909.15

The barren land indicates the most dominant class over study area due to the presence of plateau whereas agriculture class ranks second in terms of land coverage as per SVM classification results. Whereas, RF algorithm indicates urban as second largest land cover with an area of ~550 sq km. Some pixels of barren land got mix-up with urban area, therefore it's an overestimation of an urban area. Some barren land pixels in RF classification got assigned in water class as well. The visual interpretation of classified maps obtained through SVM and RF indicates that SVM classifier performed better than RF classifier to make LULC map of study area.

The central portion of the study area indicates the dominance of the agriculture area due to closeness of Pravara River. Whereas the Sangamner city could be found in the NW side of map as a urban area dominated region with red color. As per the results of RF classification, we can easily identify the issue of mix pixels between urban and barren land class.

We have calculated the overall accuracy for both SVM and RF classifiers which is are 94.50% and 78.38% respectively.

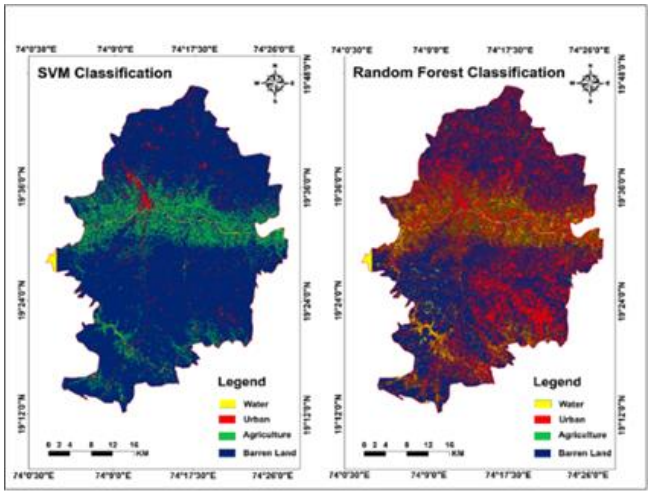

Figure 4. - Land Use Land Cover (LULC) classification of Sangamner using SVM and RF classifiers

In the SVM classification we have not observed the mix pixel problem but in case of RF classification Barren land has mixed with urban areas. The results obtained in the present study validates the same. Moreover, in some cases, RF may perform better than SVM depending on quality and quantity of training samples, dataset variations, and spatial extend of the study area

5. Conclusion

In the present study, we have compared the efficiency of SVM and RF supervised classification techniques to classify freely available sentinel-2 images of ROI. Accuracy assessment carried out for quantitative comparison of both classification techniques. We have also implemented the GEE platform as the most popular and computationally very efficient framework for spatial data analysis. It is very important to study various classification techniques, their workflow, back-end process to precise selection of classifier for various studies to improve the accuracy and quality of studies.

References

Blaschke, T., Lang, S., Lorup, E., Strobl, J., & Zeil, P. (2000). Object-oriented image processing in an integrated GIS/remote sensing environment and perspectives for environmental applications. Environmental information for planning, politics and the public, 2(1995), 555-570.

Liu, C. A., Chen, Z. X., Yun, S. H. A. O., Chen, J. S., Hasi, T., & PAN, H. Z. (2019). Research advances of SAR remote sensing for agriculture applications: A review. Journal of integrative agriculture, 18(3), 506-525. https://doi.org/10.1016/S2095-3119(18)62016-7.

Sothe, C., Almeida, C. M. D., Liesenberg, V., & Schimalski, M. B. (2017). Evaluating Sentinel-2 and Landsat-8 data to map sucessional forest stages in a subtropical forest in Southern Brazil. Remote Sensing, 9(8), 838. https://doi.org/10.3390/rs9080838.

Traganos, D., Aggarwal, B., Poursanidis, D., Topouzelis, K., Chrysoulakis, N., & Reinartz, P. (2018). Towards global-scale seagrass mapping and monitoring using Sentinel-2 on Google Earth Engine: The case study of the aegean and ionian seas. Remote Sensing, 10(8), 1227.

Enderle, D. I., & Weih Jr, R. C. (2005). Integrating supervised and unsupervised classification methods to develop a more accurate land cover classification. Journal of the Arkansas Academy of Science, 59(1), 65-73.

Duraisamy, V., Bendapudi, R., & Jadhav, A. (2018). Identifying hotspots in land use land cover change and the drivers in a semi-arid region of India. Environmental monitoring and assessment, 190(9), 535.

Kremic, E., & Subasi, A. (2016). Performance of random forest and SVM in face recognition. The International Arab Journal of Information Technolog, 13(2), 287-293.

Belgiu, M., & Drăguţ, L. (2016). Random forest in remote sensing: A review of applications and future directions. ISPRS journal of photogrammetry and remote sensing, 114, 24-31.https://doi.org/10.1016/j.isprsjprs.2016.01.011.

Wessel, M., Brandmeier, M., & Tiede, D. (2018). Evaluation of different machine learning algorithms for scalable classification of tree types and tree species based on Sentinel-2 data. Remote Sensing, 10(9), 1419. https://doi.org/10.3390/rs10091419.

Nitze, I., Schulthess, U., & Asche, H. (2012). Comparison of machine learning algorithms random forest, artificial neural network and support vector machine to maximum likelihood for supervised crop type classification. Proceedings of the 4th GEOBIA, Rio de Janeiro, Brazil, 79, 3540.

Thanh Noi, P., & Kappas, M. (2017). Comparison of random forest, k-nearest neighbor, and support vector machine classifiers for land cover classification using Sentinel-2 imagery. Sensors, 18(1), 18. https://doi.org/10.3390/s18010018.

Raczko, E., & Zagajewski, B. (2017). Comparison of support vector machine, random forest and neural network classifiers for tree species classification on airborne hyperspectral APEX images. European Journal of Remote Sensing, 50(1), 144-154. https://doi.org/10.1080/22797254.2017.1299557.

Shelestov, A., Lavreniuk, M., Kussul, N., Novikov, A., & Skakun, S. (2017, July). Large scale crop classification using Google earth engine platform. In 2017 IEEE international geoscience and remote sensing symposium (IGARSS) (pp. 3696-3699). IEEE.

Huang, S., Cai, N., Pacheco, P. P., Narrandes, S., Wang, Y., & Xu, W. (2018). Applications of support vector machine (SVM) learning in cancer genomics. Cancer genomics & proteomics, 15(1), 41-51. https://doi.org/10.21873/cgp.20063.

Son, N. T., Chen, C. F., Chen, C. R., & Minh, V. Q. (2018). Assessment of Sentinel-1A data for rice crop classification using random forests and support vector machines. Geocarto international, 33(6), 587-601. https://doi.org/10.1080/10106049.2017.1289555.

Joshi, V., & Nagare, V. (2009). Land use change detection along the Pravara river basin in Maharashtra, using remote sensing and GIS techniques. Acta geographica Debrecina Landscape & Environment series, 3(2), 71-86.

Xiong, J., Thenkabail, P. S., Tilton, J. C., Gumma, M. K., Teluguntla, P., Oliphant, A., ... & Gorelick, N. (2017). Nominal 30-m cropland extent map of continental Africa by integrating pixel-based and object-based algorithms using Sentinel-2 and Landsat-8 data on Google Earth Engine. Remote Sensing, 9(10), 1065. https://doi.org/10.3390/rs9101065.

6th Intercontinental Geoinformation Days

igd.mersin.edu.tr

Analyzing optimal routes to safe areas using OpenStreetMap and very high-resolution remote sensing imagery

Obaidurrahman Safi[*1], **Muhammed Enes Atik**[2]

[*1]*Istanbul Technical University, Informatics Applications, Türkiye*
[2]*Istanbul Technical University, Department of Geomatics Engineering, Türkiye*

Keywords
Route analysis
Satellite images
OpenStreetMap
GIS
Remote Sensing

Abstract

This study presents a study on the practical application of an integrated system of OpenStreetMap (OSM), high-resolution imagery, and Geographic Information System (GIS) for route analysis. The research findings demonstrate the effectiveness of utilizing these technologies to assess earthquake damage, evaluate transportation accessibility, and plan optimal routes to safe areas. By comparing pre- and post-earthquake images and extracting spatial data from OSM, the study accurately identifies the extent and nature of the damage, highlighting the crucial role of high-resolution imagery in resource allocation, route planning, and relief efforts. Furthermore, the research emphasizes the significance of high-resolution imagery and OSM data in urban planning and disaster preparedness. By incorporating up-to-date road networks from OSM and detailed visual information from high-resolution images, the system performs route optimization, identifies obstacles or hazards, calculates distances and travel times, and supports informed decision-making for transportation planning, logistics, or emergency response. For determining the shortest, fastest, and recommended routes to safe areas, the system considers factors such as road networks, distances, travel times, land use, and potential obstacles or hazards. These findings have significant implications for disaster preparedness, urban planning, and effective communication with government agencies and aid organizations.

1. Introduction

Natural disasters, such as earthquakes, have the potential to cause widespread devastation and disruption to communities. Understanding the extent of the damage, identifying critical areas, and facilitating effective disaster response and recovery efforts are essential for minimizing the impact on human lives and infrastructure (Erden and Karaman, 2012). In recent years, advancements in geospatial technologies and open-source data availability have revolutionized how researchers and decision-makers approach disaster management (Kamran and Saeed, 2019).

This study focuses on utilizing a methodology based on secondary data analysis to assess the impact of an earthquake and inform disaster management strategies. The methodology integrates spatial data from OpenStreetMap (OSM) and satellite imagery obtained from reliable sources. By harnessing the power of these datasets, the study aims to provide valuable insights into spatial patterns, damage distribution, and safe routes within the affected area. The primary objectives of this research are to identify blocked road segments, collapsed buildings, and changes caused by the earthquake. This information is crucial for prioritizing relief efforts, coordinating rescue operations, and planning evacuation procedures (Jaiswal and Mukherjee, 2016). Additionally, the study aims to analyze the integration of OSM spatial data and satellite imagery to create comprehensive maps and visualizations that facilitate decision-making processes in disaster management.

2. Data and Methodology

2.1. Study Area

An earthquake-affected region of Kahramanmaraş was chosen as the study area. Kahramanmaraş, commonly known as Maraş, is a province located in the Mediterranean region of Turkey. According to the Geographical Regions of Turkey, it is bordered by Sivas to the north, Adıyaman and Malatya to the east, Adana and Kayseri to the west, and Osmaniye and Gaziantep to the south. Its geographical coordinates lie between

* **Corresponding Author**

*(safio@itu.edu.tr) ORCID ID 0009-0004-6727-8004
(atikm@itu.edu.tr) ORCID ID 0000-0003-2273-7751

Cite this study

Safi, O., & Atik, M. E. (2023). Analyzing optimal routes to safe areas using OpenStreetMap and very high-resolution remote sensing imagery. Intercontinental Geoinformation Days (IGD), 6, 117-120, Baku, Azerbaijan

37°35′ N latitude and 36°56′ E longitude, encompassing an area of 14,525 km^2. On February 6, 2023, Kahramanmaraş and its surrounding region experienced two devastating earthquakes with magnitudes of 7.7 and 7.5. The Location of the study area of this research is shown in Figure 1.

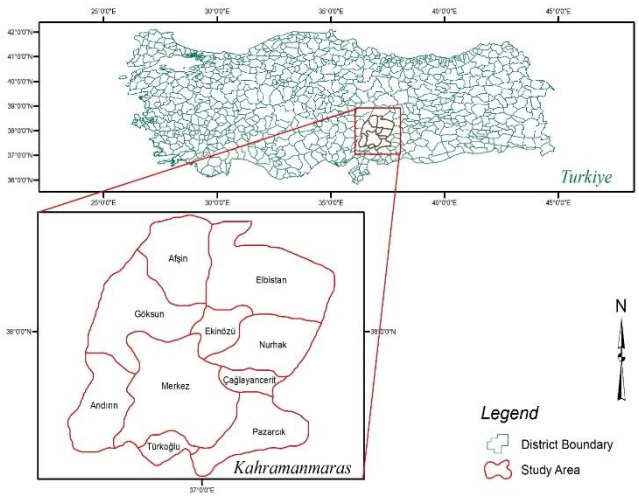

Figure 1. Location map of the study area

2.2. Data preparation and processing

The preparation and processing of spatial data from OSM and satellite images involved in this study are key components of the methodology. These steps were crucial for obtaining accurate and reliable information for analysis. To begin, the OSM spatial data was prepared by extracting relevant features such as road networks and building footprints. OSM is a collaborative project that aims to create a free and open map of the world (Haklay and Weber, 2008). It is built and maintained by a community of volunteers who contribute data on roads, buildings, and other features (Bertolotto et al., 2020). OSM data is used to create new routes and visualize road features (Mahabir, 2016). In the case of earthquake damage assessment, OSM data is used to identify blocked road networks and damaged buildings. One of the key advantages of using OpenStreetMap data is that it provides a detailed view of the road network in the affected area, including information about the width of each road and the presence of any obstacles such as buildings, trees, or other structures.

This information is overplayed on satellite imageries to determine which routes are most likely to be open and to identify any potential hazards that may need to be avoided. In addition to identifying which roads are open and which are blocked, the combination of OpenStreetMap data and high-resolution images is also used to identify safe areas where relief supplies can be delivered and where people can gather for shelter and medical assistance. This information is critical in ensuring that relief efforts are delivered efficiently and effectively, and that aid is directed to those who need it most.

This process involved filtering the OSM dataset to select the specific elements of interest within the study area. The selected features were then extracted and organized in a suitable format for further analysis. Figure 2 shows the road networks of the study area extracted for OSM and Figure 3 illustrates the building footprint of the surrounding region.

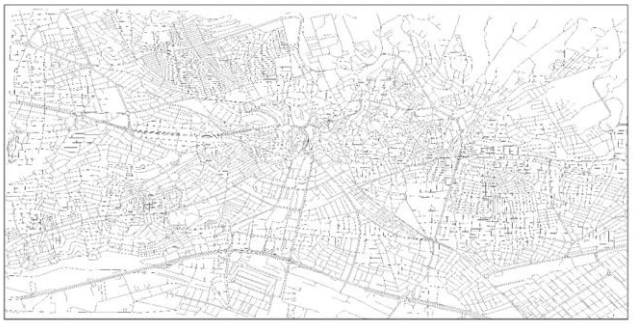

Figure 2. Road networks of the study area

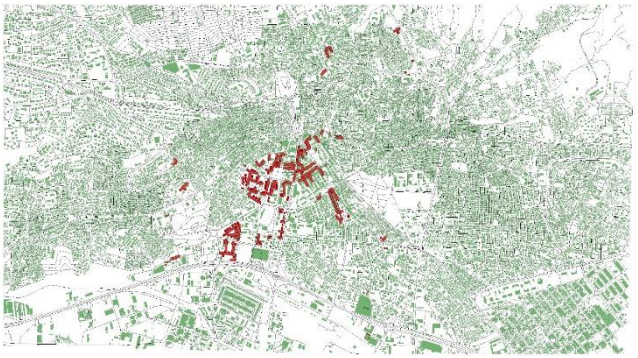

Figure 3. Building footprint of the study area

Simultaneously, the satellite images obtained from the selected source were subjected to thorough preparation and processing. The satellite images were taken from Planet SkySat satellite which has a spatial resolution of 50 cm. The images have RGB bands.

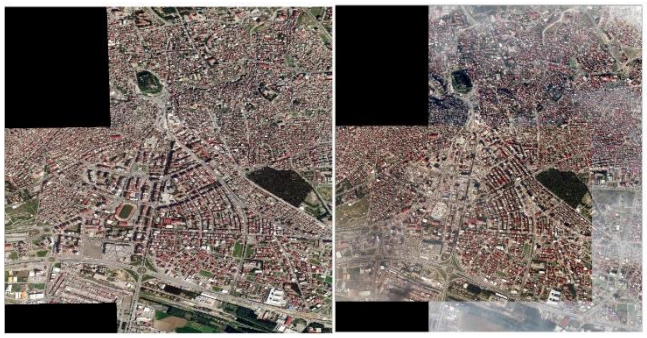

Figure 4. (a) Pre-earthquake high-resolution image (b) Post-earthquake high-resolution image

2.3. Experiment

Following data preparation, the spatial data from OSM and the processed satellite images were integrated and aligned within a consistent coordinate system. This integration facilitated the overlay and comparison of the OSM features with the corresponding features extracted from the satellite images. The combined dataset was then subjected to further processing and analysis based on the research objectives. This involves tasks such as feature extraction, feature visualization, spatial analysis, and route analysis.

The methodology employed in this research involves a systematic approach. The initial step involves identifying blocked roads, safe areas, and collapsed buildings within the earthquake zone, enabling a clear understanding of the affected areas. Subsequently, a shortest path and fastest path analysis is performed to determine the optimal routes to safe areas, considering factors such as distance, time, and recommended routes. This analysis aids in coordinating evacuation and relief efforts by identifying the most efficient pathways for affected individuals and emergency responders.

3. Results and Discussion

The analysis of the collected data in this study not only provided insights into the immediate impact of the earthquake but also yielded significant findings that contribute to a broader understanding of the event and its consequences. The results obtained from the data analysis play a pivotal role in various domains, particularly in route planning, disaster management, and response strategies.

The examination of the satellite images before and after the earthquake enabled a detailed assessment of the extent of the damage. By comparing the pre and post-earthquake images, the study identified areas where buildings had collapsed or suffered significant structural damage. This information proved vital for prioritizing relief efforts and allocating resources effectively. The integration of OSM spatial data and satellite imagery allowed for the creation of comprehensive maps and visualizations. These visual representations facilitated a clear understanding of the spatial patterns, damage distribution, and safe routes within the study area. The maps provided valuable insights for decision-makers, aiding in disaster management and post-earthquake recovery planning. Figure 5 presents the visualization of the blocked road onto the road network of the study area and Figure 6 illustrates the visual display of collapsed buildings onto buildings' footprints.

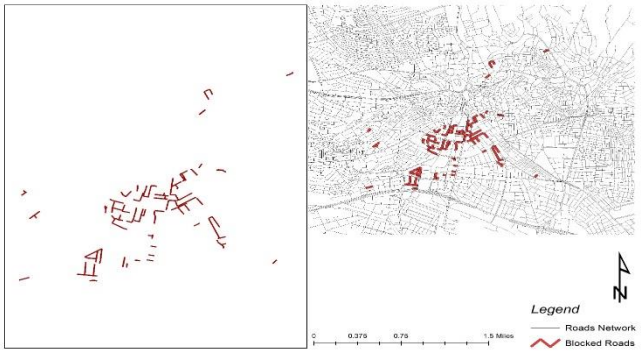

Figure 5. Visualization of blocked road onto road network

Utilizing the shortest path analysis, the study identified the optimal routes from affected areas to safe zones. By considering factors such as distance, time, blocked roads, and debris, the analysis facilitated the planning and coordination of evacuation procedures. The results provided guidance for the safe and efficient movement of individuals and emergency response teams during and after the earthquake. Figure 7 presents the shortest route to the safe area. Figure 8 presents the shortest route from affected areas to safe areas.

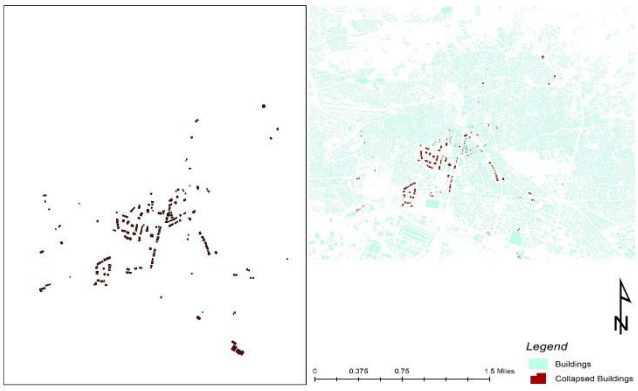

Figure 6. Visual depiction of collapsed building onto building footprint

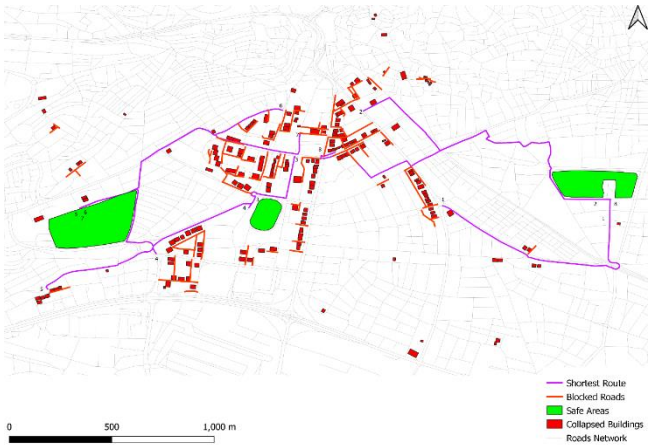

Figure 7. The shortest route to the safe zone

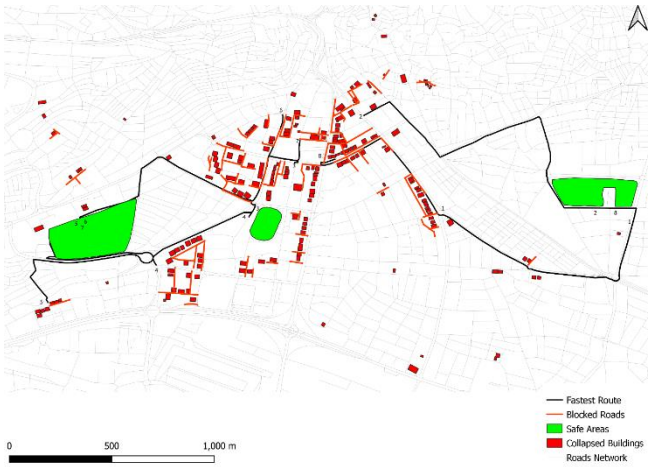

Figure 8. The fastest route to the safe zone

Recommended routes, in the context of post-earthquake scenarios, are meticulously evaluated to prioritize safety and efficiency for emergency evacuation and response efforts. While there may be instances where the recommended route coincides with the shortest or fastest route, the focus goes beyond mere distance or speed. The recommended route takes into account additional factors that can significantly impact safety, such as road conditions, potential structural damage, the presence of debris, and ongoing rescue operations.

The recommended route strikes a balance between efficiency and safety, guiding evacuees and responders through the safest and most feasible path. It may deviate slightly from the shortest or fastest route to avoid hazardous zones or blocked roads, thus providing a reliable and secure passage during the critical post-earthquake period.

Figure 9 provides an illustration of the recommended routes from the regions affected by the earthquake to the designated safe zone. This figure showcases the optimized paths that prioritize safety and efficient evacuation. By following these recommended routes, emergency responders and individuals can navigate through the affected areas with a higher level of safety and reduced risks.

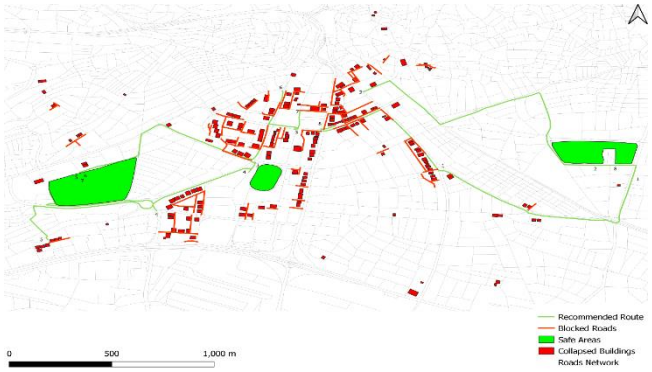

Figure 9. The recommended route to the safe areas

4. Conclusion

In conclusion, this study successfully employed a methodology based on the integration of OSM spatial data and satellite imagery to assess the impact of an earthquake and support disaster management and response efforts. The identification of blocked road segments and collapsed buildings provided crucial information for prioritizing relief operations and allocating resources efficiently. The detailed assessment of damage through pre- and post-earthquake satellite images enabled effective planning and resource allocation.

The integration of OSM spatial data and satellite imagery allowed for the creation of comprehensive maps and visualizations, enhancing the understanding of spatial patterns, damage distribution, and safe routes. These visual representations proved valuable for decision-makers involved in disaster management and post-earthquake recovery planning. In summary, the findings of this study provide valuable insights into the impact of the earthquake, supporting decision-making processes and informing strategies for disaster management and post-earthquake recovery.

Acknowledgment

Thanks to Planet Labs for providing VHR SkySat satellite images of the earthquake zone.

References

Bertolotto, M., McArdle, G., & Schoen-Phelan, B. (2020). Volunteered and crowdsourced geographic information: the OpenStreetMap project. Journal of Spatial Information Science, 20.

Erden, T., & Karaman, H. (2012). Analysis of earthquake parameters to generate hazard maps by integrating AHP and GIS for Küçükçekmece region. Natural Hazards and Earth System Sciences, 12(2), 475–483.

Haklay, M., & Weber, P. (2008). OpenStreetMap: User-Generated Street Maps. IEEE Pervasive Computing, 7(4), 12–18.

Jaiswal, A., & Mukherjee, A. (2016). Geospatial analysis of earthquake-induced damage using high-resolution satellite imagery. Natural Hazards, 81(2), 1095-1118.

Kamran, A., & Saeed, U. (2019). Advancements in geospatial technologies for disaster management: A review. Geomatics, Natural Hazards, and Risk, 10(1), 1690-1710.

6th Intercontinental Geoinformation Days

igd.mersin.edu.tr

Development of aggregated risk matrix for assessing the pipeline multiple natural disasters and their visualization using GIS

Aslan Babakhanov *[1]

[1]*Ministry of Science and Education Republic of Azerbaijan, Institute of Geography named after academician H.A. Aliyev, Azerbaijan*

Keywords
Risk assessment
Pipelines
Natural Disasters
Spatial Risk
Kernel Density Estimation

Abstract

This paper presents an approach for the computation and evaluating of an aggregated risk rating matrix to quantify the vulnerability of Baku-Tbilisi-Ceyhan pipeline to multiple natural disasters (ND) on the territory of Azerbaijan. The scope of (ND) encompasses earthquakes, floods, landslides, faults, mud volcanoes and soil erosions. Our proposed approach merges individual risk evaluations for each ND with certain intrinsic, but with generalized and aggregated calculation of final risk value smoothed by Kernel Density Estimation method. Further, we employ Geographic Information System (GIS) technology for the spatial representation of the computed risks across the pipeline network by using the final and aggregated risk values per special cell. This visual approach facilitates a better comprehension of spatially varied risks and supports the effective planning of risk mitigation measures. This visual approach aids in better understanding of the spatial distribution of risks, thereby supporting efficient strategizing of risk mitigation measures. The model was evaluated using the linear part of Baku-Tbilisi-Ceyhan pipeline as a case study, demonstrating the method's robustness and versatility. The methodology outlined in this study offers a rigorous and adaptable tool for ND risk assessment using GIS tools, but with some compute intensive methods. It aims to the enhancing pipeline safety and resilience on the territory of Azerbaijan

1. Introduction

Enhancing the resilience of the infrastructural components within the Azerbaijani hydrocarbon extraction complex to safeguard against potentially catastrophic effects of ND presents a critical and timely challenge in the scientific community. The pipeline systems, responsible for transferring hydrocarbon resources from the oil and gas deposits, constitute high-risk elements within this complex. Given the inherent flammability of these resources, they possess the capacity to initiate incidents with calamitous repercussions, resulting in irrecoverable ecological damage, loss of human lives, substantial financial and administrative losses, and infrastructural devastation (Lerche and Bagirov 2014).

As the role of pipeline interconnectivity expands among various countries, coupled with the rising incidents of natural disasters, the relevance and necessity of risk assessment methods are increasingly emphasized (Krausmann et al. 2011).

There are known ND on the territory of Azerbaijan that may directly have an impact to pipelines: earthquakes, heavy rainfalls and they are may trigger other events, such as landslides, mud volcanoes, floods, soil erosions and liquefaction (Amirova-Mammadova 2018).

It is common to visualize the impact and risk values as a single map per risk factor, but for bigger picture (here, using the single map) there is a need for an aggregation of risk values. Here comes the risk matrix, but with additional capabilities to evaluate the all required risk factor.

2. Method

In this study, the re-evaluated risk matrixes per weighted natural disaster will be used to assess each impact factor, smooth them using the Kernel Density Estimation (KDE) applied to a risk scores and at the end they will be mapped as a 2D array (Gramacki 2017). The

* **Corresponding Author**

*(aslan@babakhanov.az) ORCID ID 0000-0002-8790-7945

Cite this study

Babakhanov, A. (2023). Development of aggregated risk matrix for assessing the pipeline multiple natural disasters and their visualization using GIS. Intercontinental Geoinformation Days (IGD), 6, 121-125, Baku, Azerbaijan

values assigned to each matrix cells will be adopted in any of relational databases (Nasser 2014) or any convenient textual data format, like comma delimited text files, JSON files or any other data table format that can be used by widely used GIS tools like ESRI ArcGIS or QGIS tools.

2.1. Risk Matrix

To study the impact of natural disasters on pipelines, a risk matrix is an important component in representing the level of safety. For the risk calculation methods, I'll base it on a standard 5x5 risk matrix which evaluates hazards based on their likelihood (from rare to almost certain) and their consequences (from insignificant to catastrophic). Thus, five level is one of the optimal options for levels (Blokdyk 2018).

The more important is to identify the certain regions with certain hazards that may affect the pipelines (Han and Weng 2010). The fact that, region representing as a squared polygon area on the map, it could be of any size, from 10x10 meters up-to kilometers and classified by risk level. For this purpose, a distribution of risk levels must be prepared for squared area "Table 1".

This table is important part of all calculations and be included into the visualization of GIS maps.

Table 1. Risk level distribution per ND factor

Natural Disaster	Risk Level (1-5, 5 is highest)	Description	Color
Landslides	4	Soil movements in hilly or mountainous areas that can displace or damage pipelines	Yellow
Earthquakes	5	Ground shaking or rupture causing severe damages	Red
Flooding	3	Cause erosion or sedimentation	Yellow
Corrosion from soil chemistry	3	Certain soil conditions can enhance corrosion leading to pipeline material degradation	Yellow

2.2. Calculating Risk values

In order to deal with multiple events of hazards, each contribution to a single risk factor be aggregated to the singe risk score.

Firstly, calculate the individual risk scores ($\boldsymbol{R_i}$) for each hazard as per Equation 1.

$$\boldsymbol{R_i} = \boldsymbol{L_i} \times \boldsymbol{C_i} \quad (1)$$

where $\boldsymbol{L_i}$ is the likelihood and $\boldsymbol{C_i}$ is the consequence of the $\boldsymbol{i^{th}}$ hazard. Once we have the individual risk scores for each hazard ($\boldsymbol{R_1, R_2, \ldots, R_n}$), then calculating the average risk score ($\boldsymbol{R_{avg}}$) as follows:

$$\boldsymbol{R_{avg}} = \frac{\mathbf{1}}{\boldsymbol{n}} \sum_{i=1}^{n} \boldsymbol{R_i} \quad (2)$$

In this case, $\boldsymbol{n}$ is the total number of hazards or events being considered. Taking the average is just the one of many possible methods to aggregate the risk, but suitable for mapping purposes. Notably, the color coding of the risk scores would be: ***1-6*** as Green (low risk), ***7-12*** as Yellow (medium risk) and ***13-25*** as Red (high risk). Each value that falls into each score might be considered as a gradient color as well.

On the other hand, calculating an aggregate risk score using this method assumes each hazard is independent and equally significant, which may not always be the case. So, for such a complex situation, we will incorporate a weighting system to account for the varying significance of different hazards or correlations between events. Here we assign a weight ($\boldsymbol{w_i}$) to each hazard, which represents its relative importance or significance. This would typically be a value between 0 and 1, with total of all weights equal to 1. The next step is to calculate the weighed risk score ($\boldsymbol{R_{wi}}$) for each hazard:

$$\boldsymbol{R_{wi}} = \boldsymbol{w_i} \times \boldsymbol{R_i} \quad (3)$$

then, sum all of the weighted risk scores to get the total risk score ($\boldsymbol{R_{total}}$):

$$\boldsymbol{R_{total}} = \sum_{i=1}^{n} \boldsymbol{R_{\mathrm{wi}}} \quad (4)$$

and finally apply the color coding based on the risk score:

$$Color(\boldsymbol{R_{total}}) = \begin{cases} Green & if\ 1 \le \boldsymbol{R_{total}} \le 6 \\ Yellow & if\ 7 \le \boldsymbol{R_{total}} \le 12 \\ Red & if\ 13 \le \boldsymbol{R_{total}} \le 25 \end{cases}$$

This method gave is a risk score that takes into account both the individual risk scores and the relative importance of each hazard, but not considering the correlation between hazards.

2.3. Smoothing risk scores by categories

Mapping of granulated risk values over the map would give us coarse image even by dividing each risk score into sub-score. In order to smooth the risk values over the 2D map, we will use the Kernel Density Estimation (KDE) method to generate an estimation of the probability density function of multiple risk values (here small risk zones). So, while doing the KDE for each category, you will treat the risk values outside the category range as if they don't exist.

The equation (Equation 1) for each risk category (**c** as 1: *Green, 2: Yellow, 3: Red*) consider the data points ($\boldsymbol{x_i, y_i}$) that fall within that category's risk score range.

$$\hat{f}_c(x,y) = \frac{1}{n_c h^2} \sum_{i=1}^{n_c} \frac{1}{2\pi} e^{-\frac{1}{2}\left[\left(\frac{x - x_i^{(c)}}{h}\right)^2 + \left(\frac{y - y_i^{(c)}}{h}\right)^2\right]}$$

So, risk levels (here categories) per impact, where (n_c) is the number of data points in the (i)th category, (h) is the bandwidth parameter, (e) is the base of the natural logarithm and $x_i^{(c)}$ and $y_i^{(c)}$ are the nth pair of 2D data points.

This equation (Equation 1) assumes, that the **X** and **Y** variables are independent for each category within the Gaussian kernel. The bandwidth parameter h is very important in KDE as it determines the smoothness of the density estimate. A small **h** will make the estimate very sensitive to the data (potentially overfit), while a large **h** will make the estimate very smooth (potentially underfit). It's often chosen using cross-validation or a rule-of-thumb method (Silverman 2018).

2.4. Processing

Before starting the analyses on certain area of interest (AIO), there were made an analysis of most evident natural disaster events occurred on a territory of Azerbaijan. That analyses were a key process to determine the minimal dimension for AIO, where de identified as square of 1 km. In fact, that size is not de-facto and can be changed from places, regions, cities and etc. Changing the size of AIO is adding the more analyses to the events and their effect. The risk level determination, risk weight and score calculation of AIO is show in Figure 1.

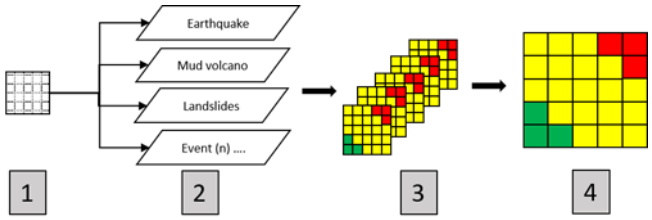

Figure 1. Processing of single AIO

The first step 1 is about to determine the AIO, where shape of pipeline must be at center of AIO. This will give us a proper and proportional GIS visualization of events area and pipeline linear part. At the step 2 we need identify the ND that may fit into this AIO. Surely, the dimension of AIO might be changed if any of identified ND has a broader effect. At the same step 2, we determine the risk parameters per event, their weights against the pipeline. Step 3 is about to calculation of risk matrixes per event. At the end (step 4) we aggregate the risks scores into a single risk score matrix.

2.5. Assessment challenges

One of challenges is the accurately description of the risk impact of a natural disaster that may affect the pipeline, then we need to disclose in a broader form the definition of the risk itself in order to give it a clearer vision of dimension of risk probability.

Here are the some of them (ordered by complexity)

1. Identification of risk parameters and their evaluations.
2. Determination of right risk weights per risk parameter.
3. Selection of proper level of granulation of area of interest to avoid coarsening.

The first challenge can be described when assessing the earthquakes effects on pipelines and triggered post events, including NATECH (Krausmann et al. 2016).

A three-parametric earthquake event that may affect the onshore pipeline is show in Figure 2. By adding color of risk category, we can see 3D view of earthquake effect on pipeline. This plot is showing only the risk at given location. Note, that location may change and values may vary.

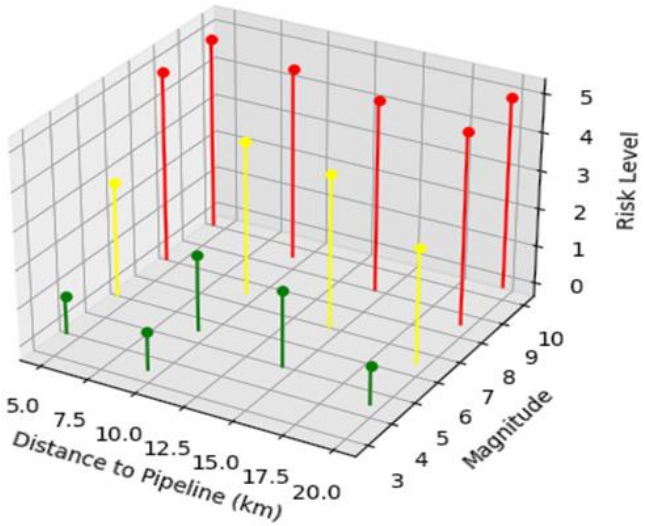

Figure 2. 3D earthquake risk assessment plot

The same 3D plot can be generated for other ND that may affect the pipelines, and they may have more parameters, adding assessment difficulties.

3. Results

As a result of study, we managed a good visualization of aggregated risk using GIS tools. Moreover, adding the buffered zones along the pipeline route providing the clearer picture of risk areas (Petersen 2020).

Figures from “Fig. 4” to “Fig. 7” are showing the evolution of aggregated fine-tuned risk scores from multiple natural hazards in a small region. The minimal area (which is AIO) is about 2 km^2 and whole assessed region is 100 km^2. The risk matrixes were based on mix of registered and assessed earth quakes, known faults and mud volcanoes.

Following tools were used to accomplish the visualizations:

- Maps were build using ESRI ArcMap 10.8
- Calculations were done in Python 3.8
- Output data format was CSV files

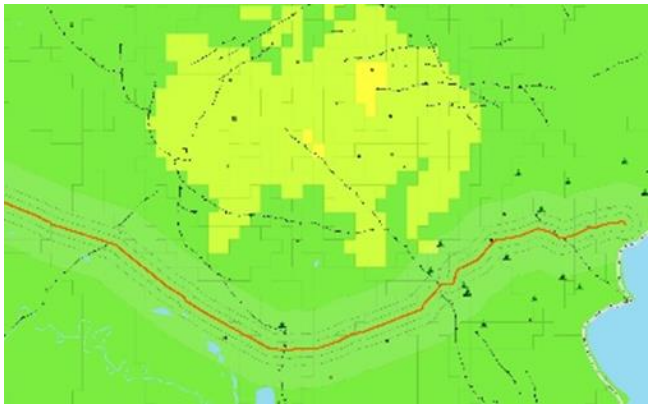

Figure 4. Coarse, aggregated risk scores

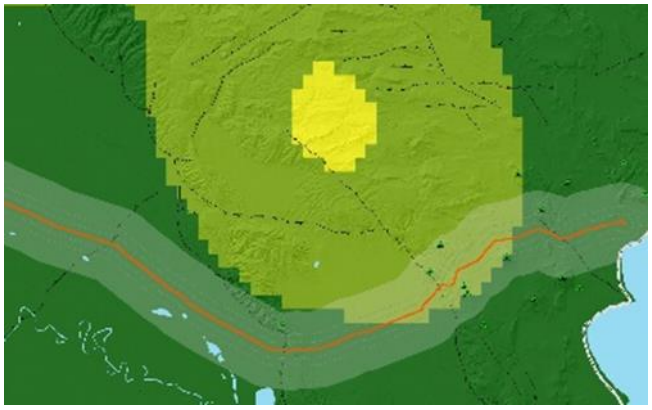

Figure 5. KDE based aggregated risk scores

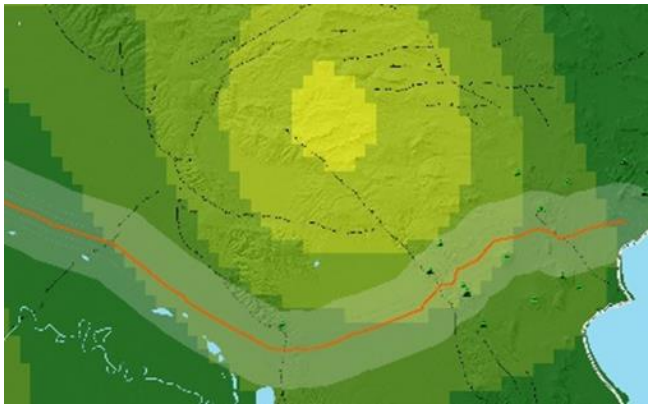

Figure 6. KDE based, small tuned risk scores

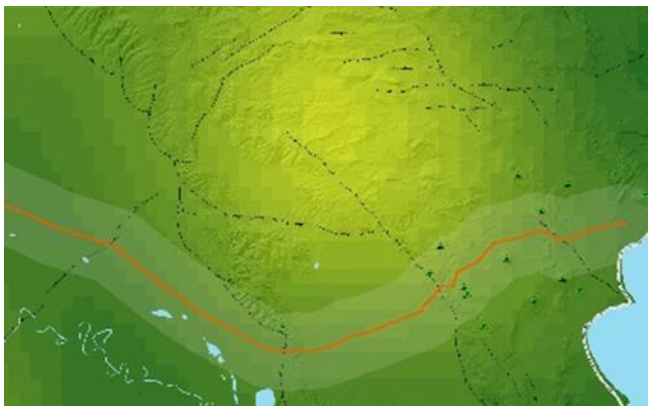

Figure 7. KDE based, fine-tuned risk scores

4. Conclusion

We identified several factors contributing to the difficulties of determination of risk weights:

1. **Complexity of Risk Interactions:** ND often do not occur in isolation. They can interact and compound in complex ways, making it difficult to accurately assign weights. For example, the risk posed by an earthquake could increase the risk of a subsequent landslide, but determining exactly how much additional risk this interaction creates can be challenging.
2. **Lack of Data:** For many risks, especially rare or unprecedented ones, there may be insufficient data to accurately estimate probabilities and impacts. This lack of data can lead to uncertainty in the risk weights.
3. **Over-simplification**: In an effort to simplify, there is a danger of oversimplifying the complexity of risks and their interactions by assigning a single risk weight. This might lead to an underestimation of the actual risk.
4. **Dependence on Model**: The assigned risk weights are only as good as the risk assessment model used. If the underlying model does not accurately represent the situation, the risk weights might be misleading.

Despite the difficulties, we were able to visualize the risk in aggregated form, using single map with fine-grained and tuned risk scores.

One of the best findings, is this model can be used to assess the other risks by using the same matrix representation and weight calculations and then we can implement the KDE method for fine tuning the final output if necessary. Also, the chained operations are giving us flexibility to include an additional function like risk score determination for relative AIO regions by implementing the Moore neighborhood (Ilachinski and Zane. 2001) algorithms.

Acknowledgement

This study was carried out as part of the master's thesis prepared by Aslan Babakhanov at Institute of Geography named after academician H.A. Aliyev.

References

Amirova-Mammadova, S. (2017). Pipeline Politics and Natural Gas Supply from Azerbaijan to Europe. Wiesbaden: Springer.

Blokdyk, G. (2018). Risk Matrix a Complete Guide. 5starcooks.

Gramacki, A. (2017). Nonparametric Kernel Density Estimation and Its Computational Aspects. Springer.

Han, Z., & Weng, W. (2010). An integrated quantitative risk analysis method for natural gas pipeline network. Journal of Loss Prevention in the Process Industries, 23(3), 428–436. https://doi.org/10.1016/j.jlp.2010.02.003

Ilachinski, A., & Zane. (2001). Cellular Automata – A Discrete Universe. Kybernetes, 32(4). https://doi.org/10.1108/k.2003.06732dae.007

Krausmann, E., Cruz, A. M., & Salzano, E. (2016). Natech Risk Assessment and Management: Reducing the Risk of Natural-Hazard Impact on Hazardous Installations. Elsevier.

Krausmann, E., Renni, E., Campedel, M., & Cozzani, V. (2011). Industrial accidents triggered by earthquakes, floods and lightning: lessons learned from a database analysis. Natural Hazards, 59(1), 285–300. https://doi.org/10.1007/s11069-011-9754-3

Lerche, I., & Bagirov, E. (2014). Impact of Natural Hazards on Oil and Gas Extraction. Springer.

Nasser, H. (2014). Learning ArcGIS Geodatabases. Packt Publishing Ltd.

Petersen, K. (2020). Visualizing Risk: Drawing Together and Pushing Apart with Sociotechnical Practices.

Silverman, B. W. (2018). Density Estimation for Statistics and Data Analysis. Routledge.

6th Intercontinental Geoinformation Days

igd.mersin.edu.tr

Production of digital maps by uncrewed aerial vehicle (UAV)

Murat Yakar [*1], **Abdurahman Yasin Yiğit** [1], **Ali Ulvi**[2]

[1]*Mersin University, Engineering Faculty, Geomatics Engineering Department, Mersin, Türkiye*
[2]*Mersin University, Institute of Science, Department of Remote Sensing and Geographic Information Systems, Mersin, Türkiye*

Keywords
UAV
Photogrammetry
DEM
Orthophoto
Digital Map

Abstract

Unmanned aerial vehicles (UAVs) have recently been used to generate digital maps. UAVs are utilized in a variety of applications today and are among the most modern measurement systems. There is a direct correlation between the calculation of the geometric components of the horizontal and vertical lines of digital maps and their accuracy and precision. Consequently, the horizontal and vertical errors of the generated digital maps are a significant factor. This study used the data collected by the unmanned aerial vehicle to investigate the creation of digital maps. Due to the photogrammetric analysis of these images, a Digital Elevation Model and orthophoto of the study area were produced. In addition to the GCP used as a reference, the location accuracy of the orthophoto map created by determining the coordinates of the detail points in the field with the RTK GPS technique was measured, and an approximation cost comparison between the two techniques was conducted.

1. Introduction

Many mapping organizations worldwide use large-format aerial cameras to acquire large-format aerial photographs for topographic map production (Ulvi et al., 2019). However, some mapping organizations have begun using various brands' digital mapping cameras (Remondino et al., 2011). However, due to the high price of the digital mapping camera alone, few mapping organizations can afford to use it, despite its accurate and swift photogrammetric output. Producing a topographic map using conventional aerial photogrammetry is typically a time-consuming and expensive process, as it involves numerous steps, such as producing a flight map, acquiring an aerial photograph, establishing a ground control point, and a lengthy image processing procedure (Colomina et a., 2008). Additionally, this method is only appropriate for mapping vast areas. However, there are times when a small-area aerial photograph is required for mapping purposes. Large-format aerial cameras are not cost-effective for imaging small areas (Yılmaz & Yakar, 2006a; Polat et al., 2020). Photogrammetrists have begun acquiring aerial photographs with small-format cameras to circumvent this issue. Small-format cameras for cartography have been the subject of research with optimistic outcomes. With a compact format camera, photogrammetric outputs such as a digital map and orthophoto can be obtained successfully. More research has been conducted on using light platforms to acquire aerial photographs for cartography and other purposes (Siebert & Teizer, 2014). Small format cameras such as high-resolution digital cameras, video cameras, and other sensors combined with light platforms such as helicopters, gliders, balloons, etc., are commonly used by people worldwide to acquire digital aerial images/photographs. It is possible to remotely control the light platform manually or operate it autonomously (i.e., automatically) based on pre-programmed flight plans or more complex dynamic automation systems. Unmanned aerial vehicle (UAV) refers to the sensor, light platform, and procedure for piloting the system without a pilot. Using UAVs for surveying and other purposes in Malaysia is still relatively novel. UAVs have been effectively utilized for large-scale mapping to produce photogrammetric outputs such as digital maps, digital orthophotos, digital elevation models (DEM), and contour lines (Yakar & doğan, 2018; Alptekin and Yakar, 2021).

The Unmanned Aerial Vehicle (UAV) system is a flexible, low-cost photogrammetry and remote sensing system. Consequently, this system represents a new revolution in photogrammetry and an appropriate alternative to other mobile mapping systems (Alptekin & Yakar, 2020). UAVs are primarily employed for military purposes before being utilized for civilian applications. The military uses UAVs for reconnaissance missions,

* **Corresponding Author**

*(myakar@mersin.edu.tr) ORCID ID 0000-0002-2664-6251
(ayasinyigit@edu.tr) ORCID ID 0000-0002-9407-8022
(aliulvi@mersin.edu.tr) ORCID ID 0000-0003-3005-8011

Cite this study

Yakar, M., Yiğit, A. Y., & Ulvi, A. (2023). Production of digital maps by uncrewed aerial vehicle (UAV). Intercontinental Geoinformation Days (IGD), 6, 126-129, Baku, Azerbaijan

unmanned weapons, and other activities (Karataş et al., 2022). UAVs are more applicable to agricultural activities, such as paddy monitoring and sprinkling, for civil applications (Kuşak et al., 2021; Ünel et al., 2020). The fundamental principle of UAVs is photogrammetry at low altitudes. Like photogrammetry, the UAV camera is utilized for flight planning, mapping, and analysis.

2. Method

UAV is a small aircraft that flies autonomously guided by an on-board Global Positioning System (GPS), stabilized by an on-board 3-axis gyro sensor and magnetometer in the autopilot microprocessor, and whose telemetry is monitored at a Ground Control Station (GSC). The aircraft is radio-controlled from the Ground Control Station (GSC) and becomes autonomous at a fixed altitude (Yılmaz & Yakar, 2006). The antenna in the GSC will transmit a communication link to the UAV, and the UAV will transmit its location, altitude, and speed back to the GSC (Karataş et a., 2022a; b; c).

UAVs fly between 100 and 300 meters above the earth and below the clouds (Colomina et al., 2008); Flying at the optimal altitude based on the earth's terrain is essential to avoid image distortion. Before flying, it is necessary to calculate the correct altitude.

The flight duration is dependent on the energy source used. Generally, oil has a much longer flight duration than batteries, though this depends on the aircraft's payload capacity (Yılmaz & Yakar, 2006). Hand-launched lightweight or micro UAVs typically have maximal payloads between 1 and 2 kilograms. A flight's duration and coverage area will vary based on the power source. The aircraft make two or three flights to conserve battery power to cover a large area (Yılmaz & Yakar, 2006b; Kanun et al., 2021a).

Geomatic applications like unmanned photogrammetry measure and map the earth's surface. The UAV (Unmanned Aerial Vehicle) has recently been adopted as a weapon by the military. The armed forces use the idea of photogrammetry to pinpoint the exact location of the adversary (Kanun et al., 2021b). UAVs have undergone a revolution in the hands of civilians for usage in fields including agriculture, surveillance, and more. Combining close-range photogrammetry, mosaicking aerial pictures, and terrestrial photogrammetry, UAV photogrammetry is the latest measuring method in photogrammetric applications (Karataş et al., 2022).

This is novel terminology for photogrammetry (Ulvi et al., 2019). Photogrammetry image processing techniques used in UAV photogrammetry include rectification, orthorectification, aerial triangulation, etc. UAV photogrammetry also details the various types of UAV platforms that can capture aerial imagery, including micro UAVs, standard UAVs, low-altitude UAVs, high-altitude UAVs, and so on (Yakar et al., 2015).

Global Positioning (GPS) technology achieves a more exact flight stabilization and navigation result. It is the same method used in photogrammetry. Camera calibration is a part of the package. However, most UAVs only employ small cameras. Lens distortion and focal length parameters may be corrected using the camera's settings. UAV pictures may be mosaicked and orthorectified using the same principle as aerial triangulation. However, many ground control points (GCPs) are required for this.

Table 1. The UAVs' classification depends on their size, endurance, range, and flying altitude

Category name	lass [kg]	Range [km]	Flight Altitude [m]	Endurance e [hours]
Micro	< 5	< 10	250	1
Mini	<25/30/150	< 10	150/250/300	< 2
Close Range	25–150	10－30	3000	2－4
Medium Range	50–250	30－70	3000	3－6
High Alt. Long Endurance	>250	>70	>3000	>6

The UAV is capable of autonomous flight and operates in a wide range of missions and emergencies that can be controlled from a ground base station or by remote control. The UAV comprises the airframe, flight computer, payload, mission/load controller, base station, and communication infrastructure. UAVs with less than 5 kg mass are known as micro UAVs. Figure 1 shows an example of a micro fixed-wing UAV and a rotary UAV system used in the study.

Figure 1. UAV used in the study (Anafi Parrot)

3. Results

After capturing UAV images, a consistent and easy-to-follow methodology in Agisoft Metashape Pro was used to modify the data. An orthorectified picture mosaic was made after creating a point cloud from the photographs using Agisoft's structure-from-motion (SfM) computation technique. Compared to the photogrammetric approach, SfM can determine camera locations and orientation parameters with or without ground control points [30]. For each picture, the scale-invariant feature transform (SIFT) technique is first used by the SfM algorithm to gather and identify local features. A comprehensive evaluation of the SfM approach is unnecessary for this investigation; for a more in-depth discussion, the interested reader is referred to the works mentioned above [15], [40], [38], [23]. More information

on the functionality of these Agisoft stages may be found in [25,27]. There are three primary phases to the processing: (1) picture alignment, (2) point cloud and mesh creation, and (3) DSM and orthophoto generation. In this research, two different types of wholly automated software were employed. Adding photos, marking features, and defining input parameters such as project datum and projection, GCPs and CheckPs, and final resolutions are all required of the user. After the cameras are correctly aligned, point clouds, DEMs, and orthomosaics may be generated.

UAV photos were processed in Agisoft Metashape Pro using a standardized, user-friendly workflow. You may learn more about the features of these Agisoft stages. The model was georeferenced using the coordinates of nine differential GPS control points installed at the site. The accumulation of smaller, more precise models in important areas allows Agisoft to estimate a horizontal spatial error of 8.23 cm for the overall model, which is within an acceptable range. The processed and georeferenced model yielded a high-resolution (2.5 cm) orthophotograph and a digital elevation model (DEM; see Figure 2). Due to the moderate vegetative cover at the site, the DEM that includes the plant heights and architecture at the site is inappropriate for mapping and spatial analysis. As a result, developing a DTM was required. As discussed in earlier articles, several ways exist to construct a DTM from datasets. However, the majority of them need a certain level of technical expertise. Agisoft Metashape's products are simple in design and operation, but they differ widely in the degree to which they automate common tasks.

Nine differential GPS control points were set up on-site, and their coordinates were used to georeference the model. Agisoft estimated a horizontal spatial inaccuracy of 8.23 cm for the whole model, which is within an acceptable range given the collection of smaller, more exact models in strategic locations. A high-resolution (2.5 cm) orthophotograph and a digital elevation model (DEM) were both produced from the processed and georeferenced model (Figure 2). With a DEM including the vegetation heights and architecture at the site, this dataset is unsuitable for mapping and spatial analysis due to the site's moderate vegetative cover. Therefore, making a DTM was essential. There are a variety of approaches to creating a DTM using datasets, as detailed in previous articles, albeit most of them need a fair amount of technical competence. However, Agisoft Metashape's offerings are generally straightforward but vary widely regarding how much automation is included and how well it works.

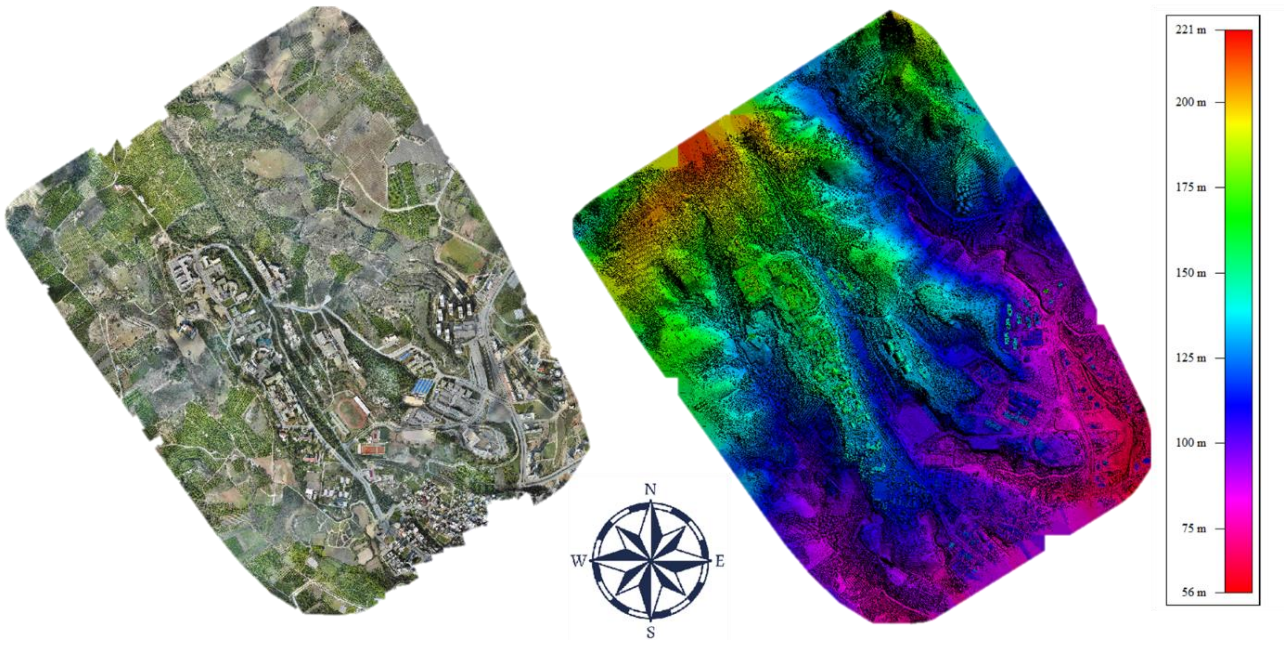

Figure 2. Orthomosaic (left) and DEM (right)

4. Conclusion

In this investigation, small-format digital camera data was processed using digital photogrammetric software. Digital orthophoto and digital maps were generated using digital photogrammetric software. The 3D stereoscopic model was quickly built with digital photogrammetric software. This study found that the most effective method for digital UAV mapping was using GPS from a fixed location with a 10-minute observation. This information demonstrates that the UAV when flying at 152m, achieved a precision of 1 m. A UAV is an invaluable tool when making a 3D model of a place, especially one with steep terrain. It was found that a UAV flying at 152m could successfully create the DEM and orthophoto, with the orthophoto having a planimetric accuracy of 2.5 cm. This study demonstrates that UAV systems can quickly and precisely capture DEM and provide high-quality mapping results. This study's methodology is applicable and valuable for high-resolution mapping of a compact area on a limited budget.

References

Alptekin, A., & Yakar, M. (2020). Determination of pond volume using an unmanned aerial vehicle. Mersin Photogrammetry Journal, 2(2), 59-63.

Alptekin, A., & Yakar, M. (2021). 3D model of Üçayak Ruins obtained from point clouds. Mersin Photogrammetry Journal, 3(2), 37-40.

Colomina, I., Blázquez, M., Molina, P., Parés, M. E. & Wis, M. (2008). Towards a New Paradigm for HighResolution Low-Cost Photogrammetry and Remote Sensing. IAPRS&SIS, 1201-1206.

Kanun, E., Alptekin, A., & Yakar, M. (2021a). Cultural heritage modelling using UAV photogrammetric methods: a Kanlıdivane archeological site case study. Advanced UAV, 1(1), 24-33.

Kanun, E., Metin, A., & Yakar, M. (2021b). Yersel Lazer Tarama Tekniği Kullanarak Ağzıkara Han'ın 3 Boyutlu Nokta Bulutunun Elde Edilmesi. Türkiye Lidar Dergisi, 3(2), 58-64.

Karataş, L., Alptekin, A., & Yakar, M. (2022a). Creating Architectural Surveys of Traditional Buildings with the Help of Terrestrial Laser Scanning Method (TLS) and Orthophotos: Historical Diyarbakır Sur Mansion. Advanced LiDAR, 2(2), 54-63.

Karataş, L., Alptekin, A., Kanun, E., & Yakar, M. (2022b). Tarihi kârgir yapılarda taş malzeme bozulmalarının İHA fotogrametrisi kullanarak tespiti ve belgelenmesi: Mersin Kanlıdivane ören yeri vaka çalışması. İçel Dergisi, 2(2), 41-49.

Karataş, L., Alptekin, A., Karabacak, A., & Yakar, M. (2022c). Detection and documentation of stone material deterioration in historical masonry buildings using UAV photogrammetry: A case study of Mersin Sarisih Inn. Mersin Photogrammetry Journal, 4(2), 53-61.

Korumaz, A. G., Dülgerler, O. N., & Yakar, M. (2012). Digital techniques in cultural heritage documentation. Selçuk University Journal of Engineering, Science and Technology.

Kusak, L., Unel, F. B., Alptekin, A., Celik, M. O., & Yakar, M. (2021). Apriori association rule and K-means clustering algorithms for interpretation of pre-event landslide areas and landslide inventory mapping. Open Geosciences, 13(1), 1226-1244.

Polat, N., Önal, M., Ernst, F. B., Şenol, H. İ., Memduhoğlu, A., Mutlu, S., Mutlu, S. İ., Budan, M. A., Turgut, M. & Kara, H. (2020). Harran Ören Yeri Arkeolojik Kazı Alanınından Çıkarılan Bazı Küçük Arkeolojik Buluntuların Fotogrametrik Olarak 3B Modellenmesi. Türkiye Fotogrametri Dergisi, 2 (2), 55-59.

Pulat, F., Yakar, M., & Ulvi, A. (2022). Comparison of photogrammetric software using the terrestrial photogrammetric method: The case of Hüsrev Paşa Mosque. Intercontinental Geoinformation Days, 4, 192-195.

Remondino, F., Barazzetti, L., Nex, F., Scaioni, M. & Sarazzi, D. (2011). UAV Photogrammetry for Mapping and 3D Modeling Current Status and Future Perspectives. ISPRS ICWG I/V UAV-g Conference, Zurich, Switzerland.

Şasi, A., & Yakar, M. (2017). Photogrammetric modelling of sakahane masjid using an unmanned aerial vehicle. Turkish Journal of Engineering, 1(2), 82-87.

Siebert, S.& Teizer, J. (2014). Mobile 3D Mapping for Surveying Earthwork Projects Using an Unmanned

Ulvi, A., Varol, F., & Yiğit, A. Y. (2019). 3D modeling of cultural heritage: the example of Muyi Mubarek Mosque in Uzbekistan (Hz. Osman's Mushafi). International Congress on Cultural Heritage and Tourism (ICCHT), 115-123, Bishkek, Kyrgzstan.

Ulvi, A., Yiğit, A. Y. & Yakar, M. (2019). Modeling of Historical Fountains by Using Close-Range Photogrammetric Techniques. Mersin Photogrammetry Journal, 1(1), 1-6.

Unal, M., Yakar, M., & Yildiz, F. (2004, July). Discontinuity surface roughness measurement techniques and the evaluation of digital photogrammetric method. In Proceedings of the 20th international congress for photogrammetry and remote sensing, ISPRS (Vol. 1103, p. 1108).

Ünel, F. B., Kuşak, L., Çelik, M., Alptekin, A., & Yakar, M. (2020). Kıyı çizgisinin belirlenerek mülkiyet durumunun incelenmesi. Türkiye Arazi Yönetimi Dergisi, 2(1), 33-40.

Yakar, M. & Dogan, Y. (2018). 3D Reconstruction of Residential Areas with SfM Photogrammetry. In Conference of the Arabian Journal of Geosciences, 73-75.

Yakar, M., & Doğan, Y. (2017). Uzuncaburç Antik Kentinin İHA Kullanılarak Eğik Fotogrametri Yöntemiyle Üç Boyutlu Modellenmesi. 16. Türkiye Harita Bilimsel ve Teknik Kurultayı. TMMOB Harita ve Kadastro Mühendisleri Odası, Ankara.

Yakar, M., Orhan, O., Ulvi, A., Yiğit, A. Y., & Yüzer, M. M. (2015). Sahip Ata Külliyesi Rölöve Örneği. TMMOB Harita ve Kadastro Mühendisleri Odası, 10.

Yakar, M., Toprak, A. S., Ulvi, A., & Uysal, M. (2015). Konya Beyşehir Bezariye Haninin (Bedesten) İHA ile fotogrametrik teknik kullanilarak üç boyutlu modellenmesi. Türkiye Harita Bilimsel ve Teknik Kurultayı, 25, 28.

Yakar, M., Ulvi, A., Yiğit, A. Y., & Alptekin, A. (2022). Discontinuity set extraction from 3D point clouds obtained by UAV Photogrammetry in a rockfall site. Survey Review, 1-13.

Yakar, M., Yılmaz, H. M., & Mutluoglu, O. (2014). Performance of photogrammetric and terrestrial laser scanning methods in volume computing of excavation and filling areas. Arabian Journal for Science and Engineering, 39, 387-394. https://doi.org/10.1007/s13369-013-0853-1

Yilmaz, H. M., & Yakar, M. (2006a). Lidar (Light Detection And Ranging) Tarama Sistemi. Yapı Teknolojileri Elektronik Dergisi, 2(2), 23-33.

Yilmaz, H. M., & Yakar, M. (2006b). Yersel lazer tarama Teknolojisi. Yapı teknolojileri Elektronik dergisi, 2(2), 43-48.

6th Intercontinental Geoinformation Days

igd.mersin.edu.tr

Utilizing UAVs for rapid spatial data acquisition in disaster management: A case study of Islahiye

Casım Öncel*[1], Bünyamin Ataş [1], Nurullah Börü [1], Nizar Polat [1]

[1]*HarranUniversity, Geomatics Engineering Department, Şanlıurfa, Türkiye*

Keywords
Earthquakes
Landslide
UAV
Photogrammetry
DEM

Abstract

This study investigates the application of unmanned aerial vehicles (UAVs) for swift spatial data acquisition in disaster management. Specifically, the focus is on monitoring a landslide and the resulting lake formation in the Islahiye district of Gaziantep, Turkey, subsequent to the Kahramanmaraş earthquakes. Using UAVs, orthophotos and elevation models were generated, enabling accurate visual representations of the affected area. Through data analysis, the landslide volume was estimated at approximately 549,183.8 cubic meters, with the water area of the formed lake measuring approximately 26,731.6 square meters. The findings underscore the value of UAVs as efficient and cost-effective tools for acquiring real-time and precise spatial data in different disaster management stages. UAVs prove advantageous for pre-disaster monitoring, prediction, early warning systems, as well as post-disaster search and rescue operations and recovery endeavors. This study contributes to the existing knowledge on UAVs in disaster management, demonstrating their crucial role in assessing the impact of natural disasters and guiding subsequent response and recovery actions. The calculated values of landslide volume and water area provide essential quantitative information for understanding the magnitude of the event and facilitating appropriate measures. Moreover the study demonstrates the valuable role of UAVs in disaster management by providing real-time and precise spatial data. UAVs prove advantageous for monitoring, early warning systems, search and rescue operations, and recovery endeavors. The findings contribute to our understanding of the impact of natural disasters and aid in guiding appropriate response and recovery actions.

1. Introduction

In today's world, any kind of natural, technological, and human-induced events that we cannot cope with using local resources are referred to as disasters. According to the definition accepted by the United Nations, a disaster is defined as "any natural, technological, or human-induced event that causes physical, economic, and social losses for people, disrupts or interrupts normal life, affects societies, and cannot be managed with local resources" (Kadıoğlu 2008). Our country, particularly Turkey, is constantly exposed to natural disasters such as earthquakes, landslides, and floods, which cause the most loss of life and property (Alptekin and Yakar 2020a; Kusak et al. 2021). Natural disaster causes damage to the surrounding lands, settlements and living creatures by not fitting the amount of water in the riverbed for various reasons (Demir 2021).

The most critical issue during a disaster is the rescue of people alive. Therefore, the first 72 hours after a disaster is a highly critical period that requires rapid and efficient search and rescue operations. In recent years, there has been an increasing demand for low-cost, small unmanned aerial vehicles (UAVs) for various purposes and applications (Alptekin and Yakar 2020b). UAVs are defined as "motorized aerial vehicles that can be remotely controlled autonomously or semi-autonomously without a human pilot, depending on the mission, capable of carrying different payloads and performing specialized tasks within a specific time interval, either in the atmosphere or outside of it, and are reusable" (Blyenburgh 1999; Erdelj 2017; Yakar and Dogan 2017). The first attempts for photogrammetric

* **Corresponding Author**

*(casmoncell@gmail.com) ORCID ID 0009-0000-7952-5827
(bunyaminatas16@hotmail.com) ORCID ID 0009-0003-7699-1664
(nrllhbr21@gmail.com) ORCID ID 0009-0006-9305-5490
(nizarpolat@harran.edu.tr) ORCID ID 0000-0002-6061-7796

Cite this study

Öncel, C., Ataş, B., Börü, N., & Polat, N. (2023). Utilizing UAVs for Rapid Spatial Data Acquisition in Disaster Management: A Case Study of Islahiye. Intercontinental Geoinformation Days (IGD), 6, 130-133, Baku, Azerbaijan

purposes with UAVs were made in 1979 (Eisenbeiss 2009) Nowadays, unmanned aerial vehicles are widely and effectively used in various fields, ranging from defense to entertainment. They are preferred as data acquisition platforms in documenting cultural heritage, archaeological studies, 3D modeling, and many other areas, especially in small areas (Uysal et al. 2017).

Unmanned aerial vehicles are used in different stages of disaster management. Generally, UAVs are used in the following areas in disaster management (Uysal et al. 2013).

- The usage of UAVs in monitoring, prediction, and early warning. UAVs are used for analyzing information for environmental monitoring and prediction, as well as for early warning purposes.
- Integration and sharing of disaster information. UAVs support other applications by bridging different information technologies or consolidating available information from various sources.
- Usage for situational awareness, logistics, and evacuation support. UAVs can assist in collecting information during a disaster, especially about affected individuals and the movements of rescue teams.
- Supporting communication systems. UAVs can help rebuild communication infrastructure that has been destroyed or damaged during a disaster.
- Search and rescue operations. UAVs can be utilized in the search and rescue of missing, injured, and trapped individuals.
- Damage assessment. UAVs can assist in assessing damage using video and imagery.

UAVs can be used for various purposes in disaster management. They offer significant opportunities for rapid and effective utilization in search and rescue operations. However, the proper and up-to-date base maps are required for conducting pre and post-disaster activities. While satellite imagery provides current data, obtaining timely and high-accuracy data is not always possible. UAVs provide valuable contributions to rapid and up-to-date data collection (Yiğit and Uysal 2019). It is necessary to determine the accuracy of the products obtained from these low-cost systems. The aim of this study is to monitor the landslide and the resulting ponding after the earthquake that occurred on February 6, 2023 in Turkey, and to produce a 3D model of the region.

As it is known, earthquakes occurred in Turkey on February 6, 2023, centered in Kahramanmaraş. Many destructions and landslides occurred with the earthquake. One of these landslides occurred in the Islahiye district of Gaziantep. Roads were closed due to landslides and a pond was formed in the area. In this study, the latest situation in the landslide region and the ponding that occurred in the region were monitored by UAV.

2. Method

This section delves into three key aspects of the study: UAV deployment, data collection methods, and UAV photogrammetry techniques, all focused on the specific study area of the landslide and lake formation in the Islahiye district of Gaziantep, Turkey.

Since the study area is mountainous and carries a risk of landslides, it was really difficult to reach the area. Since the landslide is towards a valley, water accumulation has also occurred in the region (Figure 1). For this reason, the relevant area carries more risks.

Figure 1. A general view of landslide area

The DJI Mavic 2 Pro is a successful system with features such as an effective range of 8 km, a maximum flight time of 31 minutes, 4K recording with a Hasselblad camera, a 1" CMOS sensor, GPS sensor, 4-way obstacle sensing, automatic return to home, and a weight of approximately 1 kg. The UAV used in the study is depicted in Figure 2.

Figure 2. DJI Mavic 2 Pro UAV

A photogrammetric flight plan covering 0.349 km^2 area was made and a total of 180 aerial photographs were taken with 80% overlap. After obtaining the aerial photographs, it is necessary to process them photogrammetrically and to obtain photogrammetric products that will meet the needs. At this point, unlike classical photogrammetry, the motion-based detection (Structure from Motion -SfM) approach is widely used in UAV photogrammetry. SfM operates under the same basic conditions as photogrammetry. It uses overlapping images to obtain the 3D structure of the object of interest. SfM allows to produce many products such as matching photos, generating sparse and dense point cloud, three-dimensional model, digital elevation model and orthophoto. Image processing steps can take serious time. For this reason, it is highly recommended to use high-performance computers for full software performance. Many commercial software such as Agisoft are widely used in studies using SfM.

3. Results

Aerial photographs taken within the scope of the study were processed with the SfM approach. The first product obtained in this context is the sparse point cloud. Photographs connected by 326 298 points in total were stabilized to produce a dense point cloud. Dense point cloud with 157 965 014 point gives us all the details we took in the photo in three dimensions (Figure 3).

Figure 3. UAV based photogrammetric dense point cloud

Using the 3D information we obtained, we produced the digital elevation model of the region and the high resolution orthophoto behind it (Figure 4).

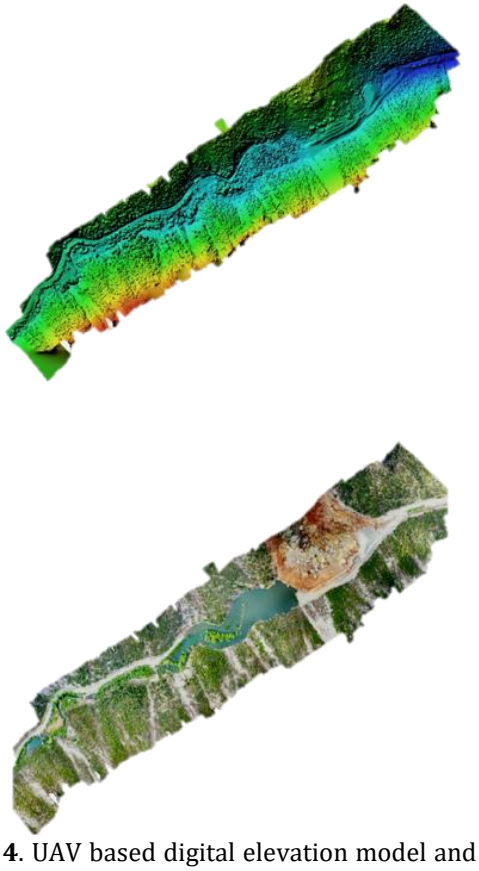

Figure 4. UAV based digital elevation model and the high resolution orthophoto of the region

4. Discussion

Some analyzes related to the study area were made. First, a sample profile of the soil pile was obtained (Figure 5). According to the profile study obtained, the height difference within a distance of 300 meters reaches 40 meters.

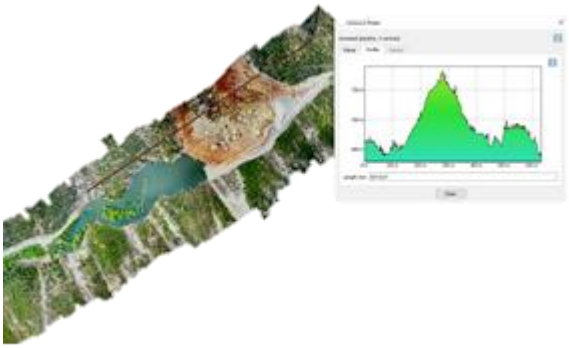

Figure 5. Investigation profile of landslide

Calculation of the approximate volume of the soil pile the spread area of the landslide was determined manually and the approximate volume was calculated using the best fit plane (Figure 6). Accordingly, the volume of 549183.8 cubic meters of soil was calculated in an area of 928 612 square meters.

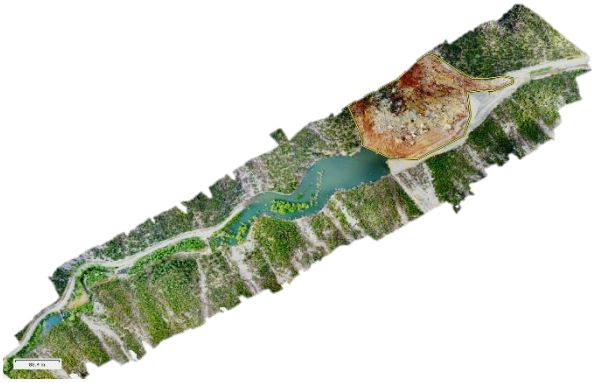

Figure 6. Calculation of the approximate volume and the spread area of the landslide

The pond area formed in the area closed as a result of the landslide was also observed with the obtained orthophoto (Figure 7). According to the calculation made, the water area is 26731.6 square meters.

Figure 7. Calculation of the approximate area of formed pond

5. Conclusion

Orthophoto, which form the basis of many engineering projects, are essential for effective and successful disaster management. In disaster management, there is a need for fast and accurate spatial data. The use of UAVs as data acquisition platforms for obtaining real-time, accurate, and reliable data is increasing in disaster management. Unmanned aerial vehicles provide significant convenience in the production of necessary spatial data in different stages of disaster management. They enable the rapid and accurate acquisition of spatial data required for monitoring work processes, prediction, and early warning during the pre-disaster stage, as well as for risk and damage reduction and preparedness. The use of UAVs in the post-disaster phase facilitates fast and efficient search and rescue operations and recovery efforts. In this study, an orthophoto and elevation model of the landslide and lake formation area that occurred after the Kahramanmaraş earthquakes was produced by using UAV, and the approximate volume (549183.8 m3) and area (928 612 m2) calculations of the landslide and the pond area (26731.6 m2) were made.

References

Alptekin, A., & Yakar, M. (2020). Heyelan bölgesinin İHA kullanarak modellenmesi. Türkiye İnsansız Hava Araçları Dergisi, 2(1), 17-21.

Alptekin, A., & Yakar, M. (2020a). Determination of pond volume with using an unmanned aerial vehicle. Mersin Photogrammetry Journal, 2(2), 59-63.

Alptekin, A., & Yakar, M. (2020b). Heyelan bölgesinin İHA kullanarak modellenmesi. Türkiye İnsansız Hava Araçları Dergisi, 2(1), 17-21.

Alptekin, A., & Yakar, M. (2021). 3D model of Üçayak Ruins obtained from point clouds. Mersin Photogrammetry Journal, 3(2), 37-40.

Alptekin, A., Çelik, M. Ö., Doğan, Y., & Yakar, M. (2019). Mapping of a rockfall site with an unmanned aerial vehicle. Mersin Photogrammetry Journal, 1(1), 12-16.

Bünyan Ünel, F., Kuşak, L., Çelik, M., Alptekin, A., & Yakar, M. (2020). Kıyı Çizgisinin Belirlenerek Mülkiyet Durumunun İncelenmesi. Türkiye Arazi Yönetimi Dergisi, 2 (1), 33-40.

Demir, V., Alptekin, A., Çelik, M. Ö., & Yakar, M. (2021). 2D Flood modeling with the help of GIS: Mersin/Lamas River. Intercontinental Geoinformation Days, 2, 175-178.

Eisenbeiss, H. (2009). UAV Photogrammetry, Doctor of Sciences, ETH Zurich, Switzerland

Erdelj, M., Natalizio, E., Chowdhury, K. R., & Akyildiz, I. F. (2017). Help from the sky: Leveraging UAVs for disaster management. IEEE Pervasive Computing, 16(1), 24-32.

Kadıoğlu, M. (2008). Afet Zararlarını Azaltmanın Temel İlkeleri, 1-34, JICA Türkiye Ofisi Yayınları No: 2, Ankara.

Kanun, E., Alptekin, A., & Yakar, M. (2021). Documentation of cultural heritage by photogrammetric methods: a case study of Aba's Monumental Tomb. *Intercontinental Geoinformation Days*, *3*, 168-171.

Karataş, L., Alptekin, A., Kanun, E., & Yakar, M. (2022). Tarihi kârgir yapılarda taş malzeme bozulmalarının İHA fotogrametrisi kullanarak tespiti ve belgelenmesi: Mersin Kanlıdivane ören yeri vaka çalışması. İçel Dergisi, 2(2), 41-49.

Kusak, L., Unel, F. B., Alptekin, A., Celik, M. O., & Yakar, M. (2021). Apriori association rule and K-means clustering algorithms for interpretation of pre-event landslide areas and landslide inventory mapping. Open Geosciences, 13(1), 1226-1244.

Mirdan, O., & Yakar, M. (2017). Tarihi eserlerin İnsansız Hava Aracı ile modellenmesinde karşılaşılan sorunlar. Geomatik, 2(3), 118-125.

Tükenmez, F., & Yakar, M. (2023). Production of road maps in highway projects by unmanned aerial vehicle (UAV). *Advanced Engineering Days (AED)*, *6*, 94-96.

Uysal, M., Toprak, A. S., & Polat, N. (2013). Photo Realistic 3D Modeling with UAV: Gedik Ahmet Pasha Mosque in Afyonkarahisar, CIPA 2013 Symposium, 3-6 September 2013, 659-662.

Uysal, M., Yılmaz, Y., Tiryakioğlu, İ., & Polat, N. (2017). İnsansız Hava Araçlarının Afet Yönetiminde Kullanımı. 4. Uluslararası Deprem Mühendisliği ve Sismoloji Konferansı, 44-47.

Van Blyenburgh, P. (1999). UAVs: an overview. Air and Space Europe, 1(5), 43-47.

Villi, O., & Yakar, M. (2022). İnsansız Hava Araçlarının Kullanım Alanları ve Sensör Tipleri. Türkiye İnsansız Hava Araçları Dergisi, 4(2), 73-100.

Yakar, M., & Doğan, Y. (2017). Uzuncaburç Antik Kentinin İHA Kullanılarak Eğik Fotogrametri Yöntemiyle Üç Boyutlu Modellenmesi. 16. Türkiye Harita Bilimsel ve Teknik Kurultayı. TMMOB Harita ve Kadastro Mühendisleri Odası, Ankara.

Yakar, M., Ulvi, A., Yiğit, A. Y., & Alptekin, A. (2022). Discontinuity set extraction from 3D point clouds obtained by UAV Photogrammetry in a rockfall site. Survey Review, 1-13

Yiğit, A., & Uysal, M. (2019). Afet yönetiminde uzaktan algilamanin kullanimi. In İdRc 2019 İnternational Disaster & Resilience Congress (Vol. 26, p. 28).

Yüksel, G., Ulvi, A., & Yakar, M. (2022). Usage of unmanned aerial vehicles in open mine sites. *Intercontinental Geoinformation Days*, *4*, 13-16.

6th Intercontinental Geoinformation Days

igd.mersin.edu.tr

Generating a thermal index map with unmanned aerial vehicles (UAVs) with thermal sensors

Yunus Kaya*[1], Abdulkadir Memduhoğlu [1] Nizar Polat [1]

[1]*Harran University, Faculty of Engineering, Department of Geomatics Engineering, Şanlıurfa, Türkiye*

Keywords
UAV
Photogrammetry
Thermal camera
Index map

Abstract

Unmanned Aerial Vehicles (UAVs) are more advantageous than traditional methods in terms of high-resolution imaging, low cost, and time. With the thermal camera placed on the UAV, the temperature reflectance values of large areas can be obtained more easily. This study produced a detailed thermal index map showing the potential of this approach with the preliminary applications using DJI Mavic 3 Pro T UAV at Harran University Osmanbey campus. Thermal index maps can be used to identify areas with different thermal properties and to detect environmental changes. Since the processing of thermal photographs does not yet allow for map production in terms of software, these images are processed with remote sensing and photogrammetric methods to obtain a thermal index map. This approach can also be used in many areas, such as urban planning, building energy efficiency assessments, and agriculture. This study investigated the effectiveness of UAVs with thermal cameras for mapping activities and many different application potentials, and preliminary results of thermal index map production studies conducted at Harran University Osmanbey campus were presented.

1. Introduction

The increasing focus on sustainable development and climate protection highlights the important role of cities in promoting energy efficiency and empowerment strategies. To achieve these goals, it is necessary to determine and analyze the thermal quality of existing structures, especially at the regional scale. The New Urban Agenda, announced by the United Nations in 2016, highlights the key role of cities in promoting sustainable development and climate protection in the building sector (UN, 2017).

Classical thermography studies examining the thermal conditions of large areas use handheld cameras at eye level to obtain high-quality thermographic images (Lucchi, 2018). However, terrestrial thermography cameras provide disadvantages in terms of time and cost in cases where many buildings at various heights and large areas need to be studied. In addition, components of buildings, such as roofs and upper floors, cannot be perceived by terrestrial methods.

Aerial photogrammetry allows us to create digital products in a short time. (Alptekin, A., & Yakar, M. (2021)Unmanned Aerial Vehicles (UAVs) have become practical imaging tools that have recently become widespread and used in many studies.(Yakar, M., & Doğan, Y. (2017), Alptekin, A., & Yakar, M. (2020).Advances in unmanned aerial vehicle (UAV) technologies have made it easier to model engineering projects Alptekin, A. & Yakar, M. (2020).In many projects The orthophoto of the region was created by unmanned aerial vehicle(Kusak et all. 2021, Yakar, M., & Doğan, Y. (2017). The UAV photogrammetry method was used to create the 3D point data and solid model (Karatas, et. al. 2022, Yakar, M., & Kocaman, (2018).

UAVs, which have found their place in many areas of use in the recent past, are also successfully used in ground observation applications, including energy transmission lines (Hartmut et al., 2020), gas and oil pipelines (Rathinam et al., 2005), agriculture (Honkavaara et al., 2013) and bridges (Metni and Hamel, 2007). Thanks to their small size, multi-rotor UAVs can move freely in the air, be easily controlled, and be easily used in many places. In addition, different sensors placed on the UAV allow more information to be collected. (Alptekin et al., 2019, Kanun et al., 2021, Şasi and Yakar (2017). While systems such as GPS and IMU placed in the UAV system ensure the correct positioning of the data obtained from the UAV, data in different formats can be

* **Corresponding Author**

*(yunuskaya@harran.edu.tr) ORCID ID 0000-0003-2319-4998
(akadirm@harran.edu.tr) ORCID ID 0000-0002-9072-869X
(nizarpolat@harran.edu.tr) ORCID ID 0000-0002-6061-7796

Cite this study

Kaya Y, Memduhoğlu A & Polat N (2023). Generating a thermal index map with unmanned aerial vehicles (UAVs) with thermal sensors. 7th Intercontinental Geoinformation Days (IGD), 6, 134-137, Baku, Azerbaijan.

collected thanks to the red, green, and blue camera (RGB), multispectral sensors, and thermal sensors.

Although various kinds of research are trying to determine the thermal values in large areas and building inspections (Vollmer and Möllmann, 2010) through thermal UAV images, there are gaps in the literature regarding the processing of thermal UAV data. This study created a detailed thermal index map showing the potential of thermal UAV data by making a sample application at Harran University Osmanbey campus. In order to determine the areas with different thermal properties and to detect environmental changes, the thermal data obtained from the UAV data were evaluated by remote sensing and photogrammetry methods, and a thermal index map was created.

2. Method and Application

DJI Mavic 3 Pro T was equipped with a thermal camera to determine the temperature difference on different surfaces, such as water, vegetation, shade, and soil in the study area. Before the aerial inspection, a visual survey was performed to determine flight height relative to observed building heights to plan a crash-safe flight mission. The mission was carried out as a planned flight with the help of Pix4D Capture software. The measurement was done at 10:00 on 15 May 2023 in one go. The aerial survey was conducted with a UAV equipped with a thermal and RGB camera that captured 4682 images (2341 thermal and 2341 RGB images). The flight altitude was 40 meters from the take-off point, and the overlap rate was 90%. The area of 4.8 hectares was measured in approximately 35 minutes. Although there is a temperature scale on the photographs taken from UAV, images can be exported in 0-255 radiometric scale. In order to transfer the temperature values read from the photographs to the orthophoto, the minimum, and maximum temperature values were determined using an experimental method. A radiometric scale from 0-255 was converted to minimum and maximum temperature values with linear contrast stretch. As a result of the study, the values obtained from the orthomosaic and the values obtained from the source photographs were compared. The flow chart of the study is given in Figure 1.

3. Results and Discussion

RGB and thermal data obtained from the UAV flight were used to examine the temperature reflectance values of areas with different characteristics on the campus. First, orthomosaic was produced by the photogrammetric process (Figure 2).

Although there is a temperature scale on the photos taken from UAV, images can be exported in 0-255 radiometric scale. For this reason, the temperature information cannot be read on the produced orthomosaic. In order to eliminate this uncertainty, the minimum and maximum temperature values in the orthomosaic were determined with samples taken from different points in the orthomosaic. For this, the minimum (16.9 °C) and maximum (52.7 °C) temperature values in the study area were determined empirically via DJI Thermal Analysis Tool. 0-255 values were converted to 16.9-52.7 values by applying linear contrast stretch. In order to determine the difference between the temperature information read on the orthomosaic and the temperature information read on the photo, samples from the green area, water, and shadow areas were compared (Table 1). The temperature values in the orthomosaic were determined from the ENVI software, and the temperature values on the photo were determined from the DJI Thermal Analysis Tool.

When Table 1 is examined, it is seen that the temperature difference is higher on the water surfaces. The temperature difference between the two data in the green area is the least. Reflection, sun exposure time, and angle will affect the results.

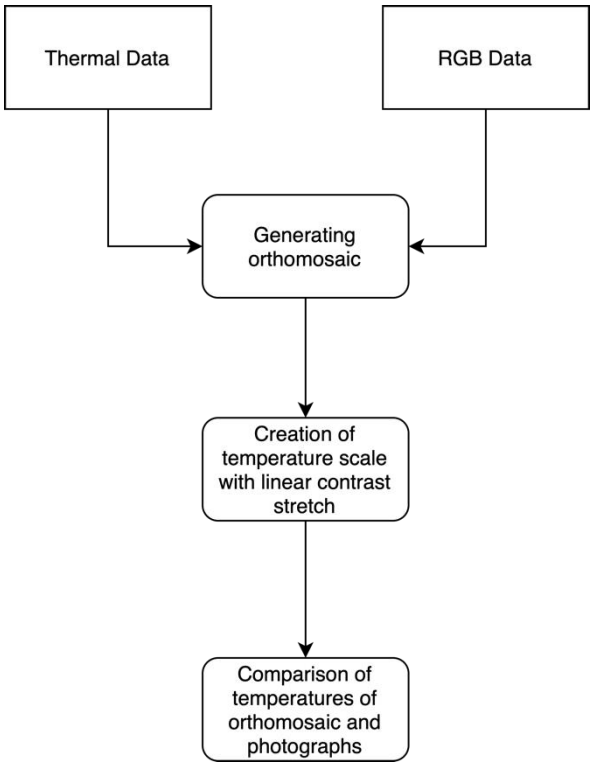

Figure 1. Workflow

Table 1. Orthomosaic and photographic temperature differences on different surface types

Surface Type	Temperature value in orthomosaic (°C)	Temperature value in the photo (°C)	Difference (°C)
Water (Lake)	19,8	21,2	1,4
Vegetation	20,2	20,3	0,1
Shadow	19,8	19,0	0,8

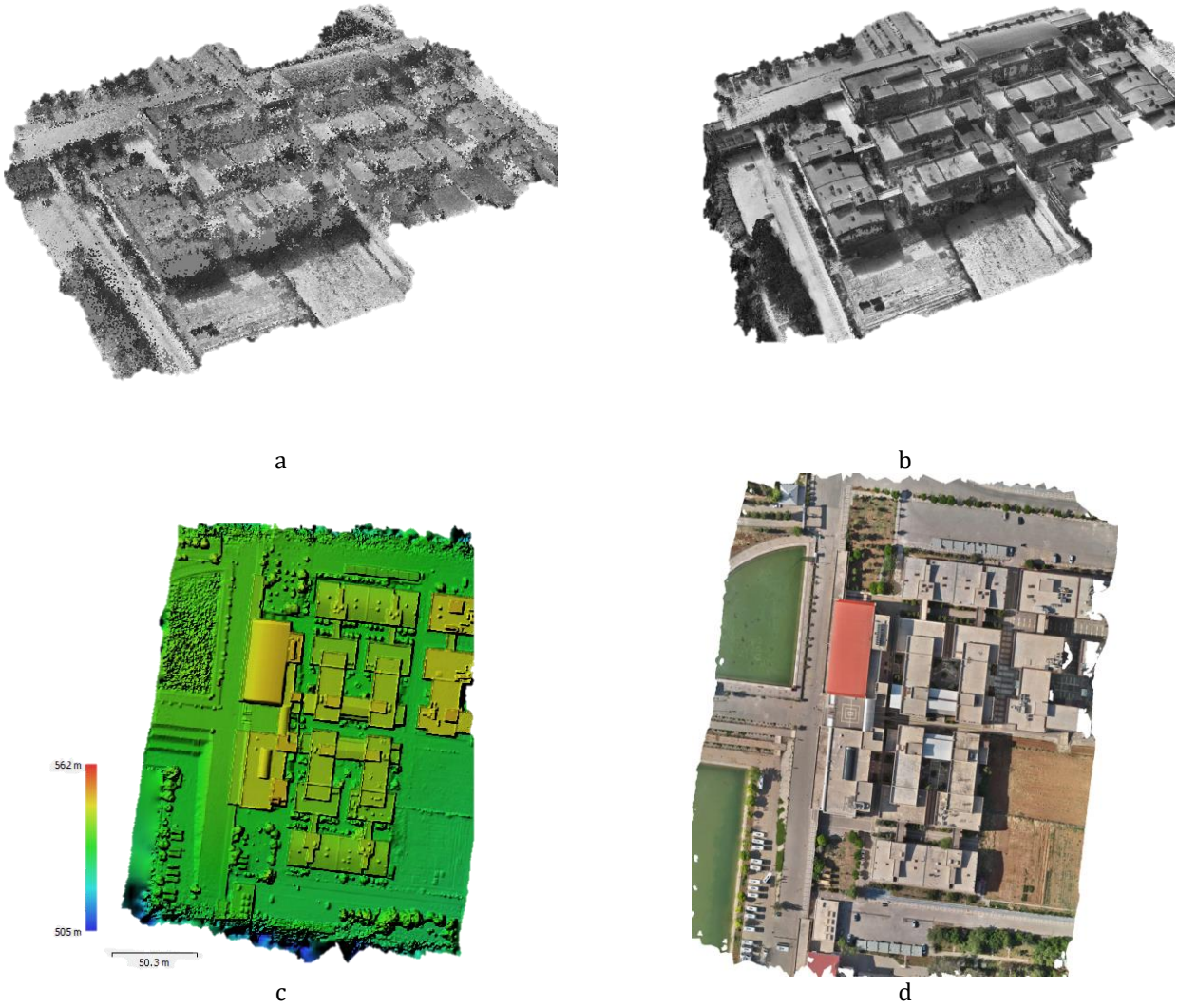

Figure 2. a) Point cloud, b) Dense point cloud, c) Digital Elevation Model, d) Orthomosaic

4. Conclusion

This study presents a method and application example for generating thermal index maps from UAV data with the thermal camera. It is unknown whether the negative aspects of the method used in the study are the same as the point determined on orthomosaic and the photo point used in orthomosaic production. In addition, among the study's shortcomings, it was not determined how much the photo shooting hours would affect the temperature. In future studies, the data obtained at different times of the day will be compared on different surface types, and a more comprehensive analysis will be carried out.

References

Alptekin, A., & Yakar, M. (2020). Determination of pond volume with using an unmanned aerial vehicle. *Mersin photogrammetry journal*, *2*(2), 59-63.

Alptekin, A., & Yakar, M. (2020). Heyelan bölgesinin İHA kullanarak modellenmesi. Türkiye İnsansız Hava Araçları Dergisi, 2(1), 17-21.

Alptekin, A., & Yakar, M. (2021). 3D model of Üçayak Ruins obtained from point clouds. Mersin Photogrammetry Journal, 3(2), 37-40.

Alptekin, A., Çelik, M. Ö., Doğan, Y., & Yakar, M. (2019). Mapping of a rockfall site with an unmanned aerial vehicle. Mersin Photogrammetry Journal, 1(1), 12-16.

Honkavaara, E., Saari, H., Kaivosoja, J., Pölönen, I., Hakala, T., Litkey, P., Mäkynen, J., & Pesonen, L. (2013). Processing and Assessment of Spectrometric, Stereoscopic Imagery Collected Using a Lightweight UAV Spectral Camera for Precision Agriculture. Remote Sensing, 5, 5006–5039.

Kanun, E., Alptekin, A., & Yakar, M. (2021). Cultural heritage modelling using UAV photogrammetric methods: a case study of Kanlıdivane archeological site. Advanced UAV, 1(1), 24-33.

Kanun, E., Alptekin, A., Karataş, L., & Yakar, M. (2022). The use of UAV photogrammetry in modeling ancient structures: A case study of "Kanytellis". *Advanced UAV*, *2*(2), 41-50.

Karataş, L., Alptekin, A., & Yakar, M. (2022). Detection and documentation of stone material deterioration in historical masonry structures using UAV photogrammetry: A case study of Mersin Aba Mausoleum. *Advanced UAV*, *2*(2), 51-64.

Karataş, L., Alptekin, A., Kanun, E., & Yakar, M. (2022). Tarihi kârgir yapılarda taş malzeme bozulmalarının İHA fotogrametrisi kullanarak tespiti ve belgelenmesi: Mersin Kanlıdivane ören yeri vaka çalışması. İçel Dergisi, 2(2), 41-49.

Kusak, L., Unel, F. B., Alptekin, A., Celik, M. O., & Yakar, M. (2021). Apriori association rule and K-means clustering algorithms for interpretation of pre-event landslide areas and landslide inventory mapping. Open Geosciences, 13(1), 1226-1244.

Lucchi, E. (2018). Applications of the infrared thermography in the energy audit of buildings: a review. Renewable and Sustainable Energy Reviews, 82, 3077–3090. doi: 10.1016/j.rser.2017.10.031.

Metni, N., & Hamel, T. (2007). A UAV for bridge inspection: Visual servoing control law with orientation limits. *Automation in construction*, *17*(1), 3-10.

Mirdan, O., & Yakar, M. (2017). Tarihi eserlerin İnsansız Hava Aracı ile modellenmesinde karşılaşılan sorunlar. *Geomatik*, *2*(3), 118-125.

Mohammed, O., & Yakar, M. (2016). Yersel fotogrametrik yöntem ile ibadethanelerin modellenmesi. *Selçuk-Teknik Dergisi*, *15*(2), 85-95.

Rathinam, S., Kim, Z., Soghikian, A., & Sengupta, R. (2005). Vision-Based Following of Locally Linear Structures using an Unmanned Aerial Vehicle. 44th IEEE Conference on Decision and Control, Seville, Spain, 15 December 2005, 6085–6090.

Surmann, H., Holz, D., Blumenthal, S., Linder, T., Molitor, P., & Tretyakov, V. (2008). Teleoperated visual inspection and surveillance with unmanned ground and aerial vehicles. *International Journal of Online and Biomedical Engineering*, *4*(4), 26-38.

Şasi, A., & Yakar, M. (2017). Photogrammetric modelling of sakahane masjid using an unmanned aerial vehicle. *Turkish Journal of Engineering*, *1*(2), 82-87.

UN. (2017). New urban agenda United Nations Conf. on Housing and Sustainable Urban Development (Quito, Ecuador). ISBN: 978-92-1-132731-1

Ünel, F. B., Kuşak, L., Çelik, M., Alptekin, A., & Yakar, M. (2020). Kıyı çizgisinin belirlenerek mülkiyet durumunun incelenmesi. *Türkiye Arazi Yönetimi Dergisi*, *2*(1), 33-40.

Villi, O., & Yakar, M. (2022). İnsansız Hava Araçlarının Kullanım Alanları ve Sensör Tipleri. *Türkiye İnsansız Hava Araçları Dergisi*, *4*(2), 73-100.

Vollmer, M., & Möllmann, K. P. (2010) Infrared Thermal Imaging (Weinheim, Germany: Wiley– VCH). ISBN: 978-3-527-41351-5.

Yakar, M., & Dogan, Y. (2019). 3D Reconstruction of Residential Areas with SfM Photogrammetry. In *Advances in Remote Sensing and Geo Informatics Applications: Proceedings of the 1st Springer Conference of the Arabian Journal of Geosciences (CAJG-1), Tunisia 2018* (pp. 73-75). Springer International Publishing.

Yakar, M., & Doğan, Y. (2017). Mersin Silifke Mezgit Kale Anıt Mezarı fotogrametrik rölöve alımı ve üç boyutlu modelleme çalışması. *Geomatik*, *2*(1), 11-17.

Yakar, M., & Doğan, Y. (2017). Uzuncaburç Antik Kentinin İHA Kullanılarak Eğik Fotogrametri Yöntemiyle Üç Boyutlu Modellenmesi. 16. Türkiye Harita Bilimsel ve Teknik Kurultayı. TMMOB Harita ve Kadastro Mühendisleri Odası, Ankara.

Yakar, M., & Kocaman, E. (2018). Kayseri-Sahabiye Medresesi 3-boyutlu modelleme çalışması ve animasyonu. *International Journal of Engineering Research and Development*, *10*(1), 133-138.

6th Intercontinental Geoinformation Days

igd.mersin.edu.tr

Documenting historical buildings using high-resolution photographs obtained with smartphones: The Case of Latifiye (Abdullatif) Mosque, Mardin/Türkiye

Lale Karataş*[1], Murat Dal [2], Aydın Alptekin [3], Murat Yakar [4]

[1]*Mardin Artuklu University, Department of Architecture and Urban Planning, Türkiye*
[2]*Munzur University, Department of Architecture, Türkiye*
[3]*Mersin University, Faculty of Engineering, Department of Geological Engineering, Türkiye*
[4]*Mersin University, Faculty of Engineering, Department of Geomatics Engineering, Türkiye*

Keywords
Smartphones
Photogrammetry
3DF Zephyr
Dense Point Cloud
Orthophoto

Abstract

In today's context, the use of technology has become increasingly widespread in the process of gathering, processing, documenting, and presenting data obtained through photogrammetry. Advancements in technology have made it easier to digitally document historical artifacts using photogrammetric methods. Traditional measurement techniques, laser scanning, and photogrammetry, or combinations of these methods, are commonly used in the documentation of historical artifacts. In this study, the focus was on the application of close-range photogrammetry, a subfield of photogrammetry, using the non-metric cameras of smartphones that we frequently use in our daily lives. The three-dimensional images of Mardin Latifiye Mosque were obtained using photographs captured with smartphones. Additionally, a panoramic view of the mosque was created, allowing for the examination of materials and material deterioration. Archaeological data was added to the obtained images, and all the work conducted in the area was made accessible through a web platform. This article provides a detailed explanation of the methods followed at every stage to generate three-dimensional models from smartphones. It also describes the necessary processes to create 360-degree panoramic images.

1. Introduction

Although laser scanning provides a faster technique for obtaining point cloud data, photogrammetric methods have gained prominence due to their economic nature, accessibility, portability, and the fact that they do not require specialized expertise (Kanun et al., 2022). Photogrammetry, particularly the production of three-dimensional (3D) models from two-dimensional (2D) photographs taken with non-metric cameras, stands out as the most widely used technique (Karataş & Menteşe, 2022).

Architectural and structural features, geometric shapes, and accurate information about materials are crucial foundations for the restoration of historical artifacts (Karataş & Dal, 2023). Therefore, documenting historical artifacts and monitoring their deformations are of vital importance (Karataş et al., 2022a). Measuring a structure using traditional methods can be costly and time-consuming, particularly when accessing and measuring the higher parts of the structure is challenging. Remote sensing and photogrammetric methods can be employed for this purpose (Karataş et al., 2022b). The integration of non-metric cameras into smartphones has made it possible to utilize photographic data obtained from them for photogrammetric evaluations (Karataş et al., 2022c). With the advent of smartphones in this field, access to data collection tools has reached a high level. As data collection materials have advanced, many individuals have started using the photogrammetry technique with photographic data obtained from smartphones (Karataş et al., 2022d).

In parallel with advancing technology, photogrammetry now utilizes images produced with cameras or videos, as well as electronically recorded images with scanners, instead of relying solely on traditional photographs. There are a limited number of studies in the literature that aim to investigate the overall

* **Corresponding Author**

*(lalekaratas@artuklu.edu.tr) ORCID ID 0000-0001-8582-4612
(muratdal@munzur.edu.tr) ORCID ID 0000-0001-5330-1868
(aydinalptekin@mersin.edu.tr)ORCID ID 0000-0002-5605-0758
(myakar@mersin.edu.tr) ORCID ID 0000-0002-2664-6251

Cite this study

Karataş, L., Dal, M., Alptekin, A., & Yakar, M. (2023). Documenting historical buildings using high-resolution photographs obtained with smartphones: The Case of Latifiye (Abdullatif) Mosque, Mardin/Türkiye. Intercontinental Geoinformation Days (IGD), 6, 138-142, Baku, Azerbaijan

photogrammetric accuracy of smartphones. The results of these studies demonstrate that smartphones can be used in digital photogrammetry (Wrózynski et al., 2017; Dabove et al., 2019; Yilmazturk & Gurbak, 2019).

The presented paper describes the generation of three-dimensional images of Mardin Latifiye Mosque using photographs captured with smartphones. Additionally, a panoramic view of the mosque was created, allowing for the examination of materials and material deterioration. Archaeological data was integrated into the obtained images, and all the work conducted in the field was made accessible through a web platform. The article provides explanations of the methods followed at every stage for generating three-dimensional models from smartphones and describes the necessary procedures for producing 360-degree panoramic images.

1.1. The location, history, and significance of the structure.

The mosque, known as Latifiye Mosque in the local community, bears the characteristics of Artukid mosque architecture. It is located south of Cumhuriyet Square, which is rich in historical fabric. It is situated in the urban conservation area of Artuklu District in Mardin Province, specifically on the southern side of the 1st Avenue in Latifiye Neighborhood, registered under parcel number 14 in Plot 309. The property is owned by the Regional Directorate of Foundations (Figure 1).

(a)

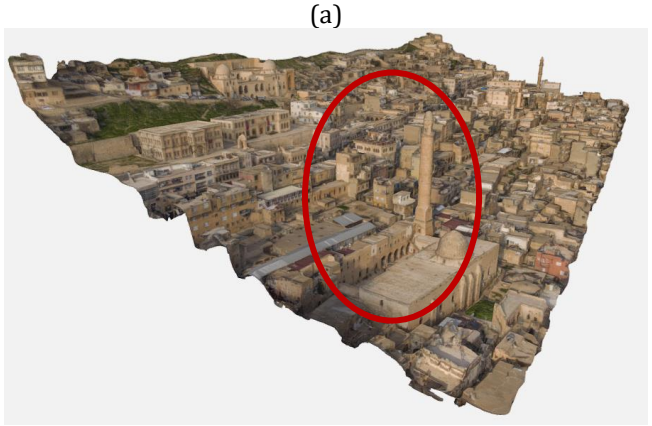

(b)

Figure 1. a) Site plan: The location of Latifiye Mosque within the topography of Mardin city is shown. b) Section: The section of Latifiye Mosque depicting its vertical representation within the city's topography.

According to the inscription on the portal, the construction of the building was commissioned by Abdullatif, who served two Artuklu sultans, in 1371 (Abdulgani Efendi, 1999; Alioğlu, 2000; Altun, 2011; Ahunbay, 2005; Gabriel, 1940) (Figure 2).

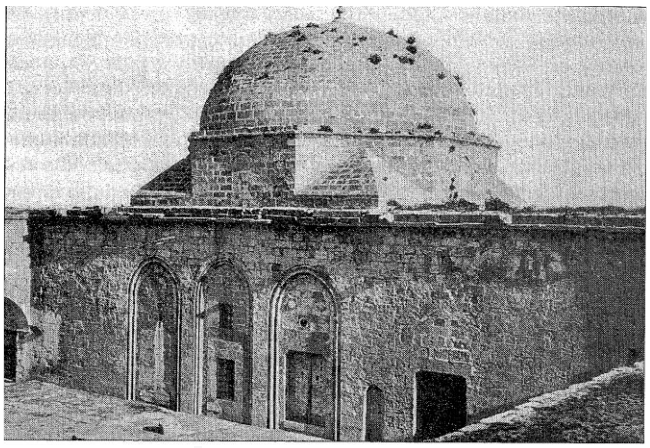

Figure 2. Latifiye Mosque (Gabriel, 1940)

The mosque is currently open for religious worship. On the east and north sides of the building, there are houses adjacent to the southern and western garden walls. Recently, the monumental features of the structure, such as the low-arched entrance door from the street to the outer courtyard and the entrance to the inner courtyard, have been modified. It is open for worship and visitation. Repair and renovation works have been carried out on the building until the present day (Mardin Governorship Provincial Directorate of Culture and Tourism, 2013).

2. Method

The study was conducted in two stages: fieldwork and office work. In the first stage, the building was examined on-site, and photographs of the structure were taken.

In the first stage of the study, the images of the historical structure obtained through fieldwork were transferred to the open-source 3DF Zephyr software for digital evaluation. 3DF Zephyr is a photogrammetry software used to create 3D models from photographs. This program utilizes photogrammetry techniques to identify 3D points in the photos and generate a point cloud (source: https://www.3dflow.net/3df-zephyr-photogrammetry-software/). In this case, 85 photos taken with the non-metric camera on the smartphone were used in 3DF Zephyr. The collected photo data was first introduced to the software. After the import process, the production of a 3D point cloud was initiated. The photos captured in the field were transformed into a point cloud using the open-source 3DF Zephyr software. Finally, material texture data was added to the completed 3D point cloud, and the documentation of the historical structure was completed.

The workflow of the study is presented below:

Step 1: Fieldwork - Obtaining photographs of the structure.

Step 2: Importing Photos - The photos are imported into the 3DF Zephyr software and used to create a 3D point cloud and model.

Step 3: Point Cloud Generation - The imported photos will appear in the "Photos" section of your project. Click on a button like "Generate Point Cloud" to initiate the process. Once completed, the point cloud will be displayed in the "Point Cloud" section of your project.

Step 4: Processing and Editing the Point Cloud - 3DF Zephyr provides various tools and options to process and edit the generated point cloud. You can make corrections, remove unnecessary points, adjust colors, apply filters, and perform other editing tasks.

Step 5: Orthophoto and 3D Model Generation - An orthophoto (or orthomosaic) is a geometrically corrected image with a uniform scale. Unlike standard images with a specific perspective, an orthophoto has the same distortion as a map and allows for accurate measurement of distances. The software can be used to generate orthophotos and 3D models based on the processed point cloud.

Within the 3DF Zephyr software, there are different options for creating orthophotos available in the "Workflow" menu. In the previous step of the study, the dense point cloud obtained can be used to create an orthophoto using the "Orthophoto from Dense Point Cloud (requires dense point cloud)" option. Additionally, the software offers the options of "Orthophoto from Sparse Points (does not require dense point cloud)" and "Orthophoto from Mesh (requires mesh)".

After generating the orthophoto automatically from the dense point cloud, it is necessary to export the orthophoto. The software allows you to select export settings and additional deliverables for the orthophoto.

3.Results

In the study, elevation drawings were created using the orthophotos obtained from the point clouds in AutoCAD 2020 software. By utilizing these drawings, the facade architecture of the mosque was explained and documented in written form. Below are the descriptions and elevation drawings related to the facade architecture of the structure.

The structure has a facade facing the front courtyard and four facades opening to the main courtyard. The north facade is referred to as facade number 1, the south facade as facade number 2, and the east facade facing the front courtyard as facade number 3. The east facade facing the main courtyard is labeled as facade number 4. The west facade of the structure is facade number 5 (Figure 4).

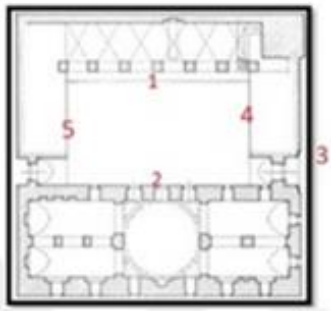

Figure 4. According to the plan drawing of Latifiye Mosque, the numbering of the facades is as follows (Karataş, 2017)

The orthophoto can be exported in image formats such as *.jpg, *.png, and *.tif.

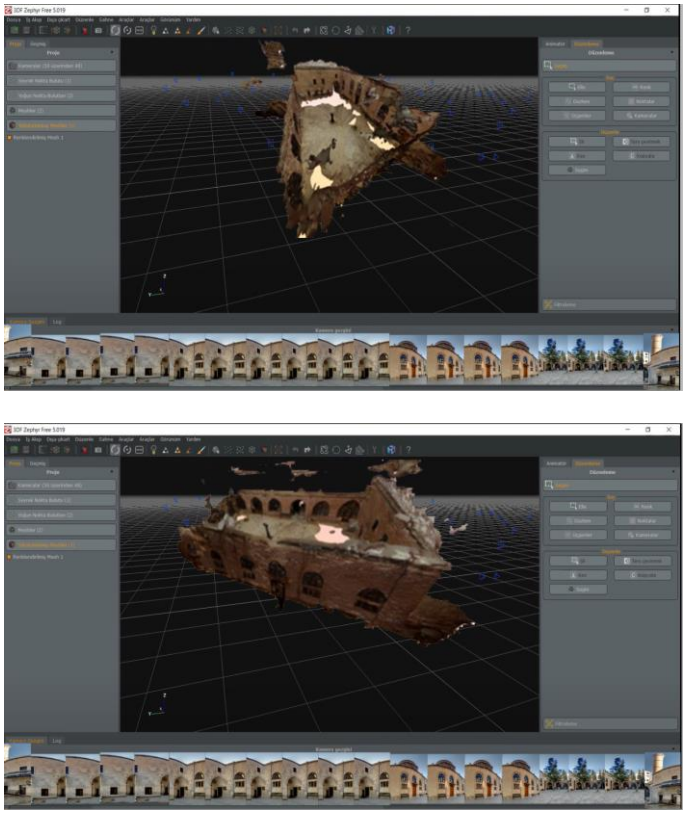

Figure 3. Some examples of dense point cloud visuals obtained using the field-acquired photo data of the Latifiye Mosque in 3DF Zephyr software

The facade numbered as 1 consists of a pointed arch arcade structure supported by thick piers, extending in the east-west direction along the northern side of the courtyard. It opens to the south with a cross-vaulted portico structure, which is the third one from the east and includes a selsebil (a public water fountain). This facade is evaluated together with the courtyard facade like the other facades. Due to later interventions, the original texture of the arcade has been compromised, and the arcade arches have been closed to create enclosed spaces. These spaces are currently used as a tea house and storage (Figure 5).

The facade numbered as 2 is located on the south side of the inner courtyard and consists of the rectangular-plan prayer hall extending in the east-west direction. It is covered with a series of five barrel vaults running parallel to the qibla wall (the wall facing Mecca). The vaults are supported by two pointed arches at the east and west, and by the southern and northern walls, dividing the space into two domed sections. The transition elements of the wide dome in front of the mihrab (prayer niche) are achieved with two-tiered muqarnas-adorned squinches. The dome, resting on an octagonal drum, provides illumination to the exterior through four windows, and its upper part displays fine stone masonry. This plan scheme represents a characteristic design of an Artukid-period mosque with a rectangular layout and a domed section in front of the

mihrab, which is also found in similar examples in Mardin and its surrounding areas (Figure 6).

The facade numbered as 3 is the entrance facade of the building facing the street (Figure 7).

The facade numbered as 4 is the eastern wing of the courtyard, constructed in two stories with finely cut limestone. This wing extends in the north-south direction and comprises the ground floor, which consists of three rooms serving as part of the mosque's madrasa section, and the upper floor, which can be accessed through a staircase opening that has been closed off in later periods. On the southern side of this wing, there is a pointed-arched iwan that provides access to the main entrance of the mosque's inner courtyard. On the north side of the iwan, there is a small room with a door, while on the south side, there is a lintelled doorway leading to the prayer hall. The second floor consists of two spaces (Figure 8).

The facade numbered as 5 is the western facade of the courtyard, constructed in two stories with smooth limestone. However, similar to the eastern facade, this facade has undergone numerous alterations over time. Only one floor of this two-story facade remains standing, and the traces of the second floor can still be observed. Currently, this facade features a semi-circular arched structure supported by piers and an entrance with a depressed arch opening, located on the southern side and adjacent to the prayer hall wall, providing access to the rear courtyard (Figure 9).

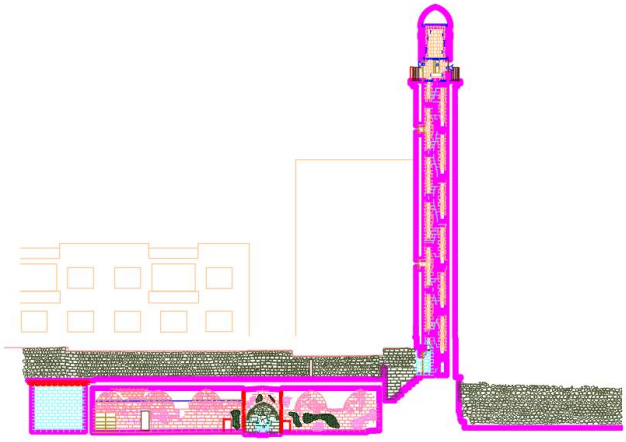

Figure 5. Analytical elevation drawing of Latifiye Mosque facade number 1

Figure 6. Analytical elevation drawing of Latifiye Mosque facade number 2

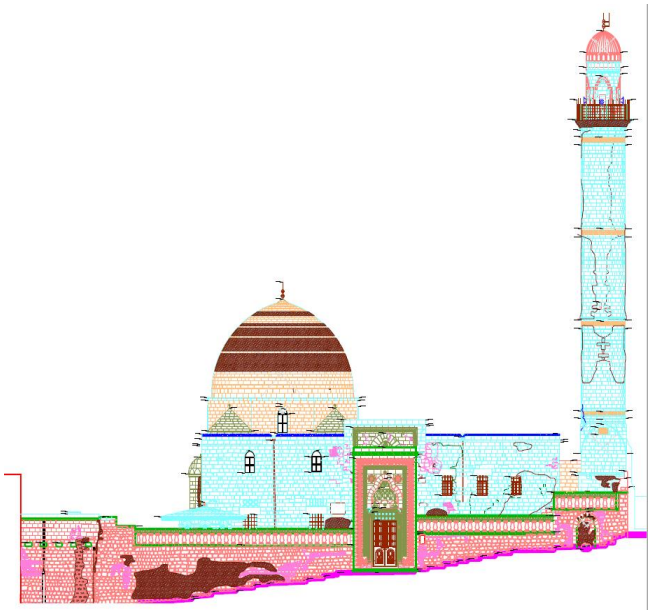

Figure 7. Analytical elevation drawing of Latifiye Mosque facade number 3

3. Discussion and Conclusion

Using photogrammetric methods for documenting historical artifacts is advantageous compared to traditional methods that require time-consuming and laborious measurements. However, photogrammetric methods have disadvantages such as expensive measurement tools, high-dimensional data, and complex modeling processes. In this study, the performance of photogrammetric methods in documenting historical artifacts was examined by utilizing non-metric cameras like smartphones, which are commonly used in our daily lives and more easily accessible compared to alternatives. The case study for this research was conducted on Latifiye Mosque, located in the city of Mardin, which holds historical significance.

The results of the study show that the proposed method can be used as a foundation for documenting and preserving cultural heritage. It has been demonstrated that high-resolution photographs taken with smartphones can be used to generate dense point clouds using various software, which in turn can provide scaled orthophotos to assist in the creation of architectural drawings. This method can be utilized in restoration projects to identify deformations occurring on historical artifacts and monitor changes that take place over time. Additionally, due to the wide user base and user-friendly nature of mobile phones, it is believed that they can contribute to the documentation of numerous cultural heritage sites.

References

Abdulgani Efendi. (1999). Mardin Tarihi. (Çev. Burhan ZENGİ). Ankara: Afşaroğlu Matbaa.

Ahunbay, Z. (2005). Antik Mardin: Taşın Belleği. Mardin, Türkiye: Yapı Kredi Yayınları.

Alioğlu, E. F. (2000). Mardin Şehir Dokusu ve Evler. Tarih Vakfı, İstanbul.

Altun, A. (2011). Mardin'de Türk Devri Mimarisi. İstanbul, 43.

Alyılmaz, C., Yakar, M., & Yılmaz, H. M. (2010). Drawing of petroglyphs in Mongolia by close range photogrammetry, 5(11), 1216-1222

Alyilmaz, C., Alyilmaz, S., & Yakar, M. (2010). Measurement of petroglyhps (rock of arts) of Qobustan with close range photogrammetry. International Archives of Photogrammetry, Remote Sensing and Spatial Information Sciences, 38(Part 5), 29-32.

Dabove, P., Grasso, N., & Piras, M. (2019). Smartphone-Based Photogrammetry for the 3D Modeling of a Geomorphological Structure. Applied Sciences, 9(18), 3884.

Gabriel, A. (1940). Voyages Archeologiques Dans La Turquie Orientale. Paris.

Kanun, E., Alptekin, A., Karataş, L., & Yakar, M. (2022). The use of UAV photogrammetry in modeling ancient structures: A case study of "Kanytellis". Advanced UAV, 2(2), 41–50.

Karataş, L. Alptekin, A., Karabacak, A. & Yakar, M. (2022c). Detection and documentation of stone material deterioration in historical masonry buildings using UAV photogrammetry: A case study of Mersin Sarisih Inn. Mersin Photogrammetry Journal, 4 (2), 53-61.

Karataş, L. & Dal, M. (2023). Deterioration analysis of historical village house structure in Mersin Kanlıdivane archaeological area by UAV method. Mersin Photogrammetry Journal, 5 (1), 32-41.

Karataş, L., & Menteşe, D. H. (2022). Dara Antik Kenti (Anastasiopolis) Nekropol Alanının Malzeme Sorunlarının Fotogrametrik Yöntemlerle Belgelenmesi. Türkiye Fotogrametri Dergisi, 4(2), 41-50

Karataş, L., Alptekin, A., & Yakar, M. (2022). Documentation of stone material deterioration on the facades of historical masonry buildings by terrestrial laser scanning: A case study of a Mansion in Mardin. Intercontinental Geoinformation Days, 5, 172-175.

Karataş, L., Alptekin, A., & Yakar, M. (2022b). Detection and documentation of stone material deterioration in historical masonry structures using UAV photogrammetry: A case study of Mersin Aba Mausoleum. Advanced UAV, 2(2), 51–64.

Karataş, L., Alptekin, A., Kanun, E., & Yakar, M. (2022a). Tarihi kârgir yapılarda taş malzeme bozulmalarının İHA fotogrametrisi kullanarak tespiti ve belgelenmesi: Mersin Kanlıdivane ören yeri vaka çalışması. İçel Dergisi, 2(2), 41-49

Korumaz, A. G., Dülgerler, O. N., & Yakar, M. (2011). Kültürel mirasin belgelenmesinde dijital yaklaşimlar. Selçuk Üniversitesi Mühendislik, Bilim ve Teknoloji Dergisi, 26(3), 67-83.

Mardin Valiliği İl Kültür ve Turizm Müdürlüğü. (2013). Mardin Kültür Envanteri. İstanbul, Türkiye.

Mohammed, O., & Yakar, M. (2016). Yersel fotogrametrik yöntem ile ibadethanelerin modellenmesi. Selçuk-Teknik Dergisi, 15(2), 85-95.

Wróżyński, R., Pyszny, K., Sojka, M., Przybyła, C., & Murat-Błazejewska, S. (2017). Ground Volume Assessment Using 'Structure from Motion' Photogrammetry with a Smartphone and a Compact Camera. Open Geosciences, 9, 281-294.

Yakar, M., & Doğan, Y. (2017). Mersin Silifke Mezgit Kale Anıt Mezarı fotogrametrik rölöve alımı ve üç boyutlu modelleme çalışması. Geomatik, 2(1), 11-17.

Yakar, M., & Kocaman, E. (2018). Kayseri-Sahabiye Medresesi 3-boyutlu modelleme çalışması ve animasyonu. International Journal of Engineering Research and Development, 10(1), 133-138.

Yakar, M., Murat Yilmaz, H., Yıldız, F., Zeybek, M., Şentürk, H., & Çelik, H. (2009). Silifke-Mersin Bölgesinde Roma Dönemi Eserlerinin 3 Boyutlu Modelleme Çalışması ve Animasyonu. Jeodezi ve Jeoinformasyon Dergisi, (101).

Yakar, M., Orhan, O., Ulvi, A., Yiğit, A. Y., & Yüzer, M. M. (2015). Sahip Ata Külliyesi Rölöve Örneği. TMMOB Harita ve Kadastro Mühendisleri Odası, 10.

Yakar, M., Uysal, M., Toprak, A. S., & Polat, N. (2013). 3D modeling of historical doger caravansaries by digital photogrammetry. The International Archives of the Photogrammetry, Remote Sensing and Spatial Information Sciences, 40, 695-698.

Yakar, M., Yılmaz, H. M., Güleç, S. A., & Korumaz, M. (2009). Advantage of digital close range photogrammetry in drawing of muqarnas in architecture, 8(2), 202-207

Yılmaztürk, F., & Gürbak, A. E. (2019). Geometric Evaluation of Mobile-Phone Camera Images for 3D Information. International Journal of Optics, 2019, 1-10.

Yilmaz, H. M., Yakar, M., & Yildiz, F. (2008). Digital photogrammetry in obtaining of 3D model data of irregular small objects. The International Archives of the Photogrammetry, Remote Sensing and Spatial Information Sciences, 37, 125-130.

6th Intercontinental Geoinformation Days

igd.mersin.edu.tr

Architectural documentation with terrestrial laser scanning (TLS) data: Case study of Lutfu Pasa caravanserai (Mathius Caravanserai), Izmir

Lale Karataş*[1], Murat Dal [2], Aydın Alptekin [3], Murat Yakar [4]

[1]*Mardin Artuklu University, Department of Architecture and Urban Planning, Türkiye*
[2]*Munzur University, Department of Architecture, Türkiye*
[3]*Mersin University, Faculty of Engineering, Department of Geological Engineering, Türkiye*
[4]*Mersin University, Faculty of Engineering, Department of Geomatics Engineering, Türkiye*

Keywords
Remote sensing
TLS
Architectural surveys
Cultural heritage
Tire

Abstract

Lutfu Pasa Caravanserai (Mathius Caravanserai), located in Yeni Mahalle, Lütfü Paşa Street, Tire district of Izmir province, is a two-story, courtyard-style, and masonry structure. The building is also known as Mathius Caravanserai, named after a former owner, a Greek businessman who operated the han during a certain period. Currently, the han is in a neglected state and privately owned. This presented paper aims to obtain survey drawings and reports regarding the historical han's current condition by utilizing observational examination and data obtained from terrestrial laser scanning, with the goal of ensuring the sustainability of the historical structure. The study intends to reveal information about the current state of the han. As a result of the study, the various stages the structure has gone through over time have been determined, and floor plan drawings and reports have been produced. Consequently, architectural drawings of the floor plan have been prepared as analytical surveys to provide information about the current state for future restoration works.

1. Introduction

Architectural documentation is a process used to preserve the design, details, and historical values of a structure. Terrestrial laser scanning is one of the most common techniques used in architectural documentation. Scanning data is utilized for measurements, geometry, material information, and documenting changes in the structure. This provides an accurate and precise foundation for restoration projects or the preservation of historical buildings, ensuring their proper conservation (Karataş, 2023a).

Analytical survey is a process used to document and record the current condition and characteristics of a structure in detail. Terrestrial laser scanning enables the creation of a complete digital replica of both the interior and exterior spaces of the building. This scanning data can be used to analyze the plans, sections, and elements of the structure in a three-dimensional format. Additionally, during the analytical survey process, it provides accurate and precise information about the measurements and geometry of the existing building (Karataş, 2023b).

The aim of the study conducted within this scope was to obtain measured drawings and survey reports of the historical han located on Lütfü Paşa Street in Yeni Mahalle, Tire district, İzmir province, using data obtained from terrestrial laser scanning. The study aimed to reveal information about the current condition of the structure. As a result of the study, the current state of the building, which has undergone various stages of transformation over time, was determined through drawings and reports.

1.1. The location, history, and significance of the structure

The caravanserai is located on Lütfü Paşa Street in Yeni Mahalle, Tire district, İzmir province. It is a one-storey, courtyard-oriented, and rubble-built structure. In some documents, the han is referred to as Mathius Caravanserai (due to its Byzantine origins), Esir Caravanserai (as it was used for buying and selling slaves), or Dellaloğlu Caravanserai. It is understood from the sources of the General Directorate of Foundations that the han was built by the foundation established by

* **Corresponding Author**

*(lalekaratas@artuklu.edu.tr) ORCID ID 0000-0001-8582-4612
(muratdal@munzur.edu.tr) ORCID ID 0000-0001-5330-1868
(aydinalptekin@mersin.edu.tr)ORCID ID 0000-0002-5605-0758
(myakar@mersin.edu.tr) ORCID ID 0000-0002-2664-6251

Cite this study

Karataş, L., Dal, M., Alptekin, A., & Yakar, M. (2023). Architectural documentation with terrestrial laser scanning (TLS) data: Case Study of Lutfu Pasa caravanserai (Mathius Caravanserai), Izmir. Intercontinental Geoinformation Days (IGD), 6, 143-147, Baku, Azerbaijan

the Grand Vizier Lütfi Pasha in Tire. The building is also known as Mathius Caravanserai, named after a Greek man who operated the han for a period of time. Currently, the han is in a neglected state and privately owned (Figure 1).

(a)

(b)

Figure 1. Lutfu Pasa Caravanserai, located in Tire, Izmir, features a captivating entrance section. a) Entrance section, b) View from a shop inside the caravanserai

2. Method

In the study, literature research, visual observation, and terrestrial laser scanning methods were used to create analytical surveys of the identified structure. The obtained information was evaluated through descriptive and systematic analysis methods. In the initial phase of the research, a situation analysis was conducted on the historical building where the case study would be applied, and general information about the structure was presented based on data obtained from an archival scan. Additionally, an observational analysis was conducted on the structure to document its material issues.

2.1. Documentation of the Architectural Features and Deteriorations of the Structure

The systematic presentation of the stages followed for documenting material deteriorations using methods derived from terrestrial laser scanning is presented in this section, following the analysis of the current condition of the structure.

2.1.1. Scanning Process and Data Processing

For the overall measurement of the structure, a 3D laser scanner of the Leica Geosystems brand, model ScanStation C10, was utilized. When examining the general technical specifications of the device, it offers wide-angle scanning and documentation capabilities, with a range of 360º horizontal and 270º vertical coverage. Additionally, it allows for focused scanning and photography of specific areas and surfaces, enabling detailed and accurate capture of these regions. The device is capable of scanning surfaces with up to 90% reflectivity at distances of up to 300 meters, with a scanning speed of 50,000 points per second. The efficient operating temperature range for the device is between 0ºC and 40ºC. It is unable to operate effectively below or above these temperature thresholds (Figure 2).

Figure 2. Leica ScanStation C10

The structure was scanned using a terrestrial laser scanning device (Leica Geosystems brand, ScanStation C10 model, 3D laser scanner) (Figure 3). Point clouds were obtained during the scanning process.

Figure 3. Lutfu Pasa Hanı during laser scanning of the inner courtyard

2.1.2. Plans and elevation drawings were derived from orthophoto images.

In this section, the steps followed for creating orthophotos using the point cloud data are presented in detail. The point cloud data obtained from the laser scanning process was processed using the software PointCab Origins 4.0 to generate 3D visualizations of the structure (Figure 3). In the next stage, using PointCab

Origins 4.0, cross-sections were taken from desired locations on the 3D visualizations of the structure to produce orthophotos (Figure 4).

Figure 3. An example scene from PointCab Origins 4.0 program where scaled orthophotos of the structure are obtained

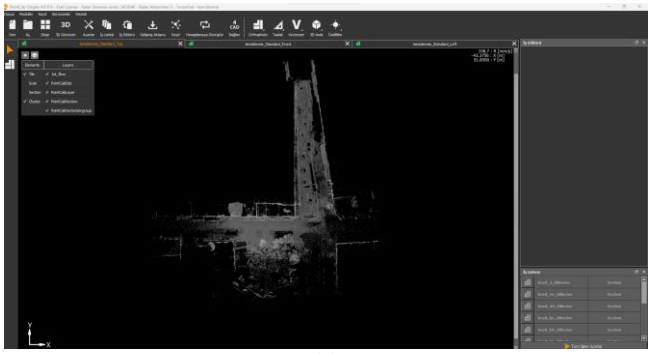

(a)

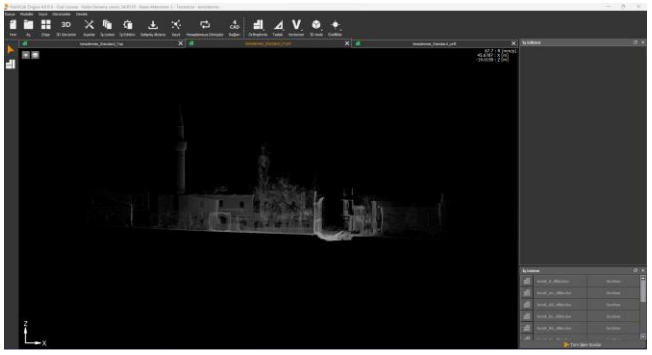

(b)

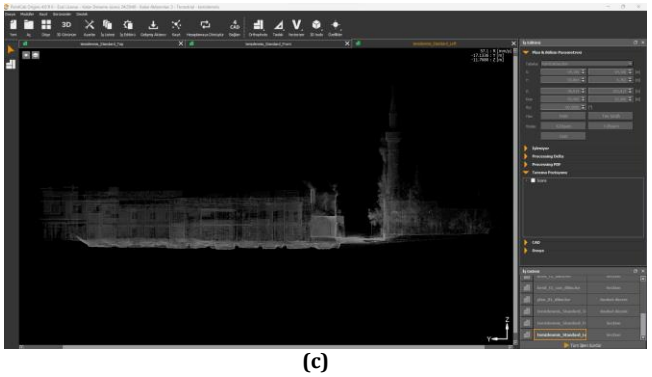

(c)

Figure 4. In PointCab Origins 4.0 program, scaled orthophotos of the structure's floor plans can be obtained. a) Floor plan orthophoto; b) Section orthophoto; c) Elevation orthophoto

In the next stage, the AutoCAD software was used to generate architectural drawings. Before the drawing process, the orthophoto images produced in PointCab Origins 4.0 software were transferred to the AutoCAD environment (Karataş et al., 2022a,b,c; Karataş et al., 2023a,b,c; Karataş & Alptekin, 2022). The AutoCAD software supports the common data format of .tif or .tiff files, which allowed for the transfer of orthophoto images to the AutoCAD environment (Karataş & Menteşe, 2022). Using the obtained scaled orthophoto images, elevation drawings of the structure were created using the AutoCAD program.

3. Results

The caravanserai located in Yeni Mahalle, Lütfü Paşa Street, Tire district of Izmir province is a two-story, courtyard-centered structure consisting of a ground floor and a single upper floor. The ground floor is devoid of arcades, while the upper floor features arcaded galleries. The han complex is comprised of 24 shops on the ground floor and 37 shops on the first floor, totaling 61 shops. The complex originally had 22 shops facing outward, but the external shops have been demolished. The shops on the other facades are currently being used with unqualified additions.

The entrance to the han is located on the eastern facade. The entrances to the rooms on the ground floor are arched, while those on the upper floor are lintel-shaped. The arcades in the courtyard have been completely demolished except for the western facade. The ground floor portion of the western facade has survived to the present day, but the upper floor section has mostly collapsed, except for the arches and supporting columns.

The caravanserai structure, measuring 40m x 43m, is constructed with rubble stone and brick. While a significant portion of the structure has been preserved to this day, unqualified additions have been made to the open shop area. The approximately 3.6m x 4m-sized shops have been altered with plaster, paint, and new joinery.

Overall, the caravanserai exhibits a traditional architectural style with its courtyard layout and arcaded galleries. Although some parts have suffered damage and alterations over time, the remaining elements provide valuable insights into the historical significance and construction techniques of the han.

The caravanserai structure features a rectangular courtyard in its interior, with a square gallery on the western facade. However, all the galleries on the other facades have collapsed on both floors. The caravanserai consists of rooms on both the lower and upper floors. The vaulted ceilings on the lower floor of the western facade remain original, while the ceiling system on the upper floor has completely collapsed. The arches and piers of the gallery are still intact.

The caravanserai has an entrance on the eastern side, and it comprises thirty-seven rooms on the upper floor and twenty-four rooms and stable compartments on the lower floor. The entrance door and corridor on the eastern facade retain their originality. The doors of the rooms on the ground floor have arches, while those on

the upper floor have lintels. Out of the twenty-two shops located on the exterior of the caravanserai, the ones facing north on the outer facade have been demolished to provide road width.

After conducting macro and micro visual observations in the previous section, a comparative evaluation was made between the current condition analysis of the structure or monument and the analytical survey drawings obtained from laser scanning and orthophotos. Based on this evaluation, the following findings were obtained regarding the architectural features of the structure (Figure 5):

1. General Layout and Form: The structure exhibits a compact layout with a ground floor and single-storey height. It has a rectangular plan and is characterized by its courtyard design.
2. Construction Materials: The structure is predominantly constructed using traditional masonry techniques, with locally sourced stone as the primary building material. The walls display a robust and solid construction, showcasing the durability of the materials used.
3. Architectural Style: The architectural style of the structure reflects the characteristics of the historical period it belongs to. It exhibits elements of Byzantine and Ottoman architectural styles, blending influences from different periods.
4. Ornamental Details: The structure features decorative elements such as carved stone reliefs, ornate arches, and decorative motifs. These details contribute to the aesthetic appeal of the building and provide insights into the craftsmanship of the era.
5. Preservation Issues: The comparative analysis reveals various preservation issues, including deterioration of the masonry, weathering of surfaces, and structural instability in certain areas. These findings highlight the need for restoration and conservation measures to ensure the long-term preservation of the structure.

(a) (b)

Figure 5. Analytical survey drawings: a) Ground floor plan b) First floor plan

4. Conclusion

The conducted study focuses on the documentation of material deteriorations in the historical structure by combining the data obtained through terrestrial laser scanning with on-site observations, aiming to analyze the current condition and architectural features of the historical building. The study exemplifies the methods of transforming the data obtained from laser scanning into orthophotos, which serve as a foundation for documentation, systematically illustrating the necessary stages of documenting the architectural features and current condition of historical structures.

References

Alptekin, A., & Yakar, M. (2020). Kaya bloklarının 3B nokta bulutunun yersel lazer tarayıcı kullanarak elde edilmesi. Türkiye LİDAR Dergisi, 2(1), 1-4.

Alptekin, A., & Yakar, M. (2020). Mersin Akyar Falezi'nin 3B modeli. Türkiye Lidar Dergisi, 2(1), 5-9.

Alptekin, A., Çelik, M. Ö., Doğan, Y., & Yakar, M. (2019, November). Illustrating of a landslide site with photogrammetric and LIDAR methods. In Conference of the Arabian Journal of Geosciences (pp. 303-305). Cham: Springer International Publishing.

Kanun, E., Metin, A., & Yakar, M. (2021). Yersel Lazer Tarama Tekniği Kullanarak Ağzıkara Han'ın 3 Boyutlu Nokta Bulutunun Elde Edilmesi. Türkiye Lidar Dergisi, 3(2), 58-64.

Karabacak, A., & Yakar, M. (2023). 3D modeling of Mersin Akyar Cliffs with wearable mobile LIDAR. Advanced Engineering Days (AED), 6, 86-89.

Karataş, L. & Alptekin, A. (2022). Kagir Yapılardaki Taş Malzeme Bozulmalarının Lidar Tarama Yöntemi ile Belgelenmesi: Geleneksel Silvan Konağı Vaka Çalışması. Türkiye Lidar Dergisi, 4 (2), 71-84.

Karataş, L. & Menteşe, D. H. (2022). Dara Antik Kenti (Anastasiopolis) Nekropol Alanının Malzeme Sorunlarının Fotogrametrik Yöntemlerle Belgelenmesi. Türkiye Fotogrametri Dergisi, 4(2), 41-50

Karataş, L. (2023a). 3D Laser Scanning and Photogrammetric Measurements for Documentation of the Facades of Mardin Castle, Türkiye. Advanced LiDAR, 3(1), 10–21.

Karataş, L. (2023b). Yersel lazer tarama yöntemi ve ortofotoların kullanımı ile kültür varlıklarının cephelerindeki malzeme bozulmalarının dokümantasyonu: Mardin Mungan Konağı örneği. Geomatik, 8(2), 152-162

Karataş, L., Alptekin, A. & Yakar, M. (2022b). Determination of Stone Material Deteriorations on the Facades with the Combination of Terrestrial Laser Scanning and Photogrammetric Methods: Case Study of Historical Burdur Station Premises. Advanced Geomatics, 2(2), 65-72.

Karataş, L., Alptekin, A. & Yakar, M. (2023c). Investigating the limestone quarries as geoheritage sites: Case of Mardin ancient quarry. Open Geosciences, 15 (1)1, 20220473.

Karataş, L., Alptekin, A., & Yakar, M. (2022a). Creating Architectural Surveys of Traditional Buildings with the Help of Terrestrial Laser Scanning Method (TLS) and Orthophotos: Historical Diyarbakır Sur Mansion. Advanced LiDAR, 2(2), 54–63.

Karataş, L., Alptekin, A., & Yakar, M. (2022c). Analytical Documentation of Stone Material Deteriorations on Facades with Terrestrial Laser Scanning and Photogrammetric Methods: Case Study of Şanlıurfa Kışla Mosque. Advanced LiDAR, 2(2), 36–47.

Ulvi, A., Yakar, M., Toprak, A. S., & Mutluoglu, O. (2014). Laser scanning and photogrammetric evaluation of Uzuncaburç Monumental Entrance. International Journal of Applied Mathematics Electronics and Computers, 3(1), 32-36.

Yakar, M., Ulvi, A., & Toprak, A. S. (2016). The Use of Laser Scanner in Caves, Encountered Problems and Solution Suggestion. Universal Journal of Geoscience, 4(4), 81-88.

Yakar, M., Yilmaz, H. M., & Mutluoglu, O. (2009). Comparative Evaluation of Excavation Volume by Terrestrial Laser Scanner and Total Topographic Station Based Methods. Lasers in Engineering, 19(5), 331.

Yılmaz, H. M., & Yakar, M. (2006). Lidar (Light Detection And Ranging) Tarama Sistemi. Yapı Teknolojileri Elektronik Dergisi, 2(2), 23-33.

Yılmaz, H. M., & Yakar, M. (2006). Yersel lazer tarama Teknolojisi. Yapı teknolojileri Elektronik dergisi, 2(2), 43-48.

6th Intercontinental Geoinformation Days

igd.mersin.edu.tr

Comparison of active and passive remote sensing data in extracting coastlines

Sheida Fathi[1], Seyed Mohamad Tavakkoli Sabour[*1], Parviz Zeaiean Firouzabadi [1], Ali Hosingholizade [2]

[1]*University of Kharazmi, Geography, Department of Remote Sensing and GIS, Tehran, Iran*
[2]*University of Tehran, Geography, Department of Remote Sensing and GIS, Tehran, Iran*

Keywords
Shoreline
Sentinel1
OLI
Optical indicators
Zarivar lake

Abstract

Coastal environments are one of the most sensitive environmental systems that are affected by hydrodynamic processes and rapid changes. Also, from an ecological point of view, coastal areas are of high value due to having sensitive and productive ecosystems. Therefore, extracting characteristics of coastlines and revealing their changes is very efficient and vital for various applications. In this research, the coastline of Zarivar Lake located in the Kurdistan province of Iran extracted thriough image processing techniques including minimum distance, maximum probability, optical indices NDVI, NDWI, TCW and band ratios of Oli bands (5/3) and (6/3). In this regard, coastlines were extracted after necessary processing. The results showed that the 5/3 band ratio method in coastline extraction has an average error of 90 meters when using OLI data, and the maximum likelihood classification has an average error of 120 meters in comparision to visual interpretation when using Sentinel 1 Microwave data

1. Introduction

Coastlines are constantly changing due to different human and natural factors (Toure et al. 2019; Ciritci and Türk. 2019). Observing these lines is necessary for constant and continuous monitoring of the lake water level (Sojka et al. 2022; Abdelhady et al. 2022). These lines have been defined by the International Committee of Geographic Data (ICGD) as one of the most important geographical complications and the intersection between water and land levels (Halder et al. 2022), which can be determined using different methods and for various applications (Tajima et al. 2021). In the past, traditional methods were used to monitor these lines. These methods were expensive and time consuming. In addition, due to the unavailability of some measuring lines, they were not done (Templin et al. 2018). Shoreline is a dynamic and unique area, and in fact, it is the junction of water and land, which is always affected by the action and reactions of the two on each other (Mutagi et al. 2022). In order to have a proper coastline detection method, it is necessary to evaluate the existing methods in order to propose better approaches to detect the coastline of each region (Abdul Maulud et al. 2022). In this research, we will investigate and compare different methods of determining coastlines using OLI (optical data) and Sentinel 1 (radar data). The results of this research can help managers and planners to adopt a suitable approach for coastal areas. Figure 1 shows the implementation of the research.

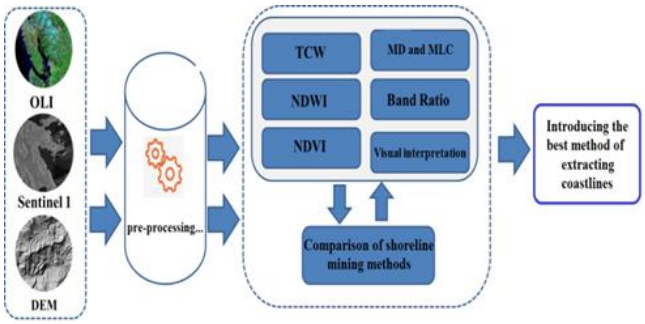

Figure 1. Research implementation process

2. Method

2.1. Study area

Zarivar Lake is a boiling water ecosystem located 3 kilometers west and northwest of Marivan city. The length of the lake perimeter is 25 km and its maximum depth is about 5.85 meters. According to the water conditions of the internal springs of the lake and the discharge of the rivers leading to it, its area fluctuates between 7.8 and 20 square kilometers. The height of the lake is about 1290 meters above sea level. The lake has an almost oval shape and is slightly bent towards the

* **Corresponding Author**

*(sheidafathi68@gmail.com) ORCID ID 0000-0002-0019-4824
(tavakkoli@khu.ac.ir) ORCID ID 3026 – 3448 – 0002 – 0000
(zeaiean@khu.ac.ir) ORCID ID 0000-0001-8407-5605
(a.hosingholizade@ut.ac.ir) ORCID ID 0000 – 0001 – 5286 – 1361

Cite this study

Fathi, S., Sabour, S. M. T., Firouzabadi, P. Z., & Hosingholizade, A. (2023). Comparison of active and passive remote sensing data in extracting coastlines. Intercontinental Geoinformation Days (IGD), 6, 148-151, Baku, Azerbaijan

west, which is caused by the accumulation of sediments that have entered this part of the lake through seasonal rivers. This lake is located inside a wide valley, which is surrounded by low mountains on three sides, north, west and east. Figure 2 shows the location of Zarivar Lake in the study area.

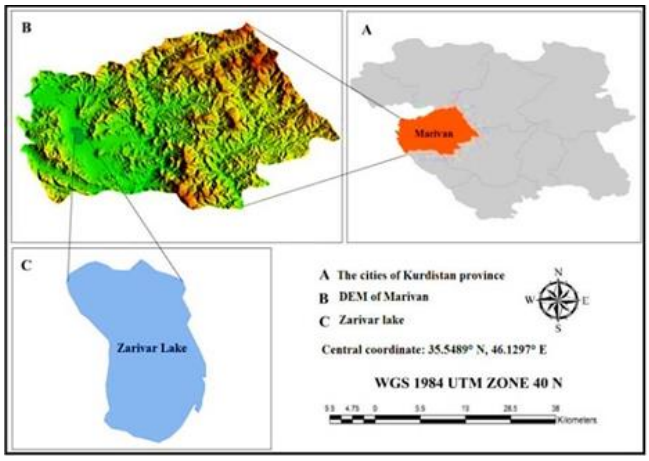

Figure 2. Location map of the study area

2.2. Data

In this study, OLI, Sentinel 1 and 2 data and DEM pertaining to study area were downloaded and used. The images were used with zero cloud cover so as not to interfere with the use of different algorithms. Table 1 shows the date of collection and the type of images used.

Table 1. Data and Date

Satellite	Sensor	Date
Landsat 8	OLI1	2015-03-10
	OLI2	2015-04-27
	OLI3	2016-03-12
	OLI4	2016-05-15
Sentinel-1	Radar1	2015-04-04
	Radar2	2015-05-21
	Radar3	2016-03-10
	Radar4	2016-05-21

2.3. Coastline extraction methods/ algorithms

Before implementing processing algorithms, preprocessing techniques including calibration were applied to all images.

2.4. Maximum likelihood algorithm

This algorithm calculates the conditional probabilities of membership in each class based on the comparison of the spectral values of each pixel with the statistics of each training set. In order to implement this method, it is necessary to have several bands and introduce land use landcover classes and samples, so that the classes used for the classification methods were considered completely identical.

2.5 Minimum distance (MD) algorithm

In this algorithm, the distance of each unclassified pixel is compared with the average pixels' values in each trainig sits, and the desired pixel is assigned to the class that has the closest distance to its average (Wicaksono et al. 2019). Table 2 shows thresholds.

2.6. Normalized Difference Vegetation Index (NDVI)

It is one of the most widely used indicators for monitoring vegetation changes, whose numerical value ranges from -1 to +1. By introducing a threshold limit for the index (Table 2), NDVI image was classified again and water was separated from soil and the coastline was extracted (Gonçalves et al. 2019).

2.7. Normalized Difference water Index (NDWI)

One of the non-normalized indicators is water and the amount of water in plants. Its value range is between -1 and +1 (Wicaksono et al. 2019). Table 2 shows thresholds.

2.8. TASSELED Cap Wetness (TCW)

It is one of the indicators of humidity, which is obtained from the comparison of a number of visible, near infrared and short infrared bands. In this method, the threshold was introduced for each image (Chen et al. 2019). Table 2 shows thresholds.

2.9. Oli Band ratio 5 to 3 and 6 to 3

The use of band ratios of 5/3 and 6/3 is because of the different water reflectances in these bands. For example, water reflection in band 6 of the OLI sensor is close to zero and band 3 is higher than this value. If the result of these ratios is smaller than 1, it means water, otherwise it is considered dryland (Liu et al. 2017). "Table 2" shows thresholds.

2.10. Estimating the accuracy of coastline extraction

Usually, to estimate the classification accuracy, the error matrix is used, which estimates the error based on the classified and ground truth observations. Considering that the aim of this research is to extract the coastline, the main classification error occurs exactly on these borders. Therefore, it is possible that the accuracy of the classification based on the error matrix even reaches 95% and has a 5% error, and it is also possible that the same 5% happened on the coastline. On the other hand, the classification accuracy through the error matrix cannot indicate the accuracy of coastline extraction. Therefore, for this estimation, the coastline distance method was used from the base data. The results of this investigation method were presented based on the calculation of absolute difference, relative difference and percentage of relative difference. The stated values are the results of the sharing process of two reference and classified data. In such a way that the layer resulting from UNION has an area, which three numbers are proposed as area:

A) The common area of the two layers detected in both waters

B) The area estimated in the water reference data, but in the classified soil data
C) The area specified in the classified water data but in the soil reference data
Absolute difference = total non-common area (b, c)
Relative difference = absolute difference/lake area
Percentage of relative difference = relative difference × 100

The absolute difference value is obtained from the sum of the areas. The sum of these distances represents the sum of absolute difference. The total size of these distances (absolute difference) indicates the amount of error in estimating the coastline, the higher this value, the greater the error.

Table 2. Methos and Threshold

Method	Threshold	Data
NDVI	0.011>	OLI1
	0.28>	OLI2
	0.10>	OLI3
	0.26>	OLI4
NDWI	>-0.05 <-0.01	OLI1
	>-0.20 <-0.02	OLI2
	>-0.15 <-0.04	OLI3
	>-0.25 <-0.07	OLI4
TCW	>-1500	OLI1
	>0	OLI2
	>-1500	OLI3
	>0	OLI4
Band ratio 5:3	<0.10	OLI1
	<0.25	OLI2
	<0.08	OLI3
	<0.23	OLI4
Band ratio 6:3	0.10>	OLI1
	0.08>	OLI2
	0.08>	OLI3
	0.05>	OLI4

3. Results

Table 3 shows the estimation error of the coastline in meters. The measuring criterion is the comparison of the obtained coastline with the Shapfile of the lake, which was obtained by the ground mapping method with the total station Leica TS02 camera with an accuracy of 7 seconds of gradation.

Table 3. Method and Error rate

Image and Method	MD	MLC	Visual	NDVI	NDWI	TCW	Band ratio 5:3	Band ratio 6:3
OLI1	23	29	18	9	104	146	7	5
OLI2	23	62	09	7	126	240	6	3
OLI3	41	26	30	7	155	166	04	9
OLI4	70	42	30	09	142	174	7	03
Radar1	78	40	40		-	-	-	-
Radar2	43	45	9		-	-	-	-
Radar3	40	47	26		-	-	-	-
Radar4	80	49	20		-	-	-	-

Figure 3 shows some of the outputs. As can be seen, Figure 3 (a) shows the lowest value of the lake area obtained by the MD classification method. Figure 3 (d) shows the largest area of the lake compared to the land estimate.

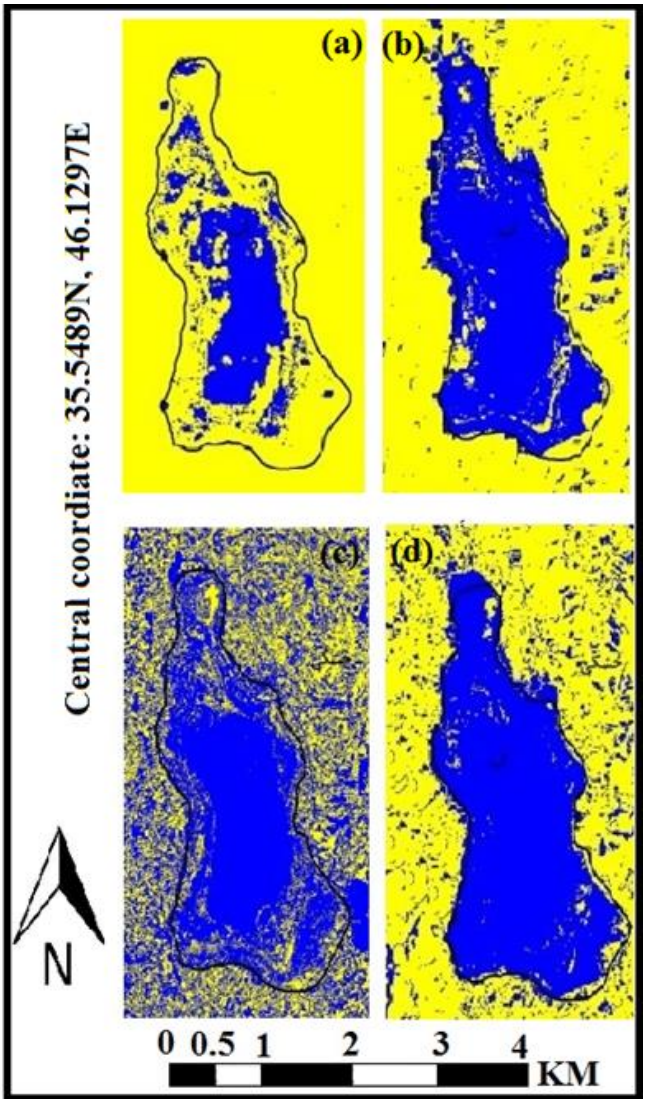

Figure 3. MD (a), NDVI (b), MLC (c), Band ratio 5/3 (d)

4. Discussion

By examining the results and comparing them, it can be found that the use of a band ratio of OLI band 3/5 is more accurate in extracting the coastline than other methods used in this research, which may be due to the strong difference in the reflection of the lake surface. (water) and beach (non-water). Based on the data in the "table 3", this value for the bandwidth ratio of 5/3 shows the value of 77 meters. Also, NDVI and NDWI indices show much better results than ML and MD classification algorithms. Regarding the use of radar data, the accuracy of determining coastlines visually and the use of MD and MLC classifications have brought better results. Therefore, it can be concluded that in order to determine the coastlines more accurately, the difference of reflection in different bands can be used as an effective basic solution in determining the coastlines.

5. Conclusion

According to the results, it can be concluded that the accurate extraction of the coastline on each image is done

with a special method. every method however complex, will not necessarily have a more accurate result than other methods. In this research, in order to accurately extract the coastline on radar images, classification methods were much less accurate than simpler methods such as visual interpretation. if radar images with more bands and polarizations are available, they can bring much better results from more accurate extraction of the coastline. Regarding the indicators, due to the difference and diversity in the lake and the coast, the method that showed the best results on Landsat images to extract the coastline was the use of a band ratio of 5 (near infrared) to 3 (green), which is due to the great difference. Water reflections were in these two spectral ranges. It is suggested that in the future research, according to the purpose and conditions of the region, if the aim is to study blue areas, radar images with different polarizations and optical images should be used simultaneously.

Acknowledgement

The authors of this article express their gratitude to the Department of Remote Sensing and GIS of Kharazmi University in Tehran for their assistance in preparing this research.

References

Abdelhady, H. U., Troy, C. D., Habib, A., & Manish, R. (2022). A simple, fully automated shoreline detection algorithm for high-resolution multi-spectral imagery. Remote Sensing, 14(3), 557. https://doi.org/10.3390/rs14030557

Abdul Maulud, K. N., Selamat, S. N., Mohd, F. A., Md Noor, N., Wan Mohd Jaafar, W. S., Kamarudin, M. K. A., & Ahmad, A. (2022). Assessment of Shoreline Changes for the Selangor Coast, Malaysia, Using the Digital Shoreline Analysis System Technique. Urban Science, 6(4), 71. https://doi.org/10.3390/urbansci6040071

Chen, C., Fu, J., Zhang, S., & Zhao, X. (2019). Coastline information extraction based on the tasseled cap transformation of Landsat-8 OLI images. Estuarine, Coastal and Shelf Science, 217, 281-291. https://doi.org/10.1016/j.ecss.2018.10.021

Ciritci, D., & Türk, T. (2019). Automatic detection of shoreline change by geographical information system (GIS) and remote sensing in the Göksu Delta, Turkey. Journal of the Indian Society of Remote Sensing, 47(2), 233-243. https://doi.org/10.1007/s12524-019-00947-1

Halder, B., Ameen, A. M. S., Bandyopadhyay, J., Khedher, K. M., & Yaseen, Z. M. (2022). The impact of climate change on land degradation along with shoreline migration in Ghoramara Island, India. Physics and Chemistry of the Earth, Parts A/B/C, 103135. https://doi.org/10.1016/j.pce.2022.103135

Gonçalves, R. M., Saleem, A., Queiroz, H. A., & Awange, J. L. (2019). A fuzzy model integrating shoreline changes, NDVI and settlement influences for coastal zone human impact classification. Applied Geography, 113, 102093. https://doi.org/10.1016/j.apgeog.2019.102093

Liu, Y., Wang, X., Ling, F., Xu, S., & Wang, C. (2017). Analysis of coastline extraction from Landsat-8 OLI imagery. Water, 9(11), 816. https://doi.org/10.3390/w9110816

Mutagi, S., Yadav, A., & Hiremath, C. G. (2022). Shoreline Change Monitoring of Karwar Coast of Karnataka, India, Using Sentinel-2 Satellite. In Sustainability Trends and Challenges in Civil Engineering (pp. 339-350). Springer, Singapore. https://doi.org/10.1007/978-981-16-2826-9_22

Sojka, M., Choiński, A., Ptak, M., Kanecka-Geszke, E., Zhu, S., & Strzeliński, P. (2022). Detection of lake shoreline active zones and water volume changes using digital lake bottom model and water level fluctuations. Geocarto International, (just-accepted), 1-21. https://doi.org/10.1080/10106049.2022.2082553

Tajima, Y., Wu, L., & Watanabe, K. (2021). Development of a Shoreline Detection Method Using an Artificial Neural Network Based on Satellite SAR Imagery. Remote Sensing, 13(12), 2254. https://doi.org/10.3390/ijgi8020075

Templin, T., Popielarczyk, D., & Kosecki, R. (2018). Application of low-cost fixed-wing UAV for inland lakes shoreline investigation. Pure and Applied Geophysics, 175(9), 3263-3283. https://doi.org/10.1007/s00024-017-1707-7

Toure, S., Diop, O., Kpalma, K., & Maiga, A. S. (2019). Shoreline detection using optical remote sensing: A review. ISPRS International Journal of Geo-Information, 8(2), 75. https://doi.org/10.3390/rs13122254

Wicaksono, A., Wicaksono, P., Khakhim, N., Farda, N. M., & Marfai, M. A. (2019, December). Semi-automatic shoreline extraction using water index transformation on Landsat 8 OLI imagery in Jepara Regency. In Sixth International Symposium on LAPAN-IPB Satellite (Vol. 11372, pp. 500-509). SPIE. https://doi.org/10.1117/12.2540967

6th Intercontinental Geoinformation Days

igd.mersin.edu.tr

Land cover classification using various remote sensing datasets with PlanetScope SuperDove Data in GEE

Gülden Reşidoğlu Şahin *[1], **Gordana Kaplan** [1]

[1]*Eskisehir Technical University, Institute of Earth and Space Sciences Institute, Eskisehir, Türkiye*

Keywords
Remote sensing
UAV
Photogrammetry
DEM
Camera calibration

Abstract

Planet operates the Earth observation satellites PlanetScope (PS) and SkySat (SS). The PlanetScope satellite constellation consists of multiple launches of groups of satellites. Consisting of approximately 130 satellites, PlanetScope is capable of examining the entire Earth's surface every day. The aim of this study is to investigate the effect of Green I (b3 band 513-549nm) and Yellow (b5 band 600-680nm) bands of PlanetScope PSB.SD sensor on different land cover classes. In addition, the interaction of these bands with various index-based algorithms calculated from Sentinel-2 satellite images was examined. The results showed that different datasets had different overall accuracies. This study was carried out with the Google Earth Engine (GEE), a cloud computing platform with a very comprehensive database of remote sensor data and satellite images designed for the analysis of geographic data. By comparing the data sets, the effect of the GreenI and Yellow bands of the Planetscope Superdove (PSB.SD) sensors in two different study areas, Karataş and Doğubeyazıt districts, also shows in different classes. As a result, a highly accurate land cover classification was established in the study areas. The results can be critical in choosing bands and indexes depending on the study area and class type decided in a land cover classification.

1. Introduction

With the commercial use of remote sensing satellites, the increase in the number of satellite systems launched for various purposes, and the general vision capabilities of satellites and the technological development of sensor systems, satellite images are used effectively in many application areas. Working on these data requires a long time and money. However, in recent years, remote sensing data processing has moved from traditional methods to cloud-based platforms. Among these systems, Google Earth Engine (GEE) is a cloud-based geospatial analytics platform that allows users to highly effectively solve key challenges of managing, storing, processing and analyzing huge volumes of data. The creation of land use/land cover (LULC) maps that show how the land is used for various human purposes or the physical features of the earth's surface is a remote sensing challange. The partnership between Google and Norway's International Climate and Forests Initiative (NICFI) has led to the addition of NICFI PlanetScope Basemaps (more than 700 geospatial high-resolution, 4.77 m, datasets) to GEE's public data catalogue. The availability of PlanetScope (PL) data at GEE is an important step forward for detecting and monitoring LULC dynamics in high resolution, including small-scale distortions in tropical landscapes. In land cover classification, machine learning techniques give better results than standard classifiers. Machine learning classifiers include RandomForest (RF); It is one of the most effective, accurate and widely used classifiers. RF for remote sensing data classifier is the most widely used machine learning method in the context of GEE. As remote sensing satellites have different spectral resolution, the comparison of the results obtained from different bands can be of great benefit for different studies. The innovative PlanetScope SuperDove (PSB.SD) collects data in the green and yellow regions of the electromagnetic spectrum, making a uniqe set of data. The aim of this study is to evaluate the accuracy advantages of combining the Green-I (b3 band) and Yellow (b5 band) bands in the 8-band satellite image of PSB.SD with variouse indexes while examining the accuracy of the LULC classification. With this methodology, the success of various datasets for multiple classes was investigated.

* **Corresponding Author**

*(e-mail) ORCID ID xxxx – xxxx – xxxx – xxxx
(e-mail) ORCID ID xxxx – xxxx – xxxx – xxxx
(e-mail) ORCID ID xxxx – xxxx – xxxx – xxxx

Cite this study

Şahin, G. R., Kaplan, G. (2023). Land cover classification using various remote sensing datasets with PlanetScope SuperDove Data in GEE. Intercontinental Geoinformation Days (IGD), 6, 152-156, Baku, Azerbaijan

2. Method

2.1. Study araea

Karataş district of Adana province was determined as the first study area (144.208 km²). Karataş was established within the natural borders of the Seyhan and Ceyhan rivers in the Mediterranean Region. The lands of the district in Çukurova have a completely flat plain land structure. The district has natural beaches on the Mediterranean coast. In Karataş the summers are hot and humid, and the winters are with a temperate climate well above the average temperatures. Therefore, it is an important region in terms of agricultural areas. It is possible to find different products in agricultural lands every period. PlanetScope satellite images in April-May were filtered in this region. At this date, while some of the agricultural lands had green crops, the crops in some of them turned yellow (brown appearance), and in some agricultural areas, the agricultural lands appear empty due to new plantings. For this reason, while determining the land cover classes, agricultural areas were expressed with 3 different classes. For the purposes of this study, a total of 7 land cover classes were determined. These; residential areas (urban), water areas (water), forest (forest), bare land (bare land), agricultural areas 3 different classes (green agriculture crops), Brown agriculture crops (brown crop), bare cropland (empty field).

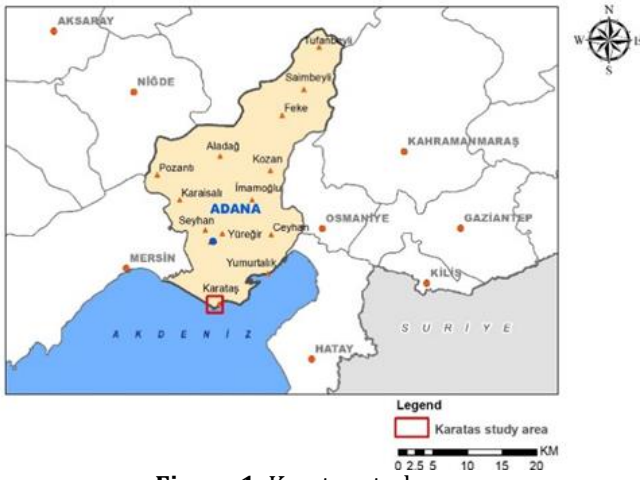

Figure 1. Karataş study area

Doğubeyazıt district of Ağrı province was determined as the second study area (150.557 km2). The lands of the district are made up of plains and volcanic mountains. Part of the plain, where rocks and hills can be seen from place to place, is barren. The high parts and foothills of the mountains are large pasture areas. The rainy season is spring and autumn. Planetscope satellite images from April-May in this region were filtered. The purpose of filtering these months is evident in the PlanetScope satellite image, due to the spring rains and pasture areas and grassland areas. The fact that the rocks and elevation are high is a factor in determining this area as the second study area. For the purposes of this study, 6 land cover classes were determined. These are; settlement areas (urban), pasture areas (pastures), bare land, cliffs (rocks), grassland (grassland) and road (road).

Figure 2. Doğubeyazıt study area

2.2. Methods

The PlanetScope satellite, launched in November 2018, has sensors with enhanced spectral resolution. Second-generation sensors from PlanetScope satellites (known as Dove-R or PS2.SD) have a sensor plane divided into four separate horizontal strips (one per radiometric band) along the flight path. Third-generation PlanetScope sensors (known as SuperDove or PSB.SD) are currently in orbit and produce images with 8 spectral bands. It is set to 0.3 pixels for PlanetScope products (PS2.SD and PSB.SD devices).

Table 1. PlanetScope PSB.SD Spectral Bands

PSB.SDSpectral Bands	Band No	Wavelength (nm)
Coastal Blue	b1	431-452 nm
Blue	b2	465-515 nm
Green I	b3	513-549 nm
Green II	b4	547-583 nm
Yellow	b5	600-620 nm
Red	b6	650-680 nm
Red-Edge	b7	697-713 nm
NIR	b8	845-885 nm

For this study, index-based algorithms created from Green I and Yellow bands from PSB.SD bands and Sentinel-2 satellite images were used.

Planet offers two geometry types (Basic and Ortho) for PlanetScope images. The basic scene products are designed for users with advanced image processing and geometric correction features. The product is not orthorectified or corrected for terrain disturbances. Ortho Scenes represent single-frame image captures with additional postprocessing as acquired by a PlanetScope satellite. PlanetScope Ortho Analytic 8B Scene Level 3D ortho geometry from Planetscope Satellite Image product processing levels was used.

In this study, we use PSB.SD sensor bands (8 bands) from Planetscope satellite for land cover classification for Karataş and Doğubeyazıt districts and Sentinel images integrated into GEE to investigate different datasets. GEE is a cloud computing platform designed to store and process huge datasets for analysis and final decision making (Kumar & Mutanga 2018). All the steps in the methodology were done in GEE. After Planetscope

images were integrated into GEE, visualization processes were performed.

The Planetscope satellite image of Karataş district was filtered for the months of April and May, when the land cover on the study area was fully developed and the land cover classes were thought to be better utilized. The first dataset of the study area includes all bands of the Planetscope satellite image dated 11 May 2021 with minimal cloudiness. Different indices (NDVI -Normalized vegetation difference index, NDWI -Normalized water difference index) were created with Planetscope satellite bands (Table1). The slope data of the study area was created using NASA SRTM Digital Elevation (30m) data integrated into GEE. Optimal datasets were searched by adding these data to the dataset.

The satellite image of Doğubeyazıt district, from April and May, which are thought to benefit better from the land cover classes on the study area, were filtered. The first dataset of the study area includes all bands of the Planetscope satellite image dated May 14, 2021, with minimal cloudiness. The slope data of the study area was created using NASA SRTM Digital Elevation (30m) data integrated into GEE. In addition, different indexes were created with Planetscope and Sentilen-2 satellite bands. NDVI (Normalized vegetation difference index) and EVI (Improved vegetation index) indexes were calculated with Planetscope, and UI (Urban index) and KBRI (Karst bare-rock index) indexes were calculated with Sentinel-2 (Table2). The slope data of the study area was created using NASA SRTM Digital Elevation (30m) data integrated into GEE. Optimal datasets were searched by adding these data to the dataset.

Table2. Spectral indices used in the Karataş study area

Index	Bands	PlanetScope-PSB.SD	Equation
NDVI	Red,NIR	b6, b8	(b8 – b6) / (b8 + b6)
NDWI	Green, NIR	b4, b8	(b4 – b8) / (b4 + b8)

Table3. Spectral indices used in the Dogubeyazit study area

Index	Bands	PSB.SD	Sentinel	Equation
NDVI	Red,NIR	b6, b8	-	(b8 – b6) / (b8 + b6)
EVI	NIR,Red, Blue	b8, b6, b2	-	2.5 * ((NIR - R) / (NIR + 6 * R - 7.5 * B + 1))
UI	SWIR2, NIR	-	B12, B8	(SWIR2-NIR)/(SWIR2+NIR)
KBRI	SWIR1, NIR	-	B11, B8	(SWIR1-NIR)/(20*sqrt (SWIR1+NIR)

RandomForest classifier, one of the GEE classification algorithms, was used for both study areas. Accuracy analysis of the classification process was performed. Accuracy analysis is based on comparison of sample classified cells selected from the classified image with reference cell classes. Accuracy assessment is an important factor in remote sensing analysis results.

In this study; While 170 sample points were randomly selected from the total land classes for the Karatas area, 280 sample points were selected for the Doğubeyazıt area. Overall accuracy and kappa values were tested as two accuracy measures for all classes. The overall accuracy provides information on the proportion of reference points mapped correctly, while the Kappa Coefficient means that the classification is based on randomly assigned sample points only.

3. Results and Discussion

The results of statistical analyzes, general accuracy and kappa values are presented in Table 3 for Karatas study area and Table 4 for Doğubeyazıt study area.

The first data set of the Karataş study area includes all of the PlanetScope PSB.SD bands (8 bands). In the second data set, the Green-I (b3) and Yellow (b5) bands are removed from the dataset, resulting in a decrease in the accuracy criteria. The addition of the slope data to the first dataset improves kappa and accuracy values. As the NDWI Index did not cause any change in the data set (dataset-5), the Coastal Blue (b1) band was removed from the dataset and the kappa value was calculated again and it was observed that the results increased slightly (dataset-6). Better accuracy values were obtained by adding the Urban index (UI) to the dataset (dataset-7). Finally, the b1 band was removed from the cluster again and the best accuracy value was achieved. As a result, the effect of certain indexes calculated from PlanetScope satellite bands and Sentinel 2 satellite bands on land cover classification accuracy was examined.

The first data set of Doğubeyazıt study area includes all of the PlanetScope PSB.SD bands (8 bands). In the second data set, the yellow (b5) band was removed and it was observed that the accuracy values decreased. It is understood that the importance of the Yellow band in the accuracy criterion is great for this study area. It is seen that the accuracy value increases when the GreenI (b3) band is removed from the data set. Adding NDVI Index and Green I (b3) band together to the data set increases the accuracy criteria again (dataset-5). This shows that the efficiency of some bands in accuracy measures increases by adding them to the data set with certain indexes. In later data sets, the best accuracy values are achieved by adding SLOPE, UI (Urban Index), KBRI (Karst Bare-Rock Index), EVI (Enhanced Vegetation Index) data. Due to the high elevation difference of the Doğubeyazit study area, the factor in reaching the best classification criterion of the SLOPE data is large.

Table4. Datasets used in Karataş study area

No	Dataset	OA	KAPPA
1	b1+b2+b3+b4+b5+b6+b7+b8	0.76	0.72
2	b1+b2+b4+b6+b7+b8	0.74	0.69
3	b1+b2+b3+b4+b5+b6+b7+b8+SLOPE	0.78	0.74
4	b1+b2+b3+b4+b5+b6+b7+b8+SLOPE+NDVI	0.80	0.76
5	b1+b2+b3+b4+b5+b6+b7+b8+SLOPE+NDVI+NDWI	0.80	0.76
6	b2+b3+b4+b5+b6+b7+b8+SLOPE+NDVI+NDWI	0.81	0.77
7	b1+b2+b3+b4+b5+b6+b7+b8 +SLOPE+NDVI +NDWI+UI	0.82	0.79
8	b2+b3+b4+b5+b6+b7+b8 +SLOPE+NDVI +NDWI+UI	0.84	0.81

Table 5. Datasets used in Doğubeyazit study area

No	Dataset	OA	KAPPA
1	b1+b2+b3+b4+b5+b6+b7+b8	0.74	0.67
2	b1+b2+b3+b4+b6+b7+b8	0.71	0.64
3	b1+b2+b4+b5+b6+b7+b8	0.75	0.68
4	b1+b2+b4+b5+b6+b7+b8+NDVI	0.75	0.69
5	b1+b2+b3+b4+b5+b6+b7+b8+NDVI	0.76	0.70
6	b1+b2+b3+b4+b5+b6+b7+b8+NDVI+SLOPE	0.81	0.77
7	b1+b2+b3+b4+b5+b6+b7+b8+NDVI+SLOPE+UI	0.83	0.79
8	b1+b2+b3+b4+b5+b6+b7+b8+NDVI+SLOPE+UI+KBRI	0.84	0.80
9	b1+b2+b3+b4+b5+b6+b7+b8+NDVI+SLOPE+UI+KBRI+EVI	0.85	0.81

Table6. Karataş user and producer accuracy for the individual classes using the investigated datasets

Class	Urban	Green Crops	water	Forest	Bare Land	Brown Crops	Bare Cropland
1	87/93	100/65	88/78	80/100	89/42	92/100	58/92
2	93/93	85/65	88/78	70/88	78/39	92/92	61/85
3	87/100	95/73	94/75	80/89	89/45	92/100	63/89
4	93/93	95/66	88/82	70/88	89/57	92/85	74/93
5	93/100	95/70	88/78	90/90	100/50	92/92	66/96
6	93/100	100/65	88/78	70/100	89/67	92/79	74/93
7	93/100	90/62	88/82	70/88	100/64	92/92	79/97
8	93/100	100/69	88/78	70/100	100/69	92/92	82/97

Table7. Doğubeyazıt user and producer accuracy for the individual classes using the investigated datasets

Class	Urban	Pastures	Bare Land	Rocks	Grassland	Road
1	99/91	79/69	73/65	0/0	88/97	48/42
2	100/89	72/61	69/66	10/20	81/97	48/45
3	100/93	77/64	78/67	16/50	81/100	48/53
4	100/93	75/66	77/64	16/45	84/100	43/53
5	100/92	75/73	78/66	10/25	88/97	48/48
6	99/93	81/69	80/70	10/25	86/95	52/55
7	99/94	89/75	78/75	60/88	83/97	52/55
8	100/96	87/77	83/77	56/93	85/97	57/57
9	100/99	85/73	85/78	60/94	83/100	57/57
10	100/99	96/76	88/78	44/92	85/98	52/65

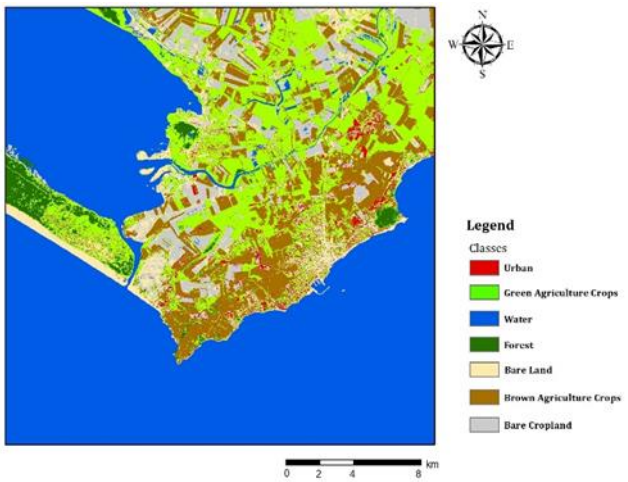

Figure 3. Karataş- sınıflandırma sonucu (dataset-8)

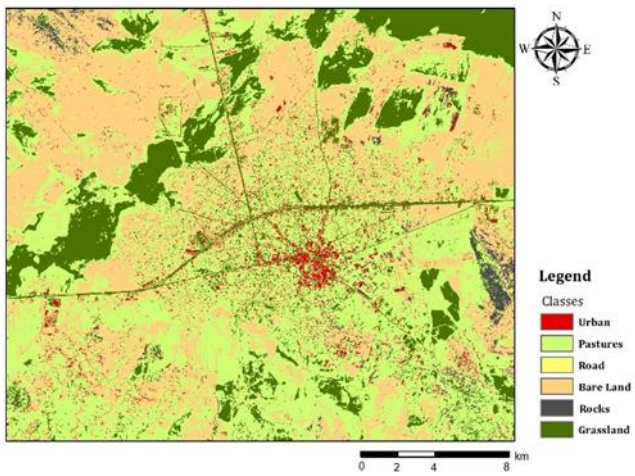

Figure 4. Doğubeyazıt- sınıflandırma sonucu (dataset-9)

References

Aghababaei, M., Ebrahimi, A., Naghipour, A. A., Asadi, E., & Verrelst, J. (2021). Vegetation types mapping using multi-temporal Landsat images in the google earth engine platform. Remote sensing, 13(22), 4683. https://doi.org/10.3390/ rs13224683

Abdollahnejad, A., Panagiotidis, D., & Surový, P. (2017). Forest canopy density assessment using different approaches–Review. Journal of forest science, 63(3), 107-116.

Brovelli, M. A., Sun, Y., & Yordanov, V. (2020). Monitoring forest change in the amazon using multi-temporal remote sensing data and machine learning classification on Google Earth Engine. ISPRS International Journal of Geo-Information, 9(10), 580. https://doi.org/10.3390/ijgi9100580

Kaplan, Gordana & Milevski, Ivica & Valjarevic, Aleksandar. (2022). National land cover mapping using various remote sensing datasets in GEE. Carpathian Journal of Earth and Environmental Sciences. 17. 297-306. https://doi.org/10.26471/cjees/2022/017/223

Kaplan, G., & Avdan, U. (2019). Evaluating the utilization of the red edge and radar bands from sentinel sensors for wetland classification. Catena, 178, 109-119. https://doi.org/10.1016/j.catena.2019.03.011

Vizzari, M. (2022). PlanetScope, Sentinel-2, and Sentinel-1 Data Integration for Object-Based Land Cover Classification in Google Earth Engine. Remote Sensing, 14(11), 2628. https://doi.org/10.3390/rs14112628

Yao, J., Wu, J., Xiao, C., Zhang, Z., & Li, J. (2022). The classification method study of crops remote sensing with deep learning, machine learning, and Google Earth engine. Remote Sensing, 14(12), 2758. https://doi.org/10.3390/ rs14122758

6th Intercontinental Geoinformation Days

igd.mersin.edu.tr

Classification of hybrid maize seeds (Zea mays) with object-based machine learning algorithms using multispectral UAV imagery

Ismail Colkesen[1*], Umut Gunes Sefercik[1], Taskin Kavzoglu[1], Hasan Tonbul[1], Muhammed Yusuf Ozturk[1], Osman Yavuz Altuntaş[1], Mertcan Nazar[1], Ilyas Aydin[1]

[1]*Gebze Technical University, Engineering Faculty, Department of Geomatics Engineering, Kocaeli, Türkiye*

Keywords
Multispectral UAV
CCF
RotFor
SVM
NDSM

Abstract

In recent years, detailed monitoring of different vegetation classes by using modern remote sensing technologies has become one of the essential issues for smart agriculture activities. In this study, using three advanced machine learning algorithms, namely canonical correlation forest (CCF), rotation forest (RotFor) and support vector machines (SVM), and object-based image classification techniques on multispectral (MS) unmanned aerial vehicle (UAV) orthomosaics, the separability of 12 maize species were investigated. The investigations were performed in Sakarya Maize Research Institute application area located in Arifiye district of Sakarya province, Turkey. In maize monitoring, besides the five spectral bands (R, G, B, red edge, NIR) of the MS UAV, the Normalized Digital Surface Model (NDSM) describing the height of maize species was generated and included as an additional band to improve classification performance, evaluated with F-score, overall accuracy (OA) and Kappa metrics. The results demonstrated that CCF and RotFor algorithms provide similar OA as 76.61% and 76.75%, respectively and the SVM algorithm has 74.18%. In parallel, the Kappa values of CCF and RotFor are 0.75 and the SVM is 0.72. In terms of class-based F-scores, by all algorithms, C. Sweet and C. Arifiye were identified with over 97% and 94% accuracies, respectively, that prove the successful determination of their boundaries using object-based classification.

1. Introduction

Cereals are grown in large quantities around the world for their edible parts and provide billions of people with more food energy than all other crops combined (Bigini et al. 2021). The maize plant, included in the cereal group, is a plant of high economic value, adaptability, and the highest productivity (Slavin 2004). The plant can be cultivated at altitudes up to thousands of meters in almost every region of the earth's surface, except in the polar regions where cold climatic conditions prevail (Kırtok 1998). Approximately 20% of the maize produced worldwide is used in human nutrition, 65-70% is used as animal feed and the remaining 10-15% is used in industry (Bilgic et al. 2012). Due to the increasing population in Türkiye, the need for maize plants is increasing day by day, and imports have been undertaken to maintain the balance between production and consumption (Akkurt and Demirbas 2021). Accordingly, the detailed monitoring of maize and increase its production have a vital importance.

Traditionally, plant monitoring studies are carried out by onerous, low-accuracy and costly terrestrial methods in under-developed or developing Countries. In contrast, modern remote sensing technologies provide easily achievable, highly accurate, low-cost data. In recent years, especially the Unmanned Aerial Vehicles (UAV) has become indispensable for large-scale mapping, smart agriculture and forest activities and image classification by means of high-resolution, high-frequency and low-cost multispectral data (Sefercik et al. 2021).

In the literature, several studies exist about plant monitoring by modern remote sensing technologies. In Yilmaz (2018), multi-temporal Sentinel-2 satellite images and object-based classification approach were used to generate crop maps of 9 different plant species growing including maize plant. In the study carried out by Öztürk (2021), multi-temporal PlanetScope satellite images were used together with texture features to map the vineyard plant. Object and pixel-based classification methods were applied with machine learning algorithms, and the highest overall accuracy (91%) was obtained in

* **Corresponding Author**

*(icolkesen@gtu.edu.tr) ORCID ID 0000-0001-9670-3023

Cite this study

Colkesen, I., Sefercik, U. G., Kavzoglu, T., Tonbul, H., Ozturk, M. Y., Altuntas, O. Y., Nazar, M. & Aydin, I. (2023). Classification of hybrid maize seeds (Zea mays) with object-based machine learning algorithms using multispectral UAV imagery. Intercontinental Geoinformation Days (IGD), 6, 157-161, Baku, Azerbaijan

object-based classification method using Random Forest algorithm. In the study conducted by Guo et al. (2022), plant heights were measured using RGB and Multispectral (MS) UAV images in three years. Using the generated digital elevation model (DEM) and vegetation and texture indices as the basic data set, the combination of DEM-RGB VI was found to adequately (90%) predict the heights of maize plants.

In this study, on generated MS UAV orthomosaic, the separability of 12 different maize species was examined by using advanced machine learning algorithms and object-based image classification method during the period of the tassel showing a strong relationship with yield. The performance of maize classification was improved with the contribution of generated Normalized Digital Surface Model (NDSM), produced with RGB UAV data.

2. Study Area and Dataset

The study area is located in the Arifiye district of Sakarya province, Türkiye. In the area, 12 agricultural parcels in rectangular shape each has 500 m^2 (20 m × 25 m) are designed and has been planted with a different type of maize species. For easier separation of parcels from each other and delineation of each parcel clearer, 2.5 m width roads were left between them. Figure 1 shows the study area and maize species.

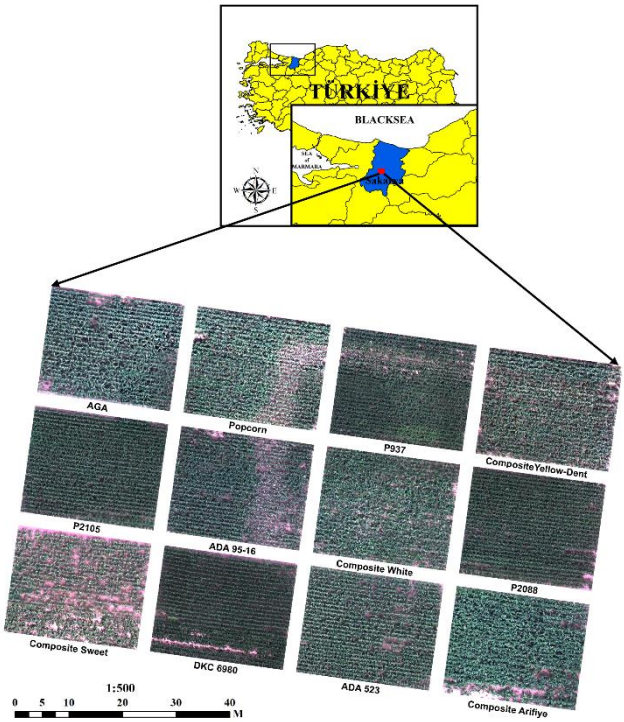

Figure 1. Study area and maize species

3. Methodology

3.1. UAV data acquisition

The flights were planned with two different UAVs as DJI Phantom 4 MS RTK and DJI Phantom 4 Pro V2.0 RGB with different imaging capabilities. While, five band (R, G, B, red edge, NIR) multispectral aerial photos were collected with 2.08 MP spatial resolution by MS UAV to create qualified orthomosaic for classification processes, 20 MP aerial photos were provided by RGB UAV to generate high resolution NDSM. The flights were implemented as polygonal and bundle grid from 50 m altitude applying 80% and 60% front and side overlap, respectively. In bundle-grid flights, 70° camera viewing angle (off-nadir 20°) was preferred while nadir view is applied in polygonal flights. The aerial photos were achieved with ground sampling distances (GSD) of 1.44 cm and 2.61 cm for RGB and MS UAV flights.

For geometric calibration of the RGB UAV aerial photos, mobile polycarbonate ground control points (GCPs) were established and measured by CHC-i80 GNSS receiver before the flights. GCPs were not required for MS UAV due to availability of RTK GNSS equipment. For radiometric calibration of MS UAV aerial photos, MAPIR V2 calibration target was observed by the UAV at the beginning of the flights.

3.2 Generation of UAV orthomosaic and NDSM

UAV orthomosaics were produced applying photogrammetric processing steps for orthomosaic generation in SfM-based Agisoft Metashape Professional Software (Sefercik et al. 2022). With the advantage of SfM approach, reconstruction of the 3D geometry in high resolution from a series of overlapping 2D sequential photos is possible (Westoby et al., 2012). In photogrammetric processing, first the UAV aerial photos were oriented in two steps as generation of the sparse point cloud by initial alignment and absolute orientation utilizing GCPs. The sparse point cloud is a low-resolution 3D vector representation of the study area and generated to increase geometric orientation accuracy however it is insufficient for further process. That's why, dense point clouds, which provide more realistic and complex characterization of the study area for producing high-quality orthomosaic, were generated utilizing depth maps. Using dense point cloud, a 10 cm grid digital surface model (DSM), the 3D digital cartographic representation of earth surface including all natural and human-made objects, was generated applying vector-raster transformation. As a last step for photogrammetric processing, orthomosaic was produced with 2.6 cm GSD.

NDSM is the differential 3D model of the DSM and the digital terrain model (DTM) which is the 3D digital representation of bare earth surface. By subtracting the bare earth surface from the crown surface of the maize using RGB UAV DSM and DTM, the exact heights were calculated by utilizing LISA software. NDSM of the maize species are shown in Figure 2.

3.3 Object-based classification

This study investigated the separability of maize species through object-based image classification. To achieve this purpose, three process steps, including i) image segmentation, ii) determination of class labels of segments via machine learning algorithm, and iii) accuracy assessment, were performed.

Due to its more effective and accurate performance in classifying high-resolution images compared to the pixel-

based technique, object-based classification has been widely utilized in many research (Whiteside et al. 2011; Georganos et al. 2018; Chen et al. 2018). Unlike traditional pixel-based mapping, the pixels are combined into meaningful objects or segments based on their spectral, spatial, and contextual specifications in the object-based classification, and this process is known as image segmentation. The multi-resolution segmentation (MRS) presented by Baatz and Schape (2000), a robust and effective algorithm, was applied to the UAV dataset to perform image segmentation. The segmentation process is controlled by three main parameters (i.e., scale, shape, and compactness) by MRS. Since the definition of scale parameter value determining the segment sizes is one of the most significant factors affecting the qualitative and quantitative results of thematic mapping, several algorithms were developed to estimate the optimal value of this parameter. In this paper, the Estimation of Scale Parameter-2 (ESP-2) algorithm developed by (Drăguţ et al. 2014) was employed to select scale parameter.

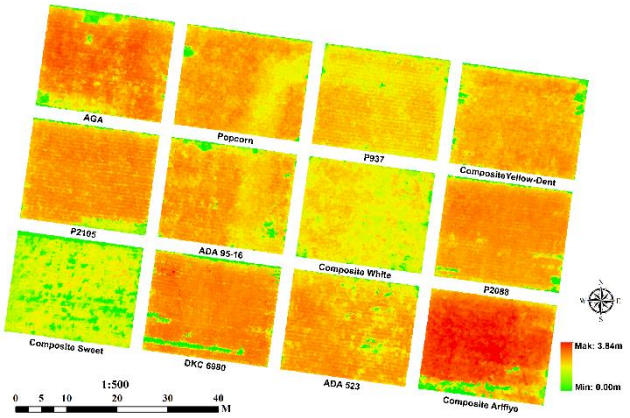

Figure 2. NDSM of maize species

3.4 Classification algorithms

Within the scope of this study, three robust machine learning algorithms, namely canonical correlation forest (CCF), rotation forest (RotFor) and support vector machine (SVM), were employed for estimating the class labels of each segment.

RotFor, presented by Rodriguez et al. (2006), is one of the most effective tree-based machine learning algorithms. RotFor, which has a similar structure to the random forest, first randomly splits the input variables into K subsets, unlike this algorithm. Then, principal component analysis is applied to each subset before constructing individual decision trees. The unknown class labels of each sample are determined by majority voting (Colkesen and Ozturk 2022).

CCF was introduced by Rainforth and Wood (2015), mainly based on applying canonical correlation analyses (CCA) to ensure maximum correlation between features and class labels before the construction of the classification model (Colkesen and Ertekin 2020). With canonical correlation, not only the relationship between features but also the relationship between features and class labels are considered.

SVM is one of the most widely used machine learning algorithms in the literature due to its robustness and success in solving complex classification and regression problems. The basic principle of the algorithm is to map the nonlinear input data (e.g., UAV imagery) into a higher-dimensional feature space through kernel functions and determine an optimum hyperplane separating two classes in the feature space (Kavzoglu and Colkesen 2009).

4. Results

In this research, the MRS algorithm was applied to UAV dataset with five spectral bands and NDSM to obtain homogeneous image objects. The shape and compactness values of the MRS algorithm were set as 0.5 and 0.9 by considering the trial-and-error strategy, while the scale parameter value was determined using an automated estimation algorithm, ESP-2, based on these parameter values. According to the ESP-2 result, the optimal scale value was estimated as 52, and input image was divided into 100,311 segments (Figure 3). A total of 68 spectral, spatial and textural features, including maximum, minimum, mean, standard deviation, mode, ratio, brightness, area of the pixel, GLCM entropy, GLCM contrast, GLCM homogeneous, GLCM mean and GLCM standard deviation values were calculated and utilized in the object-based mapping.

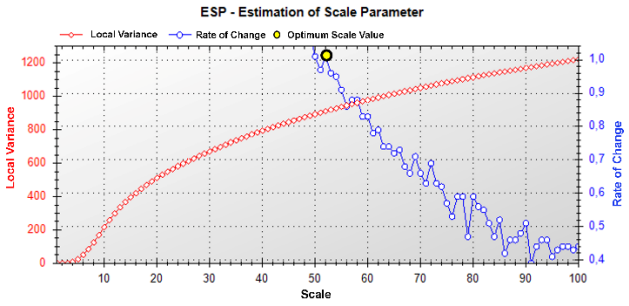

Figure 3. LV-RoC graphs produced by ESP-2.

In the prediction of class labels of each segment by CCF, RotF, and SVM algorithms, a total of 3,035 and 913 segments were utilized to construct classification models and hyperparameter optimizations, respectively. CCF and RotF algorithms were implemented in MATLAB software, while the SVM thematic mapping process was conducted in R software. In addition, 3,000 samples for each class (a total of 42,000) were selected on the UAV data to evaluate thematic maps produced by machine learning algorithms statistically. Confusion matrix-based metrics, overall accuracy (OA), Kappa coefficient, and F-Score, were calculated to assess accuracy. Estimated class-level accuracies (i.e., F-score) of hybrid maize species and map-level accuracies (i.e., OA and Kappa coefficient) were given in Table 1. As can be seen from the table, the map level accuracies of CCF and RotFor are approximately 77%, while the accuracy achieved with the SVM algorithm is 74.18%.

When class-level accuracies of each crop were analyzed, all algorithms estimated that C. Arifiye and C. Sweet maize crops with over 94% accuracy. In addition, individual class accuracies of C. White and DKC 6980

crops were about 81% and 89%. On the other hand, algorithms showed inferior performance in the determination of ADA 95-16 and ADA 523 classes, producing the lowest F-Score values. Furthermore, the boundaries of popcorn, AGA, and P2105 maize crops were separated from other crop types with a better class-based accuracy using CCF and RotF algorithms. On the other hand, SVM outperformed the other algorithms for classifying P937 maize class with approximately 4% higher accuracy.

Table 1. Object-based classification results.

Maize Crop	F-Score (%)		
	CCF	RotF	SVM
C. Yellow-Dent	64.29	62.80	56.34
P937	74.46	75.06	79.92
Popcorn	62.70	60.71	52.57
AGA	76.98	79.19	71.31
P2105	64.45	63.94	60.05
ADA 95-16	50.37	54.14	48.57
C. White	80.04	81.44	80.47
P2088	67.92	69.99	68.04
C. Arifiye	94.38	95.20	94.86
ADA 523	50.86	46.67	48.03
DKC 6980	89.01	87.67	90.11
C. Sweet	99.52	97.69	97.48
Shadow	94.73	94.40	92.40
Soil	99.92	99.98	97.30
OA (%)	76.61	76.75	74.18
Kappa	0.75	0.75	0.72

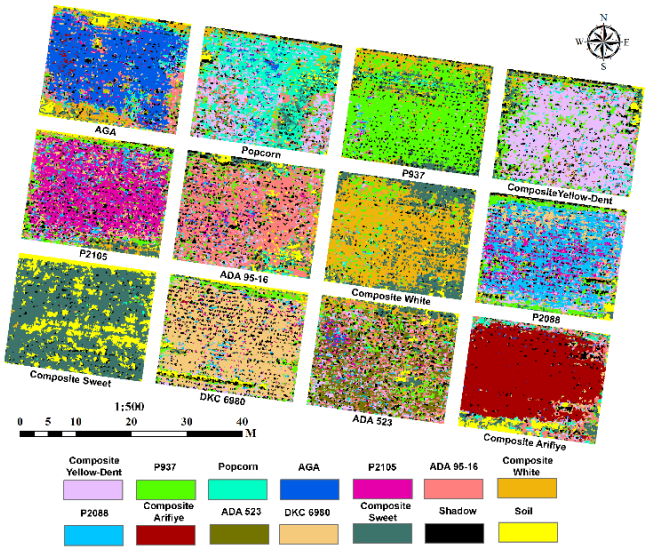

Figure 4. Thematic map of RotFor algorithm

As an example of the crop maps, a thematic map produced by of RotFor algorithm with the highest OA value was presented in Figure 4 to perform qualitative evaluations. When the figure was analyzed, it was observed that the boundaries of C. Arifiye, DKC 6980, and C. Sweet were successfully identified using object-based image classification. On the other hand, in the area where ADA 523 is cultivated, it is observed that the misclassifications are relatively high, and it cannot be distinguished due to its spectral similarity to other species. In addition, misclassification errors were also observed in the P2105 and P208 cultivated fields.

5. Conclusion

This study investigated the separability of 12 maize crop types through object-based image classification. Several important conclusions can be drawn as follow. First, object-based mapping of the C. Arifiye and C. Sweet maize crops was conducted with over 94% class-based accuracy. In addition, it was observed that the boundaries of these crop types were successfully determined by object-based mapping. The most important reason for this result is the heights of the two corn types mentioned. This finding verified that utilizing NDSM as an auxiliary dataset positively contributed to determining and identifying maize species. Secondly, all machine learning algorithms showed inadequate classification performance for ADA 523. As a result, it can be stated that ensemble-learning algorithms make statistically more accurate predictions than the SVM algorithm in the classification of maize species considered in this study. To increase the accuracy of the results obtained, there is a need for further studies to examine the spectral structure and height changes of these maize species in different phenological stages.

Acknowledgement

This work was funded and supported by the Scientific and Technological Research Council of Turkey (TUBITAK) under project no: 121Y392. Special thanks to the Ministry of Agriculture and Forestry Sakarya Maize Research Institute for their valuable contributions to the project.

References

Akkurt, E., & Demirbaş, N. (2021). Türkiye'de mısır üretiminde kendine yeterliliğin değerlendirilmesi. XV. IBANESS İktisat, İşletme ve Yönetim Bilimleri Kongreler Serisi–Plovdiv/Bulgaristan, 29-30.

Baatz, M., & Schape, A. (2000). Multiresolution segmentation: an optimization approach for high quality multi-scale image segmentation. Angewandte Geographische Informationsverarbeitung, 12(12), 12–23.

Bigini, V., Camerlengo, F., Botticella, E., Sestili, F., & Savatin, D. V. (2021). Biotechnological resources to increase disease-resistance by improving plant immunity: A sustainable approach to save cereal crop production. Plants, 10(6), 1146.

Bilgiç, S., Sade, B., Soylu, S., Bilgicli, N., Cerit, I., Öz, A., Cengiz, R. & Özkan, I. (2012). Maize report. Mısır raporu. National Grain Council.

Chen, Y., Ming, D., Zhao, L., Lv, B., Zhou, K., & Qing, Y. (2018). Review on High Spatial Resolution Remote Sensing Image Segmentation Evaluation. Photogrammetric Engineering & Remote Sensing, 84(10), 629–646. https://doi.org/10.14358/PERS.84.10.629

Colkesen, I., & Ertekin, O. H. (2020). Performance Analysis of Advanced Decision Forest Algorithms in Hyperspectral Image Classification. Photogrammetric Engineering & Remote Sensing, 86(9), 571–580. https://doi.org/10.14358/PERS.86.9.571

Colkesen, I., & Ozturk, M. Y. (2022). A comparative evaluation of state-of-the-art ensemble learning algorithms for land cover classification using WorldView-2, Sentinel-2 and ROSIS imagery. Arabian Journal of Geosciences, 15(10), 942. https://doi.org/10.1007/s12517-022-10243-x

Drăguț, L., Csillik, O., Eisank, C., & Tiede, D. (2014). Automated parameterisation for multi-scale image segmentation on multiple layers. ISPRS Journal of Photogrammetry and Remote Sensing, 88, 119–127. https://doi.org/10.1016/j.isprsjprs.2013.11.018

Georganos, S., Grippa, T., Vanhuysse, S., Lennert, M., Shimoni, M., & Wolff, E. (2018). Very High Resolution Object-Based Land Use–Land Cover Urban Classification Using Extreme Gradient Boosting. IEEE Geoscience and Remote Sensing Letters, 15(4), 607–611. https://doi.org/10.1109/LGRS.2018.2803259

Guo, Y., Xiao, Y., Li, M., Hao, F., Zhang, X., Sun, H., Beurs, K., Fu, Y. H. & He, Y. (2022). Identifying crop phenology using maize height constructed from multi-sources images. International Journal of Applied Earth Observation and Geoinformation, 115, 103121.

Kavzoglu, T., Colkesen, I., (2009). A kernel functions analysis for support vector machines for land cover classification. International Journal of Applied Earth Observation and Geoinformation, 11, 352–359. https://doi.org/10.1016/j.jag.2009.06.002

Kırtok Y. (1998). Mısır Üretim ve Kullanımı. Kocaoluk Basın ve Yayınevi, Sayfa 445, İstanbul.

Öztürk, M. (2021). Asmaların haritalanmasında farklı sınıflandırma yaklaşımları ve algoritmalarının başarılarının araştırılması. [Doctoral thesis, Eskisehir Technical University]. CoHE Thesis Center. https://tez.yok.gov.tr/UlusalTezMerkezi/giris.jsp

Rainforth, T., & Wood, F. (2015). Canonical Correlation Forests. ArXiv Preprint ArXiv:1507.05444.

Rodriguez, J. J., Kuncheva, L. I., & Alonso, C. J. (2006). Rotation Forest: A New Classifier Ensemble Method. IEEE Transactions on Pattern Analysis and Machine Intelligence, 28(10), 1619–1630. https://doi.org/10.1109/TPAMI.2006.211

Sefercik, U. G., Kavzoğlu, T., Colkesen, I., Nazar, M., Ozturk, M. Y., Adali, S., & Dinc, S. (2021). Land Cover Classification Performance of Multispectral RTK UAVs, ISPRS SCA'21 International Smart City Applications Conference, Karabuk, Turkey, 27-29 October 2021.

Sefercik, U. G., Kavzoğlu, T., Nazar, M., Atalay, C., & Madak, M. (2022). Creation of a Virtual Tour. Exe Utilizing Very High-Resolution RGB UAV Data. International Journal of Environment and Geoinformatics, 9(4), 151-160.

Slavin, J. (2004). Whole grains and human health. Nutrition research reviews, 17(1), 99-110.

Westoby, M. J., Brasington, J., Glasser, N. F., Hambrey, M. J., Reynolds, J. M. (2012). 'Structure-from-Motion' photogrammetry: A low-cost, effective tool for geoscience applications. Geomorphology, 179, 300-314.

Whiteside, T. G., Boggs, G. S., & Maier, S. W. (2011). Comparing object-based and pixel-based classifications for mapping savannas. International Journal of Applied Earth Observation and Geoinformation, 13(6), 884–893. https://doi.org/10.1016/j.jag.2011.06.008

Yılmaz, M. (2018). Tarımsal Yaz Ürünlerin Sentinel-2 Uydu Görüntülerinden Rastgele Orman Algoritması İle Nesne-Tabanlı Sınıflandırılması. MS thesis, Hacettepe University, Ankara.

6thIntercontinental Geoinformation Days

igd.mersin.edu.tr

Study of land subsidence induced by oil extraction in the Tengiz oilfield of Kazakhstan using radar interferometry (InSAR)

Emil Bayramov*[1], Manfred Buchroithner [2], Martin Kada [3], Saida Aliyeva [4]

[1] *Nazarbayev University, School of Mining and Geosciences, Astana, Kazakhstan*
[2] *Dresden University of Technology, Institute of Cartography, Dresden, Germany*
[3] *Technical University of Berlin, Institute of Geodesy and Geoinformation Science, Berlin, Germany*
[4] *ADA University, School of Education, Baku, Azerbaijan*

Keywords
SBAS
2D and 3D decomposition
Geospatial
Oil field
Interferometry

Abstract

Our studies focused on the assessment of the surface deformation velocities and cumulative displacements at Tengiz Oilfield in Kazakhstan using the Small Baseline Subset remote sensing technique followed by 3D and 2D decompositions and cosine corrections to derive vertical and horizontal movements from line-of-sight (LOS) measurements. In the present research we applied time-series of Sentinel-1 satellite images acquired during 2018-2020. All ground deformation derivatives showed the continuous subsidence at the Tengiz oilfield with increasing velocity. 3D and 2D decompositions of LOS measurements to vertical movement showed that the Tengiz Oil Field 2018-2020 continuously subsided with the maximum annual vertical deformation velocity around 70 mm. Based on the LOS measurements, the maximum annual subsiding velocity was observed to be 60 mm. The results of the present research will support operators of oil and gas fields and also other types of infrastructure to evaluate the actual differences of InSAR ground deformation measurements against the required standards and the precision of measurements depending on the operational needs, timeframes and availability of radar imagery.

1. Introduction

Tengiz is an oilfield located in NW Kazakhstan's low-lying wetlands along the northeast shores of the Caspian Sea. Recent studies by Grebby et al. (2019) and Orynbassarova (2019) proved that Tengiz Field has been for some time under the long-term influence of subsidence induced by oil and gas production. Monitoring of ground deformation processes at oil and gas fields has several business values for industry since it is one of the critical input parameters for geohazard risk assessment, induced seismicity, geomechanics surveillance programs (reservoir stress, volumetric strain, fault reactivations and dislocation), site safety for fault or landslide reactivation, well failures, environmental assessment, reservoir modelling, enhanced oil recovery (EOR), oil and gas production. Interferometric Synthetic Aperture Radar (InSAR) technology was verified as a more effective technology for the ground deformation monitoring of large oil and gas fields and their infrastructure rather than traditional geodetic measurements of single points (Bayramov et al., 2020a, Bayramov et al. 2020b, Bayramov et al., 2020c, Mirzaii et al., 2019). Even though geodetic measurements have higher accuracy, they do not reflect the large scale of deformation patterns (Shi et al., 2019). However, there have been few publicly accessible studies on the surface deformation characteristics of the Tengiz field in recent years. Therefore, monitoring recent surface deformations over the Tengiz oilfield is of great importance and business value for guiding the continued exploitation there. To the extent of our knowledge, there are also no publicly accessible studies focused on the use of 3D or 2D decomposition techniques to derive vertical and horizontal deformations for the Tengiz field in the recent years. The present studies thus offer practical scientific value and advantages for the petroleum and gas industry.

***Corresponding Author**

*(bayramov@nu.edu.kz) ORCID ID 0000-0002-3804-5373

Cite this study

Bayramov, E., Buchroithner, M., Kada, M., & Aliyeva, S. (2023). Study of land subsidence induced by oil extraction in the Tengiz oilfield of Kazakhstan using radar interferometry (InSAR), 6, 162-167, Baku, Azerbaijan

Our research focused on the quantitative assessment of the surface deformation velocities and rates and their natural and man-made controlling factors at the Tengiz oilfield using Small Baseline Subset (SBAS) remote sensing and geostatistical interpolation techniques followed by 3D and 2D decompositions and cosine corrections to derive vertical and horizontal movements from LOS measurements. Sentinel-1 satellite images acquired from ascending and descending tracks during 2018-2020 were used in our studies. The detailed research goals are as follows:

(1) Determination of ground deformation velocities and rates at the Tengiz oilfield over the period of 2018-2020 using SBAS remote sensing techniques followed by 3D and 2D decompositions and cosine corrections to derive vertical and horizontal east-west and north-south movements from LOS measurements

(2) Detection of vertical and horizontal ground deformation hotspots

(3) Quantitative comparison of the ground deformation velocities and rates derived from LOS, 3D and 2D decomposition and cosine correction measurements

(4) Assessment of the spatial relationships between the detected patterns of vertical and horizontal ground deformations, man-made oil field exploitation and natural tectonic processes

(5) Provision of recommendations to operators of oil and gas fields and other types of petroleum infrastructure.

2. Method

2.1. Study Area

The Tengiz oilfield was discovered in 1979 and it is one of the largest discoveries worldwide in recent history. It is located in north-western Kazakhstan's low-lying wetlands along the northeast shores of the Caspian Sea (Figure 1) and covers an area of 430 km2, being 19 km wide and 21 km long. It is located 150 km south-east of the city of Atyrau which is considered to be the main transport hub for Tengiz oil. Tengiz field has recoverable reserves estimated at between six billion and nine billion barrels. However, the reservoir is estimated to contain around 25 billion barrels of oil and is located at the depth of 3885-5117 m (Grebby et al., 2019). The oil comes out of wells hot at high pressure and with a large proportion of gas. Current oil production is 720,000 barrels per day. The region has a semi-arid climate, with temperatures decreasing to –30°C in winter and reaching up to 40C in summer. The average annual precipitation varies in the range of 100 - 200 mm (Klein et al., 2012). The terrain of the study area is flat, but with regular depressions formed as a result of seasonal snow melts and rainfalls (Grebby et al., 2019). The sour gas injection enhanced oil recovery method is used at the Tengiz oilfield (Bealessio et al., 2020). The Tengiz field is located within the seismically active region of Kazakhstan (Sokolova et al., 2017).

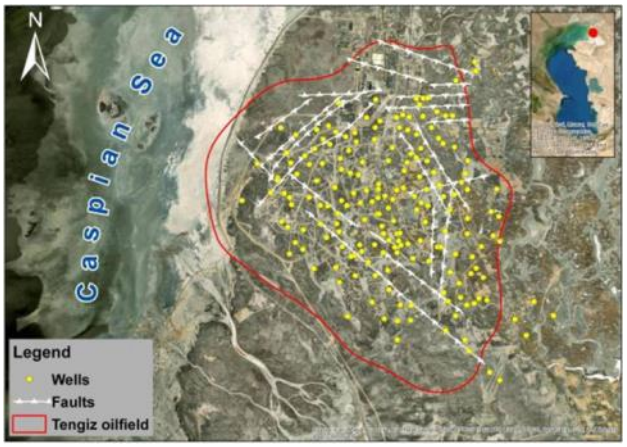

Figure1. Tengiz oilfield with the representation of wells.

2.2. Quantitative Assessment of Ground Deformations at Tengiz Oilfield using SBAS Techniques, 3D & 2D Decompositions and Cosine Corrections

C-band (5.6 cm wavelength and 5.4 GHz) Sentinel-1 A/B TOPS images from the European Space Agency (ESA) were used for the present research to map the spatial distribution and rates of ground deformation at the Tengiz oilfield. Sentinel-1 VV polarization bands were used since co-polarized bands provide higher coherence (Imamoglu et al., 2019). As it is possible to observer in Figure 2a, the study area was fully covered by all three tracks. Sentinel-1 images in wide-swath mode provide a wide coverage of about 250 km with a slant range resolution of 5 m and an azimuth resolution of 20 m (Yang et al., 2019). The connection graphs of SAR images in Figure 2b and Figure 2c show that all radar images were well connected in time in order to follow the displacement monitoring over the period of 2018-2020. The interferometric processing was performed using the Small Baseline Subset (SBAS) technique followed by 3D and 2D decompositions, cosine corrections and geospatial analysis to derive both vertical and horizontal deformations (Figure 3).

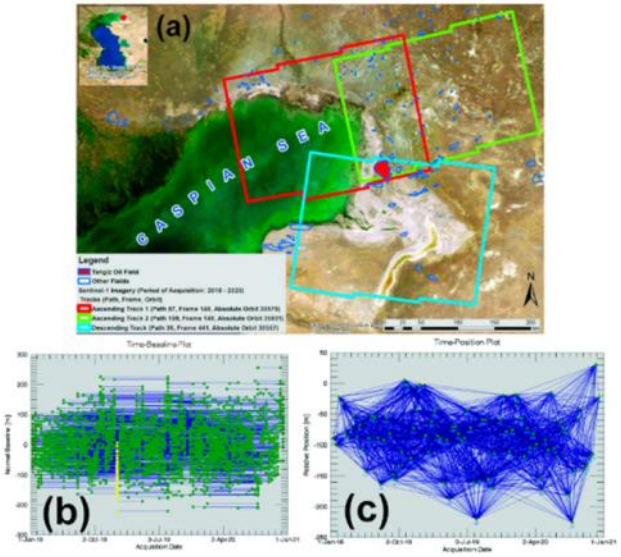

Figure 2. (a) Sentinel-1 imagery track numbers and acquisition details; connection graphs: (b) time-position plot for SBAS; (c) time-baseline plot for SBAS.

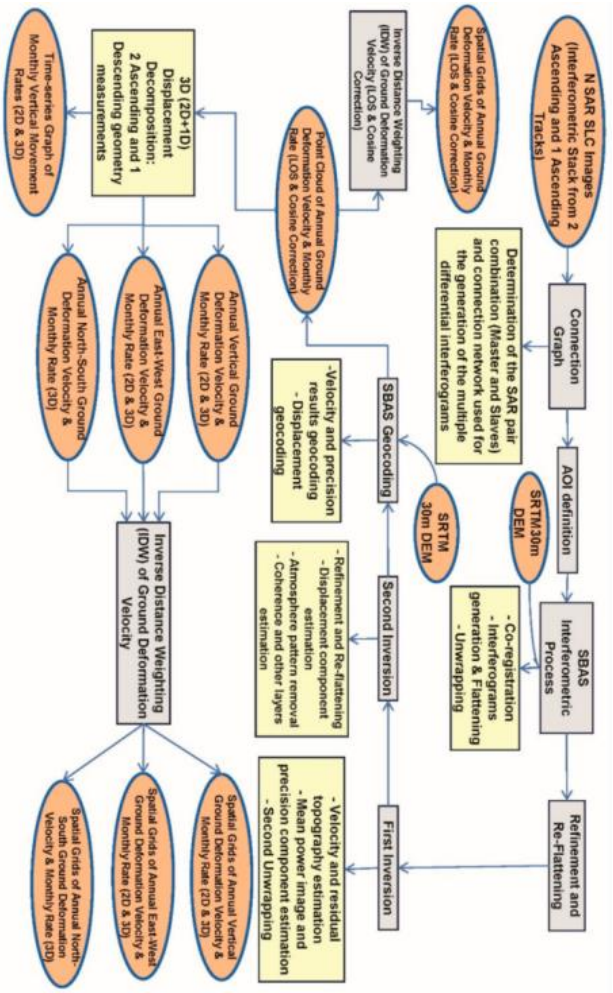

Figure 3. Workflow of SBAS interferometric processing followed by 2D and 3D decompositions, cosine correction and geostatistical interpolations.

3. Results

The 3D and 2D decompositions of LOS measurements 2018-2020 to vertical displacement allowed to determine that annual average vertical deformation velocity over the Tengiz oilfield was in the range of – 70.04-22.44 mm/year and –73.29-23.70 mm/year, respectively (Figure 4a, b).

The range of vertical subsidence velocities was observed to be slightly higher than in case of LOS measurements. Based on the Pearson Correlation Coefficient > 90 and t-test p-value > 0.05 in Figure 4c and Figure 4d, it is possible to conclude that both 3D and 2D decompositions produced identical vertical deformation velocities with an RMSE of 1.86 mm. Even though many research activities applied the LOS measurements for the operational purposes of oil and gas fields, as mentioned before, it was possible to observe differences in LOS displacements compared to 3D and 2D decomposition results (Figure 4d).

The vertical velocity obtained through the division of the LOS displacement rates by the cosine of the radar incidence angle is presented in Figure 5a-c. The histogram of vertical velocity distribution derived from cosine correction is presented in Figure 5d. Like the previously mentioned histogram of LOS measurements, in this case it was also possible to observe significant variations in the spatial distribution of ground deformation values (Figure 5d). These variations might also create a challenge and uncertainties for the oil and gas operators even though the cosine correction was applied to derive vertical deformation velocity. However, the RMSE between vertical deformation velocities derived from cosine correction and from 3D decomposition reduced twice with the variation in the range of 6-8 millimetres. Along the profiles in Figure 5a-c it was possible to observe differences between 3D decomposition vertical deformation and cosine-corrected velocities in the range of 0-17 mm (Figure 5e). It is possible to conclude that the cosine correction of LOS measurements to vertical deformation velocity obviously improved the overall reliability of ground movement measurements. However, it is still possible to observe variations along the profile which may also create a different kind of uncertainties for the operators of oil and gas fields.

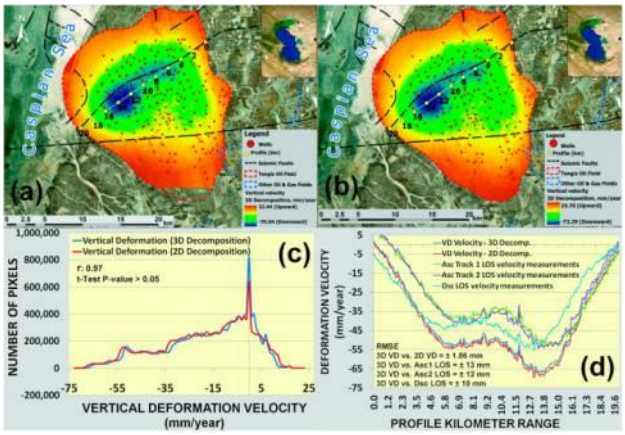

Figure 4. Vertical deformation velocity derived: (a) from 3D decomposition of 2 ascending and 1 descending LOS measurements; (b) from 2D decomposition of 1 ascending and 1 descending LOS measurements; (c) histogram of vertical deformation velocities derived from 3D and 2D decompositions; (d) profiles of vertical deformation velocities derived from 3D and 2D decompositions and LOS measurements.

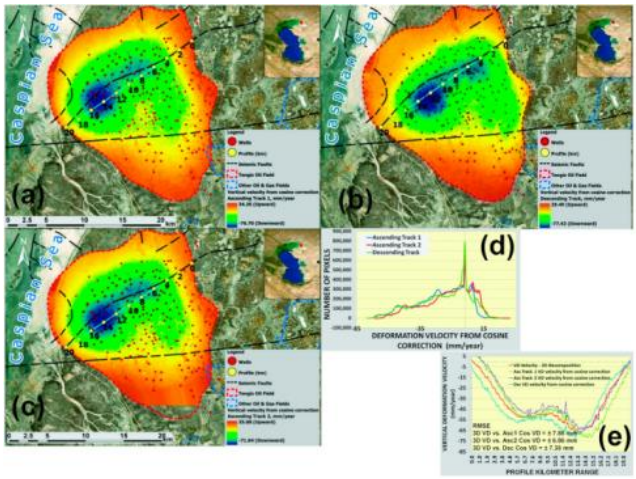

Figure 5. Vertical deformation velocity derived from cosine correction: (a) Ascending track 1; (b) Descending Track; (c) Ascending Track 2; (d) histogram of vertical velocity distribution derived from cosine correction; (e)

comparison of vertical velocity profiles derived from 3D decompositions and cosine corrections.

The hotspot of significant subsidence is located at the intersection of profile lines in Figure 6a and Figure 6b. The location of maximum subsidence velocity was also observed at the intersection of profiles indicated in Figure 6a. As it is possible to see in Figure 6b, the maximum annual vertical deformation velocity of maximum subsidence along profiles reaches about 70 mm. Location and time series of cumulative ground displacement rates of the maximum subsiding position are presented in Figure 6c and Figure 6d, respectively, for LOS measurements and their 2D and 3D decompositions to vertical movements. The ground deformation rate at the maximum subsiding location reaches about 200 mm of vertical ground movement derived from 3D decomposition of LOS measurements over the period of 2018-2020 (Figure 6c; Figure 6d). The differences of vertical deformation rates derived from 3D decomposition and cosine corrections at the maximum subsiding site vary in the range of 0-50 mm (Figure 6d). RMSE between vertical deformation rates from 3D and 2D decompositions and cosine correction was observed to be in the range of 30-40 mm (Figure 6d).

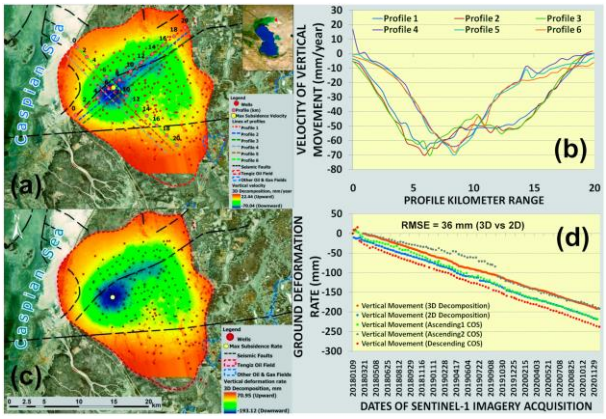

Figure 6. (a) Location of maximum subsidence in the area of vertical deformation velocity derived from 3D decomposition; (b) Profiles of vertical movement velocity; (c) Maximum subsiding location with the background of vertical deformation rate derived from 3D decomposition; (d) Vertical deformation rates derived from 3D and 2D decompositions and cosine corrections for the location of maximum subsidence.

The 3D and 2D decomposition of LOS measurements 2018-2020 to horizontal east-west displacement allowed to determine that annual average horizontal deformation velocity over the Tengiz oilfield was in the range of –25.48-21.33 mm/year and –23.17-22.82 mm/year, respectively (Figure 7a; Figure 7b). Although the annual average horizontal deformation velocity was not significant, it was interesting to find both eastward and westward horizontal movements. Based on the Pearson Correlation Coefficient > 80 and a t-test p-value > 0.05 in Figure 7c and Figure 7d, it is possible to conclude that both 3D and 2D decompositions produced identical horizontal deformation velocities with an RMSE of 1.62 mm. This allows to state that 2D decomposition of LOS measurements will be sufficient for the future deformation analysis by oil and gas operators of the Tengiz oilfield.

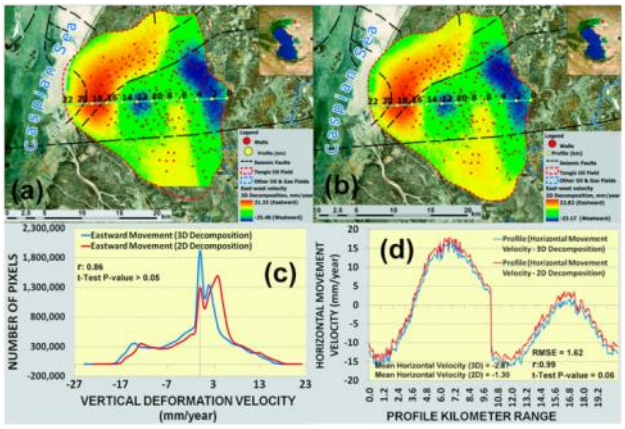

Figure 7. East-west movement velocity derived from: (a) 3D decomposition of 2 ascending and 1 descending LOS measurements; (b) 2D decomposition of 1 ascending and 1 descending LOS measurements; (c) histogram of east-west movement velocities derived from 3D and 2D decompositions; (d) profiles of east-west movement velocities derived from 3D and 2D decompositions.

The 3D decomposition of LOS measurements 2018 -2020 to horizontal north-south displacement allowed to determine an annual velocity over the Tengiz oilfield in the range of –5.54-8.12 mm/year (Figure 8a). Even though the north-south movement was not significant, the interesting pattern of the Tengiz oilfield northern area moving southward and southern area moving northward towards seismic fault was observed (Figure 8b). This, in return, allowed to assume that this area is under the impact of natural, i.e., not man-made, tectonic processes as it was also determined by Anissimov et al. (2020). This fact may increase the negative impacts on the Tengiz oilfield through the acceleration of the subsidence processes caused by the man-made oil extraction processes. The spatial relationships between the seismic faults and horizontal and vertical movements were well reflected in the 3D representation of the ground deformation velocities (Figure 9a–d).

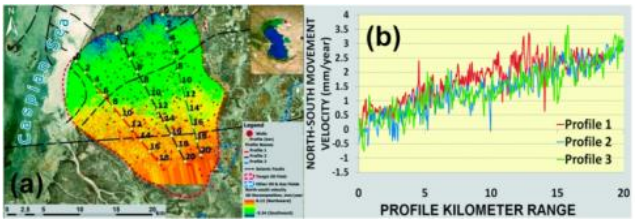

Figure 8. (a) North-south movement velocity derived from 3D decomposition of 2 ascending and 1 descending LOS measurements; (b) North-south movement velocity along profiles

Unfortunately, because of the absence of historical cumulative high-precision GPS measurements, it was not possible to validate the SBAS measurements, the results of 2D and 3D decompositions and cosine corrections. The only possible qualitative judgment was conducted based on the studies by Grebby et al. (2019)

which also revealed a continuous subsidence at the Tengiz oilfield.

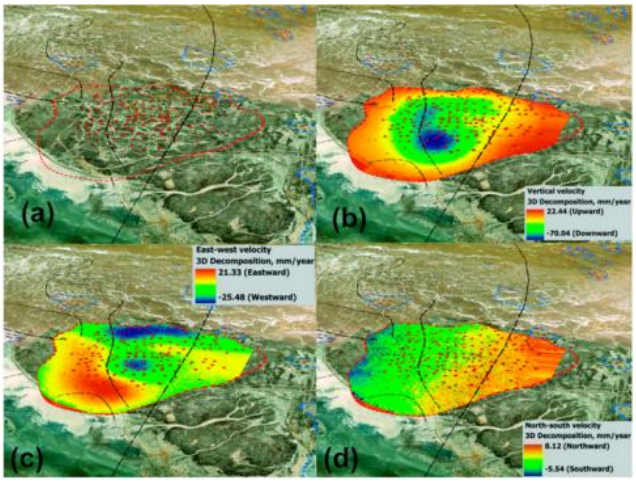

Figure 9. Oblique aerial view of: (a) Tengiz oilfield; (b) vertical deformation velocity derived from 3D decomposition; (c) east-west movement velocity derived from 3D decomposition; (d) north-west movement velocity from derived from 3D decomposition.

4. Discussion

Based on the results of the present research, it was possible to conclude that the subsidence processes in the Tengiz field continue with increasing velocity. 3D and 2D decompositions of LOS measurements concerning vertical deformation revealed twice lower differences in comparison to cosine correction than with LOS measurements. The role of 3D and 2D decompositions to vertical velocities becomes even more indicative in this case, if sufficient number of SAR data is available from ascending and descending tracks. Even though the vertical deformation confirmed typical patterns of subsidence caused by oil extraction, detected east-west and north-south movements at the Tengiz oilfield clearly indicated that the study area crossed by seismic faults is affected by natural tectonic processes. It is necessary to emphasize that the spatial patterns of east-west and north-south ground movements were observed to both sides of the seismic faults. A seismic fault was also observed crossing the detected hotspot of subsidence. This means that the natural tectonic processes at the Tengiz oilfield should also be considered as one of the significant risk factors which might have significant consequences like induced seismicity and infrastructure failure as a result of ongoing oil field exploitation.

The outcomes of the present research suggest to the operators of oil and gas fields to initially evaluate required standards and precision of measurements depending on the operational needs. In particular oil and gas operators should be aware that even though LOS measurements present the overall ground movement patterns, they do not reflect true vertical movement values at the local scale. Therefore, planning of actual risk mitigation and remediation measures on the ground might be misleading unless LOS measurements are decomposed to vertical deformation velocities and rates.

5. Conclusion

The present research investigated the surface deformations induced by man-made production and natural processes in the Tengiz oilfield using SBAS technique and 3D and 2D decompositions of LOS measurements to vertical and horizontal deformations. Our conclusions and recommendations are as follows:

(1) 3D decomposition of LOS measurements concerning vertical movements showed that the Tengiz oilfield continued to subside during 2018-2020 with a maximum annual vertical deformation velocity around 70 mm. Following LOS measurements, the maximum annual subsiding velocity was observed to be 60 mm. Cosine corrections of LOS measurements to vertical movement revealed a maximum annual vertical deformation velocity of 77 mm.
(2) Overall RMSE between 3D decomposed vertical deformation and LOS measurements was observed to be in the range of 10-13 mm. The differences on the local level were variable in the range of 7-21 mm.
(3) Overall RMSE between 3D decomposed and cosine-corrected vertical deformations was observed to be in the range of 6-8 mm. Compared to LOS measurements, the cosine-correction improved the results of vertical deformation twice relative to 3D and 2D decomposition. The differences on the local level were variable in the range of 0-17 mm.
(4) The ground deformation rate at the location of maximum subsidence reached around 200 mm of vertical ground movement derived from 3D decomposition of LOS measurements over the period of 2018–2020. The differences of vertical deformation rates derived from 3D decomposition and cosine corrections at the site of the maximum subsidence varied in the range of 0-50 mm. RMSE between vertical deformation rates from 3D and 2D decompositions and cosine correction was observed to be in the range of 30-40 mm. Besides the ground deformation velocity, it is highly important to consider the total displacement reflected in the deformation rate of individual sites of interest.
(5) The vertical deformation confirmed typical patterns of subsidence caused by oil extraction. Detected east-west and north-south movements at the Tengiz oilfield clearly indicated that the study area crossed by seismic faults is affected by natural tectonic processes. It has to be emphasized that the spatial patterns of east-west and north-south ground movements were observed on both sides of seismic fault crossing the detected hotspot of subsidence. It is possible to conclude that the natural tectonic process at the Tengiz field is one of the significant risk factors which might have significant consequences like induced seismicity and infrastructure failure as a result of ongoing man-made oil field exploitation. It is critical for operators of oil and gas fields and also other types of oil and gas infrastructure to realize the actual differences of ground deformation measurements derived from 3D and 2D decompositions,

cosine correction and LOS measurements. This will allow to initially evaluate the required standard and precision of measurements depending on operational needs, timeframes and availability of imagery. Since it was not possible to validate the results of the present research, it is planned to use higher resolution SAR sensors to cross-validate the achieved results.

Acknowledgement

This research was funded by the Nazarbayev University through the Social Policy Grant (SPG) and Faculty-development Competitive Research Grant (FDCRGP) - Funder Project Reference: 080420FD1917.

References

Anissimov, L., Postnova, E., & Merkulov, O. (2000). Tengiz oilfield: geological model based on hydrodynamic data. Petroleum Geoscience, 6(1), 59-65.

Bayramov, E., Buchroithner, M., & Kada, M. (2020a). Quantitative assessment of ground deformations for the risk management of petroleum and gas pipelines using radar interferometry. Geomatics, Natural Hazards and Risk, 11(1), 2540-2568.

Bayramov, E., Buchroithner, M., & Kada, M. (2020b). Radar remote sensing to supplement pipeline surveillance programs through measurements of surface deformations and identification of geohazard risks. Remote Sensing, 12(23), 3934.

Bayramov, E., Buchroithner, M., Kada, M., Bayramov, R. (2020c). Quantitative assessment of ground deformation risks, controlling factors and movement trends for onshore petroleum and gas industry using satellite Radar remote sensing and spatial statistics. In Georisk: Assessment and Management of Risk for Engineered Systems and Geohazards; Taylor & Francis: London, UK.

Bealessio, B. A., Blánquez Alonso, N. A., Mendes, N. J., Sande, A. V., Hascakir, B. (2020). A review of enhanced oil recovery (EOR) methods applied in Kazakhstan. Petroleum, 7, 1–9.

Grebby, S., Orynbassarova, E., Sowter, A., Gee, D., & Athab, A. (2019). Delineating ground deformation over the Tengiz oil field, Kazakhstan, using the Intermittent SBAS (ISBAS) DInSAR algorithm. International Journal of Applied Earth Observation and Geoinformation, 81, 37-46.

Imamoglu, M., Kahraman, F., Cakir, Z., & Sanli, F. B. (2019). Ground deformation analysis of Bolvadin (W. Turkey) by means of multi-temporal InSAR techniques and Sentinel-1 data. Remote Sensing, 11(9), 1069.

Klein, I., Gessner, U., & Kuenzer, C. (2012). Regional land cover mapping and change detection in Central Asia using MODIS time-series. Applied Geography, 35(1-2), 219-234.

Mirzaii, Z., Hasanlou, M., Samieie-Esfahany, S., Rojhani, M., & Ajourlou, P. (2019). Land subsidence monitoring in azar oil field based on time series analysis. Multidisciplinary Digital Publishing Institute Proceedings, 18(1), 2.

Orynbassarova, E. (2019). Improvement of the method of integrated preparation and use of space images in tasks of assessment of sedimentation of industrial surface in the conditions of operation of Tengiz oil and gas field. Ph.D. Thesis, Satbayev University, Almaty, Kazakhstan.

Shi, J., Yang, H., Peng, J., Wu, L., Xu, B., Liu, Y., Zhao, B. (2019). InSAR Monitoring and analysis of ground deformation due to fluid or gas injection in Fengcheng oil field, Xinjiang, China. J. Indian Soc. Remote Sensing, 47, 455–466.

Sokolova, I. N., Mikhailova, N. N., Velikanov, A. E., Poleshko, N. N. (2017). Induced seismicity on the territoryof Kazakhstan. In Book of Abstracts CTBT: Scienceand Technology Conference; CTBTO: Vienna, Austria.

Yang, C., Zhang, D., Zhao, C., Han, B., Sun, R., Du, J., Chen, L. (2019). Ground Deformation Revealed by Sentinel-1 MSBAS-InSAR Time-Series over Karamay Oil field, China. Remote Sensing, 11, 2027.

6th Intercontinental Geoinformation Days

igd.mersin.edu.tr

Consequent increase of the Caspian level in the coastal zone of the Republic of Azerbaijan (according to aerospace data)

Amir Aliyev [*1], **Dilshad Suleymanlı** [1], **Ramin Atakishiev** [1] **Dilara Hasanova** [1]

[1]*Institute of Geography, Caspian Sea, Baku, Azerbaijan*

Keywords
Level of the Caspian Sea
Azerbaijan coastal zone
Flooding

Abstract

The results of the study of fluctuations in the level of the Caspian Sea and its effects on the coastal zone of the Azerbaijan Republic are presented. During the period 1978 - 1995, the level of the Caspian Sea grew rapidly. Estimates of flooded areas by administrative areas are given, as well as other negative phenomena in the coastal area. For a detailed study of the state of flooding of the Azerbaijani coastal zone when raising the level of the Caspian Sea, we compile maps of flooding of all extents of coastal lines. The map of the flooding of the Azerbaijani coastal zone is made up of aerospace photographs.

1. Introduction

The Caspian Sea is of particular interest to scientists because of its history of fluctuations in both area and depth, which offer clues to the complex geological and climatic evolution of the region.

Approximately 5 million years ago, the Caspian Sea separated from the Black Sea as a result of tectonic and climatic processes and formed its own independent basin.

Its elongated form extends almost 750 miles (1200 km) from north to south, and its average width is about 200 miles (320 km). At present, it covers an area of about 145,000 square miles (391.000 km^2). The Caspian Sea is not only an economic source, but also a climatic regulator of this region.

2. Method

During these many years, there have been considerable fluctuations of the sea level (Figure 1). Short - term wind fluctuations can cause rises up to seven feet, though the average is about two feet. Barometric pressure changes can cause similar fluctuations. Tidal variations are only a few inches. And the seasonal rises, induced by high spring water in rivers, are not much more.

At present, it is established that more than half of the coastal territory of the Republic of Azerbaijan was in conditions of flooding of the coastal zone during the rise of the level of Caspian Sea by 2,5 meters between 1978 - 1995, the flooding maps of all the length (about 800 km) of coastal lines are drawn up. For this purpose, the aero - cosmic photo, data of regular instrumental measures of Sea level and expedition works in coastal zone were used. The map of the flooding of Azerbaijani coast is drawn up with materials decoding aero - cosmic photo using the literature and the fund materials, also with topographic and subject - matter plans. So, about 100 maps of flooding were drawn up in 1:25000 scales. On the basis of the coastal zone of the Republic of Azerbaijan, 26.5 mBS. (Figure 2).

The morphometric characteristics and the square of flooding of 11 administrative regions of the Republic of Azerbaijan situated in the coastal zone of the Caspian Sea are given in the Table 1.

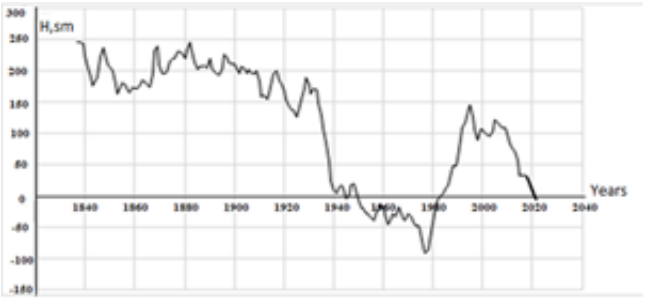

Figure 1. Change in the level of the Caspian Sea (1837 – 2021)

* **Corresponding Author**

*(e-mail) ORCID ID xxxx – xxxx – xxxx – xxxx
(e-mail) ORCID ID xxxx – xxxx – xxxx – xxxx
(e-mail) ORCID ID xxxx – xxxx – xxxx – xxxx

Cite this study

Aliyev, A., Suleymanlı, D., Atakishiev, R., & Hasanova, D. (2023). Consequent increase of the Caspian level in the coastal zone of the Republic of Azerbaijan (according to aerospace data). Intercontinental Geoinformation Days (IGD), 6, 168-170, Baku, Azerbaijan

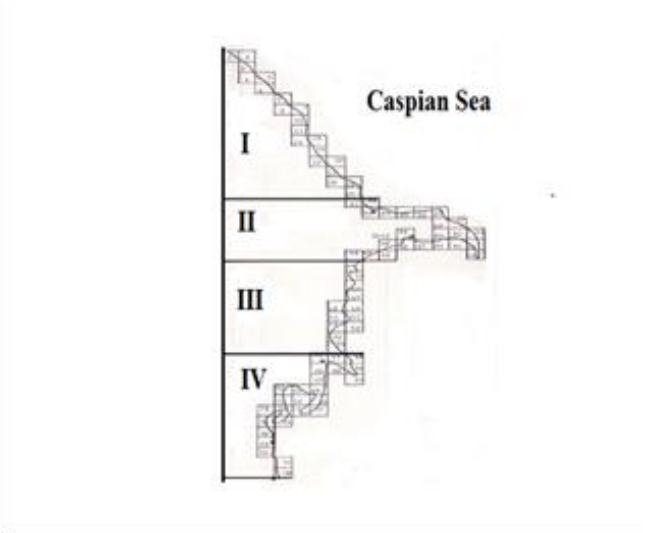

Figure 2. Layout of maps in the Caspian coastal zone (scale 1:25000)

Table 1. Areas of flood of the coastal zone in the administrative regions

The name of areas	Length of a coastal line, km	The area of flooding, sq. km
The Hachmas	66.0	20.70
The Shabran	20.7	10.40
The Siazan	39.6	6.10
The Hizy	26.1	5.10
The Baku - merry	289.6	38.20
The Saljan	11.7	0.60
The Neftchala	94.6	132.70
The Qizil– Aqaj Bay	102.0	239.00
The Masalli	31.5	26.70
The Lenkoran	35.1	4.10
The Astara	21.1	0.90
Total	738.10	484.50

It is received, that at flooding the coastal zone of the Azerbaijan Republic is divided into 4 characteristic regions:

- From river Samur to Apsheron
- Apsheron peninsula
- From Apsheron peninsula to delta of the river Kura
- From the river Kura to river Astara

It is revealed that as a result of the rising in the level of the Caspian Sea for the period 1978 - 1995 on all extent of the Azerbaijani coastal zone the processes of flooding occurred. The total area of the flooded territories is 484.5 square kilometers.

The greatest flooding comes from sea level rises, and the coastal region threatens from the delta of the river Kura in Astara River. It accounts for about 80% of the area of possible flooding at sea level. The housing and economic objects located on all extent of a coastal zone which is under the threat of flooding is defined by the flooding Atlas

- 50 settlements
- 250 industrial enterprises
- 60 km of highways
- 10 km of the railway
- 30000 hectares of winter pastures
- 10000 hectares of the irrigated earths
- Recreational objects on 200 thousand persons. (Aliyev, 2001)

Reasons for Sea fluctuations many contributing factors, that could effect the rise as runoff inflow, precipitation over the sea itself and evaporation from the sea surface. The water balance of the Caspian depends directly on climate changes, taking place on all territory of the Caspian Sea basin which, in tum, is greatly influenced by the Volga River which provides more than 80% of the lakes volume. Some scientists have suggested that sea level variations are due to tectonic processes taking place in the region of the Caspian. But a study of geomorphologic processes for the last 200 years shows that the tectonic activity in the region is very weak. (Aliyev, 2010).

Since 1996 a non-stationary regime has been observed in the level regime of the Caspian Sea, which continued until 2004. From 2005 to the present (2021), the sea level has been continuously decreasing at a rate of 7-8 sm/year. At present, the decrease is about 1.9 m (Figure 1). In forecasts based on climatic factors, it is agreed that the lowering of the Caspian Sea level will last at least until the middle of the XXI century (Aliyev, et.al. 2021, Aliyev and Veliyev, 1999).

3. Conclusion

As a result of the processing of aerial images, it was determined that during the rise of the sea level by 2.5 m in 1978-1995, approximately 50 thousand ha of our coastal area was flooded. At this time, many negative incidents occurred in the coastal areas. The sea level has been decreasing since 1996, and currently a decrease of 190 sm is observed. It is predicted that the level of the Caspian Sea will decrease by 2050 years.

References

Aliyev, A. S. (2001). Rising of level of Caspian Sea and flooding of a coastal zone of the Azerbaijan Republic. Baku, 144 p.

Aliyev, A. S., & Veliyev, S. S. (1999). Dynamics of change of level of Caspian Sea during historical time and in the near future. Meteorology and the Hydrology, N3, 79 - 87.

Aliyev, A. S. (2010) The last sharp rise of the level of the Caspian Sea. Proceedings of the international conference "The Caspian region -Environmental consequences of the climate change" Moscow, 146 – 148.

Aliyev, A. S. (1996). Present rise of the water - level of Caspian Sea and its influence on the economy of

Azerbaijan. Proceedings regional workshop Integrated coastal zone management, I.R. Iran, 59 – 62.

Aliyev, A. S., Tatliyeva, Z. I., Ahmedova, R. Y., Suleymanli, D. Q. (2021). Changes in the level of the Caspian Sea and its consequences in the coastal zone of the Republic of Azerbaijan. ANAS Transactions, Earth Sciences 75-80.

6th Intercontinental Geoinformation Days

igd.mersin.edu.tr

A GIS-Based investigation of the causes of the flood disaster in the city center of Şanlıurfa (Türkiye) in 2023

Faruk Bingöl [*1], **İbrahim Halil Yıldırım** [1], **Ahmet Serdar Aytaç** [1], **Ömer Kaylı** [1], **Sezgin Abukan** [1], **Nizar Polat** [2]

[1]*Harran University, Faculty of arts and sciences, Geography, Şanlıurfa, Türkiye*
[2]*Harran University, Engineering Faculty, Department of Geomatics, Şanlıurfa, Türkiye*

Keywords
GIS
Flood
DEM
Sustainability
Natural Hazard

Abstract

Flood events have occurred frequently in various periods in Şanlıurfa (Türkiye). There were 83 floods between 1950 and 2018 within the borders of Şanlıurfa and most of these floods also affected the city centre. The most recent flood in the city centre of Şanlıurfa took place on March 15, 2023, and 16 people lost their lives in this disaster. In addition, 27 residential buildings, 234 workplaces, 19 schools, 8 mosques and 3 underpasses were damaged in 1978 neighbourhoods. In this study, it is aimed to investigate the causes of the flood disaster in Şanlıurfa' (Türkiye) downtown based on GIS. For this purpose, the natural factors (precipitation, slope, lithology, soil) and human factors (structuring in the stream beds, intervention in the stream bed) that have an effect on the flood have been determined and mapped using GIS-based software. Each factor has been evaluated in terms of floods turning into disasters. The flood event in the study area was caused by various natural factors such as slope, soil characteristics, lithological features and weakness of vegetation, especially due to excessive and sudden downpours. Human factors (construction in the floodplain of Karakoyun, Cavsak, and Karaköprü streams) were effective in the event's becoming a disaster.

1. Introduction

Floods are ranked right after mass movements in the list of disasters causing loss of life and property in Türkiye (Dölek 2021). Flood is a natural hazard that easily turns into a disaster and causes great loss of property and life in Türkiye as it is almost everywhere in the world (Özcan, 2006). In recent years, developments in GIS have facilitated the analysis and management of data related to disasters (earthquakes, landslides, floods, etc.) and the modelling of these data (Bingöl 2023).

Şanlıurfa's downtown is located in the Middle Euphrates Section of the Southeastern Anatolia Region of Türkiye. In this study, the Karakoyun, Cavsak and Karaköprü basins, where floods occur in the city centre of Şanlıurfa, are considered. The study area is surrounded by certain units, Germüş plateau in the north, Tektek plateau in the southeast, Harran plain in the south, and Fatik plateau in the southwest and west. Due to the aforementioned plateaus, the study area is located in a low position relative to its surroundings. According to this, the flow directions of the rivers belonging to the three basins in the study (Karakoyun, Cavsak, and Karaköprü streams) are from the plateaus towards the downtown (Figure 2).

Şanlıurfa has a continental Mediterranean climate in which the summers are hot and dry and the winters are cold. Most precipitation falls in winter and spring. As it is known, precipitation in a short time and in a heavy manner plays the biggest role in the occurrence of flood disasters (Koçman et al. 1996). In areas with an arid-semi-arid climate, such as the research area, too much precipitation variability can trigger ecological and economic losses. (Sepetçioğlu, 2013). As a matter of fact, this has a great role in flooding. In the study area, while slope, lithology, and plant and soil characteristics are the preparatory factors in the formation of floods, meteorological factors enable floods to occur. Human factors come to the fore in the disaster of floods.

* **Corresponding Author**

*(bingolfaruk@harran.edu.tr) ORCID ID 0000-0002-2426-5738
(ibrahyildirim@gmail.com) ORCID ID 0000-0002-8268-2521
(aserdaraytac@harran.edu.tr) ORCID ID 0000-0001-8638-038X
(omerkayli49@gmail.com) ORCID ID: 0000-0002-9088-780X
(abukansezgin@gmail.com) ORCID ID 0000-0002-7017-1249
(nizarpolat@harran.edu.tr) ORCID ID 0000-0002-6061-7796

Cite this study

Bingöl, F., Yildirim, İ. H., & Aytaç, A. S., Kayli, Ö., Abukan, S., & Polat, N. (2023). A GIS-Based Investigation of the Causes of the Flood Disaster in the City Center of Şanlıurfa (Türkiye) in 2023. Intercontinental Geoinformation Days (IGD), 6, 171-175, Baku, Azerbaijan

2. Method

In the research, first of all, a literature review was conducted. Subsequently, the preparatory and triggering parameters that are effective in the occurrence of floods were determined and mapped with the relevant literature and field observations. The ArcMap interface of ArcGIS software was used to create these maps. In this study, flow direction, flow accumulation, flow class, drainage network, basin and sub-basin boundaries of the basins were determined by using Raster (cellular) based Digital Elevation Model (DEM) through ArcGIS software. Stream bifurcation values were determined using the Strahler method.

By using the buffer method, areas 50 and 100 meters away, which are considered to be dangerous areas in terms of flooding, were determined as buffer zones. In addition, NDVI (Normalised Difference Vegetation Index) map was produced to reveal the relationship between the vegetation cover in the study area and floods.

A slope map was produced from the digital elevation model. The geological map from MTA(general directorate of mineral research and exploration) and the soil map from OGM(Forest management) were digitized in the ArcMap interface in accordance with the purpose. Afterwards, the areas affected by the disaster that occurred on 15 March 2023 and the spatial distribution of those who lost their lives were determined and associated with.

3. Findings

On 15 March 2023, a flood disaster occurred in Şanlıurfa downtown. As a result of the flood 16 people lost their lives and 1978 houses, 234 business places, 19 schools, 8 mosques and 3 underpasses were damaged in 27 neighbourhoods. Figure 1 shows the areas where flooding occurred on this date. The flooding occurred in Karakoyun stream (Süleymaniye neighbourhood, Piazza, Balıklıgöl surroundings, areas where there is construction in Mance stream, Halepli garden), certain parts of Cavsak stream (Abide junction and its surroundings) and Karaköprü stream (Şenevler and Atakent neighbourhood) (Figure 2.).

The flood disaster that occurred in Şanlıurfa downtown was caused by natural environment features such as precipitation, slope, lithology, and soil and human factors such as construction in stream beds and interventions to the stream bed. The factors that are effective in the formation of flood are examined below.

3.1. Precipitation

Although the average annual precipitation in the downtown is 460 mm, the total amount of precipitation on 15-16 March when the disaster occurred was 146.8 mm (On 15 March 119 mm). Considering that the average annual precipitation amount in March at the research site is 68.3 mm (Figure 3) it is clearly seen that there is extreme rainfall in the field. For this reason, a flood event occurred at the study site and led to a disaster.

Figure 1. Overflow of stream beds in the study area (Karakoyun Stream)

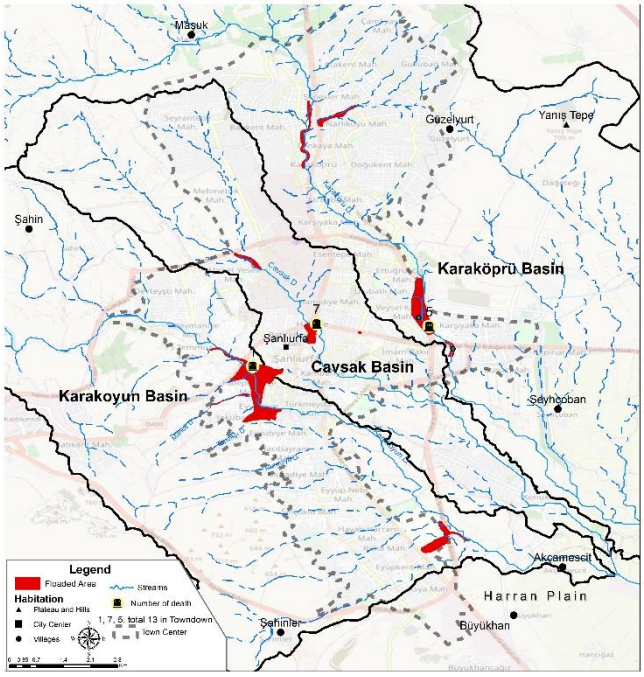

Figure 2. The areas most affected by flooding 2023

Table 1. Total daily Precipitation(m) in Şanlıurfa during the week of the flood (March 2023) (MGM 2023)

Days	11	12	13	14	15	16	17
Precipitation	0	0	1,2	0,6	119	27,8	0,6

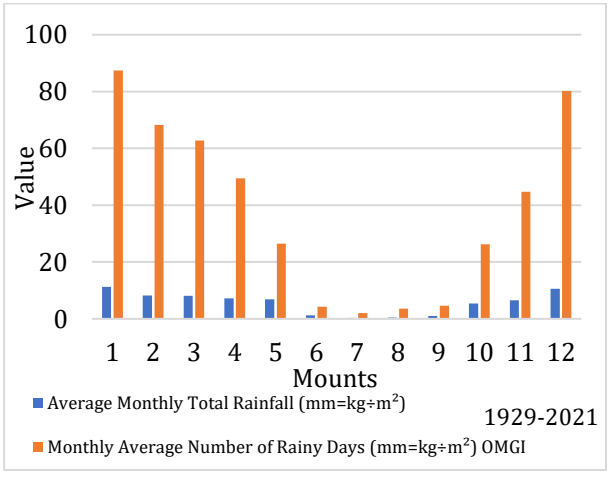

Figure 3. Precipitation (mm) graph of the study area

3.2. Slope

Slope values are an important land parameter in the evaluation of flood potential. According to the results in the literature, water collection basins are evaluated in 4 groups. Areas with slope values less than 2° have a very high potential for flooding. Generally, flat areas with low slopes are temporary water accumulation areas where surface runoff reaches a steady level (Selçuk et al., 2016). Areas with slope values between 2° and 6° have a high flood potential but a lower potential than the first group. These two slope groups cover large areas in the downtown where the flood disaster occurred (Figure 4.). The flood potential of these areas is high. While the slope values are between 6° and 16°, the flood potential is low, and slope values higher than 16° are not significant in terms of flood potential (Masoudian 2009). These classes constitute the upper level of the river basins. Due to the high slope values of these areas, precipitation is directly drained. Therefore, they have low flood potential. However, these slope groups increase the flood potential in the middle and lower reaches of the basins by providing a rapid flow of water towards the lower basins.

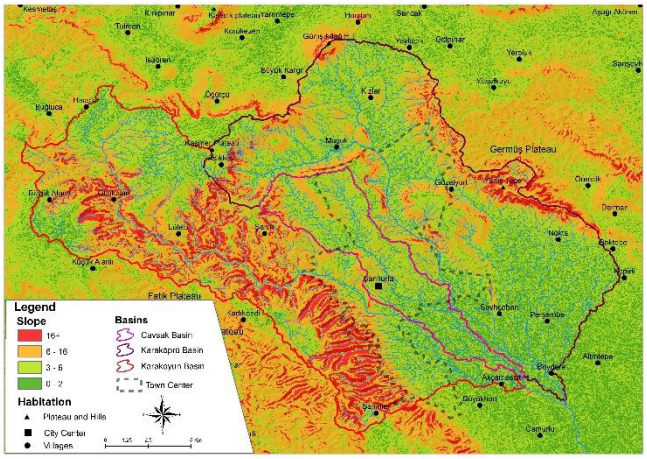

Figure 4. Slope map of the study area

3.3 Lithology

Lithology is an important factor because it affects surface flow. Especially in areas dominated by permeable rocks, water finds the opportunity to seep underground faster. In areas where the permeability property is dominated by less or impermeable rocks, the waters find little or no opportunity to penetrate underground (Şahinalp 2007). It is observed that carbonate rocks (Gaziantep and Fırat Formations) are dominant in the areas where the flood occurred (upper parts of the basin). The fact that there are many north-south and northwest-southeast oriented faults and cracks in these limestones (Kaylı 2020) shows that the permeability is high. However, the existence of limestone levels with high clay content in the solid limestones belonging to both the Gaziantep and Euphrates formations (Kaylı et al. 2022), causes the water to be unable to go deeper. And, on this occasion, the upper levels of the formations are saturated with water faster. In addition, the limestone crust formations that occur in certain parts of the Gaziantep formation also have a negative impact on the transfer of water underground. Especially the limestone shell formations formed by recrystallization form a hard shell on the Gaziantep formation. This situation has caused a decrease in permeability by disconnecting the water from the underground cracks. The above-mentioned features played an important role in causing floods in the middle and lower levels.

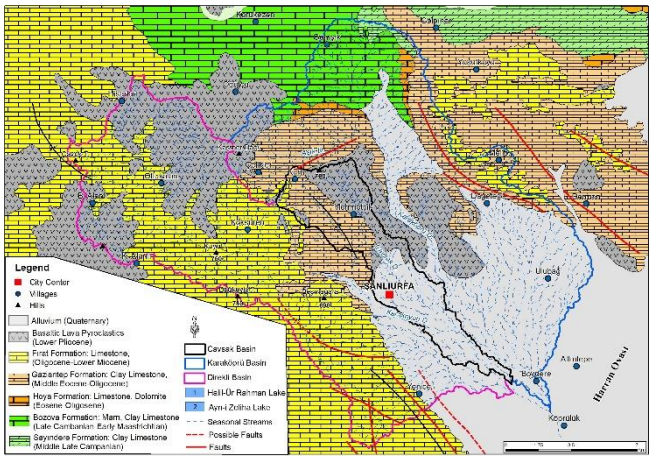

Figure 5. Geology map of the study area

3.4. Vegetation

It has a significant effect on flood formation by increasing the infiltration capacity of water into the soil and protecting the soil cover. The retention of falling precipitation through branches and leaves delays the infiltration of water to the ground. In this respect, vegetation plays a preventive role in the occurrence of floods. It is not possible to mention a significant vegetation cover that can prevent flooding in the study area. The upper reaches of the basins generally have a low plant density index of -0.13-0.09. The upper level of the basins where the flood occurred and the poor vegetation cover in the areas where it was effective increased the severity of the floods.

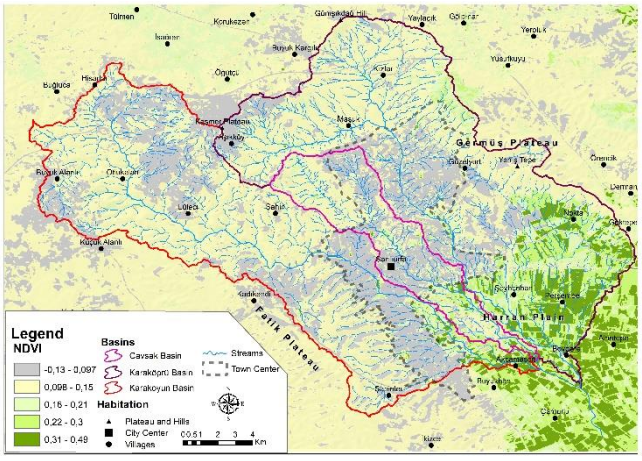

Figure 6. Landsat Normalized Difference Vegetation Index (NDVI) of Study Area

3.5. Soil

Soil structure and texture are important for the formation of floods. In general, brown and reddish-brown soils cover a large area in the study area. Besides,

colluvial soils and basaltic soils also can be seen. The clay content of the soils in the field is high. Soils with a high clay content become saturated with water in a short time, causing superficial runoff. The thickness of the soil is an important factor in terms of water infiltration. However, the fact that there is shallow soil on the upper floors and the city centre lacks soil as a result of concreting increases the potential for flooding and flooding by accelerating the surface flow.

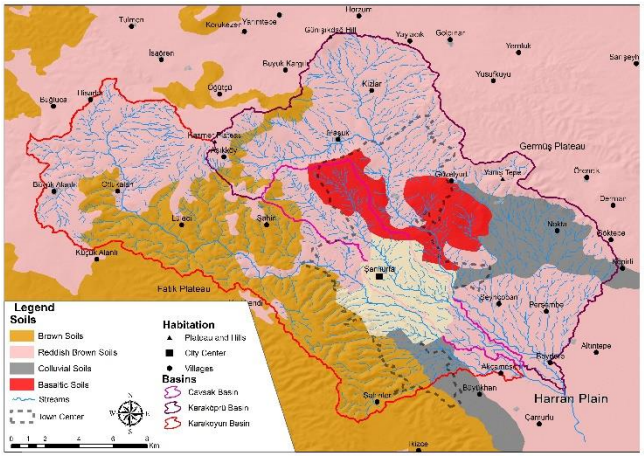

Figure 7. Soil map of the study area

3.6. Construction and intervention in stream beds

The distance to the stream beds is an important factor, especially in terms of flooding. Because the most affected areas in flood events occurring in residential areas are those close to the stream beds (Weli and Oye 2014). Human activities in stream beds cause possible floods to turn into disasters due to the alteration of the stream bed. Urbanization typically increases the amount of surface water and water to be discharged (Selçuk et al. 2016).

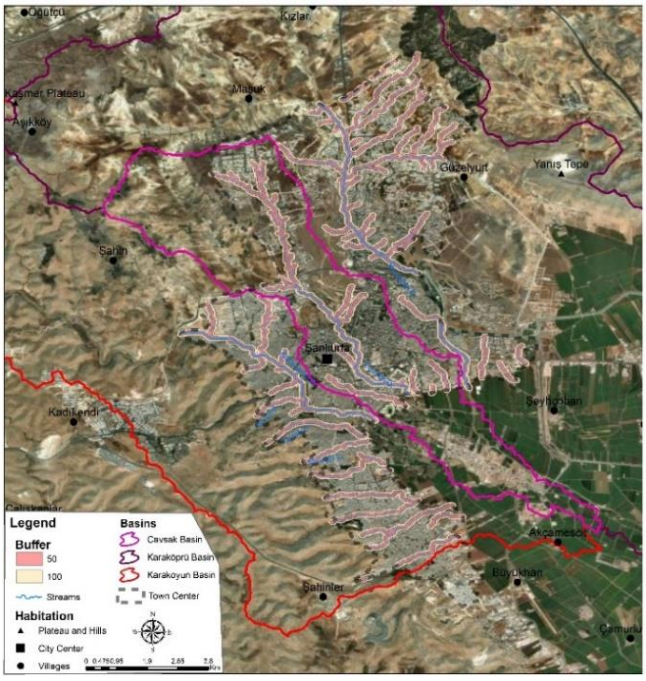

Figure 8. Buffer Map of Stream Beds

There is serious construction in the floodplains of Karakoyun, Cavsak and Karaköprü streams (Figure 8). Especially in some areas, interventions such as narrowing the stream beds and creating closed channel systems, smoothing the stream bed under the heading of riverbed reclamation, unplanned construction (squatting) and conversion of stream beds into streets by covering them with asphalt or concrete have converted flood events into natural hazards.

4. Conclusion

Firstly, excessive rains on March 15-16, 2023 caused flooding in the city of Şanlıurfa, and various natural factors such as slope features, lithological features and soil and vegetation weakness had preparatory effects on the realization of this event. In particular, human factors have been effective in the characterization of the flood as disasters. One of these factors is the structuring of the stream beds and the intervention in the stream beds for various reasons is effective.

In order to effectively combat the flood danger and possible disasters faced by the city of Şanlıurfa, a flood action plan should be prepared and possible risk areas should be identified. There is a shanty settlement in the beds of Karakoyun, Cavsak and Karaköprü streams. These areas should be transformed into green areas through urban transformation works.

References

Bingöl, F. (2023). GIS Based Sensitivity Analysis of the Cifthisar Basin and its Vicinity (Adıyaman) in terms of mass movements, Şanlıurfa. MS Thesis, Harran University Social Sciences Institute

Dölek. i, (2021)."Türkiye'de Doğal Afetler," in Türkiye`nin Fiziki Coğrafyası, Ankara, Pegem Akademi Yayıncılık, 314-366.

Kaylı, Ö. (2020). The İnvestigation Of Fatik Plateau (Şanlıurfa) İn Terms of Karst Geomorphology, Şanlıurfa. MS Thesis, Harran University Social Sciences Institute

Kaylı, Ö., Aytaç, A., & Bingöl, F. (2022). Preliminary Findings Regarding the Speleological Analysis of the Northeast of The Fatik Plateau (Şanlıurfa-Eyyübiye). International Geomorphology Symposium, Manisa.

Koçman, A., Kayan, İ., Sezer, L. İ., Gümüş, H., Emekli, G., & Mutluer, M. (1996). İzmir'de 3-4 Kasım 1995 Karşıyaka Sel Felaketi (Oluşumu, Gelişimi, Etkileri ve Alınması Gereken Önlemler). Ege Üniversitesi İzmir Araştırma ve Uygulama Merkezi Yayınları, (1).

Masoudian, M. (2006). The topographical impact on effectiveness of flood protection measures, Kassel, Germany. Ph.D. thesis, Kassel University.

Özcan, E. (2006). Sel olayı ve Türkiye. Gazi Üniversitesi Gazi Eğitim Fakültesi Dergisi, 26(1), 35-50.

Selçuk, L., Selçuk. A.S. and Kasapoğlu, D. (2016). Urban Flood Susceptibility Assessment of Central Districts of Van Province, Turkey, Using Geographic Information System (GIS)-Based Multi Criteria Decision Analysis (MCDA). Hacettepe Üniversitesi Yerbilimleri Uygulama ve Araştırma Merkezi Bülteni, 37(1), 1-18.

Sepetçioğlu, M. Y. (2013). Şanlıurfa ili taşkın sorunları ve çözüm önerileri. Engineering Sciences, 8(1), 21-38.

Şahinalp, M. (2007). Neden ve sonuçlarıyla Şanlıurfa İlinde yaşanan sel felaketleri (28-29 Ekim, 01 Kasım 2006). Türk Coğrafya Dergisi, (49), 89-122.

Weli, V. E., & Ideki, O. (2014). The Effect of Urbanization on Channel Adjustment and Flood Vulnerability of Woji Basin, River State, Nigeria. Journal of Natural Sciences Research, 4(10), 86-93.

6th Intercontinental Geoinformation Days

igd.mersin.edu.tr

The effect of climatic factors on the cotton productivity using machine learning approaches

Bakhtiyar Babashli *[1]

[1]National Aviation Academy, Faculty of Aerospace, Department of Aerospace Environmental Monitoring, Baku, Azerbaijan

Keywords
Cotton
Machine learning
Climate
Factor
Productivity

Abstract

Agriculture and the farming are two of the most important sectors of the economy. An accurate and timely assessment of cotton field productivity is useful for management decisions about cotton supply and sales. Cotton production concentration is influenced by a variety of factors. The impact of climatic conditions (rainfall, temperature, wind, etc.) on cotton productivity is studied in order to determine the quantitative relationship between these parameters and productivity. Several machine learning techniques have been researched and used to estimate crop yield. Errors like RMSE, MSE, MAE, and R2 were employed as indicators, and the polynomial regression model was chosen as the best among them.

1. Introduction

Cotton is one of the most important and widely produced products in the world. Currently, cotton (Gossypium spp.) a natural fiber produced on a large scale is a source of income for millions of farmers. Cotton cultivation is mostly adapted to temperate, tropical and subtropical climates worldwide, but its future development may take a different path due to future climate change (Bange et al., 2016). Climate change can have an impact on cotton output in both good and negative ways. Temperature influences cotton growth and development by determining fruit production, photosynthesis, and respiration rates (Turner et al., 1986).

The conducted research showed that the achievements of science and advanced practice in cotton farming the productivity of cotton can be further increased by applying it (Seyidaliyev, 2012). It is required to enhance cotton production, quality, fast-growing cotton kinds, crop collecting, and the use of new technology.

Cotton yield is statistically significantly related to both water availability and temperature (Crane-Droesch, 2018). Both of these factors have a larger effect on the cotton yield than soil acidity. This is important because it shows that many factors have an effect on cotton growth, and we must consider all of these factors when manipulating the genetic makeup of the cotton plant.

Among the most extensively produced crops for the production of fiber globally, cotton is economically important and is grown in more than 60 nations with temperate and tropical climates (Jans et al, 2021). However, a rise in temperature during the cotton growth season (CGS) had a negative impact on yield (Snider et al, 2009). Furthermore, an increased frequency of hot days may be detrimental to cotton yield.

This project's objective is to forecast cotton yield using climate information in Azerbaijan. The influence of changing climate conditions on productivity was assessed using machine learning techniques. This problem is statistically based on a regression model. As a result, our research sought to identify any quantifiable association between environmental conditions and production. Particularly, several environmental elements appear to be related to fertility. The primary goal of this research is to put to the test the current statistical link between environmental conditions and productivity.

Modern machine learning algorithms were applied to the study to increase the model's superiority. This, it is possible to predict cotton productivity by learning machine algorithms to evaluate the effect of climate elements on cotton productivity in the cotton-producing regions of Azerbaijan.

2. Method and data

Data on the climate and cotton yields from 2017 to 2021 were used in the current analysis, including information on the effects of daily temperature, wind, humidity and rainfall on cotton yields. These parameters during the previous five years varied significantly,

* **Corresponding Author**

*(bakhtiyar.babashli@gmail.com) ORCID ID 0000-0001-7931-1677

Cite this study

Babashli B (2023). The Effect of Climatic Factors on the Cotton Productivity Using Machine Learning Approaches. Intercontinental Geoinformation Days (IGD), 6, 176-179, Baku, Azerbaijan

according to the results of daily data from 16 locations for each growing season.

2.1. Climate and crop yield data

The information is gathered from several public data sources. NASA is the source of the weather information (Nasa data). Productivity use the website of the Statistical Commission of the Republic of Azerbaijan done (The State Statistical Committee of the Republic of Azerbaijan).

The climate (temperature, rainfall, humidity, wind) and soil data (soil wetness and moisture) for the last five years are considered climate data. The information on the NASA website basically consisted of the daily. Beyleqan, Fuzuli, Agcabedi, Aghdam, Terter, Yevlax, Zerdab, Kurdemir, Imishli, Saatli, Bilesuvar, Neftchala, Salyan, Sabirabad, Goranboy and Berde were the 16 regions that were taken into consideration for the study (figure 1). According to the Ministry of Science and education of the Republic of Azerbaijan "cotton-growing" textbook guidelines for field crop planting and harvesting dates, the length of the climatological growth season (CGS) was counted from May to September (Pambıqçılıq, 2017). The daily weather and yield data were collected over growing seasons.

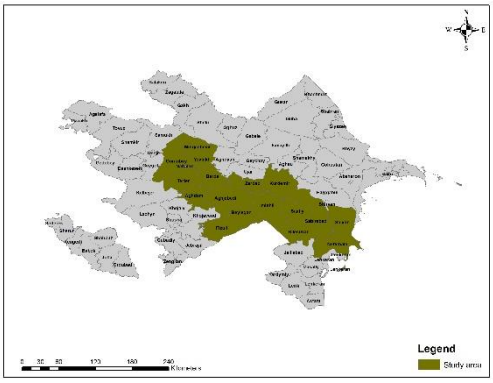

Figure 1. Study area

Using Matplotlib scatter plots were created (figure 2). The data in the first diagram in the figure 2 shows that the wind speed ranges from 0.51 to 9.47m/s. In the second of the diagrams the humidity is 13.69 and 89.94 varies between. In the third diagram shows the rainfall ranges from 0 to 62.85 mm/day. In the fourth diagram temperature ranges from 1.31 to 24.59℃. In the fifth diagram soil wetness ranges from 0.1 to 0.8. In the sixth diagram soil moisture ranges from 0.37 to 0.72. In the seventh diagram indicates surface pressure ranges from 91.83 to 82.95 kPa and the eighth diagram display cotton yield ranges from 8.2 to 40.8 cent/ha.

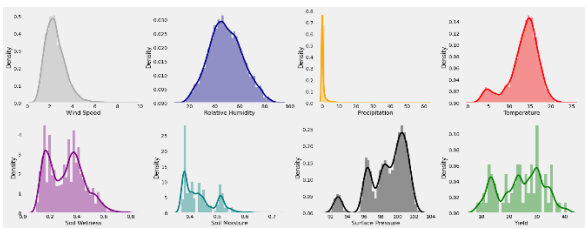

Figure 2. Distribution for climate variables

2.2. Method

In this study, trends were evaluated using the regression method. The fundamental concept of the approach is to establish an algebraic relationship between the dependent and independent variables. A model of the relationship and estimations of the parameter values are used to generate an estimated regression equation (Ostertagováa, 2012). The linear regression method was employed in this investigation. A statistical tool called linear regression can be used to determine the relationship between several "explanatory" factors and a real-valued outcome. This study use nonlinear polynomial predictors. A nonlinear polynomial predictor, also known as an n-dimensional one-dimensional polynomial function.

$$y = a0 + a1\,x + a2\,x\,2 + \bullet\bullet\bullet + an\,x\,n \quad (1)$$

where a vector of coefficients of size n + 1 is (a0, a1, a2, , an).

We have used various parameters as our independent variable (climate data) and yield value as our dependent variable to apply this methodology (Gonzalez-Sanchez et al, 2014). To distinguish between train and test data, the dichotomy of data was developed. The following variables are used in this experiment: y is the cotton yield; a0 is the intercept; a1, a2, a3... an, is the coefficient for rainfall, temperature, humidity and wind etc. The model for this experiment was built using the scikit-learn package's different regression function. Algorithms used for productivity prediction are as follows: Polynomial Regression (MPR), Random Forest Regressor (RFT), Extreme Gradient Boosting Regressor (XGBR), Cat Boost Regression (CBR), LGBM Regressor (LGBR).

Polynomial Regression is a form of regression analysis in which the relationship between independent variables and dependent variables is modeled in an nth-degree polynomial (Mohammad et al. 2022). Polynomial regression models are usually fit by the least squares method. The least squares method minimizes the variance of the coefficients according to the Gauss Markov theorem. One of the fundamental differences between Linear and Polynomial Regression is that Polynomial Regression does not require the relationship between the independent and dependent variables in the data set to be linear. Polynomial Regression is commonly employed when the Linear Regression Model fails to capture the points in the data and the Linear Regression doesn't succeed to properly describe the best outcome. Linear regression is essentially a first-degree polynomial regression.

Random Forest is a decision tree-based machine learning algorithm. Random Forest employs an ensemble approach, which is highly popular in recent years. Ensemble is a common decision-making system based on decision trees. Random Forest regressor is an approach for predicting vegetation that generates random trees (Breiman et al. 2001). The benefit of utilizing Random Forest allows us to eliminate difficulties caused by outliers in our database.

Extreme Gradient Boosting Regression is a machine learning technique for classification problems that

generates a set of prediction models, usually in the form of decision trees. The model is improved on the existing gradient boosting algorithm (Chen et al, 2016). This method combines a number of key factors to estimate complex statistical dependencies (Thomaset et al, 2018). This model is widely used because it gives positive forecast results. The main goal of XGB is to speed up and improve the performance of decision trees.

The most modern productivity boosting technique is the Cat Boost Regressor (CAT). This is due to the implementation of a more efficient gradient boosting tree algorithm (Khan et al, 2020). Categorical parameters, symmetric indicators with minimal variables and superior accuracy form the basis of this decision tree algorithmic framework. Like Gradient Boosting and XGB, the CatBoost method builds multiple decision trees at the same time each time it tries to reduce the error.

LightGBM is a histogram-based method. Learning decision trees can be done using one of the two approaches: level-wise (depth-wise) or leaf-wise (Shahhosseini et al, 2021). The equilibrium of the tree is maintained as the tree grows using the level-wise technique. The division process continues from the leaves in the leaf-wise technique, which lowers loss. LightGBM distinguishes itself from other boosting algorithms because to this property. The Leaf-wise technique reduces error rates and speeds up learning. However, the Leaf-wise growth technique causes the model to over-learn when the amount of data points is small. As a result, the technique is more suited for usage in huge data.

We are utilizing the coefficient of determination as the experiment's evaluation metric. The amount of variance in the dependent variable that can be explained by the predictors in the model is measured by the coefficient of determination R2, which is well - defined in linear regression models (Mohammed et al, 2022). R2 has a value between 0 and 1, with 0 being the worst and 1 being the greatest.

3. Results

This study used several regression models to predict climate data to increase cotton productivity and the results were compared. The accuracy of these forecasting models is measured by R Square, Root Mean Square Error (RMSE) and Mean Percent Prediction Error (MPPE).

Table 1. Accuracy Results of Algorithms

Model	MAE	MSE	RMSE	R Square
Polynomial	0.007	0.0001	0.009	0.960
XGBoost	0.012	0.0003	0.017	0.871
CatBoost	0.013	0.0003	0.017	0.867

Polynomial regression is the best model for our research, with R-squared values of 0.96, MAE of 0.0073, MSE of 0.0001, and RMSE of 0.0094 presented in table 1. This shows that the experiment's model was quite accurate. As a result, we discover that there is a quantitative association between environmental conditions and cotton output utilizing the information from the aforementioned numerous studies. The results of this experiment also show that it is possible to forecast cotton's return using a variety of environmental conditions.

4. Discussion

The relationship between mainly meteorological factors and cotton yield was analyzed by Polynomial Regression algorithm. The obtained results show that temperature, cloud cover, rain and wind are the most important factors affecting the productivity of cotton at all growth stages. So, timely action due to these factors can both increase the production and prevent the reduction of cotton productivity. Meteorological elements have different effects on cotton productivity. For example, increased rainfall, potential evapotranspiration and excess water during the cycle can lead to increased cotton yield. On the contrary, a decrease in cotton productivity is observed due to the increase in air temperature and water shortage (Silva et al. 2021). One of the main factors of climate change is the lack of water, which has a great impact on agriculture and reduces the productivity and quality of various crops.

Cotton yield potential is determined between planting and flowering dates. Climatic conditions during this period have a great impact on productivity. Climatic elements have shown different relationships and intensities with cotton productivity. Cotton grows most effective at temperatures between 25-30^{0}C. When the temperature drops below 25^{0}C, plant growth slows down. Raising the temperature to 300°C stimulates cotton development in the early stage of plant development, before budding. Above 35°C, the cotton plant's growth and development processes are halted. The seeds of the plant heat up more at this greater temperature and their development ceases.

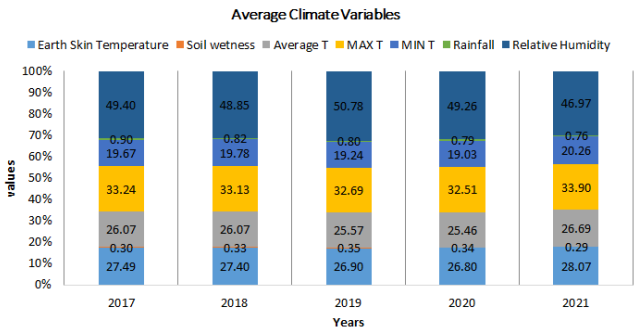

Figure 3. Average climate variables

Cotton yield in the researched area varied between 8.2 cents/ha in 2017 (Nefchala) and 40.8 cents/ha (Salyan) in 2020. İn 2017 and 2018, the productivity of cotton was observed to be lower than in other years. During these years, the average temperature was quite low, with the maximum average temperature exceeding 40^{0}C Celsius. Simultaneously, beginning in 2019, new technologies and the usage of various fertilizers and chemicals were implemented. Furthermore, as science has advanced, the sowing of new seeds has increased output. Nonetheless, while there are irrigation issues in 2020-2021, the introduction of new technology has produced circumstances for increased productivity.

The polynomial algorithm was the best performing algorithm to track all spatial variability of cotton productivity using climate elements as independent variables. As the temperature increases in the model, it tends to increase its performance. However, increasing the ranks of the model also increases the risk of overfitting and underfitting the data. Forward Selection and Backward Selection can be used to find the correct model rank to avoid excessive or inappropriate. These methods increase or decrease the rank until the best possible model is determined, as well as until it is significant.

Wind and temperature are among the climate elements that have the most influence on cotton productivity in the main production regions of Azerbaijan (Figure 3). These two variables showed positive correlation and high significance in the period from sowing to flowering. Excessive rainfall and excess water during the flowering period can lead to a decrease in cotton yield. Water shortage and maximum temperature above 34°C results in a sharp decrease in cotton productivity. Using machine algorithms, it is possible to accurately predict cotton yields in major producing regions. The best algorithm was Polynomial and the least performing algorithm was Random Forest. The polynomial algorithm is successful in predicting cotton yield with climate data from planting to flowering. It is possible to predict about 90-100 days, which gives the manufacturer enough time to plan the product.

5. Conclusion

The findings of this study demonstrate that considerable changes in both climatic variables and cotton indices occur over a 5-year period. According to the diverse behaviors of climate variables at various locations, the effect of their shifting patterns on cotton output is evaluated. We examined the data on cotton yield and daily climatic factors from May to September during vegetation process. Analysis of the effects of climate variables on cotton yield was done using the regression models. The R2 value, which is within the range of the regression equations for yield, was used to pick the regression equations.

We intend to gather more information (climate, soil) in the future to increase the model's accuracy. It will be more effective in the future with the study of other weather parameters and the addition of soil types.

References

Bange, M., Baker, J. T., Bauer, P. J., Broughton, K. J., Constable, G. A., Luo, Q., Oosterhuis, D. M., Osanai, Y., Payton, P., Tissue, K. R., and Singh, B. K. (2016). Climate Change and Cotton Production in Modern Farming Systems, CAB International, Boston, MA, 61

Breiman, L. (2001). Random forests. Machine Learning. 45, 5–32.

Chen, T., & Guestrin, C. (2016, August). Xgboost: A scalable tree boosting system. In Proceedings of the 22nd acm sigkdd international conference on knowledge discovery and data mining (pp. 785-794).

Crane-Droesch, A. (2018). Machine learning methods for crop yield prediction and climate change impact assessment in agriculture. Environmental Research Letters, 13(11), 114003.

Gonzalez-Sanchez, A., Frausto-Solis, J., & Ojeda-Bustamante, W. (2014). Attribute selection impact on linear and nonlinear regression models for crop yield prediction. The Scientific World Journal, 1-10. https://doi.org/10.1155/2014/509429.

https://power.larc.nasa.gov/data-access-viewer/

https://stat.gov.az/source/agriculture/

Jans, Y., von Bloh, W., Schaphoff, S., & Müller, C. (2021). Global cotton production under climate change–Implications for yield and water consumption. Hydrology and Earth System Sciences, 25(4), 2027-2044.

Khan, P. W., Byun, Y. C., Lee, S. J., Kang, D. H., Kang, J. Y., & Park, H. S. (2020). Machine learning-based approach to predict energy consumption of renewable and nonrenewable power sources. Energies, 13(18), 4870.

Mohammad, M. Y., & Ahmed, A. D. (2022). Estimating Parameters via L-Linear Method for Second-Order Regression of Polynomial Model. Journal of Economics and Administrative Sciences, 28(134), 160-167. https://doi.org/10.33095/jeas.v28i134.2428.

Ostertagová E. (2012). Modelling using polynomial regression. Procedia Engineering, 48, 500–506. https://doi.org/10.1016/j. proeng.2012.09.545.

Pambiqçiliq. (2017). Ministry of Education of the Republic of Azerbaijan, Baku.

Seyidaliyev, N. (2012). Pambıqçılığın əsasları, Baku, East-West

Shahhosseini, M., Hu, G., Huber, I., & Archontoulis, S. V. (2021). Coupling machine learning and crop modeling improves crop yield prediction in the US Corn Belt. Scientific reports, 11(1), 1606.

Shaik, M. A., Manoharan, G., Prashanth, B., Akhil, N., Akash, A., & Reddy, T. R. S. (2022, May). Prediction of crop yield using machine learning. In AIP Conference Proceedings (Vol. 2418, No. 1). AIP Publishing.

Silva, M. T., Andrade, A. S. D., Serrão, E. A. D. O., da Silva, V. D. P., & Souza, E. P. D. (2021). Applıcatıon of spatial modeling for upland cotton yield ın the semi-arid of Paraíba State, Brazil. Engenharia Agrícola, 41, 609-618.

Snider, J. L., Oosterhuis, D. M., Skulman, B. W., & Kawakami, E. M. (2009). Heat stress-induced limitations to reproductive success in Gossypium hirsutum. Physiologia plantarum, 137(2), 125-138.

Thomas, J., Mayr, A., Bischl, B., Schmid, M., Smith, A., & Hofner, B. (2018). Gradient boosting for distributional regression: faster tuning and improved variable selection via noncyclical updates. Statistics and Computing, 28, 673-687. https://do.iorg/10.1007/s11222-017-9754-6.

Turner, N. C., Hearn, A. B., Begg, J. E., & Constable, G. A. (1986). Cotton (Gossypium hirsutum L.): Physiological and morphological responses to water deficits and their relationship to yield. Field Crops Research, 14, 153-170.

6th Intercontinental Geoinformation Days

igd.mersin.edu.tr

Analysis of investment planning in electricity distribution systems with GIS

Kadri Kaya[*1], **Abdulkadir Memduhoğlu** [2]

[1]*Harran University, Graduate School of Natural & Applied Sciences, Department of Geomatics Engineering, Sanliurfa, Türkiye*
[2]*Harran University, Faculty of Engineering, Department of Geomatics Engineering, Sanliurfa, Türkiye*

Keywords
Electricity Investment and Planning
GIS
Electricity Distribution

Abstract

Efficient distribution of electrical energy is crucial in today's world. Geographic Information System (GIS) software plays a significant role in determining the traceability and measurability of electricity distribution. Distribution companies receive investment funds from affiliated organizations to make investments in their service areas. This study analyzes the effective utilization of these investment funds and the selection of appropriate areas for investment through geometric and semantic data using GIS applications. In this study, an investment plan was developed for the Seyrantepe neighborhood, a densely populated area in the Karaköprü district of Sanliurfa province, where energy waste occurs due to unauthorized energy consumption. Electrical grid and spatial analysis were conducted using the GIS system. Three main criteria were considered in determining the relevant area: unauthorized energy density, uninterrupted energy supply, and new subscription processes. The entire process was carried out using GIS software, which involved defining an identity (project code) for the planned area and conducting analysis and obtaining results through SQL queries. The integration of electrical measurement circuits of subscribers and provision of quality and uninterrupted electricity to new settlement areas were achieved through GIS-enabled visualization using the software. Using this software, an investment plan was identified that could reduce the region's unauthorized consumption and System Average Interruption Frequency Index by approximately three times.

1. Introduction

In today's world, the demand for electricity is increasing every day due to factors such as advancing technological investments, population growth, and unconscious consumption. The correct and efficient distribution of this energy is of vital importance for the future world, alongside the policies implemented to increase electricity production in line with these demands.

The Energy Market Regulatory Authority (EPDK) was established to ensure the efficient use of electrical energy, the seamless establishment of the supply network, and the determination and management of rules and procedures that both individual and commercial users must adhere to (EPDK, 2017). In a situation where energy has gained such importance, especially due to the absence of storage options, Geographic Information System (GIS) applications play a significant role for all distribution companies. The EPDK allocates budgets to distribution companies in order to promote the healthy use and proper transfer of energy, allowing them to perform various analyses in GIS applications using specific SQL queries to analyze and visualize the results of these budgets in the field.

To effectively utilize this comprehensive yet non-storable energy source, the key is to transmit high-quality electrical energy with minimal losses and in the shortest route from its point of generation to the end user. Significant technological advancements have been made in the field of transmission and distribution in the past to address this challenge, and this progress continues today (Rao, 2008). When considering all components of an electrical network that caters to the entire energy demand of a region, from transmission facilities to consumer meters, as spatially referenced data, it becomes inevitable to utilize GIS for data management, querying, and analysis (Ünverdi, 2021). Additionally, continuous monitoring and examination of electrical grids in a geographic sense are necessary to provide the best service to users. Performing these tasks on paper maps or using a system that cannot ensure

* **Corresponding Author**

*(kaya21kadri@gmail.com) ORCID ID 0009-0001-3775-9702
(akadirm@haran.edu.tr) ORCID ID 0000-0002-9072-869X

Cite this study

Kaya, K., Memduhoğlu, A. (2023) Analysis of Investment Planning in Electricity Distribution Systems with GIS. Intercontinental Geoformation Days (IGD), 6, 180-183, Baku, Azerbaijan.

standardization appears impractical. Updating, duplicating, sharing, analyzing, and querying operations on paper maps are time-consuming and costly, and the data integrity cannot be ensured as verbal information about objects is stored in different formats and locations (Emiroğlu, 2007).

The rate of electricity theft constitutes the majority of the overall loss and leakage rate in Türkiye. As mentioned earlier, the annual average loss and leakage rate in Türkiye is around 15%. Since technical and administrative losses are within the minimum standard, they do not pose a significant problem. On the other hand, the increasing adoption of principles such as material quality, workmanship, and the use of modern and state-of-the-art devices will pave the way for further reduction of technical and administrative losses. In our country, technical and administrative losses range from 3% to 7%, while non-technical losses range from 10% to 15%. In short, there is a leakage rate of 10% in total production. According to EPDK data, the highest rate of electricity theft occurs in the eastern regions. The Dicle, Aras, and Vangölü regions sometimes experience theft rates of up to 60% (Aksu, 2019).

For accurate analysis of investments in Sanliurfa province, a leading region in loss and leakage rate (LLR) rankings in Türkiye, it is crucial to utilize GIS applications in a highly technological and efficient manner. Spatial information, including attribute data for all inventories within the distribution area, is integrated and kept up to date in the GIS application. The current state of the field is assessed by incorporating satellite imagery obtained from various providers as the basemap, and the network infrastructure is determined based on existing structures.

Critical applications such as efficient energy distribution, real-time access to digital data, visual analysis, and investment planning to prevent energy waste have been implemented through GIS applications in the study area.

2. Study Area

The Seyrantepe neighborhood of Karaköprü district in Sanliurfa has witnessed a rapid acceleration in urbanization in recent years (Figure 1). Despite the increased risk of earthquakes due to the rocky soil structure and the general climate, there has been a rapid population growth (Gökler, 2020).

As agricultural areas rapidly diminish (Hatipoğlu, 2018), urbanization in this region naturally leads to an increased demand for electricity and the need for investment. In this context, one of the most important criteria for selecting the study area is the integration of LLR with the electrical measurement devices available in the GIS environment. Therefore, streets numbered 8030, 8071, 8069, and 8040, which show higher LLR measurements compared to other areas, have been selected as the study area for Seyrantepe neighborhood (Figure 2). In the GIS environment, a total of 385 subscriptions have been identified for this area. This value indicates that the number of subscribers in this region is suitable for electricity investment.

Figure 1. Study Area

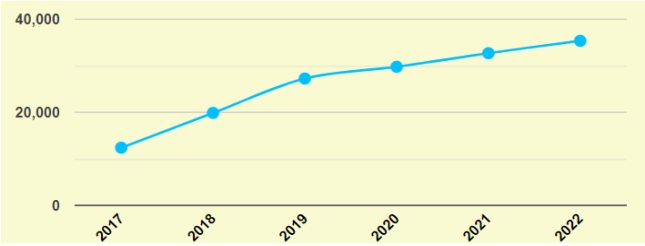

Figure 2. Annual population change of the neighborhood (TURKSTAT, 2023)

3. Material and Method

MapInfo and Edabis desktop-field-web applications were used as GIS software. The selection of the relevant area was based on factors such as loss and leakage due to unauthorized energy use, quality and uninterrupted power supply, new subscription processes, and new settlement areas. Google and Yandex satellite images were used as a base map in the GIS software for ground control of buildings and electrical networks. Geometric and semantic information, including electricity subscribers, floor count, and address (city-district-neighborhood-street), was obtained for all buildings in the study area, and a base map was provided for the use of the electrical network.

The existing condition prior to the investment in the relevant area has been recorded as the initial condition project in the Edabis application (Figure 3). Attribute information for the materials to be removed, including length, year, current condition, type, and usage method, has been determined through the query screen in the software. The amount of loss and leakage in the area has been determined through the integration of the transformer leakage analysis in the GIS software, and the undergrounding of the electrical network has been planned in the GIS environment to prevent external interventions. The installation of Field Distribution Boxes (FDB) and underground cables for each inventory to be removed from the field has also been planned in the GIS environment.

The selection of investment areas based on specific criteria and the planning of investments in these areas in the GIS environment are necessary before starting field work. This allows for a realistic assessment of the return on investment and accuracy prior to fieldwork. The criteria used in the selection of investment locations are described in the following subheadings.

3.1. Detection of unauthorized energy usage

All electrical inventory used in the field, through the electronic chips and sensors present in the inventory, performs real-time measurements and sends this

information to the Mapinfo-based Edabis GIS software using ID numbers. Based on these data, the discrepancies between the supplied energy and the billed energy can be spatially analyzed and obtained through the KKO (Loss and Leakage) system in the system. In this context, the KKO system in the study area has been measured as 47.9%. Since this value is high compared to the surrounding areas, this region has been selected for investment (Figure 4).

Figure 3. Initial condition of the study area

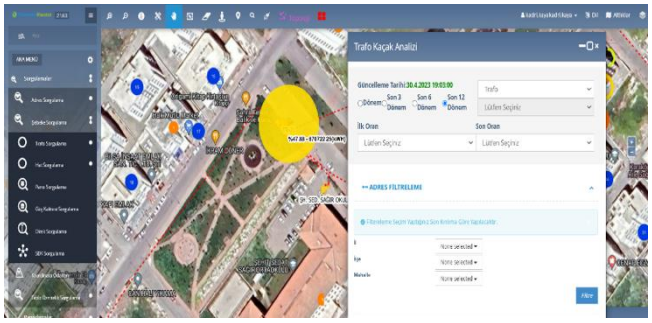

Figure 4. Integration of GIS Transformer Leakage Analysis

3.2. High-Quality and Continuous Energy Supply

The main duty of all distribution companies is to provide high-quality and uninterrupted energy. Investments are planned considering the service life of electrical inventory and the increasing use of electronic devices in today's world. Attribute information of the inventory in the field is kept up to date in the GIS software. This enables the reporting of information such as the production year and facility of the inventory through the GIS, determining the necessity of network renewal. Additionally, the consumption levels of the subscribers in the region have been analyzed using the registered measurement devices in the system, and an increasing consumption trend has been identified in the area. Taking this information into account, the investment to be implemented has been designed to accommodate the expected increase in inventory and meet the projected consumption levels.

3.3. Tracking of New Subscription Processes

When determining the investment area, the new subscriber numbers in the regions can be spatially identified through the integration of the electricity subscriber system with GIS. This situation necessitates network improvements and investment in areas where the new subscriber count is relatively high. In this context, the analysis of spatial and electrical growth can be conducted using GIS to determine the extent of investment required in these areas. In the analysis conducted within the study area, it has been determined that this region also requires investment in terms of new subscriptions.

4. Results

All GIS analyses are carried out using a GIS software called Edabis, which is specifically designed for the distribution company based on MapInfo. The initial observation status for the area to be invested in has been determined both visually and numerically, and the information regarding the list of areas for investment has been reported to the EPDK. Once the approval and budget for the investments are obtained, the relevant information for the area in question is identified in the GIS environment.

The planning phase was conducted by comparing the current situation in the field with the GIS. The inventory to be removed from the relevant area was identified numerically through SQL queries in the Edabis system, and it was recycled and recorded for use in other areas. With the assigned codes for each investment area, simple queries can be made through the GIS to continuously monitor the respective area.

The three main criteria for the investment areas, which are unauthorized consumption, quality and uninterrupted energy supply, and new subscription processes, have been identified using geometric and semantic data, and the necessary analyses have been conducted through the Edabis and MapInfo GIS software. These data have been obtained through the integration of the GIS software with electrical measuring devices, base satellite images, citizen applications, loss-leakage integration, and the semantic data of the network.

The inventory related to the planned investment has been compared in terms of pre-investment and post-investment conditions based on the current situation and analysis in the study area (Table 1).

Table 1. Pre and Post Investment Status of the Study Area

	Transformer	Pole/ FDB	LV Line (m)	Lighting pole
Pre-investment	2	72	3786	100
Post-investment	1	61	4200	120

If this planned investment is implemented, according to the analysis obtained through the GIS software, one of the most important issues for distribution companies, the System Average Interruption Frequency Index, will be reduced by three times. Furthermore, the analysis results indicate that power outages will be minimized, and no inconvenience will be experienced in new subscription applications.

By assigning a specific code to this project in the GIS software, it has been recorded and can be visualized

through SQL queries for potential fieldwork in the study area. This enables the digital monitoring of every planned scenario for electricity distribution without the need for additional fieldwork (Figure 5). Moreover, each electrical inventory item removed in the field can be recycled. The reporting of these removed inventories can also be carried out through the demolition query screen in the GIS software. These inventories can be tracked through the integration of Google Street View within the GIS software (Figure 6).

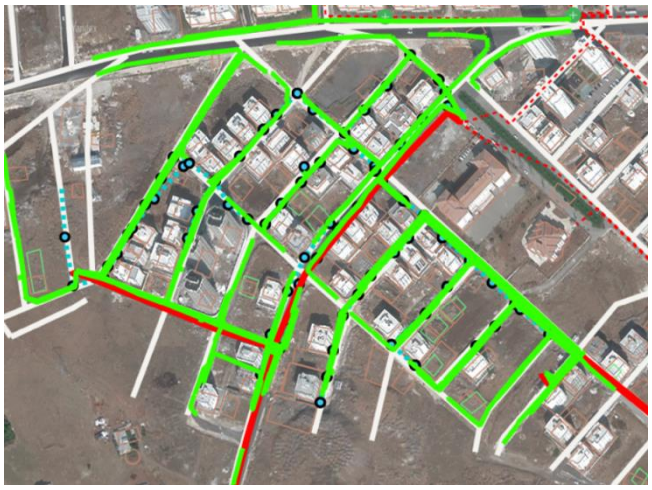

Figure 5. The Final Status of the Study Area

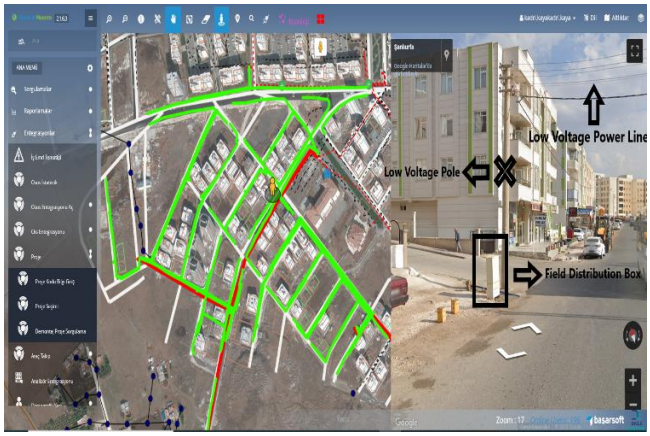

Figure 6. Google Street View of the Study Area

5. Conclusion

The main objective of this study is to analyze both pre and post-investment scenarios of all investments made by distribution companies using GIS and solve potential scenarios. The first objective of the study is to determine the suitability of making investments in the relevant area. The second objective is to observe improvements after the investment. These improvements can be measured through factors such as customer satisfaction when quality and uninterrupted energy are provided, reduction in workload, time savings, and cost savings. Additionally, the recycling of removed inventories is also an important factor. It has been demonstrated that all of these factors can be evaluated through GIS investment analysis.

With the increasing energy demand in today's world, it is observed that especially the analysis of loss and leakage amounts can be done accurately through GIS. In the study area, the loss and leakage rate, which has been determined as 47.88%, and System Average Interruption Frequency Index, projected to be reduced by three times through accurate analysis and investments.

Acknowledgement

We would like to express our sincere gratitude to Dicle Elektrik Dağıtım A.Ş. (DEDAŞ) for providing the anonymized data used in this study.

References

Aksu, A. (2019). Elektrik dağıtım şirketlerinde kayıp ve kaçağın incelenmesi. Master's thesis, Istanbul University.

Emiroğlu C., Tanrıöven K. & Akbulut F. (2007). Elektrik Dağıtım Şirketlerinde GIS Uygulamaları. Ulusal Coğrafi Bilgi Sistemleri Kongresi, 30 September –02 November, KTÜ, Trabzon, Türkiye.

EPDK, (2017), Elektrik Dağıtımı ve Perakende Satışına İlişkin Hizmet Kalitesi Yönetmeliği- Regulation on Quality of Service for Electricity Distribution and Retail Sale .

Gokler, M. E., Durmus, H., & Atesoglu, A. (2020). Evaluation and Risk Mapping of Cutaneous Leishmaniasis Cases between 2007 and 2017 in Sanliurfa, Türkiye.

Hatipoğlu, İ. H., & Ak, B. E. (2018). Kentsel dokuda Bitkilendirmenin öneminin Şanlıurfa ili Karaköprü Ilçesi örneğinde irdelenmesi: ISUEP2018 International Symposium on Urbanization and Environmental Problems, 28, 30.

Rao, M. K., Varma, B. S., & Radhakrishna, C. (2008, July). Experiences on implementation of GIS based tools for analysis, planning and design of distribution systems. In 2008 IEEE Power and Energy Society General Meeting-Conversion and Delivery of Electrical Energy in the 21st Century (pp. 1-8). IEEE.

Turksat, (2023), Population statistics by neighborhood, Turkish Statistical Institute (Turkstat).

Ünverdi, A. B. (2021). Elektrik dağıtım sisteminde cbs uygulamaları ve gerçekleşen kesintilerin cbs entegrasyonu ile raporlanması. Master's thesis, Ondokuz Mayıs University.

6th Intercontinental Geoinformation Days

igd.mersin.edu.tr

The recreational potential of waterfalls in an example of Gabala district

Ismailova Shahla *1

[1]*Geography Institution, Geomorfology, Baku, Azerbaijan*

Keywords
Waterfalls
Recreational potential
Accessibility
Gabala district

Abstract

Gabala district is a famous tourist destination in South Caucasus. Tectonic feature, lithological and topographical structure, climatic condition and river regimes of this region result in obsessing a great potential in terms of waterfalls. There is a Yeddi Gozel (Seven Beauties) waterfalls in this district which attracts both domestic and international visitors. At the same time there are other waterfalls in this district which of the value remains underestimated and their potential is not being used enough in tourism. In these articles we investigate the accessibility of these waterfalls, there altitude, proximity to the road, proximity to other attractive objects in terms of tourism. Taking all this into account we estimate their accessibility and their touristic potential. Considering the studied waterfalls make a map on ArcGIS 10.5, we proposed three touristic routes in the region and grouped other touristic objects that tourists can enjoy on that route. Thus, these routes can be used to attract more tourists and bring more income to the country and the local people.

1. Introduction

Ecotourism is a responsible tourism to the natural areas which conserves environment and improves the well-being of local people. The south slope of Great Caucasus is well known for its mountainous ecosystems, historical monuments and variety of ecotourism destinations. Among various tourism resources this region is rich with its waterfalls- must-visit sites for travelers. The purpose of this article to reveal the unfamous waterfalls of study region, to determine the way to reach them, evaluate their recreational potential and add them to the tourism route.

Waterfalls are landforms of limited occurrence, natural curiosities which are rare or absent entirely across most of the inhabited world. Waterfalls display a variety of visual characteristics and sounds that together make them particularly attractive to the beholder. Engaging with waterfalls is a part of the "adventure travel" and is attractive to travelers in search of a deeper travel experience.

2. Method

This research uses survey method. Data was collected by using field observation and Google Earth Pro. Data analysis with descriptive analysis. Research was carried out in a Gabala region in South slope of Great Caucasus. During the field observation we discuss famous and unfamous waterfalls in a mountainous region of this village, investigate their accessibility for the tourists, make a map in ARCGIS 10.8 showing the location of waterfalls and the ways which can take tourists to these objects. We evaluated the tourism potential of the area by revealing the tourism attractiveness of the surrounding areas. We grouped the waterfalls and divided them into 3 tourist routes so that the tourists who are waterfall lovers can visit several waterfalls in the same trip. We also assessed the attractiveness of tourist routes by noting other tourist facilities available along these routes.

3. Results

From the discussion we revealed that Gabala district has 3 types of waterfalls in terms of accessibility. Easily accessible waterfalls are two- Yeddi Gozal and Durja. They have 0-2 km distance from the way or village. Hard accessible waterfalls have 2-4 km distance from the way or village, very hard accessible waterfalls are situated more than 4 kilometers away from the way or village.

* **Corresponding Author**

*(e-mail) ORCID ID xxxx – xxxx – xxxx – xxxx

Cite this study

Shahla, I. (2023). The recreational potential of waterfalls in an example of Gabala district. Intercontinental Geoinformation Days (IGD), 6, 184-186, Baku, Azerbaijan

Table 1. Accessibility degree of waterfalls

Water-falls	Attitude (m)	Distance from the way or the nearst village (km)	Accessibility		
			easy	middle	hard
Yeddi Gozal	1059	0,3	+		
Durja	1608	0,82	+		
Soyuqbulaq	2180	2,44		+	
Zeylik	1496	2,2		+	
Ag chay	1419	3,3		+	
Gazan	1931	4,39			+
Mujug	1931	4,7			+
Mijixjadaur	2125	5,48			+
Gamarvan	1774	5,69			+

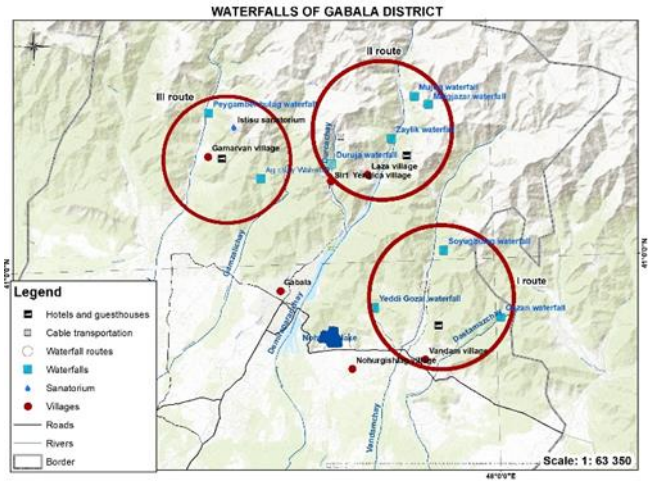

Figure 1. Tourism routes for waterfall trips

Table 2. Indicators used in the evaluation of tourism potential

Type	variables	I route	II route	III route
Natural resources	Waterfall	+	+	+
	Landscape	+	+	+
	Wildlife	+	+	+
Tourism infrastructure	Hotels, guesthouses	+	+	+
	Campsites	+	+	+
	Treatment			+
	Cable transportation		+	
	Horse riding	+	+	+
General infrastructure	National road	+		
	Village road	+	+	+

It is seen from the Table 2 that all 3 routes is rich with touristic resources. I route includes three- Soyugbulag, Yeddi Gozel and Gazan waterfalls. The nearest village is Vandan village. The region is a forested mountain region. Region provided with hotels and Baku-Balaken highway passes through from this village.

II route include four- Mujug, Mujukhjazar, Zaylik and Durja waterfalls. Mujug is the highest waterfall of Azerbaijan. The nearest villages are Laza and Durja villages. These villages also provided with hotels. In Durja village there is a cable transportation which begins from Gabaala district, III route include two waterfalls- Peygenberbulaq and Ag chay waterfalls. The nearest village is Gamarvan village. The village provided with guesthouses. There is a Istisu sanatorium in Gamarvan which theats some diseases with mineral water. Gamarvan village has a summer pasture in mountains. So, tourists can enjoy from lambs, clean and cool weather in summer.

All three routes are high estimated routes because of their listed attractions.

4. Discussion

Typically found in difficult, even dangerous, terrain waterfalls are often made easier to reach and enjoy by the construction of footpaths and other amenities. Yeddi Gozal (Seven Beauties) is a seven-storey waterfall which is located at an altitude of 1103 m at the foot of the mountain in a thick forest. These waterfalls are 6 km from the village of Vandam. This waterfall is the most easily accessible waterfall in Gabala district. Yeddi Gozal (Seven Beauties) waterfall is equipped with wooden stairs, because two of them are seen from below, to see another five waterfall tourists have to climb stairs.

Durja waterfall is in the Durja village, on 1608 m, on the Durjachay river, the tributary of Demiraparanchay. Distance from the village is 0,82 km. From Gabala to Durja village there is a cable car and highway, to the waterfall there is a hiking trail.

Many tourists dislike the commercial development at some waterfalls and so are encouraged to go to other, less developed falls. This in turn, contributes to the development and degradation of remoter, more pristine waterfalls sites, thus incurring the further spread of tourism blight.

There is The Soyugbulag waterfall which is three storey waterfalls on the Vendamchay river basin, on 2180 m altitude. This waterfall is 2,44 km away from the village way. Waterfall has a hiking route passing through the valley os the Vandam river and continues by the mountain river through the forest.

Gazan waterfall is on the Dastamazchay river basin on 1200 m altitude. is 4,39 km away from the village way. İt has very difficult and dengarous way. So, tourists who like difficulty can go and enjoy from this waterfall.

Mujug waterfall is the highest waterfall of Azerbaijan on a Demiraparanchay river basin. The waterfall is far from the settlement. İt has 4,7 km distance from Laza village. There is no road leading to this waterfall. So, getting to Mujug waterfall is an adventure tour. Tourists have to climb into the mountains, hike or horseback ride to the waterfall.

Near the Mujug waterfall there is a Michigchadaur waterfall on 2125 m altitude. Between Mucug and Michigchadaur there is a 1 km distance. And this way passes from forested mountains.

Zeylik waterfall is situated in Laza village on 1496 m, on the Demiraparanchay basin. 2,2 km far from the village. It is located 5 km deep in the forest of Shahdag National Park. The road to the waterfall passes through forest path and river bed.

Ag chay waterfall is on the 1419 m, on a Gamzelichay basin. The nearest village is Gamarvan village. The distance from the village is 5,69 km. There is a camp site on this way.

Peygamber bulaq waterfall is on the 1579 m altitude, 1,94 km from the sprinq named Chomche bulag, 3,51 km from the Campsite and 6,49 km from the Gamarvan village.

5. Conclusion

Waterfalls are the most attractive natural objects that attract tourists even though there are accessible or not. In these articles we investigate the waterfalls situated in Gabala district. We clarified their accessibility. We grouped waterfalls being near to each other in three routes. We noted another touristic resources and attractiveness of this routes and estimated all these routes with high assessment.

References

Hudson, B. J. (2006). Waterfalls, tourism and landscape. Geography, 91(1), 3-12. https://doi.org/10.1080/00167487.2006.12094145

Hudson, B. J. (2002). Best after rain: Waterfall discharge and the tourist experience. Tourism Geographies, 4(4), 440-456.

Iatu, C., & Bulai, M. (2011). New approach in evaluating tourism attractiveness in the region of Moldavia (Romania). International Journal of Energy and Environment, 5(2), 165-174.

Karadeniz, V. (2013). The recreational potential of Sızır Waterfall and its environment in terms of sustainability Sürdürülebilirlik kapsamında Sızır Şelalesi ve çevresinin rekreasyonel potansiyeli. Journal of Human Sciences, 10(1), 1098-1115.

6th Intercontinental Geoinformation Days

igd.mersin.edu.tr

Preparing soil protection map using GIS: A case study from Türkiye

Nuri Bozali [*1], **Fatih Sivrikaya** [2]

[1]*Karadeniz Technical University, Faculty of Forestry, Department of Forest Engineering, Trabzon, Türkiye*
[2]*Kastamonu University, Faculty of Forestry, Department of Forest Engineering, Kastamonu, Türkiye*

Keywords
Soil protection
Erosion risk
GIS

Abstract

Ecosystem services that exist spontaneously in forest ecosystems and benefit society are planned with a certain approach. Forest ecosystem services need to be classified, measured, mapped, planned, and managed. Due to its mountainous terrain, our country has a high disaster risk potential in terms of floods, avalanches, stone and rock rolling, landslides, and soil loss. Soil erosion is recognized as one of the most important environmental problems. Land use changes occur as a result of applications made by people other than natural factors, which increases the amount and risk of soil loss. In this study, the areas that will serve as soil protection were determined and mapped according to certain parameters. The mapping process incorporated various parameters such as slope, bedrock, crown closure, and tree root system. According to the results, approximately 41% of the area consists of areas very sensitive to erosion.

1. Introduction

Erosion is regarded as the second most significant environmental issue globally, following the rapid expansion of the population (Nikkami 2012). The phenomenon of erosion is observed in regions where there is a confluence of intense precipitation, limited vegetation cover, and areas with a sharp slope. The absence of effective erosion control measures results in soil depletion and constrains the agricultural potential of the affected regions (Yitbarek 2012). The impact of climate change on soil erosion risk is significant, as alterations in precipitation patterns have been observed to play a key role. The impacts of climate change have been observed to cause alterations in the frequency and severity of extreme weather events, such as heightened precipitation, prolonged drought, and modifications in land use practices. These changes have been found to have a significant impact on soil erosion processes (Borrelli et al. 2020). Forests play a significant role in ameliorating the adverse impacts of climate change on soil erosion. Hence, forest planners and managers formulate tactics that can safeguard the soil in situ whilst assessing the requisites for other ecosystem services.

Ecosystem services are classified into four categories in terms of their direct and indirect benefits to society: regulating (climate, water regime, ecosystem health), supportive (soil formation, food chain, basic production), production (food, fresh water, firewood, genetic resources), and cultural (recreation, ecotourism, education, cultural heritage) services (Haines-Young and Potschin 2018; ME, 2005). Soil erosion is one of the important factors affecting the sustainability of ecosystems and thus the provision of ecosystem services (Rodrigues et al. 2020). In determining the prominent areas in soil protection and erosion prevention services, it is necessary to determine not only the actual erosion areas but also the areas with hidden risks (Bozali 2020). In this study, while determining the areas to be allocated for soil protection service, the slope, the bedrock structure, the root system of the trees, and crown closure were mapped with the Geographical Information System (GIS).

2. Materials and Method

2.1. Study area

The research was conducted within the İpekyolu Forest Planning Unit, situated in the Maçka Forest Directorate of the Eastern Black Sea Region. This region is known for its mountainous terrain and is located within the country (Figure 1). The region encompasses a combined expanse of 5985.9 hectares, with 3949.8 hectares being covered by forests and the remaining

* Corresponding Author

*(nuribozali@ktu.edu.tr) ORCID ID 0000-0001-5735-3649
(fsivrikaya@kastamonu.edu.tr) ORCID ID 0000-0003-0860-6747

Cite this study

Nuri, B., & Sivrikaya, F. (2023). Preparing soil protection map using GIS: A case study from Türkiye. Intercontinental Geoinformation Days (IGD), 6, 187-190, Baku, Azerbaijan

2036.0 hectares being devoid of forestation. The dominant tree species within the planning unit are spruce, beech, and Scots pine, as determined by the prevailing habitat conditions. The study area also encompasses a variety of tree species, including alder, hornbeam, fir, and oak.

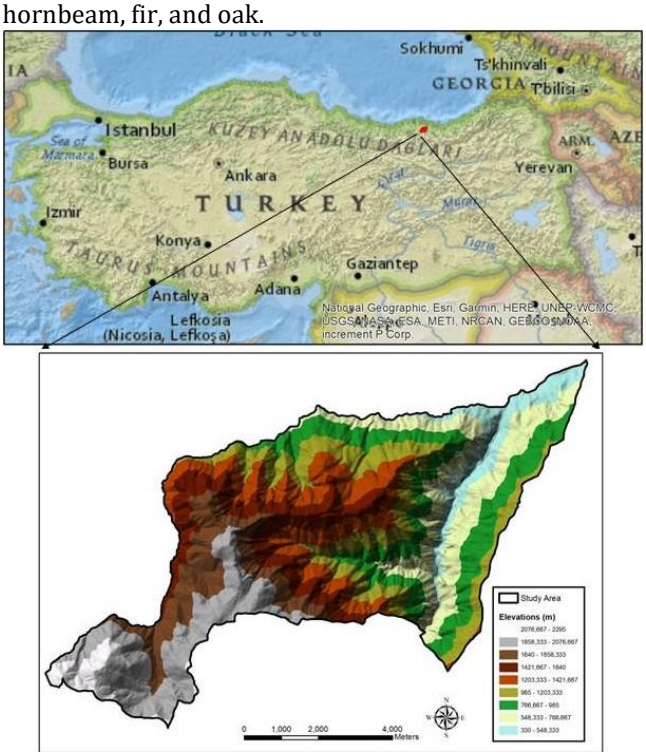

Figure 1. Study area

2.2. Dataset

The digital map of stand types and digital elevation model (DEM) data were acquired from the Maçka Forest Directorate. Furthermore, the geological configuration of the region has been digitized, and the bedrock units have been established utilizing the 1/100,000 scaled geological maps provided by the Mineral Research and Exploration General Directorate.

2.3. The map of soil protection function

The allocation of areas for soil protection service was determined by considering factors such as slope, bedrock, crown closure, and tree root system. The assessment of the soil protection function in the plan unit was based on the slope criterion. Specifically, areas with a land slope greater than 30% were identified as having a significant soil protection function, and slope groups were established accordingly, as presented in Table 1.

Table 1. Erosion risk groups according to slope classes

Slope (%)	Risk Class	Sensitivity
0-30	III	Low
31-60	II	Medium
> 60	I	High

The susceptibility of bedrock groups to erosion and the associated risk groups for the study area were given in Table 2.

Table 2. Erosion risk groups according to bedrock classes

Bedrock	Risk Class	Sensitivity
Sandstone, Schist, Sediment	I	High
Ophiolite, Sedimentary Rock	II	Medium
Gabbro, Limestone, Marble Clay	III	Low

The categorization of erosion risk groups is established in the following manner. The first risk group comprises areas with a high susceptibility to erosion and a significant amount of soil mobility. Simultaneously, the soils that have developed on this particular group of bedrock exhibit a high degree of susceptibility to erosion. Risk group II refers to regions where the likelihood of erosion is moderate and the bedrock group exhibits a moderate susceptibility to erosion. According to the classification system, risk group III denotes regions that exhibit minimal or negligible erosion hazards, and the bedrock group in these areas is comparatively less vulnerable to erosion.

The amount of vegetation and litter in forests serves to mitigate the adverse impacts of erosion. The sensitivity of the plan unit to erosion has been assessed based on its crown closure and root system (Table 3).

Table 3. Erosion risk groups according to crown closure-tree root system

Crown Closure	Risk class based on root structure		
	Tap-root	Heart root	Fringe root
Bare-land	-	-	-
Sparsely distributed	II	II	I
Low coverage	II	II	II
Medium coverage	III	III	II
Full coverage	III	III	II

Maps delineating the areas susceptible to erosion were generated individually based on slope (S), bedrock structure (B), crown closure-tree root system (C) for the study area. Erosion sensitive areas were determined by overlapping the maps, and a soil protection function map was created. The following equation was used while determining the first-, second-, and third-degree erosion sensitive areas within the scope of the soil protection function (SCF).

SCF=3S+2B+1C

It is predicted that the importance of the slope in the areas that will serve as soil protection is greater than in the others, and therefore it will have the highest weight ratio. Therefore, a hierarchical order was established, whereby slope (3) was given greater priority than bedrock structure (2), and crown closure-tree root system (1). The numerical values 1, 2, and 3 utilized in the equation denote the weight ratios. After determining the minimum and maximum limits of the equation, three groups were formed, and the areas to be allocated for SCF were determined. The equation employs the values 33 and 100 as the lower and upper bounds, respectively.

The difference between the upper limit value and the lower limit value was divided into 3 groups and the limit range values were determined for SCF (Table 4).

Table 4. Limit values of soil protection function risk groups

SCF Value	Risk Class	Description
198-332	III	Low susceptibility to erosion
333-466	II	Medium susceptibility to erosion
467-600	I	High susceptibility to erosion

3. Results and Discussion

Maps depicting the risk of erosion based on slope, bedrock, and crown closure-root system criteria were produced using ArcGIS 10.6 software, as illustrated in Figure 2, Figure 3, and Figure 4. These maps were then incorporated into the risk category database. The study has shown the spatial distribution of erosion risk categories based on three distinct criteria, as presented in Table 5. The production of the ultimate risk map involved the overlaying of slope, bedrock, and crown closure-root system maps, resulting in the generation of a soil conservation map, as depicted in Figure 5.

When evaluated in terms of risk groups, approximately 44% of the area is in the high-risk group in terms of slope, and 38% is in the high-risk group in terms of crown closure-root system. Furthermore, it can be observed that a significant proportion of the region, specifically 76%, is situated within the basaltic geological formation.

Table 5. The areal distribution of the erosion risk classes in the study area based on slope, crown closure-tree root system and bedrock

Slope		
Erosion risk	Area (ha)	%
High	2627.84	43.90%
Medium	2702.50	45.15%
Low	655.54	10.95%
Total	5985.88	100.00
Crown closure-tree root system		
High	2246.80	37.53%
Medium	341.83	5.71%
Low	2205.92	36.85%
Bare-land	1191.33	19.91%
Total	5985.88	100.00
Bedrock		
Basalt	4558.38	76.15%
Dacite	1427.50	23.85%
Total	5985.88	100.00

Based on the results, it was determined that 45.07% of the study area exhibited a moderate susceptibility to erosion, while 13.49% demonstrated a lower susceptibility to erosion. The remaining 41.4% of the area was classified as highly vulnerable to erosion.

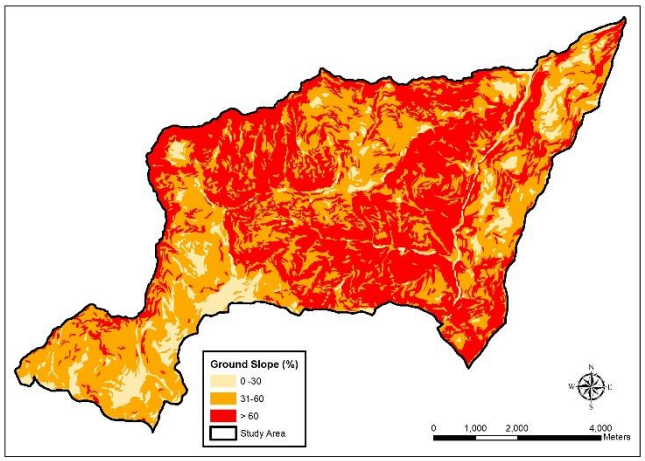

Figure 2. The slope classes map of the study area

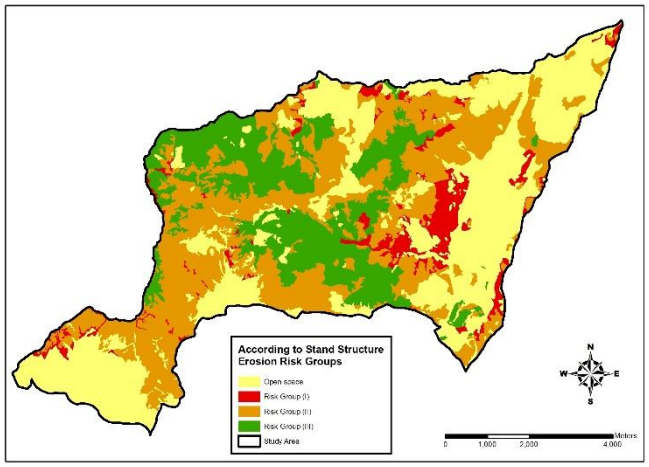

Figure 3. The crown closure-tree root system and slope classes map of the study area

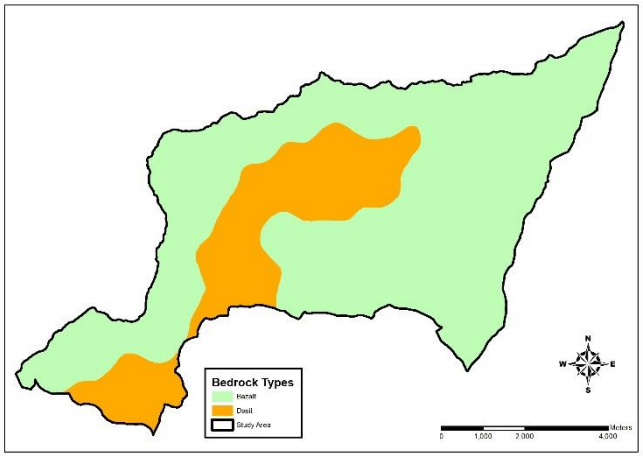

Figure 4. The bedrock classes map of the study area

Table 4. The areal distribution of the erosion risk classes in the study area

Erosion risk	**Area (ha)**	**%**
High	2480.98	41.45
Medium	2697.54	45.07
Low	807.36	13.49
Total	5985.88	100.00

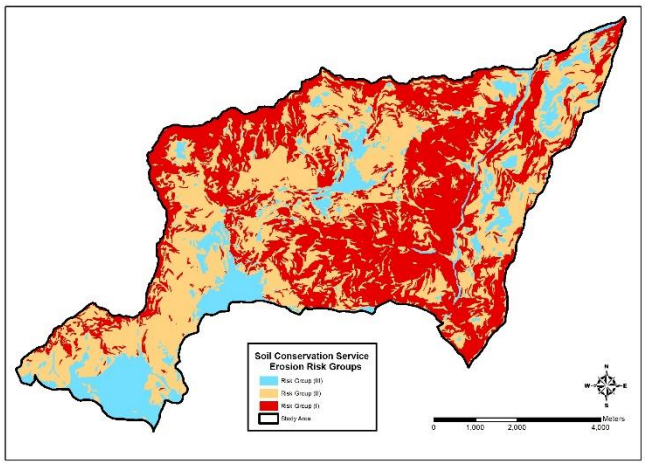

Figure 5. Soil protection map

4. Conclusion

This proposed methodology aims to incorporate slope, bedrock, crown closure, and root system criteria into the identification of soil protection areas in our country. This approach goes beyond the traditional reliance on the slope criterion alone. It enables the identification of not only visibly eroded regions but also those with concealed susceptibility to erosion. This study has facilitated the development of a methodology that forest managers can employ to pinpoint regions that will function as safeguards for soil during the formulation of forest management strategies.

Acknowledgement

We would like to thank the Trabzon Regional Directorate of Forestry for providing us with the related information.

References

Borrelli, P., Robinson, D. A., Panagos, P., Lugato, E., Yang, J. E., Alewell, C., ... & Ballabio, C. (2020). Land use and climate change impacts on global soil erosion by water (2015-2070). Proceedings of the National Academy of Sciences, 117(36), 21994-22001.

Bozali, N. (2020). Assessment of the soil protection function of forest ecosystems using GIS-based Multi-Criteria Decision Analysis: A case study in Adıyaman, Turkey. Global Ecology and Conservation, 24, e01271. https://doi.org/10.1016/j.gecco.2020.e01271.

Haines-Young, R., & Potschin, M. B. (2018). Common International Classification of Ecosystem Services (CICES) V 5.1 and Guidance on the Application of the Revised Structure.

Hurni, H., Herweg, K., Portner, B., & Liniger, H. (2008). Soil erosion and conservation in global agriculture. Land use and soil resources, 41-71.

MEA, (2005). Ecosystem and Human Well-Being: Synthesis, Island press, Washington, DC.

Nikkami, D. (2012). Investigating sampling accuracy to estimate sediment concentrations in erosion plot tanks. Turkish Journal of Agriculture and Forestry, 36(5), 583-590.

Rodrigues, A. R., Botequim, B., Tavares, C., Pécurto, P., & Borges, J. G. (2020). Addressing soil protection concerns in forest ecosystem management under climate change. Forest Ecosystems, 7(1), 1-11.

Yitbarek, T. W., Belliethathan, S., & Stringer, L. C. (2012). The onsite cost of gully erosion and cost-benefit of gully rehabilitation: A case study in Ethiopia. Land Degradation & Development, 23(2), 157-166.

6th Intercontinental Geoinformation Days

igd.mersin.edu.tr

Using EO1 hyperspectral images for rock units mapping

Parisa Safarbeyranvand [1], Parviz Zeaiean Firouzabadi [*2], Ali Hosingholizade[3], Reza Bastami[4]

[1] *Kharazmi University, Geography, Remote sensing and GIS, Tehran, Iran*
[2] *Tehran University, Geography, Remote sensing and GIS, Tehran, Iran*
[3] *Islamic Azad University Science and Research Branch, Tehran, Iran*

Keywords
Hyperspectral Images
Rock Plot
Pure Members
SAM
SVM

Abstract

The issue of mapping geological units during an evolving process has now reached a point where the detection and classification of geological units is carried out with the aid of hyperspectral sensing. In this study, using hyperspectral the image of the Hyperion sensor, related to the Khorramabad area in Lorestan province, and using Spectral Angle Mapper (SAM) and SVM (Support Vectors Machine) algorithms for detecting and separating geological units after performing the necessary preprocesses, the MNF conversion and PPI algorithm were used to reduce data and extract pure pixels on the image, respectively. From the overlapping of pure pixels with geological units and ground data, the average range for each member was extracted. Field surveys performed at the points provided by the Spectral Angle Mapter (SAM) confirm the superiority of the SVM method in separating geological units. Finally, by verifying the accuracy of the algorithms by calculating the error matrix, the accuracy of the classification of each method are (68.83) and (81.70) is for SVM and SAM respectively, it was found that at the end of the SVM algorithm with a total accuracy of 81.70 was introduced as the best classification algorithm.

1. Introduction

Using remote sensing technology and using satellite data reduced the costs and increased accuracy and speed of data collecting (Alvipanah, 2013). The use of satellite technology in the last decades as one of the most important means of information acquisition attracted the attention of many experts and specialists of various sciences, including geology, mining, environment, meteorology, agriculture and etc. From years of 1980, by introducing of Hyper-spectroscopic sensors, a major step has been taken in the area of remote sensing technology (Hasani Moghaddam, 2019). Hyper-spectral sensors, in comparison with multi-spectral sensors, produce much more accurate spectral data and therefore allow for more accurate identification of ground targets (Campsvalls et al., 2014). As the Hyper-spectral sensors are used of bands extremely large spectra produce a large amount of spectral data, so it is also necessary to use methods that are capable of processing and extracting valuable information from this high dimension data. The relationships of geological and remote sensing are nearly thirty years old (Waske et al., 2009). In the most hyper spectral sensors, reflection measurements of surface phenomena with a spectral width of 0.01 μm and spectral ranges of 0.4 to 2.5 μm are acquired, so this property makes it possible for geological unit's investigations.

The existing maps of the geological units are prepared by traditionally ways; in this research, used of remotely sensed hyperspectral images to produce more accurate maps of geological units. The data obtained from the measurements in terms of providing a wide coverage of the area and providing quantitative parameters can be a suitable source for updating geological maps (Rajendran et al., 2007). Images from remote sensing technology provide efficient data that requires processing on the image to extract information from them.

Among different methods of remote sensing, the classification techniques have a special role in analyzing, separating and detecting various geological units.

Image classification is one of the main process components of the information extracting from an object that are obtained by examining the relationship between spectral effects and classes (Oommen et al., 2008).

Ramakrishnan and Bharati (2015), review the potential of Hyperspectral Remote Sensing (HRS) technique in various geological applications ranging from lithological mapping to exploration of economic minerals of lesser crustal abundance. This work updates

* **Corresponding Author**
(pbeyranvandgis@gmail.com) ORCID ID 0000 – 0002 – 7860 – 2621
*(p.zeaiean@gmail.com) ORCID ID 0000-0001-8407-5605
(a.hosingholizade@ut.ac.ir) ORCID ID 0000 – 0001 – 5286 – 1361
(Bastami870@gmail.com) ORCID ID 0000 – 0000 – 0000 – 0000

Cite this study
Safarbeyranvand, P., Firouzabadi, P. Z., Hosingholizade, A., & Bastami, R. (2023). Using EO1 hyperspectral images for rock units mapping. Intercontinental Geoinformation Days (IGD), 6, 191-194, Baku, Azerbaijan

understanding on the subject starting from spectroscopy of minerals to its application in exploring mineral deposits and hydro-carbon reservoirs through different procedures such as atmospheric correction, noise reduction, retrieval of pure spectral endmembers and unmixing.

In this research, we specifically seek to compare the classification of geological units using SVM and SAM methods and compare them.

2. Method

2.1. Study area

The study area is located in the west of Iran, Lorestan province, Khorramabad city. Khorramabad is geographically located at 33 degrees, 29 minutes north latitude and 48 degrees, 21 minutes east.

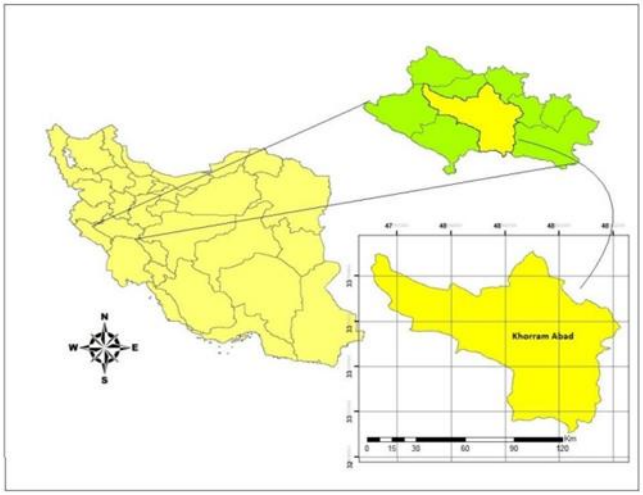

Figure1. Iran and case study

2.2. Satellite Image of EO-1 Hyperion Sensor

The image used in this study was captured in September 5, 2010, with a route number 166 and a row number 37. Its dimensions are 7.65 km wide and 185 km long. The centre of this area is the coordinates of 31° 37'00.09 "north and 47 ° 53'19.11" east.

2.3. Band Selection

Among the 242 spectral bands of the Hyperion sensor used in this research, 196 bands are calibrated and unique, and 155 bands were entered into the processing stage by removing the bands that absorb water or have a lot of noise. Table 1 shows the range of acceptable electromagnetic wavelengths for entering the processing stage.

Table 1. Acceptable bands which enter processing

Acceptable bands	Spectral range
8-57	VNIR range
79 83-119 133-164 183-184 188-1220	SWIR range

2.4. Minimum noise fraction

Transform (MNF) reduces data dimensionality and noise when using hyperspectral data. The MNF transform is considered as a noise reduction transform. It is a linear transformation that is used to determine the original dimensions and volume of the image, separate noise from other information and reduce the degree of processing in the next step. In this conversion, the image is first converted to noise and noise-free, then the noise-free part is considered as the main part and the noise is removed.

2.5. Pixel Purity Index (PPI)

PPI algorithm is used in hyperspectral images to find pure pixels (final pixels). For this purpose, the ten output bands obtained from the MNF transformation, which are noise-free, are given as input to the PPI algorithm. The output of this algorithm is an image that specifies pure pixels.

2.6. Endmember spectrum extraction through pure pixel identification

Many classification algorithms in hyperspectral images need to enter the spectral characteristics of the members (any class or complex that is classified or revealed in the hyperspectral image is called a member) to start processing.

Pure members were extracted from areas where the type of geological unit was identified. With 4 stages of surveying and field surveying and recording the coordinates of geological units using a high-precision GPS device and using the sampled points that corresponded to the pure pixels extracted from the PPI algorithm, the average reference spectrum of the units was extracted from the image itself and this reference spectrum was used as an input for the classification algorithm (Figure 2).

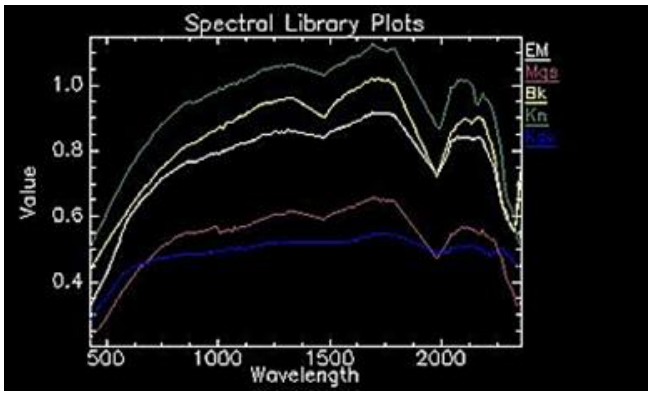

Figure 2. The spectra extraction from the geological unit's image

2.7. Spectral Angle Mapper (SAM)

Spectral Angle Surveyor as a Guided Classification Method, an Effective Method for Spectrum Comparison Images are relative to the standard range or reference spectrum. The algorithm of this method calculates the similarity between the two spectra by the spectral angle

between the two. In fact, by transforming the spectra into a vector in space, the size of the number of bands, the angle between the two vectors is calculated. In this method, for calculating the angle, the direction of the vectors is important and not their length, and therefore, the pixel brightness does not affect their classification. The angle between 0 and 1 if below, the more accurate it will be. If the angle is one, the entire image is identified as the

For example, to compare a pixel, the desired pixel spectrum with the same pixel spectrum is plotted between the reference spectra on two bands in a coordinate axis. The resulting points are then drawn to the origin and the angle between the two resulting lines is known as the pixel identification angle.

2.8. Support Vector Machine (SVM)

Support vector machine is a useful technique for data classification (Abbasi et al., 2015). A classification task usually involves separating data into training and testing sets. Each instance in the training set includes one "target value" (i.e., the class labels) and several "attributes". The goal of SVM is to produce a model which predicts the target values of the test data given only the test data attributes (Wei Hsu et al., 2003).

3. Results

After compilation of classified pictures, to assess the accuracy of each method, the GPS points taken by ground observations were used as ground maps to determine the accuracy of the error matrix, the accuracy of classification in each method, and ultimately the best way to estimate the geological map of the units introduced. The results of a accuracy assessment are usually presented as an error matrix, whereby a variety of parameters and values representing accuracy or some kind of error in the results are extracted from this matrix. This matrix is the result of a comparison of the pixels to pixels, the pixels defined with the corresponding pixels in the classification results. In the error matrix, land data in the columns and data related to the classification results are given in the rows of this matrix. The numbers on the matrix's main diameter indicate the number of pixels whose labels match the two sets of data or, in the other hand, the number of pixels that are correctly categorized over this diameter. Non-diagonal elements are the set of errors.

4. Discussion

The evaluation of the results of this research shows that the mapping of geological units mapped using SAM and SVM algorithms is highly consistent with the maps of the Geological Organization.

The SVM algorithm with overall accuracy of 81.70% and kappa coefficient of 0.72% was more accurate than the SAM algorithm with total accuracy of 68.63% and coefficient of 0.44%. Also, the results show that the SVM algorithm is an effective method for classifying the area based on the existing geological units in geological mapping research, taking into account the regional conditions. Due to the high capability of images in distinguishing phenomena, it has been shown that identification and separation of geological units using these images is easier and more accurate than other methods such as using multi-dimensional images.

According to the results of calculating the area of different formations in the study area, Keshkan formation has the largest area calculated by SVM class and Gachsaran formation has the largest area calculated by SAM classification method.

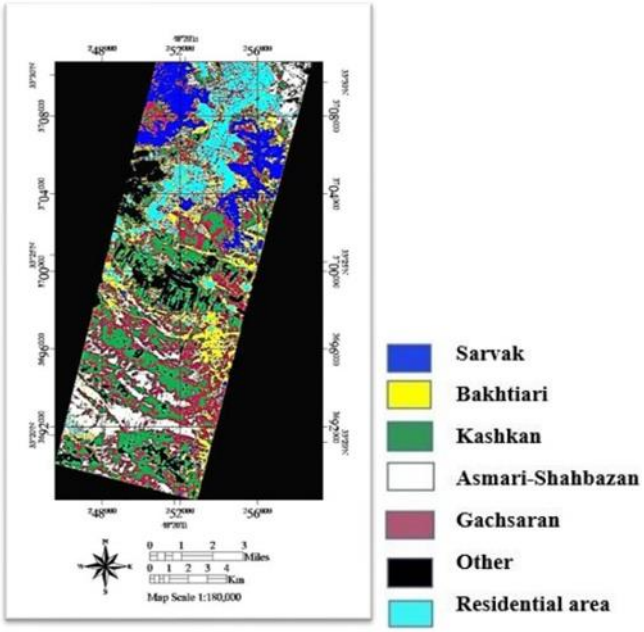

Figure 3. Classification result with SAM algorithm

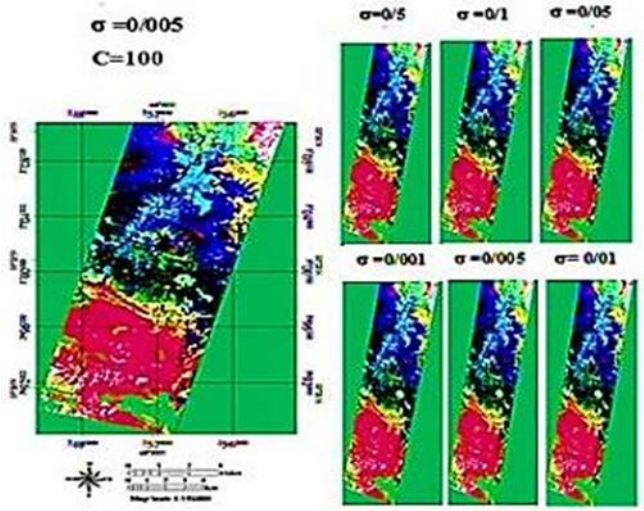

c

σ	C	Maximum precision(%)
≥0/001	100-200	62/57
0/005	100-200	81/70
0/01	100-200	59/96
0/05	100-200	63/01
0/1	100 200 200-2000	55/78 61/54 52/85
≥0/5	100-200	76/92

b

Figure 4. Classification result with SVM algorithm

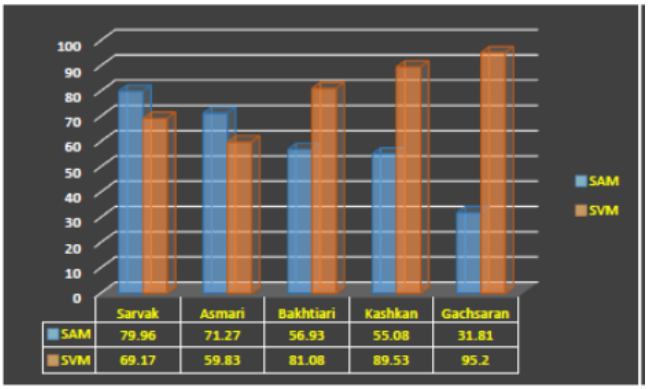

	Sarvak	Asmari	Bakhtiari	Kashkan	Gachsaran
SAM	79.96	71.27	56.93	55.08	31.81
SVM	69.17	59.83	81.08	89.53	95.2

Figure 5. Comparison of the accuracy of the different formation's detection by classification algorithms

5. Conclusion

Over the past years, geological mapping and extensive studies have reached a point where instead of doing field work and spending a lot of time and money, it is possible to study the area in a short time and with high accuracy using remote sensing images.

In this research, SAM and SVM algorithms were used to identify geological units. One of the most important factors in target detection that affects the final evaluation of algorithms is the selection of the threshold value, which was determined by trial and error in this study.

For better identification of geological units, MNF, PPI based on SVM and SAM composite were used.

References

Barton, I. F., Gabriel, M. J., Lyons-Baral, J., Barton, M. D., Duplessis, L., & Roberts, C. (2021). Extending geometallurgy to the mine scale with hyperspectral imaging: A pilot study using drone-and ground-based scanning. Mining, Metallurgy & Exploration, 38(2), 799-818.

Douglas, A., Kereszturi, G., Schaefer, L. N., & Kennedy, B. (2022). Rock alteration mapping in and around a fossil shallow intrusion at Mt. Ruapehu New Zealand with laboratory and aerial hyperspectral imaging. Journal of Volcanology and Geothermal Research, 107700. https://doi.org/10.1016/j.jvolgeores.2022.107700

Fonteneau, L. C., Martini, B., & Elsenheimer, D. (2019). Hyperspectral imaging of sedimentary iron ores–beyond borders. ASEG Extended Abstracts, 2019(1), 1-5. https://doi.org/10.1080/22020586.2019.12073201

Johnson, C. L., Browning, D. A., & Pendock, N. E. (2019). Hyperspectral imaging applications to geometallurgy: Utilizing blast hole mineralogy to predict Au-Cu recovery and throughput at the Phoenix mine, Nevada. Economic Geology, 114(8), 1481-1494. https://doi.org/10.5382/econgeo.4684

Johnson, C. L, Browning D. A., & Pendock N. E (2019). Hyperspectral imaging applications to geometallurgy: Utilizing blast hole mineralogy to predict Au-Cu recovery and throughput at the Phoenix mine, Nevada. Economic Geology, 114(8), 1481-1494.

Lorenz, S., Ghamisi, P., Kirsch, M., Jackisch, R., Rasti, B., & Gloaguen, R. (2021). Feature extraction for hyperspectral mineral domain mapping: A test of conventional and innovative methods. Remote Sensing of Environment, 252, 112129. https://doi.org/10.1016/j.rse.2020.112129

Noroozi, M., Kakaie, R., & Jalali, S. E. (2015). 3D Geometrical-Stochastical modeling of rock mass joint networks: case study of the right bank of Rudbar Lorestan Dam plant. Journal of Geology and Mining Research, 7(1), 1-10. https://doi.org/10.5897/JGMR14.0213

Qasim, M., Khan, S. D., & Haider, R. (2022). Integration of multispectral and hyperspectral remote sensing data for lithological mapping in Zhob Ophiolite, Western Pakistan. Arabian Journal of Geosciences, 15(7), 1-19. https://doi.org/10.1007/s12517-022-09788-8

Ramanaidou, E. R., & Wells, M. A. (2012). Hyperspectral imaging of iron ores. In Proceedings of the 10th International Congress for Applied Mineralogy (ICAM) (pp. 575-580). Springer, Berlin, Heidelberg.

Schodlok, M. C, Frei, M., & Segl, K. (2022). Implications of new hyperspectral satellites for raw materials exploration. Mineral Economics, 35(3), 495-502. https://doi.org/10.1007/s13563-022-00327-1

Sousa, F J, & Sousa D. J. (2022). Hyperspectral Reconnaissance: Joint Characterization of the Spectral Mixture Residual Delineates Geologic Unit Boundaries in the White Mountains, CA. Remote Sensing, 14(19), 4914. https://doi.org/10.3390/rs14194914

Stuart, M. B., Davies, M., Hobbs, M. J., Pering, T. D., McGonigle, A. J., & Willmott, J. R. (2022). High-resolution hyperspectral imaging using low-cost components: Application within environmental monitoring scenarios. Sensors, 22(12), 4652. https://doi.org/10.3390/s22124652

6th Intercontinental Geoinformation Days

igd.mersin.edu.tr

Bathymetric model generation in shallow waters with optical satellite images and machine learning algorithms

Fatma Karlığa[1], Ugur Alganci [*1], Dursun Zafer Şeker [1]

[1]*Istanbul Technical University, Civil Engineering Faculty, Geomatics Engineering Department, Istanbul, Türkiye*

Keywords
Remote sensing
Bathymetric model
Sentinel 2
Machine Learning

Abstract

Bathymetric mapping is essential for understanding ocean dynamics, mapping ecosystems, and forecasting coastal erosion. The goal of this study is to produce bathymetric models in shallow coastal area of rarely investigated Antarctic region using machine learning methods and Sentinel-2 satellite image. Based on satellite imagery and multibeam echosounder data, two algorithms, random forest (RF) and support vector machine (SVM), were used to predict ocean depths. The accuracy criteria used to evaluate the models' performance included RMSE, MAE, and R2. With an RMSE of 1.51, an MAE of 1.04, and an R2 of 0.77, the RF model produced promising results. These metrics provided low errors and a good fit between projected and observed water depths. The SVM model also provided promising results with slightly lower performance with an RMSE of 1.58, an MAE of 1.13, and an R2 of 0.75. Overall, this study showed that above mentioned algorithms can be used as viable approach for generating bathymetric models in shallow coastal areas. These models can contribute to our understanding of underwater topography, ecosystem dynamics, and the impacts of climate change.

1. Introduction

A bathymetric model is a digital representation of the ocean floor's topography, usually in the form of a map or 3D model. Bathymetric mapping of shallow waters is useful for a variety of purposes, including navigation, resource exploration, and environmental monitoring (Vojinovic et al., 2013). Bathymetry is important in many scientific fields, including oceanography, marine biology, and climate research. It gives important information on the structure and properties of the seabed, which is necessary for understanding ocean dynamics, mapping ecosystems, and forecasting coastal erosion. However, conventional techniques for gathering bathymetric data, like using sonar or performing hydrographic surveys, can be time-consuming and expensive, particularly in environments with shallow water where the water is too shallow for ships to access (Jagalingam et al., 2015). The use of optical satellite imagery and machine learning algorithms as an alternative technique for creating bathymetric models in shallow waters has gained popularity in recent years (Duan et al, 2022; Lumban-Gaol, Ohori & Peters, 2021; Misra et al, 2018; Mudiyanselage et al, 2022; Tonion et al, 2020; Wu, Mao & Shen, 2021).

Climate change's negative impacts have become increasingly visible in recent years, with rising temperatures and extreme weather events occurring all across the world. These changes have been most noticeable in the polar areas, resulting in major heatwaves and temperature rises (Gülher & Algancı, 2023). The Antarctic Peninsula and sub-Antarctic islands have been identified as hotspots of fast warming, with record-breaking temperatures and increased snowpack melt. These concerning patterns underline the critical importance of ongoing monitoring of the environment and sea level rise in shallow coastal locations. The precise evaluation of water depths, or bathymetry, is a critical component in understanding and mitigating the consequences of climate change in these locations.

To address these issues, bathymetric models are created in the study region near the Antarctic Peninsula using satellite images and machine learning methods. This study also aims to examine the viability and precision of creating bathymetric models in shallow waters using machine learning algorithms and Sentinel-2 image. To achieve this, a Sentinel-2 image and associated multibeam echosounder (MBE) bathymetric data was gathered. The Sen2Cor atmospheric correction algorithm was applied to Sentinel-2 image to investigate

* **Corresponding Author**

(karligaf18@itu.edu.tr) ORCID ID 0009-0005-5011-3489
*(alganci@itu.edu.tr) ORCID ID 0000-0002-5693-3614
(seker@itu.edu.tr) ORCID ID 0000-0001-7498-1540

Cite this study

Karlığa, F., Algancı, U., Şeker, D. Z. (2023). Bathymetric model generation in shallow waters with optical satellite images and machine learning algorithms. Intercontinental Geoinformation Days (IGD), 6, 195-198, Baku, Azerbaijan

its impact of the bathymetric model's accuracy on the Sentinel-2 satellite image that encompasses the study area.

2. Method

The proposed methodology initially starts with preprocessing of the Sentinel 2A satellite image, which includes atmospheric correction, registration and sub-setting. Then land masking was applied to imagery. As a next step random forest (RF) and support vector machine (SVM) models were trained with in-situ MBE data and resulting SDB maps were then validated with independent validation MBE data. Flowchart of the study is presented in Fig. 1.

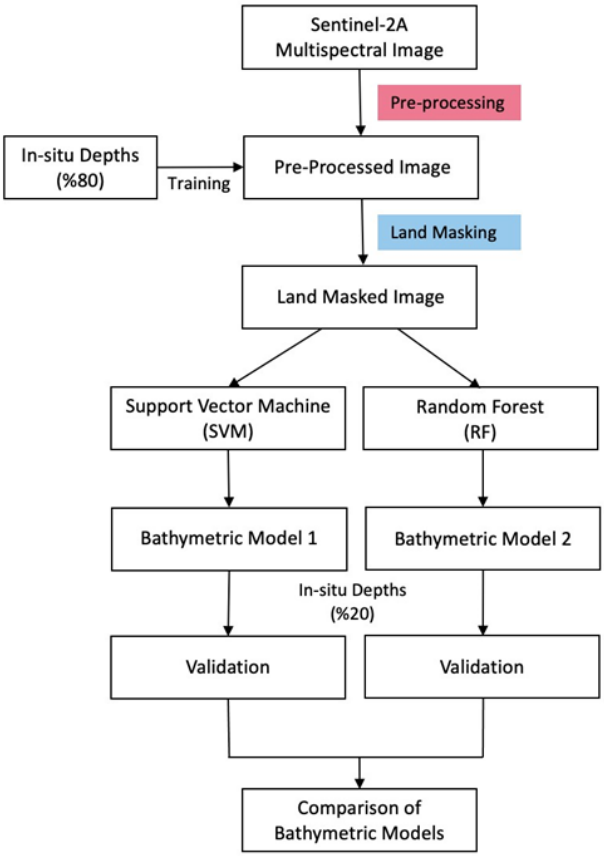

Figure 1. Flowchart of proposed methodology

2.1. Study area

This study focuses on a 22.24 km^2 study area located in Antarctica near Adelaide Island. Adelaide Island is one of the largest islands in the Marguerite Bay region, which is located on the Antarctic Peninsula's west coast. This area has a distinct arctic environment with pristine, unaffected shallow waters. Because of the varying depths and seafloor features, these waters are of particular interest for bathymetric modeling. The underwater features of the study area include complex bathymetry, channels, ridges, and submerged valleys. The chosen research area is ideal for assessing the performance of proposed bathymetric surface modeling techniques using optical satellite imagery and machine learning algorithms. Figure 2 provides the overviews of the study region.

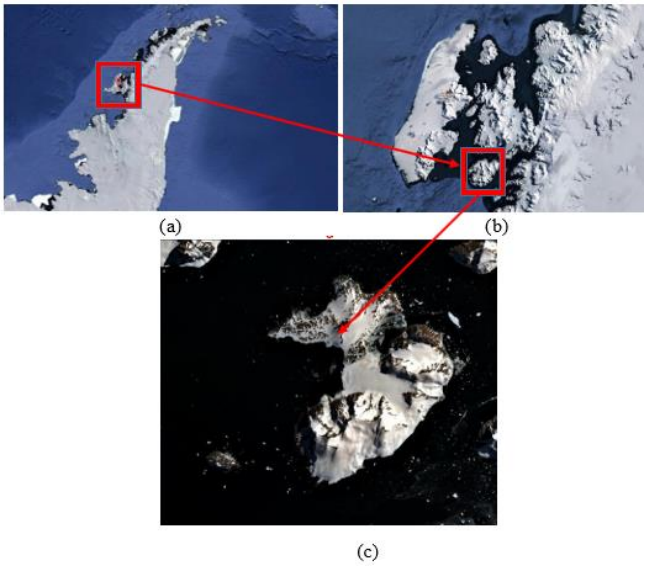

Figure 2. Study area (a), zoomed study area (b), natural color imagery of the study area derived from the Sentinel-2 satellite image (c)

2.2. Data

For SDB mapping purpose 2019 -01-24 dated Sentinel 2A image that was processed in Level 1C was used. The in situ bathymetric data was collected with an MBE with 5m horizontal spacing. A total of 18,928 bathymetry points with 0-15 m depth interval, were used to train and test machine learning algorithms. Among them, 80% (15142 points) were used to train the models, and 20% (3786 points) were used for validation.

2.3. Preprocessing and land masking

Sentinel-2 satellite image is corrected for atmospheric effects using optimized algorithms in the Sen2Cor module. It uses a set of sophisticated algorithms to calculate atmospheric scattering and absorption effects in satellite images, estimate aerosol density, and convert reflectance values into atmospherically corrected ones. A land masking technique was used on Sentinel-2 satellite imagery using the Google Earth Engine (GEE) platform to remove land masses and focus on depth analysis. Due to its inherent sensitivity to land reflectance, the near-infrared band (B8) of Sentinel-2 imagery was chosen to create the land mask. Several threshold values were experimented with and evaluated in order to determine the most accurate threshold value for detecting land pixels.

2.4. RF and SVM modeling

Both RF and SVM algorithms are used in state of regressor for this study to determine the correlative structure of surface reflectance and in situ MBE data. A parameter tuning process was carried out in order to determine the optimal parameters for the RF algorithm. The number of trees in the ensemble is a key parameter in RF, and it has a significant impact on the model's performance. The tree parameter from 10 to 1000 were experimented in this study and it was observed that the model achieved the optimum performance when the tree parameter was set to 400. The model's accuracy was

evaluated using appropriate validation techniques, and it was discovered that the tree selection had a minimal impact on overall accuracy, with an approximate impact of only 0.001. SVM is interested in two hyperparameters: gamma and C. The influence of a single training example is controlled by Gamma, while C determines the trade-off between achieving a low training error and maintaining a wide margin. To find the best combination, a grid search was run over a predefined range of gamma and C values. In the grid search, the combination of gamma: 0.1 and C: 100 produced the best results. These values were chosen as the best hyperparameters for the SVM algorithm to use when creating the bathymetric model.

3. Results

After training the both algorithms, resulting SDB surfaces were assessed through RMSE, MAE and R^2 accuracy metrics by use of independent validation points (Table 1). Results showed that RF performed slightly better for the 0-15m depth range according to all metrics.

Table 1. Error metrics for the two models

Metric/Method	RF	SVM
RMSE	1.51	1.58
MAE	1.04	1.13
R^2	0.77	0.75

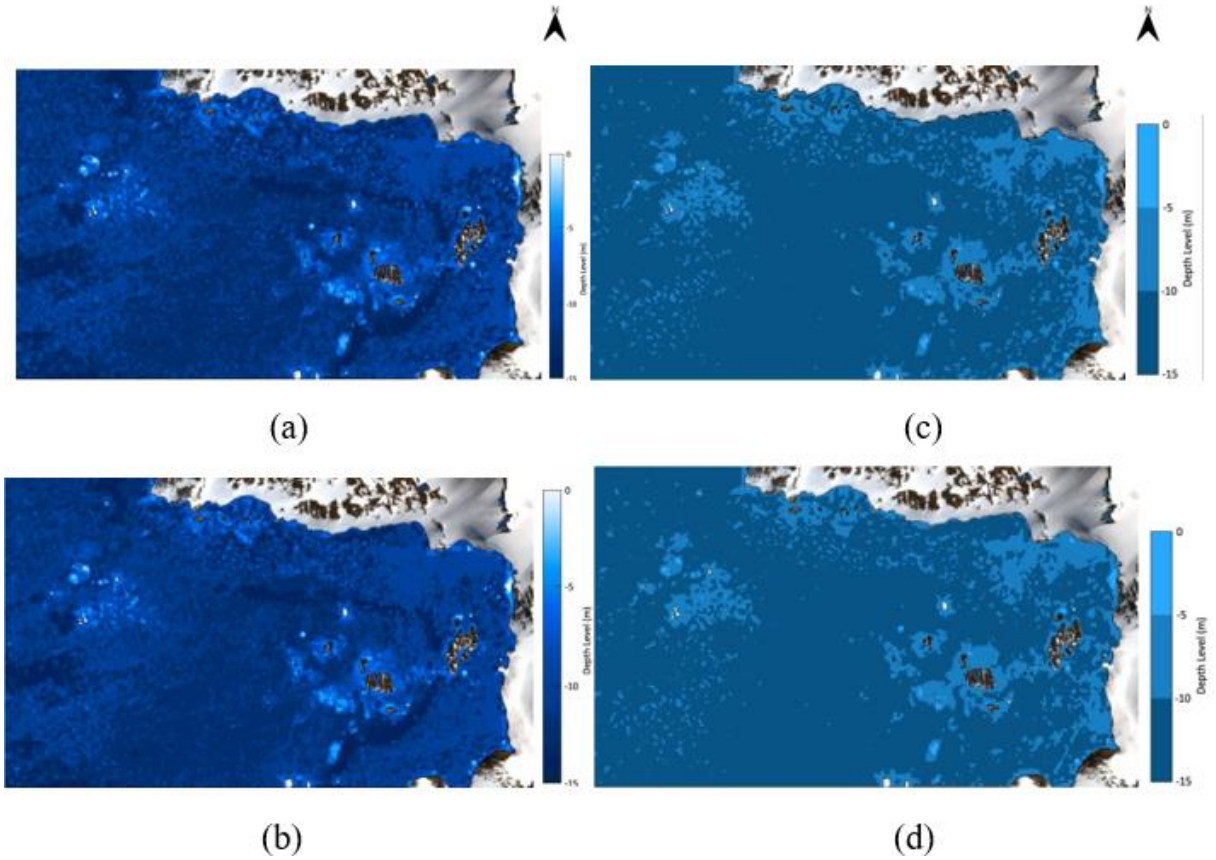

Figure 3. SDB surfaces and maps derived with RF algorithm (a, c) and SVM algorithm (b, d).

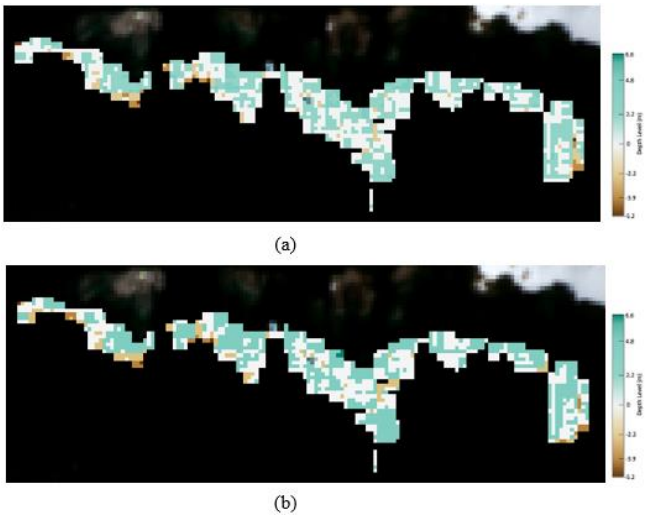

Figure 4. Reference Data–RF Difference (a), Reference Data–SVM Difference (b)

The accuracy achievement level according to MAE metric corresponds to A2/B IHO CATCOC level vertical accuracy requirements. This finding is in line with similar studies that used Sentinel 2 or better spatial resolution satellite images, however this finding is significant considering the complexity of study region and atmospheric conditions. After validating the efficient performance, SDB maps of the region were produced from surface rasters with 5m depth intervals (Figure 3).

Produced SDB maps are extracted from the same resolution grid generated from MBE point data. The difference layer is visualized for 0-15m depth range to understand the distribution of errors. This analysis provided that both algorithms showed similar error distribution with a slight overestimate of depths (Figure 4).

4. Discussion

RF model demonstrated promising performance in estimating water depths in shallow coastal areas. The RF model provided relatively low errors, with an RMSE of 1.51 and an MAE of 1.04, indicating a reasonable match between predicted and observed depths. The R^2 value of 0.77 indicates that the RF model can explain roughly 77% of the variance in water depth. These findings show the RF algorithm's ability to capture the complicated correlations between satellite images and bathymetric data. Similarly, the SVM model demonstrated bathymetric modeling capability, but with slightly more errors than the RF model. The RMSE of the SVM model was 1.58 and the MAE was 1.13, indicating a somewhat higher average difference between predicted and observed depths. The R2 value of 0.75 indicates that the SVM model can explain roughly 75% of the variance in water depth. While the SVM model has significantly lesser accuracy than the RF model, it nevertheless gives useful information for bathymetry estimate in shallow seas. The selection of these algorithms is influenced by project needs, computer resources, and the trade-offs between accuracy and computational efficiency.

In the context of bathymetric modeling, the comparison of the RF and SVM models highlights the strengths and limits of each technique. The RF model performed particularly well in estimating water depths, In the future, the findings of this study may help to a better understanding of the consequences of climate change on the arctic areas, notably in terms of sea level rise and ecosystem dynamics. Furthermore, the bathymetric models created will provide useful data for future monitoring. Using modern remote sensing techniques and machine learning algorithms, accurate bathymetric models have been created to enhance knowledge of the changing polar environment.

5. Conclusion

This study investigated the potential use of Sentinel-2 images on Antarctic region for shallow water bathymetry extraction. Overall, the integration of machine learning algorithms, particularly RF and SVM, with Sentinel-2 satellite images has shown to be a promising strategy for building bathymetric models in shallow coastal regions. This work provided how remote sensing and machine learning approaches may give excellent information on water depths, which is important for a variety of applications such as navigation, ecosystem monitoring, and climate research. Future study in this area could concentrate on improving the models by including more variables or applying more powerful machine learning techniques. Extending the investigation to larger areas or different geographic regions could also provide useful insights into the models' generalizability and performance under varying environmental conditions.

Acknowledgement

This study was funded by the Scientific and Technological Research Council of Turkey (TUBITAK), 1001 program, Project No: 121Y366. The authors would like to thank the Turkish Naval Forces Office of Navigation, Hydrography and Oceanography (ONHO) for providing the bathymetry data.

References

Duan, Z., Chu, S., Cheng, L., Ji, C., Li, M., & Shen, W. (2022). Satellite-derived bathymetry using Landsat-8 and Sentinel-2A images: assessment of atmospheric correction algorithms and depth derivation models in shallow waters. Optics Express 30, 3238-3261.

Gülher, E.; Alganci, U. (2023). Satellite-Derived Bathymetry Mapping on Horseshoe Island, Antarctic Peninsula, with Open-Source Satellite Images: Evaluation of Atmospheric Correction Methods and Empirical Models. Remote Sensing, 15, 2568.

Jagalingam, P.; Akshaya, B.; Hegde, A.V. (2015). Bathymetry Mapping Using Landsat 8 Satellite Imagery. Procedia Engineering, 116, 560–566.

Lumban-Gaol, Y., Ohori, K., Peters, R. (2021). Satellite-derived bathymetry using convolutional neural networks and multispectral sentinel-2 images. The International Archives of the Photogrammetry, Remote Sensing and Spatial Information Sciences, 43, 201–207

Misra, A., Vojinovic, Z., Ramakrishnan, B., Luijendijk, A. & Ranasinghe R. (2018). Shallow water bathymetry mapping using Support Vector Machine (SVM) technique and multispectral imagery, International Journal of Remote Sensing, 39:13,4431-4450

Mudiyanselage, S.S.J.D., Abd-Elrahman, A., Wilkinson, B. & Lecours V. (2022). Satellite-derived bathymetry using machine learning and optimal Sentinel-2 imageryin South-West Florida coastal waters, GIScience & Remote Sensing, 59(1), 1143-1158.

Tonion, F., Pirotti, F., Faina, G., & Paltrinieri, D. (2020). A machine learning approach to multispectral satellite derived bathymetry. ISPRS Annals of the Photogrammetry, Remote Sensing and Spatial Information Sciences, (3), 565–70.

Vojinovic, Z., Abebe, Y., Ranasinghe, R., Vacher, A., Martens, P., Mandl, D., Frye, S., Van Ettinger, E., & De Zeeuw, R. (2013). A machine learning approach for estimation of shallow water depths from optical satellite images and sonar measurements. Journal of Hydroinformatics, 15(4), 1408–1424.

Wu, Z., Mao, Z., Shen, W. (2021). Integrating Multiple Datasets and Machine Learning Algorithms for Satellite-Based Bathymetry in Seaports. Remote Sensing, 13, 4328.

6th Intercontinental Geoinformation Days

igd.mersin.edu.tr

Creation of land use and land cover maps of the Khachmaz-Shabran region of Azerbaijan using machine learning methods

Nariman Imranli*[1], Raziye Hale Topaloglu [2], Elif Sertel [3]

[1] *Turkish National Defence University, Atatürk Strategic Studies and Graduate Institute, Faculty of Satellite Technologies, Istanbul, Türkiye*
[2] *Yildiz Technical University, Faculty of Civil Engineering, Department of Geomatics Engineering, Istanbul, Türkiye*
[3] *Istanbul Technical University, Faculty of Civil Engineering, Department of Geomatics Engineering, Istanbul, Türkiye*

Keywords
Remote sensing
LULC
SVM
RF

Abstract

This study aims to produce Land Use/ Land Cover (LU/LC) maps of the Azerbaijan Khachmaz-Shabran region using machine learning (ML) methods and remotely sensed data. We used two common ML classification algorithms, Random Forest (RF) and Support Vector Machine (SVM). We generated two different LU/LC maps using an Azersky satellite image with a spatial resolution of 1.5 and a Sentinel-2 image with 20 m spectral bands. Both images were acquired on 1 August 2020. We implemented LU/LC class definitions of Level 2 of the CORINE nomenclature. After the classification step, an error matrix was created using the same reference points for Azersky and Sentinel-2. We compared the results of two classifications to determine the better-performing approach in obtaining the region's LU/LC maps.

1. Introduction

Remote sensing is used to map landscapes and infrastructures worldwide, manage natural resources, and study environmental change. With the emergence of high and very high-resolution satellite images with the developing technology, examining the current land use situation and the dynamic changes that have occurred over the years has become more accessible. Therefore, high and very high-resolution satellite data, which provides fast and reliable information, has become one of the practical information sources (Sertel et al., 2018; Topaloglu et al. 2022).

Information on Land Use/Land Cover (LU/LC) is essential for proper planning, management, and utilization of natural resources, including agricultural land and environmental protection (Sertel et al., 2018). Assessment of changes in LU/LC helps better understand the interactions between people and the environment, leading to better management of natural resources and sustainable development. Many methods and tools exist to classify and evaluate LU/LC and changes (Alipbeki et al. 2019; Topaloglu et al. 2022).

Machine learning (ML) techniques for LU/LC classification enable accurate and rapid analysis in many areas, such as land use planning, environmental management, monitoring of natural resources, and agricultural management (Algancı et al. 2015; Albayrak et al. 2018; Dey et al. 2021). Specifically, using ML algorithms such as Support Vector Machine (SVM), Random Forest (RF), and Neural Networks (NN), detailed LU/LC classes can be detected (Mountrakis et al. 2011; Algancı et al. 2015; Lui et al. 2016).

The RF classification algorithm is an ML method based on decision trees (Breiman 2001). Decision trees analyze the classes of training data and determine which class the test data belongs to according to the rules extracted from the training data (Algancı et al. 2015). The SVM is one of the most widely used classifiers for multispectral images. The method uses an optimal hyperplane with a maximum distance between the closest points. The reference vectors lie at the boundaries of the training samples, giving the maximum margin between the two classes and placing a separating linear hyperplane between them. An advantage of SVM is that it requires a small training sample size compared to traditional classifiers (Huang et al. 2002; Algancı et al. 2015).

The primary purpose of this study is to determine LU/LC maps of the Azerbaijan Khachmaz-Shabran region using two different ML techniques and to compare the accuracies of LU/LC maps created from Azersky and Sentinel-2 satellite data. RF and SVM were applied to classify 13 different land categories accurately, and

* **Corresponding Author**

*(imranli.nariman.94@gmail.com) ORCID ID 0009-0009-8711-9701
(haletopaloglu48@gmail.com) ORCI) ORCID ID 0000-0001-9706-8068
(sertele@itu.edu.tr) ORCID) ORCID ID 0000-0003-4854-494X

Cite this study

Imranlı, N., Topaloğlu, H., & Sertel, E. (2023). Creation of land use and land cover maps of the Khachmaz-Shabran region of Azerbaijan using machine learning methods. Intercontinental Geoinformation Days (IGD), 6, 199-203, Baku, Azerbaijan

results were examined to evaluate the performance of two algorithms and multi-sensor satellite images.

2. Study area and data

The Khachmaz-Shabran region, part of Azerbaijan's economic zone, is located in the northeast of the Greater Caucasus (Fig.1). Its primary industries are light and food industries; at the same time, the soils have a wide variety of crops and are very fertile. Various elevation ranges are observed in the region, with sea level in the coastal zone, lower elevation values in the plains adjacent to the coast, and higher elevations towards the western part, where forests and mountains are available. The region is rich in oil and gas, gravel, sand, clay, and other minerals (Bedelova and Valehov, 2019).

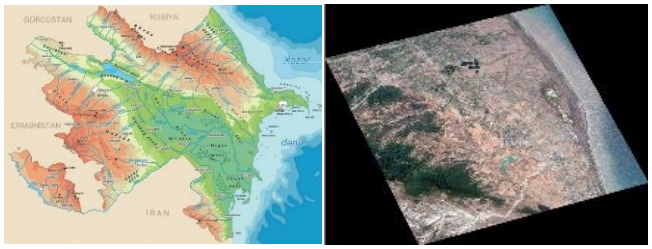

Figure 1. Study area

We used two remote sensing images; one was obtained from the Azersky and the other from the Sentinel-2 satellite. Both images were acquired on 01.08.2020 and with zero cloudiness. The Azersky and Sentinel-2 satellite data were obtained in level 2A and level 1 Ortho formats, respectively. Azersky image was pan-sharpened, including Red, Green, Blue, and Near-infrared spectral bands. We used the same spectral bands of Sentinel-2, but the spatial resolution is 20m in this case.

3. Methodology

We employed RF and SVM classification approaches to generate LU/LC maps. Figure 2 shows the whole flow chart of this study.

In this study, thirteen LU/LC classes based on Level-2 of CORINE nomenclature were mapped. These classes are:

- urban fabric
- industrial, comercial, and transport units
- mine, dump, and construction sites
- artificial, non-agricultural vegetated areas
- arable land
- pastures
- heterogeneous agricultural areas
- forests
- shrub and/or herbaceous vegetation associations
- open spaces with little or no vegetation
- coastal wetlands
- inland waters
- marine waters

Training sites were created for each class in ArcMap and ArcGIS Pro software. At least 20 samples were collected for each LU/LC class, and 300 samples were used to classify satellite images. The same training sites were utilized for Azersky and Sentinel-2 data sets and both SVM and RF classification algorithms.

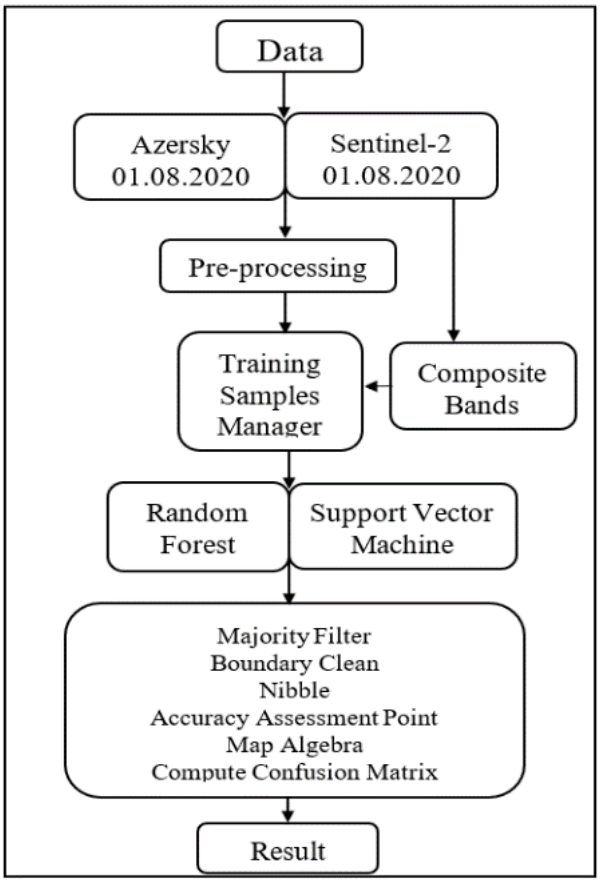

Figure 2. Flowchart of the study

3.1 Support vector machines

Support Vector Machine (SVM), a supervised and non-parametric statistical learning technique aims to find a hyperplane that divides training samples into a certain number of classes (Kavzoglu and Colkesen, 2009; Mountrakis et al. 2011; Du et al. 2019;). SVMs are classifiers that, in their most basic form, assign a binary test sample into one of two possible classes. By utilizing a kernel to translate feature space samples to a higher dimensional feature space, the SVM technique is extended to classes that cannot be separated linearly. SVMs are particularly useful in remote sensing because they can handle less training and achieve higher classification accuracy than conventional techniques (Chen and Guevara 2015).

3.2 Random forest

A group of binary decision trees makes up the ensemble method known as Random Forest (RF) classifier. By assembling a linear mixture of simpler models, it improves model performance. RF selects observations randomly for "small" binary trees. The performance of the method is enhanced by the comprehensive solution of this substantial forest (set) of trees. Based on the majority of labels from each tree, the final result is obtained (Li et al. 2020). When determining the specific classes, each classifier typically gives one vote, and classification is done by considering votes for all classifiers (Jing et al. 2020).

After the classification, we implemented a post-classification process to enhance the classification results. We employed smoothing with "Majority Filter", "Boundary Clean" and "Nibble" functions (Fig. 3), (Esri 2023).

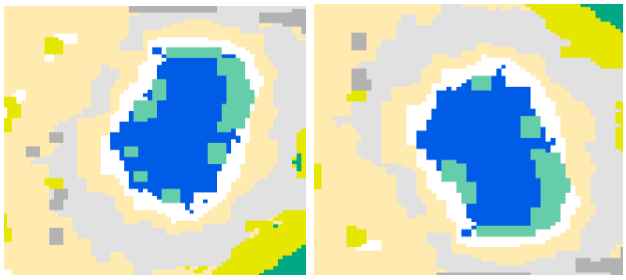

Figure 3. The difference before and after smoothing

To determine the accuracy of the final LU/LC maps, we conducted an accuracy assessment by generating an error matrix and calculating overall (OA), producer's (PA), and user's accuracy (UA) values and kappa statistics.

4. Results and Discussion

We determined 13 different LU/LC classes in the region both from Sentinel-2 and Azersky satellite images. Selected regions from LU/LC maps of Sentinel-2 and Azersky images using RF and SVM methods are shown in Figure 4. Each column represents a small area within the region. For the first region, more natural grassland areas were classified with RF-based Sentinel-2 classification. Inland water surfaces could be identified with both images and both methods. However, some parts of the shorelines of the lake were classified as the sea with the Azersky image.

We randomly generated approximately 400 reference pixels to conduct an accuracy assessment. The error matrix results are illustrated in Table 1 and Table 2.

We presented the accuracy metrics of Sentinel-2 LULC classification results in Table 1. We obtained a better OA value of 0.88 with the RF method compared to SVM which is 0.83. Specifically, for urban (1.1) and industrial, commercial, and transport units (1.2) classes, RF produced higher UA than the SVM method for Sentinel-2 classification. When we checked the confusion matrix of the Sentinel-2 RF LULC map, we observed that urban (1.1) and coastal wetlands (4.2) were mixed with the open spaces (3.3) class. In Sentinel-2 SVM, we found out that the industrial, commercial, and transport units (1.2), besides the urban (1.1) and coastal wetlands (4.2) classes, were mixed with open spaces (3.3).

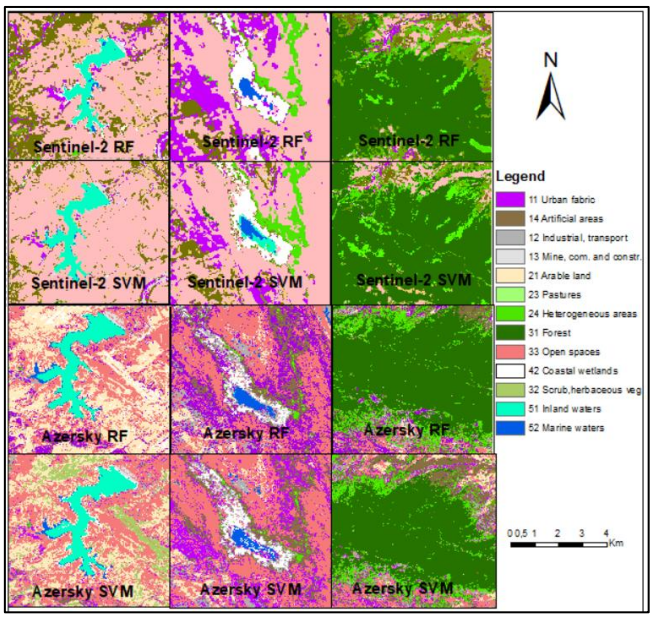

Figure 4. Classification results

On the other hand, we showed the accuracy metrics of the Azersky LULC classification results in Table 2. We acquired a better OA value of 0.78 with the SVM method. The RF method exhibited superior performance in terms of UA compared to the SVM method for the forest (3.1) and marine waters (5.2) classes in the Azersky classification. When we analyzed the RF confusion matrix of the Azersky satellite image based LULC map, we observed that the highly mixed class was the open spaces class (3.3), confused with the urban (1.1), arable land (2.1), coastal wetlands (4.2), mine, dump and construction sites (1.3) classes. In SVM based LULC mapf from the Azesky satellite image, urban (1.1), industrial, commercial, and transport units (1.2) and mine, dump, and construction sites (1.3) were mixed with the open spaces (3.3) class.

Table 1. Accuracy assessment for Sentinel-2 LULC maps

	Random Forest		Support Vector Machine	
	User's Accuracy	Producer's Accuracy	User's Accuracy	Producer's Accuracy
11 urban fabric	0.84	1	0.58	1
12 industrial, commercial and transport units	0.90	0.90	0.55	0.81
13 mine, dump and construction sites	0.87	0.96	0.87	0.90
14 artificial, non-agricultural vegetated areas	0.65	0.91	0.77	1
21 arable land	0.71	0.69	0.84	0.93
23 pastures	0.90	0.82	0.97	0.97
24 heterogeneous agricultural areas	0.94	1	0.94	1
31 forests	1	0.91	1	0.89
32 shrub and/or herbaceous vegetation associations	0.97	0.97	0.97	0.91
33 open spaces with little or no vegetation	0.97	0.65	0.97	0.40
42 coastal wetlands	0.77	0.92	0.35	0.92
51 inland waters	1	1	1	1
52 marine waters	1	0.94	1	0.86
overall accuracy	0.88		0.83	
kappa	0.81		0.82	

Table 2. Accuracy assessment for Azersky LULC maps

	Random Forest		Support Vector Machine	
	User's Accuracy	Producer's Accuracy	User's Accuracy	Producer's Accuracy
11 urban fabric	0.58	0.86	0.61	0.56
12 industrial, commercial and transport units	0.73	0.88	0.63	0.95
13 mine, dump and construction sites	0.58	0.90	0.58	0.90
14 artificial, non-agricultural vegetated areas	0.61	0.90	0.55	0.89
21 arable land	0.74	0.61	0.87	0.64
23 pastures	0.58	0.75	0.94	0.78
24 heterogeneous agricultural areas	0.94	0.97	1	1
31 forests	0.97	0.88	0.94	1
32 shrub and/or herbaceous vegetation associations	0.87	0.64	0.94	0.81
33 open spaces with little or no vegetation	0.84	0.45	0.94	0.45
42 coastal wetlands	0.42	0.38	0.48	0.50
51 inland waters	0.87	1	1	0.89
52 marine waters	0.97	0.83	1	0.90
overall accuracy	0.75		0.78	
kappa	0.73		0.75	

5. Conclusion

Our results show that the highest OA of 0.88 was obtained with the RF based classification of the Sentinel-2 image. The Coastal Wetlands, Urban, and Green Urban classes exhibited lower UA and PA values for both satellite images. The Coastal Wetlands class is mostly mixed with Open Spaces and Arable land. Some Urban areas were misclassified as the Open Spaces and some Road, Industry areas were misclassified as the Open Spaces. Inland waters, marine waters, and forest areas were easily identified from both satellite images with both classification methods.

This study showed that both Sentinel-2 and Azersky satellite images can be used to create up-to-date LU/LC maps. Although some classes suffered from mixture problems, most of the classes were accurately identified. To overcome this problem, some of the similar characteristic classes could be merged, and LULC maps could be generalized if it fits the purpose of the study.

References

Albayrak, S., Koc-San, D., & Sivrikaya, F. (2018). Land cover classification using machine learning algorithms. Journal of Environmental Management, 207, 205-214.

Alganci, U., Ozdogan, M., Sertel, E., & Ormeci, C. (2015). Estimating maize and cotton yield in southeastern Turkey with integrated use of satellite images, meteorological data and digital photographs. Field Crops Research, 157, 8-19.

Alipbeki, O. A., Alipbekova, Ch. A., & Amangaliev, K. S. (2019). Assessment of The Accuracy of Land Use Classification. International Scientific journal "Bulletin of Science" No. 12

Bedelova, A. N., & Valehov, N. S. (2019). GİS əsasında Xaçmaz rayonunun torpaq və meşə örtüyünün yamacların meylliyindən asılı olaraq ekoloji qiymətləndirilməsi.

Breiman, L. (2001). Random forests. Machine learning, 45(1), 5-32.

Chen, J., & Guevara, M. (2015). Support vector machine for land cover classification: a study from the central Amazon region, Brazil. Environmental Monitoring and Assessment, 187(3), 1-13. https://doi.org/10.1007/s10661-015-4416-4.

Esri, (2023). https://desktop.arcgis.com/en/arcmap/, accessed in May 2023.

Dey, P., Das, M., & Maiti, S. K. (2021). Land use and land cover classification of a mining region using machine learning algorithms: a case study in India. Environmental Earth Sciences, 80(2), 1-17.

Du, P., Feng, X., Li, Y., & Wan, J. (2019). Mapping land use and land cover using machine learning techniques: A comparative study of random forest and support vector machine algorithms. Remote Sensing, 11(23), 2829.

Huang, C., Davis L. S., & Townshend J. R. G. (2002). An assessment of support vector machines for land cover classification, International Journal of Remote Sensing, 23(4), 725-749.

Jing, L., Zhang, Z., Yang, X., & Wang, H. (2020). Comparison of Random Forest and SVM in the classification of land cover using Sentinel-2 imagery. Peer Journal, 8, e10105.

Kavzoglu, T., Colkesen, I. (2009). A kernel functions analysis for support vector machines for land cover classification, International Journal of Applied Earth Observation and Geoinformation, 11, 5, 352-359.

Li, W., Wu, C., Zhou, W., Li, W., Huang, X., & Zhang, W. (2020). An improved random forest algorithm for the classification of Corine land cover using Sentinel-2A data. International Journal of Applied Earth Observation and Geoinformation, 93, 102218. https://doi.org/10.1016/j.jag.2020.102218.

Lui, W., Wang, J., & Qiu, S. (2016). A random forest based approach for land use and land cover classification using Landsat 8 imagery. Remote Sensing, 8(9), 786.

Mountrakis, G., Im, J., & Ogole, C. (2011). Support vector machines in remote sensing: A review. ISPRS Journal of Photogrammetry and Remote Sensing, 66(3), 247-259.

Sertel, E., Topaloğlu, R. H., Şallı, B., Algan, I. Y., & Aksu, G. A., (2018). Comparison of Landscape Metrics for Three Different Level Land Cover/Land Use Maps. ISPRS Internatıonal Journal Of Geo-Informatıon ,7,10.

Sertel, E., Musaoğlu, N., Alp, G., Yay, I., Kaya, Ş., Yüksel, B., & Yılmaz, A. (2018). 1:25000 ölçekli ulusal Arazi Örtüsü/Kullanımı Sınıflandırma Sistemi ile HGK TOPO Veritabanının Karşılaştırılması. Harita Dergisi , 160, 34-46.

Topaloglu, R. H., Aksu, G. A., Ghale, Y. A. G., & Sertel, E., (2022). High-resolution land use and land cover change analysis using GEOBIA and landscape metrics: A case of Istanbul, Turkey. Geocarto International, 37, (25), 9071-9097.

6th Intercontinental Geoinformation Days

igd.mersin.edu.tr

Displacement analysis of aftershocks occurred after 6 February 2023 Kahramanmaraş Earthquakes

Dilara Solmaz [*1], **Nusret Demir** [2]

[1]*Akdeniz University, Institute of Science and Technology, Department of Space Sciences and Technologies, Antalya, Türkiye*
[2]*Akdeniz University, Faculty of Science, Department of Space Sciences and Technologies, Antalya, Türkiye*

Keywords
RADAR
SAR
PSI
SBAS
Displacement

Abstract

The phenomenon of shaking the environments through which the shakings that occur due to the fractures in the earth's crust spread as waves and pass through is called an earthquake. Shakings that occur during an earthquake cause displacement in their locations. Many remote sensing methods are applied to detect deformations. Turkey is located on the North Anatolian Fault Line, the West Anatolian Fault Line and the East Anatolian Fault Line, and these fault lines cause earthquakes from the past to the present. On February 6, 2023, 7.7 (Pazarcık) and 7.6 (Elbistan) earthquakes occurred in Kahramanmaraş. After these earthquakes, there were many aftershocks. In this study, in which aftershocks were examined with PSI and SBAS methods, the data obtained from the Sentinel-1 satellite was used.

1. Introduction

Earthquakes, which occur as a result of fractures in the earth's crust, are one of the natural disasters that cause loss of life and property and affect the economy. Earthquakes also cause deformation on the earth. Surface rupture, regional collapse, slope movements, volumetric compression, liquefaction, settlement and bedding failures, flow slides, lateral spreading and sand volcanoes are some of the deformations that may occur (Onur, 2007).

Since Turkey is located along the North Anatolian Fault Line, East Anatolian Fault Line and West Anatolian Fault zones, it has been under the risk of earthquakes since ages (Karslıoğlu, 2021). The seismic activities in Turkey and its surroundings have been technically monitored since the 1900s. T.R. The Disaster and Emergency Management Presidency (AFAD) of the Ministry of Interior and Boğaziçi University Kandilli Observatory and Earthquake Research Institute are the two main seismic network operators in Turkey (Kadirioğlu et al., 2018).

On February 6, 2023, 7.7 M earthquakes occurred at 4.17 in Pazarcık district of Kahramanmaraş province and 7.6 magnitude earthquakes occurred at 13.24 in Elbistan district. These earthquakes caused huge destruction in 11 provinces, including Kahramanmaraş, Gaziantep, Kilis, Adıyaman, Hatay, Malatya, Osmaniye, Şanlıurfa, Adana, Elazığ and Diyarbakır. More than 50 thousand people died in this earthquake where more than 37 thousand buildings were destroyed (AFAD, 2023).

AFAD recorded those 294 aftershocks greater than M4 occurred from 6 February 2023 to 13 April 2023 in and around Kahramanmaraş.

In this study, InSAR analysis has been used to calculate the surface displacement during the aftershocks period.

2. Method

2.1. Study area

The 7.7M earthquake that occurred at 04:17 in Kahramanmaraş's Pazarcık district on February 6, 2023, recorded by AFAD, lasted for approximately 1 minute. Then, the earthquake that occurred in the district of Elbistan at 13:24 lasted for about 45 seconds. Many aftershocks occurred after these earthquakes and are shown in Figure 1.

Between February 6, 2023 and April 13, 2023, 294 aftershocks with magnitudes greater than 4M occurred.

* **Corresponding Author**

*(dilarasolmaz02@gmail.com) ORCID ID 0000-0002-5555-1761
(nusretdemir@akdeniz.edu.tr) ORCID ID 0000-0002-8756-7127

Cite this study

Solmaz, D., & Demir, N. (2023). Displacement analysis of aftershocks occurred after 6 February 2023 Kahramanmaraş Earthquakes. Intercontinental Geoinformation Days (IGD), 6, 204-206, Baku, Azerbaijan

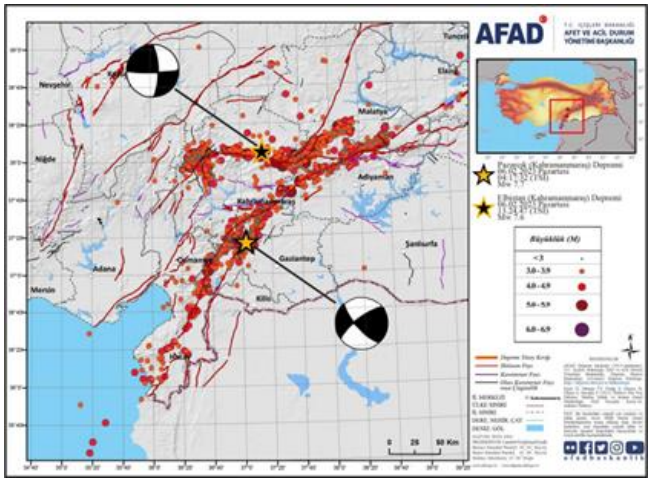

Figure 1. Kahramanmaraş earthquake location map (AFAD,2023)

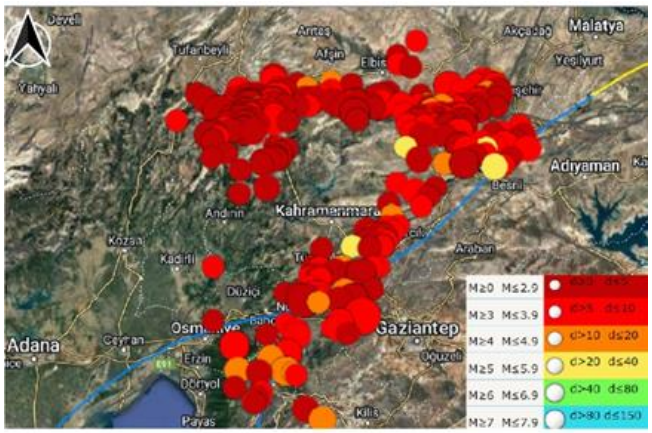

Figure 2. Kahramanmaraş aftershock's location map

2.2. SBAS

The SBAS method achieves displacement over time by stacking conventional D-InSAR interferograms (Berardino et al., 2002).

The SBAS approach has two distinct features. Multiple SAR images taken at different times in the same area are required to get started. the end is only the removal of targeted scattering.

2.3. PSI (Persistent Scatterer Interferometry)

Interferometry based on permanent scatters is an interferometry technique that studies surface movements with the help of fixed surfaces. This technique is based on the series of interferogram approach. Unlike InSAR, which detects deformations occurring on the surface with a single pair of interferograms, it makes use of multiple interferograms.

This technique was developed in 1999 by the Sar team at the Polytechnic University of Milan (POLIMI). This method, which is used to detect landslides or landslides, collapse and uplift areas, is also used to monitor urban activities such as pipelines, transportation lines, highways and railways, and to monitor seismic faults, volcanic areas and analyze their structures (Çomut, 2016).

For SBAS, we have used NASA ASF HYP3 data processing system for ascending and descending modes both.

3. Results

Between 6 February and 13 April 2023, SBAS and PSI analyzes were made using the data received from the Sentinel-1 satellite, and the displacements created by the aftershocks on the surface were obtained by two methods. The displacement results obtained and the fault line data were overlapped and the relationship between the deformation caused by the aftershocks and the ground was obtained.

4. Conclusion

According to the results of the SBAS analysis, the displacement values vary between -55.9 cm and 414,5 for the ascending satellite data, while the result of descending mode is between -26,0 cm and 34,6 cm.

Regarding PSI methodology, for the descending mode, the displacement has the values between -26,3 cm and 31 cm.

The results show that the displacement still occur with high values during the aftershocks which have been happening after the main EQs.

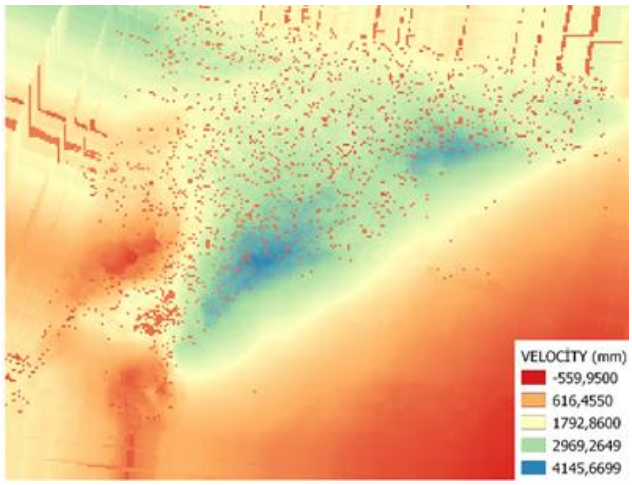

Figure 3. Displacement result from SBAS- ascending mode (mm)

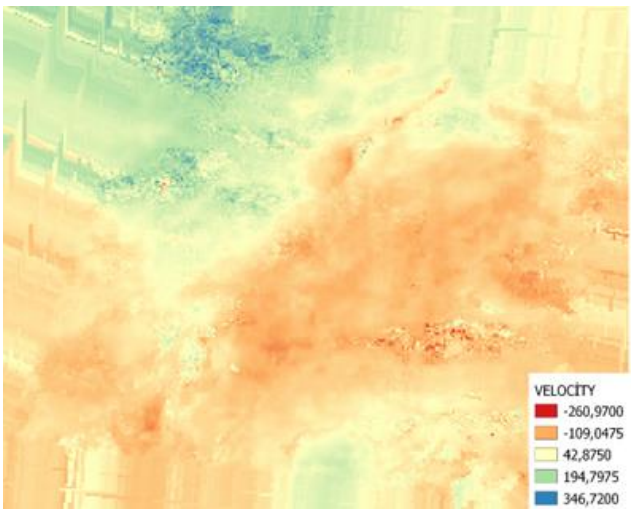

Figure 4. Displacement result from SBAS- descending mode (mm)

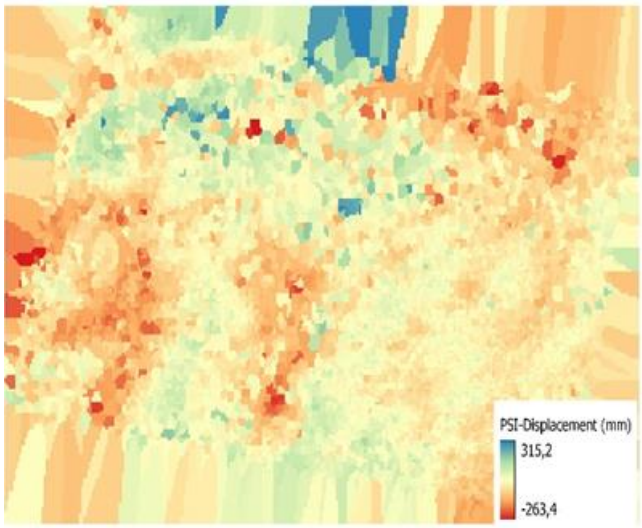

Figure 5. Displacement result from PSI - descending mode (mm)

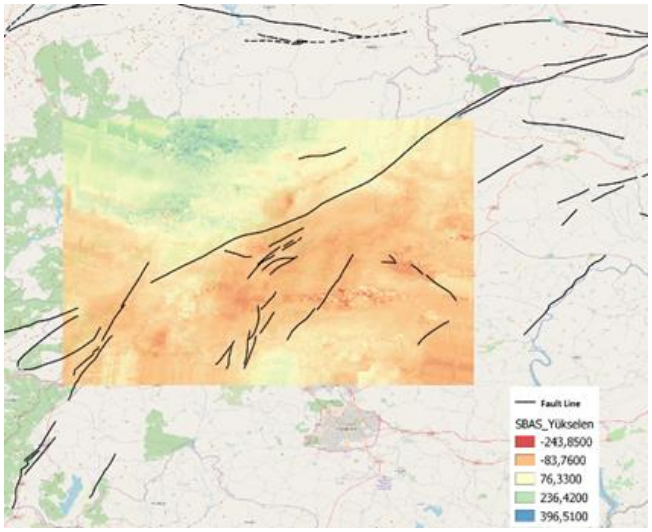

Figure 6. SBAS- descending - fault line, mm

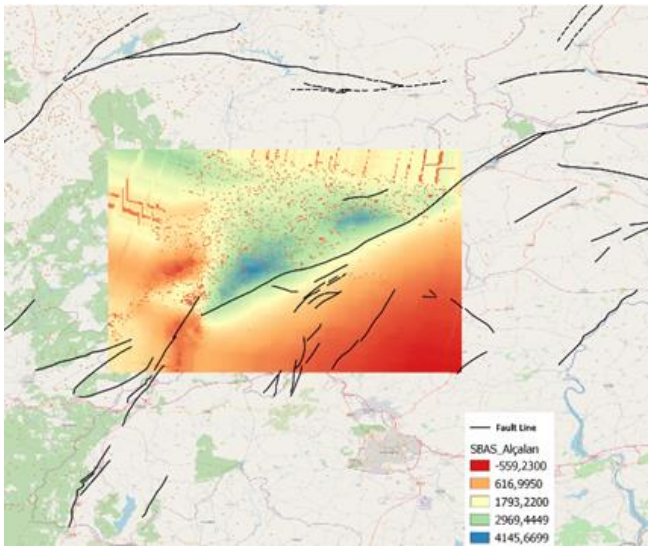

Figure 7. SBAS- ascending - fault line

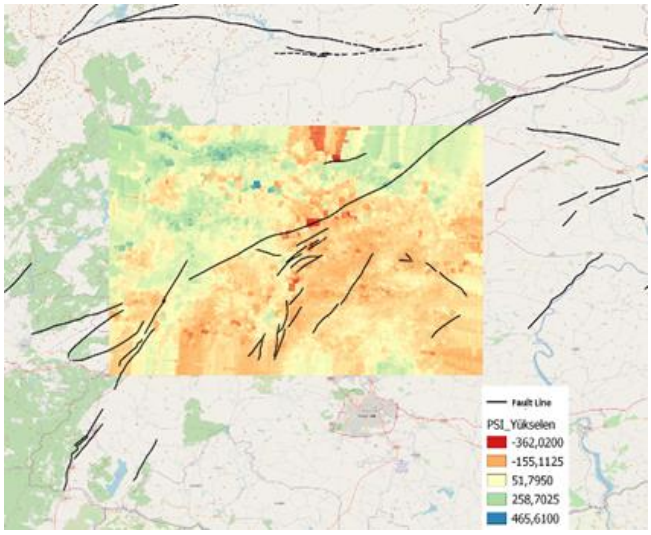

Figure 8. PSI- ascending - fault line

References

AFAD, (2023). 06 February 2023 Pazarcık-Elbistan (Kahramanmaraş) Mw: 7.7 – Mw: 7.6 Earthquakes Report.

Berardino, P., Fornaro, G., Lanari, R., & Sansosti, E. (2002). A New Algorithm for Surface Deformation Monitoring Based on Small Baseline Differential SAR İnterferograms. IEEE Transactions on Geoscience and Remote Sensing, 40, 2375-2383.

Çomut, F. C. (2016). Farklı yeryüzü özelliklerinde ileri InSAR teknikleri kullanılarak yüzey deformasyonlarının belirlenmesi. PhD Thesis, Konya

Gunce, H. B., & San, B. T. (2018). Measuring Earthquake-Induced Deformation in the South of Halabjah (Sarpol-e-Zahab) Using Sentinel-1 Data on November 12, 2017. In Proceedings, 2(7), 346; https://doi.org/10.3390/ecrs-2-05159.

Karslıoğlu, A., Alkayış, M. H., Kalkan, K., & Onur, M. İ. (2020). Sentinel-1 uydusu ile Konya Karapınar ilçesi bölgesel çökme analizi. Disaster Science and Engineering, 6 (2), 8-15

Malik, K., Kumar, D., Perissin, D., & Pradhan, B. (2022). Estimation of ground subsidence of New Delhi, India using PS-InSAR technique and Multi-sensor Radar data. Advances in Space Research, 69 (4), 1863-1882.

Mancini, F., Grassi, F., & Cenni, N. (2021). A Workflow Based on SNAP–StaMPS Open-Source Tools and GNSS Data for PSI-Based Ground Deformation Using Dual-Orbit Sentinel-1 Data: Accuracy Assessment with Error Propagation Analysis. Remote Sensing, 13(4), 753.

NASA ASF HYP3, https://github.com/ASFHyP3/hyp3-nasa-disasters

Onur, M. İ. (2007). Dinamik etkiler altında zemin deformasyonunun incelenmesi. Master Thesis, Anadolu University, İnstitute of Science Eskişehir.

Thomas, A. (2021). Mapping of surface deformation associated with the 5.2 magnitude Stilfontein earthquake of 3 April 2017 using radar interferometry. The Egyptian Journal of Remote Sensing and Space Sciences, 24, 85–108.

6th Intercontinental Geoinformation Days

igd.mersin.edu.tr

NMF-based ensemble clustering for GNSS velocity field: tectonic insights

Seda Özarpacı*[1], Batuhan Kılıç[1]

[1]*Yildiz Technical University, Faculty of Civil Engineering, Department of Geomatic Engineering, Istanbul, Türkiye*

Keywords
Block modeling
GNSS horizontal velocity field
Clustering
NMF
Ensemble clustering

Abstract

Block modeling is a frequently employed technique to yield the block motions such as block rotations and internal strains as well as to estimate fault slip rates via GNSS velocity data. The accuracy of the modeling outcomes heavily relies on the precise determination of the block boundaries. Typically, surface traces of mapped faults, seismological data, and/or GNSS velocity fields are utilized for this purpose. Nonetheless, the identification of suitable and accurate block boundaries for the velocity field is subject to interpretation and subjectivity. One method that can be used to determine block boundaries is the clustering method. Clustering analysis assigns data to similar groups based on similarities and differences in the data subject to clustering. Since the 2000s, this method has been used in the clustering of GNSS velocities and helps to determine block boundaries before block modeling. In this study, we utilized the Non-negative Matrix Factorization (NMF) method to cluster the current GNSS horizontal velocity field of Türkiye, and we compared the results with the literature. First, we clustered velocities from k = 2 to 9 using five distinct single clustering methods to determine the block boundaries. Then, we used the optimum number k = 5 to cluster the data using NMF-based ensemble clustering.

1. Introduction

The tectonics of Türkiye have a complex structure due to the collision of the Eurasian and Arabian plates, the escape resulting from this collision, and the subduction zones formed by the Anatolian and African plates along the Cyprus and Hellenic arcs. The North Anatolian Fault (NAF) and the East Anatolian Fault (EAF), which were formed as a result of these processes, are the most important strike-slip faults in the region (McClusky et al. 2000; Reilinger et al. 2006).

Although many models are used to understand and interpret these structures, block modeling produces the closest results to surface deformations. The accuracy of the modeling results depends on how well the block boundaries are defined (Thatcher 2009). Although many researchers have used mapped fault surface traces, seismology data, and/or GNSS velocity fields to determine block boundaries, the determination of block boundaries is subjective (Reilinger et al. 2006).

One method that can be used to determine block boundaries is the clustering method. Clustering analysis assigns data to similar groups based on similarities and differences in the data subject to clustering, without any prior information. This method has been used by different researches (Savage and Simpson 2013; Savage and Wells 2015; Özarpacı et al. 2023) in the clustering of GNSS velocities and helps to determine block boundaries before block modeling.

In previous studies, various clustering methods have been used to determine block boundaries from GNSS velocities, and their performances have been analyzed. However, it is also observed that different algorithms produce different results. In this study, an ensemble clustering algorithm is tested to eliminate the subjectivity arising from clustering methods. For this purpose, using the last velocity field obtained from updated, continuous, and campaign GNSS data for Türkiye (Kurt et al. 2023), first, individual clustering methods were used, and then the success of the Non-Negative Matrix Factorization (NMF) algorithm was tested based on the results obtained from these methods.

2. Method

In the clustering analysis, the horizontal velocities of 836 stations were evaluated by means of the current

* **Corresponding Author**

*(ozarpaci@yildiz.edu.tr) ORCID ID 0000-0002-1900-3725
(batuhank@yildiz.edu.tr) ORCID ID 0000-0002-0529-8569

Cite this study

Ozarpaci, S., & Kilic, B. (2023). NMF-based ensemble clustering for GNSS velocity field: tectonic insights. Intercontinental Geoinformation Days (IGD), 6, 207-210, Baku, Azerbaijan

GNSS velocity field (Kurt et al. 2023). Diverse clustering techniques were utilized to generate clustering models (k = 2 to 9) from multiple community members to form the NMF ensemble clustering approach. For each k value, the outputs of the members were subsequently combined using the NMF ensemble clustering method to derive the ultimate clustering results, and the conformity of the final solutions with the tectonic structure of the region was evaluated (Figure 1).

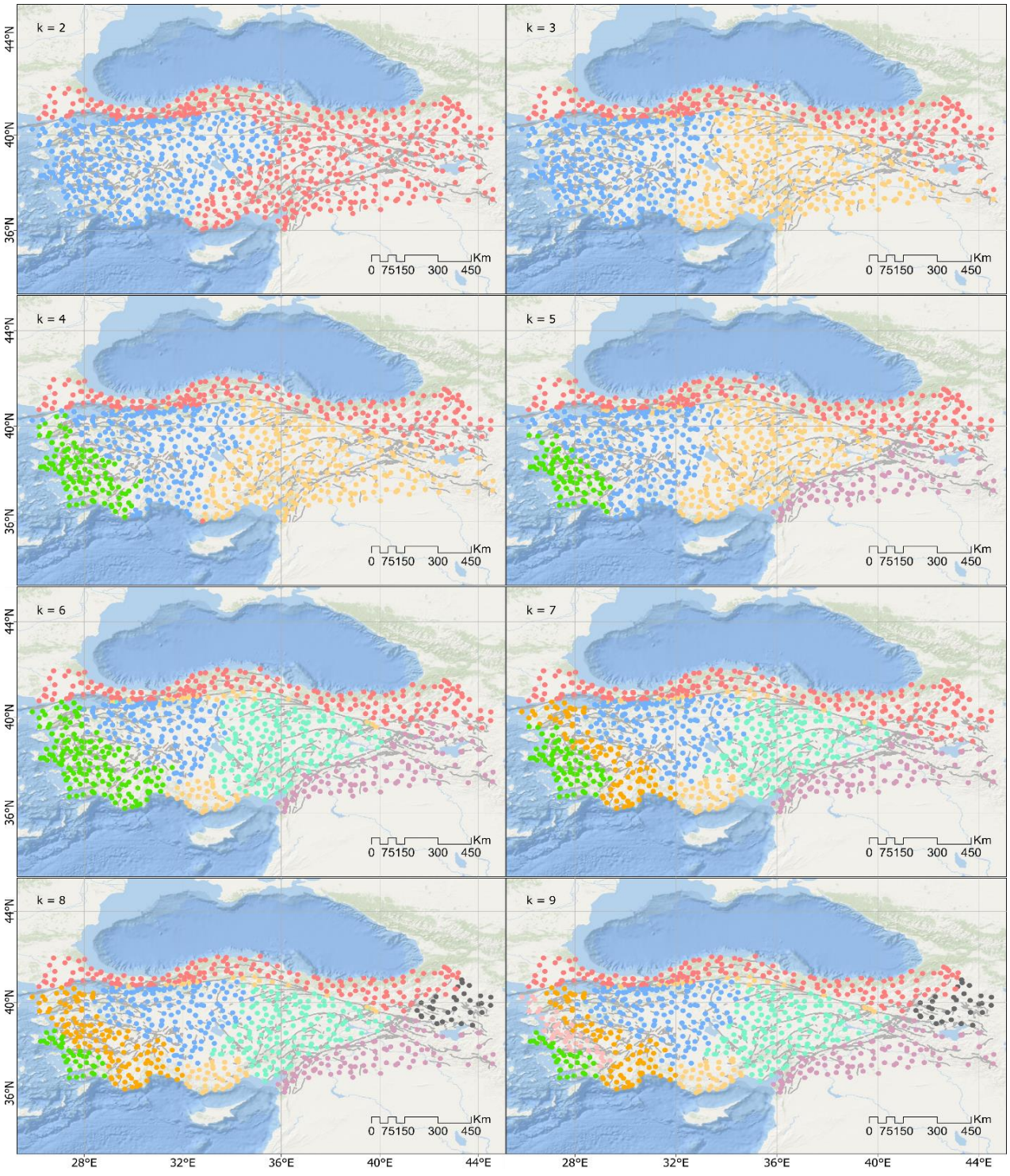

Figure 1. Ensemble clustering results with NMF (from k = 2 to k = 9). The gray thin lines indicate active faults (Emre et al. 2013)

2.1. Single clustering techniques

Each clustering technique partitions the dataset based on certain criteria and, as a result, generates different results on the same dataset from a specific perspective. Hence, in order to obtain more profound insights into the underlying patterns in the data, it is crucial to maintain a diverse range of member results (Golalipour et al. 2021; Kılıç and Özarpacı 2022). This

study utilized various clustering algorithms, including k-means, Balanced Iterative Reducing and Clustering using Hierarchies (BIRCH), Hierarchical Agglomerative Clustering (HAC), mini-batch k-means, and spectral clustering techniques, to generate diversity in the ensemble clustering member results. Among these methods, k-means and mini-batch k-means are partitioning-based, BIRCH and HAC are hierarchy-based, and spectral clustering is graph-based.

2.2. NMF ensemble clustering technique

NMF is a clustering ensemble method that contains a non-negative matrix factorization process. This approach was initially introduced by Paatero and Tapper (1994). The NMF method is characterized by factorizing a non-negative data matrix V into two matrix factors, W and H, where V ≈ WH and both W and H are constrained to be non-negative. The matrix W represents the dimensionally reduced data matrix, whereas the matrix H corresponds to the associated coefficient matrix, i.e., the weights associated with W. Despite the emergence of various extensions that incorporate the clustering feature, the initial model formulation of NMF did not explicitly include a clustering objective, as it was primarily introduced as a dimensionality reduction algorithm (Kılıç and Özarpacı 2022).

3. Results and Discussion

For each value of k, the outcomes of the NMF ensemble clustering method produced over the results obtained from single clustering techniques are shown in Figure 1. As one can see that the NAF and EAF exhibit distinct separation of clusters after k = 5. Also, after k = 4 clusters, the Aegean coast obviously creates a block with a velocity gradient. In our clustering results from k = 2 to 9, we see that Anatolia is being divided by different clusters. However, Anatolia's geological structure is widely believed to be tectonically rigid and characterized by uniform motion (McClusky et al. 2000; Reilinger et al. 2006). As pointed out by Savage and Wells (2015), "cluster boundaries that remain relatively stable as k is increased are tentatively identified as block boundaries" in geographical space. Therefore, our results demonstrate that Anatolia is a rigid block because the pattern of clusters does not remain the same as it did along NAF or EAF block boundaries (Özarpacı et al. 2023).

We take the optimal number of clusters for Türkiye as five in terms of the literature (Özdemir and Karslıoğlu 2019; Kılıç and Özarpacı, 2022; Özarpacı et al. 2023), as it is the minimum number required to adequately explain the data without over-parametrization. Furthermore, we see some stations around the 1999 Izmit and Duzce earthquakes behave differently. The underlying reason for this phenomenon can be interpreted as the block boundary that exists along the NAF being more influential as a distinctive characteristic, relative to the clustering approach employed (Savage and Simpson 2013).

Figure 2 illustrates the outcomes of the NMF ensemble clustering approach with 5 clusters applied to the GNSS velocity data of Türkiye, along with the block boundaries derived from Reilinger et al. (2006) and NMF-based analyses.

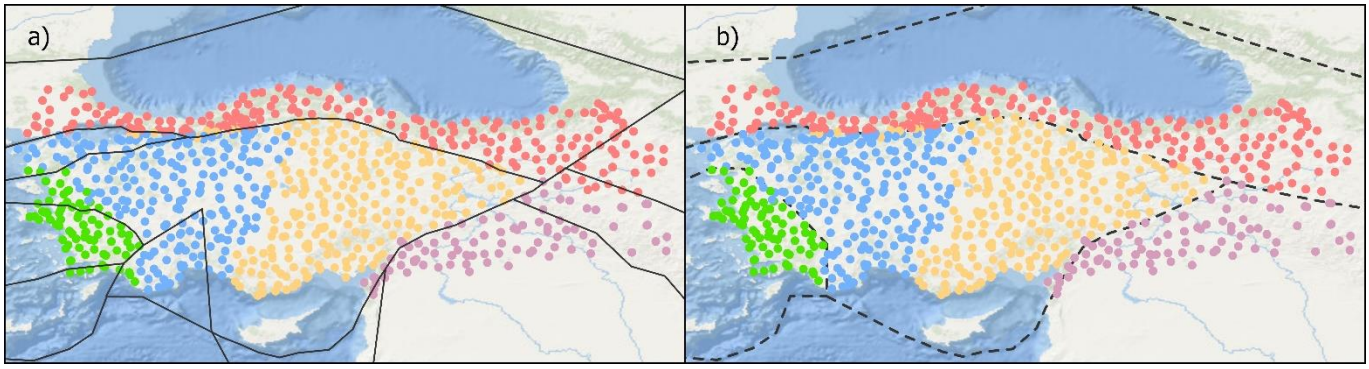

Figure 2. Horizontal velocity clustering results for k = 5 clusters with NMF: (a) black solid lines indicate block boundaries from Reilinger et al. (2006); (b) black dashed lines indicate the revised block boundaries obtained by the NMF ensemble clustering technique

Observations indicate that NAF is partitioned into two branches, namely, the southern and the northern branches, in the Marmara region. The velocity changes along the northern branch, which bears the majority of the velocity of the GNSS stations along NAF, manifest in the clustering results, and the resultant clusters are observed to be disjoined along the said branch (as depicted in Figure 2). Reilinger et al. (2006) established a block boundary along the southern branch based on their study. However, since the velocity gradients along this branch were not significant, no boundary was determined in the given study (as illustrated in Figure 2b). The present study reveals differences in the boundaries of the Aegean block compared to Reilinger et al.'s (2006) investigation. Specifically, the boundaries of the Aegean block appear to have undergone changes, and no significant velocity change was observed in the region along the triangular-shaped block boundary to the west of the Mediterranean Region (Figure 2b). Finally, upon analyzing the block boundaries of the eastern part of Türkiye in Figure 2b, it is observed that the velocity gradient in this area results in two distinct blocks, which are distinct from the findings of Reilinger et al. (2006).

4. Conclusion

In this study, the effectiveness of non-negative matrix factorization (NMF), an ensemble clustering method, in clustering the horizontal velocities obtained from the latest and most comprehensive GNSS velocity field of Türkiye and its compatibility with the tectonic structure of the region were investigated. GNSS velocities were subjected to clustering analysis ranging from 2 to 9 using five distinct single clustering methods to identify the most appropriate number of clusters for the GNSS horizontal velocity field. The outcomes yielded from each of the clustering methods were then incorporated into the NMF approach to assess the consistency with the study area. Beyond five clusters, it can be observed that the Eurasian and Arabian plates maintain their distinguishability, the Southern Aegean region exhibits consistency, and the Anatolian plate becomes increasingly partitioned into additional clusters. Furthermore, it is important to note that no block boundary exists along the southern branch of the NAF in the Marmara Region, and the velocity gradient in the eastern part appears as a single branch rather than being separated into two distinct branches.

References

Emre, Ö., Duman, T. Y., Özalp, S., Elmacı, H., Olgun, S., & Şaroglu F. (2013). Açıklamalı Türkiye Diri Fay Haritası. Ölçek 1:1.250.000; Maden Tetkik ve Arama Genel Müdürlüğü, Özel Yayın Serisi-30: Ankara, Türkiye.

Golalipour, K., Akbari, E., Hamidi, S. S., Lee, M., & Enayatifar, R. (2021). From clustering to clustering ensemble selection: A review. Engineering Applications of Artificial Intelligence, 104, 104388.

Kılıç, B., & Özarpacı, S. (2022). Ensemble Clustering in GPS Velocities: A Case Study of Turkey. Applied Sciences, 12(24), 12636.

Kurt, A. İ., Özbakir, A. D., Cingöz, A., Ergintav, S., Doğan, U., & Özarpacı, S. (2023). Contemporary velocity field for Turkey inferred from combination of a dense network of long term GNSS observations. Turkish Journal of Earth Sciences, 32(3), 275-293.

Mcclusky, S., Balassanian, S., Barka, A., Demir, C., Ergintav, S., Georgiev, I., ... & Veis, G. (2000). Global Positioning System constraints on plate kinematics and dynamics in the eastern Mediterranean and Caucasus. Journal of Geophysical Research: Solid Earth, 105(B3), 5695-5719.

Özarpacı, S., Kılıç, B., Bayrak, O. C., Özdemir, A., Yılmaz, Y., & Floyd, M. (2023). Comparative analysis of the optimum cluster number determination algorithms in clustering GPS velocities. Geophysical Journal International, 232(1), 70-80.

Özdemir, S., & Karslıoğlu, M. O. (2019). Soft clustering of GPS velocities from a homogeneous permanent network in Turkey. Journal of Geodesy, 93(8), 1171-1195.

Paatero, P., & Tapper, U. (1994). Positive matrix factorization: A non-negative factor model with optimal utilization of error estimates of data values. Environmetrics, 5(2), 111-126.

Reilinger, R., McClusky, S., Vernant, P., Lawrence, S., Ergintav, S., Cakmak, R., ... & Karam, G. (2006). GPS constraints on continental deformation in the Africa-Arabia-Eurasia continental collision zone and implications for the dynamics of plate interactions. Journal of Geophysical Research: Solid Earth, 111(B5).

Savage, J. C., & Simpson, R. W. (2013). Clustering of GPS velocities in the Mojave Block, southeastern California. Journal of Geophysical Research: Solid Earth, 118(4), 1747-1759.

Savage, J. C., & Wells, R. E. (2015). Identifying block structure in the Pacific Northwest, USA. Journal of Geophysical Research: Solid Earth, 120(11), 7905-7916.

Thatcher, W. (2009). How the continents deform: The evidence from tectonic geodesy. Annual Review of Earth and Planetary Sciences, 37, 237-262.

6th Intercontinental Geoinformation Days

igd.mersin.edu.tr

Lake level forecasting with radial based neural networks

Mehmet Fehmi Yıldız [1], Vahdettin Demir*[1]

[1]*KTO Karatay University, Civil Engineering Department, Konya, Türkiye*

Keywords
Michigan-Huron
Radial Based Neural Networks
Lake levels
Forecast

Abstract

Many water resources across the world have increasing and decreasing water levels. The change of water level in lakes, which is one of the water resources, is associated with climate change and the effects of climate change can be seen at lake levels the fastest. Lake Michigan-Huron studied in this study is an 8 km wide body of water formed by the confluence of Lake Michigan and Huron. Lake Michigan-Huron is the largest freshwater lake in the world. The aim of this study is to estimate the water level of Lake Michigan-Huron in the USA. For this purpose, radial-based artificial neural networks were used. In the forecast model, lake levels in the past months and periodicity number were used as input data. The lake water level (m) data used has a record length of 104 years (1918-2021). All data is divided into 4 parts (M1, M2, M3 and M4). 75% of all data was used for the training phase (M1+M2+M3) and 25% for the testing phase (M4). The test sections were changed from M1 to M4 so that the training and testing rates remained constant. Mean absolute error (MAE), root-mean-square error (RMSE) and coefficient of determination (R^2) were used as evaluation criteria. As a result, it is seen that the models make very good predictions in all data sets and in the training-test phases. However, according to the test results, the data set that gives the most successful results is the M1 package and the input set using data that has been lag time for 7 months.

1. Introduction

Humans have been interested in water since its inception, trying to study water movements, recognize features, identify detection hazards, and make the most of the water outside. The branch of science that manages the distribution and properties of water on Earth is called hydrology. The science of hydrology, which provides its relationship with the internal environment and efforts to control its environment, began to gain more importance. As a result of the hydrological operation, the basic structures that maintain their water consumption and attitudes can be identified (Koca, 2014).

Due to the changes in water bodies, long research has been started. Water is an indispensable resource for human life. Therefore, research on the quality and quantity of existing water resources has intensified, and the storage facility of closed water basins such as lakes has gained importance (Teltik et al., 2008).

The water level of many lakes in the world is observed to rise and fall due to various reasons. In the studies, it is thought that the reasons for the change in the lake level are meteorological and hydrological features (evaporation, precipitation, flow, etc.), tectonic movements, changes in the ozone layer and climate change (Teltik et al. 2008). In addition, the use of water resources to provide more water than normal in order to meet the water needs of agricultural activities and cities also causes the capacity of water reserves such as lakes to decrease (Albek et al., 2017).

Some studies on the use of RBANN in the literature, In the study of Desmukh and Tanty (2015), a comprehensive review was made on the artificial neural network (ANN) used in the field of hydrology-related problems. They stated that it can be well exemplified by artificial intelligence with precipitation-flow modeling, stream flow modeling, water quality modeling and its applications in groundwater (Desmukh and Tanty 2015).

In 2018, Arslan et al. A study was carried out to examine the seasonal variation of Adana Seyhan Dam Lake area. In their study, they achieved highly accurate results in the classification of water structures with the artificial neural network method (Arslan et al. 2018).

In a study conducted by Dikbaş and Fırat in 2005, a comparison of POM and ANN models was made in three-dimensional hydrodynamic modeling in lakes. When the

* **Corresponding Author**

(*mehmetfehmi.yildiz@ogrenci.karatay.edu.tr*) ORCID ID 0000-0001-6550-8401
*(*vahdettin.demir@karatay.edu.tr*) ORCID ID 0000-0002-6590-5658

Cite this study

Yıldız, M. F., & Demir, V. (2023). Lake level forecasting with radial based neural networks. Intercontinental Geoinformation Days (IGD), 6, 211-215, Baku, Azerbaijan

results obtained with both models were compared, it was seen that the methods had advantages and disadvantages compared to each other. ANN requires previously obtained observation results and calculations, while POM does not. In addition, ANN achieves results in a much shorter time than POM. As a result, it can be recommended to use the artificial neural network method in certain sections and studies that require many detailed calculations (Dikbaş and Fırat, 2005).

A study was conducted by Aksoy et al. in 2020 on the estimation of the water level in Yalova Gökçe Dam using ANN. According to the data they obtained as a result of the analyzes, the dam water level for 2019 was 73.77, while the actual water level of the dam was measured as 72.13 meters. As a result, it is thought that the use of ANN algorithms will be beneficial in estimating the water level of Gökçe Dam (Aksoy et al. 2020).

In 2012, Okkan and Dalkılıç conducted a study on the modeling of monthly flows of the Kemer Dam using radial-based neural networks. When they evaluated the results of their study in terms of minimum and maximum currents, the results of the RBANN model were successful for most months. In addition, it is thought that the problems encountered in other artificial neural network models can be overcome with RBANN (Dalkılıç and Okkan, 2012).

The purpose of this study was to analyze the water level of Lake Michigan-Huron in the United States and to determine changes in the lake's water level. For this purpose, monthly lake water levels in Lake Michigan-Huron between 1918-2021 were estimated with radial-based artificial neural networks and the predictions in various data sets (the training set is 3 parts and the test set is one part, and the test set is constantly changing.) were compared with the observed data.

2. Material and Method

2.1. Material

In the study, monthly water levels year from January 1918 to December 2021 were used. Data obtained from "https://www.lre.usace.army.mil/Missions/Great-Lakes-Information/Great-Lakes-Information.aspx#ICG_ETH_22302". Statistical information of the data used is given in Table 1.

The data are observed as monthly average (m) and there are no gaps in the data. In addition, station information in Excel format is available for all researchers free of charge.

Table 1. Statistical information for water levels (m)

Michigan-Huron	
Average	176.44
Standard error	0.0116
Median	176.45
Standard Deviation	0.410
Sample Variance	0.168
Kurtosis	-0.787
Skewness	0.101
Smallest	175.57
Largest	177.5
Number of Data	1248

2.2. Study Area

Lake Michigan is the third largest of the five great lakes in the northern United States and is connected to Lake Huron by the Strait of Mackinac (Demir, 2022). It is located 176 meters above sea level and its deepest point is 281 meters. Lake Huron is also located in North America and is the 4th largest lake in the world.

Lake Huron is connected to Lake Michigan by the Straits of Mackinac and to Lake Superior by a series of straits. Huron and Michigan are hydrologically a single lake because the flow of water through the straits keeps water levels in overall balance. Although the flow is generally eastward, water moves in both directions depending on local conditions. Combined, Lake Michigan-Huron is the world's largest freshwater lake by area (Michigan-Huron, 2023). The study area is given in Figure 1.

Figure 1. Lake Michigan-Huron (Demir and Yaseen, 2022)

The most important factor in choosing this study area is that when Michigan-Huron Lake is considered as a whole, it is the largest freshwater lake in the world in terms of surface area and the data are continuous.

2.3. Method

Artificial neural networks are a method based on the biological nervous system in humans. Artificial neural networks consist of elements called neurons, which are connected in parallel and have a non-linear structure. It is used in object recognition, system modeling, signal processing and solving complex engineering problems. Artificial neural networks realize the learning process with examples. In other words, it can be defined as the machine-transferred version of the human learning mechanism (D'Addona, 2014).

2.4. Radial based neural network

The radial-based neural network model can be considered as a combination of a data modeling technique for a high-dimensional space and a schema such as an ANN network. In the RBANN model, three layers are defined as input layer, hidden layer and output layer, but unlike the classical ANN structure, a nonlinear clustering analysis and radial based activation functions

are used in the transition from the input layer to the hidden layer in the radial-based neural network model (Dalkılıç and Okkan, 2012).

The mathematical representation of radial basis neural networks is as follows.

$$\emptyset_j = exp\left[-\|x - c_j\|/\sigma_j^2\right] \quad (1)$$

Here is x the input vector, c_j j. It is the center of the Gaussian function and σ_j is the standard deviation. Equation $\|x - c_j\|$ indicates the Euclidean distance between vectors x and c_j. j. the activation level of the intermediate node is equal to $\emptyset_j$.

Interlayer outputs;

$$y_{kj} = \prod \emptyset_j(x, c, \sigma) \quad (2)$$

k. the output of the node is given by Equation 2.

$$o_k = \sum_{j=1}^{J} w_{kj}\, y_{kj} \quad (3)$$

Here w_{kj} k. With the exit node j. is the weight between the middleware node (Kılıç et al., 2012). The basic structure of RBANN is given in Figure 2.

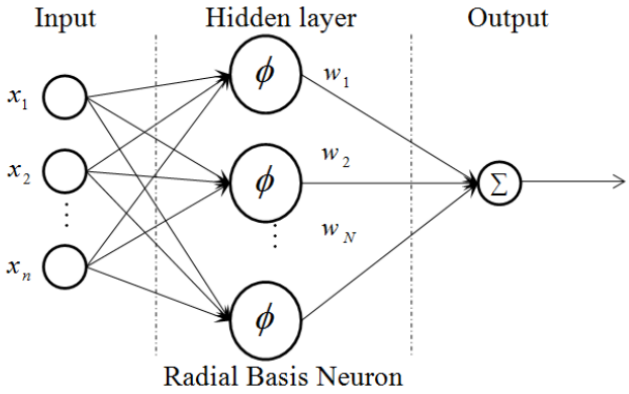

Figure 2. Radial-based neural network structure (Chen et al. 2019)

In Figure 2, the RBANN structure basically consists of three parts and the output data is obtained by multiplying the input data with the weights after reaching the hidden layer.

3. Results

In the modeling phase, the data were first shifted by lag time, and then the estimation results were obtained by separating them into training and test sets. The estimated data with the observed data were evaluated by considering the comparison criteria. Root Mean Square Error (RMSE), Mean Absolute Error (MAE) and coefficient of determination (R^2) were used as comparison criteria. The formulas of the comparison criteria are given in Equation 4-6.

$$RMSE = \sqrt{\frac{1}{N}\sum_{i=1}^{N}(Y_p - Y_o)^2} \quad (4)$$

$$MAE = \frac{1}{N}\sum_{i=1}^{N}|Y_p - Y_o| \quad (5)$$

$$R^2 = \left(\frac{N*(\sum Y_o*Y_p)-(\sum Y_o)*(\sum Y_p)}{\sqrt{(N*\sum Y_o^2)-(\sum Y_o)^2*(N*\sum Y_p^2)-(\sum Y_p)^2}}\right)^2 \quad (6)$$

N is the number of data used in the equations, Yp represents the estimated value in the model, Yo represents the observed value. Since Equation (4-5) has error results for our comparison criteria, the unit of error results in the model is m^3/s.

High error results show that the model is far from real data, that is, it gives unsuccessful results. If the error values are close to zero, it indicates that the results of the model are close to the real data.

The coefficient of determination R^2 can take a value between 0 and 1. It is interpreted that the closer the value is to 1, the higher the model's fitness and accuracy.

In the study, data sets with 12 inputs were created. These; 1 month lag (T-1), T-2, T-3, T-4 and T-5 with 1 year lag (Y-1), Y-2, Y-3, Y-4 and Y-5.

Month numbers representing the periodicity of the data were used recursively as the 12th input set. 75% of all data were used in the training phase and 25% in the testing phase. At this stage, four different combinations were tried, namely training (75%) and testing (25%). These are M1 (the part with the oldest data), M2, M3 and M4 (the part with the most recent data). Model results are given in Table 2 according to the training and testing phases.

In the table, the most successful result in the test phase was obtained in 7 inputs. The scatter plot of the best method is given in **Figure 3**.

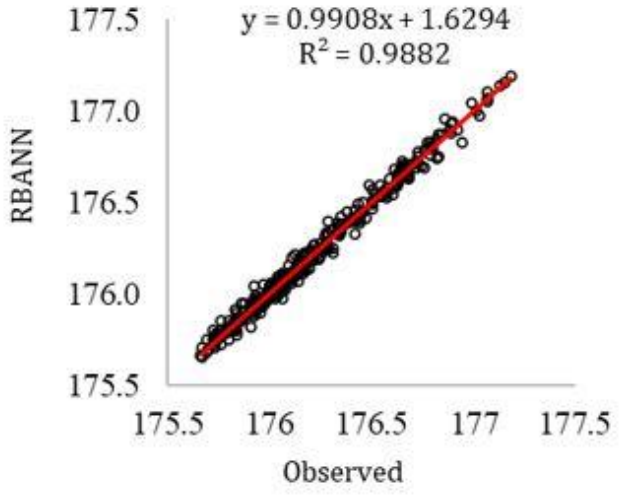

Figure 3. Scatter plot

When the values in the graph are examined, it is seen that the results obtained using the radial-based artificial neural network model are compatible with the water level data of the observed lake, and the graph equation approaches the y=x line, and the R^2 value is 0.9882. The variation of these estimates in the time series is shown in Figure 4.

Table 2. RBANN training and test results (Model: RBANN)

Part	Input	Training			Test		
		RMSE	MAE	R^2	RMSE	MAE	R^2
M1	1	0.069	0.055	0.97	0.066	0.054	0.964
	2	0.046	0.037	0.986	0.044	0.035	0.984
	3	0.044	0.034	0.987	0.042	0.033	0.986
	4	0.043	0.033	0.988	0.041	0.031	0.987
	5	0.042	0.033	0.989	0.039	0.03	0.987
	6	0.042	0.032	0.989	0.039	0.03	0.988
	7	0.041	0.032	0.989	0.038	0.03	0.988
	8	0.041	0.032	0.989	0.038	0.03	0.988
	9	0.042	0.032	0.989	0.039	0.031	0.987
	10	0.042	0.033	0.988	0.04	0.031	0.987
	11	0.043	0.033	0.988	0.04	0.031	0.987
	12	0.039	0.03	0.99	0.038	0.03	0.988
M2	1	0.067	0.054	0.973	0.071	0.057	0.962
	2	0.045	0.036	0.988	0.048	0.037	0.983
	3	0.043	0.034	0.989	0.045	0.035	0.985
	4	0.042	0.033	0.989	0.044	0.034	0.986
	5	0.042	0.033	0.989	0.043	0.033	0.986
	6	0.041	0.031	0.99	0.042	0.032	0.987
	7	0.041	0.032	0.99	0.041	0.031	0.988
	8	0.04	0.032	0.99	0.041	0.031	0.988
	9	0.041	0.032	0.99	0.042	0.031	0.987
	10	0.042	0.033	0.989	0.043	0.032	0.987
	11	0.042	0.033	0.989	0.042	0.032	0.987
	12	0.039	0.031	0.991	0.04	0.031	0.988
M3	1	0.069	0.055	0.964	0.066	0.054	0.945
	2	0.045	0.036	0.985	0.049	0.039	0.973
	3	0.043	0.034	0.986	0.046	0.036	0.975
	4	0.042	0.032	0.987	0.045	0.035	0.976
	5	0.041	0.032	0.987	0.044	0.034	0.977
	6	0.04	0.031	0.988	0.042	0.033	0.978
	7	0.04	0.031	0.988	0.043	0.033	0.978
	8	0.04	0.031	0.988	0.044	0.034	0.977
	9	0.04	0.031	0.988	0.044	0.035	0.977
	10	0.041	0.032	0.987	0.044	0.035	0.976
	11	0.042	0.032	0.987	0.047	0.037	0.975
	12	0.04	0.031	0.988	0.046	0.036	0.976
M4	1	0.068	0.055	0.971	0.068	0.055	0.963
	2	0.048	0.038	0.985	0.046	0.037	0.983
	3	0.044	0.034	0.988	0.044	0.035	0.984
	4	0.042	0.033	0.989	0.042	0.033	0.986
	5	0.041	0.032	0.989	0.041	0.033	0.986
	6	0.04	0.031	0.99	0.042	0.033	0.986
	7	0.04	0.031	0.99	0.041	0.032	0.987
	8	0.04	0.031	0.99	0.042	0.033	0.986
	9	0.041	0.032	0.99	0.042	0.033	0.986
	10	0.041	0.032	0.989	0.042	0.033	0.986
	11	0.042	0.032	0.989	0.043	0.034	0.985
	12	0.039	0.03	0.99	0.04	0.032	0.987

4. Discussion

In a study conducted by Demir in 2021, the water level changes of Lake Michigan were examined using MARS, M5-tree and LSSVR methods. These three models have gone through training and testing phases. RMSE, MAE and R^2 were used as evaluation criteria. In the study, 80% of the data was used in the training phase and the remaining 20% in the testing phase. The data period of the study is between 1918 and 2020. Data deferred up to 8 months were used as the input set. When the results were examined, it was seen that better results were obtained with the MARS method (RMSE=0.0359, MAE=0.0288, R^2=0.9922). In addition, it was stated that the periodicity effect increased the model performance. (Demir, 2022).

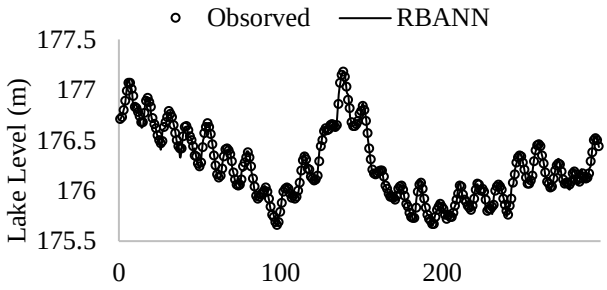

Figure 4. Timeline graph of test data

Figure 4 shows the estimates of test data for the M1 package. RBANN appears to capture the highs and lows of the test data well.

A study was conducted by Demir and Yaseen on estimating the water level in 5 large lakes in the USA by 2021. In this study, they aimed to find a reliable model for lake level estimation. In their study, they used three different models: MARS, M5-tree and LSSVR. In the study, the data set was divided into 4 parts and 75% of the data was used in the training and the remaining 25% in the testing phase. Data deferred up to 3 months were used as the input set. When the results of these three models are compared with MAE, RMSE and R^2 (RMSE=0.344, MAE=0.287, R^2=0.426), it is seen that the LSSVR model gives better results (Demir and Yaseen 2022).

In a study conducted by Çubukçu et al. in 2021 on the estimation of the monthly average water levels of Lake Michigan, data between 1981 and 2021 were used and studied with three different artificial neural network models. These models are multilayer ANN, radial basis ANN and generalized ANN models. RMSE, MAE and R2 were used as comparison criteria. In general, it was seen that all models gave good results, but according to the test results, the best training algorithm was seen as multilayer ANN, giving the best results in 12 inputs. (MAE= 0.0342, RMSE= 0.0435, R^2= 0.9906). The best method was found to be MANN, RBANN and GRNN, respectively (Çubukçu et al. 2021).

In our study, unlike the above study, when we analyze the data between 1918-2021 with the RBANN model, we see that it gives the best results in 7 entries (MAE=0.03, RMSE=0.038, R^2=0.988).

5. Conclusion

Using the monthly average lake water level data of Lake Michigan-Huron between 1918-2021, which revealed this result, estimates were made with the

radial-based artificial neural network model and the results were compared.

In the study, 75% of all data were trained and 25% were tested. At this stage, four different combinations were tried, namely training (75%) and testing (25%). Evaluation criteria include absolute mean error (MAE), root mean square error (RMSE), and determination value (R^2).

It is seen that the results obtained make very good predictions in all inputs sets and training-test tests. However, according to his tests, the most successful result was the M1 data set package and the 7 inputs.

When compared with the results of previous studies, the RBANN model has acceptable accuracy.

As a result, the use of RBANN to estimate the Michigan-Huron lakes water level would be beneficial.

References

Aksoy, A. S., Aksoy, Y. R., Keskin, M. E., & Yılmazkoç, B., (2017). Göl Seviye Tahmini: Eğirdir Gölü: Mühendislik Bilimleri ve Tasarım Dergisi, 5(3), 601-608.

Albek, E. A., Albek, M. & Göncü, S. (2017). Trend Analysis of Burdur, Eğirdir, Sapanca and Tuz Lake Water Levels Using Nonparametric Statistical Methods. Afyon Kocatepe University Journal of Sciences and Engineering, 17(2), 555–570.

Arslan, N., Çiçekli, S., Dönmez, C., Şekertekin, A., (2018). Adana Seyhan Baraj Gölü Alanının Mevsimsel Değişiminin Yapay Sinir Ağları ile Analizi. Uzaktan Algılama ve Coğrafi Bilgi Sistemi Sempozumu, Ankara.

Chen, T., Cheng, P., He, H., Yan, Y. (2019). Tree Height Estimation of Forest Plantation in Mountainous Terrain from Bare-Earth Points Using a DoG-Coupled Radial Basis Function Neural Network, 11,1271.

Çubukçu, E. A., Yılmaz, C. B., Demir, V., & Sevimli, M. F. (2021). Forecasting of monthly average lake levels of Lake Michigan with artificial neural networks. *Advanced Engineering Days (AED)*, *1*, 4-7.

D'Addona, D. M. (2014). Neural Network, in: CIRP Encycl. Prod. Eng., Springer Berlin Heidelberg, Berlin, Heidelberg, 911–918. https://doi.org/10.1007/978-3-642-20617-7_6563.

Demir, V. (2022). Enhancing monthly lake levels forecasting using heuristic regression techniques with periodicity data component: application of Lake Michigan. *Theoretical and Applied Climatology*, *148*(3-4), 915-929. https://doi.org/10.1007/s00704-022-03982-0

Demir, V., & Yaseen, Z. M. (2023). Neurocomputing intelligence models for lakes water level forecasting: a comprehensive review. *Neural Computing and Applications*, *35*(1), 303-343.

Desmukh, T., Tanty, R., (2015). Application of Artificial Neural Network in Hydrology- A Review. International Journal of Engineering Research and Technology, 4(06), 184-188.

Dikbaş, F., Fırat, M., (2006). Göllerde Üç Boyutlu Hidrodinamik Modellemede POM ve Yapay Sinir Ağları Yöntemlerinin Kullanılması: Gökpınar Baraj Gölü Örneği: Mühendislik Bilimleri Dergisi, 1(12), 43-50.

Kılıç, E., Özbalcı, Ü., & Özçalık, H. R. (2012). Comparison of MLP and RBF Structures in Modeling of Nonlinear Dynamic Systems with Artificial Neural Networks, Elektrik - Elektronik ve Bilgisayar Mühendisliği Sempozyumu, 29 Kasım - 01 Aralık 2012, Bursa.

Koca, Y. (2014). Rize İyidere Alt Havzası İkİzdere Kesiti İçin Birim Hidrografın Belirlenmesi. Uzmanlık tezi, Orman ve Su İşleri Bakanlığı, Ankara.

Michigan-Huron (2023), Lake Michigan–Huron https://en.wikipedia.org/wiki/Lake_Michigan%E2%80%93Huron, Access date: 25.05.2023

Okkan, U., & Yıldırım Dalkiliç, H. (2012). Radyal tabanlı yapay sinir ağları ile Kemer Barajı aylık akımlarının modellenmesi. *Teknik Dergi*, *23*(112), 5957-5966.

Teltik, İ., Aksoy, H., Ünal, N. E. (2008). Van Gölü Su Seviyesi Stokastik Modelleri, Van Gölü Hidrolojisi ve Kirliliği Konferansı, 21-22 Ağustos 2008, DSİ XVII. Bölge Müdürlüğü, Van, 74-81.

6th Intercontinental Geoinformation Days

igd.mersin.edu.tr

Comparison of web based online GNSS data evaluation services

Mehmet Emin Tabar*[1], Yasemin Sisman [2]

[1]*Bitlis Eren University, Vocational School of Technical Sciences, Department of Architecture and Urban Planning, Bitlis, Türkiye*
[2]*Ondokuz Mayis University, Faculty of Engineering, Department of Geomatics Engineering, Samsun, Türkiye*

Keywords
RINEX
GNSS
Precise point positioning
Relative positioning

Abstract

RINEX - Receiver Independent Exchange Format is a data exchange format for raw GNSS data. The first RINEX version was developed in 1989 by W. Gurtner (Teunissen and Montenbruck 2017). In parallel with the GNSS concept, versions such as RINEX 2.XX, RINEX 3.XX, RINEX 4.XX have been developed. There are different methods for processing RINEX data. These methods are classical GNSS data evaluation software and web-based online data evaluation services as an alternative to this software. In the study, different web-based online evaluation services will be compared and their usability in measurement applications will be examined. Online services using PPP (Precise Point Positioning) and relative technique will be used to evaluate the data. 30 seconds of RINEX data obtained from a point belonging to the CORS-TR network will be sent to different web-based online GNSS evaluation services and the services will be evaluated by comparing the coordinate values from these services.

1. Introduction

The global positioning system (GNSS) provides great convenience in scientific studies thanks to the data it provides. Satellite-based positioning systems can instantly determine the coordinates of the location with precision. These systems are generally used for navigation, surveying, geodetic measurements, determination of earth crust movements, earthquake studies, etc. extensively used in areas such as (URL1 2023). Satellite-based positioning system consisting of GPS (Global Positioning System), initially operated only by the United States; With the activation of different satellite-based systems such as Russia's GLONASS, China's COMPASS, Japan's QZSS, European Union's Galileo and India's IRNSS, a large global positioning system called GNSS (Global Navigation Satellite System) became like that (Alkan et al. 2017). Some time ago, simultaneous measurements had to be made using at least two receivers, the first of which was a reference, in order to determine the position with centimeter accuracy. In this method, which is called the relative technique and applied based on phase measurements, a data evaluation software was needed to determine the coordinates. Today, with the widespread use of systems called CORS (Continuously Operating Reference Station) and Network RTK, which emerged with the addition of RTK (Real Time Kinematic) feature to networks consisting of fixed stations that make continuous GNSS observations, users' need for a fixed receiver has largely disappeared (Alkan, Ozulu, and İlçi 2017).

Sensitive satellite orbit and clock information with different accuracy levels is produced by many organizations, especially the International GNSS Service (IGS), and presented to the users. With these data; With the application of corrections such as carrier wave phase rotation, satellite antenna phase center, solid earth tides and ocean loading, another technique that allows determination of bias with an accuracy that will be sufficient for many measurement applications is PPP (Precise Point Positioning) (Alkan et al. 2017). With the PPP technique, it is possible to determine the position kinematically or statically with centimeter accuracy (Xiaohong, Jiahuan, and Xiaodong 2020). GNSS evaluation software should be used for PPP and Relative position determination. There are commercial and scientific software for GNSS evaluation. Most of this software require a license fee. At this point, online GNSS evaluation services, which are available for free, are very useful and useful. These services evaluate on the basis of PPP or relative technique. When looking at online GNSS services, services using relative techniques such as AUSPOS, OPUS; There are services that use PPP (Precise Point Positioning) technique such as APPS, CSRS-PPP. A point data of the CORS-TR network was sent to these GNSS evaluation services and the coordinates obtained

* **Corresponding Author**

*(metabar@beu.edu.tr) ORCID ID 0000-0002-3234-5340
(ysisman@omu.edu.tr) ORCID ID 0000-0002-6600-0623

Cite this study

Tabar, M. E, & Sisman, Y. (2023). Comparison of web based online GNSS data evaluation services. Intercontinental Geoinformation Days (IGD), 6, 216-219, Baku, Azerbaijan

from the services were compared. The advantages of these services compared to each other are examined and the results are presented.

2. Method

RINEX data obtained from BOL1, ERZ2, ISTN, TOK1 TUSAGA-Active points were sent to OPUS and AUSPOS using relative technique, APPS and CSRS-PPP using PPP (Precise Point Positioning) technique, and the obtained coordinate values were examined. Precision Point Positioning is a positioning technique that uses widely and easily available GNSS orbit and clock corrections. The PPP technique is different from the differential GNSS positioning technique. Because differential techniques require access to observations of one or more reference stations whose coordinates are known (Grinter and Roberts 2011). PPP technique generally has simplified operational logistics as well as a reduction in labor and equipment costs (Gao 2006).

2.1. OPUS

NOAA's Online Positioning User Service (OPUS) provides free access to high-accuracy National Spatial Reference System (NSRS) coordinates. OPUS uses the same software which computes coordinates for the nation's geodetic control marks and the NOAA CORS Network (NCN). Under normal conditions, most positions can be computed to within a few centimeters. However, estimating the accuracy for a specific solution is difficult because formal error propagation is notoriously optimistic for GPS reductions. User errors (such as misidentification of antenna or ARP height) cannot be detected. Local multipath or adverse atmospheric conditions may also negatively impact your solution (URL3 2023). The RINEX file is loaded for processing. Antenna type, antenna height and e-mail address are entered and sent for analysis.

2.2. AUSPOS

Geoscience Australia's online GPS processing service AUSPOS analyzes RINEX data using the relative technique. The system can be used without being a member. A maximum of 20 RINEX data can be loaded at one time. The system determines the antenna type and height by scanning automatically with the scan button. The AUSPOS outputs for the ISTN point are presented in Figure 1-4.

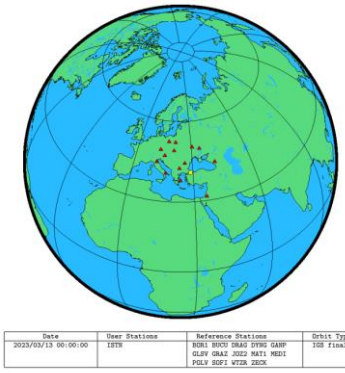

Date	User Stations	Reference Stations	Orbit Type
2023/03/13 00:00:00	ISTN	BOR1 BUCU DRAG DYNG GANP GLSV GRAZ JOZ2 MAT1 MEDI POLV SOFI WTZR ZECK	IGS final

Figure 1. AUSPOS processing summary (ISTN)

Station	X (m)	Y (m)	Z (m)	ITRF2014 @
ISTN	4223660.665	2325015.261	4161716.362	13/03/2023
BOR1	3738358.146	1148173.996	5021815.926	13/03/2023
BUCU	4093760.543	2007794.121	4445130.150	13/03/2023
DRAG	4432980.279	3149432.340	3322110.803	13/03/2023
DYNG	4595220.042	2039434.214	3912625.874	13/03/2023
GANP	3929181.229	1455237.017	4793654.074	13/03/2023
GLSV	3512888.592	2068980.138	4888903.347	13/03/2023
GRAZ	4194423.507	1162703.019	4647245.604	13/03/2023
JOZ2	3664880.241	1409190.875	5009618.625	13/03/2023
MAT1	4641951.105	1393054.005	4133281.126	13/03/2023
MEDI	4461400.409	919593.924	4449504.973	13/03/2023
POLV	3411556.967	2348464.214	4834397.019	13/03/2023
SOFI	4319371.770	1868688.113	4292064.087	13/03/2023
WTZR	4075580.253	931854.107	4801568.310	13/03/2023
ZECK	3451174.305	3060335.696	4391955.810	13/03/2023

Figure 2. AUSPOS computed cartesian coordinates (ISTN)

Station	Longitude(East) (m)	Latitude(North) (m)	Ellipsoidal Height(Up) (m)
ISTN	0.004	0.003	0.008
BOR1	0.003	0.003	0.007
BUCU	0.003	0.003	0.006
DRAG	0.004	0.003	0.008
DYNG	0.003	0.003	0.007
GANP	0.003	0.003	0.007
GLSV	0.003	0.003	0.007
GRAZ	0.003	0.003	0.007
JOZ2	0.003	0.003	0.007
MAT1	0.004	0.003	0.007
MEDI	0.003	0.003	0.007
POLV	0.003	0.003	0.007
SOFI	0.003	0.003	0.007
WTZR	0.003	0.003	0.007
ZECK	0.004	0.003	0.007

Figure 3. AUSPOS positional uncertainty (95% C.L.) (ISTN)

Baseline	Ambiguities Resolved	Baseline Length (km)
JOZ2 - POLV	82.8 %	988.489
GLSV - JOZ2	88.1 %	687.747
BOR1 - JOZ2	87.5 %	271.436
POLV - ZECK	84.6 %	839.098
GRAZ - MEDI	85.9 %	411.680
GRAZ - JOZ2	93.0 %	687.377
BUCU - DYNG	98.0 %	732.136
BUCU - JOZ2	92.7 %	927.853
BUCU - SOFI	70.2 %	306.072
DRAG - DYNG	77.9 %	1267.725
JOZ2 - WTZR	85.0 %	663.182
BUCU - MAT1	71.9 %	880.720
BUCU - ISTN	83.6 %	444.777
GANP - JOZ2	94.8 %	344.407
AVERAGE	85.4%	675.193

Figure 4. AUSPOS ambiguity resolution - per baseline (ISTN)

2.3. CSRS-PPP

CSRS-PPP is an online application for post-processing of global navigation satellite systems (GNSS) data. It uses precise satellite orbit, clock and yaw corrections derived from a global network of receivers to determine accurate user positions anywhere in the world, regardless of proximity to reference stations. It can be processed statically and kinematically. RINEX data can be processed in zip format, with a maximum of 300 MB. The data is processed in a very short time and sent to the e-mail address you entered. The processed RINEX data is sent to the e-mail address entered in the system in zip format. The zip file sent contains clk, pdf, csv, pos, sum and tro formatted files.

- **SUM File:** Contains the parameters and the results of the PPP processing.
- **POS File:** Contains the positioning information for each epoch processed.

- **CSV File:** A comma-separated (.csv) format text file containing the positioning and clock information for each epoch processed.
- **TRO File:** Contains dry and wet zenith path delay and tropospheric gradient for each epoch processed.
- **CLK File:** A RINEX_CLOCK format file containing the receiver clock offset and the clock offset sigma (95%) for each epoch processed (URL-2, 2023).

CSRS-PPP service ISTN point outputs are presented in Table 1, Figure 5, Figure 6, Figure 7, Figure 8, Figure 9 and Figure 10.

Table 1. CSRS-PPP mode, frequency and product type

Point	Mode	Frequency	Product Type
BOL1	Static	Double	NRCan/IGS Final
ERZ2	Static	Double	NRCan/IGS Final
ISTN	Static	Double	NRCan/IGS Final
TOK1	Static	Double	NRCan/IGS Final

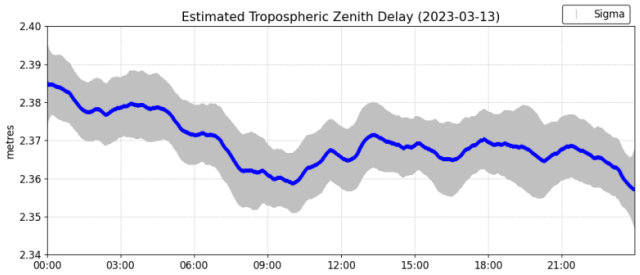

Figure 5. CSRS-PPP estimated tropospheric zenith delay (ISTN)

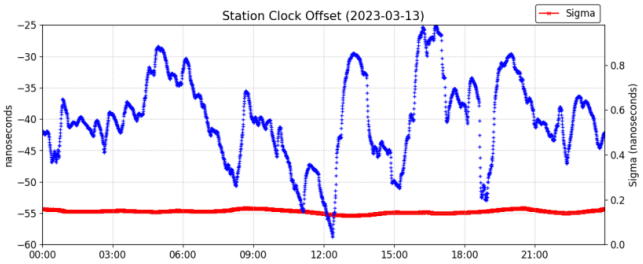

Figure 6. CSRS-PPP station clock offset (ISTN)

2.4. APPS

APPS accepts GPS measurement files, and applies the most advanced GPS positioning technology from NASA's Jet Propulsion Laboratory to estimate the position of your GPS receivers, whether they are static, in motion, on the ground, or in the air. APPS employs:

- Real-time GPS orbit and clock products from JPL's GDGPS System
- JPL's daily and weekly precise GPS orbit and clock products
- JPL's GipsyX/RTGx software for processing the GPS measurements (URL4 2023).

In order to use the APPS service, you must be a member of the service. After the RINEX file is uploaded, results can be obtained in a short time.

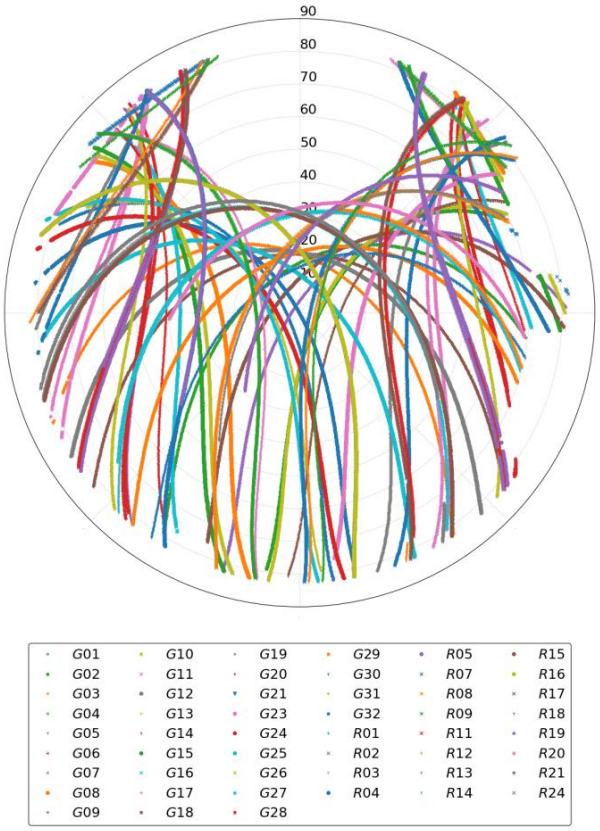

Figure 7. CSRS-PPP satellite sky distribution (ISTN)

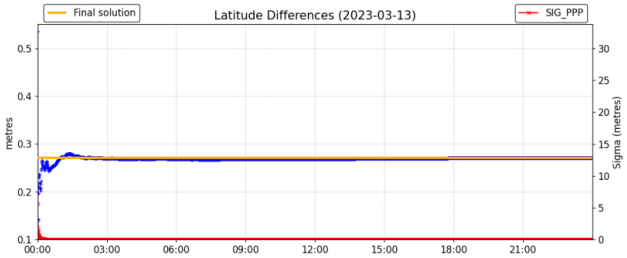

Figure 8. CSRS-PPP latitude differences (ISTN)

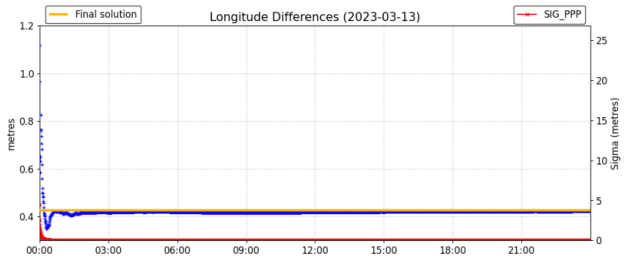

Figure 9. CSRS-PPP longitude differences (ISTN)

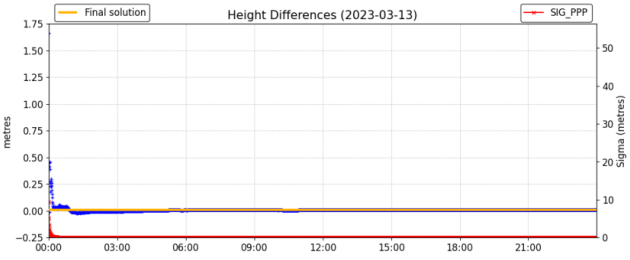

Figure 10. CSRS-PPP height differences (ISTN)

3. Results

RINEX data obtained from four CORS-TR points were sent to online GNSS evaluation services and the results in Table 2, Table 3, Table 4 and Table 5 were obtained.

Table 2. BOL1 estimated coordinates

Service	X (m)	Y (m)	Z (m)
OPUS	no solution	no solution	no solution
AUSPOS	4121753.605	2536363.599	4141652.664
CSRS-PPP	4121753.621	2536363.605	4141652.677
APPS	4121753.610	2536363.601	4141652.673

Table 3. ERZ2 estimated coordinates

Service	X (m)	Y (m)	Z (m)
OPUS	3781453.138	3139093.189	4054003.001
AUSPOS	3781453.138	3139093.193	4054003.003
CSRS-PPP	3781453.153	3139093.201	4054003.009
APPS	3781453.146	3139093.196	4054003.010

Table 4. ISTN estimated coordinates

Service	X (m)	Y (m)	Z (m)
OPUS	4223660.668	2325015.259	4161716.366
AUSPOS	4223660.665	2325015.261	4161716.362
CSRS-PPP	4223660.681	2325015.268	4161716.373
APPS	4223660.674	2325015.268	4161716.370

Table 5. TOK1 estimated coordinates

Service	X (m)	Y (m)	Z (m)
OPUS	3911480.068	2900418.942	4106499.837
AUSPOS	3911480.059	2900418.934	4106499.825
CSRS-PPP	3911480.071	2900418.942	4106499.834
APPS	3911480.060	2900418.934	4106499.827

4. Discussion

It is seen that the results obtained from the online GNSS evaluation services give very close values to each other. It has been seen that CSRS-PPP service is ahead of other services in terms of ease of application, since RINEX data can be uploaded in multiple ways as zip files up to 300 MB. When the reports sent by the services are examined, it is seen that the CSRS-PPP service provides more detailed reports than other services. In general, online GNSS assessment services have been found to process RINEX data quite quickly and easily.

5. Conclusion

It can be considered as an economical and easy-to-apply alternative that online GNSS evaluation services can determine location without the need for any data other than that collected with the GNSS receiver.

References

Alkan, R. M., Ozulu, İ. M., & İlçi, V. (2017). Klasik GNSS veri değerlendirme yazılımlarına alternatif olarak web-tabanlı online değerlendirme servisleri. Afyon Kocatepe Üniversitesi Fen ve Mühendislik Bilimleri Dergisi, 17(2), 603-619.

Gao, Y. (2006). Precise Point Positioning and its challenges. Inside GNSS, 1(8), 16-18.

Grinter, T., & Roberts, C. (2011, November). Precise point positioning: where are we now. IGNSS Symposium, 15-17.

Teunissen, P. J., & Montenbruck, O. (Eds.). (2017). Springer handbook of global navigation satellite systems (Vol. 10, pp. 978-3). Cham, Switzerland: Springer International Publishing. https://doi.org/10.1007/978-3-319-42928-1.

URL-1. (2023). Küresel Uydu Seyrüsefer Sistemi. https://tr.wikipedia.org/wiki/Küresel_uydu_seyrüsefer_sistemi.

URL-2. (2023). CSRS-PPP. https://webapp.csrs-scrs.nrcan-rncan.gc.ca/geod/tools-outils/ppp.php?locale=en.

URL-3. (2023). OPUS. 2023. https://geodesy.noaa.gov/OPUS/.

URL-4. (2023). APPS. https://pppx.gdgps.net/.

Xiaohong, Z., Jiahuan, H. U., & Xiaodong, R. (2020). New progress of PPP/PPP-RTK and positioning performance comparison of BDS/GNSS PPP. Acta Geodaetica et Cartographica Sinica, 49(9), 1084.

6th Intercontinental Geoinformation Days

igd.mersin.edu.tr

A detection method of mismatched measures in GNSS coordinate time series: Fuzzy logic and IQR (Interquartile Range) based approach

Hüseyin Pehlivan[*1]

[1]*Gebze Technical University, Engineering Faculty, Department of Surveying Engineering, Kocaeli, Türkiye*

Keywords
GNSS data
Outlier
Fuzzy Logic
IQR
Filtering

Abstract

This study presents a new approach for outlier detection aiming to enhance the accuracy and reliability of GNSS data. Unlike traditional approaches, this approach combines fuzzy logic and the Interquartile Range (IQR) method to improve outlier detection. The fuzzy logic-based method is employed to flexibly model data characteristics. Individual outlier scores are calculated for each data point using fuzzy logic, and these scores are then utilized to identify outliers in the dataset. By determining a threshold value based on the spread of the data around its center using the IQR method, data points scoring above this threshold can be considered outliers. The combination of these two methods ensures a more reliable and accurate outlier detection. When applying the proposed approach to a test signal containing obvious outlier values, it is observed that the processed time series exhibits a better normal distribution and improves performance metrics, indicating enhanced signal quality. Experimental results demonstrate the effectiveness of the proposed approach in effectively detecting outliers in GNSS coordinate time series. Overall, the proposed approach offers a promising solution for outlier detection in GNSS data by integrating fuzzy logic and the IQR method. It provides improved accuracy and reliability, leading to enhanced data analysis and interpretation in GNSS applications.

1. Introduction

GNSS (Global Navigation Satellite System) coordinate time series are widely used in determining geographical locations and serve as important data sources in various fields. However, Data obtained from GNSS systems contain outliers that can arise from measurement errors, hardware malfunctions, multipath effects, station-related errors, orbital anomalies, and unknown reasons. In addition to outliers, GNSS position time series are affected by temporally correlated noise, which includes white noise and flicker noise (Mao et al., 1999). These outliers can bias estimates in both functional and stochastic models (Koch 1999; Khodabandeh et al. 2012). Consequently, the presence of outliers can negatively affect the analysis and interpretation of GNSS data, leading to inaccurate results.

Detecting outliers in GNSS position time series is crucial, and various approaches have been proposed for this purpose. There are several approaches for detecting outliers in the GNSS position time series, such as three sigma method (3σ) (Mao et al. 1999), Bayesian method (Zhang and Gui 2013). Besides these methods, the window-opening test algorithm based on the Interquartile Range (IQR) statistic is another commonly used approach for outlier detection in the GNSS position time series (Nikolaidis 2002; Li and Shen 2018). This algorithm is fast and robust since the median and IQR values of a time series are less affected by outliers. Due to its superior performance, the outlier detection approach based on IQR criterion has been widely applied in GNSS position time series analysis.

On the other hand, Aliosmanoğlu and Akyilmaz (2002) conducted a study comparing conventional outlier testing, robust estimation, and fuzzy techniques for detecting outliers within a geodetic network. Similarly, Gökalp ve Boz (2005), Outlier data in GPS networks was identified using both traditional statistical methods and fuzzy logic approach. Cateni et al. (2007) extracted abnormal data caused by various factors using a fuzzy logic-based method and compared it with a statistical technique. Overall, these studies compare fuzzy logic and other methods with various approaches.

In this study, a novel approach is proposed that combines fuzzy logic and IQR (Interquartile Range) methods as an alternative to traditional approaches. The

* **Corresponding Author**

*(hpehlivan@gtu.edu.tr) ORCID ID 0000 – 0002 – 0018 – 6912

Cite this study

Pehlivan, H. (2023). A detection method of mismatched measures in GNSS coordinate time series: Fuzzy logic and IQR (Interquartile Range) based approach. Intercontinental Geoinformation Days (IGD), 6, 220-223, Baku, Azerbaijan

fuzzy logic-based method is employed to flexibly model data characteristics and calculate individual outlier scores for each data point. On the other hand, the IQR method identifies outliers by considering the distribution of the data around its center. By combining these two methods, the proposed approach offers a promising solution for effective outlier detection in GNSS data analysis

The method ensures effective detection of outliers in GNSS coordinate time series. Experimental studies demonstrate its superiority in terms of reliability and accuracy compared to other methods.

In summary, it is essential to accurately detect and differentiate outliers in GNSS coordinate time series. The proposed approach combining fuzzy logic and IQR methods offers an effective solution to this challenge, aiming to improve the accuracy and reliability of GNSS data analysis.

2. Method

2.1. Mamdani Fuzzy Inference System (FIS)

Mamdani Fuzzy Inference System (FIS) is a model of an inference system based on fuzzy logic. Fuzzy logic is an artificial intelligence technique used to solve problems with uncertainty and complexity. Unlike traditional binary (true/false) logic, fuzzy logic operates with fuzzy sets and fuzzy rules.

FIS aims to obtain one or more output values by performing fuzzy inference on input data. It consists of three main components: input variables, output variables, and a rule set.

Input variables are the variables that provide data to the system and define the fuzzy sets associated with them. Each input variable has membership functions that represent different value ranges and fuzzy sets.

Output variables represent the results obtained from the system. Each output variable also has membership functions that represent different value ranges and fuzzy sets.

The rule set defines the relationship between input variables and output variables through if-then rules. Each rule specifies a combination of input variables and the corresponding output variable value. These rules are based on the "if-then" logic of fuzzy reasoning.

Mamdani FIS fuzzifies the input data, applies the rules, and calculates the output values. These output values can be used to solve a specific problem or make a decision. The System is a model used to deal with uncertainty and complexity in the real world. It finds applications in various fields such as control systems, decision support systems, data analysis, artificial intelligence, and many others.

2.2. The Interquartile Range (IQR)

The method is a statistical technique used to assess the spread of a dataset and detect outliers. The IQR represents the difference between the lower quartile (25th percentile) and the upper quartile (75th percentile) of the data.

The IQR method determines outliers by measuring the dispersion around the center of the dataset. In the first step, the data is sorted, and quartiles are calculated. The lower quartile corresponds to the 25th percentile of the data and is also known as the first quartile. The upper quartile corresponds to the 75th percentile of the data.

Next, the IQR is calculated by subtracting the lower quartile value from the upper quartile value. This value represents the spread of the middle 50% of the dataset.

To detect outliers, a threshold value is established using the IQR method. Typically, the lower bound is determined by subtracting 1.5 times the IQR from the lower quartile, and the upper bound is determined by adding 1.5 times the IQR to the upper quartile. Data points outside these bounds are considered outliers.

The IQR method takes into account the density and distribution of the dataset. As a robust and statistically reliable approach based on the center of the data, it is used to identify extreme values in a dataset.

2.3. Fuzzy Logic and IQR based outlier detection

Mathematical Model and Process Steps:

1- The input data is defined.

2- Detection of outliers using Fuzzy Logic:

a. A Mamdani Fuzzy Inference System (mamfis) is created for fuzzy logic-based outlier detection.

b. Input variable (data) and output variable (outlier) are defined.

c. Three membership functions ("low", "medium", "high") are defined for the input variable "data".

d. Two membership functions ("no_outlier", "outlier") are defined for the output variable "outlier".

e. Rules are defined to establish the relationships between the input variable (data) and output variable (outlier).

f. The fuzzy logic system is constructed.

3- Calculation of the output signal:

a. The evalfis function is used on the fuzzy logic system to calculate the output value (outlier_scores) for each point in the dataset.

4- Outlier detection using the Interquartile Range (IQR) method:

a. Q1 is calculated: It represents the lower quartile (25th percentile) of the dataset.

b. Q3 is calculated: It represents the upper quartile (75th percentile) of the dataset.

c. IQR is calculated: It is the difference between Q3 and Q1.

d. The threshold value is calculated as 1.5 times the IQR: threshold = 1.5 * IQR.

e. Outliers are determined as outliers = (outlier_scores < Q1 - threshold | outlier_scores > Q3 + threshold).

5- Examination of outliers:

a. The outliers are presented on the graph.

These steps encompass the procedures and mathematical explanations used to detect outliers in the dataset and generate the output signal through fuzzy logic-based outlier detection.

Figure 1 represents the process steps of fuzzy logic-based outlier detection mentioned in the 2nd step in a

more visual manner. In this representation, the input variable "data" passes through membership functions (e.g., "low", "medium", "high"). Then, connections are established using rules (IF-THEN based statements). These rules result in the creation of a Mamdani Fuzzy Inference System (fis). This system produces the "outlier" output based on the given "data" input. Finally, the output values, referred to as "outlier_scores," are obtained and the values will be within the range of [0, 1].

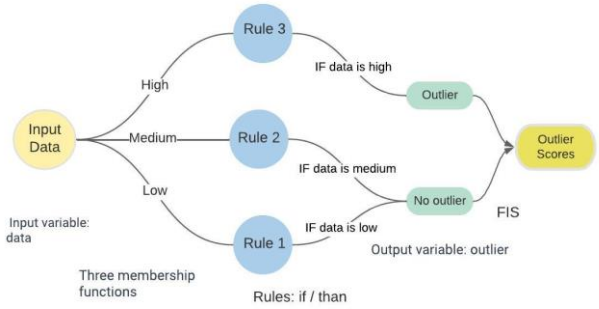

Figure 1. Fuzzy Logic-based outlier detection process.

The obtained 'outlier_scores' variable in this context is calculated for each data point in the dataset as a result of fuzzy logic-based outlier detection. These scores indicate the likelihood of data points being outliers and represent the outcome of the outlier detection process. These scores can be used for outlier detection and help identify outliers in the dataset.

In the 3rd step, the IQR method is used for outlier detection. By comparing the outlier scores obtained with the threshold values determined using IQR, we can determine the outliers. Data points in the input data that fall outside the range of (outlier_scores < Q1 - threshold) or (outlier_scores > Q3 + threshold) are identified as outliers.

3. Results

The input data used in the test consists of 1024 data points collected using the RTK GNSS method with a sampling frequency of 1 Hz over a duration of 17 seconds. This dataset contains evident outliers (Figure 2).

The 'outlier scores' obtained from applying the 2nd step of the Fuzzy Logic-based outlier detection process to the input signal can be seen in Figure 3.

The 'outlier scores' obtained from the Fuzzy Logic-based outlier detection process were used to perform outlier detection using the IQR method as described in the 3rd step. The threshold values for IQR were calculated as follows: Q1 = prctile(data, 25), Q3 = prctile(data, 75), IQR = Q3 - Q1, and threshold = 0.5 * IQR. The points that fell outside the threshold, determined as Outlier = (outlier_scores < Q1 - threshold or outlier_scores > Q3 + threshold), were identified as outliers.

Calculated index numbers of identified outliers:

Outlier indexs = [36, 116, 117, 118, 136, 137, 145, 146, 156, 157, 164, 165, 166, 167, 168, 169, 170, 171, 172, 173, 174, 175, 176, 177, 182, 183, 184, 188, 189, 190, 194, 195].

Figure 4 shows the input data, outlier values, and corrected output data.

When examining the histograms of the input and output signals, the high and narrow peak observed in the histogram graph of the input signal indicates the potential outliers in the data. It can be seen that the output signal exhibits a better normal distribution (Gaussian distribution) (Figure 5).

Additionally, to evaluate the performance of the output signal, metrics such as RMS (Root Mean Square), signal power, noise power, and SNR (Signal-to-Noise Ratio) values can provide information about the quality of the output signal.

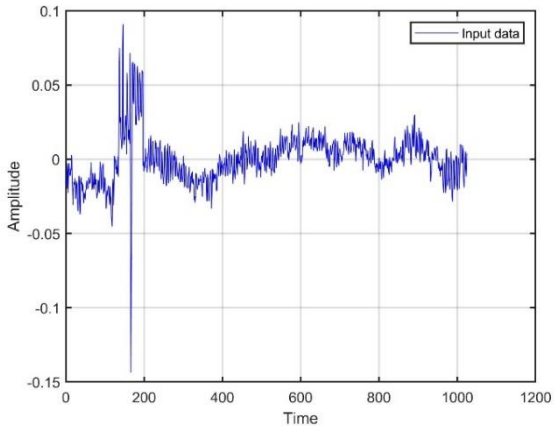

Figure 2. The input data

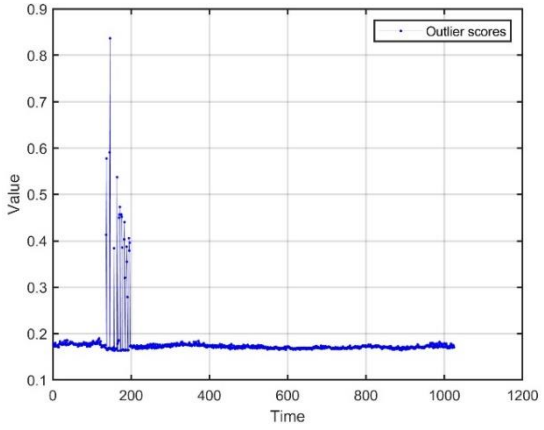

Figure 3. The "outlier scores" of the input data obtained from the fuzzy Logic-based outlier detection process

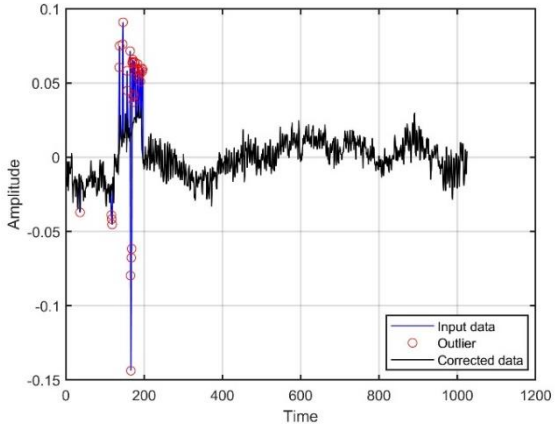

Figure 4. Fuzzy Logic and IQR based method applied signal outputs

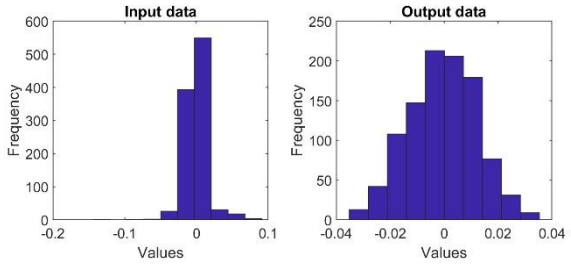

Figure 5. The histograms of input and output signals.

After applying the proposed model, the accuracy measures of the input and output signals are presented in Table 1.

Table 1. Accuracy metrics for input and output signals

Items	Input Data	Output Data
RMS	0.1670	0.1260
Signal Power	0.0028	0.0016
Noise Power	0.0027	0.0001
SNR	-0.0001	2.2182

4. Discussion

RMS value of the input dataset is calculated as 0.1670, while it is 0.1260 for the output dataset. This indicates that the output data is more stable and exhibits less variation compared to the input data. The signal power of the input dataset is 0.0028, whereas it decreases to 0.001 in the output dataset. This suggests that the output dataset has a lower signal power. The noise power of the input dataset is 0.0027, whereas it is calculated as 0.0001 for the output dataset. The significantly lower noise power in the output dataset compared to the input data indicates that the output signal contains less noise. The SNR value of the input dataset is -0.0001, while the SNR value of the output dataset is 2.2182. The positive and high SNR value of the output dataset indicates that it has a better signal-to-noise ratio compared to the input signal. These evaluations demonstrate that the output signal has lower RMS, signal power, and noise power values compared to the input signal, and it has a higher SNR value. This suggests that the output signal is cleaner, less noisy, and more stable.

5. Conclusion

In this study, a novel approach for outlier detection in GNSS coordinate time series was developed using fuzzy logic. The proposed method calculates a fuzzy logic-based outlier score for each data point, indicating its probability of being an outlier. To detect outliers, the IQR method was employed to obtain outlier scores. These outlier scores were then compared with threshold values determined by the IQR. Data points in the input data that exceeded the threshold range of outlier scores were identified as outliers. The results demonstrate that this approach is effective for outlier detection in GNSS coordinate time series.

Accurate detection of outliers enhances the overall accuracy and reliability of GNSS data. Moreover, the proposed method provides a general framework that can be applied to other domains of data analysis.

In conclusion, this study showcases the successful application of a combined fuzzy logic and IQR approach for outlier detection in GNSS coordinate time series. The proposed method offers a valuable tool for obtaining more reliable results in data analysis.

References

Aliosmanoğlu, Ş., & Akyilmaz, O. (2002). A comparison between statistical & fuzzy techniques in outlier detection. In Vistas for Geodesy in the New Millennium: IAG 2001 Scientific Assembly, Budapest, Hungary September 2–7, 2001 (pp. 382-387). Springer Berlin Heidelberg. https://doi.org/10.1007/978-3-662-04709-5_63

Cateni, S., Colla, V., & Vannucci, M. (2007, February). A fuzzy logic-based method for outliers detection. In Artificial Intelligence and Applications (pp. 605-610).

Gökap, E., & Boz, Y. (2005). Outlier detection in GPS networks with fuzzy logic and conventional methods. From Pharaohs to Geoinformatics. FIG Working Week.

Khodabandeh, A., Amiri-Simkooei, A. R., & Sharifi, M. A. (2012). GPS position time-series analysis based on asymptotic normality of M-estimation. Journal of Geodesy, 86, 15-33.

Koch, K. R. (1999). Parameter estimation and hypothesis testing in linear models. Springer Science & Business Media.

Li, W., & Shen, Y. (2018). The consideration of formal errors in spatiotemporal filtering using principal component analysis for regional GNSS position time series. Remote Sensing, 10(4), 534.

Mao, A., Harrison, C. G., & Dixon, T. H. (1999). Noise in GPS coordinate time series. Journal of Geophysical Research: Solid Earth, 104(B2), 2797-2816.

Nikolaidis, R. (2002). Observation of geodetic and seismic deformation with the Global Positioning System. University of California, San Diego.

Qianqian, Z., & Qingming, G. (2013). Bayesian methods for outliers detection in GNSS time series. Journal of Geodesy, 87(7), 609-627.

6th Intercontinental Geoinformation Days

igd.mersin.edu.tr

Evaluation of satellite altimetry-derived gravity field models with shipborne gravity data in the Mediterranean Sea

Aslınur Bahçekapılı[*1], **Bihter Erol** [1]

[1]*Istanbul Technical University, Faculty of Civil Engineering, Department of Geomatics Engineering, Istanbul, Türkiye*

Keywords
Marine gravity
Satellite altimetry
Shipborne gravity
Mediterranean Sea

Abstract

Marine gravity field models can be used in a wide range of applications such as improving marine geoid and the height system, monitoring ocean circulation, tides, the greenhouse effect and climate change and can benefit various Earth sciences such as geodesy, geophysics and oceanography. Satellite altimetry-derived gravity field models provide uniform global coverage compared to shipborne gravity data. Studies conducted about the quality assessment of the latest satellite altimetry-derived gravity field models in Turkish seas are deficient. Therefore, in this study, selected satellite altimetry-derived gravity field models (SSv29.1, DTU21, DTU17, DTU15, DTU13 and DTU10) were validated with shipborne gravity data in the Mediterranean Sea. In comparison with shipborne free-air gravity anomalies, SSV29.1 model has the lowest standard deviation with 24.096 mGal followed by DTU21, DTU17, DTU15, DTU13 and DTU10 models with standard deviations of 24.169, 24.371, 24.396, 24.416 and 24.444 mGal, respectively. It is concluded that there are no statistically significant differences between the models for the study area.

1. Introduction

Gravity field models offer valuable information about the Earth, its interior and its fluid envelope for all geosciences such as geodesy, geophysics and oceanography (Barthelmes, 2014). Gravity field models can be used in geoid modelling, defining the reference height system, determining ocean circulation models and dynamics, monitoring tides, greenhouse effect and climate change, marine transportation and fishing, weather forecasting and prediction of natural disasters, exploration of natural resources like oil and gas, and mining.

Marine gravity fields can be generated from different data sources which consist of shipborne, airborne and land measurements, satellite gravity missions and satellite altimetry. Terrestrial measurements such as shipborne gravity data have high accuracy, however, these datasets are mostly sparse, the data derivation process is costly and time-consuming, temporal variations of the gravity field cannot be determined and also systematic errors can occur. Although satellite altimetry might not provide as accurate data as shipborne gravimetry, satellite altimetry data have global and uniform coverage and can be accessed free of charge.

Satellite altimetry provides sea surface heights by measuring the time between a radar signal transmitted to the Earth's surface and reflected back to the satellite. Marine geoids generated from the sea surface height measurements enable to develop gravity field models since geoids refer to the equipotential surface of the Earth's gravity field that corresponds closely with the mean sea level (Andersen, 2012; Andersen & Knudsen, 2000). Satellite altimetry is particularly efficient over oceans and open water on land due to the excellent reflective structure of the water (GGOS, n.d.). Coastal areas are not ideal for implementing satellite altimetry. Abulaitijiang et al. (2021) stated that improvements in recent satellite altimeters enable to provide more reliable short-wavelength components of the marine gravity field than traditional altimetry.

Satellite altimetry is confirmed as a valuable observational tool for numerous research areas such as ocean and hydrosphere, due to its achievements and its level of accuracy and precision (Abdalla et al., 2021). The developments in satellite altimetry missions and data processing methods contributed to the enhancement of

* **Corresponding Author**

*(bahcekapili@itu.edu.tr) ORCID ID 0000-0001-7061-9050
(bihter@itu.edu.tr) ORCID ID 0000-0003-0854-788X

Cite this study

Bahçekapılı, A. & Erol, B. (2023). Evaluation of satellite altimetry-derived gravity field models with shipborne gravity data in the Mediterranean Sea. Intercontinental Geoinformation Days (IGD), 6, 224-227, Baku, Azerbaijan

marine gravity models in terms of accuracy and resolution (Guo et al., 2022; Zaki et al., 2018, as cited in Li et al., 2022).

Around the world, several studies were carried out in order to evaluate the accuracy of satellite altimetry-derived marine gravity fields (Kamto, 2022). There are a few related studies conducted in Turkish seas, however, studies that contain the latest satellite altimetry models are inadequate. Therefore, this study aims to fill the gap on this subject by validating satellite altimetry products in the Turkish seas. In this study, selected satellite altimetry-derived gravity field models which also consist of the recent models (SSv29.1, DTU21, DTU17, DTU15, DTU13 and DTU10) were validated with shipborne gravity data in the Mediterranean Sea.

2. Method

Shipborne gravity data were obtained from International Gravimetric Bureau (BGI). 14661 points at the Mediterranean Sea between 33°N to 38°N and 26°E to 36°E were used for the validation (Figure 1).

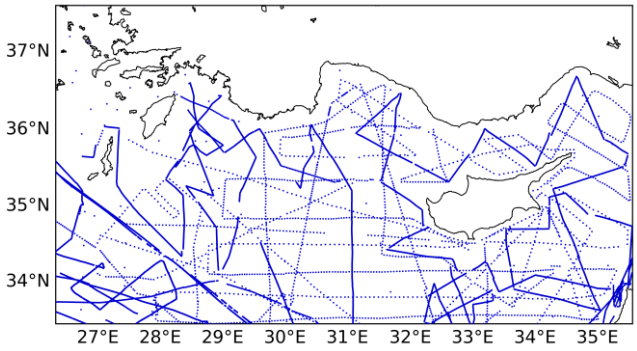

Figure 1. Spatial distribution of 14661 shipborne data points at the Mediterranean Sea

SSv29.1, DTU21, DTU17, DTU15, DTU13 and DTU10 models were selected as satellite altimetry gravity field models (Table 1). S&S series of marine gravity models were presented by the Scripps Institution of Oceanography (SIO) (Abdallah et. al., 2022). SSv29.1 gravity data were extracted from global 1 arc-minute grids from SIO's website (SIO, n.d.).

DTU21 model was obtained from the Technical University of Denmark (DTU). DTU17, DTU15, DTU13 and DTU10 models were acquired from DTU's website (DTU, 2018). All of the DTU models have 1 arc-minute resolution and the same reference gravity field with SSv29.1 which is EGM2008. DTU21 and SSv29.1 models were generated practically from the same available altimetry data. The computation algorithms of these models are different. DTU models use the residual sea surface heights while SSv29.1 model applies the residual slopes of the sea surface heights (Andersen & Knudsen, 2020; Sandwell et al., 2013, as cited in Abdallah et al., 2022).

Before the validation, SSv29.1 and DTU free-air gravity anomalies were interpolated to 14661 shipborne gravity points with a bilinear interpolation method by using Surfer® from Golden Software. Satellite altimetry-derived free-air gravity anomalies were compared with shipborne free-air gravity anomalies by subtracting shipborne gravity anomalies from satellite altimetry-derived gravity anomalies (Equation 1). For each comparison, statistical parameters were calculated and differences were visualized in order to implement both quantitative and qualitative analyses. As statistical parameters, minimum, maximum, mean and standard deviation (SD) values were computed.

$$\Delta g_{residual} = \Delta g_x - \Delta g_y \quad (1)$$

Δg_y : the shipborne-derived gravity anomaly
Δg_x : the satellite altimetry-derived gravity anomaly
$\Delta g_{residual}$: the residual gravity anomaly

Table 1. Characteristics of satellite altimetry gravity field models (Abdallah et al., 2022; Li et al., 2022)

Model	Year	Data	Coverage Range
SSv29.1	2019	T/P + J1 + E2 + En + J2 + C2 + Al + S3A + S3B	85°S ~ 85°N
DTU21	2021	T/P + GFO + E2 + J1 + C2 + J2 + Al + ICESat-1 + S3A + S3B	90°S ~ 90°N
DTU17	2017	T/P + GFO + E2 + J1 + C2 + J2 + Al + ICESat-1	90°S ~ 90°N
DTU15	2015	Ge + E1 + T/P + GFO + E2 + J1 + C2 + ICESat-1	90°S ~ 90°N
DTU13	2013	Ge + E1 + T/P + GFO + E2 + J1 + C2 + ICESat-1	90°S ~ 90°N
DTU10	2010	Ge + E1 + T/P + GFO + E2 + J1+ ICESat-1	90°S ~ 90°N

(Ge: Geosat, E1: ERS-1, T/P: Topex/Poseidon, J1: Jason-1, E2: ERS-2, En: Envisat, C2: Cryosat-2, Al: Saral/Altika, J2: Jason-2, S3A: Sentinel-3A, S3B: Sentinel-3B)

3. Results

In comparison with shipborne free-air gravity anomalies, SSv29.1 model has the lowest standard deviation with 24.096 mGal followed by DTU21, DTU17, DTU15, DTU13 and DTU10 models with standard deviations of 24.169, 24.371, 24.396, 24.416 and 24.444 mGal, respectively. SSv29.1 model also has the lowest mean value with -1.635 mGal followed by DTU21 with the mean value of -2.714 mGal (Table 2).

A similarity can be seen among the difference maps (Figures 2, 3, 4, 5, 6 and 7). In the difference map of the SSv29.1 model, the difference values are slightly lower near the coasts of Israel compared to the other models. For all models, the largest discrepancies with shipborne data belong to two tracks of the ship surveys. This could be due to some errors in shipborne data along these survey tracks.

Table 2. Statistics of the differences between satellite altimetry-derived free-air gravity anomalies and shipborne free-air gravity anomalies

Model	Minimum	Maximum	Mean	SD
SSv29.1	-94.880	163.931	-1.635	24.096
DTU21	-89.267	165.453	-2.714	24.169
DTU17	-92.523	163.977	-2.913	24.371
DTU15	-92.641	164.545	-2.968	24.396
DTU13	-91.563	164.407	-2.974	24.416
DTU10	-92.726	163.367	-2.908	24.444

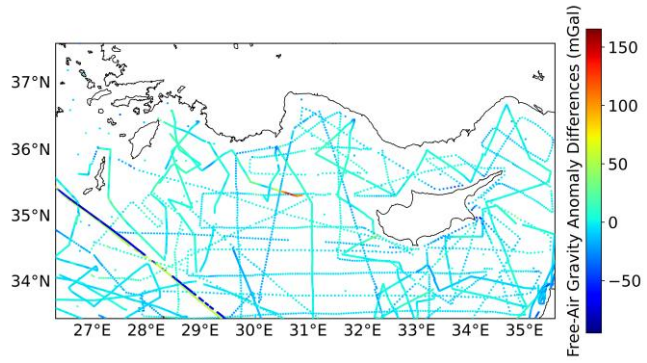

Figure 2. Differences between SSv29.1 free-air gravity anomalies and shipborne free-air gravity anomalies

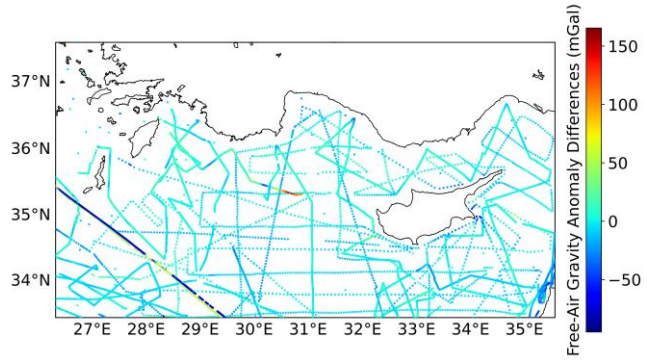

Figure 3. Differences between DTU21 free-air gravity anomalies and shipborne free-air gravity anomalies

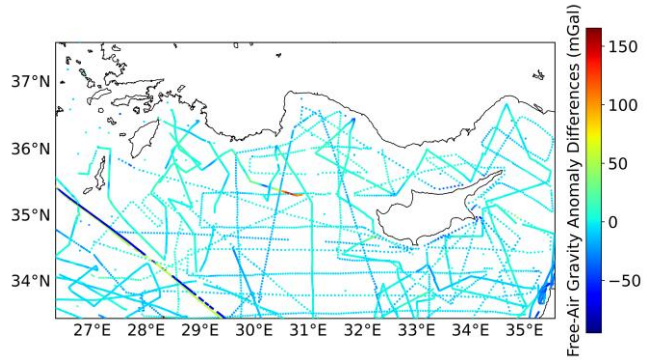

Figure 4. Differences between DTU17 free-air gravity anomalies and shipborne free-air gravity anomalies

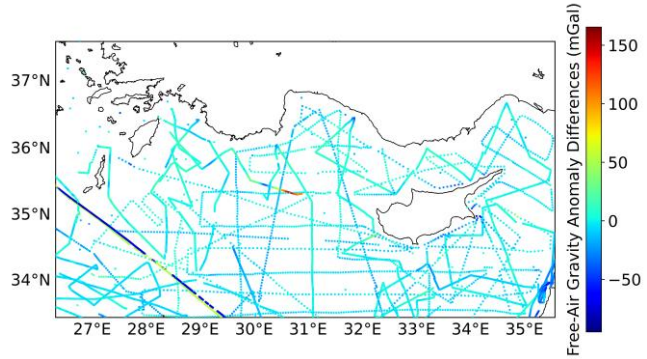

Figure 5. Differences between DTU15 free-air gravity anomalies and shipborne free-air gravity anomalies

In Figure 8, it can be seen that SSv29.1 and DTU21 model differences in comparison with the shipborne gravity data differ from each other mostly in the coastal areas.

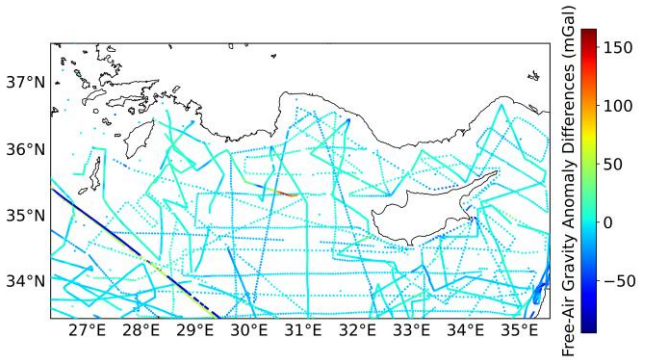

Figure 6. Differences between DTU13 free-air gravity anomalies and shipborne free-air gravity anomalies

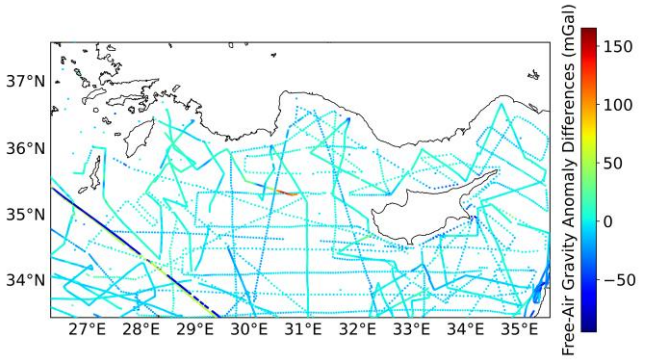

Figure 7. Differences between DTU10 free-air gravity anomalies and shipborne free-air gravity anomalies

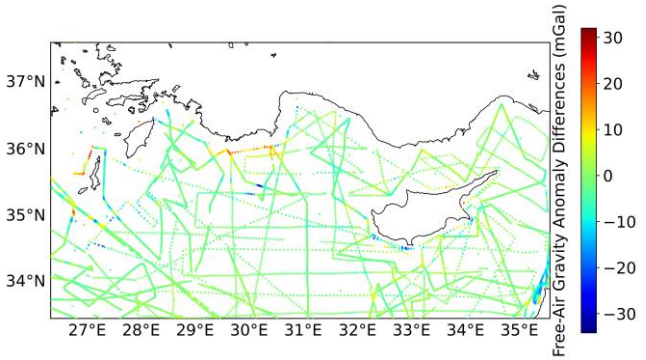

Figure 8. Differences between SSv29.1 and DTU21 models in comparison with shipborne free-air gravity anomalies

4. Discussion and Conclusion

Satellite altimetry is essential for gathering marine data for all geosciences including geodesy and oceanography. Therefore, evaluating the accuracy of satellite altimetry data is important. This study provides information about the performances of SSv29.1, DTU21, DTU17, DTU15, DTU13 and DTU10 satellite altimetry gravity models in the Mediterranean Sea. By comparing six different satellite altimetry-derived free-air gravity anomalies with shipborne free-air gravity anomalies, it is concluded that there are no statistically significant differences between the models for the study area. The reason for this can be that the models were generated from data obtained from mainly the same satellite altimetry missions.

The results of this study are preliminary for future studies and will be supported by further analyses. In future studies, it is planned to use the outputs of this

study to enhance marine geoid in coastal areas and improve the height system. Moreover, dynamic ocean topography will be modelled with satellite altimetry data. Furthermore, it is aimed to generate a combined marine geoid with shipborne gravity and satellite altimetry data in order to increase spatial resolution. Increased resolution and accuracy of the marine geoid will improve the forecasting of ocean circulation, tides, greenhouse effect and climate change, since ocean currents can be observed from sea surface heights.

Acknowledgement

This study is supported by Istanbul Technical University Scientific Research Projects (BAP) with contract number MDK-2023-44650.

References

Abdalla, S., Kolahchi, A. A., Ablain, M., Adusumilli, S., Bhowmick, S. A., Alou-Font, E., ... & Hamon, M. (2021). Altimetry for the future: Building on 25 years of progress. Advances in Space Research, 68(2), 319-363.

Abdallah, M., Abd El Ghany, R., Rabah, M., & Zaki, A. (2022). Comparison of recently released satellite altimetric gravity models with shipborne gravity over the Red Sea. The Egyptian Journal of Remote Sensing and Space Science, 25(2), 579-592.

Abulaitijiang, A., Andersen, O. B., Barzaghi, R., & Knudsen, P. (2021). Coastal marine gravity modelling from satellite altimetry–case study in the Mediterranean. Journal of Geodetic Science, 11(1), 29-37.

Andersen, O. B. (2012). Marine gravity and geoid from satellite altimetry. In Geoid determination: theory and methods (pp. 401-451). Berlin, Heidelberg: Springer Berlin Heidelberg.

Andersen, O. B., & Knudsen, P. (2000). The role of satellite altimetry in gravity field modelling in coastal areas. Physics and Chemistry of the Earth, Part A: Solid Earth and Geodesy, 25(1), 17-24.

Andersen, O.B., & Knudsen, P. (2020). The DTU17 global marine gravity field: First validation results, in: International Association of Geodesy Symposia. Springer, pp. 83–87. https://doi.org/10.1007/1345_2019_65.

Barthelmes, F. (2014). Global models. Encyclopedia of Geodesy, Springer International Publishing, 1-9.

Global Geodetic Observing System (GGOS). (n.d.). Satellite altimetry. https://ggos.org/item/satellite-altimetry/

Guo, J., Luo, H., Zhu, C., Ji, H., Li, G., & Liu, X. (2022). Accuracy comparison of marine gravity derived from HY-2A/GM and CryoSat-2 altimetry data: a case study in the Gulf of Mexico. Geophysical Journal International, 230(2), 1267-1279.

Kamto, P. G., Yap, L., Nguiya, S., Kandé, L. H., & Kamguia, J. (2022). Evaluation of latest marine gravity field models derived from satellite altimetry over the Gulf of Guinea (Central Africa) with shipborne gravity data. Studia Geophysica et Geodaetica, 66(1-2), 23-37.

Li, Z., Guo, J., Ji, B., Wan, X., & Zhang, S. (2022). A Review of Marine Gravity Field Recovery from Satellite Altimetry. Remote Sensing, 14(19), 4790.

Sandwell, D., Garcia, E., Soofi, K., Wessel, P., Chandler, M., Smith, W.H.F. (2013). Toward 1-mGal accuracy in global marine gravity from CryoSat-2, Envisat, and Jason-1. Leading Edge 32, 892–899. https://doi.org/10.1190/tle32080892.1.

Scripps Institution of Oceanography (SIO). (n.d.). Extract xyz grid - topography or gravity (SSv29.1) [Data set]. University of California San Diego. https://topex.ucsd.edu/cgi-bin/get_data.cgi

Technical University of Denmark (DTU). (2018). [DTU17, DTU15, DTU13 and DTU10] [Data set]. https://ftp.space.dtu.dk/pub/

Zaki, A., Mansi, A.H., Selim, M., Rabah, M., El-Fiky, G. (2018). Comparison of satellite altimetric gravity and global geopotential models with shipborne gravity in the Red Sea. Marine geodesy, 2018, 41, 258–269. https://doi.org/10.1080/01490419.2017.1414088.

6th Intercontinental Geoinformation Days

igd.mersin.edu.tr

Compliance analysis in polynomial surface determination with ANOVA

Ulku Kirici Yildirim[*1], **Yasemin Sisman** [1]

[1]*Ondokuz Mayis University, Engineering Faculty, Department of Geomatics, Samsun, Türkiye*

Keywords
Geoid
Polynomial geoid determination
Significant test
Regression analysis

Abstract

Geoid determination has always been an important subject of study. Geoid determination is the modelling that enables us to determine the height of a point whose position is known. While determining the geoid, it is very important to state the degree of the surface. At first sight which degree polynomial surface will be used or appropriate point distribution is unknown for the work area. A significance test should be performed to determine the most appropriate degree of polynomial with regression analysis. This study tried to determine the best fit polynomial geoid for the region where Ondokuz Mayis University is located in Samsun.

1. Introduction

The geoid determination is the most important problem for scientist interested in the earth. There are a lot of areas interested in geoid like geodesy, geophysics, geography etc. (Akçın, 2001). The geoid called the surface closed the average sea surface and formed by the combination of the points have got sea level (Sjöberg, 2023). The geoid is a complex surface and it is not easy defined as mathematically. In the geodesy the measurements on the physical earth, but the calculation of measurements is done on the reference surface (Bolat, 2011).

2. Method

2.1. The determination of the best suitable polynomial

This method is the most widely used surface fitting procedure. The function of surface is determined with basic definition of orthogonal polynomials: (Cakır, Yilmaz, 2014).

$$N_{(x,y)} = \sum_{i=0}^{m} \sum_{\substack{j=k-i \\ i=0}}^{k} a_{ij} x^i y^j \qquad (1)$$

where (x, y) is the position coordinates of points, aij the constants of the polynomial and m the order of the chosen polynomial. 2nd order polynomial equation can be written for the polynomial:

$$N_{(x,y)} = a_{00} + a_{01}y + a_{10}x + a_{02}y^2 + a_{11}xy + a_{20}x^2 \qquad (2)$$

Equation 2, the measurement and unknown numbers are equal to the point and constants number. If the measurement number (n) is bigger than the unknown number (u), the solution must be realized by using adjustment procedure. When the Equation (2) are designed according to indirect measurement adjustment mathematical model, the following equations are obtained:

$$V = AX - \ell \qquad P_{ll} = Q_{ll}^{-1} \qquad X = \begin{bmatrix} a_{00} \\ a_{01} \\ a_{10} \\ a_{02} \\ a_{11} \\ a_{20} \end{bmatrix} \quad A = \begin{bmatrix} 1 & y_1 & x_1 & y_1^2 & x_1y_1 & x_1^2 \\ 1 & y_2 & x_2 & y_2^2 & x_2y_2 & x_2^2 \\ . & . & . & . & . & . \\ . & . & . & . & . & . \\ 1 & y_n & x_n & y_n^2 & x_ny_n & x_n^2 \end{bmatrix} \quad \ell = \begin{bmatrix} N_1 \\ N_2 \\ . \\ . \\ N_n \end{bmatrix} \qquad (3)$$

This model can be solved by objective function of the least square adjustment method. The unknown parameters are obtained following equation (Sisman, 2014).

$$X = \left(A^T PA\right)^{-1} A^T P\ell \qquad (4)$$

The root mean square error formula as follows;

* **Corresponding Author**

*(ulku.kirici@omu.edu.tr) ORCID ID 0000 – 0002 – 3569 – 4482
(ysisman@omu.edu.tr) ORCID ID 0000 – 0002 – 6600 – 0623

Cite this study

Kirici Yildirim U, & Sisman Y (2023). Compliance analysis in polynomial surface determination with ANOVA. Intercontinental Geoinformation Days (IGD), 6, 228-232, Baku, Azerbaijan

$$m_0 = \sqrt{\frac{V^T PV}{n-u}} \quad (5)$$

The measurement group has got the outliers inevitably. These outliers can adversely affect the adjustment. Therefore, the outlier detection test must be done to determine the outliers' measurements, (Aksoy, 1984; Ayan, 1992; Uzun 2003; Bayrak, 2003; Teke and Yalçınkaya, 2005; Bektaş, 2005, Sisman et al. 2012). The outlier detection test is realized according to hypothesis is used for outlier detection. The test size is calculated by using the residuals of measurements and their standard deviation.

2.2. Regression analysis and ANOVA

Regression analysis involves identifying the relationship between a dependent variable and one or more independent variables. It is one of the most important statistical tools which is extensively used in almost all sciences. A model of the relationship is hypothesized, and estimates of the parameter values are used to develop an estimated regression equation. Various tests are then employed to determine if the model is satisfactory. Model validation is an important step in the modelling process and helps in assessing the reliability of models before they can be used in decision making (Ostertagova, 2012).

The degree of the polynomial was determined by regression analysis in the MiniTab program. MiniTab is data analysis, statistical and process improvement software tool used by organizations worldwide to improve quality and reduce costs. Minitab provides users with tools to perform statistical analysis, including hypothesis testing, regression analysis, and ANOVA. Additionally, Minitab provides various graphical tools to help users visualize data (Guide to the BASIC Programming Language, 03.06.2023).

Analysis of variance (ANOVA) is a technique originally developed by Fisher (1925). It has widespread applications. Its purpose is to predict a single dependent variabla on the basis of one or more predictor variables and to establish whether those predictors are good predictors (Cardinal and Aitken, 2013). ANOVA is a statistical test used to analyze the difference between the means of more than two groups. A one-way ANOVA uses one independent variable, while a two-way ANOVA uses two independent variables. One-way ANOVA is used when you have collected data about one categorical independent variable and one quantitative dependent variable. The independent variable should have at least three levels. ANOVA uses the F test for statistical significance. This allows for comparison of multiple means at once, because the error is calculated for the whole set of comparisons rather than for each individual two-way comparison (which would happen with a t test). The F test compares the variance in each group mean from the overall group variance. If the variance within groups is smaller than the variance between groups, the F test will find a higher F value, and therefore a higher likelihood that the difference observed is real and not due to chance (Büyüköztürk, 2012).

3. Results

In this study, a data set of 1765 points related to Ondokuz Mayis University was used. The points have X,Y,Z coordinates.

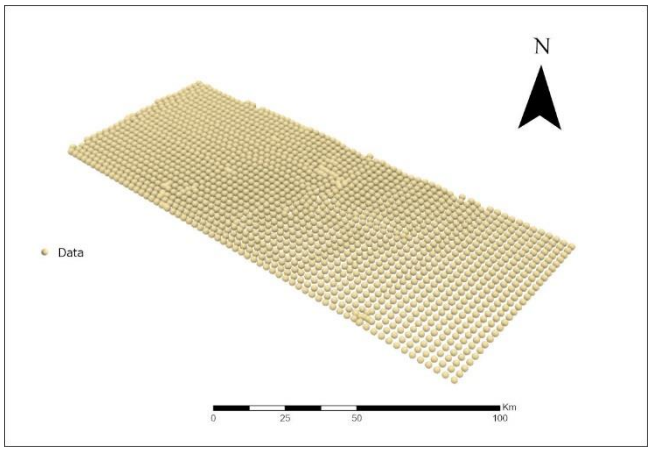

Figure 1. Data set

The data set was first tested for significance with regression analysis using the Minitab program. Polynomial degrees are tested. As a result of the regression analysis, the match and significance of the model were examined.

Then outlier measurement test was performed with the data set. The test was repeated beyond the outlier points were removed from the data set. This process was repeated until there were no outlier measurements.

3.1. The determination of the best polynomial

Firstly, the regression equation in the Minitab program was chosen as a 1st degree polynomial. The model has been found to be % 38.30 compatible. All the variables in the polynomial equation were significant.

Analysis of Variance

Source	DF	Adj SS	Adj MS	F-Value	P-Value
Regression	2	97,00	48,5009	548,45	0,000
X	1	82,66	82,6578	934,71	0,000
Y	1	13,12	13,1179	148,34	0,000
Error	1762	155,82	0,0884		
Total	1764	252,82			

Model Summary

S	R-sq	R-sq(adj)	R-sq(pred)
0,297375	38,37%	38,30%	38,16%

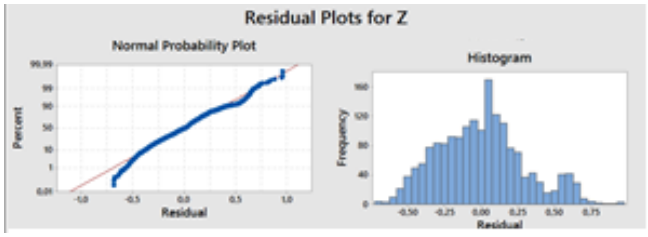

Figure 2. 1st degree polynomial regression equation

The regression equation was chosen as a 2 nd degree polynomial. The model has been found to be % 87,46 compatible. All the variables in the polynomial equation were significant.

Analysis of Variance

Source	DF	Adj SS	Adj MS	F-Value	P-Value
Regression	5	221,202	44,2405	2461,34	0,000
X	1	84,136	84,1357	4680,93	0,000
Y	1	13,087	13,0867	728,08	0,000
X*X	1	15,929	15,9295	886,24	0,000
Y*Y	1	6,925	6,9245	385,25	0,000
X*Y	1	0,086	0,0865	4,81	0,028
Error	1759	31,617	0,0180		
Total	1764	252,819			

Model Summary

S	R-sq	R-sq(adj)	R-sq(pred)
0,134068	87,49%	87,46%	87,42%

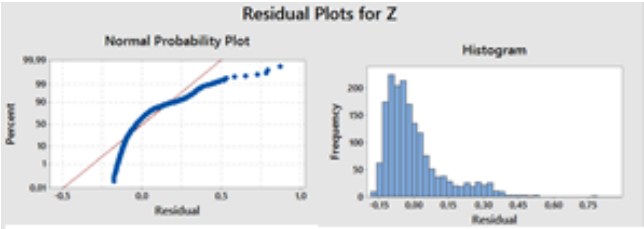

Figure 3. 2nd degree polynomial regression equation

The regression equation was chosen as a 3rd degree polynomial. The model has been found to be % 89,47 compatible. The xy^2 variable in the polynomial equation was found to be insignificant.

Analysis of Variance

Source	DF	Adj SS	Adj MS	F-Value	P-Value
Regression	9	226,338	25,1487	1666,70	0,000
X	1	14,702	14,7017	974,34	0,000
Y	1	6,590	6,5904	436,77	0,000
X*X	1	16,040	16,0401	1063,04	0,000
Y*Y	1	6,749	6,7493	447,30	0,000
X*Y	1	0,097	0,0973	6,45	0,011
X*X*X	1	0,269	0,2693	17,85	0,000
Y*Y*Y	1	0,224	0,2245	14,88	0,000
X*X*Y	1	0,108	0,1078	7,15	0,008
X*Y*Y	1	0,007	0,0074	0,49	0,484
Error	1755	26,481	0,0151		
Total	1764	252,819			

Model Summary

S	R-sq	R-sq(adj)	R-sq(pred)
0,122837	89,53%	89,47%	89,43%

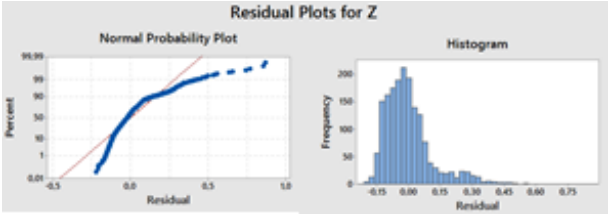

Figure 4. 3rd degree polynomial regression equation

Analysis of Variance

Source	DF	Adj SS	Adj MS	F-Value	P-Value
Regression	8	226,331	28,2913	1875,53	0,000
X	1	30,058	30,0579	1992,64	0,000
Y	1	14,907	14,9072	988,25	0,000
X*X	1	16,047	16,0466	1063,78	0,000
Y*Y	1	6,749	6,7489	447,41	0,000
X*Y	1	0,099	0,0990	6,56	0,010
X*X*X	1	0,733	0,7333	48,61	0,000
Y*Y*Y	1	1,746	1,7464	115,77	0,000
X*X*Y	1	0,778	0,7778	51,56	0,000
Error	1756	26,488	0,0151		
Total	1764	252,819			

Model Summary

S	R-sq	R-sq(adj)	R-sq(pred)
0,122819	89,52%	89,48%	89,44%

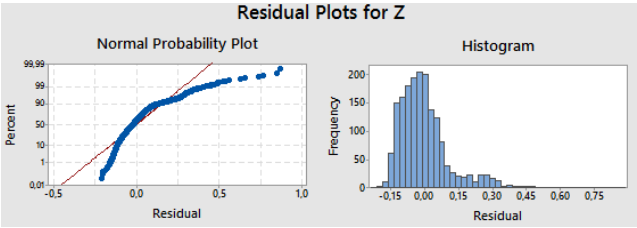

Figure 5. 3rd degree polynomial (without xy2) regression equation

Analysis of Variance

Source	DF	Adj SS	Adj MS	F-Value	P-Value
Regression	13	231,950	17,8423	1497,05	0,000
X	1	13,180	13,1795	1105,82	0,000
Y	1	27,229	27,2292	2284,66	0,000
X*X	1	1,260	1,2604	105,76	0,000
Y*Y	1	3,774	3,7744	316,69	0,000
X*Y	1	0,023	0,0232	1,95	0,163
X*X*X	1	0,220	0,2199	18,45	0,000
Y*Y*Y	1	0,296	0,2956	24,81	0,000
X*X*Y	1	0,521	0,5206	43,68	0,000
X*X*X*X	1	0,000	0,0004	0,03	0,862
Y*Y*Y*Y	1	0,119	0,1188	9,97	0,002
X*X*X*Y	1	0,028	0,0280	2,35	0,125
X*X*Y*Y	1	0,013	0,0130	1,09	0,296
X*Y*Y*Y	1	0,021	0,0212	1,78	0,182
Error	1751	20,869	0,0119		
Total	1764	252,819			

Model Summary

S	R-sq	R-sq(adj)	R-sq(pred)
0,109171	91,75%	91,68%	91,64%

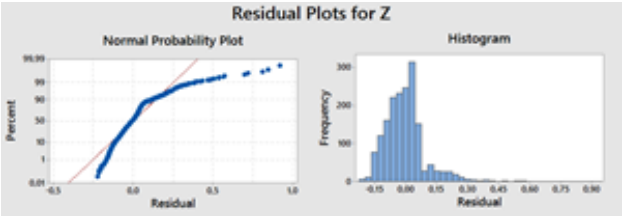

Figure 6. 4th degree polynomial regression equation

The variable xy^2 in the 3rd degree polynomial equation was removed from the equation and the regression analysis was repeated. The model has been found to be % 89,48 compatible. All the variables in the polynomial equation were significant.

The regression equation was chosen as a 4th degree polynomial. The model has been found to be % 91,68 compatible. The xy, x^2y^2, x^3y, xy^3, x^4 variable in the polynomial equation was found to be insignificant.

The variable xy, x^2y^2, x^3y, xy^3, x^4 in the 4th degree polynomial equation was removed from the equation and the regression analysis was repeated. The model has been found to be % 90,67 compatible. All the variables in the polynomial equation were significant.

3.2. Outlier measurement test

The polynomial function was obtained from 1 to 4 in order by using an adjustment solution according to the least square method. The outlier detection was realized in all solutions until there were no outlier measurements in the data. When the 1st order polynomial equation is used, 8 outlier measures are found. The root mean square error was calculated as 0.2921 m.

When the 2nd order polynomial equation is used, 353 outlier measures are found. The root mean square error was calculated as 0.0454 m.

When the 3rd order polynomial equation is used, 439 outlier measures are found. The root mean square error was calculated as 0.0266 m. When the xy^2 variable was removed from the 3rd degree polynomial equation and the outlier measurement test was repeated and 439 outlier measurement were found. The root mean square error was calculated as 0.0268 m.

When the 4th order polynomial equation is used, 403 outlier measures are found. The root mean square error was calculated as 0.0261 m. When the xy, x^3y, x^2y^2, xy^3, x^4 variables were removed from the 4th degree polynomial equation and the outlier measurement test was repeated and 284 outlier measurement were found. The root mean square error was calculated as 0.0414 m.

4. Discussion

Table 1. Significant test results

Polynomial Degree	Model fit	Insignificant Coef.
1st degree	%38,30	-
2nd degree	%87,46	-
3rd degree	%89,47	xy^2
3rd degree_withoutxy^2	%89,48	-
4th degree_withoutxy^2	%91,68	xy,x^3y,x^2y^2,xy^3,x^4

Table 2. Outlier Measurement test results and calculated mo values

Polynomial Degree	Outlier Point	m_o(m)
1st degree	8	0,2921
2nd degree	353	0,0454
3rd degree	439	0,0266
3rd degree_withoutxy^2	439	0,0268
4th degree_withoutxy^2	403	0,0261

5. Conclusion

In this study, it was tried to determine the appropriate polynomial surface model Ondokuz Mayis University in Samsun. 1765 points were used in the application. Firstly, the significance of the polynomial was tested using regression analysis. Then, an outlier measurement test was performed and m_o was compared. As a result of these process, it was decided that it would be appropriate to use the 3rd degree polynomial with the xy^2 variable removed from the equation as the surface.

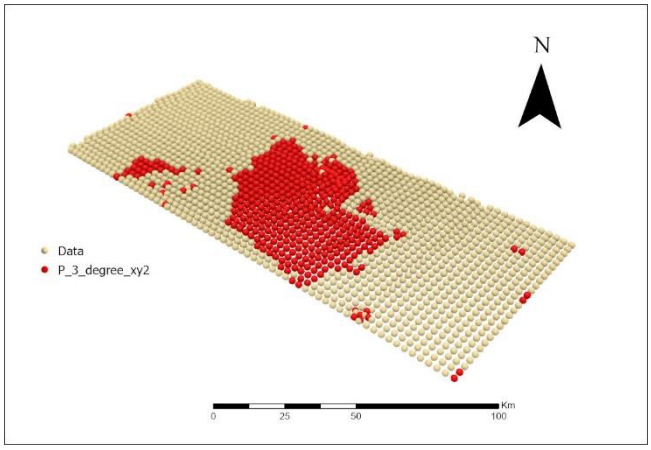

Figure 7. Outlier points in fit polynomial surface

It was observed that there was no big alteration in m_0 values after the 3rd degree. In this case, it is decided that the best suitable geoid determination function was the 6th order polynomial function for this application. The study can be improved by using different and increasing data set.

References

Akçin, H. (2001). Jeoit kavramı ve belirleme teknikleri üzerine bir inceleme. Niğde Üniversitesi Mühendislik Bilimleri Dergisi, 4(1), 37-50.

Aksoy, A. (1984). Uyuşumsuz ölçüler testi. Harita Dergisi, 93, 15-24.

Ayan, T. (1992). Uyuşumsuz ölçüler testi. Harita ve Kadastro Mühendisliği. Dergisi, (72), 38-46.

Bayrak, T. (2003). Heyelanlar için bir dinamik deformasyon ve bir dinamik hareket yüzeyi modellerinin oluşturulması. PHD Thesis, Karadeniz Teknik University, Trabzon.

Bektaş, S. (2005), Dengeleme Hesabı. Samsun: Ondokuz Mayıs Universitesi Yayınları, Samsun

Bolat, S. (2011), Lokal Jeoid Belirlemede Kullanılan Enterpolasyon Yöntemleri Samsun İli Örneği. Yüksek Lisans Tezi, Ondokuzmayıs University, Samsun.

Büyüköztürk, Ş., Kılıç Çakmak, E., Akgün, E. A., Karadeniz Ş. & Demirel, F. (2012). Bilimsel Araştırma Yöntemleri (11. Baskı). Ankara: Pegem Yayınları

Cardinal, R. N., & Aitken, M. R. (2013). ANOVA for the behavioral sciences researcher. Psychology Press.

Cakir, L., & Yilmaz, N. (2014). Polynomials, radial basis functions and multilayer perceptron neural network methods in local geoid determination with GPS/levelling. Measurement, 57, 148-153.

Guide to the BASIC Programming Language, (2023). This guide provides an overview of the built-in BASIC programming language available within SPM®,

Ostertagová, E. (2012). Modelling using polynomial regression. Procedia Engineering, 48, 500-506.

Sjöberg, L. E. (2023). On the topographic bias by analytical continuation in geoid determination. Studia Geophysica et Geodaetica, 67(1), 27-38. https://doi.org/10.1007/s11200-022-0337-4.

Sisman, Y., Dilaver, A., & Bektas, S. (2012). Outlier detection in 3D coordinate transformation with fuzzy logic. Acta Montanistica Slovaca, 17(1), 1-8

Sisman, Y. (2014). Coordinate transformation of cadastral maps using different adjustment methods. Journal of the Chinese Institute of Engineers, 37(7), 869-882.

Teke, K., & Yalçinkaya M. (2005). Yerel jeoid yüzeyinin belirlenmesinde kullanılan enterpolasyon yöntemleri. TUJK Düşey Datum Çalıştayı, Karadeniz Teknik Üniveristesi, Trabzon.

Uzun, Y. (2003). Üç boyutlu astrojeodezik dik koordinat sistemlerinde dönüşüm modelleri ve uyuşumsuz ölçülerin belirlenmesi yöntemlerinin karşılaştırılması. PHD Thesis, Karadeniz Teknik University, Trabzon.

6th Intercontinental Geoinformation Days

igd.mersin.edu.tr

Continuous decimeters level real-time Precise Point Positioning in polar high latitude region

Reha Metin Alkan [1], **Mahmut Oğuz Selbesoğlu** [1], **Hasan Hakan Yavaşoğlu** [1], **Bilal Mutlu** [1]

[1] *Istanbul Technical University, Faculty of Civil Engineering, Department of Geomatics Engineering, Istanbul, Türkiye*

Keywords
Polar region
Marine survey
Real-time Kinematic GNSS
PPP

Abstract

In this article, the usability and accuracy assessment of the real-time Precise Point Positioning (PPP) technique for dynamic positioning in application areas with difficult atmospheric and topographic conditions, such as polar regions, has been investigated. Within this frame, kinematic Global Navigation Satellite System (GNSS) data collected during the ship voyage in the Southern Ocean region for the 6th Turkish Antarctic Expedition in 2022 was used. The GNSS data were collected over approximately 9 hours with a 1 Hz sampling rate by tracking all available satellite constellations. The data were processed using Net_Diff GNSS in-house processing software with a PPP solution with an ambiguity resolution (PPP-AR solution) approach using real-time products in the real-time Precise Point Positioning (RT-PPP) mode. The State Space Representation (SSR) products were retrieved from Centre National D'Etudes Spatiales / Centre for Space Studies (CNES) Analysis Center. The results showed that the real-time GNSS PPP solution provided a cm to dm level of accuracy. The overall results obtained from the study showed that the RT-PPP technique is an alternative to the relative method in challenging high-latitude regions. The results of the study will also contribute to many researchers who will work in the polar regions and make a meaningful contribution to the limited literature.

1. Introduction

Different types of human activities in the polar regions, including the Arctic and Antarctic regions, are increasing day by day. As a result, the positioning performance of GNSS in these regions attracts more attention, and its use with different approaches is becoming widespread. The real-time centimetre-level position information has critical importance in many scientific and practical applications carried out in these regions, including precise navigation, hydrographic surveying, rig positioning, offshore platform survey, geotechnical surveying, geohazard assessment, marine construction, pipeline, and cable layout, glacial erosion monitoring, environmental mapping, and assessment, seismology, and so on. To fulfill the positioning needs in these applications, the GNSS technique has been widely used. The method has gained immense popularity owing to its ease of application, provided by its high level of accuracy. GNSS can be used at any time of the day and in all weather conditions, even in temperatures as low as -40°C and below. This makes it a highly reliable and versatile method for positioning and navigation. Furthermore, almost the 24/7/365-day measurement capability of GNSS and its ability to operate with minimal personnel requirements make it a highly efficient and cost-effective tool. As a result, the GNSS has been widely adopted across various domains, including land, sea, and air applications, where accurate positioning and navigation are critical.

The possible highest level of accurate positioning can be provided with conventional relative techniques, both in post-process or real-time modes. Indeed, this method provides reliable, robust, and highly accurate positioning. However, in order to apply the relative method, an additional measurement must be made at reference station(s) with known coordinates, and an additional effort needs to transmit the corrections for real-time applications. In the case of post-processing, GNSS data processing software and an expert user are also required. The land-based reference station requirement is an important limitation in measurements made more than hundreds of kilometres away from shores, especially for remote marine areas like open seas and oceans. As known, the accuracy of the relative GNSS positioning is affected by the baseline length. Because in

* **Corresponding Author**

*(alkanr@itu.edu.tr) ORCID ID 0000-0002-1981-9783
(selbesoglu@itu.edu.tr) ORCID ID 0000-0002-1132-3978
(yavasoglu@itu.edu.tr) ORCID ID 0000-0002-3139-4327
(mutlubil@itu.edu.tr) ORCID ID 0000-0002-9763-0345

Cite this study

Alkan, R. M, Selbesoglu, O, Yavasoglu, H. H, & Mutlu, B. (2023). Continuous decimeters level real-time Precise Point Positioning in Polar high latitude region. Intercontinental Geoinformation Days (IGD), 6, 233-237, Baku, Azerbaijan

remote areas such as the polar region, where the lack of GNSS networks consisting of points with sufficient density, sparse or low-density reference stations, environmental constraints in the establishment of new ones, the number of logistics problems, extreme atmospheric and weather conditions are limited to the usability of the conventional relative technique in high latitude regions. It should be noted that distance-dependent errors induced by the atmospheric and orbital errors cannot be minimized by establishing long baselines in relative technique. In this method, as the distance between the rover and its reference receiver increases, the positioning accuracy decreases. Furthermore, more than thousands of km baseline-length are too much in order to fix ambiguities for obtaining cm-level accuracy. Depending on all these issues, the relative method may turn into an ineffective method with very low performance in this challenging geography.

The Precise Point Positioning (PPP) technique, which has almost become a standard GNSS positioning tool, stands out as an important alternative with its ease of application and accuracy close to that of the relative method. The fact that the method needs precise orbit and clock data together with GNSS data collected with only one receiver has made the PPP an effective positioning tool used in many different fields. The PPP is not affected by baseline-dependent errors like in relative technique due to not requiring reference station data. This provides the usability of this technique anywhere in the world freely. In remote areas such as the Arctic and Antarctic, it is much more economical to log raw GNSS observations and process them with the PPP technique for accurate 3D positioning rather than using a reference station or a control network.

However, despite all this, the most important shortcoming of the PPP technique is that it needs a long convergence time (typically 20-30 minutes or more) (Qu et al., 2023). This requirement has been a serious restriction for the use of the PPP technique in RT applications (An et al., 2023). However, with the advent of the 'IGS-RTS Project', real-time precise products started to be produced by many Analysis Centres (ACs) under the umbrella of IGS. This provides the emerging real-time PPP (RT-PPP) technique as a combination of PPP and Real-Time Kinematic (RTK) methods. The RT-PPP technique has been widely used in many static and kinematic applications with cm-dm level accuracy by using only one receiver's data without the need for any additional reference station (Abdallah et al. 2016; Wang et al. 2018; Monico et al. 2019; Di et al. 2020; Di et al. 2022; Savchyn et al. 2023; Yu et al. 2023). Although there are many studies on the performance of RT-PPP in mid and lower-latitude regions, there are very few studies on the real-time positioning performance of the technique in real marine remote area applications.

In this study, GNSS data collected during a ship voyage in the Southern Ocean (South Polar Region) were used. The data were processed in simulation mode (as if it were a real-time application) using real-time precise products (precise satellite clock and orbit corrections, biases, and other necessary data) provided by CNES, and real-time PPP coordinates were obtained. Finally, the performance analysis of the method was made by comparing the PPP-derived coordinates with the reference trajectory.

2. Field Kinematic Test

2.1. Data collection

To assess the accuracy performance of the RT-PPP technique, a kinematic GNSS data set collected with a 72.05 m long and 12.50-meter-wide research ship named Betanzos sailing in the Southern Ocean within the scope of the 6th Turkish Antarctic Expedition was used. The GNSS data collected on February 07, 2022, has an occupation time of approximately 9 hours in a 1-second measurement interval by observing from all available GNSS satellites. In the study, CHCNAV i90 Pro geodetic GNSS receiver was used, which was mounted on the ship deck. The i90 Pro receiver is capable of GPS, GLONASS, Galileo, and BeiDou satellites' observations with its 336 channels. The stated accuracy is given as 2.5 mm + 1 ppm RMS (pos.), 5 mm + 1 ppm RMS (height) with post-processing kinematics (PPK) under the open sky, without multipath, optimal GNSS geometry and atmospheric condition. In the time period when the measurements were collected, the ship sailed at an average speed of appr. 15 kph. The surveying area and kinematic test measurement are given in Figure 1 (Britannica, 2023 and Google Earth).

Figure 1. The Kinematic test measurement

2.2. Data processing

The real-time PPP coordinates of each measurement epoch (total 32,638 epochs) were calculated by processing the kinematic GNSS observations, Ephemeris Products (CNES/POD Products-CNT), and State Space Representation (SSR) precise products produced by IGS-RTS CNES Analysis Centre. The used CNES products include the real-time orbit, clock corrections, and the code and phase biases (CNES/POD Products-CNT). All calculations were carried out with Net_Diff v.1.14 software developed at the GNSS Analysis Centre of Shanghai Astronomical Observatory, Chinese Academy of Sciences. Net_Diff supports all signals of GPS, GLONASS, Galileo, and BeiDou satellite systems

operating globally, as well as QZSS and IRNSS serving on a regional basis, for all single, dual, and triple frequency multi-GNSS observations (Zhang et al. 2020). The software can process the GNSS data in different ways, including RTK, PPP, PPP-AR, and PPP-RTK approaches. The software is open source on GitHub and can be downloaded at the address of http://202.127.29.4/shao_gnss_ac/Net_diff/Net_diff.html.

Although the GNSS data were collected from all satellite constellations through the measurements, only a combination of GPS (G), GLONASS (R), and BeiDou (C) observations were used. As data processing strategy for RT-PPP solution in Net_Diff v1.14 software, raw code and phase observations with undifferenced-uncombined version was processed based on kinematic RT-PPP with Ambiguity Resolution (AR) in simulation mode. According to the ambiguity fix percentage ratio results, it was found that only a few ambiguities were resolved with a ratio of 33%. Due to this low rate, the PPP-AR solution was considered to make a limited contribution to improving the results. It should be noted that the coordinates of a kinematic trajectory were estimated with forward and backward processing strategies. The priori troposphere was modelled based on Saastamoinen global model. Also, the ionosphere and wet troposphere were modelled by software, and Vienna Mapping Function (VMF1) model was used for troposphere mapping. In order to obtain the highest level of accuracy, phase wind-up, solid earth tide, and relativistic effects, corrections were applied, and Kalman Filter was used as an estimator. Besides, phase center offset values were obtained from igs14.atx file. Finally, the kinematic coordinates of the ship were obtained in the ITRF2014 reference frame.

The number of used satellites, PDOP values, and sky plot were plotted in Figure 2.

In order to demonstrate the performance of the method and to determine the provided accuracy, the reference trajectory was calculated within cm-level accuracy by resolving the carrier-phase ambiguities with the relative GNSS technique. For this purpose, a commercial software, CHCNAV Geomatics Office Software 2.0 (CGO 2.0), was used. The coordinates obtained from the RT-PPP solution were compared with the relative solutions (i.e., reference trajectory) for the horizontal position (2D) and height (Up) components for each measurement epoch and were plotted as a time series in Figure 3.

The differences in Figure 3 were summarized with accuracy measures, i.e., Standard Deviation (Std.Dev.) and Root Mean Square Error (RMSE). The calculated values were given in Table 1.

Table 1. Statistical results

	Δn (cm)	Δe (cm)	Δ2D Pos. (cm)	ΔUp (cm)
max.	110	96	140	60
min.	-9	-138	0	-106
mean	4	5	16	16
Std.Dev.	7	17	11	14
RMSE	8	18	19	21

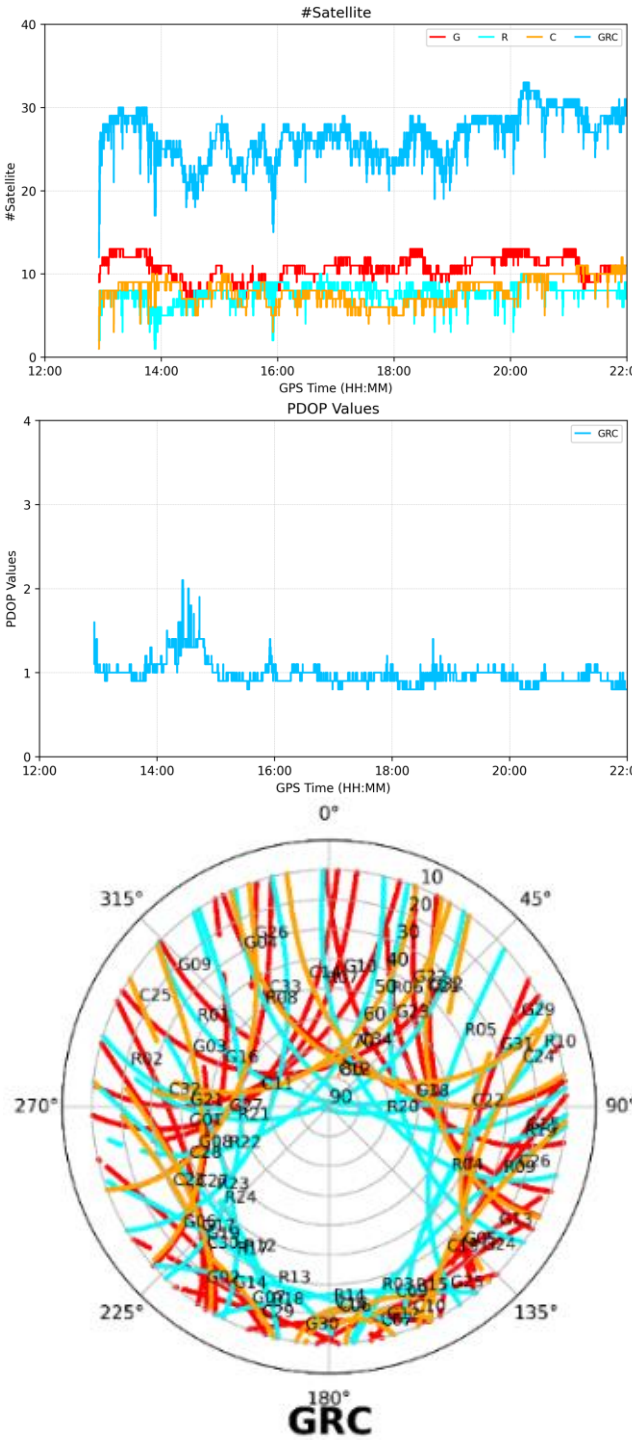

Figure 2. Satellite number (up), PDOP (middle), and sky plot (bottom)

3. Results and Discussions

In general, multi-constellation PPP significantly increased the number of satellites, and this improved the availability and reliability of positioning results (Zhao et al., 2022). This was also the case in our study. According to Figure 2, it was seen that the number of satellites for the multi-GNSS solution (GRC solution) increased significantly compared to the single-constellation systems. The mean number of observed satellites were found as 11, 8, 8, and 27 for G-alone, R-alone, C-alone, and GRC combination, respectively. In general, it was seen that the number of satellites and the PDOP value were inversely proportional; in other words, the PDOP value

improved as the number of satellites increased. In the high latitude areas, the satellites were generally observed at lower elevation angles and over a shorter continuous period due to the GNSS orbit characteristics. Thus, the multi-GNSS observations increased the signal availability, and depending on this, positioning accuracy and reliability were improved.

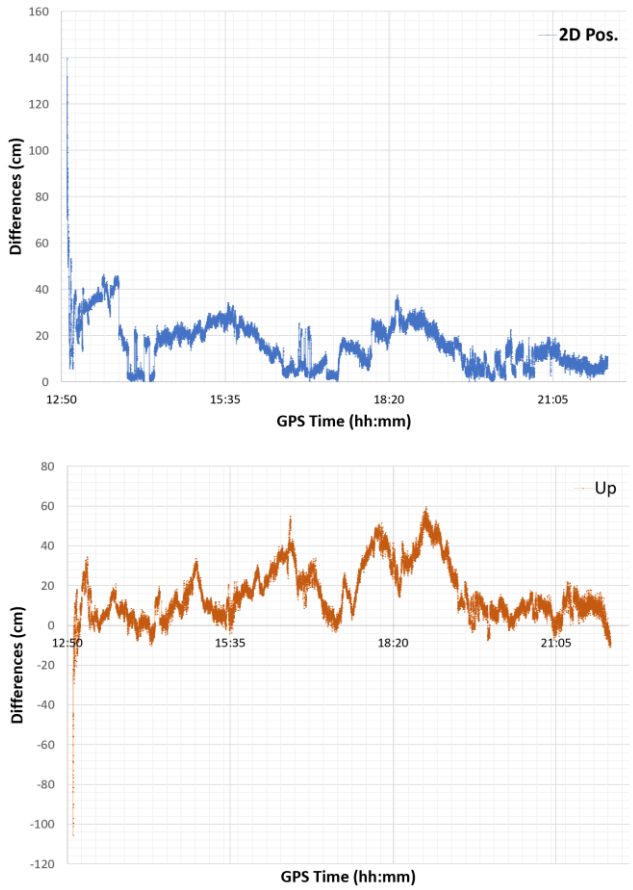

Figure 3. Comparison of the coordinates between RT-PPP and relative GNSS solutions

The results in Figure 3 showed that the multi-GNSS RT-PPP solution produced centimetre to decimetre level coordinate differences after the convergence period. The mean differences were found 16 cm for both 2D position and height components. Although this performance was generally well enough in such challenging conditions, the RT-PPP positioning accuracy in the high-latitude polar regions was found worse than that of medium and low-latitude regions. The most likely reasons for this were the configuration of the observed satellites, spatial geometric distribution of the observed GNSS satellite configuration, observing the satellites at low elevation angles, severe weather conditions, and atmospheric effects (mainly ionospheric effect).

Concerning accuracy, the RMSE of the RT-PPP solution were found as 19 cm in 2D horizontal and 21 cm in height components. As depicted in Table 1, the Standard Deviations (Std.Dev.) were found slightly better than the RMSE values as 11 cm and 14 cm for 2D horizontal and height components. The RMSE and Std.Dev. of the north-south components were found better than that of the east-west.

Due to the fact that PPP does not need base station data, the baseline length bias is not an issue like in the relative technique. Unlike the relative positioning method, the RT-PPP technique does not require additional GNSS data. So that, it has become a viable alternative to the conventional relative GNSS method.

4. Conclusion

The main goal of this paper was to evaluate the performance of the real-time PPP (RT-PPP) technique in high-latitude areas. For this purpose, a realistic kinematic test was carried out in the Southern Ocean, and 9 hours of kinematic GNSS data was collected. The dataset was processed with Net_Diff GNSS processing software in real-time mode. The overall results obtained from the study showed that the RT-PPP technique provides a centimetre to decimetre level of positioning accuracy in dynamic applications, especially for remote marine applications, without the need for additional GNSS reference data efficient and cost-effective way. These attainable accuracies satisfied the accuracy requirement of many real-time and kinematic remote marine and related applications, including the IHO, IMO accuracy standards, and others.

The overall results demonstrated that the RT-PPP technique can be successfully used for dynamic positioning under difficult atmospheric and topographical measurement conditions of polar high-latitude regions. It was clearly seen that the RT-PPP technique produces 3D position faster, allowing users to reduce the operational costs and time, and thus also the carbon footprint of each project.

Acknowledgement

The authors gratefully acknowledge the IGS and CNES Analysis Centre for providing real-time products. Dr. Yize Zhang, the developer of Net_Diff software from the Shanghai Astronomical Observatory, China, is appreciated by the authors for providing the software. This study was carried out under the auspices of the Presidency of the Republic of Turkey, supported by the Ministry of Industry and Technology, and coordinated by TUBITAK MAM Polar Research Institute.

References

Abdallah, A. M., Abd Rabbou, M., & El-shazly, A. (2016, April). Performance evaluation of real time precise point positioning (RT-PPP) in static & kinematic modes in Egypt. In Proceedings of the Arab Institute of Navigation (AIN) 2016 Melaha International Conference and Exhibition (pp. 25-27).

An, X., Ziebold, R., & Lass, C. (2023). From RTK to PPP-RTK: towards real-time kinematic precise point positioning to support autonomous driving of inland waterway vessels. GPS Solutions, 27(2), 86. https://doi.org/10.1007/s10291-023-01428-2

Britannica, (2023). The editors of encyclopaedia. "Southern Ocean", Encyclopaedia Britannica, https://www.britannica.com/place/Southern-Ocean. Accessed 31 May 2023.

Di, M., Zhang, A., Guo, B., Zhang, J., Liu, R. & Li, M. (2020). Evaluation of real-time PPP-based tide measurement using IGS real-time service. Sensors, 20(10), 2968. https://doi.org/10.3390/s20102968.

Di, M., Guo, B., Ren, J., Wu, X., Zhang, Z., Liu, Y., Liu, Q. & Zhang, A. (2022). GNSS real-time precise point positioning in Arctic Northeast Passage. Journal of Marine Science and Engineering, 10(10), 1345. https://doi.org/10.3390/jmse10101345

Monico, J.F.G., Marques, H.A., Tsuchiya, Í., Oyama, R.T., de Queiroz, W.R.S., de Souza, M.C. & Wentz, J.P. (2019). Real time PPP applied to airplane flight tests. Boletim de Ciências Geodésicas, 25(2). https://doi.org/10.1590/s1982-21702019000200009.

Qu, L., Du, Y., Wang, H., Jiang, W. & Wang, L. (2023). Multi-constellation and multi-frequency precise point positioning with fast ambiguity resolution on a global scale. Measurement, 211, 112642. https://doi.org/10.1016/j.measurement.2023.112642

Savchyn, I., Brusak, I. & Tretyak, K. (2023). Analysis of recent Antarctic plate kinematics based on GNSS data. Geodesy and Geodynamics 14(2), 99-110. https://doi.org/10.1016/j.geog.2022.08.004

Wang, Z., Li, Z., Wang, L., Wang, X. & Yuan, H. (2018). Assessment of multiple GNSS real-time SSR products from different analysis centers. ISPRS International Journal of Geo-Information, 7(3), 85. https://doi.org/10.3390/ijgi7030085

Yu, C., Zhang, Y., Chen, J., Chen, Q., Xu, K. & Wang, B. (2023). Performance assessment of multi-GNSS real-time products from various analysis centers. Remote Sensing, 15(1), 140. https://doi.org/10.3390/rs15010140

Zhang, Y., Chen, J., Gong, X. & Chen, Q. (2020). The update of BDS-2 TGD and its impact on positioning. Advances in Space Research, 65(11), 2645-2661. https://doi.org/10.1016/j.asr.2020.03.011

Zhao, J., An, J., Wang, Z., Ai, S., Zhu, L., & Zhang, B. (2022). Signal quality and positioning performance of GPS/BDS-3/GLONASS/Galileo in polar regions. Advances in Space Research, 69(6), 2541-2554. https://doi.org/10.1016/j.asr.2021.12.032

6th Intercontinental Geoinformation Days

igd.mersin.edu.tr

The importance of using GIS technology in conducting geographic research in the Republic of Azerbaijan

Zakir Eminov

Institute of Geography, Ministry of Science and Education, Baku, Azerbaijan

Keywords
Geographic maps
Eelectronic maps
Electronic databases
Atlas
GIS

Abstract

As there is a lot of information in modern times, the sources from which they are obtained are also wide and numerous. Maps which are considered one of the important scientific sources in geography are important among them. At present, maps prepared based on the use of GIS technology are of greater importance, and since they have a high level of information load, there are opportunities to continuously update the information. At the same time, the creation of electronic databases is an important source for the preparation of maps, as well as for the implementation of other socio-economic analyzes and measures.

1. Introduction

In modern times, there are quite a lot of information sources used in geographical research. The information collected in them is diverse and multi-disciplinary. The use of GIS tools and the preparation of maps based on them are of particular importance in the systematic collection, storage, and use of these data for various purposes.

In addition to complex indicators, most of the thematic maps are made based on information related to a field on the basis of modern technologies, electronic maps also have geographic components. At the same time, electronic databases prepared for countries or regions are also important. They can be continuously updated.

2. Method

It is very important to prepare maps and databases for various purposes using GIS technology. Methods such as statistics, historical-geographic analysis, cartography, comparison, analysis and comparison are used for activities in this field. Effective use of various software of computer technology is the basis of the conducted research. As the demands on databases and maps increase in modern times, it is necessary to use more methods.

3. Results and Discussions

In addition to physical-geographical components, objects and events with economic-geographical content can also be used in the prepared electronic maps. Collection and analysis of the information given on maps, and grouping. It is possible and relatively easy to enter and update new data every year, although providing regional analyzes has presented challenges. Such a situation creates opportunities to prepare electronic maps both for the country and at the level of regions and administrative areas. At the same time, it is possible to draw up maps in this direction and place information there in most areas of the economy.

The given data is subject to change in a short period in the maps on the use of population and labour resources. Every year, new information is published in the form of a report on births, deaths, natural growth of the population, migration, marriages and divorces, and employment structure by the State Statistics Committee. There are significant differences in their distribution across regions, and these differences are subject to change from year to year. Therefore, there is a need to change the information about the population in these types of maps.

Demographic indicators are presented in the form of groups in electronic population maps. First of all, it is

* **Corresponding Author**

*(zakir_eminov@mail.ru) ORCID ID 0000-0002-5967-0063

Cite this study

Eminov, Z. (2023). The importance of using GIS technology in conducting geographic research in the Republic of Azerbaijan. Intercontinental Geoinformation Days (IGD), 6, 238-240, Baku, Azerbaijan

possible to determine the distribution of the population by regions. Demographic indicators are prepared by groups in advance on the maps. It is possible to create databases on all the information the State Statistics Committee provides. In the population section, you can get information about its total number, as well as indicators such as gender composition, age composition, and the working-age population.

At the same time, the information given in the electronic maps shows one-year indicators and figures for 5-year periods or consecutive data of the last 5 years.

The number of salaried employees, employed population, economically active population, and the number of employees in separate economic fields are included in the data on the use of labour resources. The distribution of labour resources by administrative areas is given here, and the differences in the use of labour resources in regions are visible. Monitoring the distribution of information on the existing administrative-territorial units in Azerbaijan refers to the advantages of using electronic maps.

Electronic databases (EDBs) are one of the most important resources in conducting geographic research. Their grouping is required by the excessive amount of data in the system of geographical sciences. A variety of information and cartographic materials are required to prepare the physical-geographical and economic-geographical characteristics of each country.

Recently, research has been given a large place within the framework of administrative regions, provinces, and economic regions covering smaller territories. Analyzes in economic-geographical research are conducted in the directions of historical-geographical development, current situation and prospective development. For this purpose, the EDB is established primarily for the use of numerous information in the process of population settlement, demographic development, use of labour resources, and analysis of the development dynamics of separate areas of the economy. Information is obtained based on a survey from the SSC, individual ministries, other state institutions, and local government bodies. At the same time, it is important to compare data from different years. Therefore, it is important to collect data covering the last 20-30 years for each region, country and thematic direction.

In this regard, it is important to note the collection of information and the creation of a geographical base related to the East Zangezur economic regions of Karabakh.

Currently, the database is of great importance in the process of restoration and construction works carried out in both economic regions, the beginning of village, town and city restoration, the planning of cities and villages, how many people can be accommodated in each of them, and the determination of their number in the coming years and decades. At the same time, information in the appropriate directions is important for creating jobs, building social and cultural service facilities, how many people they serve, and meeting the demand for food and non-food products.

It should be noted that there have been problems in collecting data about these areas for many years. Since there is no permanent population, only the number of registered population in administrative areas was determined, there was no information about the activity of economic areas.

The physical and geographical conditions of Karabakh have completely changed. Because there was no population during the occupied period, there were no anthropogenic effects, and the environment was untouched by nature. At the same time, military operations have had a serious impact on the natural environment, soil, water, vegetation, animal world, and biodiversity. Long-term observations and data collection are required for their determination.

Atlas is a source of information of special importance in geography. Maps are carriers of important information, as well as the "second language" of geography. Although the preparation of the atlas is a time-consuming process, it is considered a very important scientific resource. Because general geographic atlases are compiled on the basis of information that covers all physical-geographical and economic-geographical processes and includes data from many years. Some of the collected information plays the role of the archive at the same time in the.

maps given here. It is always possible to compare new information with them. The maps that are included in the atlas and reflect the physical-geographical components reflect the situation at a specific time.

The Atlas published in Azerbaijan in 1963 is still used as an important source. First of all, there are maps of physical-geographical components here. A lot of rich information is reflected in the maps compiled on the basis of data collected over many years. Geological, geomorphological, climate, hydrographic network, land-vegetation, and Caspian Sea maps are the main sections.

The section of the Atlas that is still of great importance is the provision of maps of economic regions. On the basis of very rich data, the general geographical maps reflecting the industrial, agricultural and transport networks in economic regions are distinguished by their high scientific capacity.

It should be noted with great regret that the Atlas published in 2014 after a gap of many years does not include maps of economic regions. In addition, the Atlas contains numerous maps that take into account the results of recent research. It is possible to obtain geographical information based on the use of the Atlas, which is a collection of global physical-geographical and economic-geographical maps.

The information given in the atlases becomes obsolete in a very short time, and there is a need to update the figures. That's why the electronic version of the Atlases has recently been preferred. There are opportunities to continuously add new information to them. Therefore, new maps are acquired, their use becomes easier and their importance as a source of information increases.

4. Conclusion

– Maps are prepared as a result of all the studies conducted in the field of geography in the modern era. There are opportunities to continuously update data on existing maps using modern GIS technology. At the same

time, modern technical means allow for continuous updating of new maps.

– Electronic databases have important scientific and practical importance in modern times. They are also important sources in the preparation of maps, as there is always an opportunity to enter new information.

– Electronic maps can be prepared for most geographic components. The help of GIS technology is great in their design.

References

Demographic indicators of Azerbaijan (2018). Statistical yearbook. Baku: SSC, 2019.509 p.

Eminov, Z. N. (2005). Population of Azerbaijan (in Azerbaijani). Baku: Chirag, 560 p.

Eminov, Z., Imrani, Z., & Jafarov, S. The Current State of Foreign Trade Relations of the Republic of Azerbaijan. *Proceedıngs E-Book*, 52.

Geography of the Republic of Azerbaijan (in Azerbaijani) (2015). II volume. Baku: Europe, 327 p.

Industry of Azerbaijan – (2018). Statistical Yearbook, SSC AR. Baku: MP - 9, 349 p.

On the path of independence (2016). 25. ANAS. Baku: East-West, 382-486.

Population of Azerbaijan (2019). Statistical Yearbook. SSC AR. Baku: MP - 9, 140 p.

Regions of Azerbaijan – (2018). SSC AR. Baku: MP - 9, 786 p.

6th Intercontinental Geoinformation Days

igd.mersin.edu.tr

Determination of suitable areas for wind power plant installation in Şanlıurfa with GIS and AHP

Tacettin Ataş*[1], Abdulkadir Memduhoğlu [2]

[1]*Harran University, Graduate School of Natural & Applied Sciences, Department of Geomatic Engineering, Şanlıurfa, Türkiye*
[2]*Harran University, Faculty of Engineering, Department of Geomatic Engineering, Şanlıurfa, Türkiye*

Keywords
GIS
AHP
Wind Power Plant
Multi-Criteria Decision Analysis

Abstract

Despite the increasing energy consumption day by day, the demand for energy is also growing. Currently, energy is obtained in two different ways: renewable and non-renewable sources. Non-renewable sources cannot meet the increasing energy demand due to their limited availability. The use of non-renewable sources results in carbon emissions, posing a risk to living beings. Therefore, people have turned to renewable energy sources in search of alternative solutions. Wind energy, as one of the renewable energy sources, stands out as a clean and sustainable energy source. To harness this source, it is necessary to establish Wind Power Plants (WPP). For the efficient operation of these plants, proper site selection is crucial. In this study, Geographic Information Systems (GIS) and the Analytic Hierarchy Process (AHP) method were utilized to determine suitable areas for WPP installation in a part of Şanlıurfa province. Seven criteria were identified to be considered in determining the suitable areas for WPP, including wind speed, land use, slope, distance to power transmission lines, distance to highways, distance to active fault lines, and distance to residential areas. These criteria were compared with each other using the AHP method to establish a priority ranking. Based on this ranking, the areas suitable for WPP installation were evaluated. The evaluation results identified a total area of 42.68 km^2 as highly suitable for WPP installation in the study area.

1. Introduction

As a result of the increasing human population and the desire of people to sustain their lives at higher standards, industry and technology are rapidly advancing. Energy consumption and the need for energy are progressively increasing due to factors such as the development of industry and technology. Non-renewable energy sources like widely used fossil fuels are inadequate to keep up with this rapid change and also contribute to carbon emissions that negatively impact living organisms. Furthermore, the depletion of these resources is inevitable.

Human intellect has always sought to find a way out. The search for alternatives to meet the increasing global energy demand continues. The most important criteria in energy sources are their lack of harm to living organisms and their renewability.

Wind energy, as one of the renewable energy sources, is considered an alternative energy source. Reasons such as the absence of threats to living organisms such as carbon emissions and greenhouse gases, as well as its unlimited availability, have increased the interest in wind energy.

The use of wind energy is continuously increasing worldwide. It stands out as an effective tool in combating climate change and reducing dependence on fossil fuels.

In recent years, the use of wind energy has also been steadily increasing in our country. According to the statistical reports published by the Turkish Wind Energy Association, the installed capacity based on wind energy is provided in Figure 1, and its proportion within the total installed capacity is shown in Figure 2. It can be observed that the installed capacity based on wind energy in our country has increased by approximately 5 times in the last 10 years. Its share within the total installed capacity has also risen from 3.96% in 2012 to 10.81% in 2022 (TUREB, 2023).

* **Corresponding Author**

*(tacettinatas@gmail.com) ORCID ID 0009-0009-3931-3737
(akadirm@haran.edu.tr) ORCID ID 0000-0002-9072-869X

Cite this study

Ataş, T. & Memduhoğlu, A. (2023). Determination of suitable areas for wind power plant installation in Şanlıurfa with GIS and AHP. Intercontinental Geoinformation Days (IGD), 6, 241-244, Baku, Azerbaijan

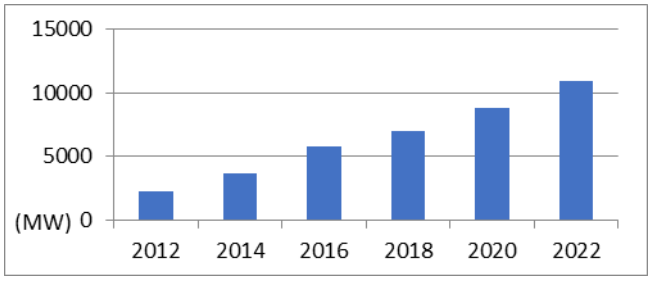

Figure 1. Installed capacity based on wind energy in Türkiye (MW)

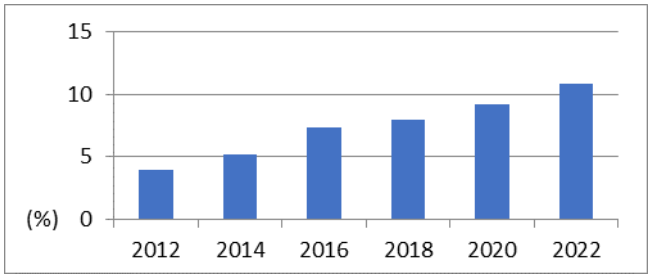

Figure 2. Proportion of wind energy in the installed capacity in Türkiye (%)

To harness wind energy, Wind Power Plants (WPP) are necessary. WPPs convert the kinetic energy of the wind into mechanical energy, which is then used to generate electricity (Hayli, 2001). These facilities consist of various wind turbines placed over large areas at different heights.

In order to obtain energy most efficiently, it is crucial to accurately determine the suitable areas for WPP installation. Environmental impacts, societal effects, geographical factors, and technical requirements should be taken into account during the site selection process. Some criteria considered in similar studies include wind speed, land use, slope, aspect, altitude, distance to residential areas, distance to power transmission lines, distance to highways, distance to airports, distance to rivers and lakes, distance to fault lines, and proximity to bird migration routes. The process of determining suitable areas involves a complex procedure that incorporates multiple disciplines.

In this study, Geographic Information Systems (GIS) were utilized, and the identified criteria were evaluated using the Analytic Hierarchy Process (AHP) method to determine suitable areas for WPP installation.

2. Method

Utilizing information systems is a fast way to process complex data and obtain final results. In this study, Geographical Information Systems (GIS) were employed to perform Multi-Criteria Decision Analysis (MCDA) using the Analytic Hierarchy Process (AHP) methodology.

The AHP method was initially developed by Thomas L. Saaty (Ekiz, Şirin, & Erener, 2022). The AHP method enables the determination of weight criteria based on priority ranking by comparing the determining criteria with each other (Saaty, 1994). AHP evaluates all criteria together and employs pairwise comparisons (Arca & Çıtıroğlu, 2020) to identify the most prioritized criteria, offering a rational and efficient approach to generate solutions (Saaty, 1994).

There are several criteria that are effective in the selection of areas for WPP installation. Since WPPs will interact with the surrounding areas, criteria that may have an impact on the environment, such as proximity to residential areas and land use, should be considered (Memduhoğlu, Özmen, Göyçek, & Kılıç, 2014). In this study, seven influential criteria have been identified. These criteria include wind speed, land use, slope, distance to power transmission lines, distance to highways, distance to active fault lines, and distance to residential areas. Due to minimal variation in altitude within the study area, it was not included in the evaluation. Furthermore, criteria such as proximity to bird migration routes, distance to airports, and distance to lakes and rivers can be considered in larger study areas but were not deemed significant criteria for this particular study area.

Once the criteria have been selected and weighted, they can be analyzed together within the GIS software to identify suitable areas for WPP installation.

2.1. Study Area and Data

The study area has been determined as a region within the boundaries of Şanlıurfa province, as depicted in Figure 3.

Figure 3. Study area

The study area consists of Şanlıurfa city settlement, partially Harran Plain, partially Tektek Mountains, forested areas, pasturelands, meadows, and mixed

agricultural lands. It has an approximate area of 2,250.74 km^2.

The summers are dry and hot, while the winters are rainy. The average wind speed varies between 3.85 m/s and 6.97 m/s at a height of 100 meters (GWA, 2023).

The data corresponding to the identified criteria in this study were obtained from various sources and adapted by cutting them according to the study area boundary. Table 1 presents the collected data.

Some of the data were used directly, while others were transformed before being utilized.

Table 1. Data types and sources of the criteria

Criteria	Data Type	Data Source
Wind Speed	Raster	Global Wind Atlas (GWA, 2023)
Land Cover	Raster	CORINE 2018 (Copernicus, 2023)
Slope	Raster	Alos Palsar DEM (ASF, 2023)
Electrical Transmission Lines	Vector	OpenStreetMap (OSM, 2023)
Highways Network	Vector	OpenStreetMap (OSM, 2023)
Live Fault Lines	Vector	Republic of Turkey, Mineral İnvestigation and Exploration General Directorate (MTA, 2023)
Residential Areas	Raster	CORINE 2018 (Copernicus, 2023)

3. Results

After determining the criteria, a comparison matrix, Table 2, was created to compare these criteria in terms of their relative importance. The comparison matrix contains values that represent the relative importance between criteria (Ömürbek & Şimşek, 2014). For example, the wind speed criterion is three times more important than the slope criterion, indicating that the weight of the wind speed criterion should be higher than the weight of the slope criterion.

All criteria were compared in this manner and assigned specific values. Based on the values obtained from the comparison matrix, the weight criteria for all criteria were determined and presented in Table 2. To assess the accuracy of the weight determination process, the Consistency Ratio (CR) was calculated, resulting in a CR value of 2%. According to Saaty's recommendation, the maximum acceptable consistency ratio is 10%. If the value exceeds this threshold, the comparison matrix needs to be reviewed and revised (Saaty, 1990).

Through the ArcGIS software, criteria were transformed, distance analysis was conducted, and reclassification processes were performed to create thematic maps for each criterion. The reclassified thematic map for the land use criterion is provided in Figure 4.

Within the study area, potential areas for wind energy installation were analyzed, and a result map, Figure 5, was created. In this map, the results were categorized into five hierarchical classes: "not suitable," "slightly suitable," "moderately suitable," "suitable," and "highly suitable."

It is observed that there is a total area of 42.68 km^2 classified as "highly suitable" for wind energy installation. The "suitable" class covers an area of 486.56 km^2, the "moderately suitable" class covers 950.42 km^2, the "slightly suitable" class covers 646.96 km^2, and the "not suitable" class covers 124.12 km^2.

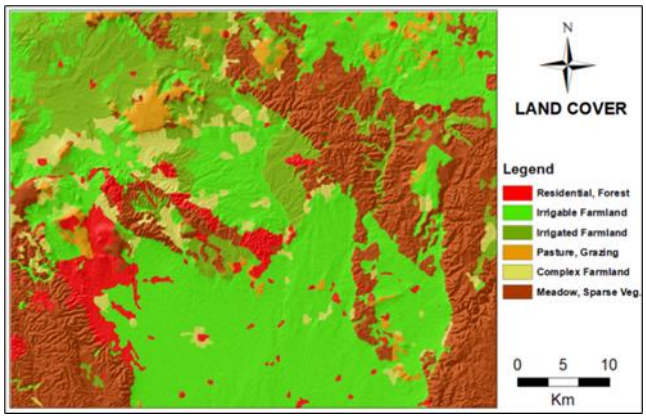

Figure 4. Reclassified land use map

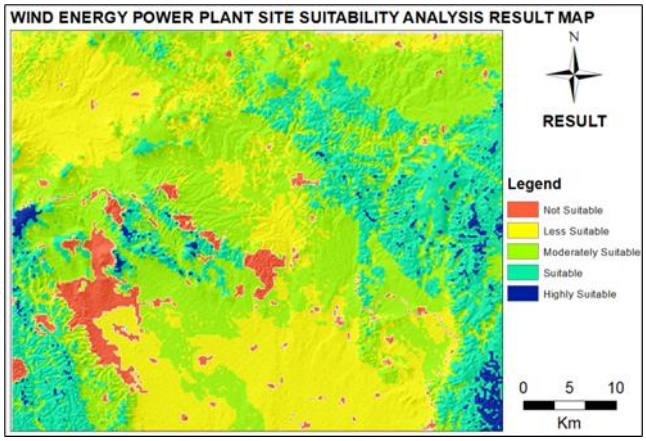

Figure 5. Suitability result map of areas for wind energy installation

4. Discussion

Upon examining the results, it is observed that the unsuitable areas for wind energy installation are mainly residential areas and forested areas, as shown in Figure 4. The most suitable areas, on the other hand, are found to be mountainous regions that are unsuitable for agriculture and classified as grasslands and pastures. Therefore, these results contribute to increasing the reliability of the analysis.

In order to install WPP in the study area, site-specific measurements need to be conducted, and information should be obtained from meteorological sources. More detailed results can be obtained by considering parameters such as wind power density, wind capacity, prevailing wind direction, and topographical factors. It is also necessary to seek support from experts in the field of WPP and individuals from various sectors (such as energy, infrastructure, etc.). Furthermore, a thorough analysis of the terrain should be conducted, taking into account biological indicators such as trees and shrubs, as well as valuable clues provided by geological features shaped by wind erosion and deposition (Memduhoğlu, Özmen, Göyçek, & Kılıç, 2014).

Table 2. Comparison matrix and criterion weight values

	Wind Speed	Land Use	Slope	Distance to Power Transmission Lines	Distance to Highways	Distance to Fault Lines	Distance to Residental Areas	Weight (%)
Wind Speed	1	2	3	4	4	5	6	34
Land Use	0,5	1	2	3	3	4	5	23
Slope	0,33	0,5	1	2	2	3	4	15
Distance to Power Transmission Lines	0,25	0,33	0,5	1	1	2	3	9
Distance to Highways	0,25	0,33	0,5	1	1	2	3	9
Distance to Fault Lines	0,2	0,25	0,33	0,5	0,5	1	2	6
Distance to Residental Areas	0,17	0,2	0,25	0,33	0,33	0,5	1	4

5. Conclusion

Based on the seven criteria determined for the study area and their calculated weight (importance) values, an analysis of suitable areas for WPP has been conducted using GIS. The analysis resulted in five different suitability classes.

In contrast to existing studies in the literature, the analysis focused specifically on identifying areas suitable for WPP within the boundaries of Şanlıurfa province.

Future studies will involve analyzing the entire Şanlıurfa province for potential WPP locations. Due to the size of the study area and the need for detailed analysis, the findings will be supported by field measurements and meteorological data. Factors such as distance to rivers and lakes, airports, bird migration routes, elevation, prevailing wind direction, aspect, wind power density, and wind capacity will be considered to enhance the analysis. Furthermore, the study will not only identify suitable areas for WPP installation but also pinpoint suitable immovable properties owned by the state. The aim is to prevent bureaucratic, legal, and social issues that may affect the WPP implementation process.

References

Arca, D., & Çıtıroğlu, H. K. (2020). Rüzgar Enerjisi Santral (RES) Yapım Yerlerinin CBS Dayalı Çok Kriterli Karar Analizi ile Belirlenmesi: Yenice İlçesi (KARABÜK) Örneği. Karaelmas Fen ve Mühendislik Dergisi, 168-176.

ASF. (2023). https://search.asf.alaska.edu/. Accessed: 5 5, 2023,

Copernicus. (2023). Copernicus. Accessed: 5 2, 2023, from https://land.copernicus.eu/

Ekiz, S., Şirin, A., & Erener, A. (2022). En uygun rüzgâr enerji santrali yerlerinin coğrafi bilgi sistemleri ile belirlenmesi: Kocaeli ili örneği. Jeodezi ve Jeoinformasyon Dergisi, 59-79.

GWA. (2023). GLOBAL WIND ATLAS. Accessed: 5 2, 2023, from https://globalwindatlas.info

Hayli, S. (2001). Rüzgâr enerjisinin önemi, Dünya'da ve Türkiye'deki durumu. Fırat Üniversitesi Sosyal Bilimler Dergisi, 1-26.

Memduhoğlu, A., Özmen, G., Göyçek, G., & Kılıç, F. (2014). Rüzgar türbini kurulacak alanlarin CBS – Çok ölçütlü karar analizi kullanilarak belirlenmesi: Davutpaşa Kampüsü. V. Uzaktan Algılama ve Coğrafi Bilgi Sistemleri Sempozyumu. İstanbul.

MTA. (2023). Maden Tetkik ve Arama Genel Müdürlüğü. Retrieved 5 5, 2023, from https://www.mta.gov.tr/

OSM. (2023). Open Street Map. Retrieved 5 5, 2023, from https://www.openstreetmap.org/

Ömürbek, N., & Şimşek, A. (2014). Analitik hiyerarşi süreci ve analitik ağ süreci yöntemleri ile online alışveriş site seçimi. Yönetim ve Ekonomi Araştırma Dergisi, 12(22), 306-327

Saaty, T. L. (1977). A scaling method for priorities in hierarchical structures. Journal of Mathematical Psychology, 234-281.

Saaty, T. L. (1990). How to make a decision: The analytic hierarchy process. European Journal of Operational Research, 9-26.

Saaty, T. L. (1994). How to Make a Decision: The Analytic Hierarchy Process. Interfaces, 24(6), 19-43.

TUREB, 2. (2023). Türkiye Rüzgar Enerjisi Birliği. Accessed: 04 28, 2023,

6th Intercontinental Geoinformation Days

igd.mersin.edu.tr

Relief morphometry as a factor of formation and spatial differentiation of highland landscapes of the major Caucasus

Ulviye Qasimova *[1]

[1] *Azerbaijan State Pedagogical University, General geography department, Baku, Azerbaijan*

Keywords
Morphometry
Relief
Hypsometry
Topography
Landscape

Abstract

The article analyzed the morphometric indicators of the topography of the highland part of the Greater Caucasus (hypsometric height, slope and aspect of topography, horizontal and vertical division). The height amplitude in this zone is high, leading to the mentioned parameters' diversity. The fact that topography plays a vital role in the formation and distribution of the landscape makes the analysis of morphometric indicators relevant in the investigated area. Landscapes spread in the mountainous zone are divided into different facies and zones depending on the slope and aspect of the topography both horizontally and vertically. The reason for this is that the topography affects climate change. Modern methods were used during the research. For this, the Digital Elevation Model of the area was processed. As a result of processing, height, slope, and aspect maps were compiled. The main goal of the research is to analyze the factors affecting the formation of the landscape, the morphometric elements of the topography based on modern methods and analyze the results. As a result of the study, it was determined that the morphometric indicators of the topography play an important role in the formation of landscapes. As a result of our analysis, it was determined that different half-types of nival, subnival, alpine, and subalpine landscape types are distributed in the research area.

1. Introduction

The relief is recognized by all researchers as the main factor in the landscape differentiation of the territory. Due to the development of digital technologies and the wide availability of remote sensing data, a detailed assessment of the relief as a landscape-forming factor has become possible. Thus, the use of digital elevation models has simplified the morphometric analysis of the relief. The relief and its parameters are recognized as the most important in the selection of natural-territorial complexes of the highest classification ranks. To identify the NTC of different levels and create a landscape map, it is necessary to analyze the relief: first of all, the distribution of heights, steepness, and exposure of slopes. Heat and water balances depend on these factors in mountainous conditions. They, in turn, directly impact the distribution of soil and vegetation cover (Budagov, 1973, 1988, Solntsev, 2001).

2. Method

Morphometric relief analysis is one of the methods of geomorphological research, in which the quantitative characteristics of landforms are studied using special measurements. Usually, the absolute and relative heights of individual landforms or their complexes, slope angles, exposure of theories, areas occupied by positive and negative forms, and some others are measured (Kirillova, 2010).

3. Results

A significant number of works are devoted to the problems of quantitative description of the relief (Kuchinskaya, 2011, Hajiyeva, 2017). Morphometric analysis of the relief today is carried out using a digital elevation model (DEM). The creation of DEMs of different resolutions has begun, which in GIS technologies perform, to a certain extent, the functions of map scales.

* **Corresponding Author**

*(qulviyesh@gmail.com) ORCID ID 0009-0000-7403-5394

Cite this study

Qasimova, U. (2023). Relief morphometry as a factor of formation and spatial differentiation of highland landscapes of the major Caucasus. Intercontinental Geoinformation Days (IGD), 6, 245-247, Baku, Azerbaijan

The territory of the high-mountainous Greater Caucasus was analyzed using the ArcGIS package based on the DEM. The Shuttle Radar topographic mission (SRTM) radar survey results, designed to build a high-precision global DEM network, were used as a basis. Its root-mean-square error is estimated at a height of about 16 m, and the accuracy of the position of the three-second grid nodes is about 20 m, while in mountainous terrain these indicators become higher. Such accuracy of the DEM corresponds to the goals set in the work.

4. Discussion

The corrected SRTM image with a resolution of about 60 m is suitable for performing morphometric analysis and building corresponding maps in a GIS environment. Image editing, related to the identification and subsequent elimination of minor errors, was carried out using the tools of the ArcGIS package and its Spatial Analyst module. The same program was used in the primary calculations and mapping. The map of slope steepness (angles of inclination of the earth's surface) was built using the Special Analyst function and its Surface analysis option. Initially, the map was obtained in raster representation and then it was converted to vector. As a result of the conversion, polygons of different steepness were obtained in the vector map of slope steepness. At the same time, a hypsometric map was initially built with given height steps, then the minimum and maximum slopes and areas of polygons were calculated by height steps. The slope exposure map was built in a similar way. According to this method, a hypsometric map and a map of the steepness of the slopes were compiled for the territory of the high-mountainous Greater Caucasus on the basis of digital elevation models. Further, thematic layers were superimposed on these maps - rock lithology (geological), distribution of climatic parameters (temperature, precipitation, moisture - Ku), hydrographic network, vegetation, soil cover, as well as available landscape maps.

Greater Caucasus major range of the Caucasus Mountains extending west-eastern for about 1200 km from the Taman Peninsula on the Black Sea to the Absheron peninsula on the Caspian Sea. Our investigation territory is a highland area of the Greater Caucasus. The territory of this area is 313486 km^2. As can be seen from the above data, the foothills occupy 35% of the entire area of the high-mountainous strip of the Caucasus (Figure 1). At the same time, altitudes 1800–2300 m - 165711 km^2 (49.9%), and 2301–3200 m - 139096 km^2 (41,9%), and above 3201 m - 26679 km^2 (8,2%). That is, in geomorphological terms, high mountains are more widely represented on the territory of the Greater Caucasus, while the middle mountains occupy a slightly smaller area.

The largest area in the low mountains is occupied by elevations of 200–400 and 400–600 m, which include the front ranges. As for the middle mountains, here the distribution of the territory is quite uniform. In the highlands (up to 3000 m), an increase in the proportion of territories with altitudes above 2500 m is noticeable, which can be explained by the presence of significant leveling surfaces both on the Skalisty Ridge and in Intramountainous Dagestan. The highest parts of the mountain structure do not occupy such a significant area. The landscapes of the foothills, low mountains, and low mountains, which rise to 1000–1200 m, are noticeable, up to 600 m, almost completely occupied by them. Territories with 600–800 m elevations gravitate towards the foothills, and with a further increase in the absolute height of the low mountains and foothills, they gradually turn into the actual mountain structure. The distribution of the territory depending on the steepness of the slopes is illustrated.

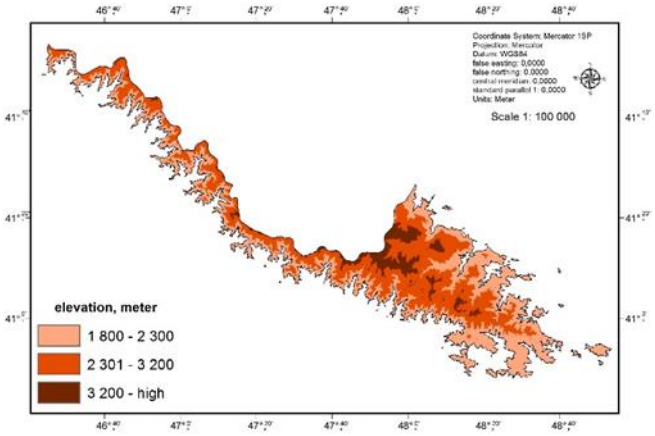

Figure 1. Hypsometric height map of the highland part of the Greater Caucasus

On the territory of the high-mountainous Greater Caucasus, there are slopes with a steepness of up to 45 °. Surfaces with a steepness of up to 10° occupy 41601 km^2 (12.5%). Geomorphologically, they correspond to the plains. In the mountainous part of the territory with such steep slopes, it is most often observed either in basins or these are leveling surfaces in rather elevated parts (mountain plateaus). Slopes with different degrees of slope (from 11^0 to 15°) occupy the largest, in comparison with other slopes - up to 48606 km^2 (14.6%). The next group of slopes is slopes of medium steepness (16–25°), occupying 120144 km^2 (36.6%). Steep slopes (26-30°) occupy 102428 km^2 (30.9%). Steep slopes (36–41°) occupy 17169 km^2 (5.2%). And, finally, sheer cliffs occupy a negligible area. As for the foothill, low-mountain, and low-mountain landscapes, here slopes with a steepness of up to 10° account for more than 50% of similar slopes that have become widespread throughout the North-Eastern Caucasus (Figure 2).

As the steepness of the slopes increases, the proportion of the territory that is located within the mountainous structure of the Greater Caucasus increases. On the whole, within foothill landscapes, a fairly significant proportion of slopes with a steepness of up to 25° is still preserved, and steeper slopes are not typical for the category of foothill, low-mountain, and low-mountain landscapes. Another important morphometric characteristic is sloping exposure (Nikolaev, 2003, Geography, 2015).

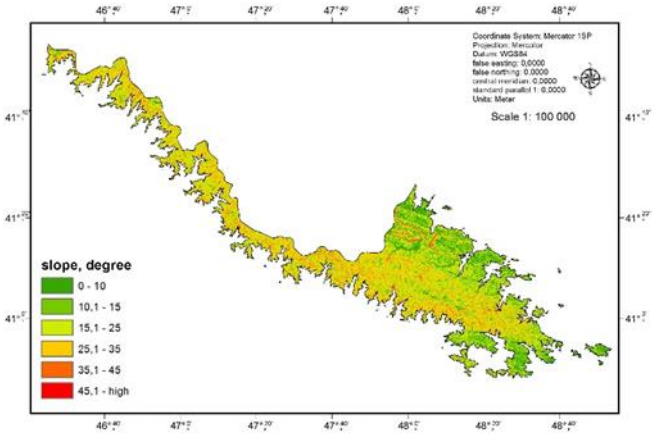

Figure 2. Slope map of the highland part of the Greater Caucasus

As can be seen from the above data, for the high-mountainous Greater Caucasus, the most characteristic are the slopes of the northern points, the total share of which is 42.9%, which is easily explained by the position of the territory on the northern macroscope of the Greater Caucasus. The slopes of the southern points account for 31.3%. From the position of atmospheric circulation, the slopes of the western points, which receive the maximum amount of precipitation in temperate latitudes, occupy more than 30% (33.2%), and the eastern ones - about 40% (39.9%). That is, the combination of these factors leads to the fact that there are more widely represented locations in which there is some lack of heat and moisture. As for foothills, low-mountain, and low-mountain landscapes, flat surfaces are absolutely typical only for foothill landscapes, since they account for 173 out of 174 km² (99.4%). The slopes of other exposures here occupy, on the whole, an area proportional to the total area (Figure 3).

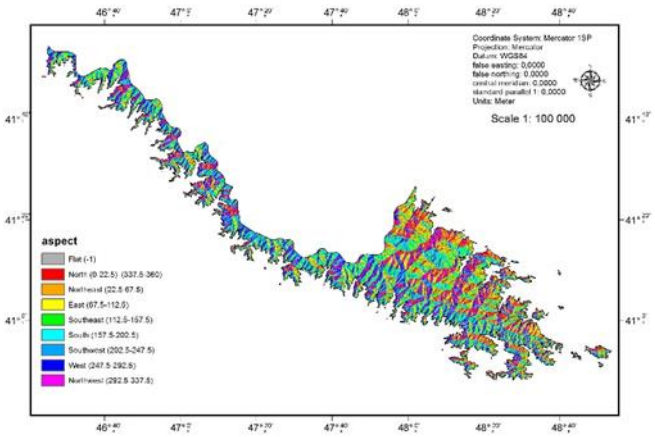

Figure 3. Aspect map of the highland part of the Greater Caucasus

5. Conclusion

Based on the research carried out, the following conclusions can be drawn. The most pronounced factor in assessing the aesthetic properties of the territory is the relief, and the assessment of landscapes should begin with it. An analysis of the relief of the territory, performed on an appropriate scale, allows you to accurately and quickly assess the aesthetic attractiveness of the routes in order to develop tourist and educational routes. Obviously, the dissected relief and the complex structure of the topological level create the most attractive view.

References

Budagov, B. A. (1973). Geomorphology and recent tectonics of the southeastern Caucasus. Baku, Elm, 66-80.

Budagov, B. A. (1988). Modern natural landscapes of the Azerbaijan SSR, Baku, "Elm", 135 p.

Geography of the Republic of Azerbaijan. (2015). Physical geography. Baku "Europe", 529 p.

Hajiyeva, G. N., & Eyubova, Z. I. (2017). Influence of relief morphometric indicators on agriculture in mountainous geosystems of the southeastern slope of the Greater Caucasus Bulletin of the KemSU, Series: Biological, technical and Earth sciences, 4, 26-31.

Kirillova, A. (2010). Some approaches to measure the landscape aesthetics in the Votkinsk region (the Eastern European part of Russia). The magazine from the European Geography Association for students and young geographers, 5, 31 - 33.

Kuchinskaya, I. Ya. (2011). Landscape-ecological differentiation of mountain geosystems. Baku, 195 p.

Nikolaev, V. A. (2003). Landscape science. Aesthetics and design. M.: Aspect Press, 176 p.

Solntsev, N. A. (2001). Teaching about the landscape (selected works). M.: Publishing House of Moscow. un-ta, 384 p.

6th Intercontinental Geoinformation Days

igd.mersin.edu.tr

Identifying urban landscape patterns and influences on Dengue Incidence in Mandaue City, Philippines

Isabella Pauline Quijano*[1,2], Jao Hallen Bañados[1]

[1]*Smart City Solutions to Urban Flooding (SMART TUrF) Program, College of Science, University of the Philippines Cebu, Cebu City, Philippines*
[2]*Department of Biology and Environmental Science, College of Science, University of the Philippines Cebu, Cebu City, Philippines*

Keywords
GIS
Flood Hazard
Morans I
Dengue Fever
Epidemiology

Abstract

Climate change-induced extreme rainfall events have become more frequent inundating large areas in highly urbanized cities in the Philippines. With these potential flood events, it is critical to investigate the potential consequences, such as vector-borne illness epidemics like dengue fever, which have been associated with the monsoon season in the Philippines. In this paper, we study the association of a dengue outbreak in Mandaue city, Philippines with independent variables including climatic variables, drainage infrastructures, urbanization levels and vegetation. We use the Global Moran's I index to measure spatial autocorrelation between the locations of dengue cases while Spearman's rank correlation was used to examine relationships between dengue cases and the chosen landscape variables. The results of this work suggest that inadequate flood control and water disposal facilities can increase the risk of a dengue outbreak especially in densely populated areas.

1. Introduction

Dengue is a mosquito-borne illness that is becoming increasingly common all around the world, especially in tropical and subtropical regions, where it affects one-third of the population. This virus is transmitted through Aedes mosquitos when the temperature is lower than 28°C and is supported by stagnant water that allows them to lay eggs and reproduce. The Philippines has one of the highest age-standardized dengue fever prevalence rates in Southeast Asia, resulting in 170,503 symptomatic cases and 750 deaths annually (Undurraga et al, 2017). In fact, the first known epidemic of the severe form of the virus, dengue haemorrhagic fever, originated in Manila in 1953 and incidences have been on the rise since then (Edillo & Madarieta, 2012). Despite being an epidemic in the country for a long time, no specific treatments or vaccines have been developed to deal with it. Mandaue City, in particular, has reported high numbers of dengue cases and fatalities in recent years, and thus, further research needs to be done to identify the factors that could be contributing to its spread (Quijano et al, 2016; Cotejo, 2022). This study aims to explore the important factors responsible for the spread of dengue and its vectors in Mandaue City, Philippines, and to find variables that could be useful in mapping the potential outbreak of dengue fever.

2. Method

Mandaue City (10.3321° N, 123.9357° E), shown in Figure 1A, is a high-income and urbanized city situated on the Province of Cebu 's central-eastern coast. It is the province's second largest city and a first-class highly urbanized city in the Philippines' Central Visayas region (Mahoney & Klitgaard, 2019). Its population was estimated at 364,116 according to the 2020 census.

Here, we use a spatial statistical approach, the Global Moran's I index, to determine any clustering of dengue incidences in the study's denominator: the barangay-level population data of the city.

2.1. Variables

The dependent variable of the study is the dengue incidence rates (Figure 1A). We collected the dataset through the number of reported dengue cases per barangay in Mandaue City from the Department of Health for the period of January to November 2022. The danger of dengue virus transmission rises as a result of female *Aedes aegypti* or *Aedes albopictus* mosquitoes biting and

* **Corresponding Author**

*(ilquijano@up.edu.ph) ORCID ID 0000-0002-7579-7267
(jlbanados@up.edu.ph) ORCID ID 0000-0002-7675-1762

Cite this study

Quijano, I. P., & Bañados, J. H. (2022). Identifying urban landscape patterns and influences on Dengue Incidence in Mandaue City, Philippines. Intercontinental Geoinformation Days (IGD), 6, 248-252, Baku, Azerbaijan

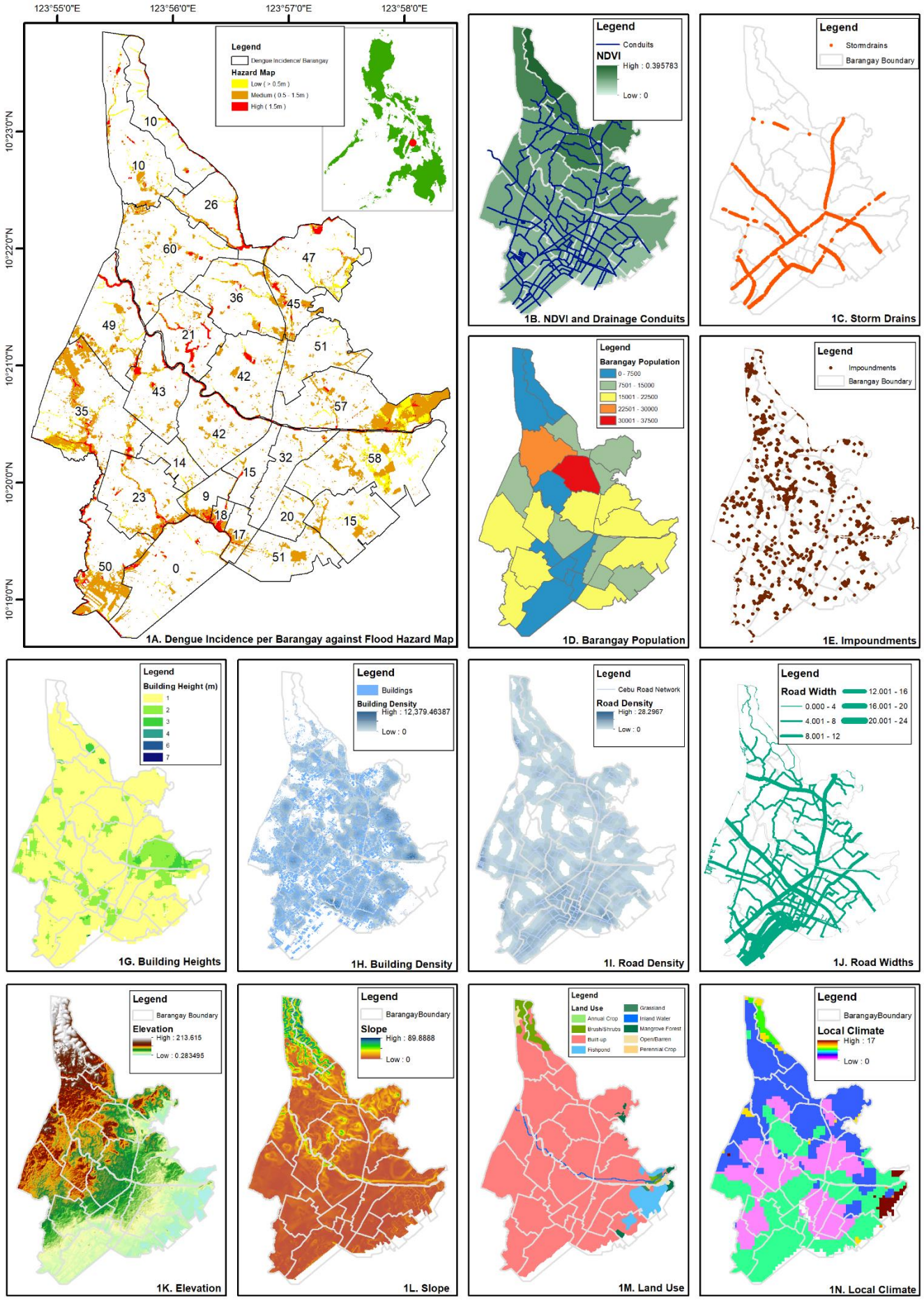

Figure 1. Variables Used as factors for determining dengue incidences in the city

sucking on human blood to get protein and iron minerals. Thirteen independent variables are used and studied to be contributing factors to dengue incidences in the city based on literature review pertaining to *Aedes* dispersal, breeding and nesting factors (Figure 1). The independent variables of the study are categorized into three: infrastructure-linked factors, anthropogenic landscape features and climate-related factors.

The infrastructure-related factors can influence the presence of *Aedes* vector-carrying mosquitoes by enabling or preventing their reproduction and nesting. This includes roof gutters, trash receptacles, sewage, and storm drainage networks in urban areas. For this study, four factors were chosen from this category that could provide *Aedes* sp. with water corridors. The first of these was the flood hazard map, which was used to identify areas that may be inundated with water and could provide a place for mosquitoes to nest in. This data was generated from the Flo-2d software. The second and third factors looked at the city's drainage network and storm drain density, which were obtained from the city's planning office (Hemme et al, 2010; Seidahmed et al, 2018). The last factor studied was the impoundment density, which refers to artificially-created bodies of standing water that could be used by *Aedes* as breeding and nesting sites (Quijano et al, 2016). This data was derived from the digital elevation model through GIS.

This second category, anthropogenic landscape features, focuses on the peridomestic environmental niche of Aedes species. Building density, building height, population density, road width, and road density are the datasets used for this category, which are all related to the dispersal patterns of Aedes species, particularly their tendency to congregate around homes and the potential for habitat fragmentation due to highways to impede their movement (Marti et al, 2020; Seidahmed et al, 2018; Hemme et al, 2010). These datasets were acquired from the city's planning office and further analyzed in a GIS environment.

The last important component of the entomological indices is a set of climate-related factors, including Normalized Difference Vegetation Index (NDVI), local climate zones, land use, elevation and slope datasets (Seidahmed et al, 2018). These datasets were obtained from the city's planning office and were processed using GIS, excluding the climate dataset which was retrieved from the global map of local climate zones and the NDVI dataset which originated from the U.S. Geological Survey's Landsat 8 imagery (Demuzere et al, 2022)..

3. Results

The Global Moran's Index of the dengue cases per barangay was 0.40 with a significant z-score of 2.30 and a p-value of 0.021. This analysis, shown in Figure 2, indicates that dengue incidence was highly spatially autocorrelated with clustering and nonuniformity. These findings imply that a dengue outbreak was experienced in the city among select barangay hotspots and that these areas merit further investigation to scrutinize environmental, anthropogenic or other contributing factors that may have influenced the high incidence of dengue cases in these barangays.

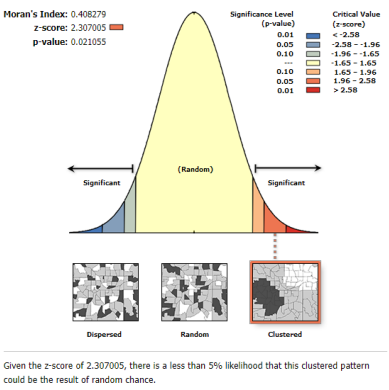

Figure 2. (Global Moran's I) Report

The susceptibility of people becoming ill can be determined by the qualities of their community. Through Spearman's rank correlation analysis, we present a correlation matrix which shows the link between multiple variable datasets (Figure 3). This matrix, when applied to raster layers, shows how the cell values from one layer are related to the cell values from another layer.

The results of our spatial correlation show most of our variables indicating a negative relationship with dengue incidence in the barangays. Unfortunately, our chosen variables for the study presented weak relationships with our dengue incidence rates. Despite this, most notable is the relationship between land use, building height and road density with moderate relationships and population density, flood hazard, building density and NDVI with weak relationships.

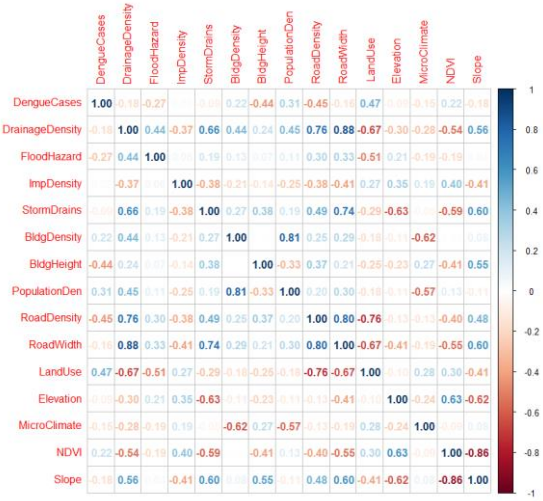

Figure 3. Correlation matrix between all associated variables used for the study and the dengue cases per barangay boundary in Mandaue City.

4. Discussion

All infrastructure-linked variables had a negative association to dengue cases, with flood hazards having the most significant negative relationship (-0.27). The drainage density, flood hazard, and storm drain density all had moderate to strong relationships, which could be due to areas with more drainage channels being connected to storm drains in flood prone areas. Although the drainage network density and storm drain density had values less than 0.2, the direction of the relationship suggests that areas with fewer drainage networks and

storm drains had higher dengue incidence rates. This contrasts with a study conducted in Pakistan by Tahir et al (2020) that showed a positive relationship between flooding and dengue incidences. However, this could be due to poor flood management and water disposal facilities, which is supported by this study's results. Further research could be done to explore the influence of standing water after flood events in Mandaue City and how it relates to dengue cases. Studies such as this one, those in Pakistan, and others (Seidahmed et al, 2018; Marti et al, 2020), show that there is a correlation between dengue occurrences and the availability of water management networks, indicating the need for upgraded drainage infrastructures to help control both floods and dengue fever preventive methods.

The most noteworthy result from the anthropogenic factors was that of road density having a negative correlation with dengue cases, meaning that barangays with fewer roads had more dengue cases. Even though the value for road width was not significant, it still demonstrated a negative relationship with dengue cases, implying that narrower roads resulted in more dengue cases. This was further supported by the strong relationship between road density and width, which indicates that more roads connected to highways and major transportation hubs impede *Aedes* migration. This coincides with an Australian study by Hemme et al (2019) showing that Aedes aegypti have difficulty crossing big highways, suggesting that greater roads networks and wider road widths can act as a form of habitat fragmentation and reduce *Aedes* species' mobility.

The study's results regarding building density and building heights are found to also be in line with other literature (Edillo & Madarieta, 2012; Seidahmed et al, 2018; Marti et al, 2020), indicating areas with higher building density and more low building structures to have higher dengue incidences.

Population density has a weak positive influence on dengue incidences, with denser human populations having more incidences. Additionally, the correlation between population density and building density, like road widths and road density, implies that there are more structures in areas with more people. Despite the findings of the study, more research should be conducted to investigate the anthropogenic and socioeconomic connections to dengue outbreaks, due to the restriction of remote sensing and GIS methods in anticipating human behavior, and the lack of consideration of artificial containers for mosquito breeding.

For climate-related factors, land use and NDVI had a positive correlation with the number of dengue cases, meaning that a greater amount of land use in an area and more vegetation can lead to a higher incidence of dengue. Additionally, our research indicated that dengue is more prevalent in lower altitude locations and flatter terrain. Furthermore, the global map of local climate zones suggests that highly urbanized areas have a higher rate of dengue cases. In relation to the climate-related variables, finer scaled dengue incidence rates or population studies of Aedes species could be done to further investigate these relationships.

5. Conclusion

This study found a positive correlation between dengue cases and their locations, indicating clustered outbreaks in some barangays of Mandaue City. Potential factors to dengue outbreaks were identified, showing the need for better flood control, including drainage network conduits and water disposal facilities, to reduce the risk of outbreaks. This study has shown that the complexity of A. aegypti's population structure, which can be impacted by location, environment, and geography, can provide insight into their dispersal patterns, microclimate preferences, and infrastructure issues. It was also observed that inadequate flood control, such as insufficient drainage networks and water disposal systems, can lead to a higher risk of dengue outbreaks.

Acknowledgement

This research was conducted by the UP Cebu CENVI. This research is an output of the Smart City Solutions to Urban Flooding (SMART TUrF) Program under the CURB Flood Project. We are grateful to the Department of Science and Technology (DOST) for the financial support, with the DOST PCIEERD as the monitoring agency and UP Cebu as the implementing agency. The authors also acknowledge our collaborators from Mandaue City for assisting us with the data used for this study.

References

Cotejo, H. I. (2022, April 2). Dengue brigades' reactivation in 27 Mandaue barangays eyed. Sunstar Publishing Inc. Retrieved from sunstar.com.ph/article/1930918/cebu/local-news/dengue-brigades-reactivation-in-27-mandaue-barangays-eyed

Edillo, F. E., & Madarieta, S. (2012). Trends of dengue infections (1997–2008) in Cebu Province, Philippines. Dengue Bulletin, 36.

Hemme, R. R., Thomas, C. L., & Severson, D. W. (2010). Influence of urban landscapes on population dynamics in a short-distance migrant mosquito: Evidence for the dengue vector Aedes aegypti. PLoS Neglected Tropical Diseases, 4(3), e634. https://doi.org/10.1371/journal.pntd.0000634

Mahoney, M., & Klitgaard, R. (2019). Revitalizing Mandaue city: obstacles in implementing a performance governance system. Policy Design and Practice, 2(4), 383-399. https://doi.org/10.1080/25741292.2019.1642072

Marti, R., Nair, K. K., Kazi, A., Dutilh, B. E., Dutta, D., Maselli, D., ... & Balmaseda, A. (2020). A mapping review on urban landscape factors of dengue retrieved from Earth observation data, GIS techniques, and survey questionnaires. Remote

Seidahmed, O. M. E., Lu, D., Chong, C. S., Ng, L. C, & Eltahir, E. A. B. (2018). Patterns of urban housing shape dengue distribution in Singapore at neighborhood and country scales. GeoHealth, 2, 54–67. https://doi.org/10.1002/2017GH000080

Tahir, M. J., Siddiqi, A. R., Ullah, I., Ahmed, A., Dujaili, J., & Saqlain, M. (2020). Devastating urban flooding and dengue outbreak during the COVID-19 pandemic in

Pakistan. Medical journal of the Islamic Republic of Iran, 34, 169. https://doi.org/10.47176/mjiri.34.169

Quijano, I. P., Banados, J. L., Vicentillo, J. K., Patino, C. L., & Sinogaya, J. R. (2016). Identifying surface impoundments on LiDAR generated DEMs to identify dengue prone areas. In The 3rd International Symposium on Environment and Health & ISEG 2016 (pp. 1-9). Galway, Ireland.

6th Intercontinental Geoinformation Days

igd.mersin.edu.tr

Investigation of effects of land use and land cover on environment of urban landscape based on GIS

Shahnaz Amanova[*1]

[1] *Research Institute of Crop Husbandry, Sustainable husbandry and plant diversification, Baku, Azerbaijan*

Keywords
Urban landscape
Environment
Saatli City
Construction density coefficient

Abstract

In the article, we have analyzed the territorial and population development of the Saatli urban landscape located in the Mugan plain in the territory of the Republic of Azerbaijan, and we have shown the results of its impact on the environment. For this purpose, a 1:10 000 scale topographic plan of the city dated 1975, and satellite and space images of the XX and XXI centuries were used. Based on Landsat 5 and 8 satellite data, the land use situation of Saatli City was analyzed. Land use in the urban landscape is affected by the relief of the area, morphometric indicators of the relief, climatic conditions and others. Therefore, we have studied these elements based on modern technologies. As a result of the analysis of the territorial development of the urban landscape, it was determined that the arable lands in the surrounding areas were replaced by construction sites, and even the 30-hectare oxbow lake of the Araz River was turned into a construction site. Intensification of land use in the urban landscape is closely related to population growth in cities. Population dynamics show that the city was included in the group of medium-sized cities in 2020.

1. Introduction

Cities cover 2% of the Earth's surface (Breuste and Qureshi, 2011). However, more than 50% of the world's population lives in cities [Arnaiz-Schmitz C. et al, 2018]. By the end of the century, this figure is forecasted at 70% (Mikadze, 2015). From this point of view, the study of cities, monitoring the dynamics of their development, and forecasting the future can be considered a topical issue of our time.

What is the city? This concept is perceived differently in different countries. For example, in Azerbaijan, a city is a settlement with a population of more than 15,000 and non-agricultural activities. There are 79 cities in the country. One of these cities is Saatli, which we studied in the article.

Cities are the most intensively developed settlements on the Earth (Forman, 2016). In this regard, their study is very important. Factors affecting urban settlement are classified as follows (Cheshmehzangi, 2015).

-historical factors
- use of natural resources
- construction of industrial enterprises
- administrative-management and trade-distribution function
- Establishment of resort-sanatorium economy
- labor resources

Cities have been studied both in terms of territory and population (Amanova, 2021, 2022]. The city of Saatli is located on the Mughan plain and forms the administrative center of the Saatli region.

2. Method

Our research is based on the processing of satellite and space images. In addition, a 1:10,000 scale topographic plan dating back to the 1970s was used to track the city's territorial development.

In order to determine the anthropogenic impact on the urban landscape, aerospace images for 1989, 2014 and 2022 were detected, construction sites were vectorized and analyzed. For the analysis of the level of urban development, satellite images for 2022 were detected by us and the surface cover was studied.

Images from Landsat 5 and 8 satellites were used to analyze the current and past situation in the vegetation and water basins.

* **Corresponding Author**

*(shahnaz.amanova@gmail.com) ORCID ID 0000-0001-7962-7073

Cite this study

Amanova, S. (2023). Investigation of effects of land use and land cover on environment of urban landscape based on GIS. Intercontinental Geoinformation Days (IGD), 6, 253-255, Baku, Azerbaijan

Based on the Digital Elevation Model of the city, maps reflecting the absolute height and exposure were prepared, analyzed in conjunction with the construction site map, and the role of these factors in the creation of construction sites was analyzed.

3. Results

The city of Saatli belongs to a group of cities descended from villages due to its favorable economic and geographical position due to its genetic characteristics (Fig. 1).

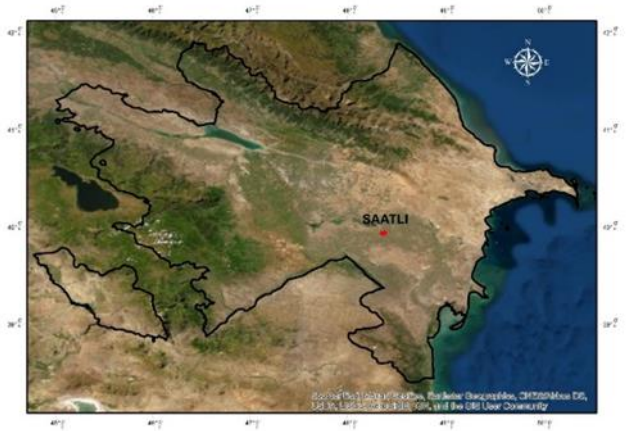

Figure 1. location of the investigation area within the Republic of Azerbaijan

Climatic conditions also affect settlement. High temperatures in the summer months require adaptation of the construction, operation of industrial enterprises and population to these conditions. High temperatures overheat the streets and walls of buildings, creating discomfort. In this case, the way out is to plant greenery, especially on the banks of the Araz River, it would be more expedient to increase the area of greenery.

The climatic factor affects the maintenance of the housing stock, the operation of enterprises, the cost of production processes. We come to the conclusion that the urban planning process should be linked to the climate.

The city of Saatli, located in the northern part of the Mugan Plain, has a temperate-hot semi-desert and dry steppe climate with dry summers. The total annual amount of total radiation is 133 kcal/cm^2, and the amount of radiation balance is 45 kcal/cm^2. The average annual temperature is 14° C. The average temperature of the coldest month is 1,4° C, and the temperature of the warmest month is 26,2° C. During the summer months, the absolute maximum temperature sometimes rises to 40° C. The average annual minimum temperature is -12° C. In the coldest months, the absolute minimum temperature is -26° C.

Temperatures above 5° are only 4900-5000°, and temperatures above 10° are only 4400-4500° C. The average annual relative humidity is 74% and varies between 60-85% during the year. Possible evaporation is 900-1000 mm per year. The average annual wind speed is 2,2 m/s.

Such favorable climatic conditions are among the factors contributing to the development and expansion of the Saatli urban landscape in the lowlands. The combination of temperatures above 5 and 10 ° C, the low number of snow and hail days, and the low average annual wind speed create favorable conditions for agriculture in the city. At the same time, the large number of sunny days in the plain relief makes it convenient to build solar power plants within the green economy. Taking into account the hydropower potential of the Araz River, we can say that there are favorable opportunities for the construction of small hydropower plants. However, due to the recent drought, it would be appropriate to delay this work to some extent.

The level of groundwater in the city is also one of the factors influencing the development of the area and the territorial organization of the economy.

The relief of the plains makes the slopes less sloping, which creates conditions for the development of agriculture and animal husbandry. From this point of view, we can note that Saatli is one of the cities of agricultural purpose.

If the area of Saatli city was 8,9 km^2 according to the topo plan of 1975, in 2022, based on the decoding of aerospace images, it was found that the city area expanded to 18.4 km2 (Fig. 2). This means that the average annual area growth is 2,27%. If we look at the direction of expansion of the city, we see that it is expanding mainly in the south-west and north-west. This is due to the existence of rural settlements in other directions, resulting in limited opportunities for expansion and the water canal passing through the area. If we look at the space image, we can see that the city has arable land in the south and south-east. This will lead to problems with food supply, destruction of fertile lands, provision of fodder base for livestock in urban landscapes.

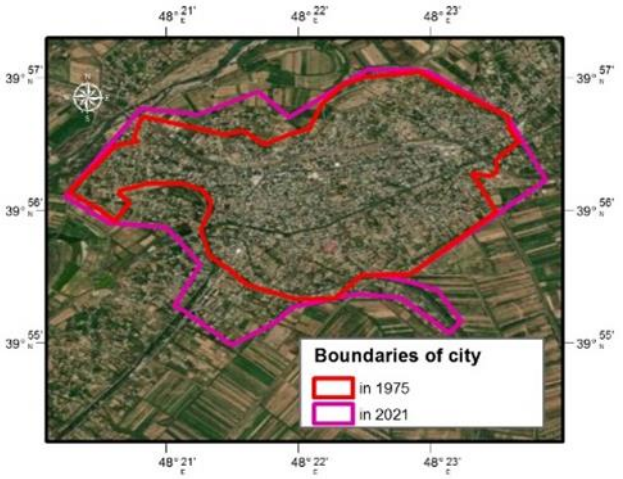

Figure 2. Dynamics of boundaries of Saatli city in 1975-2021

Most area of Saatli urban landscape is below sea level. Based on the results of the map compiled on the basis of the Digital Elevation Model of the area, we determined that 0,5% of the urban area is below (-25) m, 1,6% at a height of (-25) - (- 20) m, 17,4% at a height of (-20) - (-

15) m, 51,2% at a height of (-15) - (-10) m, 2,7% at a height of (-10) - (-5) m, 26% at a height of (-5)-0 m, and 0,5% at a height of 0-3.4 m. The most optimal height for the population is the area with an urban landscape (15) - 0 m.

Based on the DE model, a map showing the espect in the urban landscape was compiled. Based on the results, we can say that the urban area is almost evenly distributed on all aspects.

If we pay attention to the population dynamics of Saatli city in the XXI century, we can see that the population has increased from 16 thousand to 20.1 thousand in the last 20 years, which shows that in 2020 the city has received the status of a medium city. Over the past 20 years, the average annual population growth was 1.2%.

Urban development has a strong impact on the environment. Developing cities affect water, land, vegetation and the atmosphere. For this purpose, we have studied the damage caused to the environment by the dynamics of the territory and population within the urban landscape.

As a result of decoding the aerospace images of Saatli for 2000 and 2022, we found that the number of constructions has increased in 22 years. In 2000, the area with a construction density coefficient of 0-1 was 7,78 km^2, but in 2022 it was reduced to 3,33 km^2. Areas with a coefficient greater than 1, on the other hand, have increased. For example, areas with a coefficient of 1-2 increased by an average of 50%, areas with 2-3 increased by 200%, areas with 3-4 increased by 7 times, areas with 4-5 increased by 5 times, and areas with more than 5 increased by 2 times. These figures show that construction in the Saatli urban landscape, which is the study area, has been growing rapidly for 22 years.

4. Conclusion

The area of the urban landscape has increased by 106% in 47 years, which means that the average annual growth is 2,27 %.

The average annual population growth in the city was 0,9-7,4% in the XX century, but dropped to 1,2% in the XXI century.

During 2000-2022, the number of constructions in the city increased by 1162 units and reached 2124 units.

In order to prevent environmental pollution in the city, it is expedient to clear the forest strip along the banks of the Araz River.

References

Amanova, Sh. (2022). Geo-ecological situtation and forecasting of coastal cities of Azerbaijan. Grozny Natural Science Bulletin, Earth Sciences, 1 (27), 5-13

Amanova Sh. (2021) Developing cities and their problems. “Nakhchivan” University, Scientific Works, 3, 198-203

Arnaiz-Schmitz, C., Schmitz, M., Herrero-Jáuregui, C., Gutiérrez-Angonese, J., Pineda, F. & Montes, C. (2018) Identifying socio-ecological networks in rural-urban gradients: Diagnosis of a changing cultural landscape. Science of the Total Environment, 612, 625-635

Breuste, J., & Qureshi, S. (2011) Urban sustainability, urban ecology and the Society for Urban Ecology (SURE). Urban Ecosystems, 3, 313-316

Cheshmehzangi, A. (2015). Urban identity as a global phenomenon: hybridity and contextualization of urban identities in the social environment. Journal of Human Behavior in the Social Environment, 25 (5), 391-406

Forman, R. T. (2016). Urban ecology principles: are urban ecology and natural area ecology really different?. Landscape Ecology, 8, 1653-1662

Mikadze, V. (2015). Ephemeral urban landscapes of guerrilla gardeners: A phenomenological approach. Landscape Research, 40 (5), 519-529

6th Intercontinental Geoinformation Days

igd.mersin.edu.tr

Spatio-temporal appraisal of glacial lakes, susceptibility analysis and potentials of glacial lake outburst floods in the peri-glacial environment of Western Himalayas

Atta-ur Rahman[*1]

[1]*University of Peshawar, Department of Geography and Geomatics, Peshawar, Pakistan*

Keywords
Glacial Lake
Glacial Lake Outburst Flood
Astore Drainage Basin
Analytical Hierarchy Process
Susceptibility Mapping

Abstract

This study is focused on Spatio-temporal monitoring of glacial lakes, susceptibility analysis and potentials of glacial lake outburst floods (GLOF) in the Periglacial environment of western Himalayas. In the study region, parallel to recurrence of GLOF events, the number and volume of glacial lakes in the peri-glacial area are increasing. In western Himalayas, 52 out of 2,600 glacial lakes are considered as potentially dangerous. Astor Drainage Basin (on which the present study is based), host numerous glaciers and glacial lakes whereas, Glacial Lake Outburst Floods (GLOFs) are recurrently occurring phenomenon. It has a geographical area of about 3988.7 km^2 and the altitude varies from 1237m to 8105m amsl. The study area receives heavy precipitation and most of the peaks remain under snow year-round. The data were collected from Astore, Rama, and Rattu met stations, while discharge data were obtained from Doyian station. It has been calculated that there are a total of 372 small and large glaciers spread over an area of 239.59 Km^2 making 6% of the total area. The analysis revealed that the number of glacial lakes has been increased from 120 in 1989 to 128 in 2019, whereas the areal extent of the glacial lakes has been increased from 4.75 km^2 to 5.861 km^2, respectively. During the study period, out of total glacial lakes, 2 (two) were vanished whereas, 10 new lakes were formed. Furthermore, for carrying out susceptibility analysis, twelve GLOFs factors including slope, lake area expansion, aspect, lake type, distance between glacier's snout and lake, precipitation, elevation, distance to settlement, land surface temperature, distance to road network, fault lines and surface lithology were prepared and weight were assigned using Saaty's Scale. Subsequently, the final GLOF susceptibility zonation map was developed and the results were classified into free zone (20.340%: 796.4622 km^2), very low susceptible area (32.272%: 1263.6660 km^2), low (25.644%: 1004.1560 km^2), moderate (13.610%: 532.9245 km^2), high (6.154%: 241.0049 km^2) and very high susceptible zone (1.9%: 77.4288 km^2) of the total geographical area of Astore Drainage Basin, respectively. In the study area, the GLOF event frequently hit the downstream communities and poses serious threat to vulnerable communities. It is therefore, monitoring glacial lakes and GLOF susceptibility zonation may assist DRR managers and policy makers in taking appropriate measures for the reduction of GLOFs related damages.

1. Introduction

Global warming patterns are causing glaciers to retreat (Zemp et al., 2015). As a result, several glacial lakes form in, around, and under the glacier (Linsbauer et al., 2015). According to previous research, glaciers with low flow velocity or those that are stationary and have a low surface slope angle are more vulnerable to lake formation (Frey et al., 2010). These lakes grow in size and number (Wang et al., 2015), end in a cataclysmic manner (Korup and Tweed, 2007), and their consequences increase the risk of Glacial Lake Outburst Floods. A Glacial Lake Outburst Flood (GLOF) is "A form of outburst flood that occurs when the dam containing a glacial lake fails" (Hakeem et al., 2018).

Glacial lakes are found in northern Pakistan's high mountain ranges. In the Hindu Kush Himalayas (HKH) area of the country, there are currently around 2,600 glacial lakes (Rehman, 2015). According to the inventory, developed by International Centre for Integrated Mountain Development (ICIMOD), 2,500 glacial lakes were identified in ten river basins of Pakistan's HKH

* **Corresponding Author**

*(atta-ur-rehman@uop.edu.pk) ORCID ID 0000-0002-5932-2288

Cite this study

Rahman, A. (2023). Spatio-temporal appraisal of glacial lakes, susceptibility analysis and potentials of glacial lake outburst floods in the peri-glacial environment of Western Himalayas. Intercontinental Geoinformation Days (IGD), 6, 256-259, Baku, Azerbaijan

region in 2005 (ICIMOD, 2005). Nonetheless, it was estimated to be 2,420 in 2010, with 52 of them being deemed potentially hazardous. Cirque type accounts for 25% of these lakes, while End Moraine Dammed accounts for 62% (ICIMOD, 2010). The Indus, Astore, and Gilgit River Basins form the bulk of these lakes. GLOF has been increasing in this area as one of the more common natural phenomena (Ashraf et al., 2012). GLOF incidents were more common during the years 1900-1910 and 2000-2010, according to the existing records. One of the most forceful GLOF came from the Karamber valley glacier in June, 1905. The valley has a long history of generating GLOF events (Iturrizaga, 2005). In the second decade (2000-2010), five GLOF events were recorded from the Hunza valley's Gojal village alone in 2008 (Rehman, 2015).

The HKH region is highly vulnerable to glacial lake outburst floods (GLOF), and there has been very little work done here so far. Furthermore, no such research has been done in the Astore Drainage Basin. The aim of this study is to conduct a Spatio-temporal distribution of glacial lakes over a thirty-year period (from 1989 to 2019) and to conduct the susceptibility analysis of Glacial Lake Outburst Flood (GLOF) of the study area by using the available data and AHP. The proposed study's findings would act as a baseline for future research. It will also give Disaster Risk Reduction (DRR) administrators and policymakers an insight into how to minimize future damages.

2. Method

This study is conducted in Astore Drainage Basin, located in Himalayas. The study area spans between 34º 46' 31" to 35º 38' 38" North latitude and 74º 24' 12" to 75º 14' 52" East longitude. The Astore Drainage Basin is bordered on the north by Gilgit district, on the south by Neelum valley, on the east by Skardu district, and on the west by Diamir. It covers a total area of 3988.7 Km^2. The basin's elevation varies between 1237 and 8105 meters above sea level. Astore, Rama, and Rattu are the three meteorological stations, while Doyian is the only hydrometric station. There are 372 glaciers in the study area, covering a total area of 239.59 km^2. The Astore Sub-basin has the lowest ice reserves in the Upper Indus Basin (UIB), with just 16.88 km^3 of ice (ICIMOD, 2011). In the winter, this area gets heavy precipitation, and most of the peaks are snow-covered all year (Ahmad et al., 2018).

Inventories are the most basic form of mapping, and they are the first step in studying and analyzing any phenomenon. Landsat satellite images with a spatial resolution of 30m and some with 15m (panchromatic) were used to compile glacial lake inventories in Astore Drainage Basin for the observation years 1989, 1999, 2009, and 2019.

The GLOF susceptibility map was created using twelve factors that were chosen for this study based on their effectiveness and availability. Slope, aspects, elevation, lake type, lake area extension, and distance between glacier's snout and glacial lake, as well as distance to road network, distance to settlement, precipitation, land surface temperature (LST), fault line, and surface lithology, are all factors to consider. Data was gathered from secondary sources to achieve the study's objectives. It contains data from the Shuttle Radar Topography Mission Digital Elevation Model (SRTM DEM), Landsat Imageries, Google Earth Images, a Lithological Map, and Meteorological data from Tropical Rainfall Measuring Mission (TRMM) and Astore Meteorological Station. To assess GLOF susceptibility in the study area, a systematic methodology combining Analytical Hierarchy Process (AHP) and Geographic Information System (GIS) was used.

3. Results

3.1. Spatio-temporal Distribution of Glacial Lakes (1989-2019)

From 1989 to 2019, the evolution and development of glacial lakes in the Astore Drainage Basin was extremely complicated with the depletion of some lakes, the emergence of new ones, and the growth of existing glacial lakes. Between 1989 and 2019, the number and size of glacial lakes changed dramatically. The Astore Drainage Basin had 120 glacial lakes in 1989. In 1999, there were 126 lakes in the inventory. According to Landsat imagery, the number of glacial lakes increased from 127 in 2009 to 128 in 2019. Over the investigated period, the volumetric and areal extents of the lakes also grew with the growing number. The lakes' total area grew from 4.75 km^2 to 5.86 km^2, and their approximate volume increased from 2043463.17 m^3 to 2522083.32 m^3. The specifics can be found in the Table 1.

Table 1. Areal and volumetric extents of the lakes

	Areal Extent (Km^2)			Volumetric Extent (m^3)		
Year	Glacial-fed Lakes	Non-glacial-fed Lakes	Total	Glacial-fed Lakes	Non-glacial fed Lakes	Total
1989	1.93	2.82	4.75	830241.01	1213222.16	2043463.17
1999	2.282	3.175	5.457	982004.21	1366495.78	2348499.99
2009	2.278	3.298	5.576	980046.56	1419182.01	2399228.57
2019	2.491	3.370	5.861	1071887.82	1450195.50	2522083.32

3.2. GLOF Susceptibility Mapping

To create a single GLOF susceptibility map, the weighted causative factors were combined using the Weighted Sum tool in ArcMap 10.5. In the process, the net weight was used for weighting. The susceptibility to GLOFs is based on the measured weights for each parameter and its respective groups which divides the entire region into different zones. Based on the outburst weightage ranking, it was reclassified into six susceptibility zones: free susceptibility zone, very low susceptibility zone, low susceptibility zone, moderate susceptibility zone, high susceptibility zone and very high susceptibility zone.

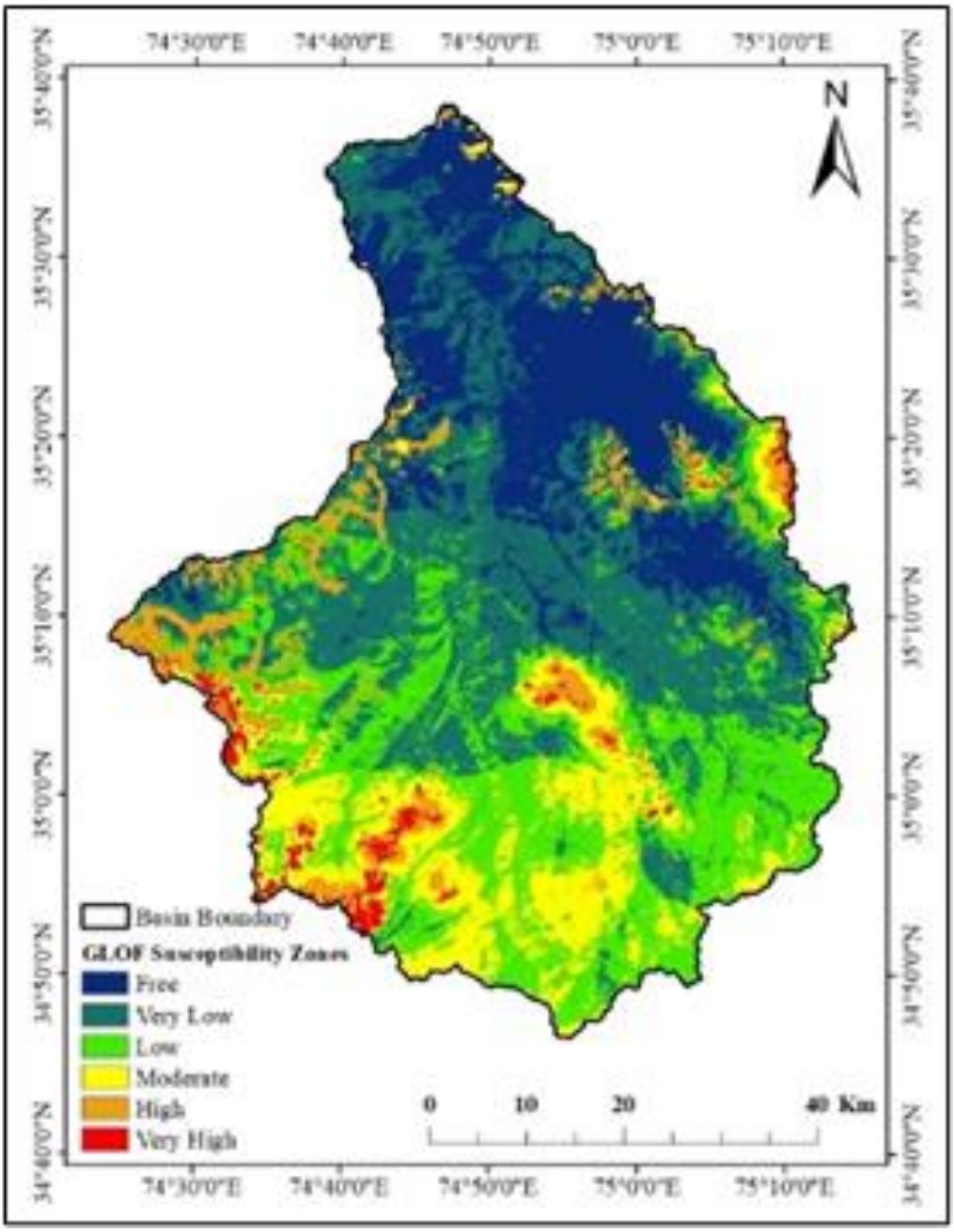

Figure 1. GLOF susceptibility map of Astore Drainage Basin

4. Discussion

From 2009 to 2019, the area of the glacial lakes expanded at a faster pace than the rest of the decades/years. Glacial-fed lakes have grown by 29.07 percent in the last 30 years from 1.93 km^2 in 1989 to 2.491 km^2 in 2019 which is considerably more than non-glacial-fed lakes which have grown by just 19.50 percent (from 2.82 km^2 in 1989 to 3.370 km^2 in 2019). Furthermore, the findings revealed that smaller lakes grew in size faster than larger lakes. According to the findings of all inventories, there is a strong correlation between elevation and the number of glacial-fed lakes, i.e., the higher the number of glacially fed lakes, the higher the elevation. The finding is not surprising since it is commonly assumed that the ponds left by Quaternary glaciers where non-glacier-fed lakes are found, are at a lower elevation than the current glacier termini where Glacier-fed lakes are found (Wang et al., 2015).

During the study period two lakes in the basin are vanished and 10 glacial lakes have appeared. Out of these ten lakes two of them are non-glacial while the others are Glacial-fed lakes. Non-glacial-fed lakes, as it is well known, are typically created in the ponds left by Quaternary glaciers. Two non-glacial-fed lakes are shown to have formed after 1989 in this study. This may be due to rainwater runoff or significant amounts of snow melting. GLOF susceptibility varies from high to very high in the Southwestern and some Eastern parts of the basin. The Southern part of the study area shows a broad distribution of moderate GLOF susceptible zones. Whereas, GLOF susceptibility varies between, low to very low in Northern and in central part of the basin. According to the results, more than 8.134 percent

(318.4337 km^2) of the basin area is occupied by high and very high susceptibility zones.

5. Conclusion

Glacier retreat results in the formation of glacial lakes. There are various forms of glacial lakes, each of which poses a serious threat to downstream communities and property. The GLOF susceptibility in the Astore Drainage Basin was assessed using the Analytical Hierarchy Process. To achieve the objective, glacial lakes inventory map of 108 lakes with an area greater than 0.01 km^2 was developed. The lakes' locations were verified using high-resolution Google Earth maps. A total of twelve GLOF influencing factors were chosen and organized in a hierarchical order. The weights of each class and class's subclasses were determined. Using Saaty's scale (1977), the CI and CR were estimated. Finally, using the Weighted Sum tool in ArcMap 10.5, the GLOF susceptibility zones were identified, ranging from free to very high. The findings revealed that high and very high zones cover more than 8.134 percent (318.4337 km^2) of the basin area while low and very low zones cover 57.916 percent (2,267.822 km^2). This study's GLOF susceptibility map is a useful guide for disaster risk reduction administrators, policymakers, and planners. They will be able to make quick decisions to reduce the losses and harm caused by current and future GLOFs. To avoid the extremely vulnerable areas, appropriate mitigation techniques and preventive measures can be implemented.

References

Ahmad, I., Ahmad, Z., Munir, S., Shah, S. R. A., & Shabbir, Y. (2018). Geo-spatial dynamics of snowcover and hydro-meteorological parameters of Astore basin, UIB, HKH Region, Pakistan. Arabian Journal of Geosciences, 11, 1-15.

Ashraf, A., Naz, R., & Roohi, R. (2012). Glacial lake outburst flood hazards in Hindukush, Karakoram and Himalayan Ranges of Pakistan: implications and risk analysis. Geomatics, Natural Hazards and Risk, 3(2), 113-132.

Frey, H., Huggel, C., Paul, F., & Haeberli, W. (2010). Automated detection of glacier lakes based on remote sensing in view of assessing associated hazard potentials. Grazer Schriften der Geographie und Raumforschung, 45, 261-272.

Abdul Hakeem, K., Abirami, S., Rao, V. V., Diwakar, P. G., & Dadhwal, V. K. (2018). Updated inventory of Glacial Lakes in Teesta Basin using remote sensing data for use in GLOF risk assessment. Journal of the Indian Society of Remote Sensing, 46, 463-470.

ICIMOD: (2005). Report on inventory of the glacier and glacial lakes of HKH region. Kathmandu, Nepal.

ICIMOD: (2010). Report on formation of glacial lakes in the Hindu Kush Himalayas and GLOF risk assessment. Kathmandu, Nepal.

ICIMOD: (2011). Report on the Status of Glaciers in the Hindu Kush-Himalayan Region. Kathmandu, Nepal.

Iturrizaga, L. (2005). The historical Saklei Shuyinj and Chateboi Glacier Dams as triggers for lake outburst cascades in the Karambar Valley, Hindukush. Island Arc, 14(4), 389-399.

Korup, O., & Tweed, F. (2007). Ice, moraine, and landslide dams in mountainous terrain. Quaternary Science Reviews, 26(25-28), 3406-3422.

Linsbauer, A., Frey, H., Haeberli, W., Machguth, H., Azam, M. F., & Allen, S. (2016). Modelling glacier-bed overdeepenings and possible future lakes for the glaciers in the Himalaya—Karakoram region. Annals of Glaciology, 57(71), 119-130.

Rehman, G. (2015). GLOF Risk and Reduction Approaches in Pakistan. Disaster Risk Reduction Approaches in Pakistan, 217-237.

Wang, W., Xiang, Y., Gao, Y., Lu, A., & Yao, T. (2015). Rapid expansion of glacial lakes caused by climate and glacier retreat in the Central Himalayas. Hydrological Processes, 29(6), 859-874.

Zemp, M., Frey, H., Gärtner-Roer, I., Nussbaumer, S. U., Hoelzle, M., Paul, F., ... & Vincent, C. (2015). Historically unprecedented global glacier decline in the early 21st century. Journal of glaciology, 61(228), 745-762.

6th Intercontinental Geoinformation Days

igd.mersin.edu.tr

Analysis of rural ethnosettlement in Balakan administrative region based on GIS method

Bayimkhanim Huseynova

Ministry of Science and Education of the Republic of Azerbaijan, Institute of Geography, Baku, Azerbaijan

Keywords
Balakan district
Rural population
Ethnic minorities
Ethno-settlement
GIS

Abstract

In the article, the analysis of the rural ethnosettlement in the Balakan administrative region based on the GIS method was studied. The main purpose of the research work is to study the national composition of the population, their distribution by residential areas and the modern problems of the villages in Balakan district located in the north-western zone of the country using the GIS method. In order to carry out the research work, fund materials were analyzed, field research works were carried out in order to get to know the local situation closely, and space images of the area were obtained. The obtained data were processed in the ArcGIS program. As a result of the conducted research, it became clear that a serious polarization process took place in the ethno-settlement system of the region. That is, although villages with a large demographic potential play a major role in their settlement, some villages are distinguished by their weak demographic potential. Some villages have no permanent population. As a result of uneven socio-economic and demographic development within the region, the population of some villages either increased or decreased at a slow pace. This was related to regular migration processes in the region. In order to closely study ethno-settlement in the study region, settlement maps were prepared. At the same time, a proposal plan was prepared in order to eliminate the problems that arose.

1. Introduction

The north-western zone of Azerbaijan is one of the areas distinguished by the diversity of its ethnic composition. Representatives of various minority ethnic groups have settled here. These areas, included in the Shaki-Zagatala economic region, mainly cover mountainous regions (Huseynova 2021). In this region, which is mainly surrounded by mountainous areas, only the population of Balakan district mainly settled in the areas up to 500 meters. Balakan administrative district, which is a part of Shaki-Zagatala economic district, is located in the far north-western part of the country. This administrative region with a total area of 923 km^2 is surrounded by the Russian Federation from the north, the Republic of Georgia from the west and southwest, and the Zagatala region of the Republic of Azerbaijan from the east. According to statistical data, the population of the region is 632,9 thousand people (Demographic indicators of Azerbaijan 2022). In total, there are 1 city, 1 settlement and 57 rural settlements within the administrative district. The population of the region is one of the areas with a rich ethnic composition. Thus, the main part of the population in the research area, i.e., 72.7%, was made up of Azerbaijanis, 26.6% of Avars, and the rest of the population consisted of Inghilois, Russians and representatives of other minority ethnic groups. The study of settlement issues in this region, which is distinguished by the diversity of its ethnic composition and is located in the remote border zone of the country, and the mapping of these data are of special political and strategic importance. The collection of such information can play a significant role in solving the settlement problems that arise in the area now and in the future.

2. Method

The research work consists of stock materials of the database, processing of space images and field studies. In order to collect information about the region's population, ethnic composition and settlement issues, it was closely acquainted with the research works of local and foreign researchers who have been conducting research in this field for many years. As examples of such researchers, we can show Eminov (2005), Javadov (2000), Ayyubov (2015), Adamovich (2022), Liu (2017),

* **Corresponding Author**

*(nane_huseinova@yahoo.com) ORCID ID 0000 – 0003 – 0975 – 0302

Cite this study

Huseynova, B. (2023). Analysis of rural ethnosettlement in Balakan administrative region based on GIS method. Intercontinental Geoinformation Days (IGD), 6, 260-262, Baku, Azerbaijan

Mihai (2020) and others. The second data base of the research consists of space images provided by the Azerbaijan Space Agency. On the basis of those space images, it was possible to see how and during which period the settlements changed, and in which parts the population was mainly concentrated. A field trip to some villages of the administrative region was organized in order to get to know the research area more closely and to learn the reasons for the change in settlement. These villages are mainly rural settlements densely populated by minority ethnic groups. At this time, questionnaires were distributed among the population, and the last collected materials were analyzed.

2.1. Settlement and ethnic composition of the region

Balakan administrative region covers altitudes from 140 meters to 3100 meters above sea level. However, the population is mainly settled in the mountainous areas. Especially the Ganikh-Ayrichay valley, which has a rich agricultural potential, is more densely populated by the population. The highest settlement of the region is Mazymchay village located at 558 meters.

As we mentioned earlier, Avars have a special role in the ethnic composition of the region. Avars are densely settled mainly in Sharif, Yeni Sharif, Shambul, Meshashambul, Ajiliqbina, Katekh and a number of villages of the region. Ititala village of the region is a village inhabited by Inghilois.

2.2. Population distribution by altitude zones

If we look at the distribution of the population by altitude zones (Table 1), although there are 4 rural settlements up to 200 meters in the region, only Ititala village has a permanent population. The other three villages - Goyamtala, Darvazbina and Bayrambina - have no population. The region has only one village located above 500 meters, which is the village of Mazymchay, which has a medium demographic potential and its population is growing at a slow pace.

As can be seen from the table, the main part of the rural population and rural settlements of the region is located within the 200-500 meter belt. However, the population is unevenly distributed within this belt (Figure 1).

Table 1. Change of settlements by altitude zones

Altitude zones	1999		2009		Indicator of increase or decrease of the population (%)
	Number of villages	Number of population	Number of villages	Number of population	
0-200	4	2029	4	2240	+10,4
201-500	52	71457	52	76913	+7,6
500 and more	1	351	1	358	+2,0
Total	57	73837	57	79511	+7,7

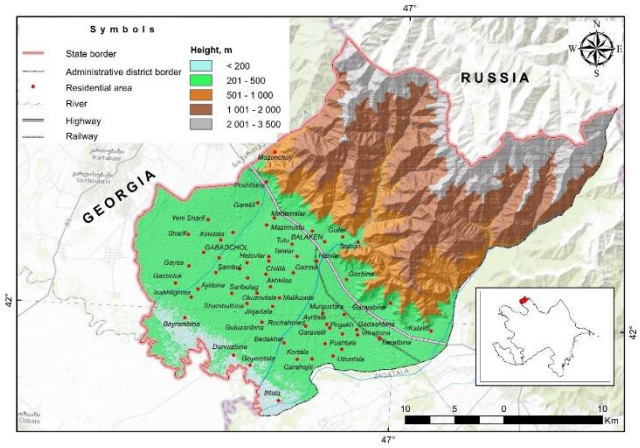

Figure 1. Map of the change of settlements by altitude zones

3. Results

Uneven socio-economic and demographic development of the region has also affected the proximity, demographic potential and density of settlements. Thus, there are villages with both large and weak demographic potential in the region (Eminov 2021). Unequivocally, villages with a large demographic potential are located close to the district center and to each other. Villages belonging to this group attract attention due to their proximity to highways. They also form large rural agglomerations.

Villages with weak demographic potential are mostly located far from the city center and on highways. The income level of the population in these villages is low. This results in the intensification of migrations in those villages and, as a result, their population decreases or increases at a slow pace.

4. Discussion

Large villages located close to each other in the region have created rural agglomerations. We can group these rural agglomerations in the following groups (Fig.2):

Rural agglomerations around the city of Balakan - Hanifa village (4693 people), Gazma (2516 people), Talalar (3098 people), Tulu village (5816 people), Mahamalar village (4276 people), Gullar village (5882 people) .)

Sharif-Shambul village agglomerations - Sharif village (3293 people), Yeni Sharif village (3118 people), Khalatala (2728 people), Meshashambul village (2498 people), Gaysa village (3602 people)

Katekh-Mazikh village agglomeration - Katekh village (7134 people), Mazikh village (1602 people Zagatala district)

Ititala (2240 people) - Ashagi Chardakhlar (1093 people Zagatala district)-Danachi (7071 people Zagatala district) triangle

Garakli village agglomeration - Gerakli village (3531 people).

The main part of the population in these villages was made up of Avars.

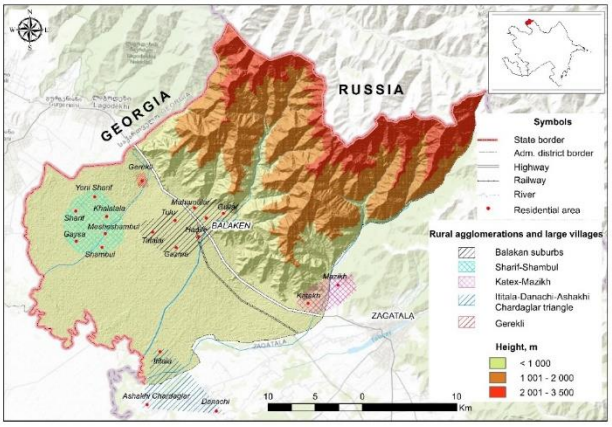

Figure 2. Rural agglomerations

Although some villages of the region have formed large agglomerations, a decrease in the population has been noted in some villages. Thus, in 1999-2009, the population of 6 villages in the region decreased, 4 villages had no population, and 2 villages had less than 100 people (Fig 3.).

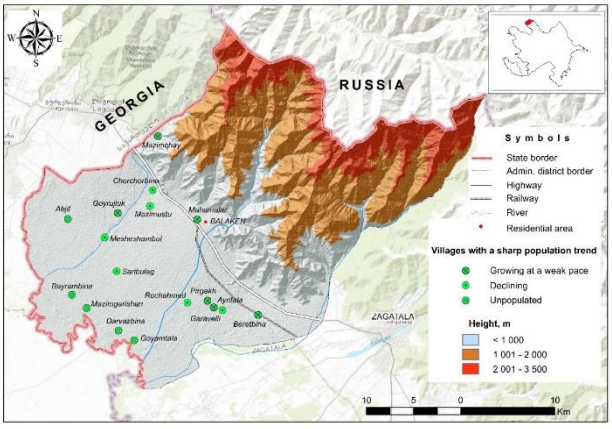

Figure 3. Map of threatened, endangered and extinct villages

The main reason for the population decline in such villages in the region is due to the lack of sources of income and the migration of the population for the purpose of earning or looking for work (Huseynova 2022). In this case, the migration process mainly involves the young population. This also results in a decrease in natural increase due to the decrease in the number of young people in the villages.

5. Conclusion

Based on the results of the conducted research, it can be said that the population is unevenly distributed in Balakan administrative district. Within the administrative district, the population is mostly settled in the height zone of 200-500 meters.

Although the large villages of the region have united to form large rural agglomerations, small villages have started to decline.

The main reason for the decline of small villages is the lack of necessary socio-economic conditions for providing employment to the population in such villages.

The lack of permanent settlement in the villages located in the border zone and the decrease in population can cause serious problems in terms of ensuring the security of the border zone.

References

Demographic indicators of Azerbaijan. (2022). State Statistical Committee of Azerbaijan, 557 p.

Eminov, Z. N. (2021). Demographic development of villages in the Republic of Azerbaijan and problems of the settlement of the rural population, 552 p.

Huseynova, B. A. (2021). The tendency and improvement of settlements of ethnic minorities on altitude zones in the rural areas of Shaki-Zagatala economic-geographical region. Journal of Young Scientist, 2, 112-120.

Huseynova, B. A. (2022). Participation of ethnic minorities living in the north-western regions of the republic of Azerbaijan in the migration process. Geographical bulletin, 3(62), 45–57. https://doi.org/10.17072/2079-7877-2022-3-45-57.

6th Intercontinental Geoinformation Days

igd.mersin.edu.tr

Relief influence on plant cover of Zangilan District

Gulnar Hajiyeva [*1], **Aytan Mammadova** [2]

[1] *Institute of Geography named after Acad. H.A. Aliyev of The Ministry of Science and Education, Landscape and Landscape Planning Department, Baku, Azerbaijan*
[2] *Institute of Soil Science and Agrochemistry of The Ministry of Science and Education, The Laboratory of Soil Information System Department, Baku, Azerbaijan*

Keywords
Relief
Plant cover
Forest
DEM

Abstract

The article is an analytical review of the literature that considers the influence of relief on the spatial distribution of individual plants and plant communities. Since time immemorial, man has learned to use the unevenness of the earth's surface, whether it be convenient bays or fertile valleys. The position in the relief plays an important role for representatives of the flora. Acting not directly, but indirectly, through the transformation of the main climate factors, it has a noticeable effect on the formation of vegetation types. In the article, each of the morphometric indicators of the relief of the vegetation cover of the studied region was analyzed in the ArcMap program. The influence of these parameters on vegetation was studied separately. Slope exposures are of great importance for the life cycle of plants. The steepness of the slope affects the species composition and structure of phytochromes. Also, the article discusses the current ecological state of the pearl of the forests of Europe and the South Caucasus - the eastern plane tree. As a result of the intensive and illegal logging of these forests by the Armenian Republic, their area has significantly decreased, and ways of their restoration are also being considered.

1. Introduction

The forest is one of the most important natural resources for humans. Humanity has been engaged in forestry and forest science for several centuries. Derivative forests are still the main building material to this day. Throughout the history of forestry, it was necessary to use the forest nationally and replenish the used resources in the most productive way (Yashina, 1960, Yantser, 2005).

The territory of Karabakh is located between the rivers Kura and Aras, it is limited in the east by the Kura-Aras lowland, in the west and northwest by Armenia, and a very small area borders Georgia. Its total area is 29,040,381 km^2, which is 25% of the territory of the Republic of Azerbaijan. The territory of Karabakh consists of mountainous and flat parts. Its length from northwest to southeast is 600 km. The territory of Nagorno-Karabakh is 4363 km^2, and the area of the plains is 24677.4 km^2. Karabakh's favorable relief and climatic conditions contributed to forming a dense river network and rich soil and vegetation cover.

2. Method

The territory of the Zangilan district is located in the zone of medium and low mountains and has a complex, fragmentary structure on the surface. The district is mountainous in the west and plain in the east. In addition to sedimentary rocks, Jurassic, Cretaceous, and Neogene-anthropogenic deposits, which are volcanic rocks, are widespread in the region. The fact that most of the region is mountainous has led to the fact that the plains cover a small area here (Figure 1).

Looking at the map of the absolute heights of the study area, we see that 3% of the area is 2000 m above sea level, 7% is 1501-2000 m, 15% is 1001-1500 m, 38% is 501-1000 m, and the rest and part of it is covered by parts below 1000 m. Such altitudinal zones in the administrative region also affect the assimilation and degradation of plants common here (Sharay and Shary, 2011, Korner, 2003).

The steepness and inclination of the slopes play an important role in the formation of the vegetation cover of the area (Figure 2, 3). Both slope maps of the study area were prepared and analyzed using the ArcMap software. It turned out that the northern slopes are a minority here.

* **Corresponding Author**

*(hgulnarn@gmail.com) ORCID ID 0000-0002-1061-1652
(aytan.amea@gmail.com) ORCID ID 0000-0002-6838-6822

Cite this study

Hajiyeva, G., & Mammadova, A. (2023). Relief influence on plant cover of Zangilan District. Intercontinental Geoinformation Days (IGD), 6, 263-265, Baku, Azerbaijan

Therefore, steppe plants are more common (Shary and Shararya, 2002).

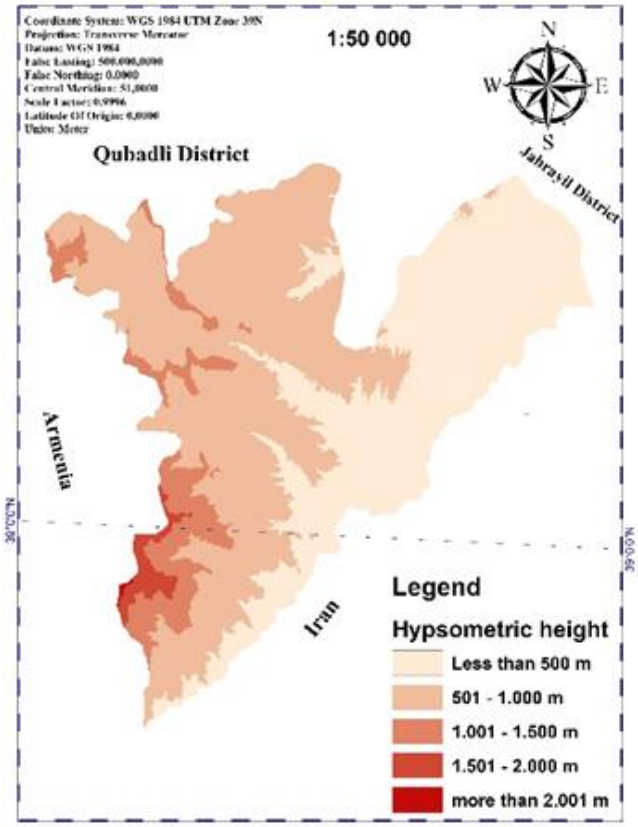

Figure 1. Hypsometric height of Zangilan district

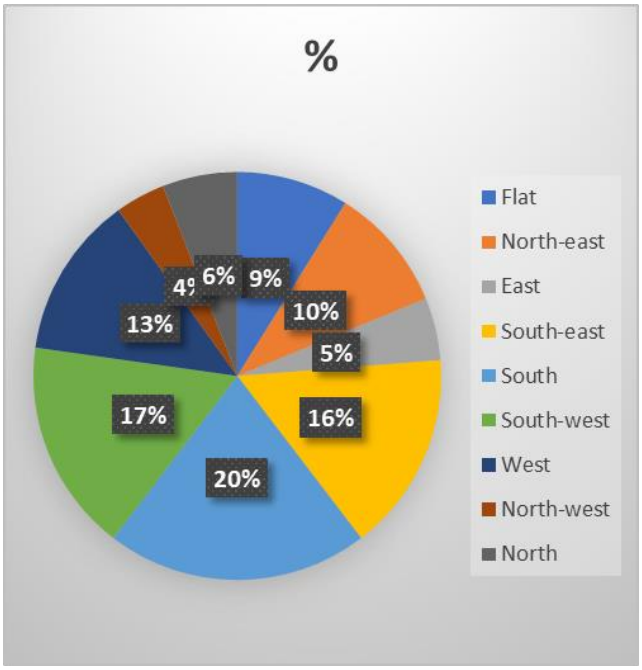

Figure 2. The aspect of slopes of the Zangilan district

Along with the visibility of the slopes, we also analyzed the slope in the same program. the lack of slope in most of the area has led to greater plant assimilation and degradation in the region (Sokolova, 2016).

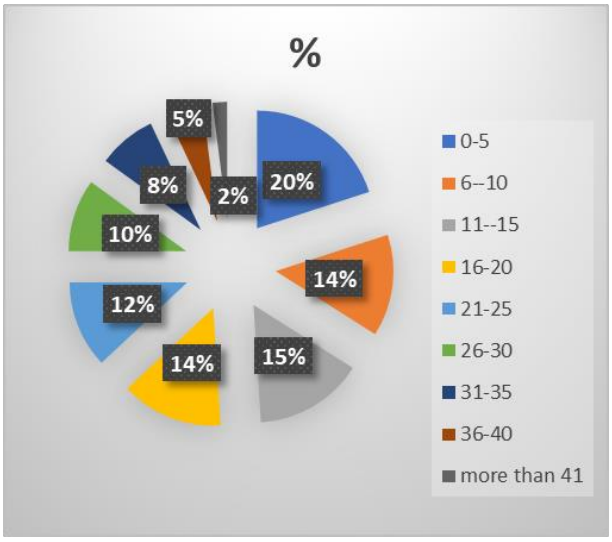

Figure 3. The inclination of the slopes of the Zangilan District

3. Results

As a result of the peculiarity of orographic conditions in the territory of Karabakh, there are landscape belts of natural complexes of mountain forests from west to east and from north to south. The forest area is 340,000 ha, of which 247,000 ha (13,000 ha are valuable forests) have been occupied by the Republic of Armenia for 27 years. Of these, state forests make up 986 hectares of forest area, 710 hectares are occupied by collective farm forests, and 560 hectares are roads, water channels, and cultivated forests. More than 460 species of wild trees and shrubs grew in these territories, of which 70 (blackberry, wormwood, Aras oak, linden, oriental plane tree, common pomegranate, forest grapes, pirkal, beech, Eldar pine, common palm, willow pear, etc.) are endemic. Currently, these species are on the verge of extinction from the face of the Earth (Khalilov and Quliyev, 2014).

4. Discussion

One of the valuable plant species is the oriental plane tree (Mammadov and Khalilov, 2002, 2005). The only natural forest of the eastern plane tree in Europe is located in the western part of the Lesser Caucasus, in the Zangilan region. These plants, located in the basin of the Basitchai River in terms of the physical condition of the trees and the area of natural tree plantation, are the largest plane tree forests in the world.

A plane tree, or as it is also called "eastern" – is one of the oldest species of flowering plants. For its beauty, picturesque view, and unique bio-ecological features, it is called the pearl of the woody flora of the East, and for its mighty trunk, majestic and dense crown - the giant tree of the South (Prilipko, 1975). Despite the wide and dense structure of the leaves in winter, he dumps them. The trunk is very powerful (up to 40-50 meters in height, and the circumference reaches 18 meters). The leaves are alternate, palmately lobed on long petioles. This plant is dioecious and has inflorescences of both female and male types. Small flowers are unisexual. Sycamore flowers are small, in dioecious inflorescences, one- and many-headed. The male flowers are yellowish in color and have

a double perianth. Female flowers are often with a simple perianth and develop in larger globular purple capitate inflorescences. Sometimes they are thin on a long peduncle, consisting of 2-7 pieces. Since both flowers are on the same tree, they are different plants of the same species.

The plane tree is a fast-growing and long-lived tree. Eighty percent of trees grow from rootstocks. The plane tree begins to bear fruit at the age of 10-15 years, the most fruitful period is 150-200 years. Chinars can live up to 2000-2300 years. Lightweight, durable wood is used in the production of plywood, parquet, furniture, shipbuilding, and also in landscaping as a decorative wood.

On the initiative of the well-known naturalist, academician Hasan Aliyev, to protect the plane tree forest in the Zangilan region, by the decision of the Council of Ministers of the Azerbaijan SSR dated July 4, 1974, the Basitchay State Reserve with an area of 117 hectares was created, which is a unique natural monument. In October 1980, the area of the reserve decreased by 10 hectares and amounted to 107 hectares, of which 100 hectares are forests, and the remaining 7 hectares are rocky and sandy areas of the Basitchay River valley (Körner, 2003). The reserve is located at an altitude of 600-800 m above sea level. Plane forests in Azerbaijan occupy 93.5% of the area of the reserve in the Basitchay Valley. Here plane trees can grow from 900m to 1200m above sea level. The total area of sycamore forest in Azerbaijan, 12 km long and 60-200 m wide, is about 120 ha. Plane trees thin out towards the source of the river and spread deep into the territory of modern Armenia for 7-8 km. This plane forest ends near the village of Baharli in the Zangilan region, at a distance of 200-300 m from the confluence of the Basitchay and Aras rivers.

According to some data, in terms of area, plane trees in the Basitchay River valley are ranked first in Europe and second in the world, and the largest plane tree forest in the world is located in North America - Canada. However, this opinion is not supported by scientific evidence.

It should be emphasized that the Armenian invaders brutally destroyed the giant plane trees, which have no analogs in Europe. They opened a woodworking workshop for plane trees near the village of Razdara, Zangilan region. The workshop worked without interruption and produced furniture materials from sycamore, walnut, and oak growing in the surrounding forests. The area was mined and burned to hide the looting of the forest. At the same time, the Isfahan Armenians built a new $100 million woodworking plant in the Muganly village of the Zangilan region. Although the raw material base of the plant is trees floated across the Araz River, studies have shown that the main raw material was the forests of Zangilan and other occupied territories. And of course, the main blow falls on the plane trees, which are the kings of trees. According to the "Bank-Information" of the International Center for Strategic Research on Combating Terrorism and Corruption on the territory of the reserve with an area of 107 hectares located on the territory of the Zangilan region, the plane tree forest is almost or completely destroyed or partially sold to Iranian furniture factories and other construction companies. As a result of the deployment of Armenian troops on 42 hectares of the reserve in this area, plane trees were completely destroyed here. In 2000, 70 plane trees were sold from the territory of the reserve to the governor of Tehran for $100 each. 110 plane trees were uprooted and replanted on the shore of Lake Goycha (Sevan) and in the vicinity of the city of Yerevan.

5. Conclusion

Using the (ETM + Landsat (4, 5, 8)) coefficient from ArcGIS and multispectral satellite photos we studied the degree of the plant covering in 1987-2017 (Yashina, 1960). As a result of our investigation in connection with the zone appropriation the zones which are weakly covered in 2017 in comparison with 1987 decreased by 24%, an average-1,7% rose, and the zones covered with the dense plant cover reduced by 30,4%.

As a result of the investigative zone appropriation, it is important to keep definite agro-technical orders during the utilization for not getting the highest value of these changes occurring in a covering degree of the plant cover. Forests in which the plant cover is dense must be prevented from cutting with the different aims, shift grazing rules must be obeyed during the utilization from summer pastures, hayfields in cattle-breeding, growing the new forage plants including the other agro-technical rule should be obeyed. If these rules aren't obeyed during the zones use then covering degree with the dense plant will be 50% after 50 years.

References

Khalilov, M. Y., & Guliev, I. A. (2014). The anti-erosion role of the root systems of forest vegetation in the Greater Caucasus. Geographic Bulletin, 4(31), 85-90.

Körner, C. (2003). Alpine Plant life: functional plant ecology of high mountain ecosystems. Berlin: Springer, 47–62.

Mammadov, G. Sh., & Khalilov, M. Y. (2005). Ecology and environmental protection Baku: Elm, 880 p.

Mammadov, G. Sh., & Khalilov, M. Y. (2002). Forests of Azerbaijan Baku: Elm, 472 p.

Prilipko, L. I. (1975). Vegetation of the Caucasus Moscow: Nauka, 35-55.

Sharay, L. S., & Shary, P. A. (2011). Study of the spatial organization of forest ecosystems using geomorphometry methods. Ecology, 1, 3-10.

Shary, P. A., Sharaya, L. S., & Mitusov, A. V. (2002). Fundamental quantitative methods of land surface analysis. Geoderma, 107(1-2), 1-32.

Sokolova, G. G. (2016). The influence of terrain altitude slope exposure and slope degree on plant spatial distribution. Acta Biologica Sibirica, 2(3), 34-45

Yantser, O. V. (2005). Spring differences in the development of vegetation on the slopes of different solar exposure. Successes of modern natural science, 1, 77–80.

Yashina, A. V. (1960). The role of snow in the formation of vegetation. Geography of snow cover. M.: Publishing House of the Academy of Sciences of the USSR, 90–105.

6th Intercontinental Geoinformation Days

igd.mersin.edu.tr

Critical issues in emergency planning for nuclear power plant accidents

Maryna Batur*[1], Reha Metin Alkan [1]

[1] *Istanbul Technical University, Faculty of Civil Engineering, Department of Geomatics Engineering, Istanbul, Türkiye*

Keywords
Nuclear accident
Emergency management
Evacuation
Three Mile Island
Fukushima
Chernobyl

Abstract

Accidents at Nuclear Power Plants (NPP) are perhaps the most alarming situations for both the public and emergency services. Nuclear accidents provide us with an opportunity to learn from the experience in order to improve the disaster response system and prevent new tragedies. Experience from past disasters clearly shows that nuclear emergencies can lead to relatively low levels of exposure, but at the same time can cause conflicting reactions among population that are almost impossible to control. We did a review of past NPP accidents including the Three Mile Island (TMI), the Chernobyl, and the Fukushima accidents, to analyze public's evacuation behavior in nuclear accidents and found that absence of people's preparedness to radiological emergency was the main indicator of uncontrolled evacuation. It is therefore necessary to increase knowledge about radiation and convey to people how to choose the right protective measures and effectively control an emergency. To do this, it is important to include special pre-accident programs in the preparation plans and rely on them during a real emergency. We believe that the implementation of such a multidisciplinary concept including engineering emergency planning along with the social aspects, can significantly improve the existing emergency plans. This paper provides policymakers with valuable recommendations to address gaps in terms of nuclear disaster preparedness and assistance.

1. Introduction

Ask yourself how well do you know what to do in case of a nuclear emergency? If so, will you strictly follow all the pre-agreed actions? Today, nuclear power industry is one of the most reliable sources of energy, both economically and environmentally sustainable, and also meets the many challenges of a rapidly developing world. Nuclear energy has proven its effectiveness over many decades, becoming an integral part of the global energy balance (Saidi and Mbarek, 2016). Hovewer, while this greatly improves people's quality of life and contributes to zero carbon emissions, there may be critical safety concerns as most of the substances involved in manufacturing processes are hazardous materials with radiological characteristics. For instance, in the event of a nuclear accident, the subsequent release of radioactive components into the environment often results in serious losses of life and property which usually lasts for years and are difficult to eliminate. Nuclear accidents such as the Three Mile Island (USA, 1979), the Chernobyl (Ukraine, 1986), and the Fukushima (Japan, 2011) led to various serious causalities and environmental damages (Fesenko et al., 2021; Flynn, 1982; Kawaguchi and Yukutake, 2017). To be prepared for a nuclear disaster, the community living near a Nuclear Power Plants (NPP) must have appropriate response and training plans in place (Handl, 2016). Evacuation in case of nuclear accident is considered one of the most effective ways to respond, prevent and mitigate hazards from the disaster. Fast evacuation is needed in order to avoid the harmful impact of radiation. However, evacuation is a complex process that involves either technical or phycological aspects. It includes the removal of the population from risk areas, their shelter, return home or even permanent displacement. In addition, there are such approaches as mandatory evacuation, voluntary evacuation, and recommended evacuation when residents are given a choice to leave or to stay. There is another term for evacuation – a shadow evacuation or "spontaneous" evacuation. The so-called shadow evacuees are a group of people who decide to leave despite being advised to stay (Zhang et al., 2020). Shadow evacuation occurs for a variety of reasons, but it is mainly influenced by the perception that the impending hazard will be hostile,

* **Corresponding Author**

*(baturm20@itu.edu.tr) ORCID ID 0000-0001-9284-8858
(alkanr@itu.edu.tr) ORCID ID 0000-0002-1981-9783

Cite this study

Batur M & Alkan RM (2023). Critical issues in emergency planning for nuclear power plant accidents. 6th Intercontinental Geoinformation Days (IGD), 6, 266-269, Baku, Azerbaijan

whether it is so or not. Therefore, in conditions of urban evacuation, the mobility and responsiveness of people do not always have positive results, but rather can exacerbate the situation. But there were also cases when people delayed the decision to evacuate, exposing themselves to unnecessary risks (Shimada et al., 2018). Evacuation planning and its further implementation should be built on the principle of socio-psychological foundations and rely on the empirical data relevant to mass behavior in such situations. To develop an effective evacuation policy, it is critical to understand how residents respond to evacuation warnings, including their choices of stay or leave, if to leave then when, which routes to take, etc.

The main objective of this research is devoted to the review and analysis of public response and behavior during the evacuation in past nuclear accidents with the aim to identify the major problems in emergency evacuation planning.

2. Overview of evacuation following the past NPP accidents

The extent of the radiological disaster is measured by the so-called International Nuclear and Radiological Event Scale (INES), which has seven levels of severity (Webb et al., 2006). Events are ranked by degree of impact on people and the environment, starting with the first and ending with the seventh. There have been several accidents since the advent of nuclear energy and throughout its history, but only three accidents have been termed as the gravest technological catastrophes. Below are their brief descriptions.

2.1. The Three Mile Island experience

Three Mile Island catastrophe, accident in 1979 at the American NPP, was the most serious in the history of the USA. A series of equipment and technical failures, human mistakes in operating procedures and wrong decisions in the first minutes of the failure led to the partial reactor core, thus assigning the fifth level of accident on the INES scale (Bavelacqua, 2016).

Fortunately, it was concluded that there were no contamination of soil and water and little number of radioactive materials were released into the atmosphere, which had a negligible effect on public's health and environment. Therefore, the emergency response included advisory evacuation on the initial stages and voluntary evacuation in subsequent days. Fig.1 shows the map of evacuation zones around the NPP. On the first day, government announced advisory evacuation within the area of 0-8 km only for pregnant women and pre-school children along with the shelter-in-place for all others within 8-16 km. On the second day, voluntary evacuation was stated for the entire 0-16 km area, and later next day, for the entire 0-32 km zone. Despite no formal evacuation order was done in the first day, more than 100,000 people decided to leave the area. As a result, the total evacuation amounted to 63% from the 0-32 km zone, and only 37% of the entire population within this area preferred to stay. As the questionary surveys showed, the main factors influencing the decision to evacuate were spatial proximity to the station, the inability to assess the risk of danger, as well as initial fear and a sense of not knowing what to expect (Stallings, 1984).

After the accident, the exclusion zone was not established, and after a few months, residents were able to return home.

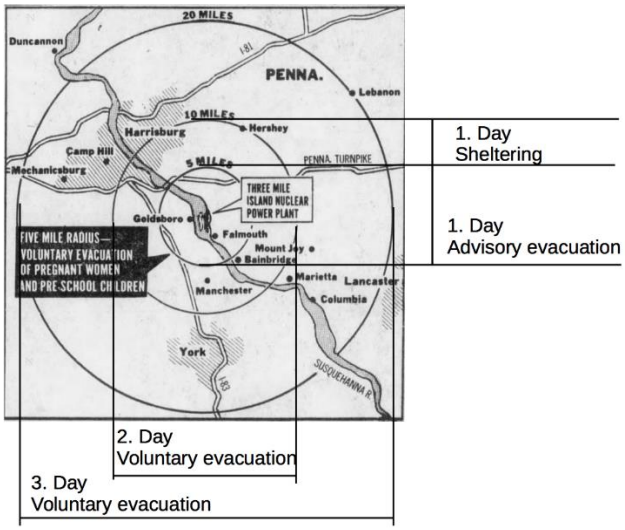

Figure 1. Map of evacuation zones following the Three Mile Island accident (modified from the original source https://www.newspapers.com).

2.2. The Chernobyl experience

The Chernobyl disaster occurred in 1986 in the Ukrainian Soviet Socialist Republic, is still considered to be the worst accident in the history of nuclear power industry having the level 7 of INES (Bavelacqua, 2016). During a technical test, one of the reactors went out of control, which led to an explosion and subsequent fire. As the result, the reactor building was completely destroyed, and large amounts of radiation was released into the atmosphere.

Unfortunately, information about the accident was withheld on the political grounds, residents learned rumors and could not believe that accident was true. Even when officials announced the evacuation, it was said that it would be temporary and implemented as a protective measure in the event of a sudden hazard. However, by that time, all population living in the immediate vicinity of the station had already received the highest doses of radiation. In the long run, all people from the 30-km radius zone were displaced, as well as from other “hotspots” identified over time, which still remain abandoned. Evacuation was carried out only as mandatory and under the strict control of the government. Ukraine still continues to bear – by itself – the main social burden of dealing with the consequences of the Chernobyl disaster.

2.3. The Fukushima-Daiichi experience

The last major accident in the nuclear industry occurred in Japan in 2011 as the result of the Tohoku Earthquake of magnitude of 9.0-9.1 (Bavelacqua, 2016). Earthquake-induced tsunami struck the reactor’s building resulting in power loss at the Fukushima-Daiichi NPP. In the absence of power, the cooling systems failed in three of the six reactors, and their cores thereafter

overheated thus, joining Chernobyl to have the level 7 according to the INES.

Post-Fukushima emergency response included mandatory and voluntary evacuations, temporary sheltering, and relocation (The National Diet of Japan, 2012). On the fifth day after the accident, Japanese authorities ordered a compulsory evacuation within a radius of 0-20 km and a simultaneous shelter-in-place within 20-30 km radius (Fig.2). And ten days after this decision, a voluntary evacuation was announced in the radial zone between 20-30 km (what was previously under the sheltering order). However, by the time the order for voluntary evacuation was adopted, almost the entire population in the 20-30 km zone had already left. Risk and a sense of fear led many people to perceive the situation as more critical than it really was. In addition, due to traffic congestions caused by this excessive evacuation, many people accidentally fled to much more polluted areas.

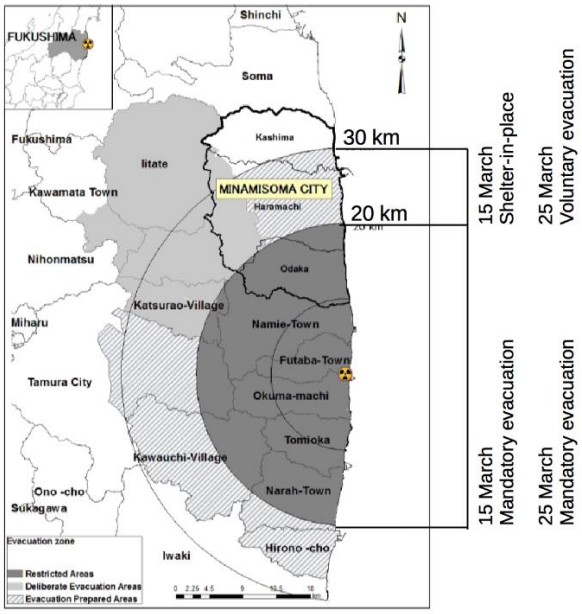

Figure 2. Map of evacuation zones following the Fukushima disaster, 2011 (modified from the original source (Do, 2019).

Table 1. People's returns after the lifting of evacuation orders (Do, 2019).

Region	Date of lifting the evacuation order	Population prior to accident	Population as of 2020
Futaba	March 2020	6,932	0
Katsuaro	June 2016	1,530	420
Kawamata	March 2017	15,569	**12,170**
Kawauchi	October 2014	2,820	**2,044**
Litate	March 2017	6,209	1,318
Minamisoma	July 2016	70,878	**59,005**
Namie	March 2017	20,905	1,923
Naraha	September 2015	7,700	3,710
Okuma	April 2019, March 2020	11,570	847
Tomioka	April 2017, March 2020	16,000	2,128
Tamura	April 2014	40,422	**35,503**

Note: The rate of returns more than 70% are marked in bold. Naraha's returns rate is 48% and all the rest are less that 30%.

Sometime later, owing to the decontamination efforts, Japan managed to recover some of the affected regions and lift the evacuation orders there, allowing people to return home (Table 1). A few chose to return, but the majority refused. Evidence from several cohort studies have shown that the main reason evacuees do not return home is the fear of radiation (Do, 2019).

3. Results and discussions: Issues to which attention should be paid in emergency preparedness

It is clear from the brief overview above that the scale of human response immediately following the nuclear accident can be uncertain. In case of Chernobyl, when the government did not release even sketchy details of the accident and generally tried to minimize its severity, the residents, having no idea what was happening, continued to live their normal lives not even trying to shelter in the safer place. In case of the accidents at the Three Mile Island and the Fukushima-Daiichi NPPs, when local authorities declared an emergency almost immediately after the accident, the population perceived the situation ambiguously. Nevertheless, actual nuclear emergencies have shown a high rate of self-evacuation, especially when residents receive incomplete or unclear information about the accident. Communicating with the public immediately after a disaster, when risk perception is low may result in messages being ignored, and vice versa, a sharp convey of information may lead to public panic, limiting the management of the situation. On the whole, we offer the following recommendations for improving the emergency response:

- It is important to focus on pre-accident communication – to develop an educational program on preparedness actions, where people living near the NPP should receive guidance on how to respond immediately after an accident.
- Residents should understand in advance which action is most appropriate for them, if it is evacuation or shelter.
- Information about the possible consequences of a nuclear accident should be clearly explained and detailed, including situations where non-compliance with government requirments could be dangerous.
- Information should aim to minimize uncertainty among the public by providing the most requested information, including the effects of radiation exposure, the protective measures to be taken first, and the length of time people may need to shelter.
- All information and communications should use basic terminology and plain language, avoiding technical legal terms.
- Information provided in the event of an emergency should sound the same as information presented in pre-emergency communication.

Ultimately, without the proper practice of informing the public about nuclear emergencies, a catastrophic accident could become more serious than we can

imagine. It is imperative that we look for and plan ways to inform the public about protective actions in the event of a radiological emergency.

4. Conclusion

In this study, we examined public response to the decision to evacuate in the radiological accident. As an example, we used three accidents at NPP – the Three Mile Island, the Chernobyl, and the Fukushima-Daiichi accidents, since these disasters are the most serious of all that have occurred. The results of this study directly pointed to the urgent need to improve the nuclear emergency management through an interdisciplinary approach by integrating engineering methods and social disciplines. In our future work, we plan to develop and implement these suggestions.

Acknowledgement

This study was carried out as part of the Ph.D. Thesis prepared by authors at Istanbul Technical University, Graduate School. The corresponding author expresses her gratitude to Prof. Dr. Reha Metin Alkan for his continuous support and assistance.

References

Bevelacqua, J. J. (2016). The Three Mile Island, Chernobyl, and Fukushima Daiichi accidents and their radiological impacts. International Nuclear Safety Journal, 5(1), 21-79.

Do, X. B. (2019). Fukushima Nuclear Disaster displacement: How far people moved and determinants of evacuation destinations. International journal of disaster risk reduction, 33, 235-252. https://doi.org/10.1016/j.ijdrr.2018.10.009

Fesenko, S. V., Sanzharova, N. I., Isamov, N. N., & Shubina, O. A. (2021). The Chernobyl Nuclear Power Plant Accident: Countermeasures and Remedial Actions in Agriculture. Biology Bulletin, 48, 2127-2140. https://doi.org/10.1134/S1062359021120049

Flynn, C. B. (1982). Reactions of local residents to the accident at Three Mile Island. In D.L. Sills (Ed.). Accident at Three Mile Island (pp. 49-63). New York: Routledge. https://doi.org/10.4324/9780429048647

Handl, G. (2016). Nuclear Off-site Emergency Preparedness and Response: Some International Legal Aspects. In: Black-Branch, J., Fleck, D. (eds) Nuclear Non-Proliferation in International Law-Volume III. T.M.C. Asser Press, The Hague. https://doi.org/10.1007/978-94-6265-138-8_11

Kawaguchi, D., & Yukutake, N. (2017). Estimating the residential land damage of the Fukushima nuclear accident. Journal of Urban Economics, 99, 148-160. https://doi.org/10.1016/j.jue.2017.02.005

Saidi, K., & Mbarek, M. B. (2016). Nuclear energy, renewable energy, CO2 emissions, and economic growth for nine developed countries: Evidence from panel Granger causality tests. Progress in Nuclear Energy, 88, 364-374. https://doi.org/10.1016/j.pnucene.2016.01.018

Shimada, Y., Nomura, S., Ozaki, A., Higuchi, A., Hori, A., Sonoda, Y., & Tsubokura, M. (2018). Balancing the risk of the evacuation and sheltering-in-place options: a survival study following Japan's 2011 Fukushima nuclear incident. BMJ open, 8(7), e021482. https://dx.doi.org/10.1136/bmjopen-2018-021482

Stallings, R. A. (1984). Evacuation behaviors at Three Mile Island. International Journal of Mass Emergencies & Disasters, 2(1), 11-26. https://doi.org/10.1177/028072708400200102

The National Diet of Japan, 2012. The official report of the Fukushima nuclear accident independent investigation commission. The official report of the Fukushima nuclear accident independent investigation commission, Tokyo.

Webb, G. A. M., Anderson, R. W., & Gaffney, M. J. S. (2006). Classification of events with an off-site radiological impact at the Sellafield site between 1950 and 2000, using the International Nuclear Event Scale. Journal of Radiological Protection, 26(1), 33. doi:10.1088/0952-4746/26/1/002

Zhang, Z., Herrera, N., Tuncer, E., Parr, S., Shapouri, M., & Wolshon, B. (2020). Effects of shadow evacuation on megaregion evacuations. Transportation research part D: transport and environment, 83, 102295. https://doi.org/10.1016/j.trd.2020.102295

6th Intercontinental Geoinformation Days

igd.mersin.edu.tr

Vegetation indices in the assessment and management of soil fertility

Matanat Asgarova*

Azerbaijan State Pedagogical University, Faculty History and Geography, Department General Geography, Baku, Azerbaijan

Keywords
Soil assessment
Soil management
Vegetation indices

Abstract

Spatial information technologies are deeply rooted in all spheres of human activity, including agriculture. Today we're talking about smart, precise, digital farming. Soil fertility assessment, field monitoring, yield forecasting, proper farming, soil fertility management include not only the collection and analysis of soil data, but also collection spatial information. In GIS Technologies, vejetatife indices provide information for precision farming, providing data on crop growth and health. With the help of global positioning, it is possible to accurately determine the location on the ground of each site, as well as monitor the development of crops from sowing to harvesting, identify moisture and nutrient deficiencies in time, and identify plant diseases. GIS technologies allow you to manage soil fertility and crop quality to the level of private fields. The study area was irrigated soils in the northern part of the Imishli region of the Republic of Azerbaijan, with an area of 3211.9 hectares. Important branches of agriculture in the region are cotton growing and grain growing. When assessing and managing soil fertility, we tried to use some vegetation indices, such as NDVI, MSAVI, NDRE, as a criterion for assessing fertility. Spatial analysis of soil data helps in agricultural planning and helps to make quick and correct decisions on soil fertility and land use management. Within the framework of agricultural fields, GIS technology is used to apply soil fertilizers with certain standards in accordance with the condition of the site, as well as for the proper organization of irrigation.

1. Introduction

Spatial information technologies have penetrated deeply into all areas of human activity, including agriculture. Today we are talking about smart, precise, digital agriculture. Soil fertility assessment, crop monitoring, yield forecasting, proper farming and soil fertility management include not only soil data collection and analysis, but also spatial information about the terrain and the environment.

Geographic information system and remote sensing are widely used in modern farming systems. Global positioning can be used to determine the exact location of each plot on the land, as well as to monitor crop development from sowing to harvesting, identify moisture and nutrient deficiencies, and detect plant diseases. GIS technology makes it possible to manage soil fertility and crop quality down to the level of private fields. Every farmer can obtain a forecast for the timing of sowing, irrigation, fertilisation and harvesting. Geographic information systems make it possible to store, retrieve and analyse spatial data based on satellite images and drone imagery, using computer hardware and software.

2. Method

Modern soil and land-use mapping requires three basic elements - topographic maps at different scales, aerospace imagery and GIS mapping software.

According to the methodology of soil mapping, an electronic soil map of the district was prepared and soil fertility was assessed on a closed scale using a 100-point system and on an open scale using coefficients on limiting factors (Mammadov, 2020).

We applied NDVI (Normalized Difference Vegetation Index), the most used index in agricultural research, to assess productivity and soil fertility management (Asgarova, 2021). This index is a numerical index using spectral bands and is closely related to moisture and green vegetation.

Besides NDVI, ArcGIS Pro has a large number of vegetation indices for different applications, such as

* **Corresponding Author**

*(matanat_askerova@mail.ru) ORCID ID 0000-0002-6396-6828

Cite this study

Asgarova, M. (2023). Vegetation indices in the assessment and management of soil fertility. Intercontinental Geoinformation Days (IGD), 6, 270-273, Baku, Azerbaijan

SAVI (Soil Adjusted Vegetation Index), MSAVI (Modified Soil-Adjusted Vegetation Index), NDRE (Normalized Difference RedEdge), etc.

2.1. Study Area

Crops in the northern part of Imishli district of Azerbaijan Republic, at coordinates 48°5'17,157", 39°59'20,536", an area of 3210 ha "Fig.1" were selected as the study area. More than 90% of the area is between -7 and -12 m above sea level. The important spheres of agriculture in this area are cotton growing and grain farming. As can be seen from the picture, a new irrigation system "Figure 1" has been fully implemented in the district. The district was developed a few years ago. On the classic soil map, the area is marked as winter pasture "Figure 2".

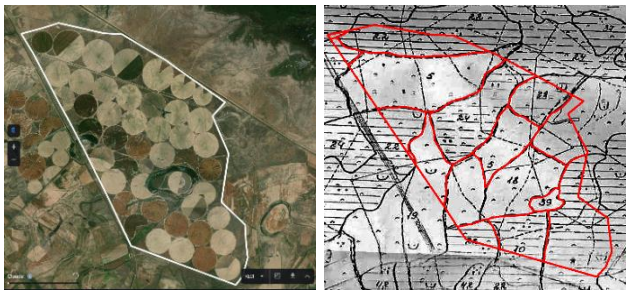

Figure 1-2. The study area in the 2021 satellite image and the classic soil map

The study area is fully irrigated and mainly used for cereals and cotton cultivation “Figure 3”.

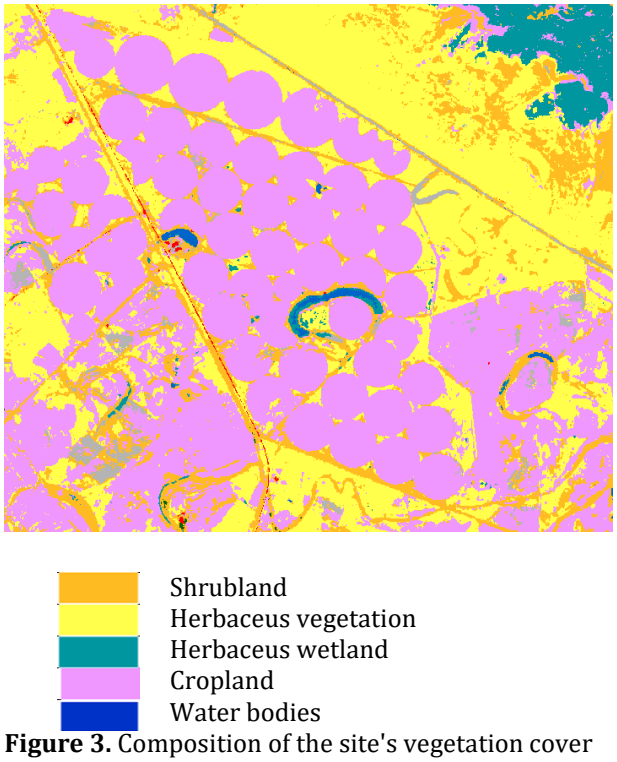

Figure 3. Composition of the site's vegetation cover

Satellite imagery is very effective in dynamically updating field boundaries to the farm level. Using fuzzy object-oriented image analysis (OBIA) we have carried out for the first time in our republic the delineation of agricultural fields at a specific site (Rasouli 2021, 2022).

2.2. Normalized Difference Vegetation Index

NDVI is calculated using the Equation 1

$$NDVI = (NIR-RED) / (NIR+RED) \quad (1)$$

where NIR is light reflected in the near-infrared spectrum, RED is light reflected in the red spectrum. NDVI is expressed as -1 to 1. Negative NDVI values mainly show clouds, water and snow, while values close to zero show rocks and bare ground. NDVI values between 0.2 and 0.3 represent shrubland and grassland and between 0.6 and 0.8 represent forest. NDVI can identify fields with dense, moderate or sparse vegetation at any time. If NDVI values are between 0.95 and 1.00 it is considered better to use NDRE "Table 1".

Table 1. NDVI values

Land cover	Values NDVI
Better to use NDRE	0,95 – 1,00
Dense vegetation	0.60 – 0.95
Moderate vegetation	0.40 – 0.60
Sparse vegetation	0.20 – 0.40
Open soil	-1.00 – 0.20

We compared the NDVI on 2 June and 15 September 2021 "Figure 4". Note the areas where the NDVI value is very different. For example, areas of a field with too low NDVI indicate pest or plant problems; areas with abnormally high NDVI indicate an admixture of weeds.

Figure 4. NDVI - June 2, and September 15, 2021

The values in the figures and in the graph are very different. While in early June the NDVI dense vegetation index was 2.58% within the study area, in the first half of September it was 36.70% "Figure 5".

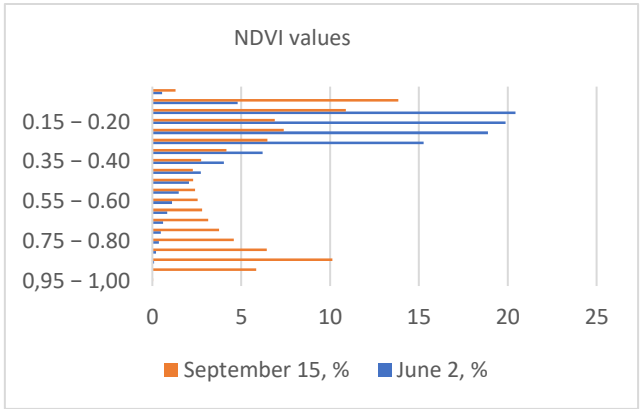

Figure 5. NDVI values on June 2, September 15, 2021

These NDVI properties enable you to predict crop yields and monitor crop condition throughout the growing season, as well as properly organize the rates and timing of irrigation, fertilization and other agronomic measures.

2.3. Soil evaluation

Soil fertility was assessed based on 100-point diagnostic indicators in a closed scale and taking into account coefficients on salinity, granulometric composition, irrigation, etc. in an open scale. A soil fertility assessment map has been drawn up. “Fig. 6”.

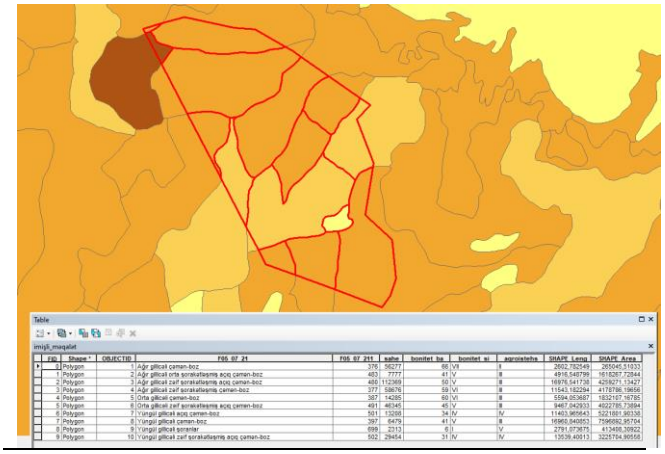

№	Soil names	Area, ha
1	Heavy loamy meadow-gray soils	56277
2	Heavy loamy medium saline light meadow-gray soils	7777
3	Heavy loamy slightly saline light meadow-gray soils	112369
4	Heavy loamy slightly saline meadow-gray soils	58676
5	Medium loamy meadow-gray soils	14285
6	Medium loamy slightly saline light meadow-gray soils	46345
7	Light loamy light meadow-gray soils	13208
8	Light loamy meadow-gray soils	6479
9	Light loamy salt pans	2313
10	Light loamy slightly saline light meadow-gray soils	29454
	Sum:	**347183**

Figure 6. Soils assessment cartogram

Each soil contour of the cartogram has attribute information - name, area, perimeter, coordinates, bonitet point, also each immet additional information (i) agrochemical, agrophysical and environmental data "Figure 7".

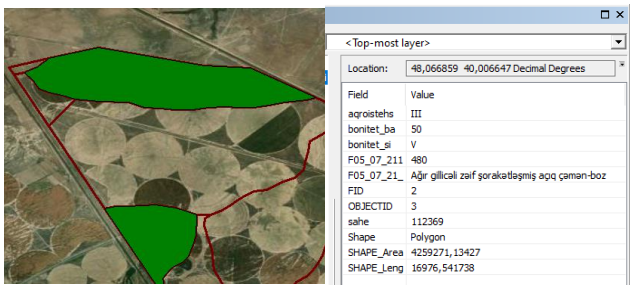

Figure 7. Information on the soil contours

3. Results

While in early June the NDVI dense vegetation index was 2.58% within the study area, in the first half of September it was 36.70%

Varieties of irrigated meadow-gray and light meadow-gray soils are common in the area. 32% of the site is occupied by heavy loamy light saline light meadow-gray soils, which scored 50, 17% by heavy loamy light saline meadow-gray soils, which scored 59, and 13% by medium loamy light saline light meadow-gray soils, which scored 60. Heavy loamy meadow-gray soils received the highest score of 66, with an area of 16%.

4. Discussion

NDVI has the advantage of identifying problematic fields and improving the accuracy of fertiliser and irrigation applications. Crop indices are tools for remote monitoring of crop health. Crop indices can be used to monitor crop rotation patterns, current vegetation intensity, temperature, precipitation, growth stage and much more.

Based on NDVI measurements, zoning can be carried out. This allows the creation of special maps for the application of seed rates and fertilisers. NDVI makes it possible to identify weak and strong zones of productivity throughout the field, measured over a long period of time. Based on NDVI, time and resources can be saved by providing farmers with accurate geolocation of problem fields. Farmers can get information about field conditions via mobile phones and mobile platforms. Based on each new satellite image, optimal and prompt decisions can be made.

5. Conclusion

Spatial analysis of soil data helps in agricultural planning and helps to make quick and right decisions for land cover and management. Within the limits of agricultural fields, GIS technology is used for the application of soil fertilizers with certain norms according to the condition of the site, as well as the correct organization of irrigation.

The use of NDVI makes it possible to identify fields with dense, moderate or rare vegetation at any time, so this index is very relevant for the assessment and management of soil fertility.

Environmental factors may affect the accuracy and reliability of vegetation index measurements. These factors should be taken into account when analyzing data to ensure that measurements are meaningful. Sizing is also an important factor, as vegetation indices should be calibrated to take account of differences in sensor characteristics, atmospheric conditions and other factors that may affect the accuracy of measurements. The lack of proper calibration of vegetation indices may lead to the use of multiple vegetation indices for proper interpretation and decision-making in the assessment and management of soil fertility.

Acknowledgement

Thank you to Professor Aliakbar Rasouli for supporting the paper.

References

Asgarova, M. M. (2021). Application of CIS technologies in managing soil fertility. 3rd International November 24 Head Teacher Education and Innovative Sciences Symposium, 24-25 May, 2021, Baku, Azerbaijan, 58-63

Mammadov, G. Sh., Hasanov, V. H., Mammadova, S. Z., & Askerova, M. M. (2020). Guidelines for the preparation of interactive soil maps and maps of ecological assessment of soils at a scale of 1:100000. Baku: Elm, 88 p.

Radočaj, D., Šiljeg, A., Marinović, R., & Jurišić, M. (2023). State of major vegetation indices in precision agriculture studies indexed in web of science: A review. Agriculture, 13(3), 707. https://doi.org/10.3390/agriculture13030707

Rasouli, A. A., Asgarova, M. M., & Safarov, S. H. (2021). Mapping of LC/LU changes inside the Aghdam district of the Karabakh economics region applying object-based satellite image analysis. Journal of Life Sciences & Biomedicine, 3(76), 54-69.

Rasouli, A. A., Mammadov, G. Sh., Asgarova, M. M. (2021). Mastering Spatial Data Analysis Inside the GIS Setting. Azerbaijan, Baku: "Science" publishing house of Azerbaijan National Academy of Sciences, 398 p.

Rasouli, A., & Asgarova, M. (2022). Boundary delıneatıon of agrıcultural fıelds by applyıng fuzzy object-based ımage analysıs. Reliability: Theory & Applications, 17(SI 4 (70)), 94-105.

6th Intercontinental Geoinformation Days

igd.mersin.edu.tr

Wildfire hazard and risk assessment at the instance of Gabala district

Aghayeva Firuza[*1]

[1]*Institute of Geography named after akademicain Hasan Aliyev, Geoekology, Baku, Azerbaijan*

Keywords
Remote sensing
Wildfire
Fire risk assessment

Abstract

As one of the main natural resources for humans, protection of forest resources is one of the main ecological problems of the world. Forests are a source of oxygen, as well as they have some features that can ensure ecological balance. For example, forests are one of the major factors that prevent landslides, erosion processes, flood events, as well as protecting land resources, hydrological resources and optimization micro climatic condition. Decreasing of forest stock affects the fauna directly. There are some factors that impact decreasing of forest resources, for example, settlements, industry and forest supply and etcetera. Forest fires occurring in different parts of the world every year eradicated acres of forest stock. The formation of forest fires is influenced by factors such as climate, anthropogenic and topological effects. Research area is district of Gabala which is situated at south slopes of Greater Caucasus. Gabala is distinguished by the abundance of forest resources in the territory of Azerbaijan, which is poorly provided with forest reserves. XX hectares of this district are covered with forests. Taking into account that XX% of the fire incidents that occurred on the southern slope of the Greater Caucasus in 2021 and 2022 took place here, this place was taken as a research area. Wildfire hazard and risk assessment and fire risk zonation, anthropogenic and topological effects are considered in this article and mapping had been done. The resulting values were classified according to the risk group and the results were compared with the fire area data. As a result of the comparison, was not found fire process in the categories of no risk or low risk. 90% of fire incidents could be classified as medium risk, high risk and critic high risk categories. Consequently, this is an indicator of the validity of the selected parameters and the conducted assessment.

1. Introduction

Research area is located South slopes of Great Caucasus and Qanıx-Ayricay valley .Qabala is old district of azerbaijan. The region is located at an altitude of 68-4466 m. It covers an area of 1548600 ha. Forest area occupies 21% of the territory. Fauna and flora species included in the red book of Azerbaijan are spread in the area. Azerbaijan is a country with few forest resources. Forests covered 11% of the country's total area. The south slope of the Greater Caucasus stands out in the country for its percentage of forests (40% of the area). On the South slopes of Great Caucasus, which is well provided with forest resources, nature protection is considered one of the urgent issues. 45 percent of the territory is occupied by Specially Protected Nature Areas. There are a part of the Shahdag National Park, Gabala and Turyanchay nature reserves, 28 biological nature monuments and specially important forest areas taken under state control in the territory of Gabala region. Despite this, 40% of the fires that occurred on the south slopes of the Greater Caucasus in 2021 and 2022 fall on the territory of Gabala region. During the research period, 1826.3 ha of forest area was burned. This is 5.64% of the total forest area of the district. During the research period, 1826.3 ha of forest area was burned. This is 5.64% of the total forest area of the district. 2021 and 2022 were taken as research years. Wildfire hazard and risk assessment and fire risk zonation of Gabala district was carried out taking into account factors such as anthropogenic and effects of topography. In order to assessment the obtained result, it was compared with the fire data of recent years and the areas covered by the fire.

2. Method

Remote Sensing data programs and ArcGIS/ArcGIS map 10.8 Software were used for fire risk assessment in Gabala region during the research. Effects of topography (slope, elevation, aspect) and anthropogenic parameters were taken as criteria. when assessing the fire risk of

* **Corresponding Author**

*(firuzaaghayeav.geoph@gmail.com) ORCID ID xxxx – xxxx – xxxx – xxxx

Cite this study

Firuza, A. (2023). Wildfire hazard and risk assessment at the instance of Gabala district. Intercontinental Geoinformation Days (IGD), 6, 274-277, Baku, Azerbaijan

the area, it is divided into 5 categories; no risk; low risk; medium risk; high risk; critical risk. Here, the slope, elevation, aspect and land use and land cover parameters were reclassified .Then overlay and map algebra operations were performed. Using this information, a fire risk assessment and risk zonation map was created. 30 m resolution SRTM DEM data provided by NASA, USGS were used to study Aspect, Slope and Elevation parameters. To investigate the land use and land cover parameters, the "Landsat 8" data provided by USGS Earth Explorer dated 17.07.2022 was used.

Data on wildfires and burned agricultural residues were obtained from the Moderate Resolution Imaging Spectroradiometer (MODIS), a satellite-based sensor. Information about Forest and agricultural resides active fire location data was taken "NASA FIRMS" application which is uses different type of satellite-based sensor (Landsat, VIRS (S-NPP & NOAA 20), MODIS (Aqua & TERRA). Using in this data was created wildfire burned area and active wildfire location map and graphs. Also, using the existing stock literature materials, information on climate was investigated and certain results were obtained.

Table 1. Wildfire risk assessment criteries

Risk assess-ment	aspect	slope	Eleva-tion	Land use and land cover
No risk	0°-45°, 315°-360°	0-8°	3500-4466	Water bodies, bare earth, bare soil
Low risk	45°-90°, 270°315°	8-15°	3000-3500	Selitep areas
Moderate risk	90°-135°,	15-25°	68-500	Agriculture land
High risk	135°180°, 225°270°	25-35°	2000-3000	Pasture
Critic risk	180°-225°	35-68°	500-2000	Forest

3. Results

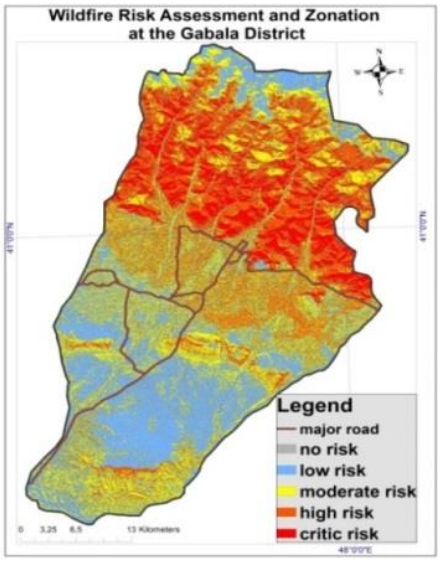

Figure 1. Wildfire risk assessment and zonation

Based on the effects of topography (slope, aspect, elevation) and Land use and Land cover parameters of the study area, fire risk classification was carried out.A fire risk assessment and a zonation map were drawn up according to the obtained categories. As a result, based on the obtained values, overlay and map algebra operations were performed, and the WildFire Assessment and Zonation map was drawn up and the area of the areas included in the risk categories was calculated (Figure 2).

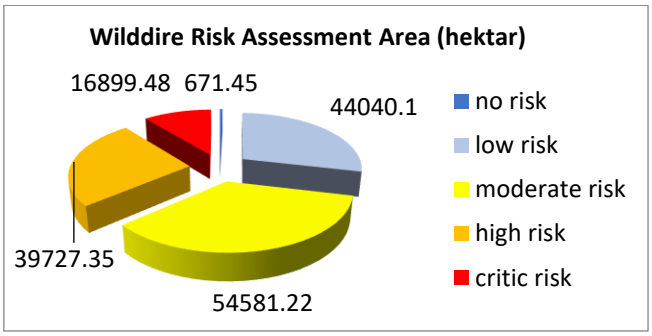

Figure 2. Wildfire risk assessment areas (hektar)

In general, 0.43% of the territory corresponds to no risk, 28.24% to low risk, 35.01% to moderate risk, 24.48% to high risk, and 10.84% to critical risk classification.

The resulting values were classified according to the risk group and the results were compared with the fire area data. In total, 108 fire incidents occurred in the area in 2021 and 11 in 2022 year. As a result of the comparison, no fire process was found in the non-risky area. There were 2 fire incidents in the low risk category, 10 in the moderate risk category and 107 in the high and critical risk categories. Thus, we can see that 90% of fire incidents correspond to the high risk and critical risk category (Figure 3-4)

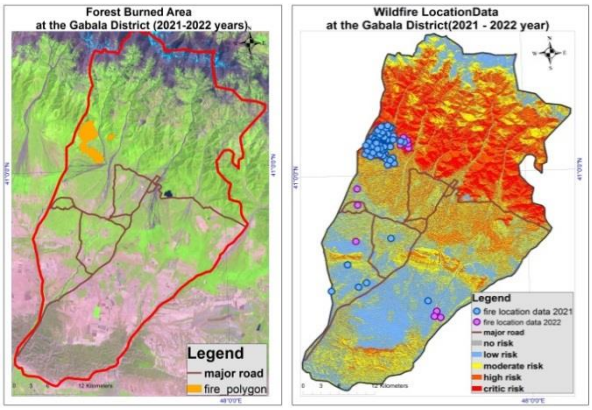

Figure 3-4. Forest burned area on the left and Wildfire location data on the left (2021-2022 year).

When the obtained results are compared with the fire area data, we can see that 100% of the area corresponds to the high risk and critical risk category. In general, during the study period, it was determined that 5.4% of the forest resources were destroyed based on the fire area data (Figure 2).

In these results, it is an indication that the selected parameters and the evaluation are reasonable.

4. Discussion

As one of the main natural resources for humans, protection of forest resources is one of the main ecological problems of the world. Forests are a source of oxygen, as well as they have some features that can ensure ecological balance. For example, forests are one of the major factors that prevent landslides, erosion processes, flood events, as well as protecting land resources, hydrological resources and optimization micro climatic condition. Decreasing of forest stock affects the fauna directly. There are some factors that impact decreasing of forest resources, for example, settlements, industry and forest supply and etcetera. Forest fires occurring in different parts of the world every year eradicated acres of forest stock.

The formation of forest fires is influenced by factors such as climate, anthropogenic and topological effects. Research area is district of Gabala which is situated at south slopes of Greater Caucasus. Gabala is distinguished by the abundance of forest resources in the territory of Azerbaijan, which is poorly provided with forest reserves. In the north of Gabala, alpine and subalpine meadows, mountain forests, bushy and sparsely wooded meadows in the central part, and wormwood and wormwood-saline semi-desert plants, xerophytic sparse forests occupy a large area. It is an area with high tourism potential. It has a dense river network system (Türyan, Demiraparan and their tributaries Tikanlıchay, Bum, Vandam, etc.).

When assessing the occurrence and spread of forest fires, it is important to consider parameters such as climate, anthropogenic and effects of topography. In this article, the classification was made mainly based on anthropogenic and relief factors. The following table lists the parameters of the classification and the results of research conducted based on these parameters in the area.

Table 1. Areas calculated based on wildfire risk assessment criteria.

Risk assess-ment	aspect	slope	Eleva-tion	Land use and land cover
No risk	34142,9	74666,7	2032,7	20802,2
Low risk	395550,7	19792,9	6413,82	32495,19
Moderate risk	15961,1	24991,2	58011,6	24395,95
High risk	47370,8	25011,1	12593,3	46371,68
Critic risk	28897,6	11459,8	42198,3	32405,15

Climate factor. The climate is mild-warm with dry winters in the lower part, and cold and humid in the highlands. Annual precipitation is 500-600 mm in the lower part, up to 1600 mm in the highlands. Average monthly temperature decreases with increasing altitude. While the average temperature in July is 24-27 C° in the plain part of the region, it drops to 20-15 C° in the middle highlands, and 10-5 C° in the highlands. While the average January temperature is 2 C° in the plains, it drops from -10-(-11) C° to even -14-(-15) C° in the high mountain peaks. Taking into account climate parameters (temperature and humidity), the risk of fire decreases with increasing altitude. The increase in temperature in the summer months and the partial decrease in precipitation increase the risk of fire. During the research period, according to the data we took from the "NASA FIRMS" platform, it can be seen that 93.27% of fire incidents happened in the summer months (August, early September). It should be noted that the fire events that occurred in September coincided with the first 5 days of the month.

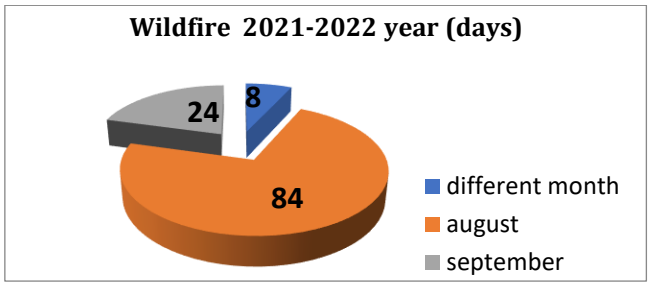

Figure 5. Wildfire events 2021-2022 year (days)

Anthropogenic factors are one of the main factors we should pay attention to when assessing fire risk. A number of anthropogenic effects, which we have listed below, cause forest fires.

- carelessness, negligence and intentional burning.
-making campfires in the forest without observing safety rules
-Throwing unextinguished cigarette butts and matches on the ground
- throwing glass and broken glass into the forest
- stubble burning
- intentional fires

The distance from residential areas and highways was taken into account when assessing the risk. Looking at the map of highways in Figure 3-4, it is clear that most of the fires classified as moderate risk occur in the buffer zone of 2000 m, which is defined as a risk area. (Figure 5).

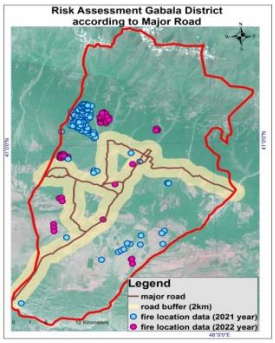

Figure 6. Risk Assessment according to major road.

The settlement factor was taken into account during the research. After the 2000s, the rapid development of tourism in the region has led to an increase in anthropogenic loads in the area. Resort-recreation centers created in the forest area increase the risk of forest fires of anthropogenic origin. As we can see in Map1, the central part of the area (200-800 m) is more densely populated. This corresponds to the lower

border of the forest. Settlements exist in the middle forest (800-1200 m) zone.

The map was prepared using arcgis 10.8 software from Landsat 8 data dated 17.07.2022 provided by USGS EarthExplorer. At this time, forest, agriculture land, urban areas, pastures, bare soil and earth land areas were classified using 1, 2, 3, 4, 5, 6, 7 band combinations and a land use and land cover map was drawn up. The resulting values were classified according to the risk group. The forest area of the total area is 20.71%. Settlement and appropriated areas cover 36.36%, summer and winter pastures cover 29.64%. In general, it is classified as water bodies, bare earth and soil land no risk, selteps low risk, agricultural area medium risk, pastures high risk, forest critical risk. In Figure 5, the Land use and Land cover map of the area was drawn up, then fire risk classification was made based on it.

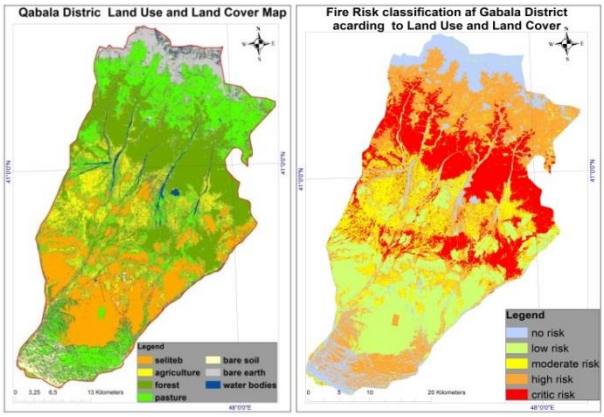

Figure 7-8. Land use and land cover on the left and fire risk classification acording to land use and land cover on the right

Elevation, slope and aspect parameters of the area are the main relief features that affect the risk of forest fires. It provides important information about the determination of the fire area, the speed and direction of its spread. Assuming other risk factors are constant, fire will move fastest on steep slopes. That said, increased inclination also increases the risk of fire.

The territory of Gabala district has an inclination interval of 7° - 68°. The inclination increases from south to north. 5 classifications were used when assessing forest fire risk based on slope inclination: 0-8° no risk, 8-15° low risk, 15-25° medium risk, 25-35° high risk and 35-68° critical risk areas. 47.9% of the total area of the territory is classified as no risk, and 23.4% as high and critical risk (Figure 6).

Fire conditions vary greatly depending on the aspect. In general, the south and southwest sides have good conditions for fire initiation and spread. These areas receive more sunlight. Increases the temperature of air and combustible material (Figure 7-8).

Elevation data is closely related to the distribution of vegetation. Vegetation in the study area is distributed along the vertical zonation of the mountainous area. Bushy and sparse meadows are spread in the central part, and semi-desert plants with wormwood and sorrel in the south, and arid type forests in the steppe plateau area. At altitudes of 600-2000 m, there are oak, beech and walnut forests. Subalpine (1700-2600 m) and alpine meadows (2500-3100 m) are common in the high mountain zone. At 3100-3500 m above sea level, subnival plants of the tundra type are found. Above 3500 m, the vegetation-free nival zone begins. Taking these into account, Elavatian classification was made again. Areas with an altitude of 500-2000 m are classified as critical risk zone, while areas higher than 3000 m are included in no-risk and low-risk categories (Figure 9-10-11).

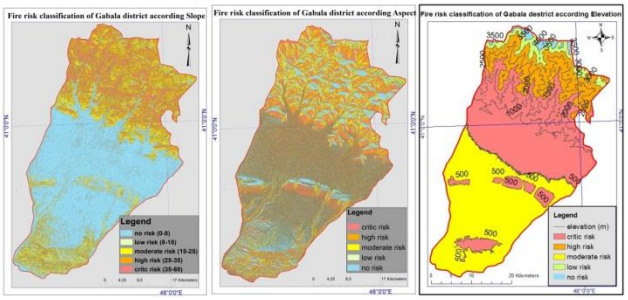

Figure 9-10-11. Fire risk classification according slope on the left , fire risk classification according aspect on the middle and fire risk classification acording elevation on the right.

5. Conclusion

Burned area data was used to verify the obtained data. The data is taken from the FIRMS database with 1000 m resolution from MODIS/MOD 14 sensors from the earth.data.nasa.gov application. Vectorized and area calculated using ArcGis 10.8 software. Data covers 2021 and 2022. The burnt forest area is 1826.3 ha, which is 5.4% of the forest area of Gabala district. 100 percent of the burned area corresponds to the high and critical risk classification zone. 2021 and 2022 data from MODIS (Aqua and Terra) sensors provided by NASA FIRMS are taken. In Gabala district, 11 fire incidents occurred in 2021 and 108 in 2022. 90% of recorded fire events correspond to the high and critical risk classification area, 8.4% to the moderate risk zone, and 1.6% to the low risk zone.

References

Atun, R., Kalkan, K., & Gürsoy, Ö. (2020). Determining The Forest Fire Risk with Sentinel-2 Images. Turkish Journal of Geosciences, 1(1), 22–26.

Bar, S., Parida, B. R., & Pandey, A. C. (2020). Landsat-8 and Sentinel-2 Based Forest Fire Burn Area Mapping Using Machine Learning Algorithms on GEE Cloud Platform over Uttarakhand, Western Himalaya. Remote Sensing Aplications: Society and Environment, 18, 100324.

Məmmədov, Q., & Xəlilov M. (2022). Azərbaycan meşələri. 26 Müseyibov, M. (1998). Azərbaycanın fiziki coğrafiyası. 127-131

Rawat, J. S., & Kumar, M. (2015). Monitoring land use/cover change using remote sensing and GIS techniques: A case study of Hawalbagh block, district Almora, Uttarakhand, India. Egyptian Journal of Remote Sensing and Space Science, 18(1), 77–84.

6th Intercontinental Geoinformation Days

igd.mersin.edu.tr

What is the best spatial interpolation technique for evaluating droughts?

Ahmad Abu Arra*[1], Eyüp Şişman [1] Mehmet Emin Birpınar[2]

[1]*Yildiz Technical University, Civil Engineering Faculty, Hydraulics Department, Istanbul, Türkiye*
[2]*Ministry of Environment and Urbanization, Çankaya, Ankara, Türkiye*

Keywords
Drought analysis
SPI
Spatial Interpolation
IDW
Kriging

Abstract

Drought is a destructive phenomenon that negatively impacts the environment and socioeconomic aspects. Drought can be evaluated temporarily and spatially based on drought indices, such as Standardized Precipitation Index (SPI). Spatial evaluation of drought has been conducted in the literature using many spatial interpolation methods without mentioning the difference between these methods and their accuracy. This research paper aims to find the accuracy of using Inverse Distance Weighted (IDW) and Kriging methods in evaluating drought based on SPI. Monthly precipitation data from 21 stations in Istanbul were used, 16 stations were used for interpolation, and 5 stations were used for validation. The results showed that the IDW method has more extreme drought values, which means more conservative regarding drought analysis and monitoring than the Kriging method. However, IDW and Kriging have approximately the same correlation coefficient (0.6) with observed values. Also, the correlation between IDW and Kriging was about 0.8. Generally, for drought analysis and monitoring, IDW is more conservative and gives more extreme drought values. Subsequently, validating and using the most suitable method and more research about using interpolation methods in drought are suggested before using any interpolation method.

1. Introduction

Drought is a complicated phenomenon with many definitions, such as an environmental and ecological catastrophe, and has been monitored and evaluated by environmentalists, agriculturists, and hydrologists. Drought has a hugely destructive impact on the environment and socioeconomic aspects. Also, drought occurs in any climate and area and is related to a precipitation deficit in a specific period (Wilhite 2016). Drought is classified into four types. One of the most common droughts is metrological drought. The most crucial variable in this type of drought is precipitation, and to avoid and prevent the negative impacts of droughts, a comprehensive understanding of drought and its characteristics has a leading role. Subsequently, the first step is using drought indices for drought assessment and monitoring (Van Loon 2015).

Several drought indices have been developed, and each one of them has its methodology and variables. Some of these indices are the Standardized Precipitation Evapotranspiration Index (SPEI) (Vicente-Serrano et al. 2010) and the Actual Precipitation Index (API) (Şen 2021). SPI is the most used drought index worldwide because of its simplicity. SPI depends only on one variable, which is precipitation. SPI is calculated for each metrological station (for a specific point), and the obtained results are used for a specific metrological station. Spatial interpolation is used to calculate and evaluate the spatial distribution of the SPI values over a specific study area like a city, country, or continent. Using spatial interpolation helps us measure the unknown values, produce maps, and improve the methodologies by validating data. The term interpolation estimates the unknown and non-observed values using the measurements of observed values at specific locations within the same location and area. Spatial interpolation converts the point observed data into surface data. The most common spatial interpolation techniques are: 1) Inverse distance weighted (IDW) and Kriging (Esri 2012).

In the literature, many articles evaluated the spatial distribution of drought indices using several methods without mentioning the accuracy and difference between these methods. Considering the importance of drought, and spatial evaluation of drought, this research is done to calculate the accuracy of IDW and Kriging methods. Also, to compare these spatial interpolation methods regarding drought analysis based on SPI. Istanbul is an ideal area for this research because of its large database (21 metrological stations), and covers considerable variations in terrain.

* **Corresponding Author**

*(ahmad.arra@std.yildiz.edu.tr) ORCID ID 0000-0001-8679-1752
(esisman@yildiz.edu.tr) ORCID ID 0000-0003-3696-9967
(mehmeteminbirpinar@gmail.com) ORCID ID 0000-0002-5703-6341

Cite this study

Abu Arra, A, Şişman, E., & Birpınar, M. E. (2023). What is the best spatial interpolation technique for evaluating droughts? Intercontinental Geoinformation Days (IGD), 6, 278-281, Baku, Azerbaijan

2. Method

2.1. Data

To investigate the accuracy and compare the Kriging and IDW spatial methods in evaluating droughts based on SPI, the application is conducted for the monthly precipitation records between 2014 and 2020 from 21 metrological stations in Istanbul (MGM). 15 metrological stations were used to get the drought map, and 6 metrological stations were used as observed data to validate the obtaining results from spatial interpolation. All monthly precipitation data were checked for consistency and continuity. Table 1 summarizes the main information about metrological stations.

2.2. Standardized precipitation index (SPI):

The SPI method was developed in 1993 by Mc Kee et al. The precipitation data is fitted to a suitable probability density function (PDF), and the goodness-of-fit tests are controlled and checked by Kolmogorov-Simirnov and Chi-Square (Stephens 1970). The last step is the standardization of probabilities into normal PDFs. More information about SPI can be found in (McKee et al. 1993).

2.3. Spatial interpolation

Inverse Distance Weighted (IDW) is a non-statistical and spatial interpolation method. In the IDW method, the unknown values are calculated and affected more by observed points near the unknown points than points far away. The original / observed data are placed on a surface-distributed grid, and the interpolation procedure is done on this regular grid to generate a spatial map. The simplest form of IDW interpolation is linear interpolation. The quality of the resulting map depends on the validated input points.

Kriging is a geostatistical interpolation method. It estimates the unknown values using the known values and semivariograms. The Kriging procedure incorporates error measures and uncertainty while determining the unknown values (Loquin and Dubois 2010). Depending on the semivariogram, optimal weights are given to known values to calculate unknown values.

2.4. Validation data

One of the main objectives of this research is to find the accuracy of IDW and Kriging spatial interpolation methods, and it is done by using 6 metrological stations as observed data to validate and check the accuracy of resulting data. These stations are distributed over the study area and indicated with a star (*) in Table 1. The validation process is done using Pearson correlation analysis. Figure 1 shows the location of the metrological and validation stations in Istanbul.

3. Results

Drought was analyzed using SPI at a 3-month timescale. SPI was calculated between 2014 and 2020 over Istanbul using 16 metrological stations. The results showed that there is a huge variation in SPI values within this period. Moderate drought ($-1.50 \leq SPI \leq -0.99$), Severe drought ($-2.00 \leq SPI \leq -1.49$), and extreme drought ($-2.00 > SPI$) were noticed within the 7 years in the study area. Figure 2 shows the temporal evaluation of SPI3 from 2014 to 2020 using the average value of the stations for each month.

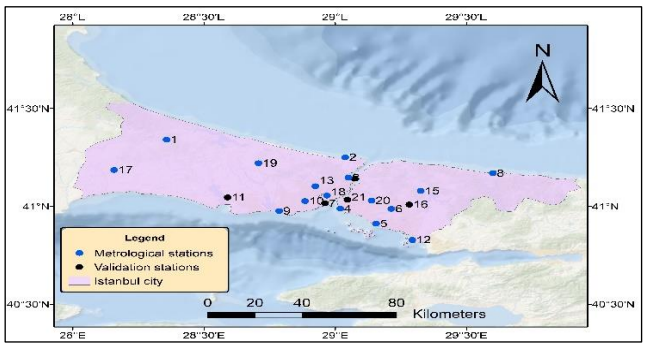

Figure 1. Location of metrological stations in Istanbul

Table 1. Geographical information of the metrological stations

#	Code	Name	Lat (N)	Long (E)
1	17047	ÇATALCA RADAR	41.34	28.36
2	17059	SARIYER/KUMKÖY	41.25	29.04
3	17061	SARIYER	41.15	29.05
4	17062	KADIKÖY RIHTIM	40.99	29.02
5	17064	İSTANBUL BÖLGE	40.91	29.16
6	17065	SAMANDIRA	40.99	29.21
7	17603	FATİH *	41.02	28.96
8	17610	ŞİLE	41.17	29.60
9	17636	FLORYA	40.98	28.79
10	17814	GÜNGÖREN	41.03	28.89
11	18099	BÜYÜKÇEKMECE *	41.05	28.59
12	18100	TUZLA	40.83	29.29
13	18101	EYÜPSULTAN	41.10	28.92
14	18396	BEYKOZ *	41.14	29.07
15	18397	ÇEKMEKÖY	41.08	29.33
16	18399	SANCAKTEPE *	41.01	29.28
17	18400	SİLİVRİ	41.19	28.16
18	18401	ŞİŞLİ	41.05	28.97
19	18402	ARNAVUTKÖY	41.22	28.71
20	18403	ÜMRANİYE	41.03	29.14
21	18404	ÜSKÜDAR *	41.03	29.05

* is the stations used as observed data to validate the results.

The calculated SPI3 values were used as Z values in the IDW and Kriging spatial interpolation methods. The interpolation was done for 4 selected months in 2020 (the last year of the period): March, June, September, and December, using the ArcMap program. Figure 3-Figure ***10*** show the SPI3 maps using IDW and Kriging methods for Mar, Jun, Sep, and Dec 2020.

The first result is that IDW has more extreme values than Kriging. For the same month and same data, the max. extreme value, according to IDW, is more than obtained from Kriging. For example, the most extreme value of SPI3 in Mar. 2020 based on IDW is -2.00, but based on Kriging, the SPI3 was -0.97. This can be attributed to the main concept of each method. IDW uses and keeps the observed values; otherwise, the Kriging method is a geostatistical method that changes the values regarding the created model. For all resulting maps, the

IDW gave more extreme SPI3 values. In literature, both IDW and Kriging were used as interpolation methods without mentioning the effect of using these methods on the resulting spatial maps.

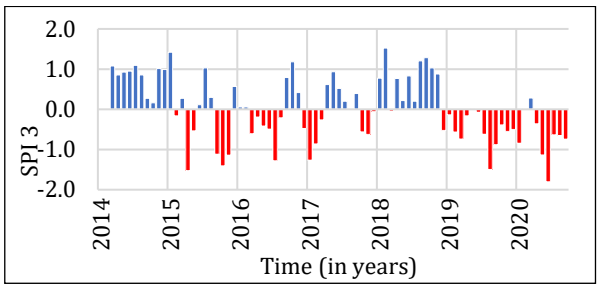

Figure 2. Temporal evaluation of SPI3 using the average value for all stations

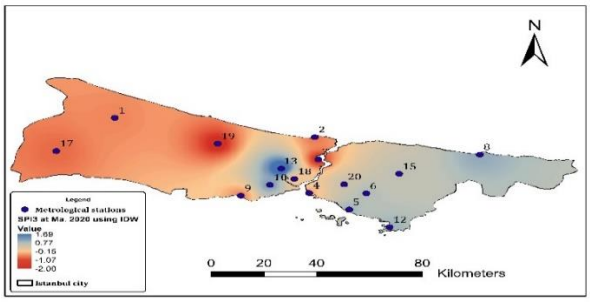

Figure 3. SPI3 in March 2020 using the IDW method

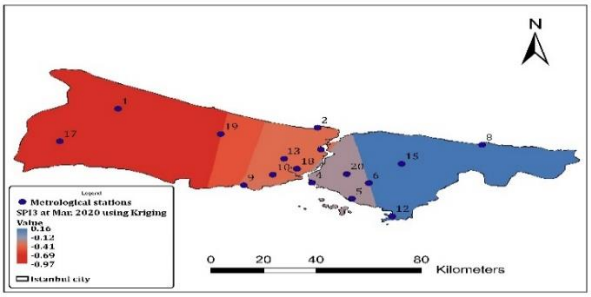

Figure 4. SPI3 in March 2020 using the Kriging method

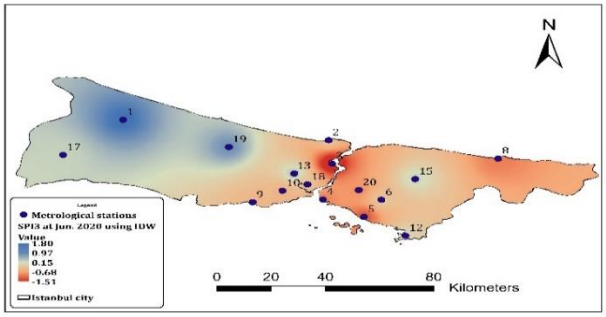

Figure 5. SPI3 in June 2020 using the IDW method

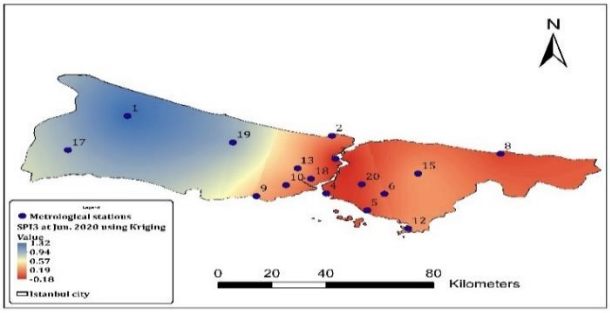

Figure 6. SPI3 in June 2020 using the Kriging method

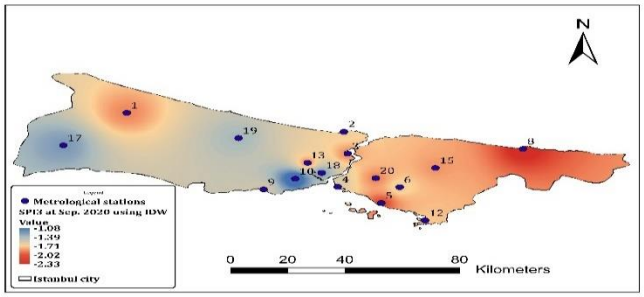

Figure 7. SPI3 in September 2020 using the IDW method

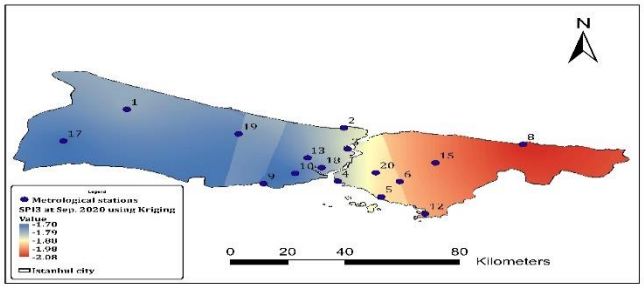

Figure 8. SPI3 in September 2020 using the Kriging method

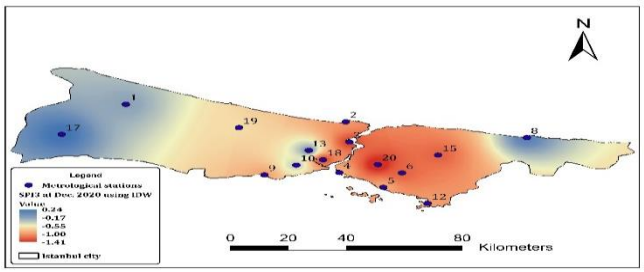

Figure 9. SPI3 in December 2020 using the IDW method

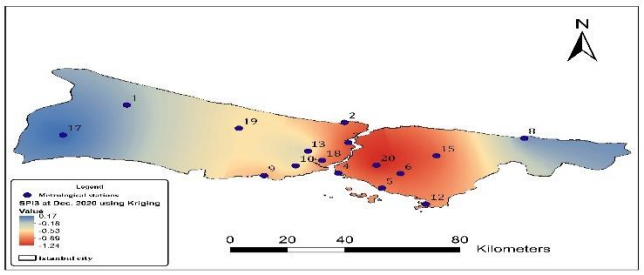

Figure 10. SPI3 in December 2020 using the Kriging method

To find the accuracy of the IDW and Kriging methods, 5 metrological stations were used as observed stations. Then, the Pearson correlation (R) was conducted between the interpolated values obtained from IDW and Kriging and observed values. Figure 11 shows the correlation between interpolated values from Kriging and observed values. The R was 0.6, which is a moderate positive relationship (Irhoumah et al. 2017). However, Figure 12 shows the correlation between interpolated values from IDW and observed values with R equal to 0.57, which is also a moderate positive relation.

Another novelty of this research paper is finding the difference between IDW and Kriging methods in evaluating droughts. Figure 13 shows the correlation between IDW and Kriging methods for drought analysis. The R was 0.8, which is a fairly strong positive relationship.

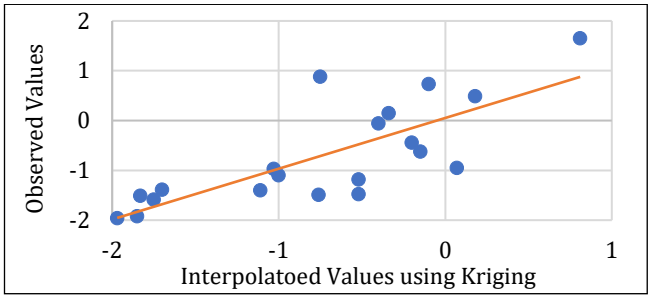

Figure 11. Correlation between Interpolated values using Kriging and the observed data

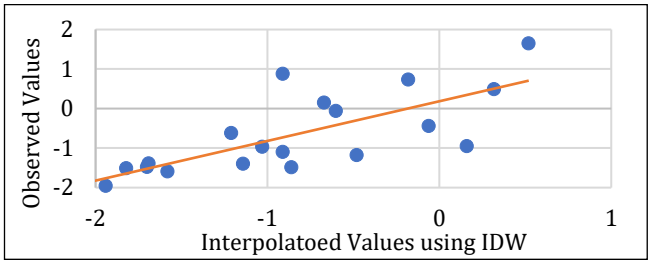

Figure 12. Correlation between Interpolated values using IDW and the observed data

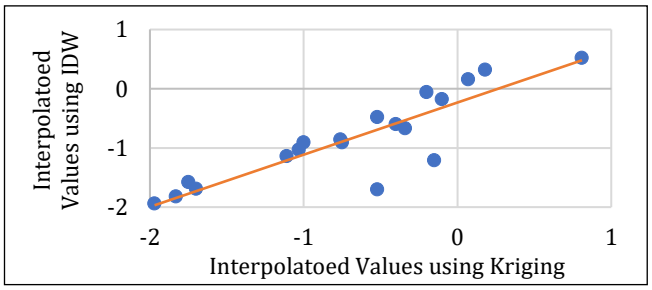

Figure 13. Correlation between Interpolated values using Kriging and IDW

4. Discussion

Generally, according to the drought analysis, IDW gives more conservative results. Due to the geostatistical method used, the origin data may be changed, which makes the Kriging interpolation method unsuitable for drought analysis. Both IDW and Kriging have approximately the same correlation coefficient regarding observed data.

5. Conclusion

Because of the importance of drought analysis and the vital role of spatial interpolation in creating drought maps, this research has two main objectives: to find the accuracy of using IDW and Kriging spatial interpolation methods and to investigate the difference between IDW and Kriging in evaluating drought.

It can be concluded that using the IDW method is more conservative and gives high and more extreme drought values. Regarding the observed data, IDW and Kriging have approximately the same R (0.6), which is a moderately positive relationship. Furthermore, the correlation between IDW and Kriging was 0.8, which is fairly strong.

It can be concluded that using the IDW method is more conservative and gives high and more extreme drought values. Regarding the observed data, both IDW and Kriging have approximately the same R (0.6), which is a moderately positive relationship. Furthermore, the correlation between IDW and Kriging was 0.8, which is fairly strong.

It is complex and impossible to find and evaluate the drought analysis at each point, and it is very complicated to put a metrological station at each meter or kilometer, so spatial interpolation is vital in studying the drought analysis and its negative impacts. The results are significant and useful for the water authorities and decision-makers.

References

Esri, (2012). An Overview of the Interpolation Toolset.(http://help.arcgis.com/en/arcgisdesktop/10.0/help/index.html#/An_overview_of_the_Interpolation_tools/ 009z00000069000000/.

Irhoumah, M., Pusca, R., Lefèvre, E., Mercier, D., & Romary, R. (2017, August). Diagnosis of induction machines using external magnetic field and correlation coefficient. In 2017 IEEE 11th International Symposium on Diagnostics for Electrical Machines, Power Electronics and Drives (SDEMPED) (pp. 531-536). IEEE.

Loquin, K., Dubois, D. (2010). Kriging with ill-known variogram and data [Internet]. In: Deshpande, A., Hunter, A. (Eds.), Scalable Uncertainty Management. Springer Berlin Heidelberg, Berlin, Heidelberg, pp. 219–235.

Mckee, T. B., Doesken, N. Y., & Kleist, Y. (1993). The relationship of drought frequency and duration to time scales. 8th Conference on Applied Climatology, Anaheim, CA, 179–184.

MGM, (2010). Turkish State Metrological Service: https://www.mgm.gov.tr/.

Şen, Z., & Almazroui, M. (2021). Actual precipitation index (API) for drought classification. Earth Systems and Environment, 5, 59-70.

Stephens, M. A. (1970). Use of the Kolmogorov–Smirnov, Cramer–Von Mises and related statistics without extensive tables. Journal of the Royal Statistical Society Series B: Statistical Methodology, 32(1), 115-122.

Van Loon, A. F. (2015). Hydrological drought explained. Wiley Interdisciplinary Reviews. Water, 2(4), 359–392.

Vicente-Serrano, S. M., Beguería, S., & López-Moreno, J. I. (2010). A multiscalar drought index sensitive to global warming: The standardized precipitation evapotranspiration index. Journal of Climate, 23(7), 1696–1718.

Wilhite, D. A. (2016). Managing drought risk in a changing climate. Climate Research, 70(2–3), 99–102.

6th Intercontinental Geoinformation Days

igd.mersin.edu.tr

Investigating urban livability using global TOPSIS in Bojnord city

Foroogh Khazaei Nezhad*[1], Ali Hosingholizade[2], Kimiya Momen[3]

[1] *Kosar University of Bojnord, Humanities, Geography, Bojnord, Iran*
[2] *University of Tehran, Geography, Remote sensing and GIS, Tehran, Iran*
[3] *Kosar University of Bojnord, Humanities, Geography, Bojnord, Iran*

Keywords
Livability
GIS
Global Topsis
Neighbourhood
Bojnord

Abstract

With the increase in the population living in cities, the need to adapt urban development to the priorities of citizens more than before. In order to achieve a livable city must to examine the current state of the city and inform the city managers about planning. For this purpose, there are various methods to check the current situation of the city. One of these location-based methods is the use of the global Topsis with GIS. In this study, livability was analyzed using 6 layers including: access to green space, transportation, public libraries and museums, urban traffic, restaurants and medical services in 49 neighborhoods of Bojnord city. The results showed that the development of Bojnord city has not been the same and the central part is better than the new parts of the city despite the older texture. Also, its central and eastern parts have better conditions than other parts of the city, and the southern part was shown to be very unsuitable. The results of this research are highly consistent with previous research. Therefore, it is suggested that, in addition to the development of all neighborhoods of the city, the southern, southwestern and eastern parts of the city should be prioritized.

1. Introduction

At the beginning of the 20th century, only about 15% of the world's population lived in cities, but with the intensification and growth of urbanization since 1950, in 2007, more than half of the world's population lived in urban areas (Baker et al. 2022; Buckner et al. 2019). It is estimated that by 2050, more than 72% of the world's population will live in cities. Therefore, nowadays, special attention has been paid to the quality and living conditions of people and human settlements in cities, and concepts such as livability have become the subject of interest in research and research in recent decades (Bayat et al. 2019; Pilleron et al. 2019). At this time, being among the most livable cities in the world is an honor for policymakers and planners who seek to improve the position of their cities at the top of the sustainable urban development competition (Oviedo et al, 2022; Carpentieri et al. 2020). Livability, which is a concept with multiple interpretations and definitions (Sujatha et al, 2023; Huang et al. 2018), is often defined as suitable for humans, for life and providing good quality of life, sustainability, identity and community health (Yeung et al. 2022; Leng et al. 2022). This concept is used to evaluate the performance of cities, in terms of the standard of living that it provides for residents, and includes the best to the worst standard of living. Although the history of studies in this field goes back to the 1970s, the recent popularity of research on this concept is related to the diverse measurable characteristics and criteria of livability at different local, urban and rural scales (Noroozian et al, 2012; Steels 2015). The selection of indicators for studying and measuring viability is very vital and important, it has considerable variety and frequency (Srichuae et al. 2016). Obviously, the indicators are a tool for understanding the existing conditions, and on the other hand, they show the trends and transformations that have occurred during a certain period. Therefore, their choice is an important and debatable issue (Chen et al. 2016; Plouffe et al, 2010). In this regard, it is important to pay attention to the indicators and variables that have the most repetition in livability studies at the city level, and to pay attention to the facilities, infrastructure and native culture of the studied community, on the other hand (Hosingholizade et al. 2020; Ezeh et al. 2017). Bojnord city is the capital of the newly established province of North Khorasan, which has grown and

* **Corresponding Author**

*(f.khazaee@kub.ac.ir) ORCID ID 0000-0000-0000-0000
(a.hosingholizade@ut.ac.ir) ORCID ID 0000 – 0001 – 5286 – 1361
(mkimiya16@gmail.com) ORCID ID 0000-0000-0000-0000

Cite this study

Nezhad, F. K., Hosingholizade, A., & Momen, K. (2023). Investigating urban livability using global TOPSIS in Bojnord city. Intercontinental Geoinformation Days (IGD), 6, 282-285, Baku, Azerbaijan

expanded rapidly since 2004, with a population, and various rool.

Due to the extensive economic, social and cultural changes caused by the political consequences of Bojnord city, which have affected the city and urbanization process in this region. Therefore, information and study of the livability of the current situation and future plans for the city of Bojnord are essential.

The current research was conducted with the aim of evaluating the livability of Bojnord city using Topsis techniques. By studying the literature and the background of the research done in measuring and evaluating livability inside and outside the country, in this study, access to green spaces, restaurants, libraries and museums, medical services such as hospitals and pharmacies, the state of transportation and traffic as the indicators affecting the livability of Bojnord city are studied.

2. Method

2.1. Study area

Bojnord city is the capital of North Khorasan province and is located in the northeast of Iran. This city is built in the foothills of Aladagh mountain range. According to the census of Iran Statistics Center, this city has a population of 233,810 people and 68,753 households. Bojnord city has 49 neighborhoods, which is the study area of the current research. This city has a cold and semi-arid climate based on Kopen criteria. The average rainfall of Bonjord city is 260 mm per year.

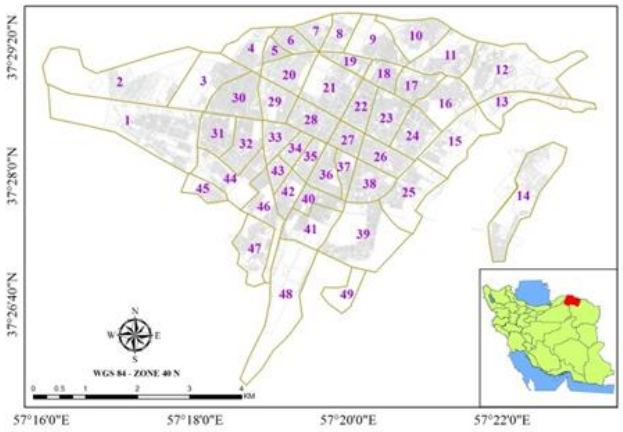

Figure 1. Iran and the study area

2.2. Determining criteria and collecting data

To select the evaluation criteria, first, a number of available sources in this field were reviewed and then the expert's point of view related to urban livability was collected. Since the local conditions are different in each place, similar criteria were combined with each other and the existing criteria were localized at the local level. In this research, six criteria were used to investigate urban livability: green space, restaurants, traffic, medical centers, transportation, and restaurants. In selecting data, the full year of 2022 was used as the basis for data collection, and all data was extracted from Google map and Google traffic archive.

2.3 Global Topsis

2.3.1. Assign weight to criteria

The weight of the criteria obtained is based on the best-worst method. So, the most weight was given to the criteria of access to medical services. The least weight was given to the criterion of access to restaurants.

Table 1. criteria and weights(uncertainty=0.08)

Criteria	W	Criteria	W
medical services	0.3	traffic	0.11
green space	0.19	Transportation	0.23
Library and museum	0.09	Restaurant	0.08

2.3.2. Standardization of criteria

The requirement for combining the criteria layered in MCDA methods is their scaling (without dimensioning). This was done by the score range method. In this method, each of the criteria is normalized based on its minimum or maximum nature with one of the Equations 1 or 2 and it was placed in the range between zero and one.

$$V(a_{ik}) = (a_{ik} - \min(a_{ik})) / r_k \quad (1)$$

$$V(a_{ik}) = (\max(a_{ik}) - a_{ik}) / r_k \quad (2)$$

In Equations 1 and 2, V(aik) is the normalized value of the criterion, aik is the initial value of the criterion, min(aik) and max(aik) are the minimum and maximum values of the criterion. Also, rk is the range of changes initial values of the criterion.

2.3.3. Calculation the distance between each option from positive and negative ideal points

The geometric distance between each option for positive and negative ideal points, also known as similarity to positive and negative points, is calculated using Equations 3 and 4:

$$si = \sqrt{\sum (W_k \times (V_k^* - V_{ik}))^2} \quad (3)$$

$$d_i = \sqrt{\sum (W_k \times (V_{ik} - V_{k*}))^2} \quad (4)$$

In equations 3 and 4, si is the distance between the positive ideal point of the i-th option, di is the distance between the negative ideal point of the i-th option, Wk is the total weight of the criterion, Vk* and Vk* are the maximum and minimum standardized values of the kth criterion, respectively.

2.4. Determining how close each option is to the ideal solution

At this stage, using two parameters obtained from equations 3, 4 and 5, the degree of proximity of each option to the ideal solution is calculated.

2.5. Ranking criteria

In the last step, the criteria available in the study area are ranked with integers and positive numbers starting from one. The number one represents the best Criteria, while the quality of the Criteria decreases as the rank increases.

3. Results

Livability is a broad concept and has various dimensions, so it can be measured based on various criteria. In this research, according to the available data, the urban livability of Bojnord has been studied by emphasizing the criteria of medical centers, green spaces, libraries and museums, transportation, traffic and restaurants using the global Topsis model.

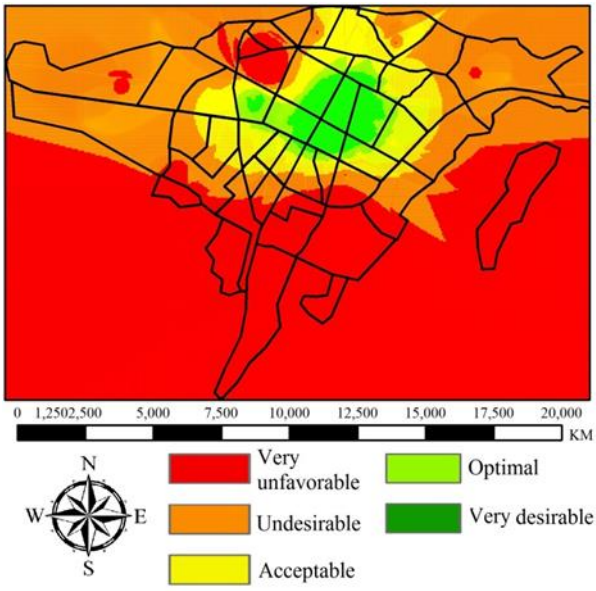

Figure 2. The results of the global Topsis in 5 different classes

4. Discussion

According to the processing done on the data and analysis of the results, it can be seen that the city of Bojnord has many inconsistencies in different localities. If we examine each of the six criteria case by case, we can see that the central parts of the city, with an older texture, have relatively better conditions for urban livability, but in the southern parts, these accesses are weaker.

By processing every layer used in this research and examining their perspective, we can have a better understanding of the situation of each parameter in the city. By combining 6 layers using the global Topsis and preparing the output map and classifying the results into 5 classes including very favorable, favorable, acceptable, unfavorable, completely unfavorable, a suitable location for urban areas can be found. The results of the research are largely consistent with the research of Hosingholizade et al in 2023. In their research, they used the Global OWA method with an ORness of 0.5.

5. Conclusion

The output of the map from global Topsis and the examination of each of the six layers will lead to a better understanding of the distribution of the previous facilities and will show a clear vision of the path ahead to achieve the planned goals. Therefore, due to the importance of studying urban livability in recent years and the direct impact of these evaluations on the planning and design of cities and various industries, it is necessary to be careful in determining the weight, choosing the appropriate layer and pixel size. Also, the results of this study can lead to the evaluation of policies, the ranking of places, the development of management strategies and urban planning with the view of livability in the studied area. On the other hand, facilitating the understanding and prioritization of issues for urban planners and managers in order to promote urban livability, and to city managers help with prioritizing and meeting the needs of different neighborhoods. Another important result is the new residential settlements that, despite the design in the last few years, did not give any priority to livability, and the older neighborhoods are in a much better condition.

References

Baker, R. E., Mahmud, A. S., Miller, I. F., Rajeev, M., Rasambainarivo, F., Rice, B. L., ... & Metcalf, C. J. E. (2022). Infectious disease in an era of global change. Nature Reviews Microbiology, 20(4), 193-205. https://doi.org/10.1038/s41579-021-00639-z

Bayat, R., Ashrafi, K., Motlagh, M.S., Hassanvand, M.S., Daroudi, R., Fink, G., and Künzli, N., 2019, Health impact and related cost of ambient air pollution in Tehran, Environmental research, 176, P.108547. https://doi.org/10.1016/j.envres.2019.108547

Buckner, S., Pope, D., Mattocks, C., Lafortune, L., Dherani, M., and Bruce, N., 2019, Developing age-friendly cities: an evidence-based evaluation tool, Journal of Population Ageing, 12(2), 203-223. https://doi.org/10.1007/s12062-017-9206-2

Carpentieri, G., Guida, C., and Masoumi, H.E., 2020, Multimodal Accessibility to Primary Health Services for the Elderly: A Case Study of Naples, Italy, Sustainability, 12(3), 781. https://doi.org/10.3390/su12030781

Chen, S., Cerin, E., Stimson, R., and Lai, P.C., 2016, An objective measure to assessing urban quality of life based on land use characteristics, Procedia Environmental Sciences, 36, 50-53. https://doi.org/10.1016/j.proenv.2016.09.009

Ezeh, A., Oyebode, O., Satterthwaite, D., Chen, Y. F., Ndugwa, R., Sartori, J., & Lilford, R. J. (2017). The history, geography, and sociology of slums and the health problems of people who live in slums. The lancet, 389(10068), 547-558. https://doi.org/10.1016/S0140-6736(16)31650-6

Hosingholizade, A., Jelokhani, M., Mahsa, N., & Hajilo, F. (2020). Spatial analysis and evaluation of urban spaces from the elderly-friendly city perspective (Study area: District 6 of Tehran, Iran). Geographical Urban Planning Research (GUPR), 8(2), 371-389. https://doi.org/10.22059/JURBANGEO.2020.295771.1215

Huang, N. C., Kung, S. F., & Hu, S. C. (2018). The relationship between urbanization, the built environment, and physical activity among older adults in Taiwan. International journal of environmental research and public health, 15(5), 836. https://doi.org/10.3390/ijerph15050836

Leng, H., & Han, B. (2022). Effect of Environmental Planning on Elderly Individual Quality of Life in Severe Cold Regions: A Case Study in Northeastern China. Sustainability, 14(6), 3522. https://doi.org/10.3390/su14063522

Noroozian, M. (2012). The elderly population in iran: an ever-growing concern in the health system. Iranian journal of psychiatry and behavioral sciences, 6(2), 1-6.

Oviedo, D., Sabogal, O., Duarte, N. V., & Chong, A. Z. (2022). Perceived liveability, transport, and mental health: A story of overlying inequalities. Journal of Transport & Health, 27, 101513. https://doi.org/10.1016/j.jth.2022.101513

Pilleron, S., Sarfati, D., Janssen-Heijnen, M., Vignat, J., Ferlay, J., Bray, F., & Soerjomataram, I. (2019). Global cancer incidence in older adults, 2012 and 2035: a population-based study. International journal of cancer, 144(1), 49-58.

Plouffe, L., & Kalache, A. (2010). Towards global age-friendly cities: determining urban features that promote active aging. Journal of urban health, 87(5), 733-739. https://doi.org/10.1007/s11524-010-9466-0

Srichuae, S., Nitivattananon, V., & Perera, R. (2016). Aging society in Bangkok and the factors affecting mobility of elderly in urban public spaces and transportation facilities. Iatss Research, 40(1), 26-34. https://doi.org/10.1016/j.iatssr.2015.12.004

Steels, S. (2015). Key characteristics of age-friendly cities and communities: A review. Cities, 47, 45-52. https://doi.org/10.1016/j.cities.2015.02.004

Sujatha, V., Lavanya, G., & Prakash, R. (2023). Quantifying Liveability Using Survey Analysis and Machine Learning Model. Sustainability, 15(2), 1633. https://doi.org/10.3390/su15021633

Yeung, W. J. J., & Lee, Y. (2022). Aging in East Asia: new findings on retirement, health, and well-being. The Journals of Gerontology: Series B, 77(3), 589-591. https://doi.org/10.1093/geronb/gbab055

6th Intercontinental Geoinformation Days

igd.mersin.edu.tr

Studying the distribution of population of Mountain Shirvan in the GIS environment

Rovshan Karimov*[1], Natavan Jafarova[1]

[1] *Institute of Geography, Ministry of Science and Education, Baku, Azerbaijan*

Keywords
Resettlement
GIS mapping
Geostatistical
Rural
Shirvan

Abstract

The paper deals with studying of resettlement of population of Mountain Shirvan region in the GIS environment. This mountain region for long has been known as one of lagging economic regions of Azerbaijan with its very low urbanization rate. Mountain Shirvan for decades experienced continuous out-migration. In this paper, upon conducting a comparative analysis of the two last population censuses we found that tens of settlements have experienced depopulation in the region. Moreover, through GIS mapping which included data collection (aerospace images and statistical information), mapping in ArcMap 10.8 program with using Overlay tool, and geostatistical analysis in ArcToolBox, we defined the features of spatial distribution of the population, and the geographical coverage of rural areas in the territory of Mountain Shirvan region.

1. Introduction

Sustainable demographic development of rural settlements is very crucial factor for mountain regions. These regions recently were less preferred by the population since they became less attractive in economic and social terms. Tens of villages experienced depopulation or faced depopulation in recent decades in various mountain areas of Azerbaijan. Out-migrations and the intensity of these processes are influenced by specific economic activities. The less profitable the jobs are, the more willingness of people to leave the place of residence in favor of regions with much higher economic opportunities.

We carried our study on the example of Mountain Shirvan region of Azerbaijan. Studying the distribution of population and the resettlement processes on the example of Mountain Shirvan is very topical issue, since demographically it is less competitive than other regions of the country.

The aim of this paper is to determine the distinguishing features of geographical distribution of population, and assess the demographic sustainability of rural areas and settlements of Mountain Shirvan through revealing the changes going in the population number.

2. Methods

To assess the demographic situation and favorability of demographic tendencies going in Mountain Shirvan in the last two decades, we reviewed relevant scientific literature. Based on available literature and fieldworks, we also considered the influencing role of geographical conditions and factors in resettlement. Analysis of the statistical data on the population number of rural settlements by region's 4 administrative districts – Shamakhi, Ismayilli, Aghsu, and Gobustan was carried out. We compared the results of the two censuses (of 1999 and 2009 years) on the region's villages to define where either population growth or depopulation has occurred.

Meantime, the territory of Mountain Shirvan was studied in the GIS environment which allowed make both the relief properties and the geographical distribution of the region's population more clrealy visible. Studying in this context includes the compilation of three maps by us to demonstrate how the population is distributed in Mountain Shirvan, and at what degree in geographical terms, the studied territory is occupied by population. To examine the role of relief (altitude) factor in resettlement, we created a relief model in the ArcGIS 10,8 program which included the steps below:

* **Corresponding Author**

*(rovshan_karimov@yahoo.com) ORCID ID 0000-0001-5059-2735
(jafarova.nata83@hotmail.com) ORCID ID 0000-0002-1745-0919

Cite this study

Karimov, R., & Jafarova, N. (2023). Studying the distribution of population of Mountain Shirvan in the GIS environment. Intercontinental Geoinformation Days (IGD), 6, 286-289, Baku, Azerbaijan

1. DEM model.
2. Heights are revealed by using the Extract_Point tool.
3. The obtained heights were used in the IDW tool.
4. Shapefile of settlements was integrated to the map. The outcome: Integrated maps of the relief model and the location of settlements done.

Figure 1. Interpolation analysis of the relief of Mountain Shirvan

Following this, Landslide model, for which DEM-model served as the primary data, was created. This was achieved in SAGA GIS program (Figure 3).

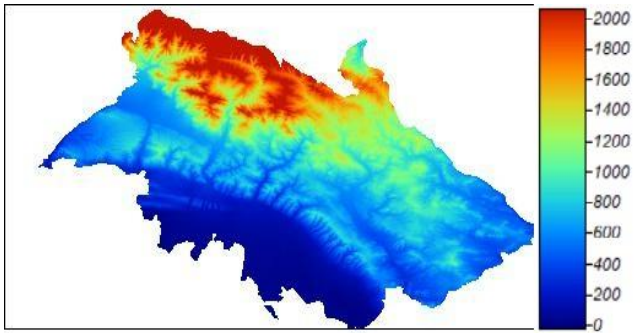

Figure 2. Digital Elevation Model (SAGA GIS) of Mountain Shirvan

To demonstrate the distribution of the settlements present in the studied region, a map of settlement was compiled in ArcGIS (Figure 3) that allows compare the density of existing settlements (rural areas) within the boundaries of Ismayilli, Aghsu, Shamakhi, and Gobustan districts of the region.

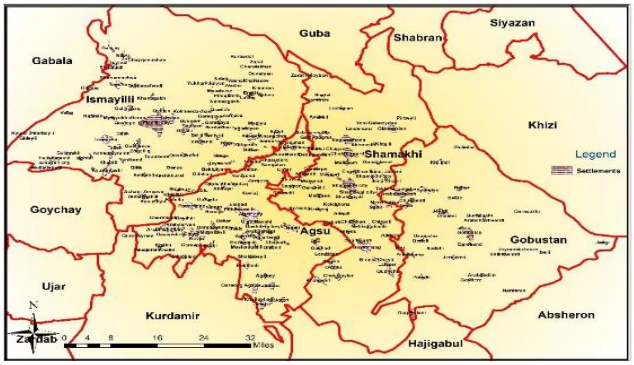

Figure 3. Distribution of settlements in the territory of Mountain Shirvan

3. Data analysis

In the Mountain Shirvan region, natural conditions are different, and natural resources, suitable (fertile land resources, fresh water resources, etc.) for economic activities are distributed unevenly in its territory (Tanriverdiyev and Safarov 1999). Fragmentation of the relief as well as the presence of inclined hills and descents and ascents may challenge the settlement process in some parts of the region (Budagov and Mikayilov 1996). From west to east in most part of the region, the altitude of relief increases. The foothills and low mountain areas of Shamakhi and Ismayilli districts are more populous, and the number of rural settlements in such areas is higher than others. Arid climatic conditions, scarce water resources, lack of irrigation canals, limited access to irrigation conditions, and low soil fertility are the adverse factors affecting the distribution of population in Gobustan and in part in Shamakhi districts (Abbasov et al. 2022). Upper parts of the region with more than 2000 m of altitude have cold climate and are relatively unsuitable for residence of population. The Mountain Shirvan is the most landslide-prone region of Azerbaijan. Here certain settlements are regularly affected and devastated by heavy landslides which are driven by both natural and human factors (Ismayilov and Mustafayev 2012). This factor challenges the sustainable development of many settlements in the region. The areas alongside the rivers of Aghsu, Pirsaat and Gozluchay, as well as the transport and infrastructure facilities have been devastated over and over by heavy landslides and long-term influence of active erosional processes [Budagov and Mikayilov 1996]. There are 69 settlements with totally about 44 thousand residents, which live under certain risk of landslide in the region (Pashayev and Karimov 2012). Beside with relatively flat plains and foothill areas, widely spread in the economic region, the medium and high mountain areas and high valleys altitude of which may reach up 1200-1300 m (Lahij, Mudri, Chukhuryurd etc.) are useful for settlement and agriculture (Tanriverdiyev and Safarov 1999).

There are significant differences in population number and density throughout the territory of the Mountain Shirvan. The villages in this region are of different sizes, thus, depending on relief, they are grouped in smaller areas constituting group of rural settlements, whereas in other places are evidently scattered and located far from each other, in particular in Gobustan district.

Population number of the Mountain Shirvan region is 326.8 thousand, consisting 3.2% of Azerbaijan's population. There are 272 villages in the region. 67.6% of all villages are in the territory of Shamakhi (38.6%) and Aghsu (29.0%) districts. Shamakhi with 105.1 thousand residents is the largest district, combining 33% of the region's total population, while Ismayilli is the second and Aghsu is the third (Table 1). The latter has the highest population density. The average size of rural settlements is very different by four districts: 970 persons in Shamakhi, 730 persons in Aghsu, 555 persons in Ismayilli, and 1190 persons in Gobustan, while the average figure by the region is about 770

persons, as calculated based on the 2009 census. 65.8% of the population of Mountain Shirvan is composed of rural population, and only 34.2% are urban residents [PoA, 2022].

Table 1. The main demographic data of the Mountain Shirvan region

Territory	Territ. area in thous. km^2	Popul. number. in thous. pers (2022)	Pop. density, thous. per/km^2	Urban popul. (thous. person) person)	Rural popul. (thous. person)
Shamakhi district	1.67	108.1	65	50.8	57.3
Ismayilli district	2.07	88.2	43	28.6	59.6
Aghsu district	1.02	80.5	79	22.4	59.7
Gobustan district	1.37	48.4	35	10.0	38.4
Mountain Shirvan region	6.13	326.8	53	111.8	215.0

Source: Population of Azerbaijan. Yearbook of the State Statistical Committee of the Azerbaijan Republic, 2022.

4. Results

Upon comparing the census data of 1999 and 2009 years we found that decline in population number has been common for 55 settlements present in the region.

In Shamakhi district, 1 urban type settlement (Sabir) and at least 11 villages (Talishnuru, Birinji Chayli, Ikinji Chabani, Avakhil, Adnali, Hajigadirli, Yenikand, Karkanj, Gurdtepe, Nagharakhana, Pirbayli) have reduced in number of dwellers. Even larger villages (e.g., Birinji Chayli with 1603 residents) were among them. Highest decline at 181 persons has been fixed by Ikinji Chabani village. The small village of Ajidere almost disappeared by 2009. Growth in population number was lower in Sabir settlement, as well as in the villages of Hajili, Dedegunesh, Birinji Chaghan, Sefali, Chabani, Chiragli, Shirvan, Sabirli, Melhem, Angakharan, Kechmedin, Galaderesi, Sis, Chol Goyler etc.

In Aghsu, where tens of smaller villages with around 100-200 residents are present, 9 villages out of 79, experienced decline in population number. Decline equaled 102 persons in Shahbeyli village, 34 persons in Nuran, 22 persons in Muradli, etc. In at least 8 smaller villages, the risk of depopulation is relatively higher.

Among the four districts of the Mountain Shirvan region, highest concern over depopulation is in Ismayilli, where 27 settlements out of 105 one's experienced decline in population number. They are the urban settlement of Lahij, and the villages of Ivanovka, Gubakhalilli, Girk, Nanij, Guyum, Namazgah, Keyvandi, Mulukh, Qoydan, Zarat, Ustalgishlag, Shabiyan, Bahliyan, Kelbend, Shukurchu, Yenikend, Garagaya, Goshakend, Tubukend, Gezli, Mudri, Gersele, Zergeran, Machakhy, Keshkhurt, and Pireganim. Almost every fourth village in Ismayilli district has experienced depopulation.

In Ismayilli, the villages facing very high risk of disappearance are quite in number as well (such as Piraganim, Garcha, Dahar, Keshkhurt, Tubukend, Kenaa, Khimran, Mulukh, Zarat, Gersele, Dvoryan and many others). A few of them with around 10-20 residents or lesser, indeed, are either almost disappeared or will disappear in the next future.

In Gobustan district, population number of 9 villages has been decreased, including of Nardaran (as less as 63 persons), Gurbanchi (38 p.), Mudrise (36 p.), Julyan (30 p.), and others. Several rural settlements such as Dagh Kolani, Shikhlar and Damlamaja actually have disappeared long ago. More than a third part of all villages in Gobustan are currently have a risk of depopulation.

Our numerous visits to the region of Mountain Shirvan proved the presence of depopulation problem here. The actual population number of many villages in the region is lower than the figures shown in the official statistics. Typically, big portion of younger and medium generation (some also with their family members) currently lives and works actually not in their home villages but in other places, mostly in the city of Baku.

The map of settlement compiled (Figure 1) shows how unevenly the population is distributed across the region of Mountain Shirvan. In Shamakhi district, where 1 city, 5 urban settlements and 57 villages are present, the density of settlements and population is very different. Some settlements are in the areas close to Shamakhi city. To the south, as well as in the areas over 1500 m, the density is low. With 41.2 thous. Inhabitants, Shamakhi city accounts for 38% of the population of the same district (PoA, 2022). With more than 40 thousand residents, it is the biggest city in the region. We identified 6 small rural areals in Shamakhi.

The villages belonging to the first group are located south of the district center – in the Langebiz range district, mainly on the right bank of the Pirsaat river. It includes Kalakhana, Kerkanec, Adnalı, Sabirli, Charhan, Nuydü, Dag Bagırli, Yenikend, Goyler Dag, Lalazar, Birinci Chayli, Gushchu, etc.

Another rural area covers the direction of Langebiz ridge with the highest demographic potential in Shamakhi district. There are Bagırli (2.1 thousand people), Ovchulu and other relatively villages here. All are located in relatively flat areas.

The third important rural area includes the villages located around the highway from the city of Shamakhi to the city of Ismayilli. This area is located in the northwestern end of the Langebiz range. Garavalli, Malcak, Gurdtape, Shirvan, Saghian, Sharadil, Mirikend, Muganli, and Biguk Khirisli villages are located within the area.

The fourth village area of Shamakhi district is a group of villages located geographically close to the district center, a little to the east and northeast of it. There are villages such as Chabani, Ikinji Chabani, Hamyali, and Gonagkend. This area, which belongs to the low and medium highlands, is also one of the landslide-prone areas.

The fifth village area of Shamakhi district is a group of villages located in the north-west of the district center, mainly in the middle highlands. Here,

Dedagunesh, First Jagan, Second Jagan, Kechmeddin, Galeybugurd, Galadaresi, Sis and other villages are more compactly located than others.

Angakharan, Chukhuryurd, Nagarakhana, etc. from Shamakhi in the direction of Yusif Mammadaliyev settlement. villages are found. They form the sixth rural area.

In Aghsu district, where, unlike Shamakhi, Ismayilli and Gobustan districts, the territory is composed mainly of plains, relatively high density of villages is present. The city of Aghsu, a center of the district, has 22.4 inhabitants [PoA, 2022]. Aghsu district is distinguished by the presence of numerous small villages. There are 6 villages only in Aghsu with population number at 3000-5500 persons. There are relatively large villages such as Gagali, Bijo, Kandoba, Kalva, Arabushagi, Padar, Arabmehdibay etc. in the region.

Based on the mapping, we identified 9 small village rural areas in Aghsu: Bozavand-Agharkh, Gagali-Arabushagi-Chaparli, Bijo-Langabiz, Garagoyunlu-Novju-Arabsarvan, Padar-Pirhasanli, Kandoba-Abbaskhanly, Gurjuvan, Nuyudlu-Girlar, and Kalva (Figure 1). Most of these rural areas involve smaller villages only.

In Ismayilli district, where the relief and biodiversity conditions are complex and various by areas, and where certain part of the territory is not only landslide-prone but is also vulnerable towards rockfall and talus processes, a few rural areas are evidently seen (Figure 1). Due to the relatively large area of Ismayilli district, and because of various relief features, and climatic conditions, the villages here are geographically scattered at higher degree.

Concentration of settlements in the territory of Ismayilli district can be grouped as follows:

1. Villages located to the right of Shamakhi-Aghsu-Ismayilli highway, either in the vicinity or relatively far to this main transport road of transitional importance.
2. Highland villages located higher than the Lahij area, those scattered towards the Burovdal village.
3. High Mountain villages on the right bank of the upper flow of Girdimanchay River.
4. Mountain villages occupying the northwest from Ismayilli city.
5. Villages located on the plateau of Gash, the western part of the district.
6. Villages spread to the southwest and south from Ismayilli city.
7. Villages located to the east from the Ismayilli-Kurdmashi highway.
8. Villages located to the southeast of Ismayilli city, the foothills of the Langabiz mountain ridge and adjacent areas.

The city of Ismayilli, located in the center of the district, and thus, having almost same proximity to most villages present, has 26.2 inhabitants (PoA, 2022).

Gobustan district is located in the eastern part of the Mountain Shirvan, and it is characterized by the high territorial capacity and the lower number of populations. Its center, the town of Gobustan has only 9.5 thousand residents (PoA, 2022). No big rural settlements are available around this town (Figure 2). Settlements are scarce. The demographic capacity of both the administrative center and rural settlements is low.

5. Conclusion

As our studies show, the process of formation of rural agglomerations is weak in the region. This concerns particularly Ismayilli and Shamakhi districts, while in Gobustan district the villages are scattered at high extent and unfavorable to form rural agglomerations at all. Most of rural settlements present in mountain areas is typically lagging compared to foothill rural settlements for demographic development.

Though rural settlements have formed 6 rural agglomerations in Shamakhi, 9 villages in Aghsu and 8 villages in Ismayilli, most of these rural settlements are smaller in size, and of high concern in terms of depopulation and even disappearance driven by the continuing out-migration. The presence of villages of the disappearance risk is typical mostly for Ismayilli, and at lesser extent for Shamakhi and Gobustan districts.

Upon exploring the distribution of settlements in the territory of Mountain Shirvan region, we found out that totally 55 settlements in this region have already experienced depopulation. About 8-10 villages have been disappeared or almost disappeared in the first decade of the twenty first century, given the condition that the number of their residents is extremely small. As our study showed, around 30 villages in the region are under the high risk of disappearance, while, a few tens of others are also associated with presence of such risk at relatively lesser degree.

References

Abbasov, R., Karimov, R. & Jafarova, N. (2022). Environmental migration: cultural losses. In a book: Ecosystem services in Azerbaijan: values and losses. Springer Publications. https://doi.org/10.1007/978-3-031-08770-7

Budagov, B. A. & Mikayilov, A. A. (1996). Physical and geographical landscape zoning. In a book: Constructive geography of the Azerbaijan Republic. 1, 173-186.

Ismayilov, M. J. & Mustafayev, N. M. (2012). Features of the landslide development on the south-eastern slope of Greater Caucasus. Transactions of Azerbaijan Geographical Society. 12, 95-103. Baku.

Pashayev, N. H. & Karimov, R. N. (2012). Economic and geographical impact of landslides on the distribution of population in the Azerbaijan Republic. “Vestnik” of Moscow Region State University (Series of "Economy”), 4 (3), 130-139. (In Russian).

Population of Azerbaijan (PoA). (2022). Yearbook of the State Statistical Committee of the Azerbaijan Republic. Baku.

Tanriverdiyev, Kh. K. & Safarov, A. S. (1999). The relief and opportunities for its rational use in agriculture. In a book: Constructive geography of the Azerbaijan Republic, 2, 8-13.

6th Intercontinental Geoinformation Days

igd.mersin.edu.tr

Modern methods of studying inaccessible mountain relief with GIS technology

Kazimova Latifa *1

[1]Azerbaijan State Oil and Industry University, Azadliq avenue. 34, AZ1010, Baku, Azerbaijan

Keywords
GIS
DEM
Morphometric analysis
Range relief
SRTM

Abstract

The application of these methods, in addition to remote means of studying the Earth's surface, makes it possible to carry out complex studies of the modern condition of mountain ranges and mountain villages. The development of such a system is complicated by different levels of accessibility information for each key site, so creating a project GIS that concentrates data on a single cartographic basis with an appropriate database for subsequent automated analysis of this information is the most effective way to address assigned tasks. On-based SRTM DEM using GIS technology performed morphometric analysis of relief Shinchay-Damiraparanchay mudflow basins. With these purpose-built maps of hypsometry, slopes, aspect, range relief and drainage density, indexes, dissection and ruggedness, and surface curvature. Also analyzed the areal distribution of these parameters by grade. Now, in connection with the development of digital technologies and the broad availability of data of remote sensing, detailed assessment of relief became possible. Application of the digital models of a relief (DMR) considerably simplified the morphometric analysis of a relief.

1. Introduction

Modeling of the mountain terrain was carried out with the help of GIS ArcGIS, which provides the ability to create and analyze maps. ArcGIS interacts with web mapping services that allow users to display any structure and any location on the map via web-platform, which also helps in the transmission of data or information through various web platforms from anywhere in the world.

Two terrain models can be used for web mapping GRID and TIN, which are widely used in GIS. GRID and TIN models are well enough to display geographical objects or phenomena that fluctuate in space, as they are different methods of construction and visualization of relief, which allows them to be used for different purposes depending on the tasks. The advantages of such a model include simplicity and speed of computer processing, it is connected with the very essence of the raster model. Output devices, such as monitors, printers, and plotters to show images use point sets (pixels), t. e. also have raster format, resulting in the GRID image being quickly visualized on the screen.

The drainage basin is the fundamental unit in fluvial geomorphology within which the relationships between landforms and the processes that modify them have been studied. The study of the geometry of the basin and the way in which it changes in response to processes has become a major part of modern geomorphology. Morphometric analysis of a drainage basin is a quantitative description of a basin and an important aspect to know the character of the basin (Ivanov, 2018).

In foreign literature, this direction gained development under the name "geomorphometry" (Piriev, 1986).

There are also synonyms for this term such as "quantitative morphology" (the quantitative morphology) and "quotative terrain analysis" (the quantitative analysis of a relief).

The area of the explored region is 3220 sq.km (Figure 1).

Figure 1. A geographical location of the explored region

* **Corresponding Author**

*(latifa.ismaylova@gmail.com) ORCID ID 0000-0002-0254-1746

Cite this study

Latifa, K. (2023). Modern methods of studying inaccessible mountain relief with GIS technology. Intercontinental Geoinformation Days (IGD), 6, 290-293, Baku, Azerbaijan

2. Method

The ILRIS Optech laser scanning system is the most modern tool for geodetic surveying of inaccessible surfaces. It allows you to get thousands of X, Y, Z points per second, from which can then be built accurate 3D models. To shoot a single point from which the entire surface of the relief is seen (Piriev, 1986). As input data for the GIS analysis of morphometric indexes of relief materials of satellite photos of SRTM are used (Figure 2).

Data of SRTM (Shuttle Radar Topographic Mission) represent the processed results of a radar survey of the surface of the globe made from the board of the American Shuttle spaceship by the method of radar interferometry, in February of the 2018 th year. This survey was conducted almost in all territories of the water area of Earth between 60 ° north lat., 54 ° south lat. by means of the radar SIR-C and X-SAR (Alizade, 2004).

The main operations were carried out in the ArcGIS - Spatial Analyst applications, 3D analyst, and geostatistical Analyst. The Hydro Tools tool model operations of watersheds, reservoirs, and drainage networks perform functions of processing and preparation of the digital models of a relief (DMR).

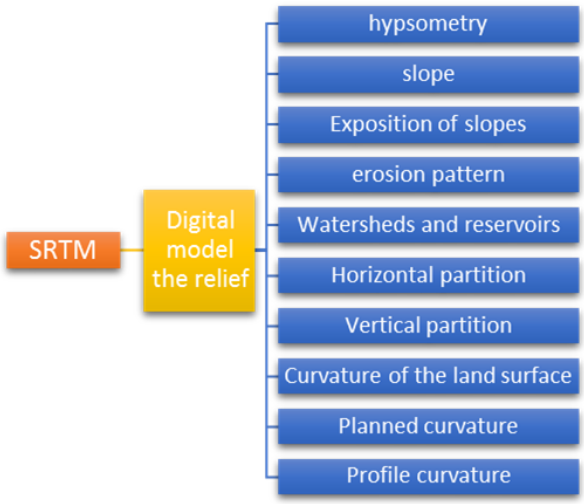

Figure 2. Scheme of creation of morphometric maps

The DEM Tools applications which contain a number of functions, for the calculation of some morphometric indexes, was useful for realization in some of the operations (Piriev, 1986). The scheme of creation of the morphometric maps on the basis of digital models of relief on ArcGIS (Figure 3).

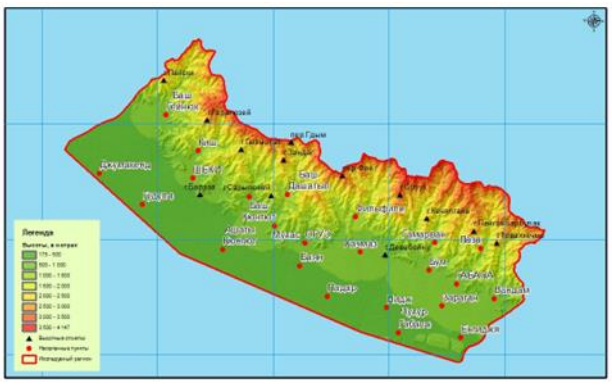

Figure 3. The hypsometric map of the explored region

2.1. Hypsometry

The analysis of the Digital model of relief (DMR) shows that absolute heights fluctuate here from 175 m to 4147 m. The analysis of the hypsometric map (Figure 3) shows that the largest space (54% in the explored region) is occupied by the range of height 175-1000 m (Table 1).

Table 1. Distribution of the total areas on a hypsometry

Hypsometry, m	175 - 500	500 - 1000	1000 - 1500	1500 - 2000
Area, км²	1003	760,8	407	391,5
Area, %	31,1	23,6	12,6	12,1

2.2. Biases of a surface (steepness) and exposition of slopes

Calculations of the biases of a surface it is necessary for the assessment of slope processes, soil erosion calculations, assessment of lands, etc. According to the calculations received from the map (Figure 4) slopes with the 10° occupy 49.5% of the total area (Table 2).

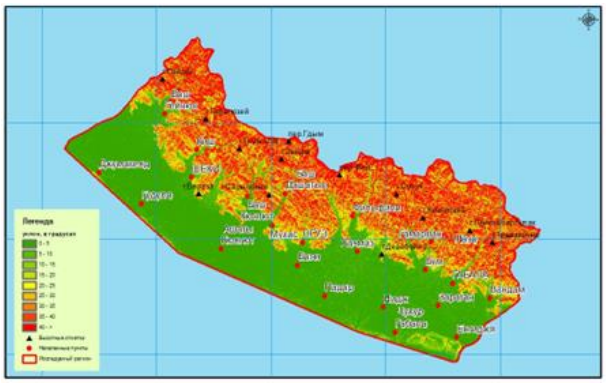

(a)

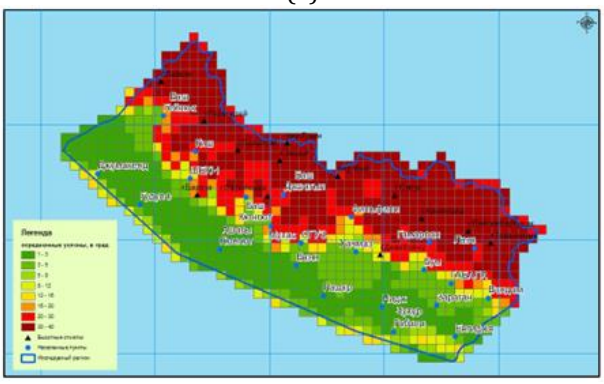

(b)

Figure 4: The map of slope angles of the explored region received by reference by method (a) and the card of average slope angles received by the method of Zone statistics (b)

Table 2. Distribution of the total areas on slope angles

Angles	5-10°	10-15°	15-20°	20-25°	25-30°
Area, км²	233	104	115	161	234
Area, %	7,23	3,22	3,57	5,01	7,27

Slopes of more than 10° where slope processes proceed more intensively, is occupied 50.5% of the

territory, at the same time the large territory is covered with the slopes by the steepness more than 40° [3].

The exposition of a slope characterizes the slope relation to the multi-scale processes (insolation, gravitation, circulation etc.).

The exposition can be considered as the direction of a bias (Alekperova et al. 2017; Ivanov, 2018).

The exposition of a slope is one of the morphometric characteristics of relief, characterizing the dimensional orientation of the elementary slope (Figure 5, Table 3).

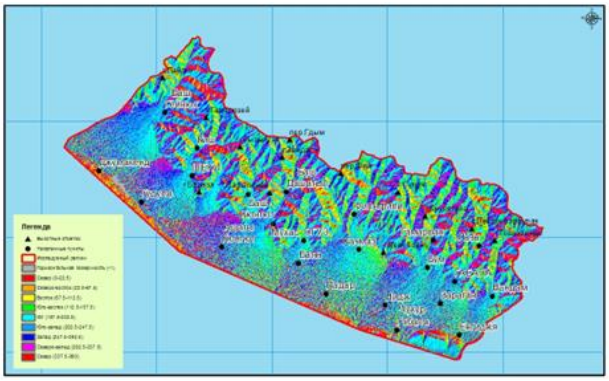

Figure 5. The map of an exposition of slopes of the explored region

Table 3. Distribution of the total areas on an exposition of slopes

Exposition	Flatness	North	East	South	west
Area, км²	47,29	231,07	200,83	762,79	419,73
Area, %	1,47	7,18	6,24	23,69	13,03

As seen from the table, the southern exposition slopes (southern, southern, western, southern, and eastern) are composed of half a total of 56.5%. The slopes with anti-polar orientation (northern, southern-western and northern-western) have more than twenty-eight percent of the total area.

2.3. Vertical and horizontal partition

Calculates vertical scattering by using a cartogram, which is a tool used by ArcGIS (Spatial Analyst Tools → Zonal Statistics), which calculates the amplitude (in meters) of the DMR values in the calculable cells (Figure 6). The vertical clearance, more than 350 m, was discovered in the main section of the Caucasus Quarter and in the high-altitude zone (Piriev, 1986.

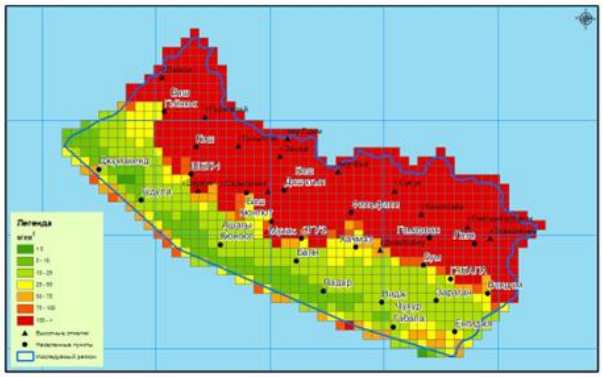

Figure 6. Map of vertical spreading relief of the region

For horizontal computing, has been used the Hydrology Tool (Spatial Analyst) to create all erosion network (Figure7).

(a)

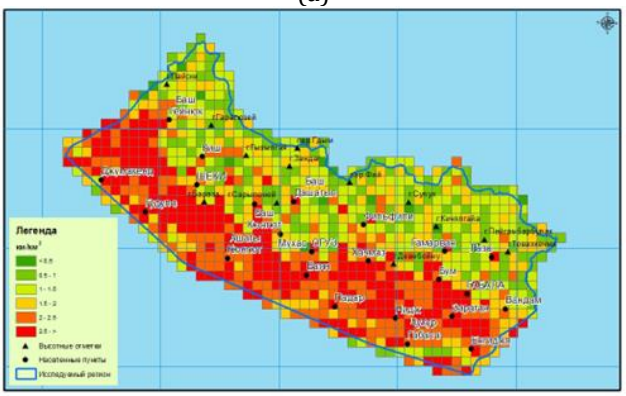

(b)

Figure 7. Resistance to CMS Erosion network (a) and map horizontally-distal relief region of the method zonal statistics (b)

The erosion network was the base for the calculation of horizontal partition. The analysis of the map (figure 7 b) shows that the maximum marks* of horizontal partition are found for the Qanix-Ayrichay plain, the least – for water separate zones.

2.4. DI, dissection index

This index expresses a ratio of the relative relief (in this case vertical partition) to an absolute relief (i.e., to the maximum indicators of a relief, so-called topmost surfaces).

$$DI = (Zmax - Zmin)/Zmax$$

It is an important index of the partition of a surface and indicates a vertical partition. The high value of the index indicates orogeny, low value corresponds to stable areas. The analysis of literary data and morphometric features of the explored territory allows us to choose on the basis of this index five class scale system - such as very low DI (<0,1), low DI (0,1-0,2), temperate DI (0,2-0,3), high DI (0,3-0,4) and very high DI (>0,4) (Figure 8). More detailed characteristics of this index are given in Table 4.

Figure 8. Distribution of the index of a partition

Table 4. Distribution of the total areas by the index of a partition (DI)

Class	DI	Area, km²	Area, %
very low	<0,1	1067,6	33,17
very low	0,1-0,2	594,94	18,49
T, °C	0,2-0,3	1225,4	38,08
High	0,3-0,4	312,82	9,72
Very high	>0,4	17,44	0,54

2.5. Ruggedness index

This index describes complexity and roughness of a land relief. The ruggedness defines extent of crossing of area where the drainage (erosive) network acts as key parameter. Chorley (1972) developed a formula for this index [4-6]:

$$(Deep\ partition\ (m/\ 〖km〗\ ^2\ ) * horizontal\ partition\ (km/\ 〖km〗\ ^2\ ))/1000$$

This index is widely used by scientists in morphological research for the best comprehension of the formation of elements of a relief in the difficult geomorphological conditions [5-8]. Results of the analysis show that the maximum values are partition are observed in mountain and mid-mountain zones of the territory (Figure 9).

Figure 9. Distribution of the index of ruggedness

3. Conclusion

GIS technologies for remote data and map analysis significantly simplify and expedites the collection and analysis of materials, and provide an opportunity to obtain intermediate and preliminary results, to better identify and follow the main objectives of the study, as well as operationalize results in the form of appropriate maps or spatial data infrastructures.

1. So, for the first time for the explored territory is carried out the complex morphometric analysis according to the radar interferometric topographic trajectory SRTM, with the software of ArcGIS.

2. On the basis of the created DMR and the modern GIS technologies are calculated morphometric parameters of a relief. This way allows one to carry out the assessment of the modern erosive processes on a quantitative basis and to create a set of geomorphological maps.

3. By means of our research materials is possible to study characteristic of processes of an erosion and accumulation and also assessment of potential stability or tendency to an erosion of various sites of the explored territory.

Acknowledgement

This work was done under the grant № EİF/GAM-3-2014-6(21) – FA.

References

Alizade, E. K. (2004). Zakonomernosti morfo-strukturnoj differenciacii gornyh sooruzhenij vostochnogo segmenta central'noj chasti Al'pijsko-Gimalajskoj shovnoj zony. Avtoref. dis. …dokt. geogr. nauk. Baku: Institut geografii NAN, 53 s.

Alekperova, S. O., Mamedov, S. G., Gamidova, Z. A., & Ismajlova, L. A. (2017). Izuchenie morfometricheskih pokazatelej rel'efa seleopasnyh bassejnov po dannym radarnyh sputnikovyh snimkov (na primere mezhdurech'ja shinchaj-damiraparanchaj) //«Vestnik Moskovskogo Gosudarstvennogo oblastnogo universiteta», №2, str.71-83, Moskva

Piriev, R. H. (1986). Metody morfometricheskogo analiza rel'efa: na primere territorii Azerbajdzhana. Baku: Jelm, 117 s.

Ivanov, E. N. (2018). Sovremennye metody nazemnogo izuchenija gornyh lednikov juga Vostochnoj Sibiri //Serija «Nauki o Zemle» T. 25. S. 54–65

Ismaylov, M. J., & Ismaylova, L. A. (2014). Scientific-methodological approaches of revelation of land-scape-recreation potential of mountain geosystems (on example of southern slopes of the greater Caucasus) // НАНА, Извест. №3-4, Баку, стр. 86-92.

6th Intercontinental Geoinformation Days

igd.mersin.edu.tr

Efficient use of wind energy in Lankaran zone

Vusala Rasulzade *[1]

[1]Azerbaijan National Academy of Science, Caspian Sea Problems Department, Baku, Azerbaijan

Keywords
Lankaran
Caspian Sea
Wind speed
Wind direction
Renewable energy

Abstract

Depletion of traditional energy resources and deterioration of ecology is one of the main issues on the agenda of the whole world in modern times. A number of developed countries are promoting the use of alternative energy sources as one of the ways to solve the problem. Currently, the most widely used alternative energy sources are solar and wind. The advantages of wind energy are that it is inexhaustible and the cost is relatively low. Aerological research results are used in wind energy. Based on these results, the wind energy cadastre is being developed. In this way, the regions where the application of wind energy is profitable are determined. Coastal zones are considered the most promising place to get energy from the wind. Offshore farms are built in the sea at a distance of 10-12 kilometers from the coast, and sometimes more. Towers of wind generators are built on foundations buried up to 30 meters deep, floating foundations are also used. The energy of the wind is directly proportional to the cube of its speed. But unfortunately, not all wind energy can be usefully used. According to theoretical calculations, the value of the coefficient of useful use of the energy of the air flood is 59.3%. Only a certain part of this energy is converted into useful energy. The performance factor of the most modern wind turbines is about 50%.

1. Introduction

One of the most developed sectors of Azerbaijan's economy is the energy sector. At a time when the countries of the world are using alternative energy on a large scale, important work is being done in this field as well in Azerbaijan. Increasing the production of ecologically clean energy is one of the most important priority issues of the economic development of our republic. Being a land of natural resources, Azerbaijan is rich in alternative energy resources such as wind, sun, wave and etc. The goal set in this area is to increase the share of renewable energy produced in the country to 24% in 2025 and 30% in 2030. Currently, this indicator is 17.3%.

There are a number of compelling reasons to switch to green energy in modern times. The most important of these is that traditional energy production damages the environment and has a negative impact on ecology. The increase in carbon dioxide emissions released into the air in Azerbaijan, which is known as a supplier of oil and gas in the world, is also an important reason for the transition to green energy. Another reason is the possibility of future depletion of traditional energy resources, which are increasingly expensive (Cəlilov, 2009).

A number of countries around the world have reduced the use of coal by switching to renewable energy, and as a result, a positive change in the amount of harmful waste emitted into the air has stimulated the improvement of the environmental situation. Currently, steps are being taken in this direction in our country as well. In particular, significant work is being done in our republic to obtain energy from the sun and wind. By studying and researching the areas rich in wind energy in Azerbaijan, it is possible to determine the amount of energy that can be obtained from it. It has been determined that the Caspian Sea coastal zone and the Absheron peninsula are among the areas with the highest wind energy potential. The purpose of this work is to determine the feasibility and usefulness of wind energy production in the Lankaran zone.

2. Method

To achieve this goal, the research was conducted in the following manner. For this, wind rose graphs were drawn up to show the change in wind speed and

* **Corresponding Author**

*(resulzade323@gmail.com) ORCID ID 0000-0002-0575-6101

Cite this study

Rasulzade, V. (2023). Efficient use of wind energy in Lankaran zone. Intercontinental Geoinformation Days (IGD), 6, 294-297, Baku, Azerbaijan

direction over the years. Hourly satellite data obtained from the MERRA-2 satellite with a resolution of 0.5x0.625 at a height of 10 meters from the NASA site was used to determine the wind rose in the given coordinates in Lankaran region.

2.1. Statistical Characteristics of wind speed based on space data

As can be seen from the picture, during both years, easterly winds prevail. To be more precise, in 2001, the phase index of east wind was 8.4%. This indicator increased slightly in 2021 and was 8.9% for eastern winds. At the same time, in 2001, northeast winds accounted for 5.5%, and southeast winds accounted for 5%. In 2021, southeast winds increased by 6.9%, while northeast winds decreased by 4%.

Both westerly and southerly winds show slight annual variations. These changes tend to decrease in the western direction and increase in the southern direction. No significant difference was observed in the north winds.

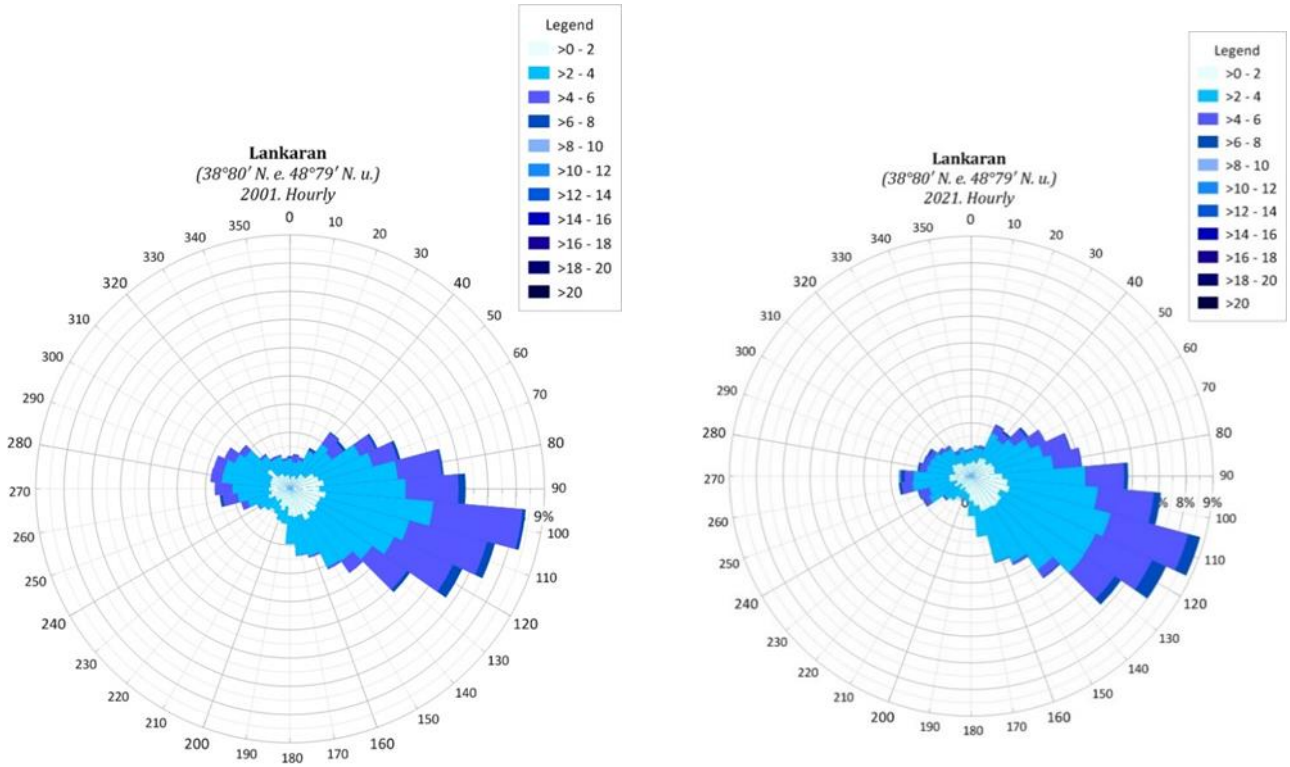

Figure 1. Wind roses for Lankaran for 2001 and 2021

2.2. Determination of wind distribution

The Rayleigh distribution is the simplest parameter to determine the wind resource because it only requires information about the average wind speed. To estimate prospective wind energy sites, a probability distribution function is often fitted to observed wind speed data. Wind speed distributions will be different in different locations (Siddiqui, M. M. 1964). The Weibull model closely reflects the actual hourly/ten-minute wind speed distribution at many locations. The Weibull factor is often close to 2, and therefore the Relay distribution can be used as a less accurate but simpler model. The Rayleigh distribution of the random quantity x is expressed by the Equation 1.

$$W(x) = \frac{x}{s^2}\exp\left(-\frac{x^2}{2s^2}\right) \quad , \quad 0 \le x \le +\infty, \quad s > 0; \qquad (1)$$

s - is a parameter of the distribution (Rəsulzadə 2022).

3. Results

Statistical indicators of wind speed and direction by year are given in Table 1.

The data given in Table 1 were obtained according to the wind roses built for 21 years and the calculations made in the "Fortran" program. As in 2001 and 2021, in other years included in this time interval, the predominance of east and southeast winds is evident. Looking at the average wind speed, 2-3 m/s winds are more frequent and the average wind speed for 21 years is 2.89 m/s.

It should be noted that the values of the mean square deviation are slightly different from each other when calculated based on the histogram and the Rayleigh parameter.

In the table, the most frequent wind directions (φ_{max}), average wind speeds ($\vec{v}$), mean square deviation according to histogram $\sqrt{\sigma_v}^2$ (H), mean square deviation according to Rayleigh parameter $\sqrt{\sigma_v}^2$ (R) and Rayleigh distribution parameter values (S_R) are shown for Lankaran.

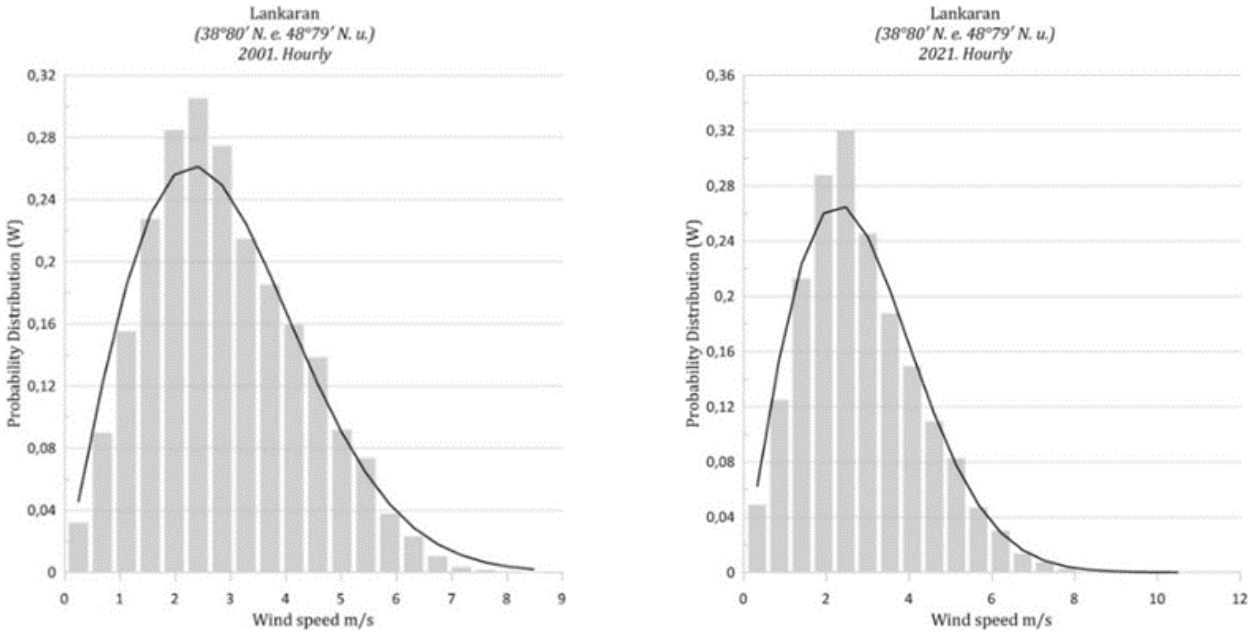

Figure 2. Rayleigh distribution graphs for Lankaran for 2001 and 2021

Table 1. Wind characteristics in Lankaran

Years	φ_{max}	$\vec{v}$ (m/s)	S_R (m/s)	$\sqrt{\sigma_v}^2$ (H) (m/s)	$\sqrt{\sigma_v}^2$ (R) (m/s)
2001	100°	2,90	2,32	1,38	1,52
2002	110°	2,86	2,28	1,39	1,49
2003	90°	2,80	2,24	1,37	1,47
2004	110°	3,02	2,41	1,48	1,58
2005	110°	3	2,39	1,39	1,56
2006	110°	3,05	2,44	1,44	1,60
2007	120°	3,05	2,44	1,42	1,60
2008	110°	2,94	2,34	1,41	1,53
2009	120°	2,86	2,28	1,39	1,49
2010	110°	2,81	2,24	1,38	1,47
2011	110°	2,82	2,25	1,31	1,47
2012	120°	2,78	2,22	1,31	1,45
2013	120°	2,88	2,30	1,39	1,51
2014	120°	2,88	2,30	1,47	1,51
2015	100°	2,88	2,30	1,38	1,51
2016	110°	3,02	2,41	1,39	1,58
2017	120°	2,96	2,36	1,39	1,54
2018	110°	2,82	2,25	1,36	1,47
2019	100°	2,73	2,17	1,31	1,42
2020	110°	2,88	2,29	1,39	1,50
2021	110°	2,85	2,28	1,43	1,49
2001-2021	110°	2,89	2,31	1,39	1,51

4. Discussion and Conclusion

The assessment of the wind energy potential of the territory is carried out on the basis of data on wind speed and wind power density (W/m²) at various heights, which is the most important parameter for the calculation and selection of wind turbines.

The power of the wind flow P (W) is proportional to the third power of the wind speed $\vec{v}$ (m/s) and is determined by the formula: $P = \frac{\rho}{2} A \overline{v^3}$, where A is the cross-sectional area perpendicular to the wind direction; $\rho = 1.225$ kg/m³ – air density. If the radius of the wind turbine blade is equal to r then $A = \pi r^2$. The quantity $\frac{P}{A} = \frac{\rho}{2} \overline{v^3}$ is wind power density (Alireza and Onar 2010).

As can be seen from figure 2, the distribution of wind speed in the considered area is expressed quite well by the Rayleigh distribution (Trevor, 2017). Accordingly, the following formula is obtained for calculating wind power density:

$$\frac{P}{A} = 1.88\, \rho\, {S_R}^3$$

If we take the average value of S_R given in Table 1 (2.31), we get the result of $\frac{P}{A} = 28.4$ (W/m²). This shows that the wind energy potential of the considered area is very weak.

Figure 3. Distribution of the average wind power density in the Lankaran region

For the 10% of the windiest areas in the Lankaran region, the average wind power density at a height of 50 m is 400 (W/m^2) and the average wind speed is 5.31 m/s. These areas are located at an altitude of approximately 1000 meters (Figure 3).

Application of green technologies and meeting the requirements of energy efficiency in the territory of the Republic of Azerbaijan requires the most accurate assessment of the renewable energy potential of each region of the country.

References

Alireza, K., & Onar, O. C. (2010). Energy harvesting, London.

Cəlilov, M. (2009). Alternativ regenerativ enerji sistemləri, Bakı.

Manwell, J. F., Mcgowan, J. G., & Rogers, A. L. (2009). Wind energy explained, Washington.

Rəsulzadə, V. (2022). Pirallahı stansiyasında küləyin sürət və istiqamətinin tədqiqi. Coğrafiyanın müasir problemləri: Elm və təhsilin inteqrasiyası beynəlxalq elmi-praktiki konfransının materialları,136-140, Bakı.

Siddiqui, M. M. (1964). Statistical inference for Rayleigh distributions. The Journal of Research of the National Bureau of Standards, Sec. D: Radio Science, 68D(9), 1007.

Trevor, M. L. (2017). Wind energy engineering, London.

6th Intercontinental Geoinformation Days

igd.mersin.edu.tr

Innovative trend analysis of downward surface shortware radiation in Türkiye during 1984-2021

Şeyma Akca*[1], Eyüp Şişman [2]

[1] *Harran University, Geomatics Engineering Department, Sanliurfa, Türkiye*
[2] *Yildiz Technical University, Civil Engineering Department, Istanbul, Türkiye*

Keywords
DSSR
ITA
Trend Analyses
Forest fire

Abstract

Downward Surface Shortwave Radiation (DSSR) is a crucial factor that plays a significant role in maintaining the Earth's surface energy balance. It refers to the solar radiation that reaches the surface, contributing to various environmental processes and influencing climatic conditions. Understanding the trends in DSSR is particularly important in areas prone to forest fires, as it can provide valuable insights into the underlying factors that contribute to fire risk. To investigate the trends of DSSR data in regions susceptible to forest fires, this study employed an innovative trend analysis methodology. The focus was on three provinces in Turkey: Antalya (specifically Manavgat and Akseki), Mugla (particularly Datça), and Rize (specifically the Central area). These provinces were chosen due to their high incidence of fires, making them ideal study areas for examining the relationship between DSSR and fire occurrences. The analysis covered a significant time span from 1984 to 2021 and relied on the Merra-2 dataset, a reliable and comprehensive dataset provided by NASA. This dataset includes a wide range of atmospheric parameters, including DSSR, allowing researchers to assess long-term trends and patterns. By analyzing the DSSR trends in these regions, the study aimed to gain insights into the potential connections between variations in DSSR and the occurrence of forest fires.

1. Introduction

Downward Surface Shortwave Radiation (DSSR) plays a fundamental role in maintaining the radiation balance at the Earth's surface, serving as a primary source of energy that drives heat (sensible and latent) and gas (such as water vapor and carbon dioxide) exchanges between oceanic ecosystems (or terrestrial) and the atmosphere. DSSR provides the energy necessary for various ecological and atmospheric processes, influencing temperature patterns, evaporation rates, and the overall dynamics of the Earth's climate system. Understanding the characteristics and trends of DSSR is essential for comprehending the intricate interactions between the land, ocean, and atmosphere, and for studying the impacts of climate change and human activities on these crucial exchanges of energy and gases. (Lorenzo et al., 2015).

The MERRA-2 utilized in this analysis incorporates spectral channels from both the infrared and visible spectra, along with information on atmospheric composition and albedo, to calculate the DSSR reaching the Earth's surface. DSSR, as a vital component of the surface energy budget, holds significant importance in climate studies and serves as a crucial input for various applications. It is employed in land surface assimilation models and surface energy budget models, aiding in the estimation of components of heat flux components over coastal areas for the purpose of driving models of ocean circulation (Ilčev, 2017). Additionally, in the domain of agriculture, DSSR data is employed as an input parameter for crop modeling (Ilčev, 2017). Moreover, in hydrology science, DSSR plays a key role in drainage basin and run-off analysis, enabling the assessment of flood risks and facilitating dam monitoring. Notably, DSSR is also employed in monitoring fire risks since high irradiance values can contribute to surface drying, impacting fire conditions.

This study focused on conducting a trend analysis of DSSR and at the same time investigating its potential role as a contributing factor in forest fires risk.

* **Corresponding Author**

*(seymakca@harran.edu.tr) ORCID ID 0000 – 0002– 7888– 5078
(esisman@yildiz.edu.tr) ORCID ID 0000– 0003 –3696 – 9967

Cite this study

Akca S, Sisman E (2023). Innovative trend analysis of downward surface shortware radiation in Türkiye during 1984-2021. Intercontinental Geoinformation Days (IGD), 6, 298-301, Baku, Azerbaijan

2. Method

2.1. MERRA-2

Within the scope of the study, NASA's MERRA-2 reanalysis data, which is a NASA mission, was utilized.

MERRA-2 (Modern-Era Retrospective Analysis for Research and Applications, Version 2) offers data starting from 1980 and serves as a replacement for the original MERRA dataset. The transition was prompted by notable improvements in the assimilation system, allowing for the integration of cutting-edge microwave observations and hyperspectral radiance, coupled with GPS-Radio Occultation data. Additionally, MERRA-2 incorporates NASA's ozone profile observations, which commenced in late 2004. Notable advancements have been made in both the GEOS model and the GSI assimilation system within MERRA-2 (Nakkazi et al., 2022). The spatial resolution remains comparable to MERRA, with an approximate resolution of 50 km in the latitudinal direction.

Monitoring of DSSR (Downward Surface Shortwave Radiation) from ground-based stations began around the world in the late 1950s. However, because these stations are sparse and heterogeneous, ground measurements alone do not provide adequate information to derive the global radiation distribution. In addition to satellite remote sensing techniques, reanalysis estimates represent a feasible approach for generating long-term global DSSR data that is practical in terms of time and cost. (Zhang et. al.,2016)

Evaluating the spatial and temporal trends of DSSR is crucial for understanding weather and climate variability, as well as for investigating its potential impact on forest fires (Zuluaga et. al., 2021).

2.2. Study Area

In recent years, Türkiye has experienced extreme weather events such as floods and fires, which can be attributed to global climate change (Şahan et al.,2022, Tuğaç, 2023). These events have been characterized by excessive and irregular precipitation, as well as extreme temperatures. In order to better understand these phenomena, the DSSR data of Antalya province, known for having the highest number of fires in the country, and the neighboring province of Muğla, were analyzed for the period of 1984 to 2021. Furthermore, the DSSR data of Rize province, which receives consistent precipitation and has a lower incidence of fires, was also examined. Innovative trend analysis methods were employed to determine the trends in these provinces and gain insights into their respective climatic patterns. All study points shown in Figure 1.

2.3. Innovative Trend Analysis (ITA) Methodology

The innovative trend analysis (ITA) method, developed by Şen (2012), has introduced a novel approach to trend research by allowing for time series analysis without any assumptions. This method has gained popularity due to its simplicity, as it can be easily applied without requiring any specific assumptions, and trends and variations can be identified through graphical representations. The ITA methodology also offers the flexibility to determine trends within visually distinct sub-groups, such as low, medium, and high, rather than analyzing the data as a whole. The adaptability of the methodology and its outputs have captured the interest of numerous researchers in the scientific field (Birpınar et al., 2023, Şişman et al., 2022, Dabanlı et al., 2016).

$$S = \frac{m_2 - m_1}{\frac{n}{2}}$$

where, S is the innovative trend slope, m_1 and m_2 are the arithmetic average of the first and second halves of the series, and n represent the total number of data.

The whole application was implemented in Excel and MATLAB Environment.

Figure 1. Study Area

3. Results

Within the scope of this research, an innovative trend analysis method has been utilized to examine the monthly trends of Merra-2 DSSR data from 1984 to 2021 in regions prone to forest fires namely Antalya (Manavgat, Akseki), Muğla (Mesudiye), and flood risk e.g., Rize.

In this study, trend direction and trend slope of monthly DSSR data in determined locations have been analyzed using ITA methodology, trend magnitude calculated with the equation 1 for each location are given in Table 1. When ITA graphs and Table 1 are examined, it is seen that DSSR trends are generally increasing. When the ITA graphs are commented in detail, the trend increases in high DSSR values in July and August, the forest fires are frequently obtained in Manavgat, Akseki and Datça, are at crucial levels to be followed. On the other hand, if we discussed the ITA graph prepared for Rize, it is seen that DSSR trends increasing in summer months when floods occurs.

The DSSR trend slope reaches its maximum of 0.093 %, 0.048% and 0.053% in April for Manavgat, Datça and Rize respectively.

4. Discussion

This study has assesed DSSR trends in Türkiye during 1984-2021, utilizing MERRA 2 gridded products as the primary data resources. While numerous research works have identified the trends of DSSR in Asia, Europe and America, there has been few investigation DSSR trends in Türkiye.

The existing researches indicates that there has been noteworthy decadal variability in Surface Solar Radiation, characterized by an increase known as "global brightening" from 1980s across the globe (Stanhill and C. S, 2008; Takemura and Ohumura, 2009). Our results are consistent with the prevailing trends observed in the current body of literature.

Increases in the frequency of forest fires events show similarities with the increasing trends in the DSSR data, especially in July and August of the summer shown as Figure 2.

Table 1. Trend slope (%) for DSSR during 1984-2021

Location Months	Manavgat	Akseki	Datça	Rize
January	-0.002	-0.077	-0.009	0.017
February	0.011	-0.087	-0.025	0.025
March	0.058	-0.071	0.036	0.014
April	0.093	0.016	0.048	0.053
May	0.044	-0.007	0.038	0.041
June	0.022	-0.007	0.021	0.032
July	0.021	0.032	0.047	0.019
August	0.023	0.034	0.040	0.046
September	0.020	-0.002	0.039	0.027
October	0.025	0.021	0.013	0.019
November	0.041	0.037	0.021	0.033
December	0.045	0.008	0.026	0.034

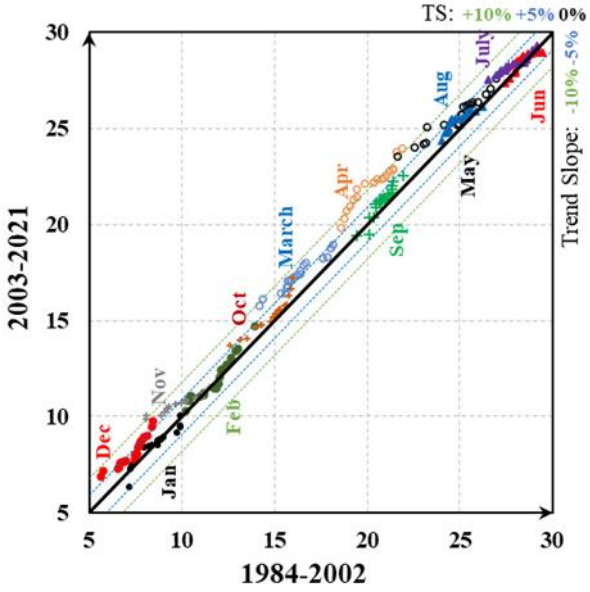

Manavgat ITA graph

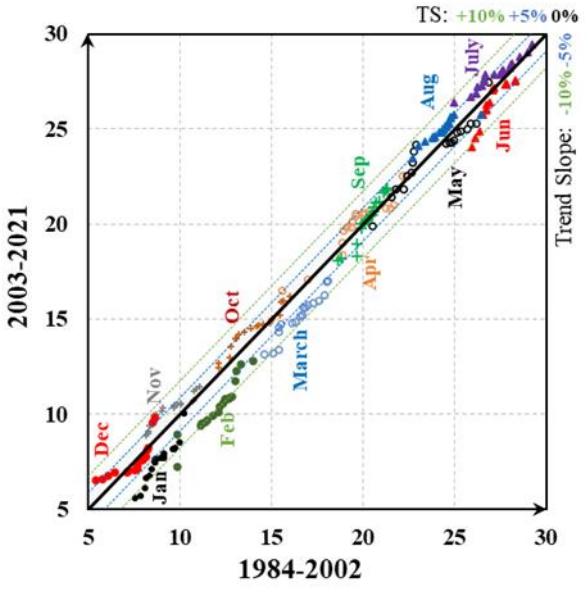

Akseki ITA graph

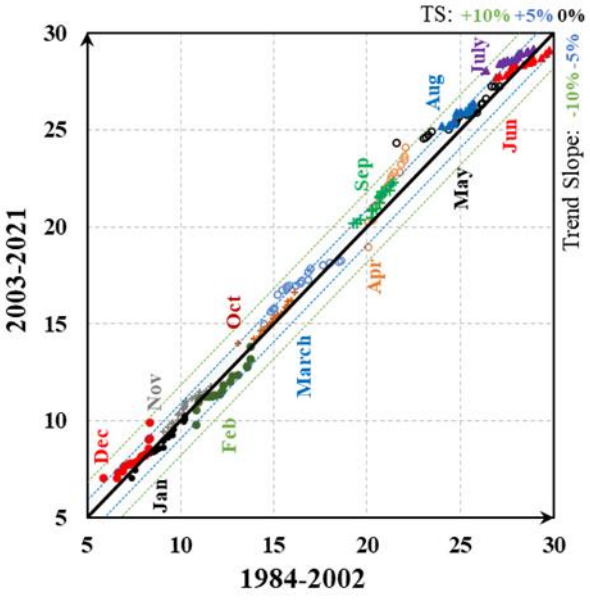

Datça ITA graph

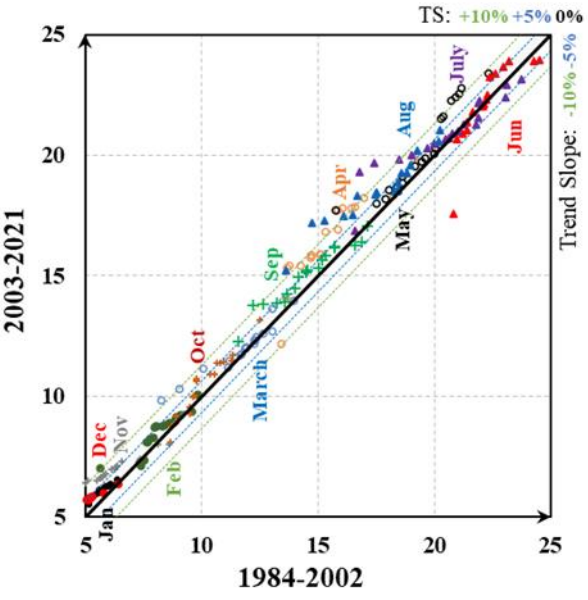

Rize ITA graph

Figure 2. Antalya (Manavgat Akseki), Muğla (Datça) and Rize ITA graphs during1984-2021 years

5. Conclusion

The trends of DSSR data should be expected to have an impact on the hydrological cycle, agricultural production and natural ecosystem. The findings of this study have the potential to contribute to advancing knowledge in the field of increasing DSSR trend' impacts on Türkiye, specifically with regard to fire and flood risk

management, solar energy production, hydrological and agricultural modeling.

As a result, accurate identification of the DSSR trends specifically holds great significance in the realms of fire risk management.

References

Birpınar, M. E., Kızılöz, B., & Şişman, E. (2023). Classic trend analysis methods' paradoxical results and innovative trend analysis methodology with percentile ranges. Theoretical and Applied Climatology, 1-18.

Cheng, L., Tang, B. H., He, Z., Fu, Z., & Li, M. (2023). Time-series variation and attribution analysis of downward shortwave radiation over the Yunnan-Kweichow plateau from 1984 to 2018. International Journal of Digital Earth, 16(1), 337-354.

Dabanlı, İ., Şen, Z., Yeleğen, M. Ö., Şişman, E., Selek, B., & Güçlü, Y. S. (2016). Trend assessment by the innovative-Şen method. Water resources management, 30, 5193-5203.

Ilčev, S. D. (2017). Global satellite meteorological observation (GSMO) theory. Springer.

Nakkazi, M. T., Sempewo, J. I., Tumutungire, M. D., & Byakatonda, J. (2022). Performance evaluation of CFSR, MERRA-2 and TRMM3B42 data sets in simulating river discharge of data-scarce tropical catchments: a case study of Manafwa, Uganda. Journal of Water and Climate Change, 13(2), 522-541.

Sanchez-Lorenzo, A., Wild, M., Brunetti, M., Guijarro, J. A., Hakuba, M. Z., Calbó, J., Mystakidis, S., & Bartok, B. (2015). Reassessment and update of long-term trends in downward surface shortwave radiation over Europe (1939–2012). Journal of Geophysical Research: Atmospheres, 120(18), 9555-9569.

Stanhill, G., & Cohen, S. (2008). Solar radiation changes in Japan during the 20th century: Evidence from sunshine duration measurements. Journal of the Meteorological Society of Japan. Ser. II, 86(1), 57-67.

Şahan, E. A., Köse, N., Güner, H. T., Trouet, V., Tavşanoğlu, Ç., Akkemik, Ü., & Dalfes, H. N. (2022). Multi-century spatiotemporal patterns of fire history in black pine forests, Turkey. Forest Ecology and Management, 518, 120296.

Şen, Z. (2012). Innovative trend analysis methodology. Journal of Hydrologic Engineering, 17(9), 1042-1046.

Şen, Z. (2017). Innovative trend significance test and applications. Theoretical and applied climatology, 127, 939-947.

Şişman, E., Kizilöz, B., & Birpinar, M. E. (2022). Trend Slope Risk Charts (TSRC) for piecewise ITA method: an application in Oxford, 1771–2020. Theoretical and Applied Climatology, 150(1-2), 863-879.

Takemura, T. & Ohumura, A. (2009) Trend of surface solar radiation over Asia simulated by aerosol transport-climate model. In: AGU Fall Meeting. San Francisco: AGU

Tuğaç, Ç. (2023). Evaluation of urban infrastructure policies in Turkey for climate resilience and adaptation. Sustainable and Resilient Infrastructure, 8(sup1), 190-202.

Zhang, X., Liang, S., Wang, G., Yao, Y., Jiang, B., & Cheng, J. (2016). Evaluation of the reanalysis surface incident shortwave radiation products from NCEP, ECMWF, GSFC, and JMA using satellite and surface observations. Remote Sensing, 8(3), 225.

Zuluaga, C. F., Avila-Diaz, A., Justino, F. B., & Wilson, A. B. (2021). Climatology and trends of downward shortwave radiation over Brazil. Atmospheric Research, 250, 105347.

6th Intercontinental Geoinformation Days

igd.mersin.edu.tr

Rapture and surface deformation mapping of Türkiye 2023 earthquake using DInSAR with Sentinel-1 satellite data

Pouya Mahmoudnia[*1], **Mohammad Sharifikia** [1]

[1]*Tarbiat Modares University, Faculty of Humanities, Department of Remote Sensing and GIS, Tehran, Iran*

Keywords
Remote sensing
DInSAR
Geo-Hazard
Earthquake

Abstract

This paper showcases the utility of the Differential Interferometric Synthetic Aperture Radar (DInSAR) technique in mapping the surface deformation caused by the 7.8 M_w earthquakes that hit the southern pate of Türkiye on February 6, 2023. By processing SAR data acquisition by Sentinel-1A satellite. The study result demonstrates the ability of DInSAR to provide highly accurate and comprehensive information on rupture caused over the known fault as well as jolting and land deformation area from strong seismic events. Furthermore, the observed significant surface deformation, including both uplift and subsidence, highlights the potential of DInSAR in geo-hazard study which can mitigate the risk and disaster caused by earthquakes. The results underline the importance of real-time earthquake detection and monitoring and can do early warning to the policies and other emergencies time to save life as more as possible close to the shake.

1. Introduction

Earthquakes are damaging geo-hazard that affect many people each year. Real-time earthquake detection and monitoring are vital for mitigating loss of life and property damage.

Differential Interferometric Synthetic Aperture Radar (DInSAR) is an effective remote sensing technique for seismic detection and monitoring. It provides comprehensive data on ground alterations and surface dislocation from seismic events (Vaka et al. 2021; Vaka et al. 2020; Xu et al. 2020).

On February 6, 2023, a 7.8 M_w earthquake hit southern Türkiye, followed by a 7.5 Mw earthquake about 90km to the north 9 hours later. The epicenters of these earthquakes are shown in Figure 1. The 7.8 M_w earthquake and its aftershocks occurred in the transition zone between the Dead Sea and East Anatolian faults, while the epicenter of the 7.8 M_w earthquake was located near the triple junction of the Arabian, African, and Anatolian plates. The Anatolian fault moves Türkiye toward the Aegean Sea, while the Dead Sea fault moves Arabia northward on the African plate.

In this study, we employed the Differential Synthetic Aperture Radar Interferometry (DInSAR) technique to cartographically depict the seismic surface deformation that resulted from the 7.8 M_w earthquake of 2023 using Sentinel-1 satellite data.

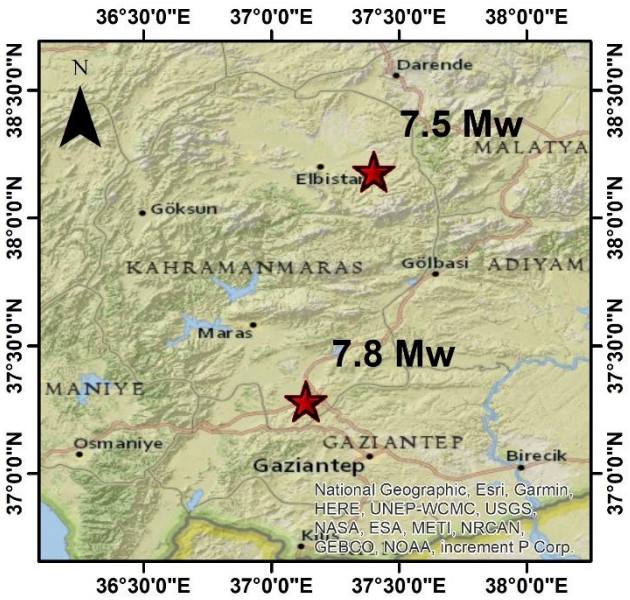

Figure 1. The epicenters of the earthquakes

* **Corresponding Author**

*(po.mahmoudnia@gmail.com) ORCID ID 0009-0000-5189-8429
(sharifikia@modares.ac.ir) ORCID ID 0000-0003-3563-8816

Cite this study

Mahmoudnia P & Sharifikia M (2023). Rapture and surface deformation mapping of Türkiye 2023 earthquake using DInSAR with Sentinel-1 satellite data. Intercontinental Geoinformation Days (IGD), 6, 302-304, Baku, Azerbaijan

2. Data and Method

2.1. Data

The present study employed SAR imagery derived from the European Space Agency's (ESA) C-band Sentinel-1 data, obtained from both ascending and descending orbits in the VV polarization (i.e., vertical transmit and vertical receive), to delineate the topographic changes resulting from the earthquake. The data was collected before and after the seismic event (see Table 1).

Table 1. Satellite dataset information used in this study

Items	Ascending	Descanting
Master	2023/01/28	2023/01/29
Slave	2023/02/09	2023/02/10
Baseline(m)	168.324	106.558
Incidence angle	43.92°	39.39°

2.2. Method

DInSAR is a technique that employs Synthetic Aperture Radar (SAR) images to measure land deformation by comparing two or more radar images taken at different times. Images are processed to obtain an interferogram, showing phase differences between two radar images caused by changes in ground displacement.

The total differential phase difference (Δφ) through fringes that account for various factors, including topography (φtopo), orbital fringe or baseline (φorbit), and movement (φmov) caused by natural occurrences such as seismic or aseismic activities Additionally, the representation incorporates fringes originating from atmospheric effects (φatmos) and phase noise (φnoise).

Δφ = φtopo+ φorbit+ φmov+ pathos+ φnoise

ALOS WORLD 3D-30m (AW3D30 DEM) is used to remove topographic fringes in interferograms. To reduce phase error caused by decorrelation, using an adaptive filter can enhance phase quality. We applied an adaptive filter, a modified version(Baran et al. 2003) of Goldstein's filtering method(Goldstein and Werner, 1998). After phase unwrapping, we refined the orbital parameters by selecting control points across interferograms to eliminate phase ramps. The unwrapped phase values were converted into line of sight (LOS) displacement and geocoded into a map projection. All procedures were executed utilizing the SARscape 5.4.1 software.

3. Results and Discussion

The interferograms resulting from the earthquakes, acquired via Sentinel-1 ascending and descending data, are depicted in Figure 2 and Figure 3. Each individual fringe correlates with a complete cycle of phase variation and corresponds to a displacement of 2. 8 centimeters in line-of-sight (LOS) in C-band interferograms.

The observed interferograms exhibit intricate and dense fringes. The patterns observed on the fringes exhibit inverse characteristics in terms of their densities and contrasts.

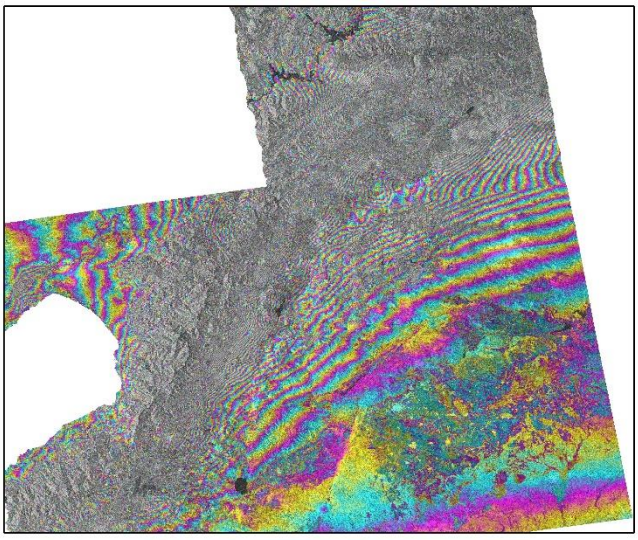

Figure 2. Interferogram of the Ascending pair

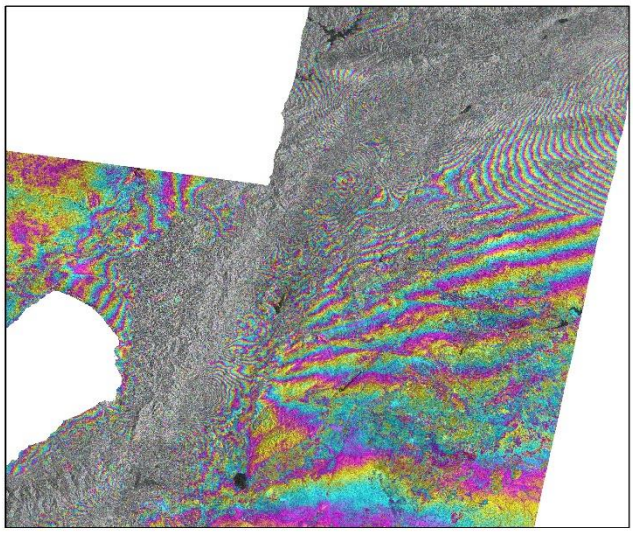

Figure 3. Interferogram of the descending pair

The figures presented in Figure 4 and Figure 5 illustrate LOS displacement maps. The observations indicate that the Sentinel-1 ascending data recorded a displacement of 1.68 m for uplift and -1.26 m for subsidence. Similarly, the Sentinel-1 descending data recorded a displacement of 1.08 m for uplift and -1.42 m for subsidence. The differences observed in the maximum and minimum displacements between the two measurements appear to be the result of alterations in the satellite pass and look direction. The standard deviation values for the observed displacements were determined to be 0.29 and 0.23 meters for the Sentinel-1 ascending and Sentinel-1 descending data sets, respectively.

4. Conclusion

In conclusion, the present study demonstrated the effectiveness of Differential Interferometric Synthetic Aperture Radar (DInSAR) as a remote sensing technique for seismic detection and monitoring, using Sentinel-1 satellite data to analyze the surface deformation resulting from the February 6, 2023earthquake in southern Türkiye. The observed significant surface

deformation, including both uplift and subsidence, highlights the potential of DInSAR in mitigating the loss of life and property damage caused by earthquakes. The study provides valuable insights into the use of DInSAR for real-time earthquake detection and monitoring, which can aid in disaster preparedness and response efforts. Further research in this area can help to improve our understanding of the impact of earthquakes on the earth's surface and inform policies and strategies for earthquake risk reduction.

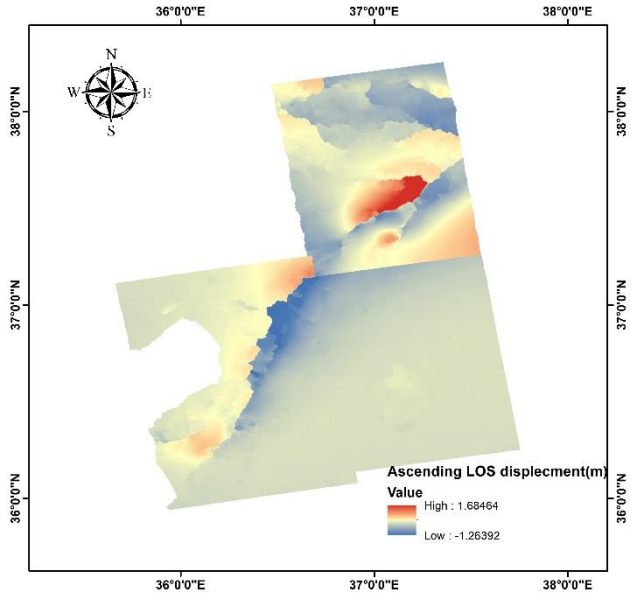

Figure 4. LOS displacement of the ascending pair

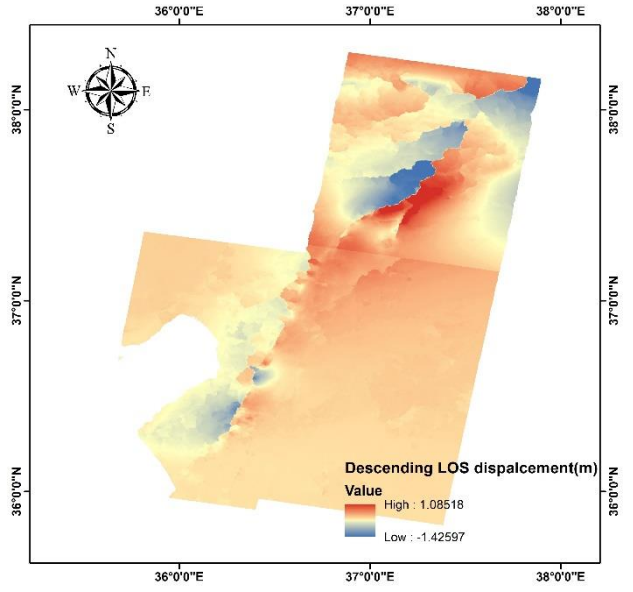

Figure 5. LOS displacement of the descending pair

References

Baran, I., Stewart, M. P., Kampes, B. M., Perski, Z., & Lilly, P. (2003). A modification to the goldstein radar interferogram filter. IEEE Transactions on Geoscience and Remote Sensing, 41(9 PART II), 2114–2118. https://doi.org/10.1109/TGRS.2003.817212

Goldstein, R. M., & Werner, C. L. (1998). Radar interferogram filtering for geophysical applications. Geophysical Research Letters, 25(21), 4035–4038. https://doi.org/10.1029/1998GL900033

Vaka, D. S., Rao, Y. S., & Bhattacharya, A. (2021). Surface displacements of the 12 November 2017 Iran–Iraq earthquake derived using SAR interferometry. Geocarto International, 36(6), 660–675. https://doi.org/10.1080/10106049.2019.1618927

Vaka, D. S., Rao, Y. S., & Singh, T. (2020). Surface deformation of the 2019 mirpur earthquake estimated from sentinel-1 insar data. 2020 IEEE India Geoscience and Remote Sensing Symposium, InGARSS 2020 - Proceedings, 130–133. https://doi.org/10.1109/InGARSS48198.2020.9358915

Xu, X., Sandwell, D. T., & Smith-Konter, B. (2020). Coseismic displacements and surface fractures from sentinel-1 InSAR: 2019 Ridgecrest earthquakes. Seismological Research Letters, 91(4), 1979–1985. https://doi.org/10.1785/0220190275

6th Intercontinental Geoinformation Days

igd.mersin.edu.tr

Comparison of different land surface temperature (LST) estimation algorithms using remotely sensed images

Ali Hosingholizade [1], Parviz Zeaiean Firouzabadi *[2] Foroogh Khazaei Nezhad [3] Mozhban Dehghani Aghchekohal [2]

[1]*University of Tehran, Geography, Remote sensing and GIS, Tehran, Iran*
[2]*Kharazmi University, Geography, Remote sensing and GIS, Tehran, Iran*
[3] *Kosar University of Bojnord, Humanities, Geography, Bojnord, Iran*

Keywords
Remote sensing
LST
Emissivity
Stefan_Boltzman
Tehran

Abstract

Earth Surface Temperature is a key indicator of energy balance on Earth. In recent years, several methods for obtaining temperature using satellite images have been provided. This study aimed to compare the performance of different methods to estimate Land Surface Temperature (LST).Here, LST over Tehran metropolitan city has been estimated through three methods including Artis, Mono_window and Stefan_Boltzman algorithms applied to Landsat (TM, ETM +, OLI) and MODIS image, Emissivity obtained through image classification, the vegetation index (NDVI) and MODIS emissivity product, Then, using an accurate thermometer, surface and air temperature at a height of one and a half meters were taken the linear relationship between surface temperature and corresponding air temperature has been established. A statistical measure namely mean absolute error and T test for selection of best method were used. The results show that Stefan_Boltzman method with mean absolute error of 1.540 °C was the best one. Therefore, it is suggested that the Stefan_Boltzman method be used For other areas with the same weather conditions and geographical parameters.

1. Introduction

Today, with the expansion of urban areas, accurate thermal data are essential for managing, designing and planning cities (Deng et al. 2023; Sidiqui et al. 2016). Analysing the trend of existing hot spots can have a direct impact on the design of new urban fabric and the process of renovation of old fabrics, especially in developed countries (Mullerova and Williams, 2019). Progress and development in remote sensing technology has made it possible to extract accurate thermal data from urban environments, which has drawn many researchers' attention to this issue and its different methods in cities (Orusa and Mondino, 2019).

Selection of accurate method to obtain temperature, even in a wider dimension, is an important factor in the study of global changes as a heat balancer and controller of climate models (Halder et al. 2021; Sidiqui et al. 2016). The knowledge of the surface temperature is very important for a wide range of issues in earth sciences, including the temperature of different regions, wide changes and interactions between human activities and the surrounding environment (Perera et al. 2022). Although the temperature difference in different regions may not be very large, this small amount can cause many disorders (Shang and Dick. 2006).

To date, various algorithms have been provided to obtain the temperature of the earth's surface. From methods that are based on classifing NDVI through thresholding (Guha et al. 2018; Hossingholizade et al. 2021) to the use of MODIS ready products (Yu et al. 2022) and other relatively older methods such as station-based observations interpolation and the use of mobile stations that do not consider the emission and instead use special thermometers to calculate the air temperature (Ozelkan et al. 2015). Since last years, various formulas have been presented to calculate the temperature. Each formula is used separately. (Mia et al. 2014).

The aim of this study is to find the best method in estimating surface temperature via comparison different methods.

The results of this research can significantly enhance the knowledge of scientists in estimation of earth surface temperature with different algorithms.

* **Corresponding Author**

(a.hosingholizade@ut.ac.ir) ORCID ID 0000 – 0001 – 5286 – 1361
*(zeaiean@khu.ac.ir) ORCID ID 0000-0001-8407-5605
(f.khazaee@kub.ac.ir) ORCID ID 0000-0000-0000-0000
(Dehghanim848@gmail.com) ORCID ID 0000-0000-0000-0000

Cite this study

Hosingholizade A, Zeaiean Firouzabadi P, Khazaee Nezhad F & Dehghani aghchekohal M (2023). Comparison of different land surface temperature (LST) estimation algorithms using remotely sensed images. Intercontinental Geoinformation Days (IGD), 6, 305-308, Baku, Azerbaijan

2. Method

2.1. Study area

The studied area is a part of Tehran province in latitude˚35˚20 to˚36˚00˚N and longitude˚50˚48 to˚52˚E. This region has a lot of diversity in terms of climate. It starts from the desert climate in the southern parts and continues to the humid climate in the north and mountainous in the eastern parts. In terms of the UTM classification system, it is also in the 39th North zone, and its height ranges from 1050 in the South to 1800 meters in the North.

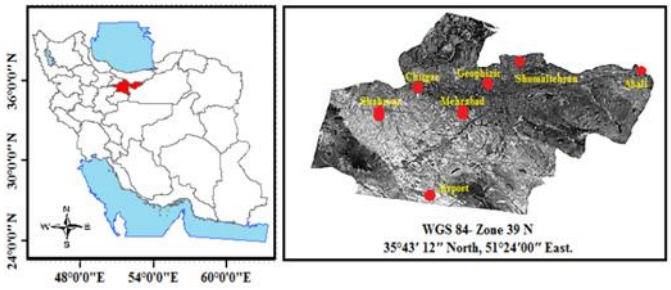

Figure 1. Iran (left)and Theran seven synoptic stations(right)

Table 1. Geographical coordinates of stations

NO	Station	Latitude	Longitude
1	Chitgar	35 44	51 10
2	Mehrabad	35 41	51 19
3	Airport	35 25	51 10
4	Abali	35 44	51 53
5	Geophizic	35 45	51 23
6	Shahryar	35 40	51 02
7	Shomal Tehran	35 48	51 29

2.2. Data

In this research, images of TM, ETM+ and TIRS sensors and the ready product of MODIS satellite, meteorological data including air temperature (Ta) and relative humidity (RH) data as well as surface and air temperature of some sample points were used. The number of rows and paths used for all images are 35 and 164, respectively. It was also tried to select images with the least amount of cloud to avoid mulfunction of different algorithms.

2.2.1. Estimation of temperature from emissivity based on classification

Here, using the SVM method, the image was divided into 6 separate classes and each class was assigned an emissivity based on available scientific sources. Finally, the emissivity map entered to the surface temperature estimation algorithms. (Chen, 2015).

Table 2. Emissivity of different classes

NO	Class	Emissivity
1	Water	0.992
2	Soil	0.962
3	Aqriculture	0.942
4	Dence Cover	0.975
5	Cover non-Cindensing	0.924
6	Urban	0.918

2.2.2. Estimating temperature from emissivity based on NDVI

After calculating NDVI, a specific emissivity value was given to each NDVI interval based on different formulas presented in Table 3 (Zhang et al. 2006).

Table 3. Division of NDVI ranges

NO	NDVI	Emissivity
1	-1<NDVI<-0.185	0.985
2	-0.185<NDVI<+0.157	0.955
3	+0.157<NDVI<0.727	1.0094 + 0.047ln (NDVI)
4	+0.727<NDVI<+0.8	0.99
5	+0.8<NDVI<1	0.99

2.2.3. Estimation of temperature with emissivity obtained from MODIS ready product

In this method, using bands 31 and 32 MODIS satellite, which is special for emission and has a pixel size of one kilometer, and resampling this product to reach a pixel size of 30 meters and enter it into the temperature estimation equations, the land surface temperature of the earth is calculated.

2.3. Mono-window

In Mono-Window algorithm, spectral radiance for each band is obtained with the following relationship (Eq. 1-7), gain and offset can be extracted from the attached Header File and follow the rest of the steps with the following relationships.

$$L_\lambda = \text{gain} \times DN \times \text{offset} \quad (1)$$

$$L_\lambda = \frac{L_{max} - L_{min}}{Qcal_{max} - Qcal_{min}} \times (DN - Qcal_{min}) + L_{min} \quad (2)$$

$$T_{sensor} = \frac{K_2}{Ln(\frac{K_1}{L_\lambda} + 1)} \quad (3)$$

$$W_i = 0.0981 \times \left\{ 10 \times 0.6108 \times \exp\left[\frac{17.27 \times (T_0 - 273.15)}{237.3 + (T_0 - 273.15)} \right] \times (RH/100) \right\} + 0.1697 \quad (4)$$

$$D = (1 - \tau_i) \times [1 + (\varepsilon_i \times \tau_i)] \quad (5)$$

$$C = \varepsilon_i \times \tau_i \quad (6)$$

$$T_s = \frac{\{a(1-C-D) + [b(1-C-D) + C + D] \times T_{sensor} - (D \times T_a)\}}{C} \quad (7)$$

Table 4. Estimating τ_i based on W_i

Temperature	W_i	$\tau_i$euation
High	0.4 – 1.6	$0.97429 - 0.08007 W_i$
High	1.6 - 3	$1.031412 - 0.11536 W_i$
Low	0.4 – 1.6	$0.982007 - 0.09611 W_i$
Low	1.6 - 3	$1.05371 - 0.14142 W_i$

Where, K1 and K2 First and second calibration constant. L_λ Spectral radiance. BT Effective temperature (Kelvin). W_i water vapor. T_0 Air temperature. RH relative humidity. a=-67.355351, b=0.458606. T_s Earth surface temperature. ε_iEmissivity. τ_i Air permeability.

2.4. Artis method

After calculating the spectral radiance, the brightness temperature at the measuring surface and the emissivity with the Normalized Differential Vegetation Index (NDVI), the MODIS classification or ready product, surface temperature is obtained by this method, is calculated using the following formula (Eq. 8) (Tan et al., 2010).

$$S_t = \frac{T_{sensor}}{1+\left(\lambda\times\left(T_{sensor}/\rho\right)\right)\mathrm{Ln}\varepsilon} \quad (8)$$

2.5. Stefan-Boltzmann method

Thermal infrared sensors measure the radiation in the upper part of the atmosphere (Top Of Atmosphere), which is called the brightness temperature (as well as the black body temperature), which is obtained using the Equation 9-11.

$$B_\lambda = \frac{C_1}{\lambda^5 \exp\left(\frac{C_2}{\lambda\times T}\right)-1} \quad (9)$$

$$TB = \left(\frac{1}{Ln\left(\frac{2hc^2\lambda^{-5}}{B_\lambda}+1\right)}\right)\left(\frac{hc}{kh}\right) \quad (10)$$

$$T_s = \frac{T_B}{\sqrt[4]{\varepsilon}} \quad (11)$$

Where, C1 = 1.19104×10^8, C2 = 14387.7, h=6.62×10^{-34}, C = 2.998×10^8, K = 1.38066×10^{-23}, B_λ= Blackbody radiation

3. Results

Hourly meteorological data of synoptic stations in Tehran city were used to calculate the parameters related to temperature extraction. Considering that the time of taking the images is approximately 6:00 a.m. Greenwich time and the time difference between Greenwich and Tehran time is three and a half hours, the data related to 6:00 a.m. (GMT) of Tehran synoptic stations were used. These data include temperature and relative humidity data that were prepared from the Iranian Meteorological Organization. After calculating the temperature by the mentioned methods, their RMS error values were presented as described in the following table (Table 5).

Table 5. Error rate (Celsius) of temperature calculation after conversion to air temperature

	Mono Window	Artis	Stefan_Boltz
TM 2010/6/4	1.56	1.70	1.42
ETM 2002/8/9	2.17	1.81	1.52
TIRS 2015/9/6	2.19	2.16	1.74
TM 2008/6/30	1.43	1.35	1.28
TM 2009/7/19	2.30	2.12	1.98
ETM 2002/10/12	1.50	1.14	1.09
ETM 2001/6/30	1.98	1.93	1.75
ETM 2002/10/12	1.58	1.39	1.26
TM 2010/6/4	1.99	1.72	1.5
TIRS 2015/9/6	1.62	1.39	1.14
ETM 2001/6/03	2.05	1.66	1.59
ETM 2002/8/9	1.52	1.44	1.34
TM 2008/6/30	1.64	1.4	1.35
TM 2009/7/19	2.16	2.09	1.82
MODIS 2009/6/30	1.95	1.65	1.48
MODIS 2009/7/19	2.37	2.25	2.22
MODIS 2015/9/6	2.64	2.49	2.38

4. Discussion

In this research, the methods of single window, Stefan-Boltzman and Landsat Science Office were used in TM, TIRS(OLI), ETM+ images. Then the results were analyzed using statistical methods. The influential parameter in estimating the best value of the earth's surface temperature is the radiation power, which is calculated in the first method through NDVI for each separate image, which is separate and constant in all stages of using the three methods mentioned for each image, and in the second method, the emissivity from The obtained classification method is calculated for each image separately, and for this method, it is separate and fixed in all stages of using the three methods mentioned for each image. Eventually in the third method "MODIS ready products" were used.

The results of all the methods were compared on different dates using the widely used statistical meature of mean absolute error. The results showed that among the methods used, the best method in estimating the temperature of the earth's surface closer to the ground data of air temperature in all three gauges and in three modes of obtaining the amount of emissivity (NDVI method, classification and MODIS ready product) The Stefan-Boltzman method had the best results, so that among the methods used, the values of the average absolute error index for the three single-window methods, Artis and Stefan-Boltzman were 1.877, 1.744 and 1.540 degrees Celsius, respectively. Therefore, it is suggested that for other areas that Use this method if it is close to the study area in terms of weather conditions and other geographical parameters.

5. Conclusion

Considering that temperature is a fleeting and highly variable quantity, the algorithm used to estimate it should be chosen correctly. Also, in addition to the type of algorithm, the emissivity estimation method directly affects the output result. On the other hand, by calculating Sig (significance level) which is considered 0.05 in the t-test, it is more than 5 percent in all methods,

which indicates that the results obtained from our samples is suitable for larger values. In other words, the results can be generalized to other samples. Therefore, it is suggested to use the appropriate method in the areas that have the same conditions as our study area, according to the purpose of the research and the existing conditions.

Acknowledgement

The authors would like to thank the Department of RS and GIS, Kharazmi University, Tehran.

References

Chen, C. (2015). Determining the Leaf Emissivity of Three Crops by Infrared Thermometry. Sensors, 15(5), 11387-1140.https://doi.org/10.3390/s150511387

Deng, X., Gao, F., Liao, S., Liu, Y., & Chen, W. (2023). Spatiotemporal evolution patterns of urban heat island and its relationship with urbanization in Guangdong-Hong Kong-Macao greater bay area of China from 2000 to 2020. Ecological Indicators, 146, 109817. https://doi.org/10.1016/j.ecolind.2022.109817

Guha, S., Govil, H., Dey, A., & Gill, N. (2018). Analytical study of land surface temperature with NDVI and NDBI using Landsat 8 OLI and TIRS data in Florence and Naples city, Italy. European Journal of Remote Sensing, 51(1), 667-678. https://doi.org/10.1080/22797254.2018.1474494

Halder, B., Bandyopadhyay, J., & Banik, P. (2021). Evaluation of the climate change impact on urban heat island based on land surface temperature and geospatial indicators. International Journal of Environmental Research, 15(5), 819-835. https://doi.org/10.1007/s41742-021-00356-8

Hossingholizade, A., Zeaiean, P., & Beyranvand, P. (2021). Comparison of Different Retrieval Temperature algorithms With different Emissivity by Using remote sensing images. Geographic Space, 20(72), 39-56.

Mia, M. B., Nishijima, J., & Fujimitsu, Y. (2014). Exploration and monitoring geothermal activity using Landsat ETM+ images: A case study at Aso volcanic area in Japan. Journal of Volcanology and Geothermal Research, 275, 14-21. https://doi.org/10.1016/j.jvolgeores.2014.02.008

Mullerova, D., & Williams, M. (2019). Satellite monitoring of thermal performance in smart urban designs. Remote Sensing, 11(19), 2244. https://doi.org/10.3390/rs11192244

Orusa, T., & Mondino, E. B. (2019, October). Landsat 8 thermal data to support urban management and planning in the climate change era: A case study in Torino area, NW Italy. In Remote Sensing Technologies and Applications in Urban Environments IV (Vol. 11157, pp. 133-149). SPIE. https://doi.org/10.1117/12.2533110

Ozelkan, E., Bagis, S., Ozelkan, E. C., Ustundag, B. B., Yucel, M., & Ormeci, C. (2015). Spatial interpolation of climatic variables using land surface temperature and modified inverse distance weighting. International Journal of Remote Sensing, 36(4), 1000-1025. https://doi.org/10.1080/01431161.2015.1007248

Perera, T. A. N. T., Nayanajith, T. M. D., Jayasinghe, G. Y., & Premasiri, H. D. S. (2022). Identification of thermal hotspots through heat index determination and urban heat island mitigation using ENVImet numerical micro climate model. Modeling Earth Systems and Environment, 8(1), 209-226. https://doi.org/10.1007/s40808-021-01091-x

Shang, L., & Dick, R. P. (2006). Thermal crisis: challenges and potential solutions. IEEE Potentials, 25(5), 31-35. https://doi.org/10.1109/MP.2006.1692283

Sidiqui, P., Huete, A., & Devadas, R. (2016, July). Spatio-temporal mapping and monitoring of Urban Heat Island patterns over Sydney, Australia using MODIS and Landsat-8. In 2016 4th International Workshop on Earth Observation and Remote Sensing Applications (EORSA) (pp. 217-221). IEEE. https://doi.org/10.1109/EORSA.2016.7552800

Tan, K., Lim, H., MatJafri, M., & Abdullah, K. (2010). Land surface temperature retrieval by using ATCOR3_T and normalized difference vegetation index methods in Penang Island. American Journal of Applied Sciences, 7(5), 717.

Yu, P., Zhao, T., Shi, J., Ran, Y., Jia, L., Ji, D., & Xue, H. (2022). Global spatiotemporally continuous MODIS land surface temperature dataset. Scientific Data, 9(1), 1-15. https://doi.org/10.1038/s41597-022-01214-8

Zhang, J., Wang, Y., & Li, Y. (2006). A C++ program for retrieving land surface temperature from the data of Landsat TM/ETM+ band6. Computers & Geosciences, 32(10), 1796-1805. https://doi.org/10.1016/j.cageo.2006.05.001

6th Intercontinental Geoinformation Days

igd.mersin.edu.tr

Index-based mapping of floating algae blooms observed on Lake Iznik using Landsat-8 imagery

Ismail Colkesen*[1], Muhammed Yusuf Ozturk [1], Osman Yavuz Altuntas [1]

[1]*Gebze Technical University, Engineering Faculty, Department of Geomatics Engineering, Kocaeli, Türkiye*

Keywords
Harmful algal blooms
AMEI
NDWI
Freshwater
Remote sensing

Abstract

As one of the most important members of the freshwater ecosystem, lakes have been under pressure in recent years, mainly due to climate change, population growth and anthropogenic activities, which adversely affect water quality and cause several environmental disasters such as harmful algal blooms. Remote sensing technologies have been widely used for their advantages in monitoring rapid changes in freshwater resources at global and local scales. The main goal of this study is to detect and map the dense floating algae formations observed in Lake Iznik, the largest freshwater source of the Marmara region, in 2022. For this purpose, Automatic Mucilage Extraction Index (AMEI), initially proposed for mucilage detection, and the well-known Normalized Difference Water Index (NDWI) were utilized, and their performances were compared in mapping algal formations using the Landsat-8 image. The results showed that the floating algae formations covered 12.1% (about 36.35 km^2) of Lake Iznik on June 5, 2022. In addition, the high-density algal formations were detected with 99% accuracy, while high- and low-algae formations were detected with 77% accuracy in the AMEI index map produced with appropriate threshold values. As a result, it can be concluded that the AMEI, initially formulated by considering the spectral bands of Sentinel-2, can be easily adapted to Landsat imagery to extract floating algal blooms.

1. Introduction

Lakes are one of the most important members of the inland water ecosystem, playing an essential role in many aspects, such as agricultural activities, biodiversity, and meeting drinking water needs. Pressure on freshwater resources has increased in recent years due to rapid global climate change and impacts from anthropogenic activities, resulting in a significant decline in the surface water quality of the aquatic environment. Pressure on the aquatic environment leads to significant changes in the physicochemical parameters of lakes, resulting in significant environmental problems such as harmful algal blooms (Moss et al. 2011; Zhang et al. 2023).

Remotely sensed images are the most important data source for monitoring water resources and detecting changes over time. Recently, considerable literature has grown around the monitoring and mapping of floating algae formations observed on inland waters using remotely sensed imagery at different spatial and spectral resolutions (Sun et al. 2022; Laneve et al. 2022; Rodríguez-López et al. 2023).

Water indices have been widely used in mapping algae formation using satellite datasets. For example, the Floating Algae Index (FAI) was applied by Hu (2009) to detect floating algae in the open ocean using the Moderate Resolution Imaging Spectroradiometer (MODIS) imagery. Furthermore, Rodríguez-López et al. (2023) investigated Chlorophyll-a concentration in Andean Lake using the FAI and surface algal bloom index (SABI) calculated from multitemporal Landsat imagery. More recently, Colkesen et al. (2023) introduced and applied an Automatic Mucilage Extraction Index (AMEI) for mapping massive mucilage formations observed on the Sea of Marmara using Sentinel-2 imagery.

In this study, the performance of the mucilage-specific AMEI index in mapping floating algal blooms observed intensively in Lake Iznik in June 2022 was analyzed, and its performance was compared with the Normalized Difference Water Index (NDWI), which is commonly used in algae detection. A Landsat-8 satellite image captured on June 5, 2022 was used as the primary

* **Corresponding Author**

*(icolkesen@gtu.edu.tr) ORCID ID 0000 – 0001 – 9670 – 3023
(m.ozturk2020@gtu.edu.tr) ORCID ID 0000 – 0001 – 6459 – 9356
(o.altuntas2022@gtu.edu.trl) ORCID ID 0000-0001-5940-4091

Cite this study

Colkesen, I., Ozturk, M. Y., & Altuntas, O. Y. (2023). Index-based mapping of floating algae blooms observed on Lake Iznik using Landsat-8 imagery. Intercontinental Geoinformation Days (IGD), 6, 309-312, Baku, Azerbaijan

data source in the application, and the results were compared thoroughly.

2. Material and Methods

2.1. Study area and dataset

Lake Iznik, also known as Lake Nicaea, is a freshwater lake located in the Bursa Province of Turkey (Fig 1.) It is characterized by specific physicochemical properties that play a crucial role in its ecosystem dynamics. Oktem et al. (2012) stated that rapid population growth, regional urbanization, and agricultural activities in the basin negatively impact the lake's ecosystem. It was also underlined that the lake shows a eutrophic characteristic due to the large amounts of nitrogen and phosphorus returned to the lake. Yağcı and Ustaoğlu (2012) highlighted that the lake has a mesotrophic-eutrophic character regarding zooplankton and is extremely sensitive to eutrophication. Derin et al. (2013) underlined that the lake has switched from mesotrophic to eutrophic in the past thirty years.

In this study, the Landsat-8 (Collection 2 level-2) image captured on June 5, 2022 was the primary data source for mapping floating algae formations. Seven bands of Landsat-8 at 30 m spatial resolution, consisting of coastal aerosol, blue, green, red, near-infrared (NIR), shortwave infrared-1 (SWIR-1), and shortwave infrared-2 (SWIR-2), were used for index-based extraction of algal formations.

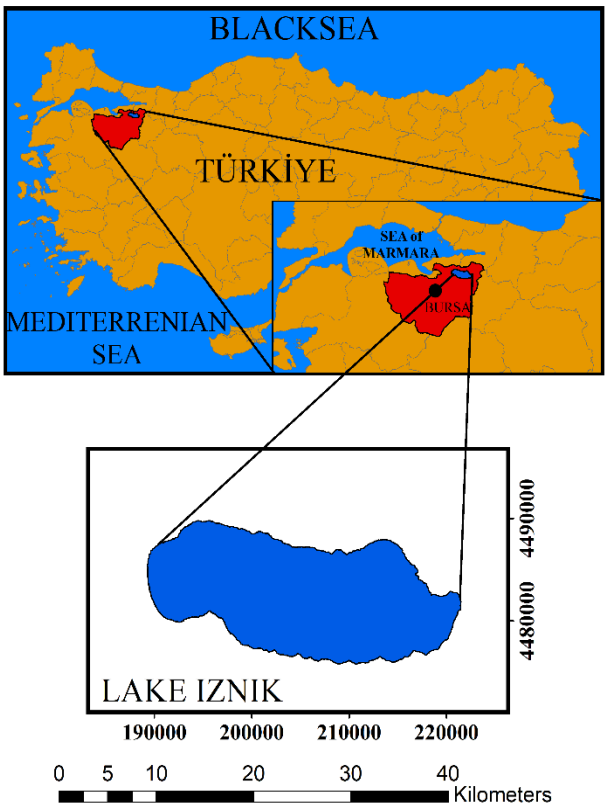

Figure 1. The location of the study area

2.2. Method

Index-based feature extraction methodology based on the utilization of AMEI and NDVI indices was followed to extract floating algal formations observed on the Landsat-8 image dated June 5, 2022. For this purpose, a ground truth dataset consisting of 1500 pixels (i.e., 500 pixels for each class) representing water and algae formations (i.e., high-density and low-density) was selected from the image. The mean spectral curves of these samples are given in Fig. 2 to analyze the spectral characteristics of water and the algae formation observed on the lake surface. As shown in the figure, high-density algal formations could be identified with the NIR band, whereas the difference between the DNs of low-density algae and water pixels was relatively lower in this band. On the other hand, it can be stated that algae and water pixels have similar spectral characteristics in the other bands of the Landsat image (except for the green and red bands). Therefore, it is not easy to distinguish pixels containing low-density algae from water pixels.

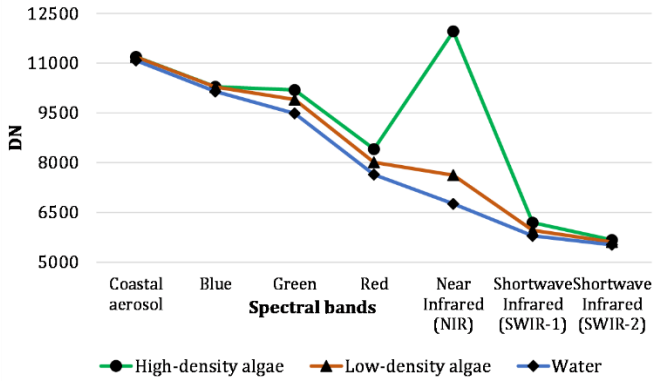

Figure 2. Spectral signatures of algae and water pixels

Considering the above-mentioned spectral features, the AMEI and NDVI indices based on the use of green (B3), red (B4), NIR (B5), and SWIR-1(B6) bands of the Landsat-8 image were used in this study. The basic formulations of the indices are given in Table 1 with references. The AMEI and NDWI indices were calculated to perform an index-based approach and derived grey-level images were used as the primary data sources for mapping algal formations.

Table 1. Formulas of NDWI and AMEI indices used in this study

Index	Formula	Reference
NDWI	$\frac{B5-B6}{B5+B6}$	Gao, 1996
AMEI	$\frac{(2\times B4)+B5-(2\times B6)}{B3+(0.25\times B6)}$	Colkesen et al. 2023

3. Results

In order to achieve the ultimate goal of the study, grey-level AMEI and NDWI index maps were produced. The resulting index maps and the false-colour Landsat image captured on June 5 2022, are given in Fig. 3. As shown in the false-colour image, high- and low-intensity floating algal formations, which appeared in green colour on the image, are mainly located in the middle and northern-east part of the Lake Iznik. Furthermore, cumulus cloud formations are observed in the eastern

and western parts of the lake. On the grey-level index maps, the highest index values indicate a high level of alg concentration, whereas the lowest index values depict a water surface. In addition, it was seen that the effects of cumulus clouds were reduced by applying AMEI and NDWI indices, and algae formations with high- and low-density can be easily identified on the maps.

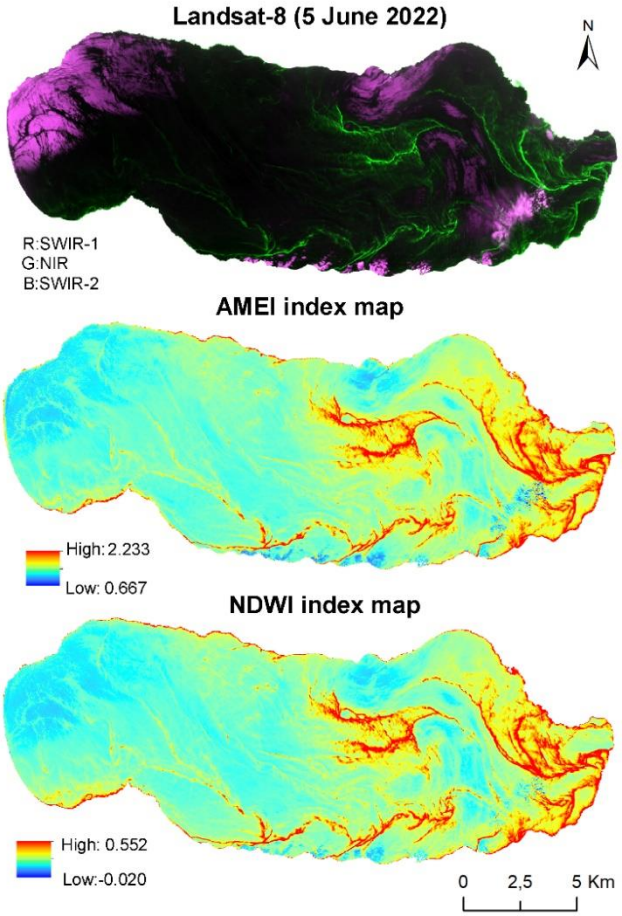

Figure 3. Index maps produced with AMEI and NDWI

The grey-level index maps were classified into two-class using multiple threshold values to investigate the spatial distributions of the algal formations and calculate algae-covered areas on the lake. Based on the natural break thresholding algorithm, four threshold values ensuring appropriate differentiation between algae and water pixels were determined for the AMEI index map, whereas two threshold values were optimal for classifying the NDWI index map. It should be noted that the class defined on the left side of the histogram, consisting of pixels having low index values, was named as water class in both index maps. On the other hand, the remaining classes on the histograms (i.e., three classes on the AMEI histogram and two classes on the NDWI histogram) were merged into one class and named as algae class. The resulting two-class index maps are given in Figure 4. According to the two-class AMEI map, the floating algae formations covered 36.35 km^2 (12.1% of the total area) of Lake Iznik on June 5, 2022. On the other hand, the algae-covered area was calculated as 27.63 km^2 corresponding to 9.21% of the total lake area on the classified NDWI map. The ground truth dataset representing water and floating algae formation was also used to assess the accuracy of the two-class index maps.

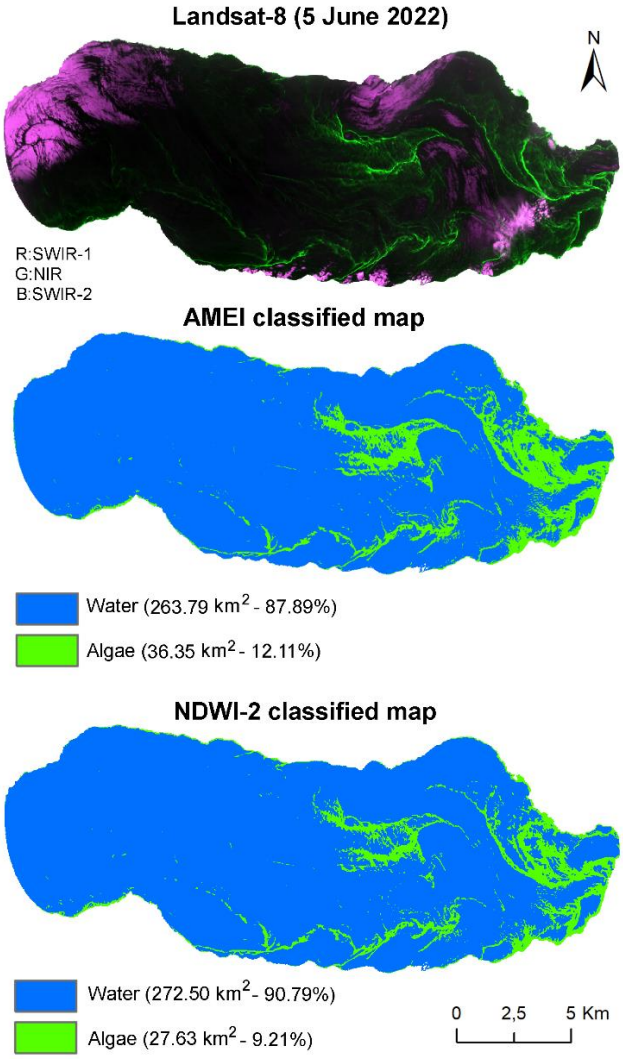

Figure 4. Classified index maps of Lake Iznik representing water and floating algae formations

The overall accuracy (OA) value, derived from the standard confusion matrix, was used as a map accuracy measure. When the accuracy analysis was performed based on water and high-density algae samples, it was seen that the classification accuracies calculated for the AMEI and NDWI maps were 99.9% and 99.5%, respectively. On the other hand, when the accuracy analysis was performed considering the whole algae samples, consisting of high- and low-density algae pixels, it was observed that the classification accuracies decreased significantly and calculated as 76.7% and 69.7% for AMEI and NDWI, respectively. This finding indicates that high-density algae formations can be accurately detected with an index-based approach, while the accuracy is relatively low in distinguishing pixels containing low-density algae formations from water pixels. On the other hand, the mucilage-specific index, AMEI, was superior to the popular NDWI index, especially in extracting low-density floating algal formations.

4. Conclusion

This study evaluated the performance of AMEI and NDWI indices in mapping the algal blooms observed in Iznik Lake with the help of Landsat 8 images. More specifically, the performance of the AMEI index, initially proposed for detecting mucilage-covered areas from Sentinel-2 imagery, was evaluated in terms of the extraction of floating algal blooms and its applicability to Landsat-8 satellite imagery. The results showed the effectiveness of the AMEI index map produced with appropriate threshold values in mapping algal blooms observed in inland waters using Landsat-8 imagery. The estimated map accuracy was 99% for the AMEI map, indicating algae formations covered 12.1% (about 36.35 km^2) of Lake Iznik on June 5, 2022. Results also indicated that distinguishing pixels containing low-density algae from water pixels was challenging due to their spectral similarity. However, it should be noted that the effectiveness of the index should be assessed in different fields and with different data sets.

References

Colkesen, I., Kavzoglu, T., Sefercik, U. G., & Ozturk, M. Y. (2023). Automated mucilage extraction index (AMEI): a novel spectral water index for identifying marine mucilage formations from Sentinel-2 imagery. International Journal of Remote Sensing, 44(1), 105-141, https://doi.org/ 10.1080/01431161.2022.2158049

Derin, Y., Milewski, A., Fryar, A. E., & Schroeder, P. (2013). An integrated approach for understanding anthropogenic and climatic impacts on lakes: a case study from Lake Iznik, Turkey. American Geophysical Union, Fall Meeting 2013, abstract #H31H1320

Gao, B. (1996). NDWI—A Normalized Difference Water Index for Remote Sensing of Vegetation Liquid Water from Space. Remote Sensing of Environment 58(3), 257–266. https://doi.org/10.1016/S0034-4257(96)00067-3.

Hu, C. (2009). A Novel Ocean Color Index to Detect Floating Algae in the Global Oceans. Remote Sensing of Environment 113(10), 2118–2129. https://doi.org/ 10.1016/j.rse.2009.05.012

Laneve, G., Bruno, M., Mukherjee, A., Messineo, V., Giuseppetti, R., De Pace, R., Magurano, F., & D'Ugo, E.. (2022). Remote Sensing Detection of Algal Blooms in a Lake Impacted by Petroleum Hydrocarbons. Remote Sensing 14(1), 121. https://doi.org/10.3390/rs14010121

Moss, B., Kosten, S., Meerhoff, M., Battarbee, R. W., Jeppesen, E., Mazzeo, N., Havens, K., Lacerot, G., Liu, Z., De Meester, L., Paerl, H., & Scheffer, M. (2011). Allied attack: climate change and eutrophication. Inland waters, 1(2), 101-105. https://doi.org/10.5268/IW-1.2.359

Oktem, Y. A., Gumus, M., & Yilmaz, G. B. (2012). The potential sources of pollution affecting the water quality of Lake Iznik. International Journal of Electronics Mechanical and Mechatronics Engineering, 2(3), 225-233.

Rodríguez-López, L., Duran-Llacer, I., Bravo Alvarez, L., Lami, A. & Urrutia, R. (2023). Recovery of Water Quality and Detection of Algal Blooms in Lake Villarrica through Landsat Satellite Images and Monitoring Data. Remote Sensing 15(7), 1929. https://doi.org/10.3390/rs15071929

Sun, Z., Chang, N. B., Chen, C. F., & Gao, W. (2022). Lake Algal Bloom Monitoring via Remote Sensing with Biomimetic and Computational Intelligence. International Journal of Applied Earth Observation and Geoinformation 113, 102991. https://doi.org/ 10.1016/j.jag.2022.102991

Yağci, M. A., & Ustaoğlu, M. R. (2012). Zooplankton fauna of Lake İznik (Bursa, Turkey). Turkish Journal of Zoology, 36(3), 341-350. https://doi.org/10.3906/zoo-1001-36

Zhang, C., Kong, X., Xue, B., Zhao, C., McGowan, S., Lin, Q., Zhang, K., & Shen, J. (2023). Double-edged effects of anthropogenic activities on lake ecological dynamics in northern China: Evidence from palaeolimnology and ecosystem modelling. Freshwater Biology, 68(6), 940-955. https://doi.org/10.1111/fwb.14077

6th Intercontinental Geoinformation Days

igd.mersin.edu.tr

3D modeling of historically significant columns

Abdurahman Yasin Yiğit*[1], Murat Yakar[1], Ali Ulvi[2]

[1]Mersin University, Engineering Faculty, Geomatics Engineering Department, Mersin, Türkiye
[2]Mersin University, Institute of Science, Department of Remote Sensing and Geographic Information Systems, Mersin, Türkiye

Keywords
Photogrammetry
3D model
Column
Cultural heritage

Abstract

The Anatolian region has been home to countless civilizations throughout known history. As can be imagined, this region is also home to various buildings that differ in size and type. There are many essential cities where these structures were built. However, many of the artifacts in these cities have been destroyed due to natural or unnatural causes. Various analyzes can be made by modeling and digitizing the parts of the buildings. Especially the 3D models of the parts of the buildings in the digital environment can provide information about the rest of the building and the urban structure of the city where it is located. In this study, the stunning part of a building was modeled in 3D using the photogrammetric modeling technique. It is thought that this study will be helpful in terms of guiding future studies.

1. Introduction

Anatolia, also formerly known as Asia Minor, has been home to numerous civilizations throughout history, and each has secured its position in history by leaving corresponding traces on this land. This region's fertile lands have witnessed the rise and collapse of many empires, including the Romans, Byzantium, Seljuks, and Ottomans. Due to their geopolitical significance, the cities, which are located in a first-degree seismic zone, have been affected by both natural disasters, such as earthquakes and wildfires, and manufactured disasters. Due to these damages, most of the structures and artifacts from these ancient civilizations have not survived to the present day. Those who have made it to the present day are protected through restoration. Most of Amasya's extant structures date back to the Seljuk and Ottoman empires. Religious and civil architectural structures, such as bridges, inns, hammams, mosques, madrasas, mansions, and clock towers, remain from these eras. Preserving these historical structures for future generations is of the utmost importance. Even though factors such as war do not exist in the region, the city is still susceptible to earthquakes. Similarly, to other types of structures in the region, earthquakes pose the highest threat to such structures. Therefore, it is essential to identify historical and valuable structures susceptible to these factors and take the necessary precautions.

The photogrammetry technique, an excellent alternative to traditional methods in documenting cultural heritage, can take photographs of the object and create a 3D model with the help of specific mathematical models. Ulvi et al. (2019) conducted a study on modeling historical fountains using close-range photogrammetry. Yakar and Dogan (2018) examined the use of the SfM method in different fields of study and reported consistent results in archaeological areas. Nowadays, due to the relatively cheap and portable nature of digital handheld cameras, terrestrial photogrammetry is frequently used in archaeological areas (Ulvi et al., 2019). Digital handheld cameras used in terrestrial photogrammetry can be calibrated before and during the mission and store the necessary information for 3D modeling. In this way, 3D models can be obtained with calibrated cameras. Using motion-based structural sensing (SfM), a 3D model of the object can be created using superimposed photographs. Nowadays, with the development of photogrammetry and computer vision disciplines, image-based modeling techniques have become a serious competitor to laser scanning

* **Corresponding Author**

*(ayasinyigit@edu.tr) ORCID ID 0000-0002-9407-8022
(myakar@mersin.edu.tr) ORCID ID 0000-0002-2664-6251
(aliulvi@mersin.edu.tr) ORCID ID 0000-0003-3005-8011

Cite this study

Yiğit, A. Y., Yakar, M., & Ulvi, A. (2023). 3D modeling of historically significant columns. Intercontinental Geoinformation Days (IGD), 6, 313-316, Baku, Azerbaijan

(Remondino et al., 2011). Some crucial advantages of image-based modeling are its low cost and include color information, calibrated or uncalibrated cameras are acceptable (Colomina et a., 2008), and it can produce a denser point cloud than a laser scanner. This is where the SfM approach, different from classical photogrammetry, is widely used (Polat et al., 2020). SfM works under the same primary conditions as Photogrammetry. Overlapping images are used to obtain the 3D structure of the object of interest. Much commercial software, such as Agisoft Photoscan, is also widely used for 3D modeling. In general, photo matching allows the production of many products, such as sparse and dense point clouds, three-dimensional models, digital elevation models, and orthophotos. Image processing steps can take considerable time. For this reason, it is recommended to use exceptionally high-performance computers to produce a full-performance 3D model (Siebert & Teizer, 2014). In this study, a column fragment of a historical building was 3D documented using photogrammetric techniques.

2. Method

Using stereo vision principles, photogrammetry as a mapping technique attempts to convert two-dimensional images into three-dimensional coordinates (Alptekin and Yakar, 2021). While such concepts were initially implemented empirically, as with analog photogrammetry, mathematical relations were quickly devised to facilitate an analytical approach to the 3D reconstruction problem. The collinearity and coplanarity conditions were crucial in establishing a relationship between 2D and 3D space (Alptekin & Yakar, 2020). Photogrammetry has focused on the issue of precision for the majority of its history and continues to do so today. This is consistent with photogrammetry's original remote sensing mapping instrument purpose. The prevalence of Structure-from-Motion as a solution to image pose estimation (Karataş et al., 2022a) demonstrates that significant advances were made almost simultaneously in computer vision. This advancement, along with other advancements in imaging sensors and computational technologies, facilitated the unprecedented automation of the traditional photogrammetric workflow, albeit occasionally at the expense of stringent quality control (Kuşak et al., 2021; Ünel et al., 2020). Image matching algorithms reduce the need for manual measurements, such as the conventional six Von Grüber points (Yılmaz & Yakar, 2006).

Bundle adjustment refers to the simultaneous computation of image exterior orientation parameters (also known as extrinsic parameters in computer vision (Karataş et a., 2022b) and point coordinates in the 3D space. It evolved from previous solutions for the problem of aero triangulation, i.e., the densification of ground controls (Yılmaz & Yakar, 2006) in analytical photogrammetry. Typically, it requires a nonlinear optimization calculation based on collinearity or coplanarity equations. This simultaneous "block" modification of the entire system offers a rigorous solution to the exterior orientation issue (Kanun et al., 2021a). In a process known as self or auto-calibration (Kanun et al., 2021b), the bundle adjustment may also comprise the resolution of the camera's internal parameters. In addition, modern bundle adjustment solutions may employ attenuation techniques (e.g., the Levenberg–Marquardt algorithm) to aid the classical Gauss–Newton least-squares method in achieving final convergence (Karataş et al., 2022c). This is the case, for instance, with the Agisoft Metashape software utilized in this investigation.

The invention of dense image matching was an additional significant advance in photogrammetry. Patch-based Multi-View Stereo (PMVS) and Semi-Global Matching (Yakar et al., 2015) may be two of the most significant advances. Dense image matching is a crucial development for photogrammetry, as it generates dense point clouds comparable to those produced by lidar. This enables photogrammetry to compete with lidar systems, although, in practice, they are frequently complementary, particularly for large-scale applications. There are numerous commercial and open-source photogrammetric solutions available on the market today. A traditional photogrammetric workflow begins with image acquisition. Certain principles must be followed to ensure excellent photogrammetric results, such as sufficient image overlap, image network configuration, and photographic quality. Before proceeding with dense image matching in order to generate dense point clouds, image orientation with bundle adjustment is typically conducted. However, these point clouds represent the object in question primarily from a geometric standpoint.

2.1. Material and Method

In the study, a mobile phone camera was used for photogrammetric photography. The sfM algorithm and photogrammetry technique were used to produce 3D models. 3D models were produced in Agisoft Metashape software.

The technical specifications of the phone camera used are given in Table 1.

Table 1. Samsung M31 technique specification

Parameters	Value
Focal Lenght	35 mm
Aperture	F 2.0
Camera Resolution	32 MP

The representation of the photogrammetric picture attraction centers of the object is given in Figure 1.

Photogrammetry is a method in which a 3-dimensional geometric model is created through photographs, allowing us to measure these models. The photogrammetry technique is frequently used when measuring environments. The principle we take as a basis in the photogrammetry technique is to pay attention to the photographs of a point taken from at least two different angles. This technique is used in many areas, including indoors and outdoors. It should be said that the photogrammetry technique has a wide application area. In many fields, such as architecture and engineering, 3D measurements can be made with the photogrammetry technique and photorealistic models of spaces and objects with this method. Photogrammetry,

which has become an important technique, especially in the measurement of open areas, is a technique that is valid for many different sectors. The best use of this technique is the most critical factor in increasing the accuracy of the measurements. Agisoft Metashape produces reliable solutions with years of experience in photogrammetry. Agisoft Metashape, which performs photorealistic, coordinated 3D model analysis using photogrammetry and high-resolution photographs, is among the software experts in its field. It is a method in which we produce photorealistic 3D models by photographing the structure or object to be modeled. We can throw these models into virtual and augmented reality environments.

As a result of the photogrammetry study, the 3D point cloud data of the object is obtained. A 3-dimensional point set where you can examine all the details of the object is given in Figure 2. The 3D model of the object is given in Figure 3.

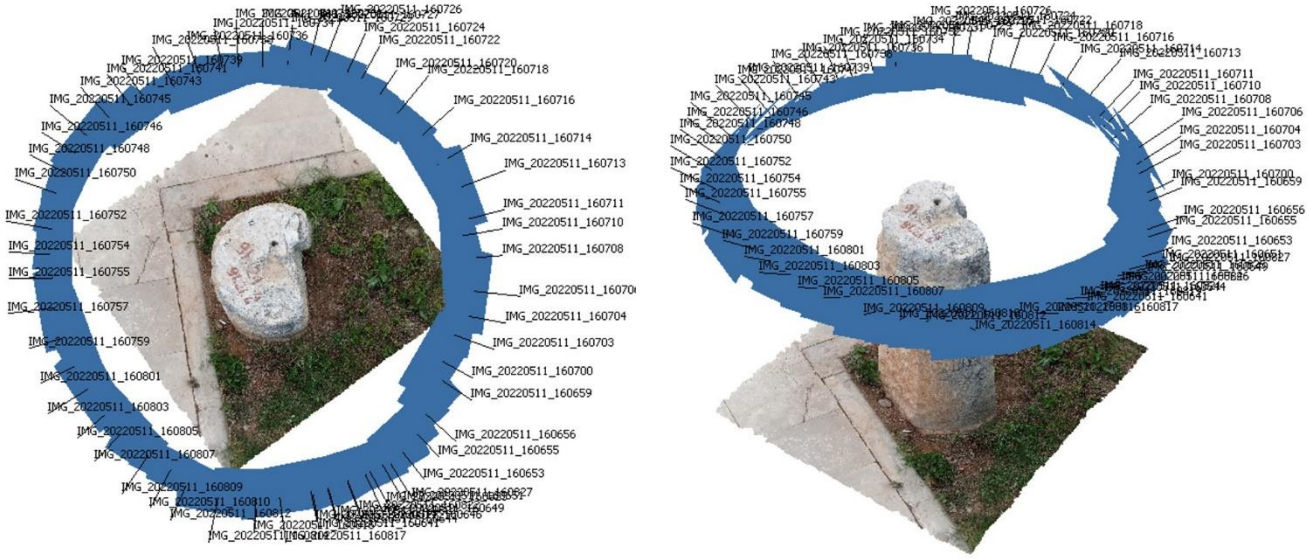

Figure 1. Photogrammetric photography method and camera positions based on the SfM algorithm

Figure 2. Point Cloud of object

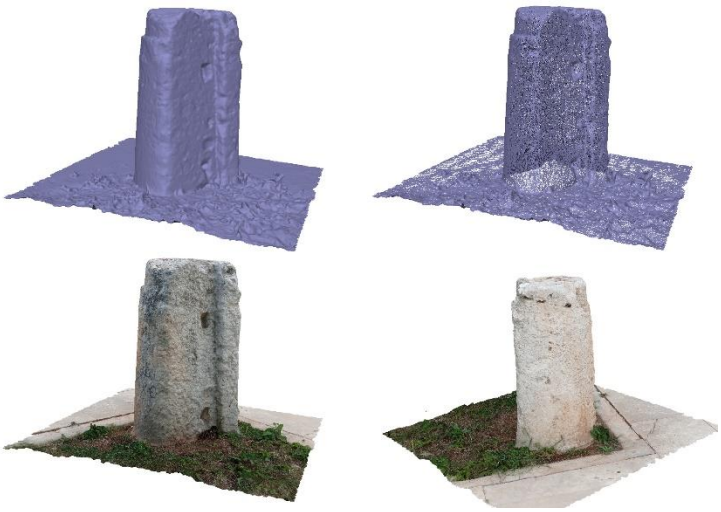

Figure 3. 3D model of the object. Top left Solid model, Top suitable wireframe model, bottom 3D model (different angle).

3. Discussion and Conclusion

In order to transfer cultural heritages to future generations, they need to be protected from natural and artificial dangers, but these dangers cannot be avoided altogether. For this reason, it is necessary to document not only the external and internal structure of the cultural heritage but also the entire historical texture, including the broken parts, for the repair and reconstruction of the damaged structures. This study has tried to document a column fragment broken off from a historical artifact using digital photogrammetry tools. In the study, the point cloud and 3D model of the column piece were produced by photogrammetric methods. The modeling process was done by taking terrestrial photographs. As a result of the study, more than 5 million points were produced by terrestrial photogrammetry. Documentation of archaeological artifacts is essential because of their reaching future generations and the restoration work that can be done on them. Documented archaeological artifacts will also shed light on future generations.

References

Alptekin, A., & Yakar, M. (2020). Determination of pond volume using an uncrewed aerial vehicle. Mersin photogrammetry journal, 2(2), 59-63.

Alptekin, A., & Yakar, M. (2021). 3D model of Üçayak Ruins obtained from point clouds. Mersin Photogrammetry Journal, 3(2), 37-40.

Colomina, I., Blázquez, M., Molina, P., Parés, M. E. & Wis, M. (2008). Towards a New Paradigm for HighResolution Low-Cost Photogrammetry and Remote Sensing. IAPRS&SIS, 1201-1206.

Kanun, E., Alptekin, A., & Yakar, M. (2021a). Cultural heritage modeling using UAV photogrammetric methods: a Kanlıdivane archeological site case study. Advanced UAV, 1(1), 24-33.

Kanun, E., Metin, A., & Yakar, M. (2021b). Yersel Lazer Tarama Tekniği Kullanarak Ağzıkara Han'ın 3 Boyutlu Nokta Bulutunun Elde Edilmesi. Türkiye Lidar Dergisi, 3(2), 58-64.

Karataş, L., Alptekin, A., & Yakar, M. (2022a). Creating Architectural Surveys of Traditional Buildings with the Help of Terrestrial Laser Scanning Method (TLS) and Orthophotos: Historical Diyarbakır Sur Mansion. Advanced LiDAR, 2(2), 54-63.

Karataş, L., Alptekin, A., Kanun, E., & Yakar, M. (2022b). Tarihi kârgir yapılarda taş malzeme bozulmalarının İHA fotogrametrisi kullanarak tespiti ve belgelenmesi: Mersin Kanlıdivane ören yeri vaka çalışması. İçel Dergisi, 2(2), 41-49.

Karataş, L., Alptekin, A., Karabacak, A., & Yakar, M. (2022c). Detection and documentation of stone material deterioration in historical masonry buildings using UAV photogrammetry: A case study of Mersin Sarisih Inn. Mersin Photogrammetry Journal, 4(2), 53-61.

Kusak, L., Unel, F. B., Alptekin, A., Celik, M. O., & Yakar, M. (2021). Apriori association rule and K-means clustering algorithms for interpreting pre-event landslide areas and inventory mapping. Open Geosciences, 13(1), 1226-1244.

Polat, N., Önal, M., Ernst, F. B., Şenol, H. İ., Memduhoğlu, A., Mutlu, S., Mutlu, S. İ., Budan, M. A., Turgut, M. & Kara, H. (2020). Harran Ören Yeri Arkeolojik Kazı Alanınından Çıkarılan Bazı Küçük Arkeolojik Buluntuların Fotogrametrik Olarak 3B Modellenmesi. Türkiye Fotogrametri Dergisi, 2 (2), 55-59.

Remondino, F., Barazzetti, L., Nex, F., Scaioni, M. & Sarazzi, D. (2011). UAV Photogrammetry for Mapping and 3D Modeling Current Status and Future Perspectives. ISPRS ICWG I/V UAV-g Conference, Zurich, Switzerland.

Siebert, S.& Teizer, J. (2014). Mobile 3D Mapping for Surveying Earthwork Projects Using an Unmanned

Ulvi, A., Varol, F., & Yiğit, A. Y. (2019). 3D modeling of cultural heritage: the example of Muyi Mubarak Mosque in Uzbekistan (Hz. Osman's Mushafi). International Congress on Cultural Heritage and Tourism (ICCHT), 115-123, Bishkek, Kyrgyzstan.

Ulvi, A., Yiğit, A. Y. & Yakar, M. (2019). Modeling of Historical Fountains by Using Close-Range Photogrammetric Techniques. Mersin Photogrammetry Journal, 1(1), 1-6.

Unal, M., Yakar, M., & Yildiz, F. (2004, July). Discontinuity surface roughness measurement techniques and the evaluation of digital photogrammetric method. In *Proceedings of the 20th international congress for photogrammetry and remote sensing, ISPRS* (Vol. 1103, p. 1108).

Ünel, F. B., Kuşak, L., Çelik, M., Alptekin, A., & Yakar, M. (2020). Kıyı çizgisinin belirlenerek mülkiyet durumunun incelenmesi. Türkiye Arazi Yönetimi Dergisi, 2(1), 33-40.

Yakar, M. & Dogan, Y. (2018). 3D Reconstruction of Residential Areas with SfM Photogrammetry. In Conference of the Arabian Journal of Geosciences, 73-75.

Yakar, M., & Doğan, Y. (2017). Uzuncaburç Antik Kentinin İHA Kullanılarak Eğik Fotogrametri Yöntemiyle Üç Boyutlu Modellenmesi. 16. Türkiye Harita Bilimsel ve Teknik Kurultayı. TMMOB Harita ve Kadastro Mühendisleri Odası, Ankara.

Yakar, M., Orhan, O., Ulvi, A., Yiğit, A. Y., & Yüzer, M. M. (2015). Sahip Ata Külliyesi Rölöve Örneği. *TMMOB Harita ve Kadastro Mühendisleri Odası*, *10*.

Yakar, M., Toprak, A. S., Ulvi, A., & Uysal, M. (2015). KONYA BEYŞEHİR BEZARİYE HANININ (BEDESTEN) İHA İLE FOTOGRAMETRİK TEKNİK KULLANILARAK ÜÇ BOYUTLU MODELLENMESİ. Türkiye Harita Bilimsel ve Teknik Kurultayı, 25, 28.

Yakar, M., Yılmaz, H. M., & Mutluoglu, O. (2014). Performance of photogrammetric and terrestrial laser scanning methods in volume computing of excavation and filling areas. Arabian Journal for Science and Engineering, 39, 387-394. https://doi.org/10.1007/s13369-013-0853-1

Yilmaz, H. M., & Yakar, M. (2006a). Lidar (Light Detection and Ranging) Tarama Sistemi. Yapı Teknolojileri Elektronik Dergisi, 2(2), 23-33.

Yilmaz, H. M., & Yakar, M. (2006b). Yersel lazer tarama Teknolojisi. Yapı teknolojileri Elektronik dergisi, 2(2), 43-48.

6th Intercontinental Geoinformation Days

igd.mersin.edu.tr

Modeling of ancient period Sarcophagus with close-range photogrammetry

Ali Ulvi*[1], Abdurahman Yasin Yiğit [2], Murat Yakar [2]

[1]*Mersin University, Department of Remote Sensing and Geographic Information Systems, Institute of Science, Mersin, Türkiye*
[2] *Mersin University, Engineering Faculty, Geomatics Engineering Department, Mersin, Türkiye*

Keywords
Close Range
Photogrammetry
3D Model
Sarcophagus

Abstract

Throughout history, Anatolia has been home to numerous societies with diverse customs. Every civilization has left behind too many cultural artifacts from its era to count after withdrawing from the historical arena. This heritage includes knowledge that dates back hundreds or even thousands of years. To be passed on to other generations, this heritage must be preserved. Technological ones have replaced traditional techniques of protection. Registering the work is the first step in the conservation and documentation process. The photogrammetric approach is one of the methods used today to recognize and capture the 3D model of the work without physically touching it. Actual texture can be applied to images using the photogrammetric approach, and a 3D model of the piece can be created. In this project, a 3D model of a Roman-era sarcophagus was created using photogrammetric methods. The Samsung M31 mobile phone camera was used to take pictures. By analyzing these data in Agisoft software, a 3D model of the sarcophagus was created with a dense point cloud with 0.3 mm spacing and an average position accuracy of 2.18 cm over the pairs of pictures. As a result of the study, using photogrammetric techniques in conservation and documentation studies to protect historical and cultural heritage and transfer it to the next generations has provided a significant advantage in terms of accuracy, speed, and cost.

1. Introduction

Türkiye is situated where three continents converge. As a result, the nation serves as a natural link between the three continents. Because of this benefit, it has become the intersection of significant roadways throughout history and into the present. This characteristic has led to significant civilizations in these countries (Yilmaz & Yakar, 2006a; 2006b; Alptekin & Yakar, 2020; 2021). We have acquired a variety of artifacts from several cultures that once flourished in Anatolia and left behind rich civilizational legacies (Alyilmaz et al., 2010; Yilmaz et al., 2007). The preservation of historical monuments or sites necessitates the creation of the initial technical papers of these works or fields and the coordinating of the relevant plans and research.

It will be feasible to quickly access all the information needed for any work that needs to be done on historical relics or locations using these documents. For work in the architectural fields, terrestrial photogrammetry offers several advantages that traditional approaches cannot swiftly and affordably supply (Yakar et al., 2014; Kanun et al., 2021a, b; Kuşak et al., 2021).

These benefits include:

-offering a high-quality graphical database;

-giving multidisciplinary research an essential tool and data sharing;

-making information easier to access and keep up with;

-Reduces costs because the information gathered throughout the preservation, restoration, and documentation process will be used in the future.

Documenting a historical relic has several advantages, such as:

-It has been noted that the work's physical description can be provided, the destruction's present state is disclosed, and it is possible to assess the building's current uses, Survey sample data will be gathered for architectural research; in rehabilitation efforts, a base is formed. It can be processed digitally for various purposes working in this industry. It serves as a model for scientists. With technology, new methods for

* **Corresponding Author**

*(aliulvi@mersin.edu.tr) ORCID ID 0000-0003-3005-8011
(ayasinyigit@mersin.edu.tr) ORCID ID 0000-0002-9407-8022
(myakar@mersin.edu.tr) ORCID ID 0000-0002-2664-6251

Cite this study

Ulvi, A., Yiğit, A. Y., & Yakar, M. (2023). Modeling of ancient period Sarcophagus with close-range photogrammetry. Intercontinental Geoinformation Days (IGD), 6, 317-320, Baku, Azerbaijan

accurately documenting cultural heritage have emerged due to research on the subject. For this reason, the first step before beginning the work to be done in line with the goal is the documentation of historical objects. In this regard, photogrammetric techniques have been employed in the literature to chronicle a variety of cultural heritages. According to Arca et al. (2011), surveys of several structures in the historic city of Safranbolu that were chosen based on their characteristics were prepared using terrestrial photogrammetry technology, and 3D models of these buildings were created. The pros and cons of several data-gathering techniques, including tachometer, photogrammetry, and terrestrial laser scanning, which are typically chosen in cultural heritage documentation projects, were covered by Grussenmeyer et al. (2008). The photogrammetry technique is suggested by Arias et al. (2005) as a preventive method that enables the detection, measurement, and monitoring of the temporal variation of some structural problems about a group of monuments belonging to the Spanish historical heritage, as well as the assessment of the level of material preservation.

Through the use of photogrammetry, volumetric data describing surface structures can be derived from parallax, or the variation in an object's apparent position as a result of the changing perspective offered by overlapping photos taken from various angles (Yakar, 2011; Karataş et al., 2022a). Structure-from-motion (SfM) photogrammetry implements and expedites the digital photogrammetric procedure using advancements in computer vision techniques. Because of this, SfM photogrammetry can employ unregistered image sets from consumer cameras that are not calibrated, but users must be aware of how camera settings might affect the quality of the data and products they produce (O'Connor et al., 2017). Prior to recently, institutions and organizations having access to expensive technology (such as laser scanners on piloted planes) frequently collected and provided topographic point cloud data to science consumers, and raw data required vital computers for data processing (Yakar & Doğan, 2018; Karataş et al., 2022b). Some users cannot access this data due to logistical requirements (Westoby et al., 2012). Contrarily, the development of SfM photogrammetry as a low-cost measurement instrument offered a more open method for scientists to gather and analyze their point cloud data (Karataş et al., 2022c). As a result, SfM photogrammetry is now recognized as a critical method of data gathering and analysis within the earth and environmental sciences. Scientists are now becoming data providers due to a shift in the geographical research paradigm (Garrett and Anderson, 2018); Consumer-grade cameras can be used to gather data, which can then be processed using SfM techniques to address various environmental science queries.

2. Material and Methods

In photogrammetry, the overlapping photos' camera locations and external orientation parameters are used to calculate the 3D coordinates of points on an object's surface. If there are at least three control points between the overlapping images, external orientation parameters can be determined. Internal orientation parameters must be known beforehand. However, the self-calibration technique does away with this requirement thanks to modern algorithms like Structure from Motion (SfM). The SfM algorithm-based photogrammetric software has made it incredibly simple to create 3D models from images taken with standard cameras and recreate surfaces (Ulvi et al., 2017; 2019). SfM is a photogrammetric approach or algorithm that automatically resolves the scene's geometry, camera positions, and orientation without the need to define a target mesh with predetermined 3D positions (Unal et al., 2014; Ünel et al., 2020). SfM is a measurement approach based on computer visualization techniques. It has grown in popularity because of the widespread usage of digital cameras, video cameras, and cell phones with cameras in this field (Uysal et al., 2013; Yakar et al., 2005; 2015). Due to its low cost, rapid results, and simple 3D measurement, its application in scientific studies has grown widely and has had a transformative impact on earth science research. The SfM technique builds 3D structures out of a series of overlapping photo frames. It functions by matching and identifying similarities among a collection of overlapping photographs. In this investigation, close-range photogrammetry techniques were used to record a sarcophagus of historical significance. A 32-megapixel smartphone camera captured 41 photographs (Table 1). When taking photos, the photogrammetric picture-shooting technique was considered (Figure 1). Agisoft Meteshape software created the monument's 3D model (Figure 2).

Table 1. Samsung M31 technique specification

Parameters	Value
Focal Lenght	35 mm
Aperture	F 2.0
Camera Resolution	32 MP

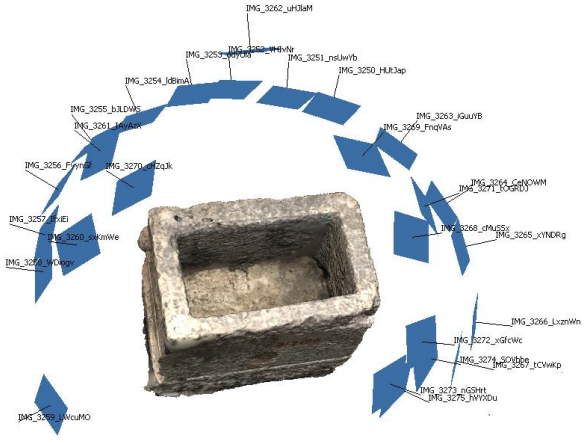

Figure 1. Photogrammetric picture-taking technique

The accuracy of the work on the 3D model has been checked. Control was made over the width and length of the sarcophagus. In reality, the width is 1,25 cm, and the height is 2,40 cm. In the control made on the model, the width is 1,25 cm, and the height is 2.38 cm. The difference of 2 cm height is the absence of sharp detail on the model to be measured. It is because the corner point is broken.

Figure 2. The 3D model obtained in Agisoft software

Figure 3. Controlling the dimensions of the 3D model

3. Conclusion

With the advancement of computer software and technology, it is now much simpler to make digital models of historical and cultural heritage buildings and use them to predict the behavior of complicated structures using 3D modeling. Since 3D models include a wealth of structural information, they are widely employed in documentation studies. The photogrammetry technique produces 3D models that are accurate in terms of appearance and size. Systems for photogrammetric measurement make it possible to model an item and determine its actual geometry. Additionally, because they are created from the actual image of the object, these technologies enable 3D models to contain accurate images.

References

Alptekin, A., & Yakar, M. (2020). Determination of pond volume using an uncrewed aerial vehicle. Mersin photogrammetry journal, 2(2), 59-63.

Alptekin, A., & Yakar, M. (2021). 3D model of Üçayak Ruins obtained from point clouds. Mersin Photogrammetry Journal, 3(2), 37-40.

Alyılmaz, C., Alyılmaz., S., & Yakar, M. (2010). Measurement of petroglyhps (rock of arts) of Qobustan with close range photogrammetry. International Archives of Photogrammetry, Remote Sensing and Spatial Information Sciences, 38(Part 5), 29-32.

Arca, D., Bayık, Ç., Acar, H., Alkan, M., ve Şeker, D.Z. (2011). Safranbolu Tarihi Kenti Örneğinde Dökümantasyon Çalışmalarında Fotogrametri Ve Cbs'nin Birlikte Kullanımı. TMMOB Harita ve Kadastro Mühendisleri Odası 13. Türkiye Harita Bilimsel ve Teknik Kurultayı 18-22 Nisan, Ankara.

Arias, P., Herráez, J., Lorenzo, H., ve Ordóñez, C. (2005). Control of Structural Problems in Cultural Heritage Monuments Using CloseRange Photogrammetry and Computer Methods Control of Structural Problems in Cultural Heritage Monuments Using Close-Range Photogrammetry and Computer Methods. Computers and Structures, 83(21–22), 1754-1766

Garrett B and Anderson K (2018) Drone methodologies: Taking flight in human and physical geography. Transactions of the Institute of British Geographers 43, 341–359

Grussenmeyer, P., Landes, T., Voegtle, T., ve Ringle, K. (2008). Comparison Methods of Terrestrial Laser

Scanning, Photogrammetry and Tacheometry Data for Recordıng of Cultural Heritage Buildings. The International Archives of the Photogrammetry, Remote Sensing and Spatial Information Sciences. Vol. XXXVII. Part B5. Beijing.

Kanun, E., Alptekin, A., & Yakar, M. (2021a). Cultural heritage modelling using UAV photogrammetric methods: a case study of Kanlıdivane archeological site. Advanced UAV, 1(1), 24-33.

Kanun, E., Metin, A., & Yakar, M. (2021b). Yersel Lazer Tarama Tekniği Kullanarak Ağzıkara Han'ın 3 Boyutlu Nokta Bulutunun Elde Edilmesi. Türkiye Lidar Dergisi, 3(2), 58-64.

Karataş, L., Alptekin, A., & Yakar, M. (2022a). Creating Architectural Surveys of Traditional Buildings with the Help of Terrestrial Laser Scanning Method (TLS) and Orthophotos: Historical Diyarbakır Sur Mansion. Advanced LiDAR, 2(2), 54-63.

Karataş, L., Alptekin, A., Kanun, E., & Yakar, M. (2022b). Tarihi kârgir yapılarda taş malzeme bozulmalarının İHA fotogrametrisi kullanarak tespiti ve belgelenmesi: Mersin Kanlıdivane ören yeri vaka çalışması. İçel Dergisi, 2(2), 41-49.

Karataş, L., Alptekin, A., Karabacak, A., & Yakar, M. (2022c). Detection and documentation of stone material deterioration in historical masonry buildings using UAV photogrammetry: A case study of Mersin Sarisih Inn. Mersin Photogrammetry Journal, 4(2), 53-61.

Korumaz, A. G., Dülgerler, O. N., & Yakar, M. (2011). Kültürel mirasin belgelenmesinde dijital yaklaşimlar. Selçuk Üniversitesi Mühendislik, Bilim ve Teknoloji Dergisi, 26(3), 67-83.

Kusak, L., Unel, F. B., Alptekin, A., Celik, M. O., & Yakar, M. (2021). Apriori association rule and K-means clustering algorithms for interpretation of pre-event landslide areas and landslide inventory mapping. Open Geosciences, 13(1), 1226-1244.

O'Connor J, Smith MJ and James MR (2017) Cameras and settings for aerial surveys in the geosciences: Optimising image data. Progress in Physical Geography: Earth and Environment, 41, 325–344.

Ulvi, A., Yakar, M., Alyilmaz, C., & Alyilmaz, S. (2017). Using the close range photogrammetry technique in 3-dimensional work: History of obrukhan sample. International Multidisciplinary Scientific GeoConference: SGEM, 17, 347-355.

Ulvi, A., Yiğit, A. Y. & Yakar, M. (2019). Modeling of Historical Fountains by Using Close-Range Photogrammetric Techniques. Mersin Photogrammetry Journal, 1(1), 1-6.

Unal, M., Yakar, M., & Yildiz, F. (2004, July). Discontinuity surface roughness measurement techniques and the evaluation of digital photogrammetric method. In Proceedings of the 20th international congress for photogrammetry and remote sensing, ISPRS (Vol. 1103, p. 1108).

Ünel, F. B., Kuşak, L., Çelik, M., Alptekin, A., & Yakar, M. (2020). Kıyı çizgisinin belirlenerek mülkiyet durumunun incelenmesi. Türkiye Arazi Yönetimi Dergisi, 2(1), 33-40.

Uysal, M., Polat, N., Toprak, A. S., & Yakar, M. (2013). 3D modeling of historical doger caravansaries by digital photogrammetry.

Westoby MJ, Brasington J, Glasser NF, et al. (2012) 'Structure-from-Motion' photogrammetry: A low-cost, effective tool for geoscience applications. Geomorphology 179: 300–314.

Yakar, M. & Dogan, Y. (2018). 3D Reconstruction of Residential Areas with SfM Photogrammetry. In Conference of the Arabian Journal of Geosciences, 73-75.

Yakar, M. (2011). Using close range photogrammetry to measure the position of inaccessible geological features. Experimental Techniques, 35, 54-59.

Yakar, M., & Doğan, Y. (2017). Mersin Silifke Mezgit Kale Anıt Mezarı fotogrametrik rölöve alımı ve üç boyutlu modelleme çalışması. Geomatik, 2(1), 11-17.

Yakar, M., & Doğan, Y. (2017). Uzuncaburç Antik Kentinin İHA Kullanılarak Eğik Fotogrametri Yöntemiyle Üç Boyutlu Modellenmesi. 16. Türkiye Harita Bilimsel ve Teknik Kurultayı. TMMOB Harita ve Kadastro Mühendisleri Odası, Ankara.

Yakar, M., & Kocaman, E. (2018). Kayseri-Sahabiye Medresesi 3-boyutlu modelleme çalışması ve animasyonu. International Journal of Engineering Research and Development, 10(1), 133-138

Yakar, M., Karabörk, H., Yılmaz, H.,M. (2000). Yersel Fotogrametrinin Kullanım Alanları. Niğde Üniversitesi Mühendislik Bilimleri Dergisi, 4, (1), 18-28.

Yakar, M., Orhan, O., Ulvi, A., Yiğit, A. Y., & Yüzer, M. M. (2015). Sahip Ata Külliyesi Rölöve Örneği. TMMOB Harita ve Kadastro Mühendisleri Odası, 10.

Yakar, M., Toprak, A. S., Ulvi, A., & Uysal, M. (2015). Konya Beyşehir Bezariye Haninin (Bedesten) İHA ile fotogrametrik teknik kullanilarak üç boyutlu modellenmesi. Türkiye Harita Bilimsel ve Teknik Kurultayı, 25, 28.

Yakar, M., Yıldız, F., & Yılmaz, H. M. (2005). Tarihi ve Kültürel Miraslarin Belgelenmesinde Jeodezi Fotogrametri Mühendislerinin Rolü. TMMOB Harita ve Kadastro Mühendisleri Odası, 10.

Yakar, M., Yılmaz, H. M., & Mutluoglu, O. (2014). Performance of photogrammetric and terrestrial laser scanning methods in volume computing of excavation and filling areas. Arabian Journal for Science and Engineering, 39, 387-394. https://doi.org/10.1007/s13369-013-0853-1

Yilmaz, H. M., & Yakar, M. (2006a). Lidar (Light Detection and Ranging) Tarama Sistemi. Yapı Teknolojileri Elektronik Dergisi, 2(2), 23-33.

Yilmaz, H. M., & Yakar, M. (2006b). Yersel lazer tarama Teknolojisi. Yapı teknolojileri Elektronik dergisi, 2(2), 43-48.

Yilmaz, H. M., Yakar, M., Gulec, S. A., & Dulgerler, O. N. (2007). Importance of digital close-range photogrammetry in documentation of cultural heritage. Journal of Cultural Heritage, 8(4), 428-433.

6th Intercontinental Geoinformation Days

igd.mersin.edu.tr

Comparing conventional and photogrammetric methods for volume calculation of stone piles: A case study in the Karacadağ Region

Cömert Oso*[1], Hasan Lafci [1], Nizar Polat [3]

[1]*Harran University, Faculty of Engineering, Department of Geomatics Engineering, Şanlıurfa, Türkiye*

Keywords
GPS
UAV
Photogrammetry
DEM
Agisoft

Abstract

Several years ago, the erupting Karacadağ volcano spread basalt stones across the Karacadağ region, causing difficulties for farmers engaged in agricultural activities in the area. This situation led to the State Hydraulic Works aiming to provide access to each parcel of land in some villages through land consolidation efforts. During the road opening process, the stones that formed were piled up in a specific area. However, the volume calculation of this stone pile is performed using a dangerous conventional method, namely the collection of GPS points by surveyors. In this study, volume calculations were conducted using both the conventional method and the photogrammetric methods utilizing Unmanned Aerial Vehicles (UAVs) on the example of a stone pile located in the rural neighborhood of Dönemeç, affiliated with Siverek district of Şanlıurfa province. The differences and advantages between the two methods were examined.

1. Introduction

Please In engineering projects (such as road construction, building construction, mining, etc.), it is necessary to calculate the volumes of soil to be excavated and filled in order to be able to make cost estimations during land-related works. These volume calculations are typically performed using cross-sections, prisms, surface leveling measurements, and contour maps (Yakar ve ark., 2009).

Volume calculations play a significant role in engineering projects. The quantities of excavation, fill, and other volume data provide essential information and various methods are employed for these calculations. In this study, a comparison will be made between local measurements using GPS and photogrammetric measurements obtained through the use of Unmanned Aerial Vehicles (UAVs) for volume calculations. The use of photogrammetric techniques has become increasingly widespread in solving different engineering problems. UAVs contribute significantly to obtaining photographs of natural and man-made structures for photogrammetric purposes (Seki et al., 2017).

Located in the center of the Southeastern Anatolia Region, Mount Karacadağ is a volcanic mountain that has formed a vast rocky terrain as the lava cooled and transformed into basalt stones. However, in a significant portion of this area, the stones are scattered over fertile soil, making it easily cleared and suitable for agriculture. Karacadağ is known for receiving heavy rainfall, particularly during the winter months, and it has a cool climate. However, over the past few centuries, due to harsh winters, the local population turned to illegal logging, resulting in significant reduction of forest areas as a result of livestock grazing and the use of branches. Today, the region mostly appears as empty and unproductive land covered with stones. However, this area actually holds tremendous potential for organic farming, which has gained importance worldwide. It can be easily cleared and used for agriculture. Rice, in particular, is the most important crop cultivated in Karacadağ. Additionally, livestock farming is one of the main livelihoods for the people living in the Karacadağ region.

Under the scope of Land Consolidation carried out by the State Hydraulic Works (DSİ), in certain parts of the

* **Corresponding Author**

*(gomard.oso@gmail.com) ORCID ID 0009 – 0000 – 8197 – 8817
(nizarpolat@harran.edu.tr) ORCID ID 0000-0002-6061-7796
(hasanlafci.02@gmail.com) ORCID ID 0000-0002-2049-9940

Cite this study

Oso, C., Lafcı, H., & Polat, N. (2023). Comparing conventional and photogrammetric methods for volume calculation of stone piles: A case study in the Karacadağ Region. Intercontinental Geoinformation Days (IGD), 6, 321-323, Baku, Azerbaijan

region, the stones have been removed from the road and piled up in a designated area to provide access roads to the fields that farmers have cleared on their own.

The basalt stones found in the Karacadağ region are used in the restoration of historical sites in Diyarbakır (Haspolat,2013).

In this study, the volume calculation of the collected stones based on road construction was carried out in the rural neighborhood of Dönemeç in Siverek district of Şanlıurfa province. Initially, the classical method was employed, where points were captured using GPS, and subsequently, aerial photographs were taken using an Unmanned Aerial Vehicle (UAV) for volume calculation through the photogrammetry method. Furthermore, the data obtained through photogrammetric method were compared with the data obtained through the classical method in terms of time and accuracy, and the advantages and disadvantages of both methods were discussed.

2. Method

The stone pile located in Dönemeç village has been selected as the study area (Figure 1). The area covered by the stones has been measured as 15,868 square meters.

Figure 1. The study area

2.1. Classic field method

In this method, a total of 433 points were collected from the field using CORS (Sokkia GNSS GRX2) equipment. During the measurement process, the surveyor had to climb on top of the stones, which posed a safety risk and resulted in significant time loss in the field.

Later, the collected points were processed in the office using CAD software and the triangulation method. This resulted in the formation of a Digital Elevation Model (DEM) with a total of 786 triangles (Figure 2). Cross-sections were extracted from the model, and the volume of the stone pile was calculated to be 133,635 cubic meters.

2.2. Photogrammetric Method

In the study, high-quality aerial photographs were taken using a DJI Mavic 2 Pro drone, resulting in a total of 510 images with a size of 6.3 GB. On the ground, seven control points were assigned using CORS (Continuously Operating Reference Station). All the processes were efficiently carried out in the field within a short period of time.

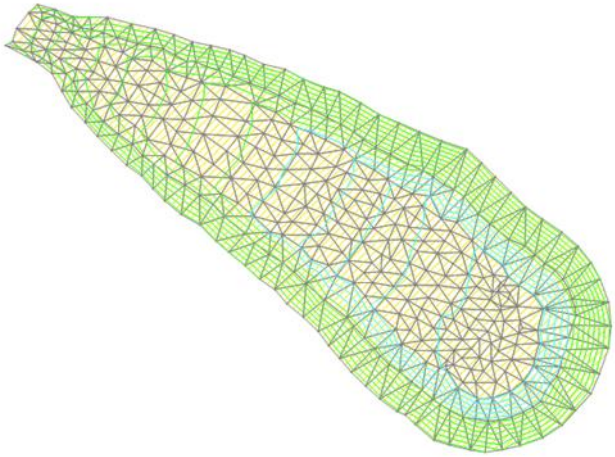

Figure 2. Triangles

Subsequently, in the office, the photographs were processed using Agisoft software to generate a 3D model of the stone pile. This was achieved by utilizing a sparse point cloud with 395,342 points and a dense point cloud with 15,837,172 points (Figure 3). A Digital Elevation Model (DEM) was then generated (Figure 4), and the volume calculation was performed, resulting in a volume of 135,500 cubic meters.

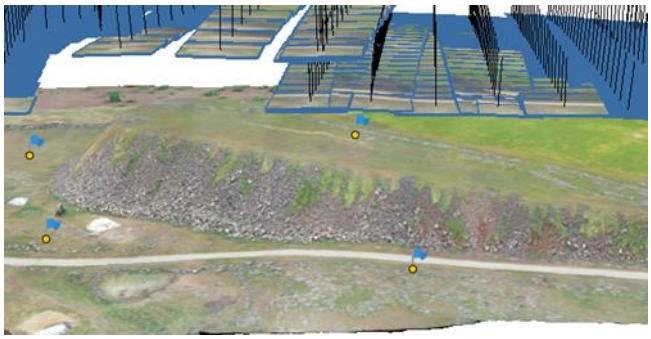

Figure 3. 3D model

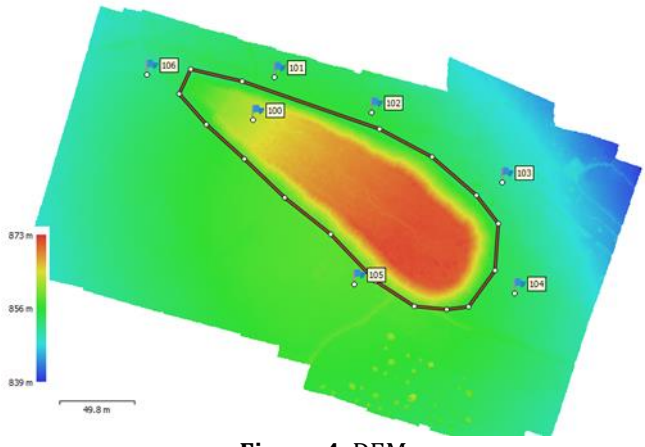

Figure 4. DEM

3. Analysis

In the study, the classic field method and the photogrammetric method were compared in terms of time and accuracy.

In terms of time, for the classic field method, the field measurements of 433 points took approximately 1.5 hours. The triangulation and volume calculation processes in the office took about 30 minutes. Overall, the classic method took approximately 2 hours.

For the photogrammetric method, the assignment of 7 ground control points and the flight time using the UAV took approximately 30 minutes. However, due to the large size of the photographs (totaling 6.3 GB), the processing time took approximately 5 hours. The total time for the photogrammetric method was approximately 5.5 hours.

In terms of accuracy, the volume of the stone pile was calculated as 133,635 cubic meters from 433 points using the classic method. On the other hand, using the photogrammetric method and analyzing 510 photographs, the volume of the stone pile was calculated as 135,500 cubic meters.

It should be noted that the measurements were conducted in May 2023, and it was found that the stone pile was old (constructed in 2019). Additionally, the presence of weeds on top of the stone pile indicated that the photogrammetric measurements might have overestimated the volume compared to the actual volume.

.

4. Result

In this study, a comparison was made between the classic field method and the photogrammetric method for the volume calculation of a stone pile in the rural neighborhood of Dönemeç in Siverek district. In the classic method, points were collected using GPS, and a Digital Elevation Model (DEM) was created using the triangulation method for volume calculation. In the photogrammetric method, high-resolution photographs were captured using Unmanned Aerial Vehicles (UAVs), and a 3D model and DEM were generated using Agisoft software for volume calculation.

In terms of time, the comparison in the field showed that the photogrammetric method yielded faster results compared to the classic method, ensuring safety as well. The assignment of ground control points and the UAV flight for capturing photographs were completed in a short period, but the processing of photographs took longer.

Regarding accuracy, slight differences were found between the volume values calculated using the classic method and the photogrammetric method. The presence of weeds on top of the stone pile contributed to the overestimation of volume in the photogrammetric method.

In conclusion, the photogrammetric method is a preferred option for volume calculations in engineering projects due to its fast results and acceptable level of accuracy. However, it is crucial to assign accurate ground control points in the field and carefully carry out the photo processing phase to obtain accurate results.

References

Alptekin, A., & Yakar, M. (2020). Determination of pond volume with using an unmanned aerial vehicle. Mersin Photogrammetry Journal, 2(2), 59-63.

Alyilmaz, C., Alyilmaz, S., & Yakar, M. (2010). Measurement of petroglyhps (rock of arts) of Qobustan with close range photogrammetry. International Archives of Photogrammetry, Remote Sensing and Spatial Information Sciences, 38(Part 5), 29-32.

Haspolat, K. (2013). Diyarbakır Karacadağ Bazalt Taşı Özellikleri ve Kullanım Alanları.

Kanun, E., Alptekin, A., & Yakar, M. (2021). Cultural heritage modelling using UAV photogrammetric methods: a case study of Kanlıdivane archeological site. Advanced UAV, 1(1), 24-33.

Karataş, L., Alptekin, A., Karabacak, A., & Yakar, M. (2022). Detection and documentation of stone material deterioration in historical masonry buildings using UAV photogrammetry: A case study of Mersin Sarisih Inn. Mersin Photogrammetry Journal, 4(2), 53-61.

Kusak, L., Unel, F. B., Alptekin, A., Celik, M. O., & Yakar, M. (2021). Apriori association rule and K-means clustering algorithms for interpretation of pre-event landslide areas and landslide inventory mapping. Open Geosciences, 13(1), 1226-1244.

Seki, M., Tiryakioğlu, İ., & Uysal, M. (2017). Farklı Veri Toplama Yöntemleriyle Yapılan Hacim Hesaplarının Karşılaştırılması. Geomatik, 2(2), 106-111. DOI: 10.29128/geomatik.322901.

Yakar, M., & Doğan, Y. (2017). Uzuncaburç Antik Kentinin İHA Kullanılarak Eğik Fotogrametri Yöntemiyle Üç Boyutlu Modellenmesi. 16. Türkiye Harita Bilimsel ve Teknik Kurultayı. TMMOB Harita ve Kadastro Mühendisleri Odası, Ankara.

Yakar, M., & Yilmaz, H. M. (2008). Using in volume computing of digital close range photogrammetry. The International Archives of the Photogrammetry, Remote Sensing and Spatial Information Sciences. Vol. XXXVII. Part B3b.

Yakar, M., Ulvi, A., Yiğit, A. Y., & Alptekin, A. (2022). Discontinuity set extraction from 3D point clouds obtained by UAV Photogrammetry in a rockfall site. Survey Review, 1-13.

Yakar, M., Yılmaz, H. M., & Mutluoğlu, Ö. (2009). Hacim Hesaplamalarında Laser Tarama ve Yerel Fotogrametrinin Kullanılması. TMMOB Harita ve Kadastro Mühendisleri Odası 12. Türkiye Harita Bilimsel ve Teknik Kurultayı.

Yılmaz, H. M., & Yakar, M. (2008). Computing of volume of excavation areas by digital close range photogrammetry.

Yilmaz, H. M., Yakar, M., & Yildiz, F. (2008). Digital photogrammetry in obtaining of 3D model data of irregular small objects. The International Archives of the Photogrammetry, Remote Sensing and Spatial Information Sciences, 37, 125-130.

6th Intercontinental Geoinformation Days

igd.mersin.edu.tr

Comparative analysis of semantic segmentation of terrestrial images using DeepLabv3+

Ahmet Verani*[1], Muhammed Enes Atik [1], Zaide Duran [1]

[1]*Istanbul Technical University, Faculty of Civil Engineering, Department of Geomatics Engineering, Istanbul, Türkiye*

Keywords
Deep Learning
Semantic Segmentation
Terrestrial
DeepLabv3+

Abstract

Feature extraction from images by semantic segmentation method with the help of deep learning algorithms is one of the methods in the sub-discipline called computer learning. Basically, the process is to give loaded data to deep artificial neural networks and train the artificial neural network with this data again and again until it creates correct predictions. In this study, DeepLab v3+ algorithm and two deep learning architectures such as Resnet18 and Resnet50 were chosen as backbone for feature extraction task from terrestrial images. The application was carried out on MATLAB. CamVid and Cityscapes datasets were used as datasets. Among the models applied, the one with the highest evaluation accuracy is, where the backbone is Resnet50 with 93.53% on Camvid and 89.29% on Cityscapes. The best results were applied to the images, which were taken for the study outside the data sets, and the results were evaluated visually.

1. Introduction

Deep learning is widely used for automated data processing as it requires less human intervention. (Atik and Ipbuker, 2021). Deep learning-based systems, both in the production and usage of products, is an issue on which studies are increasing (Sertkaya, 2022). Along with the developing hardware technologies (graphics cards, etc.), many new algorithms have been developed for the processing of big data with deep learning (Biyik *et al.*, 2023). Deep learning architectures are used for fast and automatic data extraction in large data sets (Atik *et al.*, 2022). Deep learning algorithms have a great importance in the field of image processing, which aims to obtain information from images by performing different operations on digital images (Ozgunluk *et al.*, 2022). Deep learning algorithms be trained with images, and it performs tasks such as object recognition and semantic segmentation in the field of image processing by using complex mathematical models containing multi-layer artificial neural networks. It has been shown in many studies that deep learning algorithms can detect complex patterns and show high performance in image processing thanks to its multi-layered structure.

In this study, deep learning models are trained using datasets made up of images prepared in accordance with semantic segmentation for the automatic recognition of objects in terrestrial images. DeepLab v3+ architecture (Chen et al. 2018) was used to capture the multi-scale context in images. Cambridge-driving Labeled Video Database (CamVid) is used for training and testing the algorithms. It is aimed to make high-accuracy predictions during the testing phase of the deep learning models used after the trainings.

2. Material and Method

In this section, DeepLabv3+ architecture used for feature extraction in semantic segmentation task and ResNet18 and ResNet50 models used as backbone structure will be discussed. In addition, information will be given about the data set and the metrics used in the evaluation.

2.1. Dataset

Cambridge-driving Labeled Video Database (CamVid) (Brostow *et al.*, 2009) was created by Cambridge University for autonomous driving and image processing studies. It contains 701 street images with a resolution of 720 x 960 with 32 classrooms. The data set is used in the training, testing and development of algorithms developed for autonomous driving and image processing. Label images are also available for each image, showing which class each pixel belongs to. The samples from the dataset are presented in Figure 1.

* **Corresponding Author**

*(verani19@itu.edu.tr) ORCID ID 0000-0001-9532-1138
(atikm@itu.edu.tr) ORCID ID 0000-0003-2273-7751
(duranza@itu.edu.tr) ORCID ID 0000-0002-1608-0119

Cite this study

Verani, A., Atik, M. E., & Duran, Z. (2023). Comparative analysis of semantic segmentation of terrestrial images using DeepLabv3+. Intercontinental Geoinformation Days (IGD), 6, 324-326, Baku, Azerbaijan

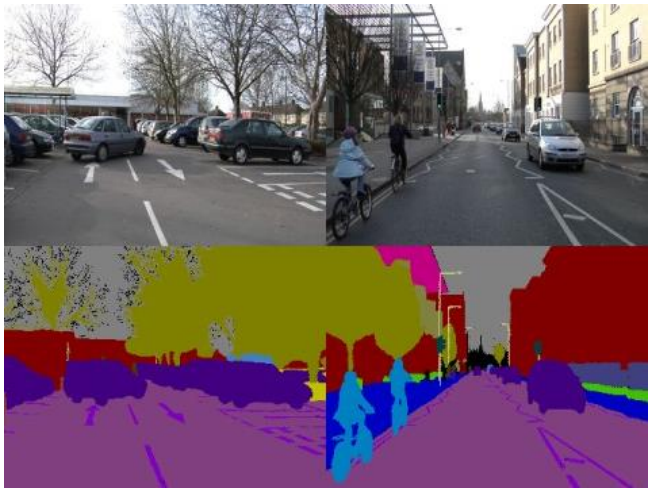

Figure 1. Image and ground truth samples from the CamVid dataset

2.2. DeepLab v3+

The algorithm used in the study uses the encoder-decoder module to capture semantic and spatial information from feature maps in the semantic segmentation task, and the spatial pyramid pooling module to capture object edge information (Chen et al., 2018). DeepLabv3 includes an ASPP module with batch normalization and image-level features. Atrous convolutions determine the density of features in convolutional networks.

In the DeepLabv3+ architecture, different deep learning networks are used as backbones. In this study, ResNet (He et al., 2015) versions were tested. Stacked residual units have been added to improve accuracy despite increased network depth in the ResNet architecture. Skipping connections solves the gradient disappearance problem by creating alternative shortcuts between connections (Atik et al., 2022). In other words, it implements the deep residual learning method, which performs identity matching with shortcut links that bypass one or more layers, and adds its outputs to the outputs of the other layer, to avoid deteriorating the training accuracy (He et al. 2015).

The ResNet architecture is named according to the number of layers. In this study, 18-layer and 50-layer models of the network are used. ResNet-18 has eighteen weight layers. ResNet-50 is designed in bottleneck structure to reduce training time. In ResNet-50, the bottleneck structure with three-layer blocks has been introduced instead of the two-layer blocks found in ResNet-34 (Atik et al., 2022).

2.3. Metrics

Two different metrics were used for the test set results of the data set. Overall accuracy is a metric calculated by taking the ratio of the total number of correct predictions obtained by a classification model to all predictions, and is designed so that classes are proportionally present and important. Unbalanced classes can prevent the metric from giving accurate results. Mean accuracy is obtained by calculating and averaging the accuracy for individual classes. It gives more effective results in cases where there is class imbalance.

2.4. Experiment

The images to be used are divided into 3 clusters as 60%, 20% and 20% as training, validation and test data, respectively. The training parameters are 15 epoch, sgdm optimizer, 0.001 learning rate were chosen. The optimum parameters were determined experimentally. For the experiments, HUAWEI D16 model computer with AMD Ryzen 5 4600H processor, 16 GB RAM, 512 SSD HD was used. All experiments are implemented in MATLAB environment.

3. Results

The test results obtained after the CamVid dataset training, in which ResNet18, ResNet50 networks that were used as the backbone infrastructure in the pre-trained DeepLab v3+ architecture, are presented in Table 1. Class-based accuracies have been found to differ according to the frequency, level of detail, and object sizes of the classes in the images. Given the uneven distribution of classes, the DeepLab v3+ResNet50 model produced more accurate prediction results than their average accuracy. In the test set, 85.65% accuracy was obtained with ResNet18 and 87.83% accuracy with ResNet50.

Table 1. CamVid Test Data Accuracies (%)

Model	Overall Acc.	Mean Acc.
DeepLabv3+ResNet18	91,20	85,65
DeepLabv3+ResNet50	92,49	87,83

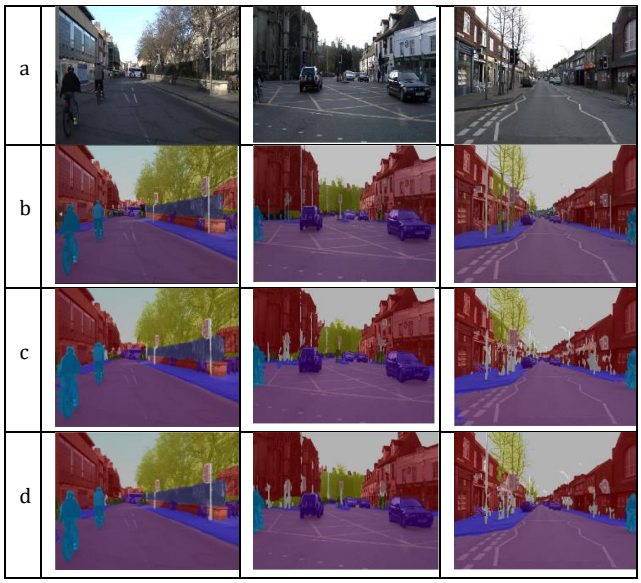

Figure 2. The result samples from the experiment. a) Image b) Ground truth c) Prediction of ResNet18 d) Prediction of ResNet50.

4. Discussion

In the study, ResNet18 and ResNet50 architectures were used in the backbone structure of the DeepLab v3+ network. As expected, ResNet-50 has higher accuracy.

However, the difference in accuracy between architectures is low. The model with ResNet 18 reduced the feature extraction time by 42.7%, while the average accuracy was reduced by 2.18%. Training times are 897 minutes for Resnet-50 and 514 minutes for ResNet-18. Since Resnet-50 is a deeper architecture, the training time is longer. Two different models were created that can generate predictive maps with semantically good accuracy.

5. Conclusion

In this study, research on semantic segmentation of terrestrial images with DeepLabv3+ architecture is presented. DeepLabv3+ which captures semantic information, spatial information and object edge information with its modules, is combined with ResNet which increases training accuracy with residual learning method. In future studies, the research can be expanded by including different datasets and architectures. Semantic segmentation of aerial images can also be studied.

References

Atik, M. E., Duran, Z., & Özgünlük, R. (2022). Comparison of YOLO versions for object detection from aerial images. International Journal of Environment and Geoinformatics, 9(2), 87-93.

Atik, S. O., & Ipbuker, C. (2021). Integrating convolutional neural network and multiresolution segmentation for land cover and land use mapping using satellite imagery. Applied Sciences, 11(12), 5551.

Atik, S. O., Atik, M. E., & Ipbuker, C. (2022). Comparative research on different backbone architectures of DeepLabV3+ for building segmentation. Journal of Applied Remote Sensing, 16(2), 024510-024510.

Biyik, M. Y., Atik, M. E., & Duran, Z. (2023). Deep learning-based vehicle detection from orthophoto and spatial accuracy analysis. International Journal of Engineering and Geosciences, 8(2), 138-145.

Brostow, G. J., Fauqueur, J., & Cipolla, R. (2009). Semantic object classes in video: A high-definition ground truth database. Pattern Recognition Letters, 30(2), 88-97.

Chen, L. C., Zhu, Y., Papandreou, G., Schroff, F., & Adam, H. (2018). Encoder-decoder with atrous separable convolution for semantic image segmentation. In Proceedings of the European conference on computer vision (ECCV) (pp. 801-818).

He, K., Zhang, X., Ren, S., & Sun, J. (2016). Deep residual learning for image recognition. In Proceedings of the IEEE conference on computer vision and pattern recognition (pp. 770-778).

Sertkaya, C. (2022). Derin Öğrenme Tabanlı Nesne Tanıma Yeteneklerine Sahip Akıllı Robot Sisteminin Geliştirilmesi. European Journal of Science and Technology, (34), 211-216.

6th Intercontinental Geoinformation Days

igd.mersin.edu.tr

Possibilities of applying smart technologies in agriculture (after the Pandemic)

Garayli Nazim Tazim[*1]

[1] *The Minister of Science and Education, Institute of Geography, Baku, Azerbaijan*

Keywords
Smart agriculture
Geographic Information Systems
Pandemic
Environment
Organic

Abstract

In addition to the rapid increase in the number of people in the world, the food needs of people are also changing with the same dynamics. This dynamic leads to a decrease in the number of economically important plant and animal species every day. Development directions of agriculture depend on social, economic and natural factors. Climate change and the problems underlying it leads to a crisis situation in some areas of agriculture. The influence of concepts such as food safety, healthy nutrition, and environmental protection on people encourages agricultural entrepreneurs to produce environmentally friendly products. The IV industrial revolution creates an opportunity to build agrarian complexes that meet modern requirements using the opportunities created by technology in farms located in cities and surrounding areas. Analysis and evaluation of spatial data is carried out using information technologies. After calculating the economic efficiency of the obtained results, a road map is prepared for conducting economic activities in the evaluated area. With the help of geographic information systems, preliminary analyzes of any type of economic subject can be calculated. The records of all components are digitized and the potential cropping structure for the area is determined. In some countries, the economic decline during the pandemic was directly related to agriculture. Territorial organization of agriculture in Azerbaijan is developing in a different direction over the years. In the post-pandemic period, this process has accelerated somewhat. Application tools were expanded to eliminate deficiencies in sectors.

1. Introduction

Azerbaijan is among the countries with ancient agricultural traditions. Throughout history, the main occupation of the peoples living in the territory of Azerbaijan has been agriculture and animal husbandry. The favorable climate, fertile lands, and the fact that the Kür and Araz rivers largely pass through our lands have paved the way for the development of the occupation of the people in this direction. The establishment of a sustainable agricultural system through a comprehensive analysis of the agricultural sector and the application of modern science means the beginning of a new stage in Azerbaijan's economic and social life. The possibilities of using technology for agricultural optimization are considered among the greatest innovations of the 21st century.

2. Method

It is important to apply several methods in farm evaluation. Years ago, potential development directions were determined using the observation method, but now the latest innovations are being applied to agriculture using the opportunities created by technology. Research conducted with the help of IoT and GIS technologies encourages the creation of large-scale farm complexes.

3 Agriculture as a priority area

As an alternative to oil in Azerbaijan, the government has announced several priority areas. One of them was tourism. The year 2020 was considered a lost year for world tourism. The tourist season in Azerbaijan ended before it started. The agricultural sector has potential. In recent years, we have seen a certain growth in this sector in terms of quantity and quality (Arampatzis et al. 2005).

It is plausible that there will be changes in the development aspects of agriculture before and after the pandemic. Of course, the importance given to agriculture in the last 10 years cannot be ignored. Due to the closure of borders during the pandemic process, the volume of imported agricultural products decreased several times. Therefore, it can be assumed that the food

* **Corresponding Author**

*(e-mail) ORCID ID **0009-0007-8000-7614**

Cite this study

Tazim, G. N. (2023). Possibilities of applying smart technologies in agriculture (after the Pandemic). Intercontinental Geoinformation Days (IGD), 6, 327-329, Baku, Azerbaijan

shortage in the Republic is at a visible level. The supply base with agricultural products has been established in recent years. In this respect, the existence of food shortages in the country was prevented. In addition, winter wheat and barley crops were planted before the spread of the coronavirus in the country. These crops are harvested during the summer months. In fact, it can be noted that the favorable agro-climatic resources of the country give us a great advantage in being able to harvest twice a year from the same region. Government subsidies provide a great incentive to plant a second crop in the same area. As a result, farmers in lowland areas start planting corn after the grain harvest is complete. Agricultural products with import dependency are as follows.

1. Cereal crops
2. Raw Materials of Sugar
3. Raw Materials of Sunflower and Corn Oils
4. Tea raw materials
5. Brass
6. Tobacco

Both the state and the private have warehouse infrastructure to store 1.5 million tons of grain stock. 80-90% of the meat and dairy supply is at the expense of the local economy.

The lack of agricultural machinery to meet the agrotechnical maintenance requirements causes farmers to pull machinery from other regions. For some time, the restriction of movement between counties has been implemented with exception rules for people engaged in agriculture (Devi et al. 2013). Machinery and agricultural products are transported seamlessly between regions. For the first time in Azerbaijan, preferential and unsecured loans are offered to farmers. Government investments in the agricultural sector are increasing every year. New equipment is purchased, subsidies are allocated by the state, agricultural service areas are created, fertilizers, fuel oil and rentals are provided on preferential terms. Agricultural Credit from the reserve fund of the President of the Azerbaijan Republic to the Ministry of Agriculture of the Republic of Azerbaijan has been provided in the 2020 state budget of the Republic of Azerbaijan to provide unsecured micro-credits in the agricultural sector to meet the need. For the financing resources of agricultural producers, 30.0 (thirty) million manats were allocated to the Development Agency on April 14, 2020, in the conditions of the Corona virus pandemic and in the following period.

4. Pandemic period

During the years of Soviet rule, agriculture was unable to become the leading sector of the economy. Agriculture, which was in a state of crisis during the Second World War, experienced a period of decline in the post-war years. In the 60s, the republic's economy and one of its main sectors, agriculture, was in a state of prolonged crisis and decline. The average annual growth rate of the total agricultural output was lagging behind other republics. In 1969, 574 thousand tons of grain, 299 thousand tons of cotton, 372 thousand tons of vegetables, 272 thousand tons of grapes, 52 thousand tons of fruit, 113 thousand tons of potatoes, 24.5 thousand tons of tobacco were produced. The productivity of the main agricultural crops was decreasing. This year, an average of 9.5 centners of cereals, 15.1 centners of cotton, 120 centners of vegetables, 43.63 centners of grapes, 10.4 centners of fruit, 18 centners of tobacco, and 79 centners of potatoes were produced per hectare. The situation in public animal husbandry was more deplorable. The number of livestock in collective farms and state farms is decreasing year by year, their productivity is decreasing, and their cost has increased. In the republic in 1969, only 49 calves and calves were obtained from every hundred cows and buffaloes, 43 lambs and goats from every hundred born sheep and goats, 677 kg of milk was milked from each cow and buffalo, and 1.6 kg of wool was sheared from each sheep. For the Union, this figure was 2253 kg and 2.8 kg, respectively.

Starting from 1975, there was a noticeable increase in agricultural products. Average indicators have increased 3 times compared to the previous decade. Advances in all fields of agriculture radically changed the socio-economic face of the Azerbaijani countryside, the country as a whole turned into an agro-industrial republic. The Corona virus pandemic, which suddenly took over the agenda by having a negative impact on the economy of the world's leading countries, has seriously affected Azerbaijan as well (Wang et al. 2010). The pandemic tested not only the sustainability of healthcare, but also the economic strength of countries. Of course, in this case, it is inevitable that the countries that strengthen their economic stability with oil will fall into a crisis situation. However, it should not be forgotten that the attention given to the development of the non-oil sector adds new priority directions to the restoration of the lost power of the economy in this period. Tourism and agriculture are considered the most profitable sectors of the non-oil sector. During the pandemic, it remains impossible to use tourism opportunities. The world's leading developed countries are planning to use the power of agriculture to the maximum to soften the economic blow caused by the pandemic. In the recently globalized world, where capitalism has developed - the urbanization of cities in the society of the IV industrial revolution, in a word, the principle of village-to-city has resulted in the agrarian sector moving into the background.

The decrease in the volume of oil and its price below 30 dollars is due to the sharp drop in demand for oil during the pandemic. The limited number of activities of industrial enterprises, plants and factories, and the decrease in the consumption capacity of oil products directly lead to changes in the demand and supply indices in the oil market. Of course, these processes form a chain connection (Liu et al. 2007).

5.Results

As a result, it should be noted that the importance of using information technologies in agriculture should be maintained. A development dynamics map should be

created based on analyzes and analyzes and this process should be accelerated with state support. All information centers related to geographic information systems should be able to help the farmer in a comprehensive way. This support should be done closely between farmers and official institutions.

6.Discussion

40-42 percent of wheat and barley is covered by import account. It should be noted that 60% of the arable land is cultivated with grain. Although 28-30 kuruş yield is obtained from 1 decare area, the most imported agricultural product is grain. When we optimize regular planting and agrotechnical maintenance, productivity can reach up to 40 cents. Currently, the amount of imported grain will vary by 20-25%. The government's efforts to ensure food security will be directed directly at local production. Subsidies and aid should be distributed more intensively to farmers and entrepreneurs to expand their farms and reuse arable or unused land for reproduction. Our country should focus on the development of the agricultural sector, the efficient use of water, soil and resources, reproduction and most importantly saving. Azerbaijan has land, irrigation and labor potential. These should be applied on a scientific basis. In other words, the agricultural sector is such that it should develop more with the application of innovative technologies.

Special attention should be paid to the production and processing of agricultural products, increasing the production capacity of existing agro-processing enterprises through the application of modern technologies and implementing comprehensive measures in the direction of creating new enterprises in this field will be the main contributor to ensuring food security in the coming years.

7.Conclusion

The social distance factor, which is one of the main ways to protect against the pandemic, does not allow people to gather together. At this time, cases of weakening of the production capacity of labor-intensive industries (cotton, cocooning, etc.) can be observed. Involvement of people in mass planting and later harvesting processes increases the speed of virus spread. Using the power of modern techniques as a tool means reducing the labor force by half. Using information technology, you can control your farm from your workplace or home. Planting should be planned and excessive production should be avoided. The fact that the product exceeds the production norm creates a problem in its sale. Sometimes the product is offered at a price below cost. The concept of management of agricultural products should be formed in the republic. The training of qualified personnel in this field should expand the possibilities of selling local products in foreign markets.

References

Arampatzis, T., Lygeros, J., & Manesis, S. (2005, June). A survey of applications of wireless sensors and wireless sensor networks. In Proceedings of the 2005 IEEE International Symposium on, Mediterranean Conference on Control and Automation Intelligent Control, 2005. (pp. 719-724). IEEE.

Devi, D. V. V., & Kumari, G. M. (2013). Real-time automation and monitoring system for modernized agriculture. International Journal of Review and Research in Applied Sciences and Engineering (IJRRASE) Vol3, 1, 7-12.

Liu, H., Meng, Z., & Cui, S. (2007, September). A wireless sensor network prototype for environmental monitoring in greenhouses. In 2007 International Conference on Wireless Communications, Networking and Mobile Computing (pp. 2344-2347). IEEE.

Mirabella, O., & Brischetto, M. (2010). A hybrid wired/wireless networking infrastructure for greenhouse management. IEEE transactions on instrumentation and measurement, 60(2), 398-407.

Nandurkar, S. R., Thool, V. R., & Thool, R. C. (2014, February). Design and development of precision agriculture system using wireless sensor network. In 2014 First International Conference on Automation, Control, Energy and Systems (ACES) (pp. 1-6). IEEE.

Wang, Q., Terzis, A., & Szalay, A. (2010, May). A novel soil measuring wireless sensor network. In 2010 IEEE Instrumentation & Measurement Technology Conference Proceedings (pp. 412-415). IEEE.

6th Intercontinental Geoinformation Days

igd.mersin.edu.tr

Studying the influence of mudflows on the geomorphological structure of rivers using by GIS technologies

Abushova Samira Nasib[*1], **Maharramova Aytan Rufat**[*2]

[1] *The Minister of Science and Education, İnstitute of Geography, Baku, Azerbaijan*
[2] *Baku State University, Baku, Azerbaijan*

Keywords
Mudflows
Geomorphological structure
Rivers
GIS technologies
Sediment dynamics

Abstract

This scientific article aims to investigate the influence of mudflows on the geomorphological structure of rivers through the utilization of Geographic Information System (GIS) technologies. By integrating field observations with GIS data, the study assesses the impact of mudflows on river channels, sediment dynamics, and overall river morphology. The results highlight the significant role of mudflows in shaping river systems and emphasize the importance of incorporating GIS technologies in the study and management of these dynamic environments.

1. Introduction

Rivers are intricate and dynamic natural systems that are shaped by various processes, one of which is mudflows. Mudflows, characterized by the rapid movement of water and sediment, have the potential to significantly alter the geomorphological structure of river channels. These events result from factors such as heavy rainfall, slope instability, and land cover conditions. Understanding the interactions between mudflows and river morphology is crucial for effective river management, hazard assessment, and the development of mitigation strategies. By studying the influence of mudflows on river systems, we can gain valuable insights into the dynamics of these environments.

The use of GIS (Geographic Information System) technologies has revolutionized the study of natural phenomena, including the impact of mudflows on the geomorphological structure of rivers. GIS technologies provide powerful tools for data acquisition, integration, visualization, and analysis, enabling researchers to gain comprehensive insights into the complex interactions between mudflows and river systems. In the context of studying the influence of mudflows on river geomorphology, GIS technologies offer several key advantages and methodologies that enhance our understanding of this dynamic process.

Firstly, GIS technologies enable the collection and integration of various geospatial data sets essential for studying the impact of mudflows on river morphology. These data sets may include topographic maps, aerial imagery, satellite images, LiDAR (Light Detection and Ranging) data, bathymetric surveys, and hydrological data. By combining these data sets within a GIS framework, researchers can create detailed and accurate representations of the study area, providing a solid foundation for further analysis.

One important aspect of studying the impact of mudflows on river geomorphology using GIS is the analysis of channel morphology changes. GIS allows researchers to compare pre- and post-mudflow channel conditions by utilizing high-resolution topographic data. By employing techniques such as digital elevation models (DEMs), researchers can assess changes in channel width, depth, cross-sectional area, and planform geometry. These spatial analyses provide quantitative data on the alterations caused by mudflows, aiding in the characterization of channel response and understanding the processes of channel widening, deepening, and avulsion.

The primary objective of this study is to comprehensively investigate the influence of mudflows on the geomorphological structure of rivers by utilizing Geographic Information System (GIS) technologies. We aim to examine the changes occurring in channel

* **Corresponding Author**

*(samira.abushova88@gmail.com) ORCID ID 0000-0002-2567-8876
(meherremova.ayten@inbox.ru) ORCID ID xxxx-xxxx-xxxx-xxxx

Cite this study

Nasib, A. S. & Rufat, M. A. (2023). Studying the influence of mudflows on the geomorphological structure of rivers using by GIS technologies. Intercontinental Geoinformation Days (IGD), 6, 330-334, Baku, Azerbaijan

morphology, sediment transport patterns, and river hydraulics resulting from mudflow events. By doing so, we seek to gain insights into the long-term effects of mudflows on river systems, including their ecological implications and potential risks to human activities and infrastructure.

2. Method

To address the research questions and achieve the objectives, this study employs a comprehensive research methodology comprising field observations, data collection, and GIS analysis. Field observations and sampling activities are conducted in areas prone to mudflows to gather detailed information on channel morphology and sediment characteristics. These activities include surveying cross-sections of river channels, measuring sediment grain sizes, and recording channel roughness.

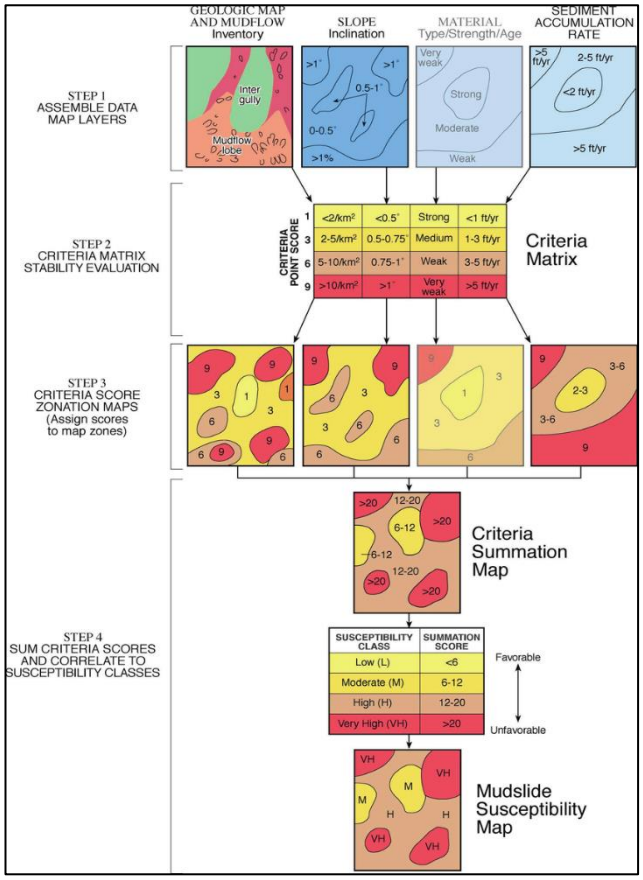

Figure 1. Analysing geomorological effect of mudflow by GIS

GIS data acquisition is a crucial component of the methodology, involving the collection of topographic, hydrological, and geological data for the study area. This includes obtaining high-resolution digital elevation models (DEMs), river network data, land cover information, and geological maps. These datasets serve as essential inputs for subsequent analysis and modeling.

The field and GIS data are integrated and analyzed within a GIS environment to assess the influence of mudflows on the geomorphological structure of rivers. Various GIS techniques are employed, such as spatial analysis, data interpolation, and hydrodynamic modeling. These methods facilitate the examination of channel changes, sediment transport patterns, and hydraulic impacts resulting from mudflows (Figure 1).

The analysis of the collected data and GIS-derived outputs provides valuable insights into the influence of mudflows on river systems. The results contribute to a better understanding of the complex interactions between mudflows and river geomorphology, aiding in the development of effective river management strategies and hazard mitigation measures.

Furthermore, GIS technologies facilitate the study of sediment transport patterns associated with mudflows. By integrating flow velocity data, sediment concentration measurements, and hydraulic modeling within a GIS environment, researchers can simulate and analyze the movement and deposition of sediment during mudflow events. This analysis helps identify sediment deposition areas, erosion hotspots, and patterns of sediment transport along the river course. GIS also allows for the visualization of sediment dynamics through thematic maps, contouring, and flow path analysis, providing a comprehensive understanding of the spatial distribution of sediment deposits and erosion zones.

Another key aspect of studying the impact of mudflows on river geomorphology using GIS is the assessment of river hydraulics. GIS technologies enable the integration of hydraulic models with spatial data, allowing for the simulation of flow characteristics, water velocities, and water depths under different scenarios. By incorporating mudflow-induced changes, such as alterations in channel roughness or increased flow resistance due to sediment deposition, researchers can evaluate the impacts on flow regimes and hydraulic conditions. This analysis helps in understanding the potential for increased flood risk, changes in water levels, and the effects on riverine ecosystems.

In addition to studying immediate impacts, GIS technologies also facilitate the analysis of long-term effects of mudflows on river systems. By integrating historical data, long-term monitoring data, and paleo-environmental records, researchers can examine the evolutionary changes in river morphology and the response of river systems to multiple mudflow events over time. GIS allows for the creation of time-series analyses, trend mapping, and change detection techniques, enabling the identification of long-term trends, patterns, and thresholds in river system response to mudflows.

Overall, GIS technologies offer a comprehensive and powerful approach to studying the impact of mudflows on the geomorphological structure of rivers. They provide the means to acquire, integrate, visualize, and analyze geospatial data, enabling researchers to examine changes in channel morphology, sediment dynamics, river hydraulics, and long-term effects on river systems. By employing GIS technologies, scientists and practitioners can gain a better understanding of the complex interactions between mudflows and river geomorphology, contributing to effective river management strategies, hazard assessment, and the preservation of riverine ecosystems.

2.1. Impact on River Hydraulics

Mudflows have a significant impact on river hydraulics, altering flow regimes and water velocities within the river system. The presence of mudflow deposits can modify the flow path, channel roughness, and cross-sectional shape, ultimately affecting the hydraulic conditions of the river.

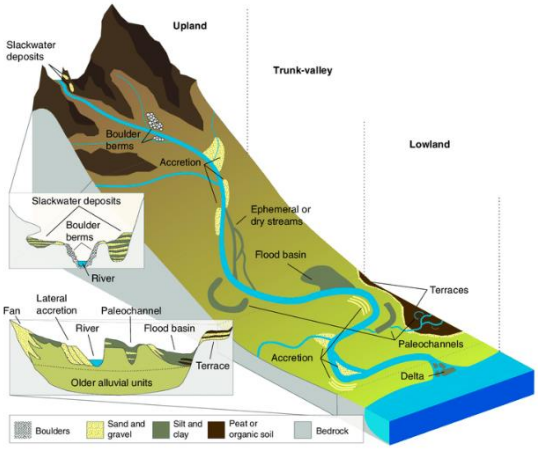

Figure 2. Simulation

The accumulation of mudflow sediments in the channel can impede flow, creating obstacles that cause flow diversions and changes in the velocity distribution. These sediment deposits can act as barriers, influencing the hydraulic capacity of the river channel and leading to increased water levels during flood events. The altered hydraulic conditions resulting from mudflows can have significant implications for flood risk management, river engineering, and the maintenance of navigation channels.

Additionally, the changes in hydraulic conditions induced by mudflows can have ecological consequences. Altered flow patterns may affect the distribution of aquatic habitats, the availability of food resources, and the movement of sediment-dependent species. These impacts highlight the intricate relationships between mudflows, river hydraulics, and riverine ecosystems.

2.2. Methods of data analysis for mudflow prevention using GIS technologies

Mudflows are natural hazards that can cause significant damage to human settlements, infrastructure, and the environment. To effectively prevent and mitigate mudflow risks, it is crucial to employ advanced technologies such as GIS (Geographic Information System). GIS technologies offer powerful tools for data analysis, visualization, and decision-making, enabling researchers and practitioners to assess potential mudflow hazards, identify vulnerable areas, and design effective prevention strategies. In the context of mudflow prevention, several key methods of data analysis using GIS technologies can be employed.

2.3. Terrain Analysis

Terrain analysis is a fundamental method for mudflow prevention using GIS. It involves the analysis of topographic data to identify areas susceptible to mudflow initiation and pathways of potential flow. GIS can process high-resolution digital elevation models (DEMs) to extract relevant terrain parameters such as slope, aspect, curvature, and flow accumulation. By applying slope and flow accumulation thresholds, GIS can delineate areas with high potential for mudflow initiation and route the flow paths through the terrain. This analysis helps identify critical zones where preventive measures can be implemented, such as the construction of debris basins, retention ponds, or channel diversions.

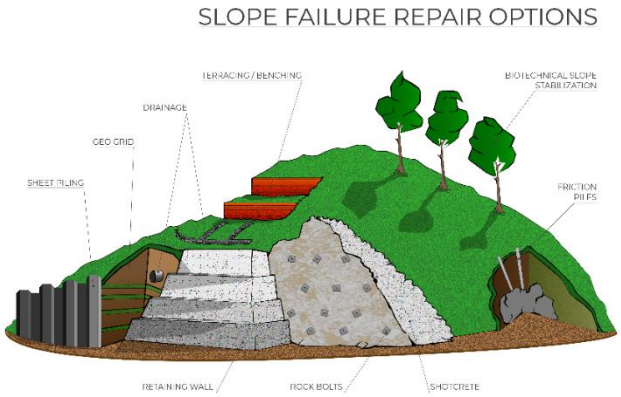

Figure 3. Simulation

2.4. Hydrological Analysis

Hydrological analysis using GIS allows for the assessment of surface water runoff and the estimation of flow volumes during rainfall events, which can trigger mudflows. GIS can incorporate rainfall data, land cover information, and digital hydrological models to simulate the runoff generation and flow paths. By analyzing the hydrological connectivity of the landscape, GIS can identify areas prone to high runoff accumulation, which increases the likelihood of mudflow occurrence. This analysis aids in the identification of potential areas for the implementation of hydrological measures, such as the installation of drainage systems, erosion control structures, or vegetative buffers.

2.5. Hazard Zoning and Risk Assessment

GIS technologies enable the creation of hazard zoning maps and risk assessment models to prioritize areas for mudflow prevention measures. By integrating multiple datasets, such as topography, hydrology, soil characteristics, land use, and infrastructure vulnerability, GIS can assign hazard levels and risk scores to different zones. This analysis helps identify areas with high susceptibility to mudflows and their potential impacts on critical infrastructure, human settlements, and environmentally sensitive areas. The outputs can be used to inform land-use planning, infrastructure development, and emergency response strategies.

2.6. Spatial analysis of historical events

GIS can facilitate the spatial analysis of historical mudflow events to identify patterns, trends, and hotspots. By incorporating historical data on mudflow occurrence, GIS can analyze the spatial distribution of past events, their frequencies, and their relationships with terrain and hydrological variables. This analysis helps in understanding the spatial-temporal patterns of mudflows, identifying areas prone to recurring events, and assessing the effectiveness of previous prevention measures. The findings can inform targeted prevention strategies and the allocation of resources for high-risk areas.

2.7. Modeling and scenario analysis

GIS technologies enable the development of mudflow prediction and scenario modeling, which aid in understanding the potential impacts of different factors and interventions. GIS can integrate various data inputs, such as precipitation data, soil properties, vegetation cover, and land-use scenarios, into predictive models. These models can simulate mudflow initiation, propagation, and deposition patterns under different scenarios, such as varying rainfall intensities, land-use changes, or the implementation of preventive measures. This analysis helps in evaluating the effectiveness of different prevention strategies and optimizing resource allocation for maximum risk reduction.

2.8. Decision Support Systems

GIS can be utilized to develop decision support systems (DSS) for mudflow prevention. A DSS integrates all relevant data, analysis tools, and visualization techniques into a user-friendly interface. It allows decision-makers and practitioners to access and analyze data, run simulations, evaluate scenarios, and visualize results. By incorporating spatial analysis capabilities, risk assessment models, and cost-benefit analysis tools, GIS-based DSS assists in making informed decisions regarding mudflow prevention measures. It facilitates the evaluation of different intervention options, cost-effectiveness analyses, and the development of comprehensive prevention plans.

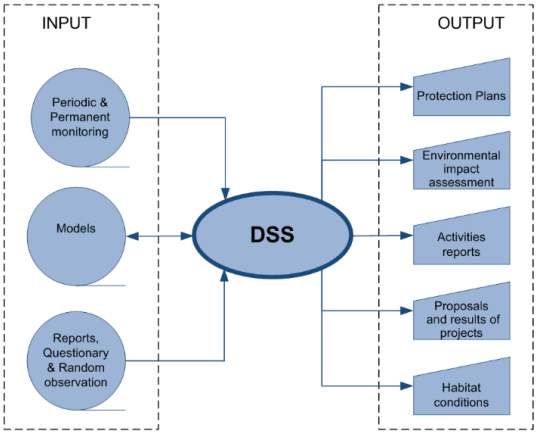

Figure 4. Simulation

In conclusion, GIS technologies provide a wide array of data analysis methods for mudflow prevention. These methods include terrain analysis, hydrological analysis, hazard zoning, risk assessment, spatial analysis of historical events, modeling, scenario analysis, and the development of decision support systems. By harnessing the power of GIS, researchers and practitioners can analyze and interpret geospatial data to identify high-risk areas, evaluate prevention strategies, and make informed decisions for effective mudflow prevention and mitigation. The application of GIS technologies in mudflow prevention plays a crucial role in safeguarding human lives, infrastructure, and the environment from the destructive impacts of these natural hazards.

3. Conclusion

The comprehensive study conducted on the influence of mudflows on the geomorphological structure of rivers using GIS technologies has yielded significant findings. The analysis revealed that mudflows have a profound impact on river systems, resulting in notable changes in channel morphology, sediment dynamics, river hydraulics, and long-term effects on river systems.

The examination of channel morphology indicated that mudflows lead to channel widening, deepening, and avulsion, altering the shape and dimensions of river channels. These changes have implications for river connectivity, sediment transport, and floodplain development. The study of sediment transport patterns associated with mudflows demonstrated the complex dynamics of sediment movement, with sedimentation occurring in certain areas and erosion in others. The spatial distribution of sediment deposits is influenced by flow velocity, channel morphology, and topographic characteristics.

The analysis of the impact on river hydraulics revealed that mudflows modify flow regimes and water velocities within the river system. The presence of mudflow deposits can impede flow, increase water levels, and alter hydraulic conditions, thereby affecting flood risk and riverine ecosystems. Furthermore, the long-term effects of mudflows on river systems encompass changes in the river network, floodplain development, nutrient cycling, and habitat availability.

References

Brierley, G. J, & Fryirs, K. A. (2005). Geomorphology and river management: applications of the river style framework. Blackwell, Oxford, UK

Brierley, G. J., Fryirs, K., Cullum, C., Tadaki, M., Huang, H. Q., & Blue, B. (2013). Reading the landscape: integrating the theory and practice of geomorphology to develop place-based understandings of river systems. Progress in Physical Geography 37(5), 601-621

Entwistle, N., Heritage, G., & Milan, D. (2011). River Habitat Survey: A useful tool for hydromorphological assessment. Advances in River Sciences 2011, Swansea UK, Abstracts

Feld, C. K. (2004). Identification and measure of hydromorphological degradation in Central European lowland streams. Hydrobiologia, 516(1), 69-90

Imanov, F. A. (2002). River flow, Baku, 207 p.

Imanov, F. A. (2011). Statistical methods in Hydrolometeorology" Baku, 270 p.

Lehotský, M, & Grešková, A. (2007). Fluvial geomorphological approach to river assessment – methodology and procedure. Geograficky Casopis 59(2), 107-129

Museyibov, M. A. (1998). Physical geography of Azerbaijan, Baku, p. 301.

Rustamov, S. G. (1961). Hydrological parameters of the Maximum Flood Costs in Azerbaijan. Math. AS SSR, Geography, 2, 119-131.

Thorne, C. R., (1998). Stream Reconnaissance Guidebook: Geomorphological Investigation and Analysis of River Channels, J Wiley and Sons, Chichester, UK, ISBN 0-471-968560, 127p.

Yovan, D. (2009). Drainage of Rainwater. Belgrade, p. 418.

6th Intercontinental Geoinformation Days

igd.mersin.edu.tr

Getting disaster information through the web

Lutfiye Kuşak[*1]

[1]*Mersin University, Engineering Faculty, Department of Geomatics Engineering, Mersin, Turkiye*

Keywords
Disaster
News
Internet
Text Mining
Sentiment Analysis

Abstract

In the world and in Türkiye, there are numerous geological, climatic, biological, social, and technical disasters. While some of these disasters occur for natural reasons, others are caused on by humans. Numerous factors, such as population growth, varying meteorological conditions, and an unplanned and unregulated rise in impermeable surface area, negatively impact the impact on areas of disasters. Today, disaster management, documentation, and monitoring are the primary concerns in various countries. For example, there is not any doubt about the amount of work, time, and expense involved in gathering disaster data. Alternative techniques should be considered as supporting evidence in addition to terrestrial observations. Data collection via the internet is a topic of interest nowadays, especially given how widely it is used. This study has therefore looked into how to collect disaster data from online sources.

1. Introduction

Numerous financial and environmental costs result from disasters. This condition causes people to die, get injured, lose their residences, and suffer economic and psychological damage. Disasters are typically divided into two categories: natural and man-made. The categories of geological, climatic, biological, social, and technological disasters are addressed all over the world. Geological disasters include earthquake, landslide, rockfall, volcanic explosion, mudflow, and tsunami. Climate disasters include heat waves, cold waves, droughts, hailstorms, tornadoes, lightning, hurricanes, typhoons, floods, cyclones, tornadoes, blizzards, avalanches, and extreme snowfall. Biological disasters include erosion, forest fires, epidemics, and insect invasion. Among the social disasters are migration, wars, terrorist acts, and fires. Technological disasters include mining accidents, incidents involving biological, nuclear, and chemical weapons, accidents involving industrial equipment, and accidents involving transportation. Nuclear, biological, and industrial disasters are the most common created by humans'. Disasters like avalanches, earthquakes, floods, and storms develop quickly but disasters like famine and drought take time to develop. One of the most frequent types of natural disasters is the climactic one.

Records should be maintained on a regular basis in order to control disasters and take precautions. In terms of time, effort, and cost, collecting and storing disaster data is a hard task. For this reason, remote sensing data collected using a variety of platforms, including UAV, satellite, and airborne, is employed in research together with ground measurements and observations. In order to carry out disaster analysis and management in a healthy way, the attribute data, which includes information such as time, disaster location, and impact area of these data, must be very carefully recorded. This is why online resource-based feature extractions have been used in studies recently.

As of April 2023, approximately 5 billion users are actively using the internet, while there are 4.8 billion active social media users (Statista, 2023). This number of users means a large data set for all commercial and non-commercial environments. For this reason, many studies are carried out to extract information by making the data meaningful.

Web usage mining, web content mining, and web structure mining are the three primary categories that web mining is analyzed under. Web mining is a sub-branch of data mining that attempts to analyze and process information on the web. The main focus of his research is web content mining, which involves activities like identifying the languages used on the pages of

* **Corresponding Author**

*(lutfiyekusak@mersin.edu.trl) ORCID ID 0000-0002-7265-245X

Cite this study

Kusak, L. (2023). Using online news to find disasters. Intercontinental Geoinformation Days (IGD), 6, 335-340, Baku, Azerbaijan

websites, disclosing the word density, locating the keywords, and categorizing the websites. Image processing or natural language processing techniques are employed for this.

Web mining generally uses text mining methods. However, unlike text mining, the preprocessing process is a little different because web pages contain html tags. Today, there are many studies in which social media content is used as a data set.

1.1. Related Works

Web content mining has been the subject of many studies. These studies may be intended to find social media content, track national and international news, and highlight people's emotional responses to some significant events.

In the study conducted by Duan et al., up-to-date data set was obtained for social media contents and management information system. Tweets were analyzed using text mining methods and Supervised machine learning algorithms (Duan et al., 2023).

In the study conducted in 2020, one-week agenda topics for Kuwait were determined using Twitter data. It has been determined that the most topics are opened on religion, emotions, laws and education in the selected date range, and different topics are trending in different locations every day of the week. In the study, as in all previous studies, data crawling was done first, then data filtering was performed and word frequencies were determined. Subject headings were created according to the results obtained (Almatar et al., 2020).

In the Sewol ferry disaster that took place in South Korea in 2014 and 300 people died, it was tried to understand the trauma and modes of the public by using social media data. For this, twitter data belonging to 3 different periods, pre-event, during the event and after the event, were analyzed using natural language processing and text mining. It has been determined that anger and sadness data are high in the period of approximately 1 month after the event, and anger increases in every 5-day period at various times until May 30 (Woo et al., 2015).

Web mining techniques are often applied in healthcare environments. Preprocessing steps were carried out with NLP and data cleaning methods in the study in which the comments made by the patients on the web sites were acquired by web scraping method. The data was analyzed using Nvivo software, correlation analysis, and sentiment analysis methods, and it was presented using a word cloud, tabular sheet, and graphic representations (Hameed, 2023).

Geotagged information makes it easier to show the location of data and to make decisions. In the 2017 study, two separate investigations were conducted on Twitter, consisting of geotagged and non-geotagged flu and a movie. According to the findings of the study, geotagged data is significantly more consistent with events, noise data is much lower, and correlations are high (Issa et al., 2017).

Web mining applications may be used in the monitoring, tracking, and analysis of epidemics in the context of biological disasters. COVID-19, which affects the entire world, is one of the diseases for which social media is employed in the context of biological disasters. The correspondence linked to COVID-19 over a period of around one month was analyzed in a study conducted in China utilizing Weibo, China's most popular social platform. The most time periods of the comments submitted on COVID-19 were gathered using the Seasonal-trend decomposition approach based on Loess (STL), one of the time series analyses. Furthermore, LDA, a Topic extraction algorithm, and Random Forest, a classification model, were merged. Furthermore, the Kernel density analysis indicated the densities of Weibo messages associated with COVID-19 based on geographical locations (Han et al., 2020).

COVID-19 has had numerous results, not just in terms of health, but also in terms of economics. To study these effects, data on agriculture and COVID-19 were acquired from the WEChat and WEibo platforms using a web crawler and text mining. First, data denoising was conducted, followed by word segmentation. LDA was used to create high frequency word groupings and determine the topic. The impact of the COVID-19 pandemic on the agriculture industry was disclosed following these steps (Pan et al., 2020).

The use of social media in disaster-related studies was examined by Said et al. and Zhang et al. in 2019.The studies in the first review article examined were grouped under three main headings. The first title is disaster detection in texts from Disaster and related social media content, the second title is disaster-related visual content analysis in social media, and the third title is disaster detection in satellite images (Said et al., 2019).In the second review study, in which social media was examined for public information and disaster warnings, the social media platforms used in the first place were evaluated, and then the regional distribution of such studies on disasters was examined (Zhang et al., 2019).

Studies conducted in general terms without focusing on any specific disaster are also included in the literature. In a study conducted in 2019, a very complex approach was put forward in which multimedia and satellite images were evaluated together. The disasters that occurred were first questioned with the countries where they occurred, then content analysis was made using social media texts, pictures and videos with the help of crawlers. Coordinate information obtained through tweets and satellite images were matched and presented to the user (Ahmad et al., 2019).

There are studies on the use of social media in disaster management. By using social media platforms such as Facebook and Twitter, the process of revealing previously occurring disasters was carried out (Kankanamge, Yigitcanlar, & Goonetilleke, 2020).

It is observed that the use of social media, especially Twitter, increases remarkably when natural disasters occur. For this reason, NLP techniques have been used in the study on information extraction to be used in future disasters based on the sharings of previously experienced disasters. Sentiment analysis, topical modeling procedures were applied (Karimizarani et al., 2023).

In a study conducted to understand the dynamics of communication when natural disasters occur, calls made by people on the web and on the phone were evaluated according to gender, ethnicity, and educational status (Pourebrahim et al., 2019).

Mobile social media data is used for real-time disaster damage assessment model. Accordingly, among the data sets obtained from Weibo, the damage data is divided into two main headings as the effect of people and the effect of structures. While data such as loss and injury were used to affect people, words such as collapse were used for structures such as buildings, traffic and agriculture. Topical models were created with LDA. The DUTIR dictionary was used for sentiment analysis. This dictionary is mainly used in Chinese natural language processing. Each category is numbered according to emotional intensity (Shan et al., 2019).

During the disaster, classification and location estimation studies were carried out with the help of tweets. With the help of the Twitter API as a data set, the data was obtained for the floods that occurred in the southern and eastern regions of India. In the study, a total of 32400 tweets were examined, the Tweets were collected in English, Hindi and other regional languages. In the study, the event was evaluated under two main headings: low importance and high importance. According to the information of whether there is an address in the tweets of high importance, information is extracted for the rescue teams, and if not, it is determined whether the user has location information with the help of previous tweet records. For this, the Markov model was used and it was planned to be sent to the rescue teams when the location was determined (Singh et al., 2019).

It is also noteworthy that social media data is used in studies for a specific disaster such as flood, earthquake, storm.With the effective use of social media, many information, including disaster information, have begun to be shared by many people who are experts in the subject or not. Posts on Weibo on the flood disaster that occurred after heavy rains in Wuhan in 2016 were examined by Fang and his friends. Hotspot analyzes of the flood-affected areas in Wuhan, the largest metropolis of China, were revealed with the help of Weibo topics. Frequency analysis method was preferred as the method in the study (Fang et al., 2019).

Social media data can be used to decide the severity of the disaster. The tweets shared during the flood disaster in South East Queensland were analyzed. First of all, it was tried to understand the trend topics of the people with descriptive analysis. With content analysis, tweets have been made meaningful. With the help of spatial analyses, regions where the disaster is intense were determined with the help of geotagged tweets (Kankanamge, Yigitcanlar, Goonetilleke, et al., 2020).

In another remarkable study, sentiment analysis was conducted with the help of twitter data in the flood disaster in Jakarta (Saddam et al., 2023).

When the literature is examined, it is seen that the focus of attention of the studies is the studies on storms and other climatic disasters. The reason why this issue is specifically addressed is that climatic disasters are much more common, as stated in the introduction.

In another study in which Twitter was preferred, text and image content were evaluated together. For the study in which the Harvey, Maria and Irma hurricanes were evaluated, sentiment classification and clustering methods were preferred in the evaluation of the text content, and the most shared entity was revealed with topic modeling and Named Entity recognition. Especially in hurricanes, the preferred organizations for aid and the people who were mentioned the most were revealed. Finally, sentiment analysis, tweets and the levels at which people felt disasters were tagged on the map (Alam et al., 2020).

The power of social media can be used to evaluate the impact of the disaster on people after a disaster has occurred. In the study conducted in 2019, the shares of people affected and unaffected by the disaster after Hurricane Sandy were evaluated. Twitter data were analyzed on the topics of faith-based, community, assets and financial. In addition, the correlation between demographic, socioeconomic, spatial attributes and topics in the region was revealed with the Dirichlet regression model (Jamali et al., 2019).

In another study to extract useful and immediate information from social media content, Machine learning and Rule-based classification were used. In the study using Weibo, the heavy storm that occurred in Zhengzhou on July 20 was discussed. As a result of the natural disaster, the city was seriously flooded, floods occurred in the streams and landslides took place. In the disaster, where 380 people were reported dead or missing, the economic loss was quite high (Tchounwou, 2004).

Investigation of Hurricanes Sandy, Harvey and Irma with CNN model using real-time social media data. In the study, in which approximately 5000-15,000 tweets were examined for each hurricane, 5 main topics were examined: warning and advice, damage, information resources, aid and people (Yu et al., 2019).

Another study under the title of special disasters is about earthquakes. The texts, pictures, videos and links shared by Weibo users after the earthquake in Sichuan constitute the main subject of the study. First of all, time-dependent analyzes of the data were made and the temporal intensities of the shares related to the earthquake were revealed. In addition, maps showing the location distribution of the shared information were created. The frequencies of the words from the shared texts were revealed. In the texts shared for the earthquakes that occurred at 3 different times, the information about the earthquake and its results were revealed with sentiment analysis (He et al., 2023).

2. Method

The aim of the study is to evaluate the results of the web mining study conducted in two different languages, Turkish and English.

Data crawling, data pre-processing, topic modelling and sentiment Analysis were done in the study.

2.1. Study Area

In the study carried out on the scale of the world and Türkiye, web pages were crawled according to both scales.

2.2. Data Set

The investigation made use of Wikipedia data. Some of the word titles were derived from the most common natural disasters in the world and in Türkiye. As a result, two distinct content analyses were carried out, one in Turkish and one in English (Table 1).

Table 1. Query words

Query (TR)	Query (EN)
Deprem	Earthquake
Afet	Disaster
Fay Hattı	Fault line
Yağmur	Rain
Fırtına	Storm
Dolu	Hail
Heyelan	Landslide
Toprak	Soil
Toprak Kayması	Mudslide
Kaya Düşmesi	Rock fall
Pandemi	Pandemic
Corona	Corona
Veba	Plague
Sel	Flood

2.3. Method

2.3.1. Data Crawling

Data crawling is a process of extracting data from various web sources. Crawling data is quite similar to what major search engines do. Data crawling is a technique for identifying web links and extracting information from them.

2.3.2. Data Preprocessing

Transformation, Tokenization, filtering can be used in this stage.

Transformation: In this section, lower keys, parse HTML and remove URL operations are done.

Tokenization: At this stage, word punctuation, regular expression and extraction of data showing only word characteristics were performed.

Filtering: This stage consists of detecting and creating stop words in order to extract Turkish words, and filtering punctuation marks and remove numerical information if you don't need.

2.3.3. Topic Modeling

Topic modeling is a statistical modeling technique that employs unsupervised Machine Learning to discover clusters or groupings of related terms within a body of text. This text mining method understands unstructured data by using semantic structures in text rather than predefined tags or training data. Latent Dirichlet Allocation (LDA) is a topic model that is used to assign text in a document to a certain topic.

3. Results

3.1. Preprocessing

Wikipedia was preferred in the study. 5 articles per query in Turkish Wikipedia and 3 articles in English Wikipedia were examined in order to make the process faster for this mini study.

In the study, both Turkish and English Wikipedia web pages were obtained as a result of the disaster words queries.

According to the search results created by using the query words in table, a total of 79 articles were found in Turkish searches and a total of 59 articles in English web sites. As a result of the pre-processing, word clouds were created. Frequency of word clouds in Turkish is 294, and 2419 in English (Figure 1).

a. Turkish Wikipedia Disaster Results

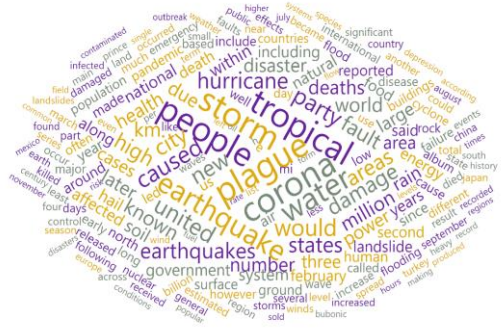

b. English Wikipedia Disaster Results

Figure 1. Word Cloud Results After preprocessing

3.2. Topic modeling Results

In addition, in the study, topic determination was made with the help of word frequencies according to the LDA (Latent Dirichlet allocation). LDA is a particularly popular method for fitting a topic model. 10 different topics have been determined (Figure 2).

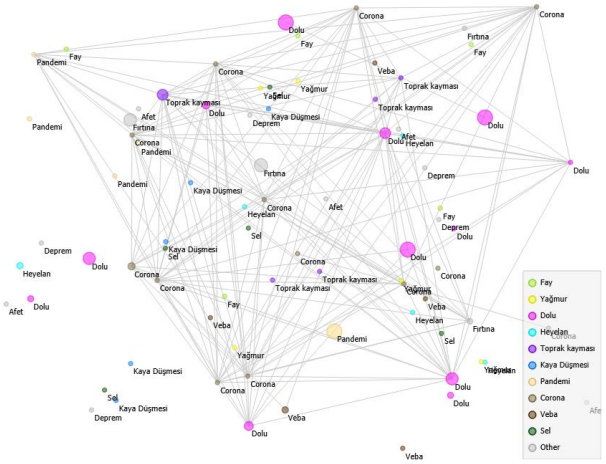

a. Topic 2 and Query Results of Turkish Wikipedia

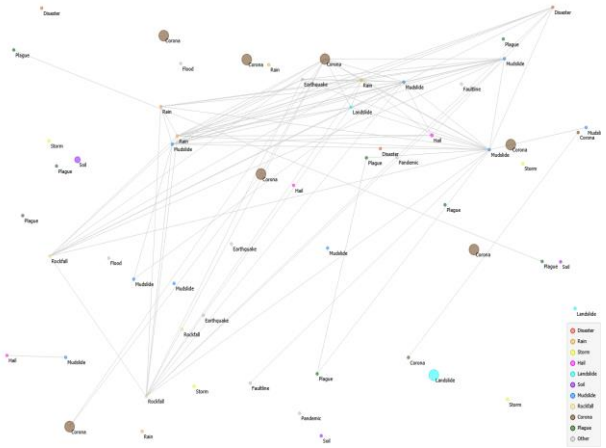

b. Topic 3 and Query Results of English Wikipedia

Figure 2. Topic modeling results

4. Conclusion

Since the study is only for Wikipedia data, it contains more academic information. Therefore, the results obtained should be improved, even if they are not worthless. In such studies, other platforms such as twitter and news, which show much more variability, may be preferred. However, supporting local data with this type of data can provide many advantages for both the government and local governments in the management of disasters.

Acknowledgement

The open source software Orange Data Mining and free information resource Wikipedia were used by the author. Thank you to both supporters.

References

Ahmad, K., Pogorelov, K., Riegler, M., Conci, N., & Halvorsen, P. (2019). Social media and satellites: Disaster event detection, linking and summarization. Multimedia Tools and Applications, 78(3), 2837–2875. https://doi.org/10.1007/s11042-018-5982-9

Alam, F., Ofli, F., & Imran, M. (2020). Descriptive and visual summaries of disaster events using artificial intelligence techniques: Case studies of Hurricanes Harvey, Irma, and Maria. Behaviour & Information Technology, 39(3), 288–318. https://doi.org/10.1080/0144929X.2019.1610908

Duan, H. K., Vasarhelyi, M. A., Codesso, M., & Alzamil, Z. (2023). Enhancing the government accounting information systems using social media information: An application of text mining and machine learning. International Journal of Accounting Information Systems, 48, 100600. https://doi.org/10.1016/j.accinf.2022.100600

Fang, J., Hu, J., Shi, X., & Zhao, L. (2019). Assessing disaster impacts and response using social media data in China: A case study of 2016 Wuhan rainstorm. International Journal of Disaster Risk Reduction, 34, 275–282. https://doi.org/10.1016/j.ijdrr.2018.11.027

G. Almatar, M., Alazmi, H. S., Li, L., & Fox, E. A. (2020). Applying GIS and Text Mining Methods to Twitter Data to Explore the Spatiotemporal Patterns of Topics of Interest in Kuwait. ISPRS International Journal of Geo-Information, 9(12), 702. https://doi.org/10.3390/ijgi9120702

Hameed, A. Z. (2023). A hybrid Fifth Generation based approaches on extracting and analyzing customer requirement through online mode in healthcare industry. Computers and Electrical Engineering, 106, 108550. https://doi.org/10.1016/j.compeleceng.2022.108550

Han, X., Wang, J., Zhang, M., & Wang, X. (2020). Using Social Media to Mine and Analyze Public Opinion Related to COVID-19 in China. International Journal of Environmental Research and Public Health, 17(8), 2788. https://doi.org/10.3390/ijerph17082788

He, W., Yuan, Q., & Li, N. (2023). Research on the Characteristics of Internet Public Opinion and Public Sentiment after the Sichuan Earthquake Based on the Perspective of Weibo. Applied Sciences, 13(3), 1335. https://doi.org/10.3390/app13031335

Issa, E., Tsou, M.-H., Nara, A., & Spitzberg, B. (2017). Understanding the spatio-temporal characteristics of Twitter data with geotagged and non-geotagged content: Two case studies with the topic of flu and Ted (movie). Annals of GIS, 23(3), 219–235. https://doi.org/10.1080/19475683.2017.1343257

Jamali, M., Nejat, A., Ghosh, S., Jin, F., & Cao, G. (2019). Social media data and post-disaster recovery. International Journal of Information Management, 44, 25–37. https://doi.org/10.1016/j.ijinfomgt.2018.09.005

Kankanamge, N., Yigitcanlar, T., & Goonetilleke, A. (2020). How engaging are disaster management related social media channels? The case of Australian state emergency organisations. International Journal of Disaster Risk Reduction, 48, 101571. https://doi.org/10.1016/j.ijdrr.2020.101571

Kankanamge, N., Yigitcanlar, T., Goonetilleke, A., & Kamruzzaman, Md. (2020). Determining disaster severity through social media analysis: Testing the

methodology with South East Queensland Flood tweets. International Journal of Disaster Risk Reduction, 42, 101360. https://doi.org/10.1016/j.ijdrr.2019.101360

Karimiziarani, M., Shao, W., Mirzaei, M., & Moradkhani, H. (2023). Toward reduction of detrimental effects of hurricanes using a social media data analytic Approach: How climate change is perceived? Climate Risk Management, 39, 100480. https://doi.org/10.1016/j.crm.2023.100480

Pan, D., Yang, J., Zhou, G., & Kong, F. (2020). The influence of COVID-19 on agricultural economy and emergency mitigation measures in China: A text mining analysis. PLOS ONE, 15(10), e0241167. https://doi.org/10.1371/journal.pone.0241167

Pourebrahim, N., Sultana, S., Edwards, J., Gochanour, A., & Mohanty, S. (2019). Understanding communication dynamics on Twitter during natural disasters: A case study of Hurricane Sandy. International Journal of Disaster Risk Reduction, 37, 101176. https://doi.org/10.1016/j.ijdrr.2019.101176

Saddam, M. A., Dewantara, E. K., & Solichin, A. (2023). Sentiment Analysis of Flood Disaster Management in Jakarta on Twitter Using Support Vector Machines. Sinkron, 8(1), 470–479. https://doi.org/10.33395/sinkron.v8i1.12063

Said, N., Ahmad, K., Riegler, M., Pogorelov, K., Hassan, L., Ahmad, N., & Conci, N. (2019). Natural disasters detection in social media and satellite imagery: A survey. Multimedia Tools and Applications, 78(22), 31267–31302. https://doi.org/10.1007/s11042-019-07942-1

Shan, S., Zhao, F., Wei, Y., & Liu, M. (2019). Disaster management 2.0: A real-time disaster damage assessment model based on mobile social media data—A case study of Weibo (Chinese Twitter). Safety Science, 115, 393–413. https://doi.org/10.1016/j.ssci.2019.02.029

Singh, J. P., Dwivedi, Y. K., Rana, N. P., Kumar, A., & Kapoor, K. K. (2019). Event classification and location prediction from tweets during disasters. Annals of Operations Research, 283(1–2), 737–757. https://doi.org/10.1007/s10479-017-2522-3

Statista (2023), (https://www.statista.com/statistics, Access Date: 10 June, 2023

Tchounwou, P. (2004). Environmental Research and Public Health. International Journal of Environmental Research and Public Health, 1(1), 1–2. https://doi.org/10.3390/ijerph2004010001

Woo, H., Cho, Y., Shim, E., Lee, K., & Song, G. (2015). Public Trauma after the Sewol Ferry Disaster: The Role of Social Media in Understanding the Public Mood. International Journal of Environmental Research and Public Health, 12(9), 10974–10983. https://doi.org/10.3390/ijerph120910974

Yu, M., Huang, Q., Qin, H., Scheele, C., & Yang, C. (2019). Deep learning for real-time social media text classification for situation awareness – using Hurricanes Sandy, Harvey, and Irma as case studies. International Journal of Digital Earth, 12(11), 1230–1247. https://doi.org/10.1080/17538947.2019.1574316

Zhang, C., Fan, C., Yao, W., Hu, X., & Mostafavi, A. (2019). Social media for intelligent public information and warning in disasters: An interdisciplinary review. International Journal of Information Management, 49, 190–207. https://doi.org/10.1016/j.ijinfomgt.2019.04.004

6th Intercontinental Geoinformation Days

igd.mersin.edu.tr

Defining the specific weights of morphometric indicators of relief for the evaluation of the ecological-geomorphological condition: A case study of the Eastern part of the Kura depression

Gasimov Jeyhun Yashar *[1]

[1] *Institute of Geography named after academician H. A. Aliyev Ministry of Science and Education, Baku, Azerbaijan*

Keywords
Morphometric indicators
Correlation
AHP
Zoning,
GIS

Abstract

Morphometric indicators of the relief (horizontal and vertical fragmentation, hypsometry, slope), which are an integral part of the environment, play a major role in assessing the ecological-geomorphological condition in the territory, and quantitatively assessing its morphology. For this reason, the morphometric quantitative indicators of the relief of the territory were divided into gradations expressing the degree of ecological-geomorphological condition and evaluated on an 8-point scale, and the correlation coefficients were calculated, expressing the relations between them. The binary comparison matrix was constructed using the analytical hierarchical process method. Using mathematical formulas, weights, that reflect the influence of morphometric indicators in the formation of ecological-geomorphological condition in the territory, were calculated: average slope – 47.9%, horizontal fragmentation – 23.9%, vertical fragmentation – 18.8%, and hypsometry – 9.4%. At the final stage, an integrated map of geomorphological risks of the territory was compiled using GIS technology, taking into account the specific weights of morphometric indicators, expressed as a percentage. On the map of ecological-geomorphological condition of the assessed territory on an 8-point scale, four regions were identified: low (1-2 points), moderate (3-4 points), medium (5-6), and high (7-8 points) risk zone.

1. Introduction

The relief of the earth's surface, which plays an important role in the creation of the environment (Khalilov 2010, Khalilov and Abushova 2014), is one of the leading natural components of the geographic stratum (Kurlovich 2012) and the basic element of the human ecosystem (Veselova 2008). The dynamics of the development of endogenous and exogenous processes of relief formation and their interaction (Timofeev 1972) which create a ecological-geomorphological condition, is reflected in the quantitative morphometric indicators of the relief, establishing the presence or absence of links between the factors and conditions of formation and its morphological appearance, commensurability and spatial coincidence of structural and orographic elements (Alizade and Tarikhazer 2015a,b, Kharchenko 2020) In general, morphological, genetic, age, morphodynamic, morphometric and other quantitative and qualitative characteristics of the terrain determine the ecological condition of the territory under study. When ecological-geomorphological mapping and assessment of the ecological state, it is more expedient to take the morphometric indicators of the relief, since they reflect the statistical and quantitative characteristics of the relief (Tanriverdiyev and Gasimov 2017, Gasimov 2019).

According to the scheme of geomorphological zoning of the territory of the Republic of Azerbaijan, the object of study consists of Shirvan, Southeast Shirvan, Kurboyu, Mugan, Salyan geomorphological zones of Kur-Araz lowland sub-region, Langabiz-Alat, Harami zones of Ajinohur-Jeyranchol foothills sub-region and Mil, Garabagh zones of Lesser Caucasus sloping plains sub-region (Shirinov 1973, Alizade et al. 2014, Gasimov 2021).

* **Corresponding Author**

*(jeyhungasimov@mail.ru) ORCID ID 0000-0001-7516-9319

Cite this study

Yashar, G. J. (2023). Defining the specific weights of morphometric indicators of relief for the evaluation of the ecological-geomorphological condition: A case study of the Eastern part of the Kura depression. Intercontinental Geoinformation Days (IGD), 6, 341-344, Baku, Azerbaijan

2. Method

When assessing the ecological and geomorphological conditions, the following morphometric indicators were taken in the East Kura depression: horizontal fragmentation as a result of long-term work of linear erosion, vertical fragmentation showing the degree of vertical tectonic uplift and arid-denudation processes, hypsometry, which is the statistical distribution of absolute height in general and its spatial distribution over the territory, the average slope, which plays an important role in the development of exodynamic and gravitational processes.

To calculate and map the horizontal fragmentation of the relief in the ArcGIS 10.2 program, a geospatial database of linear erosional landforms (modern and ancient river valley, ditches, ravine-gully network) was created based on the interpretation of satellite images (Landsat-8 OLI, Google Sattelite, Bing Image, ESRI Basemap and topographic maps at a scale of 1:100,000). When determining the average slope, vertical fragmentation and hypsometric levels in the Eastern Kura depression, a digital elevation model (SRTM - Shutle Radar Topographic Mission) was used, which is the processed results of a radar topographic survey and has a resolution of 28 m.

When assessing the ecological-geomorphological condition in the study area, correlation coefficients between morphometric factors (average slope, horizontal and vertical dissection, and hypsometry) the specific weights of these individual indicators (Gasimov 2022, Gasimov 2023), were calculated for the first time using the method of analytical hierarchical process (Saaty 1987).

At the final stage, using ArcGIS 10.2 (ArcMap - Spatial Analyst - Weighted Overlay), an integrated map of the ecological and geomorphological assessment of the territory was prepared, taking into account the specific weight of morphometric indicators.

3. Results and Discussion

The slope of the relief is an important morphometric indicator that affects the intensity of slope processes, the energy of the relief, the development of slopes, solar radiation, the circulation of substances, and ecogeomorphological conditions in general (Kuliyev 2010). The slope of the surface also determines the degree of dissection of the relief - an indicator of vertical and horizontal fragmentation. The intensity of denudation directly depends on the slope of the surface. That is, the rate of erosion on slopes and the movement of erosive materials depends on a number of factors (lithological composition, climate, impact, etc.), including slope slope (Simonov et. al. 1988).

The territory of the eastern part of the Kura Depression is less horizontally dissected. First of all, this is due to the poor development of the hydrographic network of the region, which is characterized by arid climatic conditions. The surface of the terrain is mainly divided by the Kura and Araz rivers and their ancient and modern tributaries, oxbow lakes, and a network of ravines. There is also an increase in the natural horizontal fragmentation in the foothills and lowlands behind a well-developed network of ravines and gorges.

Judging by the values of the vertical fragmentation, one can put forward a certain opinion about the intensity of endogenous and exogenous processes in a given territory. For this reason, the values of vertical fragmentation, expressed as relative (difference in extreme heights) or average heights, depend on the amplitude of vertical (rising and descending) tectonic movements and the intensity of erosion-denudation processes (Piriyev 1986). As we approach the foothills of the Greater and Lesser Caucasus, a gradual increase in vertical fragmentation is observed due to an increase in absolute heights.

The East Kura depression is inclined towards the course of the Kura River. Due to this, its height decreases from west to east to 200 m, 100 m, 20-35 m, 0 m and -25-27 m. Relief hypsometry determines the morphology of lowlands, the degree of dissection, the course of exogenous processes, microclimate conditions, the formation of soil and vegetation, and affects the location and productivity of agricultural lands.

The determination of the degrees of relevance according to the mentioned scale in the method of analytical hierarchical process is based on the personal choice of the expert (researcher). In our opinion, such an approach is subjective and may lead to certain errors in the calculation of the specific weights of individual factors. Based on these considerations, we put forward and applied the initiative to take into account the correlation coefficients between these factors when determining the degree of correlation of individual factors on the indicated scale. In fact, for each of the 4 parameters, the weight coefficient is proportional to the average value of the coefficient of linear correlation of the values of one parameter to all the others. As a result, the higher the average value of the correlation coefficient, the more the parameter has weight and the more it affects the final tension value. Thus, our approach, in our opinion, makes it possible to obtain more accurate results when calculating the specific weights of individual factors by applying the method of multi-criteria analysis.

In morphometric risk assessment, the calculated correlation coefficient between horizontal fragmentation and hypsometry was 0.58, between horizontal and vertical fragmentation, 0.63, between horizontal fragmentation and mean slope, 0.65, and a moderate relationship was found. Accordingly, among the morphometric indicators mentioned above in the binary comparison matrix constructed using the method of analytical hierarchical process, the significance value was estimated as 2 - “slightly more important than the same degree”. The correlation coefficient between mean slope and hypsometry is estimated to be high and equal to 0.71, between vertical fragmentation and hypsometry is 0.74, mean slope and vertical fragmentation is 0.81. Mutual significance between them was rated as “slightly more important than important” with an absolute value of 4.

In our study, the consistency coefficient (CI) is 0.086 with four morphometric parameters (n = 4), the random instability coefficient (RI) is 0.9, and the consistency ratio

(CR) is 0.096, which satisfies the condition (CR < 0.1) on the accuracy of the binary significance matrix between morphometric parameters (Table 1).

Table 1. Binary matrix based on morphometric indicators

M*	*A**	*B**	*C**	*D**	*W**	*W*, %
*A**	1	2	2	2	0.54	54.0
*B**	0.5	1	4	4	0.28	28.0
*C**	0.25	0.25	1	4	0.13	13.0
*D**	0.5	0.25	0.25	1	0.05	5.0
∑*	2.25	3.5	7	11	1	100
*Λ**	4.257					
*CI**	0.086					
RI	0.9					
*CR**	0.096					

*M – morphometric indicators, A – horizontal fragmentation, B – vertical fragmentation, C – hypsometry, D- mean slope, W – special weights, ∑- sum of values, Λ – constant, CI- consistency coefficient, RI- random instability coefficient, CR- consistency ratio.

Based on the assessment of ecological-geomorphological condition on an 8-point scale (Figure 1), four zones were identified according to the morphometric indicators of the relief in the Eastern Kura depression: weak (1-2 points), moderate (3-4 points), medium (5-6 points) and high (7 8 points) tension zones.

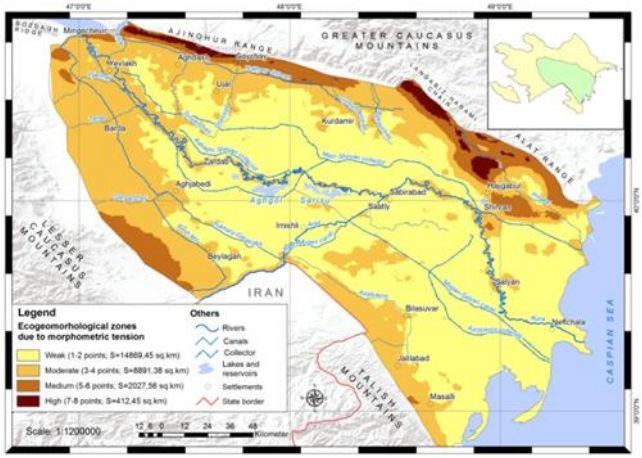

Figure 1. Ecogeomorphological zoning map of eastern Kura depression due to morphometric tension

Territories with weak tension zones (14866.87 sq.km; 56.75%) cover plains (0–1°) with weak erosion and intensive development of accumulative processes, except for the inner heights of the Eastern Kura depression. Against the background of general accumulation, eolian processes, salinization, swamping and flooding developed in the region. Zones of moderate tension (8889.843 sq.km; 33.94%) cover alluvial, alluvial-proluvial and foothill deluvial, proluvial-deluvial plains along the Kura and Araz rivers. The dissection of the relief within the area was caused by gully erosion and moderate tectonic uplift. The medium (2027.213 sq.km; 7.74%) and high (412.379 sq.km; 1.58%) tension zones are located mainly in the northern and northeastern parts of the structural-denudation ranges and ridges of depressions, in the sloping foothills of the Mil Plain in the southwest. Intense tectonic movements and intense arid-denudation processes in these areas led to a high degree of dissection of the relief, as a result, unsuitable territories for agricultural activity appeared that would cause greater damage to the crop, the so-called "badlands" (Figure 1).

4. Conclusion

An average correlation was found between horizontal and vertical fragmentation, horizontal fragmentation and hypsometry, horizontal fragmentation and average slope, as well as a high correlation between vertical fragmentation and hypsometry, average slope and vertical fragmentation, average slope and hypsometry. Significance between horizontal and vertical fragmentation, horizontal fragmentation and hypsometry, horizontal fragmentation and mean slope, taking into account the correlation coefficients, was assessed as “slightly more important than the same degree”, between vertical fragmentation and hypsometry, mean slope and hypsometry, mean slope and vertical fragmentation was rated as "slightly more important than more important." During the ecological-geomorphological assessment, special weights (weight coefficients) were calculated expressing the influence of the listed morphometric indicators in the occurrence of geomorphological risk in the territory: horizontal fragmentation - 54.0%, vertical fragmentation - 28.0%, hypsometry - 13.0%, and mean slope - 5.0%,

In general, an increase in ecological-geomorphological tension is observed due to the increase of morphometric quantitative indicators in the study area, going to the foothills of the Greater and Lesser Caucasus, to the heights within the depression.

References

Alizade, E. K., Tanriverdiyev, X. K., Khalilov, H. A. et al. (2014). Geomorphological zoning. Geography of the Republic of Azerbaijan: in 3 volumes, v 1. Physical geography. Baku: Europe, 127-132.

Alizade, E. K., & Tarikhazer, S. A. (2015a). Ecogeomorphological danger and hazards at Greater Caucasus (in limits of Azerbaijan). M.: Maks Press, 208 p.

Alizade, E. K., & Tarikhazer, S. A. (2015b). Modern eco-geomorphological problems of Azerbaijan. Proceedings of the Azerbaijan Geographical Society, Geography and natural resources. 1, 4-11.

Gasimov, J. Y. (2019). Ecogeomorphological assessment of the Kura-Araz lowland and the surrounding areas by morphometric factors. Innovative approaches in the modern science: Proceedings of XLVIII international scientific-practical conference. Moscow: 12(48), 36-42.

Gasimov, J. Y. (2021). Ecogeomorphological zoning of the Kura-Araz lowland and the surrounding areas by morphometric factors. Proceedings of the Azerbaijan Geographical Society, Geography and natural resources. 13, 40-45.

Gasimov, J. Y. (2022). Ecogeomorphological zoning of the Kura-Araz lowland and adjacent territories based on

complex factors. Materials of the XXV International Scientific Symposium. on the subject of "Civilizational bridges between people and cultures". Kiev: Kafkars Education Publications, 187-190.

Gasimov, J. Y. (2023). The application of Geographic Information Systems in ecological-geomorphological researches (Case study of Kura-Araz plain and surrounding areas). Materials of the republican scientific-practical conference on the subject of "XXI century: Infrastructure of Geospatial data and space Information. Innovations". Baku, 6-7th december, 2022, 68-74.

Khalilov, H. A. (2010). Environmental formation function of relief in the Talysh mountain system (ecogeomorphological aspect of research). Proceedings of Azerbaijan National Academy of Sciences, The Sciences of Earth, 2, 24-27.

Khalilov, H. A., & Abushova, S. N. (2014). Morphometric method of ecogeomorphological estimation relief of the of the Azerbaijan Republic (On example between river of Khram-Zayam). Geographical Bulletin of PSU. 4(31), 17-21.

Kharchenko, S. V. (2020). New Challenges of Geomorphometry and Automatic Morphological Classifications in Geomorphology. Geomorphologiya (Geomorphology RAS). 2020. No. 1. P. 3–21. https://doi.org/: 10.31857 / S043542812001006X

Kuliyev, R. Y. (2010). Angles of relief surface slopes and assessment of ecogeomorphological stress of the mountainous regions of the Azerbaijan Republic. News of Baku University. Series of natural sciences. 3, 154-159.

Kurlovich, D. M. (2012). Computer modeling of morphometric indicators of the relief of Belarus. Problems of nature management: results and prospects. Minsk. 301–304.

Piriyev, R. Kh. (1986). Methods of morphometric analysis of the relief (on the example of the territory of Azerbaijan. Baku: Elm, 114 p.

Saaty, R. W. (1987). The Analytical Hierarchy Process. Mathi Modeling. Great Britain. 9, 161-176.

Shirinov, N. Sh. (1973). Geomorphological structure of the Kura-Araks depression (Morphosculptures). Baku: Elm, 215 p.

Simonov, Yu, G., Timofeev, D. A., Ufimtsev, G. F. et al. (1988). Problems of Theoretical Geomorphology. Moscow: Nauka, 255 p.

Tanriverdiev, Kh. K., & Gasimov, J. Y. (2017). Analysis of morphometric factors affecting ecogeomorphological conditions of eastern Kura depression. Proceedings of the Azerbaijan Geographical Society, Geography and natural resources. 1, 6-13.

Timofeev, D. A. (1972). On some geomorphological laws. Geomorphologiya. 2, 3–12.

Veselova, L. K. (2008). Problems of ecological geomorphology of Kazakhstan. Materials of the 30th Plenum of the Geomorphological Commission of the Russian Academy of Sciences. St. Petersburg. 114-115.

6th Intercontinental Geoinformation Days

igd.mersin.edu.tr

Determination of fire susceptible areas and location selection of fire stations by geographical analytical method

Sayed Payamuddin Danish [1], Mevlut Uyan *[2], Mehmet Ertaş [2]

[1]*Konya Technical University, Graduate Education Institute, Konya, Türkiye*
[2]*Konya Technical University, Vocational School of Technical Sciences, Konya, Türkiye*

Keywords
Fire Station
GIS
Network Analysis
Spatial Analysis

Abstract

Fire is one of the biggest disasters that can jeopardize people's life and property safety. In the event of a fire, any delay in firefighting response can result in serious injury or death. First responders need experience, good equipment, communication and teamwork for emergency response. Today, effective response for all emergency teams is achieved through good planning, risk management, comprehensive training and preparation. GIS technology is a powerful tool to improve all aspects of fire brigade systems. This study involves a series of spatial analyses of data for the construction of fire stations in Kabul, Afghanistan, and the relocation of existing fire stations from unsuitable locations to locations where they can respond to fires in a shorter time. The aim of the study is to identify fire-prone areas in Kabul, identify suitable locations for fire stations and create access routes from fire stations to fire trucks.

1. Introduction

Fire incidents cause huge losses of life and property every year all over the world. Failure to provide the necessary coordination between the relevant units at the time of fire, uncertainty of the areas opens to fire, uncertainty of the roads leading to the fire zone, lack of coordination maps and maps indicating which area the fire station belongs to, various difficulties such as traffic density prevent fire prevention and timely intervention.

Due to the presence of worn-out and old buildings in the cities, rapid population growth and irrational growth, the security system of the city also needs to be developed to cover the whole city. The civil war in Afghanistan over the last four decades has destroyed much of its socio-economic infrastructure, one of which is the firefighting stations in Kabul. The difficulties in this regard cause serious problems for the residents of Kabul. It is clear that the current situation directly affects the process of emergency access to fire zones and the performance of the fire brigade in Kabul. Kabul is one of the busiest cities of the country and traffic congestion in this city is known as one of the main difficulties in the performance and actions of the fire brigade and other relevant units to immediately reach the fire zones.

In recent years, rapidly developing information technologies are also used in fire management. With the development of Geographical Information Systems (GIS), better results are obtained in the production of analytical maps. GIS offers very effective analysis possibilities for many disciplines that study spatial phenomena (Uyan and Dursun, 2021). Many spatial decisions problems lead to GIS-based multi-criteria decision analysis (Ertunç and Uyan, 2022). By analyzing large-scale data, GIS can answer spatial questions that can be used in analytical data on urban fires. One of the important factors in fire services in metropolises is the shortening of the time to reach the fire zone. GIS provides a valuable tool to study the spatial structure of transport networks (Sert et al. 2017). This issue should be carefully considered for fire stations and a sufficient number of fire stations should be established to provide fair services to all local residents. By using network methods, spatial analysis and GIS network analysis, possible fire locations and the best location for the fire station and the shortest route to the fire area can be determined.

GIS is a powerful information management system with a unique ability to collect, analyses and visualize location-based information. As most firefighting tasks are spatially based, GIS has emerged as an important

* **Corresponding Author**

(payamdanish@gmail.com) ORCID ID 0000-0002-0988-0804
*(muyan@ktun.edu.tr) ORCID ID 0000-0002-3415-6893
(mertas@ktun.edu.tr) ORCID ID 0000-0002-9458-3395

Cite this study

Danish, S. P., Uyan, M., & Ertaş, M. (2023). Determination of fire susceptible areas and location selection of fire stations by geographical analytical method. Intercontinental Geoinformation Days (IGD), 6, 345-348, Baku, Azerbaijan

component of information platforms built to support firefighting services. In this study, by using network analysis and spatial analysis with the help of GIS, important data were determined for the effective determination of possible fire points, firefighting stations and the areas covered by these stations in Kabul/Afghanistan.

2. Method

2.1. Study area

Kabul Province, located in the central part of Afghanistan, is surrounded by the provinces of Laghman in the east, Kapisa in the northeast, Logar in the south, Parwan in the northwest and Maidan Wardak in the southwest. Geographically, it lies between 34° 8′ 60″ and 34° 54′ 36″ north latitude and 68° 49′ 48″ and 69° 57′ 0″ east longitude. Administratively, Kabul is not only a province, but also a capital city and has 15 districts.

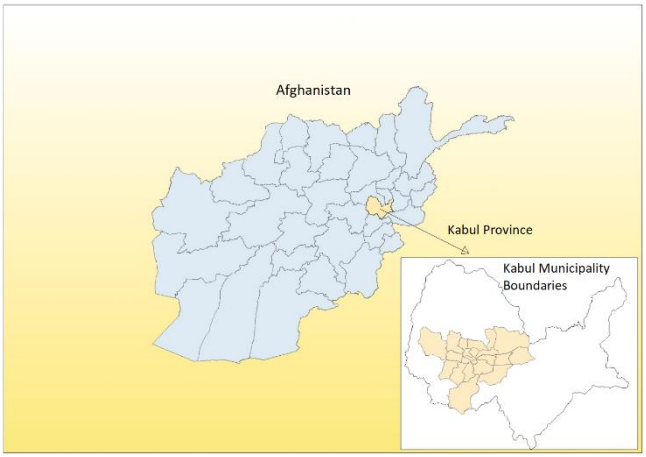

Figure 1. Afghanistan and Kabul city map

2.2. Methodology

The main objective of this study is to propose a model that supports the decision. Decision makers decide on the most suitable locations for fire stations. In this context, the following steps are followed:

- Problem/objective definition (site selection for fire stations)
- Considering the main technical tools to analyses the service area and the optimal route of the fire stations.
- Data collection, preparation and transfer to GIS software.
- Preparation of network analysis maps of roads to reach the fire scene by the shortest route.
- Preparation of density map for traffic congestion in Kabul.
- Proposing a site for new fire stations in Kabul.

In this research, two analytical methods were used to solve the above-mentioned problems.

1. Spatial Analysis
2. Density analysis
3. Network Analysis

3. Results

3.1. Density analysis

We converted our vector data into raster data to better visualize the region and the density of roads in Kabul. In Figure 2, we can better see the areas where traffic density is high and fire trucks cannot easily reach these areas. It is understood that the fire brigade should pay more attention to these areas in order to reach the fire scene immediately or at least normally in case of an accident. Some work has been done to cover these areas in the proposed part of the fire stations and the previous stations have been relocated to suitable places.

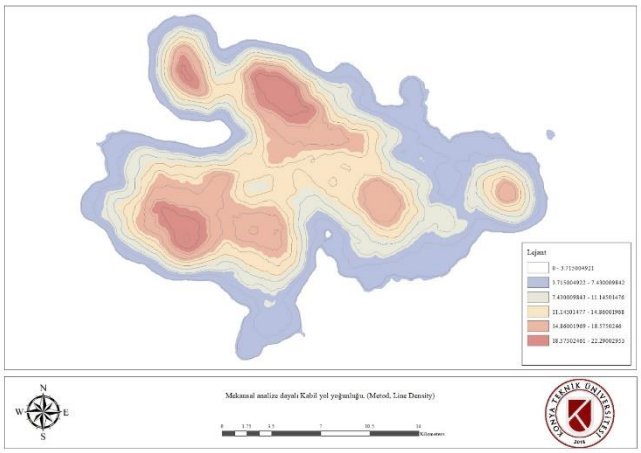

Figure 2. Road density map in Kabul

3.2. Network Analysis

Two methods were used in this research.

3.2.1. Closest facility

Finding the nearest fire station, the nearest police car to the scene, and the nearest shop to a customer's address are examples of nearest facility problems. Once you have found the nearest facilities, you can determine how many to find and whether to move towards or away from them. Once you have found the nearest facilities, you can show the best route to them, for example, you can pinpoint the nearest fire station for the scene. Or we can get help from two or more fire stations at the same time, which is the method used in this study. In the study, the closest and most suitable route from two fire stations to 25 possible fire points was determined.

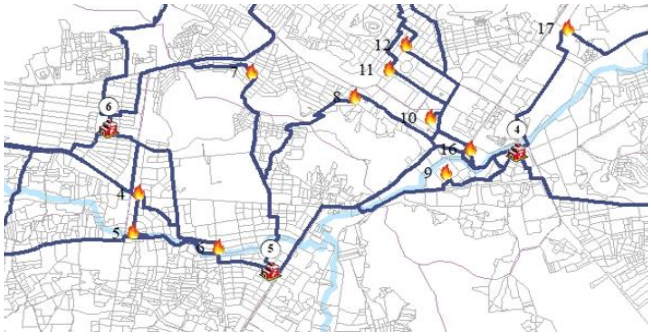

Figure 3. The closest and most convenient routes from the two existing fire stations to 25 possible fire points

3.2.2. Service areas

With this network analysis method, we can find service areas anywhere on the network. The network service area is the area covering all accessible streets, i.e. streets with a certain impedance. For example, the five-kilometer service area of a fire station includes all streets that can be reached within five kilometers of the fire station. Accessibility refers to the ease of travelling to a site. In Network Analyst, accessibility can be measured in terms of travel time, distance or any other impedance on the network. Accessibility assessments help answer basic questions such as which road is blocked by a fire truck or which house is covered by a station.

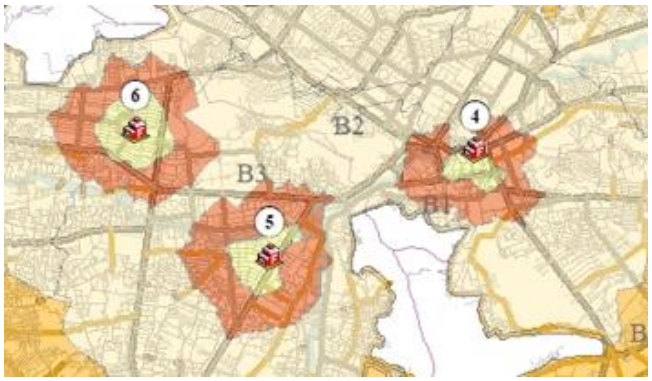

Figure 4. 5 km radius of some existing stations

There are currently six field fire stations in Kabul, but the area covered by each station is not known in advance. In case of fire, the Central Fire Brigade, after receiving information from the fire area, decides which field station to send to the fire area. For studies that consider existing stations, the definition of demand usually starts with an assessment of the effective response area for each of these stations using time or distance limits (Isa et al. 2016). It is clear that the six existing stations cannot cover all 22 districts of Kabul. With the possible locations of fires and fire stations in Kabul identified, the basic analysis of these points using the spatial and network analysis method will be described.

1. Two analyses were performed, one to find the closest facility to the incident and the other to find the shortest route to the incident.

2. For the first analysis, the location of the incident is as important as its location.

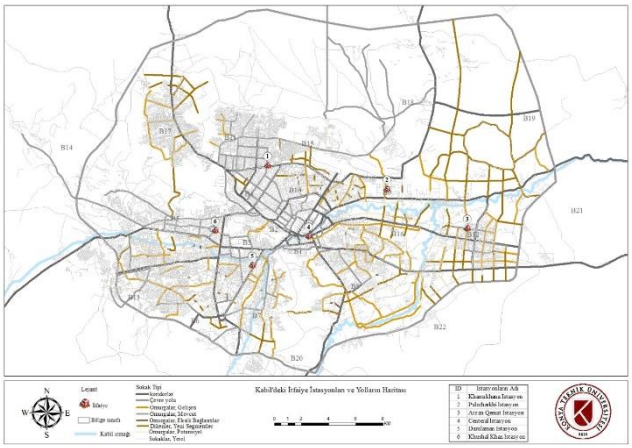

Figure 5. Location of six existing fire stations in Kabul

50 roads with a length of 257.34 kilometers were created with Closest facility for 6 stations. This is too long in terms of firefighting; therefore 5 new fire stations are proposed to cover the entire city of Kabul in a timely manner (Figure 5).

In Figure 6, 5 new stations are proposed in addition to the previous stations. These stations have been determined to reach the farthest points of Kabul city. In Figure 6, as in Figure 5, 50 routes are created from each station to the scene of the incident.

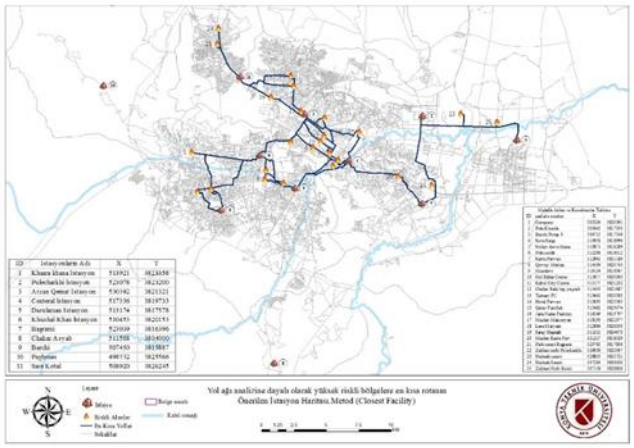

Figure 6. Location of six existing and 5 proposed fire stations in Kabul

50 roads with a length of 204.77 kilometers were created for 11 fire stations. The establishment of 5 new fire stations in Kabul reduced the total length of roads from 257 km to 204 km.

Service Area - for 6 stations

Route analysis can be used to find the optimal route between two locations, while service areas analysis can create a multigene around a point of interest covering all accessible locations and streets within a given km or driving time (Chen 2017). In this section, we tried to determine the areas covered by each existing fire station. The areas covered by each fire station were calculated for 1000 meters, 2000 meters, 5000 meters, 7500 meters.

Figure 7 shows that the coverage range of each station is between 1 km and 7.5 km. The existing areas covered by the six stations were calculated as 538.15 km^2 and subtracted from the total area of the municipal boundary, which is 1030.5 km^2. It is calculated that the existing stations cover 52.24% of the total area. 47.76% of Kabul city up to 7.5 km is not covered by firefighting.

Service Area - for 11 stations

Five new stations have been proposed for increased fire coverage in Kabul, two of which are located in District 20 and one in the most remote district, District 14. The coverage length of these stations is the same as the previous stations. All roads around the 11 stations are marked at distances of 1 km, 2 km, 5 km and 7.5 km.

The existing areas covered by the eleven stations were calculated as 815.49 km^2 and subtracted from the total area of the municipal boundary of 1030.5 km^2. It

was calculated that the existing and proposed stations cover 79.13% of the total area. 20.87% of Kabul city up to 7.5 km is not covered by firefighting. The majority of these areas are areas without an existing road network.

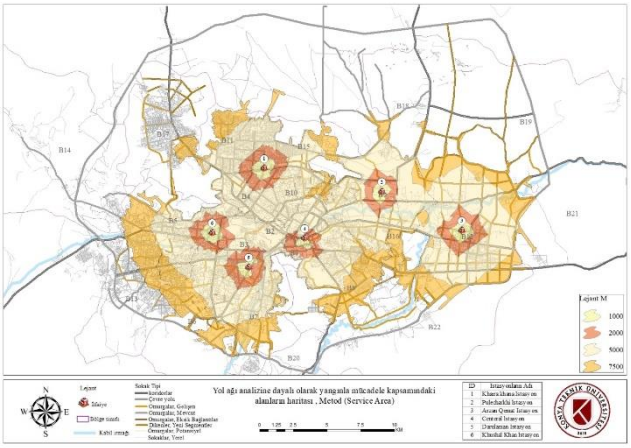

Figure 7. The areas covered by all roads around the six existing stations at distances of 1 km, 2 km, 5 km and 7.5 km

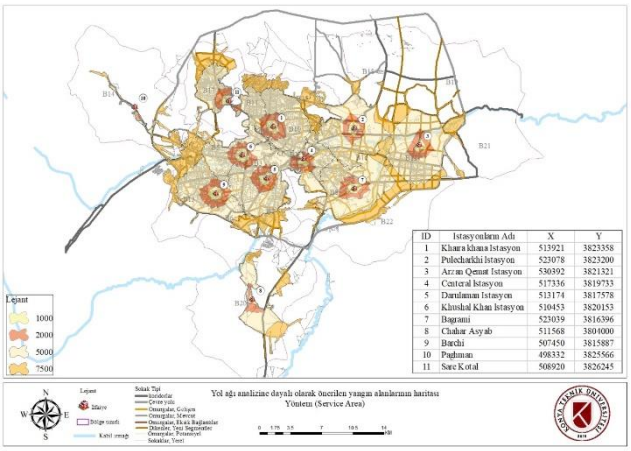

ID	İstasyonların Adı	X	Y
1	Khana khana İstasyon	513921	3823358
2	Pulecharkhi İstasyon	523078	3823200
3	Arzan Qemat İstasyon	530392	3821321
4	Cenferal İstasyon	517336	3819733
5	Darulman İstasyon	513174	3817578
6	Khushal Khan İstasyon	510453	3820153
7	Bagrami	523039	3816396
8	Chahar Asyab	511568	3804000
9	Barchi	507450	3815887
10	Paghman	498332	3825566
11	Sare Kotal	508920	3826245

Figure 8. The areas covered by all roads around the existing and proposed 11 stations at distances of 1 km, 2 km, 5 km and 7.5 km

4. Conclusion

In this research, spatial analysis was used to determine important data for the effective determination of possible fire points, fire extinguishing stations and the areas covered by these stations.

In this study, it can be ensured that all people living in cities and neighbourhoods can benefit from fire brigade services in a fair manner in case of an accident. The spatial analysis tools provided by GIS provide the most reliable analyses for such studies. The results show that a GIS-based system can be effectively used to assist firefighters in managing fires and locating potential firefighters in a short time and assessing the location of existing firefighters.

References

Chen, J. Y. L. (2017). California public electric vehicle charging stations' accessibility to amenities: A GIS network analysis approach.

Ertunç, E., & Uyan, M. (2022). Land valuation with Best Worst Method in land consolidation projects. Land Use Policy, 122, 106360. https://doi.org/10.1016/j.landusepol.2022.106360

Isa, U., Liman, M., Mohammed, M., Mathew, O., & Yayo, Y. (2016). Spatial Analysis of Fire Service Station in Kano Metropolis, Nigeria. IOSR Journal of Humanities And Social Science, 21(9), 45-52. https://doi.org/10.9790/0837-2109014252

Sert, E., Osmanli, N., Eruc, R., & Uyan, M. (2017). Determination of transportation networks base on the optimal public transportation policy using spatial and network analysis methods: a case of the Konya, Turkey. International Journal of Engineering and Geosciences, 2(1), 27-34. https://doi.org/10.26833/IJEG.286034

Uyan, M., & Dursun, A. E. (2021). Determination and modeling of lignite reserve using geostatistical analysis and GIS. Arabian Journal of Geosciences, 14(4), 312. https://doi.org/10.1007/s12517-021-06633-2

6th Intercontinental Geoinformation Days

igd.mersin.edu.tr

Comparison of soil moisture estimation based on LST-NDVI of Landsat 8 images with field soil sampling

Mozhgan Dehghani Aghchekohal [1], Parviz Zeaiean Firouzabadi *[1] Ali Hosingholizade [2]

[1] *Kharazmi University, Geography, Remote sensing and GIS, Tehran, Iran*
[2] *University of Tehran, Geography, Remote sensing and GIS, Tehran, Iran*

Keywords
NDVI
LST
Emissivity
Moisture
Tehran

Abstract

Estimation of soil moisture is very important to soil and agricultural scientists and requires many attentions towards obtaining high and accurate results. So, satellite remote sensing data and images have been extensively used to determining soil moisture especially with the help of Landsat 8 OLI sensor images. In this research, 39 points were sampled for soil moisture at the same time of Landsat 8 satellite overpass. LST and NDVI indices were used for modelling. In order to estimate the accuracy of the results, the soil moisture obtained from the images was compared with the results obtained from the soil science laboratory. The results showed that the estimated moisture by the slope method of the Temperature Vegetation index (TVX) and the percentage of soil moisture measured by use of LST-NDVI indices has a correlation of R2=0.64. The validation results of soil moisture estimation model also showed that the model is able to predict surface soil moisture with RMSE of 3.14. Also, for the study area, the equation %SM=-0.936LST-0.515NDVI+36.7 was proposed to estimate the percentage of soil moisture

1. Introduction

Surface soil moisture and estimating its quantity is an important factor in the cycle of nature (Babaeian et al. 2019). This factor plays a key role in many hydraulic models (Wang et al. 2019). With the help of this role, the direction and extent of drought can be determined in regular intervals in areas with different climates (Palagiri and pal. 2023). Continuous monitoring of soil moisture in agricultural areas effectively helps to formulate policies and determine policies in the field of crop irrigation (Pramanik et al. 2022). Soil moisture is also used to identify areas prone to forest fires (Romano and Ursino. 2020). Therefore, it is important to monitor soil moisture in each region and at different times (Amani et al. 2016). Due to the diversity of environmental factors such as non-uniformity in soil physical characteristics, topography, land vegetation, evaporation and transpiration and rainfall, soil moisture is known as a variable factor in spatial and temporal intervals (Korres et al. 2015). ; Bidgoli et al. 2020). In addition, the relative humidity parameter plays a direct role in cases such as the ability of plants to access water, the penetration of runoff into the ground, the creation of runoff, temperature, control of soil salinity, the determining factor in smart agriculture, the creation and development of watershed plans. Ghazali et al. 2020; Ezenne et al. 2019). Therefore, its accurate, continuous and extensive estimation can be the basis for solving many problems. Since this phenomenon has a very variable spatial and temporal distribution (Mälicke et al. 2020), it is not possible to measure it only with fixed ground stations for all areas and hours, because in many areas there are as many permanent and active stations. There is not enough, and this issue makes relative humidity measurements face many challenges (Su et al. 2014; Acharya et al. 2021). On the other hand, the interpolation of the relative humidity parameter with the help of existing stations cannot solve the accuracy required for research activities and projects that require it. Therefore, it is necessary to have a method that can measure the relative humidity of the soil economically, continuously and for a very long time (Sadeghi et al. 2017; Xu et al. 2018). Remote sensing, having suitable capabilities and many applications in determining relative humidity, has attracted the attention of many researchers (Wang et al. 2020; Li et al. 2016). In this research, Landsat 8 satellite images is used to estimate soil relative humidity using NDVI and LST indices simultaneously.

* **Corresponding Author**

(Dehghanim848@gmail.com) ORCID ID 0000-0000-0000-0000
*(zeaiean@khu.ac.ir) ORCID ID 0000-0001-8407-5605
(a.hosingholizade@ut.ac.ir) ORCID ID 0000 – 0001 – 5286 – 1361

Cite this study

Aghchekohal, M. D., Firouzabadi, P. Z., & Hosingholizade, A. (2023). Comparison of soil moisture estimation based on LST-NDVI of Landsat 8 images with field soil sampling. Intercontinental Geoinformation Days (IGD), 6, 349-352, Baku, Azerbaijan

2. Method

2.1. Study area

The study areas include the research farm of the Faculty of Agriculture of Tehran University with an area of approximately 5 square kilometers from 35 degrees 48 minutes 40 seconds to 35 degrees 47 minutes 49 seconds north and 50 degrees 57 minutes 8 seconds to 50 degrees 57 minutes and 19 seconds east, and the research farm of the Ministry of Water and Soil with an area of approximately 3.5 square kilometers from 35 degrees 47 minutes 26 seconds to 35 degrees 67 minutes 45 seconds north and 50 degrees 56 minutes 17 seconds to 50 degrees and 56 minutes and 13 seconds east in Mohammad Shahr located in the southeast side of Alborz province. The climate of the region is temperate and semi-arid and has harsh winters and hot summers. Also, the region is subject to the Mediterranean Sea in terms of climate and is affected by the climate of this geographical region. The average rainfall of the province reaches 450 mm.

Figure 1. Iran and the study area

2.2. Data

In this research, various data were used, including Landsat 8 satellite image and field sampling of ground surface temperature and soil depth of 5 cm, as well as soil moisture at a depth of 5 cm. The number of selected samples is 39 in order to obtain field information. Then the coordinates of the points on the ground were implemented by two-frequency GPS. To increase the accuracy, sampling was done during the satellite overpass. After sampling, all samples were placed in plastic bag to preserve moisture and transferred to the laboratory to obtain moisture. In the laboratory, the weight of wet soil was measured with an accuracy of 0.01 and then it was placed in an oven with a temperature of 105 degrees Celsius for 24 hours to completely remove the soil moisture. Then the percentage of soil moisture was calculated per following sections.

Table 1. Specifications and image date

Sensor	OLI	Number of bands	11
Date	2016-04-24	Elevation angle	54.86
Local Time	11:30	Azimuth	142.54

$$\text{soil moisture}(\%)=\frac{\text{Wet soil weight}-\text{Dry soil weight}}{\text{Dry soil weight}}\times 100$$

2.3 Estimating temperature from emissivity based on NDVI

After calculating NDVI, a specific emissivity value was given to each NDVI interval based on different formulas presented in Table 3 (Zhang et al. 2006).

$$NDVI=\frac{band\,5-band\,4}{band\,5+band\,4}$$

Table 2. Division of NDVI ranges

NO	NDVI	Emissivity
1	-1<NDVI<-0.185	0.985
2	-0.185<NDVI<+0.157	0.955
3	+0.157<NDVI<0.727	1.0094 + 0.047ln(NDVI)
4	+0.727<NDVI<+0.8	0.99
5	+0.8<NDVI<1	0.99

2.4. Artis method

In order to obtain the temperature by this method, it is necessary to calculate the spectral radiance, the brightness temperature at the surface of the sensor, the normalized differential vegetation index and the emissivity, respectively. This method is also known as the Artis method (Farina, 2012; Feng et al, 2014).

$$L_\lambda=\text{gain}\times DN\times\text{offset}$$

$$L_\lambda=\frac{L_{max}-L_{min}}{Qcal_{max}-Qcal_{min}}\times(DN-Qcal_{min})+L_{min}$$

$$T_{sensor}=\frac{K_2}{Ln(\frac{K_1}{L_\lambda}+1)}$$

$$S_t=\frac{T_{sensor}}{1+(\lambda\times(T_{sensor}/\rho))Ln\varepsilon}$$

S=Kelvin-273.15

Table 3. Calibration coefficients for Landsat 8 thermal bands

Calibration factor	K_1	K_2
OLIBAND10	774.89	1321.08
OLIBAND11	480.89	1201.14

2.5. Extraction of surface soil moisture using temperature and vegetation index (slope of TVX relationship)

In this method, the NDVI index, the brightness temperature of bands 10 and 11, and the temperature of the earth's surface were extracted from the images, and the slope of the TVX relationship between NDVI, the temperature of the earth's surface, and also the values of the brightness temperatures were calculated. The TVX relationship uses the relationship between surface temperature and vegetation index to estimate the volumetric moisture content of the soil surface layer (Thomas et al., 2023).

3. Results

Through the combination of reflective and thermal data, this study has estimated the moisture of the surface layer of the soil according to the state of the natural vegetation of the area. The obtained results indicate the relative position of this method in predicting the moisture of the surface layer of the soil using the slope of TVX in the study area. The TVX method uses the relationship between surface temperature and vegetation index to estimate the moisture content of the soil surface layer. Table 3 shows the amount of RMSE and R^2 (Table 4, Figure 2).

Table 4. The model estimated from examining the relationship between moisture percentage and LST-NDVI method

Model	Equation	R^2	RMSE
LST-NDVI	%SM=-0.936LST 0.515NDVI+36.7	0.64	3.14

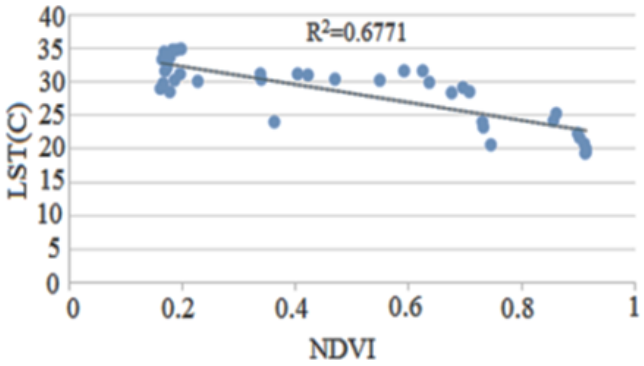

Figure 2. The relationship between land surface temperature and NDVI index in the studied samples

Correlation tests were conducted to determine the relationship between the slope of the TVX relationship and the observed soil moisture data. Figure 4-4 shows the slope regression diagram of the TVX relationship resulting from the correlation of LST and NDVI with the moisture percentage of the surface layer of the soil during the study period (Figure 3).

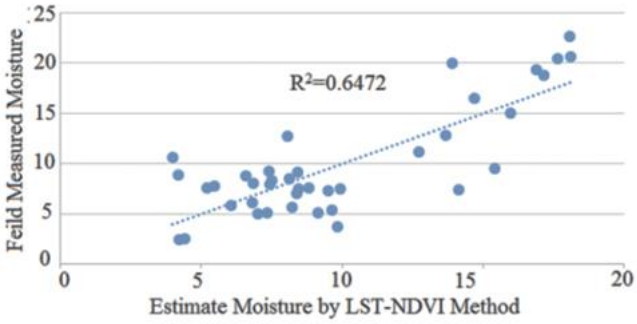

Figure 3. Moisture estimated by the slope method of the TVX relationship (LST-NDVI) against the measured soil moisture percentage

4. Discussion

The results obtained from this research showed that the model derived from the slope of the TVX relationship (LST-NDVI model), the model derived from the linear regression relationship between soil moisture values and NDVI and LST index values have a significant correlation with soil surface layer moisture. And they can provide a good estimation of soil surface layer moisture in arid, semi-arid and moderate semi-arid regions (Figure 4, Table 5 and 6).

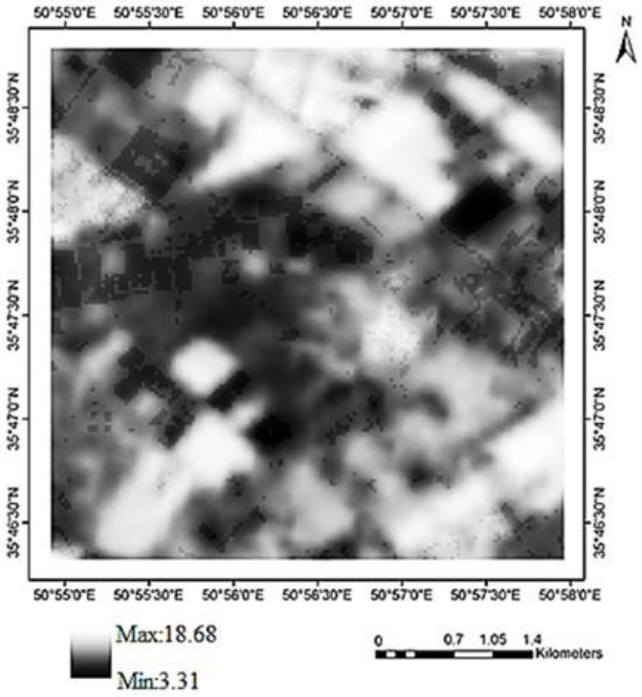

Figure 4. Soil moisture percentage obtained from TVX model (LST-NDVI)

Table 5. The results of the normality test of the indices used in the soil moisture estimation model

N		39
Normal Parameters	Mean	9.95
	Std.Deviation	4.26
Most Differences	Extreme Absolute	0.194
	Positive	0.194
	Negative	-0.090
Kolmogorov-Smirnov Z		1.215
Asymp.sig. (2-tailed)		0.105

Table 6. Validation of methods using T-test

Sig	0.890
T	0.139-

5. Conclusion

The science and technological methods are always transforming and progressing, and every day we see the improvement of the previous methods and the replacement of technology and methods of obtaining data and information from various phenomena on the surface of the earth. New sources of information and optimal methods have also been effective in estimating and measuring soil surface layer moisture. By using Landsat 8 images and performing various stages of data processing and correction, it is now possible to extract indicators such as normalized vegetation difference

(NDVI) and land surface temperature (LST). In order to determine the accuracy of the obtained model, real soil moisture data is needed at the same time as the satellite passes. In this way, by using the indices obtained from Landsat 8 images and the actual values of soil moisture, it is possible to analyze the data in order to obtain soil surface layer moisture estimation models.

References

Acharya, U., Daigh, A. L., & Oduor, P. G. (2021). Machine Learning for Predicting Field Soil Moisture Using Soil, Crop, and Nearby Weather Station Data in the Red River Valley of the North. Soil Systems, 5(4), 57. https://doi.org/10.3390/soilsystems5040057

Amani, M., Parsian, S., MirMazloumi, S. M., & Aieneh, O. (2016). Two new soil moisture indices based on the NIR-red triangle space of Landsat-8 data. International Journal of Applied Earth Observation and Geoinformation, 50, 176-186. https://doi.org/10.1016/j.jag.2016.03.018

Babaeian, E., Sadeghi, M., Jones, S. B., Montzka, C., Vereecken, H., & Tuller, M. (2019). Ground, proximal, and satellite remote sensing of soil moisture. Reviews of Geophysics, 57(2), 530-616. https://doi.org/10.1029/2018RG000618

Bidgoli, R. D., Koohbanani, H., Keshavarzi, A., & Kumar, V. (2020). Measurement and zonation of soil surface moisture in arid and semi-arid regions using Landsat 8 images. Arabian Journal of Geosciences, 13(17), 1-10. https://doi.org/10.1007/s12517-020-05837-2

Ezenne, G. I., Jupp, L., Mantel, S. K., & Tanner, J. L. (2019). Current and potential capabilities of UAS for crop water productivity in precision agriculture. Agricultural Water Management, 218, 158-164. https://doi.org/10.1016/j.agwat.2019.03.034

Ghazali, M. F., Wikantika, K., Harto, A. B., & Kondoh, A. (2020). Generating soil salinity, soil moisture, soil pH from satellite imagery and its analysis. Information Processing in Agriculture, 7(2), 294-306. https://doi.org/10.1016/j.inpa.2019.08.003

Korres, W., Reichenau, T. G., Fiener, P., Koyama, C. N., Bogena, H. R., Cornelissen, T., ... & Schneider, K. (2015). Spatio-temporal soil moisture patterns–A meta-analysis using plot to catchment scale data. Journal of hydrology, 520, 326-341. https://doi.org/10.1016/j.jhydrol.2014.11.042

Li, B., Ti, C., Zhao, Y., & Yan, X. (2016). Estimating soil moisture with Landsat data and its application in extracting the spatial distribution of winter flooded paddies. Remote Sensing, 8(1), 38. https://doi.org/10.3390/rs8010038

Mälicke, M., Hassler, S. K., Blume, T., Weiler, M., & Zehe, E. (2020). Soil moisture: variable in space but redundant in time. Hydrology and Earth System Sciences, 24(5), 2633-2653. https://doi.org/10.5194/hess-24-2633-2020

Palagiri, H., & Pal, M. (2023). Agricultural Drought Assessment Using Satellite-Based Surface Soil Moisture Estimate. In River Dynamics and Flood Hazards (pp. 411-431). Springer, Singapore. https://doi.org/10.1007/978-981-19-7100-6_22

Pramanik, M., Khanna, M., Singh, M., Singh, D. K., Sudhishri, S., Bhatia, A., & Ranjan, R. (2022). Automation of soil moisture sensor-based basin irrigation system. Smart Agricultural Technology, 2, 100032. https://doi.org/10.1016/j.atech.2021.100032

Romano, N., & Ursino, N. (2020). Forest fire regime in a Mediterranean ecosystem: unraveling the mutual interrelations between rainfall seasonality, soil moisture, drought persistence, and biomass dynamics. Fire, 3(3), 49. https://doi.org/10.3390/fire3030049

Sadeghi, M., Babaeian, E., Tuller, M., & Jones, S. B. (2017). The optical trapezoid model: A novel approach to remote sensing of soil moisture applied to Sentinel-2 and Landsat-8 observations. Remote sensing of environment, 198, 52-68. https://doi.org/10.1016/j.rse.2017.05.041

Thomas, J., Gupta, M., Srivastava, P. K., Pandey, D. K., & Bindlish, R. (2023). Development of High-Resolution Soil Hydraulic Parameters with Use of Earth Observations for Enhancing Root Zone Soil Moisture Product. Remote Sensing, 15(3), 706. https://doi.org/10.3390/rs15030744

Su, S. L., Singh, D. N., & Baghini, M. S. (2014). A critical review of soil moisture measurement. Measurement, 54, 92-105. https://doi.org/10.1016/j.measurement.2014.04.007

Wang, C., Fu, B., Zhang, L., & Xu, Z. (2019). Soil moisture–plant interactions: an ecohydrological review. Journal of Soils and Sediments, 19(1), 1-9. https://doi.org/10.1007/s11368-018-2167-0

Wang, Q., Li, J., Jin, T., Chang, X., Zhu, Y., Li, Y., ... & Li, D. (2020). Comparative analysis of Landsat-8, Sentinel-2, and GF-1 data for retrieving soil moisture over wheat farmlands. Remote Sensing, 12(17), 2708. https://doi.org/10.3390/rs12172708

Xu, C., Qu, J. J., Hao, X., Cosh, M. H., Prueger, J. H., Zhu, Z., & Gutenberg, L. (2018). Downscaling of surface soil moisture retrieval by combining MODIS/Landsat and in situ measurements. Remote Sensing, 10(2), 210. https://doi.org/10.3390/rs10020210

6th Intercontinental Geoinformation Days

igd.mersin.edu.tr

High resolution remote sensing data and environmental data for the classification of a square in Rome, Italy

Lorenza Fiumi [*1], **Francesco Atanasio Carolei** [2], **Fabrizio Filiberti** [2], **Marco Torre** [3]

[1] *National Research Council (CNR), INM, Rome, Italy*
[2] *Sysdeco, Rome, Italy*
[3] *National Research Council (CNR) IIA, Rome, Italy*

Keywords
Remote sensing
High resolution
Spaces public
Traffic flow
OBIA method

Abstract

The goal of work is to characterize and quantify the vehicles, with a synoptic vision. With data from the very high resolution Pléiades Neo sensor captured in a public space (square) of the city of Rome, the object-based image analysis (OBIA) method is applied. Traffic flow data expressed as equivalent vehicles/hour and relating to the peak hour of the winter weekday morning, made it possible to calculate the total polluting emissions expressed in g/h, indicative of local air quality conditions in the two study areas. The results achieved, while needing further checks on other areas of study, they have highlighted the validity of method and its large-scale reproducibility for support in urban planning. The work with a multidisciplinary character intends to offer a starting point for reflection on the use of spaces public places of historical architectural value, which over the centuries have seen the conditions worsen accessibility and usability for people of different age groups

1. Introduction

In this work, with a multidisciplinary and original approach, using high spatial resolution satellite data acquired in a public space of the city of Rome, respectively Square Mazzini (Figure 1), we apply a method that will allow:

- validate the usefulness of the data coming from the very high resolution Pléiades Neo sensor for the characterization and quantification of the different vehicles present (parking and transit);
- understand the dynamics of use and reflect on the critical issues in progress, through the results obtained from the processing integrated with punctual data on punctual traffic;
- present an analysis technique that can be reproduced on a large scale which, through the synoptic vision, can help reflect on the use of our heritage of historical architectural value and which can become a valid support for urban planning, aimed at environmental sustainability, preparatory to the development of new technologies and methodologies;
- offer food for thought as well as stimulate and carry on the discussion on the use of public spaces, especially in squares.

Figure 1. Study area , Square Mazzini, Rome, Italy

* **Corresponding Author**

*(lorenza.fiumi@cnr.it) ORCID ID 0000-0001-6720-601X
(e-mail) ORCID ID xxxx – xxxx – xxxx – xxxx
(e-mail) ORCID ID xxxx – xxxx – xxxx – xxxx
(e-mail) ORCID ID xxxx – xxxx – xxxx – xxxx

Cite this study

Fiumi, L., Carolei, F. A., Filiberti, F., Torre, M. (2023). High resolution remote sensing data and environmental data for the classification of a square in Rome, Italy. Intercontinental Geoinformation Days (IGD), 6, 353-356, Baku, Azerbaijan

2. Method

The images used for this study were delivered with geometric processing and with radiometric processing, they have the characteristics indicated in the Table 1, 2.

Table 1. Pléiades Neo data characteristics

Bande	Lunghezza d'onda (µm)	Risoluzione (m)
Deep Blue (VIS)	0,4 – 0,5	1,2
Blue (VIS)	0,45 -0,52	1,2
Green (VIS)	0,53 – 0,59	1,2
Red (VIS)	0,62 -0,69	1,2
Bande (NIR)	0,7 – 0,75	1,2
Neear Infrared (NIR)	0,77- -0,88	1,2
Pancromatico (VIS)	0,45-0,8	0,3

Table 2. Pléiades Neo data characteristics

Altitude Km	Fligh Date	Flight Time
620	16 october 2021	10:06:55

The workflow used is typical of Deep Learning (DL) and other supervised automatic DL approaches. In this case a combination of DL functionality within eCognition Developer and OBIA was used to detect cars with only optical data. In the first phase, some samples were collected for the recognition of cars and buses. The samples were identified in various areas of the image and chosen in different contexts, shapes and colors to guarantee a very high level of variables [Mohammad, 2019; Arch, 2017].

In the second phase of the work, the central phase, it was necessary to generate a Convolutional Neural Networks (CNN) model of DL and train it using the previously collected samples. Subsequently, the model was validated targeting new image data (other areas) [De Maria et al., 2021]. Once validated following the verification of good accuracy, the model was used in production mode and applied to new data. Finally, some samples have been added for the recognition of buses and articulated buses of ATAC (public transport of Rome). Figures 3 and 4 show the results obtained by processing the data with the DL - CNN in eCognition

Figure 2. OBIA-based object detection flowchart

2.1. Traffic flow data

To support the calculations, data on the traffic flow were used (data provided by the Mobility Office of the Municipality of Rome).

Starting from the data on the traffic flow expressed as equivalent vehicles/hour and relating to the peak hour of the winter weekday morning, the following simplifications were made: the category of cars for private transport was considered as the only component of the traffic flows.

As a function of the flows then broken down by power supply category respectively; petrol, diesel, LPG, hybrid, CNG (methane), electric and by environmental class (from Euro 0 to Euro 6), a calculation was made of the emissions for the pollutants: nitrogen dioxide (NO_2), nitrogen monoxide (NOx), Atmospheric particulate less than or equal to 10 µm (PM10) and less than or equal to 2.5 µm (PM2.5) (by power supply category and expressed in mg/h).

3. Results

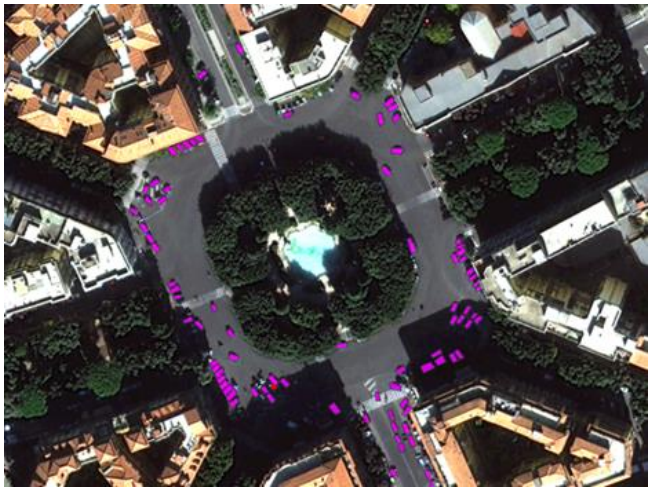

Figure 3. Rome Piazza Mazzini. The processing highlights the cars present in the study area in pink

Figure 4. Rome, Square Mazzini. The processing highlights the total emissions g/h calculated from the traffic flow data

Table 3. Processing results

Square	Car	Car parked	Bus	Total
Square Mazzini	11	78	-	89

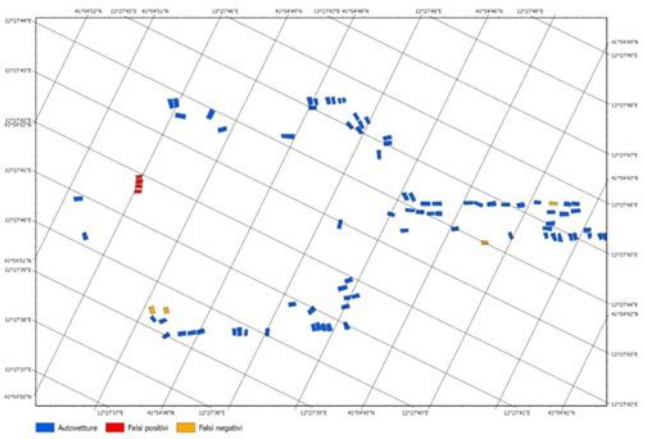

Figure 5. Square Mazzini confusion matrix. The processing shows correctly identified cars in blue, false negatives in yellow (not correctly identified) and false positives in red (wrongly classified as cars)

4. Discussion

The processing of the remote sensing data of Square Mazzini (16,600 m^2) confirms that the asphalted surface destined for traffic corresponds to almost 2/3 of the square and of this, approximately 25% is occupied by car parks located at the edges of both the square and the flowerbed central, delimiting the carriageway to a single direction of travel (Figure 3,4). The processing results in 78 parked cars and 11 in the lane. Although the presence of trees that delimit the central area, shelter from noise, absorb part of the greenhouse gases produced by cars and mitigate the heat island, the square does not offer the ideal conditions to be used appropriately by the inhabitants, declining it towards a condition of residuality. Figure 4 summarizes with the colors the presence of traffic coinciding with the trend of emissions, this reaches the maximum values (red) in the stretch of the square that goes from street Luigi Settembrini towards street Mazzini, discouraging the use of the space central.

In order to have a view that is not limited to just the moment of the acquisition of 16 october 2021, at 10.06, the integration with the data relating to car flows in the study area allows us to have a broader view. The rush hour of traffic in the square is between 7-10 and between 12-13 with a peak between 8-9. The analysis of the data relating to the flows of equivalent vehicles/hour quantifies an average value of 532 vehicles/hour, with maximum peaks at the end of via Settembrini on the square equal to 1132 vehicles/hour [Piano della Mobilità Sostenibile, 2021].

The presence of traffic and the effects due not only to pollution but also to noise represents a powerful obstacle to the usability and perception of the central space, discouraging pedestrian mobility towards the central garden, impoverishing the "social" potential of the central public space.

It would be desirable that the municipal administrations listen to and adapt to these new needs and give a new life to public spaces by equipping them adequately. From a practical point of view, it means making them accessible and usable by people with different needs and abilities. Of course, it is not always easy or obvious to give meaning and functions to historic squares, to make sure that they become places at the service of the community, or to implement effective regeneration strategies over time. The redevelopment interventions should at least try to give (or restore) a role of public space also through the integration of urban facilities that invite users to use them. For example limiting traffic or with slow-moving vehicular traffic where cars adapt to pedestrians and not vice versa, with safe routes and crossings, quality collective equipment such as benches to sit on, games for children, spaces for animals, temporary exhibitions , outdoor entertainment organizations that foster relationships and social relationships and contribute to the construction of a sense of belonging [Lauria, 2017].

5. Conclusion

Through the use of high-resolution remote sensing data from the Pléiades Neo sensor, in this work we have validated the utility of the OBIA method for the characterization and quantification of the different vehicles present (parking and transit); in a square of historic value in Rome. Furthermore, the integration with traffic data has made it possible to identify some critical issues and make a series of considerations on the use of public space.

The method, which can be reproduced on a large scale, once developed and validated in other places, in fact, can be used for environmental audits related to motorized and non-motorized activities, the presence of tourists, the sense of safety and environmental comfort, and more generally to study social phenomena, through the latest high-resolution remote sensing data, in order to inform the decision-making process.

References

Aly, M., & El-Naggar, E. (2018). Determination of optimum segmentation parameter values for extracting building from remote sensing images. Alexandria Engineering Journal, Volume 57, Issue 4 Pages 3089-3097, ISSN 1110-0168, https://doi.org/10.1016/j.aej.2018.10.001

De Maria, M. D., Fiumi, L., Mazzei, M., & Bon, V. (2021). A System for Monitoring the Environment of Historic Places Using Convolutional Neural Network Methodologies. Heritage 2021, 4, 1429–1446. https:// doi.org/10.3390/heritage4030079https://doi.org/10.3390/heritage4030079

ElMikaty, M., & Stathaki, T. (2014). Car detection in high-resolution urban scenes using multiple image descriptors, Proc. Int. Conf. Pattern Recognit., pp. 4299-4304, 2014. Available online: https://ieeexplore.ieee.org/abstract/document/6977449

Fatima, S. A., Kumar, A., Pratap, A., & Raoof, S. S. (2020). Object Recognition and Detection in Remote Sensing Images: A Comparative Study. International Conference on Artificial Intelligence and Signal Processing (AISP), 1-5, https://doi.org/10.1109/AISP48273.2020.9073614

Fiumi, L. (2012). Surveying the roofs of Rome. Journal of Cultural Heritage, 13, 304–313, https://doi.org/10.1016/j.culher.2011.12.003

Ma, L., Li, M., Ma, X., Cheng, L., Du, P. & Liu, Y. (2017). A review of supervised object-based land-cover image classification. ISPRS Journal of Photogrammetry and Remote Sensing, 130 (2017) (2017), pp. 277-293 https://doi.org/10.1016/j.isprsjprs.2017.06.001

Simons, A. (2013). Road transport: new life cycle inventories for fossil-fuelled passenger cars 989 and non-exhaust emissions in ecoinvent v3. The International Journal of Life Cycle Assessment, 1-15, 990 http://dx.doi.org/10.1007/s11367-013-0642-9

Taylor, B. T., Fernando, P., Bauman, A. E., Williamson, A., Craig, J. C., & Redman, S. (2011). Measuring the quality of public open space using Google Earth. American Journal of Preventive Medicine, 40, 105–112, https://doi:10.1016/j.amepre.2010.10.024

Wang, Y. (2014). Research on urban green surveying based on ZY 3 satellite. Engineering of Surveying and Mapping, 23(7), 65-67. https://doi.org/10.19349/j.cnki.issn1006-7949.2014.07.017

Wu, W., & Liu, W. (2018). Remote sensing recognition of residential areas based on GF-4 satellite image. In 2018 Fifth International Workshop on Earth Observation and Remote Sensing Applications (EORSA) (pp. 1-4). IEEE. https://doi.org/10.1109/EORSA.2018.8598622

Zhao, Z. M., Zhou, C., Wang X., & Fu, Q. (2015). Method for extraction of building height information based on ZY-3 image. Remote Sensing of Land and Resources, 03 (2015), 19-24. https://doi.org/10.6046/gtzyyg.2015.03.04

6th Intercontinental Geoinformation Days

igd.mersin.edu.tr

Comprehensive soil erosion risk assessment using remote sensing (on the example of Zangilan region)

Guliyev İsmail Ahliman Oghlu [1], Huseynov Rauf Adalat Oghlu *[1]

[1]*Ministry of Science and Education, İnstitute of Geography, Geography of Land Resources of Azerbaijan, Baku, Azerbaijan*

Keywords
NDVI
USLE
Afforestation
Deforestation
Remote sensing

Abstract

Determining the nature, extent and direction of changes is essential to determine the potential and future direction of ecosystem expansion. The article used GIS to track changes in the ecosystem and compare the results. It has been established that some parameters of the ecosystem have a positive trend, and some parameters have a negative trend. Thus, changes in the area of forest ecosystems due to negative environmental and anthropogenic impacts over different years (1990-2022) were compared. Change detection was determined by remote sensing from satellite images (LANDSAT 4-9 OLI/TIRS C2 L1) within the study area. The area of optimally developed forests decreased by 84.5% (10,838.05 ha). There has been a serious degradation of the currently existing forest area in a negative direction. In addition, a Universal Soil Loss Equation (USLE) was developed based on various geographic parameters (rain kinetic energy, average annual precipitation, soil erosion coefficient, slope length, slope steepness, land use/land cover) and erosion prevention methods a corresponding map was drawn up. The lands of the plains and foothills of the region have undergone all types of degradation (physical, chemical, biological) as a result of military-technical impact. As a result, the need to apply these parameters in the implementation of large-scale projects in the Zangilan administrative region, liberated from occupation, was determined.

1. Introduction

In the last 100-150 years, as a result of uncontrolled deforestation, the process of soil erosion has accelerated, and the unsystematic use of natural fodder lands has led to an intensification of this process. As the anthropogenic impact intensifies, the erosion process accelerates, and the soil formation process develops in a negative direction. Every year in the world, as a result of the erosion process, about 25-40 billion tons of arable soil are destroyed. If the erosion process develops so rapidly, then by 2050 1.5 million/km^2 of arable land will remain unused (Poluetkov, 2003). To assess the actual course of the erosion process, long-term management of soil resources in erosion-prone areas is necessary. Industrial concentration and population growth have led to a significant transformation of geographical components in space and time. All forms of anthropogenic impact (urbanization, mining, wars, etc.) have a negative impact on the environment.

In the selected study area, a 30-year period of occupation and the repetition of a phase of active hostilities led to the destruction of all ecosystems and infrastructure. In this direction, research work is being carried out in different regions of the world (Khrushch et.al. 2023; Ordway 2015). However, the research work carried out in this direction is devoted to the ethical, socio-economic and ethnic consequences of the war (Wirtz, Känel 2017). The effect of war on surrounding ecosystems has been little studied. Baumann (Baumann 2015) notes that as a result of the war, more than 60% of the agricultural land in Karabakh remained unused. Also, 30% of these lands were compensated by new agricultural land. As a result, the pressure on the surrounding areas has increased, pastures have turned into arable land.

2. Method

The study covers the territory of the Zangilan administrative region (70,099,177 ha). The description of the area is given on the basis of a digital elevation model (Figure 1).

* **Corresponding Author**

(mamed.1952@bk.ru) ORCID ID 0009 – 0003 – 1501 – 8852
*(rauf554@bk.ru) ORCID ID 0000 – 0002 – 3900 – 272X

Cite this study

Oghlu, G. I. A., Oghlu, H. R. A. (2023). Comprehensive soil erosion risk assessment using remote sensing (on the example of Zangilan region). Intercontinental Geoinformation Days (IGD), 6, 357-359, Baku, Azerbaijan

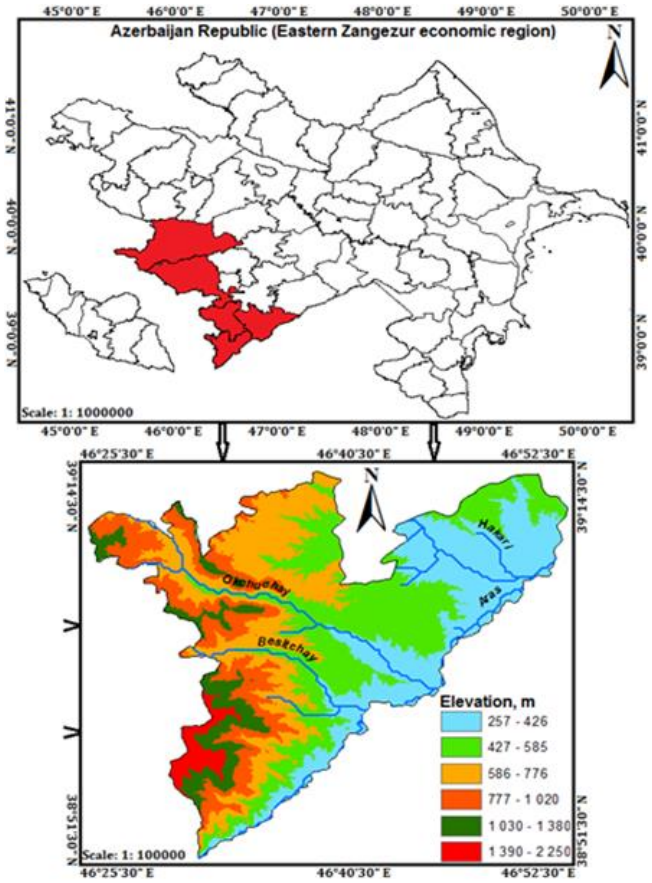

Figure 1. The geographic location of Zangilan district in Azerbaijan

The Universal Soil Loss Equation (USLE) was used to estimate the risk of erosion in the study area (Foster 2008). Universal soil loss equation (USLE) estimates long-term avarage annual rate of erosion on a field slope based on rainfall pattern, soil type, topography, crop system and management practices.

$$A=R\times K\times LS\times C\times P$$

A – is the avarage annual soil loss (tons, ha, year)
R – is the rainfall erosivity, rainfall erosivity is the kinetic energy of raindrops`s impact and the rate of sociated runoff;
K – is the soil erodibility factor, soil erodibility represents the effect of soil properties and soil profile characteristics on soil loss;
LS – is the topographic factor, topographic factors consist of slope lenght and slope steepness. İncrease in the slope lenght L causes increase in erosion due to a progressive accumulation of runoff in the direction of downslope. Increase in slope steepness factor S increase the soil erosion as a result of increasing velocity (SRTM 30 m);
C – is the crop/vegetation management factor, used to the relative effectivness of soil and crop management systems in preventing soil loss (data source: Sentinel-2 Land use/ land cover (10 m).
P – is the practice support, it reflects the effects of practices that will reduce the amount and rate of the water runoff and thus reduce the amount of erosion.

Values obtained from literatures based on the farmers practices. According to the degree of erosion, the assessment was carried out in 5 categories (Table 1).

Vegetation changes are regularly monitored locally and globally using remote sensing. The received multispectral data are involved in research in the form of vegetation indices (NDVİ, EVİ, SAVİ, etc.) (Guha 2018; Li 2011). The Normalized Different Vegetation İndex (NDVİ) is mainly used. NDVI values range from -1 to 1.

Table 1. Soil erosion classification

Level	Soil loss (tons ha^{-1} $year^{-1}$)
Very low erosion	0 – 1
Low	1 – 5
Medium	5 – 10
High	10 – 50
Extreme	>50

Vegetation changes were analyzed through satellite images (LANDSAT 4-5; LANDSAT 8-9 OLİ/TİRS C2 L1) for the years 1990-2022. Coordinates of the center point of the image were 38°54'16.27"N, 46°41'39.66"E

The evaluation of the changes in the vegetation was carried out in 5 categories (Table 2):

Table 2. NDVI classification

NDVİ class	NDVİ value	The greenness level of the vegetation
1	<-0,03	non-vegetation area, open area, waterbody
2	-0,03-0,15	very low dense vegetation
3	0,15-0,25	low dense vegetation
4	0,26-0,35	moderately dense vegetation
5	>0,35	highly dense vegetation

3. Results

On the basis of the universal soil loss equation, soil erosion losses in the study area were calculated. (Table 3).

Table 3. Soil loss

Soil loss, tons, h/yr	Area, ha	Persentage of total, %
0 – 1	32602,89	46,51
1 – 5	6821,867	9,73
5 – 10	4709,621	6,72
10 – 50	16965,96	24,2
50 >	5691,568	8,12
Relative error	3307,271	4,72
Total	70099,177	100

According to the NDVI, the dynamics of the vegetation process by categories was studied, the areas of plots with stable and variable vegetation were calculated (Table 4).

Table 4. Direction of the vegetation process

Changes	Area, ha	Persentage of total, %
No veg.	37303,19	53,2
No veg - veg.	2762,847	3,9
Veg - no veg.	10838,05	15,5
Veg.	19195,09	27,4
Total	70099,177	100

4. Discussion

As a result of 30 years of occupation and 44 days of active war, the ecosystems of the study area were severely damaged, and the integrity of the ecosystem was violated. A soil loss map was developed for the assessment of erosion risk (Figure 2).

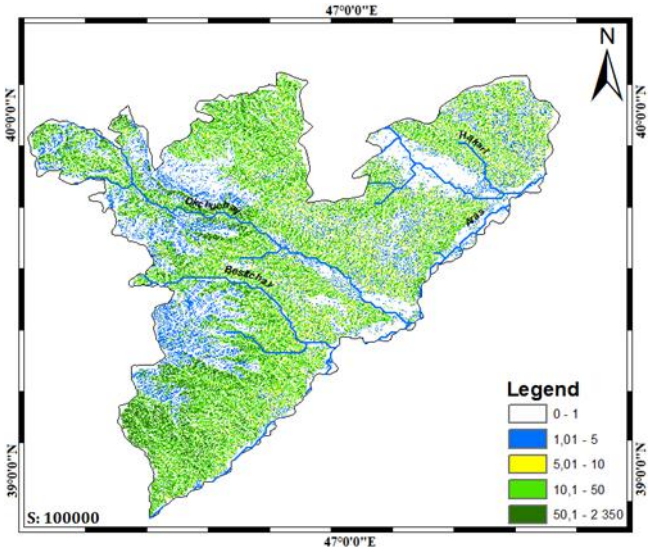

Figure 2. Soil loss equation map (2022)

The ecosystem of the region is sensitive and unstable to the influence of exodynamic processes. There was a serious degradation (physical, chemical and biological) of vegetation, which negatively affected the process of natural regeneration. The direction of transformation reflects a negative trend.

Based on the soil loss equation, it was determined that 43.76% (30,674.42 ha) of the research area has changed in a negative direction. This change was caused by the movement of military equipment, burying of mines, construction of defense fortifications, setting fires, cutting trees.

During the 30-year period of occupation, 10,838.05 hectares of forest area were cut down, and the process of natural regeneration took place on an area of 2762,847 hectares.

5. Conclusion

During the occupation, the area of heavily degraded territories increased by 14.55% (10202.76 ha) in 2022 compared to 1990 in the Zangilan administrative region, and the area of degraded territories at the background level decreased by 14.78% (10357.91 ha). Currently, work to restore the ecological balance should be carried out taking into account the balance between these two classes.

References

Baumann, M., Radeloff, V. C., Avedian, V., & Kuemmerle, T. (2015). Land-use change in the Caucasus during and after the Nagorno-Karabakh conflict. Regional environmental change, 15, 1703-1716.

Foster, G. R. (2008). Draft science documentation: Revised Universal Soil Loss Equation. Version 2. USDA-Agriculture Research Service, Washington (DC), 349 p.

Guha, S., Govil, H., Dey, A., & Gill, N. (2018). Analytical study of land surface temperature with NDVI and NDBI using Landsat 8 OLI and TIRS data in Florence and Naples city, Italy. European Journal of Remote Sensing, 51(1), 667-678.

Khrushch, O., Moskalets, V., Fedyk, O., Karpiuk, Y., Hasiuk, M., Ivantsev, N., ... & Aijjumend, H. (2023). Environmental and psychological effects of Russian war in Ukraine. Grassroots Journal of Natural Resources, 6(1), 37-84.

Li, H. X., Liu, G. H., & Fu, B. J. (2011). Response of vegetation growth to climate change and human activities in the Headwaters of three Rivers based on NDVİ / Acta Ecol. Sinica, 31, 5495–5504.

Ordway, E. M. (2015). Political shifts and changing forests: Effects of armed conflict on forest conservation in Rwanda / Journal Global Ecology and Conservation, 3, 448–462.

Poluetkov, E. V. (2003). Erosion and deflation of agrolandscapes of the North Caucasus: monograph. Novocherkassk: NGMA, 298 p.

Wirtz, P. H., & von Känel, R. (2017). Psychological stress, inflammation, and coronary heart disease. Current cardiology reports, 19, 1-10.

6th Intercontinental Geoinformation Days

igd.mersin.edu.tr

An evaluation of the effectiveness of spectral bands and indices on semantic segmentation with Attention U-Net using Sentinel-2A imagery and ESA WorldCover products

Elif Ozlem Yilmaz[*1], **Taskin Kavzoglu** [1]

[1]*Gebze Technical University, Faculty of Engineering, Department of Geomatics Engineering, Kocaeli, Türkiye*

Keywords
Attention U-Net
Deep Learning
Semantic Segmentation
Sentinel-2A
Spectral Index

Abstract

In remote sensing applications, semantic segmentation is applied to assign a semantic label (e.g., settlement, forest, and meadow) to the pixels of an image. Due to the diversity of natural and unnatural landscapes, semantic segmentation remains a difficult task for remotely sensed imagery. In this study, the Attention U-Net model was trained as a deep learning network for semantic segmentation of a Sentinel-2A image together with the WorldCover reference dataset to generate the land cover map of the study site covering Bolu, Duzce and Zonguldak provinces of Turkey. The Attention U-Net was applied to two datasets (original Sentinel-2A dataset with 10 spectral bands and Sentinel-2A dataset with additional spectral indices including Normalized Difference Vegetation Index-NDVI, Soil Adjusted Vegetation Index-SAVI, Normalized Difference Build-Up Index-NDBI and Normalized Difference Water Index-NDWI) and performance comparison was performed. The performances of deep learning models were investigated using Intersection Over Union (IoU) for segmentation model training and mean IoU for model results. The results show that the use of spectral indices as auxiliary data in semantic segmentation increases the mean IoU by approximately 10%. The results indicate that spectral indices have a higher degree of effectiveness in accuracy assessment than the original spectral bands.

1. Introduction

The capability of remote sensing (RS) platforms to gather diverse data has significantly increased with the recent technological developments in sensors. Remotely sensed data that are currently accessible have emerged as crucial components for environmental surveillance as they facilitate the identification of developments, alterations, and modifications on the Earth's surface (Shafique et al., 2022). They have been widely utilized for land cover and land use mapping, urban planning, change detection, object detection, and disaster management (Kavzoglu and Colkesen, 2013; Kavzoglu and Mather, 2003). The increasing accessibility of remotely sensed imagery, as a result of the accelerated development of remote sensing technology, provides broader opportunities for image databases (van der Meer, 2012). There exists great potential for data-driven applications, given the coverage capacity, high spatial resolution, high frequency of acquisition, and rich spectral resolution of remotely sensed imagery. In addition, numerous artificial intelligence (i.e., machine learning and deep learning) based techniques have been presented to analyze and process these data (Tsagkatakis et al., 2019). The deep learning approach has important advantages including the minimum level of human intervention, the ability to solve complex problems, and effectiveness in processing high-resolution satellite images (Yılmaz and Kavzoğlu, 2021). To date, various deep learning models have been suggested for applications (Kavzoglu et al., 2021). In particular, semantic segmentation of satellite imagery based on deep learning has been one of the substantial research topics providing essential data for geoscience applications. Semantic segmentation is the technique of assigning a class categorization to each pixel of an image (Kushwah and Markam, 2021). Unlike image classification, it is a high-level process that facilitates scene comprehension. The segmentation of image objects has a substantial impact on the precision of the classification process because segmentation is a processing stage before land use/land cover (LULC) map classification. In the last two decades, image segmentation has been conducted through region-based and edge-based algorithms. One of the most popular

* **Corresponding Author**

*(eoyilmaz@gtu.edu.tr) ORCID ID 0000-0002-6853-2148
(kavzoglu@gtu.edu.tr) ORCID ID 0000-0002-9779-3443

Cite this study

Yilmaz, E. O., & Kavzoglu, T. (2023). Evaluating the impact of spectral indices on land cover semantic segmentation with Attention U-Net architecture utilizing Sentinel-2A WorldCover reference dataset. Intercontinental Geoinformation Days (IGD), 6, 360-363, Baku, Azerbaijan

methods has been multi-resolution segmentation having scale, shape and compactness parameters (Kavzoglu et al., 2016; Tonbul et al., 2020; Yildiz et al., 2012). Evaluation of segmentation is critical to evaluate the segmentation quality qualitatively and quantitatively (Kavzoglu and Tonbul, 2017; Kavzoglu and Tonbul, 2018; Tonbul and Kavzoglu, 2017; Maxwell et al., 2021).

Existing research has highlighted problems related to the low spatial resolution of satellite imagery, the inability to fully exploit spectral information, the use of traditional methods as classifiers, and the difficulty in selecting the ideal patch size for image classification (Kavzoglu and Yilmaz, 2022). In addition, semantic segmentation applications using deep learning methods suffer from missing or insufficiently accurate reference data. To address these issues, a semantic segmentation model based on deep learning (i.e., the Attention U-Net architecture) was applied to WorldCover reference maps provided by ESA, and the influence of spectral indices, namely Normalized Difference Vegetation Index-NDVI, Soil Corrected Vegetation Index-SAVI, Normalized Difference Buildup Index-NDBI and Normalized Difference Water Index-NDWI was also investigated.

2. Study Area and Dataset

The western side (Duzce, Bolu and Zonguldak provinces) of the Black Sea region was selected as the study area, covering approximately 100 km^2 (Figure 1). In addition, the study area has a wide coastline and is known to contain mainly forest and grassland areas.

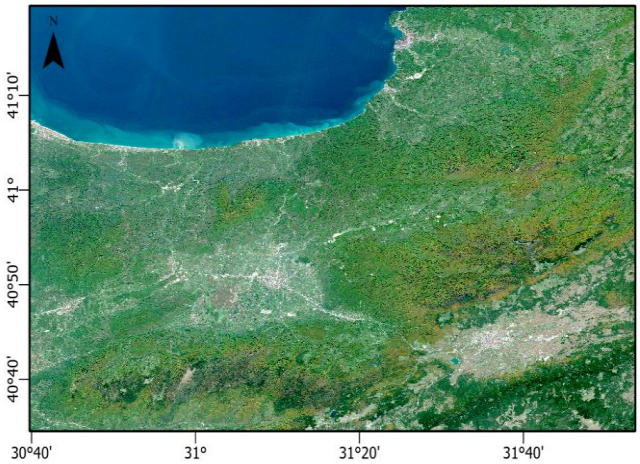

Figure 1. The location of the study area

The high-resolution, cloud-free Sentinel-2A satellite image acquired in October 2021 and the Earth Cover reference datasets produced and provided by (European Space Agency) ESA for 2021 were used for semantic segmentation and LULC labels, respectively. Prior to the training phase, the dataset underwent a process in which three bands of the Sentinel-2 image with a spatial resolution of 60 m were excluded. Furthermore, the Normalized Difference Vegetation Index (NDVI), the Soil Adjusted Vegetation Index (SAVI), the Normalized Difference Build-Up Index (NDBI) and the Normalized Difference Water Index (NDWI) were created and then used to investigate the contribution of the spectral indices to the semantic segmentation based on U-Net (Table 1).

Table 1. Formulations of Spectral Indices

Abbr.	Formula
NDVI	(NIR – Red) / (NIR + Red)
SAVI	((NIR – R) / (NIR + R + L)) * (1 + L)
NDBI	(SWIR – NIR) / (SWIR + NIR)
NDWI	(NIR – SWIR) / (NIR + SWIR)

The study area contains eight major land cover classes according to the Earth Cover reference dataset with a spatial resolution of 10 meters, produced using Sentinel-2A imagery and an overall accuracy of approximately 74% (https://esa-worldcover.org). However, as it is assumed that the limited number of pixels belonging to some land classes may affect the accuracy of the segmentation models, some land classes have been combined. As a result, the dataset included five land cover classes: tree cover, meadows, cultivated land, impervious surface including man-made structures such as roads and buildings, water bodies consisting of herbaceous vegetation, and sea (Figure 2).

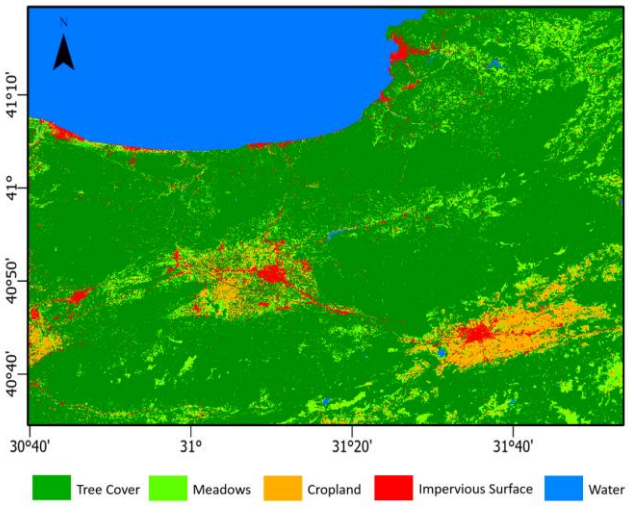

Figure 2. The study area is based on WorldCover reference data with five land cover classes

3. Methodology

In this study, the Attention U-Net was employed for semantic segmentation (Chen et al., 2023). The attention module is added to the U-Net architecture to draw attention to prominent features passing through the skip links. To distinguish between irrelevant and noisy details in skip connections, information derived from a rough scale is employed in the attention function. This occurs just prior to the concatenation process to ensure that only pertinent activations are combined. Moreover, the U-net architecture includes 2D convolutional and up-sampling layers of encoder and decoder blocks. Attention gates are located between the encoding and decoding layers to emphasize the important features of the image. Furthermore, the optimizer function of Adamax was chosen for the model, and categorical cross entropy was used as the loss function to solve the multiclass segmentation problem. After arranging the architecture

of the model, it was created with 10,000,000 trainable parameters.

The Attention U-Net architecture inherently requires inputs in the form of patches. Therefore, the satellite image and reference data were separately divided into 256x256 patches. In total, 811 patches were created for training and 542 patches were produced for both testing (271 patches) and validation (271 patches) analyses. After the datasets were normalized, the training of Attention U-Net architectures was completed. In the section on performance analysis of the deep learning models, Intersection Over Union (IoU) and meanIoU metrics were employed in the training stage while the meanIoU metric was calculated for the model findings. IoU, is characterized as the region of overlap between the anticipated and the ground truth region, which is then divided by the region of combination between both regions. Moreover, the evaluation of segmentation algorithms for multiclass problems often involves the utilization of meanIoU metric to assess their efficacy throughout all classes (Yeghiazaryan & Voiculescu, 2018).

4. Results

Semantic segmentation models trained on two datasets were completed without overfitting in the training phase. In both applications, the training and validation accuracies of the models exceeded 0.92 while the training and validation losses of the models converged to 0.1 (Figure 3). Furthermore, 270 patches were used as test data to measure the accuracy of the trained models. Some of the predicted images are shown in Figure 4. In addition, both meanIoU values and class based IoU values were calculated separately for the two semantic segmentation outputs for accuracy evaluation (Table 2).

When examining the class-based IoU values in both datasets, it was observed that the dataset containing spectral indices related to water yielded the highest IoU value of 0.991, while the dataset containing only spectral bands yielded an IoU value of 0.899 (Table 2). Conversely, it was observed that the datasets consisting of spectral indices and spectral bands for the meadow class yielded the minimum IoU values of 0.597 and 0.570 in both datasets. Furthermore, one of the reasons for the low IoU of the meadow class is that it is mixed with cropland and impervious surface classes. The findings prove that using spectral indices obtained from satellite images for land cover classification improves the accuracy of semantic segmentation applications.

Table 2. Class-based IoU values for both datasets

LULC Class	Spectral Bands	Spectral Indices
Tree cover	0.832	0.956
Meadows	0.570	0.597
Cropland	0.721	0.820
Impervious Surface	0.593	0.733
Water	0.899	0.991
mIoU	0.723	0.819

5. Conclusion

In recent years, significant progress has been made in image segmentation applications. Recent research based on deep learning approaches has improved segmentation accuracy. In general, the main challenge in deep learning image segmentation is the lack of reference data or problems in generating such data. This study proves that the reference data, namely WorldCover provided by ESA, is useful for image segmentation applications. Furthermore, the effect of spectral indices to improve the accuracy of semantic segmentation was investigated and an increase in accuracy of about 10% was achieved. In other words, the use of spectral indices in addition to spectral bands significantly improves the accuracy of semantic segmentation applications. It can be deduced that semantic segmentation and deep learning models have the capacity to make significant contributions in a wide range of areas, such as visual understanding, object recognition and image classification/segmentation. Future work includes the development of a deep learning model that uses semantic segmentation techniques for multispectral remote sensing images to produce results with superior accuracy compared to machine learning with OBIA.

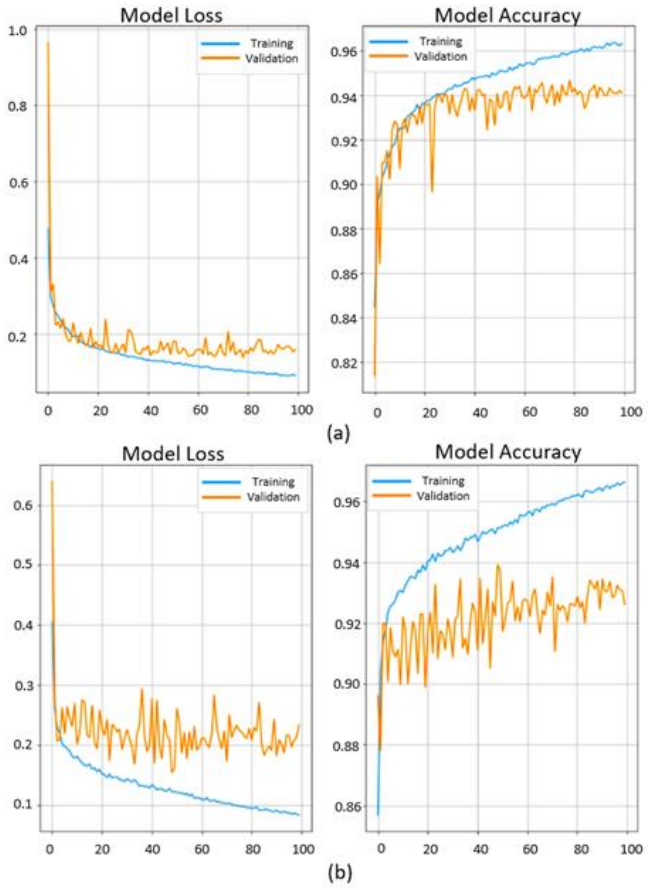

Figure 3. The learning curves for (a) Sentinel-2A with spectral indices and (b) Sentinel-2A spectral bands

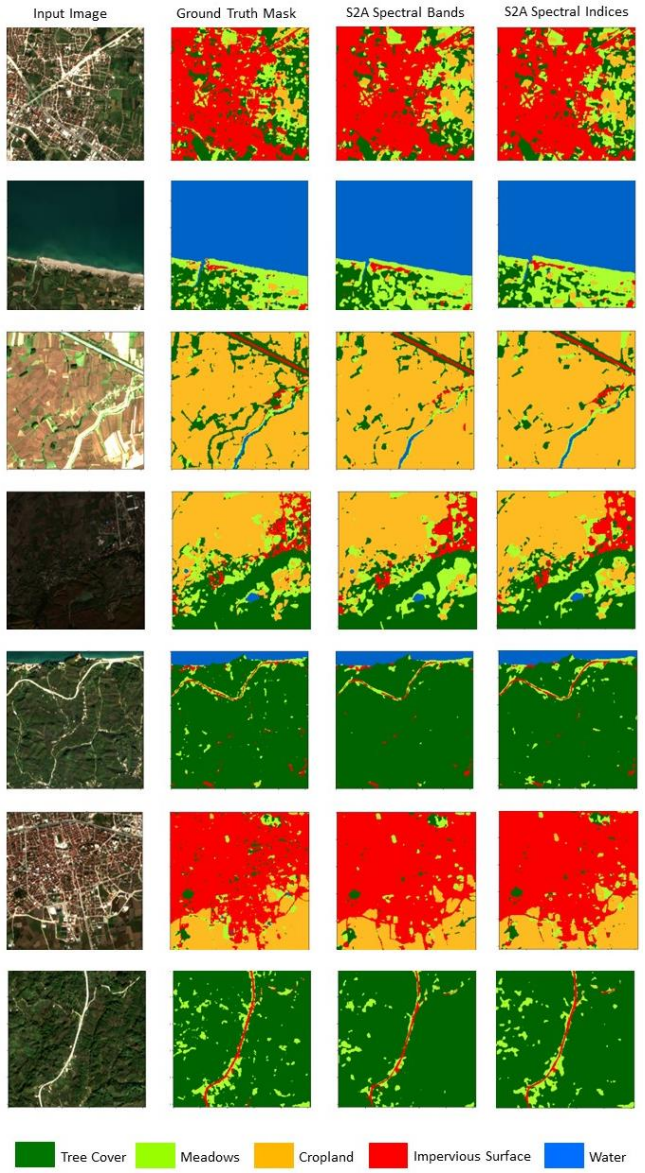

Figure 4. Predictions of semantic segmentation models

References

Chen, W., Hua, W., Ge, M., Su, F., Liu, N., Liu, Y., & Xiong, A. (2023). Severe Precipitation Recognition Using Attention-UNet of Multichannel Doppler Radar. Remote Sensing, 15(4), 1111.

Kavzoglu T. & Colkesen I. (2013). An assessment of the effectiveness of a rotation forest ensemble for land-use and land-cover mapping, International Journal of Remote Sensing, 34(12), 4224–4241.

Kavzoglu T., & Mather P. M., (2003), The use of backpropagating artificial neural networks in land cover classification, International Journal of Remote Sensing, 24(23), 4907–4938.

Kavzoglu, T., Erdemir, M. Y. & Tonbul, H. (2016). A region-based multi-scale approach for object-based image analysis. The International Archives of the Photogrammetry, Remote Sensing and Spatial Information Sciences, Volume XLI-B7, 241-247.

Kavzoglu, T., Teke, A. & Yilmaz, E.O. (2021). Shared blocks-based ensemble deep learning for shallow landslide susceptibility mapping, Remote Sensing, 2021, 13, 4776. https://doi.org/10.3390/rs13234776

Kavzoglu, T. & Tonbul, H. (2017). A comparative study of segmentation quality for multi-resolution segmentation and watershed transform. 8th International Conference on Recent Advances in Space Technologies (RAST'2017), 113-117.

Kavzoglu, T. & Tonbul, H. (2018). An experimental comparison of multi-resolution segmentation, SLIC and K-means clustering for object-based classification of VHR imagery. International Journal of Remote Sensing, 39(18), 6020-6036.

Kavzoglu, T. & Yilmaz, E.O. (2022). Analysis of patch and sample size effects for 2D-3D CNN models using multiplatform dataset: hyperspectral image classification of ROSIS and Jilin-1 GP01 imagery. Turkish Journal of Electrical Engineering and Computer Sciences, 30(6), 2124-2144.

Kushwah C. P. & Markam K., (2021), Semantic segmentation of satellite images using deep learning, International Journal of Innovative Technology and Exploring Engineering, 10(8), 33–37.

Maxwell A. E., Warner T. A., Guillén L. A., (2021a), Accuracy Assessment in Convolutional Neural Network-Based Deep Learning Remote Sensing Studies—Part 1: Literature Review, Remote Sensing, 13(13), 2450.

van der Meer F., (2012), Remote-sensing image analysis and geostatistics, International Journal of Remote Sensing, 33(18), 5644–5676.

Shafique, A., Cao, G., Khan, Z., Asad, M., & Aslam, M. (2022). Deep learning-based change detection in remote sensing images: A review. Remote Sensing, 14(4), 871.

Teke, A., Yilmaz, E. O. & Kavzoglu, T. (2021). Comparative assessment of deep learning and machine learning learning models in shallow landslide susceptibility. International Symposium on Applied Geoinformatics (ISAG2021) 2-3 December 2021, Riga, Latvia.

Tonbul, H., Colkesen, I. & Kavzoglu, T. (2020). Classification of poplar trees with object-based ensemble learning algorithms using Sentinel-2A imagery. Journal of Geodetic Science, 10(1), 14-22.

Tonbul, H., & Kavzoglu, T. (2017). Investigation of the effect of segmentation quality on object-based classification accuracy, Afyon Kocatepe University Journal of Science and Engineering, 17, 118-125.

Tsagkatakis G., Aidini A., Fotiadou K., Giannopoulos M., Pentari A., Tsakalides P., (2019), Survey of deep-learning approaches for remote sensing observation enhancement, Sensors (Switzerland), 19(18), 3929.

Yeghiazaryan, V., & Voiculescu, I. (2018). Family of boundary overlap metrics for the evaluation of medical image segmentation. Journal of Medical Imaging, 5(1), 015006-015006.

Yılmaz, E. Ö. & Kavzoğlu, T. (2021). Basic principles of deep learning and its applications in remote sensing. Map Journal (Harita Dergisi), 87(166), 25-43.

Yildiz, M., Kavzoglu, T., Colkesen, I. & Sahin, E. K. (2012). An assessment of the effectiveness of segmentation methods on classification performance. In 10th International Symposium on Spatial Accuracy Assessment in Natural Resources and Environmental Sciences, 133-138.

6th Intercontinental Geoinformation Days

igd.mersin.edu.tr

Analysis of the sea surface temperature (SST) of the Caspian Sea from NOAA Satellites

Ismayil Zeynalov [*1], **Rena Akhmedova** [1], **Aybeniz Akhmedova** [1] **Almaz Rustamova** [1]

[1]*Institute of Geography, Caspian Sea Department, Baku, Azerbaijan*

Keywords
Sea surface temperature
Water masses
Marine ecosystems
Salinity
NOAA

Abstract

The sea surface temperature (SST) of the Caspian Sea as a whole is determined by air temperature, depth, that is, heat reserve, wind characteristics (mixing) and advection. In different regions of this continental sea, in addition to the connection with air temperature common to all regions, their own factors dominate. For the Northern Caspian, this is primarily the influence of river runoff - warm continental runoff in spring and cool in autumn. In the Middle Caspian, deep-water rises near the eastern and western shores, reaching temperature contrasts of up to 15°C near the eastern shore. In the South Caspian, this is winter wind mixing and advection of waters from the Middle Caspian. In the daytime, in the spring-summer months, the heating of the sea manifests itself everywhere in the form of patches of warm water with temperature contrasts of more than 3°C - calm zones. In shallow water in the spring and autumn months, zones of heating and cooling are clearly visible, respectively, and the rate of heating and cooling is the higher, the shallower the depth of the sea, that is, the lower its heat reserve. The paper analyzes the available modern methods and means for determining the surface water temperature of the Caspian Sea. For their detection, data obtained by NOAA satellites and the AVHRR Pathfinder instrument (high-resolution radiometer) installed on them are used. And the main regularities in the atmosphere-sea system are revealed according to the average annual values of their changes over a long period of time.

1. Introduction

Information about the temporal variability of the surface temperature is required to study biological communities, ice regime, evaporation amount, heat balance, climate conditions of the adjacent sea area etc. The temperature change during the month, depending on season and meteorological conditions, in different areas of the sea goes in different ways. This work considers the temporal structures of the surface temperature. This makes it possible to compile maps of temperature fields both on the basis of individual contact measurements, and from satellite remote sensing data (Zeynalov and Makhmudova, 2021).

Information about the temporal variability of the surface temperature is required to study biological communities, ice regime, evaporation amount, heat balance, climate conditions of the adjacent sea area etc. The temperature change during the month, depending on season and meteorological conditions, in different areas of the sea goes in different ways. This work considers the temporal structures of the surface temperature. This makes it possible to compile maps of temperature fields both on the basis of individual contact measurements, and from satellite remote sensing data (Zeynalov and Makhmudova, 2021).

The main systematized data of the ground hydrometeorological network stations and satellite supervision for the whole of globe can be received by using the server network of the USA National Ocean and Atmosphere Administration (NOAA). There is a separate entity of NOAA Satellites and Information with the body of the National Environmental Satellite, Data and Information Service (NESDIS). Within the framework of the NESDIS is functioning the Office of Satellite Data Processing and Distribution (OSDPD) for processing and distribution of satellite data which provides processing, systematization and supply to users in the USA and other countries data and information from the environmental satellites. The final goal of user`s maintenance is reaching by appropriate information production over the following three institutions: Satellite Service Division

* **Corresponding Author**

*(ismayil_zeynalov@outlook.com) ORCID ID 0000-0001-9391-583X
(rena.ahmedova.67@mail.ru) ORCID ID xxxx-xxxx-xxxx-xxxx
(aybenizahmedovageoph@gmail.com) ORCID ID xxxx-xxxx-xxxx-xxxx
(almaz rustamova 2@gmail.com) ORCID ID xxxx-xxxx-xxxx-xxxx

Cite this study

Zeynalov, I., Akhmedova, R., Akhmedova, A., & Rustamova, A. (2023). Analysis of the sea surface temperature (SST) of the Caspian Sea from NOAA Satellites. Intercontinental Geoinformation Days (IGD), 6, 364-367, Baku, Azerbaijan

(SSD); Information Processing Division (IPD): Direct Services Division (DSD).

There are number of other institutions for maintenance of the initial data for monitoring of the environment. For the considered purposes in the paper has been used the data from the IPD divisions of the Satellite Active Archive (SAA) through the Internet network. In the network is presented an opportunity of selection of such information which refers to Advanced Very High-Resolution Radiometer (AVHRR); Pathfinder – specialized software. Information production of the AVHRRPF (sometimes calls as PATMOS) with a free of access represents of the number of USA satellites NOAA-7-9 – and 14.

Within the framework of the PATMOS- A1 statistical characteristics have been calculated using the indicated above satellites for intensive outgoing radiation in all five channels of visible area of the spectrum, two channels as called "atmosphere transparency windows" for 10-12 micrometers and near infrared area for elimination of impact of atmospheric cloudless and cloudy conditions. Cloudy cover statistical characteristics have been calculated where condition describes by a huge of parameters.

Based on the PATMOS – A2 version statistical characteristics of the atmospheric aerosol optical thickness above oceans as well as values of the absorbed solar (short wavelength) radiation and thermal (long wavelength) radiation have been calculated which define radiation balance on the top of an atmosphere. In the climate and climate change investigations usually use a monthly average value of appropriate characteristics.

Below presents some of data analysis results off the PATMOS- A2 information production for the term of 1982-2000 in two allocated areas of Near - Caspian region (from 38^0 up to 42^0 north longitude from 44^0 to 52^0 east latitude; and from 34^0 up to 50^0 north longitude, from 44^0 up to 56^0 east latitude) incorporation with data of a ground measuring network based on characteristics, as monthly average values of air temperature, atmospheric pressure and average speed of a wind at the surface level. The first of selected areas approximately covers the territory of Azerbaijan and second - wider area of territory of Russia, Azerbaijan, Georgia, Iran, Turkmenistan, and Kazakhstan. The specified data of a ground network are accessible through the Internet network and other information center of the USA national climate data center (NCDC).

It can be considered some of examples of interpretation to be received information production for the purposes of investigation of climate variability of selected two foregoing mention Near Caspian region for the last 20 years (Sefer et al. 2009).

2. Method

The paper analyzes the changes in the values of sea surface temperature (SST) for individual sections of the Caspian Sea, taking into account various manifestations of an anthropogenic nature. The surface temperature of the waters of the Caspian Sea as a whole is determined by air temperature, heat storage, wind characteristics (mixing) and advection. In different regions of this continental sea, in addition to the connection with air temperature common to all regions, some of their own factors also dominate.

For the Northern Caspian, this is primarily the influence of river runoff - warm continental runoff in spring and cool in autumn. In the middle of the Caspian Sea, the rise of deep waters near the eastern and western shores reaches temperature contrasts of up to 15^0C near the eastern shore. In the South Caspian, this is winter wind mixing and advection of waters from the Middle Caspian. In the daytime in the spring-summer months, the heating of the sea manifests itself everywhere in the form of patches of warm water with temperature contrasts of more than 3^0C - a calm zone. In shallow water in the spring and autumn months, zones of heating and cooling are clearly visible, respectively, and the rate of heating and cooling is the higher, the shallower the depth of the sea, that is, the lower its heat reserve. 19 The work carried out by the author confirmed the correctness of the proposed methodological approach and the basic assumptions for organizing experimental satellite monitoring of sea surface temperature fields: - the use of an algorithm for taking into account the distorting influence of the atmosphere makes it possible to reduce both geographical due to shallow water and meteorological due to taking into account the distorting influence of aerosol formations, limitations in interpretation of satellite spectrum-zonal information; - the choice of satellite NOAA as a satellite platform for operational background monitoring of the sea surface and TERRA, ESA as platforms for episodic surveys under existing conditions is the only possible one in case of extreme situations (Mekhtiyev M.G., 2022). Both geographical due to shallow water, and meteorological due to taking into account the distorting influence of aerosol formations, limitations in deciphering satellite spectral-zonal information; - the choice of satellite NOAA as a satellite platform for operational background monitoring of the sea surface and TERRA, ESA as platforms for episodic surveys under existing conditions is the only possible one in case of extreme situations (Mekhtiyev, 2022). both geographical due to shallow water, and meteorological due to taking into account the distorting influence of aerosol formations, limitations in deciphering satellite spectral-zonal information; - the choice of satellite NOAA as a satellite platform for operational background monitoring of the sea surface and TERRA, ESA as platforms for episodic surveys under existing conditions is the only possible one in case of extreme situations (Mekhtiyev, 2022).

The change in temperature during the month, depending on the time of year and meteorological conditions, occurs differently in different areas of the sea. In this paper, the time structures of the surface temperature are considered. Knowledge of such a structure makes it possible to construct maps of the temperature field both on the basis of individual contact and satellite remote measurements (Mekhtiyev, 2022).

For the selected research region, Figure 1 shows the values of the water surface temperature for the selected 14 years of continuous observations (from January 2001 to December 2015). The left side of Fig. 1 shows the corresponding average annual values (averaged over 12

months) for each year of the observations under consideration. One can see a fairly smooth course of monthly averages for the selected region with maxima in 2002, 2005, 2013. The average annual values of the corresponding values vary approximately from 14.2^{0}C to 15.8^{0}C. The presence of such smooth curves for monthly averages reflects the time course of the temperature of the "earth's surface-atmosphere" system over a given region. Much more complex is the behavior of the average annual values of the studied quantities for each year out of the selected 14 years of observations. One can note an almost systematic deviation in the average annual values of the water surface temperature for the selected region. For example, according to the curve in Fig. 1 in 2002, these values were 15^{0}C and 15.06^{0}C for the selected “square” of the territory of Azerbaijan and the entire Caspian region, respectively; in 2001 - 14.5^{0}C and 15.2^{0}C; in 2004 - 15.3^{0}C and 13.4^{0}C in 2014 (the minimum values for the entire observation period under consideration); in 2008 - 15.4^{0}C and 15.9^{0}C (maximum values for the entire period under review). The curve in Fig. 1 does not show such significant discrepancies for the corresponding value, nevertheless demonstrating a clear similarity in the extreme events of 2003, 2010, 2015, and other years of observations. These discrepancies can probably be explained by the more complex nature of the impact of climate systems on the final values of the quantity under study. Other characteristic explanations for these discrepancies are also possible. From the analysis of the data, it can be seen that 2007 and 2013 are extreme in terms of the variability of the average annual temperature observed from satellites.

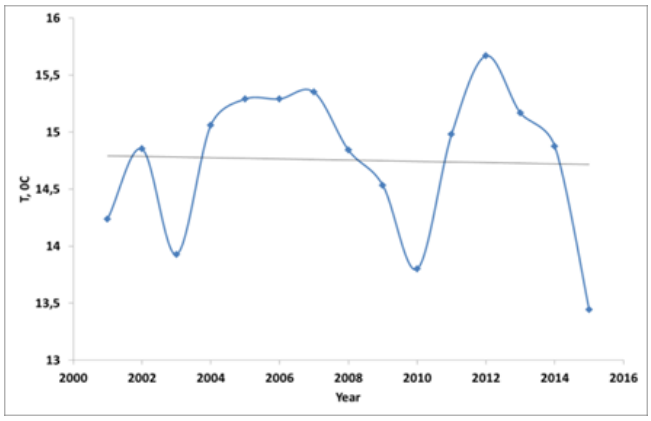

Figure 1. Data of water surface temperatures in the Caspian Sea from satellites of the NOAA series with a resolution of 50 km

Table 1. Average monthly values of SST for the Caspian Sea

Year	January	February	March	April	May	June	July	August	September	October	November	December
2001	7.87	4.03	6.99	9.47	16.17	18.20	24.91	24.91	21.15	15.55	12.71	8.90
2002	7.52	6.28	7.91	10.22	15.55	15.55	25.82	26.38	22.69	18.37	13.21	8.73
2003	6.86	5.58	5.11	7.11	14.80	16.70	24.24	26.30	21.64	17.50	12.40	8.87
2004	7.90	7.59	8.62	10.13	15.59	19.43	25.36	26.35	22.14	15.73	13.52	8.38
2005	7.43	5.30	6.09	10.21	16.91	20.08	26.03	26.01	24.13	17.44	13.45	10.41
2006	6.97	5.74	7.03	10.39	15.54	23.94	25.79	26.49	23.22	17.74	12.57	8.08
2007	7.36	6.33	6.99	8.96	16.12	22.62	26.17	26.74	23.93	17.34	12.82	8.82
2008	5.38	5.87	6.28	10.85	15.95	19.65	25.25	26.24	21.93	17.40	13.60	9.71
2009	6.06	5.41	6.89	8.89	15.33	20.16	25.55	24.54	22.08	17.84	12.48	9.17
2010	8.02	4.96	5.89	9.72	15.76	7.26	26.74	23.00	22.42	16.89	13.19	11.75
2011	8.22	6.54	5.66	9.26	16.43	23.56	26.04	26.27	22.12	16.39	11.37	7.90
2012	6.31	5.71	5.66	10.96	17.68	24.14	26.45	24.61	22.76	19.21	14.30	10.24
2013	7.00	5.95	7.15	10.85	16.33	22.55	26.26	25.85	21.75	16.28	13.35	8.69
2014	7.45	5.32	6.38	9.98	16.91	22.03	25.94	26.29	22.13	16.31	11.28	8.48
2015	6.96	5.46	6.65	9.67	16.09	22.28	7.71	24.95	24.41	16.49	12.12	8.51
Total	7.15	5.74	6.62	9.78	16.08	19.88	24.55	25.66	22.57	17.10	12.82	9.11

Which characterize the thermal features of the Caspian Sea observed from satellites for some model representations. The fact is that during a separate day it is possible to receive information on the same territory from several orbits of NOAA satellites. The corresponding territories can be covered during separate revolutions by clouds or be free from it. When presenting the final information product in the form of average monthly values, some of the corresponding scenes are inevitably "burdened" by the presence of cloud cover, while the other part may not contain clouds. It can be seen that the average annual values of the water surface temperature with a cloudless sky for individual years differ little from the similar curves in Fig. 1. The maximum of these deviations is again noticeable for the territory of Azerbaijan (absolute value is about 14.9^{0}C) followed by a fairly even course of the corresponding values of about 14.9^{0}C for the rest of the observation years. Even more unexpected is the appearance of the maximum of these deviations for the entire Caspian region (its absolute value reaches 15.8^{0}C) with a subsequent fairly smooth course near 15^{0}C for the rest of the observation years. It is possible that these incomprehensible things are related to the small amount of sample data in the territory under consideration. The data are similar to the data in Fig. 1, but characterize the values of the absorbed solar radiation flux by the "earth's surface-atmosphere" system. Again, one can note a fairly monotonous course of the annual values illustrated in Figure 1 at the top of the values for the selected region with maxima in 2007-2013 (about 15.3 - 15,5^{0}C) in 2003-2015 year.

These data characterize the thermal features of the Caspian Sea observed from satellites for some model representations. The fact is that during a separate day it is possible to receive information on the same territory from several orbits of NOAA satellites (in reality, up to four orbits from two simultaneously functioning

satellites). The corresponding territories can be covered during separate revolutions by clouds or be free from it. When presenting the final information product in the form of average monthly values, some of the corresponding scenes are inevitably "burdened" by the presence of cloud cover, and the other part does not contain clouds (Mekhtiyev, 2022). The analysis of the available archives of satellite observation data of the Caspian Sea showed the characteristic features of the interannual values of the corresponding value for 14 years of observations (2001 - 2015). The results obtained showed statistical patterns in the behavior of the studied quantity, but also introduced uncertainties into some results of the interpretation of the available data. These are the first results of such studies of the total set of parameters characterizing the state and variability of the biosphere and climate of the selected region. The basis for further research in this direction should be the study of the criteria for the statistical significance of the results obtained (Ismailov, 2023).

3. Conclusion

In the work, an analysis was carried out on the basis of the available SST values of the Caspian Sea in order to develop a further methodology for collecting and analyzing satellite data.

The data obtained from the NOAA series satellites improve the ability to consider the re-analysis of the average annual values of the characteristics of the water surface temperature intensities.

These studies further consider the atmosphere-sea system, which is necessary in solving the problems associated with the environmental problems of the Caspian Sea.

References

Ismailov, V. Kh. (2023). Study of temperature anomalies in the Caspian Sea using satellite data. Astrakhan Bulletin of Environmental Education., 2 (74), 16-21

Mekhtiev, M. G. (2022). The role of the use of data from low-orbit satellites in the study of the water surface temperature of the Caspian Sea. Astrakhan Bulletin of Environmental Education., 6 (72), 140-148 https://doi.org/10.36698/2304-5957-2022-6-140-148

Mekhtiyev, M. G. (2022). Estimation of the role of greenhouse gases in climate formation on the territory of Azerbaijan using data from low-orbit satellites. Astrakhan Bulletin of Environmental Education, 5 (71), 44-54 https://doi.org/10.36698/2304-5957-2022-5-44-54

Sefer, K., Rustam, B., Rustamov, I. Z. (2009). Alternative Energy-Environment Safety. International Journal of Aeronautical and Space Sciences. The Korean Society for Aeronautical and Space Sciences, 91-97

Zeynalov, I. M., & Makhmudova, U. Kh. (2021). The role of using data from satellite observation systems in the study of the water surface temperature of the Caspian Sea. International Scientific Conference "Climate Change in the Caspian Sea Region", 97-100

6th Intercontinental Geoinformation Days

igd.mersin.edu.tr

Contemporary characteristics of air temperature distribution in the territory of Azerbaijan

Jamal Surkhay Huseynov *

Azerbaijan Airlines CJSC, Azeraeronavigation ATD, Baku, Azerbaijan

Keywords
Climate changes
Air temperature
Statistical significance
Cartographic method
ArcGIS

Abstract

In the article, the distribution of air temperature in the territory of the Republic of Azerbaijan in 1961-2020 and its dynamics compared with 1881-1960 are determined. As a result of mathematical, statistical, and cartographic analyses, it was confirmed once again that the temperature regime of the republic has characteristics of change from the north to the south and from the plain to the highlands. In addition to this, multi-year average, seasonal indicators of temperature quantity in individual regions of the territory of the republic were determined. The maximum indicators of the perennial average temperature quantity were observed in the Kura-Araz plain in the range of 14.6-15.4 0C. The results of the research can be used in the future in the research of the climate regime, and its changes, during the creation of agriculture, tourism industry, and other large-scale industries in the area.

1. Introduction

All climate parameters, including pressure, wind, evaporation, and precipitation, are distributed completely differently on the non-uniformly heated Earth's surface (Huseynov, 2011). Each region is characterized by its own climate character. The complexity of the relief of the Republic of Azerbaijan, located in the Southern Caucasus region, and its location on the shores of the Caspian Sea play a major role in the creation of diversity in climate distribution (Atlas, 2014; Tanriverdiyev et al. 2015). According to A.M. Shikhlinsky, 8 of the 11 climate types distinguished by V.P. Keppen exist in the territory of the republic (Shikhlinsky, 1968).

By studying the temperature regime in the territory of the Republic, A.M. Shikhlinsky, A.A. Madatzade, A.M. Ayyubov, G.A. Hajiyev, A.S. Mammadov, Said H. Safarov, Surkhai H. Safarov, R.N. Mahmudov, N. Sh. Huseynov and other scientists were engaged.

The current global climate changes affect the climate of all regions. The increase in the effects of climate change and the time series of observations makes it necessary to conduct new research in this direction.

2. Method

The analyzes were carried out based on the primary data of 58 operating in Azerbaijan, including the main 32 hydrometeorological stations with complete observation series for the years 1961-2020. Mathematical, statistical, and geographical methods were used in the research. The statistical significance of the series was checked (Imanov, 2011). SBSS and Stokstat programs were used in the statistical analyses. Tables, histograms, and graphs from the obtained results were processed in Microsoft Excell, electronic map ArcGIS software.

2.1. The second level headings

The purpose of the study is to determine the regularities of the territorial distribution of changes in the temperature regime over a long period of time in the influence of regional climate changes in the territory of Azerbaijan. One of the main goals is to revise the characteristics of the vertical and horizontal distribution of air temperature and map their results with modern cartographic methods.

2.2. The second level headings

The moderating effects of the Caspian Sea can always be felt in the coastal regions of Azerbaijan. The maritime factor moderates the harsh effects of air masses from the north (cold), east (warm, dusty), and south (warm, dry) throughout the year on coastal plains, islands, and peninsulas.

In the northeastern slope of the Greater Caucasus region, the average annual temperature from 1961 to 2020 decreases from 12.9^{0}C to -5.1^{0}C from the coastal plains to the highlands. In 1881-1960, the average annual temperature for the area was determined in the range of 12.2-4.5^{0}C.

* **Corresponding Author**

*(camal_huseynov_88@mail.ru) ORCID ID 0000-0002-7878-578X

Cite this study

Huseynov S.J., (2022). Contemporary characteristics of air temperature distribution in the territory of Azerbaijan. Intercontinental Geoinformation Days (IGD), 6, 368-370, Baku, Azerbaijan

3. Discussion

This also indicates that there was an increase of 0.6-1.1^{0}C in the average annual temperature index from 1961-2020. There is a different temperature regime in the south of the Greater Caucasus region. Starting from the low mountains and reaching the height of 1500-1600 m, the average annual temperature decreases in the range of 13.3-6.4 ^{0}C.

Table 1. The perennial average temperature trend at hydrometeorological stations from 1961-2020, ^{0}C

№	Station	Altitude, m	1961-2020	1881-1960
1	Khachmaz	27	12,9	12,2
2	Guba	550	10,7	9,6
3	Gyryz	2071	5,1	4,5
4	Altiaghaj	1099	9,0	8,1
5	Sumgait	-20	14,7	13,6
6	Mashtagha	27	14,5	13,5
7	Pirallahi	-25	14,8	14,0
8	Chilov	-17	14,7	14,0
9	Oil Rocks	-17	14,8	14,0
10	Alibey	1540	6.4	5.7
11	Zagatala	487	13,3	12,5
12	Shaki	639	12,6	12,0
13	Gabala	679	11,7	10,6
14	Maraza	775	11,1	10,5
15	Mingachevir	93	15,5	14,8
16	Yevlakh	13	15,3	14,6
17	Goychay	107	15,1	14,2
18	Kurdamir	2	15,3	14,5
19	Zardab	-5	15,2	14,3
20	Beylegan	62	14,7	14,0
21	Japharkhan	-16	14,7	14,0
22	Hajigabul	-7	15,5	14,5
23	Bilasuvar	75	15,0	14,2
24	Neftchala	-24	15,2	-
25	Lankəran	-20	14,5	14
26	Gadabay	1480	8,2	7,4
27	Ganja	312	13,9	13,2
28	Aghstafa	331	13,2	12,2
29	Shamkir	404	14,2	12,9
30	Nakhchivan	875	12,7	12,7
31	Shahbuz	1205	11,7	11,2
32	Ordubad	861	13,9	11,6

According to the vertical temperature variation (0.65^{0}C/100 m), it takes values below 0^{0}C at an altitude of 2400-2500 m. Temperature indicators in the region for the period 1961-2020 differ by an increase of 0.8^{0}C compared to the period 1881-1960 (Table 2).

The average annual temperature in the Absheron aquatorium during the research period was 14.7^{0}C in the peninsula. Compared to the years 1881-1960, the average annual temperature increased by 0.8^{0}C during the multi-year period. The temperature rises slightly towards the south of the province.

Since the Kura Valley depression physical-geographical region is surrounded by mountains from the northeast and southwest, the influence of air masses coming from the Iranian plateau from the south, the Caspian Sea from the southeast, and the Jeyranchol plain from the northwest is dominant. Although the humid air masses formed over the sea affect the coastal areas, they cannot enter the interior of the plain (Shikhlinsky, 1968; Safarov et al. 2022). The northwestern part of the province is relatively high and the average annual temperature is 13.2^{0}C, the average annual temperature in the Kura-Araz plain is 15.1^{0}C (14.6-15.5^{0}C). From 1881-1960, the average annual temperature for these areas was 14.3^{0}C (14.0-14.8^{0}C), however, now this indicator has increased by 0.8^{0}C (Mahmudov, 2018; Pykhtunova, 1966).

The perennial (1961-2020) average temperature of the Lesser Caucasus Mountains, located in the west of the country, was in the range of 14.3-7.5^{0}C from lowland (300-400 m) to mid-mountain (1450-1650 m) in the west. Considering the vertical zonation, the average annual temperature is below 00C at an altitude of about 2900 m. The average annual temperature here has increased by 1.0^{0}C compared to 1881-1960. The influence of hot and dry air masses coming from the south is felt throughout the year in the eastern and southeastern parts of the Lesser Caucasus region (Huseynov, 2022). The average annual temperature in the lowlands (150-200 m) is 14.6^{0}C, 15^{0}C in the Arazboyu (areas along the Araz River) area in the south, 13-14^{0}C in the lowlands, 12^{0}C in the lower parts of the middle highlands, and 11^{0}C in the upper part of the middle highlands. Compared to the years 1881-1960, the increase in the area was 0.80C. At an altitude above 3000 m, which is the permanent frost zone of the Lesser Caucasus, the temperature is below 0^{0}C in all seasons of the year [2].

Starting from the Sharur-Ordubad plain in Nakhchivan province, the area surrounded by mountains plays a major role in the large gradient distribution of temperature along the slope. The average annual temperature in the Sharur-Ordubad plain in 1961-2020 is 2.6-13.9^{0}C. In the high altitude zone of the highlands (2100-2200 m), this quantity decreases to 7.2^{0}C. The multi-year average temperature is below 00C starting from 3300 m altitude. Compared to the previous period, the average annual temperature in the region increased by 0.9^{0}C from 1961-2020.

The Talysh mountain ranges (Talysh, Peshtasar, and Burovar) located to the west of the coastal plains in the Lankaran natural province prevent the westward movement of the humid air mass evaporating from the sea (Tanriverdiyev, 2015). A temperate warm climate type with evenly distributed rainfall in all seasons is widespread on the sea coast of the area. Thus, the perennial average temperature decreases from 14.6^{0}C to 8.9^{0}C from the coastal plains to an altitude of 1500-1600 m. There is no permanent frost zone in the Talysh mountains. Although for the years 1881-1960 [9, 10], the average annual temperature in these areas was 12.8^{0}C, from 1961-2020, it increased by 0.8^{0}C to 13.6^{0}C.

In the analysis, the dynamics of average annual air temperatures of hydrometeorological stations in the country from 1961-2020 were investigated. The multi-year trend graphs of some of them are given below (Figure 1).

If we refer to the graph, it can be said that the average annual temperature in all stations during 1961-2020 changed mostly synchronously. It can also be observed that the air temperature was colder in 1964, 1969, 1976, 1982, 1993, 2004, and 2011, and warmer in 1966, 1971, 1989, 1995, 1998, 2010, and 2017. The linear trends of the trend curves indicate an increase in average annual temperature at all stations over the perennial period.

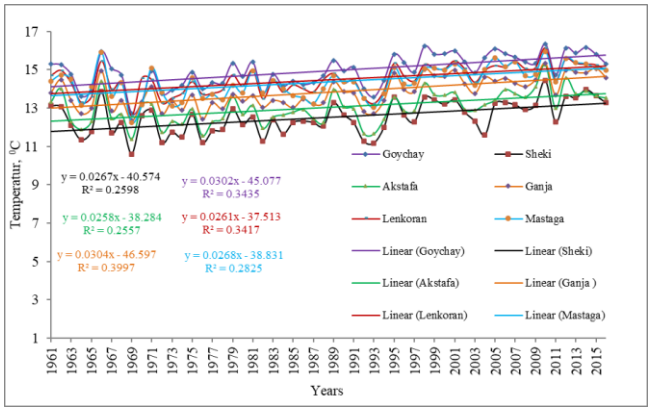

Figure 1. Average annual temperature changes at hydrometeorological stations from 1961-2020

Figure 2 indicates the distribution of perennial average annual temperature by area. The representation is illustrated by means of the IDW model of interpolation in the ArcGIS program. As can be seen from the figure, the higher temperature quantity is typical in the Absheron peninsula, coastal plains, Kura-Araz lowland, Jeyranchol, and Arazboyu plains. The average annual temperature decreases from the plains to the highlands.

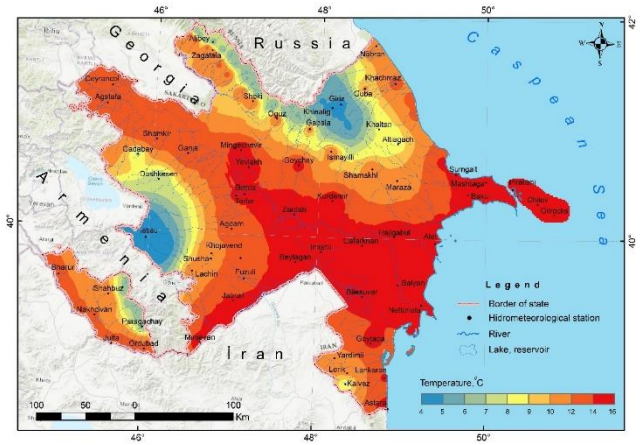

Figure 2. Distribution of average annual temperature over the period 1961-2020

4. Conclusion

A number of results were obtained during the study of the distribution of average multi-year quantities of temperature in the territory of the Republic of Azerbaijan from 1961-2020.

In the territory of Azerbaijan, the average annual air temperature decreases from the sea coast to the west and towards the mountainous belt. During the period 1961-2020, an increase in the average annual air temperature is observed in the territory of the country. Compared to 1881-1960, the average multi-year temperature in 1961-2020 increased by 0.8^{0}C across the country. The highest quantity of the average temperature of the country was 15.0-15.4^{0}C and it was observed in the south of Lankaran province, Kur-Araz plain, Arazboyu.

The results obtained during the conducted climate research can be used during the formation of the economy in the country in the future. In areas with high-temperature values, global warming will further accelerate its effects and vulnerabilities such as salinization, scouring, and lowering of the underground water level will appear in these lands. An increase in the annual amplitude is expected in the middle and high mountain zone. In connection with the hardening of the climate, it can be recommended to cultivate livestock and plant species that will tolerate the harsh continental climate.

References

National Atlas of the Republic of Azerbaijan [Atlas] (2014). State Land and Mapping Committee, 444 Baku, Azerbaijan (In Aze.)

Tanriverdiyev, Kh, K. Khalilov, H.A., & Khalilov, M. Y. (2015). Geography of the Republic of Azerbaijan-Physical Geography [I vol.]. Avropa, 530, Baku, Azerbaijan

Huseynov, N. Sh. (2011). Synoptic meteorology. Sada, 316, Baku, Azerbaijan

Imanov, F. A. (2011). Statistical methods in hydrometeorology. MBM, 272, Baku, Azerbaijan

Mahmudov, R. N. (2018). Modern climate changes and dangerous hydrometeorological phenomena. National Aviation Academy, 232, Baku, Azerbaijan

Shikhlinsky, E. M. (1968). Climate of Azerbaijan. Academy of Sciences of Azerbaijan. 360, Baku, Azerbaijan

Safarov, S. H., Huseynov, D. S., & Guliyev, Z. G. (2022). Spatio-temporal features of the distribution of precipitation in the territory of Azerbaijan. Hydrometeorological research and forecasts, 1, 77–94, Moscow, Russia

Pykhtunova, V. M. (1966). Reference book on the climate of the USSR, Temperature of air and soil. (Dagestan ASSR, Azerbaijan SSR, and Nakhchevan ASSR). Gidrometeoizdat, 267, Leningrad, CCR

Mammadov, R. M., Safarov, S. H., Safarov, E. S. (2009). Current changes of the atmospheric precipitation regime on the territory of Azerbaijan. Geography and Natural Resources, 30 (4), 403–407, Elsevier

Huseynov, N. Sh., Huseynov, J. S. (2022). Distribution of the Contemporary Precipitation Regime and the Impact of Climate Change on it within the Territory of Azerbaijan. Journal of Geography & Natural Disasters, 12(4), 1000254.1-7, Barcelona, Spain

6th Intercontinental Geoinformation Days

igd.mersin.edu.tr

How is mathematics popularized as the basis of engineering education?

Nuri Erdem[*1], **Battal Yıldırım** [2]

[1] *Engineering Faculty, Department of Geomatic Engineering, Osmaniye Korkut Ata University, Osmaniye, Türkiye*
[2] *Şehit Mehmet Karacatilki Anatolian Imam Hatip High School, Math Teacher, Osmaniye, Türkiye*

Keywords
Mathematics Teaching
Mathematics Favorite
Mathematics in Engineering
Education

Abstract

Mathematics in engineering is very large areas of use. In fact, it is so much that engineering is the profession that uses mathematics the most. Especially survey engineering is an engineering field that uses mathematical knowledge so much since it has already entered the field of Applied Mathematics as a branch of Science. As a science fiction, mathematics, which has been active in all periods of human history, is a "very lovely" by some of today's students and a "never loving" one for some. In this study; a questioner has been conducted on the questionnaire "How is Mathematics endeared?" with approximately 445 students at different grade levels in different schools who teach different types of education in Osmaniye province and 20 mathematics teachers who work in these schools participated. The answers are analyzed and interpreted with Excel graphs, and it is aimed to contribute to ingratiate and liking of the mathematics course in this way. After all; with this study, awareness about mathematics has been formed in teachers and students, negative factors that decrease mathematics success have been determined, everyone has offered suggestions for solution of the problem and it has been reached that mathematics can be ingratiate and liked when appropriate methods and techniques are used.

1. Introduction

There is a historical background that is matched to the history of mankind, science fiction mathematics. It is a fact that it is always used by people, even when it is not known when, where it is shaped and how it is used. Today, every person knows and uses the word "mathematics". Mathematics in our age; it can be likened to a magnificent multi-story building with beautiful architecture and acoustics. Many scholars have contributed to the construction of this building. Most of these scientists have gained an international character, representing the whole world, out of a nationality. Some of those are Euclid, El-Harezmi, Ömer Hayyam, Ebu Reyhan Biruni, Archimet, Ebu Ali İbn-i Sina (Avisenna), Nasireddin Tusi, Ebul Fazl Tebrizi, Ebul Vefa, A. Cauchy, G. Leibniz, Leonard Euler, Friedrich Gauss, Nils Abel, Evarista Galois, Ramanajuan. These great people continue to be a model for anyone interested in science today (Nasibov and Kaçar, 2005). Leonardo Da Vinci, a famous painter and scientist, said about the metamorphic: “no research can be worthy of taking the name of Science after math has been proved.”

The famous mathematician Einstein said that prejudice is difficult to break down atomic atoms. This prejudice is the duty of the educators to destroy, as well as the duties of the students and the parents in this regard. Many of the people who succeed in mathematics are mathematics-loving people. When the popularity of mathematics is gained, mathematical success is also achieved. A person with good mathematics can think rationally, fluently and rationally. This opens the door to success in other areas and increases the overall level of success in life (URL_1).

In primary and secondary schools, many students find it difficult, uncomfortable and boring to learn mathematics (Sedighian and Sedighian, 1996). Therefore, students do not want to learn mathematics. Studies conducted in Turkey and in various countries; demonstrates that there are many factors that negatively affect students' math learning and math thinking. Some of those; teachers' lack of field knowledge, inability to use effective teaching techniques, low level of students' readiness, interaction with the student's environment, learning environment (Fuys, et al., 1988; Messick and Reynolds, 1992; Wentzel, 1997; Freitas and Jameson, 2006; Yalçınkaya and Özkan, 2012).

New alternative teaching methods are being developed instead of methods that have been going on for years in mathematics teaching and can no longer yield. Accordingly, in mathematics education in Turkey; there are being made studies on alternative learning

* **Corresponding Author**

* nurierdem@osmaniye.edu.tr, http://orcid.org/0000-0002-1850-4616
battalkerem@hotmail.com, http://orcid.org/0000-0003-4161-5434

Cite this study

Erdem, N., & Yıldırım, B. (2023). How is mathematics popularized as the basis of engineering education? Intercontinental Geoinformation Days (IGD), 6, 371-374, Baku, Azerbaijan

methods and techniques such as computer assisted instruction, collaborative learning, probing based learning, drama and games learning, concept mapping learning, visual learning, full learning model and problem-solving method (Yalçınkaya and Özkan, 2012).

The map is an example of a bird's eye view of all or part of the earth, drawn on a plane with special signs, scaled down by the mathematical methods according to the desired scale. Because the map is the most important way to transmit geographical information, we know from the works that thinkers (especially ancient Greek) and mathematicians are dealing with the purpose of knowing the world. For example, Miletus Anaksimandros, who observed and described the progress of the Great Menderes River Delta in Turkey, speaks more about geographical relations (Çobanoğlu, 2016).

2. Method

This study has emerged from the movement of "Why mathematics achievement in Turkey is not at the desired level?" question. The ideas of students and mathematics teachers, both sides of mathematics teaching, are considered to contribute more to mathematics success by increasing the liking of mathematics lessons.

Firstly, a preliminary study was carried out with the student group to work with, and directed the students and mathematics teachers in Osmaniye Şehit Mehmet Karacatilki AİHL to ask "How is Mathematics endeared?". A questionnaire form was prepared by organizing answers. The survey was conducted with 526 students from different levels (1st, 2nd, 3rd and 4th grade students) in different high schools in Osmaniye province (Imam Hatip, Anatolia, Science, Social Sciences etc.) and 20 mathematics teachers who participated in these schools. However, some of the students did not answer some questions. The answers are analyzed and interpreted with Excel graphs, and it is aimed to contribute to the endearing and liking of the mathematics course in this way.

2.1. Questionnaire Study Applied to Students

The suggestions/thoughts used in the questionnaire study applied to students and the answers are given in Table 1.

Table 1. The suggestions/thoughts used in the questionnaire study applied to students and their answers

No.	Suggestions / Thoughts	Answers						
		Agree	Rate (%)	Partially	Rate (%)	Disagree	Rate (%)	Total
1	I already like mathematics.	236	52.8	160	35.8	51	11.4	447
2	I don't think it's possible to like mathematics.	32	7.2	95	21.3	319	71.5	446
3	It is wrong to try to make everyone like math. I think everyone should learn the lesson he likes.	239	53.5	122	27.3	86	19.2	447
4	Mathematics can be liked by giving more responsibility and ensuring student attendance.	135	30.3	141	31.7	169	38.0	445
5	Mathematics can be liked if it is explained by being related to real life and being more concrete.	287	65.1	118	26.8	36	8.2	441
6	Mathematics can be liked if the student is taught directly in private lesson format.	168	37.8	174	39.2	102	23.0	444
7	Mathematics can be liked by adding more activity, music and games according to age groups.	286	64.6	101	22.8	56	12.6	443
8	Mathematics can be liked if the reason of putting curriculum of the mathematics course is explained nicely.	181	40.7	176	39.6	88	19.8	445
9	Mathematics can be liked if explanatory explanations of the areas in which mathematics are used are arranged.	269	60.3	106	23.8	71	15.9	446
10	Referring to the history of the formulas in mathematics and explaining the mathematics related to the history can make him like.	100	22.6	136	30.8	206	46.6	442
11	Mathematics can be liked by telling the events and the miracles in the natural world.	233	53.0	128	29.1	79	18.0	440
12	Mathematics can be liked if teachers are able to reach the teachers more easily if the students can't solve them.	320	72.1	92	20.7	32	7.2	444
13	Mathematics can be liked by creating competition among students and organizing entertaining math competitions.	254	57.0	120	26.9	72	16.1	446
14	Teachers should be encouraged to tell fun lessons and to give students self-confidence for math lessons. This is the only way math can be liked.	335	75.8	84	19.0	23	5.2	442
15	Mathematics is learned when studied very regularly, and it is liked when it is learned.	303	68.2	104	23.4	37	8.3	444
16	A student in secondary education should have good mathematical background in elementary school to like mathematics.	323	72.4	79	17.7	44	9.9	446
17	Studies should be carried out to ensure that students are patient by saving them from the perception that mathematics is difficult and that they can't do it.	397	75.5	41	7.8	88	16.7	526

2.2. Questionnaire study applied to teachers

The suggestions/thoughts used in the questionnaire study applied to teachers and the answers are given in Table 2.

3. Conclusions and Recommendations

In this study, it is aimed to contribute to endear and liking of mathematics course. While searching for an answer to the question "How is Mathematics endeared?", awareness about mathematics was formed in the teachers and students, negative factors reducing the mathematics success were determined, everyone thought about their deficiencies and empathized and made suggestions for solution of the problem. It was concluded that mathematics can be endeared and liked when appropriate methods and techniques are used. For this, firstly;

- When teaching mathematics, not only theoretical courses should be taught, but also practical activities should be used.
- Students' expectations should be taken into consideration while teaching mathematics.
- Such researches should be done constantly and the obstacles in front of the math loving and the student should be detected and this obstacle should be removed.
- Students should be informed about mathematical study techniques.
- Methods and techniques used in mathematics lessons should be diversified.
- Mathematics teachers should research and update themselves according to changing and developing conditions.
- We need to think about ways to make the curiosity in the students act and want them to explore the mysterious world of mathematics.
- In fact, the growing conditions and psychological conditions of today's young people are also important factors affecting teaching mathematics. According to our observations, today's young people often give up quickly when they see it hard. However, mathematics needs to be patient and to work steadily and regularly.

Table 2. The suggestions/thoughts used in the questionnaire study applied to teachers and their answers

No.	Suggestions / Thoughts	Answers						
		Agree	Rate (%)	Partially	Rate (%)	Disagree	Rate (%)	Total
1	I do not think it's possible to like mathematics.	0	0	1	5	19	95	20
2	It is wrong to try to endear mathematics to everyone. I think everybody learn the lesson they like.	3	15	10	50	7	35	20
3	Mathematics can be liked by giving more responsibility and ensuring student participation.	8	40	9	45	3	15	20
4	Mathematics can be liked if it is explained by being associated with real life and being more concrete.	17	85	1	5	2	10	20
5	Mathematics can be liked if the student is taught directly in a private lesson format.	7	35	12	60	1	5	20
6	More activity in mathematics can be endeared by adding games according to music and age groups.	14	70	4	20	2	10	20
7	Mathematics can be liked if the reason for putting curriculum is explained well.	9	45	11	55	0	0	20
8	If introductory trips are organized in the areas where mathematics is used, mathematics can be liked.	15	75	5	25	0	0	20
9	The history of the formulas in mathematics is mentioned and the description of mathematics in connection with the history allows liking mathematics.	7	35	11	55	2	10	20
10	Mathematics can be liked by telling the events and miracles in the nature to be connected with mathematics.	16	80	3	15	1	5	20
11	Mathematics can be liked if teachers are provided with more convenient access to questions that students can't solve.	12	60	8	40	0	0	20
12	Mathematics can be endeared by creating competition among students and organizing entertaining math competitions.	13	65	6	30	1	5	20
13	Mathematics can be liked by teaching funny lessons to teachers and providing them with self-confidence in solving mathematics lessons.	15	75	4	20	1	5	20
14	Mathematics is learned if studied very regularly, and it is liked as well.	19	95	0	0	1	5	20
15	In order for a pupil in secondary education to like mathematics, he must have a good mathematical background in primary education.	18	90	1	5	1	5	20
16	Students should be aware of the difficulty of mathematics, and I should not be able to do, so that they can be patient.	19	95	0	0	1	5	20

Acknowledgement

The present study was produced from TUBITAK (The Scientific and Technological Research Council of Turkey) Project (Project No: L18B486). It was titled "How is Mathematics Endeared?" supported by the 4006-TUBITAK Science Fairs Support Program. It was prepared by Osmaniye Şehit Mehmet Karacatilki AIHL. We thank TUBITAK and Osmaniye Şehit Mehmet Karacatilki AIHL for this project. We also thank the participating schools, teachers and students.

References

Allen, H. G. (2000). Civil and Structional Engineering Education in the 21st Century: A Review of Papers Presented at the Conference, The Structional Engineer, 78(17), 17-20.

Çobanoğlu, S. (2016). Kartografya ve Uygulamalari Ders Notlari, Harita Genel Komutanlığı, Ekim, Ankara.

Freitas, S. D., & Jameson, J. (2006). Collaborative E-Support for Lifelong Learning, British Journal of Educational Technology, 37 (6)

Fuys, D. J. (1988). The Van Hiele Model of Thinking in Geometry among Adolescents, Journal for Research in Mathematics Education, Monograph, Number 3.

Palancıoğlu, H. M., Erkaya, G., & Hoşbaş, G. (2007). Avrupa Birliği Sürecinde Jeodezi ve Fotogrametri Mühendisliği'nin Durumu, TMMOB Harita ve Kadastro Mühendisleri Odası 11. *Türkiye Harita Bilimsel ve Teknik Kurultayı, Ankara*.

Kent, P., & Noss, R. (2000). The Visibility of Models: Using Technology as a Bridge between Mathematics and Engineering, International Journal of Mathematics Education in Science and Technology, 31(1), 61-69.

Messick, R. G., & Reynolds, K. E. (1992). Middle Level Curriculum in Action, White Plains, Longman, New York.

Nasibov, F., & Kaçar, A. (2005). On the Mathematıcs and Mathematıcs Educatıon, Kastamonu Education Journal, October, 13(2).

Sedighian, K., & Sedighian, A. (1996). Can Educational Computer Games Help Educators Learn About the Psychology of Learning Mathematics in Children?, In 18th Annual Meeting of the International Group of the Psychology of Mathematics Education, The North American Chapter, Florida,

Sutherland, R., & Pozzi, S. (1995). The Changing Mathematical Background of Undergraduate Engineers: A Review of the Issues. London: The Engineering Council.

Uçar, D., Ipbüker, C., & Bildirici, İ. Ö. (2011). Matematiksel Kartografya,Nobel Akademik Yayıncılık.

Uçar, D., İpbüker, C., Bildirici, İ. Ö. (2004). Matematiksel Kartografya, Harita Projeksiyonları Teorisi ve Uygulamaları, Atlas Yayın Dağıtım, İstanbul, http://www.karto.itu.edu.tr/derslerimiz/projeksiyonlar/

URL_1:http://www.gencgelisim.com/v2/kategoriler/63-egitim/5305-matematik-nasil-sevilir.html,

URL_2: http://yumurtaliekmek.com/matematik-nasil-sevilir/?share=email&nb=1

URL_3: Yahnioğlu, N., Matematik Mühendisliğine Giriş, http://slideplayer.biz.tr/slide/11635781/

URL_4: Ubuz, B., Tosmur, N., Elektrik-Elektronik Mühendislerinin Matematik ve Matematik Eğitimine İlişkin Görüşleri

URL_5:https://www.turkcebilgi.com/harita_ve_matematik

Wentzel, K. R. (1997). Students Motivation in Middle School: The Role of Perceived Pedagogical Caring, Journal of Educational Psychology, 89(3), 411

Yalçinkaya, Y., & Özkan, H. H. (2012). Content Analysis of The Articles About Alternative Methods of Mathematics Teaching in Journals Published by Education Faculties Between the Years 2000-2011, Journal of Süleyman Demirel University Institute of Social Sciences, 2(16), 31-45

Yenioğlu, Z. A. (2017). Bilişim ve Mühendislik İçin Bir Gereklilik: Matematik.

6th Intercontinental Geoinformation Days

igd.mersin.edu.tr

Compilation of environmental protection maps by region, economic area and scale

Magsad Gojamanov*[1], Ilhama Garibova [1]

[1]*Baku State University, Geography, Geodesy and cartography, Baku, Azerbaijan*

Keywords
Nature protection maps
Scaling order
Landscape zone
Azonal
Interzonal

Abstract

Environmental protection maps are divided into groups according to their purpose: maps describing protected natural areas and maps of environmental protection measures, and according to their content, by region, economic area and scale. When compiling regional EPM maps, the area is divided mainly by the principle of landscape zoning, and in special cases by the principle of administrative territory or basin (hydrographic network). Such maps contain various types of protection measures, the interrelationships of processes, and the regularity of change in space and time. The content elements in the specialized series of EPM of economic area include measures such as reclamation, restoration, cleaning of the area, reorientation of the enterprise to other economic spheres, regulation of the economic purpose of the territories. Large-scale EPMs describe regions with a complex landscape structure and a wide variety of nature protection objects. In the dissertation, the framework requirements for the content and legend load of all three groups of EPM maps were developed, the design methodology was improved, and the author's map copies were compiled.

1. Introduction

Geographically, the main purpose of nature protection is to create specially protected objects in order prevent the disturbance of nature as a result of economic activities. Depending on the object of environmental protection research, the direction of environmental protection mapping is determined and maps are compiled in accordance with the content of this direction [1]. The scientific basis of environmental protection maps (EPM) is formed by general landscape-territorial maps. In general, EPM is mainly divided into two main groups:

- maps describing protected natural areas;
- maps of environmental protection measures.

Compilation of environmental protection maps is very important in the development of methodological bases of environmental protection measures. It is possible to conduct a comprehensive assessment for any area based on environmental protection maps.

Compilation of environmental protection maps of the region is a very important and integral part of the whole complex of work on environmental protection. When choosing thematic content elements for EPM maps, these maps should clearly indicate which natural components are planned to be protected and restored, the measures to be taken, and the area in which they will be placed. The content elements of EPM maps are also selected depending on the size and purpose of the area they cover. In general, in accordance with the above features, EPM maps are divided into specialized groups by region, economic region and scaling order.

2. Regional order of EPM

Small-scale regional EPMs mainly reflect the resistance of territories to anthropogenic impacts on the environment and their livelihoods, and only a general view of specially protected natural areas can be presented. At the same time, the areas of distribution of rare flora and fauna, the boundaries of reservoirs, areas of reforestation, etc., measures are described. In the legend of small-scale regional EPM, information on the characteristics of conservation measures can be presented in the form of diagrams, histograms, schemes and pictures. It is not necessary to reflect all environmental protection measures on these maps. If it is necessary to show more fully the area of protected objects, cartogram and diagram methods should be used. It is recommended to use a quality background method when creating a map of large regions.

* **Corresponding Author**

*(m.goja@yandex.ru) ORCID ID 0000 – 0002 – 5653 – 5675
(qaribovailhama.ahmad@bsu.edu.az) ORCID ID 0000-0003-4874-1927

Cite this study

Gojamanov, M., & Garibova, I. (2023). Compilation of environmental protection maps by region, economic area and scale. Intercontinental Geoinformation Days (IGD), 6, 375-378, Baku, Azerbaijan

Table 1 lists the elements that will be included in the regional EPM legend, compiled by terrain types located in different zones and belts. Table 2 shows the regional EPM legend elements for the landscapes of the azonal and interzonal regions.

Table 1. Regional EPM legends by zone and zone

In the forest-tundra landscape zone	It is a description of measures for the protection of fire-hazardous areas, vegetation and soil cover from transport, rocks from decomposition, rare species of birds and animals, spawning grounds for fish, riparian forest areas.
In forest zone	Protection of forests from fires and floods and protection of swamps, reservoirs, berry fields, rare fauna, rare and relict plants; Thermokarst and the fight against excess moisture; Reforestation measures should be described.
In the steppe landscape zone	Measures to protect soils from water and wind erosion, salinization, raw soil steppes, rare bird and animal species should be described.
In the zone of mountain landscapes	Protection of soils from erosion and rare wild animals; Prohibition of deforestation, stripping of slopes, even selective thinning of trees in the forest; Measures to prevent avalanches, floods and landslides; It is necessary to describe the regulation of animal grazing on mountain pastures, plowing of fertile lands in a scheme that stops the development of landslides, phytomelioration measures.

3. EPM of economic area

When creating an EPM of an economic area, it is important to carry out economic zoning of the country's territory in accordance with economic activity and economic concentration. In this case, environmental protection mapping and the content of the analysis to be carried out on its basis consists of studying the effects of specific field complexes (pollution, disturbance, degradation, etc.) on natural objects located in the area. The complexes are mainly divided into industrial, agricultural and recreational areas.

During the period when Azerbaijan was part of the USSR, inefficient use of natural resources and low level of nature protection work had a serious negative impact on the environment in the country. Lack of regulatory facilities in industry, excessive use of toxic chemical fertilizers in agriculture have led to pollution of our lands and atmosphere. During the years of independence, our country has made a radical turn in the field of ecological balance, protection of the environment, consistent measures have been taken to protect natural resources, including minerals, water, soil, air, forests and biodiversity.

It should also be noted that the areas with the highest environmental problems are mainly industrial and agricultural areas. The Caspian Sea, the Absheron Peninsula, the southeastern Shirvan and Mugan plains, where the oil industry is located, are the areas with the highest environmental problems.

Table 2. The legend of the azonal and inter-zonal regional EPM

Great river valleys	The spawning grounds of rare species of plants and living creatures, valuable commercial fish, measures to protect the upper reaches of water bodies are described.
Swamps	Measures for the protection of rare plant and species species, berry fields are described.
Areas where geological rocks are collected	Measures for the detection and protection of geological objects and paleontological objects are indicated.
Areas of anthropogenic impact	Archaeological monuments (kurgans, ancient cities, places inhabited by ancient people); measures for the protection of natural objects in the places where politicians, scientists and artists live and work is described.
Afforestation areas	Given protection measures of green areas in residential areas; trees on the side of roads; forest protection strips; construc-tion of monuments of horticultural art and resort-recreation forests.
Hydrographic objects	Rivers, lakes, seashores; creation of basin protection zones in the coastal Special Protection Areas (SPA); Detection and protection of hydrological SPAs (reserves, waterfalls, groundwater sources, etc.); Measures against the collapse of coastal areas should be reflected.
Historical-landscape and ethnographic-landscape monuments	Should be reflected measures for protection of places of historical events (geographical discoveries, battles); the lands inhabited by local peoples and arable lands.

There is a special need for nature protection measures in the man-made degraded lands of Dashkasan, Balakan and Nakhchivan AR, as well as large industrial cities Baku, Sumgayit, Ganja, Shirvan and Mingachevir, where the mining industry is developed. It is necessary to take more active measures to protect and restore the saline, eroded soils of the Kura-Araz lowland, as well as to protect and restore light forests.

In this complex of activities, environmental protection maps are very important. In these maps environmental protection areas are shown in different colors and objects in circles. In the legend of the map, the area of objects is determined by the diameter of the circles. The diagrams show the components that are considered environmentally important. We have compiled maps of the areas where some industries of Azerbaijan are located. Examples of these maps are pollution maps of the Absheron Peninsula and Dashkesan region (Figures 1 and 2) When designing EPM for industrial areas, special attention is paid to the protection of water bodies (Caspian Sea, lakes of Azerbaijan, main rivers, reservoirs, etc.), atmosphere,

groundwater, soil and plant resources. These areas can be shown as species distribution areas, special boundaries and etc. These maps should also show the areas on which reclamation works are carried out and are proposed (mining areas).

The main elements of the content are the description of such activities as reclamation, restoration, cleaning of the territory, reorientation of the enterprise to other economic regions, regulation of the economic purpose of areas in the specialized line of EPM.

For industries, it is important to indicate the following protection measures in EPM maps:

- an indication of the sites for the extraction of minerals;
- boundaries of sanitary protection zones created around industrial facilities;
- areas for collection and processing of industrial waste;
- observation points for continuous environmental monitoring;
- Proposed measures for carrying out restoration work in the territories where industrial zones are located (Gadabay, Dashkesan ore deposits).

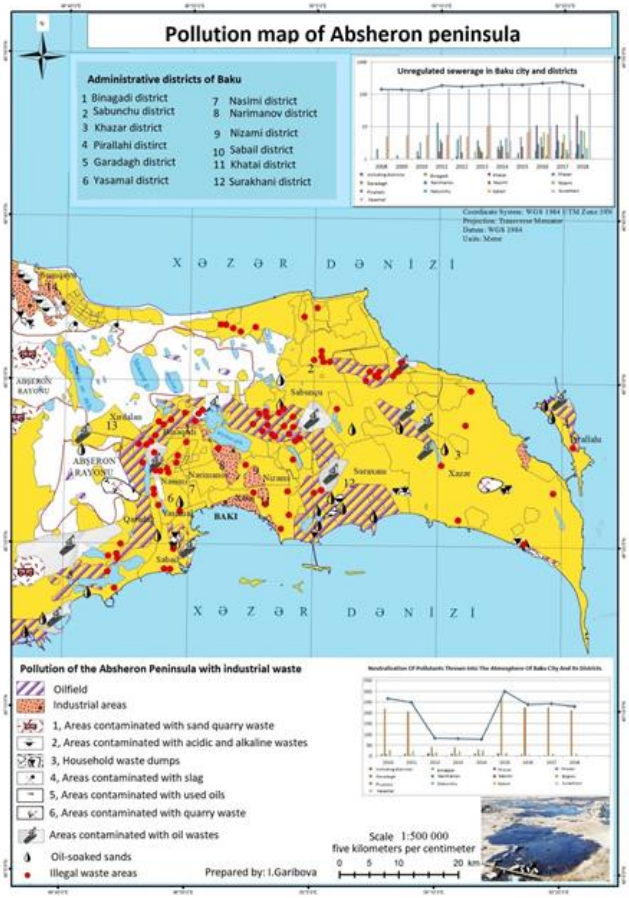

Figure 1. Pollution map of Absheron peninsula

When describing the development of agricultural lands in the EPM, the scheme of regular distribution of grazing and pastures (mainly in the foothills), the areas where reclamation measures are carried out and proposed (many areas of the Kur-Araz lowland) should be reflected. It is known that some areas of the Absheron Peninsula and the Kura-Araz lowland have been exposed to salinization. Washing of these territories and the areas that need to be washed, normalization of fertilization, etc. should be specified in the EPM. Water erosion is common in areas where agriculture is widespread.

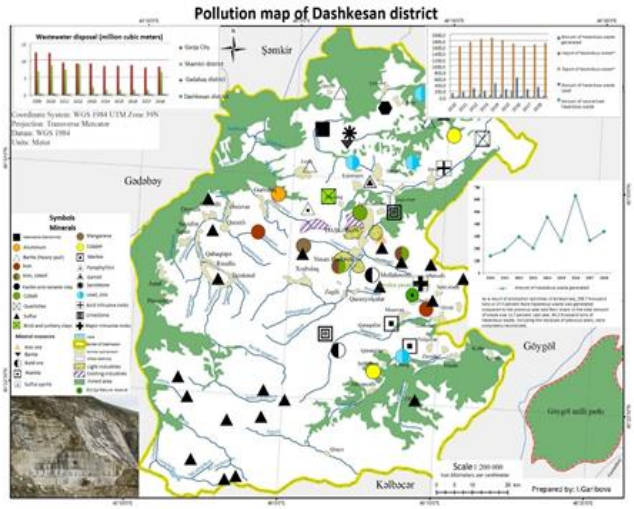

Figure 2. Pollution map of Dashkesan district

As it is more common in arable land, it is preferable to take measures against erosion in these areas. The maps should also indicate legally protected areas, natural objects, underutilized areas, and environmental agencies.

When showing the boundaries of recreation areas in the EPM, it is necessary to pay attention to specially protected natural areas, natural monuments, resort forests and beach areas. Depending on the degree of protection the zoning of national parks and depending on the tourist load the regulation of these zones should be carried out correctly. Pollution prevention measures should be specified. The content of existing recreational maps should provide information on the implementation of security rules and the state of protected objects.

4. Scale range of EPM maps

Scale EPMs are primarily designed in regions with complex landscape structures and a wide variety of nature protection areas. It is known from the cartography course that maps are usually divided into large-scale (1: 200,000 and more), medium scale (1: 200,000–1: 1,000,000) and small scale maps (less than 1: 1,000,000). Similarly, the scale range of EPM can be classified. However, the scale of these maps can be drawn not only on the scale of 1: 10000, 1: 25000, 1: 50000 and others, as in the state standard, but also on an arbitrary intermediate scale.

Generalization of EPM is sometimes associated with great difficulties. It mainly depends on the level of detail of nature protection problems. One of the reasons for the difficulty of generalization is that protection measures can be given in EPMs of different scales with completely different cartographic methods, and therefore the transition from scale to scale requires individual decisions in each case. In some cases, it is also possible to indicate the SPA and the Natural-Technical System (NTS) in scaleless characters or numbers (Table 3).

Table 3. Content elements of scale range EPM

Map scale and mapping area	Degree of description of SPA and NTS			
	Large area NTS	Small area NTS	Reserve, national parks	Dotted SPA historical, cultural, natural monuments
Summary and small scales: 1: 1 000 000 - 1:10 000 000 (maps of large countries and ad-ministrative-terri-torial divisions)	In full	With certain restrictions	With certain restrictions	-
Average scales: 1: 200 000-1: 1 000 000 (maps of small countries and ad-ministrative-terri-torial divisions)	With certain restrictions	In full	In full	With certain restrictions
Large scales: 1: 10000-1: 200000 (map of districts, SPAs and land-scape complexes)	-	With certain restrictions	In full	In full
Very large scales: 1: 2,000 -1: 10,000 (SPA plans)	-	-	With certain restrictions	In full

The results of the landscape planning should also be used in the compilation of the EPM. Landscape planning aims to maintain soil health and protect its physical and biological environment and is a system that serves to presserve the characteristics of the landscape. Landscape planning is the process of collecting and studying information about the current state of the environment in an area, its importance for the country's economy, its attractiveness and vulnerability. It then examines the impact of current and future projects in the area on these components and identifies parameters that are important for the sustainable development of the area. An action plan is also being developed to ensure the vital functions of the natural environment, maps are published with recommendations for the use and management of the landscape. In recent years, extensive research in the field of landscape planning has been carried out in Azerbaijan under the leadership of academician Ramiz Mammadov.

5. Conclusion

Based on the analysis and study of the features of the maps, the following conclusions were drawn:

1. When compiling regional EPM maps, the area is divided mainly by the principle of landscape zoning, and in special cases by the principle of administrative territory or basin (hydrographic network). Such maps contain various types of protection measures, the interrelationships of processes, and the regularity of change in space and time.
2. The content elements in the specialized series of EPM of economic area include measures such as reclamation, restoration, cleaning of the area, reorientation of the enterprise to other economic spheres, regulation of the economic purpose of the territories. Large-scale EPMs describe regions with a complex landscape structure and a wide variety of nature protection objects. The framework requirements for the content and legend load of all three groups of EPM maps were developed, the design methodology was improved and the author's map copies were compiled.
3. Maps of the regional EPM series mainly reflect the stability and vital activity of areas to man-made environmental impacts and can only give the appearance of specially protected natural areas. Cartogram and diagram methods can be used in the preparation of regional EPMs, in large regions the quality background method can be used, and in the legend information on environmental protection measures can be given in the form of diagrams, histograms, schemes and pictures.
4. When creating a series of EPM for the field of economy, the content of environmental mapping and analysis based on it is directed to the study of the impact of specific field complexes (pollution, disturbance, degradation, etc.) on natural objects located on the territory.
5. When compiling a large-scale EPM, the map should reflect suggestions for agricultural land, mineral deposits, forestry, the boundaries of recreational zones and the state of these territories, protected areas, rational use of natural resources.

References

Gojamanov, M. H., Garibova, I. A., & Smirnov, A. A. (2020). Recreational zoning of the lesser Caucasus. Proceedings of the International conference InterCarto. InterGIS Support of sustainable Development of territories, 26(3), 416-423.

Gojamanov, M. H, & Garibova, I. A. (2019). Theoretical and methodological bases of nature protection maps "Modern Problems of water management, Environmental protection, architecture and construction" IX International Scientific and Technical conference "Modern Problems of water management, Environmental protection, architecture and construction" (Tbilisi,Georgia)

Maquire, D. J. (2005). CİS Spatial Analysis and Modeling. Redlands, CA: ESRİ Press, 480 p.

Berlyant, A. M., Vostokova, A. V., & Kravtsova, V. I. (2003). Cartography. /edited by A.M.Berlyant , Aspect Press.

Garibova, I. A. (2018). Requirements for the thematic content of nature protection maps. Journal of the Institute of Geography of the Republic of Kazakhstan. Questions of geography and Geoecology, 1, 76-80.

Diakonov, K. N. (2005). Environmental design and expertise. M.: Aspect Press, 384 p.

Kochurov, B. I., Shishkina, D. Yu., Antipova, A. V., & Kostovka, S. K. (2012). Geoecological mapping. – M.: Publishing Center "Academy", 224 p

Mammadov, R. M. (2017). Landscape planning: essence and application. Baku, 292 p.

6th Intercontinental Geoinformation Days

igd.mersin.edu.tr

Obtaining ground points using CSF Filter algorithm in various airborne LIDAR point cloud data

Berkan Sarıtaş*[1], Gordana Kaplan [2]

[1]*Eskisehir Technical University, Graduate School of Science, Eskisehir, Türkiye*
[2]*Eskisehir Technical University, Institute of Earth and Space Sciences Institute, Eskisehir, Türkiye*

Keywords
Remote sensing
CSF Filter
Point Cloud
SAM
LIDAR

Abstract

Airborne laser scanning (ALS) is a remote sensing method widely recognized for its efficiency in acquiring data quickly and delivering accurate results. To ensure the reliability of ALS data, effective decontamination is crucial. This study aims to enhance the data quality of three distinct LIDAR datasets representing urban, rural, and forest environments by applying the CSF Filter algorithm in the CloudCompare software, an open-source tool widely used in point cloud processing. The impact of various data characteristics and input parameters on the filtering results was assessed through a series of comprehensive tests. The results of our analysis revealed a notable relationship between the selected parameters and the quality of the filtered data. Specifically, when the cover value within the CSF Filter parameters was increased, a corresponding increase in data loss was observed, leading to significantly flawed outcomes. These findings emphasize the importance of carefully selecting and fine-tuning the input parameters to avoid undesirable consequences. The findings underscore the importance of combining automated filtering algorithms with manual cleaning to achieve high-quality and reliable point cloud data for various geospatial analyses and applications.

1. Introduction

Modern remote sensing technologies have revolutionized the way we monitor and map large-scale regions, gradually replacing traditional measurement methods. Aerial laser scanning, a prominent laser scanning technology, has emerged as one of the most effective remote sensing methods (Uray, 2022). This technique involves transmitting lasers from scanning devices mounted on aircraft or helicopters, which reflect off objects. The distance between the scanning device and the scanned object is then calculated based on the pulse's return time. Aerial LIDAR systems typically comprise three components: GPS, IMU, and a scanner. The scanner records the reflection values, GPS captures location information of the point cloud, and the IMU-derived orientation parameters of the aircraft assist in calibrating the point cloud (Civelekoğlu, 2015).

Remote sensing methods, such as LIDAR, facilitate the creation of numerical elevation models that encompass comprehensive elevation information of the Earth's surface. Models containing three-dimensional information about various structures on the Earth's surface are known as numerical elevation models, while those representing only the bare land surface are referred to as numerical terrain models (Uray, 2022).

LIDAR technology enables the collection of raw data on both natural and man-made objects present on the Earth's surface (Kostrikov, 2019). It allows for rapid and precise acquisition of physical data in a non-contact manner, facilitating the creation of accurate 3D models (Fidan and Fidan 2021).

This study aims to investigate the performance of different filtering algorithms, specifically focusing on the CSF filter algorithm, in determining ground points for classification in point clouds obtained using LIDAR technology. The research examines various point clouds with distinct properties and compares the accuracy rates of different classification and filtering algorithms. The objective is to determine which algorithm delivers more successful filtering results for specific feature-bearing point clouds.

Previous studies in the literature have employed the CSF filtering algorithm for filtering ground points, such as the study titled "Performance Analysis of the CSF Algorithm for Filtering Ground Points." This research focused on an area characterized by challenging terrain with steep slopes and dense forest cover. Orthophotos

* **Corresponding Author**

*(berkansrts@gmail.com) ORCID ID 0000 – 0003 – 1429 – 0304
(kaplangorde@gmail.com) ORCID ID 0000-0001-7522-9924

Cite this study

Sarıtaş, B. & Kaplan, G. (2023). Obtaining ground points using CSF Filter algorithm in various airborne LIDAR point cloud data. Intercontinental Geoinformation Days (IGD), 6, 382-385, Baku, Azerbaijan

obtained simultaneously with the LIDAR data served as reference data for the study. Point cloud data were processed using the CloudCompare software, with specific parameter values selected for filtering operations. The study employed a classification threshold value of 0.5, a repetition time of 1000, and varied grid resolutions of 0.2, 0.3, 0.4, 0.5, 1, and 2. The results demonstrated distortions in the surface model with increasing grid resolution values, resulting in a reduced number of ground-class points. Consequently, manual filtering was deemed necessary to eliminate non-ground points.

By conducting an in-depth analysis of different filtering algorithms, this study contributes to the field of current research topics in LIDAR technology. The findings offer insights into the most effective filtering algorithms for specific types of feature-bearing point clouds, facilitating accurate data analysis and interpretation for various applications (Karasaka and Keleş, 2020).

2. Materials and Methods

2.1. Point Cloud Filtering

In order to create a SAM with LIDAR, the points belonging to the ground class must be cleared of objects that do not belong to the ground class, such as trees and buildings. This process in question is called filtering (Soycan et al., 2011b).

When the physical properties of the ground points are taken into consideration, they are grouped in four different ways (Süleymanoğlu and Soycan, 2017; Meng et al., 2010):

- **The lowest height:** Ground points are points located at an additional low altitude in the available October LIDAR data.
- **The steepness of the floor surface:** When looking at the Declivity between the ground and points that do not belong to the ground, it is steeper than the Declivity between neighboring ground points.
- **The height difference between the decking points:** The high elevation differences of the points between each other indicate the points belonging to objects such as buildings and trees, while the low elevation differences indicate that it is the declivity point.
- **Homogeneity of the floor surface:** The points belonging to the ground are partly smoother and more continuous than the points belonging to other objects.

2.2. Method

In this study, we investigate the effectiveness of the CSF Filter algorithm, implemented in the CloudCompare software, for filtering LIDAR point cloud data with urban, rural, and forest characteristics. By varying the input parameter values, we aim to determine which parameter values yield more accurate ground point classification. The study involves the creation of Surface Models (SAM) for each parameter value applied in the filtering algorithm, followed by an accuracy analysis of the resulting SAMs.

During the acquisition of LIDAR point clouds, atmospheric conditions like fog or rain can lead to the formation of noise points. Manual cleaning methods using the CloudCompare software are employed to remove these noise points. Subsequently, the CSF Filter algorithm, available in CloudCompare, is utilized for ground point classification. The cover value parameter is assessed using different combinations to determine its impact on the filtering results.

Through this research, we aim to identify the most effective parameter values for accurate ground point classification in LIDAR point cloud data. The findings will contribute to enhancing the data quality and reliability of LIDAR-based applications in urban, rural, and forest environments. Additionally, the study highlights the importance of pre-processing steps, such as manual noise removal, and provides insights into the optimization of the CSF Filter algorithm for improved point cloud filtering.

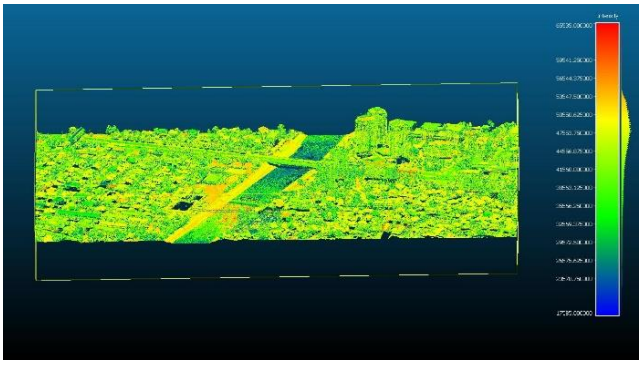

Figure 1. Display of urban area LIDAR data in CloudCompare software

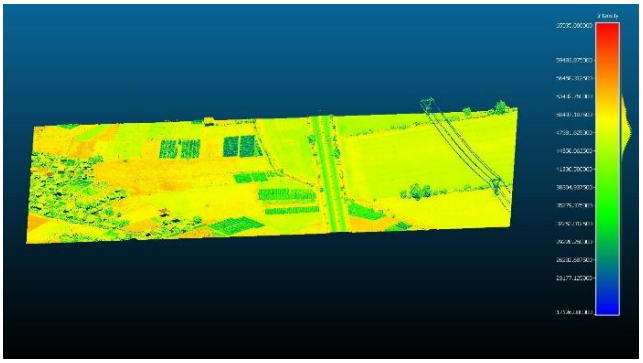

Figure 2. Displaying rural area LIDAR data in CloudCompare software

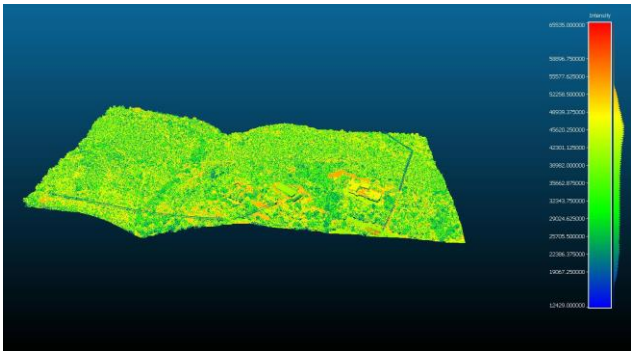

Figure 3. Displaying forest area LIDAR data in CloudCompare software

2.3. Filtering of LIDAR data – urban area

The urban area with a total of 312 buildings, is a part in the western part of Skopje, the capital of North Macedonia (Figure 1). The study area is divided into two parts by the Vardar river, which is about 60 m wide, while there are dense and low residential grid-like buildings with a maximum height of 10 m on the left side of the study area, and there are taller residential and commercial buildings on the right side. The maximum height is 70 m. The working area is generally flat, and the surface height of the working area varies between 250-327, while the terrain height is between 25 Dec-Dec 325. Besides the buildings, there are many trees, bridges and a river bank 20 m wide on both sides in the study area (Kaplan et al. 2022).

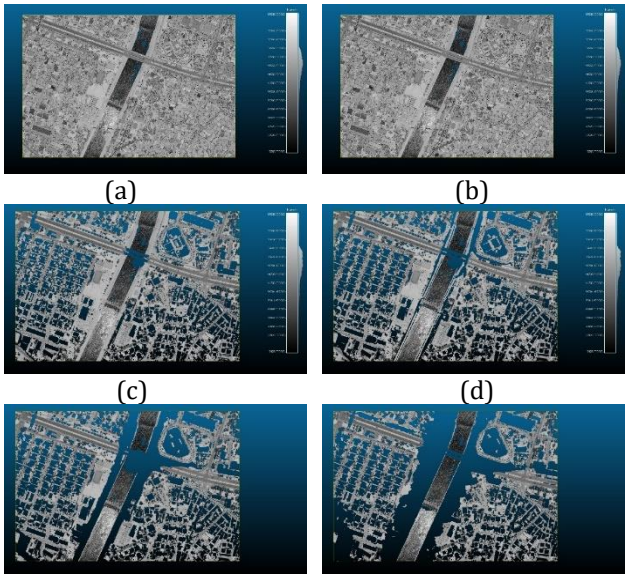

Figure 4. For an urban LIDAR point cloud; (a) The Original Point Cloud, (b) Data Obtained As a Result of Entering the CSF Filter Algorithm Cover Value as 0.1, (c) Data Obtained as a Result of Entering the CSF Filter Algorithm Cover Value as 0.5, (d) Data Obtained As a Result of Entering the CSF Filter Algorithm Cover Value as 1, (e) Data Obtained as a Result of Entering the CSF Filter Algorithm Cover Value as 2, (f) Data Obtained as a Result of Entering the CSF Filter Algorithm Cover Value as 5.

2.4. Filtering of LIDAR data – rural areas

The agricultural study area is flat and consists of corp fields, divided with a road. The main part of the crops is empty, while smaller part of the area consists of green crop lands (Figure 5).

2.5. Filtering of LIDAR data – forest area

The forest area is characterized by its abundant growth of dense and towering trees, which create a captivating and enchanting environment. The natural landscape is further enhanced by the presence of rugged mountains.

The terrain within the forest area is undulating, with varying altitudes and steep slopes that add a sense of adventure and challenge to exploring the region (Figure 6).

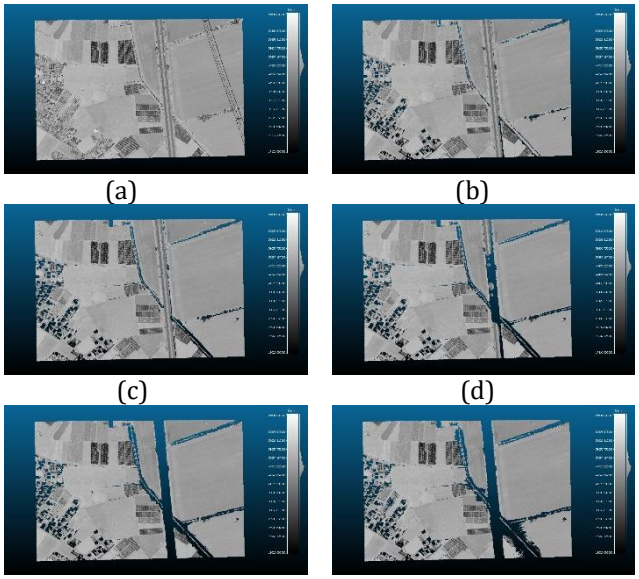

Figure 5. For rural LIDAR point cloud; (a)The Original Point Cloud, (b)The Data Obtained As a Result of Entering the CSF Filter Algorithm Cover Value as 0.1, (c) The Data Obtained as a Result of Entering the CSF Filter Algorithm Cover Value as 0.5, (d) The Data Obtained as a Result of Entering the CSF Filter Algorithm Cover Value as 1, (e) The Data Obtained as a Result of Entering the CSF Filter Algorithm Cover Value as 2, (f)The Data Obtained as a Result of Entering the CSF Filter Algorithm Cover Value as 5.

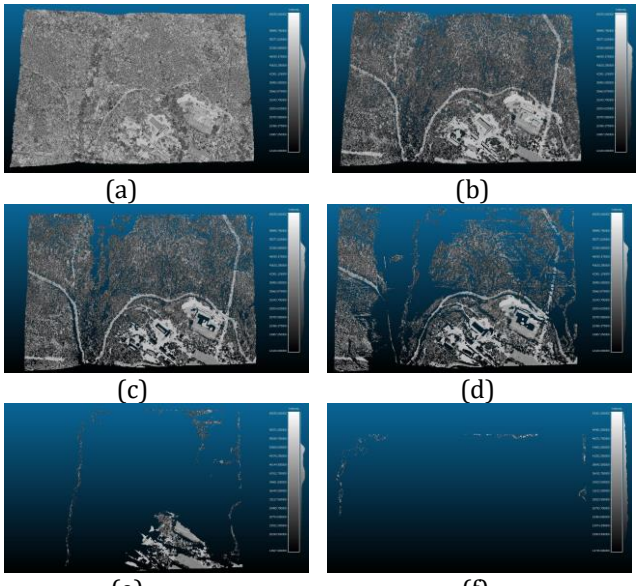

Figure 6. For Forest LIDAR point cloud; (a)The Original Point Cloud, (b)The Data Obtained As a Result of Entering the CSF Filter Algorithm Cover Value as 0.1, (c) The Data Obtained as a Result of Entering the CSF Filter Algorithm Cover Value as 0.5, (d) The Data Obtained as a Result of Entering the CSF Filter Algorithm Cover Value as 1, (e) The Data Obtained as a Result of Entering the CSF Filter Algorithm Cover Value as 2, (f) The Data Obtained as a Result of Entering the CSF Filter Algorithm Cover Value as 5.

3. Results

When examining the ground points classified by the CSF Filter algorithm, it becomes evident that there is a loss of data in the ground points as the cover value increases, leading to noticeably incorrect classifications. While it was initially assumed that the decrease in the cover value would accurately determine the actual ground points, it is observed that planar areas such as building roofs are mistakenly classified as ground points.

In assessing the urban, rural, and forest characteristics of the data, it becomes apparent that the most successful results are achieved in rural areas. However, this assessment has been primarily based on visual analysis. In future studies, it is crucial to perform a statistical accuracy assessment to obtain more reliable and objective results. By conducting such an assessment, the outcomes can be quantitatively compared and analyzed to validate the algorithm's performance across different landscapes.

This statistical accuracy assessment would involve rigorous data analysis and comparison of ground truth data with the algorithm's classifications. Furthermore, the assessment should consider factors like the complexity of urban and forest environments, as they pose additional challenges for accurate ground point classification.

By conducting a thorough statistical accuracy assessment, it will be possible to gain a deeper understanding of the algorithm's limitations and strengths across various landscape types. This assessment will provide more robust evidence to evaluate the algorithm's effectiveness and guide future improvements and optimizations.

In conclusion, while the CSF Filter algorithm exhibits data loss and incorrect classifications in ground points with increasing cover values, a more comprehensive and statistically rigorous accuracy assessment is required to assess its performance accurately. By conducting such an assessment and comparing the results across different urban, rural, and forest landscapes, a clearer understanding of the algorithm's performance can be obtained, leading to further improvements and advancements in the future.

4. Discussion

In the process of removing ground points, which is being performed using the CSF Filter algorithm, manual cleaning operation is required in the remaining parts due to the fact that planar areas are considered as ground. In this way, the process of obtaining ground points will reach a more accurate result.

5. Conclusion

In order for the accuracy analysis to be performed with more precise results, reference SAM data are needed. As a result of comparing the obtained data with the reference data, the accuracy rates of the parameters will be determined more accurately.

Acknowledgement

This study is adapted from Berkan Saritas's master's thesis.

References

Civelekoğlu. B. (2015). Hava LİDAR Verilerinin Sınıflandırılması Ve Orman Ağaçlarına Ait Öznitelik Değerlendirilmesi İstanbul Belgrad Ormanı Örneği Master's Thesis, Yıldız Teknik Üniversitesi.

Fidan, D., & Fidan, Ş. (2021). Yersel lazer tarama teknolojileriyle oluşturulan 3B modellerin akıllı kent uygulamalarında kullanımı: Mersin Süslü Çeşme örneği. Türkiye LİDAR Dergisi, 3(2), 48–57. https://doi.org/10.51946/melid.1021819

Kaplan, G., Comert, R., Kaplan, O., Matci, D. K., & Avdan, U. (2022). Using Machine Learning to Extract Building Inventory Information Based on LİDAR Data. ISPRS International Journal of Geo-Information, 11(10). https://doi.org/10.3390/IJGI11100517

Karasaka, L., & Keleş, H. (2020). CSF (Cloth simulation filtering) Algoritmasının Zemin Noktalarını Filtrelemedeki Performans Analizi. Afyon Kocatepe Üniversitesi Fen ve Mühendislik Bilimleri Dergisi, 267–275. https://doi.org/10.35414/akufemubid.660828

Meng, X., Currit, N., & Zhao, K. (2010). Ground Filtering Algorithms for Airborne LİDAR Data: A Review of Critical Issues. Remote Sensing 2010, Vol. 2, Pages 833-860, 2(3), 833–860. https://doi.org/10.3390/RS2030833

Soycan, M., Tunalioğlu, N., Öcalan, T., Soycan, A., & Gümüş, K. (2011). Three Dimensional Modeling of a Forested Area Using an Airborne Light Detection and Ranging Method. Arabian Journal for Science and Engineering, 36(4), 581–595. https://doi.org/10.1007/S13369-011-0054-8/METRICS

Süleymanoğlu, B., & Soycan, M. (2017). Hava Lidar Verilerinde Kullanılan Filtreleme Algoritmalarının İncelenmesi. TMMOB Harita ve Kadastro Mühendisleri Odası, 16.

Uray, F. (2022). Derin öğrenme tekniklerini kullanarak hava LİDAR nokta bulutlarının sınıflandırılması Doktora Tezi. Necmettin Erbakan Üniversitesi.

6th Intercontinental Geoinformation Days

igd.mersin.edu.tr

3D visualization of pavement distress using terrestrial LIDAR data

Riyaz Khan Noordeen Haroon Rashid[*1], **Vasantha Kumar Selvaraj** [1]

[1]*Vellore Institute of Technology (VIT), School of Civil Engineering, Department of Environmental and Water Resources Engineering, Vellore, India*

Keywords
Pavement distress
3D visualization
Terrestrial laser
Point cloud
LIDAR

Abstract

Terrestrial Laser Scanning (TLS) is a primal technique to obtain high quality 3D visualization models from dense point cloud data. TLS data is being used in several civil engineering fields such as Building Information Modelling (BIM), Pavement Condition Monitoring, etc. This paper focuses on the potential application of TLS point cloud data in the visualization of pavement distresses and in particular, the potholes on roads. Currently, the distresses like potholes are evaluated either through visual examination or images with the approximations. Nevertheless, the precise representation of the pothole is vital to appraise the severity of the distress and be efficacious in the maintenance of the pavement structure. The objective of this study is to use the point cloud data obtained from a terrestrial laser scanner for 3D visualization of potholes on a bituminous pavement and also to quantify it by measuring its accurate area. A road stretch in Vellore, India was taken and LIDAR survey was carried out with a terrestrial laser scanner. The collected point cloud data was then postprocessed to prepare a single LAS dataset with 6 mm accuracy. The area covered by the pothole was then clipped from the point cloud and then visualized three dimensionally by creating different perspective views in ArcGIS software. The results revealed that the LIDAR point clouds are one of the promising data sources for accurate 3D representation of pavement distresses.

1. Introduction

At present, India's National Highway (NH) system gauges around 1.5 lakh km. Of this total network, more than 77,000 km of highways has been constructed, expanded and strengthened between April 2014 and October 2022. This is greater than half of the nation's entire NH network (The Times of India, 2022). Also, through Pradhan Mantri Gram Sadak Yojana (PMGSY) scheme, the government of India has laid almost 430,000 km length of rural roads (Tawalare & Vasudeva Raju, 2016). At present the national highways authority of India (NHAI) is constructing 30 kms of new highways every day and as a result, the pavement evaluation, maintenance and management after completion of the work become very essential.

Pavement evaluation is generally carried out through field-testing and measurements or sometimes visual observation to describe the pavement's structural and functional integrity. The structural evaluation of the pavement deals with its ability to carry the present and future traffic, whereas the functional evaluation indicates its potential to supply a smooth, safe and a perfect ride quality surface (Joni et al., 2020). Functional evaluation holds the information on the characteristics of pavement, which are having significant impact on the safety and comfort of road users (Rusmanto et al., 2018).

Skid resistance, surface distress and road roughness are the primary qualities examined during the functional evaluation of pavement. Surface distress is basically the indication of upcoming failure or poor performance of the pavement through one or more of its signs such as cracking, rutting, potholes, bleeding, shoving, etc. They basically indicate the decline in pavement surface conditions. If unnoticed, they may even lead to safety issues in addition to vehicle delay, increase of fuel cost, etc. For example, in Bengaluru city in India, 6 deaths were reported due to potholes alone in a year (The Indian Express, 2022). Surface distress is generally measured through manual method (visual observation) and video recording methods (Kumar & Chandra, 2022). Even though science and technology is improving day by day, but still the majority of developing nations use the manual or visual observation technique for surface

* **Corresponding Author**

*(riyazkhan.nh2020@vitstudent.ac.in) ORCID ID 0000 – 0003 – 4022 – 8547
(svasanthakumar@vit.ac.in) ORCID ID 0000 – 0002 – 7202 – 4584

Cite this study

Rashid, R. K. N. H. & Selvaraj, V. K. (2023). 3D Visualization of pavement distress using terrestrial LIDAR data. Intercontinental Geoinformation Days (IGD), 6, 386-389, Baku, Azerbaijan

distress evaluation. The road maintenance organization's actual needs cannot be satisfied by these traditional detecting methods as its practically difficult to manually observe thousands of kilometers of roads across a country. Also, this visual observation and evaluation heavily dependent on the investigator's experience in identification as well as ranking of the distress. For example, a distress may be heavy but it may be wrongly recorded as medium or low. There may be combination of distresses at a location but instead it may be wrongly entered as single distress. In order to avoid all these issues with manual observation, nowadays sensor fitted vehicles are being employed. Distress data can be gathered using vehicles as road networks expanded over time and road data gathering using equipment also lowers rater's error, but it comes with a greater realization cost (Silyanov et al., 2020). To overcome all these drawbacks, rapid measurement techniques using terrestrial laser scanner, Unmanned Aerial Vehicles (UAV) mounted laser scanners have been widely employed nowadays (Valaskova et al., 2021). Point cloud data obtained through the Laser Scanning instrument has proved to be effectual in allowing engineers to build a 3D model of the all forms of distresses (De Blasiis et al., 2020; Ravi et al., 2020). Though there are many advantages in using laser scanning for distress evaluation, however only limited studies have been reported (Feng et al., 2022; Elseicy et al., 2022; Azam et al., 2023). Hence, in this study, LIDAR survey was carried out in order to explore its feasibility for distress identification and visualization. One of the popular distresses namely, the potholes were taken and the potential of the LIDAR in pothole identification and measurement was examined.

2. Method

2.1. Study Area

A pilot study was carried out to explore the feasibility of using laser point clouds to visualize the pothole in a three-dimensional way. For this, a 110 m long stretch of a flexible pavement near our Vellore Institute of Technology (VIT) campus was selected. A pothole of considerable dimension was found on this stretch as seen from Fig.1.

Figure 1. Pothole in the study stretch

2.2. Data Collection

The Leica BLK 360 terrestrial laser scanner was employed for laser scanning of the road section with potholes. The scanner works based on the remote sensing technique of Light Detection and Ranging (LIDAR), where the scanner emits 360,000 laser pulses per second and thus can produce a point cloud of millions of data points of X, Y, Z values finally. The scanner can scan up to a range of 60m and it is placed on the footpath of the roadway so that it can cover the entire pavement width along with the pothole. Two scans were taken on April 12, 2022 during high noon and Fig. 2 shows the HD photo of the study stretch taken by the BLK 360 scanner.

Figure 2. High-definition photo taken by the laser scanner showing the pavement with potholes

2.3. Methodology

The collected LIDAR Data were processed in Leica Cyclone Register 360 software. Point cloud created by laser scanning of the pavement and its surroundings is plotted in Fig.3. The pavement surface and its surroundings were exhibited as a cloud of points with spatial coordinates.

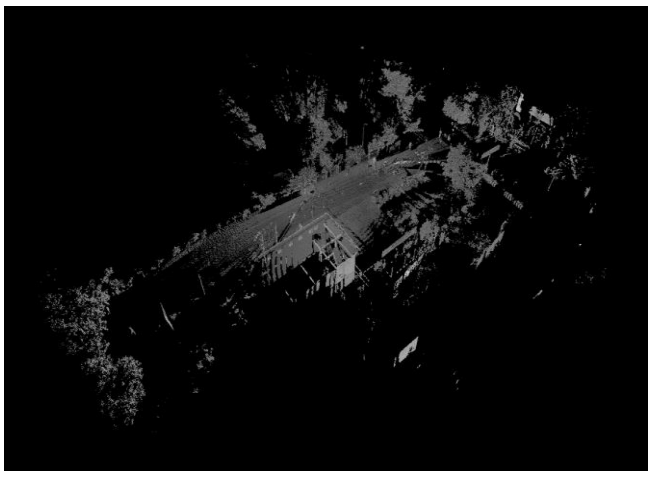

Figure 3. Point cloud from laser scanner

In the first step of post-processing of point cloud data, the scanned setups in BLK format are imported into the Leica Cyclone Register 360 software and the two scans were registered with an accuracy of 6 mm. This registered point cloud has 14,402,526 points. These points are returned from all the objects such as walls of the buildings, cars, moving objects, cables, tress etc. So, pavement surface should be extracted by removing the unwanted noises and the outliers from this cloud. By

using the predefined tools in the processing software, the unwanted objects have been removed for further analysis. The point cloud after extracting the pavement surface is shown in Figure 4.

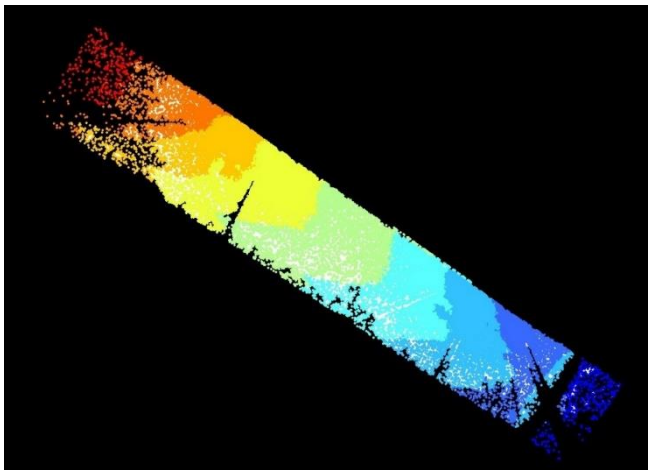

Figure 4. LAS dataset of the pavement surface

After removing the outliers, the remaining section alone has been exported to the .pts (a plain text file that stores point data, typically collected using a LIDAR scanner) format for further analysis. Next, the .pts file format has been converted into the .las format (which is a file format designed for the interchange and archiving of lidar point cloud data) using the Autodesk Recap software as shown in Fig.5. Finally, the .las format has been exported in to the ArcGIS platform for creating 3D scenes of the distress. By using 3D view option in the LAS Dataset toolbar, various 3D views of the pavement and the pothole were obtained.

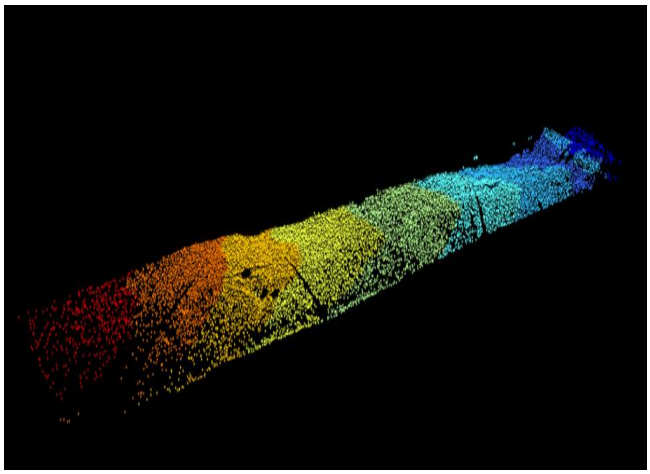

Figure 5. 3D view of the pavement surface

3. Results and Discussion

As we are interested in visualization of potholes, the same has been cut from the original LAS dataset and shown in Fig.6. The dense point cloud of the potholes captured from the TLS enable us in viewing the pothole from different perspectives. The top and side views of the potholes were showed in Figs. 7-9. One can nicely see the 3D model of the pothole and its extent from the Figs. 7-9. The depth of pothole is also pictured in Fig.10. As compared to the normal image, the views from the TLS derived point cloud gives more insight in determining the severity of the pothole. In addition to 3D visualization of potholes, one can also quantify the distress by measurement of its depth, area, etc. using the collected LIDAR data. Using Cyclone Register 360 software, the area of the pothole was measured as 4.644 sq.m. Thus, with the help of LIDAR data, one can visualize three dimensionally the distress condition and also can quantify it accurately.

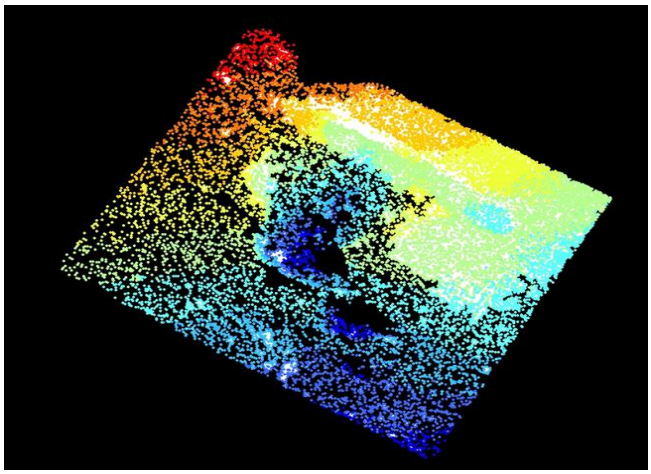

Figure 6. LAS dataset of the pothole

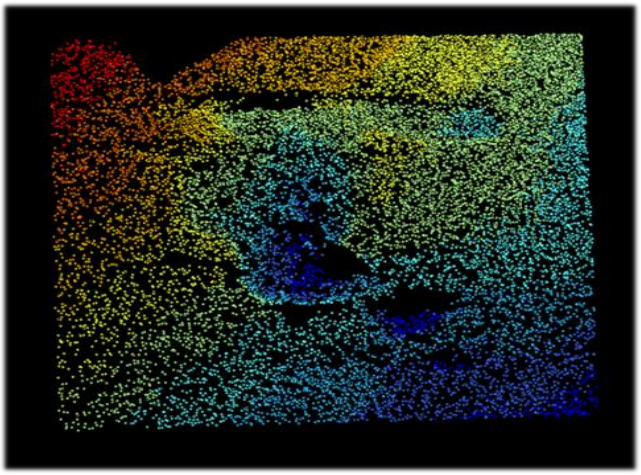

Figure 7. Top 3D view of the pothole

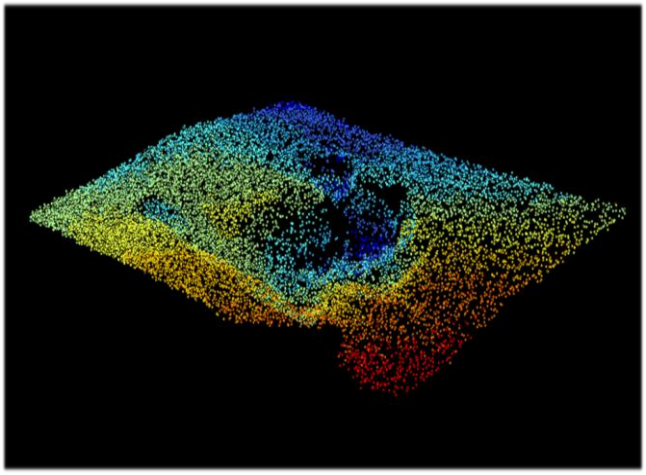

Figure 8. Side 3D view of the pothole

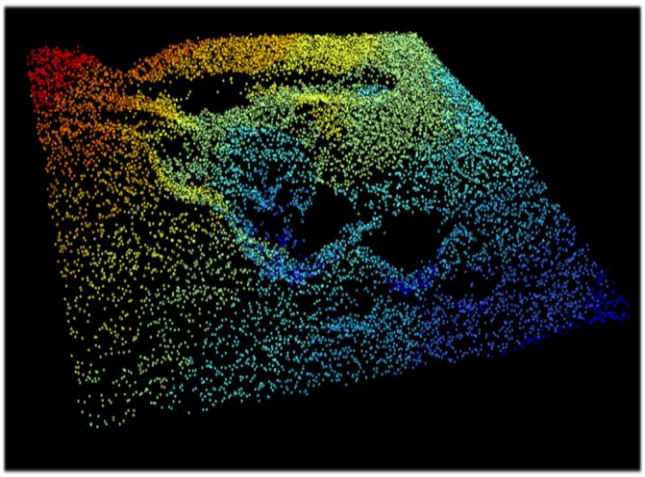

Figure 9. Side 3D view of the pothole

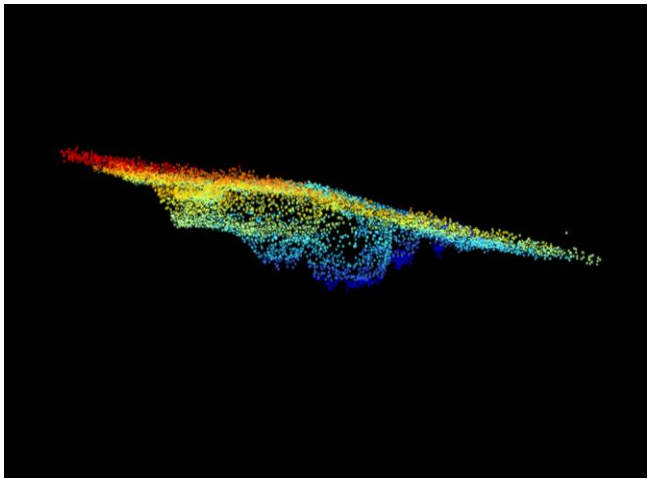

Figure 10. Side 3D view showing the depth of pothole

4. Conclusion

In this study, we showed the potential of TLS data for visualizing the pavement distresses mainly the potholes through various views and also the measurement of its areal extent. The results of our study demonstrate the effectiveness of using point cloud from LIDAR for the visualization of road surface distresses in a precise manner as the accuracy achieved was just '6 mm', less than a centimeter. A high density 3D model of the distress was created from the TLS point cloud data through laser scanning using terrestrial scanner and post processing using the TLS software. The results of this study are promising and thus suggests that LIDAR data can be used for functional evaluation of pavements rather than cumbersome manual methods.

References

Azam, A., Alshehri, A. H., Alharthai, M., El-banna, M. M., Yosri, A. M., & Beshr, A. A. A. (2023). Surface Defects. 1–18.

De Blasiis, M. R., Di Benedetto, A., & Fiani, M. (2020). Mobile laser scanning data for the evaluation of pavement surface distress. Remote Sensing, 12(6). https://doi.org/10.3390/rs12060942

Elseicy, A., Alonso-Díaz, A., Solla, M., Rasol, M., & Santos-Assunçao, S. (2022). Combined Use of GPR and Other NDTs for Road Pavement Assessment: An Overview. Remote Sensing, 14(17). https://doi.org/10.3390/rs14174336

Feng, Z., El Issaoui, A., Lehtomäki, M., Ingman, M., Kaartinen, H., Kukko, A., … Hyyppä, J. (2022). Pavement distress detection using terrestrial laser scanning point clouds – Accuracy evaluation and algorithm comparison. ISPRS Open Journal of Photogrammetry and Remote Sensing, 3(December 2021),100010. https://doi.org/10.1016/j.ophoto.2021.100010

Joni, H. H., Hilal, M. M., & Abed, M. S. (2020). Developing International Roughness Index (IRI) Model from visible pavement distresses. IOP Conference Series: Materials Science and Engineering, 737(1). https://doi.org/10.1088/1757899X/737/1/012119

Kumar, P., & Chandra, S. (2022). Manual on pavement evaluation techniques (1st ed.). Delhi, India: Khanna Publishers.

Ravi, R., Habib, A., & Bullock, D. (2020). Pothole mapping and patching quantity estimates using lidar-based mobile mapping systems. Transportation Research Record, 2674(9), 124–134. https://doi.org/10.1177/0361198120927006

Rusmanto, U., Syafi'I, & Handayani, D. (2018). Structural and functional prediction of pavement condition (A case study on south arterial road, Yogyakarta). AIP Conference Proceedings, 1977(June 2018). https://doi.org/10.1063/1.5042984

Silyanov, V. V., Sodikov, J. I., Kiran, R., & Sadikov, A. I. (2020). An overview road data collection, visualization, and analysis from the perspective of developing countries. IOP Conference Series: Materials Science and Engineering, 832(1). https://doi.org/10.1088/1757899X/832/1/012056

Tawalare, A., & Vasudeva Raju, K. (2016). Pavement Performance Index for Indian rural roads. Perspectives in Science, 8, 447–451. https://doi.org/10.1016/j.pisc.2016.04.101

The Indian Express. (2022). 6 deaths in a year: Pothole-linked accident claims another life in Bengaluru. Retrieved from https://indianexpress.com/article/cities/bangalore/6-deaths-year-pothole-accident-claims-life-bengaluru-8113083/

The Times of India. (2022). Over 50% of national highways built, expanded since 2014. Retrieved from https://timesofindia.indiatimes.com/business/india-business/over-50-of-national-highways-built-expanded-since-2014/articleshow/96241231.cms

Valaskova, V., Vlcek, J., & Kowalska-Koczwara, A. (2021). On the Applicability of Laser Scanning for Evaluation of the Pavement Serviceability Parameters. IOP Conference Series: Earth and Environmental Science, 906(1). https://doi.org/10.1088/1755-1315/906/1/01213

6th Intercontinental Geoinformation Days

igd.mersin.edu.tr

Extraction of tree parameters using terrestrial 3D LIDAR data

Sangeetha Gaikadi*[1], Vasantha Kumar Selvaraj [1]

[1]*Vellore Institute of Technology (VIT), School of Civil Engineering, Department of Environmental and Water Resources Engineering, Vellore, India*

Keywords
Urban green spaces
Terrestrial laser scanner
Point cloud data
Tree parameters

Abstract

Availability of sufficient green spaces becomes one of the mandatory requirements nowadays for any cities of the world as the growing population and urban sprawl leads to reduction to green cover. Popularly called as urban green spaces (UGS), they not only help to reduce the heat islands in a city but also ensure healthy well-being of the city residents. UGS extraction from satellite images as attempted in many studies has many limitations. For example, one can see only two-dimensional spread of UGS and it may not be possible to extract the tree parameters such as height, diameter, etc. as one can measure only area of UGS that too not at individual tree level if medium and low-resolution satellite images are used. To overcome all these drawbacks with satellite images, LIDAR technology can be used by laser scanning of trees and the collected LIDAR data can then be used to built the 3D models of trees. The present study did the same by carrying out the LIDAR survey for a sample tree located on a highway side in Vellore, India. The LIDAR scans were then registered at an accuracy of 6 mm in order to get a single point cloud which is free from noises and was then used to extract the required parameters, namely, the height of tree, diameter at breast height and crown base height. The results revealed that terrestrial LIDAR survey is one of the potential data sources for extracting the tree parameters precisely.

1. Introduction

In any city or town, it is generally good to have greener in the form of trees, shrubs, meadows, grasslands, parks etc. as UGS helps to alleviate the urban heat islands in the city and also help to reduce the stress levels and improve the well-being of the city inhabitants. Even though shrubs, grasslands, and other forms of UGS play an important role, predominantly urban trees act as an important resource in order to preserve and to protect the aesthetical and ecological balance (Ning et al., 2019). Because of rapid urbanization in recent decades, migration of people in need of jobs and better life is witnessed in almost all the cities of developing nations like India and this results in increase of urban areas or lead to urban sprawl. One of the major ill effects of urban sprawl is loss of tree coverage and thereby reduction in UGS extent. Thus, it becomes essential to map urban trees in a city which will help to examine the extent of green spaces and also aid in development of planning and policy regulations. Manual survey of UGS is not an easy task as it demands high manpower, huge time and also it is a costly affair. To overcome this laborious task, researchers started using remote sensing satellite images, where the images of resolution 10 m to 60 m were mostly employed (Chen et al., 2021; Wei et al., 2023). The major advantage of using remote sensing images for UGS extraction is medium and low-resolution images can be obtained at free of cost. But the problem is it is difficult to locate individual trees on a medium and low-resolution satellite image. The alternative option is to use high- and very high-resolution satellite images but the problem is they are very costly. Apart from the cost, one major drawback of satellite images is we can only see plan view or two-dimensional representation of the UGS area and thus one cannot get three-dimensional view of trees. Because if we have 3D data, then we can easily obtain all the tree parameters such as tree height, diameter, crown area, etc. at individual tree level. Such 3D data can be obtained using advanced techniques like Light Detection and Ranging (LIDAR).

Terrestrial LIDAR, mobile LIDAR, airborne LIDAR, and Unmanned Aerial Vehicle (UAV) LIDAR are the four categories of LIDAR technology based on various platforms. In contrast to other platforms, UAV and Terrestrial LIDAR achieve a reasonable balance between practicality, spatial coverage, and data quality (Hui et al., 2021). Though there are more UAV based studies (Wagner & Egerer, 2022; Xiao et al., 2022; Yang et al., 2022), however they need more technical skills and also

* **Corresponding Author**

*(svasanthakumar@vit.ac.in) ORCID ID 0000 – 0002– 7202-4584
(sangeetharao888@gmail.com) ORCID ID 0000 – 0003 – 3669 – 1571

Cite this study

Gaikadi, S., & Selvaraj, V. K. (2023). Extraction of tree parameters using terrestrial 3D LIDAR data. Intercontinental Geoinformation Days (IGD), 6, 390-393, Baku, Azerbaijan

the permission issues for LIDAR data collection. On the other hand, terrestrial LIDAR technology does not require permission issues as they are tripod based and they can easily measure the 3D spatial structure of trees by gathering signals from backscattered laser pulses (Hui et al., 2021). Terrestrial LIDAR technology has been evolving incredibly as it has been the latest active distant sensing technology in recent years (Sun et al., 2022). LIDAR technology can collect data more quickly and precisely than conventional passive optical remote sensing measures. It can also acquire laser pulses from the ground, multiple stems of trees and is less impacted by the lighting conditions outside. As the laser pulses scan the trees in 360 degrees, measurements can be visualized in three-dimensional (3D) structure. As a result, LIDAR has been used extensively in forest inventories, particularly for extracting the tree parameters. Tree extraction is the process of extraction of individual trees from LIDAR point clouds in order to estimate the tree parameters such as its spatial position, tree height, diameter, and crown base height, etc. Investigating a precise, effective, and reliable method of tree extraction is of tremendous practical significance and production application value. Hence in the present study, an attempt has been made to perform LIDAR survey and carryout suitable post processing techniques for tree extraction and accurate measurement of its parameters.

2. Method

2.1 Study area, Data Collection & Methodology

Figure 1 shows the flowchart of the proposed methodology. The first step is to choose a suitable LIDAR instrument for our survey. In the present study, BLK 360 laser scanner was employed. It is one of the popular laser scanners in the terrestrial category and the scanner range is 60 m which means all the objects which are at a distance of 60 m or less will be covered. The instrument is handy as it weighs less than a kg and thus easy to take to the field and perform survey. The second step is selecting a suitable location where the LIDAR survey can be carried out without any obstruction or disturbances. After seeing many locations, finally the study area was located in Tiruvalam - Katpadi road in Vellore city of Tamil Nadu, India where a tree on the roadside was found. Figure 2 shows the actual photo of the tree selected. The reason for taking this particular location is sufficient space was there on the road side at this location without any shops or houses so that tripod can be kept and survey can be carried out without any hindrances. A clear sky day was taken for the survey so that the laser scanning should not be disturbed by rain or water droplets. The BLK 360 was kept on the tripod, levelled and scanning was then started. During survey, the scan duration was set as medium so that the scan will complete in 3 minutes. Hence the scanner was kept near to the tree within a distance of 60 m so that laser scanning will cover the entire tree. The scanner can emit 360000 pulses per second, so in a 3-minute duration, millions of laser pulses will hit the target (tree) and thus finally we can get a dense point cloud of X, Y, Z values.

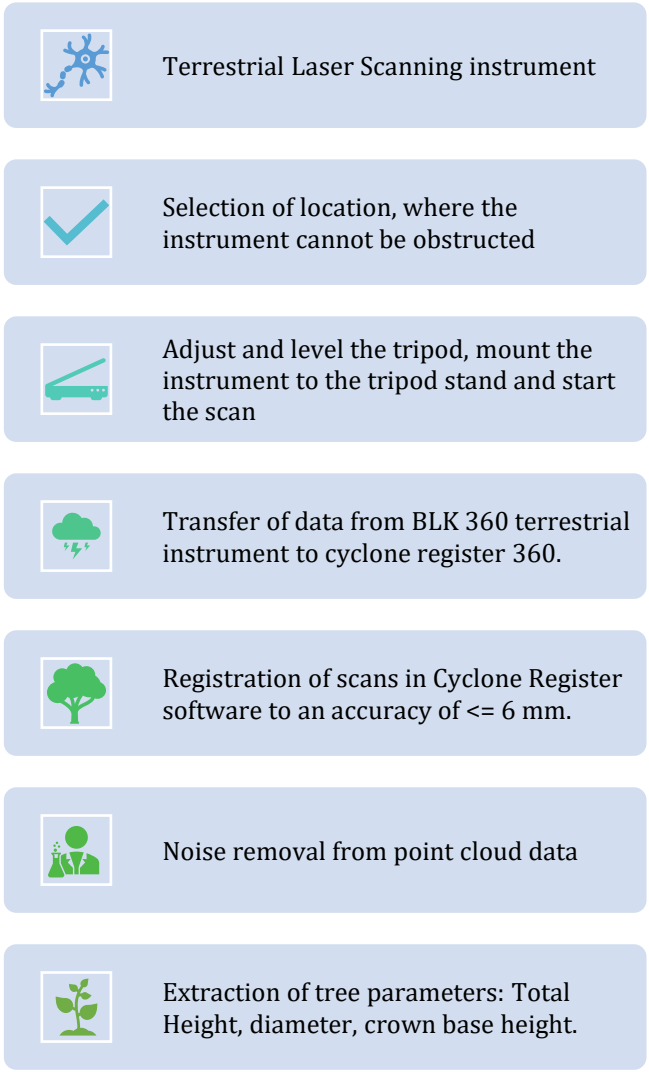

Figure 1. Methodology for tree extraction from LIDAR data

Figure 2. Photo showing the tree selected for LIDAR survey

Once the survey is over, the next step is to transfer the data to postprocessing software. Cyclone register 360 is the postprocessing software for BLK 360 and the same has been used in the present study. Each scan would normally occupy 250 MB space and hence a computer system with high end specifications would be better. The data was finally transferred to the software from BLK and the scans were registered to get an accuracy of 6 mm.

Both manual and automatic registration options were available in the postprocessing software. As the scans were taken within the range of 60m, they were automatically registered by the software with an accuracy of 6 mm. Once the registration is over, the next step is removal of noise. Because sometimes, the collected LIDAR data may have unwanted noises such as adjacent trees, buildings, electric wires, vehicles, roads, pedestrians, etc. Those noises need to be removed and the same has been done in Cyclone register 360 during the postprocessing stage. Once the noise removal is done, the last step is to extract the required tree parameters such as height, diameter, etc. using the measurement tool in Cyclone register 360. Finally, the required tree parameters were extracted precisely using the point cloud data as it contains millions of accurate X, Y, Z values.

3. Results

The result of point cloud data before removal of noises is shown in Figure 3. We can see adjacent trees and other noises in Figure 3 which need to be removed before we can start the measurement process. The 3D model of the tree as seen from Figure 3 can be obtained only from LIDAR surveys and not from conventional field surveys or satellite imaging approaches, where only two-dimensional representation of tree is possible.

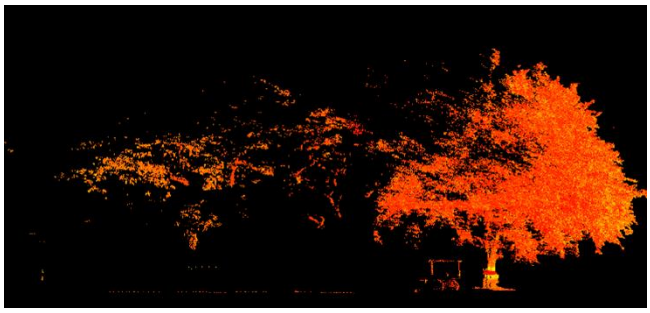

Figure 3. Side view of the LIDAR point cloud before noise removal

The point cloud data after removal of noises is shown in Figure 4. Though the trees in Figure 4 a & b looks slightly different, but they are actually the same tree. Figure 4a is the side view of the tree taken in Cyclone Register 360 software and 4b is the same tree viewed in ArcGIS software. The advantage of ArcGIS software is we can view in different angles by converting the data to LAS dataset and view it using 'LAS dataset 3D view' tool in ArcGIS software. Once the tree is extracted as shown in Figure 4, the next step is to perform the required measurements in Cyclone Register 360 using the measurement tool. In the present study, three parameters were measured from the point cloud data, namely, height of the tree, diameter at breast height and crown base height.

To measure the tree height (TH) in cyclone software, we zoomed to the maximum extent of the individual tree to clearly see the bottom and top points of the LIDAR data. Then using measuring tool, the total height of the tree from bottom to top was then measured accurately as shown in Figure 5a. Traditionally the diameter at breast height (DBH) should be measured around the trunk of the tree at 1.3m height from the base. In case if tree has a split in trunk portion at 1.3m height from the base, then we need to take an average of the trunks diameter to get the DBH. However, in our case, we didn't find any split-ups in the trunk portion of the tree at 1.3 m from base and splits were there only above 1.3m as seen from Figure 4b. As like before, using the measuring tool of Cyclone software, the DBH was measured as shown in Figure 5b. Finally, crown base height (CBH) was measured from bottom of the tree points to the slit where the living branches of the tree begin as shown in Figure 5c. Thus, the TH, DBH, CBH was calculated as 13.135 m, 3.252 m and 2.11 m respectively. It is important to mention here that, with the help of 3D LIDAR data, one can easily measure the required tree parameters in a precise manner which is not possible with even very high satellite images as they are limited to exhibit only two-dimensional representation of any objects on the earth.

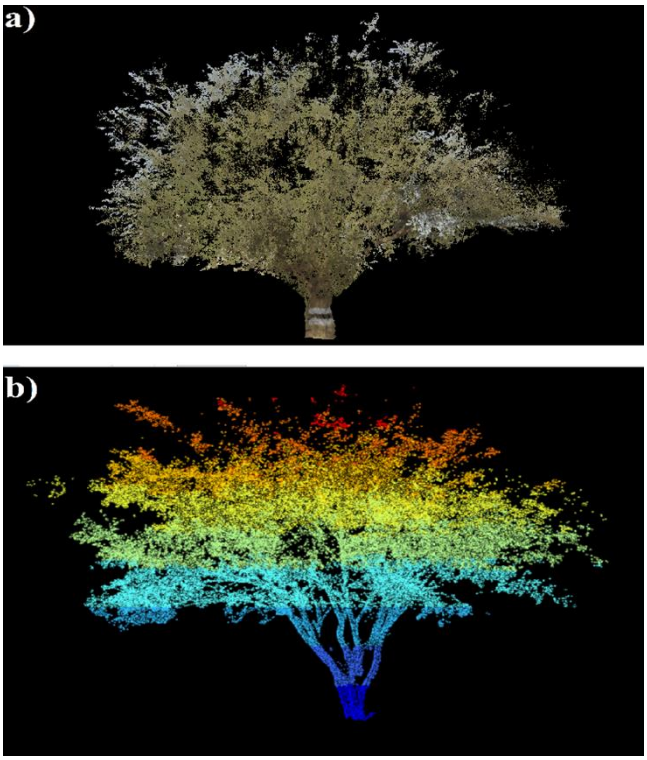

Figure 4. Tree after removal of noises a) View from Cyclone Register 360 b) View from ArcGIS after LAS conversion

4. Conclusion

UGS in any city or town is essential both from environmental and social point of view as it helps to reduce the city heat waves and at the same time ensure healthy well-being of the city residents. UGS extraction from satellite images as attempted in many studies has many limitations such as only two-dimensional representation possible, insufficient data for extracting tree parameters, etc. Hence the feasible option is to use the LIDAR data where one can built 3D models easily and accurately and the same can be used to extract the required parameters too. The present study showed the same for a sample tree on a highway by performing LIDAR survey and postprocessing of the collected data.

The tree was extracted by removing all the unwanted noises and required parameters such as height, diameter were then extracted. The results suggests that LIDAR data is a promising data source for extracting tree level data.

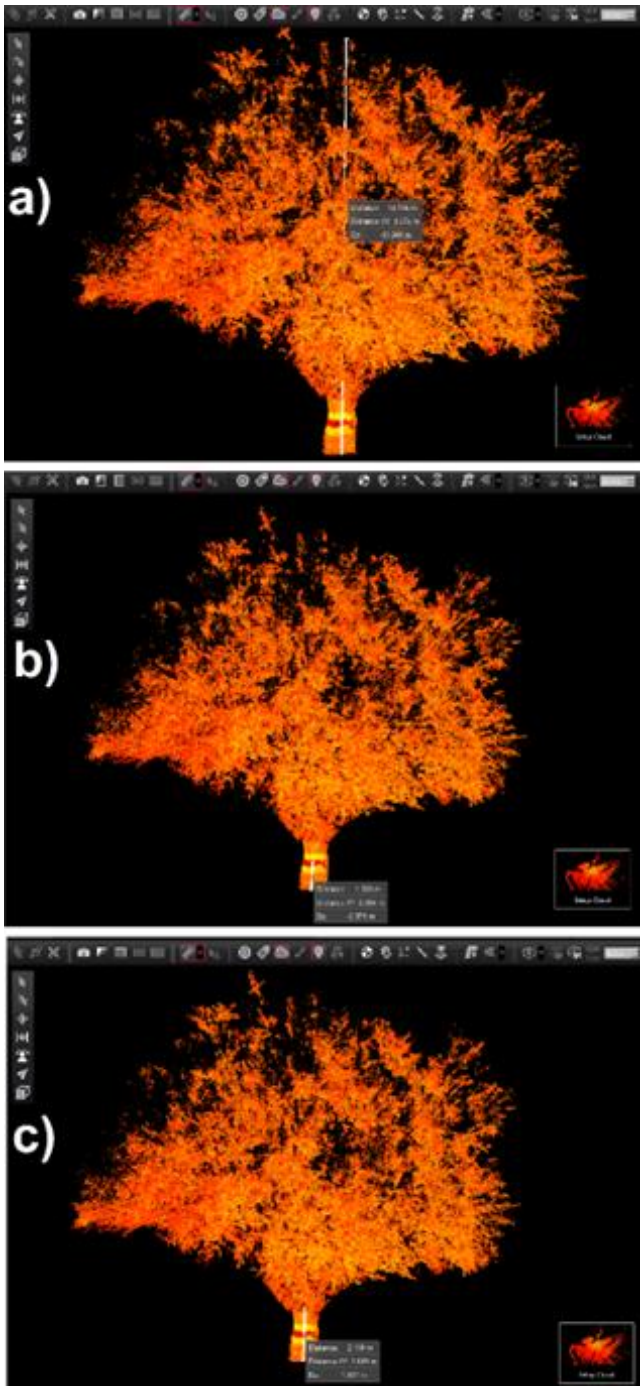

Figure 5. Extracting tree parameters: a) Tree height, b) Diameter at breast height, c) Crown base height

References

Chen, Y., Weng, Q., Tang, L., Liu, Q., Zhang, X., & Bilal, M. (2021). Automatic mapping of urban green spaces using a geospatial neural network. GIScience and Remote Sensing, 58(4), 624–642. https://doi.org/10.1080/15481603.2021.1933367

Hui, Z., Li, N., Xia, Y., Cheng, P., & He, Y. (2021a). Individual tree extraction from UAV LIDAR point clouds based on self-adaptive mean shift segmentation. ISPRS Annals of the Photogrammetry, Remote Sensing and Spatial Information Sciences, 5(1), 25–30. https://doi.org/10.5194/isprs-annals-V-1-2021-25-2021

Hui, Z., Jin, S., Li, D., Ziggah, Y. Y., & Liu, B.(2021b). Individual tree extraction from terrestrial LIDAR point clouds based on transfer learning and gaussian mixture model separation. Remote Sensing, 13(2), 1–32. https://doi.org/10.3390/rs13020223

Ning, X., Tian, G., & Wang, Y. (2019). Top-down approach to the automatic extraction of individual trees from scanned scene point cloud data. Advances in Electrical and Computer Engineering, 19(3), 11–18. https://doi.org/10.4316/AECE.2019.03002

Sun, C., Huang, C., Zhang, H., Chen, B., An, F., Wang, L., & Yun, T. (2022). Individual Tree Crown Segmentation and Crown Width Extraction From a Heightmap Derived From Aerial Laser Scanning Data Using a Deep Learning Framework. Frontiers in Plant Science, 13(June), 1–23. https://doi.org/10.3389/fpls.2022.914974

Wagner, B., & Egerer, M. (2022). Application of UAV remote sensing and machine learning to model and map land use in urban gardens. Journal of Urban Ecology, 8(1), 1–12. https://doi.org/10.1093/jue/juac008

Wei, X., Hu, M., & Wang, X. J. (2023). The Differences and Influence Factors in Extracting Urban Green Space from Various Resolutions of Data: The Perspective of Blocks. Remote Sensing, 15(5). https://doi.org/10.3390/rs15051261

Xiao, X., Zhang, L., Xiong, Y., Jiang, J., & Xu, A. (2022). Influence of spatial characteristics of green spaces on microclimate in Suzhou Industrial Park of China. Scientific Reports, 12(1), 1–23. https://doi.org/10.1038/s41598-022-13108-1

Yang, B., Wang, S., Li, S., Zhou, B., Zhao, F., Ali, F., & He, H. (2022). Research and application of UAV-based hyperspectral remote sensing for smart city construction. Cognitive Robotics, 2(December), 255–266. https://doi.org/10.1016/j.cogr.2022.12.002

6th Intercontinental Geoinformation Days

igd.mersin.edu.tr

Analysis of the vulnerability of rural settlements to earthquakes in TMA using fuzzy inference system and spatial statistics techniques

Bahman Tahmasi *[1], **Hassan Ali Faraji Sabokbar** [1], **Seyed Ali Badri** [1]

[1] *University of Tehran, Faculty of Geography, Department of Human Geography, Tehran, Iran*

Keywords
Vulnerability
Rural settlements
Earthquake
TMA
Spatial analysis

Abstract

The Tehran metropolitan area, encompassing Tehran and Alborz provinces in Iran, is characterized by a high risk of earthquakes due to multiple active faults and a dense population. The uncoordinated and unprincipled growth of rural settlements in this region, coupled with non-standard construction near fault lines, poses a significant potential for vulnerability to earthquakes. This research paper aims to spatially assess the vulnerability of rural settlements located in the Tehran metropolitan area to earthquakes by analyzing factors such as earthquake risk, population density, and building types. The study encompasses the entire rural settlements situated in Tehran and Alborz provinces. Based on the 2016 census, the total number of such villages was reported to be 1519. From this population, a sample of 472 villages for which data were available was selected to serve as representative units for analysis. To analyze the data, a fuzzy inference system (FIS) was employed. This involved the construction of a database comprising fuzzy rules and the integration of diverse indicators within MATLAB software. The resulting output was subjected to analysis utilizing spatial statistics techniques. This study shows the high potential for the vulnerability of rural settlements located in the Tehran metropolitan area to earthquakes.

1. Introduction

Historically, droughts and floods were fatal disaster events. Deaths from these events are now very low, and today's most deadly event is an earthquake. We know from historical data that the world has seen a significant reduction in disaster deaths through earlier prediction, more resilient infrastructure, emergency preparedness, and response systems. But earthquake is a natural disaster that is still not preventable and affects many people (Global Change Data Lab 2020). Earthquake is recognized as the most serious disaster and an obstacle to the development of human society (Xu et al. 2020). According to CRED data, earthquakes killed 72,114 people worldwide between 2000 and 2020 and affected 118,344,322 people (Lian et al.2021).

It is necessary to have a thorough knowledge of the earthquake and an understanding of its potential vulnerability and response capability. Being fully prepared can help mitigate the negative consequences of disasters (Kusumastuti et al. 2021; Basolo et al. 2009; Morrissey 2004). According to studies, those who are more aware of the dangers of various earthquakes are less affected (Santos-Reyes 2020; Xu et al. 2018; Kusumastuti et al. 2021; Lian et al. 2021). For this reason, assessing the current situation, gaining sufficient understanding, and analyzing the various dimensions of disasters are essential to presenting vulnerability reduction programs. Vulnerability assessment is a key component of disaster management, especially earthquakes, and it helps to ensure human society's safety (Huq et al. 2020).

The Tehran metropolitan area (TMA) is Iran's most populated, accounting for over 20% of the country's total population. Throughout history, this region has been subjected to major earthquakes. Data from paleontological seismology and historical knowledge show a high probability of earthquake occurrence and the potential for large earthquakes in the Tehran metropolitan area (Zare, 2014). The uncoordinated and unprincipled growth of villages in the Tehran metropolitan area, particularly in recent decades, construction near faults and areas prone to geological instability, indicates that serious damage will occur in the case of a large earthquake in this area (Darban Astane et al. 2018). As a response, preparing to minimize

* **Corresponding Author**

*(bahman.tahmasi@ut.ac.ir) ORCID ID 0000-0002-7742-814X
(hfaraji@ut.ac.irl) ORCID ID 0000-0002-5470-4287
(sabadri@ut.ac.ir) ORCID ID 0000-0001-7422-7281

Cite this study

Tahmasi B, Faraji Sabokbar H. A., & Badri, S. A. (2023). Analysis of the vulnerability of rural settlements to earthquakes in TMA using fuzzy inference system and spatial statistics techniques. Intercontinental Geoinformation Days (IGD), 6, 391-395, Baku, Azerbaijan

vulnerability has become a need. Due to the high risk of earthquakes, earthquake vulnerability assessment in rural settlements of the Tehran metropolitan area is critical. Therefore, this article aims to identify and combine multiple indicators to make an integrated assessment of the potential for earthquake vulnerability in rural settlements in the Tehran metropolitan area. Furthermore, this article aims to providing a vulnerability map of rural settlements in the Tehran metropolitan area.

2. Method

This research is descriptive in nature and is based on practical research. The research population includes all rural settlements in the TMA, which, according to the 2016 census, equaled to 1519 villages (Statistical Centre of Iran, 2016), with 472 villages having access to their data being selected as a sample in this study based on access to case data and data needs. The criteria used to determine vulnerability in this article are based on a survey of theoretical literature and research background, and their scientific validity has also been confirmed. Finally, according to the availability of data, a total of 7 main indicators were determined, including the 1) ratio of buildings with resistant materials, 2) ratio of buildings with non-resistant materials, 3) residential units' area, 4) population density per residential unit, 5) the ratio of vulnerable population, 6) sex ratio, and 7) earthquake risk.

Data related to residential units and the population of the studied villages have been collected from the 2016 statistics of general population and housing census of Iran (Statistical Centre of Iran, 2016). Also, the earthquake risk indicator is based on the zoning of earthquake risk in Iran according to the standard 2800 of the Iran Ministry of Roads & Urban Development in 2014. Then the fuzzy inference system (FIS) was used in the MATLAB software. The vulnerability was assessed for each indicator by creating a fuzzy rules database. The fuzzy rules database is defined in 4 stages (each stage defining 27 rules) to complete this process and determine the overall vulnerability (a total of 108 rules) for the studied Rural settlements. ArcMap software was used to visualize the spatial distribution of the outputs after assessing the degree of potential vulnerability, and performing spatial analysis of vulnerability

2.1. Study Area

The study area is two provinces of Iran including Tehran and Alborz provinces, which are referred to as the Tehran metropolitan area (TMA) in this study. Tehran province has an area of about 13842 square kilometers. Tehran province is divided into 16 counties, 46 cities, and 1048 villages. Tehran province has a population of 13267637 people. Alborz province comprises 6 counties, 17 cities, and 471 villages. Alborz province was previously known as one of Tehran province's counties, but it was separated from Tehran province in 2011 and became a new province. Alborz province has a population of 2,712,400 people (Figure 1).

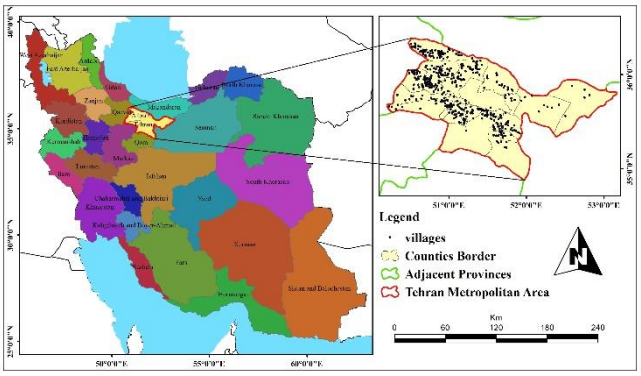

Figure 1. Map of the study area (TMA)

3. Results

According to a TMA earthquake risk survey, 494 square kilometers, or 2.63 percent of the whole area, are in a moderate risk zone, 4966 square kilometers, or 26.39 percent of the whole area, are in a high-risk zone, and 13356 square kilometers, or 70.98 percent of the whole area, are in a very high-risk zone "Table 1".

Table 1. Earthquake risk zoning in the TMA

Risk level	Area (Km²)	Percent	Cumulative percent
Moderate	494	2.63	2.63
High	4966	26.39	29.02
Very high	13356	70.98	97.37
Total	18816	100	100

According to the examined factors, none of the rural settlements are in a moderate earthquake risk zone, and most of them are in a very high earthquake risk zone. So, 75.2% of the total population and vulnerable population of the investigated rural settlements live in the zone with very high earthquake risk. 77.1% of total residential units are located in very high earthquake risk zone. Furthermore, 77.6% of buildings with resistant materials, 76.2% of buildings with non-resistant materials, 77.1% of residential units with an area of 100 square meters or less, 76.9% of residential units with an area of 101 to 200 square meters, and 77.1% of residential units with an area of 200 square meters or more are in a very high earthquake risk zone. According to the average of the eight variables investigated, 23.5% of TMA rural settlements are in the high earthquake risk zone, and 76.5% are in the very high earthquake risk zone. These statistics show very high risk, an unfavorable condition, and a high potential for vulnerability to earthquakes in rural settlements located in TMA.

By combining the indicators using a fuzzy inference system, the potential vulnerability of rural settlements in the metropolitan area of Tehran was obtained. The potential vulnerability of residential units was determined in this step by combining three indicators: (1) the ratio of buildings with resistant materials, (2) the ratio of buildings with non-resistant materials, and (3) potential vulnerability due to the area of residential units (less than 100 m^2, 101 to 200 m^2, and more than 200 m^2). The level of vulnerability in TMA rural settlements ranges from 11.48 (low) to 69.76 (high). Based on this output, as shown in Figure 2-A, the small zone in the

center of the TMA have low and moderate potential vulnerabilities, and wider zones in the west, south, and east of the TMA have high potential vulnerabilities. In the next step, by combining three population-related indicators, including: (1) population density per residential unit, (2) the ratio of the vulnerable population, and (3) sex ratio, the potential vulnerability of the population at risk was discovered. The vulnerability of the population ranges from 9.74 (low) to 71.86 (high) in the TMA rural settlements. As shown in Figure 2-B, one zone in the south of the TMA and small zones in the east and west of the TMA have high vulnerabilities, while wider zones of the TMA have mainly low and moderate vulnerabilities. Also, as previously mentioned, the TMA is classified as moderate risk, high risk, and very high risk according to the earthquake risk index. Most of the TMA is located in a high-risk zone (Figure 2-C).

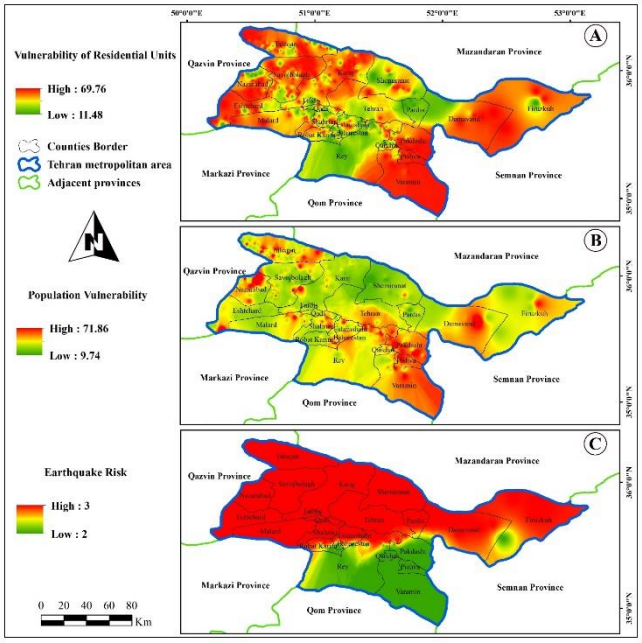

Figure 2. Spatial distribution of vulnerability of rural residential units (A), the vulnerability of rural population (B), and earthquake risk (C) in the TMA

The final value of the potential vulnerability index for each of the analyzed rural settlements in the TMA was calculated by combining three key research indicators, including population vulnerability index, residential unit vulnerability index, and earthquake risk. The spatial distribution of the vulnerability index ranges from 11.64 (low vulnerability) to 74.09 (high vulnerability) among the studied rural settlements. According to the developed spatial model, as shown in Figure 3.

A major portion of the TMA is vulnerable to earthquake risk. Only a few areas in the north, south, west, and east of TMA rural settlements have a low and moderate vulnerability to earthquakes.

In order to determine the cluster or randomness of the spatial pattern of the vulnerability of rural settlements located in the Tehran metropolitan area, spatial autocorrelation analysis (Morans I) has been used. According to the results of the spatial autocorrelation test conducted on the vulnerability data of rural settlements, it has been found that there exists a cluster spatial pattern at the level of the Tehran metropolitan area. The value of Moran's index for the vulnerability of rural settlements is 0.053, and since this value is greater than zero, it indicates the presence of a cluster spatial pattern. Furthermore, the Z value is calculated to be 3.58, with a corresponding P-value of zero. This confirms the existence of a cluster spatial pattern with a confidence level of 99%. As depicted in Figure 4, the spatial cluster pattern can be observed through the placement of the standard Z scores on the right side of the normal distribution, highlighted in red.

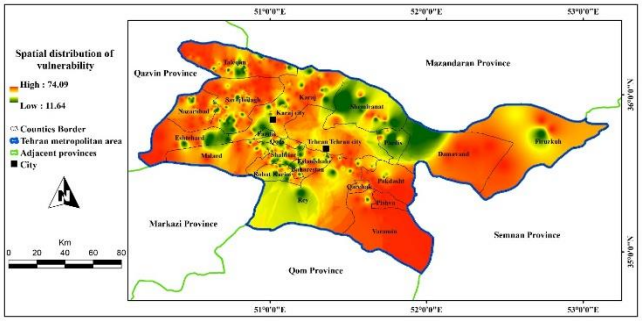

Figure 3. Spatial distribution of rural settlements vulnerability to earthquakes in the TMA

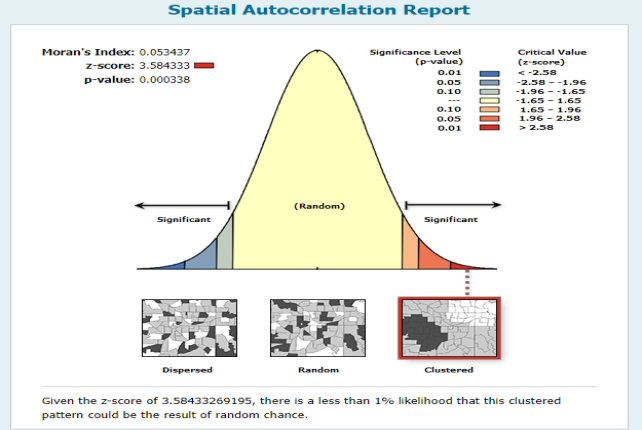

Figure 4. Spatial autocorrelation test for the vulnerability of rural settlements

The application of Hot Spot analysis has facilitated the identification of spatial areas exhibiting concentrated clusters with high and low values, displaying spatial correlation. The outcomes of the hot spot analysis conducted on the vulnerability of rural settlements demonstrate the existence of two hot clusters in the southeast and northwest regions of the Tehran metropolitan area. Furthermore, two cold clusters have formed in the southwest and northeast areas of Tehran city (Figure 5).

4. Conclusion

Earthquakes pose a grave threat to communities, leading to substantial loss of life and property. Iran is renowned for being one of the most earthquake-prone countries globally, experiencing frequent seismic activity with some instances causing significant devastation. Notably, the Tehran metropolitan area (TMA), encompassed by multiple fault lines, stands as a region in

Iran with a considerable risk of earthquakes. Throughout history, this area has witnessed major seismic events. The conjunction of high earthquake risk and the dense population and concentrated residential units in the TMA raises concerns regarding the vulnerability of cities and villages to potential earthquakes.

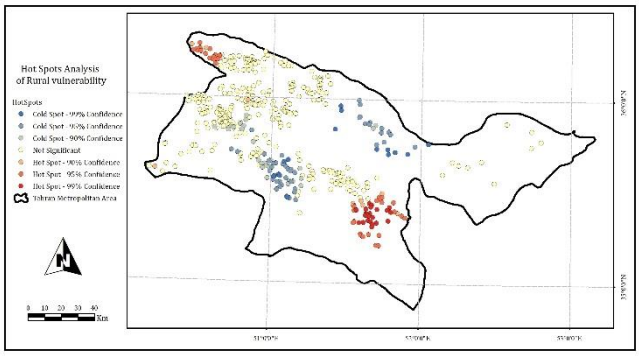

Figure 5. Hot and cold clusters of vulnerability of rural settlements

The TMA, with its substantial population, accounting for 20% of Iran's total, has drawn increased attention to the vulnerability of this region to earthquake risks. While previous research has primarily focused on evaluating the vulnerability of cities within the TMA, consisting of 63 cities, limited attention has been given to the vulnerability of rural settlements. It is plausible that researchers may have overlooked this aspect concerning natural disaster risks, potentially due to the notable political and administrative significance associated with the metropolises of Tehran and Karaj. The study findings indicate that the majority of rural settlements within the Tehran metropolitan area (TMA) are situated in zones characterized by a very high risk of earthquakes. Conversely, only a limited number of rural settlements are located in high-risk zones, and no rural settlements are found in zones with moderate earthquake risk. This condition is considered one of the primary reasons contributing to the increased potential vulnerability in the event of an earthquake.

The results further reveal that most of the investigated rural settlements exhibit high levels of vulnerability across population indicators, indicators related to residential units, and earthquake risk. When these indicators are evaluated individually, the importance of this issue and the level of vulnerability may not be readily apparent. For instance, when solely examining and evaluating indicators related to population vulnerability, the results may not appear particularly alarming or extraordinary. However, when these indicators are combined with earthquake risk and indicators of vulnerability pertaining to residential units, the overall picture becomes considerably more alarming. As a result, a significant number of rural settlements in the TMA have a high potential for vulnerability in the face of possible earthquakes.

In summary, effective strategies are necessary for the planning and resilience of rural settlements in the Tehran metropolitan area (TMA). These strategies should encompass residential unit resilience, education, health interventions, and macro-policy measures. Key measures include establishing requirements and guidelines for housing reconstruction, promoting the use of resistant materials, providing financial support for repairs, and implementing expert monitoring. Equipping medical facilities, enhancing crisis management centers, expanding educational services, and raising awareness among residents about earthquakes are also crucial.

Acknowledgement

This article has been extracted from Mr. Bahman Tahmasi's doctoral thesis titled "Spatial Pattern Analysis of Reducing Vulnerability of Rural Settlements to Earthquakes."

References

Basolo, V., Steinberg, L. J., Burby, R. J., Levine, J., Cruz, A. M., & Huang, C. (2009). The effects of confidence in government and information on perceived and actual preparedness for disasters. Environment and behavior, 41(3), 338-364.

Darban Astane, A. R., Sheykhzadeh, M., & Bazgeer S. (2018). The Strategies for Vulnerability Mitigation of Residential Context against the Earthquake (A Case Study for 6th Region of Tehran City). Geographical urban planning research 6(2), 265-288.

Global Change Data Lab. (2020). Natural Disasters Data. https://ourworldindata.org/natural-disasters.

Huq, M. E., Shoeb, A. Z. M., Hossain, M. A., Fahad, S., Kamruzzaman, M. M., Javed, A., ... & Sarven, M. S. (2020). Measuring vulnerability to environmental hazards: qualitative to quantitative. Environment, climate, plant and vegetation growth, 421-452.

Kusumastuti, R. D., Arviansyah, A., Nurmala, N., & Wibowo, S. S. (2021). Knowledge management and natural disaster preparedness: A systematic literature review and a case study of East Lombok, Indonesia. International journal of disaster risk reduction, 58, 102223.

Lian, P., Zhuo, Z., Qi, Y., Xu, D., & Deng, X. (2021). The impacts of training on farmers' preparedness behaviors of earthquake disaster—evidence from earthquake-prone settlements in rural China. Agriculture, 11(8), 726.

Morrissey, M. (2004). Curriculum innovation for natural disaster reduction: lessons from the Commonwealth Caribbean. International perspectives on natural disasters: Occurrence, mitigation, and consequences, 385-396.

Santos-Reyes, J. (2020). Using logistic regression to identify leading factors to prepare for an earthquake emergency during daytime and nighttime: the case of mass earthquake drills. Sustainability, 12(23), 10009.

Statistical Centre of Iran. (2016). General population and housing census.

Xu, D., Zhou, W., Deng, X., Ma, Z., Yong, Z., & Qin, C. (2020). Information credibility, disaster risk perception and evacuation willingness of rural households in China. Natural Hazards, 103, 2865-2882.

Xu, D., Peng, L., Liu, S., & Wang, X. (2018). Influences of risk perception and sense of place on landslide disaster preparedness in southwestern China. International Journal of Disaster Risk Science, 9, 167-180.

Zare, M. (2014). A Study on the Earthquake Hazard and Risk in the Underdeveloping NW Tehran; on the North Tehran Fault zone. The first conference of geographical sciences of Iran.Tehran: 37-43.

6th Intercontinental Geoinformation Days

igd.mersin.edu.tr

Assessing land use/land cover change in Kigali City, Rwanda

Katabarwa Murenzi Gilbert[1], Yishao Shi[1*]

[1]*Tongji University, Surveying, and Geo-informatics, Shanghai, China*

Keywords
GIS
Land cover decrease
Land use prediction
Remote analysis
Satellite images

Abstract

The unsustainable impact of global urbanization has had a profound effect on urban landscapes across the globe. This study comprehensively assesses spatial characteristics, causes, and negative effects of Land Use and Land Cover Changes in Kigali City over the past two decades. Landsat images from 2003, 2013, and 2023 were classified using ArcMap software to assess LULC dynamics. Furthermore, the Molusce plugin in QGIS was employed to compute and forecast the expansion of built-up areas from 2023 to 2033. (1) The classified images' findings show that the built-up surface's expansion experienced substantial growth. (2) Additionally, the predicted changes reflect the persistent increase in the built-up surface and reduction of the non-built-up surface. (3) Besides, the study highlights the challenges of population growth, contributing to negative impacts on agricultural land, global warming, and the urban heat island effect. In light of ongoing development and expansion in Kigali, researchers have advised implementing integrated land-use planning strategies, such as establishing compact and mixed-use areas (comprising Midrise or Highrise apartments). These strategies seek to manage urban sprawl, maintain a harmonious relationship between urban growth and the environment, and foster a sustainable and livable city for its inhabitants.

1. Introduction

Land plays a crucial role in shaping human existence and serves as a fundamental source of essential resources: including energy, water, and food, which are essential for humanity to survive (Li et al., 2021). Throughout history, humans have continuously discovered diverse ways to utilize and benefit from the land through human interaction and the natural environment (Liu et al., 2021). However, the strain on the land has intensified with the world population rapidly expanding and its accompanying demands increasing. As a result, fragile ecosystems, particularly forest-covered areas of wetlands, have become vulnerable in the direction of human-induced land modifications. (Çağlıyan, & Dağlı, 2022)

Globally, persistent LULC significantly impacts the planet's atmosphere system functioning, immediately influencing biodiversity and contributing to climate change (Jung et al., 2020). These ecosystem service alterations disrupt biological systems' capacity to meet human needs (Regasa et al., 2021). Intense agricultural development and population growth are major drivers of LULC (Alemayehu et al., 2019). East Africa, including Rwanda, experiences land cover and land use alterations due to factors like high population pressure and other human and natural-caused forces (Nkundabose, 2021). Mugiraneza et al. (2020) state that LULC change is a trending research topic, particularly in rapidly developing urban centers such as Kigali City in Rwanda.

Understanding the dynamics of land transformation and its impacts on the environment, socioeconomic conditions, and urban development is crucial for sustainable planning and decision-making (Dong, 2020). This study aims to extensively analyze LULC in Kigali City between 2003 and 2023, integrating evidence-based data and rational discourse from various academic fields. It also emphasizes the anticipated alteration in land use and land cover (LULC) that will likely occur in the built-up areas from 2023 to 2033. This change is expected to affect the people living in Kigali adversely.

2. Method

Three Landsat images were downloaded from the USGS to analyze LULC shifts in Kigali City. The images comprised Landsat 7 for 2003, 7 for 2013, and 8 for 2023. All images had a grid cell size of 30 meters and shared the same WRS path/row of 172/161. The projection used was UTM, zone 36. In addition to the satellite images, spatial locational data for the wetland and Kigali city were obtained from Rwanda Spatial Data Hub and DIVA-GIS. Regarding the mapping and computation aspect, the classification of Landsat images from 2003,

* **Corresponding Author**

*(hata2020@yahoo.fr) ORCID ID 0009-0005-4789-275X
(e-mail) ORCID ID 0000-0002-0048-6958

Cite this study

Gilbert, K. M., & Shi, Y. (2023). Assessing land use/land cover change in Kigali City, Rwanda. Intercontinental Geoinformation Days (IGD), 6, 396-399, Baku, Azerbaijan

2013, and 2023 using ArMap 10.8.2. Additionally, the Molusce plugin in QGIS Desktop 2.16.3 was utilized to calculate and predict the dynamıc of built-up areas between 2023 and 2033. The analysis results were then interpreted and discussed within the context of the research objectives. It is shown in the following workflow chart.

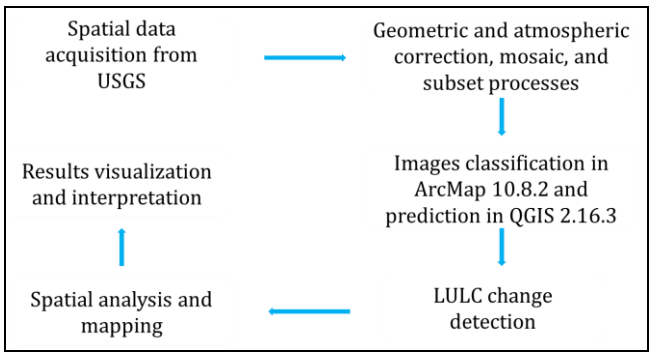

Figure 1. Research design chart

2.1. Study area

Kigali, the capital city of Rwanda in East Africa, at Latitude: -1° 56' 22.79" S and Longitude: 30° 03' 20.40" E. The main urban center of Kigali has undergone significant development and growth over time (Nduwayezu et al., 2021). The city was founded as a German colonial administrative settlement in 1907, and it experienced growth beyond its humble origins as a small neighborhood on Nyarugenge Hill. It encompasses 730 square kilometers (sq. km). In terms of population growth, in 1907 and 2002, the city had approximately 357 and 608,141 individuals, respectively, and in 2022, the population was about 1,745,555 (NISR, 2023). In 2006, administrative reorganization transformed Kigali into a metropolitan area comprising three districts, namely Nyarugenge, Kicukiro, and Gasabo (Mugiraneza et al., 2020).

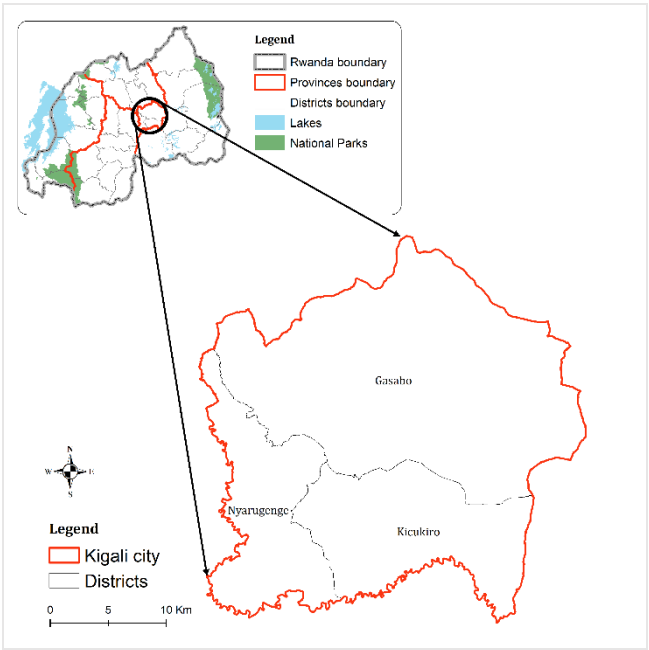

Figure 2. Study area map

3. Results

The LULC maps of the city of Kigali were classified in ArcMap using 2003, 2013, and 2023 Landsat images. The classified images and prediction results are shown in Fig 3.

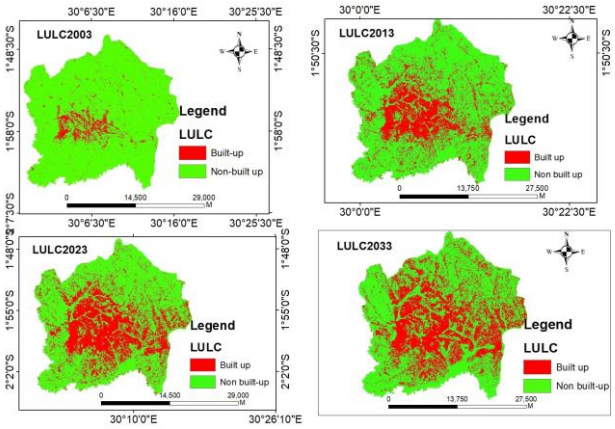

Figure 3. LULC change and prediction maps

Table 1. The summary of the area in sq. km changed in two past decades.

LULC\Year	2003	2013	2023
Built up	48.59	184.88	238.07
Non-built-up	681.41	545.12	491.93

The change detection map of Kigali between 2003 and 2023 is shown in Fig 4. It also illustrates the expansion of built-up surfaces over the city's outskirts.

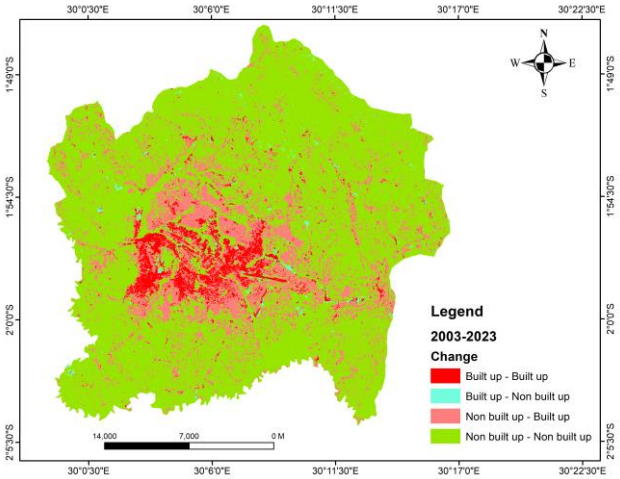

Figure 4. Change detection map of Kigali (2003-2023)

The calculated and extracted areas of Kigali city converted into another use and cover are shown in hectares in Table 2.

Table 2. LULC conversion between (2003-2023)

LULC change	Area in sq. km
Non-built-up to built-up	142.4
Built-up to non-built-up	8.6

4. Discussion

Over two past decades, from 2003 to 2023, notable transformations have occurred in LULC. In the range of ten years between 2003 to 2013, built-up areas increased from 6.6 % to 25.3%, whereas non-built-up reduced

from 93.3% to 74.6%. This means approximately 18.6% of non-built-up was converted to built-up, as shown in the figure below.

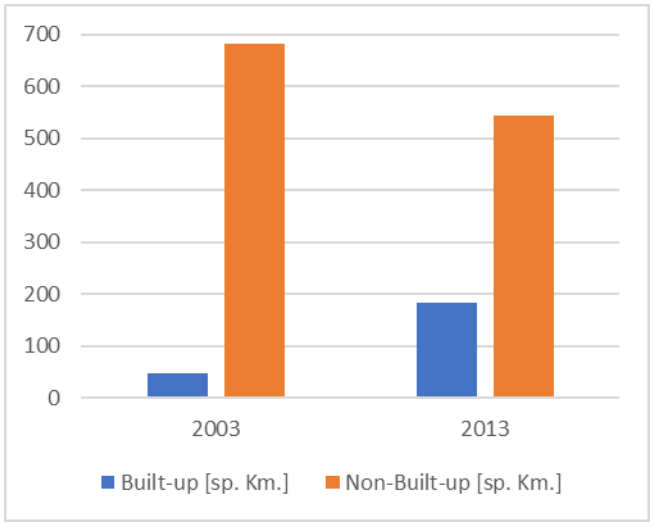

Figure 5. LULC between 2003 and 2013

The Figure 6 highlights that in the range of ten years between 2013 to 2023, built-up areas increased from 25.3% to 32.6%, whereas non-built-up reduced from 74.6% to 67.3%. This means that approximately 7.2% of non-built-up was converted to built-up.

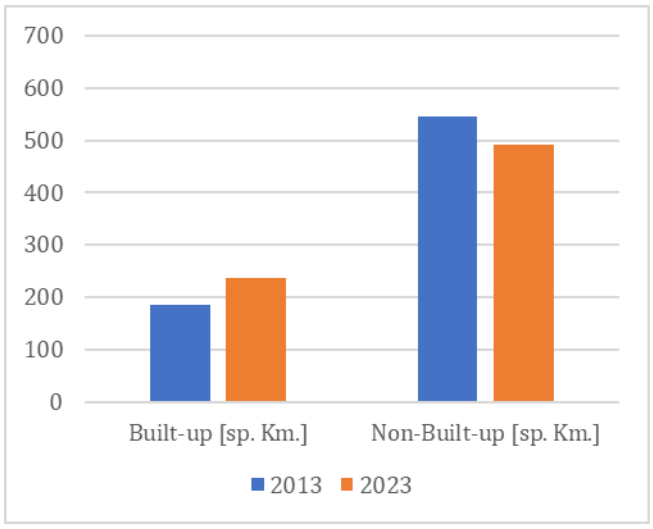

Figure 6. LULC between 2013 and 2023

The primary driver behind these changes is the population increase, followed by poor sustainable planning. Notably, in the range mentioned above of 20 years, approximately 8.6 sq. km of built-up land was converted into non-built-up. This indicates the efforts of the Rwandan government in resettling people from areas such as wetlands and landslide-prone regions, prioritizing their safety and well-being. This strategy is commendable as it helps to safeguard lives and mitigate the risks associated with natural hazards.

However, despite these measures, the study reveals that the population continues to increase steadily. This poses a challenge as it contributes to the negative change observed; urban built-up areas, in particular, have experienced significant growth, expanding approximately 5 times since 2003. This translates to 189.48 sq. km of new built-up areas, compared to the initial 48.59 sq. km in 2003. This change has adverse effects not only on human beings but also on the environment. It leads to a reduction in agricultural land and the depletion of oxygen-producing trees, which are vital for maintaining ecological balance. Additionally, since feeding a growing population requires more land, this non-built-up to built-up conversion increases global warming and the urban heat island effect through construction activities and deforestation.

Figure 7 indicates that if no serious precautions are implemented to stop the urban sprawl problem, in the coming ten years, between 2013 to 2023, built-up areas will increase from 32.6% to 36.3%, whereas non-built-up will reduce from 67.3% to 63.6%. This means that approximately 3.6% of non-built-up will change to built-up. Figure 7 shows how the problem will be in the coming decade.

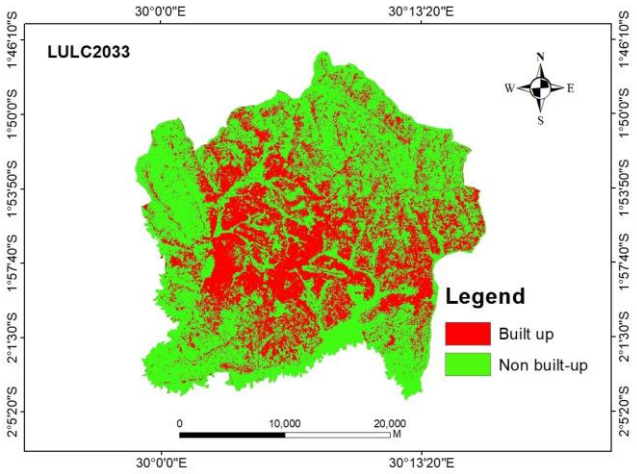

Figure 7. LULC prediction map of 2033

Figure 8 illustrates the significant decline in vegetation cover within Kigali over three decades. This stands for climate change negatively.

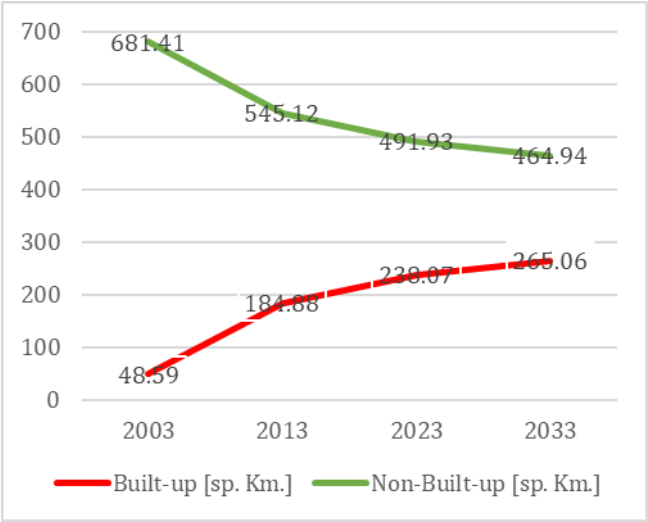

Figure 8. LULC trend between 2003 and 2033

Regarding the afore-highlighted graphs, it is evident that the built-up areas will persistently grow at a high rate without serious measures to curtail the uncontrolled expansion of settlements. The prediction indicates that by 2033, the non-built-up land area available in

2023 will diminish to a mere 3.6%. This projection underscores a profoundly negative impact that will have far-reaching consequences like losing valuable space for essential purposes such as urban parks, agriculture, and open spaces.

Several valuable mechanisms can be considered to ensure sustainable land management, urban planning, and policy formulation in light of the LULC spotted in Kigali, Rwanda. Firstly, it is crucial to prioritize integrated land-use planning approaches that balance urban development with preserving natural resources and green spaces. This can be achieved by establishing compact and mixed land use patterns, promoting efficient land use, and minimizing urban sprawl. Secondly, there should be a focus on enhancing environmental conservation and biodiversity by preserving and restoring ecosystems, including wetlands and forests, which provide vital ecosystem services. Thirdly, sustainable transportation systems and infrastructure should be prioritized to reduce the dependence on private vehicles and promote public transit, cycling, and pedestrian-friendly designs. Also, sustainable land management practices should be promoted, such as sustainable agriculture, reforestation initiatives, and green building standards.

Collaboration among stakeholders, including government authorities, communities, and researchers, is crucial to develop and implementing effective policies and strategies that ensure the long-term sustainability and resilience of Kigali City's land use and urban development.

5. Conclusion

In conclusion, the LULC of Kigali during the past two decades has been thoroughly analyzed, shedding light on the spatial patterns, drivers, and negative effects of these changes. Significant changes to the LULC map were uncovered through the study, emphasizing the noticeable growth in built-up areas. The research findings highlight the efforts of the Rwandan government in resettling people from vulnerable areas, demonstrating a proactive strategy to safeguard lives. However, population growth remains a challenge, contributing to the negative impacts of LULC on agricultural land, oxygen production, climate change, and urban heat island effects. It is of utmost importance to adopt integrated land-use planning strategies that prioritize sustainable transportation systems and environmental conservation in order to ensure the long-term sustainability and resilience of Kigali City. By promoting compact and mixed-use developments, including midrise or highrise apartments, and encouraging the preservation of green spaces, the city can effectively manage and prevent urban sprawl. Furthermore, implementing sustainable land management practices, such as optimizing resource utilization and minimizing land degradation, will foster a harmonious relationship between urban development and the environment. These measures collectively aim to create a city that is both livable and sustainable, offering residents a high-quality urban experience while simultaneously safeguarding natural resources and minimizing the ecological impact.

Acknowledgment

The authors express their gratitude to their colleagues and university administrators in a general sense.

References

Alemayehu, F., Tolera, M., & Tesfaye, G. (2019). Land use land cover change trend and drivers in Somodo watershed Southwestern, Ethiopia. African Journal of Agricultural Research, 14(2), 102-117.

Çağlıyan, A., & Dağlı, D. (2022). Monitoring Land Use Land Cover Changes and Modelling of Urban Growth Using a Future Land Use Simulation Model (FLUS) in Diyarbakır, Turkey. Sustainability, 14(15), 9180.

Dong, Y., Ren, Z., Fu, Y., Miao, Z., Yang, R., Sun, Y., & He, X. (2020). Recording urban land dynamic and its effects during 2000–2019 at 15-m resolution by cloud computing with Landsat series. Remote Sensing, 12(15), 2451.

Jung, M., Scharlemann, J. P., & Rowhani, P. (2020). Landscape-wide land use and cover changes correlate with, but rarely explain, local biodiversity change. Landscape Ecology, 35, 2255-2273.

Li, C., Yang, M., Li, Z., & Wang, B. (2021). How will Rwandan land use/land cover change under high population pressure and changing climate? Applied Sciences, 11(12), 5376.

Liu, B., Pan, L., Qi, Y., Guan, X., & Li, J. (2021). Land use and land cover change in the Yellow River Basin from 1980 to 2015 and its impact on the ecosystem services. Land, 10(10), 1080.

Mugiraneza, T., Nascetti, A., & Ban, Y. (2020). Continuous monitoring of urban land cover change trajectories with Landsat time series and landtrendr-google Earth Engine cloud computing. Remote Sensing, 12(18), 2883.

Nduwayezu, G., Manirakiza, V., Mugabe, L., & Malonza, J. M. (2021). Urban Growth and Land Use/Land Cover Changes in the Post-Genocide Period, Kigali, Rwanda. Environment and Urbanization ASIA, 12(1_suppl), S127-S146.

NISR (2023). The Fifth Rwanda Population and Housing Census, Main Indicators Report.

Nkundabose, J. P. (2021). Employing remote sensing tools to assess land use/land cover (LULC) changes in Eastern Province, Rwanda. American Journal of Remote Sensing, 9(1), 23-32.

Regasa, M. S., Nones, M., & Adeba, D. (2021). A review on land use and land cover change in Ethiopian basins. Land,10(6), 585.

6th Intercontinental Geoinformation Days

igd.mersin.edu.tr

Comparison of different valuation methods in land consolidation studies

Tayfun Çay *[1], **Musa Nehir Sözen**[2]

[1] *Konya Teknik University, Faculty of Engineering and Natural Sciences, Surveying Engineering, Konya, Türkiye*
[2] *Kastamonu University, Ihsangazi Vocational School, Department of Architecture and Urban Planning, Kastamonu, Türkiye*

Keywords
Land consolidation
Valuation
Number of parcel values

Abstract

One of the most important tools to increase productivity in rural areas is land consolidation. Land consolidation has laid the foundations for in-field development services and sustainable agricultural structuring while reducing agricultural costs. Valuation is one of the most important stages of the land consolidation works carried out intensively in the world and in Turkey. Land valuation is a large-scale land valuation process within the project area. The valuation process of land consolidation studies in Turkey has been carried out using different methods. These methods can be listed as the method specified in the Law No. 3083, the new valuation method, the method specified in the Land Consolidation Regulation and the method specified within the scope of the law amendment made on February 7, 2019. In this study, the land consolidation project carried out in 2012 in Yuvalak village of Tefenni district of Burdur province was selected as the sample area. Different valuation approaches in land consolidation projects in Turkey have been applied in our sample project. As a result of the examination, it was observed that many parcels were classified in different degree classes according to different valuation methods.

1. Introduction

In order for Türkiye to be able to compete with the world in the agricultural sector, it is necessary to provide the expected benefit from the investments made in rural areas. The ability to bring agricultural innovations to agricultural areas depends on the correction of the disorder in agricultural structures (Yıldız 1983). Sustainable agricultural practices are of great importance in terms of protecting agricultural lands and other natural resources and transferring them to future generations (Çukur et al. 2008). Land Consolidation (LC) ranks first among the structural problems of our agriculture sector that await improvement (Sönmez et al. 2005). In addition to being technical projects, land consolidation works are also social projects due to the sense of belonging of the landlords (Demiraslan et al. 2019). Land grading is the process of determining the values of lands. The criteria of land grading are a process based on the interpretation of the productivity, qualities and topography of the land (Gündoğdu et al. 2003). In order for EC studies to be carried out in a healthy way, a fair rating is required.

2. Method

In this study, the LC project, which was built according to the new rating method in the Yuvalak Village of the Tefenni District of the Burdur Province, was re-rated according to the Law No. 3083, according to the Land Consolidation Regulation and according to the regulation made in 2019. While making the rating process, the data used in the new rating method was used.

2.1. Implementation Area

The LC project was carried out by the General Directorate of Agricultural Reform in Yuvalak Village in 2012 "Figure 1-a". The data used in the study were obtained from the relevant administration. Rating studies were carried out according to the new rating method of the Law No. 3083.

2.2. Grading studies according to Yuvalak Village land consolidation regulation (ATT)

The soil score in Yuvalak village was calculated using the formula 100xTP/40. Soil map was created as in

* **Tayfun ÇAY**

*(tcay@ktun.edu.tr) ORCID ID 0000 – 0002– 4661 – 5583
(musanehirsozen@kastamonu.edu.tr) ORCID ID 0000 – 0003 – 1326 – 370X

Cite this study

Cay T, Sozen MN (2023). Comparison of different valuation methods in land consolidation studies. Intercontinental Geoinformation Days (IGD), 6, 400-402, Baku, Azerbaijan

Figure 2. All parcels in the application area were given 10 points as efficiency points. In the project made according to the new rating method, up to 20 points are given as location points.

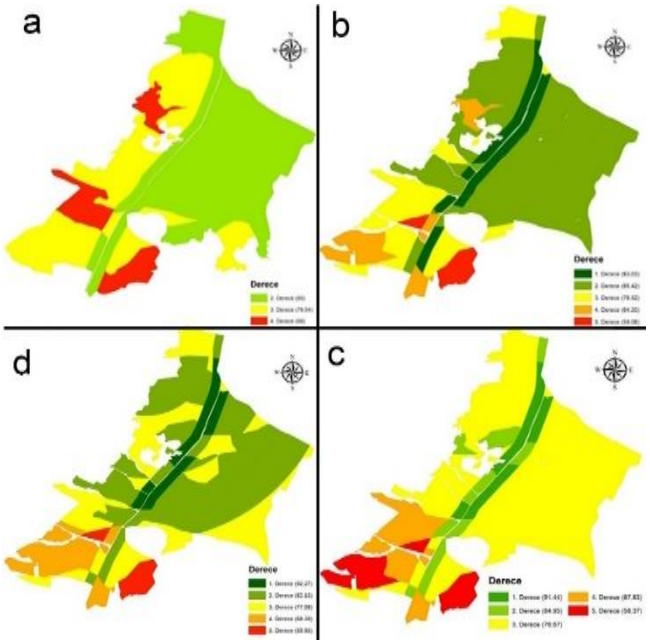

Figure 1. Yuvalak Village Rating Maps

Burdur-Antalya highway passes through the middle of Yuvalak plain. For this reason, roadside lands were given up to 10 points. Parcels close to the village center were given up to 10 points and a maximum of 20 points were given in total (R.G., 1982). Since location points can be given up to 20 points according to ATT, location points are taken into account without changing them as in the map in the figure "Fig. 2". As a result of the calculations, the rating map was formed as in "Fig 1-b".

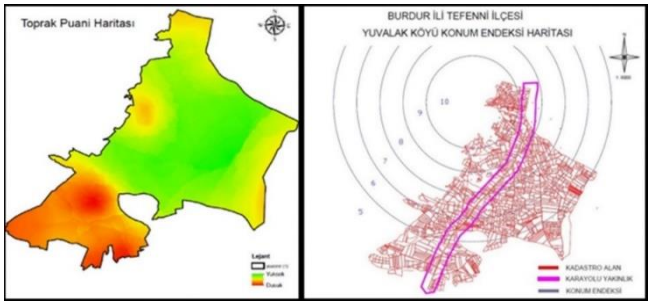

Figure 2. Yuvalak Village Soil Index / Location Index Maps

2.3. Yuvalak Village Rating Studies According to the Law No. 3083

While determining the current prices in the study area, up to 100 points are given considering the proximity to the road and the village (TRGM, 2005). While determining the soil index (TE), the scores given in the new grading method were calculated with the TEx100/40 equation, and the parcel value numbers (PDS) were calculated by scoring up to 100 points "Figure 1-c".

2.4. Rating study according to the LC and TİGH implementation regulations published in 2019

When calculating the parcel index according to the regulation, the soil index score is applied at a rate of 60%, and the score related to location and other characteristics is applied at a rate of 40%. Soil indices in Yuvalak village EC studies are given up to 40 points (R.G 2019). Soil index was calculated with the formula TE*60/40. In order to calculate the location score, the score was calculated according to the proximity to the main road with the formula 15xroad score/10, and the location score was calculated by adding the score of proximity to the village center. The other feature score was created by calculating the commission score*15/10 formula. The rating map is as in "Figure 1-d".

3. Results

Different grading methods applied in Turkey to date have been applied to our exemplary project, Yuvalak village LC project. In the grading study carried out according to the new grading method, it is not in the 1st Degree, but there is an area of 55.65 ha according to the law numbered 3083, 83.34 ha according to the ATT and 58.63 ha according to the regulation published in 2019. According to the grading study carried out according to the law numbered 3083, while the 3rd degree areas are dense, the 2nd degree areas form the density according to other methods.

Table 1. Table of Area Changes According to Different Grading Methods (ha)

	New Rating Method	According to the Law No. 3083	Land Consolidation Regulation	LC and TİGH Implementation Regulations Published in 2019
1.Degree		55.65	83.34	58.63
2.Degree	452.35	65.47	508.64	416.37
3.Degree	300.59	565.22	160.02	259.49
4.Degree	101.47	98.53	72.92	50.39
5.Degree		69.54	29.49	69.53

Yuvalak Village LC project block 146 is mapped according to 4 different grading methods and shown in Figure 3.

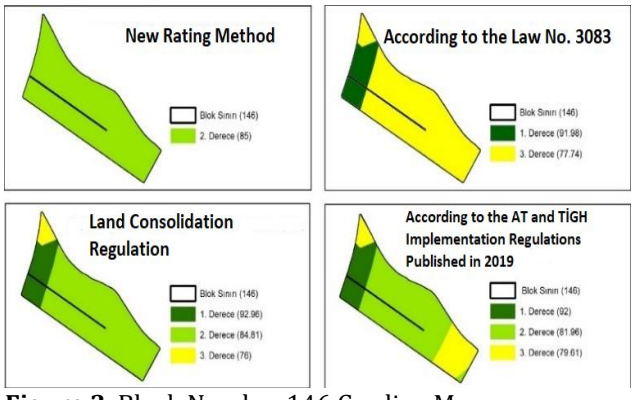

Figure 3. Block Number 146 Grading Maps

According to the new grading method, the entire block is seen as 2nd Degree. In the rating map made according to the law numbered 3083, the majority of the block numbered 146 was calculated as the 3rd degree, and the part of the main road was calculated as the 1st degree with the location points. In the rating map made according to ATT, 1,2 and 3 degree areas are seen. It was formed in 3 different degrees according to the implementation regulation published in 2019.

4. Conclusion

In order to make the rating studies more sensitive and fairer, different approaches have been developed in our country so far. According to the law no. 3083, projects were carried out according to the new rating method, according to the ATT and with the latest law amendment on February 7, 2019. The grading process was applied to Yuvalak village LC study with these methods. As a result of the study, rating maps were examined. As a result of the analysis, it has been observed that some parcels are in different grade classes according to the grading method. While some regions are calculated as 2nd Degree according to the new rating method, they are calculated as 1st Degree according to other methods. In the sample block numbered 146 of Yuvalak village, the effect of different approaches in rating methods on the rating map is shown in the figure. When analyzed spatially and formally, it is seen that different approaches in rating studies cause great changes in rating maps. It is thought that the different calculation of PDS numbers will have a positive or negative impact on the businesses of some parcels during distribution. This shows how important rating studies are.

References

Cay, T., & Uyan, M. (2013). Evaluation of reallocation criteria in land consolidation studies using the Analytic Hierarchy Process (AHP). Land Use Policy, 30(1), 541-548.

Çukur, T., & Ferruh, I. (2008). İzmir ili torbalı ilçesinde sanayi domatesi üreticilerinin sürdürülebilir tarım uygulamaları. Ege Üniversitesi Ziraat Fakültesi Dergisi, 45(1), 27-36.

Demiraslan, M., Özer, U., & Eraslan, H. (2019). Arazi Toplulaştırması Uygulamalarında Karşılaşılan Sorunlar ve Çözüm Önerileri.

Gündoğdu, K. S., Akkaya Aslan, Ş., & Arıcı, İ. (2003). Arazi toplulaştırmasında parsel değer sayılarının coğrafi bilgi sistemi kullanılarak belirlenmesi. Uludağ Üniversitesi Ziraat Fakültesi Dergisi, 17(1), 137-148.

Resmi Gazete (1982). Arazi Toplulaştırma Yönetmeliğinin 4. Maddesinin Değiştirilmesine Dair Yönetmelik. Köy isleri ve Kooperatifler Bakanlığı, 17687, 21.

Resmi Gazete (2019). Arazi Toplulaştırma ve Tarla İçi Geliştirme Hizmetleri Uygulama Yönetmeliği, Yayımlandığı Resmi Gazete Tarihi: 7/2/2019 Sayı: 30679.

Sönmez, N. K., Sari, M., Demirtaş, E., & Altunbaş, S. (2005). Arazi Toplulaştırmasında Kullanılan Farklı Toprak Derecelendirme Yöntemlerinin Karşılaştırılması. Akdeniz Üniversitesi Ziraat Fakültesi Dergisi, 18(3), 425-435.

TRGM, (2005). Toprak Sınıflaması Teknik Talimatı. Tarım Reformu Genel Müdürlüğü Tarım Arazilerini Değerlendirme Dairesi Başkanlığı, 150 s.

TRGM, (2010). Tarım Reformu Genel Müdürlüğü Arazi Toplulaştırması Teknik Talimatı. Kamulaştırma Toplulaştırma ve Dağıtım Dairesi Başkanlığı, 15 s.

Yıldız, N. (1983). Arazi toplulaştırması. Yıldız Üniversitesi Yayınları Sayı, 167.

Yoğunlu, A. (2013). Arazi Toplulaştırma Faaliyetleri. Trb1 Bölgesi (Bingöl, Elazığ, Malatya, Tunceli), Fırat Kalkınma Ajansı.

6th Intercontinental Geoinformation Days

igd.mersin.edu.tr

Four-Dimensional cadastre modeling with UML Diagram

Tayfun Çay *[1], **Hasan Çevik** [2]

[1] *Konya Technical University, Faculty of Engineering and Natural Sciences, Geomatics Engineering Department, Konya, Türkiye*
[2] *Burdur Mehmet Akif Ersoy University, Gölhisar Vocational School, Department of Architecture and Urban Planning, Burdur, Türkiye*

Keywords
Cadastre
UML
Fourth Dimension
Temporal Dimension

Abstract

In addition to the third dimension in the cadastre, the need for temporal information about the past is also increasing. Changes may occur in real estate, both legally and geometrically, over time. It is of great importance in terms of four-dimensional cadastre that these changes can be monitored instantly in the four-dimensional environment together with the vertical dimension. In this study, a four-dimensional cadastre design was made using the UML modeling language, which is a visual modeling language. In this design, along with the horizontal and vertical positions of the real estates, the fourth dimension, which shows the temporal changes, and the value element, which is thought to be the fifth dimension of the cadastre in the future, are partially included. In addition, in this study, using the UML modeling language, the zoning status of the immovables, the lines passing under and above the immovable, the type of changes that occurred in the immovables, the time and explanation of the change were included and their relations with each other were examined.

1. Introduction

Due to the two-dimensional cadastral systems in the world, the legal status of the three-dimensional rights and restrictions that are the subject of ownership above or below the land cannot be determined. The need for three-dimensional information, especially in cities that develop in a vertical direction, increases its importance day by day (Ayazlı & Batuk, 2007).

In our country, temporal Land Registry and Cadastre data are needed intensively. Land Registry and Cadastre data are constantly changing over time as a result of practices such as subdivision, development plan implementation, sales, donations, and mortgages. (Cömert & Alkan, 2004).

In addition to the vertical dimension, the need for temporal knowledge of the past is also increasing. Changes may occur in real estate, both legally and geometrically, over time. It is of great importance in terms of four-dimensional cadastre that these changes can be monitored instantly in the four-dimensional environment together with the vertical dimension.

One of the reasons for the need for four-dimensional cadastral information is that a historical record is required for a particular property. Time always plays an important role in cadastral systems. (Van Oosterom, Ploeger, Stoter, Thompson, & Lemmen, 2006).

Although there have been great changes in the Turkish cadastre in recent years, the problems for the transition to the three-dimensional cadastre have not been solved. The third dimension was neglected in the cadastral renewal studies in Turkey, only the elevation of the land was measured. Infrastructure facilities were not measured and not associated with the cadastre. Therefore, the renovation works were incomplete and insufficient. With the developments in technology and studies in spatial information systems, the need for a four-dimensional cadastre has become a necessity (Nacar, 2021).

Due to the fact that cadastre is a living phenomenon, the importance of the fourth dimension, the time factor, is increasing (Çay et al., 2007).

2. Method

In this study, the four-dimensional cadastral design was modeled with the UML modeling language.

UML, which is the abbreviation of "Unified Modeling Language", can be translated into Turkish as "Unified Modeling Language". Rather than being a programming

* **Corresponding Author**

*(tcay@ktun.edu.tr) ORCID ID 0000-0002-4661-5583
(hcevik@mehmetakif.edu.tr) ORCID ID 0000-0001-6359-3251

Cite this study

Çay, T., & Çevik, H. (2023). Four-Dimensional cadastre modeling with UML Diagram. Intercontinental Geoinformation Days (IGD), 6, 403-406, Baku, Azerbaijani

language, UML is a collection of methods that define and describe how business systems can be modeled. A good modeling in the analysis and design phase prevents many problems that may arise in the software phase. UML is more suitable for object-oriented programming languages. A software prepared with UML is both less costly, more effective and longer lasting. The birth of UML can be considered as one of the biggest developments in the software industry in recent years. (Uymaz, 2007).

Class Area
Structure and Attribute Area
Behavior and Methods Area

Figure 1. Structure of UML

As shown in Figure 1, UML consists of three different areas: the class area, the structure and attribute area, and the behavior and methods area. Among these fields, the class field is the field where the names of the classes are written. The structure and attribute area are the area where the elements of the class and their descriptors are located. The behavior and methods area are the area where the methods of the class elements are located.

Here the relationships between classes are specified. These relationships can be one-to-one, one-to-many, etc. may form. Figure 2 shows the UML diagram of the second dimension of the cadastre. Here, the immovable's ID number, block and parcel number, point number, slice meridian, coordinate values, datum and projection variables and data types of these variables are shown.

2D
-Id: Int -Block: Int -Parcel: Int -Point number: Int -Y : Double -X: Double -Datum: String -Projection: String -Slice Meridian: Int
-List ( ) : void -Save ( ) : void -Delete ( ) : void -Update ( ) : void -Clean ( ) : void

Figure 2. UML representation of 2D

Figure 3 shows the UML diagram of the third dimension of the cadastre. Here, immovable's ID number, the block and parcel number, the average elevation of the parcel, the registration object type, the elevation of the registered object, the elevation difference and the explanation variables and the data types of these variables are shown. In addition, the relationship of 3D with the registered object type is also shown.

Figure 4 shows the UML diagram of the fourth dimension of the cadastre. Here, immovable's ID number, the block and parcel number, the change type, the change time and the description variables and the data types of these variables are shown. Also, the relationship of 4D with the type of change is shown.

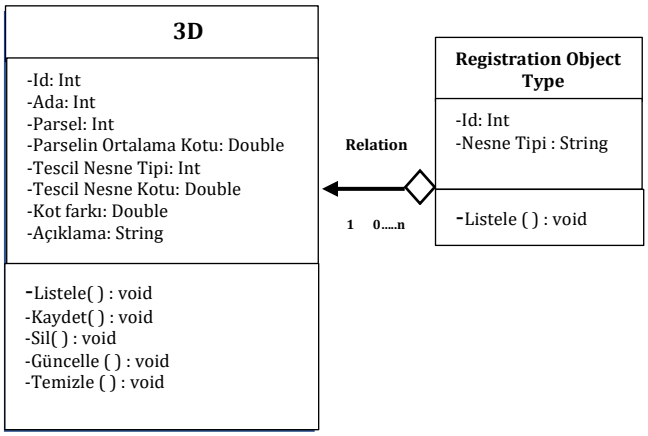

Figure 3. UML representation of 3D

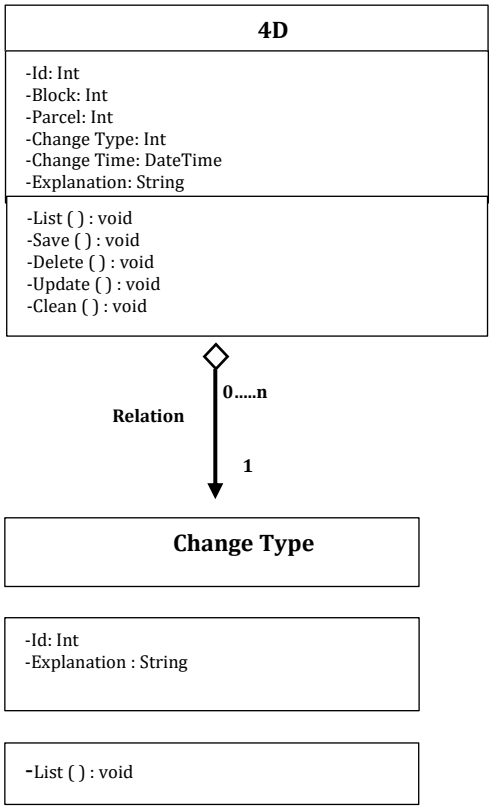

Figure 4. UML representation of 4D

Figure 5 shows the UML diagram of the zoning status of the immovable. Here, immovable's ID number, the block and parcel number, current zoning plan, plan function, approval date, scale, floor area ration (TAKS) and floor area coefficient (KAKS), building height, number of floors, construction layout, front, side and back garden distances variables and data types of these variables shown.

Figure 6 shows the UML diagram about the general information of the immovable. In the general information class, immovable's ID number, province, district, neighborhood/village, location, address, block, parcel number, title deed area, owner, father's name, qualification, numerator and denominator amount variables and the data types of these variables are shown.

In addition, the relations of the general information class with the province and district classes are shown.

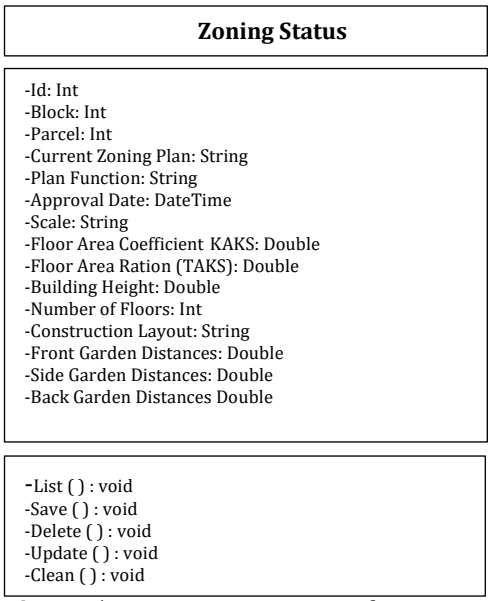

Figure 5. UML representation of zoning status

In Figure 7, the interface design of the desktop application that is desired to be made according to this UML diagram is shown. In this design, by entering the province, district, neighborhood/village, block and parcel information of the immovable whose information is desired to be accessed, the 2D, 3D, 4D and 5D buttons of that immovable appear on the screen. If two-dimensional information of the immovable is desired to be accessed, the 2D button should be pressed, if three-dimensional information is desired to be accessed, the 3D button, if four-dimensional information is desired to be accessed, the 4D button should be pressed, and if five-dimensional information is desired, the 5D button should be pressed. Here, the two-dimensional information of the immovable is meant by its horizontal coordinates, projection and datum information, ownership and share information. What is meant by the three-dimensional information of the immovable is the lines passing under and over the immovable and displaying the vertical coordinates of these lines as well as the horizontal coordinates of these lines. What is meant by the four-dimensional information of the immovable is the chronological display of the changes that have occurred in the immovable over time. What is meant by the five-dimensional information of the immovable is the value of the immovable.

In Figure 8, the third-dimensional interface design of the desktop application that is required to be written according to this UML diagram is shown. Here, after pressing the 3D button, the registration object types that pass under and over the immovable appear. The elevation differences of the selected registration object type according to the parcel can be accessed here. The main registration object types here are drinking water, rain water, sewage, natural gas, energy transmission lines, bridges, viaducts, drilling, buildings, etc.

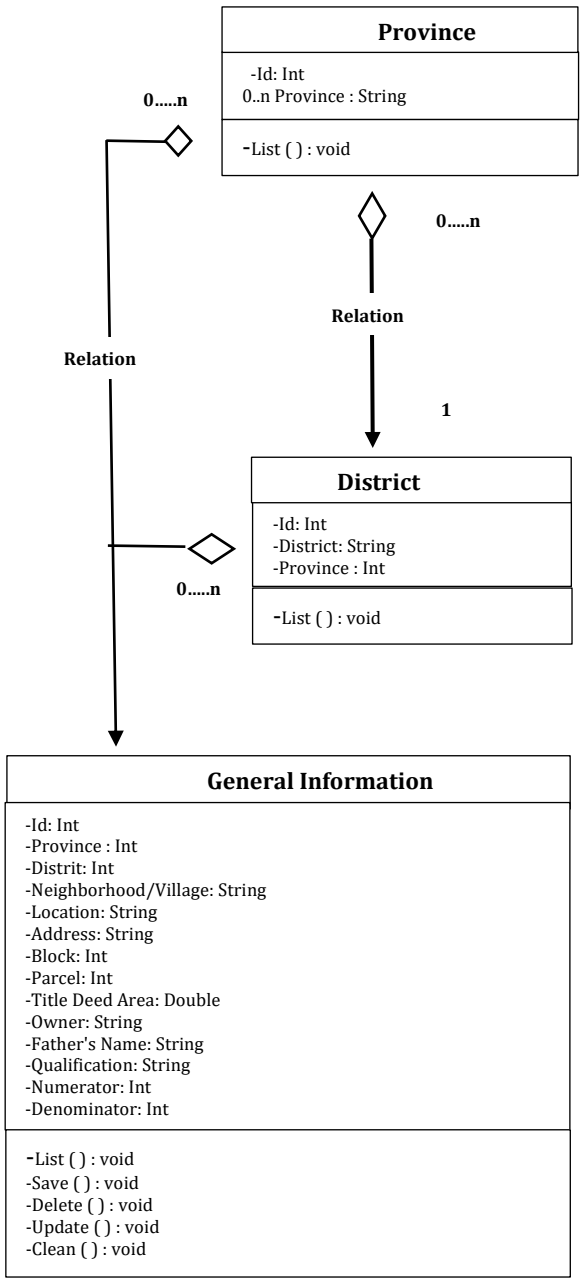

Figure 6. UML representation of general information

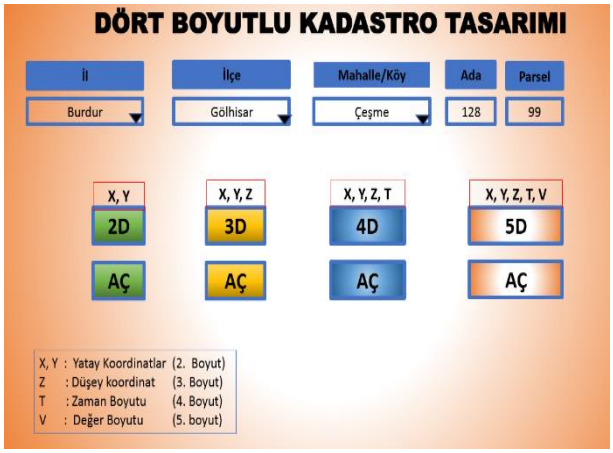

Figure 7. Interface design of the home page

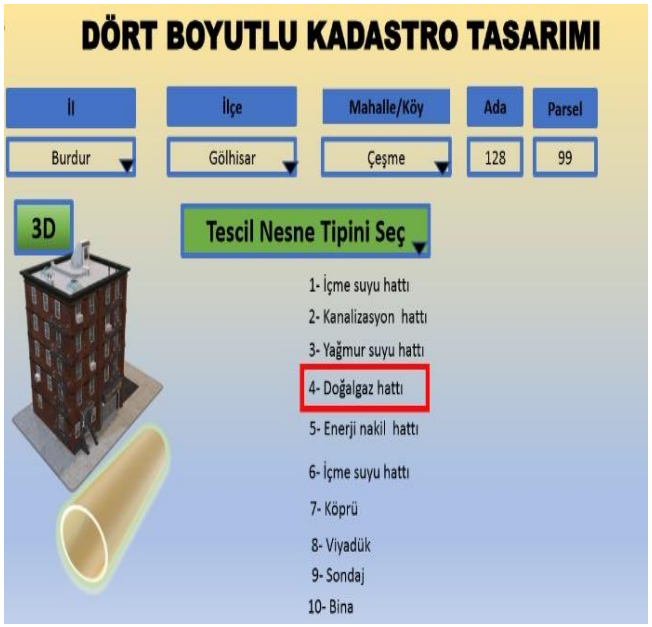

Figure 8. Interface of the third dimension

In Figure 9, the interface design of the fourth dimension of the desktop application that is desired to be made according to this UML diagram is shown. Here, after pressing the 4D button, the geometric and legal changes that occurred in the immovable over time are listed chronologically. Here, changes in the geometric sense are changes such as subdivision, amalgamation, renuniation for road, development plan implementation, expropriation. Changes in the legal sense, on the other hand, are changes such as liens and mortgages that do not change the geometric shape of the parcel.

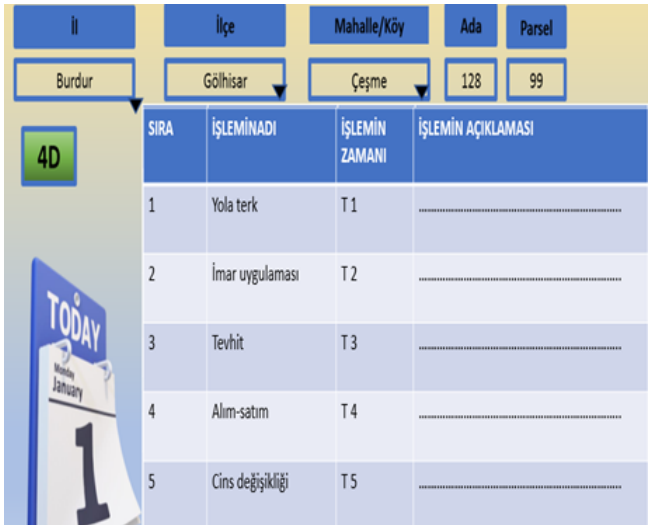

Figure 9. The interface of the fourth dimension

3. Results

As a result, it has been seen that the UML diagram is suitable in four-dimensional cadastral design, the UML diagram can be used easily with any programming language, and the UML diagram can be easily understood by every user regardless of the program language. Since many public institutions and organizations in Türkiye need historical temporal data of immovables, such a design is needed.

References

Ayazlı, E., & Batuk, F. (2007). Üç Boyutlu Kadastro Gereksinimi. TMMOB Harita ve Kadastro Mühendisleri Odası 11. Türkiye Harita Bilimsel ve Teknik Kurultayı 2-6 Nisan 2007, Ankara.

Cömert, Ç., & Alkan, M. (2004). The design and development of a temporal GIS for cadastral and land title data of Turkey. Commission IV, WG IV, 1.

Çay, T., Erdi, A., Özkan, G., İnam, Ş., Durduran, S. S., Yalpır, Ş., & İşcan, F. (2007). An investigation on Integration of Turkish Cadastre to "Cadastre 2014 Vision". Chamber of Surveying and Cadastre Engineers Geodesy Geoinformation and Land Management Journal, 2(97), 40-46 (in Turkish).

Nacar, F. (2021). The need for 4D in Turkish cadastre. Arabian Journal of Geosciences, 14(7), 542. https://doi.org/10.1007/s12517-021-06809-w

Uymaz, S. A. (2007). UML ile Sanal Kampüs Modellemesi. Yüksek Lisans Tezi, Selçuk Üniversitesi Fen Bilimleri Enstitüsü, Bilgisayar Mühendisliği Anabilim Dalı.

Van Oosterom, P., Ploeger, H., Stoter, J., Thompson, R., & Lemmen, C. (2006). Aspects of a 4D Cadastre: A First Exploration. Paper presented at the Shaping the Change XXIII FIG Congress Munich, Germany.

6th Intercontinental Geoinformation Days

igd.mersin.edu.tr

Analysis of real estate values and economic indicators in extraordinary situations

Fatma Bunyan Unel[*1]

[1]*Mersin University, Engineering Faculty, Department of Geomatics Engineering, Mersin, Turkiye*

Keywords
Real Estate Values
Economic Indicators
Economic Analysis
State of Extraordinary

Abstract

State of emergency (OHAL); It includes situations such as natural disasters, pandemic, economic crisis. In the world and Turkiye, the 17 November 2019 epidemic, the 24 February 2022 war and the 6 February 2023 earthquake caused extreme differences in economic indicators. As a result of social mobility, social, cultural, economic and geographical changes occur. The extraordinary situations are; it also causes an abnormal increase/decrease in real estate values. In this study, it is aimed to reveal the differences between economic indicators and real estate values. As economic indicators; Consumer Price Index (CPI), Producer Price Index (PPI), exchange rate, commodity, precious metals, energy resources and car prices were taken into consideration and analyzed with real estate values and economic analyzes were carried out. Considering the increase rates between 2018-2023, it is seen that the rate tends to increase as the value of the asset increases.

1. Introduction

The state of emergency (OHAL), briefly referred to as the State of Emergency, includes extraordinary situations, and measures to be taken throughout the country or region are implemented during the state of emergency. In the State of Emergency Law No. 2935 (1983), these situations are stated as follows;

• Natural disaster, dangerous epidemics or severe economic depression,

• The emergence of serious signs of widespread acts of violence aimed at destroying the free democratic order established by the Constitution or fundamental rights and freedoms, or serious disruption of public order due to acts of violence,

After the state of emergency is declared, decisions regarding the extraordinary administration procedures are taken and implemented. Under the state of emergency; Criteria are determined on how to limit or stop fundamental rights and freedoms, which are valid separately for money, property and work obligations to be imposed on citizens and for each type of state of emergency. The provisions of how and in what form the necessary measures for the State of Emergency will be taken, what powers will be given to public service officials, and what changes will be made in the status of officials are explained.

Most natural disasters are caused by meteorological reasons. The most important meteorological natural disasters in our country; hail, flood, overflow, frost, forest fires, drought, heavy rain, strong wind, lightning, avalanche, snow and storms. Disasters such as sudden earthquakes, volcanic eruptions, and fires, all of which are states of emergency (AFAD, 2023).

Pandemic, war and earthquake extraordinary situations in the world and in our country in recent years; It has affected people socially, culturally and economically. Pandemia cases started to be seen on 17 November 2019 in the world and COVID-19 originated December 2019 in Wuhan City, China. It spread very quickly to all continents by human means. It was officially announced that it was first seen in Turkiye on March 11, 2020. In this process, it has been tried to prevent the spread of the virus by taking decisions to stay home from time to time. With the support of the World Health Organization, companies and research institutes started vaccine development studies and vaccines such as Pfizer-BioNTech and Sinovac were developed for virus protection *(*Kusak & Kucukali, 2023; *Unel & Yalpir, 2023).*

Wars in different parts of the World outbreak. Finally, the invasion of Ukraine by Russia on February 24, 2022. War forces people to migrate and causes changes in population and demographic structure in both abandoned and settled areas.

According to Kandilli Observatory's (2023) the data, two earthquakes occurred on 06 February 2023 at intervals of 9 hours. One of them was a very strong earthquake with an instrumental magnitude of Ml=7.4

* **Corresponding Author**

*(fatmabunel@mersin.edu.tr) ORCID ID 0000 – 0002 – 9949 – 640X

Cite this study

Unel, F. B. (2023). Analysis of real estate values and economic indicators in extraordinary situations. Intercontinental Geoinformation Days (IGD), 6, 407-410, Baku, Azerbaijan.

(Mw=7.7) at 4.17 local time, in the Sofalaca Neighborhood (37.1757 N 37.085 E) of the Şehitkamil district of Gaziantep province. The other was a very strong earthquake with an instrumental magnitude of Ml=7.5 (Mw=7.6) occurred at 13:24 local time in Ekinözü district of Kahramanmaraş province (38.0818 N - 37.1773 E). The earthquake was felt in a wide region covering 11 provinces in Southeastern Anatolia, Eastern Anatolia, Central Anatolia and Mediterranean Regions. In the earthquake, in which a significant number of lives were lost, the biggest damage in terms of the Turkish economy in terms of 54.9% was 1.073.9 billion ₺/56.9 billion $ worth of residences, 242.5 billion ₺/12.9 billion $ public infrastructure and service buildings. (222.4 billion ₺/11.8 billion $ damage occurred) related to industry, energy, communication, tourism, health and education sectors, small tradesmen and places of worship (SSB, 2023).

The extraordinary situations experienced in the years 2020-2023 cause social, cultural, economic and geographical differences in the society. Changing people's preferences and behaviours means the interaction of their whole lives. These, in turn, affect the real estate value and change the sales and rental values in the form of a sudden increase or decrease.

2. Material and Method

The field of study is Turkiye, and the economic values of the extraordinary situations that occur in the world and in the country are examined (Figure 1).

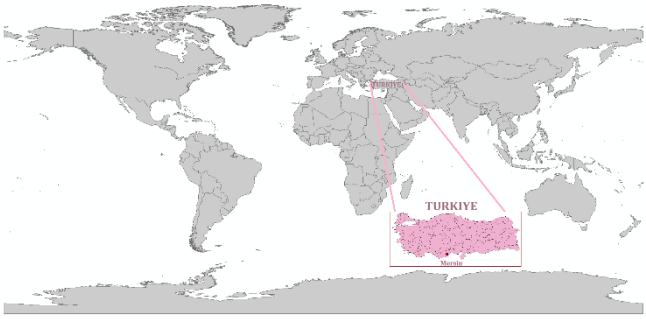

Figure 1. The study area

Data consist of economic indicators, cars and real estate values. Economic indicators are Consumer Price Index (CPI), Producer Price Index (PPI), exchange rate, commodity, precious metals, energy resources and car prices were taken into consideration and analysed with real estate values (Figure 2). The data between the years 2019-2023, when the states of emergency occurred, were collected and analysed.

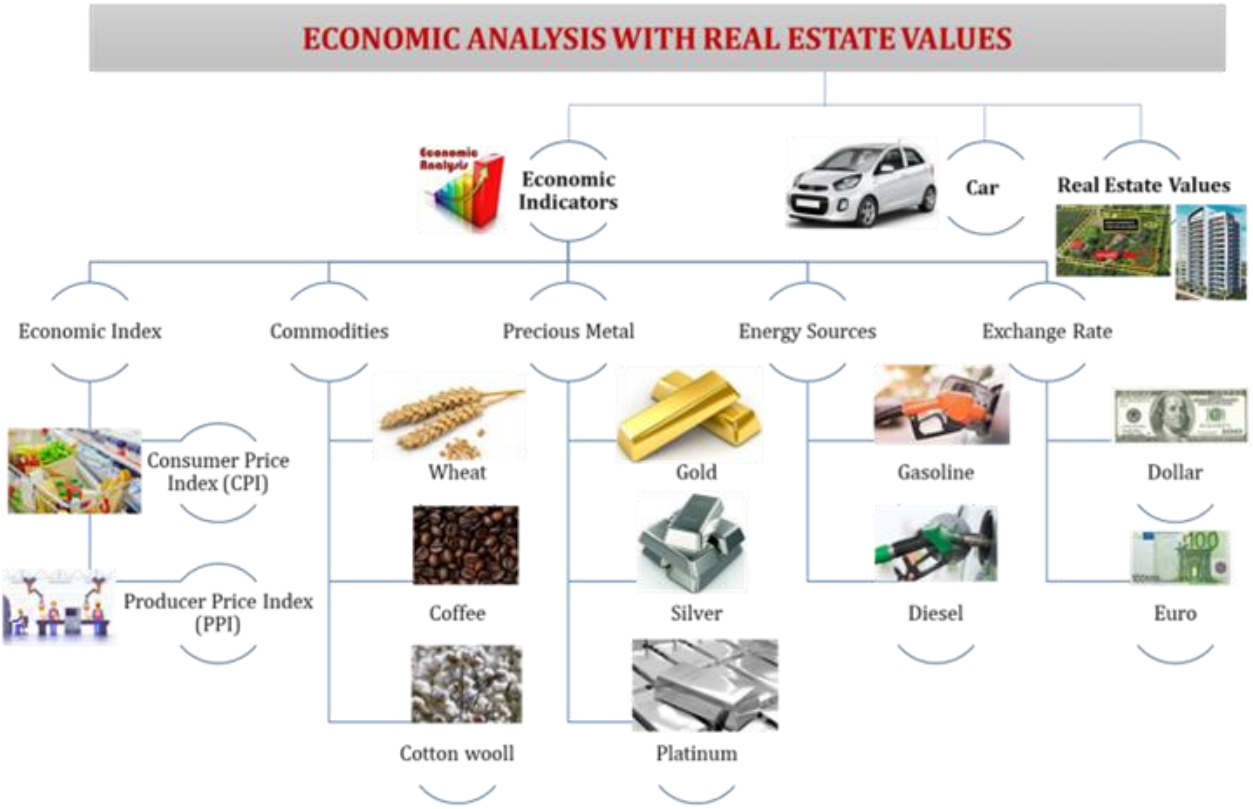

Figure 2. Economic indicators and Real estate values

Economic analysis is to evaluate costs and benefits to check the viability of an event, a project, investment opportunity, or any other situations. In other words, it involves identifying, comparing, and evaluating, costs and benefits (Vaidya, 2023).

3. Results

Indexes (PPI and CPI), commodities, precious metals, energy resources and exchange rate data were collected from economic indicators. Price changes occur in all

commercial production and consumer goods in line with supply/demand. As a result of these, overall economic indicators are obtained. The annual percentage change of PPI and CPI (TUIK, 2023) is highest in September 2018 and December 2021. In the monthly change, it was observed that it was the highest in all months of 2022 (Figure 3).

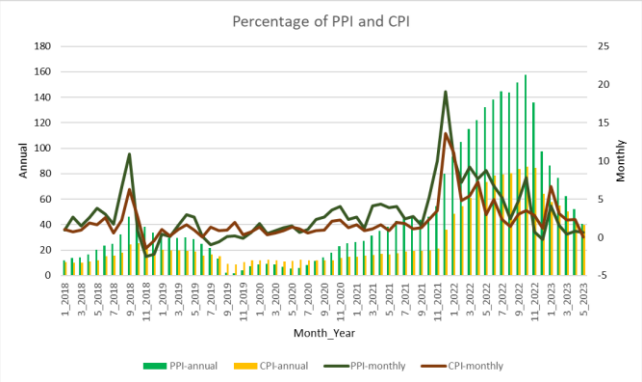

Figure 3. Percentage Change of PPI and CPI

The price changes of wheat, coffee and cotton thought of as a commodity between 2018-2023 were examined. In addition, the percentage changes in the purchase prices of gold, silver and platinum as precious metals were found. The price changes of gasoline and diesel from energy sources were investigated. Most of this data changes every second. For this study, average annual values were collected (Figure 4) (IMF, 2023; TCMB, 2023).

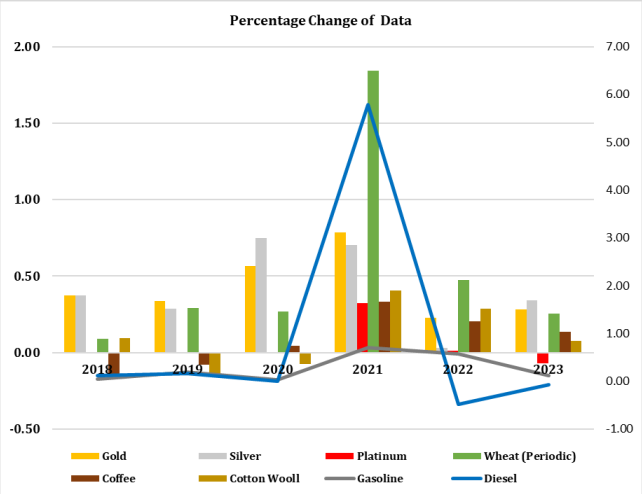

Figure 4. Percentage Changes of the others data

The values of the Turkish Lira against a unit of currency of a country, namely the US Dollar and the European Currency Euro buying/selling values (TCMB, 2023) were discussed as the exchange rate. While the purchase and sale values continue parallel to each other, the highest increase rate is seen in September 2018 and 2022. In this dataset, there was only a decrease in September 2019 (Figure 5).

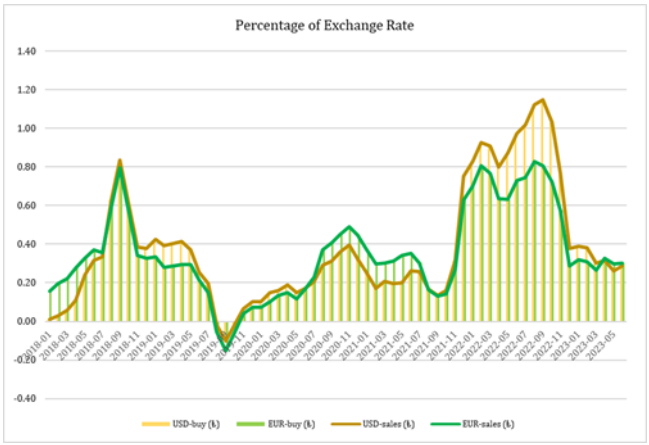

Figure 5. Percentage of exchange rate

There are also significant differences in the prices of automobiles (Car, 2023) (Figure 6) and real estate (Figure 7), which are influenced by economic indicators. In this study, these price differences according to years were analyzed. It is seen that it was increased a lot in January-June 2022 (the first six months of 2022) (Figure 6).

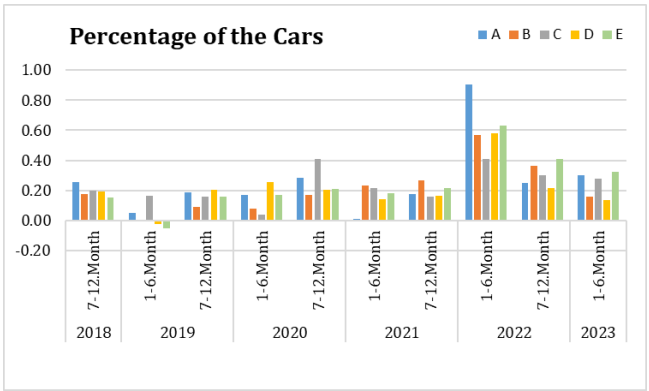

Figure 6. The change of A-E brand cars's prices

The data pertaining to real estate were collected in Mersin province, Yenişehir district, Çiftlikköy District (Figure 7).

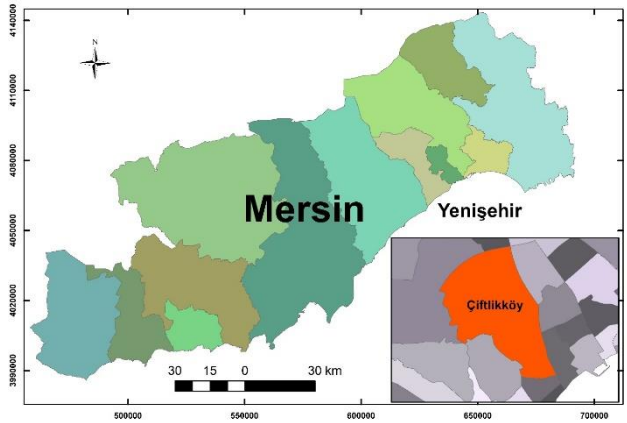

Figure 7. Ciftlikkoy Neighborhood, Mersin/Yenişehir

The residences and plots are considered as the type of real estate. The data set was created by collecting the values of those with the same characteristics as possible (Real Estate, 2023). The residences have features such as

a gross area of 110 m², 2+1 rooms, and individual natural gas (combi boiler). On the other hand, the plots are created for housing or housing + commercial construction by applying the zoning plan to the land. The plots values were also collected separately. It has been determined that it has increased approximately 3.50 times in 2022 (Figure 8).

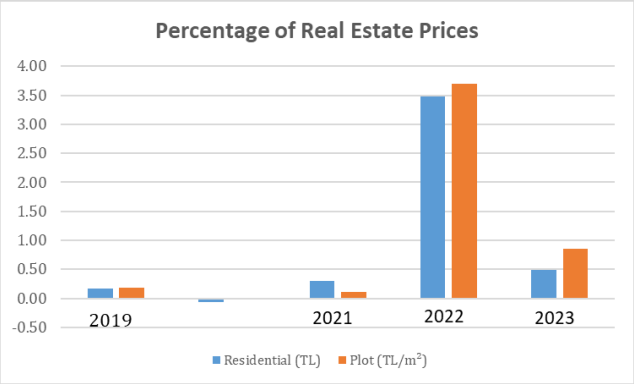

Figure 8. The residences and plots values changes

The economic value of real estate has been increasing over the years. Although most of the literature is residential (Bozdağ, & Ertunç, 2020; Ertaş & Bahadır, 2017; Ulvi & Özkan, 2019); there are different studies on value of plot (Unel & Yalpir, 2023), commercial real estate (Yüksel, et al., 2022), public institution assets (Ünel, et al., 2023).

4. Conclusion

In this study, changes of economic indicators, car and real estate values were analyzed. To investigate the effects of extraordinary situations experienced since 2018 on assets, the value changes between the years 2018-2023 were found and graphs were prepared. It has been determined that economic indicators, cars and real estate values' increase rates are different.

Turkiye economy is affected by both the crises in the world and the internal crises. It is seen that the effects of the world-wide pandemic and the Russian-Ukrainian War are experienced in Turkiye in the following months. After the 6 February 2023 earthquakes, it is observed that the upward movement in the values of real estate, cars and other assets continues.

In future studies, it is designed to analyze Gross National Product, interest rates, inflation, and unemployment rates from macro-economic indicators. In addition, it is planned to renew the analyzes with data such as Manufacturing Industry Price Index, total exports, total imports, number of housing sales, and the total number of automobile sales and continue to investigate the effects.

References

AFAD, (2023). Afet ve Acil Durum Yönetimi Başkanlığı (AFAD), T.C. İçişleri Bakanlığı, Ankara. Access Date: 07.05.2023 https://www.afad.gov.tr/afadem/dogal-afetler

Bozdağ, A. & Ertunç, E. (2020). CBS ve AHP Yöntemi Yardımıyla Niğde Kenti Örneğinde Taşınmaz Değerleme. Geomatik, 5(3), 228-240.

Car, (2023). Araba Fiyatları (The car prices), Access Date: 25 Mayıs 2023 http://www.arabalar.com.tr

Ertaş, M. & Bayındır. B. (2017). Valuation of residences through utilizing ratio of integrated capitalization, International Journal of Engineering and Geosciences, 2(3), 91 – 99.

https://www.sahibinden.com/kategori/emlak

IMF, (2023). IMF Data, Access to macroeconomic & Financial Data, Primary Commodity Price System, https://data.imf.org/?sk=471dddf8-d8a7-499a-81ba-5b332c01f8b9

Kandilli Observatory, (2023). 06 Şubat 2023 Ekinözü Kahramanmaraş Depremi Basın Bülteni. Boğaziçi Üniversitesi Kandilli Rasathanesi ve Deprem Araştırma Enstitüsü, Bölgesel Deprem-Tsunami İzleme ve Değerlendirme Merkezi, İstanbul.

Kusak, L., & Kucukali, U. F. (2023). Investigating the relationship between COVID-19 shutdown and land surface temperature on the Anatolian side of Istanbul using large architectural impermeable surfaces. Environment, Development and Sustainability, 1-38.

Real Estate, (2023). Online Real Estate Sites, Access Date: 25 May 2023

SBB, (2023). SBB Deprem Sonrası Değerlendirme Raporu. T.C. Strateji ve Bütçe Başkanlığı, Ankara.

TCMB, (2023). Electronic Data Distribution System, Elektronik Veri Dağıtım Sistemi (EVDS), Türkiye Cumhuriyeti Merkez Bankası (TCMB), https://evds2.tcmb.gov.tr/index.php?/evds/serieMarket

The State of Emergency Law, (1983). Olağanüstü Hal Kanunu, Kanun Numarası: 2935, Kabul Tarihi: 25/10/1983, Yayımlandığı Resmi Gazete; Tarih: 27/10/1983 Sayı: 18204, Yayımlandığı Düstur: Tertip: 5 Cilt: 22 Sayfa: 815.

TUIK, (2023). Türkiye İstatistik Kurumu (TUIK)- Turkish Statistical Institute, Merkezi Dağıtım Sistemi, (TÜİK), Access Date: 25 Mayıs 2023 https://biruni.tuik.gov.tr/medas/?locale=tr

Ulvi, C. & Özkan, G. (2019). Taşinmaz Değerlemede Yapay Zekâ Tekniklerinin Kullanilabilirliği ve Yöntemlerin Karşilaştirilmasi. Geomatik, 4 (2), 134-140.

Unel, F. B., & Yalpir, S. (2023). Sustainable tax system design for use of mass real estate appraisal in land management. Land Use Policy, 131, 106734.

Ünel, F.B., Kuşak, L. & Yakar, M. (2023). Bulanık Analitik Hiyerarşi Prosesi Kullanılarak Üniversite Taşınmazları için Mekansal Değer İndeks Haritasının Oluşturulması, III. Uluslararası Gayrimenkul Geliştirme ve Yönetimi Konferansı (ICREDM2023), Ankara, Turkiye.

Vaidya, (2023). Economic Analysis, https://www.wallstreetmojo.com/economic-analysis-2/ Access Date: 17.05.2023

Yüksel, G., Ünel, F. B., & Ulvi, A. (2022). Valuation of commercial real estate in Ankara middle east industry and trade center (MEITC). Advanced GIS, 2(2), 70-78.

6th Intercontinental Geoinformation Days

igd.mersin.edu.tr

Value based land regulation model and its applicability in Türkiye

Mehmet Koçoğlu [1], Mehmet Ertaş *[2], Mevlüt Uyan [2]

[1]*Munzur University, Vocational School of Pertek Sakine Genç, Tunceli, Türkiye*
[2]*Konya Technical University, Vocational School of Technical Sciences, Konya, Türkiye*

Keywords
Land readjustment
Value-based land readjustment
Cadastral parcels

Abstract

Land and land arrangement works in Türkiye are carried out in accordance with Article 18 of the Zoning Law No. 3194. According to the legislation, all cadastral parcels within the regulation boundary are considered as a whole and converted into zoning parcels. It is usual to experience an increase in value in these areas that gain the status of zoning parcel. However, in practice, while some cadastral parcels within the regulation boundary benefit a lot from this increase in value, some parcels are satisfied with less value increase. This problem experienced in practice often leads to objection to the application or legal process for citizens. According to Article 18 of the Zoning Law No. 3194, the implementation of value-based distribution instead of area-based distribution, which is created by making a deduction at the same rate from all parcels within the regulation boundary, is of great importance in terms of eliminating the existing problems. However, the uncertainties regarding the valuation of the land and land arrangement weaken the strength of the value-based land and land arrangement approach. In this study, in order for the value-based land and land arrangement model to be applicable and adopted by practitioners, the "development right", which directly and most affects the value of immovable property, is taken as the basis.

1. Introduction

With population growth and urbanisation, the planned and healthy development of built-up areas depends on the preparation of zoning plans and the reflection of the prepared plans to the land in terms of technical and legal aspects.

In Türkiye, "Land and Land Arrangement" (AAD) applications, which is one of the methods of implementing large area zoning plans, are carried out in accordance with Article 18 of the Zoning Law No. 3194.

With the Land and Land Regulation (AAD) applications, the cadastral parcels within the regulation boundary according to the zoning plans are transformed into zoning parcels, and the economic values of the immovables change along with the cadastral boundaries. The fact that the gain provided to the owners by this economic change is not of the same value for all immovable properties brings along certain problems.

The approach of Yıldız (1977), who presented the value-based distribution proposal for the first time in Türkiye, has been evaluated by many researchers and studies have been carried out on its applicability in Türkiye with various methods. However, regional differences in the parameters affecting the value of immovable property and the existence of uncertainties regarding the value calculation weaken the strength of the value-based approach method (Ertunç and Uyan 2022).

"In order to eliminate these weaknesses, there is a need for an allocation model based on another criterion other than value but directly affecting the value, such as development rights or construction area" (Çağdaş 2019).

In this study, in order for the value-based ECL model to be applicable and adopted by the practitioners, the amount of the debiting of the value differences arising from the length of the parcel frontage and the width of the road frontage (road debt) is evaluated as the progress payment construction area and included in the equalisation based on the "zoning right", which directly and most directly affects the value of the immovable. The allocation values calculated by applying this method in a pilot study area were compared with the current application method.

* **Corresponding Author**

(mehmetkocoglu@munzur.edu.tr) ORCID ID 0000-0002-3583-0544
*(mertas@ktun.edu.tr) ORCID ID 0000-0002-9458-3395
(muyan@ktun.edu.tr) ORCID ID 0000-0002-3415-6893

Cite this study

Koçoğlu, M., Ertaş, M., & Uyan, M. (2023). Value based land regulation model and its applicability in Türkiye. Intercontinental Geoinformation Days (IGD), 6, 411-414, Baku, Azerbaijan

2 Regulation model based on zoning rights

The development right-based AAD is a method that ensures that the value increases that will occur after the implementation are transferred to the public and the zoning parcels formed are allocated at their pre-regulation values. The model developed by Çağdaş (2019) was applied in the determined regulation area.

In the model; in addition to the increase in value generated by the EAD, the theoretical construction area deserved by the parcel before the plan is equalised with the construction area of the parcel that will be formed after the implementation according to the zoning plan, and the total construction area increase provided is transferred to the public. The value difference arising according to the emsale can be distributed to the owners in a fair manner when desired. Spatial value differences are prevented by preserving the rule of allocation to the parcel from its current location (Ertaş and Uşak, 2020).

According to the AAD model based on the zoning right, the construction areas of participation and allocation should be equal, as shown in Equation (1).

$$\sum_{i=1}^{n} İ A_{k_i} = \sum_{j=1}^{m} İ A_{t_j} \quad (1)$$

A_{k_i} = Participation construction area of cadastral parcel before the arrangement
A_{t_j} = Construction area allocated to the zoning parcel after the arrangement

Total participation and allocation construction areas are found by Equation (2). In the proposal approach, the construction precedent before the regulation is determined according to the Regulation on Unplanned Areas, and the construction precedent after the regulation is determined according to the implementation zoning plan.

$$\sum_{i=1}^{n} A_i \, e_i = \sum_{j=1}^{m} A_j \, e_j \quad (2)$$

A_i = Area of the parcel before regularisation
e_i = Precedent before adjustment
A_j = Area of the parcel after regularisation
e_j = Precedent after adjustment

Since the total participation and allocation values will vary with the zoning plan decisions, the equivalence cannot always be achieved and there will be an increase in the ratio (δ). This ratio is obtained by dividing the total allocation construction area by the total participation construction area as in Equation (3).

$$\delta = \frac{\sum_{j=1}^{m} İ A_{t_j}}{\sum_{i=1}^{n} İ A_{k_i}} \quad (3)$$

The difference between the total area of the parcels participating in the implementation and the total area of the allocation parcels formed after the implementation meets the public service areas in the regulation area according to the zoning plan. The amount of public service areas is found by Equation (4).

$$\sum A_{kh} = \sum_{i=1}^{n} A_i - \sum_{j=1}^{m} A_j \quad (4)$$

A_{kh} = Public service areas

The proposed method aims to allocate zoning parcels equivalent in size to the pre-application construction area, while at the same time transferring the excess construction area gained through the zoning plan to the public. The amount of land to be transferred to the public ($\sum\Delta$) can be found by both Equations (5) and (6).

$$\sum \Delta = \sum_{j=1}^{m} İ A_{t_j} - \sum_{i=1}^{n} İ A_{k_i} \quad (5)$$

$$\sum \Delta = (\delta - 1) \cdot \sum_{i=1}^{n} İ A_{k_i} \quad (6)$$

In cases where the increase in construction area is large, it may be possible to allocate some of this increase to the parcels that will be affected by the regulation and some of it to the public instead of transferring it to the public. In this case, the value increases to be allocated to the parcels and the public are found by Equations (7) and (8), respectively. The expressions p_p and p_k in the equations denote the sharing ratio of the increase in construction area between the public and the parcels.

$$\sum \Delta_p = \sum \Delta \cdot p_p \quad (7)$$

$$\sum \Delta_k = \sum \Delta \cdot p_k \quad (8)$$

$\sum \Delta_p$ = Construction area to be allocated to parcels
$\sum \Delta_k$ = Construction area to be allocated to the public

The progress payment value of a parcel within the regulation boundary is equal to the sum of the parcel participation value and the value increase amount allocated to the parcel in Equation (2.10), as given in Equation (9).

$$İA_{h_i} = İA_{k_i} + \Delta_{p_i} \quad (9)$$

$$\Delta_{p_i} = A_{k_i} \cdot (\delta - 1) \cdot p_p \quad (10)$$

$İA_{h_i}$ = Parcel progress payment area after adjustment
$İA_{k_i}$ = Pre-regulation construction area
Δ_{p_i}= Amount of increase in construction area allocated to the parcel

The area of the zoning parcel to be allocated is calculated by proportioning the progress payment construction area calculated for the parcel to the precedent of the zoning island to be allocated, as given in Equation (11).

$$A_j = \frac{İA_{h_i}}{e_j} \quad (11)$$

A_j = Area of zoning parcel to be allocated
$İA_{h_i}$ = Parcel progress payment construction area
e_j = Development island precedent value

Construction progress payment and construction allocation areas should be equal to each other. If the parcel area is not sufficient and this equivalence cannot be achieved, the difference (γ) between the construction progress payment and construction allocation areas found by equation (12) can be converted into a price (B_i) by multiplying it with the official building unit cost price

(M) of that year according to the date of application by Equation (13).

$$\gamma_i = İA_{t_i} - İA_{h_i} \quad (12)$$

$$B_i = \gamma_i \cdot M \quad (13)$$

According to the proposal method, the areal deduction rate of a parcel is calculated by dividing the allocated parcel area by the participation parcel area as in Equation (14).

$$k_i = 1 - \frac{A_j}{A_i} \quad (14)$$

According to the arrangement model based on the zoning right, the allocation schedule in the application area is created.

2.1 Debiting the value differences arising from the length of the parcel frontage and the width of the road frontage

Taking into account the frontage lengths and road widths of the zoning parcels after the arrangement, the resulting value differences were debited as "road debt" (Yıldız et al., 2008). The road debt amounts were evaluated as progress payment construction area according to the method based on development rights and included in equalisation. In the distribution model based on development rights, while the value differences arising from the increase in precedent are taken into consideration, road widths and frontage lengths are not evaluated. As the precedents of the development islands may be different, the road widths surrounding the development islands may also be different.

According to the frontage lengths and road widths of the regulation area, the weighted frontage length is calculated for each zoning parcel separately by Equation (15).

$$AC = \frac{\sum_{i=1}^{n} YG_i \cdot PC_i}{\sum_{i=1}^{n} YG_i} = \left(\frac{YG_1 \cdot PC_1 + YG_2 \cdot PC_2 + YG_3 \cdot PC_3}{YG_1 + YG_2 + YG_3} \cdot n\right) \quad (15)$$

AC = Weighted façade length
YG = Road width
PC = Parcel frontage length
n = Number of facades

At the same time, since the road widths of each parcel cannot be the same, weighted road widths are calculated by Equation (16).

$$AYG = \frac{YG_1 \cdot PC_1 + 2 \cdot YG_2 \cdot PC_2 + 3 \cdot YG_3 \cdot PC_3}{\sum_{i=1}^{n} PC_i} \quad (16)$$

AYG = Weighted road width

According to the suggestion of (YALPIR, 2007); the multiplication coefficient of the widest road was taken as 1, and the weights of the road widths were determined by successively increasing towards the narrowest road.

The overall weighted road width on island basis was found by Equation (17).

$$GAYG = \frac{\sum_{i=1}^{n} YG_i \cdot PC_i}{PC_i} \quad (17)$$

GAYG = General weighted road width

Then, the weighted road debt is calculated for each zoning parcel using Equation (18). Since the amounts of receivables or payables are assessed on an island basis, the average road debt for each zoning island is calculated. The difference between the weighted road debt and the average road debt calculated on an island basis will constitute the actual road debt.

$$Road\ Debt\ (YB) = \frac{AC_i(AYG_i - GAYG)}{10} \quad (18)$$

According to the result obtained, negative values are considered as creditor while positive values are considered as debtor. The debts and credits of the parcels on island basis should be equal to each other. Thus, it will be mathematically controlled.

2.2 Evaluating the road debt amounts as progress payment construction area and including them in equalisation

In land use right based land use applications, the value differences that occur according to the precedent values that change with the zoning plans are not sufficient for equalisation alone. As the precedents may differ in zoning islands, the frontage lengths and frontage road widths of the zoning parcels formed after the arrangement may also differ. A more equitable distribution will be ensured with the approach of mathematically evaluating the road debt as the progress payment construction area according to the method based on the development right and including it in the equalisation. Thus, it can be realised that the right holders gain the same value.

The inclusion of the road debt amounts in the equalisation is achieved by using the generated Equation (19).

$$YBD = (Y_b \cdot E) \cdot M \quad (19)$$

YBD = Road debt equalisation
Y_b = Amount of road debt
E = Precedent
M = Construction cost

For the construction cost (M); the value determined for 2019 based on the Building Approximate Unit Costs schedule used in the calculation of the compensation fee based on the development right was taken into consideration.

With the Equation (19), the road debt amounts of the zoning parcels in the regulation area are evaluated together with the right of way construction area and included in the equalisation

2.3 Area Based Distribution of the Regulation Area

In the area determined as the study area, DOP calculation should be made after the regulation limit is passed according to the AD regulation.

3 Results and Conclusions

The distribution method based on area, which is one of the methods for the comprehensive reflection of zoning plans on the land, is constantly criticised due to legal and technical problems. Because, due to the nature of this application, the parcel values before and after the regulation are not taken into consideration. In addition, the DOP deductions made from the cadastral parcels subject to the regulation in proportion to their area are not parallel to the increase in value after the implementation. Although this situation leads to value differences, it does not change the value of the parcels within the regulation boundary at the same rate. Considering the location and characteristics of the parcels, the value parameters affecting the parcel values before and after the implementation should be determined and evaluated according to objective methods.

In value-based AD applications, it is desired that the values of the parcels entering the regulation should be parallel to their values after the regulation. The increase in value should be a gain for the public. For a proposal approach that will be accepted by the practitioners and the society, each parameter should be evaluated. The proposal method provides the rule of allocating parcels from the same or close to the same place as in the existing AD applications. In addition, the construction areas of the parcels before the regulation and the construction areas of the parcels after the regulation are equalised and the increase in value gained with the zoning plan is provided to the public.

The value differences arising from the frontage lengths of the zoning parcels formed after the arrangement and the width of the road frontage, which are considered as a deficiency of the application method based on the zoning right, have been included in the application. In practice, the value expressed as road debt is found on parcel basis. The road debt amounts are evaluated as progress payment construction area and included in equalisation.

Before the implementation of value-based AD in Türkiye, a valuation system is needed in order to produce the parameters affecting the value fairly and objectively. Academicians, practitioners and legislators should act in coordination on a good valuation system and value-based AD application method and meet the need for regulation clearly. Effective utilisation of technology and computer software will accelerate the transition process. In particular, value maps to be created with the effective use of Geographical Information Systems within the Land Registry and Cadastre Directorates should be made available to practitioners through databases.

It should be ensured that the interview stage in land consolidation applications is also carried out with value-based AD, and the opinions of the owners in the area where the implementation decision is taken should be taken into consideration. In this way, objections to the courts will be reduced and the judicial burden will be lightened.

Before the implementation of value-based AD in Türkiye, a valuation system is needed in order to produce the parameters affecting the value fairly and objectively. Academicians, practitioners and legislators should act in a coordinated manner and clearly meet the need for regulation regarding a good valuation system and value-based AD application method. Effective utilisation of technology and computer software will accelerate the transition process. In particular, value maps to be created with the effective use of Geographical Information Systems within the Land Registry and Cadastre Directorates should be made available to practitioners through databases.

It should be ensured that the interview stage in land consolidation applications is also carried out with value-based AD, and the opinions of the owners in the area where the implementation decision is taken should be taken into consideration. In this way, objections to the courts will be reduced and the judicial burden will be lightened.

In value-based AD applications, the creation and use of advanced software where the distribution can be calculated and made easily and quickly according to the parameters and weight ratios affecting the immovable value will make a great contribution to the transition process.

Training should be provided to the students studying Surveying Engineering at universities, especially to the practitioners, and the technical and legal infrastructure should be established by academicians.

Existing implementation proposals should be revised by stakeholders and an implementation method that will be accepted by both implementers and right holders should be established.

References

Çağdaş, V. (2019). İmar Hakkı Esasına Dayalı Arazi ve Arsa Düzenlemesi Modeli, Harita Dergisi, 161, 57-66.

Ertunç, E., & Uyan, M. (2022). Land valuation with Best Worst Method in land consolidation projects. Land Use Policy, 122, 106360.

Koçoğlu, M. (2019). Değer Esasli Arsa Düzenlemesi Modeli ve Ülkemizde Uygulanabilirliği, YL Tezi, Konya Teknik Üniversitesi, Konya

Ertaş, M., & Uşak, B, (2020). İmar Planlarında Farklı Yoğunlukların Taşınmaz Birim Değerine Etkisi, Türkiye Arazi Yönetimi, 2(2), 48-55

Yalpır, Ş. (2007). Bulanık Mantık Metodolojisi ile Taşınmaz Değerleme Modelinin Geliştirilmesi ve Uygulaması: Konya Örneği, Selçuk Üniversitesi, Fen Bilimleri Enstitüsü, Doktora Tezi, 245s, Konya.

Yıldız, F., Özkan, G., Yalpır, Ş., Yıldırım, H., Gökmen, A., & Öztaş, M. (2008). Alan Düzenleme Esaslarının Belirlenmesinde Değer Eşitliğini Esas Alan Modellerin Uygulanması Üzerine Bir Araştırma, Jeodezi, Jeoinformasyon ve Arazi Yönetimi Dergisi, 99, 5-14.

Yıldız, N. (1977). Arsa Düzenlemesi, Yıldız Teknik Üniversitesi, Profesörlük Takdim Tezi, 62s, İstanbul.

3194 Sayılı İmar Kanunu, R.G.: 18749/ 09.05.1985. www.mevzuat.gov.tr

6th Intercontinental Geoinformation Days

igd.mersin.edu.tr

Geospatial technologies for early warning and assessment of climate change impacts on wheat yields in Azerbaijan

Sona Guliyeva[*1,2]

[1]*Space Agency of the Republic of Azerbaijan (Azercosmos), GIS center, Baku, Azerbaijan,*
[2]*National Aviation Academy, Aerospace Faculty, Aerospace Monitoring of Environment Department, Baku, Azerbaijan*

Keywords
Global warming
Agriculture
Climate change
Earth Observation
Crop yield

Abstract

Global warming presents significant challenges to global agriculture, with notable implications for the Republic of Azerbaijan's economy and food security. This paper focuses on the use of Earth Observation data and geoinformation systems to provide early warning detection of climate-related risks to crop growth and yields. By analyzing satellite imagery and automated calculation of vegetation indices, the study models the relationship between climate effects and crop yield. Initial assessments using satellite images revealed that over 15% of Azerbaijani territory was affected by drought in 2021, making it the most drought-affected year in the past two decades. Test fields were selected based on this data, considering different adaptation capabilities to changing environmental conditions, focusing on the main crop type, wheat. Comparative analyses were conducted to assess crop growth and predict yields under various climate change scenarios. By developing maps and collecting statistical data, the study uncovered the dynamics of crop condition changes and forecasted yields during growing seasons. The research also tested a model for assessing climate change effects on crop yields. The findings of this study provide a valuable foundation for the efficient planning of climate adaptation and mitigation strategies in agriculture.

1. Introduction

Today, in the face of increased climate change impacts, early-warning and assessment systems play a crucial role in helping decision-makers anticipate agricultural needs, identify yield gaps, and comprehend the response of crops to local climatic conditions, especially for wheat. Earth observation (EO) data, specifically satellite-based remote sensing, have proven to be effective and scalable tools for monitoring crop growth and estimating yields (Majorova V.I, 2013).

The significance of this study lies in its contribution to the development of methodological support for early warning and assessment of climate change impacts on crop yields, as well as the formulation of mitigation plans. It aligns with national-level initiatives and the global sustainable development goals (SDGs). The primary objective is to explore the potential of remote sensing data and geoinformation technologies to develop dynamic decision support systems for wheat production in Azerbaijan, integrating satellite-based drought assessment with available climate data. Specifically, the study aims to develop an empirical model capable of predicting crop yields at the beginning of the growing season under climate change effects.

To achieve this goal, the study sets the following objectives: (1) assessing agricultural drought at the national level, (2) local monitoring of agricultural lands throughout the growing season, (3) testing a crop model for rainfed areas focusing on wheat cultivation.

2. Material and methods

2.1. Study area

The climatic conditions in Azerbaijan are diverse and unique, with over half of the territory covered by mountains and the remaining portion consisting of plains, lowlands, intermountain hollows, valleys, and volcanic highlands formed over geological periods. Wheat cultivation occurs in both irrigated and non-irrigated lands, with the duration from planting to full maturity varying from 228 days in the plains to 305 days in mountainous regions. Rainfed agriculture is predominantly practiced in mountainous regions and foothills, characterized by low productivity and agricultural communities that often face poverty. Harsh conditions often lead to migration and abandonment of land, with subsistence sustained through the cultivation of drought-resistant crops.

* **Sona Guliyeva**

*(sguliyeva@naa.edu.az) ORCID ID 0000-0002-3833-3738

Cite this study

Guliyeva S. (2023). Geospatial technologies for early warning and assessment of climate change impacts on wheat yields in Azerbaijan. Intercontinental Geoinformation Days (IGD), 6, 415-419, Baku, Azerbaijan

For this research, two test fields were selected, one on irrigated land and the other on non-irrigated land, focusing on the main crop type, wheat. These fields were chosen due to their different adaptation capabilities to changing environmental conditions. The locations of these test fields are depicted in the map below (Figure 1).

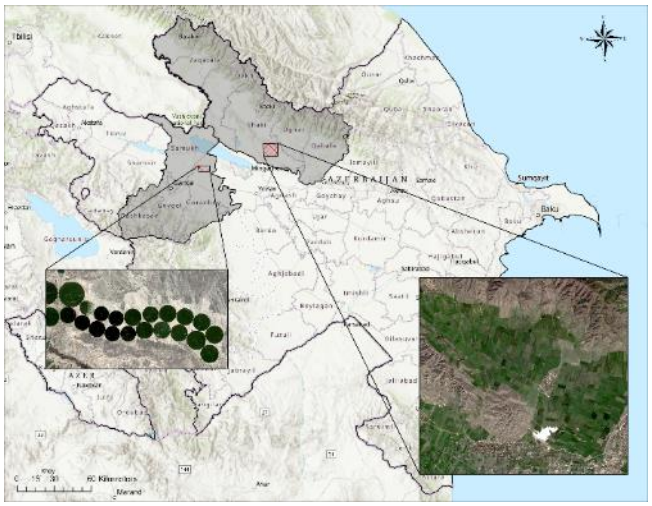

Figure 1. Location of Selected Test Fields

Two test fields were selected for this study, both primarily dedicated to cereal crops, specifically wheat. The first test field is an irrigated area located in the Ganja-Dashkasan economic region, while the second test field is a non-irrigated area in the Sheki-Zagatala region.

2.2. Dataset

Remote sensing plays a crucial role in agricultural drought assessment, providing valuable data on Earth's surface processes through various satellite missions worldwide (Liu, X., 2016). In this study, remote sensing data from two EO satellites, Aqua and Azersky, were utilized for national and local monitoring. Open-source data from the Aqua satellite's MODIS sensor were employed to determine the drought levels across the entire country. The assessment of long-term agricultural drought for the entire country relied on 21-year data from MODIS, employing the Vegetation Condition Index (VCI) developed by Kogan (Kogan F., 1995) and following the recommended practices by the UN-SPIDER (UN-SPIDER, 2017).

Based on the findings from the national assessment, specific test fields were selected. Recognizing the significance of spatial resolution in local monitoring, high-resolution imagery from the Azersky satellite was utilized in this study. Images taken from Azersky satellite images have been shown in figure 2.

Figure 2. Azersky satellite images, 15 April 2021

For this research, all available archive datasets of Azersky images were examined to analyze the phenological regime of the main study area. Data from the period of April to June, specifically from 2018 to 2021, were selected for analysis.

Wheat is a versatile crop that can thrive in various climates, with heat being a key factor for its growth. Temperature data plays a crucial role in providing essential climate information for studying its influence. Additionally, the research examined climate change scenarios proposed by the IPCC to understand the impact of climatic factors. To ensure accurate and reliable data, Climate Hazards Group InfraRed Precipitation with Station data (CHIRPS) was utilized, which has demonstrated a high accuracy rate of up to 90% in previous studies. Specifically, precipitation data during the wheat growing period were analyzed in this research. CHIRPS precipitation data, a combination of satellite estimates and ground-based rainfall data from weather stations, provides accurate and reliable information on precipitation. These data have been available since 1981, ensuring a comprehensive analysis of rainfall patterns (Funk, C. C. et al, 2014).

Ground data for this research were collected through collaboration with the research center and a survey conducted among farmers in the main test field selected. Figure 3 displays an image of the wheat crop taken from the field site.

Figure 3. Sheki Region Wheat Crop, 25 March 2022

To simulate the model, field data collected from land surveys were utilized, including crop types and corresponding coordinates. The field coordinates and crop types were recorded using a GPS E-Trex 10 device.

2.3. Methodology

The research methodology, as depicted in Figure 4, utilizes a modified crop model that combines drought-based indices using satellite imagery.

In the initial stage, the assessment of agricultural drought was conducted at a national level, covering the entire territory of the country. Satellite data from the Aqua satellite, based on international experience and recommended practices by UN-Spider, were employed for long-term agricultural drought monitoring over a period of 21 years.

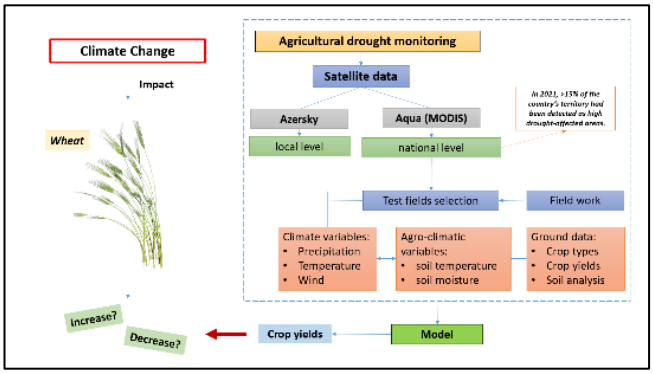

Figure 4. Methodological scheme

The results of the first stage revealed that more than 15% of the country's land is affected by severe drought conditions. These findings facilitated the identification of areas prone to extreme drought through national monitoring. Additionally, a survey was conducted among farmers and residents in the study area to gather local insights on agricultural drought and to test the Aquacrop model (Vanuytrecht, et al, 2014). The aim was to assess the impact of climate change on the yield of wheat cultivated in this specific area.

3. Results and Discussion

Initially, the VCI was tested in the first study area, yielding positive results. Subsequently, the obtained accuracy was applied to the entire country. The overall trend indicates an increased prevalence of drought compared to the 5-year period. However, there may be exceptions in specific months. For instance, in October 2020 (autumn), drought was observed in fewer territories compared to 2015, while dry areas expanded in other observed months. Notably, a significant difference was observed in April 2020 (spring) compared to previous periods.

In 2020, agricultural lands in the Ganja-Dashkasan region experienced a significant prevalence of drought, covering approximately 42% of the territory. To compare and validate the results, CHIRPS precipitation data was utilized. The analysis revealed an inverse relationship between the extent of drought and the amount of precipitation. Specifically, lower-than-average rainfall in March and early April led to a peak in drought during those months. Conversely, increased precipitation in May resulted in a decrease in drought levels, reaching a minimum during that month.

The experiments involved automated processing of a substantial amount of data using the Jupyter Notebook web-based computing platform. By comparing all the obtained results, it was determined that 2021 exhibited the highest drought severity compared to previous years. Figure 5 illustrates the spatial distribution of drought levels across the country in 2021.

Based on the classification of the obtained results, the study identified five levels of drought severity: no drought, light, medium, severe, and extreme. The analysis revealed that the extreme level of drought, represented by the color red on the map, covers an area of 13,809.1 km^2, accounting for 15.53% of the country's total territory.

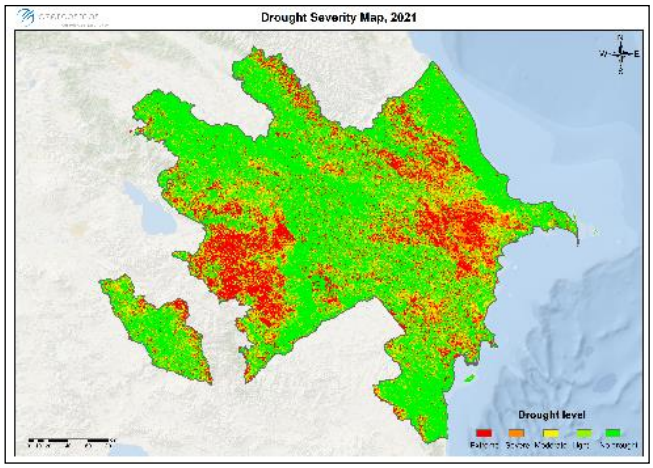

Figure 5. Drought Severity Map in Azerbaijan, 2021

The widely-used Normalized Difference Vegetation Index (NDVI) was computed. Additionally, the Chlorophyll Index (CI) was used to estimate the total amount of chlorophyll in plants. CI plays a crucial role in modern agriculture, providing valuable insights into crop development and aiding decision-making for food producers. CI values were computed for both test fields using Azersky satellite images taken on April 15, 2021. The resulting Chlorophyll concentration maps are depicted in Figure 6.

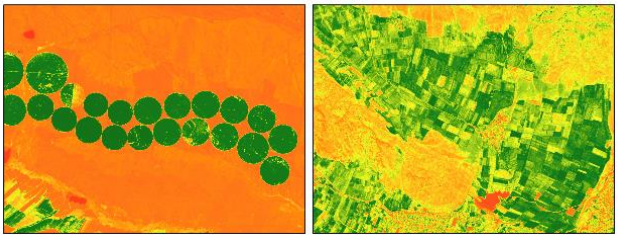

Figure 6. Chlorophyll concentration maps, 15 April 2021

In the chlorophyll concentration maps, green indicates high levels of chlorophyll during active vegetation growth, yellow represents average levels, and red represents low levels. The maps highlight the differences between irrigated and non-irrigated fields, with irrigated fields displaying a pronounced green color indicating high chlorophyll content. The chlorophyll content also varies within different crop parcels in the non-irrigated test area.

To monitor the crops, three images representing the 2022 growing season were processed on April 3rd, May 19th, and May 30th. These dates were selected for their minimal cloud cover. Figure 7 depicts the graphical representation of NDVI dynamics within three selected crop parcels. During the 2022 growing season, NDVI dynamics reflect the growth and biomass changes of crops. NDVI shows an increase at the beginning of the season, a plateau during flowering, and a decrease as the grain ripens.

The graph reveals a significant decline in NDVI from April 30 to May 19, indicating water scarcity due to drought in the region. Among the three index maps obtained, the highest vegetation level was observed in April 2022.

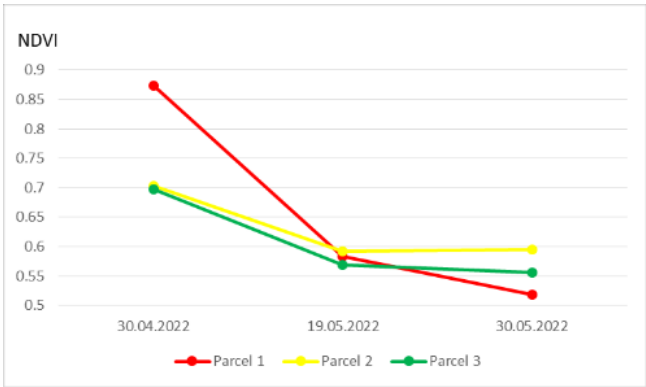

Figure 7. NDVI dynamics, growing season 2022

To assess temporal changes, images from 2018 were processed and compared with images from the same period in May, when vegetation is in the developmental and flowering stage. The vegetation index was calculated using Azersky images, as shown in Figure 8.

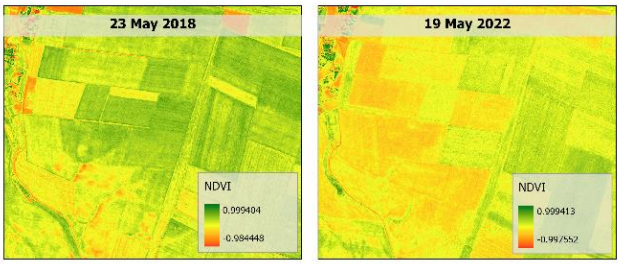

Figure 8. NDVI maps, May 2018 and 2022

The map highlights that vegetation development in May 2018 was superior to 2022, suggesting changes over the five-year period. However, it is important to acknowledge that these changes may be influenced by various natural factors not considered in this study. Comprehensive research combining remote sensing with ground-based work and long-term measurements is necessary for a more comprehensive understanding.

The third objective of this study was to evaluate the AquaCrop model's performance in simulating winter wheat growth under water deficit conditions in a rainfed test area. The model incorporates features such as canopy cover simulation, wheat growth simulation, and estimation. The AquaCrop model will be used to assess the impact of climate change on crop productivity through various scenarios.

The graph presented in Figure 9 reflects the crop's state on March 29th, showing normal development with a biomass of 4.716 t/ha. The absence of dry output indicates no water stress. It is important to note that the meteorological data used in the model came from a nearby meteorological station in Sheki city.

However, it is crucial to validate and refine the model results by incorporating accurate field-specific data, such as soil characteristics, temperature, precipitation, and evapotranspiration. Obtaining precise data has been challenging due to the lack of coordinated and parcel-specific information provided by farmers. To effectively utilize soil analysis information in GIS, it is necessary to plan fieldwork in the areas of interest over recent years.

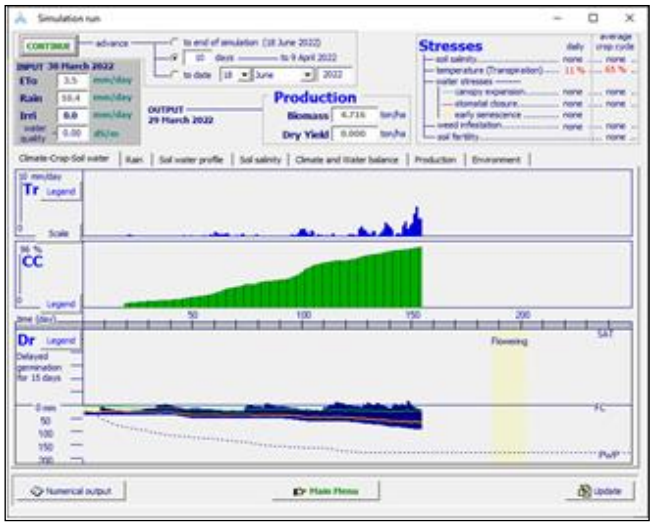

Figure 9. Simulation Results of AquaCrop Model for Winter Wheat in 2022

4. Conclusion and Future Work

In the context of this scientific study, the following key findings have been obtained: (1) assessment of agricultural drought at the national level helped identify and quantify the areas affected by drought in the previous year; (2) monitoring of agricultural fields using vegetation indices revealed a strong correlation between NDVI and CI values and crop productivity in the selected parcels; (3) testing of the crop model for wheat production provided insights into the impact of climate change on crop yields, highlighting the importance of temperature and precipitation variations.

The research results have significant implications for understanding the potential effects of climate change on crop yields. They provide valuable knowledge for stakeholders and planners to develop appropriate strategies and plans to mitigate the impacts of climate change on agriculture.

Future research will focus on modifying and validating crop models to forecast crop yields more accurately. The development of a refined crop model will enable the tracking of changes in crop yields under different climate change scenarios. This information will be instrumental in implementing effective agricultural management systems and guiding land use and ecosystem management strategies.

Overall, the study highlights the role of geoinformation technologies in assessing and monitoring agricultural fields, including the impacts of climate change such as agricultural drought. The findings contribute to the understanding of ecological balance and provide a foundation for informed decision-making in agriculture and land management.

Acknowledgement

Special acknowledgments go to Mr. Elchin Hasanov from Sheki Regional Center of Agrarian Services Agency, Ministry of Agriculture of the Republic of Azerbaijan, for his continuous support and provision of necessary ground data for this research. Significant thanks to various international programs and open-source data platforms that greatly contribute to scientific

advancements worldwide, notably NASA for Aqua data, ESRI for free training and software, UN General Assembly (UN-SPIDER), and the University of California, Santa Barbara for CHIRPS data.

References

Funk, C. C., Peterson, P. J., Landsfeld, M. F., Pedreros, D. H., Verdin, J. P., Rowland, J. D., ... & Verdin, A. P. (2014). A quasi-global precipitation time series for drought monitoring. US Geological Survey data series, 832(4), 1-12.

Kogan F., «Application of vegetation index and brightness temperature for drought detection» Advances in Space Research, 15(11), 100, 1995.

Liu, X., Zhu, X., Pan, Y., Li, S., Liu, Y., & Ma, Y. (2016). Agricultural drought monitoring: Progress, challenges, and prospects. Journal of Geographical Sciences, 26, 750-767. https://doi.org/10.1007/s11442-016-1297-9

Majorova, V. I. (2013). Kontrol' sostojanija sel'skohozjajstvennyh polej na osnove prognozirovanija dinamiki indeksa NDVI po dannym kosmicheskoj mul'tispektral'noj i giperspektral'noj s'jomki / V.I. Majorova, A.M. Bannikov, D.A. Grishko [i dr.] // Nauka i obrazovanie: jelektronnoe nauchno-tehnicheskoe izdanie, 199–228.

UN-SPIDER. (2017). Recommended Practice: Drought Monitoring Using the Vegetation Condition Index (VCI). Accessed, 10, 9206.

Vanuytrecht, E., Raes, D., Steduto, P., Hsiao, T. C., Fereres, E., Heng, L. K., ... & Moreno, P. M. (2014). AquaCrop: FAO's crop water productivity and yield response model. Environmental Modelling & Software, 62, 351-360.

6th Intercontinental Geoinformation Days

igd.mersin.edu.tr

Investigation of drought-threatened areas through different drought indexes: A case study in Mersin, Türkiye

Mehmet Özgür Çelik*[1], Murat Yakar[1]

[1]*Mersin University, Engineering Faculty, Geomatics Engineering Department, Mersin, Türkiye*

Keywords
Drought
PDSI
PHDI
SPI
SPEI

Abstract

Global climate change is having a growing impact all around the world. Drought is one of the most destructive effects of global climate change in the Mediterranean basin. The study area is Mersin, which is located in southern Türkiye and is threatened by drought. Therefore, a drought analysis of the research area was conducted. Palmer Drought Severity Index (PDSI), Palmer Hydrological Drought Index (PHDI), Standardized Precipitation Index (SPI), and Standardized Precipitation-Evapotranspiration Index (SPEI) were chosen as drought indices that employ climatic data. The indices were calculated, and graphs were created. As a result, it was concluded that Mersin is at risk of drought.

1. Introduction

The harmful effects of global climate change are becoming more widespread and directly endanger the lives of all living beings. The world has currently warmed by 1.1°, while the agreed climate limit is 1.5° (Öztürk & Gürsoy, 2022). If the current trend continues, global warming will increase, and the adverse impacts of climate change on the world will gradually worsen. Natural disasters including floods, wildfires, and droughts will become increasingly common (Demir et al., 2021). At this point, these disasters will strike different regions based on their meteorological and geographical characteristics. Drought will be one of the most significant effects of climate change in Mediterranean basin regions (Hadri et al., 2021). This basin is currently becoming dry in some areas (İban, 2022).

Drought is a natural disaster that has a long-term detrimental impact with far-reaching implications. Drought is classified as meteorological, agricultural, and hydrological (Hobbins et al. 2008). A meteorological drought is defined as a drought that lasts months or years as a result of below-normal precipitation (Palmer, 1965). Agricultural drought is described as periods of below-average precipitation, substantial but infrequent precipitation, or higher-than-normal evaporation (Liu et al., 2016). In contrast, hydrological drought is defined as periods when stream flow and water storage fall below the long-term average level (Van Loon, 2015). Drought's harmful consequences must be identified, eliminated, or minimized (Alahacoon & Edirisinghe, 2022).

The study area, Mersin, is threatened by drought because of its location in the Mediterranean basin. At this point, it is critical to do a drought analysis. The Palmer Drought Severity Index (PDSI), Palmer Hydrological Drought Index (PHDI), Standardized Precipitation Index (SPI), and Standardized Precipitation-Evapotranspiration Index (SPEI) are standard drought indices that use climatic data (temperature and precipitation) during this time. These indices were utilized in this study to analyze Mersin's drought.

2. Study Area

Mersin province is the study area (Figure 1). Drought is a hazard in the region, which has a Mediterranean climate and is located in the Mediterranean basin. According to data from the General Directorate of Meteorology (MGM), Mersin has experienced severe drought in recent years (MGM, 2023). It was chosen as the study area for the investigation of the growing impact of drought.

* **Corresponding Author**

*(mozgurcelik33@gmail.com) ORCID ID 0000-0003-4569-888X
(myakar@mersin.edu.tr) ORCID ID 0000-0002-2664-6251

Cite this study

Çelik, M. Ö., & Yakar, M. (2023). Investigation of Drought-Threatened Areas through Different Drought Indexes: A Case Study in Mersin, Türkiye. Intercontinental Geoinformation Days (IGD), 6, 420-423, Baku, Azerbaijan.

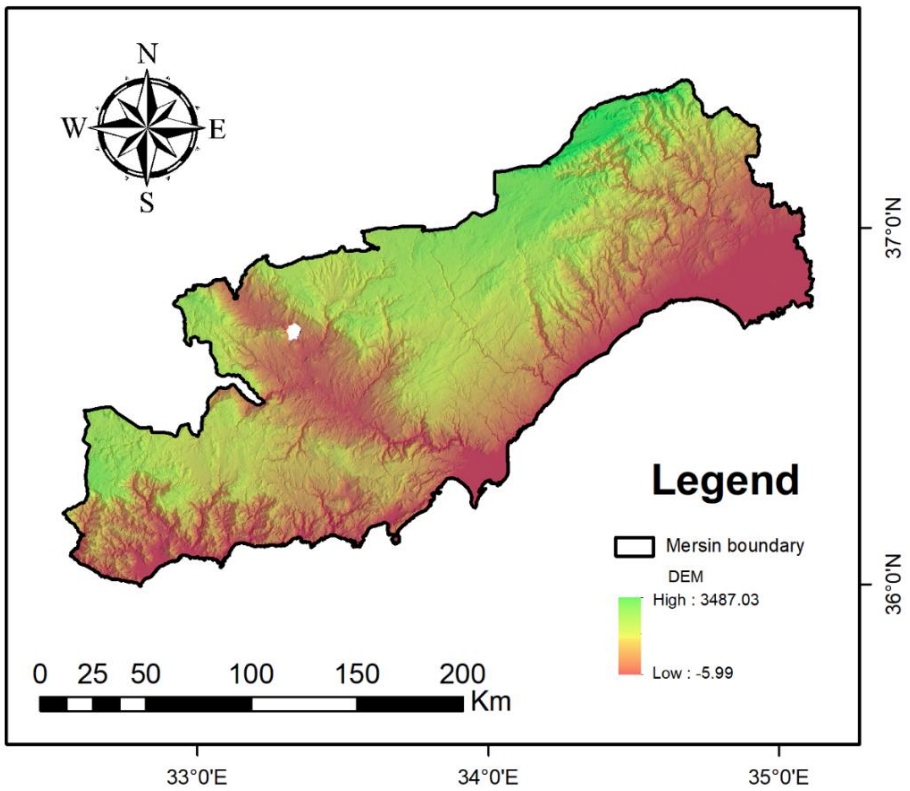

Figure 1. Study area

3. Material and Method

Drought analysis was performed using the PDSI, PHDI, SPI, and SPEI indices. A three-stage procedure was used for this. First, fundamental climate data, including maximum and minimum temperatures and precipitation, were gathered from the NASA Prediction Of Worldwide Energy Resources (POWER) website (NASA POWER, 2023). According to the World Meteorological Organization (WMO), at least 30 years of data should be available to generate drought indices and perform analysis (European Comission, 2013). Working with data over extended time periods improves accuracy. In this direction, 42 years of data from the research area's 1981-2023 time period were used for calculations. Second, after arranging the data, the PDSI, PHDI, SPI, and SPEI indices were calculated in R Studio. This application offers an environment for R, a computer language that permits statistical calculations and graphic creation. Finally, graphs for the calculated indices were constructed.

3.1. Palmer drought severity index (PDSI)

Temperature and precipitation data are used to calculate PDSI (Ramirez, 2023). Furthermore, drought analysis is carried out with the potential evapotranspiration (PET) parameter. PDSI was estimated in the study using PET data from Mersin province based on temperature, precipitation, and maximum and minimum temperature differences. PDSI values are classified into specified classes. As a result, scores range from -10 (dry) to +10 (wet), with values below -4 representing extreme drought and values over +4 representing extreme wet.

3.2. Palmer hydrological drought index (PHDI)

PHDI is a derivative of PDSI that was designed to study water storage, stream flow, and hydrological drought. Temperature and precipitation data are employed in its calculation, much like in PDSI.

3.3. Standardized precipitation index (SPI)

The standardized precipitation anomaly is generated using precipitation data from regions with varying climatic conditions, and SPI values are computed. Thus, drought analysis is carried out. SPI values are classified into standard classes. Extreme drought is represented by -2 and above, whereas extreme wetness is represented by +2 and above.

3.4. Standardized precipitation-evapotranspiration index (SPEI)

SPEI is a more advanced variant of SPI that employs PET data computed from precipitation and temperature changes (NCAR, 2023). The SPEI compares evaporation to available water capacity. Precipitation and PET data are used for this, and SPEI is calculated during the specified period.

4. Results

Drought indices were developed for the years 1981-2023, and the graphs are shown in Figure 2-6. When the PDSI graph is analyzed, it is clear that drought has been more prevalent, particularly in recent years (2018, 2019, and 2020) (Figure 2). In addition, when PDSI values were examined over 42 years, it was discovered that the

maximum values did not approach the extreme wet value (+4 and above). Drought did, however, grow in five separate times, notably 1989-1991, 1996-1998, 2003-2006, and 2018-2020. These findings may be said to overlap with the region's geographical location and climate data.

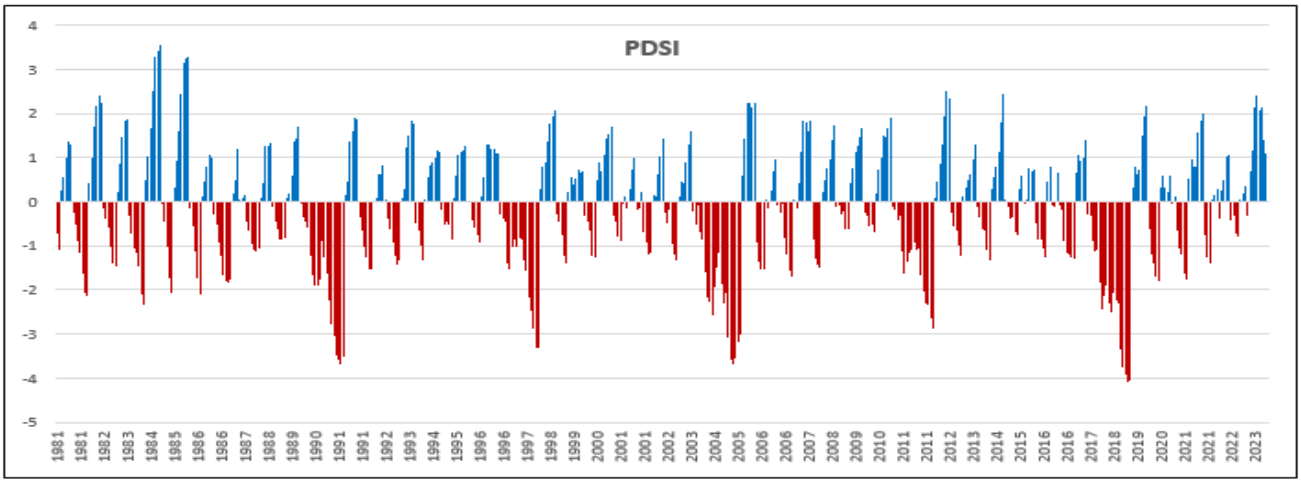

Figure 2. PDSI

Because PHDI is derived from PDSI, the values in the graph are similar (Figure 3). PHDI, on the other hand, gives reliable information regarding the research area's hydrological drought. This drought has been becoming worse in recent years (2018-2023). Indeed, the level of natural and artificial water resources decreased in the same period.

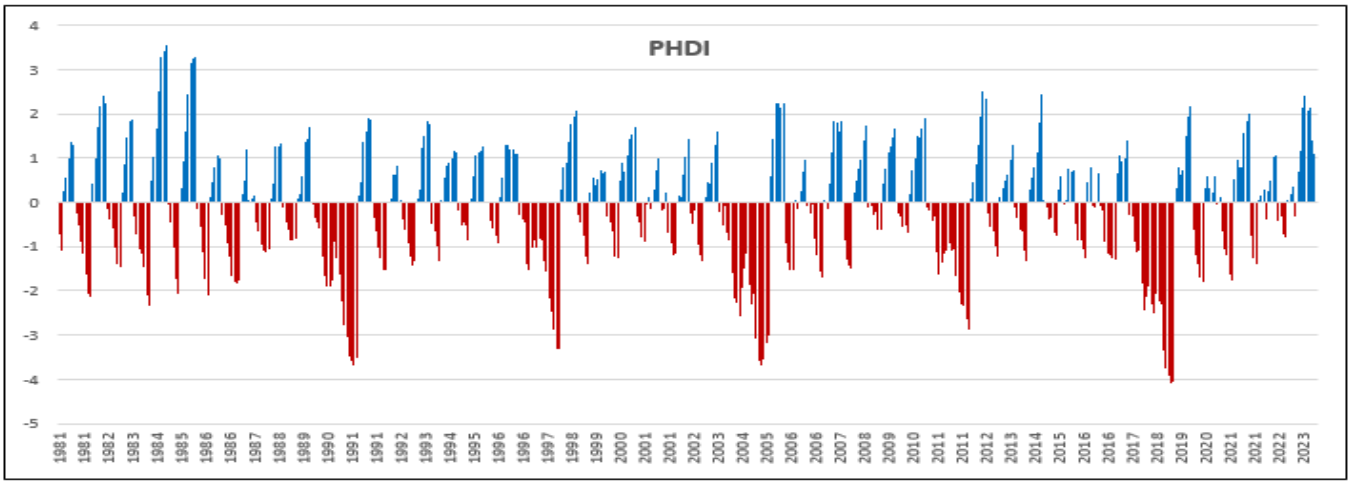

Figure 3. PHDI

The SPI graph (Figure 4) depicts value variations over 42 years. Similarly to the PDSI, the highest values did not exceed the excessive wet value (+2 and above), whereas the minimum values did (-2 and below).

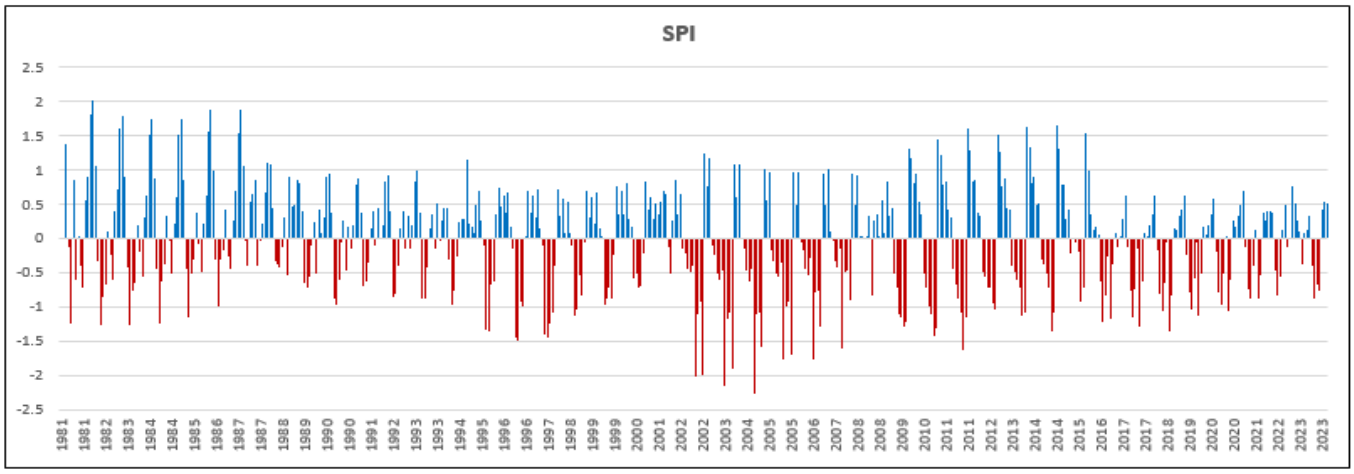

Figure 4. SPI

SPEI is a PET-based index that is a more advanced variant of SPI. As a result, looking at the SPEI values allows for more detailed analyses. In the last two years (2021, 2022) and today (2023), it is observed that drought has increased in the study area located in the Mediterranean basin with the effect of global warming (Figure 5).

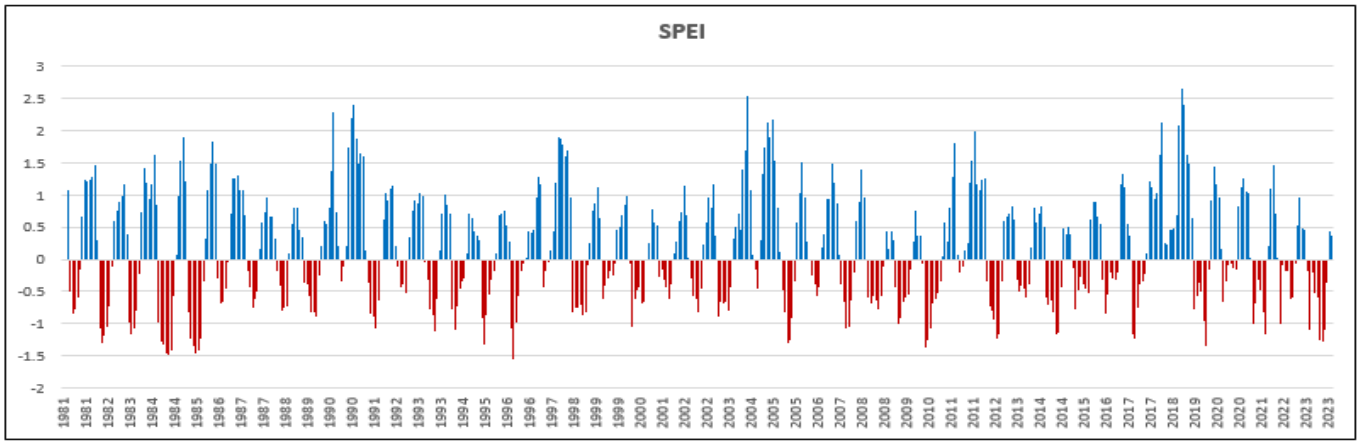

Figure 5. SPEI

5. Conclusion

Mersin, the study area, is vulnerable to the harmful consequences of global warming due to its location in the Mediterranean basin. Drought is one of these impacts. Furthermore, inappropriate land use and irresponsible land management practices contribute to global warming. All of these factors inspired the study that was completed. Four separate indices were calculated and graphs were made to analyze the drought. The obtained values were interpreted, and a drought analysis was carried out. The values obtained for sustainable land management and usage are expected to help decision-makers as a result of the implementation.

References

Alahacoon, N., & Edirisinghe, M. (2022). A comprehensive assessment of remote sensing and traditional based drought monitoring indices at global and regional scale. Geomatics, Natural Hazards and Risk, 13(1), 762-799. https://doi.org/10.1080/19475705.2022.2044394

Demir, V., Alptekin, A., Çelik, M. Ö., & Yakar, M. (2021). 2D Flood modeling with the help of GIS: Mersin/Lamas River. Intercontinental Geoinformation Days, 2, 175-178.

European Commission, (2023). Standardized Precipitation Index (SPI) [Retrieved 30.05.2023], https://edo.jrc.ec.europa.eu/documents/factsheets/factsheet_spi_ado.pdf

Hadri, A., Saidi, M. E. M., & Boudhar, A. (2021). Multiscale drought monitoring and comparison using remote sensing in a Mediterranean arid region: a case study from west-central Morocco. Arabian Journal of Geosciences, 14, 1-18. https://doi.org/10.1007/s12517-021-06493-w

Hobbins, M. T., Dai, A., Roderick, M. L., & Farquhar, G. D. (2008). Revisiting the parameterization of potential evaporation as a driver of long-term water balance trends. Geophysical Research Letters, 35(12). https://doi.org/10.1029/2008GL033840

İban, M. C. (2022). Monitoring Drought Severity in Mersin and Adana using MODIS Data and the VHI Index (MODIS Verileri ve VHI İndeksi ile Adana ve Mersin'de Kuraklık Şiddetinin İzlenmesi –in Turkish). 11. Türkiye Ulusal Fotogrametri ve Uzaktan Algılama Birliği (TUFUAB) Teknik Sempozyumu, 12-14 Mayıs 2022, Mersin, Türkiye, 16-19.

Liu, X., Zhu, X., Pan, Y., Li, S., Liu, Y., & Ma, Y. (2016). Agricultural drought monitoring: Progress, challenges, and prospects. Journal of Geographical Sciences, 26, 750-767. https://doi.org/10.1007/s11442-016-1297-9

MGM, (2023). General Directorate of Meteorology (MGM) drought analysis, [Retrieved 30.05.2023], https://www.mgm.gov.tr/veridegerlendirme/kuraklik-analizi.aspx?d=aylik&k=spi#sfB

NASA POWER, (2023). NASA Prediction of Worldwide Energy Resources (POWER), [Retrieved 30.05.2023], https://power.larc.nasa.gov/data-access-viewer/

NCAR, (2023). National Center for Atmospheric Research (NCAR), Standardized Precipitation Evapotranspiration Index (SPEI) [Retrieved 30.05.2023], https://climatedataguide.ucar.edu/climate-data/standardized-precipitation-evapotranspiration-index-spei

Öztürk, T., & Gürsoy, F. (2022). Geopolitical Impact of Global Climate Change on the Arctic Ocean. Akdeniz İİBF Journal, 22(1), 117–31. https://doi.org/10.25294/auiibfd.1053878

Palmer, W. C. (1965). Meteorological drought. US Department of Commerce, Weather Bureau.

Ramirez, S. G. (2023). Applied Machine Learning in Development of Geospatial Information Tools for Sustainable Groundwater Management. PhD thesis, Brigham Young University, USA.

Van Loon, A. F. (2015). Hydrological drought explained. Wiley Interdisciplinary Reviews: Water, 2(4), 359-392. https://doi.org/10.1002/wat2.1085

6th Intercontinental Geoinformation Days

igd.mersin.edu.tr

Analysis of land surface temperature distribution in response to land use land cover change in agroforestry dominated area, Gedeo Zone, Southern Ethiopia

Wendwesen Taddesse Sahile [*1], **Gashaw Kibret Goshem** [1], **Seid Ali Shifaw** [1], **Muh Rais Abidin** [2]

[1]*Dilla University, College of Agriculture, Department of Land Administration and Surveying, Dilla, Ethiopia*
[2]*Universitas Negeri, Makassar, Indonesia*

Keywords
Agroforestry
Gedeo Zone
Land Surface Temperature
Support Vector Machine

Abstract

Land Use Land Cover (LULC) changes have a significant impact on Land Surface Temperature (LST) by altering the surface properties and energy balance. The current study aimed to analyze the LST distribution due to LULC change over the agroforestry-dominated Gedeo Zone, Southern Ethiopia. Multi-temporal satellite images acquired by Landsat 5 TM, Landsat 7 ETM+, and Landsat 8 using OLI-TIRS sensors in 2005, 2011, and 2017, respectively, and a Sentinel 2A MSI in 2017 and 2022 were corrected for radiometric using and geometric errors and processed to classify LULC classes and extract LST. The study result revealed that the temperature varies through the surface according to LULC classes. It was identified that the Agroforestry and Built-up coverage has increased by 1520 and 2600 km^2, respectively, from 2005 to 2022. On the other hand, the Bare Land and Farm Land coverage decreased by 1554 and by 2565 km^2, respectively, in the same period. The LST result has shown that there has been a remarkable variation in the spatial pattern of the LST between 2005 and 2022. The average LST in Agroforestry, Bare Land, Farm Land, and Built-up area has progressively increased over the years, from 19.6, 26, 20.2, and 25.58 ^{0}C in 2005 to 25, 32.16, 28.23, and 30.62 ^{0}C in 2022, respectively. While in 2005 the maximum recorded LST did not exceed 37.3°C, by 2022 it had increased by close to 3°C, reaching 40.6°C. Even though the coverage of Agroforestry has increased in the last 17 years, the mean LST has increased. From the result, it was concluded that LST may not be dependent on the local LULC change only; other factors like urbanization and global warming could play a significant role in changing LST locally as well as globally. So, the results of this study are important

1. Introduction

Land Use Land Cover (LULC) changes can have a significant impact on Land Surface Temperature (LST) by altering the surface properties and energy balance(Govind & Ramesh, 2019; Tan, Yu, Li, Tan, & Zhou, 2020). Studies showed the conversion of forested areas to agricultural land results in a decrease in evapotranspiration and an increase in surface temperature due to reduced vegetation cover and increased soil exposure(Bounoua, DeFries, Collatz, Sellers, & Khan, 2002; Defries, Bounoua, & Collatz, 2002; Pramova, Locatelli, Djoudi, & Somorin, 2012).

Land surface temperature (LST) is a measure of the surface temperature of the Earth, and it is an important variable in climate modeling and environmental monitoring(Hulley et al., 2019). It is affected by various factors, including solar radiation, air temperature, humidity, wind speed, and surface properties such as albedo and emissivity(Hofierka, Gallay, Onačillová, & Hofierka Jr, 2020).

Even though several studies were conducted to observe the impact of LULC change on LST, the extent and direction of these changes remain poorly understood, and there is a need to investigate the impact of LULC on LST in the agroforestry-dominated Gedeo Zone.

2. Method

2.1. Study area

The study was conducted in the Gedeo zone Southern Nations Nationalities and Peoples (SNNP) region, Ethiopia. Geographically, the study area is located

* **Corresponding Author**

*(wendwesent@du.edu.et) ORCID ID xxxx – xxxx – xxxx – xxxx
(e-mail) ORCID ID xxxx – xxxx – xxxx – xxxx
(e-mail) ORCID ID xxxx – xxxx – xxxx – xxxx

Cite this study

Sahile, W. T., Goshem, G. K., Shifaw, S. E., & Abidin, M. R. (2023). Analysis of land surface temperature distribution in response to land use land cover change in agroforestry dominated area, Gedeo Zone, Southern Ethiopia. Intercontinental Geoinformation Days (IGD), 6, 424-427, Baku, Azerbaijan

from 5°53' N to 6°27' N latitude and from 38° 8' to 38° 30'E longitude. The altitude ranges from 1500 to 3000 m above mean sea level. The area experiences annual rainfall that ranges from 800 to 1800 mm and the mean annual temperature varies from 12.5°C to 25°C (Negash, Yirdaw, & Luukkanen, 2012).

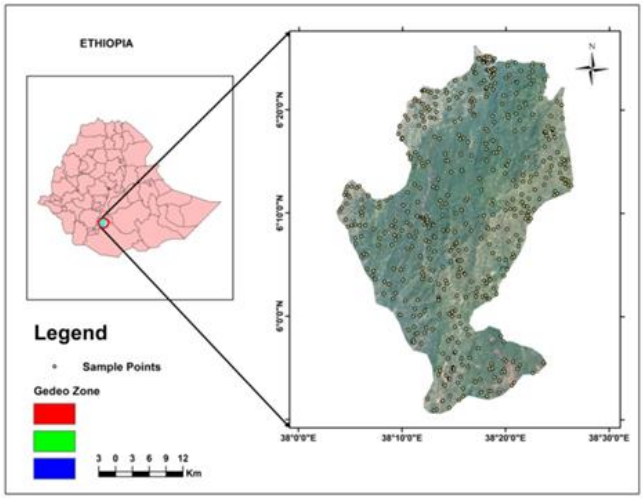

Figure 1. Study Area

5 images for the years 2005 and 2011 using a Support Vector Machine (SVM) classification algorithm. The SVM is a commonly used supervised machine learning algorithm that is widely used for classification techniques for image classification(Foody & Mathur, 2004).

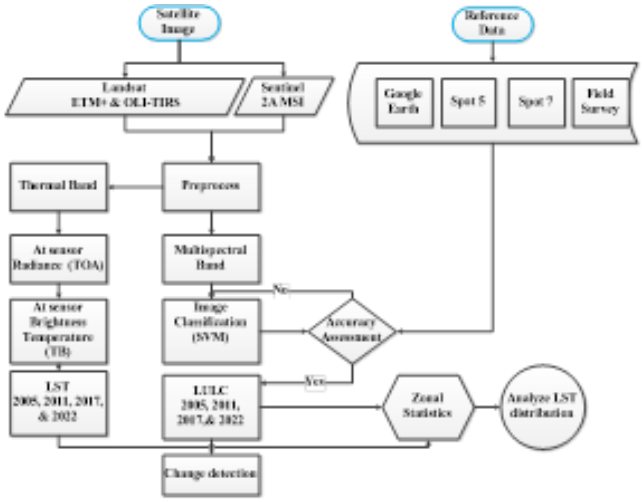

Figure 2. Methodology Flowchart

2.2. Data

Two years of Cloud-free Sentinel-2A MSI images were downloaded from European Space Agency (ESA) website for land use land cover classification in 2017 and 2022. Sentinel image has a 10 m spatial resolution relatively higher resolution than Landsat images. To address the study area extent, three scenes of sentinel images were mosaicked and subsetted to the study area extent. Additionally, four different years of Landsat imageries with a path/row 168/56 were downloaded from the USGS-EROS website (https://eros.usgs.gov/) for land cover classification and LST extraction. A 1.5 m and 5 m spatial resolution Spot images and Google Earth historical images were utilized for assessing the accuracy of classification for 2005, 2011, and 2017.

Table 1. Data and Data Source

Sensor Name	Acquisition Date	Spatial Resolution (m)	Source
ETM+	01/01/2005	30	USGS
"	01/01/2011	"	
OLI_TIRS	01/01/2017	"	"
"	01/01/2022	"	"
Sentinel 2A	01/01/2017	10	ESA
"	01/01/2022		
Spot 5	2005	5	GII
Spot 7	2017	1.5	"

2.3. LULC mapping and accuracy assessment

Before starting the classification, all stated satellite images' atmospheric errors were corrected by applying Dark Object Subtraction (DOS1) method under the preprocessing tool in Quantum GIS 3.10. The land cover maps for the years 2017 and 2022 were derived from 10 m reflective bands of Sentinel 2A and 30 m Landsat 7, and

3. Results

3.1. Spatio-temporal distribution of LULC in Gedeo Zone between 2005 and 202

We can observe that the area of Agroforestry has increased steadily from 104,071 km² in 2005 to 105,591 km² in 2022. On the other hand, the Bare-land area decreased from 6725.7 km² in 2005 to 4163.13 km² in 2011, but it slightly increased again to 5169.78 km² in 2022 indicating the efforts to reforest and restore degraded lands have been partially successful. The built-up area has consistently increased over the years, from 1092.6 km² in 2005 to 3693.87 km² in 2022. The area of Farmland has been decreasing over the years, from 36,515.7 km² in 2005 to 33,950.3 km² in 2022 at the expense of other LULC changes.

3.2. Spatio-temporal distribution of LST in Gedeo Zone between 2005 and 2022

The average LST in Agroforestry, Bare Land, Farm Land, and Built-up area has progressively increased over the years, from 19.6 ^{0}C, 26^{0}C, 20.23^{0}C, and 25.58^{0}C in 2005 to 25^{0}C, 32.16^{0}C, 28.23^{0}C and 30.62 in 2022, respectively. The overall result revealed that the average LST in ^{0}C has increased from 2005 to 2022.

The maximum change in mean LST was observed between 2005 and 2011. Accordingly, the mean LST abruptly increased by 3.53^{0}C, 3.96^{0}C, 4.27^{0}C, and 2.14^{0}C in Agroforestry, Bare Land, Farm Land, and Built-up, respectively. On the other hand, the minimum mean LST change was detected from 2011- 2017 and 2017- 2022. In the last 17 years, the mean LST increased even though the coverage area of agroforestry increased; a slight analogous relationship was detected between LST and agroforestry area coverage.

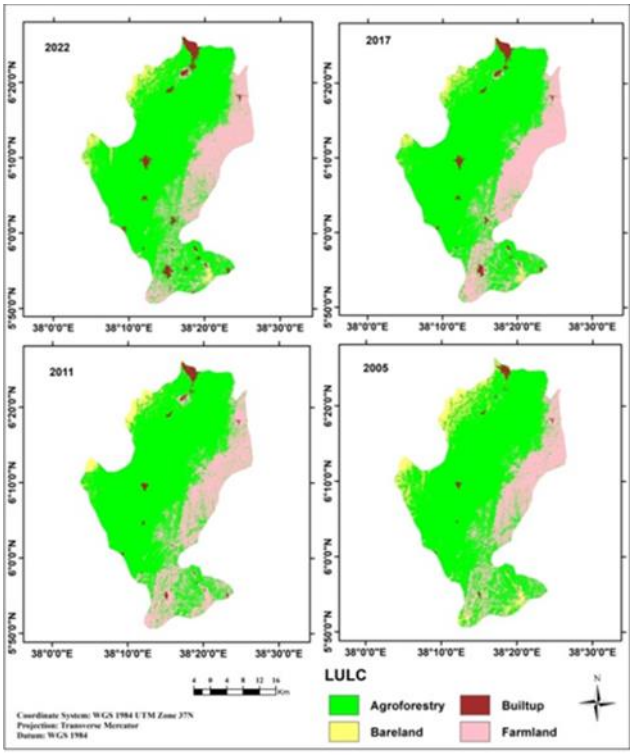

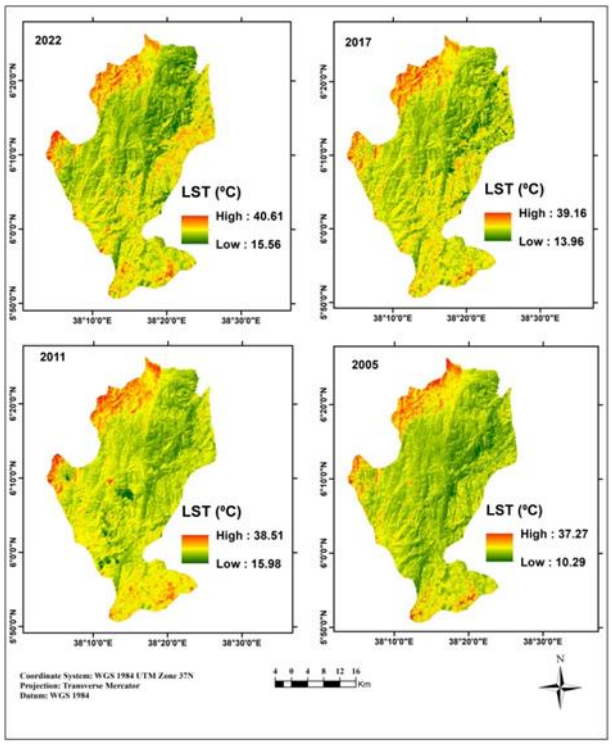

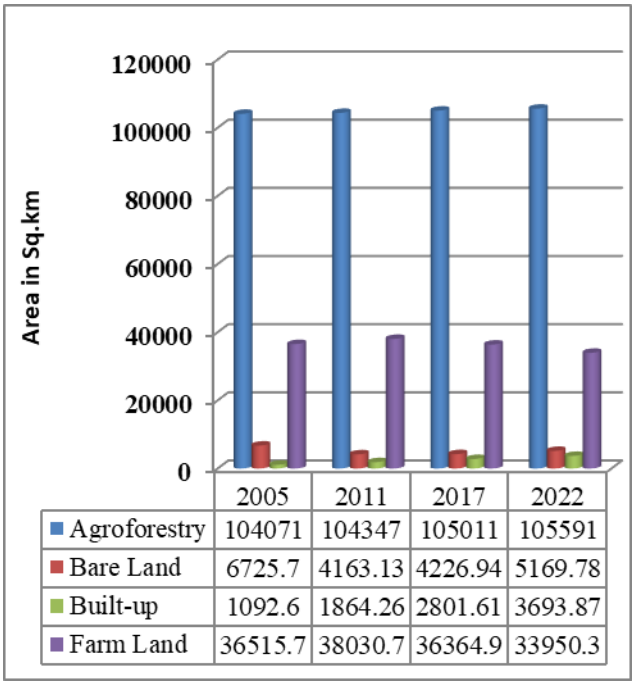

	2005	2011	2017	2022
Agroforestry	104071	104347	105011	105591
Bare Land	6725.7	4163.13	4226.94	5169.78
Built-up	1092.6	1864.26	2801.61	3693.87
Farm Land	36515.7	38030.7	36364.9	33950.3

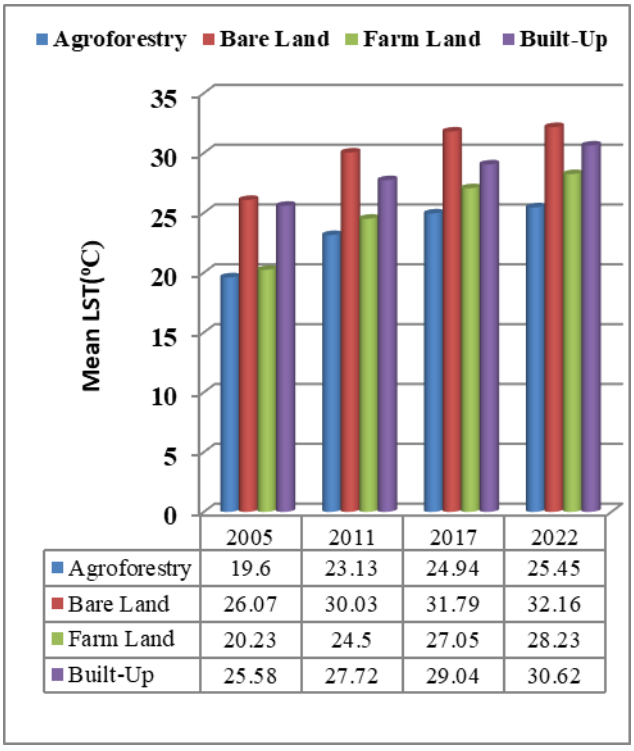

	2005	2011	2017	2022
Agroforestry	19.6	23.13	24.94	25.45
Bare Land	26.07	30.03	31.79	32.16
Farm Land	20.23	24.5	27.05	28.23
Built-Up	25.58	27.72	29.04	30.62

4. Discussion

An investigation of the dynamics of LULC across the Gedeo Zone revealed the increased need for land for urban expansion. Accordingly, the built-up area coverage has increased by 2601 km^2 from 2005 to 2022. Similar studies in Ethiopia revealed the need for land by the cities and towns due to urban expansion (Terfa, Chen, Liu, Zhang, & Niyogi, 2019). The coverage of Agroforestry has increased steadily by 1520 km^2 from 2005 to 2022. This indicates that agroforestry practices have been successful in maintaining and even expanding the forest cover while also providing for agricultural needs (Bishaw, 2001). This suggests that the Gedeo Zone is actively engaging in agroforestry practices to sustainably manage the land and maximize productivity(Shanka, 2022).

The overall analysis of the LST distribution result revealed that the mean LST in ^{0}C has increased from 2005 to 2022. This could be due to various factors such as urbanization, changing agricultural practices, and land degradation (Tsegaye, 2019; Wassie, 2020). Even though the area coverage of Agroforestry increased, the dynamics of other LULC and other factors like global warming could play a vital role in the rise of average LST. Other factors like urbanization and global warming could

play a significant role in changing LST locally as well as globally(Murray, Quam, & Wilder-Smith, 2013). Thus, the rise of LST may not be dependent on the local LULC change only.

The Northern areas including Dilla Town and its surrounding have experienced significant urbanization with a maximum recorded mean LST between 2002 and 2022. Understanding the impact of LULC on LST is important for identifying areas where agricultural productivity may be at risk(Parven et al., 2022). The Northwest and Southern parts of the study area; the area bounded by the West Guji zone has dominated by Bare Land and negatively influenced agricultural productivity(Kafy et al., 2021). These areas should be targeted for interventions such as irrigation and shade management. These interventions can help to mitigate the negative effects of high temperatures on agricultural productivity and ensure sustainable agricultural production in the region.

5. Conclusion

The overall dynamics of LULC in the study area indicated a gradual shift towards sustainable practices such as agroforestry, as well as urbanization and changes in agricultural practices. Policymakers need to monitor and manage these changes to ensure sustainable land use and minimize negative impacts on the environment and livelihoods. From the result of the study, the next conclusions were attained: The area coverage of the built-up area and bare land has increased rapidly while the coverage of agroforestry increased slightly from 2002 to 2022; leading to the rise of LST. The increased area coverage of agroforestry may not guarantee the cooling down of LST; other factors like urbanization and global warming could play a significant role in changing LST locally as well as globally.

Acknowledgement

I would like to express my gratitude to Co-authors Mr. Gashaw Kibret, Mr. Sied Ali, and Mr. M Muhammed Rais. Their contributions were critical to the success of this research.

References

Bishaw, B. (2001). Deforestation and land degradation in the Ethiopian highlands: a strategy for physical recovery. Northeast African Studies, 7-25.

Bounoua, L., DeFries, R., Collatz, G. J., Sellers, P., & Khan, H. (2002). Effects of land cover conversion on surface climate. Climatic Change, 52, 29-64.

Defries, R. S., Bounoua, L., & Collatz, G. J. (2002). Human modification of the landscape and surface climate in the next fifty years. Global Change Biology, 8(5), 438-458.

Foody, G. M., & Mathur, A. (2004). A relative evaluation of multiclass image classification by support vector machines. IEEE Transactions on geoscience and remote sensing, 42(6), 1335-1343.

Govind, N. R., & Ramesh, H. (2019). The impact of spatiotemporal patterns of land use land cover and land surface temperature on an urban cool island: a case study of Bengaluru. Environmental monitoring and assessment, 191, 1-20.

Hofierka, J., Gallay, M., Onačillová, K., & Hofierka Jr, J. (2020). Physically-based land surface temperature modeling in urban areas using a 3-D city model and multispectral satellite data. Urban Climate, 31, 100566.

Hulley, G. C., Ghent, D., Göttsche, F. M., Guillevic, P. C., Mildrexler, D. J., & Coll, C. (2019). Land surface temperature Taking the Temperature of the Earth (pp. 57-127): Elsevier.

Kafy, A.-A., Rahman, A. F., Al Rakib, A., Akter, K. S., Raikwar, V., Jahir, D. M. A., . . . Kona, M. A. (2021). Assessment and prediction of seasonal land surface temperature change using multi-temporal Landsat images and their impacts on agricultural yields in Rajshahi, Bangladesh. Environmental Challenges, 4, 100147.

Murray, N. E. A., Quam, M. B., & Wilder-Smith, A. (2013). Epidemiology of dengue: past, present and future prospects. Clinical epidemiology, 299-309.

Negash, M., Yirdaw, E., & Luukkanen, O. (2012). Potential of indigenous multistrata agroforests for maintaining native floristic diversity in the south-eastern Rift Valley escarpment, Ethiopia. Agroforestry Systems, 85(1), 9-28.

Parven, A., Pal, I., Witayangkurn, A., Pramanik, M., Nagai, M., Miyazaki, H., & Wuthisakkaroon, C. (2022). Impacts of disaster and land-use change on food security and adaptation: Evidence from the delta community in Bangladesh. International Journal of Disaster Risk Reduction, 78, 103119.

Pramova, E., Locatelli, B., Djoudi, H., & Somorin, O. A. (2012). Forests and trees for social adaptation to climate variability and change. Wiley Interdisciplinary Reviews: Climate Change, 3(6), 581-596.

Shanka, T. S. (2022). Characterizing to sustain the agrobiodiversity in the Gedeo Zone, Southern Ethiopia Natural Resources Conservation and Advances for Sustainability (pp. 581-612): Elsevier.

Tan, J., Yu, D., Li, Q., Tan, X., & Zhou, W. (2020). Spatial relationship between land-use/land-cover change and land surface temperature in the Dongting Lake area, China. Scientific reports, 10(1), 1-9.

Terfa, B. K., Chen, N., Liu, D., Zhang, X., & Niyogi, D. (2019). Urban expansion in Ethiopia from 1987 to 2017: Characteristics, spatial patterns, and driving forces. Sustainability, 11(10), 2973.

Tsegaye, B. (2019). Effect of land use and land cover changes on soil erosion in Ethiopia. International Journal of Agricultural Science and Food Technology, 5(1), 26-34.

Wassie, S. B. (2020). Natural resource degradation tendencies in Ethiopia: a review. Environmental Systems Research, 9, 1-29.

MERSİN UNİVERSİTY

Intercontinental Geoinformation Days

ISBN: 978-605-72800-4-6

https://igd.mersin.edu.tr/